SILICATE GLASSES AND MELTS

SECOND EDITION

Bjorn Mysen

Pascal Richet

ELSEVIER

SILICATE GLASSES AND MELTS

SILICATE GLASSES AND MELTS

SECOND EDITION

Bjorn Mysen
Pascal Richet

ELSEVIER

Elsevier
Radarweg 29, PO Box 211, 1000 AE Amsterdam, Netherlands
The Boulevard, Langford Lane, Kidlington, Oxford OX5 1GB, United Kingdom
50 Hampshire Street, 5th Floor, Cambridge, MA 02139, United States

© 2019 Elsevier B.V. All rights reserved.

Cover photo (courtesy N. Villeneuve): LAVA flow from the Piton de la Fournaise, La Réunion island.

No part of this publication may be reproduced or transmitted in any form or by any means, electronic or mechanical, including photocopying, recording, or any information storage and retrieval system, without permission in writing from the publisher. Details on how to seek permission, further information about the Publisher's permissions policies and our arrangements with organizations such as the Copyright Clearance Center and the Copyright Licensing Agency, can be found at our website: www.elsevier.com/permissions.

This book and the individual contributions contained in it are protected under copyright by the Publisher (other than as may be noted herein).

Notices
Knowledge and best practice in this field are constantly changing. As new research and experience broaden our understanding, changes in research methods, professional practices, or medical treatment may become necessary.

Practitioners and researchers must always rely on their own experience and knowledge in evaluating and using any information, methods, compounds, or experiments described herein. In using such information or methods they should be mindful of their own safety and the safety of others, including parties for whom they have a professional responsibility.

To the fullest extent of the law, neither the Publisher nor the authors, contributors, or editors, assume any liability for any injury and/or damage to persons or property as a matter of products liability, negligence or otherwise, or from any use or operation of any methods, products, instructions, or ideas contained in the material herein.

Library of Congress Cataloging-in-Publication Data
A catalog record for this book is available from the Library of Congress

British Library Cataloguing-in-Publication Data
A catalogue record for this book is available from the British Library

ISBN: 978-0-444-63708-6

For information on all Elsevier publications
visit our website at https://www.elsevier.com/books-and-journals

ELSEVIER
Book Aid
International
Working together
to grow libraries in
developing countries
www.elsevier.com • www.bookaid.org

Publisher: Candice Janco
Acquisition Editor: Amy Shapiro
Editorial Project Manager: Tasha Frank
Production Project Manager: Divya KrishnaKumar
Cover Designer: Victoria Pearson

Typeset by SPi Global, India

Preface

This work is an updated and augmented version of the book published under the same title in 2005, which was itself a complete rewriting and considerable expansion of a first work written in 1988 by the senior author. A quick comparison between these three versions would at once reveal the considerable advances made during the past three decades in the study and understanding of amorphous silicates. Of particular interest has been the development of a great many probes with which the structure of these phases can now be determined with an amazing wealth of details. Thanks in particular to the availability of intense laser and X-ray sources, other experimental advances have made a variety of high-pressure and high-temperature experiments possible, with obviously important petrological implications for the earth's interiors. In parallel, atomistic simulations and even first-principles methods have been improved to the point that they not only can throw valuable light on a variety of observed features, but also can make predictions of practical interest.

There are thus many good reasons for continuing to investigate the various aspects of these materials, which are in some ways unique in view of their dual industrial and natural importance. As stated in the previous edition, the yearly production of silicate glasses is approaching 100 million tons. From traditional vessels, bottles, window panes, or lenses to modern insulating stone and rock wools, reinforcement and optical fibers, thin films, flat-display panels or even biological prostheses, silicate glasses fulfill an ever-increasing diversity of uses. Of course, these achievements illustrate the long way followed since the beginnings of real glassmaking 4000 years ago. For millennia, progress was empirical. For more than a century, however, basic glass research has been a key factor to meet successfully the competition with other materials, to optimize glass production, and to develop new products tailored for specific applications. For these purposes, chemical composition is an essential parameter that is acted upon, given the strong influence it exerts on the structure and properties of silicates. As a result, deciphering the mutual property-structure relationships as a function of temperature and chemical composition remains a major goal of glass and melt science.

Although magma is also essentially made up of silicates, the importance of understanding such relationships has been perceived more recently in earth sciences. The $21\,\mathrm{km}^3$ (i.e., about 60 billion tons) of lava that each year reach the earth's surface are the most spectacular manifestation of magmatic processes. This amount, however, represents just a tiny fraction of the actual volume of rising magma that is transferring heat and matter within the earth and is eventually forming igneous rocks at or near the surface. Magmatic activity has, in fact, been a major factor in shaping our planet throughout its 4.5 billion years long history.

Magma and industrial glass share a great many features, in particular a great diversity of chemical composition. Of course, the complexity of magma composition is not human choice but Nature's will. Another difference is that industry deals with a greater number of major chemical elements, whereas earth sciences are facing the formidable challenge raised by high pressures and high temperatures. In both cases, however, the methods of investigation are the same—at least at low pressures—and the results obtained in one field are of direct relevance to the other.

Keeping in mind this dual natural and industrial importance, we have again attempted to picture in a consistent manner the physical chemistry of silicate glasses and melts. Not expecting this book to be read from the first to the last page, we have written the chapters in such a way that they can be read independently of each other. To limit the growth of the book and avoid abusing the readers' patience, we have tried to avoid any useless duplication between chapters by making instead frequent cross-referencing between them. In a literature that has grown so large that it cannot be reviewed comprehensively, we also attempted to limit the usual bias due to the authors' research interest while not overlooking important papers relevant to our story. The approximately 2600 papers quoted should then give an adequate representation of the current literature.

As a side effect of the emphasis now put on structure, sometimes the actual macroscopic features to be accounted for are either overlooked or not clearly identified, so for every chapter, or sometimes for two consecutive related chapters, we first give a summary of physical properties before describing structures. In this respect, we have thought it useful to recall that, despite often being more than 50 years old, basic information such as phase diagrams has not lost any of its importance.

An introductory chapter is devoted to a short history of glass and magma. In the following chapters we present the general physical and structural features of glasses and viscous liquids. With pure SiO_2 as a starting point, we proceed to compositions of increasing chemical complexity in the second part of the book. The effects of network-modifying cations are first exemplified using alkali and alkaline earth elements. The specific influences of aluminum, iron, titanium, and phosphorus are then reviewed. The influence of volatile components (water, fluids of the system CHOS, noble gases, and halogens) is also dealt with. Application of these results to complex systems is finally discussed.

Concentrating on properties of more direct relevance to phase equilibria and mass transfer, we have for the most part left aside electrical, optical, or mechanical properties. Information on these themes will be found in the publications in the following list, which also includes a few older books that still provide very helpful insights.

At the end of our project, it is a pleasure to thank S. Hardy and M. Woolf for the efficient way they have gathered many of the additional papers discussed in this new edition. And we also acknowledge again the valuable criticism or help provided by Y. Bottinga, J. Dyon, J. Roux, and J.F. Stebbins on many chapters of the first edition, fruitful collaboration with R. Conradt, G. Ottonello and A. Takada, and the cover picture provided by N. Villeneuve.

Silicate Glasses and Melts–Structure and Properties first introduces the reader to the principles that govern the physical and chemical properties of these materials and in particular to the mutual relations between their properties and structure. With pure SiO_2 as a starting point, compositions of increasing chemical complexity are dealt with in the second part of the book. The effects of network-modifying cations are first exemplified using alkali and alkaline earth elements. The specific influence of aluminum, iron, titanium, and phosphorus are then reviewed. The influence of volatile components (water, fluids of the system CHOS, noble gases, and halogens) is also dealt with. Application of these results to complex systems such as natural melts is finally discussed.

Bjorn Mysen is a senior scientist at the Geophysical Laboratory of the Carnegie Institution of Washington. His research interests include relationships between structure and properties of silicate melts and aqueous fluids at high temperature and high pressure and relationships between energetics and structure of minerals, melts, and fluids, with authorship of more than 250 articles. He has served as author, editor, and coeditor of several books on these subjects (*Magmatic Processes: Physicochemical Principles*, The Geochemical Society 1987; *Structure and Properties of Silicate Melts*, Elsevier 1988; *Phase Diagrams for Ceramists*, Vol. 8, American Ceramic Society, 1989; *Phase Equilibria—A Memorial to A. Muan*, American Ceramic Society, 1992; *The Role of* Magmas *in the Evolution of the Earth*, Elsevier, 1998; *Mantle Petrology: Field Observations and High Pressure Experimentation*, The Geochemical Society, 1999).

Pascal Richet is senior physicist at the Institut de Physique du Globe de Paris. He has been a visiting professor at Stanford University and at the Tokyo Institute of Technology. Within his main research area, the physical chemistry of oxide materials, he has authored numerous papers on the high-temperature properties of crystalline and amorphous silicates. He has also published *The Physical Basis of Thermodynamics* (Plenum Publishing, New York, 2001), as well as books dealing with either popularization or history and philosophy of science. These include *A Natural History of Time* (The University of Chicago Press, 2007) and, in French, *The Age of Glass* (Gallimard, Paris, 2000), *A Guide to the Volcanoes of France* (Belin, Paris, 2003), *Fire, At the Source of Civilization* (Gallimard, Paris, 2004), and *A Guide to the Volcanoes of French Overseas Territories* (Belin, Paris, 2007).

Further Reading

Affatigato, M. (Ed.), 2015. Modern Glass Characterization. John Wiley & Sons, Hoboken, NJ.

Bansal, N.P., Doremus, R.H., 1986. Handbook of Glass Properties. Academic Press, Orlando.

Cable, M., Parker, J.M., 1992. High-Performance Glasses. Blackie, Glasgow.

Carroll, M.R., Holloway, J.R. (Eds.), 1994. Volatiles in Magmas. In: Reviews in Mineralogy, 30. Mineralogical Society of America, Washington, DC.

Donth, E., 2001. The Glass Transition. Springer, Berlin.

Doremus, R.H., 1994. Glass Science, second ed. John Wiley & Sons, New York.

Mackenzie, J.D. (Ed.), 1960–1964. Modern Aspects of the Vitreous State, 3 vols. Butterworth, London.

Gutzow, I. and Schmelzer J. (2013) The Vitreous State: Thermodynamics, Structure, Rheology, Crystallization. Springer, Heidelberg.

Leuzzi, L., Nieuwenhuizen, L., 2008. Thermodynamics of the Glassy State. Taylor & Francis, New York.

Mazurin, O.V., Streltsina, M.V., Shvaiko-Shvaikovskaya, T.P., 1987a. Handbook of Glass Data. Part A. Silica Glass and Binary Silicate Glasses. Elsevier, Amsterdam.

Mazurin, O.V., Streltsina, M.V., Shvaiko-Shvaikovskaya, T.P., 1987b. Handbook of Glass Data. Part C. Ternary Silicate Glasse. Elsevier, Amsterdam.

Mazurin, O.V., Streltsina, M.V., Shvaiko-Shvaikovskaya, T.P., 1993. Handbook of Glass Data. Part E. Single-Component, Binary, and Ternary Oxide Glasses: Supplements to Parts A, B, C, and D. Elsevier, Amsterdam.

Morey, G.W., 1938. The Properties of Glass. ACS Monograph SeriesReinhold Publishing Co., New York

Mysen, B.O., 1988. Structure and Properties of Silicate Melts. Elsevier, Amsterdam.

Nemilov, S.V., 1995. Thermodynamic and Kinetic Aspects of the Vitreous State. CRC Press, Boca Raton.

Nicholls, J., Russell, J.K. (Eds.), 1990. Modern Methods of Igneous Petrology: Understanding Magmatic Processes. In: Reviews in Mineralogy, 24. Mineralogical Society of America, Washington, DC.

Paul, A., 1990. Chemistry of Glass, second ed. Chapman and Hall, London.

Pye, L.D., Montenero, A., Joseph, I., 2005. Properties of Glass-Forming Melts. CRC Press, Boca Raton.

Rao, K.J., 2002. Structural Chemistry of Glasses. Elsevier, Oxford.

Rawson, H., 1967. Inorganic Glass Systems. Academic Press, London.

Richardson, F., 1974. Physical Chemistry of Melts in Metallurgy. 2 vols. Academic Press, London.

Richet, P. (Ed.), 2018. Encyclopedia of Glass Science, Technology, History and Culture. John Wiley & Sons, Hoboken, NJ.

Scholze, H., 1991. Glass. Nature, Structure, and Properties. Springer, New York.

Shelby, J.E., 1997. Introduction to Glass Science and Technology. The Royal Society of Chemistry, Cambridge.

Simmons, C.J., El-Bayoumi, O.H., 1993. Experimental Techniques of Glass Science. The American Ceramic Society, Westerville, OH.

Stebbins, J.F., McMillan, P.F., Dingwell, D.B. (Eds.), 1995. Structure, Dynamics and Properties of Silicate Melts. In: Reviews in Mineralogy, 32. Mineralogical Society of America, Washington, DC.

Tammann, G., 1933. Der Glaszustand. Leopold Voss, Leipzig.

Turkdogan, E.T., 1983. Physicochemical Properties of Molten Slags and Glasses. The Metals Society, London.

Uhlmann, D.R., Kreidl, N.J., 1983–1990. Glass Science and Technology, 1. Glass-Forming Systems; 4A Structure, Microstructure, and Properties; 4B Advances in Structural Analysis. Academic Press, New York.

Varshneya, A., 2014. Fundamentals of Inorganic Glasses. Soc. Glass Technology, Sheffield.

Vogel, W., 1994. Glass Chemistry, second ed. Springer, New York.

Wolf, M.B., 1984. Chemical Approach to Glass. Elsevier, Amsterdam.

Zanotto, E.D., 2013. Crystals in Glass: A Hidden Beauty. John Wiley & Sons, Hoboken, N.J.

Zarzycki, J. (Ed.), 1991a. Glasses and Amorphous Materials. In: Materials Science and Technology, 9. VCH, Weinheim.

Zarzycki, J., 1991b. Glasses and the Vitreous State. Cambridge University Press, Cambridge.

Index

Note: Page numbers followed by *f* indicate figures and *t* indicate tables.

CHAPTER

1

The Discovery of Silicate Melts: An Applied and Geological Perspective

OUTLINE

1.1 INTRODUCTORY COMMENTS

Under a thin sedimentary layer, the rocks that make up the continents and the ocean floor were formed by cooling of magma. The name igneous rocks (*ignis*, fire in Latin) is a reminder of this origin. Today, such a magmatic source is taken for granted, although such an origin was established only about two centuries ago. In fact, since the beginnings of glass four millennia ago to the end of the 18th century, molten silicates were of concern solely to glass makers and subsequently to metallurgists. Hence, it is hardly a novelty that the properties of silicate melts are as important in materials sciences as in the earth sciences.

https://doi.org/10.1016/B978-0-444-63708-6.00001-6

1.2 THE EARLY HISTORY OF GLASS

1.2.1 The Beginnings of an Art

Glass is one of the earliest man-made materials (e.g., Bimson and Freestone, 1987; Tait, 1991; Shortland and Degryse, 2018). It appeared more than 4000 years ago in the Middle East, about five millennia after other oxide-based materials (ceramics, plaster, and lime), but it closely followed the first metals, copper and lead, and even preceded iron.

It is not known whether glass was first produced in Mesopotamia, Egypt, or Syria, and whether it was made during ceramic or metallurgical operations. In fact, a single origin is unlikely. Similar sequences of discoveries probably led to similar processes and products in different places in the Middle East. Their common feature was to be small, imperfect pieces that might have originally been accidental by-products of glazing applied to stone and faience before repeated efforts allowed bulk glass to be produced, mainly as beads.

What may actually be termed glassmaking apparently dates back to the 16th century BC, as real glass pieces appear in the archeological record in the Late Bronze age. These early glasses have familiar compositions (Table 1.1). They are not translucent but opaque and vividly colored by various metals such as copper (red and blue-red), iron (black, brown, and green), antimony (yellow), cobalt (blue), or tin (white) (Oppenheim et al., 1970). The substances that yielded these various colors were thus already identified empirically at these early stages. In Egypt, it is not fortuitous that glassmakers were called "makers of lapis lazuli." As a matter of fact, this was the first time that a given property of a material—its color—could be varied almost at will. Unknowingly, glassmakers had thus discovered the rich possibilities offered by continuous solid solutions, and they also observed that small changes in ingredients (i.e., in chemical composition) could result in marked changes in a physical property.

For a very long time, glassmakers would use raw materials of variable quality and were, of course, ignorant of the importance of controlling redox conditions when working with

TABLE 1.1 Composition of Some Ancient Glasses (wt%)[a]

	SiO_2	Na_2O	Al_2O_3	K_2O	CaO	MgO	Fe_2O_3	PbO
Babylonian, 14th cent. BC	61–71	9–14	1–3	1–3	5–8	3–6	1–2	
Blue glaze, 6th cent. BC	64.0	17.8	1.9	4.3	5.9	3.6	1.4	
Egypt, 18th dynasty, translucent	62–66	17–22	1–2	0–1	8–12	4–5	0–1	
India (3rd–5th cent. BC)	58–71	13–19	2–6	2–5	5–9	1–5	1–2	
Alexandria	72.7	19.0	1.8	0.39	5.2	0.4	0.12	
Soda glass, Europe, 1st–9th cent.	65–73	14–20	2–5	0–2	4–9	0–2	0–3	
Potash glass, Europe, 9th cent.	51–54	1–2	1–3	14–18	12–16	5–7	1–3	
Islamic glass, 13th cent.	68	14	3	3	8	4		
English crystal	57–72	0–3	0–1	8–14	0–1			9–29
Bohemia	55			32	12			

[a] *See Brill (1999) for a comprehensive review; English crystal with 0%–6% B_2O_3, from Moretti (2004).*

multivalent elements. Their operations were tricky and not necessarily reproducible because their knowledge was strictly empirical. Hence, rites were practiced to ensure success through the protection of gods. This is revealed by extant 7th-century BC cuneiform tablets from Niniveh, found in King Assurbanipal's library, which report the earliest known procedures for making kilns and glass (Oppenheim et al., 1970):

> When you set up the foundation of a kiln to [make] glass, you [first] search in a favorable month for a propitious day, and [then only] you set up the foundation of the kiln. As soon as you have completely finished […] no outsider or stranger should [thereafter] enter [the building], an unclean person must not [even] pass in front of [ritual *Kùbu*-images]. You regularly perform libations offerings before them. On the day when you plan to make the "metal" in the kiln, you make a sheep sacrifice before the *Kùbu*-images, you place juniper incense on the censer and [then only] you make a fire in the hearth of the kiln and place the "metal" in the kiln.

Early glassmakers shared many points with metallurgists in their use of earthy materials and operation of their furnaces, as testified in this tablet by the use of the term metal, which would be used in Europe until the late 19th century. More importantly, glassmakers were good observers. The very existence of these cuneiform tablets shows that keeping written records of technical processes was already considered important in Mesopotamia. This first kind of quality control included instructions on how to estimate the most important practical property of glass, viscosity. For this purpose, tablets from the 14th or 12th century BC advised the glassmaker to observe how droplets of glass were sticking to the tip of the rake used to stir the melt. Such records would eventually be lost after the collapse of Mesopotamian states, to be recovered only in the early 20th century AD, when these tablets would be deciphered and their meaning ascertained.

As other examples of their craft, Mesopotamian glassmakers were aware of the deleterious effects of fumes (through vapor-melt interactions) and thus kept recommending, "You keep a good and smokeless fire burning." They used bellows to achieve sufficiently high temperatures and knew which colors would be obtained (through redox reactions) depending on whether their pots were covered or not and the doors of their kilns open or closed. They were familiar with sintering, grinding, and stirring (to achieve chemical homogeneity). Glassmakers also mastered quenching procedures by dipping or immersing glass pots in water and practiced annealing at appropriate temperatures in dedicated furnaces to prevent a piece from breaking spontaneously on cooling (as a result of the internal stresses that build up through the glass transition). A testimony of high achievements was the ability of early glassmakers to imitate obsidians, which thus belonged to two different categories, namely, "genuine" and "from the kiln" (Oppenheim et al., 1970). Another interesting feature of this activity was the production of synthetic basalt through firing of local silts (Stone et al., 1998). No connection seems to have been made with the actual rock, however, although basalt was well known since it was brought from the mountains of Zagros or High Mesopotamia to be used extensively in Assyrian and Babylonian steles and statues.

The chemical inertness and nonporous nature of glass were important features of the material and were put to good use to conserve unguents or perfumes. To make small containers, the viscous melt was, for example, spread over a core made up of a mixture of dung and clay, which was subsequently scraped from the inside of the newly made piece. Many other ways of working or molding glass were invented (see Stern and Schlick-Nolte, 1994; Sternini, 1995). A very high level of artistry was rapidly reached although (or because?) glass remained an

FIG. 1.1 Millefiori glass cup (size: 10cm) from Alexandria probably made about 2000 years ago. *Redrawn from Corning Glass Museum, Corning, New York.*

expensive material, catering to the elites in eastern Mediterranean and western Asian areas. These skills are attested by pieces made up of glasses of different colors, sometimes intermingling in a very complex pattern, like the so-called *millefiori* glass cup of Fig. 1.1 (cf. Charleston, 1980; Richet, 2000).

Glasses of similar compositions were also deposited as thin layers on a variety of surfaces (Matson, 1985). The vitrified bricks of Mesopotamian monuments of the 6th–4th centuries BC are famous for their ornamental value. For such fragile building materials, glass was also valuable because it offered protection against alteration.

When deposited on metals, glass is called enamel (Colomban, 2018). In this form, it was extensively used in jewelry. And, from the 4th century BC, very fluid lead-based glasses gave rise to glazes that allowed pottery to be impermeable to liquids. When welding different glasses or depositing glass onto another substrate, glassmakers had to use materials having similar thermal expansion coefficients. In all these endeavors, thermal expansion had thus to be controlled empirically.

1.2.2 An Industrial Revolution

Slowly, glassmaking spread from the Middle East. Beads made during the late second millennium BC have been found from Italy to central Asia and China. Glass vessels followed suit later, reaching Greece, Italy, and China toward the 13th, 8th, and 5th centuries BC, respectively; present-day France in the 1st century AD; and then Belgium and the Rhine Valley in the 3rd–4th centuries. Glass did not gain importance in Japan because of the lack of siliceous sand. It would remain unknown in America until the Spanish conquest.

Two most important inventions were made at the beginning of the Christian era, probably in Phoenicia, in the large workshops of Sidon. These inventions were transparent glass and glassblowing (see Grose, 1986; Freestone, 2018). Transparency requires the raw materials to be of high purity with less than a few wt‰ of iron oxides, in particular. This could be achieved only in places where sand and natron, i.e., naturally occurring sodium carbonate [$Na_2CO_3 \cdot NaHCO_3 \cdot 2H_2O$], were available. The border between Phoenicia and Egypt owes its importance to the local availability of such materials. It was discovered early on that transparency was improved upon addition of substances we now call antimony oxide [Sb_2O_3] and especially manganese oxide [pyrolusite, MnO], the famous *glassmaker's soap*. The explanation is that these transition elements oxidize most of the trace amounts of Fe^{2+} present into the less-absorbing Fe^{3+} and, along with their own optical bands, cause the rather continuous absorption in the visible that makes the glass colorless with a slightly reduced light transmission.

Glassblowing was an early industrial revolution. With this new process, shaping glass became much easier, less time consuming, and thus less expensive. As a result, melting furnaces with capacities of up to 20 tons of glass were constructed, as shown by remains recently excavated in Egypt and Israel (Freestone, 2018). The size and shape of pieces were no longer restricted as they were with earlier methods, thus allowing glass to become a basic commodity in the Roman empire (e.g., Stern, 1995; Sternini, 1995), with a technological level that would not be matched again before the 18th century in Europe. Glassblowing required strict control of viscosity during the alternating periods of working and reheating before the final annealing. Good use was also made of thermal shock to cut the piece at the desired place and also for severing it from the blowing pipe.

Because glasses found in widely different places show a definite similarity of chemical composition (Table 1.1), Velde (1990) suggested that, until the 8th or 9th century, glass was essentially made in the Middle East and exported as ingots or final products to the Western world, where only small furnaces were operated for remelting the imported ingots along with cullet (scrap glass) that was extensively recycled. This view is supported by glass cargo found in ships wrecked in the Mediterranean Sea and by the fact that remains of glassworks from this period have not been unearthed in Europe (Foy et al., 1998). The composition of this glass (Table 1.1) is similar to that of modern window glass (Table 1.2).

When the ancient trade routes were cut following the Arab conquest, glass had to be made from starting materials available locally. In Western Europe, the ashes of ferns, which are potassium-rich, were commonly used as a flux to melt siliceous sand. In the long run, this change had the unfortunate consequence that the resulting glasses were more prone to alteration by atmospheric and meteoric waters than the former soda-lime glasses. Then, around the 11th century AD, the soda-rich ashes of marine plants such as *Salicornia* were imported from Spain, so glass compositions became more similar to the ancient ones. This is the reason why stained glass from the late Middle Ages tends to be better preserved than that of earlier periods. By that time, flat glass had already been made for a long time from blown glass by the two different processes that would be used until the end of the 19th century (Fig. 1.2).

Variations in chemical composition also resulted in changes in the melting, working, and annealing conditions because viscosity depends strongly on the nature and amount of the constituting oxides. Everything else being equal, the difference between the annealing temperatures of the sodium- and potassium-based glasses of Fig. 1.3 reaches 120 degrees. Moreover, the former had to be melted and homogenized at temperatures about 200 degrees higher than the latter.

As shown by Turner (1956a,b), much can be learned about glass technology in antiquity from modern investigations of the physical and chemical properties of ancient glasses. This statement has actually become increasingly true, thanks to the progress made since then in analytical capabilities. Isotope-based geochemical methods are in particular used to determine the origins of glasses or those of their raw materials. For example, lead and neodymium

TABLE 1.2 Composition of Some Industrial Glasses and Melts (wt%)[a]

	SiO_2	Al_2O_3	B_2O_3	Fe_2O_3	FeO	MgO	CaO	Na_2O	K_2O	TiO_2
Window glass	72.6	0.6			0.8	3.6	8.7	14.3	0.2	
Thermometer[b]	53.0	21.0	10.0			10.0	5.0			
CRT, panel[c]	60.5	2.0						8.0	7.5	0.5
CRT, funnel[d]	50.0	4.0				2.0	4.0	6.0	8.5	
FDP[e]	69.0	11.5	7.3			1.4	5.0			
Pyrex	81.1	2.0	12.3				0.1	5.2	0.2	
Neutral glass[f]	74.8	6.2	10.5				0.5	7.5	0.8	
E glass	56.5	14.3	6.4		0.5	2.6	18.4	0.4	0.4	0.6
Vycor[g]	62.7	3.5	26.9					6.6		
Glass wool[h]	65.0	2.5	4.5			2.5	8	16.5	0.7	
Rock wool[h]	46.6	13.3		6.4	4.8	9.1	10.0	5.6	1.4	2.4
Ash[i]	37.0	9.8			2.3	2.0	42.6	2.2	1.1	3.0
Slag[j]	36–7	5–35				16–4	43–54			

[a] *Compositions may vary from one manufacturer to another, and with time for a given manufacturer. 2003 world glass production: 120 × 10^6 tons. In the European Union (29 × 10^6 tons), container glass: 63%; flat glass: 27%; tableware: 4%; reinforcement fibers: 2%; specialty glasses: 4%.*

[b] *Jena 2950^{III} (supremax).*

[c] *Cathode ray tube for color television, with 9.5% SrO, 9% BaO, 0.5% ZnO, 1.5% ZrO^2, 0.2% CeO_2, 0.3% Sb_2O_3.*

[d] *With 23% PbO, 1% SrO and BaO, and 0.3% Sb_2O_3.*

[e] *Flat display panel, Corning code 1737, with 4.4% BaO, 1.2% SrO, and 0.2% As_2O_3.*

[f] *For pharmaceuticals.*

[g] *As melted, vitroceramics.*

[h] *For thermal insulation.*

[i] *From incineration of household waste.*

[j] *Optimal sulfur retention for slags with two extreme Al_2O_3 contents.*

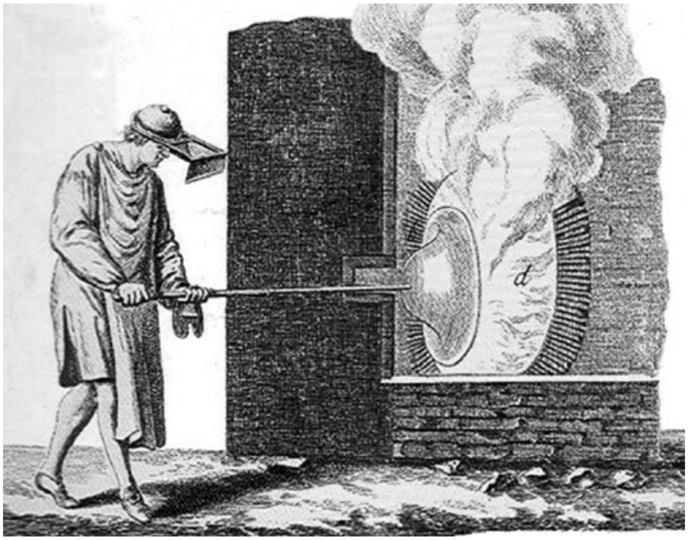

FIG. 1.2 Making of crown, flat glass from a bulb rapidly rotated in front of a furnace after having been opened opposite to the end through which it was first blown (Diderot and D'Alembert, 1751). Alternatively, as described by the German monk Theophilus in the 12th century, flat glass could be made from a large cylinder which was split longitudinally and flattened in an annealing furnace after its two ends had been cut out. In both cases, controlling the viscosity at the various stages of the process was of paramount importance.

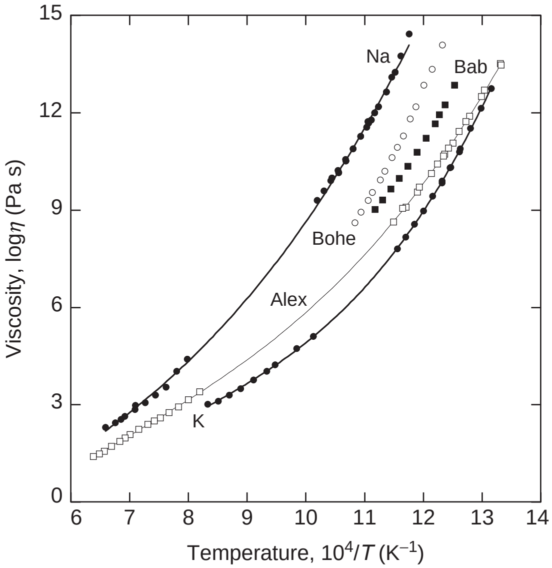

FIG. 1.3 Viscosity of antique glasses (Vo Thanh and P. Richet, unpub. res.). Glass is said to be short or long when the temperature interval of the 10^5–10^8 Pa s working viscosity interval is narrow or large, respectively. Compositions listed in Table 1.1 for Bab (Babylonia), Bohe (Bohemia), and Alex (Alexandria). Na: 66% SiO_2, 20% Na_2O, 8% CaO 2.5% Al_2O_3; K: 54% SiO_2, 20% K_2O, 15% CaO, 6% MgO, and 2% Al_2O_3 (other oxides as in Table 1.1 for soda and potash glass).

isotopes may discriminate between possible sources of silica and strontium and antimony isotopes for those of plant ashes and opacifiers, respectively (Shortland and Degryse, 2018).

A continuous link between late antiquity and modern times was ensured in Venice, which was originally a distant outpost of Byzantium. There, natron-based glass was remelted as early as in the 7th or 8th century, shortly before plant ashes had to be used (Verità, 2018). However, Venetian glass acquired its famous reputation much later, after quartzite pebbles had been substituted for imported sand as a purer source of silica in the early 14th century. In the middle of the following century the famous *cristallo* was then invented by Angelo Barovier (d. ~1480). The secret of the new glass was an initial purification step of the soda plant ash consisting of dissolution in boiling water, decantation, filtration, and drying of the *sale de cristallo* eventually obtained. It was with this product that Venice reigned supreme in the glass industry for two and a half centuries.

1.3 GLASS AND SCIENCE

1.3.1 A Scientific Material

The beginnings of glass as a scientific material probably date back to the optical experiments made in Alexandria by Ptolemy (AD ~90 to ~168), still better known as an astronomer. As investigated with glass, air, and water, refraction occurs "not only in the passage from rarer and more tenuous to denser media—as happens in the case of reflection—but also in the passage from a denser to a rarer medium" in a way such that the angles of incidence and refraction "do bear a certain consistent qualitative relation to one another with respect to the normals." As a technical material, glass was also put to use in various devices designed

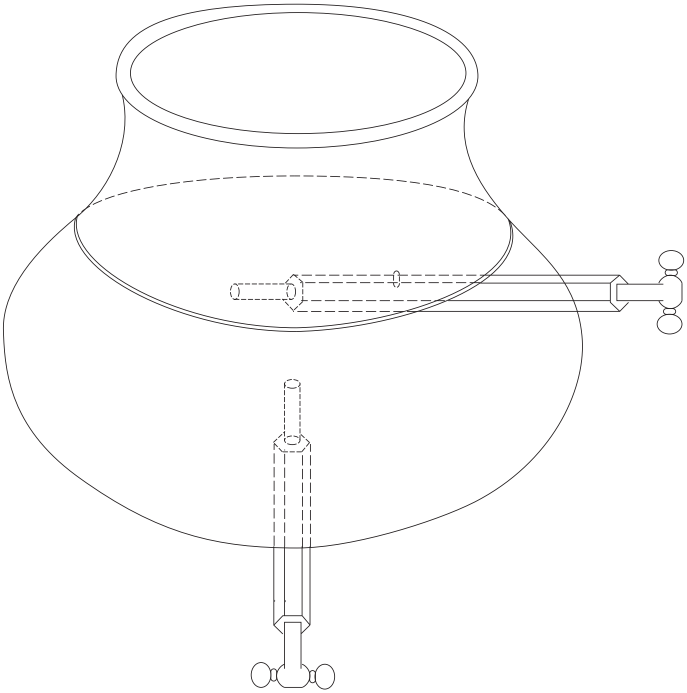

FIG. 1.4 The complex shape of "a Cupping-Glass, to which is attached, an Air-exhausted Compartment" in the Pneumatics of Hero of Alexandria (section 56, 19th-century drawing of the English translation).

by Greek inventors, for instance by Hero of Alexandria (1st century AD) in his *Pneumatics*, where the power of fluids was used in a variety of automata and recreational devices (Fig. 1.4).

Glassmaking represented a dramatic transformation of a variety of humble earths into wonderful substances akin to gems. By its special properties, glass was thus raising fundamental questions, especially because its fusibility placed it in the same category as the metals then known. Glass thus attracted the alchemists' interest as a model substance to explain a variety of phenomena related to the philosophy of matter (Beretta, 2018), and also because it was playing a great role in their practical operations. Since the beginning of their *Sacred Art*, alchemists had thus taken advantage of glass transparency, chemical inertness, and plasticity to make vessels of any shape for any purpose (Fig. 1.5). A most important piece from this period is the still, which led to the discovery of alcohol. Another was the *philosopher's egg*, a large egg-shaped vessel in which the desired transmutation of base metals into silver or gold was supposed to operate, under the right heat conditions, in contact with the mysterious philosopher's stone.

In physics, the manner in which glass distorts vision had already been noticed in antiquity. For a long time, this effect was judged to be more a problem than an asset because the shape of objects could not be reliably observed. This drawback was, for instance, emphasized by Seneca (4 BC to AD 65). Hence glass by itself attracted little interest from the first Greek and Arab theoreticians of optics. It is only when it was realized that distortion of images is determined by the shape of glass, and not by its nature, that optical applications became possible. Apparently, this happened in the 13th century in Italy, when glass was ground to form concave

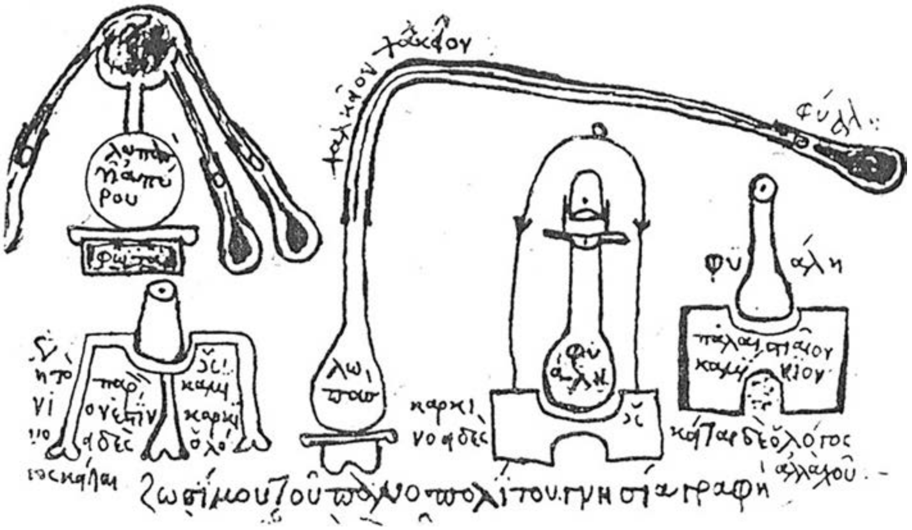

FIG. 1.5 One of the earliest representations of alchemical glassware, in a 13th century manuscript copy of a work by the 3rd–4th century AD Greek alchemist Zosimus (MS 2327, BN Paris, in Berthelot, 1887).

lenses to be used to correct farsightedness (Clay and Court, 1932; Ilardi, 2007). Because of the isotropy of its optical properties and relative ease of production, glass rapidly proved to be more appropriate for optics than crystals like quartz and beryl, which had also been used. Later on, convex and different sorts of lenses allowed other kinds of visual impairments to be corrected. In this way, glass transformed the daily lives of laymen and scholars alike.

Of fundamental importance were also the inventions that glass made possible in the 17th century, when lenses became used in telescopes and microscopes (Fig. 1.6). With these new

FIG. 1.6 Hooke's (1665) microscope. Glass was used not only for the two lenses of the instrument, but also for the fuel flask (on the left side) and the spherical water bulb which served to focus the light on the small lens placed near the sample holder.

instruments, scientists like Galileo Galilei (1564–1642), Robert Hooke (1635–1703) and Antonie van Leeuwenhoek (1632–1723) began to explore the marvels of the outer and inner reaches of the world. They discovered a universe much greater and more populated than hitherto thought and the existence of innumerable living species that were invisible to the naked eye. Glass, in the form of prisms, also had the intriguing ability to decompose natural light in a rainbow-like manner. This was the basis of Isaac Newton's (1642–1727) famous 1666 investigation on the nature of light.

All branches of physics would, in fact, depend on glass to a very large extent. To give a first example, the existence of atmospheric pressure and its measurement by the mathematician Evangelista Torricelli (1607–48) in 1644 relied on the outstanding mechanical quality of Venetian glass (Fig. 1.7). Glass tubes also were used by Robert Boyle (1627–91) to establish in 1662 the well-known law that bears his name from measurements of the volume of air compressed by mercury (Fig. 1.8). Indeed, without glass there would have been no thermometers or barometers and it would have been much more difficult to arrive at the concepts of temperature and pressure. In the early 18th century, sap pressure in vascular plants as well as blood pressure in animals could also not have been discovered and measured without mercury tubes (Hales, 1723, 1733). (For thermometers, however, problems raised by the nonequilibrium nature of glass would last more than two centuries!) Thanks to its insulating properties, glass would also play a major role in electrostatics through rubbing of various materials on glass rods and disks. When in

FIG. 1.7 Torricelli's experiment illustrated by various kinds of large glass tubes in which the height of mercury is independent of both the shape and inclination of the device (Maignan, 1653).

FIG. 1.8 The U-shaped glass tube used by Boyle (1661).

1733 he discovered two different kinds of electricity, Charles Du Fay (1698–1739) called them “vitreous” [positive] and “resinous” [negative]. This nomenclature would hold until the end of the 19th century and in particular would be used when voltages as high as 30 kV were produced in the 18th century with electrostatic machines through rubbing on pads of large glass disks (Hackmann, 1978).

1.3.2 Descartes and the Foundation of a Science

Of course, curious minds were not satisfied with empiricism. René Descartes (1596–1650) had a strong interest in glass because of his optical research activities. He had, for example, theoretically explained the law of refraction discovered in 1620 by Willebrord Snell (1580–1626) in the Netherlands. The famous philosopher was especially fascinated by the “transmutation of ashes into glass.” This wide-ranging interest led him to give, in 1644, an insightful picture of vitrification in his extremely ambitious *Principles of Philosophy*, a treatise aimed at deriving a comprehensive description of the world from a few first mechanical principles. A glass, thus wrote Descartes,

> when still glowing with heat, is fluid because its particles are easily moved [separately from one another] by that force of fire which previously smoothed and bent them. However, when it begins to be cooled, it can take on any figures whatever. And this is common to all bodies which have been liquefied by fire; for while they are still fluid, their particles effortlessly adapt themselves to any figures whatever, and when such bodies subsequently harden with cold, they retain the figures which they last assumed.

At a time when nothing was known about the microscopic constitution of matter, Descartes was able to describe in this way not only what we now refer to as the atomic configurations of a material but also the manner in which these vary with temperature. Descartes went on to explain why glass should be annealed because of differential volume contraction on cooling and build-up of what we call internal stress, saying that glass

> is also more fragile when it is cooled quickly than when it is cooled slowly; for its pores are fairly open while it is glowing with heat […]. However, when glass cools naturally, these pores become narrower. […] And if the cooling occurs too rapidly, the glass becomes hard before its pores can thus contract. As a result, those globules subsequently always make an effort to separate its particles from one another.

But Descartes’s groundbreaking conceptions on glass probably suffered from the general criticism laid upon the Principles of Philosophy. This treatise was judged by many as a “romance” even before the vortices, which played so prominent a role in his system, had been attacked by the Newtonians. Although they were heralding the beginnings of glass science, Descartes’ ideas thus did not attract much attention. They have even remained completely forgotten until the present time (Richet, 2000). Yet, these concepts would have helped to find explanations to a great many glass properties in the following centuries.

A case in point is *tempered* glass, which was presented in 1661 as *Prince Rupert’s drops* before the Royal Society of London (Merret, 1662). Brought from Germany by the English Prince Rupert, these glass beads are produced through quenching of melt droplets into water (Fig. 1.9). Their particularity is to be remarkably shock resistant until a final blow makes them explode

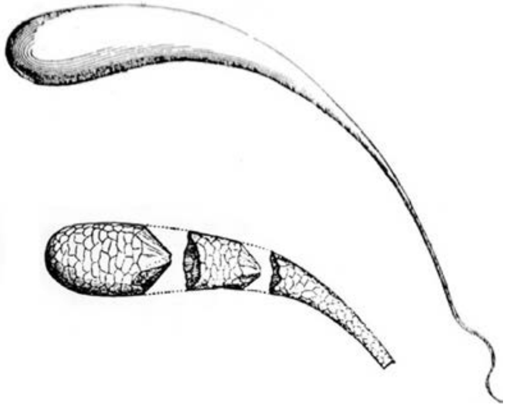

FIG. 1.9 Prince Rupert's drops (Péligot, 1877). Their weak point is their thin tail, which lacks a core, so that a slight shock on it triggers shattering of the whole piece.

and shatter into a very fine powder.[1] In a dramatic way, this phenomenon illustrates the role played by internal stresses that develop when glass is not annealed. Tempered glass would remain a scientific curiosity until the late 19th century, however, when fast cooling by compressed air came into use and made it possible to cool a piece of glass in such a way as to ensure a smooth, homogeneous distribution of internal stress.

1.3.3 The Effects of Composition

Environmental issues have long confronted the uses of glass. As early as the beginning of the 17th century, excessive consumption of charcoal for metallurgy and glassmaking in England gave rise to laws designed to preserve forests. However, substitution of coal for charcoal resulted in serious difficulties because the glass had to be protected from the corrosive (sulfurous) fumes released by the burning of coal. Melting pots had to be covered, with the consequence that heating was made more difficult because of the lack of heat radiated from the furnace vault. Consequently, new, more effective fluxes had to be found to alleviate the problem. A result was the invention in 1676 of *crystal glass* by George Ravenscroft (1632–83) through addition of large amounts of lead oxide to the composition (Moody, 1988; Moretti, 2004).

Even though lead oxide had been used in antiquity, crystal glass was a forerunner of future changes made in glass composition to yield new, special properties. Because index of refraction scales with density, crystal glass had a distinctly bright and vivid appearance, which instantly met with popular success. Of course, it also proved valuable to optics, a branch of physics where it became known as *flint* glass because it was made from ground flint in a country (England) where pure enough siliceous sand was badly lacking.

---

[1] In modern terms, the explanation is as follows. Owing to faster cooling, the surface of the drop is slightly less dense than its core. As a result, the core is under extension whereas the surface is under compression. Because a material breaks much more readily under extension than under compression, strong shocks are needed to produce the extensive stresses needed to initiate rupture on the glass surface. The mechanical energy that was stored through tempering is then released so violently that the glass shatters completely.

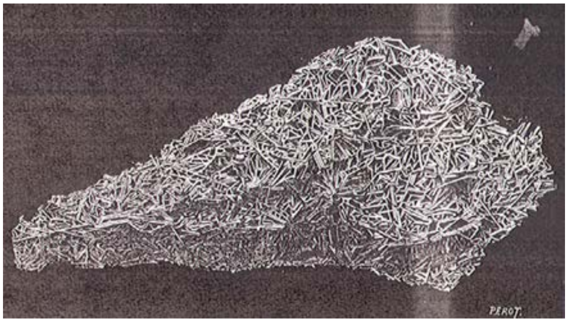

FIG. 1.10 Réaumur's porcelain, an engraving from Péligot (1877).

Another new family of glass appeared at about the same time in Bohemia. There, potash-lime glass was made as a substitute for quartz, which had been extensively mined for the purpose of carving beautiful vessels out of large single crystals. The new glass ensured great clarity, even for big pieces, and it could be ornamented with enamel because it could sustain high temperatures without softening.

Actually, glassmakers had long noticed that excessive time spent at temperatures appropriate for blowing induces partial transformation to a whitish material that could no longer be blown. It is only in 1727 that the naturalist and physicist René-Antoine Ferchault de Réaumur (1683–1757) observed that this was the result of devitrification of the melt. Réaumur also discovered that porcelain was a partially melted material and was, thus, an intermediate product between terracotta and glass. Through extensive devitrification, he could then create new products later called Réaumur's glass porcelains (Fig. 1.10).

Réaumur's experiments exemplified the extensive ceramic work of the period connected with the search for raw materials that would allow imitation of China's porcelain. Rocks appeared to differ widely in the way they reacted at high temperature. Granite, for instance, was readily melted. To Georges Louis Leclerc, count of Buffon (1707–88), this observation suggested that granite had formed by cooling of a melt. For reasons that will be given shortly, however, the evidence was not considered overwhelming by many scientists of the time.

1.4 THE DISCOVERY OF NATURAL MELTS

1.4.1 The Origin of Neptunism

Early glassmakers were familiar with an uncommon rock, obsidian. As already noted, they even succeeded in imitating this rock as small pieces because its special aspect, color, luster, and fracture made it a valuable commodity used for a wide variety of tools, jewels, or even mirrors. Long before the emergence of agriculture, these natural glasses had been traded far and wide within Eurasia, North and South America, and other parts of the world. In Eurasia, outcrops were mined in Sardinia, Lipari Islands (north of Sicily), Pantelleria (between Sicily and Tunisia), Armenia, Ethiopia, or Turkey. Today, these obsidians are of interest for archeological purposes because their specific trace element composition makes it possible to identify their source and thus to reconstruct prehistoric routes along which they were traded (see Dixon et al., 1968; Tykot, 2018).

Before the beginnings of geology, however, the origin of rocks in general, and obsidians in particular, was not of great concern. Without adequate means of investigation, people remained mostly interested in the practical uses of different kinds of rocks in the way already described by Pliny the Elder (23–79) in the 36th and 37th books of his famous *Natural History*. Until the middle of the 18th century, volcanic products were identified as such only when their origin was obvious from field relationships. This applied to cinders, ashes, scoriae, and solid lava that had been clearly issued from the crater of a volcano. At a time when the world was still believed to have been created about 6000 years earlier, it was difficult to think of extinct volcanoes because the earth could not be much different from what it had been at the Creation (Richet, 2007).

Since antiquity, it had been held that volcanoes resulted from subterranean fires fueled, not by exhalations of subterraneous winds as guessed by Aristotle (~384 to ~322 BC), but by bitumen, sulfur, or coal as reported by Lucretius (~98 to ~55 BC) or Strabo (~−64 BC to AD +25). There was, in fact, no room for alternative theories because, as explained by Aristotle, each of the four elements that were combined to make matter had a *natural place* such that *earth* tended to fall toward the center of the earth, followed by *water*, *air*, and *fire* in successively superimposed shells such that the spherical figure of the earth was in particular very simply and convincingly explained. It followed that any subterranean fire could not be permanent. Volcanoes had to be considered instead as local accidents, scattered throughout the earth's surface, which could not have been of any real importance in the past. Volcanoes were thus known only in volcanically active areas.

Although this view would dominate among naturalists until the 18th century, an enigmatic 12th-century author named Marius showed remarkable insight in explaining the formation of what we now call metamorphic and igneous rocks in terms of an increasingly strong action of subterranean heat on muds, whose deposition in water bodies he had likely observed himself. He did it in his book *On the Elements*, perhaps written in France toward 1160, where he described on the basis of actual observations how the four elements were combining to make up all things from minerals to man. As Marius asked his readers:

> Do you also know that the jar of a potter is a kind of glass? But because it was not cooked long, it is therefore not glass. But if it were cooked for a long time by the fire, it would be turned into clear and glittering glass, like the pot of the goldsmith. Now, therefore, you can observe how stones are created in the body of the earth because of insufficient fire; if the fire were greater, the process would be completed and these stones would be turned into glass. Of this sort are the stones we use for the constructions of houses, and marbles of various colors, and the little white stones which are found on the banks of rivers.

And Marius concluded that "there are many kinds of these because of the varieties of earth of which there are many kinds—I do not mean earth properly speaking—and because of the variation in the amount of heat they receive." These ideas received little attention, however, as indicated by the fact that a single manuscript of his book is known, which had to wait until 1976 to be at last edited and printed.

In contrast, there were actually many good reasons to think that most rocks were formed in water. Wasn't water the ubiquitous agent at the earth's surface? And didn't the Scriptures assert that the sole extraordinary episode of the earth's history had not been a volcanic conflagration, but the Deluge? When laying the foundations of geology in 1669, Nicolaus Steno (1638–86) indeed explained that strata had first been sediments deposited at the bottom of the sea before being consolidated as rock. In addition, chemists had observed that aqueous solutions precipitated solid material with a geometrical shape. The prismatic shape of rocks such as basalt (Figs. 1.11 and 1.12) thus was clearly indicative of an aqueous origin.

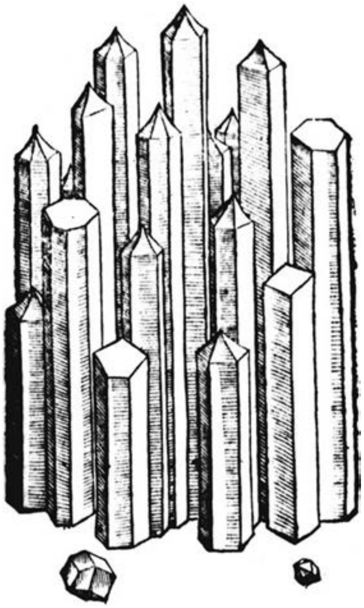

FIG. 1.11 Basalt prisms whose idealized apices are a testimony of the confusion that would beset the distinction between minerals and rocks until the end of the 18th century (Gesner, 1565).

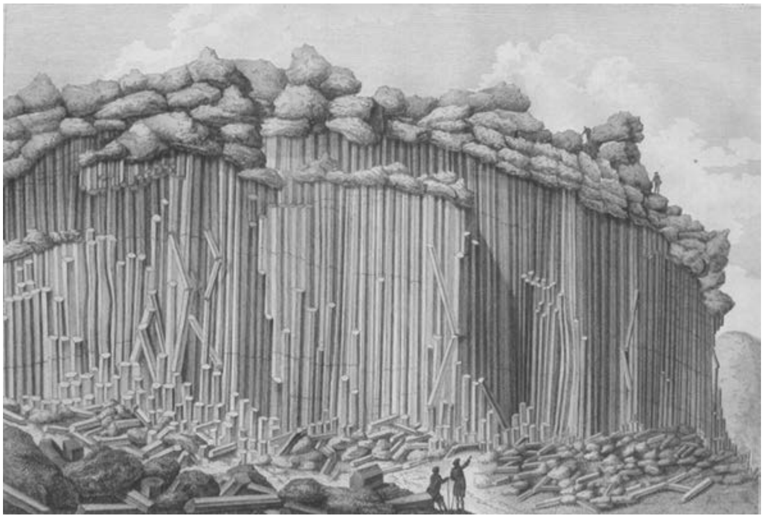

FIG. 1.12 Basalt prisms in Chenavari, near Montélimar in the Rhône valley (Faujas de Saint-Fond, 1778).

Even the bold theoreticians who followed Descartes and wrote their own *Theories of the Earth* did not challenge such ideas. Descartes himself thought that the earth was an "encrusted" sun whose center was filled with a fiery matter. But he did not make any connection between such hot, deep interiors of the earth and volcanism, which he also ascribed to as subterranean fires. When Gottfried Wilhelm Leibniz (1646–1716) and Buffon later considered the earth as still cooling from an initially molten state, they, too, held that water was the main geological agent. They were both *neptunists*, as they would have been called at the beginning of the 19th century. Following the ideas that Leibniz expounded in the 1690s in his *Protogaea*, published posthumously, it was generally assumed instead that granite, the rock considered at that time to be primordial because it was consistently overlaid by sedimentary rocks, had deposited from a primitive, strongly mineralized aqueous ocean.

1.4.2 From Extinct Volcanoes to Magma

To appreciate better how the existence of *igneous* rocks came to be recognized, we must start with the field trip made by the naturalist Jean-Étienne Guettard (1715–86) in central France in July 1751. In Moulins, he was struck by the town's fountains because these were made from a stone that resembled some Italian lavas of the Parisian rock collection of which he was curator. By asking where this stone was quarried, he ended up near Clermont-Ferrand where he discovered the typical volcanoes which make up the now-famous *Chaîne des Puys*. Far away from any active volcanic province, Guettard pointed out, there were extinct volcanoes which some day would perhaps erupt anew. Guettard, however, was himself a neptunist. He was a proponent of subterranean fires as the source of volcanic activity, and he was sharing the common idea held since antiquity that volcanoes are located near the sea because eruptions are triggered by interactions of infiltrated sea water with molten lava. He would also long believe that basalt could not have a volcanic origin because its columnar nature was a testimony to an order inconsistent with the confusion that is the hallmark of the action of fire (Guettard, 1770).

Later, however, Guettard (1779) would yield to the new ideas that were being propounded by Nicolas Desmarest (1725–1815), a government official who was also a part-time naturalist. Of still greater importance was in effect the second step made in 1763 when Desmarest traveled to Auvergne to see for himself the volcanoes described by Guettard. Near the Puy de Dôme, he immediately realized that basalt had been flowing out from the crater of volcanoes. This he demonstrated by careful observations that led him to make a detailed cartography of lava *flows* in the whole region. Thanks to its prismatic nature, basalt was soon identified not only in various parts of France by Faujas de Saint-Fond (1778), Guettard (1779), and other naturalists, but throughout Europe (Fig. 1.13). As made in Hessia by Rudolf Erich Raspe (1737–94)—better known as the author of the *Adventures of Baron Münchausen*—the existence of former volcanoes was recognized in Italy, Spain, Portugal, Germany, Ireland, and Scotland. In the past, volcanism thus appeared to have been much more important than previously thought. But Desmarest and his fellow naturalists were also neptunists. They held that lavas were just rocks melted at shallow depths in which phenocrysts were the remnants of former rocks that had been incompletely melted. The mineral pyroxene [*pyros*, fire, and *xenos*, foreign] described by Buffon's aide Louis Jean-Marie Daubenton (1716–1800) and by the famous mineralogist René-Just Haüy (1743–1822), is a reminder of these ideas.

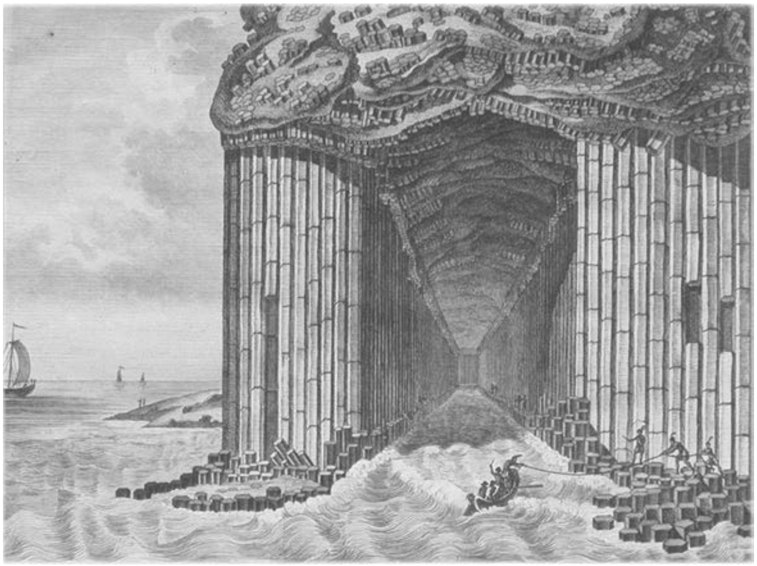

FIG. 1.13 The basaltic Fingal cave in Staffa Island (Hebrides, Scotland) as depicted by Faujas de Saint-Fond (1797).

At that time, thermodynamics was still in limbo so it is not surprising that the nature of "volcanic fire" was debated. Was it the same as that of "common fire"? Scientists like the abbot Lazzaro Spallanzani (1729–99) thought that melting experiments could solve the problem. But the answer remained elusive because the difference between temperature (an intensive thermodynamic property) and heat (an extensive property) had not yet been worked out properly. Spallanzani (1792–1797) himself incorrectly believed that, over long enough periods of time, the fire of furnaces would reach an intensity sufficient to melt lavas. A more lasting observation reported by Spallanzani in his great book was that exsolution of dissolved gases is the driving force of volcanic eruptions, as he daringly recognized in 1790 during an eruption of Vesuvius.

The breakthrough on the origin of lava eventually came from Déodat de Dolomieu (1750–1801), a famous geologist of the period who left his name on the dolomite rock and the Dolomites Mountains. Back from volcanological field work in Italy and Auvergne, he elegantly demonstrated in 1797 that lavas originate from a great depth below the primordial granite, an idea that ruled out water-melt interactions as the cause of eruptions. Although Dolomieu remained cautious about the source of lava, he correctly concluded that it extends all over the earth. Adumbrating the concepts of isostasy and asthenosphere, he also inferred that this reservoir is "viscous and pasty" and can, thus, feed the biggest volcanoes indefinitely without causing any underground collapse (see Richet, 2005). It was at that time that the word *magma* began to take on its modern meaning (Gohau, 1998). Until then, it had meant viscous or gelatinous pastes used in pharmacy. This new importance of volcanism even misled the great astronomer William Herschel (1738–1822) to observe in April 1787 at 10:36 p.m. three volcanoes in the dark part of the new moon. He then concluded that "two of them are either already nearly extinct, or otherwise in a state of going to break out, which perhaps may be decided next lunation. The third shows an actual eruption of fire, or luminous matter."

1.4.2.1 *The New Importance of Silicate Melts*

In Scotland, the physician James Hutton (1726–97) had already assumed that the earth was hot at depth. He was, in fact, claiming that fire, and not water, is the main natural agent. According to the theory he first sketched in 1785—late in his life—the earth is a heat engine that gives rise to the great geological cycles of erosion, sedimentation, petrification, and finally mountain-building. For Hutton, there was no doubt that granite had an *igneous* origin, a term whose oldest known occurrence is found in a 1792 book by the Irish scientist Richard Kirwan (1733–1812). Although Dolomieu's views fitted well within this *plutonist* scheme, there was considerable reluctance to admit that basalt is indeed a volcanic rock. During the first decades of the 19th century, the neptunist school would follow Abraham Gottlob Werner (1749–1817), the most famous geologist of his time, and continue to defend the old ideas of an aqueous origin for granite and basalt through deposition of both rocks in highly mineralized primitive solutions (e.g., Werner, 1791).

Another Scot, James Hall (1761–1832) resolved to provide an experimental basis for his friend Hutton's ideas. With great ingenuity, and a certain contempt of danger, he showed that pressure is an important factor for phase stability within the earth (Hall, 1806–1809). Limestone, for instance, does not decompose when heated under pressure, but transforms into marble. Hall's other main achievement was his discovery, in 1790, that glass forms when the cooling rate of the melt is too high for crystallization to proceed, a result that he published only 8 years later. This discovery marked an abrupt change in perspective because phenocrysts could no longer be considered as the remnants of former rocks but were recognized to be the first minerals to form on cooling. These conclusions were soon put to practical use. In France, the chemist Jean-Antoine Chaptal (1756–1832) attempted to use basalt as a starting product to make bottles, but his efforts ended in failure because devitrification could not be avoided on cooling.

These advances had obvious consequences on the still fledging discipline of petrology. The presence of coarse minerals pointed to very slow cooling, whereas that of glass was clear evidence for rapid cooling of volcanic origin. From careful observations made on crushed rocks with the use of the optical microscope and the blowpipe, Louis Cordier (1777–1861) concluded in 1816 that all volcanic rocks are essentially made up of a few minerals: feldspar, pyroxene, olivine, and iron titanates first, and also amphibole, mica, leucite, and hematite. Of course, the same minerals were observed in coarse-grained rocks, consistent with their igneous origin. Another significant result achieved at that time was melting of quartz under the blowpipe. Vitrification of pure SiO_2 was achieved in tiny amounts by Marcet (1813) and in larger quantities by Marc-Antoine Gaudin (1801–80) who, in 1839, drew fibers which were "resembling steel in elasticity and tenacity." After four millennia of glassmaking, it had at last become possible to melt silica without a flux.

Considerably more important were the temperature measurements made by Cordier in mines. He reported in 1827 that the geothermal gradient is about 1°C per 30 m and concluded that, at some depth, temperatures are much higher than the melting point of any rock. Below a solid crust thinner than 100 km was lying a boundless "sea of fire" from which all igneous rocks derived (Fig. 1.14). This view of an earth made up mostly of silicate melts would be immensely popular. Temperatures of about 2×10^5°C were estimated at the center of the earth from the hypothesis of a constant geothermal gradient, even though this assumption was inconsistent with the theory of heat conduction published in 1822 by Joseph Fourier

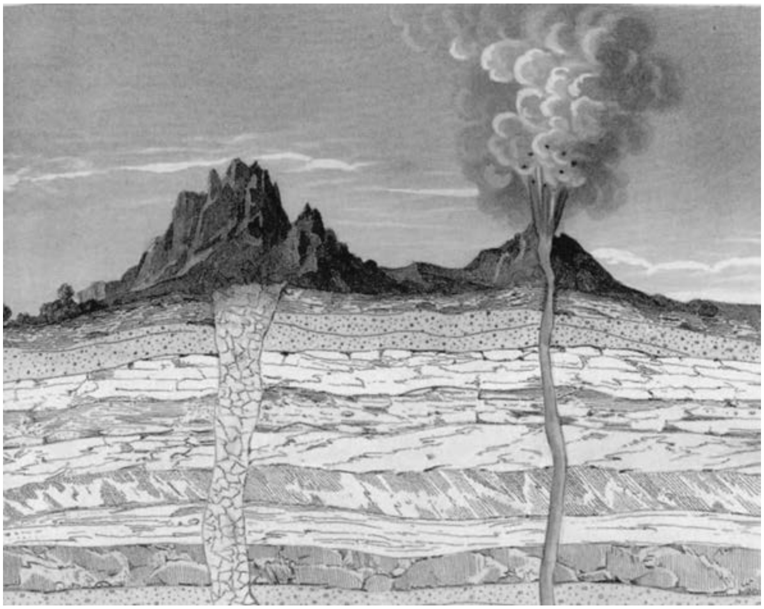

FIG. 1.14 A 19th century concept which is still present in the popular mind: the sea of fire with its direct connection with active and extinct volcanoes (With, 1874).

(1768–1830). In fact, Fourier's main goal when he set up his famous theory had been to determine the age of the earth from its cooling history (see Richet, 2007). For lack of relevant thermal conductivity and heat capacity measurements, however, Fourier (1820, 1824) had himself refrained from any real numerical application.

The real attack against the sea of fire would come from one of the founders of thermodynamics, William Thomson (1824–1907), later known as Lord Kelvin of Largs. As a great pioneer of geophysics, Thomson set out to place geology on a rigorous, quantitative footing. In 1863, he first demonstrated that the earth is not liquid, but essentially solid and "at least as rigid as steel." By using Fourier's theory of heat conduction, he then attempted to determine the age of the earth from current surface temperature and geothermal gradient (e.g., Burchfield, 1990; Richet, 2007). When following Buffon and Fourier, without their cautiousness, Thomson (1895) thus was mistaken when he eventually limited the age of the earth to about 24 million years. But the stress he had put on the need for good physical measurements for rocks and melts was already bearing fruit.

1.5 THE PHYSICAL CHEMISTRY OF MELTS

1.5.1 The Measurements of Physical Properties

For basalt, Thomson inspired in England the first measurements of the enthalpy of melting (Roberts-Austen and Rücker, 1891) and in the United States of the variation of the melting temperature of a rock with pressure (Barus, 1893). It was at that time that geologists began to show serious interest in melt viscosity. While Becker (1897) tried to estimate it from field observations, Doelter (1902) was measuring it to compare it to that of various molten minerals and rocks. Such physical work complemented well the systematic efforts made since the middle of the 19th century to reproduce the mineralogy and texture of igneous rocks in the laboratory (see Gohau, 1997; Young, 2003).

Following Kelvin's recommendations, a group of scientists was willing to make geology benefit from the new science of chemical thermodynamics, whose principles had been laid out by Josiah Willard Gibbs (1839–1903). With the support of the steel tycoon Andrew Carnegie (1835–1919), they created in 1905 the Geophysical Laboratory of the Carnegie Institution of Washington. One of the first goals was the establishment of a thermodynamic temperature scale up to 1755°C (see Sosman, 1952). In addition, the quenching method was designed to determine phase equilibria of materials whose transformations tend to be extremely sluggish (Day et al., 1906; Shepherd et al., 1909). Interest in the physical chemistry of silicate melts and glasses ranked high in the geological work to be performed and in its potential industrial applications (e.g., Bowen, 1918; Fenner and Ferguson, 1918; Morey, 1919; Morey and Merwin, 1932). Other early major achievements were the determination of the $CaO\text{-}Al_2O_3\text{-}SiO_2$ phase diagram by Rankin and Wright (1915), the annealing studies (see the following) of Adams and Williamson (1920), the recognition of the importance of experimental studies of diffusion by Bowen (1921), and the discovery by Greig (1927) of liquid immiscibility in binary alkaline earth silicates.

Glass also played a major role in the theory of rupture published in 1920 by Alan A. Griffith (1893–1963). For practical reasons, glass fibers had been selected by Griffith to demonstrate the considerable lowering of breaking stress by surface defects. A tremendous increase of this stress with decreasing fiber diameter was indeed observed (Fig. 1.15); this effect was ultimately due to the fact that "a fiber consisting of a single line of molecules must possess

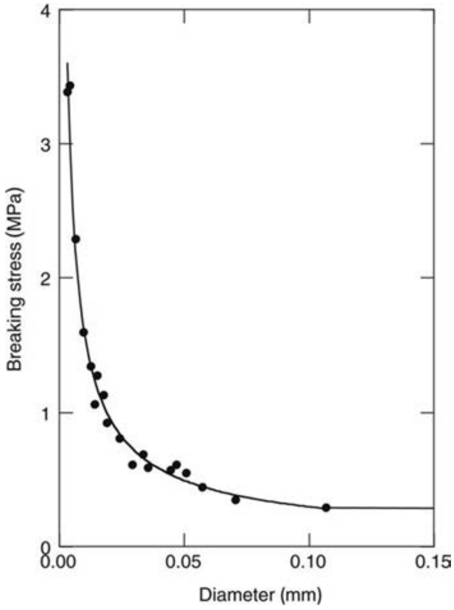

FIG. 1.15 Breaking stress against diameter of glass fibers. Data of Griffith (1920) for a glass of unspecified composition (1 MPa = 10 bars).

the theoretical molecular tensile strength." In the form of fibers, glass had more strength than steel, but it would take two decades to put this advantage to practical use for materials reinforcement.

The physical chemistry of liquid silicates also became of great importance to metallurgy. Slags, which are silica-poor melts, had been known ever since the beginnings of iron metallurgy because the ore impurities, mostly silicates, melted and coalesced as inclusions in the metal sponge that was obtained at the end of the process (e.g., Tylecote, 1992). The smith was getting rid of them by hammering the sponge, but there was no apparent need to pay attention to their properties. This situation had begun to change when the blast furnace was invented in the 13th century and pig iron—a liquid carbon-metal alloy—was recovered at the bottom of the furnace, with the molten slag left above. Then, it was realized in the 19th century that desulfurization and dephosphorization of the metal could be controlled through exchange reactions with the slag phase (Mills, 2018).

Eventually, thermodynamic modeling of such reactions became an important goal. Hence, metallurgists were among the first to measure extensively activities of oxides in melts (e.g., Rein and Chipman, 1965) and to perform phase equilibria calculations (see Richardson, 1974). Especially in Germany, metallurgists also pioneered measurements of physical properties such as density and viscosity (see the studies listed by Bottinga and Weill, 1970, 1972). Likewise, it was with the support of the metallurgical industry that Bockris and coworkers measured the electrical conductivity (Bockris et al., 1952) and viscosity (e.g., Bockris and Lowe, 1954) of silicate melts and arrived at the modern picture of partially ionic liquids made up of groups of various sizes.

1.5.2 Toward the Glass Transition

From the mid-19th century, glass, in turn, had benefited from the progress of chemistry and physics to which it had contributed so much. It was known that vitrification is not restricted to silicates but can also obtain in organic substances such as sugars. Even an element—selenium—had a vitreous form. These substances had strange properties, as revealed by measurements that had either fundamental or industrial motivations. Chevandier and Wertheim (1845) observed that the density and "elasticity coefficient" of quenched glass increases upon annealing, on average by 4.5‰ for the density. Because of their rigidity, glasses were considered as particular forms of solids but their relationships to crystalline polymorphs were not clear. As they were assigned definite melting temperatures, another curious observation was made in 1851 by Johann Wilhelm Hittorf (1824–1914), when he noticed that selenium glass was "melting" without any heat effect.

At the end of the 19th century, work by Gustav Tammann (1861–1938) marked an important turning point. While investigating the relationships between glass and crystal, Tammann (1898a) found that crystallization proceeds in two steps, namely, formation of "crystallization centers" followed by growth of crystals. For both nucleation and growth, the rate varies with temperature according to a bell-shaped curve (Fig. 1.16). From cooling experiments performed on scores of liquids of many kinds, Tammann (1898b), in addition, established the kinetic nature of the glass transition and stated that, at least in small amounts, most liquids could vitrify if cooled rapidly enough. Because the glass-forming ability of a liquid was determined by its reluctance to crystallize, Tammann could define glass as "a non-crystalline, strongly supercooled melt."

FIG. 1.16 Rates of crystal growth and nucleation against extent of supercooling for a glass-forming liquid whose viscosity increase is also illustrated. *Redrawn from Tammann (1925).*

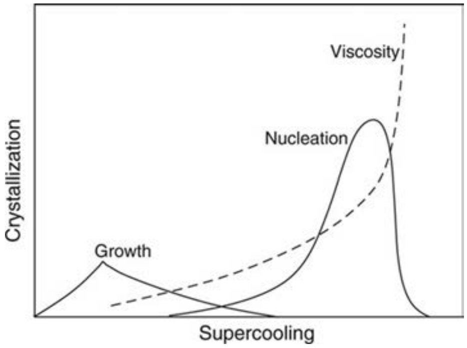

Following the discovery that glasses with high electrical conductivities could act as electrolytes, another important observation was made at the same period during which the glass electrode was invented by Haber (of ammonia synthesis fame) and Klemensiewicz (1909). The notion of pH had just been formulated so that, after optimization of its chemical composition, the glass electrode became in a few decades the most widely used chemical instrument in both academic and industrial contexts (Belyustin and Ivanovskaya, 2018).

In addition, abrupt variations of properties were observed when a glass is heated during measurements of thermal expansion (Callendar, 1887) or dielectric constant (Flemming and Dewar, 1897). Curiously, however, these anomalies elicited little interest.

The development of platinum-based thermocouples, calibrated through gas thermometry, made accurate measurement of high temperatures possible at the beginning of the 20th century. The improved measurements of physical properties made over large temperature ranges led to a better understanding of the glass and melt relationship. Viscosity, for instance, was extensively studied for soda-lime compositions by Washburn and Shelton (1914).

In his pioneering high-temperature calorimetric investigation of silicate glasses and crystals (Fig. 1.17), White (1919) lucidly reported that several of the glasses “show a decided increase in specific heat at some fairly elevated temperature. No explanation has been

FIG. 1.17 Glass transition of $NaCaAl_{1.5}Si_{2.5}O_8$ observed in drop calorimetry experiments (White, 1919) as a break in the mean heat capacity curve, $C_m = (H_T - H_{298})/(T - 298)$, where H is enthalpy.

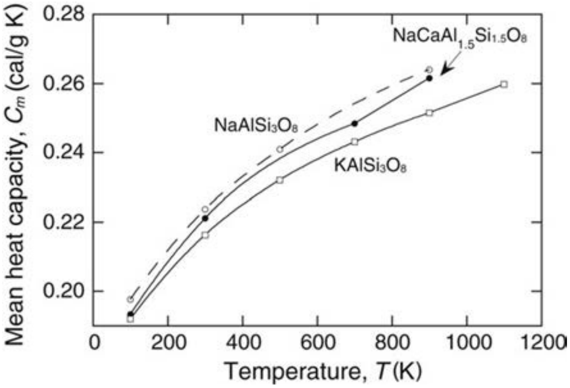

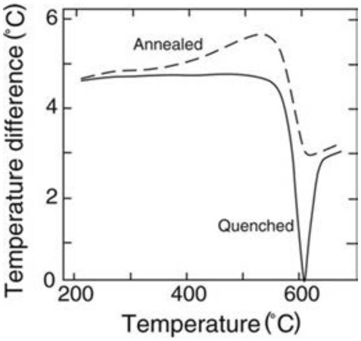

FIG. 1.18 Glass transition of annealed and quenched samples of window glass in differential thermal analysis experiments (Tool and Eichlin, 1925).

established for any of these facts. It seems probable that the increase in specific heat would have appeared if they had been carried higher. It may be a phenomenon of considerable importance."

At about the same time, So (1918) and Tool and Eichlin (1920) also observed anomalous thermal effects for silicate glasses in narrow temperature intervals near the empirical annealing temperatures (Fig. 1.18). Similar observations were made by Gibson et al. (1920) for some alcohols, while Peters and Cragoe (1920) described analogous variations of the thermal expansion coefficient of silicate glasses (see Richet and Bottinga, 1983). Glass formation was thus associated, not with any discontinuous change in first-order thermodynamic properties (e.g., volume, enthalpy), but with rapid variations of second-order thermodynamic properties.

It is during this period that Adams and Williamson (1920) heralded the beginning of relaxation studies when they investigated the internal stresses that build up when a glass-forming liquid is cooled and made their famous analysis of the rate at which the ensuing strain and birefringence can be released on annealing. This work was of particular importance for optical glass. An important practical outcome would be standardization of working operations in terms of viscosity for the strain point ($10^{13.5}$ Pa s), the annealing point (10^{12} Pa s), the deformation point ($10^{10.3}$ Pa s) and the softening point ($10^{6.6}$ Pa s).

Before any structural information was available, even for silicate crystals, Alexander A. Lebedev (1893–1969) noted that the birefringence of optical glass disappeared upon annealing near the 575°C temperature of the α-β transition of quartz. In 1921, he assumed that glass contained "minute quartz crystals," forming themselves solid solutions, such that "annealing is not so much the removal of stress as the attaining of complete polymorphic transformation." These views formed the basis for the microcrystalline hypothesis, according to which glass was made up of a disordered arrangement of very small crystals whose structure was similar to that of a stable crystalline form (see Evstropyev, 1953).

In other measurements, Tool and Eichlin (1924) observed that thermal effects in the annealing range depend on cooling rate, which in turn causes glass properties to depend on thermal history (Fig. 1.18). Extensive work by a number of investigators, especially Tool and Eichlin (1924, 1931, and references therein), revealed that a state of equilibrium could be attained through "molecular rearrangement" in crystallite-free materials. There was, therefore, still no hint of a glass-to-liquid transition. Tool and Eichlin (1931) noted that these transformations were taking place at "effective" temperatures, later called *fictive* temperatures (Tool, 1946), which were slightly higher than the annealing temperatures. For viscosity,

FIG. 1.19 Structural relaxation in viscosity measurements at 486.7°C on fibers of a window glass (Lillie, 1933). The *lower curve* refers to a newly drawn sample whose fictive temperature was higher than the run temperature, the upper curve to a sample first annealed at 477.8°C for 64h. The convergence of the curves indicates attainment of thermodynamic equilibrium in about 2000min.

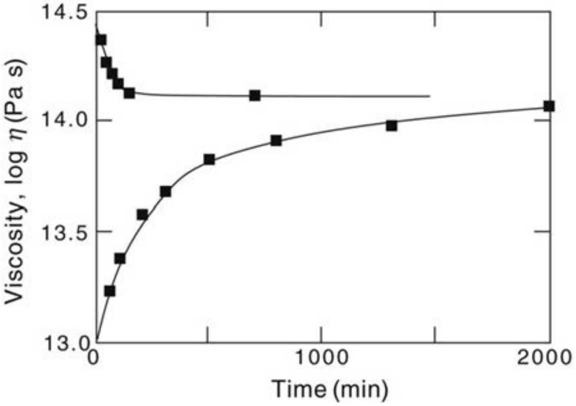

Lillie (1933) then showed how equilibrium properties can be measured through reversal experiments made on samples whose fictive temperature is initially higher and lower than the run temperature (Fig. 1.19; see also Section 2.1.1).

Another important step was recognition that the viscosity of glass-forming liquids does not follow Arrhenius laws,

$$\eta = \eta_0 \exp\left(\Delta H\eta / RT\right), \tag{1.1a}$$

$$\log \eta = A + 2.303\, \Delta H\eta / RT, \tag{1.1b}$$

where $A = \log \eta_0$ is a preexponential term and $\Delta H\eta$ the activation enthalpy for viscous flow. To account for the nonlinear variations of $\log \eta$ against reciprocal temperature, Fulcher (1925), Vogel (1921), and Tammann and Hesse (1926) proposed instead the equation

$$\log \eta = A + B/(T - T_1), \tag{1.2}$$

where A, B, and T_1 are constants. This TVF Eq. (1.2) embodies the fact that viscosity would become infinite at the T_1 temperature. This intriguing feature is intimately connected with the still unsolved fundamental problem of the glass transition. Further work would show that equations of the same form also account for the temperature dependence of other transport and relaxation properties (i.e., electrical conductivity, atomic diffusivity, dielectric and structural relaxation times, or even spin-lattice relaxation). However, the parameter, T_1, which is sometimes called the Vogel temperature, is specific to each property considered.

Although they could not determine unambiguously the nature of glass, Parks and Huffman (1927) recognized early its specificity as a distinct state of matter. Relying on their heat capacity measurements on organic substances (Fig. 1.20), they wrote:

> While there is no definite temperature, comparable to the melting point of a crystal, at which all properties undergo a sharp change, there is nevertheless a temperature interval, definite and reproducible, in which a number of properties change with a rapidity approaching that observed in the case of the melting process of a crystal. In brief, there is a softening region instead of a melting point. The glass as it exists below the softening region differs so markedly from the liquid existing above that it might well be considered as a different state of the substance. For this reason we have recently suggested the possibility of regarding glass as a fourth state of matter, distinct from both the liquid and crystalline states and yet showing to some extent characteristics of both these states.

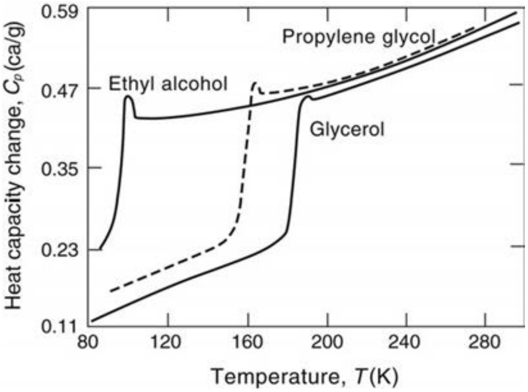

FIG. 1.20 Heat capacity changes of organic substances in the glass transition region (Parks and Huffman, 1927).

At last, consistent with Descartes' ideas, a new kind of transition, the glass transition, was defined from such variations of second-order thermodynamic properties. Without any reference to the polymorphic-like transformations assumed by Lebedev, Tool and Eichlin, or other workers, the very viscous liquid (at high temperature) was separated from the glass (at low temperature) by a transition at a temperature denoted by the symbol T_g. This new field of glass science was ably reviewed in books by Tammann (1933) and by Morey (1938) for silicates. Glass had definitely taken a much broader meaning by designating as glass any material that does not crystallize on cooling from the molten state, including the ubiquitous organic polymers today known as plastics.

1.5.3 The First Glimpses of Structure

Whereas a glass is a hybrid phase characterized by a fixed atomic arrangement, like in a crystal, and by the lack of long-range order, like in a liquid, a melt is a phase whose structure changes rapidly in response to temperature or pressure variations. Because the term *configuration* designates any microscopic arrangement of matter consistent with a given macroscopic state of the system, in the 1930s the physicists Franz Simon (1893–1956) and John D. Bernal (1901–71) termed *configurational* those contributions to physical properties that are associated with structural changes within the liquid. Deciphering the nature of these changes has proven to be an extremely difficult task. For a long time, structural studies have been restricted to glasses. Conclusions have often been applied without the necessary caution when using glass as a proxy for the liquid state. Direct investigation of the structure of liquid at high temperature has become possible only recently, as will be described in later chapters.

The starting point of structural studies is that glass lacks long-range order, but also that some short-range order necessarily exists because the bonding requirements of each kind of atom prevent complete bond disorder. From the mid-1920s, X-ray diffraction methods have allowed the structure of the main crystalline silicates to be determined (e.g., Bragg, 1937). The young William H. Zachariasen (1906–79) was struck by the small energy and volume differences between glasses and crystals. By assuming that the principles of structural chemistry newly established for crystal should also apply to glass, Zachariasen posited that both phases share the same basic structural elements. Because glasses lack symmetry and periodicity, they differ from crystals by the fact that disorder begins right at the scale of first-neighbor distances. In his famous 1932 paper, Zachariasen went on to summarize in three rules the conditions for glass formation:

> An oxide glass may be formed
>
> 1. If the sample contains a high percentage of cations which are surrounded by oxygen tetrahedra or by oxygen triangles
> 2. If these tetrahedra or triangles share only corners with each other
> 3. And if some oxygen atoms are linked to only two such cations and do not form further bonds with any other cations

From the beginning, two extreme situations have thus been depicted by the Lebedev and Zachariasen schools, the disagreement dealing with the extent of medium-range order that prevails in glass. The first structural studies of glass made with X-ray diffraction had been inconclusive for lack of adequate methods to deal with the experimental X-ray scattering curves of amorphous substances (e.g., Wyckoff and Morey, 1925; Randall et al., 1930). The situation changed when the method of Fourier analysis was designed by Zernicke and Prins (1927) to determine radial distribution functions of liquids. As shown in Fig. 1.21, the method was pioneered by Bertram E. Warren (1902–91) for oxide and silicate glasses. In studies of SiO_2 and B_2O_3 glass, Warren (1934) and Warren et al. (1936) confirmed Zachariasen's first rule by showing that Si and B are coordinated by four and three oxygens, respectively, and each oxygen by two Si or B. They also coined the term *random network* to describe the three-dimensional disordered arrangement described by Zachariasen. Work on soda-silica glass (Warren, 1934, Warren and Biscoe, 1938) then showed that two different kinds of oxygen (later called bridging and nonbridging) must be distinguished depending on whether they are bonded to only one or to two silicons (Fig. 1.22).

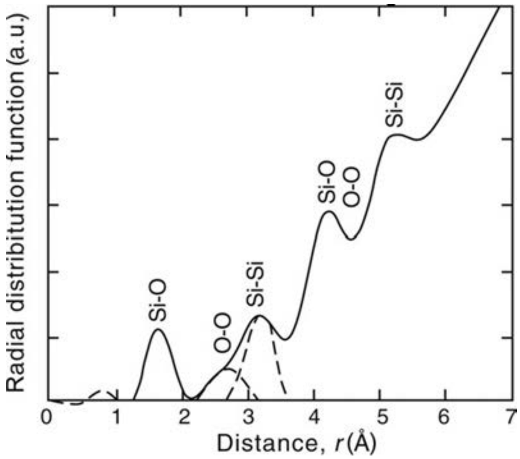

FIG. 1.21 The X-ray radial distribution function of SiO_2 glass (Warren et al., 1936), the first to be determined for silicate glasses. The peak positions yield the distances between first- and second-nearest neighbors, which can be assigned from known ionic radii or interatomic distances in relevant crystals. For well-resolved peaks, the number of neighboring atoms involved can be derived from the peak areas.

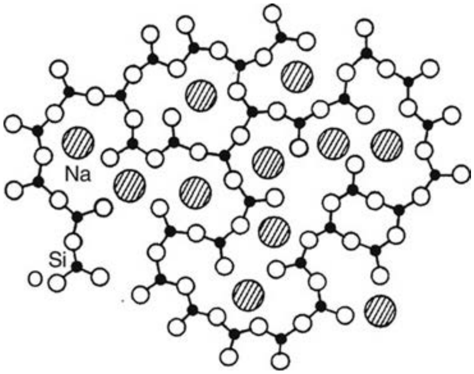

FIG. 1.22 Two-dimensional projection of the structure of a soda-silica glass. As derived from X-ray data, this random network also accounted structurally for the existence of gradual (instead of abrupt) softening, viscosity decrease upon Na_2O addition (through fragmentation of the silicate network), and electrical conduction (through hopping of the loosely bound Na atoms). *From Warren and Biscoe (1938).*

Other methods began to be used to investigate glass structure. Right after the discovery of the Raman effect (Raman and Krishnan, 1928), the spectrum of quartz was recorded by a number of spectroscopists (e.g., Pringsheim and Rosen, 1928). The resemblance of the Raman spectrum of quartz with the spectra of silica, crown, and flint glasses was pointed out by Gross and Romanova (1929). Despite the technical difficulties of Raman work made with mercury lamps, a variety of glasses were studied in more detail by Kujumzelis (1936). His spectra for SiO_2 and B_2O_3 glasses (Fig. 1.23) compare remarkably well with modern results (for SiO_2, see the background corrected spectrum of Fig. 5.21). Each glass was found to have a characteristic spectrum that was determined by the kinds of molecular groups present in the structure. In accord with the ideas of Zachariasen and Warren, Kujumzelis correctly attributed the

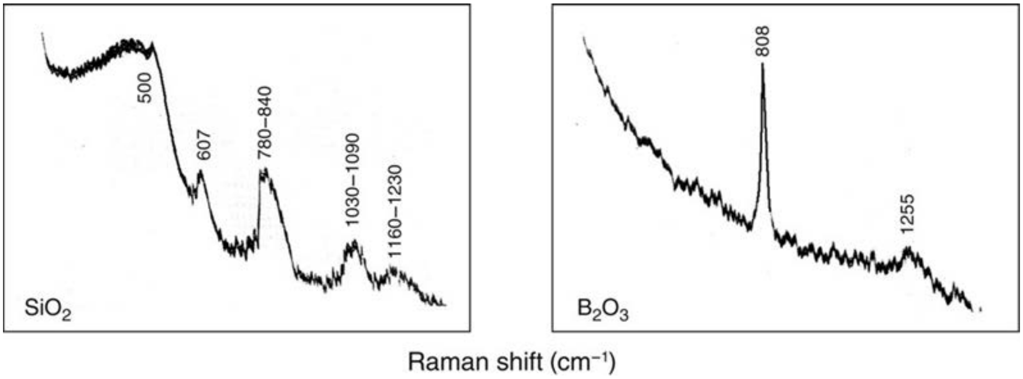

FIG. 1.23 Raman spectra of SiO_2 and B_2O_3 glasses. The sharp peak at 808 cm^{-1} in the B_2O_3 spectrum would later be shown to be characteristic of the so-called boroxol rings. *From Kujumzelis (1936).*

bands below 550 cm^{-1} to lattice modes and noted that Al could substitute for Si without marked structural changes. Although the basis for such work would not be available for a few more decades, he also pointed out that systematic measurements were needed to make reliable specific band assignments.

Together with the notion of bridging and nonbridging oxygens, the distinction between network-former and network-modifier cations was another concept of fundamental importance. Warren and Pincus (1940) used it to discuss liquid immiscibility in binary metal oxide-silica systems in terms of competition of cations for bonding with nonbridging oxygens, whose outcome is determined by the ratio Z/r_c of the electric charges and ionic radii of cations. Along similar lines, Adolf Dietzel (1902–93) introduced in 1942 the notion of field strength, $I = Z/a^2$, where a is the distance between ions (metal cation and oxygen, in general), to rationalize the systematic variations of devitrification, compound formation, and melting temperatures as a function of the nature of cations. Later, Stevels (1953, 1954) would recognize the control exerted on physical properties by the degree of polymerization through a parameter X designating the average number of nonbridging oxygens per tetrahedrally coordinated cation (which is now more explicitly denoted by NBO/T).

As will be described in other chapters of this book, random network models are probably too extreme in denying significant medium-range order. Nonetheless, Zachariasen's rules still represent a useful starting point for discussion of glass structure. On the other hand, it is ironic that the strongest evidence for structural microheterogeneity presented by the microcrystalline school (see Evstropyev, 1953) was the result of metastable liquid-liquid phase separation that would be discovered in the early 1960s (see Mazurin et al., 1984).

1.5.4 The Search for New Compositions

From prehistory until the end of the 19th century, the oxides of very few elements had been used for making glass. Leaving aside coloring elements, whose concentration is low, these were silicon, sodium, calcium, aluminum, potassium, and lead. In England, a minister named Harcourt and the physicist George Gabriel Stokes (1819–1903) succeeded in incorporating a variety of other elements in glass (see Vogel, 1994). Harcourt even discovered the glass-forming ability of B_2O_3 and P_2O_5, but his efforts had few practical applications.

In Germany, the great optician Ernst Abbe (1840–1905) wondered whether the narrow range of chemical composition of glass was why both refractive index and dispersion were always increasing in a way similar to density. Was it also the reason that lenses had known little improvement since the invention of flint glass? At Abbe's instigation, Otto Schott (1851–1935) had begun in 1881 systematic investigations of the density-optical property relationships of silicate glasses in a work supported by a scientifically oriented German government. By using all the elements known at that time, he could incorporate 28 of them in concentrations higher than 10 wt% (see Hovestadt, 1900). For instance, introduction of barium, a heavy element, caused an increase of the refractive index of glass without increasing the dispersion. Such observations proved especially useful for microscopy and photography applications. From this work, it was becoming possible to tailor a glass composition for a given specific application.

At the turn of the 20th century, the various processes used to make flat and container glass underwent mechanization (see Cable, 1990), but such an industrial mutation did not induce any important change in glass composition. Further progress in this respect resulted from specific needs. In the United States, a search was, for example, made for glasses with low thermal expansion coefficients because the lights of train cars were breaking under the thermal shock caused by heavy rains. Addition of boron oxide for improving the homogeneity of optical glass had already been described by Faraday (1859). After having also been used by the Schott company to make glass for thermometers, borosilicates resulted in 1908 in the invention of Nonex glass by Corning Glass Works. This lead borosilicate glass was an instant success, but sales soon dropped because the material no longer needed replacement (see Dyer and Gross, 2001). The use of glass for cookware was then considered, but lead-bearing materials were unsuitable for such an application.

Further research eventually resulted, in 1915, in the famous sodium borosilicate glass dubbed Pyrex, which has an extremely small coefficient of thermal expansion ensured by the presence of about 12 wt% B_2O_3. Since then, borosilicates have found innumerable uses, thanks to their chemical inertness combined with lower temperatures of melting and homogenization than for silicates (Youngman, 2018). These advantages result from the facts that B_2O_3 has itself a very low melting temperature of 712 K and that mixing of B^{3+} and Si^{4+} in the anionic framework, made possible by association of boron with charge-compensating cations, enhances this effect through the entropy of Si, B mixing. Hence, the depressing effects of B_2O_3 as a flux on liquidus temperatures are similar to those of alkalis, but with the important advantage of not significantly affecting the polymerization state of the material and thus not degrading its stability.

The increasing diversity of chemical composition made possible prediction of a given physical property from the composition of the glass. Near room temperature, linear variations of various properties of silicate glasses were observed as a function of the concentration of oxide components (e.g., Winkelmann, 1893). Further experimental work revealed deviations from additivity, which were incorporated in more complex models (Gehlhoff and Thomas, 1926). However, no such effort could be attempted for melts because experimental data would be badly lacking for a very long time.

Chemistry could also help improve properties without changing the bulk composition of the glass. This is the case of chemical tempering, which ensures shock resistance much greater than with the usual quenching procedure. The internal stresses that ensure resistance to shocks are achieved through replacement of sodium by potassium via chemical exchange between the surface of the glass and a molten salt (Karlsson and Wondraczek, 2018). New applications could otherwise be found for existing glasses. A calcium borosilicate, the so-called E glass, was extensively used for electrical insulation before its excellent mechanical properties were recognized. From the middle of the 20th century, it has been with this glass and new related compositions that mechanical reinforcement by glass fibers has been realized in composite materials (Li and Watson, 2018).

More recently, new uses of silicate glasses have been made possible by either their extremely high purity or, in contrast, by the very wide extent of their solid solutions. Whereas the optical fiber, without which the internet would not exist, thus relies on high-purity, defect-free SiO_2 fibers (Ballato, 2018), borosilicate glasses have been selected for nuclear waste disposal because of their ability to dissolve large amounts of many different nuclides, combined with their low melting temperature and high resistance to corrosion by aqueous solutions (see Wicks, 1985; Pinet et al., 2018). Likewise, incineration of municipal and industrial waste produces a variety of glass phases that result in a considerable volume reduction of the residues, stabilizes them against weathering, and may even yield products of practical interest (Heuss-Aßbichler and Bayuneso, 2018).

Other completely new glass families have been invented in the last few decades formed, for instance, from sol-gel processes (Almeida and Gonçalves, 2018; Malfait et al., 2018), from fluorides and chalcogenides (Bureau and Lucas, 2018), or in metallic systems (Louzguine-Luzgin and Inoue, 2018). These glasses have found many applications, thanks to their specific optical, mechanical, or thermal properties. Referring to Kurkjian and Prindle (1998) for other insights on glass compositions, we will conclude this short description by mentioning that important uses of some glasses in fact rely instead on the intrinsic instability of the material. This point is particularly well exemplified by the silica-poor, alkali-rich *water glasses*, which are important binders or precursors in industrial chemical syntheses (Rogendorff, 2018), and also by the very rapidly developing field of bioglasses, in which large concentrations of modifier ions and nonbridging oxygens allows for in vivo degradation and concomitant regeneration of soft or bone tissue (Brauer and Jones, 2018).

1.5.5 A Geological Outlook

At the end of this fast journey through time, the considerable interest raised by silicate melts in earth sciences does not need to be emphasized. The data of Table 1.3 illustrate the diversity in chemical composition of lavas. A noteworthy feature of these analyses is the continuous increase in SiO_2 content observed throughout magmatic evolution. This trend is the result of partial melting and fractional crystallization events grouped under the term of magmatic differentiation (see Young, 1998).

In the late 19th century, it was assumed that liquid-liquid immiscibility was another process effective in nature. Ironically, the observation of liquid unmixing in simple iron and alkaline earth silicates by Greig (1927) ruled out this process as a cause of magmatic differentiation because it was also observed that miscibility gaps disappear rapidly upon addition of alumina at concentrations much lower than those found in igneous rocks. This was not the final answer to the question, however. The actual occurrence of liquid immiscibility in terrestrial and lunar lavas has later been demonstrated (Roedder and Weiblen, 1970), triggering new experimental studies (e.g., Philpotts, 1976) and illustrating once more the fruitful interplay of field and laboratory observations.

Magmas are important not only in continents, but also in the oceanic crust. In the 1950s, exploration of the sea revealed that ocean floors are made up of basalt, implying that this igneous rock covers 70% of the earth's surface (Shand, 1949; Heezen et al., 1959). In the theory of plate tectonics (Dietz, 1961; Hess, 1962), magma plays a key role in creating new ocean floor when emerging at midocean ridges. Adiabatic melting in the rising part of the convection cells that circulate through the mantle is a fundamental aspect of the earth's activity.

Planetary exploration has also shown volcanic activity to be present on Mars and Venus and in the satellites of giant planets. Glass more than 4 billion years old has been brought

TABLE 1.3 Compositional Diversity of Natural Glasses and Igneous Rocks (wt%)[a]

	SiO_2	Al_2O_3	Fe_2O_3	FeO	MgO	CaO	Na_2O	K_2O	TiO_2
Fulgurite (Libya)	97.6	1.5		0.2		0.4	0.3		
Darwin glass[b]	87.4	8.0	0.2	1.9	0.8		0.1	1.0	0.5
Obsidian[c]	74.7	13.7	1.0	0.6	0.1	0.8	3.9	4.0	
Rhyolite[d]	73.9	13.5	1.5	1.1	0.4	1.1	3.6	4.4	0.3
Obsidian[e]	70.3	16.4	1.0	1.0	1.1	2.6	4.3	2.9	0.3
Trachyte glass[d]	62.3	17.3	3.1	3.4	0.5	2.4	6.8	4.4	
Phonolite[d]	57.9	19.6	2.9	2.1	1.1	2.1	8.0	5.4	0.6
Pele hair (Hawaii)	51.2	14.8	2.9	9.9	6.5	11.1	2.7	0.9	
Basalt glass[f]	50.9	15.7		9.1	8.6	12.1	2.2	0.2	1.2
Tephrite[d]	48.8	17.3	4.2	5.3	4.8	9.4	3.8	4.6	1.9
Peridotite[d,g]	42.3	4.2	3.6	6.6	31.2	5.0	0.5	0.3	0.6
Dunite[d,g]	41.1	1.9	3.9	10.1	40.6	1.1	0.2	0.1	0.1
Silica glass, Luna 20	98.9	0.7					0.1	0.1	0.2
Granite glass	72.9	14.8		2.5	0.3	2.7	2.2	4.2	0.5
Basalt glass[h]	52.8	15.4	0.2	10.0	6.8	10.8	1.1	1.1	1.8
Low SiO_2 glass	32.3	38.9		0.1	7.1	21.6			0.1

[a] *Compositions normalized to 100 wt% by neglecting the reported H_2O^+ and H_2O^- contents. The small MnO and P_2O_5 contents are not listed. See* Richet and Bottinga (1983) *and* Cox et al. (1979) *for references of analyses.*

[b] *Tasmania.*

[c] *Obsidian Cliff, Yellowstone.*

[d] *Average compositions, see* Cox et al. (1979).

[e] *Big Butte, Montana.*

[f] *Mid-ocean ridge, Famous zone.*

[g] *Melt not vitrifying.*

[h] *Fra Mauro.*

back from the moon's surface. It even appears that the surface of the primitive earth was probably covered by a magma ocean, more than 1000 km deep, at temperatures higher than 2000°C (Abe, 1997; Rama Murthy and Karato, 1997). From the long-gone magma ocean to the smallest currently active volcano, magma owes its fundamental importance to the fact that, at all scales, it is the most efficient agent for transporting matter, and energy, throughout the earth.

References

Abe, Y., 1997. Thermal and chemical evolution of the terrestrial magma ocean. Phys. Earth Planet. Inter. 100, 27–39.

Adams, L.H., Williamson, E.D., 1920. Annealing of glass. J. Franklin Inst.. 190, 597–631 and 835–870.

Almeida, R., Gonçalves, C., 2018. Sol-gel processes and products. In: Richet, P. (Ed.), Encyclopedia of Glass Science, Technology, History and Culture. J. Wiley & Sons, Hoboken, NJ.

Ballato, J., 2018. Optical fibers. In: Richet, P. (Ed.), Encyclopedia of Glass Science, Technology, History and Culture. J. Wiley & Sons, Hoboken, NJ.

Barus, C., 1893. The fusion constants of igneous rock. III. The thermal capacity of igneous rock, considered in its bearing on the relation of melting-point to pressure. Philos. Mag. 35, 296–307.

Becker, G.F., 1897. Some queries on rock differentiation. Am. J. Sci. 3, 21–40.

Belyustin, A.A., Ivanovskaya, I.S., 2018. The glass electrode and electrode properties of glasses. In: Richet, P. (Ed.), Encyclopedia of Glass Science, Technology, History and Culture. J. Wiley & Sons, Hoboken, NJ.

Beretta, M., 2018. Glass and the philosophy of matter in antiquity. In: Richet, P. (Ed.), Encyclopedia of Glass Science, Technology, History and Culture. J. Wiley & Sons, Hoboken, NJ.

Berthelot, M., 1887. Collection des anciens alchimistes grecs. vol. I. Georges Steinhel, Paris.

Bimson, M., Freestone, I.C., 1987. Early Vitreous Materials. British Museum occasional papers N°56, British Museum, London.

Bockris, J.O.M., Lowe, D.C., 1954. Viscosity and the structure of molten silicates. Proc. Roy. Soc. A226, 423–435.

Bockris, J.O.M., Kitchener, J.A., Ignatowicz, S., Tomlinson, J.W., 1952. Electric conductance in liquid silicates. Trans. Faraday Soc. 48, 75–91.

Bottinga, Y., Weill, D.F., 1970. Densities of liquid silicate systems calculated from partial molar volumes of oxide components. Am. J. Sci. 269, 169–182.

Bottinga, Y., Weill, D.F., 1972. The viscosity of magmatic silicate liquids: a model for calculation. Am. J. Sci. 272, 438–475.

Bowen, N.L., 1918. The significance of glass-making processes to the petrologist. J. Wash. Acad. Sci. 8, 88–93.

Bowen, N.L., 1921. Diffusion in silicate melts. J. Geol. 29, 295–317.

Boyle, R., 1661. Nova experimenta physico-mechanica de vi areis elastica et ejusdem effectibus facte maximam partem in nova machina pneumatica. A. Vlacq, The Hague.

Bragg, W.L., 1937. Atomic Structure of Minerals. Cornell University Press, Cornell.

Brauer, D.S., Jones, J.R., 2018. Bioactive glasses. In: Richet, P. (Ed.), Encyclopedia of Glass Science, Technology, History and Culture. J. Wiley & Sons, Hoboken, NJ.

Brill, R.H., 1999. Chemical Analyses of Early Glasses. vols. 2. Corning Museum of Glass, Corning.

Burchfield, J., 1990. Lord Kelvin and the Age of the Earth, second ed. The University of Chicago Press, Chicago.

Bureau, B., Lucas, J., 2018. Fluoride and chalcogenide glasses for mid-infrared optics. In: Richet, P. (Ed.), Encyclopedia of Glass Science, Technology, History and Culture. J. Wiley & Sons, Hoboken, NJ.

Cable, M., 1990. Classical glass technology. In: Zarzycki, J. (Ed.), Glasses and Amorphous Materials. In: Material Science and Technology, vol. 9. VCH, Weinheim.

Callendar, H., 1887. On the practical measurement of temperature: experiments made at the Cavendish Laboratory. Philos. Trans. R. Soc. Lond. A178, 161–230.

Charleston, R.J., 1980. Masterpieces of Glass from the Corning Museum of Glass. Henry Abrams, New York.

Chevandier, E., Wertheim, G., 1845. Notes sur l'élasticité et la cohésion de différentes espèces de verres. C. R. Acad. Sci. 20, 1637–1640.

Clay, R.S., Court, T.H., 1932. The History of the Microscope. Charles Grifin, London.

Colomban, P., 2018. Glazes and enamels. In: Richet, P. (Ed.), Encyclopedia of Glass Science, Technology, History and Culture. J. Wiley & Sons, Hoboken, NJ.

Cox, K.G., Bell, J.D., Pankhurst, R.J., 1979. The Interpretation of Igneous Rocks. George Allen & Unwin, London.

Day, A.L., Shepherd, E.S., Wright, F.E., 1906. The lime-silica series of minerals. Am. J. Sci. 22, 265–302.

Diderot, D., D'Alembert, J.L.R., 1751. Encyclopédie, ou dictionnaire raisonné des arts, des sciences et des métiers. Briasson, Paris.

Dietz, R.S., 1961. Continent and ocean evolution by spreading of the sea floor. Nature 190, 854–857.

Dixon, J.E., Cann, J.R., Renfrew, C., 1968. Obsidian and the origins of trade. Sci. Am. 218, 38–46.

Doelter, C., 1902. Die chemische Zusammensetzung und die Genesis Monzonitgesteine. Tschermaks Mineral. Petr. Mitt. b 195–225.

Dyer, D., Gross, D., 2001. The Generations of Corning. The Life and Times of a Global Corporation. Oxford University Press, Oxford.

Evstropyev, K.S., 1953. The Crystalline Theory of Glass Structure. The Structure of Glass. Proceedings of a Conference Held in Leningrad. Consultants Bureau, New York, pp. 9–15.

Faraday, M., 1859. On the manufacture of glass for optical purposes. In: Experimental Researches in Chemistry and Physics. Taylor and Francis, London, pp. 231–291.

Faujas de Saint-Fond, B., 1778. Recherches sur quelques volcans éteints du Vivarais et du Velay. Cuchet, Grenoble.

Faujas de Saint-Fond, B., 1797. Voyage en Angleterre, en Écosse et aux îles Hébrides. H.J. Jansen, Paris.

Fenner, C.N., Ferguson, J.B., 1918. The effect of certain impurities in causing milkiness in optical glass. J. Am. Ceram. Soc. 1, 468–476.

Flemming, J., Dewar, J., 1897. On the dielectric constants of certain frozen electrolytes at and above the temperature of liquid air. Proc. R. Soc. Lond. 61, 299–330.

Fourier, J., 1820. Extrait d'un mémoire sur le refroidissement du globe terrestre. Ann. Chim. Phys. 13, 418–437.

Fourier, J., 1824. Remarques générales sur les températures du globe terrestre et des espaces planétaires. Ann. Chim. Phys. 27, 136–167.

Foy, D., Vichy, M., Picon, M., 1998. In: Lingots de Verre en Méditerranée Occidentale (IIIe Siècle av. J.-C. - VIIe Siècle ap. J.-C.). Approvisionnement et Mise en Oeuvre, Données archéologiques et Données de Laboratoire. Annales du 14e congrès de l'Association Internationale d'Histoire du Verre, pp. 51–57.

Freestone, I., 2018. Roman glass. In: Richet, P. (Ed.), Encyclopedia of Glass Science, Technology, History and Culture. J. Wiley & Sons, Hoboken, NJ.

Fulcher, G.S., 1925. Analysis of recent measurements of the viscosity of glasses. J. Am. Ceram. Soc. 8, 339–355.

Gehlhoff, G., Thomas, M., 1926. Die physikalischen Eingenschaften der Gläser in Abhängigkeit von der Zusammensetzung. Z. Techn. Phys. 7, 105–126.

Gesner, K., 1565. De Omni rerum fossilium genere, gemmis, lapidibus, metallis et hujusmodi, libri aliquot, plerique nunc primum editi. Jacobus Gesnerus, Zürich.

Gibson, G., Parks, G., Latimer, W., 1920. Entropy changes at low temperatures. II. Ethyl and propyl alcohols and their equal molal mixtures. J. Am. Chem. Soc. 42, 1542–1550.

Gohau, G., 1997. Expériences anciennes sur la formation des roches cristallines, du dernier quart du XVIIIe siècle aux années 1850. Bull. Soc. Géol. Fr. 168, 813–820.

Gohau, G., 1998. L'origine de l'usage du mot magma en sciences de la terre. C. R. Acad. Sci. II 326, 743–750.

Greig, J.W., 1927. Immiscibility in silicate melts. Am. J. Sci. 13, 1–44 and 133–154.

Griffith, A.A., 1920. The phenomena of rupture and flow in solids. Philos. Trans. R. Soc. Lond. A221, 163–198.

Grose, D.F., 1986. Innovation and change in ancient technologies: the anomalous case of the Roman glass industry. In: Kingery, W.D. (Ed.), Ceramics and Civilization. III. High-Technology Ceramics, Past, Present, and Future. The American Ceramic Society, Columbus, pp. 65–79.

Gross, E., Romanova, M., 1929. Über die Lichtzerstreuung in Quarz und festen amorphen Stoffen, welche die Gruppe SiO_2 enthalten. Z. Phys. 55, 744–752.

Guettard, J.-É., 1770. Neuvième mémoire. Sur le basalte des Anciens et des Modernes. In: Mémoires sur différentes parties des sciences et arts. vol. 2. Laurent Prault, Paris, pp. 226–277.

Guettard, J.-É., 1779. Minéralogie du Dauphiné. vols. 2. Paris.

Haber, F., Klemensiewicz, Z., 1909. Über electrische Phasengrenzekräfte. Z. Phys. Chem. 67, 385–431.

Hackmann, W.D., 1978. Electricity from Glass: The History of the Frictional Electrical Machine 1600–1850. Sijthoff & Noordhoff, Alphen aan den Rijn.

Hales, S., 1723. Vegetable Staticks: or, an Account of Some Statical Experiments on the Sap in Vegetables. T. Woodward, London.

Hales, S., 1733. Haemastaticks: or, an Account of Some Hydraulic and Hydrostatical Experiments Made on the Blood and Blood-Vessels of Animals. W. Innis R. Mamby and T. Woodward, London.

Hall, J., 1806–1809. Accounts of a series of experiments, shewing the effects of compression in modifying the action of heat. Trans. R. Soc. Edinb. 6, 71–184.

Heezen, B., Tharp, M., Ewing, M., 1959. The floors of the oceans. I. The North Atlantic. Geol. Soc. Am. Spec. Paper. 65.

Hess, H.H., 1962. The history of ocean basins. In: Engel, A.E.J., James, H.L., Leonard, B.F. (Eds.), Petrologic Studies: A Volume in Honor of A. F. Buddington. Geol. Soc. Am., Washington, DC, pp. 599–620.

Heuss-Aßbichler, S., Bayuneso, A., 2018. Immobilization of municipal and industrial waste. In: Richet, P. (Ed.), Encyclopedia of Glass Science, Technology, History and Culture. J. Wiley & Sons, Hoboken, NJ.

Hooke, R., 1665. Micrographia: Or Some Physiological Descriptions of Minute Bodies Made by Magnifying Glasses with Observations and Inquiries Thereupon. James Allestry, London (Repr. Dover, New York, 1961).

Hovestadt, H., 1900. Jenaer Glas und seine Verwendung in Wissenschaft und Technik. Fischer, Jena (transl. by Everett, J.D., Everett, A. as Jena Glass and its Industrial Applications, MacMillan, London, 1902).

Ilardi, V., 2007. Renaissance Vision From Spectacles to Telescopes. Am. Philos. Soc., Philadelphia.

Karlsson, K.S.R., Wondraczek, L., 2018. Strengthening of oxide glasses. In: Richet, P. (Ed.), Encyclopedia of Glass Science, Technology, History and Culture. J. Wiley & Sons, Hoboken, NJ.

Kujumzelis, T.G., 1936. Raman-Effekt und Struktur der Gläser. II. Mitteiltung. Z. Phys. 100, 221–236.

Kurkjian, C.R., Prindle, W.R., 1998. Perspective on the history of glass composition. J. Am. Ceram. Soc. 81, 795–813.

Li, H., Watson, J.C., 2018. Continuous glass fibers for reinforcement. In: Richet, P. (Ed.), Encyclopedia of Glass Science, Technology, History and Culture. J. Wiley & Sons, Hoboken, NJ.

Lillie, H.R., 1933. Viscosity-time-temperature relations in glass at annealing temperatures. J. Am. Ceram. Soc. 2, 619–631.

Louzguine-Luzgin, D.V., Inoue, A., 2018. Structures, properties and uses of metallic glasses. In: Richet, P. (Ed.), Encyclopedia of Glass Science, Technology, History and Culture. J. Wiley & Sons, Hoboken, NJ.

Maignan, E., 1653. Cursus philosophicus concinnatus ex notissimis cuique principiis ac praesertim quoad res physicas instauratus ex lege naturae sensatis experimentis passim comprobata. R. Bosc, Toulouse.

Malfait, W.J., Wernery, J., Zhao, S., Brunner, S., Koebel, M.M., 2018. Silica aerogels. In: Richet, P. (Ed.), Encyclopedia of Glass Science, Technology, History and Culture. J. Wiley & Sons, Hoboken, NJ.

Marcet, A., 1813. On an easy method of procuring a very intense heat. Ann. Philos. 2, 99–100.

Matson, F.R., 1985. Glazed bricks from Babylon—historical setting and microprobe analyses. In: Kingery, W.D. (Ed.), Ceramics and Civilization. II. Technology and Style. The American Ceramic Society, Columbus, pp. 133–156.

Mazurin, O.V., Roskova, G.P., Porai-Koshits, E.A., 1984. Immiscibility diagrams of oxide glass-forming systems. In: Mazurin, O.V., Porai-Koshits, E.A. (Eds.), Phase Separation in Glass. North Holland, Amsterdam, pp. 103–142.

Merret, C., 1662. An Account of the Glass Drops Made by the Royal Society Meeting at Gresham College, appendix p. 353–362 to His Translation of Antonio Neri's Art of Glass, Wherein are Shown the Wayes to Make and Colour Glass, Paste, Enamels, Lakes, and Other Curiosities. O. Pulleyn, London.

Mills, K.C., 2018. Metallurgical slags. In: Richet, P. (Ed.), Encyclopedia of Glass Science, Technology, History and Culture. J. Wiley & Sons, Hoboken, NJ.

Moody, B.E., 1988. The life of George Ravenscroft. Glass Technol. 29, 198–210.

Moretti, C., 2004. La realizzazione del cristallo al piombo in Inghilterra. Analisi critica della ricetta attribuita a George Ravenscroft e aspetti ancora oscuri nel processo di sviluppo del vetro "flint" Rev. Staz. Sperim. Vetro 34 (1), 19–33.

Morey, G.W., 1919. An improved method for optical glass making. J. Am. Ceram. Soc. 2, 146–150.

Morey, G.W., 1938. The Properties of Glass. Reinhold Publishing Co., New York.

Morey, G.W., Merwin, H.E., 1932. The relation between the composition and the density and the optical properties of glass. I. The soda-lime-silica glasses. J. Opt. Soc. Am. 22, 632–662.

Oppenheim, A.L., Brill, R.H., Barag, D., von Saldern, A., 1970. Glass and Glassmaking in Ancient Mesopotamia. An Edition of the Cuneiform Texts Which Contain Instructions for Glassmakers, With a Catalogue of Surviving Objects. The Corning Museum of Glass Press, Corning.

Parks, G., Huffman, H., 1927. Studies on glass. I. The transition between the glassy and liquid states in the case of simple organic compounds. J. Phys. Chem. 31, 1842–1855.

Péligot, E., 1877. Le verre, son histoire, sa fabrication. Masson, Paris.

Peters, C., Cragoe, C., 1920. Measurements on the thermal dilation of glass at high temperatures. J. Opt. Soc. Am. 4, 105–144.

Philpotts, A.R., 1976. Silicate liquid immiscibility: its probable extent and petrogenetic significance. Am. J. Sci. 276, 1147–1177.

Pinet, O., Vernaz, E., Ladirat, C., Gin, S., 2018. Nuclear waste vitrification. In: Richet, P. (Ed.), Encyclopedia of Glass Science, Technology, History and Culture. J. Wiley & Sons, Hoboken, NJ.

Pringsheim, P., Rosen, B., 1928. Über den Ramaneffekt. Z. Phys. 50, 741–755.

Rama Murthy, V., Karato, S.I., 1997. Core formation and chemical equilibrium in the Earth; II, chemical consequences for the mantle and core. Phys. Earth Planet. Inter. 100, 81–95.

Raman, C.V., Krishnan, K.S., 1928. A new type of secondary radiation. Nature 121, 501.

Randall, J.T., Rooksby, H.P., Cooper, B.S., 1930. X-ray diffraction and the structure of vitreous silica. Z. Kristall. 75, 196–214.

Rankin, G.A., Wright, F.E., 1915. The ternary system CaO-Al_2O_3-SiO_2. Am. J. Sci. 39, 1–79.

Rein, R.H., Chipman, J., 1965. Activities in the liquid solution SiO_2-CaO-MgO-Al_2O_3 at 1600°C. Trans. AIME 233, 415–425.

Richardson, F., 1974. Physical Chemistry of Melts in Metallurgy. vols. 2. Academic Press, London.

Richet, P., 2000. L'âge du verre. Gallimard, Paris.

Richet, P., 2005. Dolomieu et l'origine profonde des laves. In: Gaudant, J. (Ed.), Dolomieu et la Géologie de Son Temps. Presses de l'Ecole des Mines, Paris, pp. 95–108.

Richet, P., 2007. A Natural History of Time. The University of Chicago Press, Chicago.

Richet, P., Bottinga, Y., 1983. Verres, liquides et transition vitreuse. Bull. Mineral. 106, 147–168.

Roberts-Austen, W., Rücker, A., 1891. On the specific heat of basalt. Philos. Mag. 32, 353–355.

Roedder, E., Weiblen, P.W., 1970. Silicate liquid immiscibility in lunar magmas as evidenced by melt inclusions in lunar rocks. Science 167, 641–644.

Rogendorff, H., 2018. Water glass. In: Richet, P. (Ed.), Encyclopedia of Glass Science, Technology, History and Culture. J. Wiley & Sons, Hoboken, NJ.

Shand, S.J., 1949. Rocks of the mid-Atlantic ridge. J. Geol. 57, 89–92.

Shepherd, E.S., Rankin, G.A., Wright, F.E., 1909. The binary systems of alumina with silica, lime, and magnesia. Am. J. Sci. 38, 293–333.

Shortland, A., Degryse, P., 2018. Ancient glass, Late Bronze age. In: Richet, P. (Ed.), Encyclopedia of Glass Science, Technology, History and Culture. J. Wiley & Sons, Hoboken, NJ.

So, M., 1918. Expansion of glass in connection with its optical and thermal properties. Proc. Tokyo Math. Phys. Soc. 9, 426–441.

Sosman, R.B., 1952. Temperature scales and silicate research. Am. J. Sci. 250A, 517–528.

Spallanzani, L., 1792–1797. Viaggi alle Due Sicilie e in alcune parti dell' Appennino. Stamperia di B. Comini, Pavia (tr. 1798. Travels in the Two Sicilies and Some Parts of the Appenines, J. Robinson, London).

Stern, E.M., 1995. Roman Mold-Blown Glass, the First Through Sixth Centuries. The Toledo Museum of Art, Toledo.

Stern, E.M., Schlick-Nolte, B., 1994. Frühes Glas der alten Welt. Verlag Gerd Hatje, Stuttgart.

Sternini, M., 1995. Le fenice di sabbia, Storia e tecnologia del vetro antico. Edipuglia, Bari.

Stevels, J.M., 1953. Le verre considéré comme polymère. Verres Réfract. 7, 91–104.

Stevels, J.M., 1954. Networks in glass and other polymers. Glass Ind. 35, 657–662.

Stone, E.C., Lindsley, D.H., Pigott, V., Harbottle, G., Ford, M.T., 1998. From shifting silt to solid stone: the manufacture of synthetic basalt in ancient Mesopotamia. Science 280, 2091–2093.

Tait, H., 1991. Five Thousand Years of Glass. British Museum Press, London.

Tammann, G., 1898a. Ueber die Krystallisationsgesschwindigkeit. II. Z. Phys. Chem. 26, 307–316.

Tammann, G., 1898b. Ueber die Abhängigkeit der Zahl der Kerne, welche sich in verschiedenen unterkühlten Flüssigkeiten bilden, von der Temperatur. Z. Phys. Chem. 28, 441–479.

Tammann, G., 1925. Glasses as supercooled liquids. J. Soc. Glass Technol. 9, 166–185.

Tammann, G., 1933. Der Glaszustand. Leopold Voss, Leipzig.

Tammann, G., Hesse, W., 1926. Die Abhängigkeit der Viskosität von der Temperatur bei unterkühlten Flüssigkeiten. Z. Anorg. Allg. Chem. 156, 245–257.

Thomson, W., 1871. Inaugural address, British Association. Nature 4, 262–270.

Thomson, W., 1895. The age of the Earth. Nature 51, 1438–1444.

Tool, A.Q., 1946. Relation between inelastic deformability and thermal expansion of glass in its annealing range. J. Am. Ceram. Soc. 29, 240–252.

Tool, A.Q., Eichlin, C.G., 1920. The absorption of heat in glass. J. Opt. Soc. Am. 4, 340–363.

Tool, A.Q., Eichlin, C.G., 1924. Certain effects produced by chilling glass. J. Opt. Soc. Am. 8, 419–449.

Tool, A.Q., Eichlin, C.G., 1925. Variations in glass caused by heat treatment. J. Am. Ceram. Soc. 8, 1–17.

Tool, A.Q., Eichlin, C.G., 1931. Variations caused in the heating curves of glass by heat treatment. J. Am. Ceram. Soc. 14, 276–308.

Turner, W., 1956a. Studies in ancient glasses and glassmaking processes. Part III. The chronology of the glassmaking constituents. J. Soc. Glass Technol. 40, 39–52.

Turner, W., 1956b. Studies in ancient glasses and glassmaking processes. Part IV. The chemical composition of ancient glasses. J. Soc. Glass Technol. 40, 162–186.

Tykot, R., 2018. Obsidian in prehistory. In: Richet, P. (Ed.), Encyclopedia of Glass Science, Technology, History and Culture. J. Wiley & Sons, Hoboken, NJ.

Tylecote, R.F., 1992. A History of Metallurgy, second ed. The Institute of Metals, London.
Velde, B., 1990. Alumina and calcium oxide content of glass found in Western and Northern Europe, first to ninth centuries. Oxf. J. Archaeol. 9, 105–117.
Verità, M., 2018. Venetian glass. In: Richet, P. (Ed.), Encyclopedia of Glass Science, Technology, History and Culture. J. Wiley & Sons, Hoboken, NJ.
Vogel, H., 1921. Das Temperaturabhängigkeitsgesetz der Viskosität von Flüssigkeiten. Phys. Z. 22, 645–646.
Vogel, W., 1994. Glass Chemistry, second ed. Springer, Berlin.
Warren, B.E., 1934. X-ray determination of the structure of glass. J. Am. Ceram. Soc. 17, 249–254.
Warren, B.E., Biscoe, J., 1938. Fourier analysis of X-ray patterns of soda-silica glass. J. Am. Ceram. Soc. 21, 259–265.
Warren, B.E., Pincus, A.G., 1940. Atomic considerations of immiscibility in glass systems. J. Am. Ceram. Soc. 23, 301–304.
Warren, B.E., Krutter, H., Morningstar, O., 1936. Fourier analysis of x-ray patterns of vitreous SiO_2 and B_2O_3. J. Am. Ceram. Soc. 19, 202–206.
Washburn, E., Shelton, G., 1914. The viscosities of soda-lime glasses. University of Illinois Bulletin, vol. 140.
Werner, A.G., 1791. Observations sur les roches volcaniques et sur le basalte. J. Phys. Chim. Hist. Nat. 38, 409–420.
White, W., 1919. Silicate specific heats. Second series. Am. J. Sci. 47, 1–43.
Wicks, G.G., 1985. Nuclear waste glass. In: Tomozawa, M., Doremus, R.H. (Eds.), Treatise on Materials Science and Technology, vol. 26, Glass IV. Academic Press, Orlando, pp. 57–118.
Winkelmann, A., 1893. Ueber die specifischen Wärmen verschieden zusammengesetzer Gläser. Ann. Phys. Chem. 49, 401–420.
With, E., 1874. L'écorce terrestre. Plon, Paris.
Wyckoff, R.W.G., Morey, G.W., 1925. X-ray diffraction measurement of some soda-lime-silica glasses. J. Soc. Glass Technol. 9, 265–267.
Young, D.A., 1998. N. L. Bowen and Crystallization-Differentiation. Mineralogical Society of America, Washington, DC.
Young, D.A., 2003. Mind Over Magma: The Story of Igneous Petrology. Princeton University Press, Princeton.
Youngman, R.E., 2018. Borosilicate glasses. In: Richet, P. (Ed.), Encyclopedia of Glass Science, Technology, History and Culture. J. Wiley & Sons, Hoboken, NJ.
Zachariasen, W.H., 1932. The atomic arrangement in glass. J. Am. Chem. Soc. 54, 3841–3851.
Zernicke, F., Prins, J.A., 1927. Die Beugung von Röntgenstrahlen in Flüssigkeiten als Effekt der Molekülanordnung. Z. Phys. 41, 184–194.

Further Reading

Aristotle. Meteorology, book II, ch. 8, transl. by Webster, E.W., 1984. The Complete Works of Aristotle. Princeton University Press, Princeton.
Bernal, J.D., 1936. An attempt at a molecular theory of liquid structure. Disc. Farad. Soc. 336, 27–40.
Buffon (Leclerc de), G.L., 1779. Époques de la nature. Critical edition with introduction and notes by J. Roger, repr. 1988. Mém. Mus. Nat. Hist. Nat. 10, 1–316.
Cordier, L., 1816. Mémoire sur les substances minérales dites en masse, qui entrent dans la composition des roches volcaniques de tous les âges. J. Phys. Chim. Hist. Nat. 83. 135–163, 285–307 and 352–387.
Cordier, L., 1827. Essai sur la température de l'intérieur de la Terre. Mém. Acad. R. Sci. 7, 473–555.
Daubenton, L., 1797. Tableau méthodique des minéraux, suivant leurs différentes natures, et avec des caractères distinctifs, apparens ou faciles à reconnoître, 5ème éd. Du Pont, Paris.
Descartes, R., 1644. Principia Philosophiae. Elsevier, Amsterdam (transl. by Miller, V.R., Miller, R.P., 1984 as The Principles of Philosophy. D. Reidel Pub. Co., Amsterdam).
Desmarest, N., 1774. Mémoire sur l'origine et la nature du basalte à grandes colonnes polygones, déterminées par l'histoire naturelle de cette pierre, observée en Auvergne. Mém. Acad. R. Sci. 705–775.
Dietzel, A., 1942. Die Kationenfeldstärken und ihre Beziehungen zu Entglasungsvorgängen, zur Verbindungsbildung und zu den Schemlzpunkten von Silicaten. Z. Elektrochem. 48, 9–23.

Dolomieu (de), D., 1797. Rapport fait par le citoyen Dolomieu, Ingénieur des Mines, sur ses voyages de l'an V et de l'an VI. J. Mines 7, 385–402.

Du Fay (de Cisternai), C.F., 1735. Quatrième mémoire sur l'électricité. De l'attraction et répulsion des corps électriques. Mém. Acad. R. Sci., 457–476.

Fourier, J., 1822. Théorie analytique de la chaleur. Firmin Didot, Paris (transl. by Freeman, A. as Analytical Theory of Heat, Repr. Dover, New York, 1955).

Galilei, G., 1610. Sidereus nuncius, magna, longeque admirabilia spectacula pandens, suspiciendaque proponens unicuique, præsertim vero. T. Baglionum, Venezia (transl. by A. van Helden as The Sidereal Messenger, The University of Chicago Press, Chicago, 1989).

Gaudin, M.A., 1839. Sur les propriétés du cristal de roche fondu. C. R. Acad. Sci. 8, 678–679 and 711–713.

Gibbs, J.W., 1874–1876. On the equilibrium of heterogeneous substances. Trans. Connect. Acad. Arts Sci. 3, 103–248 and 343–524.

Guettard, J.-É., 1752. Mémoire sur quelques montagnes de la France qui ont été des volcans. Mém. Acad. R. Sci., 363–392.

Hall, J., 1798. Curious circumstances upon which the vitreous or stony character of whinstone and lavas respectively depend; with other facts. J. Nat. Philos. Chem. Arts 2, 285–288.

Hall, J., 1805. Experiments on whinstone and lava. Trans. R. Soc. Edinb. 5, 42–75.

Haüy, R., 1801. XXe espèce. Piroxène. In: Traité de minéralogie. vol. 3. Louis, Paris, pp. 80–93.

Hero of Alexandria (1st c. AD), Pneumatica, transl. by Woodcroft, B. reed, 1971. The Pneumatics of Hero of Alexandria. McDonald, London.

Herschel, W., 1787. An account of three volcanoes in the Moon. Trans. R. Soc. Lond. 77, 29–32.

Hittorf, J.W., 1851. Ueber die Allotropie des Selens. Ann. Phys. Chem. 84, 214–220.

Hutton, J., 1788. Theory of the Earth; or an investigation of the laws observable on the composition, dissolution, and restauration of land upon the globe. Trans. R. Soc. Edinb. 1, 209–304.

Hutton, J., 1795. Theory of the Earth, With Proofs and Illustrations. W. Creech, Edinburgh.

Kirwan, R., 1792. Elements of Mineralogy, second ed. P. Elmsly, London.

Lebedev, A.A., 1921. Polymorphism and annealing of glass. Trans. Opt. Inst. Petrograd 2, 1–20 (abstract in J. Soc. Glass Technol., 6, 110–112, 1922).

Leeuwenhoek (van), A., 1939–1999. The Collected Letters. vols. 15. Swets & Zeitlinger, Amsterdam.

Leibniz G.W. (1749) Protogaea. Scheidt, Göttingen, transl. by Cohen, C., Wakefield, A., 2008. Protogaea. Scheidt, Göttingen.

Lucretius (1st c. BC). De Natura Rerum, transl. by Watson, J.S., 1997. On the Nature of Things. Prometheus Books, Amherst.

Marius (12th cent.) De Elementis, transl. by Dales, R.C., 1976. Marius: On the Elements. Univ. Calif. Press, Berkeley.

Newton, I., 1671. A letter of Mr. Isaac Newton, professor of Mathematicks in the University of Cambridge; containing his new theory about light and colors. Philos. Trans. R. Soc. Lond. 6, 3075–3087.

Pliny the Elder (23–79), Historia naturalis, books 36 and 37 transl. by Eicholz, E., 1966. Natural History. Harvard Univ. Press, Harvard.

Theophilus Presbyter (12th c.). De diversis artibus, transl. by Hawthorne, J.G., Smith, C.S., 1963. On Divers Arts. The University of Chicago Press, Chicago.

Ptolemy (2nd cent. A.D.), Optika, transl. by Smith, A.M., 1996. Ptolemy's Theory of Visual Perception. Am. Philos. Soc., Philadelphia.

Raspe, R.E., 1771. A letter containing a short account of some basalt hills in Hessia. Phil. Trans. R. Soc. Lond. 61, 580–583.

Raspe, R.E., 1776. An Account of Some German Volcanoes and Their Productions. With a New Hypothesis of the Prismatical Basaltes; Established Upon Facts. Lockyer Davis, London.

Réaumur (Ferchaut de), R.A., 1727. Idée générale des différentes matières dont on peut faire la Porcelaine; et quelles sont les véritables matières de celle de la Chine. Mém. Acad. R. Sci., 185–203.

Réaumur (Ferchaut de), R.A., 1739. Art de faire une nouvelle espèce de porcelaine par des moyens extrêmement simples et faciles, ou de transformer le Verre en Porcelaine. Mém. Acad. R. Sci., 370–388.

Seneca, Quaestiones naturales, transl. by Hine, H., 2010. Natural Questions. The University of Chicago Press, Chicago.

Simon, F., 1931. Ueber den Zustand der unterkuhlten Flüssigkeiten und Gläser. Z. Anorg. Allg. Chem. 203, 219–227.

Steno, N. (1669) De solido intra solidum naturaliter contento dissertationis prodromus, transl. by Winter, J.G., 1916. The Prodromus of Nicolaus Steno's Dissertation Concerning a Solid Body Enclosed by Process of Nature Within a Solid. MacMillan, London.

Strabo, n.d. Geography (transl. by Jones, H.L., Harvard University Press, Cambridge, 1960).

Tammann, G., 1903. Kristallisieren und Schmelzen, Ein Beitrag zur Lehre des Änderungen des Aggregatzustandes. J.A. Barth, Leipzig.

Thomson, W., 1863. On the rigidity of the Earth. Philos. Trans. R. Soc. Lond. 153, 573–582.

Torricelli, E., 1644. Letters to Michelangelo Ricci, p. xxvii-xxx and xxxi-xxxv in Lezioni accademiche (1715). T. Bonnaventuri, Florence.

CHAPTER

2

Glass Versus Melt

OUTLINE

2.1 INTRODUCTORY COMMENTS

The ease with which a liquid adjusts to the shape of its container is a familiar consequence of atomic mobility. This is a hallmark of the molten state. Atomic mobility is the very reason why liquids flow, even though another salient feature evident through daily experience is that viscosity (η) increases markedly with decreasing temperatures, which can be accounted for quantitatively in various ways (Deubener, 2018). If crystallization does not occur when a liquid is cooled below its liquidus temperature, viscosity eventually becomes so high that flow can no longer take place on the timescale of an experiment. The liquid transforms to a glass, i.e., to a solid with a disordered atomic arrangement. From an essentially phenomenological perspective, the glass transition and the resulting close connection between glasses and melts

https://doi.org/10.1016/B978-0-444-63708-6.00002-8

are the main themes reviewed in this chapter. A variety of other relaxation mechanisms operates in glass-forming liquids (e.g., Debenedetti, 1997; Angell et al., 2000; Donth, 2001; Fotheringham, 2018). As a result of difficulties in high-temperature experiments, such secondary relaxation mechanisms have not been documented extensively for silicate melts. This is not a serious problem as they are of little influence on the structural and physical properties dealt with in this book.

2.2 RELAXATION

The glass transition is not abrupt but typically occurs over a few tens of degrees. Depending on heating or cooling rate, it can take place at widely differing temperatures. In all cases, however, the time dependence of the investigated physical property reveals that the kinetics of structural relaxation are slow at the timescale of the measurement.

2.2.1 Glass Transition Range

In general, the glass transition temperature (T_g) is defined as the temperature at which the tangents to the glass and liquid curves of a given property intersect (Fig. 2.1). At the particular timescale of the experiment, T_g is that temperature at which the configuration of the liquid is frozen in (here, configuration designates any microscopic arrangement of the material consistent with a given macroscopic state of the system). Contrary to the temperature of an equilibrium transition, T_g is not a fixed point because it varies with the experimental conditions. It is higher for higher cooling rates or shorter experimental timescales. This effect demonstrates the kinetic, nonequilibrium nature of the glass transition. Such variations of T_g can amount to hundreds of degrees. They are shown in Fig. 2.2 for the glass transition of $CaAl_2Si_2O_8$ as determined under the experimental conditions of viscometry, ultrasonic, and Brillouin scattering experiments, which are made at experimental timescales of the order of 10^2, 10^{-6} and 10^{-10} s, respectively (see Section 2.3.2). Hence, the glass or liquid nature of the substance does not depend only on temperature but also on the timescale at which its properties are probed.

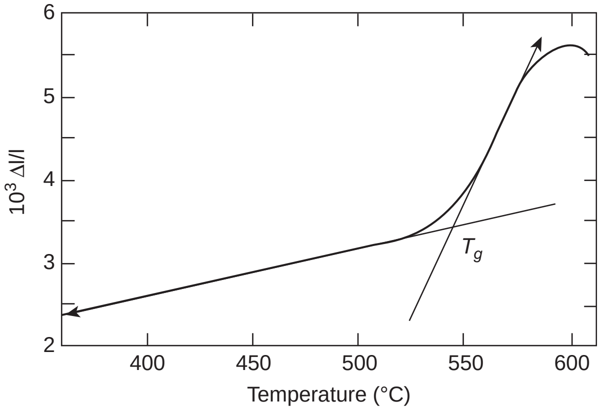

FIG. 2.1 Dilatometric glass transition temperature of E glass (composition in Table 1.2), as determined from the break in the thermal expansion curve. The decrease of the sample length (l) above 600°C is due to flow of the sample under its own weight slightly above the glass transition.

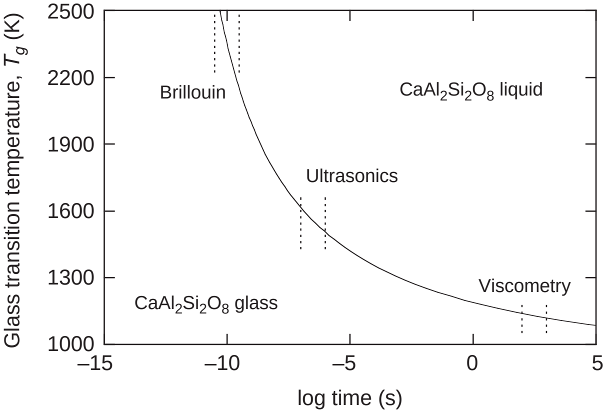

FIG. 2.2 Time-dependence of the glass transition for $CaAl_2Si_2O_8$ (from data of Askarpour et al., 1993). The transition curve separates the fully relaxed liquid from the unrelaxed glass. It is plotted against experimental timescale to show the conditions under which the glass transition takes place for the three kinds of experiments indicated.

More precisely, the glass transition does not manifest itself as a sharp discontinuity, but as a temperature interval where the properties of the material depend on time as well as on thermal history. Under given experimental conditions, the width of this *glass transition range* is typically a few tens of degrees, as illustrated in Fig. 2.3 by the viscosity of a window glass. The viscosities in this figure were measured with timescales of minutes, first in order of decreasing temperatures and then in order of increasing temperatures. Time-dependent viscosity was observed from about 800 to 775 K. The viscosity increased with time when the liquid was cooled down to the temperature of the measurement, whereas it decreased with time if it was heated up first. Like any physical property, the viscosity of a liquid in internal thermodynamic equilibrium is determined by only two variables, pressure (ambient, in this case) and temperature (that of the experiment). The differences between the values observed at the beginning of each series of isothermal measurements (i.e., after cooling and after heating) demonstrate that the melt was not in internal equilibrium until a common, constant value was attained.

Equilibrium viscosities of up to about 10^{15} Pa s can be reached through complete relaxation achieved in reversal experiments lasting a few days, as shown in Fig. 2.3, for example. Still higher viscosities could be measured, but the experimental timescales would rapidly exceed

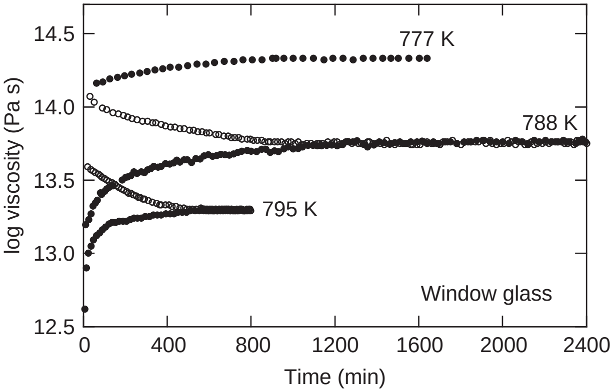

FIG. 2.3 Time dependence of the viscosity of a window glass (see Table 1.2) at several temperatures in the glass transition range. Isothermal measurements made in order of decreasing *(open symbols)* and then increasing *(solid symbols)* temperatures (Sipp et al., 1997).

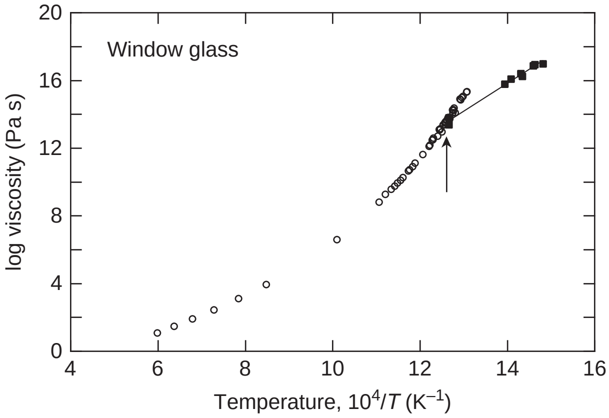

FIG. 2.4 Equilibrium *(open circles)* and isostructural *(solid squares)* viscosity of window glass. For the latter data, the fictive temperature of the material is indicated by the arrow. Measurements from Mazurin et al. (1979) and Sipp et al. (1997).

the lifetime of the experimentalist![1] Leaving aside for the moment a discussion of the configurational changes that take place during relaxation, we emphasize that equilibrium is out of reach if experiments are made quickly well below the glass transition range. Measurements can nevertheless be made under such conditions. Then, the resulting viscosity is lower than the equilibrium value because the sample has been previously held at a temperature higher than that of the experiment (Fig. 2.3). This viscosity is termed *isostructural* because the structure of the sample cannot adjust to the new temperature conditions during the timescale of the experiment. It varies with temperature according to an Arrhenius law (Mazurin et al., 1979), in contrast with the generally strong departures from Arrhenian variations found for the liquid (see Bottinga and Richet, 1996). It is even possible to determine the temperature at which the structure of the glass has been frozen in. This temperature is given by the intersection of the Arrhenius law of the glass with the non-Arrhenian curve of the liquid (Fig. 2.4).

Depending on the kind of measurement performed, the glass transition thus manifests itself either as a continuous or as a discontinuous transformation. Similar to first-order thermodynamic properties (volume, enthalpy, entropy), there is no discontinuity of transport properties (viscosity, electrical conductivity, etc.), but a change in temperature dependence across the glass transition range. In contrast, the variations of second-order thermodynamic properties are rapid enough to be considered practically as discontinuities such as illustrated in Fig. 2.5 with the heat capacity of a sodium silicate.

2.2.2 Vibrational Versus Configurational Relaxation

Relaxation does not represent a response of the material to temperature changes only, but to variations of any intensive variable. In experiments made at constant temperature, stress

---

[1] It is often said that thicker stained glass at the bottom of panes in medieval churches resulted from long-term flow at room temperature under the own weight of the material. As pointed out by Zanotto and Gupta (1999), timescales of the order of 10^{23} years would be needed to produce such an effect. The likely explanation is that stained-glass masters simply installed the thickest side of glass panes at the bottom when they were not getting panes of even thickness.

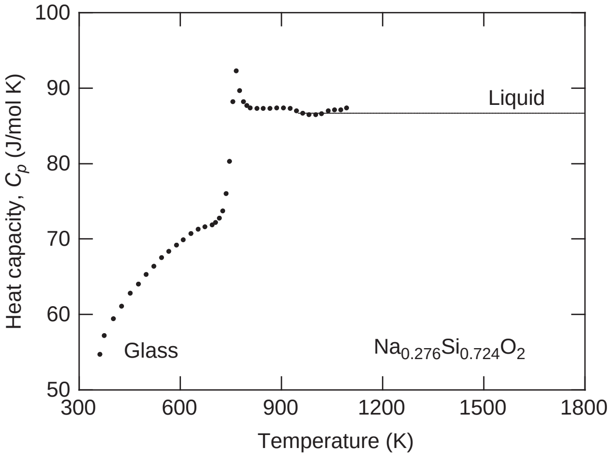

FIG. 2.5 Heat capacity change at the glass transition for a sodium silicate. Adiabatic measurements *(solid points)* by Yageman and Matveev (1982) and drop calorimetry data *(solid line)* by Richet et al. (1984). The bump near 800 K is the relaxation peak discussed in Section 2.3.2.

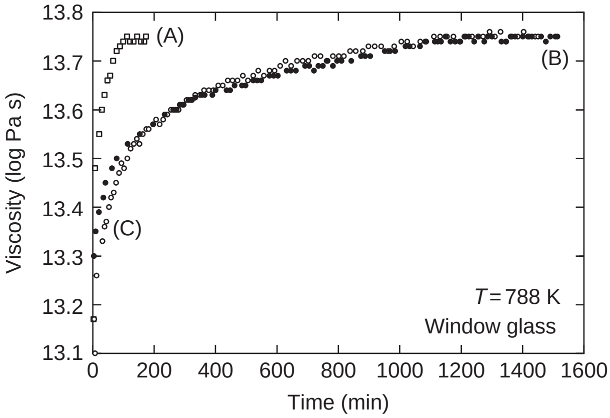

FIG. 2.6 Approach to equilibrium of the viscosity of a window glass: (A) After a stress change at constant temperature; (B) After a temperature change at constant stress. (C) And after a combination of such two changes (Sipp et al., 1997). The departure from equilibrium in (C) is the sum of the responses in (A) and (B).

changes can cause viscosity to be time-dependent. Relaxation tends to be much faster after a stress change than after a temperature change, however, as illustrated by the ninefold difference between the data plotted in Fig. 2.6 for a window glass. When the so-called Boltzmann (1874) superposition principle holds true, relaxation after simultaneous different perturbations is the sum of the individual responses (see Hodge, 1994). This is illustrated in Fig. 2.6 by the stress and temperature perturbations and their combined effects on a window glass.

Specifically, two kinds of relaxation, vibrational and configurational, must in general be distinguished. When energy is delivered quickly to a substance, for example with laser pulses, the conversion of light into heat takes place at the 10^{-12} to 10^{-14} s timescale of atomic vibrations. Because of such very short timescales, vibrational relaxation can be considered as instantaneous during physical measurements. The observed relaxation results instead from configurational changes within the substance. In accordance with Le Chatelier's Laws, these changes represent additional entropy and volume changes, which allow the Gibbs free energy to decrease further in response to variations of temperature and pressure. Configurational changes thus take place whenever the structure of a substance can vary. This is the case of liquids, of course, as well as of crystals during phase transitions or at high temperatures. These phenomena will be described in the following chapter.

Now consider any first-order thermodynamic property, Y, such as volume, enthalpy, entropy, etc. In view of the very strong temperature dependence of relaxation kinetics, three cases must be distinguished with regard to the variation of a property following a temperature jump ΔT (Fig. 2.7):

1. At high temperatures, relaxation time is short with respect to the timescale of a measurement. The equilibrium value Y_1 is reached instantly in such a way that an apparent discontinuity, ΔY, is observed, which is the sum of vibrational and configurational contributions.
2. At lower temperatures, relaxation takes longer because the time needed to reach the equilibrium value, Y_2, becomes similar to the experimental timescale. A smaller jump of Y is first observed, which is due to instantaneous vibrational relaxation. This jump is followed by a configurational relaxation, which progressively brings Y to its new equilibrium value. The lower the temperature, the longer is the time required to reach equilibrium, as illustrated with the plots of Y_2 and Y_3 in Fig. 2.7.

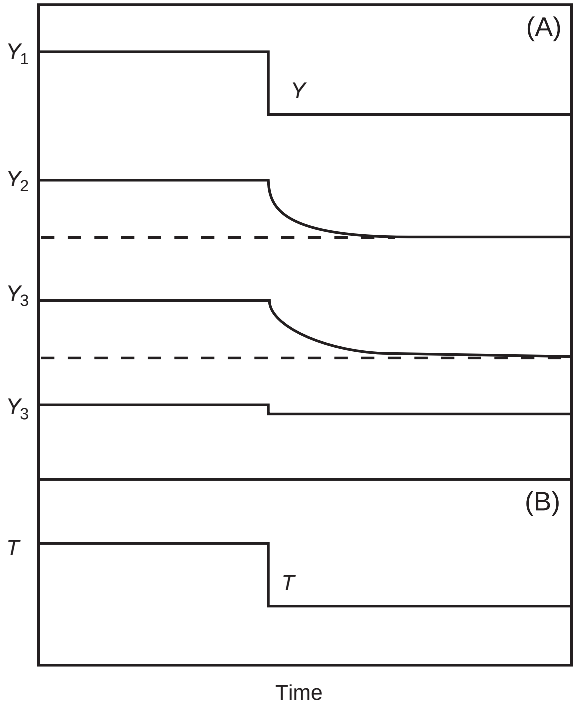

FIG. 2.7 Vibrational and configurational relaxation shown in (A) at four different temperatures for a given property Y, consecutive to an abrupt change in temperature ΔT represented in (B). In order of decreasing temperature, Y_1 refers to a fully relaxed phase (e.g., a liquid), Y_2 and Y_3 to a relaxing material, and Y_4 to a fully unrelaxed phase (e.g., a glass). For Y_2 and Y_3, the equilibrium values are shown by a *dashed line*.

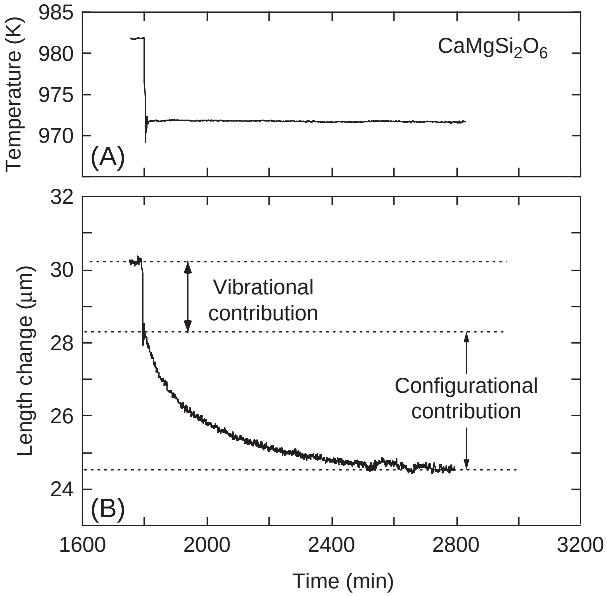

FIG. 2.8 Vibrational (instantaneous) and configurational (delayed) contributions to volume relaxation in dilatometry experiments made on supercooled liquid $CaMgSi_2O_6$ (Toplis and Richet, 2000). In response to the temperature change from 982 to 972 K shown in (A), the vibrational component of length change is much faster than the changes due to relaxation of the liquid structure apparent in (B). Sample length: 12 mm.

3. When the temperature has decreased even further, relaxation has become so long that no configurational changes can take place in the course of the measurement. The structure of the phase has been frozen in. Only a small instantaneous change in Y due to atomic vibrations is observed. The glass transition has occurred because configurational changes are no longer possible at an appreciable rate.

When relaxation requires times that are long with respect to the 10^{-12} to 10^{-14} s period of atomic vibrations, vibrations in a liquid can be considered as taking place in a fixed structural environment. Physical properties can then be separated into independent vibrational and configurational contributions. As will be shown from the simple Maxwell model, this situation obtains in liquids when the viscosity is higher than about 0.1 Pa s. An example of volume relaxation is provided by the dilatometry experiments of Fig. 2.8 where both vibrational and configurational contributions can be observed directly. The former is instantaneous, whereas the latter is delayed and slowly leads to the equilibrium length of the sample.

2.2.3 Relaxation Times

Relaxation is relevant to silicate melts from both a theoretical and practical standpoint. This has been reviewed elsewhere (Moynihan et al., 1976; Hessenkemper and Brückner, 1989, 1990; Dingwell and Webb, 1990; Dingwell, 1995; Moynihan, 1995; Fotheringham, 2018) or shown by a variety of measurements (e.g., Webb, 1992a,b; Stevenson et al., 1995; Sipp et al., 1997). To characterize the rate at which a given property, Y, approaches the new equilibrium value, Y_e, one defines the relaxation time, τ, as:

$$\tau_Y = -(Y_t - Y_e)/(\partial Y/\partial t), \tag{2.1}$$

where Y_t is the value actually measured at instant t. If τ_Y were constant, i.e., not depending on the instantaneous value of Y, relaxation would be described by a simple exponential law:

$$(Y_t - Y_e) = (Y_0 - Y_e)\exp\left(-t/\tau_Y\right), \tag{2.2}$$

where Y_0 is the initial Y value. In other words, after a time τ_Y the variation of Y would represent a fraction $1/e$ of the initial difference from the equilibrium value.

Relaxation times depend not only on temperature (Fig. 2.3), but also on the extent of departure from the equilibrium state, i.e., on thermal history. In addition, relaxation kinetics do not follow exponential laws of the form (2.2) at constant temperature because either individual relaxation times are intrinsically nonexponential or the actual transformation is made up of many mechanisms with different relaxation times. In a phenomenological way, quantitative modeling of experimental relaxation measurements can be achieved in two different ways. One can assume that there is a distribution of relaxation times and then express relaxation as the sum of a number of equations of the form (2.2). Alternatively, nonexponentiality can be built into Eq. (2.2) through replacement of the variable $(-t/\tau_Y)$ by $(-t/\tau_Y)^{\beta}$, where β is a constant, ranging from 0 to 1, first introduced by Kohlrausch (1863) in torsion experiments on rubber and glass fibers. Because a review of relaxation studies and models is beyond the scope of this book (see Scherer, 1986; Hodge, 1994; Angell et al., 2000), we will now turn to a few points of more direct relevance.

The first point is whether or not the relaxation kinetics (and relaxation times) are the same for various physical properties of the same substance. From comparisons between their own photon correlation spectroscopy results with literature data on enthalpy or viscosity, Siewert and Rosenhauer (1997), for instance, concluded that relaxation in SiO_2-$NaAlSiO_4$ melts is slower for thermal than for mechanical perturbation. It is not easy to answer such a question rigorously, however, because the effects of differing samples, temperature conditions, experimental timescale, thermal history, or data analysis are not readily disentangled.

Because the glass transition occurs when relaxation times become greater than the timescale of an experiment, differences between the glass transition temperatures measured under similar conditions for different properties reflect possible differences in relaxation kinetics for a given substance. Such comparisons made for many silicates and aluminosilicates by Webb and Knoche (1996) show that these temperatures agree to within experimental errors for enthalpy and volume. Webb and Knoche (1996) also concluded that, for all their samples, the viscosity at the glass transition lies in the rather narrow range $10^{9.71} - 10^{12.08}$ Pa s, with a standard deviation from the mean of only $10^{0.33}$ Pa s. From simultaneous enthalpy and volume measurements, Sipp and Richet (2002) investigated a wider composition range in which titano- and borosilicates were included. The correlation between glass transition temperatures (Fig. 2.9) is still better and the viscosity interval at T_g narrower than reported by Webb and Knoche (1996). In spite of glass transition temperatures spanning the wide range 750–1160 K, the viscosity interval is $10^{10.1} - 10^{11.7}$ Pa s with a standard deviation from the mean of $10^{0.11}$ Pa s.

The similarity of relaxation times for different properties can be confirmed directly by measurements performed on samples with the same thermal history. For such comparisons, the results are expressed as dimensionless variables:

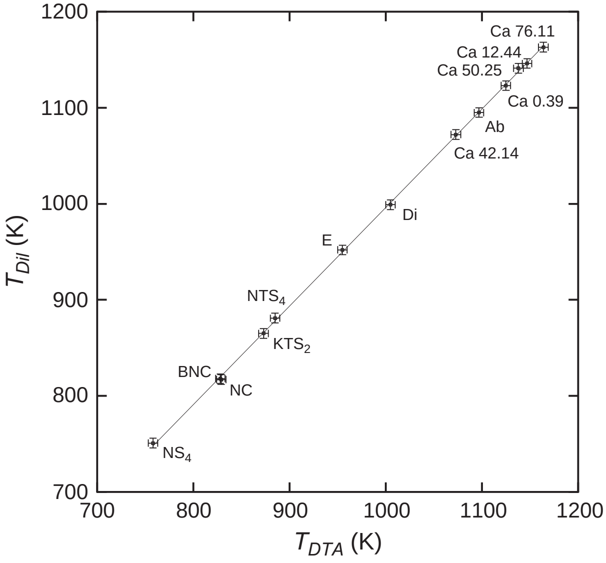

FIG. 2.9 Correlation between the volume and enthalpy glass transition temperatures as measured by dilatometry (T_{Dil}) and by differential thermal analysis (T_{DTA}), respectively (Sipp and Richet, 2002). Abbreviations: Ab ($NaAlSi_3O_8$); Di ($CaMgSi_2O_6$); K (K_2O); N (Na_2O); S (SiO_2); T (TiO_2); Ca *x.y* (*x* mol% SiO_2, *y* mol% Al_2O_3, (100-*x*-*y*) mol% CaO); BNC and E: complex calcium borosilicates (see Sipp et al., 1997).

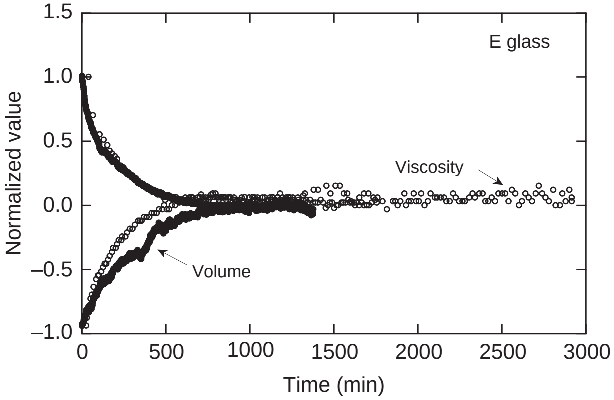

FIG. 2.10 Viscosity and volume relaxation for E glass shown in a normalized form with Eq. (2.3). Data from Sipp and Richet (2002), with viscosity measurements from Sipp et al. (1997).

$$Y = (Y_t - Y_e)/(Y_0 - Y_e), \tag{2.3}$$

where Y_t, Y_e, and Y_0 are the values of property Y at time t, at equilibrium, and at time 0, respectively. Over a few-hour intervals, the volume and viscosity of a window glass relaxed at the same rate (Rekhson et al., 1971). The same conclusion has been arrived at for E glass (Fig. 2.10) over longer duration for wider departures from equilibrium (Sipp and Richet, 2002). Although relaxation is a complicated function of temperature and thermal history, the equivalence of relaxation rates for different properties of silicate melts is a welcomed simplifying feature. It is of great practical use, especially in allowing relaxation times for any property to be estimated from viscosity through Maxwell's model.

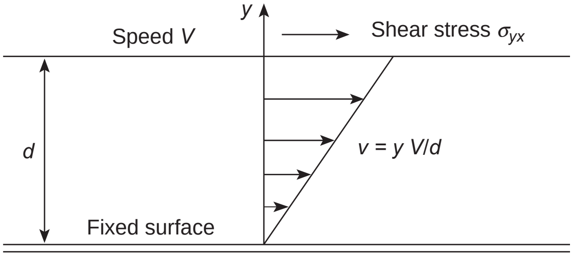

FIG. 2.11 Schematic plot of velocity gradients in a liquid between two infinite planes separated by a distance d, the upper plane moving at a speed V.

2.2.4 Maxwell Model

Referring to Fotheringham (2018) for a general review of relaxation models of practical interest, we will now deal with the very simple treatment of viscoelastic media proposed by Maxwell (1868), as it represents a very convenient way to describe their main features. Its starting point is the flow of liquids where shear stresses resulting from interatomic forces yield velocity gradients perpendicular to the stream direction (Fig. 2.11). The simplest case holds when "the resistance arising from the want of lubricity in the parts of a fluid is, other things being equal, proportional to the velocity with which the parts of the fluid are separated from one another" (Newton, 1725). Shear stresses then are proportional to velocity gradients. For a homogeneous relative deformation, or strain, ε (= $\Delta l/l$, l = sample length), one has:

$$\sigma = \eta\,\partial\varepsilon/\partial t, \tag{2.4}$$

and the shear viscosity, η, is *Newtonian* as long as η is independent of the stress, σ, and strain rate, $\delta\varepsilon/\delta t$, of the sample.

In view of the continuous pathway between the liquid and glass states, glass-forming liquids cannot be purely Newtonian when they approach the glass transition. In fact, they are *viscoelastic*, with an elastic component that becomes increasingly important near T_g. More precisely, application of a shear stress first causes an elastic strain, which would be recovered if the stress were released, and then a viscous deformation. The relation between the elastic stress and strain is given by Hooke's law. Originally stated as "*Ut tensio, sic vis*," that is, "the power of any spring is in the same proportion with the tension thereof," this law is written in modern terms as:

$$\sigma = G_\infty\,\varepsilon, \tag{2.5}$$

where G_∞, also known as the shear rigidity, is the shear modulus at infinite frequency. Hence, the elastic stress rate is:

$$\mathrm{d}\sigma/\mathrm{d}t = G_\infty\,\mathrm{d}\varepsilon/\mathrm{d}t. \tag{2.6}$$

The second component is the aforementioned Newtonian, nonrecoverable viscous deformation that tends to relax the stress built up macroscopically through strained bond lengths and angles. The applied stress does not remain constant but tends to disappear at a rate depending on the value of σ and on the nature of the substance. Assuming that this rate was proportional to σ, Maxwell (1868) rewrote Eq. (2.6) as:

$$d\sigma/dt = G_\infty \, d\varepsilon/dt - \sigma/\tau, \tag{2.7}$$

and introduced in this way the stress relaxation time, τ, as a measure of the rate of the process. In practice, stress and structural relaxation times are about the same and both terms are used synonymously in the viscoelastic literature. If the strain, ε, is constant, Maxwell noted that:

$$\sigma = G_\infty \, \varepsilon \exp(-t/\tau), \tag{2.8}$$

so that the stress eventually vanishes and the pressures are distributed as in a fluid at rest. If, alternatively, the deformation rate $d\varepsilon/dt$ is kept constant, the instantaneous stress is readily obtained by integration of Eq. (2.7):

$$\sigma = \eta \, d\varepsilon/dt + C e^{-t/\tau}, \tag{2.9}$$

where C is a constant.

By combining the simplest representations of elasticity and viscous flow, the Maxwell model has as a mechanical analog a spring and a dash pot placed in series. The response of a viscous melt subjected to stress thus is made up of an instantaneous, elastic response, which is vibrational in origin, along with a delayed response whose nature is configurational. We refer to Richet and Bottinga (1995) for a discussion of the usefulness and limitations of the Maxwell model. Here, we simply note that $d\sigma/dt$ in Eq. (2.7) becomes very small when stresses are applied at low frequencies, in which case one finds:

$$\eta = G_\infty \, \tau. \tag{2.10}$$

Another important point is that the shear modulus G_∞ is insensitive to composition. From a review of literature data for amorphous silicates, Dingwell and Webb (1989) pointed out that G_∞ varies by less than a factor of 10 with either temperature or composition, with a mean value of 10 GPa. Since atomic vibrations typically have a period of 10^{-12} to 10^{-14} s, configurational relaxation remains much slower than vibrational relaxation as long as viscosity is higher than about 0.1 Pa s. By rewriting Eq. (2.10) as:

$$\eta(T) = G_\infty(T) \, \tau(T), \tag{2.11}$$

we see that the variations of G_∞ can be estimated from the width of the viscosity interval at the glass transition. The value of $10^{10.9\pm0.11}$ Pa s given for this interval in the preceding section points to a possible spread of only half an order of magnitude for G_∞ is consistent with the conclusion of Dingwell and Webb (1989). Compared with the tremendous variations of viscosity with temperature and composition, G_∞ thus is almost constant. If the viscosity is known, structural relaxation times can be readily estimated from Eq. (2.10).

The temperature dependence of G_∞ can be determined directly from sound velocity measurements made at extremely short timescales because $G_\infty = \rho \; v_s^2$, where ρ is the density and v_s the velocity of shear acoustic waves at infinite frequency. This is the situation in Brillouin scattering experiments during which inelastic scattering of phonons by photons takes place at timescales of about 10^{-10} s (see Askarpour et al., 1993). Above the glass transition range, Brillouin and density data yield values of G_∞ in the range 34–36 GPa and indicate that dG_∞/dT is about -0.02 GPa/K for pure SiO_2 (Polian et al., 2002) and $CaMgSi_2O_6$, $CaAl_2Si_2O_8$, and $Ca_3Al_2Si_3O_{12}$ melts (Askarpour et al., 1993). As a result, G_∞ decreases by less than 8 GPa in the 400 K interval spanned by the data of Fig. 2.9 and remains close to the 3–32 GPa range delineated by Dingwell and Webb (1989).

2.2.5 Local Versus Bulk Relaxation

Even though the shear modulus is a property closely connected to viscosity, it is insensitive to temperature and composition. Hence, there is not much structural information to be drawn from its determination. For silicates, it is tempting to assume that the 34–36 GPa value, which pertains to melts ranging from pure SiO_2 to SiO_2-poor melts, results from common structural features. This inference would be misleading, however, for similar G_∞ values of the order of 10^{10} GPa apply to all kinds of glass-forming liquids in spite of the major composition and bonding differences that they represent. This is the reason why these liquids share the common feature that their viscosity is about 10^{12} Pa s when they pass through the glass transition with a cooling rate of a few degrees per minute, i.e., with experimental timescales of the order of 100 s.

Although silicate melts are made up of a variety of structural entities, there is a single glass transition, not different points at which mobility would successively set in for different kinds of atoms or atomic groups. This feature reflects the cooperative nature of the glass transition. As described in more detail in Chapter 4, the bulk dynamics of silicate liquids are controlled by the strong Si—O bonds of the anionic framework (Farnan and Stebbins, 1994; Stebbins et al., 1995). Structural, enthalpy, and volume relaxations are determined by the rate of exchange of these bonds. This does not mean, however, that atomic mobility completely vanishes below the glass transition. Measurements of electrical conductivity or element diffusivity indicate that matter is still transported, although it does so at too slow a rate for the bulk properties of the glass to be affected.

It is possible to determine the characteristic times for various relaxation mechanisms. In a nuclear magnetic resonance (NMR) study of a sodium silicate (Fig. 2.12), George and Stebbins (1998) observed that, with decreasing temperatures, the correlation time for Na site hopping (τ_{Na}) derived from ^{23}Na spin-lattice relaxation data becomes much shorter than the viscosity relaxation time (τ_η) determined from the Maxwell relation (2.10). Similar results have been obtained for three different processes in calcium aluminosilicates over wider temperature intervals extending to below the standard glass transition (Fig. 2.13). In this study, Gruener et al. (2001) determined the rate of exchange of Al—O bonds from ^{27}Al spin-lattice NMR

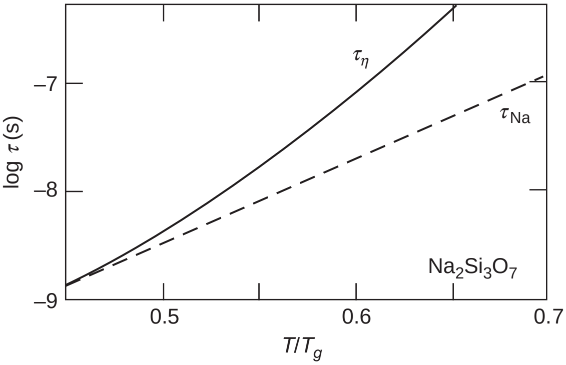

FIG. 2.12 Decoupling of viscosity and Na hopping in $Na_2Si_2O_7$ melt as evidenced by increasing differences between the characteristic times τ_η and τ_{Na} of these processes. *Redrawn from George and Stebbins, (1998).*

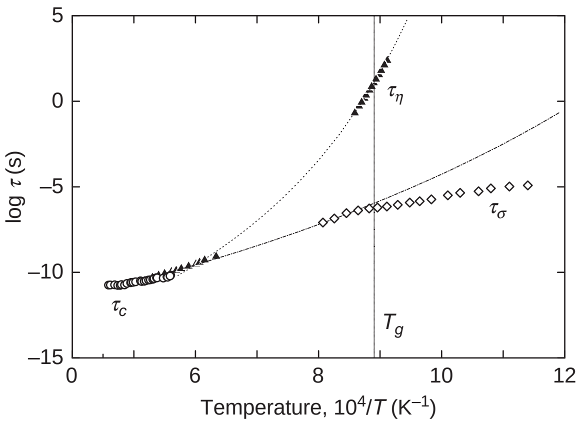

FIG. 2.13 Decoupling of calcium mobility from network relaxation (Gruener et al., 2001). Characteristic times as determined from measurements of viscosity (τ_η), electrical conductivity (τ_σ) and, at high temperature, from ^{27}Al spin-lattice relaxation (τ_c). The effect of the glass transition (T_g) on τ_σ is shown as the difference between the measurements and the curve fitted to the high-temperature data.

experiments, the characteristic time for calcium hopping from electrical conductivity measurements, and structural relaxation times from viscosity and Maxwell model (Fig. 2.13). Whereas all three times are similar above 1600 K, decoupling between structural relaxation and calcium hopping becomes considerable at lower temperatures. At the standard T_g, the relaxation times for these processes differ by seven orders of magnitude. The glass transition itself has little effect on the calcium-hopping frequency, for Fig. 2.13 merely shows a slight change in slope between the data for the liquid above T_g and the "isostructural" data at lower temperatures. Decoupling between alkali mobility and network relaxation was also observed near T_g through lineshape analyses in a Brillouin scattering study of alkali silicates (Kieffer et al., 1995). Likewise, in neutron scattering experiments the dynamic timescale was still found 100 times shorter for Na diffusion than for network relaxation at 1300°C (Meyer et al., 2002).

For a soda-lime silicate melt (Fig. 2.14), decoupling is also attested to by a change in diffusion regime occurring near the glass transition for oxygen, but not for calcium and sodium. These and other observations on simple silicates (e.g., Yinnon and Cooper, 1980; Braedt and Frischat, 1988) indicate that the mechanisms of diffusion differ for network-modifying cations and for oxygen (and silicon as well). For oxygen, there exist at least two different mechanisms. As shown in Chapter 4 (Section 4.5.2), the high-temperature process is closely related to viscous flow. Accordingly, oxygen diffusion varies as strongly as viscosity with the silicate composition. For network-modifying cations, a single mechanism might instead operate from low to high temperature. The diffusivities of these cations tend to vary less with composition because they are not controlled by the bulk of the structure.

Decoupling of bulk and local relaxation has many important implications. As a single example, note fact that element diffusivities differ much less at high temperature, where they tend to converge, than near and below the glass transition, where considerable differences are observed. Besides, this high-temperature convergence points to a linear correlation between the activation enthalpies for diffusion and the preexponential terms of Arrhenius laws. Empirically, this relationship is known as a compensation law (see Winchell, 1969; see also Chakraborty, 1995).

FIG. 2.14 Self diffusion of oxygen, calcium, and sodium in a soda (16 wt%)-lime (12 wt%) silica melt down to the glass transition. Data from Johnson et al. (1951) for ^{22}Na, Wakabayashi (1977) for ^{45}Ca at high temperature, and Terai and Oishi (1977) for ^{18}O and ^{45}Ca at lower temperatures. The standard glass transition is indicated by the *arrow*.

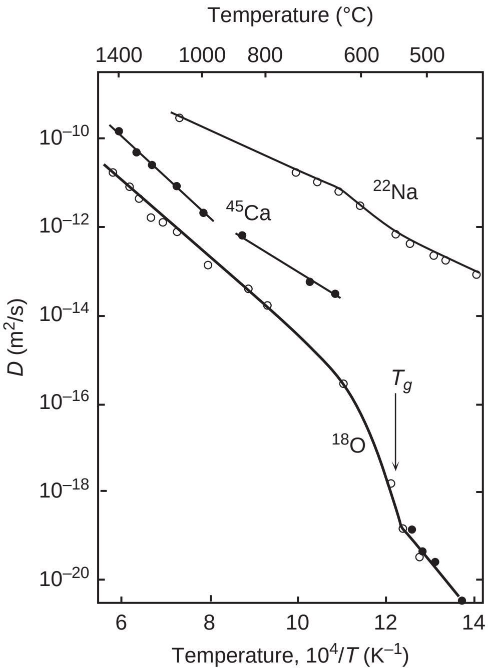

2.3 GLASS TRANSITION

Equilibrium phase transitions have a thermodynamic origin because they allow the Gibbs free energy of the system to decrease in response to pressure or temperature changes. Kinetic phase transitions are quite different because they result from the fact that, under given circumstances, the system has not sufficient time to minimize its Gibbs free energy through adjustments of its configuration. When the system is trapped in such a state of high Gibbs free energy, which does not correspond to the equilibrium configuration, it ceases to be in internal equilibrium and its properties depend on its previous history. This is one of the main consequences of the glass transition whose purely theoretical aspects are beyond the scope of this chapter (see for instance Berthier and Biroli, 2011; Biroli and Garrahan, 2013).

2.3.1 A Microscopic Picture

In this section, we will describe how the changes in second-order thermodynamic properties through the glass transition are related to atomic mobility in the liquid. Referring to early (Davies and Jones, 1953) or more recent (Richet, 2001; Gujrati, 2018; Garden and Guillou, 2018) reviews of the thermodynamics of glasses, we will restrict ourselves to a schematic one-dimensional picture of interatomic potentials (Fig. 2.15). Contrary to crystals, where these

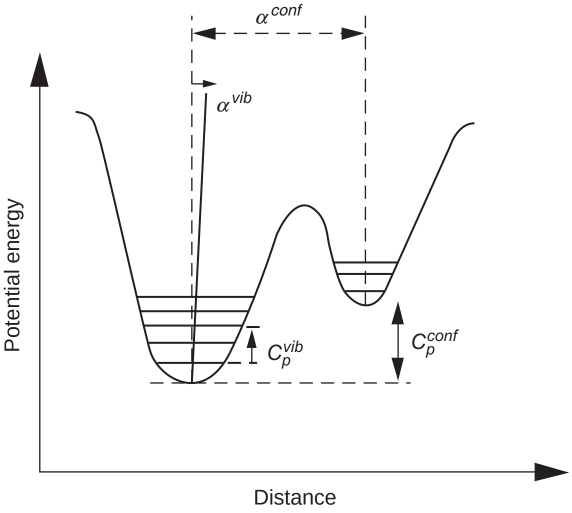

FIG. 2.15 Schematic representation of potential energy in a glass as a function of interatomic distance. Also shown is the manner in which potential energy is related to vibrational energy levels and to the configurational parts of heat capacity and thermal expansion coefficient. The zero-point energy is neglected (from Richet, 2001).

potentials have a long-range symmetry, glasses have essentially a short-range order because the bond angles and distances between next-nearest neighbor atoms are not fixed but spread over a range of values. As originally described by Goldstein (1969), the minima of potential energy, which determine the glass configuration, are separated by barriers with varying heights and shapes in a so-called configurational energy landscape. When thermal energy is delivered to the glass, the temperature rise is associated only with increasing amplitudes of vibration of atoms within their potential energy wells. The heat capacity of the glass is, therefore, only vibrational in nature, which is similar to that of any other solid.

At sufficiently high temperature, thermal energy increases to the point that atoms can overcome the barriers that separate their own from the neighboring potential energy wells (Fig. 2.15). This onset of atomic mobility signals structural relaxation. If, however, the relaxation time is longer than the experimental timescale, only the vibrational heat capacity is measured. If the temperature is increased further, or if time is sufficient for the new equilibrium configuration to be attained during the measurement, then the configurational heat capacity is also measured. When integrated over all atoms, the configurational heat capacity represents the energy differences between the minima of the potential energy wells that are explored as temperature increases (Fig. 2.15).

Hence, the glass transition can be viewed as the point from which atoms begin to explore positions characterized by higher potential energies. Regardless of the complexity of this process at a microscopic level, this spreading of configurations over states of higher and higher potential energy is the main feature of atomic mobility. As a consequence, configurational heat capacities are positive. This feature, in turn, is consistent with the fact that any configurational change must cause an entropy rise when the temperature increases. As for relaxation times, they decrease with rising temperatures because large thermal energies allow potential energy barriers to be overcome more easily.

2.3.2 Rate Dependence of the Glass Transition

If enthalpy is measured, not as a function of time at constant temperature but as a function of temperature at constant cooling rate, configurational changes gradually vanish because of the continuous increase of relaxation times. Both the enthalpy and its derivative, the heat capacity, also decrease smoothly (Fig. 2.16). At the same (absolute) rate, however, a different pathway is followed on heating and on cooling. Relaxation does resume at the temperature at which it vanished on cooling, but the first effect of heating is to lower the enthalpy of the glass and bring it closer to the equilibrium values of the supercooled liquid. At higher temperatures, the enthalpy curve of the material has already crossed that of the supercooled liquid when relaxation becomes almost complete at the timescale of the experiment. The heat capacity then increases rapidly (Fig. 2.16) in a way that depends on thermal history. The rise is highest for samples initially cooled down at the slowest rates or for samples heated at the highest rates.

For all substances, the glass transition occurs when the viscosity is about 10^{12} Pa s for cooling rates of 1–10 K/min. In accordance with the Maxwell model, such a viscosity holds for macroscopic measurements whose timescale of $10^2 - 10^3$ s is typical of calorimetry or dilatometry experiments. This is why we term *standard* T_g the temperature at which the viscosity is 10^{12} Pa s. Consistent with this close link between viscosity and glass transition, the variation of T_g with the heating or cooling rate, q, is described by the empirical relation proposed by Moynihan et al. (1974):

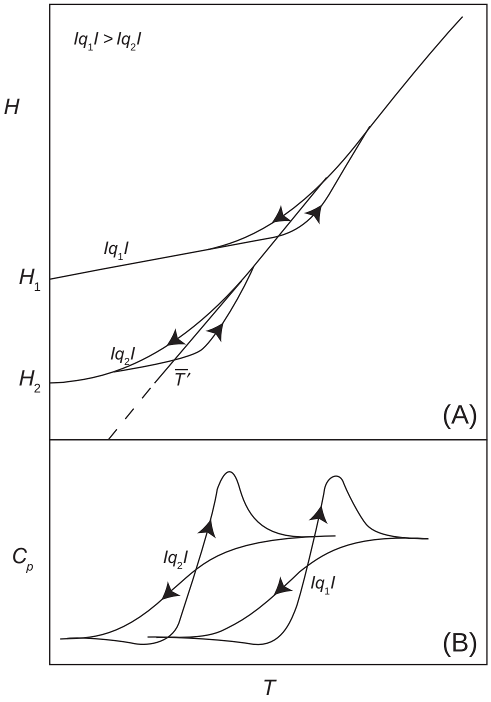

FIG. 2.16 (A) Enthalpy variations through the glass transition and associated changes in heat capacity. (B) The glass transition is cycled with two different heating and cooling rates $q_1$and q_2 (Moynihan et al., 1976). Note the higher enthalpy of the glass quenched with the fastest cooling rate, and the hysteresis observed for H and C_p at the transition.

$$d \ \ln |q|/d(1/T_g) = -\Delta H_\eta / R, \tag{2.12}$$

where R is the gas constant, and $\Delta H_\eta = R \ \partial \ \ln \eta / \partial(1/T)$, the activation enthalpy for viscous flow, which also characterizes the temperature dependence of relaxation times over restricted temperature intervals. For a typical ΔH_η-value of 500 kJ/mol and a standard glass transition temperature of 1000 K, Eq. (2.12) indicates that T_g increases by only 30 K when the cooling rate varies from 0.01 to 100 K/s. Such a width is small. Nonetheless, it allows structural studies made on glasses quenched at different rates to yield valuable information on configurational changes induced by larger temperature variations (Geissberger and Galeener, 1983). This intimate connection between dT_g/dq and viscosity, in turn, allows ΔH_η to be estimated from the observed width of the glass transition (Moynihan, 1993).

Shorter experimental timescales shift the glass transition to higher temperatures (Fig. 2.2) just like faster heating or cooling rates. The rate dependence of the glass transition temperature is seen most clearly in measurements of the adiabatic compressibility (β_s) by sound velocity experiments. This compressibility is obtained from:

$$\beta_s = 1/\rho v_p^2, \tag{2.13}$$

where ρ is the density and v_p the compressional (or longitudinal) sound velocity. Equilibrium values are measured only if the pressure changes induced by the acoustic wave are short with respect to the time needed by the fluid to adjust its structure in response to this perturbation. Ultrasonic velocities and glass and melt compressibilities are then frequency independent (e.g., Rivers and Carmichael, 1987; Kress et al., 1989).

Ultrasonic measurements are made at megahertz frequencies, i.e., with timescales of the order of 10^{-6} s. From the Maxwell relationship (2.10), the relaxation times of the liquid are shorter than such a value only if the viscosity is lower than 1 Pa s. The glass transition thus occurs at much higher temperatures in ultrasonic measurements than in calorimetry or dilatometry experiments, as illustrated in Fig. 2.17 for sodium disilicate (Nikonov et al., 1982). Below 700°C, relaxation times are so long that configurational changes do not take place during the passage of acoustic waves. The liquid exhibits instead solid-like properties so that velocities do not depend on frequency. Configurational changes are revealed above 700°C by a temperature interval where v_p decreases markedly and becomes frequency dependent. The onset of this v_p decrease is found at lower temperatures for lower frequencies (i.e., shorter timescales). Then, the equilibrium state is reached at higher temperatures when a single linear temperature dependence is finally observed for v_p, shown as v_∞ in Fig. 2.17.

The effect of frequency on the glass transition temperature is even more dramatic when hypersonic sound velocities are measured by Brillouin scattering with timescales of the order of 10^{-10} s (see Masnik et al., 1993 for details). These timescales are so short that relaxed velocities are typically observed only above 2000 K for silicate melts (Vo-Thanh et al., 1996). At such high temperatures, the observed velocities are similar to the values determined by ultrasonic methods (Fig. 2.18). With decreasing temperatures, the loss of equilibrium is signaled by a progressive increase of the sound velocity. That Brillouin scattering begins to probe the acoustic properties of a material with a fixed configuration is also indicated by the possibility of measuring shear wave velocities (v_s), which are zero in a relaxed liquid, well above the standard glass transition temperature (Askarpour et al., 1993). The material is not really a "glass" because its configuration changes rapidly with temperature, but a "glass-like" material.

FIG. 2.17 Relaxation effects on the longitudinal sound velocity, v_p, of sodium disilicate melt as determined by ultrasonic measurements made at the frequencies indicated. The dashed lines v_∞ and v_{p0} indicate the unrelaxed velocity in the glass and the relaxed, equilibrium velocity in the liquid, respectively. By comparison, the standard glass transition is 450°C. *Redrawn from* Nikonov et al. (1982).

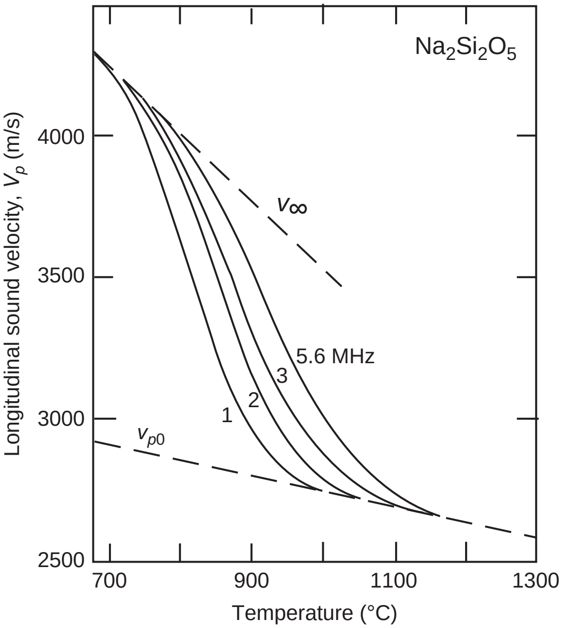

FIG. 2.18 Compressional sound velocity in a calcium aluminosilicate as measured ultrasonically (Webb and Courtial, 1996) and by Brillouin scattering (Vo Thanh, unpub. results). The *arrow* indicates the standard T_g. Because sound velocity in solids depends primarily on density, the break in Brillouin data around T_g is not due to the onset of configurational changes, but to the increase of thermal expansion at this temperature.

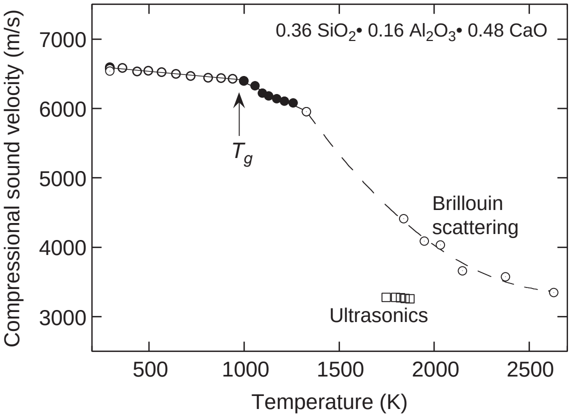

Only the solid-like part of its acoustic properties is probed. Its adiabatic compressibility is not the equilibrium value, but that of an isotropic solid:

$$\beta_s = 1/\rho\left(v_p^2 - 4/3v_s^2\right), \tag{2.14}$$

which joins smoothly with that of the real glass at the glass transition.

2.3.3 Fictive Temperature

The rate dependence of T_g has the important consequence that the enthalpy, entropy, or volume of a glass depend on thermal history and not only on pressure (P) and temperature (T). Ritland (1956) showed that all physical properties of a glass at given T and P cannot be specified by a single additional parameter. A number of parameters are required instead for rigorous descriptions of the index of refraction or electrical conductivity. For thermodynamic properties, however, a simple empirical description is generally appropriate because the heat capacity or thermal expansion coefficient of silicate glasses are not very sensitive to thermal history. For example, the enthalpy or volume curves of a glass formed with different cooling rates are practically parallel. Knowledge of the actual glass transition temperature thus enables the enthalpy or volume to be determined. For continuous cooling, this temperature is a third variable describing the state of a glass called the fictive temperature, $\overline{T}$. As an example, the enthalpy and entropy differences between two glasses having fictive temperatures $\overline{T}_1$ and $\overline{T}_2$ are given by:

$$\Delta H_a = \int_{\overline{T}_1}^{\overline{T}_2} (C_{pl} - C_{pg})dT, \quad \Delta S_a = \int_{\overline{T}_1}^{\overline{T}_2} (C_{pl} - C_{pg})/T\,dT, \tag{2.15}$$

where C_{pl} is the heat capacity of the equilibrium liquid and C_{pg} that of the glass. Analogous equations can be written in terms of thermal expansion coefficients for volume differences between glasses having differing thermal histories.

The fictive temperature is well defined only for glasses cooled rapidly below the glass transition range. What happens if the glass is heated back up to the glass transition range, i.e., in a temperature interval where structural relaxation will resume? Like enthalpy and volume, the fictive temperature must vary to approach the equilibrium value, which is the actual temperature of the experiment. Hence, the fictive temperature is more precisely defined as the temperature at which the glass configuration would be the equilibrium configuration of the supercooled liquid.

Although it cannot be measured directly, the fictive temperature is related to observable properties. The simplest way of doing so is to define it as that part of the given property (H, V, etc.) that relaxes, expressed in temperature units (Moynihan et al., 1976). Accordingly, we write for enthalpy relaxation:

$$H(T) = H_l(\overline{T}) - \int_{T}^{\overline{T}} C_{pg} dT, \tag{2.16}$$

where $H_l(\overline{T})$ is the equilibrium enthalpy at temperature $\overline{T}$. Differentiation of Eq. (2.16) with respect to T then yields the variation of $\overline{T}$ with temperature under the particular conditions of the experiment:

$$\mathrm{d}\overline{T}/\mathrm{d}T = (C_p - C_{pg})|_T / (C_{pl} - C_{pg})|\overline{T}. \tag{2.17}$$

This derivative is the relaxational part of the heat capacity, whose instantaneous value is denoted by C_p. It is zero for the glass and unity for the liquid. At equilibrium, the fictive temperature is equal to the actual temperature, i.e., $\overline{T}(T) = T$. For continuous cooling, Eqs. (2.16), (2.17) indicate that $\overline{T}$ tends to a limiting value $\overline{T}$, which depends on the cooling rate and is equal to the previously defined glass transition temperature.

2.3.4 Kauzmann Paradox and Residual Entropy

When viscous liquids escape crystallization, why do they eventually vitrify instead of remaining in the supercooled liquid state? One answer to this question is purely kinetic and relies only on increasingly long relaxation times on cooling. If experiments could last forever, any glass would eventually relax to the equilibrium state. Then, the glass transition would result only from the limited timescale of feasible measurements. In fact, a simple thermodynamic argument proposed by Kauzmann (1948), known as Kauzmann's paradox, indicates that this answer is incorrect.

The reason originates in the existence of a configurational contribution that causes the heat capacity of a liquid to be generally higher than that of a crystal of the same composition. As a consequence, the entropy of the liquid decreases faster than that of a crystal when the temperature is lowered (Fig. 2.19). If the entropy of the supercooled liquid is extrapolated to temperatures below the glass transition range, it will become lower than that of the crystal at a temperature T_K that is high enough for such an extrapolation to remain reasonable. This situation is not thermodynamically forbidden, but it seems unlikely, indeed, that an amorphous phase could have a lower entropy than a crystalline material of the same composition.

The conclusion is that an amorphous phase cannot exist below T_K. The temperature of such an entropy catastrophe constitutes the lower bound to the metastability limit of the supercooled liquid. As internal equilibrium cannot be reached below T_K, the liquid must undergo a phase transition before reaching it. This is, of course, the glass transition. Kauzmann's paradox suggests that, although it is kinetic in nature, it anticipates a thermodynamic transition whose nature is still debated extensively (e.g., Donth, 2001). In its original form, Kauzmann's paradox implicitly neglects possible differences in vibrational entropy between the amorphous and crystalline phases. This simplification is actually incorrect but it does not

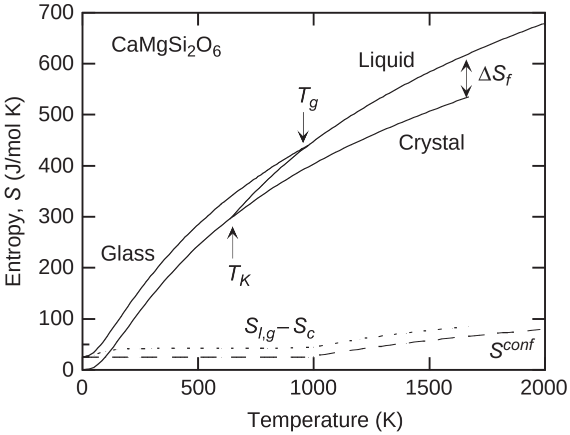

FIG. 2.19 Standard glass transition temperature, T_g, and temperature of Kauzmann paradox, T_K, for CaMgSi$_2$O$_6$. The entropy difference between the amorphous and crystalline phases, $S_{i,g} - S_c$, and the configurational entropy, S^{conf}, are also plotted. Calorimetric data as indicated by Richet et al. (1986).

detract from the gist of the argument, for taking into account such differences would only shift T_K slightly. A more rigorous statement of the paradox is that the catastrophe would occur when the configurational entropy of the supercooled liquid vanishes.

Although well established experimentally, the notion of residual entropies at 0 K for amorphous or disordered substances has been doubted lately (Mauro et al., 2007; Gupta and Mauro, 2008) on the grounds that the excess entropy of the liquid is completely lost at the actual glass transition when the system ceases to be ergodic, i.e., becomes unable to explore all its configurational states when its structure is frozen in. This statement has sparked a lively controversy, especially since simple statistical mechanical models had long been accounting quantitatively for the residual entropies measured for disordered crystals such as ice or CO. In contrast to this "kinetic" view, the "traditional" picture then has been defended on the basis of simple theoretical considerations (e.g., Goldstein, 2008) or of careful analysis of calorimetric measurements (Johari, 2011).

At the root of the disagreement are the ways in which microstates are counted in statistical mechanical models (Takada et al., 2015). Two different treatments are possible depending on whether Gibbs or Bolzmann entropy is considered. With the *kinetic* approach, on which the "entropy-loss" view rests, one counts only the number of states actually visited by the system at the observational timescale. With the *probabilistic* approach of the "conventional" standpoint, what matters instead is the probability of occurrence of the relevant states regardless of whether they are actually explored by the system. All extensive variables such as energy, volume, and entropy then remain state variables in nonequilibrium even though more than two of them are needed to characterize the overall state of the system. Their values thus keep well defined at each instant, in agreement with the equivalence of the kinetics of structural, enthalpy, and volume relaxation observed for silicate melts (Takada et al., 2015). Such a *spatial* sampling is consistent with the recent, extensive analysis made by Gujrati (2010), which relies on the "additivity" of extensive variables over different macroscopic parts of a system and dismisses the relevance of ergodicity and "temporal sampling" to the entropy of glasses and supercooled liquids. Of more practical interest for our purpose is the fact that the traditional standpoint is also strongly supported experimentally by the nice agreement found between entropies at the glass transition determined from calorimetric and rheological measurements (see the following) as well as by the composition dependence of calorimetric residual entropies, which are making sense in structural terms (see the next chapter).

2.4 CONFIGURATIONAL PROPERTIES

The configurational contributions to physical properties are a macroscopic consequence of atomic mobility. The second-order thermodynamic properties of liquids thus differ from those of glasses. Specifically, the configurational heat capacity and compressibility are necessarily positive. The reason is found in Le Chatelier's Laws, which dictate that the temperature dependence of entropy and the pressure dependence of volume are greater for the liquid than for the glass phase of a substance. Although there is no such thermodynamic constraint on the configurational thermal expansion coefficient, experience shows that it is also generally positive.

A practical difficulty in determination of configurational properties is the so-called crystallization curtain, which generally prevents observations in temperature intervals between T_g and the liquidus. When physical measurements can be performed accurately, however, the difficulty is not serious as long as experiments are made even over a narrow temperature range just above the glass transition and above the liquidus. As shown for the heat capacity (Richet and Bottinga, 1984) or the density (Bottinga et al., 1982; Lange, 1996), interpolations between the two ranges then yield reliable values because of the smooth variations of properties that prevail in the whole liquid range (Richet and Bottinga, 1980). In particular, there is no singularity at the liquidus temperature since the properties of supercooled liquids cannot be influenced by the possible formation of a crystalline phase.

2.4.1 Thermal Properties

Whereas the heat capacity is an additive function of composition for silicate glasses (Richet, 1987), it varies in a complex way for melts (Fig. 2.20). In practical terms, the distinction between vibrational and configurational contributions is useful only if their relative importance can be evaluated. One can write:

$$C_p = C_p^{vib} + C_p^{conf}, \tag{2.18}$$

but determination of the configurational part requires knowledge of the baseline vibrational C_p. Strictly speaking, these contributions are not mutually independent. Configurations of higher energy tend to be associated with lower vibrational frequencies and, thus, with higher vibrational heat capacities and entropies. Fortunately, silicates exhibit a very useful simplifying feature, first pointed out by Haggerty et al. (1968). With usual cooling rates, the glass transition occurs when the isobaric heat capacity of the glass is close to $3R/g$ atom ($R =$ gas constant). This is the Dulong-and-Petit harmonic limit for the isochoric heat capacity (from which, as already noted, C_p differs little).

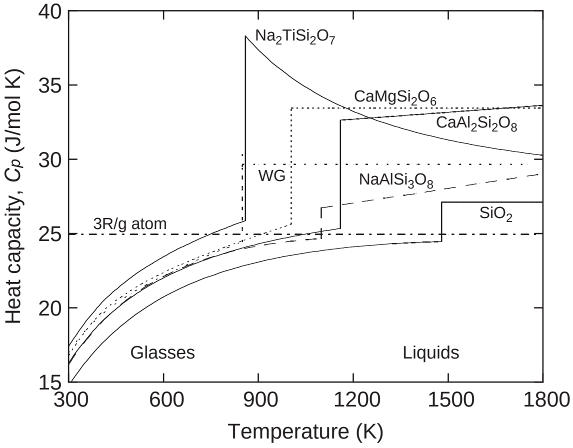

FIG. 2.20 Heat capacity of a variety of silicates glasses and melts. Data for WG (window glass) from Richet et al. (1997). See Richet and Bottinga (1995) for other data sources.

As listed by Richet and Bottinga (1986) and illustrated in Fig. 2.20, subsequent measurements have confirmed this correlation although both the magnitude of the heat capacity change at T_g and the temperature dependence of the liquid heat capacity depend markedly on chemical composition. The only exceptions to this rule are some borosilicates and hydrous silicates (Richet et al., 1997; Bouhifd et al., 2006). For reasons discussed by Richet et al. (1986), the vibrational C_p should not vary significantly with temperature above T_g. It follows that the configurational heat capacity (C_p^{conf}) can be determined from the equation:

$$C_p^{conf} = C_{pl} - C_{pg}(T_g). \tag{2.19}$$

This expression also shows that most of the temperature dependence of C_{pl}, if any exists, can be ascribed to temperature-dependent configurational changes in the liquid. Likewise, the composition dependence of C_{pl} is the same as that of the configurational heat capacity.

The existence of a configurational heat capacity implies that configurational parts can also be defined for the enthalpy and entropy. Their variations with temperature are given by:

$$C_p^{conf} = \left(\partial H^{conf}/\partial T\right)p = T\left(\partial S^{conf}/\partial T\right)_p. \tag{2.20}$$

Between any two temperatures, T_1 and T_2, the variations of configurational enthalpy and entropy are:

$$H^{conf} = H^{conf}(T_1) + \int_{T_1}^{T_2} C_p^{conf}\, dT, \tag{2.21}$$

and

$$S^{conf} = S^{conf}(T_1) + \int_{T_1}^{T_2} C_p^{conf}/T\, dT. \tag{2.22}$$

2.4.2 Volume Properties

Another general feature of interatomic potentials is their anharmonic nature, because displacements of the vibrating atoms from their equilibrium positions are not strictly proportional to the forces exerted on them. Because increasing vibrational amplitudes result in increasing interatomic distances (Fig. 2.15), the thermal expansion coefficient is generally positive for glasses. In the liquid, it increases markedly when even greater interatomic distances result from configurational changes. Because melts are isotropic, their volume thermal expansion coefficient is three times the linear coefficient derived from dilatometry experiments. In such experiments, the increase of thermal expansion is revealed by the important variation of the slope of the length-temperature relationship (Fig. 2.1). Because measurements are generally made at a constant heating rate, relaxation is not complete when the length of the sample begins to decrease at the so-called softening point as a result of not so high a viscosity. It follows that the configurational thermal expansion coefficient (α^{conf}) differs from the observed change in thermal expansion coefficient ($\Delta\alpha$) at T_g.

Experimentally, the difficulties due to incomplete relaxation can be obviated in three different ways. First, one can take advantage of the equivalence of relaxation kinetics for enthalpy and volume so that calorimetric data can serve as templates for deriving α_l through extrapolation of the dilatometric measurements (Knoche et al., 1992). Second, thermal expansion can be measured for a sample enclosed in an appropriate container in which softening does not affect the dilatometric experiment (Gottsmann et al., 1999). Third, vibrational and configurational relaxation can be observed directly in high-precision dilatometric experiments made at constant temperature (Fig. 2.8), and the equilibrium thermal expansion coefficient (α_l) can be determined for the supercooled liquid (Toplis and Richet, 2000).

Compressibility is also made up of vibrational and configurational contributions just like other physical properties discussed in this chapter. Because the shape of interatomic potentials determines the vibrational energy levels, compression is termed vibrational for the elastic part of the deformation. As for the configurational contribution, it manifests itself when the applied pressure changes the potential energy wells and causes modifications in short-range order through shorter equilibrium distances and steeper slopes around the minima pictured in Fig. 2.15. These two contributions can be separated by a combination of experiments made at different timescales. As described in Section 2.3.2, ultrasonic measurements yield the equilibrium adiabatic compressibility, whereas Brillouin scattering experiments probe only its vibrational part. The configurational compressibility is then given by the difference between these two results (Askarpour et al., 1993).

2.4.3 Permanent Compaction of Glass

In the same way that glasses can have different fictive temperatures, glasses with different fictive pressures can be prepared (Fig. 2.21). The compact configuration achieved by a melt at high pressure is frozen in if the glass transition takes place at the pressure of the experiment (Tammann and Jenckel, 1929). Because the melt is necessarily more compressible than the glass, permanent compaction arises from the fact that only the elastic part of compression is released when the glass is eventually decompressed to ambient pressure at room temperature. The density of a glass thus increases with the pressure at which the liquid is quenched.

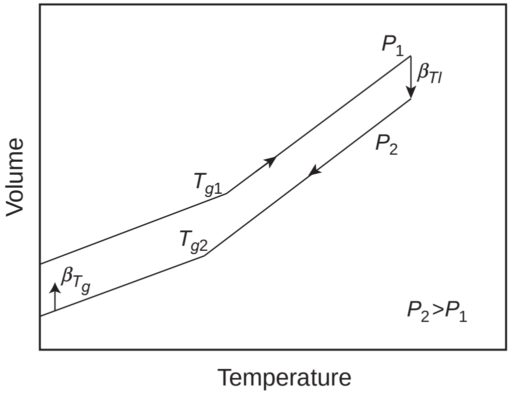

FIG. 2.21 Permanent compaction of a glass that has been frozen in at temperature T_{g1}, at the high pressure P_1, and then brought back to room pressure (P_2). The difference between the isothermal compressibilities of the liquid (β_{T_l}) and the glass (β_{T_g}) phases originates in the existence of a configurational contribution in the former.

This feature is another indication that glasses are nonequilibrium substances. It offers an indirect way to estimate the compressibility of the liquid (Maurer, 1957).

As shown in Fig. 2.22 for a series of hydrous tephrite glasses, permanent compaction becomes significant for synthesis pressures of a few hundred megapascals (i.e., a few kilobars). Because the pressure dependence of T_g is small for amorphous silicates (Rosenhauer et al., 1979), the effect depends primarily on the pressure at which vitrification occurs and on the compressibility contrast between the liquid and glass. If the compacted glass is heated at room pressure, its density decreases to the value of the same glass formed at this pressure. Such a volume relaxation begins well below the standard T_g (Mackenzie, 1963a). For compacted hydrous phonolite glasses (Fig. 2.23), it causes the thermal expansion coefficient to become anomalously high at temperatures at which the viscosity is about 10^{16} Pa s (Bouhifd et al., 2001). On further heating after complete relaxation, a "normal" expansivity is, in contrast, observed (Fig. 2.23).

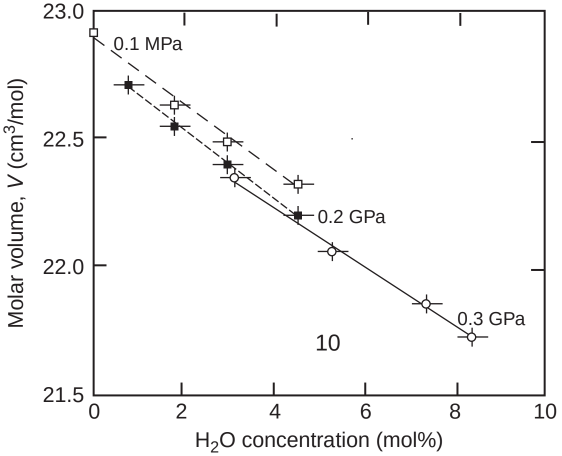

FIG. 2.22 Molar volume of a Fe-free hydrous "tephrite" glasses against water content for samples synthesized at the indicated pressures (Richet et al., 2000). The 0.1 MPa (room pressure) data refer to glasses relaxed at this pressure.

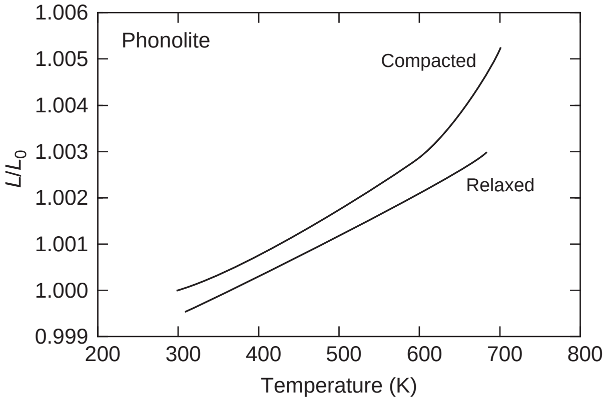

FIG. 2.23 Volume relaxation of a Fe-free hydrous "phonolite" glass during dilatometric experiments (Bouhifd et al., 2001) with 1.6 wt% H_2O synthesized at 0.3 GPa (3 kbar, *compacted curve*) and after relaxation to the room-pressure density *(relaxed curve)*.

Interestingly, glasses compressed at low temperature to pressures of a few gigapascals also undergo permanent compaction. This effect was discovered by Bridgman and Simon (1953) for SiO_2 glass compressed beyond 10 GPa in minute-long experiments at room temperature. For example, an 18% compaction was observed for a peak pressure of 20 GPa. Especially under nonhydrostatic stresses (see Mackenzie, 1963b), high pressure can induce large irreversible configurational changes at temperatures at which the substance is said to be a glass. For given frequencies or experimental timescales, the kinetics of pressure- and temperature-induced configurational modifications are thus markedly different. This dissimilarity exists because potential energy wells vary much less with temperature than with pressure. At elevated temperatures, high kinetic energy simply allows states of higher potential energy to be explored. At sufficiently high pressure, the shape of the potential energy wells change, even at low temperature, in a way that gives rise to new configurations.

2.4.4 Permanent Compaction and Volatile Solubility

Variable permanent compaction at room temperature and pressure is the clearest illustration that the thermodynamic state of a glass cannot be described by only two state variables. This issue has an important bearing on the notion of volatile solubility, which will thus be reviewed briefly here.

Especially under the high pressures of the earth's interiors, the solubility of various volatiles can be high enough to affect melt properties markedly (Chapters 14–17). Considerable difficulties are raised, however, by experiments at simultaneously high pressures and temperature so that much information, especially on structure, has been derived from volatile-bearing glasses studied at ambient conditions. For the parent melt, solubility is well defined by the equalities of the chemical potentials of the volatile and silicate components in both the fluid and melt phases at the P,T conditions of the experiment. For melt quenching, temperature is reduced quickly to ensure a temperature drop so rapid that the compositions of both phases are actually preserved. The P,T pathway followed varies somewhat not only when the experimental conditions are varied, but especially when different setups are used. The fictive temperatures and pressures are not well known and, more seriously, no chemical potential equalities can be written under ambient conditions between the quenched fluid and nonequilibrium glass.

When dealing with volatile-bearing *glasses*, one should thus use terms like *content* instead of *solubility*, and *bonding* or *insertion in the glass network* instead of *solubility mechanisms*. In accordance with these statements, we know that, except for the small and chemically inert noble gases (Chapter 17), there is no way to dissolve significant amounts of volatiles in a glass (i.e., below T_g). In other words, a reported volatile content of a glass as a proxy for its melt is meaningful only if reference is made to the equilibrium parent melt under well-defined P,T conditions.

2.4.5 Configurational Entropy and Viscosity

Configurational properties have proven most useful for dealing with the temperature, composition, and pressure dependence of the viscosity of silicate melts (Richet, 1984). We first note that any process induced by a temperature decrease is necessarily accompanied by an entropy decrease. This is the simplest evidence for the importance of entropy in glass transition and, thus, in glass formation. Among the many statistical mechanical models that have attempted to account for the glass transition and solve Kauzmann's paradox, the early one proposed by Gibbs and Di Marzio (1958) is of special interest. This model predicts that the supercooled liquid would transform to an "ideal" glass through a second-order transition at the temperature T_0 at which its configurational entropy would vanish.

Since then, the existence and the nature of such a transformation have been much debated. This discussion notwithstanding, the important point for our discussion is the result subsequently derived by Adam and Gibbs (1965) on the basis of a lattice model of polymers. This result is a very simple relationship between relaxation times and the configurational entropy of the melt, viz.:

$$\tau(T) = A \exp\left(B_e / TS^{conf}\right), \tag{2.23}$$

where A is a preexponential term and B_e is approximately a constant proportional to the Gibbs free energy barriers hindering the cooperative rearrangements of the structure. Qualitatively, the idea behind this theory is that structural rearrangements would be impossible in a liquid with zero configurational entropy so that relaxation time would be infinite. If two configurations only were available for an entire liquid volume, mass transfer would require a simultaneous displacement of all structural entities. The probability for such a cooperative event would be extremely small, but not zero, and the relaxation times would be extremely high, but no longer infinite. When configurational entropy increases, the cooperative rearrangements of the structure required for mass transfer can take place independently in smaller and smaller regions of the liquid. As embodied in Eq. (2.23), relaxation times thus decrease when configurational entropy increases.

As described by Goldstein (1969), such a relaxation model, relying on potential energy barriers, would apply to melts whose viscosity is higher than about 1 Pa s. Except for SiO_2-poor compositions, this is generally the case of silicate liquids. From a structural standpoint, nanoscale heterogeneities near the glass transition are a key ingredient of the model. Their existence has been established spectroscopically (e.g., Malinovsky and Sokolov, 1986). Moynihan and Schroeder (1993) have shown that these heterogeneities can indeed be interpreted as configurational entropy fluctuations and, in addition, that they can account for the aforementioned nonexponentiality of the kinetics of structural relaxation.

In a wide variety of contexts, the Adam-Gibbs (1965) theory of relaxation processes has received continuous interest (see McKenna and Glotzer, 1997). In this section, we will discuss briefly its application to the viscosity of silicate melts, referring to other papers for more detailed accounts (Richet, 1984; Richet and Bottinga, 1995; Toplis, 1998, 2001) or for connections with TVF equations and Kauzmann paradox (Sipp et al., 2001). In preamble, note that the two main parameters in Eq. (2.23), B_e and S^{conf}, have to be dealt with separately. The former is related to bond strength. Here, we will focus on the latter and examine how it accounts quantitatively for the temperature and composition dependences of viscosity over ranges which can cover more than 10^{13} orders of magnitude.

Quantitative applications of Adam-Gibbs theory, however, have long suffered from the difficulty in evaluating configurational entropy. A common approximation is to take the entropy difference between a melt and a crystal of the same composition. The data of Fig. 2.19 illustrate that this procedure is not warranted.

Silicates have the important advantage that their configurational heat capacity can be determined readily, which makes reliable calorimetric determinations of S^{conf} possible. By combining the Maxwell relationship (2.10) and Eq. (2.23), one finds that:

$$\log \eta = A_e + B_e / TS^{conf}, \tag{2.24}$$

where A_e is a constant. Richet (1984) thus pointed out that this equation could be checked quantitatively against experimental viscosity data if S^{conf} was evaluated with Eq. (2.22).

According to Eq. (2.24), the manner in which log η deviates from Arrhenius laws (Fig. 2.24A) as a function of composition is determined by the temperature dependence of S^{conf} (Fig. 2.24B) and thus by the magnitude of the configurational heat capacity. When calculating S^{conf} from Eq. (2.22), for reasons of consistency one generally takes the temperature T_1 as the fictive temperature of the glass used in calorimetric measurements. If the residual entropy of the glass has been measured, then Eq. (2.24) is a two-parameter equation. If not, the configurational entropy at T_g can also be determined from the observed viscosity-temperature relationship.

In fact, such a rheological approach has many advantages over calorimetric determinations of $S^{conf}(T_g)$ whose principle is depicted in Fig. 2.19. The viscosity experiments are much less tedious to perform than the comprehensive calorimetric measurements required to evaluate $S^{conf}(T_g)$. Viscosity data are also more accurate because the viscosity data do not represent small differences between large numbers, as do the calorimetric values. But a most useful feature is that this procedure is not restricted to the few mineral compositions for which the whole set of calorimetric measurements can be performed. From a theoretical standpoint, therefore, Eq. (2.24) is important because it represents the only means to determine configurational entropies for solutions and to calculate the thermodynamically important entropies of mixing (Fig. 2.25).

A general feature of viscosity is that its composition dependence is much stronger at low than at high temperatures. That viscosities should actually converge at infinite temperature is borne out by the Maxwell relationship (2.10) because relaxation times would then become

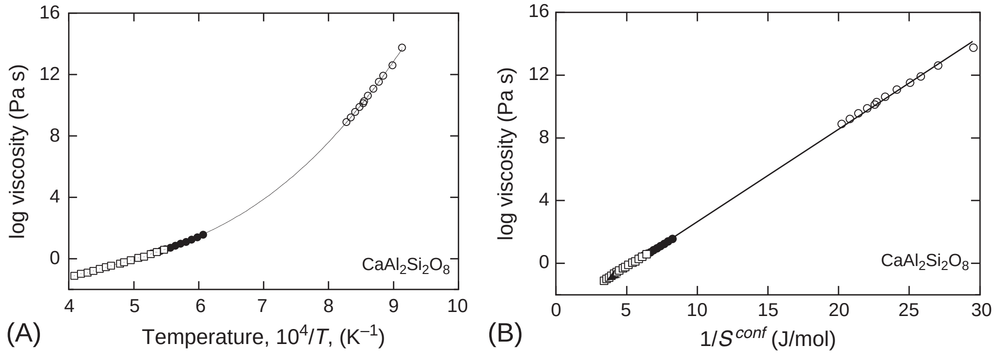

FIG. 2.24 Viscosity of stable and supercooled $CaAl_2Si_2O_8$ liquid. (A) Against reciprocal temperature. (B) Against $1/TS^{conf}$. Data from Urbain et al. (1982; *open squares*), Scarfe et al. (1983; *solid circles*), and Sipp et al. (2001; *open circles*).

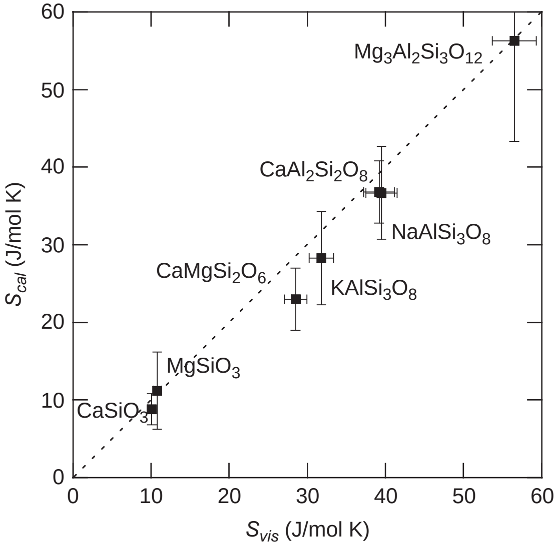

FIG. 2.25 Comparison between the configurational entropies at the standard glass transition temperature determined from calorimetric (S_{cal}) and viscosity (S_{vis}) measurements. *Redrawn from Richet and Bottinga (1995).*

nearly independent of any structural feature and be determined instead only by similar periods of atomic vibrations. At low temperature, the composition dependence of viscosity is, in contrast, extremely large with differences of more than 10^{12} orders of magnitude (e.g., Richet, 1984). According to the empirical TVF equation:

$$\ln \eta = A + B/(T - T_1), \tag{2.25}$$

the temperature T_1 at which the viscosity would diverge is a strong function of composition. This temperature is similar to the Kauzmann temperature at which the configurational entropy would vanish (see Sipp et al., 2001). Analytically, Eq. (2.25) might be derived from Eq. (2.24) under the assumption that C_p^{conf} is of the form a/T, where a is a constant. Such a temperature dependence does not hold true for silicates. The numerical equivalence of Eqs. (2.24), (2.25) has nonetheless been demonstrated from high-precision viscosities measured to more than 10^{13} Pa s (Sipp et al., 2001).

At constant temperature, configurational entropy depends on chemical composition. This is why Eq. (2.24) can also account for the composition dependence of viscosity (Richet, 1984). Many different factors contribute to S^{conf}. Their relative importance can vary markedly with temperature, with the result that the composition dependence of viscosity is generally much stronger near the glass transition than at higher temperatures (Fig. 2.26). A case in point is the entropy due to mixing of network-forming cations (e.g., Si and Al) or of network-modifier cations, such as alkali or alkaline earth cations, which can be assumed to mix ideally within a fixed silicate framework. For one mole of melt, Richet (1984) noted that the configurational entropy of mixing is:

$$\Delta S_m = -R \Sigma x_i \ln x_i, \tag{2.26}$$

FIG. 2.26 Viscosity of mixed (Ca, Mg) SiO_3 melts at the indicated temperatures (Neuville and Richet, 1991).

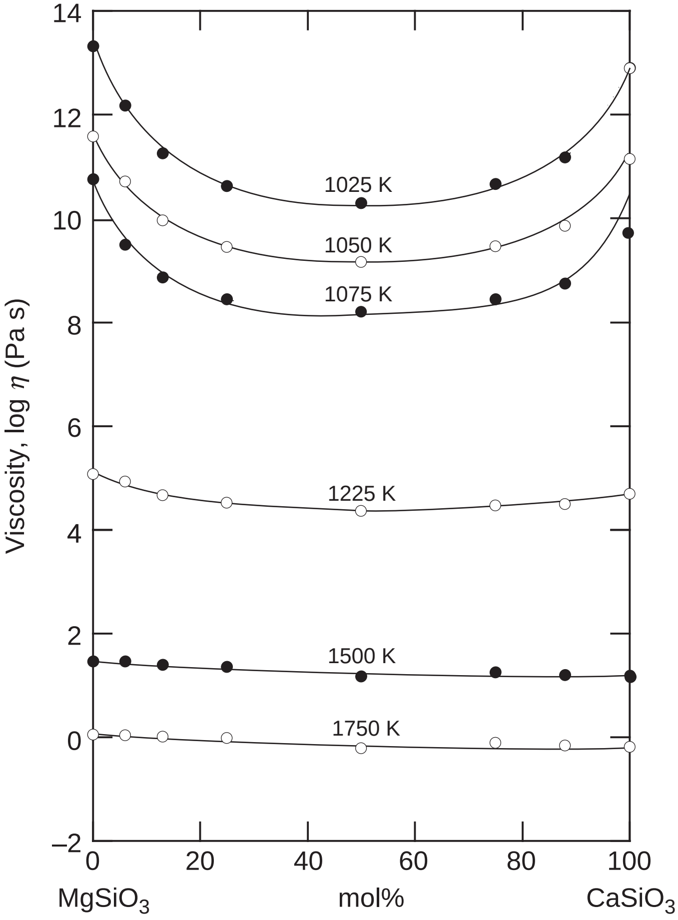

where the x_i are the mol fractions of the cations that mix, for instance Na and K, or Ca and Mg as considered in Fig. 2.26. For a given mixed melt, we then write:

$$S^{conf} = \Sigma x_i S_i^{conf} + \Delta S_m, \tag{2.27}$$

where ΔS_m is given by Eq. (2.26).

In $CaSiO_3$-$MgSiO_3$ melts, the good fit to the experimental data indicates that the deep viscosity minimum at low temperatures results directly from mixing of the $CaSiO_3$ and $MgSiO_3$ endmembers. However, the entropy of mixing as given by Eq. (2.25) does not vary with temperature. Its relative contribution to the total entropy, Eq. (2.27), thus decreases with increasing temperatures to the point that the viscosity becomes an almost linear function of composition (Fig. 2.26). Analogous trends are observed when structurally similar ions are exchanged. Examples include melts along the joins $K_2Si_3O_7$-$Na_2Si_3O_7$ (Richet, 1984) or

$Ca_3Al_2Si_3O_{12}$-$Mg_3Al_2Si_3O_{12}$ (Neuville and Richet, 1991), and molten $NaAlSi_3O_8$ mixed with H_2O and F (Dingwell and Mysen, 1985). Such trends do not hold true if mixing cannot be described with Eq. (2.26), for example because of differences in ionic radius or electrical charge. In such cases, mixing of two different silicate frameworks also contributes to the configurational entropy of mixing and Eq. (2.26) is no longer valid.

2.4.6 Glass Formation

Knowledge of composition ranges of glass formation is useful for a variety of practical reasons. In view of the rate dependence of the glass transition, the boundaries of such domains refer to specific conditions. These include not only the average cooling rate and size of the sample, but also the nature of the container or of the melting atmosphere because crystal nucleation is generally heterogeneous. Under well-defined conditions of homogeneous nucleation, a more precise approach consists of determining the critical cooling rate to be achieved for restricting the crystal volume fraction to a given value, generally taken as 10^{-6}, which is the resolution limit of the optical microscope. Such data are scarce, but they nonetheless demonstrate that critical rates depend strongly on composition. In particular (Fig. 2.27A), it appears that glass formation tends to be markedly favored around eutectic compositions (Richet et al., 2006).

The Maxwell relationship and the operational definition of the standard glass transition as the temperature at which viscosity is 10^{12} Pa s embody the intimate relationship between viscosity and vitrification. Any factor that causes a viscosity increase thus favors glass formation. Other things being equal, vitrification is easier near eutectics because freezing-point depression enables lower temperatures and higher viscosities to be reached. But this explanation is just a starting point because the viscosity variations along the liquidus curve represent a complex interplay of temperature and composition changes for alkali silicate melts (Fig. 2.27B). The viscosity first drops at high SiO_2 contents because the effects of the breakup of the SiO_2 structure predominate over those of rapidly decreasing liquidus temperatures (see

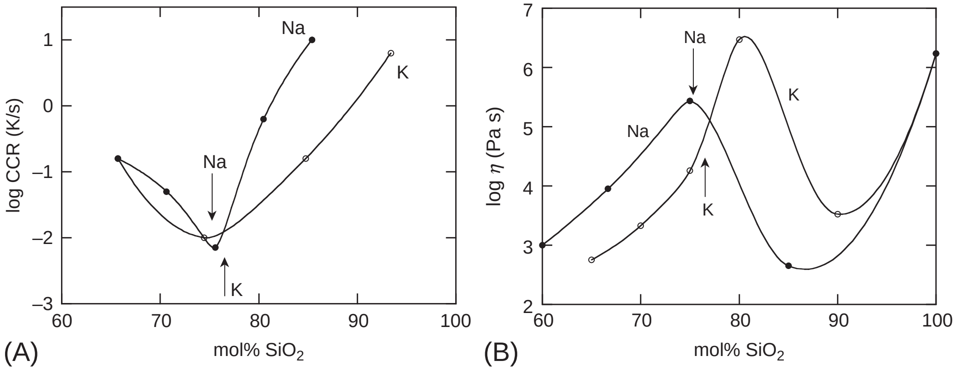

FIG. 2.27 Glass formation in the Na_2O-SiO_2 and K_2O-SiO_2 systems. (A) Critical cooling rate for vitrification (CCR) from Sipp et al. (2001, referring to crystal volume fractions lower than 10^{-6}). (B) Viscosity along the liquidus; data from Poole (1948), Bockris et al. (1955) and Urbain et al. (1982). The *arrows* indicate the positions of the SiO_2-$Na_2Si_2O_5$ and $K_2Si_2O_5$-$K_2Si_4O_9$ eutectics (see Fig. 6.1).

Fig. 6.16). The converse holds true for alkali oxide contents higher than about 12 mol%. The viscosity increases to a maximum value and then eventually falls off. Correspondence between the eutectic composition and the viscosity maximum is observed only for the Na_2O-SiO_2 system. For K_2O-SiO_2 melts, this explanation accounts for only part of the observed composition dependence of vitrification.

Deep freezing-point depressions at eutectic points are associated with negative enthalpies of mixing, i.e., with predominantly attractive interactions between the melt components. Because such negative values also result in compound formation, glass formation should take place in composition domains where compounds form within a given system. Such seemingly paradoxical correlations will indeed be observed repeatedly in the following chapters. Enthalpies of mixing must not be of too high a magnitude, however, or compounds with high liquidus temperatures will form and the kinetics of crystal growth will be too rapid even slightly below the liquidus because of too low a viscosity.

Glass formation is often discussed within the framework of crystal nucleation and growth. Unfortunately, not much information can be drawn in this respect, for the "classical" nucleation theory underestimates experimentally observed rates by tens of orders of magnitude (e.g., Fokin and Zanotto, 2000). One reason for this failure is that, especially at high degrees of supercooling, crystallization tends to produce metastable phases whose composition differs markedly from that of the stable liquidus phases (Roskosz et al., 2005). That kinetics takes over thermodynamics in the process is exemplified by supercooled $Mg_3Al_2Si_3O_{12}$ liquid which crystallizes congruently to aluminous enstatite instead of incongruently to the equilibrium assemblage forsterite + sapphirine + cordierite (Lejeune and Richet, 1995). Because crystallization is in this case accompanied by a 20% density increase, the factor limiting nucleation is clearly element diffusion to form three different phases and not the large structural rearrangements required for congruent crystallization of aluminous enstatite. However, the difficulty of incorporating kinetics in theories of glass formation is compounded by the fact that, owing to the decoupling between local and bulk relaxation, the diffusivity of network-modifying cations does not scale with viscosity. The consequence is that crystals are nonstoichiometric and enriched in the most mobile network-modifying cation (Roskosz et al., 2005).

A rigorous theory of glass formation has yet to be established (see the review by Ojovan, 2018). Configurational entropy is a factor that must be considered in this respect because of its close connection with viscosity. Of course, the important parameter is not viscosity at the liquidus temperature, where the driving force for crystallization is zero, but at large degrees of undercooling. Everything else being equal, melts lose entropy faster and thus vitrify less readily when they have high (e.g., alkaline earth silicates) rather than low (e.g., alkali silicates) configurational heat capacities. As an example, glasses with the M_2SiO_4 (orthosilicate) stoichiometry are extremely difficult to quench. For Mg_2SiO_4, the standard glass transition should be about 1000 K, as determined from extrapolations of data for joins in the MgO-Al_2O_3-SiO_2 system (Richet et al., 1993) or from a comparison with a molten peridotite (Dingwell et al., 2004). At this temperature, however, configurational entropy has nearly vanished (Fig. 2.28). To obtain the significant configurational entropy of 2–3 J/g atom K typical of silicate glasses, the fictive temperature should be in the range 1200–1300 K. This, in turn, requires high cooling rates of at least 700 K/min (Tangeman et al., 2001).

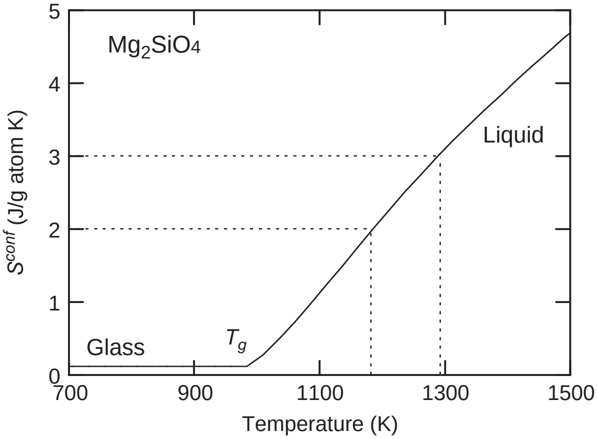

FIG. 2.28 Configurational entropy of Mg_2SiO_4 glass and liquid. The standard T_g of about 1000 K, estimated from data for magnesium aluminosilicate melts, is 130 K higher than the Kauzmann temperature Data from Richet et al. (1993).

Additional evidence supporting the importance of entropy in vitrification is provided by the so-called "invert" glasses (Hänlein, 1933; Trap and Stevels, 1960). These materials are SiO_2-poor but bear a number of other oxides such that configurational entropy of mixing is high and predominates over the topological contribution. For silicates, these glasses illustrate what is informally termed the "principle of confusion" in the literature on chalcogenide and other exotic glasses (e.g., Lucas, 1999). According to this rule, a more complicated chemical composition translates into a greater number of compounds that could nucleate and, thus, in mutual competition such that crystal nucleation and growth is frustrated and does not take place on sufficiently rapid cooling. In other words, the probability of forming viable nuclei through composition fluctuations of the melt is lower when several compounds can form than when a single crystal structure is available.

A last point must be mentioned to conclude this brief review. It has long been known that the state of a given glass depends on its pressure and temperature history so that one might distinguish an infinity of states through which the material would pass in a continuous way. The new idea that some of these states are in fact separated by abrupt discontinuity resembling crystal phase transitions has thus led to the concept of polyamorphism. As defined for a variety of systems (e.g., amorphous ice, Si or Ge semiconductors, SiO_2, GeO_2 or metallic glasses), these transitions are driven by density and entropy contrasts between low- and high-density liquid phases (e.g., McMillan and Wilding, 2018). Although their relevance to geological processes is doubtful, these phases are receiving much attention not only in view of the theoretical problems they are raising, but also because they could be used to design new nanomaterials.

References

Adam, G., Gibbs, J.H., 1965. On the temperature dependence of cooperative relaxation properties in glass-forming liquids. J. Chem. Phys. 43, 139–146.

Angell, C.A., Ngai, K.L., McKenna, G.B., McMillan, P.F., Martin, S.W., 2000. Relaxation in glass-forming liquids and amorphous solids. J. Appl. Phys. 88, 3113–3157.

Askarpour, V., Manghnani, M.H., Richet, P., 1993. Elastic properties of diopside, anorthite, and grossular glasses and liquids: a Brillouin scattering study up to 1400 K. J. Geophys. Res. 98, 17683–17689.

Berthier, L., Biroli, G., 2011. Theoretical perspective on the glass transition and amorphous materials. Rev. Mod. Phys. 83, 587–645.

Biroli, G., Garrahan, J.P., 2013. Perspective: the glass transition. J. Chem. Phys. 138, 12A301.

Bockris, J.O.M., Mackenzie, J.D., Kitchener, J.A., 1955. Viscous flow in silica and binary liquid silicates. Trans. Faraday Soc. 51, 1734–1748.

Boltzmann, L., 1874. Zur Theorie der elastichen Nachwirkung. I. Aufsuchung des matematischen Ausdruckes für die elastische Nachwirkung. Sitzber Kgl. Akad. Wiss. Wien. Math-Naturw Klasse 70, 275–306.

Bottinga, Y., Richet, P., 1996. Silicate melt structural relaxation; rheology, kinetics, and Adam-Gibbs theory. Chem. Geol. 128, 129–141.

Bottinga, Y., Weill, D., Richet, P., 1982. Density calculations for silicate liquids. I. Revised method for aluminosilicate compositions. Geochim. Cosmochim. Acta 46, 909–919.

Bouhifd, M.A., Whittington, A., Richet, P., 2001. Partial molar volume of water in phonolitic glasses and liquids. Contrib. Mineral. Petrol. 142, 235–243.

Bouhifd, M.A., Whittington, A., Roux, J., Richet, P., 2006. Effect of water on the heat capacity of polymerized aluminosilicate glasses and melts. Geochim. Cosmochim. Acta 70, 711–722.

Braedt, M., Frischat, G., 1988. Sodium self diffusion in glasses and melts of the system Na_2O-Rb_2O-SiO_2. Phys. Chem. Glasses 29, 214–218.

Bridgman, P.W., Simon, I., 1953. Effects of very high pressures on glass. J. Appl. Phys. 24, 405–413.

Chakraborty, S., 1995. Diffusion in silicate melts. In: Stebbins, J.F., McMillan, P.F., Dingwell, D.B. (Eds.), Structure, Dynamics and Properties of Silicate Melts, Reviews in Mineralogy. vol. 32, pp. 411–504.

Davies, R.O., Jones, G.O., 1953. Thermodynamic and kinetic properties of glasses. Adv. Phys. 2, 370–410.

Debenedetti, P.G., 1997. Metastable Liquids. Princeton University Press, Princeton.

Deubener, J., 2018. Viscosity of glass-forming melts. In: Richet, P. (Ed.), Encyclopedia of Glass Science, Technology, History and Culture. J. Wiley & Sons, Hoboken, NJ.

Dingwell, D.B., 1995. Relaxation in silicate melts: some applications. Rev. Mineral. 32, 21–66.

Dingwell, D.B., Mysen, B.O., 1985. Effects of water and fluorine on the viscosity of albite melt at high pressure: a preliminary investigation. Earth Planet. Sci. Lett. 266–274.

Dingwell, D.B., Webb, S.L., 1989. Structural relaxation in silicate melts and non-Newtonian melt rheology in geologic processes. Phys. Chem. Miner. 16, 508–516.

Dingwell, D.B., Webb, S.L., 1990. Relaxation in silicate melts. Eur. J. Mineral. 2, 427–449.

Dingwell, D.B., Courtial, P., Giordano, D., Nichols, A.R.L., 2004. Viscosity of peridotite liquid. Earth Planet. Sci. Lett. 226, 127–138.

Donth, E., 2001. The Glass Transition. Relaxation Dynamics in Liquids and Disordered Materials. Springer, Berlin.

Farnan, I., Stebbins, J., 1994. The nature of the glass transition in a silica-rich oxide melt. Science 265, 1206–1209.

Fokin, V.M., Zanotto, E.D., 2000. Crystal nucleation in silicate glasses: the temperature and size dependence of crystal/liquid surface energy. J. Non-Cryst. Solids 265, 105–112.

Fotheringham, U., 2018. Relaxation. In: Richet, P. (Ed.), Encyclopedia of Glass Science, Technology, History and Culture. J. Wiley & Sons, Hoboken, NJ.

Garden, J.-L., Guillou, H., 2018. Thermodynamics of glasses. In: Richet, P. (Ed.), Encyclopedia of Glass Science, Technology, History and Culture. J. Wiley & Sons, Hoboken, NJ.

Geissberger, A.E., Galeener, F.L., 1983. Raman studies of vitreous SiO_2 versus fictive temperature. Phys. Rev. B 28, 3266–3271.

George, A., Stebbins, J.F., 1998. Structure and dynamics of magnesium in silicate melts: a high-temperature ^{25}Mg NMR study. Am. Mineral. 83, 1022–1029.

Gibbs, J.H., Di Marzio, E., 1958. Nature of the glass transition and the glassy state. J. Chem. Phys. 28, 373–383.

Goldstein, M., 1969. Viscous liquids and the glass transition: a potential energy barrier picture. J. Chem. Phys. 51, 3728–3739.

Goldstein, M., 2008. On the reality of residual entropies of glasses and disordered crystals. J. Chem. Phys. 128, 154510.

Gottsmann, J., Dingwell, D.B., Gennaro, C., 1999. Thermal expansion of silicate liquids: direct determination using container-based dilatometry. Am. Mineral. 84, 1176–1180.

Gruener, G., Odier, P., De Sousa Meneses, D., Florian, P., Richet, P., 2001. Bulk and local dynamics in glass-forming liquids: a viscosity, electrical conductivity and NMR study of aluminosilicate melts. Phys. Rev. B. 64, 024206.

Gujrati, P.D., 2010. Loss of temporal homogeneity and symmetry in statistical systems: deterministic *versus* stochastic dynamics. Symmetry 2, 1201.

Gujrati, P.D., 2018. The glass transition and the entropy crisis. In: Richet, P. (Ed.), Encyclopedia of Glass Science, Technology, History and Culture. J. Wiley & Sons, Hoboken, NJ.

Gupta, P.K., Mauro, J., 2008. The laboratory glass transition. J. Chem. Phys. 126, 224504.

Haggerty, J.S., Cooper, A.R., Heasley, J.H., 1968. Heat capacity of three inorganic glasses and supercooled liquids. Phys. Chem. Glasses 5, 130–136.

Hänlein, W., 1933. Die physikalischen Eigenschaften des Systems SiO_2-Na_2O-K_2O-CaO. Z. Techn. Phys. 14, 418–424.

Hessenkemper, H., Brückner, R., 1989. Relaxation behaviour, high-temperature tensile strength and brittleness of glass melts. Glastechn. Ber. 62, 399–409.

Hessenkemper, H., Brückner, R., 1990. Some aspects of the workability of glass melts. Glastechn. Ber. 63, 19–23.

Hodge, I.M., 1994. Enthalpy relaxation and recovery in amorphous materials. J. Non-Cryst. Solids 169, 211–266.

Johari, G.P., 2011. Specific heat relaxation-based critique of isothermal glass transition, residual entropy and time-average formalism for ergodicity loss. Thermochim. Acta 523, 97–104.

Johnson, J.R., Bristow, R.H., Blau, H.H., 1951. Diffusion of ions in some simple glasses. J. Am. Ceram. Soc. 34, 165–172.

Kauzmann, W., 1948. The nature of the glassy state and the behavior of liquids at low temperatures. Chem. Rev. 43, 219–256.

Kieffer, J., Masnik, J.E., Reardon, B.J., Bass, J.D., 1995. High-frequency relaxational spectroscopy in liquid borates and silicates. J. Non-Cryst. Solids 183, 51–60.

Knoche, R., Dingwell, D.B., Webb, S.L., 1992. Temperature-dependent thermal expansivities of silicate melts: the system anorthite-diopside. Geochim. Cosmochim. Acta 56, 689–699.

Kohlrausch, F.W., 1863. Ueber die elastische Nachwirkung bei der Torsion. Ann. Phys. Chem. 119, 337–368.

Kress, V.C., Williams, Q., Carmichael, I.S.E., 1989. When is silicate melt not a liquid? Geochim. Cosmochim. Acta 53, 1687–1692.

Lange, R.A., 1996. Temperature independent thermal expansivities of sodium aluminosilicate melts. Geochim. Cosmochim. Acta 60, 4989–4996.

Lejeune, A.-M., Richet, P., 1995. Rheology of crystal-bearing silicate melts: an experimental study at high viscosities. J. Geophys. Res. 100, 4215–4229.

Lucas, J., 1999. Les verres de fluorures. Actual. Chim. 14–18.

Mackenzie, J.D., 1963a. High-pressure effects on oxide glasses: II. Subsequent heat treatment. J. Am. Ceram. Soc. 46, 470–476.

Mackenzie, J.D., 1963b. High-pressure effects on oxide glasses. I. Densification in rigid state. J. Am. Ceram. Soc. 46, 461–470.

Malinovsky, V.K., Sokolov, A.P., 1986. The nature of the boson peak in Raman scattering in glasses. Solid State Commun. 57, 757–761.

Masnik, J.E., Kieffer, J., Bass, J.D., 1993. Structural relaxations in alkali silicate systems by Brillouin light scattering. J. Am. Ceram. Soc. 76, 3073–3080.

Maurer, R.D., 1957. Pressure effects in the transformation range of glass. J. Am. Ceram. Soc. 40, 211–214.

Mauro, J., Gupta, P.K., Loucks, R.J., 2007. Continuously broken ergodicity. J. Chem. Phys. 126, 224504.

Maxwell, J.C., 1868. On the dynamical theory of gases. Philos. Mag. **35**, 129–145. 185–217.

Mazurin, O.V., Startsev, Y.K., Potselueva, L.N., 1979. Temperature dependences of the viscosity of some glasses at a constant structural temperature. Sov. J. Glass Phys. Chem. 5, 68–79.

McKenna, G.B., Glotzer, S.C., 1997. 40 years of entropy and the glass transition. J. Res. Nat. Inst. Stand. Technol. 102, 135–248.

McMillan, P.F., Wilding, M., 2018. Polyamorphism and liquid-liquid phase transitions. In: Richet, P. (Ed.), Encyclopedia of Glass Science, Technology, History and Culture. J. Wiley & Sons, Hoboken, NJ.

Meyer, A., Schober, H., Dingwell, D.B., 2002. Structure, structural relaxation and ion diffusion in sodium disilicate melts. Europhys. Lett. 59, 708–713.

Moynihan, C.T., 1993. Correlation between the width of the glass transition region and the temperature dependence of the viscosity of high-T_g glasses. J. Am. Ceram. Soc. 76, 1081–1087.

Moynihan, C.T., 1995. Structural relaxation and the glass transition. Rev. Mineral. 32, 1–19.

Moynihan, C.T., Schroeder, J., 1993. Non-exponential structural relaxation, anomalous light scattering and nanoscale inhomogeneities in glass-forming liquids. J. Non-Cryst. Solids 160, 52–59.

Moynihan, C.T., Easteal, A.J., Wilder, J., Tucker, J., 1974. Dependence of the glass transition temperature on heating and cooling rate. J. Phys. Chem. 78, 2673–2677.

Moynihan, C.T., Macedo, P.B., Montrose, C.J., Gupta, P.K., De Bolt, M.A., Dill, J.F., Dom, B.E., Drake, P.W., Easteal, A.J., Elterman, P.B., Moeller, R.P., Sasabe, M., Wilder, J.A., 1976. Structural relaxation in vitreous materials. Ann. N. Y. Acad. Sci. 279, 15–35.

Neuville, D.R., Richet, P., 1991. Viscosity and mixing in molten (Ca, Mg) pyroxenes and garnets. Geochim. Cosmochim. Acta 55, 1011–1020.

Newton, I., 1725. Philosophiae Naturalis Principia Philosophica, lib. II, cap. IX, third ed. (transl. by A. Motte as Mathematical Principles of Natural Philosophy, 1729, rev. by F. Cajori, University of California Press, Berkeley, 1934).

Nikonov, A.M., Bogdanov, V.N., Nemilov, S.V., Shono, A.A., Mikhailov, V.N., 1982. Structural relaxation in binary alkalisilicate melts. Fys. Khim. Stekla 8, 694–703.

Ojovan, M., 2018. Glass formation. In: Richet, P. (Ed.), Encyclopedia of Glass Science, Technology, History and Culture. J. Wiley & Sons, Hoboken, NJ.

Polian, A., Vo-Thanh, D., Richet, P., 2002. Elastic properties of a-SiO_2 up to about 2300 K from Brillouin scattering measurements. Europhys. Lett. 57, 375–381.

Poole, J.P., 1948. Viscosité à basse temperature des verre alcalino-silicatés. Verres Refract. 2, 222–228.

Rekhson, S.M., Bulaeva, A.V., Mazurin, O.V., 1971. Changes in the linear dimensions and viscosity of window glass during stabilization. Inorg. Mater. 7, 622–623.

Richet, P., 1984. Viscosity and configurational entropy of silicate melts. Geochim. Cosmochim. Acta 48, 471–483.

Richet, P., 1987. Heat capacity of silicate glasses. Chem. Geol. 62, 111–124.

Richet, P., 2001. The Physical Basis of Thermodynamics. Plenum Publishing, New York.

Richet, P., Bottinga, Y., 1980. Heat capacity of silicate liquids: new measurements on $NaAlSi_3O_8$ and $K_2Si_4O_9$. Geochim. Cosmochim. Acta 44, 1535–1541.

Richet, P., Bottinga, Y., 1984. Anorthite, andesine, wollastonite, diopside, cordierite and pyrope: thermodynamics of melting, glass transitions, and properties of the amorphous phases. Earth Planet. Sci. Lett. 67, 415–432.

Richet, P., Bottinga, Y., 1986. Thermochemical properties of silicate glasses and liquids: a review. Rev. Geophys. 24, 1–25.

Richet, P., Bottinga, Y., 1995. Rheology and configurational entropy of silicate melts. In: Stebbins, J.F., McMillan, P.F., Dingwell, D.B. (Eds.), Structure, Dynamics and Properties of Silicate Melts. In: Reviews in Mineralogy, vol. 32. Mineralogical Society of America, Washington, DC, pp. 67–93.

Richet, P., Bottinga, Y., Téqui, C., 1984. Heat capacity of sodium silicate liquids. J. Am. Ceram. Soc. 67, C6–C8.

Richet, P., Robie, R.A., Hemingway, B.S., 1986. Low-temperature heat capacity of diopside glass: a calorimetric test of the configurational entropy theory as applied to the viscosity of liquid silicates. Geochim. Cosmochim. Acta 50, 1521–1533.

Richet, P., Leclerc, F., Benoist, L., 1993. Melting of forsterite and spinel, with implications for the glass transition of Mg_2SiO_4 liquid. Geophys. Res. Lett. 20, 1675–1678.

Richet, P., Bouhifd, M.A., Courtial, P., Téqui, C., 1997. Configurational heat capacity and entropy of borosilicate melts. J. Non-Cryst. Solids 211 (3), 271–280.

Richet, P., Whittington, A., Holtz, F., Behrens, H., Ohlhorst, S., Wilke, M., 2000. Water and the density of silicate glasses. Contrib. Mineral. Petrol. 138, 337–347.

Richet, P., Roskosz, M., Roux, J., 2006. Glass formation. Insights from composition. Chem. Geol. 225, 388–401.

Ritland, H.N., 1956. Limitations of the fictive temperature concept. J. Am. Ceram. Soc. 39, 403–406.

Rivers, M., Carmichael, I.S.E., 1987. Ultrasonic studies of silicate melts. J. Geophys. Res. 92, 9247–9270.

Rosenhauer, M., Scarfe, C.M., Virgo, D., 1979. Pressure dependence of the glass transition temperature in glasses of diopside, albite, and sodium trisilicate composition. In: Carnegie Instn. Washington Year Book. vol. 78, pp. 547–551.

Roskosz, M., Toplis, M.J., Besson, P., Richet, P., 2005. Nucleation mechanisms: a crystal chemical investigation of highly supercooled aluminosilicate liquids. J. Non-Cryst. Solids 351, 1266–1282.

Scarfe, C.M., Cronin, D.J., Wenzel, J.T., Kauffmann, D.A., 1983. Viscosity-temperature relationships at 1 atm. in the system diopside-anorthite. Am. Mineral. 68, 1083–1089.

Scherer, G.W., 1986. Relaxation in Glasses and Composites. John Wiley & Sons, New York.

Siewert, R., Rosenhauer, M., 1997. Viscoelastic relaxation measurements in the system SiO_2-$NaAlSiO_4$ by photon correlation spectroscopy. Am. Mineral. 82, 1063–1072.

Sipp, A., Richet, P., 2002. Equivalence of volume, enthalpy and viscosity relaxation kinetics in glass-forming silicate liquids. J. Non-Cryst. Solids 298, 202–212.

Sipp, A., Neuville, D.R., Richet, P., 1997. Viscosity, configurational entropy and structural relaxation of borosilicate melts. J. Non-Cryst. Solids 211 (3), 281–293.

Sipp, A., Bottinga, Y., Richet, P., 2001. New viscosity measurements for 3D network liquids and new correlations between old parameters. J. Non-Cryst. Solids 288, 166–174.

Stebbins, J.F., Sen, S., Farnan, I., 1995. Silicate species exchange, viscosity, and crystallization in a low-silica melt: *in situ* high-temperature MAS NMR spectroscopy. Am. Mineral. 80, 861–864.

Stevenson, R.J., Dingwell, D.B., Webb, S.L., Bagdassarov, N.S., 1995. The equivalence of enthalpy and shear stress relaxation in rhyolitic obsidians and quantification of the liquid-glass transition in volcanic processes. J. Volcanol. Geotherm. Res. 68, 297–306.

Takada, A., Conradt, R., Richet, P., 2015. Residual entropy and structural disorder in glass: a review of history and an attempt to resolve two apparently conflicting views. J. Non-Cryst. Solids 429, 33–44.

Tammann, G., Jenckel, E., 1929. Die Zunahme der Dichte von Gläsern nach Erstarrung unter erhöhtem Druck und die Wiederkehr der natürlichen Dichte durch Temperatursteigerung. Z. Anorg. Allg. Chem. 184, 416–420.

Tangeman, J.A., Phillips, B.L., Navrotsky, A., Weber, J.K.R., Hixson, A.D., Key, T.S., 2001. Vitreous forsterite (Mg_2SiO_4): synthesis, structure, and thermochemistry. Geophys. Res. Lett. 28, 2517–2520.

Terai, R., Oishi, Y., 1977. Self-diffusion of oxygen in soda-lime silicate glass. Glastechn. Ber. 50, 68–73.

Toplis, M.J., 1998. Energy barriers associated with viscous flow and the prediction of glass transition temperatures of molten silicates. Am. Mineral. 83, 480–490.

Toplis, M.J., 2001. Quantitative links between microscopic properties and viscosity of liquids in the system SiO_2-Na_2O. Chem. Geol. 174, 321–331.

Toplis, M.J., Richet, P., 2000. Equilibrium expansivity of silicate liquids in the glass transition range. Contrib. Mineral. Petrol. 139, 672–683.

Trap, H.J.L., Stevels, J.M., 1960. Conventional and invert glasses containing titania. Part 1. Phys. Chem. Glasses 1, 107–118.

Urbain, G., Bottinga, Y., Richet, P., 1982. Viscosity of liquid silica, silicates and aluminosilicates. Geochim. Cosmochim. Acta 46, 1061–1072.

Vo-Thanh, D., Polian, A., Richet, P., 1996. Elastic properties of silicate melts up to 2350 K from Brillouin scattering. Geophys. Res. Lett. 23, 423–426.

Wakabayashi, H., 1977. Self-diffusion coefficients of calcium in molten soda-lime-silica glass. J. Non-Cryst. Solids 24, 427–429.

Webb, S.L., 1992a. Shear, volume, enthalpy and structural relaxation in silicate melts. Chem. Geol. 96, 449–457.

Webb, S.L., 1992b. Low-frequency shear and structural relaxation in rhyolite melt. Phys. Chem. Glasses 19, 240–245.

Webb, S.L., Courtial, P., 1996. Compressibility of melts in the CaO-Al_2O_3-SiO_2 system. Geochim. Cosmochim. Acta 60, 75–86.

Webb, S.L., Knoche, R., 1996. The glass transition, structural relaxation and shear viscosity of silicate melts. Chem. Geol. 128, 165–183.

Winchell, P., 1969. The compensation law for diffusion in silicates. High Temp. Sci. 1, 200–215.

Yageman, V.D., Matveev, G.M., 1982. Heat capacity of glasses in the system SiO_2-$Na_2O.SiO_2$. Fiz. Khim. Stekla 8, 238–245.

Yinnon, H., Cooper, A.R., 1980. Oxygen diffusion in multicomponent glass forming silicates. Phys. Chem. Glasses 21, 204–211.

Zanotto, E.D., Gupta, P.K., 1999. Do cathedral glasses flow? Additional remarks. Am. J. Phys. 67, 260–262.

CHAPTER

3

Glasses and Melts Versus Crystals

OUTLINE

3.1 INTRODUCTORY COMMENTS

Although much information has been gathered on glasses and melts, crystals remain useful references for discussing the structure and properties of these materials. The reason is, of course, that long-range symmetry makes structural determinations much easier for crystals than for glasses and liquids. If a property-composition-structure relationship is known for crystals, then comparisons with glasses or melts can provide valuable insights into structural features relevant to the same property of the amorphous phases. In this respect, however, an important simplifying feature of glasses and melts is that their properties tend to vary smoothly with composition, without the irregularities of crystal properties that originate in the specificity of each crystal structure. In other words, conclusions drawn from a few amorphous compositions can in general be extended to a much wider composition range than those made for crystals.

Glasses are solids that share with crystals common features determined by atomic vibrations in a fixed configuration. At the atomic scale, the structure of both kinds of phases can be

https://doi.org/10.1016/B978-0-444-63708-6.00003-X

considered as a three-dimensional arrangement of the oxygen coordination polyhedra. This arrangement is disordered in glasses because of lack of long-range order, but there nevertheless remain definite short-range order similarities with crystals. As will be seen, these manifest themselves in two important thermochemical properties, the low-temperature heat capacity and entropy.

Because liquids undergo configurational changes, they differ from both glasses and crystals for all features related in some way to atomic mobility. As described in Chapter 2, the physical properties of glasses and liquids do join smoothly at the glass transition. It follows that any difference in structure and properties between melts and solids, whether vitreous or crystalline, are highest at higher temperatures in spite of the extensive disordering that can manifest itself in crystals near the melting point (Fig. 3.1). Moreover, thermochemical data demonstrate that structural differences between a glass and a melt at superliquidus temperatures can be as great as those between a glass and a crystal of the same composition.

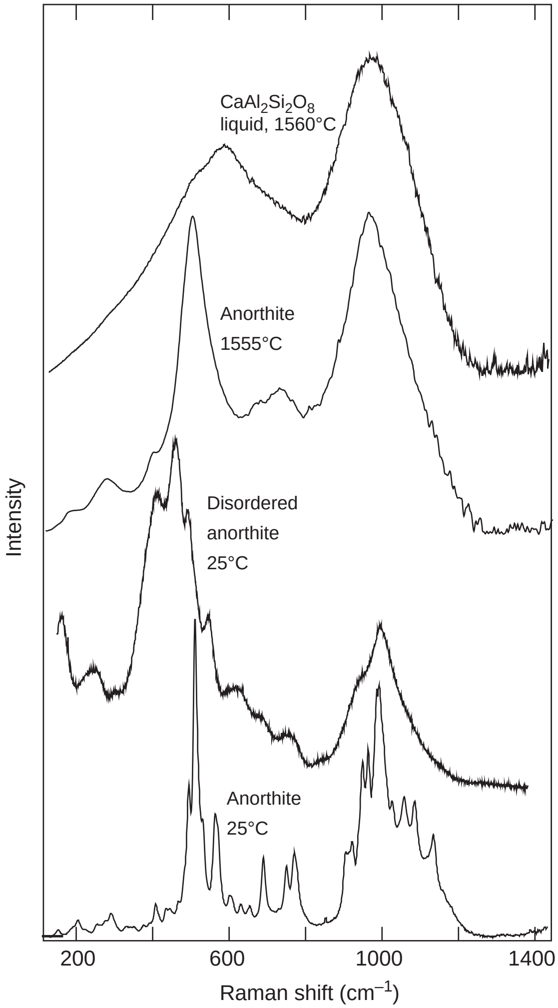

FIG. 3.1 Raman spectra of anorthite and $CaAl_2Si_2O_8$ liquid (Mysen, unpub.). The spectrum of a disordered anorthite grown near the glass transition is included for comparison (Roskosz et al., 2005).

In view of such differences, the specific features of the liquid state must be understood. For this purpose, silicate crystals again represent a useful starting point. At temperatures that can be more than 200 K lower than the reported melting points, they show anomalous variations of physical properties that also are due to configurational changes. In the last part of this chapter, attention will thus be paid to cation disorder, α-β transitions, and premelting effects, whose mechanisms give some insights on similar rearrangements that operate in melts, in particular upon crystallization and melting.

It may, nonetheless, be useful to recall that the glimpses provided by high-temperature studies of crystals do not represent a comprehensive picture of atomic mobility and associated structural changes in liquids. Because of lack of long-range order, melts can sample a much wider configurational space than crystals. In particular, rare structural units in crystals could be common in melts. As a single example, temperature increases appear to induce a change to the unusual fivefold coordination for a small fraction of the network-forming cations Si^{4+} and Al^{3+} (Stebbins, 1991; Stebbins and McMillan, 1993). In spite of usefulness of crystal structure information, comparisons with crystals cannot be a complete substitute for direct structural investigations of glasses and melts.

3.2 THERMODYNAMIC PROPERTIES

From a thermochemical standpoint, crystals are the necessary starting point for determinations of melt properties. This holds especially true for entropy, whose "absolute" value can be determined only from a cycle that begins with the third-law zero value of the crystal (see Chapter 2; Fig. 2.19). Hence, it is appropriate to first review a few aspects of heat capacity, C_p, and entropy, S, of crystals relevant to amorphous phases. In preamble, note that the difference between the isobaric and isochoric heat capacity is equal to $TV\alpha^2/\beta_T$ where α is the thermal expansion coefficient and β_T the isothermal compressibility. For glasses, this difference is so small that it will be consistently neglected in the following discussion (Richet and Bottinga, 1980).

Leaving aside the theoretical aspects briefly alluded to in Chapter 2, Section 2.3.4, practical application of equilibrium thermodynamics to glasses might seem unwarranted because the existence of a reversible pathway between any two temperatures is required to define the entropy of a phase. Now, the heat capacity hysteresis represented in Fig. 2.16 indicates that some entropy is created when C_p/T is integrated along a heating and cooling cycle through the glass transition range. This is, indeed, an intrinsic feature of the irreversibility of a nonequilibrium transformation. In practice, however, the entropy created is small relative to the vibrational entropy of the glass (Bestul and Chang, 1965). Hence, the deviations of experimental pathways from reversible ones are not a significant problem in calorimetric measurements so that they do not prevent the entropy of a glass from being defined operationally.

3.2.1 High-Temperature Enthalpy and Entropy

In solids, the isobaric heat capacity (C_p) is the physical property most directly related to atomic vibrations (Hehlen and Rufflé, 2018). For silicates above ambient temperature, its value is already close to the Dulong-and-Petit limit of 3R/g atom K. It cannot depend sensitively on vibrational density of states and, thus, on structure because this limit depends only on the number of atoms in the selected gram formula weight. This is the reason why glasses and crystals have similar heat capacities, except at low temperatures and in phase transition regions.

As discussed in the previous chapter, there is an abrupt C_p increase at the glass transition, T_g, caused by the onset of configurational changes in the liquid. For enthalpy, this implies that differences between crystals and melts increase markedly from T_g to superliquidus conditions (Fig. 3.2). The effect is similar to that already pictured in Fig. 2.19 (Chapter 2) for the entropy in connection to Kauzmann's paradox. For both enthalpy and entropy, the differences between glasses and crystals at the glass transition temperature can be half of those observed between liquids and crystals at the liquidus. These variations demonstrate unambiguously the importance of temperature-induced structural changes in liquids. When investigating the structure of glasses near room temperature, it should thus be kept in mind these differences between a glass at T_g and a liquid at high temperature can be as great as those between a crystal and a glass at room temperature.

The enthalpy and entropy differences between crystals and melts—the enthalpy and entropy of fusion for short—play a fundamental role in determining solid-liquid equilibria. These properties must be known accurately for thermodynamic calculations. As shown in Fig. 3.3 for lithium and sodium metasilicates, the simplest way would be to measure the enthalpy released by a melt when it crystallizes. The sluggish nature of crystallization in silicate systems usually makes such experiments impossible, however, because often melts vitrify or undergo only partial crystallization on cooling.

The problem raised by the glass-forming tendency may be circumvented through solution calorimetry. After complete dissolution in an appropriate solvent, the same final state (i.e., the same speciation) is obtained for initially amorphous and crystalline phases. The enthalpy differences between both phases (the enthalpy of vitrification) then is simply the difference, $\Delta H_v(T_v)$, between the enthalpies of solution measured at temperature T_v. Experiments are made either in HF solutions near room temperature (e.g., Hovis et al., 1998), or in molten lead borate near 700°C (e.g., Navrotsky, 1997).

Denoting by C_{pc}, C_{pg}, and C_{pl} the heat capacities of the crystal, glass, and liquid, respectively, the enthalpy of fusion at any temperature, T, is calculated from:

$$\Delta H_f(T) = \Delta H_v(T_v) + \int_{T_v}^{\overline{T}} \left(C_{pg} - C_{pc}\right) dT + \int_{\overline{T}}^{T} \left(C_{pl} - C_{pc}\right) dT, \tag{3.1}$$

where $\overline{T}$, the fictive temperature of the glass investigated in solution calorimetry, must be known as accurately as possible.

The enthalpy versus temperature plots of Fig. 3.2 illustrate the calculations made with Eq. (3.1). A summary of enthalpies of fusion was published by Richet and Bottinga (1986). Since then, additional measurements have been made by Zigo et al. (1987) for gehlenite ($Ca_2Al_2SiO_7$: $\Delta H_f = 172 \pm 6$ kJ/mol at $T_f = 1863$ K); by Richet et al. (1993a) for spinel ($MgAl_2O_4$: $\Delta H_f = 107 \pm 11$ kJ/mol at $T_f = 2408$ K), and forsterite (Mg_2SiO_4: $\Delta H_f = 142 \pm 14$ kJ/mol at $T_f = 2174$ K); by Sugawara and Akaogi (2003) for Ni_2SiO_4 ($\Delta H_f = 221 \pm 26$ kJ/mol at $T_f = 1923$ K) and Co_2SiO_4 ($\Delta H_f = 103 \pm 15$ kJ/mol at $T_f = 1688$ K); by Sugawara and Akaogi (2004) for

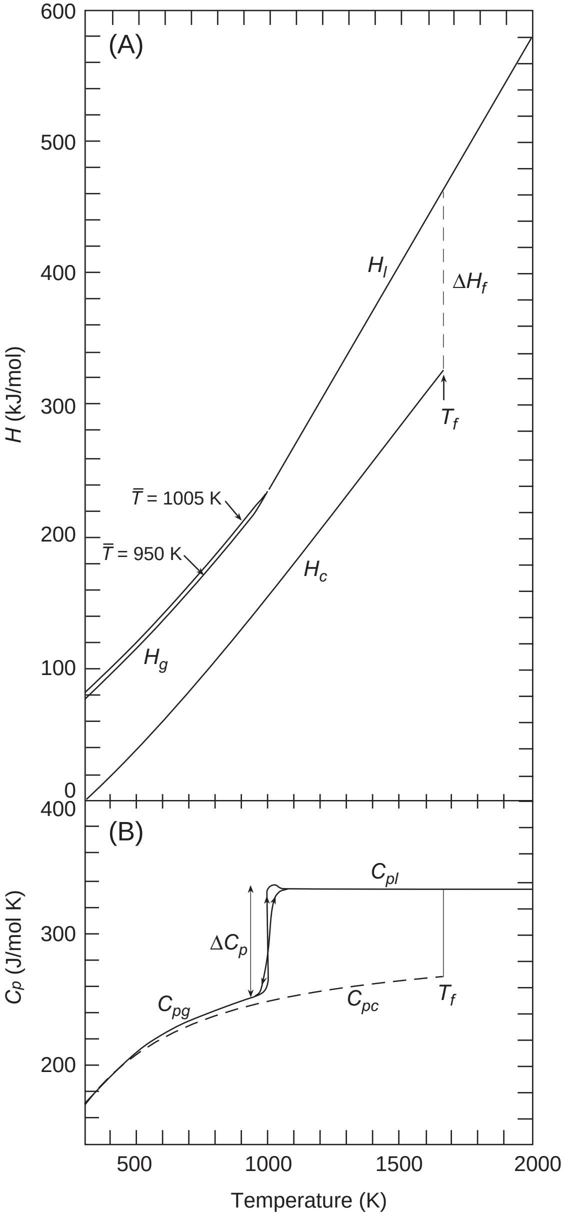

FIG. 3.2 High-temperature enthalpy (A) and heat capacity (B) of diopside and glassy and liquid $CaMgSi_2O_6$, to which the subscripts *c*, *g*, and *l* refer, respectively. The enthalpy of the crystal at 298 K is taken as 0; that of the glass is plotted for the two different fictive temperatures indicated. The C_p hysteresis at the glass transition was actually not observed. The temperature and enthalpy of melting are denoted by T_f and ΔH_f. From Richet and Bottinga (1986).

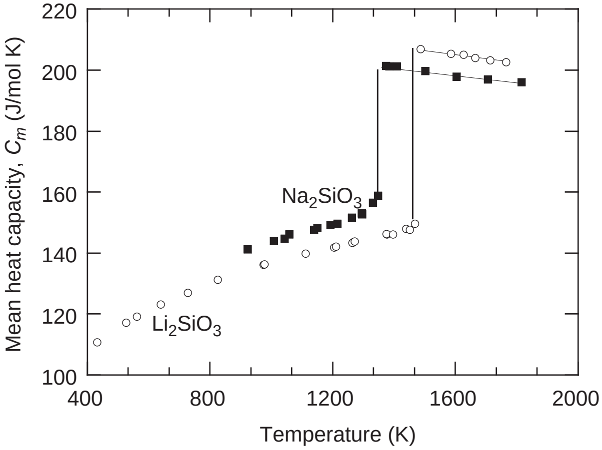

FIG. 3.3 Fusion of Na_2SiO_3 and Li_2SiO_3 as observed in relative enthalpy experiments (Téqui et al., 1992). Measurements plotted as mean heat capacities, $C_m = (H_T - H_{273})/(T - 273)$, to show at an expanded scale the enthalpy data on both sides of the melting point.

hematite (Fe_2O_3: $\Delta H_f = 133 \pm 10\,\text{kJ/mol}$ at $T_f = 1895\,\text{K}$) and acmite ($NaFeSi_2O_6$: $\Delta H_f = 70.5 \pm 9.4\,\text{kJ/mol}$ at $T_f = 1373\,\text{K}$); and by Nerád et al. (2006) for titanite ($CaTiSiO_5$: $\Delta H_f = 139 \pm 3\,\text{kJ/mol}$ at $T_f = 1656\,\text{K}$).

If melting is congruent, the entropy of fusion of a mineral is given by:

$$\Delta S_f(T) = \Delta H_f\left(T_f\right)/T, \tag{3.2}$$

where T_f is the equilibrium melting temperature. If melting is incongruent, only the temperature dependence of the entropy of fusion can be determined from calorimetric measurements with:

$$\Delta S_f(T) = \Delta S_f\left(T_f\right) + \int_{T_f}^{T} \left(C_{pl} - C_{pc}\right)/T\,dT, \tag{3.3}$$

where T_r is an arbitrary reference temperature. With an equation analogous to Eq. (3.1), the calculation may be extended to below T_g if the fictive temperature of the glass is known.

As described in Section 2.4.1 (Chapter 2), both the enthalpy and entropy of liquids can be split into vibrational and configurational parts. In the absence of any phase transition, crystals have only vibrational properties. This feature suggests that the configurational enthalpy and entropy of liquids could be approximated by the enthalpy and entropy differences between liquids and crystals. Such an approximation is incorrect, however, especially for entropy (Figs. 2.19 and 3.4). First, small C_p differences between crystals and glasses can translate into significant enthalpy and entropy differences when integrated over wide temperature intervals. Second, these C_p differences can be large at the low temperatures from which integrations must be performed to derive entropies. This is illustrated by the large variations of the entropy differences shown in Fig. 3.4 below 300 K. For this and other reasons, low-temperature heat capacities must also be considered.

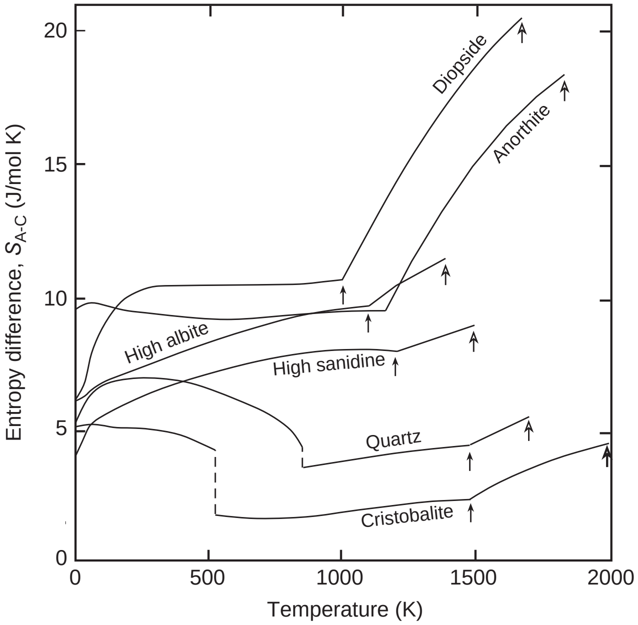

FIG. 3.4 Entropy differences between amorphous and crystalline silicates (see Richet and Bottinga, 1986, for data sources). The *open arrows* indicate the congruent melting temperatures, and the *solid arrows* the calorimetric glass transition temperatures.

3.2.2 Low-Temperature Heat Capacity and Vibrational Entropy

The low-temperature heat capacity is needed to determine the standard entropy of a phase or, more precisely, its vibrational entropy, with

$$S_{298} - S_0 = \int_0^{298} C_p/T\,dT, \tag{3.4}$$

where the residual entropy, S_0, cannot be omitted because it does not vanish for disordered substances such as glasses. For minerals, it has long been known that $S_{298} - S_0$ depends on volume or, more precisely, on atomic packing. In other words, short-range order around cations, and especially on oxygen coordination of cations are the most important factors (Robinson and Haas Jr., 1983; Holland, 1989). These effects are summarized by the entropy of the isostructural forms of SiO_2 and GeO_2 (Fig. 3.5). In both instances, the entropy is markedly lower for the tetragonal ("rutile") polymorphs, where Si^{4+} and Ge^{4+} are octahedrally coordinated, than for the hexagonal ("quartz") forms where both cations are in tetrahedral coordination. For the latter forms and the glass as well, the entropy is only a slight positive function of molar volume.

Qualitatively, these variations are readily accounted for. In a solid, the isochoric heat capacity of a single oscillator of frequency, v, is given by the Einstein function:

$$C_v(T) = x^2 e^x / \left(e^2 - 1\right)^2, \tag{3.5}$$

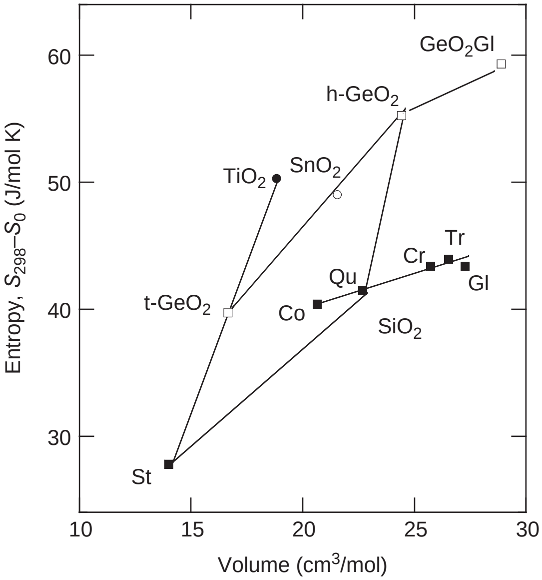

FIG. 3.5 Entropy against volume for SiO_2 and GeO_2 glasses and polymorphs. Co: coesite; GeO_2Gl: GeO_2 glass; Gl: SiO_2 glass; h-GeO_2: hexagonal GeO_2; Qu: quartz; St: stishovite; t-GeO_2: tetragonal GeO_2; Tr: tridymite. Data for rutile (TiO_2) also included. See Richet et al. (1993b, 2003) for data sources.

where $x = hv/kT$, and h and k are Planck and Boltzmann constants, respectively (see, e.g., Kittel, 1996). The only assumption made is that vibrations are harmonic, which is justified at low temperatures where vibrational amplitudes are small. If the vibrational density of states is known, the calculated molar heat capacity of the material is;

$$C_v(T) = \int_0^{v_m} C_v g(v) dv, \tag{3.6}$$

where v_m is the highest vibrational frequency in the solid, and the integration is made over a total of $3N$ modes for a substance with N atoms in its gram formula weight.

The Einstein function, Eq. (3.5), tends to 0 at 0 K and to the Boltzmann constant, k, in the high-temperature limit. Hence, the Dulong and Petit high-temperature limit of C_v is $3R$ if N is taken to be the Avogadro number. In general, $g(v)$ is not sufficiently well known to predict accurately $C_v(T)$. At least qualitatively, the trends of Fig. 3.5 are nonetheless accounted for readily in terms of the variations of the vibrational density of states induced by the change from four- to sixfold coordination of either Si^{4+} or Ge^{4+}.

At a given temperature, the heat capacity of an oscillator increases when its frequency (or bond distance), decreases. For SiO_2 and GeO_2 polymorphs, Si—O and Ge—O bond distances are longer in the tetragonal than in the hexagonal phases. Lengthening of Si—O (and Ge—O) bonds thus leads to lower vibrational frequencies for Si—O stretching modes. However, the ensuing higher heat capacity of the internal modes of SiO_4 and GeO_4 tetrahedra are more than compensated for by the C_p decreases of the lattice modes, which are due to shorter Si—Si and Ge—Ge distances between second-nearest neighbors in the more compact tetragonal structure of the high-coordination polymorphs. The net effect is a decrease of the heat capacity and entropy (Gillet et al., 1990).

Heat capacity thus appears to be a useful structural probe in addition to be needed for thermodynamic calculations. For silicates, sensitivity to short-range order becomes obvious below about 200 K and can be extremely important below 100 K. The effect has been most clearly documented for aluminum speciation in calcium aluminosilicates (Richet et al., 2009), thanks to a very wide range of vitrification through which the proportions of four-, five-, and sixfold coordinated aluminum vary to a rather large extent. At 50 K, the partial molar isobaric heat capacity is several times smaller for $^{[5]}Al_2O_3$ and $^{[6]}Al_2O_3$ than for $^{[4]}Al_2O_3$ (Fig. 3.6). Although the partial molar C_p of $^{[5]}Al_2O_3$ then rapidly increases to match that of $^{[4]}Al_2O_3$, at 200 K the values for both components remain higher by about 25% than that of $^{[6]}Al_2O_3$. As a result, there are large $S_{298} - S_0$ differences for the three Al_2O_3 species (Table 3.1).

In agreement with these trends, the $S_{298} - S_0$ data plotted in Fig. 3.7 for sodium and calcium aluminosilicates indicate that the transformation from four- to sixfold coordination has similar effects for aluminum as for silicon (Richet et al., 1993b). In both Na and Ca series, the glasses define smooth entropy trends. These trends are also consistent with the data for the low-pressure crystal phases in which Al^{3+} is tetrahedrally coordinated. In contrast, the high-pressure crystalline phases jadeite (Jd, $NaAlSi_2O_6$) and Ca-Tschermak pyroxene (CaTs, $CaAl_2SiO_6$), where all or some Al^{3+} is sixfold coordinated, have entropies departing negatively from these trends. Without any structural information for glasses of these compositions, we could, therefore, conclude that Al^{3+} is essentially fourfold coordinated in all glass samples of these series. This conclusion is valid at least for all peralkaline and peralkaline earth compositions (de Ligny et al., 1996).

Low-temperature heat capacity also provides information on the local environment of network-modifying cations, especially for binary SiO_2-M_2O systems for which measurements are the most extensive (Labban et al., 2007). The observations for $M_2Si_2O_5$ glasses and crystals

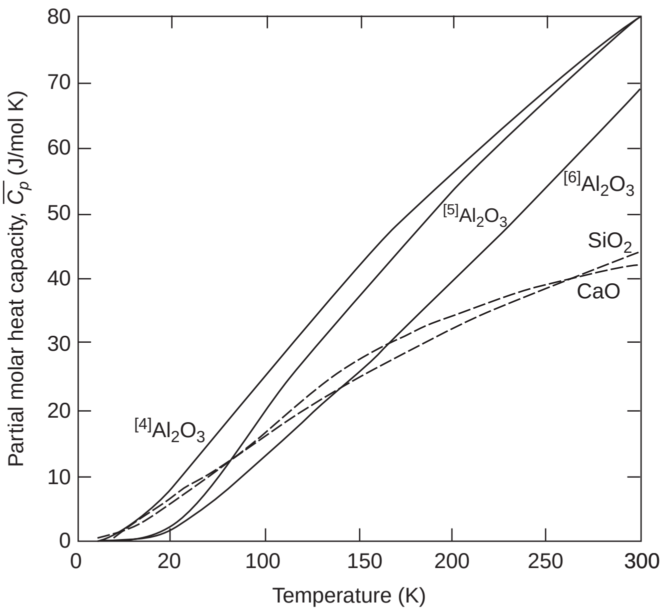

FIG. 3.6 Partial molar heat capacities of Al_2O_3 with four-, five-, and sixfold coordinated aluminum derived from a calorimetric study of 10 CaO-Al_2O_3-SiO_2 glasses (Richet et al., 2009).

TABLE 3.1 Partial Molar Relative Entropies of Oxides in Silicate Glasses, and Entropy Coefficients of Oxides in Crystals for the Coordination Numbers Listed in Roman Numbers

Oxide	Glasses[a]	Crystals[a]
SiO_2	43.4	40.3 (IV)–27.8 (VI)[b]
Li_2O	49.0	38.5 (IV–V)
Na_2O	85[c]	76 (IV–V)
	96.7[b]	97.3 (IX)
K_2O	108[c]	101 (V–VI)
	119.1[b]	114.3–120.4
MgO	30.7	26.7 (VI)–27.7 (VII)
CaO	42.8	39.6 (VI)–38.7 (VIII)
FeO	56.7	43.2 (IV–VIII)
$^{IV}Al_2O_3$	72.81	72.1 (IV)
$^{V}Al_2O_3$	48.5	
$^{VI}Al_2O_3$	45.0	43.8 (VI)
Fe_2O_3	116	80.5 (VI)
Y_2O_3	91.81	[99.08]
Si_3N_4	75.95	[113.0]

[a] *Data in J/mol K for glasses from Richet et al. (1993b, 2009), N.F. Richet et al. (2010a), and Sipowska et al. (2009) and, when available for crystals, from the entropy-coordination model of Holland (1989).*

[b] *For Al-charge compensating alkali cation.*

[c] *In Al-free silicates.*

FIG. 3.7 Vibrational entropy of aluminosilicate glasses *(open symbols)* and crystals *(solid symbols)*. Ab (albite): $NaAlSi_3O_8$; An (anorthite): $CaAl_2Si_2O_8$; CaTs (calcium Tschermak molecule): $CaAl_2SiO_6$; Jd (jadeite): $NaAlSi_2O_6$; Ne (nepheline) and Ca (camegieite): $NaAlSiO_4$. The data for An and $CaAl_2Si_2O_8$ glass plot at the same point. See Richet et al. (1993b) for data sources.

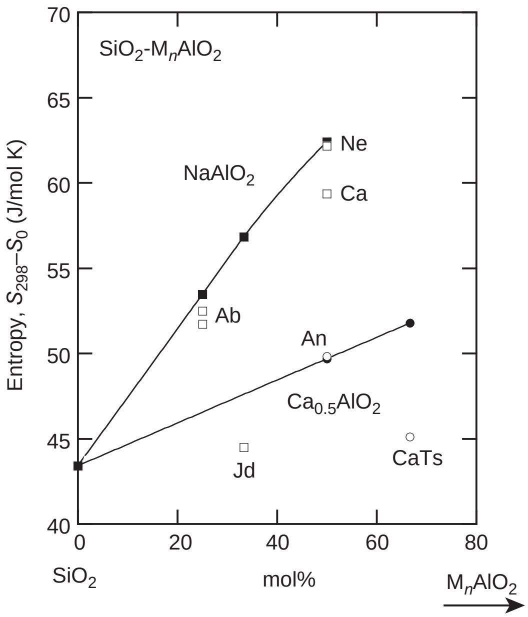

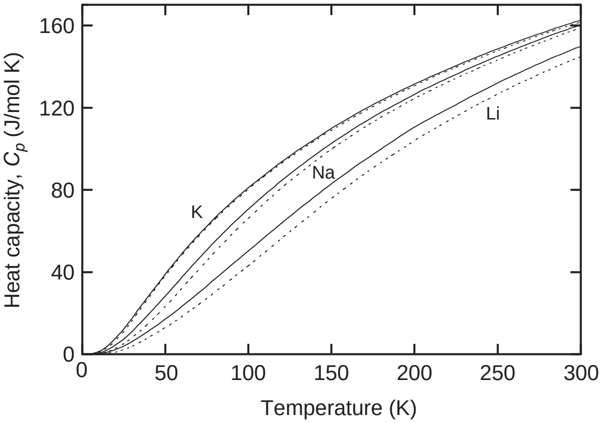

FIG. 3.8 Low-temperature heat capacity of binary $M_2Si_2O_5$ glasses *(solid curves)* and crystals *(dashed curves)*, with M = Li, Na, and K. Data from Labban et al. (2007).

plotted in Fig. 3.8 illustrate two general trends. First, at a given temperature the heat capacity decreases regularly in the order K, Na, Li, which is a direct consequence of the increase in average bond strength in the same order resulting from the decrease of the ionic radius of the alkali. Second, the heat capacity of a glass is higher than that of its crystalline counterpart, which correlates with the lower density of the glass and the correlative decrease in bond strength within this phase. Again, there is a regular trend since these differences increase in the order K, Na, Li. If this volume effect is taken into account, then the small C_p differences, and particularly their systematic nature, rule out markedly differing coordination numbers for alkali ions in glasses and crystals of the same composition.

The entropy of silicate crystals may be approximated as the sum of entropy coefficients pertaining to each oxide in which the cation has the appropriate coordination number (Holland, 1989; see also Table 3.1). Owing to the continuous nature of glass solutions, an analogous procedure allows partial molar relative entropy of oxides in glasses to be determined from an analysis of available data (N.F. Richet, 2009a,b; Richet et al., 1993b; N.F. Richet et al., 2010a; de Ligny et al., 1996; Sipowska et al., 2009). The additive nature of $S_{298} - S_0$ suggested by the linear trends of Fig. 3.7 is borne out by an analysis of the data available for more than 30 different glasses. The experimental results are reproduced to better than 1% with a set of composition-independent partial molar entropies (Table 3.1). This is another way of stating that short-range order around cations does not depend strongly on composition in glass-forming silicates.

A distinction must be made, however, in that two different values are found for Na_2O and K_2O depending on whether the alkali element is a network-modifier or serves as a charge compensator for tetrahedral Al^{3+} (Table 3.1). The higher entropy derived in the latter case indicates that when the alkali associates with Al^{3+}, its coordination number has increased from about 5 to a higher value similar to those determined for crystalline tectosilicates. This conclusion agrees with the analogous increase of the size of the oxygen shell around sodium determined early by Isard (1959) from electrical conductivity measurements on aluminosilicates. In contrast, a single partial molar entropy obtains for the oxides of Ca and for Mg when these cations switch from a network-modifying to a charge-compensating role. As will be seen in Chapter 8, this contrast between alkali and alkaline earth cations translates into different composition dependences of physical properties of melts at high temperatures. This is another way of stating that configurational properties are sensitive functions of cation coordination.

3.2.3 Boson Peak

Although the vibrational entropy of glasses is essentially a linear function of composition (see previous section), additivity does not necessarily hold true for heat capacity because data close to 0 K contribute little to entropy. As a matter of fact, additivity of heat capacity breaks down below about 50 K so that two different temperature ranges must be distinguished in low-temperature C_p analyses. Graphical integration of the $g(v)\ c_v(T)$ functions in Fig. 3.9 indicates that only modes with frequencies lower than 200 cm^{-1} really contribute to C_p below 50 K. Of course, these regimes have no sharp boundaries, as illustrated by the C_p calculations made for SiO_2 glass from a reported vibrational density of states (Fig. 3.9).

Those low-frequency modes involve either weak bonds or motion of a large number of atoms. As such, they could be probes of medium-range order. For example, the negligible C_p differences found between anorthite crystals and $CaAl_2Si_2O_8$ glass (Robie et al., 1978) indicate a great structural similarity that extends beyond short-range order. A similar conclusion probably holds true for cordierite and $Mg_2Al_4Si_5O_{18}$ glass (de Ligny et al., 1996). In contrast, there exists a large heat capacity difference between albite and $NaAlSi_3O_8$ glass (Fig. 3.4), which also points to stronger association with Al^{3+} for alkali than for alkaline earth cations and possibly to different local structure of albite crystals and $NaAlSi_3O_8$ glass. This conclusion is consistent with the structural interpretation discussed in Chapter 9. Likewise, it is only below 50 K that a dependence of C_p on the thermal history of the glass has been detected. The heat capacity is higher for samples with higher fictive temperatures and lower densities (Westrum Jr., 1956; Richet et al., 1986; Pérez-Encisco et al., 1997).

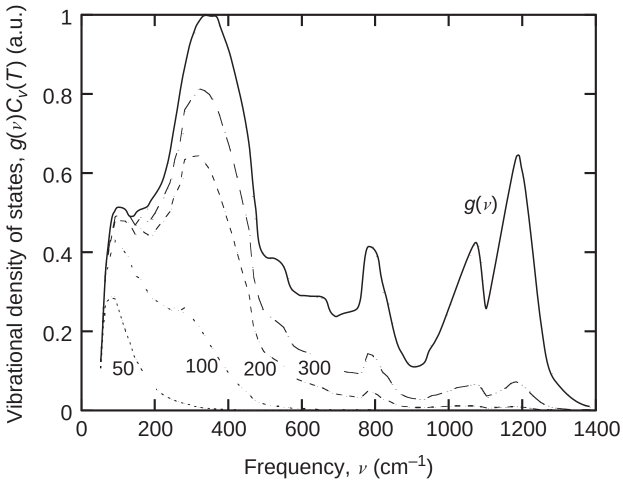

FIG. 3.9 Heat capacity of SiO_2 glass as determined from its vibrational density of states, $g(v)$ (*solid curve*, from Galeener et al., 1983). At each temperature indicated (in K), the heat capacity is given by the area under the $g(v)\ c_v(T)$ function, plotted as a dashed curve, where $c_v(T)$ is the Einstein function for a single oscillator (see de Ligny et al., 1996).

Near 0 K, the heat capacity of crystals is generally proportional to T^3. This feature is simply accounted for by the Debye model that considers a crystal as an isotropic continuum in which longitudinal and transverse acoustic waves propagate with constant velocities. The constancy of C_p/T^3 predicted by the Debye model at very low temperature is not borne out by the experimental data, however, which show instead a sharp maximum at temperatures below 50 K. In other words, the heat capacity is much greater and the number of low-frequency modes much higher than indicated by the Debye model. At low frequencies, there indeed exists a broad feature known as the boson peak, observed by inelastic neutron scattering or Raman spectroscopy. Its extent depends on thermal history and correlates with the magnitude of excess heat capacities, being higher for quenched than for annealed glasses (e.g., Ahmad et al., 1986).

It is often assumed that such deviations from the Debye model are typical of glasses and other disordered materials (e.g., Pohl, 1981). However, deviations have also been observed for crystalline materials. For example, the data for SiO_2 polymorphs (Fig. 3.10) clearly show that the anomaly can be greater for a crystalline polymorph—cristobalite—than for SiO_2 glass (Bilir and Phillips, 1975). The boson peak is almost nonexistent for stishovite and, among phases with fourfold coordinated Si, it is smallest for coesite, the densest phase. Qualitatively, the explanation is the same as for the C_p decreases resulting from the change of Si^{4+} (and Ge^{4+}) from four- to sixfold coordination described in the previous section. Lengthening of Si—O (and Ge—O) bonds leads to lower vibrational frequencies for Si—O stretching modes, but this effect is overwhelmed by the increases of the frequencies of lattice modes such that the boson peak becomes much smaller. Similar trends are observed for other crystalline silicates. The magnitude of the boson peak decreases with decreasing degree of polymerization, as illustrated by the SiO_2 polymorphs (Fig. 3.10) and enstatite and forsterite (Fig. 3.11). Boson anomalies as observed for $MgSiO_3$ glass exist because of atomic disorder in this material.

Many general interpretations have been proposed for the boson peak. For SiO_2 glass, Buchenau et al. (1986) concluded from neutron scattering and C_p measurements that it is essentially due to coupled librations of the corner-shared SiO_4 tetrahedra at 0.3–4 THz

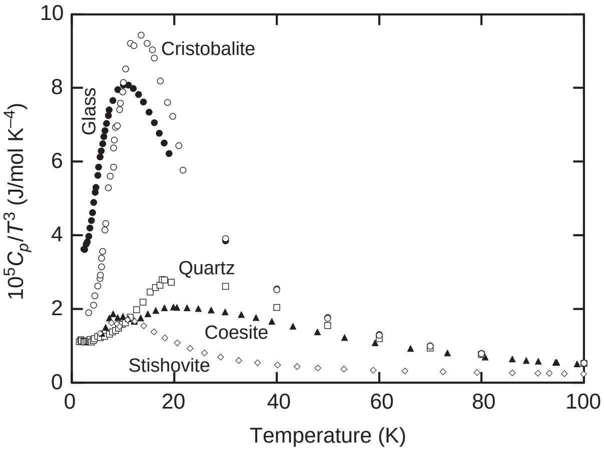

FIG. 3.10 Boson peak of SiO_2 glass and polymorphs See Richet et al. (2003) for data sources. The slight boson peak of stishovite likely results from small amounts of an amorphous SiO_2 phase in the natural sample investigated by Holm et al. (1967).

FIG. 3.11 Boson peak of forsterite (Mg_2SiO_4), enstatite ($MgSiO_3$), and $MgSiO_3$ glass. Similar results are observed for geikielite ($MgTiO_3$). Data from Robie et al. (1982, 1989), Richet et al. (1993b), and Krupka et al. (1985).

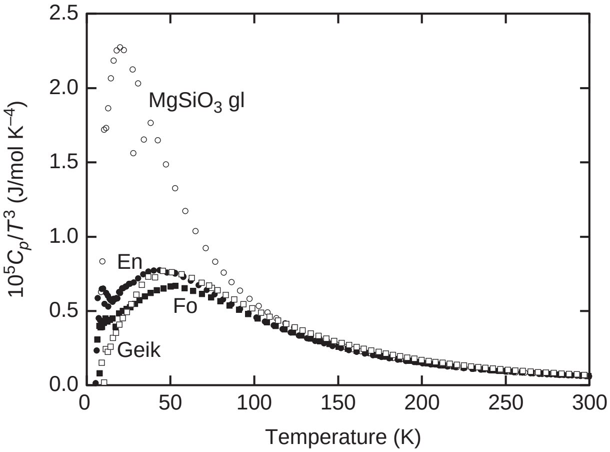

frequencies. This statement has been confirmed by hyper-Raman scattering measurements (Hehlen et al., 2000). Other salient features of the boson anomaly have been determined from low-temperature calorimetric data, which have the advantage of sampling all vibrational excitations and not only the optically active vibrational modes observed by Raman or IR spectroscopy.

From C_p data of alkali silicate glasses with SiO_2 contents ranging from 50 to 100 mol% (Labban et al., 2007; de Ligny, unpub. data), an inversion procedure applied to Eq. (3.6) yields reliably the vibrational density of states up to about 400 cm^{-1} (N.F. Richet, 2009a). A well-defined peak is systematically found at frequencies below 200 cm^{-1} (Fig. 3.12), with an intensity and peak frequency that increases with decreasing SiO_2 content and, at constant stoichiometry, with the mass of network-modifying cation (Fig. 3.13). Analogous trends have been found for alkaline earth silicate glasses (N.F. Richet, 2009b), such that the excess heat capacities and vibrational densities of states with respect to the Debye model also depend more strongly on the nature of the network-modifying cation than on the degree of polymerization of the anionic framework. These smooth variations can be accounted for simply in terms of two different contributions, namely, coupled librations of corner-sharing SiO_4 tetrahedra and localized vibrational modes associated with network-modifying cations, which appear to be insensitive to the overall glass structure with frequencies decreasing, as they should, with the mass of the cation (N.F. Richet, 2009b). Another noteworthy feature is an almost linear relationship between the temperature of the calorimetric boson peak and the transverse sound velocity, although pure SiO_2 and SiO_2-rich glasses are exceptions to this trend because of the weak transverse character of SiO_4 librations.

Such calorimetric data are thus useful not only to determine the energetics of the mechanisms involved in the boson peak, but also to check atomistic simulations performed to arrive at a more precise description of the excitations that cause the excess heat capacity and vibrational density of states. The potential interest of the method is especially great given the wide composition ranges covered by the calorimetric data now available. Besides, such calculations should also throw some light on another striking feature of the boson peak, namely, its

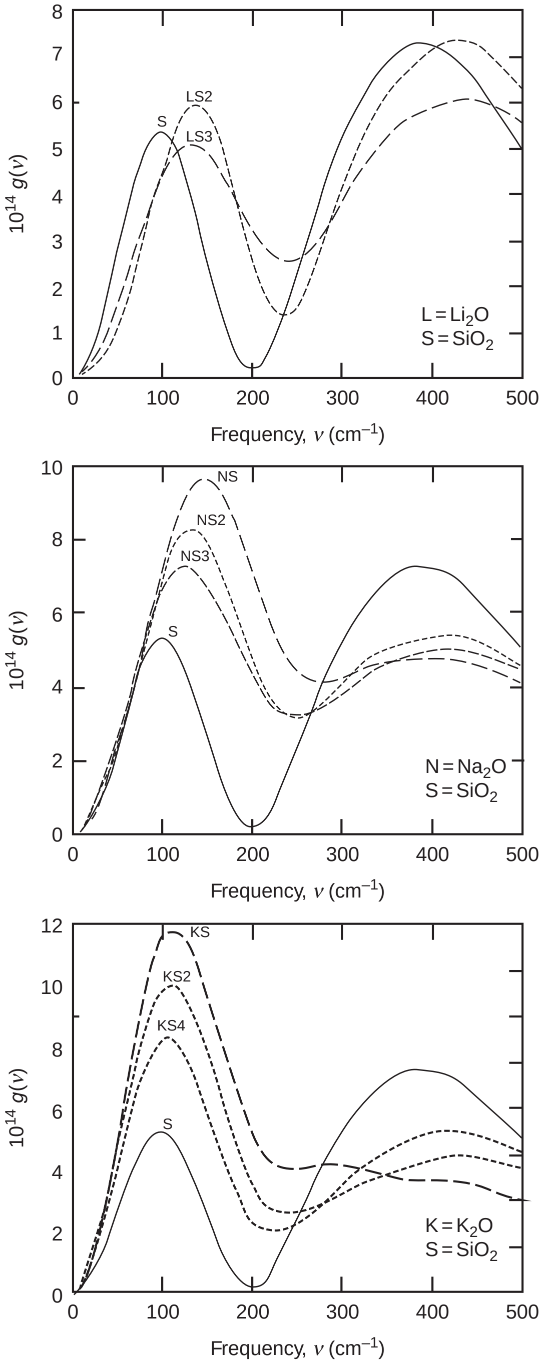

FIG. 3.12 Low-frequency part of the vibrational densities of states of alkali silicate glasses as determined from inversion of low-temperature heat capacities (N.F. Richet, 2009a,b).

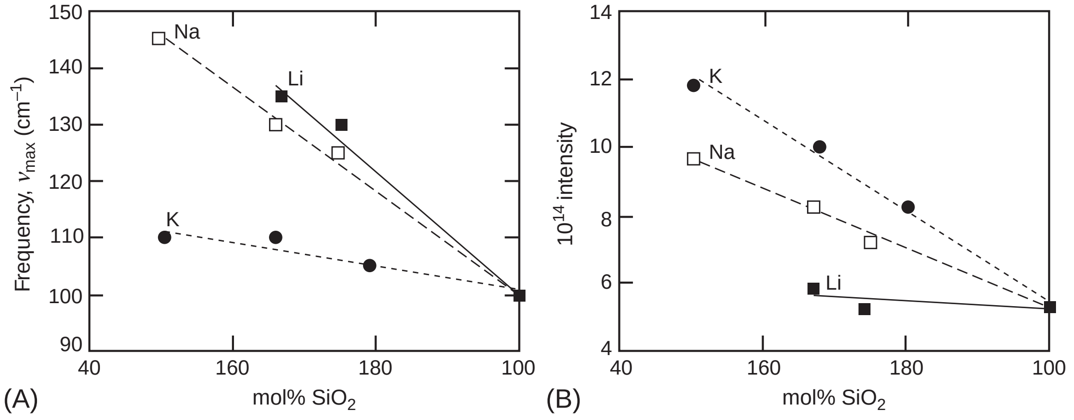

FIG. 3.13 Frequency (A) and intensity (B) of the first peak of the vibrational densities of states of alkali silicates glasses (N.F. Richet, 2009a,b).

FIG. 3.14 Universal representation of the calorimetric boson peak when the temperature and maximum of the C_p/T^3 peaks (cf. Figs. 3.10 and 3.11) are used as scaling parameters in plots of the available data for silicates, aluminosilicates and oxynitride glasses (N.F. Richet et al., 2010b). N.B. Data for amorphous silicon (Si) departing markedly from the single silicate relationship.

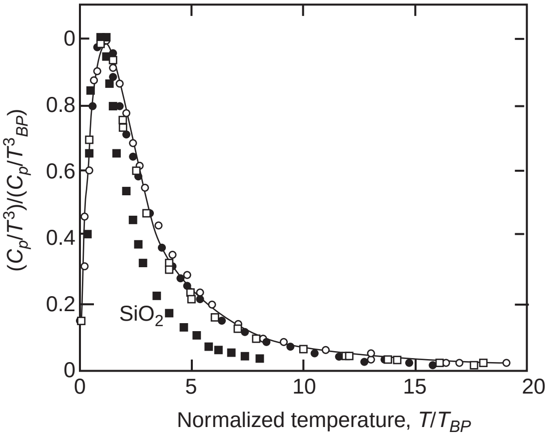

universal character apparent in the fact that all calorimetric data for silicate glasses collapse on the same master curve when plotted in a reduced form $(C_p/T^3)/(C_p/T^3)_b$ versus T/T_b, where the subscript b denotes the temperature and magnitude of the boson peak (Fig. 3.14).

3.2.4 Configurational Entropy

The residual entropy of a glass, $S_g(0)$, is the configurational entropy frozen in at the glass transition. As apparent in Fig. 2.19 (Chapter 2), this entropy represents a small difference between the large variations of the melt and crystal entropies from the melting point to 0 K. As such, it is sensitive to the various structural features discussed in previous sections. But an important difficulty is that $S_g(0)$ can be determined by calorimetric means only for a small

TABLE 3.2 Residual Entropy of Glasses, $S_g(0)$, and Entropy of Ca ⇔ Mg or Si ⇔ Al Disordering, S_d[a]

	$S_g(0)$		S_d
	J/mol K	**J/g atom K**	**J/g atom K**
B_2O_3	11.2 (0.8)	2.24 (0.16)	
GeO_2	6.6 (1.1)	2.20 (0.37)	
SiO_2	5.1 (1.2)	1.70 (0.4)	
Na_2SiO_3	3.7 (2)	0.6 (0.3)	
K_2SiO_3	12.6 (4)	2.1 (0.7)	
$K_2Si_2O_5$	18.0 (4)	2.0 (0.4)	
$CaSiO_3$	8.54 (2)	1.76 (0.4)	
$CaMgSi_2O_6$	24.3 (3)	2.30 (0.4)	1.1
$MgSiO_3$	11.2 (5)	2.24 (1.0)	
$NaAlSiO_4$	9.7 (2)	1.38 (0.3)	1.6
$NaAlSi_2O_6$	16.5 (5)	1.7 (0.5)	
$NaAlSi_3O_8$	36.7 (6)	2.82 (0.46)	1.4
$KAlSi_3O_8$	28.3 (6)	2.18 (0.46)	1.4
$CaAl_2Si_2O_8$	36.8 (4)	2.83 (0.31)	1.8
$Mg_3Al_2Si_3O_{12}$	56.3 (13)	2.81 (0.65)	1.4
$Mg_2Al_4Si_5O_{18}$	94.0 (13)	3.24 (0.45)	1.8

[a] *Calorimetric values as listed by Richet and Neuville (1992), de Ligny et al. (1996), and Richet et al. (2003). Unpub. values for NS, KS, and KS$_2$.*

number of compositions because the entropy cycle necessarily involves fusion of a congruently melting compound. Available data are summarized in Table 3.2 where results for other related glass-forming oxides are included.

On a g-atom basis, $S_g(0)$ varies with composition by more than a factor of two. To examine these results, it is useful to split the configurational entropy into two parts (Richet and Neuville, 1992). The first is *topological* and accounts for the distribution of bond angles and bond distances. It is specific to the amorphous state and varies in a complex manner with the melt composition. The second contribution to configurational entropy is termed *chemical* and is analogous to that of crystalline solid solutions where cations substitute for one another on sites of the structure. Even though such sites are less well defined in glasses than in crystals, at least to a first approximation one can assume that mixing is ideal and that the resulting entropy is given by:

$$\Delta S_m = -nR\sum x_i \ln x_i, \tag{3.7}$$

where R is the gas constant and n the number of moles of atoms being mixed. As long as mixing is complete, this expression applies to mutual substitution of both network-modifying cations, such as Na^+ and K^+ or Ca^{2+} and Mg^{2+}, and network-forming cations (Si^{4+}, Al^{3+}, B^{3+}, Ti^{4+}) within the anionic framework. When several substitutions take place simultaneously, an interesting feature is that, in analogy with the case of crystalline substitutions, Eq. (3.7) can be applied properly regardless of possible complexity of chemical composition (Weill et al., 1980).

The calorimetric data of Table 3.2 indicate that chemical and topological contributions are comparable in the glassy state. An interesting exception is $NaAlSiO_4$ glass whose residual entropy is only 1.4 J/g atom K, a value lower than the 1.7 J/mol K found for pure SiO_2 glass (Table 3.2). The entropy of SiO_2 glass represents a reference for that of other three-dimensional open networks because it is purely topological. Even if topological entropy were lower in $NaAlSiO_4$ than in SiO_2 glass, one concludes that these data leave little room for significant $Si \Leftrightarrow Al$ disordering in the former (Richet et al., 1990). As predicted by the Loewenstein avoidance principle, a ^{17}O NMR study subsequently has indeed shown that the $Si \Leftrightarrow Al$ distribution is highly ordered in $NaAlSiO_4$ glass where there is less than 10% of Al—O—Al linkages (Lee and Stebbins, 2000; see also Chapter 9).

In analogy with crystals, the ensuing question is how $Si \Leftrightarrow Al$ ordering in melts varies with temperature above the glass transition. Discussion of this question is postponed until the next section because another complexity must be mentioned first. This has to do with the fact that glasses and melts benefit from their disordered structures, which allow a variety of elements to coexist in a single phase over wide composition regions. Specifically, elements such as boron and titanium likely mix with silicon only at high temperatures. In contrast to Al^{3+}, they tend to form their own network at lower temperatures without, however, causing macroscopic phase separation. As a result, the distinction between chemical and topological entropy becomes blurred and their estimation still more difficult.

The point to be stressed here is that topological entropy raises major difficulties in thermodynamic modeling. It cannot be estimated because only part of the structural entities that mix have been identified, and its evaluation would remain a very difficult theoretical problem even if the structure of the melt were known exactly. This problem is compounded by the fact that the relative importance of topological entropy increases with temperature whenever cation mixing is complete at the glass transition, in which case chemical entropy as given by Eq. (3.7) is constant. As described in Section 2.4.5 (Chapter 2), the possibility of determining configurational entropies from analyses of viscosity data thus represents a valuable source of thermochemical and structural information.

3.3 LIQUID-LIKE CHARACTER OF CRYSTALS

Crystals are often considered to be perfect up to their melting point. Of course, the existence of point defects or dislocations is acknowledged, but it is rightly held that, however important these defects may be for plasticity or atomic diffusion, they are of little relevance to phase equilibria and thermodynamic properties. What is less well known is that high temperatures generally confer a specific liquid-like character to a crystal. This feature is linked to atomic mobility and can have significant thermodynamic implications. As a complement to analyses of low-temperature properties, which bring information on static structural features, a review of high-temperature properties sheds some light on the dynamics of phases and especially on the energetics of these processes. In this section our purpose is, therefore, to take advantage of the simplicity afforded by the existence of long-range order in crystals to derive some information on atomic mobility in melts.

3.3.1 Glass-Like Transitions

The most conspicuous effect is the actual glass transition observed in *plastic*, or glassy crystals, which are good examples of disordered systems with three-dimensional long-range order. These crystals are characterized by a low entropy of fusion and an unusually high plasticity. They possess weakly bonded molecular groups whose orientation can change around the lattice points at higher temperatures, but become frozen in on cooling (Suga and Seki, 1974). These transformations are phenomenologically similar to the glass transition. Instead of relating a liquid to a crystal, Kauzmann's paradox involves in this case metastable and stable crystals. The familiar ice I polymorph is probably the most common glassy crystal. Its residual entropy of 3.4 J/mol K (Haida et al., 1974) results from a random orientation of the hydrogen bonds linking different H_2O molecules into H_4O tetrahedra in the hexagonal lattice defined by the oxygen atoms.

The large bond strength differences that allow some molecular groups to reorient freely do not generally exist in silicates. Although one cannot exclude that some hydrous minerals might be considered as glassy crystals, the important point is that the common order-disorder reactions involving cations should also follow the same phenomenology. The best documented transition is that of hercynite ($FeAl_2O_4$) spinel. It will be described in some detail as an example of observations that might be made for silicates.

In spinels, the divalent cation, A (e.g., Fe^{2+}, Mg^{2+}), and trivalent cation, B (e.g., Al^{3+}, Cr^{3+}), distribute themselves over one tetrahedral site and two octahedral sites in an approximately cubic close-packed arrangement. Accordingly, the general formula $A_{1-x}B_x(A_{x/2}B_{1-x/2})_2O_4$ can be written, where the parentheses indicate those cations that occupy octahedral sites. The *degree of inversion*, x, varies from 0 for ordered, "normal" spinels, to 2/3 for a random cation distribution, and even to 1 for "inverse," ordered spinels where all A cations occupy a tetrahedral site.

For $FeAl_2O_4$, Harrison et al. (1998) found that x varies strongly with temperature (Fig. 3.15). The measurements were made on heating on a sample that had first been rapidly quenched to room temperature. On reheating, x remained constant at about 0.13 as long as the relaxation kinetics for the ordering reaction were slow. Relaxation set near 800 K when x began to decrease and approached the equilibrium value. Within the timescale of the experiment, equilibrium was reached from about 900 K, above which x increased steadily. Conversely, the data of Fig. 3.15 show that the partially disordered Fe/Al cation distribution over the two kinds of crystallographic sites was frozen in at about 980 K during the initial quench of the sample. For $FeAl_2O_4$, calorimetric measurements are lacking to evaluate the thermal effects of this transition. For $MgAl_2O_4$, in which similar changes in the degree of inversion take place (e.g., Maekawa et al., 1997), the data plotted in Fig. 3.16 suggest an excess C_p of only 6 and 8 J/mol K at 1100 and 2000 K, respectively.

FIG. 3.15 Temperature dependence of the degree of inversion, x, revealing the glass-like transition of hercynite ($FeAl_2O_4$). The *arrow* indicates the decrease of x caused by relaxation on annealing near 900 K. Data of Harrison et al. (1998).

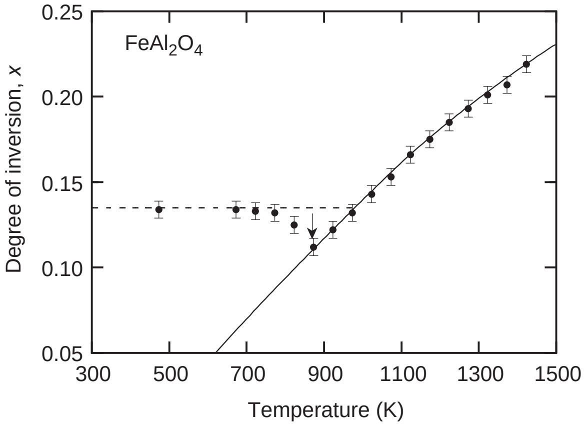

FIG. 3.16 Configurational heat capacity of $MgAl_2O_4$ spinel approximated by the difference between the heat capacity of the mineral and the values calculated from summation of the data for MgO and Al_2O_3. *Redrawn from Richet and Fiquet (1991).*

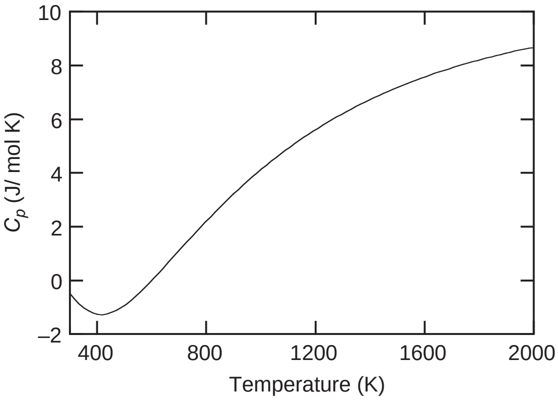

In silicates, cation order-disorder is a common kinetically controlled transformation. The reactions involving divalent cations in olivines and pyroxenes are cases in point which have long been investigated (e.g., Mueller, 1967; Virgo and Finger, 1972). Experimentally, the problem encountered is that the kinetics of such a process are generally either very fast or very slow, because relaxation times vary strongly with temperature. In the latter case, the transition temperature does not change much with cooling rate. As a result, it is difficult to quench crystals with different structural states or to measure the rate of cation exchange among the crystallographic sites of the structure. Neutron and X-ray diffraction measurements have, nonetheless, revealed variations in site occupancies with temperature (Akamatsu and Kumazawa, 1993; Artioli et al., 1995; Henderson et al., 1996; Schlenz et al., 2001). The important result is that the cation distributions measured under ambient conditions represent those frozen in upon cooling and differ from the distributions prevailing at higher temperatures.

If configurational heat capacity is small, then residual entropy of partially disordered crystals does not depend appreciably on thermal history. For ice, for instance, $S(0)$ varies by only

0.06 J/mol K between samples quenched rapidly and those equilibrated at 89 K (Haida et al., 1974). By assuming ideal mixing, one finds that the effect would be more significant for hercynite, with residual entropies of 7.4 and 6.5 J/mol K for quenched ($x = 0.134$) and annealed samples ($x = 0.112$), respectively. No such data are available for olivines or pyroxenes because the range of structural states that can be preserved on quenching is not well known. But it is tempting to suggest that because of intrinsic atomic mobility in the liquid state, disordering should be effective in melts for network modifier cations whenever charge and ionic radius constraints are satisfied. As shown in the previous chapter, the existence of mixed alkali and mixed alkaline earth effects on viscosity is consistent with this view.

From an entropy standpoint, the other important case is that of order-disorder reactions involving network-forming cations. It is beyond our scope to review the literature devoted to this subject, especially for Si ⇔ Al ordering in crystals whose kinetics can be neither too fast nor too slow in temperature ranges of present interest (e.g., Dove et al., 1997). What is relevant for this discussion is that variations of Si ⇔ Al ordering are associated with large entropy and heat capacity changes. As already mentioned, the two limiting cases are complete order, at low temperature and complete disorder at high temperature; the possible intermediate situation of obeying the Loewenstein avoidance principle lies in between. For albite ($NaAlSi_3O_8$), these three cases correspond to configurational entropies of 0, 18.7, and 12.6 J/mol K, respectively, as calculated with the assumption of ideal mixing.

The prevalence of order-disorder reactions in the crystalline state leaves no doubt as to their existence and to a likely larger extent in glasses and melts. Little is known, however, about the temperature and composition dependences of Si ⇔ Al ordering, although information on the extent of Al—O—Si bonding (and B—O—Si bonding as well) has been obtained by NMR spectroscopy (Lee and Stebbins, 2002; Du and Stebbins, 2003). A case in point is $NaAlSiO_4$ glass, whose residual entropy is lower than that of pure SiO_2 glass. Because Si ⇔ Al disorder necessarily prevails at high temperature, the disordering process should contribute to the configurational heat capacity of the melt, and more specifically, to its strong temperature dependence (Richet et al., 1990).

3.3.2 α-β Transitions

Although α-β transitions have been detected in only a few tectosilicates such as SiO_2 and $NaAlSiO_4$ polymorphs, they deserve attention because such transitions represent evidence for extensive oxygen dynamics in crystalline silicates. These transitions are reversible and their enthalpy changes seem modest but, because transition temperatures can be rather low, the entropy changes represent high fractions of entropies of fusion (Table 3.3). The importance of structural rearrangements occurring at the transition is borne out by the considerable broadening of bands in the Raman spectra of crystalline SiO_2 and $NaAlSiO_4$ crystals (crisbalite and carnegieite) with increasing temperature (Fig. 3.17). This is especially the case for the spectral features near 400 cm^{-1}, which involve extensive oxygen motion, whereas the changes in high-frequency modes, representing mainly Si—O stretching vibrations, can be assigned to rigid tetrahedra in a constant averaged environment. This dynamic nature of β-cristobalite is also borne out by the strong similarity of its low-frequency Raman spectra with that of SiO_2 liquid close to its melting temperature (Richet and Mysen, 1999).

TABLE 3.3 Thermodynamics of α-β Transitions and of Fusion of Tectosilicates[a]

	α-β Transition			Fusion		
	T_t	ΔH_t	ΔS_t	T_f	ΔH_f	ΔS_f
Quartz[b]	847	0.65	0.76	1700	9.4	5.5
Cristobalite	525	1.32	2.50	1999	8.9	4.5
Carnegieite	966	8.10	8.38	1799	21.7	12.1

[a] *Data in K, J/mol, and J/mol K, from Richet et al. (1982) and Richet and Mysen (1999).*
[b] *Small transition effects because of extensive premonitory effects.*

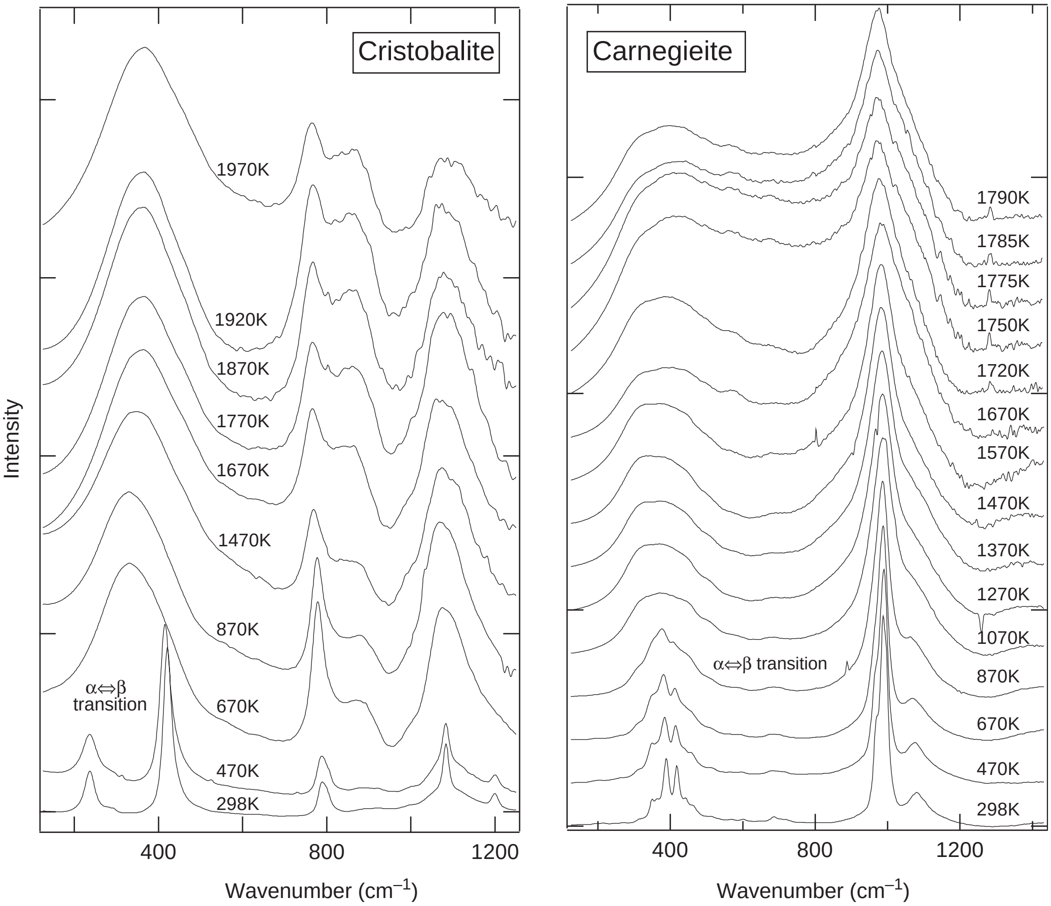

FIG. 3.17 Raman spectra of cristobalite and carnegieite on both sides of α-β transitions (Richet and Mysen, 1999).

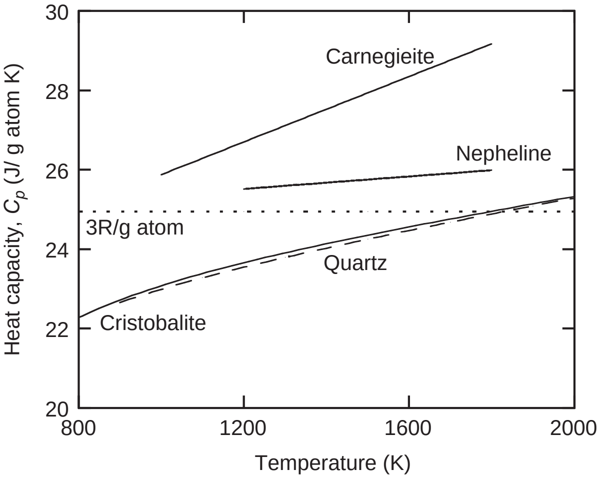

FIG. 3.18 Heat capacity of the β-phases of SiO_2 and $NaAlSiO_4$; see Richet and Mysen (1999) for data sources. The Dulong and Petit limit of 3R/gatomK is shown as a reference to reveal configurational heat capacities.

Cristobalite has been studied extensively. It has long been recognized that the structure of the β-phase is a dynamic average. Averaging could be made over α-type domains (Hatch and Ghose, 1991), but the dynamics more likely result from free rotation of rigid SiO_4 tetrahedra caused by precession of Si—O bonds with respect to their average orientation (Swainson and Dove, 1995; Dove et al., 1997). Once the dynamics has set in at the α-β transition, little energy is required in view of the insensitivity of potential energy surfaces to changes in O—Si—O angles. This agrees with the calorimetric data that do not point to significant configurational heat-capacity changes with temperature of cristobalite (Fig. 3.18). In other words, the important result is that the onset of atomic mobility at the α-β transition through movement of oxygen atoms entails similar entropy variations as disappearance of long-range order at the melting point.

As indicated by molecular dynamics simulations, another interesting feature is that the dynamics can be related to the existence of three slightly different crystal structures between which β-cristobalite keeps switching (Bourova et al., 2000). With its higher density, quartz has sharper interatomic potentials and has only two such structures for its β-phase. As for coesite, oxygen motion is less extensive and sets in without any α-β transition because there is only one possible structure for this dense polymorph (Bourova et al., 2004). As a matter of fact, this crystal structure is remarkably metastable because it can be preserved up to 1776K, i.e., more than 900K above the 1-bar melting point of the mineral, thus representing an extreme case of the rare phenomenon of crystal superheating (Bourova et al., 2006). That the number of possible configurations is much reduced for coesite at high pressure is also shown by the fact that, in contrast to the situation at ambient pressure where a great many SiO_2 polymorphs are known, coesite is the only known high-pressure SiO_2 polymorph with tetrahedral Si^{4+} coordination. Owing to the structural similarities of cristobalite with SiO_2 glass (Chapter 5), the configurational entropy of amorphous SiO_2 should thus decrease at high pressure.

Structurally, carnegieite can be considered as a stuffed derivative of cristobalite. An interpretation similar to that presented for cristobalite should obtain for its α-β transition, with the difference that the heat capacity of β-carnegieite is anomalously high, being from 5% to 20% higher than the Dulong and Petit value (Fig. 3.18). Other configurational changes thus take place, which are superimposed on the dynamics of oxygen atoms. Consistent with the considerable broadening of the high-frequency features in the Raman spectra (Fig. 3.17), which is not seen for cristobalite, these could be temperature-induced disordering of silicon and aluminum. Such disordering, which has been invoked in the previous section to account for the high temperature dependence of the heat capacity of $NaAlSiO_4$ liquid (Richet et al., 1990), would take place to a lesser extent in nepheline, the other $NaAlSiO_4$ polymorph (Fig. 3.18).

3.3.3 From Premelting to Melting and Crystallization

Premelting probably represents the most conspicuous evidence for configurational changes in crystals. Macroscopically, it manifests itself as an anomalous increase of the heat capacity when the melting temperature of a crystal is approached (Fig. 3.19). Such increases typically begin from 80 to 250 K below the reported congruent melting points and are associated with enthalpy and entropy effects that represent from 7% to 22% of the enthalpies and entropies of fusion (Richet and Fiquet, 1991; Thiéblot et al., 1999; Courtial et al., 2000; Nerád et al., 2013). The reversible nature of the phenomenon as well as the lack of any microtextural differences between samples heated below and in the premelting range indicate that these anomalies are not due to partial melting of the crystal but to nonquenchable, temperature-induced configurational changes within a solid substance (Richet et al., 1994). This is also consistent with the fact that premelting is not observed for minerals exhibiting α-β transitions, for which such changes are activated at the transition temperature.

At the scale of the unit-cell, X-ray diffraction experiments do not reveal anomalies in thermal expansion in the premelting range (Richet et al., 1996, 1998). Since there is no evidence for anomalously high concentrations of crystal defects, which could affect molar volume, volume effects do not seem to contribute to the enthalpy anomalies shown by the calorimetric data.

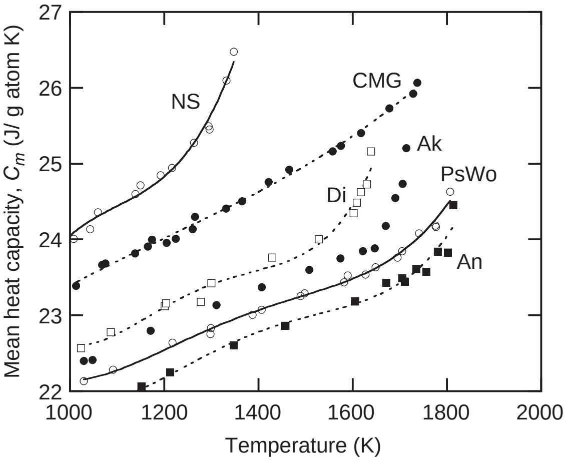

FIG. 3.19 Premelting effects in calorimetric measurements. Mean heat capacity, $C_m = (H_T - H_{273})/(T - 273)$, of Na_2SiO_3 (NS), $CaMgGeO_4$ (CMG), diopside (Di, $CaMgSi_2O_6$), åkermanite (Ak, Ca_2MgSiO_7), pseudowollastonite (PsWo, $CaSiO_3$), and anorthite (An, $CaAl_2Si_2O_8$). Data from Richet et al. (1994) and Courtial et al. (2000).

That these anomalies are associated with configurational changes within a crystalline phase is clearly apparent in Raman spectra where considerable band broadening and loss of resolution are observed (Richet et al., 1996, 1998).

Anorthite is probably the mineral that has been subjected to the most thorough structural and calorimetric investigations after heat treatments at high temperatures. Samples show an increasing degree of Al ⇔ Si disorder when quenched from temperatures increasingly higher than 1670 K, whereas little effects are apparent after annealing below 1670 K where the disordering kinetics become very slow (Benna et al., 1985). It is unlikely to be fortuitous that this temperature is the same as that of the onset of premelting (Richet et al. 1994). Compared to completely ordered samples, anorthites quenched from 1800 K have an excess enthalpy of about 3 kJ/mol (Carpenter et al., 1990). Even including the premelting enthalpy, the total excess enthalpy at the melting point is about 13 kJ/mol. This number is smaller than the enthalpy difference of 15 kJ/mol, which has been estimated between completely disordered and ordered samples (Carpenter et al., 1990). Without the (unknown) entropy frozen in during quenches from 1800 K, the entropy of premelting represents 25% of the 23 J/mol K of complete, ideal Si ⇔ Al disordering. Hence, this process alone is more than sufficient to account for the observed calorimetric effects, which suggests that it should also contribute to the configurational heat capacity of aluminosilicate liquids.

Disorder is also related to premelting of alkaline earth silicates or aluminosilicates. In this case, marked band broadening is observed only in the low-frequency part of the Raman spectra, which involves mainly T—O—T bending and M—O stretching and bending (Richet et al., 1998; Bouhifd et al., 2002). Whereas the silicate framework is not affected much, the onset of premelting correlates with the temperature at which the self-diffusion of Ca^{2+} begins to increase markedly in diopside (Dimanov and Ingrin, 1995), and that at which electrical conductivity rises sharply in pseudowollastonite and gehlenite (Bouhifd et al., 2002). As discussed previously, such cation mobility could give rise to glass-like transitions. However, a much more detailed interpretation can likely be derived from the study of the structurally much simpler alkali metasilicate crystals, which have the same pyroxene stoichiometry.

Premelting is observed a few degrees below the congruent melting temperature for Li_2SiO_3 and about 150 K below it for Na_2SiO_3 (Richet et al., 1996; see also Fig. 3.2). That Li^+, and especially Na^+, are highly mobile even below these premelting ranges is indicated by "liquid-like" spin-lattice relaxation times determined by ^{7}Li and ^{23}Na NMR spectroscopy (George et al., 1998). Such high mobility involves exchange among many sites, without any disordering of silicon or oxygen positions, but it is not associated with any significant C_p anomaly. The onset of premelting correlates instead with structural rearrangements of the silicate chains, which, in turn, enhances alkali hopping and gives rise to a distribution of Q^n-species in the crystal that prefigures the melt structure. These structural changes manifest themselves in NMR spectroscopy as variations in the lineshapes of ^{29}Si spin echo spectra, which become similar to those of a melt (Fig. 3.20). Likewise, the Raman spectra show an asymmetric broadening of the distribution of Si—O stretching mode frequencies. The similarity with the liquid is even such that the high-frequency Raman spectrum of Na_2SiO_3 shows, in addition to the most intense band assigned to Q^2-species, bands pertaining to the other Q^n-species observed in the melt (Fig. 3.21).

As deduced by Nesbitt et al. (2017) from the calorimetric and spectroscopic observations, actual melting is the result of three successive reactions (Fig. 3.22). First, breakage of weak

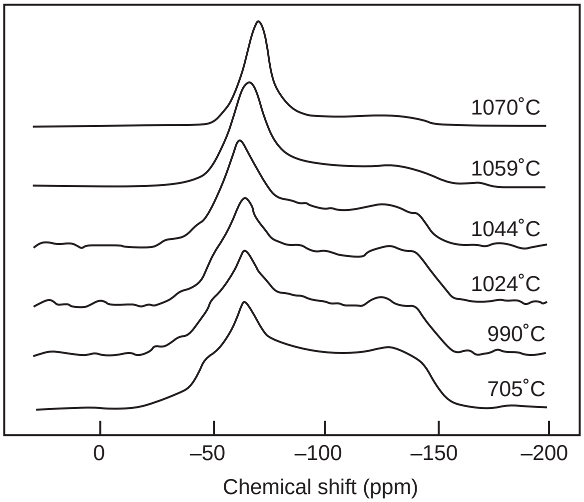

FIG. 3.20 Dynamics of silicate chains in the premelting range crystalline of Na_2SiO_3 as indicated by ^{29}Si NMR spin echo spectra plotted for the indicated temperatures (George et al., 1998).

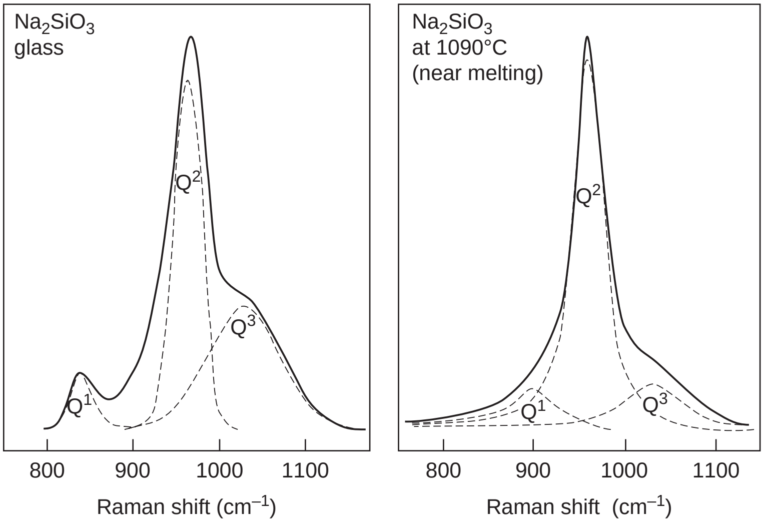

FIG. 3.21 Raman spectra of Na_2SiO_3 glass and crystal near the melting temperature of 1089°C. The individual bands that make up the high-frequency part of the spectra are shown in both cases (Frantz and Mysen, 1995; Richet et al., 1996; Nesbitt et al., 2017).

Na—O bonds without significant enthalpy effects produces mobile Na^+ ions and $Si—O^-$ moieties that remain part of the silicate chains as negatively charged Q^2 species. Second, from about 800 K these species react with "normal" Q^2 units to cross-link the chains with Q^3 species, liberating along the way "free" oxygen O^{2-} ions. Not only is the onset of this reaction coincident with that of the calorimetric premelting effects, but it is accompanied by a slight phase transition above which the *a* and *b* unit-cell parameters remain nearly constant. Finally,

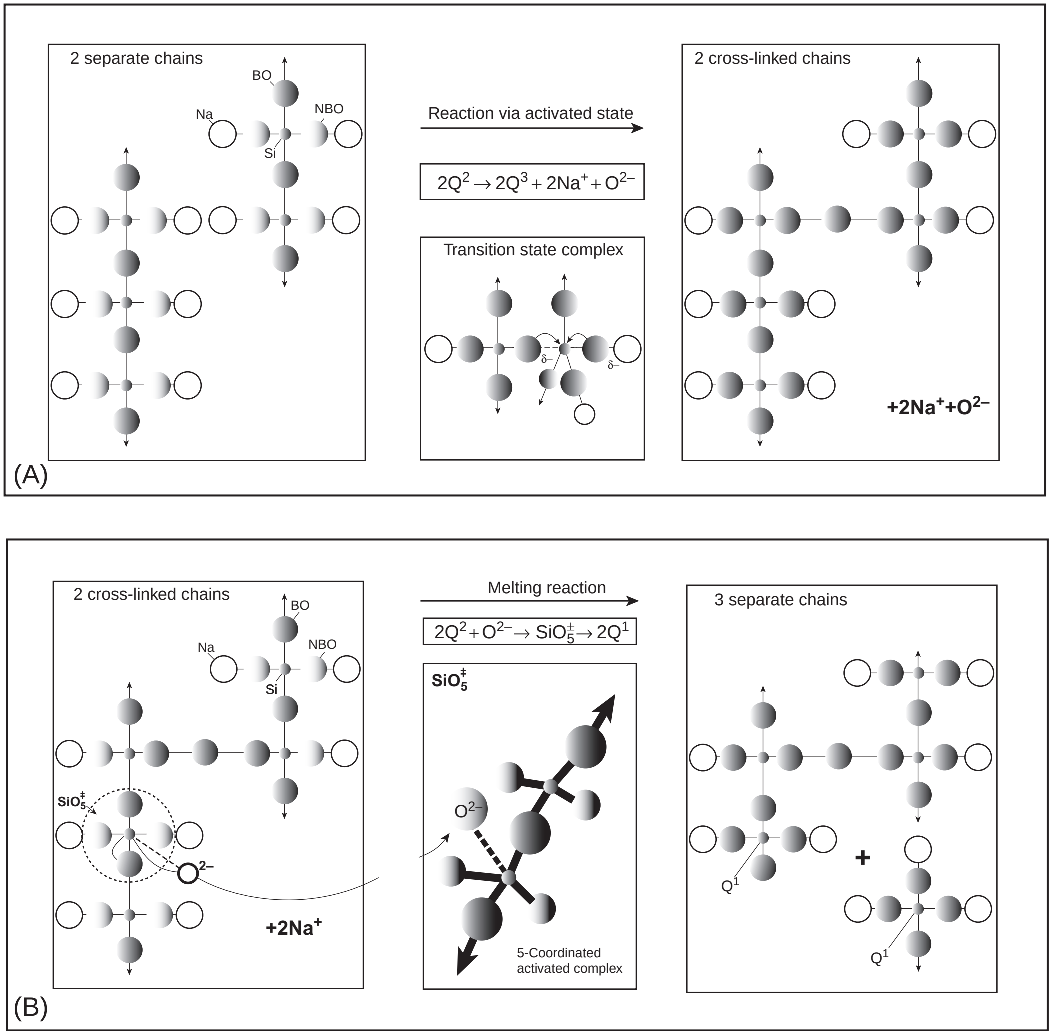

FIG. 3.22 Premelting and melting mechanisms of Na_2SiO_3 (Nesbitt et al., 2017). (A) Cross linking of Q^2 chains through production of mobile Na^+ ions and formation of Q^3 species in the premelting step. (B) Destruction of the chain structure upon actual melting.

actual melting takes place with a sharp enthalpy change in the third step whereby the silicate chains are depolymerized upon interaction with the free O^{2-} ions to form the Q^1 species also observed spectroscopically.

An important feature is that melting of Na_2SiO_3 is a congruent transformation occurring under equilibrium conditions. It follows that the reaction is reversible, even at a microscopic scale. In other words, crystallization necessarily takes place according to the same series of reactions taken in reverse order. The simple picture of crystallization as the growth of a nucleus through continuous attachments of unit cells is thus much too simplistic to be practically useful. Hence, the complete theoretical failures to predict nucleation rates, which can be 10^{20}–10^{50} times greater than observed (e.g., Fokin et al., 2006), more likely originate in the neglect of such reaction steps than other features recently considered, such as the roughness of the liquid-nuclei interface, variations of the surface energy with temperature and the size of nuclei, or initial nucleation of metastable crystals.

Coming back now to diopside, we note that the increase of calcium diffusivity is indicative of the production of mobile ions that is a prerequisite for the occurrence of configurational changes in silicate chains. Formation of Q^3 and Q^1 species can then take place as observed in Raman spectra (Richet et al., 1998), with the minor complication that melting of diopside is actually slightly incongruent (Nesbitt et al., 2017). Although similar mechanisms can also be applied to stoichiometries other than that of pyroxene, there is one class of silicates to which they are inapplicable. This class includes SiO_2 polymorphs as well as tectosilicates in which alkalis have a very low mobility as a result of their charge-compensating role for aluminum in tetrahedral coordination. These minerals do not undergo premelting, but instead the aforementioned first-order α-β transitions at temperatures through which atomic mobility sets in as dynamically averaged substructures. It is unlikely fortuitous that these minerals melt or precipitate sluggishly because (i) a surface rather than a bulk mechanism has been described for quartz and cristobalite (Ainslie et al., 1961; Wagstaff, 1969); (ii) as already noted, the high-pressure form of SiO_2, coesite, may superheat metastably by more than 900 K (Bourova et al., 2006); and (iii) albite ($NaAlSi_3O_8$) has been kept for more than 5 years 90 K below its melting temperature without any incipient crystallization (Schairer and Bowen, 1956). Because these minerals lack a simple mechanism to produce free oxygen, their peculiar properties in turn represent circumstantial evidence for the basic role of these anions in melting and crystallization.

References

Ahmad, N., Hutt, K.W., Phillips, W.A., 1986. Low-frequency vibrational states in As_2S_3 glasses. J. Phys. C Solid State Phys. 19, 3765–3773.

Ainslie, N.G., Mackenzie, J.D., Turnbull, D., 1961. Melting kinetics of quartz and cristobalite. J. Phys. Chem. 65, 1718–1724.

Akamatsu, T., Kumazawa, M., 1993. Kinetics of intracrystalline cation redistribution in olivine and its implication. Phys. Chem. Miner. 19, 423–430.

Artioli, G., Rinaldi, R., Wilson, C.C., Zanazzi, P.F., 1995. High-temperature Fe-mg partitioning in olivine: *in-situ* single crystal neutron diffraction study. Am. Mineral. 80, 197–200.

Benna, P., Zanini, G., Bruno, E., 1985. Cell parameters of thermally treated anorthite. Al, Si configurations in the average structures of the high temperature calcic plagioclases. Contrib. Mineral. Petrol. 90, 381–385.

Bestul, A.B., Chang, S.S., 1965. Calorimetric residual entropy of a glass. J. Chem. Phys. 40, 3731–3733.

Bilir, N., Phillips, W.A., 1975. Phonons in SiO_2: the low-temperature heat capacity of cristobalite. Philos. Mag. 32, 113–122.

Bouhifd, M.A., Gruener, G., Mysen, B.O., Richet, P., 2002. Premelting and calcium mobility in gehlenite ($Ca_2Al_2SiO_7$). Phys. Chem. Miner. 29, 655–662.

Bourova, E., Parker, S.C., Richet, P., 2000. Atomistic simulations of cristobalite at high temperatures. Phys. Rev. B62, 12052–12061.

Bourova, E., Parker, S.C., Richet, P., 2004. High-temperature structure and dynamics of coesite (SiO_2) from numerical simulations. Phys. Chem. Miner. 31, 569–579.

Bourova, E., Richet, P., Petitet, J.P., 2006. Coesite (SiO_2) as an extreme case of superheated crystal: an X-ray diffraction study up to 1776 K. Chem. Geol. 229, 57–63.

Buchenau, U., Prager, M., Nücker, N., Dianoux, A.J., Ahmad, N., Phillips, W.A., 1986. Low-frequency modes in vitreous silica. Phys. Rev. B34, 5665–5673.

Carpenter, M.A., Angel, R.J., Finger, L.W., 1990. Calibration of Al/Si order variations in anorthite. Contrib. Mineral. Petrol. 104, 471–480.

Courtial, P., Téqui, C., Richet, P., 2000. Thermodynamics of diopside, anorthite, pseudowollastonite, $CaMgGeO_4$ olivine and åkermanite up to near the melting point. Phys. Chem. Miner. 27, 242–250.

de Ligny, D., Westrum Jr., E.F., Richet, P., 1996. Entropy of calcium and magnesium aluminosilicate glasses. Chem. Geol. 128, 113–128.

Dimanov, A., Ingrin, J., 1995. Premelting and high temperature diffusion of Ca in synthetic diopside: an increase of the cation mobility. Phys. Chem. Miner. 22, 437–442.

Dove, M.T., Keen, D.A., Hannon, A.C., Swainson, I.P., 1997. Direct measurements of the SiO bond length and orientational disorder in the high-temperature phase of cristobalite. Phys. Chem. Miner. 24, 311–317.

Du, L.S., Stebbins, J.F., 2003. Nature of silicon-boron mixing in sodium borosilicate glasses: a high-resolution ^{11}B and ^{17}O NMR study. J. Phys. Chem. 107, 10063–10076.

Fokin, V.M., Zanotto, E.D., Yuritsyn, N.S., Schmelzer, J.W.P., 2006. Homogeneous crystal nucleation in silicate glasses: a 40 years perspective. J. Non-Cryst. Solids 352, 2681–2714.

Frantz, J.D., Mysen, B.O., 1995. Raman spectra and structure of $BaO-SiO_2$, $SrO- SiO_2$, and $CaO-SiO_2$ melts to 1600°C. Chem. Geol. 121, 155–176.

Galeener, F.L., Leadbetter, A.J., Stringfellow, M.W., 1983. Comparison of the neutron, Raman, and infrared vibrational spectra of vitreous SiO_2, GeO_2 and BeF_2. Phys. Rev. B27, 1052–1078.

George, A.M., Richet, P., Stebbins, J.F., 1998. Cation dynamics and premelting in lithium metasilicate (Li_2SiO_3) and sodium metasilicate (Na_2SiO_3): a high-temperature NMR study. Am. Mineral. 83, 1277–1284.

Gillet, P., Le Cléac'h, A., Madon, M., 1990. High-temperature Raman spectroscopy of the SiO_2 and GeO_2 polymorphs: anharmonicity and thermodynamic properties at high-temperature. J. Geophys. Res. 95, 21635–21655.

Haida, O., Matsuo, T., Suga, H., Seki, M., 1974. Calorimetric study of the glassy state. X. Enthalpy relaxation at the glass transition temperature of hexagonal ice. J. Chem. Therm. 6, 815–825.

Harrison, R.J., Redfern, S.A.T., O'Neill, H.S.C., 1998. The temperature dependence of the cation distribution in synthetic hercynite ($FeAl_2O_4$) from in-situ neutron structure refinements. Am. Mineral. 83, 1092–1099.

Hatch, D.M., Ghose, S., 1991. The α–β phase transition in cristobalite, SiO_2. Phys. Chem. Miner. 17, 554–562.

Hehlen, B., Rufflé, B., 2018. Atomic vibrations in glasses. In: Richet, P. (Ed.), Encyclopedia of Glass Science, Technology, History and Culture. J. Wiley & Sons, Hoboken, NJ.

Hehlen, B., Courtens, E., Vacher, R., Yamanaka, A., Kataoka, M., Inoue, K., 2000. Hyper-Raman scattering observations of the boson peak in vitreous silica. Phys. Rev. Lett. 84, 5355–5358.

Henderson, C.M.B., Knight, K.S., Redfern, S.A.T., Wood, B.J., 1996. High-temperature study of octahedral cation exchange in olivine by neutron powder diffraction. Science 271, 1713–1715.

Holland, T.J.B., 1989. Dependence of entropy on volume for silicate and oxide minerals: a review and a predictive model. Am. Mineral. 74, 5–13.

Holm, J.L., Kleppa, O.J., Westrum Jr., E.F., 1967. Thermodynamics of polymorphic transformations in silica. Thermal properties from 5 to 1070°K and pressure-temperature stability fields for coesite and stishovite. Geochim. Cosmochim. Acta 31, 2289–2307.

Hovis, G.L., Roux, J., Richet, P., 1998. A new era in hydrofluoric acid solution calorimetry; reduction of required sample size below ten milligrams. Am. Mineral. 83, 931–934.

Isard, J.O., 1959. Electrical conduction in the aluminosilicate glasses. J. Soc. Glass Technol. 43, 113–123.

Kittel, C., 1996. Introduction to Solid State Physics. John Wiley & Sons, New York.

Krupka, K.M., Robie, R.A., Hemingway, B.S., Kerrick, D.M., Ito, J., 1985. Low-temperature heat capacities and derived thermodynamic properties of antophyllite, diopside, enstatite, bronzite, and wollastonite. Am. Mineral. 70, 249–260.

Labban, A., Berg, R., Zhou, J., Johnson, D.A., Westrum Jr., E.F., 2007. Heat capacities and derived thermodynamic properties of lithium, sodium, and potassium disilicates from $T = (5 \text{ to } 350)$ K in both vitreous and crystalline states. J. Chem. Therm. 39, 991–1000.

Lee, S.K., Stebbins, J.F., 2000. Al-O-Al and Si-O-Si sites in framework aluminosilicate glasses with Si/Al = l: quantification of framework disorder. J. Non-Cryst. Solids 270, 260–264.

Lee, S.K., Stebbins, J.F., 2002. Extent of intermixing among framework units in silicate glasses and melts. Geochim. Cosmochim. Acta 66, 303–309.

Maekawa, H., Kato, S., Kawamura, K., Yokokawa, T., 1997. Cation mixing in natural $MgAl_2O_4$ spinel: A high-temperature ^{27}Al NMR study. Am. Mineral. 82, 1125–1132.

Mueller, R.F., 1967. Model for order-disorder kinetics in certain quasi-binary crystals of continuously variable composition. J. Phys. Chem. Solids 28, 2239–2243.

Navrotsky, A., 1997. Progress and new directions in high temperature calorimetry revisited. Phys. Chem. Miner. 24, 222–241.

Nerád, I., Kosa, L., Mikšíková, E., Adamkovičová, K., 2006. Enthalpic analysis of the $CaTiSiO_5$ system. System. Chem. Pap. 60, 274–278.

Nerád, I., Mikšíková, E., Kosa, L., Adamkovičová, K., 2013. Premelting at fusion of titanite ($CaTiSiO_5$): a calorimetric study. Phys. Chem. Miner. 40, 597–602.

Nesbitt, W., Bancroft, G.M., Henderson, G.S., Richet, P., O'Shaughnessy, C., 2017. Melting, crystallization and the glass transition: toward a unified description for silicate phase transitions. Am. Mineral. 102, 412–420.

Pérez-Encisco, E., Ramos, M.A., Vieira, S., 1997. Low-temperature specific heat of different B_2O_3 glasses. Phys. Rev. B56, 32–35.

Pohl, R.O., 1981. Low-temperature specific heats of glasses. In: Phillips, W.A. (Ed.), Topics in Current Physics. In: vol. 24. Springer Verlag, Berlin, pp. 27–52.

Richet, N.F., 2009a. Heat capacity and low-frequency vibrational density of states. Inferences for the boson peak of silica and alkali silicate glasses. Physica B404, 3799–3806.

Richet, N.F., 2009b. Boson peak of alkali and alkaline earth silicate glasses: influence of the nature and size of the network-modifying cation. J. Chem. Phys. 136, 034703.

Richet, N.F., Rouxel, T., Kawaji, H., Nicolas, J.-M., 2010a. Boson peak, elastic properties, and rigidification induced by the substitution of nitrogen for oxygen in oxynitride glasses. J. Am. Ceram. Soc. 93, 3214–3222.

Richet, N.F., Kawaji, H., Rouxel, T., 2010b. The boson peak of silicate glasses: the roles of Si-O, Al-O and Si-N bonds. J. Chem. Phys. 133, 044510.

Richet, P., Bottinga, Y., 1980. Heat capacity of liquid silicates: new measurements on $NaAlSiO_4$ and $K_2Si_4O_9$. Geochim. Cosmochim. Acta 44, 1535–1541.

Richet, P., Bottinga, Y., 1986. Thermochemical properties of silicate glasses and liquids: a review. Rev. Geophys. 24, 1–25.

Richet, P., Fiquet, G., 1991. High-temperature heat capacity and premelting of minerals in the system MgO-CaO-Al_2O_3-SiO_2. J. Geophys. Res. B96, 445–456.

Richet, P., Mysen, B.O., 1999. High-temperature dynamics in cristobalite (SiO_2) and carnegieite ($NaAlSiO_4$): a Raman spectroscopy study. Geophys. Res. Lett. 26, 2283.

Richet, P., Neuville, D.R., 1992. Thermodynamics of silicate melts. Configurational properties. In: Saxena, S.K. (Ed.), Thermodynamic Data; Systematics and Estimation. In: vol. 10. Springer, New York, pp. 132–161.

Richet, P., Bottinga, Y., Deniélou, L., Petitet, J.P., Téqui, C., 1982. Thermodynamic properties of quartz, cristobalite and amorphous SiO_2: drop calorimetry measurements between 1000 and 1800 K and a review from 0 to 2000 K. Geochim. Cosmochim. Acta 46, 2639–2658.

Richet, P., Robie, R.A., Hemingway, B.S., 1986. Low-temperature heat capacity of diopside glass: a calorimetric test of the configurational entropy theory as applied to the viscosity of liquid silicates. Geochim. Cosmochim. Acta 50, 1521–1533.

Richet, P., Robie, R.A., Rogez, J., Hemingway, B.S., Courtial, P., Téqui, C., 1990. Thermodynamics of open networks; ordering and entropy in $NaAlSiO_4$ glass, liquid, and polymorphs. Phys. Chem. Miner. 17, 385–394.

Richet, P., Leclerc, F., Benoist, L., 1993a. Melting of forsterite and spinel, with implications for the glass transition of Mg_2SiO_4 liquid. Geophys. Res. Lett. 20, 1675–1678.

Richet, P., Robie, P.A., Hemingway, B.S., 1993b. Entropy and structure of silicate glasses and melts. Geochim. Cosmochim. Acta 57, 2751–2766.

Richet, P., Ingrin, J., Mysen, B.O., Courtial, P., Gillet, P., 1994. Premelting effects in minerals: an experimental study. Earth Planet. Sci. Lett. 121, 589–600.

Richet, P., Mysen, B.O., Andrault, D., 1996. Melting and premelting of silicates: Raman spectroscopy and X-ray diffraction of Li_2SiO_3 and Na_2SiO_3. Phys. Chem. Miner. 23, 157–172.

Richet, P., Mysen, B.O., Ingrin, J., 1998. High-temperature Raman spectroscopy and X-ray diffraction of diopside and pseudowollastonite. Phys. Chem. Mineral. 25, 401–414.

Richet, P., de Ligny, D., Westrum, E.F.J., 2003. Low-temperature heat capacity of vitreous GeO_2 and B_2O_3: thermophysical and structural implications. J. Non-Cryst. Solids 315, 20–30.

Richet, P., Nidaira, A., Neuville, D.R., Atake, T., 2009. Aluminum speciation, vibrational entropy and short-range order in calcium aluminosilicate glasses. Geochim. Cosmochim. Acta 73, 3894–3904.

Robie, R.A., Hemingway, B.S., Wilson, W.H., 1978. Low-temperature heat capacities and entropies of feldspar glasses and of anorthite. Am. Mineral. 63, 109–123.

Robie, R.A., Hemingway, B.S., Takei, H., 1982. Heat capacities and entropies of Mg_2SiO_4, Mn_1SiO_4, and CO_2SiO_4 between 5 and 380 K. Am. Mineral. 67, 470–482.

Robie, R.A., Haselton Jr., H.T., Hemingway, B.S., 1989. Heat capacities and entropies at 298.15 K of $MgTiO_3$ (geikielite), ZnO (zincite) and $ZnCO_3$ (smithsonite). J. Chem. Therm. 21, 743–749.

Robinson, G.R., Haas Jr., J.L., 1983. Heat capacity, relative enthalpy, and calorimetric entropy of silicate minerals: an empirical method of prediction. Am. Mineral. 68, 541–553.

Roskosz, M., Toplis, M.J., Besson, P., Richet, P., 2005. Nucleation mechanisms: a crystal-chemical investigation of phases forming in highly supercooled aluminosilicate liquids. J. Non-Cryst. Solids 351, 1266–1282.

Schairer, J.F., Bowen, N.L., 1956. The system Na_2O-Al_2O_3-SiO_2. Am. J. Sci. 254, 129–195.

Schlenz, H., Kroll, H., Phillips, M.W., 2001. Isothermal annealing and continuous cooling experiments on synthetic orthopyroxenes: temperature and time evolution of Fe, Mg distribution. Eur. J. Mineral. 13, 715–726.

Sipowska, J.T., Atake, T., Mysen, B.O., Richet, P., 2009. Entropy and structure of oxidized and reduced iron-bearing silicate glasses. Geochim. Cosmochim. Acta 73, 3905–3913.

Stebbins, J.F., 1991. Experimental confirmation of five-coordinated silicon on a silicate liquid structure: a multinuclear, high temperature NMR study. Science 255, 586–589.

Stebbins, J.F., McMillan, P., 1993. Compositional and temperature effects on five coordinated silicon in ambient pressure silicate glasses. J. Non-Cryst. Solids 160, 116–125.

Suga, H., Seki, M., 1974. Thermodynamic investigation on glassy states of pure simple compounds. J. Non-Cryst. Solids 16, 171–194.

Sugawara, T., Akaogi, M., 2003. Calorimetric measurements of fusion enthalpies for Ni_2SiO_4 and CO_2SiO_4 olivines and application to olivine-liquid partitioning. Geochim. Cosmochim. Acta 67, 2683–2693.

Sugawara, T., Akaogi, M., 2004. Calorimetry of liquids in the system Na_2O-Fe_2O_3-SiO_2. Am. Mineral. 89, 1586–1596.

Swainson, I.P., Dove, M.T., 1995. Molecular simulation of α- and β-cristobalite. J. Phys. Condens. Matter 7, 1771–1778.

Téqui, C., Grinspan, P., Richet, P., 1992. Thermodynamic properties of alkali silicates: Heat capacity of Li_2SiO_3 and lithium-bearing melts. J. Am. Ceram. Soc. 75, 2601–2604.

Thiéblot, L., Téqui, C., Richet, P., 1999. High-temperature heat capacity of grossular ($Ca_3Al_2Si_3O_{12}$), enstatite ($MgSiO_3$) and titanite ($CaTiSiO_5$). Am. Mineral. 84, 848–855.

Virgo, D., Finger, L.W., 1972. Temperature-dependent Mg, Fe distribution in a lunar olivine. Earth Planet. Sci. Lett. 14, 305–312.

Wagstaff, F.E., 1969. Crystallization and melting kinetics of Cristobalite. J. Am. Ceram. Soc. 52, 650–654.

Weill, D.F., Hon, R., Navrotsky, A., 1980. The igneous system $CaMgSi_2O_6$-$CaAl_2Si_2O_8$-$NaAlSi_3O_8$: variations on a classical theme by Bowen. In: Hargraves, R.B. (Ed.), Physics of Magmatic Processes. Princeton University Press, Princeton.

Westrum Jr., E.F., 1956. In: The low-temperature heat capacity of neutron-irradiated quartz.Trav. 4ième Congr. Int. Verre, Paris, pp. 396–399.

Zigo, O., Adamkovicova, K., Kosa, L., Nerad, I., Proks, I., 1987. Determination of the heat of fusion of $2CaO\bullet Al_2O_3\bullet SiO_2$ (gehlenite). Chem. Pap. 41, 171–181.

CHAPTER

4

Structure and Property Concepts

OUTLINE

4.1 INTRODUCTORY COMMENTS

Variations in bond length, bond angle, and bond strength are central to our understanding of structure and properties of silicate melts and glasses. Here, we will discuss how these parameters vary with chemical composition, and how properties of melts and glasses can be related to these variables. Data from specific chemical systems will be used to illustrate the general concepts. Details of property-structure relationships will be discussed in later chapters.

https://doi.org/10.1016/B978-0-444-63708-6.00004-1

4.2 BOND LENGTH, BOND ANGLE, AND BOND STRENGTH IN SILICATES

The energetics of bonding in silicates are governed by the types and proportions of oxygen polyhedra, their linkages, and the manner in which all polyhedra mix in the structure. These concepts, as well as some definitions and terms used here and elsewhere in the book, are discussed in the following paragraphs.

4.2.1 Definitions and Concepts of Bonding

Many of the principles that describe bonding in crystalline materials can also be used in examination of properties and structure of melts and glasses. In crystal chemistry, the four basic types of bonds are ionic, covalent, van der Waals, and metallic. On the basis of current understanding of structure and energetics in melts and glasses, which is more limited than in crystalline materials, we will consider only ionic and covalent bonding.

In a situation of pure ionic bonding, the interaction between ions is purely coulombic with no shared electrons. Individual cations may be considered to have undeformable symmetry such that the interatomic distance, d, is simply the sum of the ionic radii of the two cations, r_i, and r_j:

$$d = r_i + r_j. \tag{4.1}$$

In purely covalent bonding, atoms are linked to form a molecule by sharing outer electrons (Lewis, 1916).

In silicate systems, be they molten, glassy, or crystalline, bonds are neither ionic nor covalent, but may be viewed as having a fractional ionic character where the fraction, f_i, depends on the structure and atoms involved. A number of definitions of this fraction have been proposed. A common expression is that of Phillips (1970):

$$f_i = E_i^2/\left(E_i + E_j\right), \tag{4.2}$$

where E_i and E_j are ionic energy gaps and f_i is the fractional ionic character. An earlier and commonly used definition is that of Pauling (1960), where the fractional ionic character is related to the electronegativity, χ_i and χ_j, of the two atoms in a bond:

$$f_i = 1 - \exp\left[-0.25\left(\chi_i - \chi_j\right)\right]. \tag{4.3}$$

The electronegativity, χ_i, is the tendency to attract electrons and has been defined in a number of ways (Mulliken, 1935; Gordy, 1946; Sanderson, 1960). A convenient operational definition of electronegativity is that of Sanderson (1960):

$$\chi_i = 3\delta/4\pi r_i, \tag{4.4}$$

where δ is the atomic number and r_i is the covalent nonpolar radius.

The concept of ionization potential is useful when describing melt and glass structure in terms of systematic relations to properties of the metal cations. In this book, we will use the definition:

$$X_i = Z_i / r_i^2, \tag{4.5}$$

where Z_i is formal electrical charge and r_i is ionic radius. We must recognize, however, that this definition is one of convenience because it assumes that the bonding is fully ionic, which it is not. Furthermore, because ionic radius depends on the number of ligands in a polyhedron of interest, ionization potential depends on the coordination number. In silicate glasses and melts, this coordination number is not always well known.

4.2.2 Bond Strength, Bond Angle, and Composition

A central feature of melt and crystal structure is bond strength, which ultimately is related to bond energy. Among the earliest to use this term, Pauling (1929) defined mean bond strength, $\overline{S}$, as the ratio of the valence over coordination number. It is necessary, however, to consider the fact that most bonds have a partial covalent character. To this end, Donnay (1969) proposed the expression

$$S = S_o \left(r_i^o / r_i \right)^{n_i}, \tag{4.6}$$

where S is the strength of a bond with length, r_i, S_0 is an ideal bond strength of length r_i^o, and n_i is a constant.

The electrostatic energy of metal-oxygen bonds—an expression of bond strength—tends to fall in reasonably well-defined ranges depending on the particular cation of interest and on the oxygen coordination number (Smyth and Bish, 1988; see also Table 4.1). The electrostatic energy is related to site potential simply by dividing the electrostatic energy with the electrical charge. For a given coordination number, the site potential is positively correlated with the ionization potential of the metal cation. For a given metal cation, the site potential, or bond strength, decreases as the oxygen coordination number increases.

Theoretical studies have shown that bond strength is a systematic function of bond distance (Fig. 4.1). The shorter a metal-oxygen bond, the greater is its strength (Pauling, 1960). For obvious geometrical reasons, metal-oxygen bond distances are a positive function of the oxygen coordination number. Everything else being equal, it follows that bond strength decreases when the oxygen coordination number increases. This simple view holds well for highly ionic crystals and led to Pauling's rules (Pauling, 1929), for example. These relationships become less clear in crystals with mixed ionic and covalent bonding (e.g., Gibbs et al., 2000). In other words, in silicate crystals where bonds often are significantly covalent, the relationship illustrated in Fig. 4.1 should be treated with some caution. The same caution likely applies to melts and glasses.

The basic building block in silicate structure is the oxygen tetrahedron. This tetrahedron may be treated as a near-rigid unit regardless of the extent of polymerization of the tetrahedra (e.g., Hazen and Finger, 1982). In crystalline silicate structures, bond length variation is accommodated by changes in intertetrahedral angle. Such relationships have been observed in naturally occurring minerals (e.g., Brown et al., 1969) and shown in numerical simulations

TABLE 4.1 Site Potential, Oxygen Coordination Number, and Cation Types in Minerals

Cation	Coordination Number	Ionic Radius (Å)[a]	Site Potential Energy Range (eV)[b]
Al^{3+}	4	0.47	105–166
Al^{3+}	5	0.56	111
Al^{3+}	6	0.61	92–117
Ca^{2+}	6	1.08	33–50
Ca^{2+}	7	1.15	37–83
Ca^{2+}	8	1.20	38–51
Fe^{2+}	6	0.69	46–107
K^+	6	1.46	8–19
K^+	8	1.59	7–12
Mg^{2+}	6	0.80	47–77
Mg^{2+}	8	0.97	49–50
Na^+	6	1.10	4–17
Na^+	7	1.21	14–34
Na^+	8	1.24	14–18
Si^{4+}	4	0.34	145–207

[a] *From Whittaker and Muntus (1970).*
[b] *Site potential = electrostatic energy/electrical charge; eV = electron volt.*
Data from Smyth and Bish, 1988.

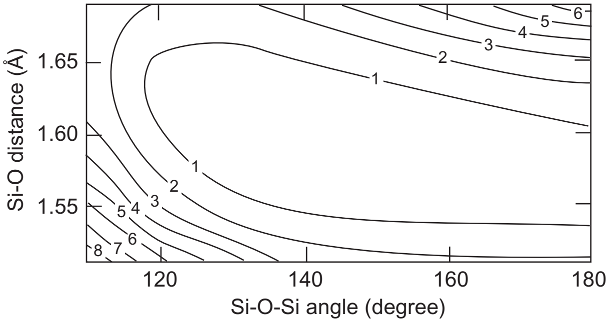

FIG. 4.1 Relationships between bond distance, Si—O, and intertetrahedral bond angle, Si—O—Si, calculated for $H_6Si_2O_7$ clusters. Numbers on curves denote atomic units, a.u. $1\,a.u. = 2.625 \times 10^3\,kJ/mol$ (Gibbs et al., 1981; Poole et al., 1995).

of the potential energy surface for $H_6Si_2O_7$ clusters (e.g., Gibbs et al., 1981; Poole et al., 1995; see also Fig. 4.1). In the simulations in Fig. 4.1 bond length is negatively correlated with intertetrahedral angle (see also Gibbs et al., 1981; Poole et al., 1995). The minimum of this energy surface correlates decreasing bond angle with increasing bond length in the silicate tetrahedra. This relationship is similar to that observed in the crystal structures of natural silicates and aluminosilicates (Fig. 4.2) as well as aluminosilicate glasses

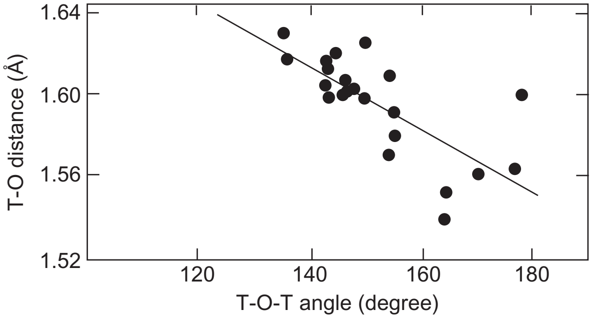

FIG. 4.2 Relationships between bond distance, T—O (T = Si, Al), and intertetrahedral bond angle, T—O—T, for natural silicate and aluminosilicate minerals (Brown et al., 1969).

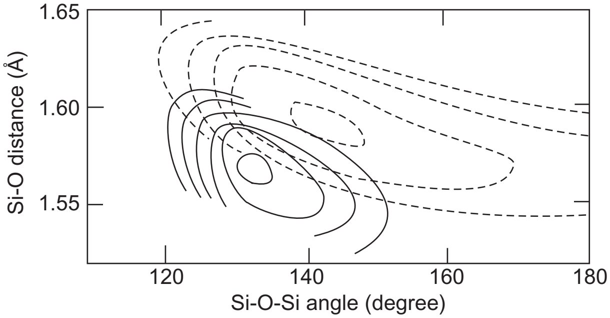

FIG. 4.3 Relationships between bond distance, Si—O, and intertetrahedral bond angle, Si—O—Si, calculated for $H_6Si_2O_7$ clusters at ambient pressure *(dashed lines)* and at 1 GPa *(solid lines)*. Divisions represent 1 a.u. (see also Fig. 4.1) (Ross and Meagher, 1984).

(Taylor and Brown, 1979). Here, the Al—O bond distance is about 1.72 Å so that the greater the Al/(Al + Si) of a glass, melt, or crystalline materials, the longer is the T—O bond length (T = Al + Si) and the smaller is the intertetrahedral angle, T—O—T (Fig. 4.1). By increasing the pressure the relationships between angle and distance remain, with the energy surfaces qualitatively resembling those at ambient pressure (Fig. 4.3). However, for a given T—O bond distance, the intertetrahedral angle (T—O—T angle) is smaller.

The greater compressibility of molten and glassy silicates compared with their crystalline equivalents (e.g., Levien et al., 1980; Seifert et al., 1983) may result from greater flexibility of intertetrahedral, Si—O—Si, angle and therefore of Si—O bond length (Seifert et al., 1983; Kubicki and Lasaga, 1987). However, in aluminosilicates the strength of the Al—O bond plays an important role. This strength is governed not only by bond angles, but also by the electronic properties of the cation(s) that serve to charge-balance tetrahedrally coordinated Al^{3+}. (For further discussion of this concept, see Section 4.4.3.) It should also be noted that in silicate structures containing bridging oxygens, variations in intertetrahedral angles may also be driven by changes in the number of oxygen bridges, whether for minerals (e.g., Liebau, 1981) or for glasses and melts (e.g., Soules, 1979; Furukawa et al., 1981). When the proportion of oxygen bridges decreases, the intertetrahedral angle becomes larger. This proportion is a direct function of the abundance ratio of metal oxide components to tetrahedrally coordinated cations (see also Chapters 7 and 9).

4.3 BASICS OF SILICATE STRUCTURE

The actual ionic charges in silicates are much smaller than the formal charges of 2− for O, 4+ for Si, etc., because of the partially covalent nature of bonding. For liquid SiO_2, charges of 2.76 and −1.38 for Si and O, respectively, have been derived from ab initio calculations (Tangney and Scandolo, 2002). Even for the archetypal ionic crystal, MgO, charges of ±1.44 have been calculated in the same way for Mg and O (Tangney and Scandolo, 2003).

To a first approximation, silicates can, nonetheless, be considered as ionic substances in which a single anion, oxygen, forms chemical bonding with a wide variety of cations of different sizes and electrical charges. Given that the actual charge of an ion depends on the overall composition and can vary from one structural position to another, this approximation represents the only way to rationalize simply the structure of silicates, be they crystalline or amorphous. Empirically, it is justified by the fact that the charge ratios between cations and oxygens remain close to the nominal values. The fundamental assumption thus made is that, with the exception of the constraints imposed by long-range order, the principles established for ionic crystals (Pauling, 1929) are applicable to amorphous phases (Zachariassen, 1932). Here, only those structural aspects relevant for comparisons of crystalline and amorphous silicates will be summarized along these lines. More detailed descriptions will be given in later chapters.

4.3.1 Oxygen Coordination Polyhedra

Oxygen is the main constituent of silicates. Not only are there always more oxygens than atoms of any other elements, but the ionic radius of the O^{2-} ion, which is about 1.30 Å, is so large compared to the radii of most cations that oxygen atoms occupy, for example, 100 times more space than Si^{4+} in pure SiO_2. Even in olivine, oxygen occupies about eight times the volume of all the other cations combined (in these calculations, all ionic radii were from Whittaker and Muntus, 1970). Hence, deciphering the structure of silicates is tantamount to describing how cations fit in between oxygen anions. This is conveniently accomplished in terms of polyhedra whose apices are the oxygens that form bonding to a given cation (the ligand). Such oxygen coordination polyhedra are determined by a complex balance of electrostatic interactions. They are characterized by the number of ligands, the so-called coordination number, and by the various cation-oxygen distances. Both kinds of parameters are primarily determined by ionic radius ratios between O^{2-} and cations.

Cations and their effects on structure and properties can be compared in terms of their electrical charge, Z, and ionic radius, r. Among major elements in silicates, silicon is the most efficient because it has the smallest radius and the highest formal charge (4+). At low pressure, its optimum coordination is achieved in the form of SiO_4 tetrahedra with Si—O distances near 1.60 Å (Fig. 2.4). At high pressures, at least in crystalline SiO_2, SiO_6 octahedra with Si—O distances near 1.90 Å are formed instead (Fig. 4.4). Such a transformation is abrupt in crystals, as exemplified by the coesite-stishovite transition near 10 GPa, but progressive in liquids in which it likely begins at lower pressures than in equivalent crystals (Fukui et al., 2009; Sato and Funamori, 2010). Other cations then share oxygens with SiO_4 tetrahedra at low pressure (Fig. 4.5), or with SiO_6 octahedra at high pressure.

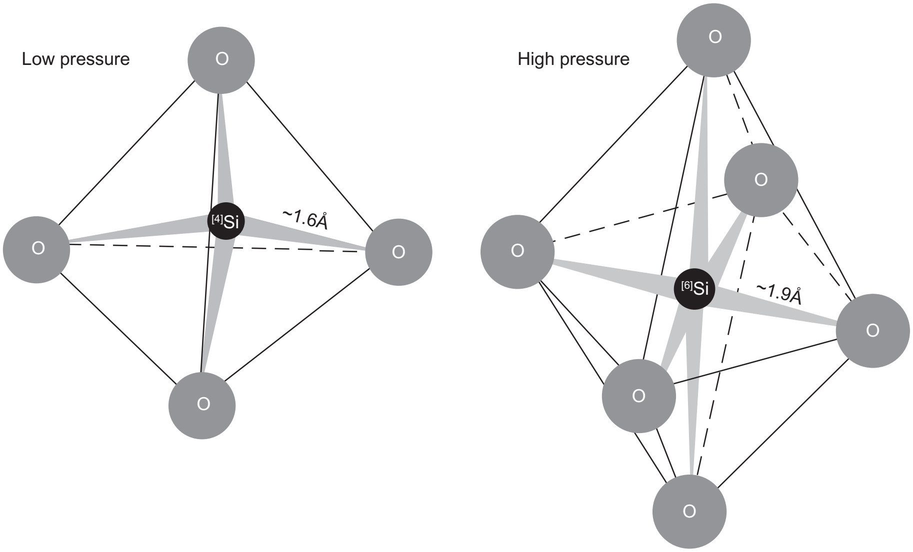

FIG. 4.4 Low-pressure SiO_4 tetrahedra vs high-pressure SiO_6 octahedra. In the SiO_2 polymorphs, these types of oxygen polyhedra are exemplified by quartz and stishovite, respectively.

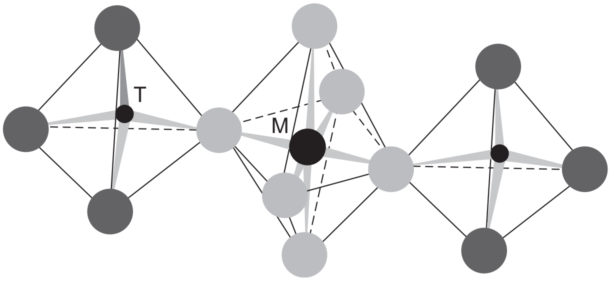

FIG. 4.5 Connection by nonbridging oxygens *(light gray)* between the oxygen coordination of tetrahedrally coordinated cations, T and the octahedron of another cation, M (*dark gray*: bridging oxygens).

A dramatic illustration of the difference in bond strength between Si^{4+} and other cations is provided by Mg_2SiO_4 glass. The structure of this material is made up of isolated, regular SiO_4 tetrahedra, similar to those of the crystalline form (forsterite). These tetrahedra are randomly oriented and linked through a variety of highly distorted MgO_n polyhedra, with $4 < n < 6$ (Kohara et al., 2011). This contrast between SiO_4 and MgO_n polyhedra illustrates the fact that, although Si^{4+} ions are half as abundant as Mg^{2+}, they control the structure and leave to Mg^{2+} ions a simple role of "space fillers."

Between these two extremes, the number of nonbridging oxygens per silicon atom increases from 0 as in SiO_2 to 4 as in Mg_2SiO_4. This number is an average value that characterizes the degree of polymerization of the silicate framework. Various kinds of SiO_4 tetrahedra must be distinguished to describe the structure in more detail because oxygens are either bridging

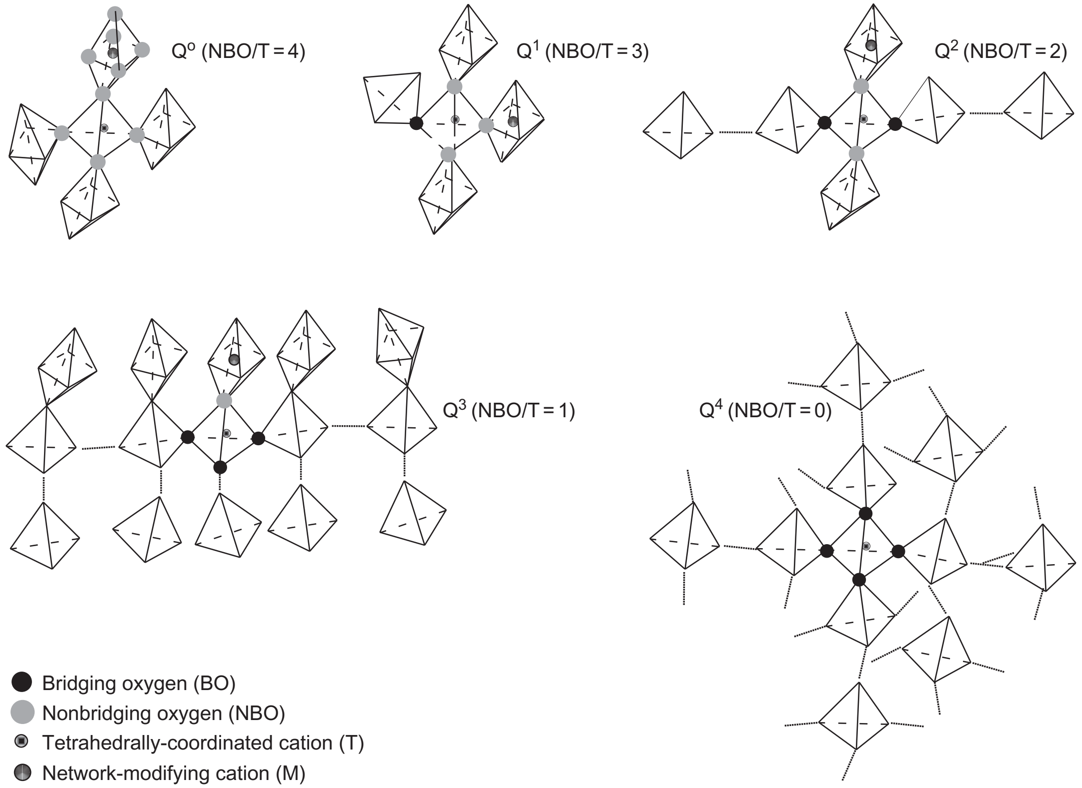

FIG. 4.6 Schematic representation of interconnected silicate tetrahedra and larger oxygen polyhedra with a central metal cation in the various Q^n structural units. In the Q^4 sketch, the *short lines* indicate effectively infinite extension of the structure.

or nonbridging. Following Schramm et al. (1984), one characterizes this difference in terms of Q^n-species comprising an SiO_4 tetrahedron in which n oxygens are bridging and 4-n are nonbridging (Fig. 4.6). The silicate chains of pyroxene ($MSiO_3$) crystals are, for example, made up of only Q^2 species, but there is, in contrast, a distribution of Q^n-species around a mean value of 2 in amorphous phases of the same stoichiometry (Etchepare, 1972; Brawer and White, 1975; Maekawa et al., 1991; Polyakov et al., 2010).

Whereas tetrahedral coordination always holds for Si^{4+} at low pressure, the coordination number of oxygen increases from 2, for pure SiO_2, to higher values for depolymerized structures. These coordination numbers depend on the manner in which other cations form bonds to nonbridging oxygens by forming additional oxygen polyhedra between SiO_4 tetrahedra (Fig. 4.6). The latter cations will be referred to as M-cations. In olivine crystals, for instance, divalent metal cations are sixfold coordinated by oxygens, which are themselves bound to 4 M-cations. Although the number of cations to which oxygen can be coordinated changes widely in oxide compounds, the ionic radius of O^{2-} varies only from 1.27 to 1.34 Å between twofold and eightfold coordination. Such variations are very small compared to those experienced by cations when their coordination changes. This is illustrated by Si^{4+} (see previous) or Na^+ ($r = 1.07$ Å and 1.40 Å for four- and ninefold coordination, respectively). This sensitivity difference is the main reason why attention is paid to cation coordination by oxygen and not to oxygen coordination by cations.

As already noted, the actual charges of cations and anions are not only lower than the formal charges that are usually assumed, but they are not constant for a given ion. According to ab initio calculations on sodium tetrasilicate, the charge of Si within Q^4- and Q^3-species is on average 0.14 and 0.10 higher, respectively, than in Q^2-species, whereas nonbridging oxygens are more negatively charged than bridging oxygens by 0.15 charge units (Ispas et al., 2002). An important consequence of such charge distributions is that bonding of bridging oxygens with silicon leaves a residual charge, which is used for bonding with other cations. The relative contribution of bridging and nonbridging oxygens to the oxygen coordination of these cations is poorly known. In molecular dynamics simulations of soda-lime silicates, this contribution is in a ratio varying from 1:5 to 1:10 for glasses quenched from the very high temperature of 6000 K (Cormack and Du, 2001). Such calculations do not allow the actual ratio to be determined for the actual temperature ranges of interest, but this important feature should be kept in mind when discussing silicate structures.

4.3.2 Network-Formers and Network-Modifiers

When an alkali or alkaline earth oxide is mixed with pure SiO_2, the ensuing decrease of the Si/O ratio causes depolymerization of the silicate framework. According to a terminology already used by Warren and Pincus (1940), in these situations silicon is a network-former and most other metal cations are network-modifiers.

A few elements can be both network-modifiers and network-formers. Aluminum is the most important in this category. At low pressure, its ionic radius ($r = 0.47$ Å) is comparable to the 0.34 Å of Si^{4+}, but its formal charge is only 3+ so that it can enter tetrahedral sites of the silicate framework only by associating with a neighboring charge-compensating cation to achieve the 4+ formal charge of Si. This role is generally played by an alkali (univalent) cation, as illustrated by albite ($NaAlSi_3O_8$), for example, or by an alkaline earth (divalent) cation, which compensates for two different Al^{3+} as illustrated in crystals by anorthite ($CaAl_2Si_2O_8$). Whether a charge-balancing cation associates with one or two Al^{3+} cations has profound effects on the Al—O bond strengths and, therefore, properties of the material (see Chapter 8 for detailed discussions of such property behavior).

Other cations achieve tetrahedral coordination when their ionic radii are not too different from that of Si^{4+} and their mismatch in electrical charge can be compensated. In crystalline silicates, P^{5+} is such a cation ($r = 0.25$ Å), at least at low pressures. The same applies to Fe^{3+} ($r = 0.57$ Å), although this cation sometimes has more than four oxygen ligands, in particular in crystalline materials. Boron may occur either in ${BO_4}^{5-}$ tetrahedra ($r = 0.20$ Å) and in ${BO_3}^{3-}$ triangles ($r = 0.10$ Å). Titanium, with its somewhat greater ionic radius of 0.61 Å when existing as Ti^{4+}, is usually coordinated by more than four oxygens but there is also evidence for fourfold coordination. For convenience, any network-forming, tetrahedrally coordinated cation will be denoted by T.

Characterization of the anionic framework of amorphous silicates becomes more complicated when several of these cations are present in appreciable amounts, for example in aluminosilicates. The distances between the central T-cation in a tetrahedron and an oxygen, whether bridging or nonbridging, are sensitive functions of the type of T-cation (Marumo and Okuno, 1984; Henderson et al., 1984; Cormier et al., 2003). Similar principles apply to the intratetrahedral (O—T—O) and intertetrahedral (T—O—T) angles because of the correlations between bond angle and distance. In addition, the bond angles also depend on the polymerization state of the silicate framework and increase as a silicate species becomes more depolymerized (Soules, 1979; Furukawa et al., 1981).

Network-modifying cations serve as links between the oxygen tetrahedral. These cations most commonly are alkali metals and alkaline earths. In cases where there are multiple network-modifying cations, the nonbridging oxygens in the most depolymerized of Q^n-species tend to form oxygen polyhedra with the most electronegative cation available as this is the environment with the least steric hindrance. Equilibria among Q^n-species will, therefore, be affected by the electronic properties of the network-modifying cation or cations.

4.3.3 The NBO/T Parameter

The NBO/T (nonbridging oxygen, NBO, per tetrahedrally coordinated cation, T) atomic ratio represents the simplest way to characterize the degree of polymerization of the structure. As will be shown in following chapters, this parameter has proven useful for rationalizing glass and melt properties. It is necessarily an approximate description, however, for it does not take into account the nature of the network-forming and of the network-modifying metal cations.

The NBO/T can be calculated from melt composition provided that the proportion of tetrahedrally coordinated cations is known. A procedure that may be used for this purpose is given in Table 4.2. At present, this calculation can be conducted at comparatively low pressures for which the necessary information is available. At high pressures, such as in the deeper portion of the earth's upper mantle and below, both Si^{4+} and Al^{3+} may undergo partial or complete coordination transformation (Lee et al., 2006; Kelsey et al., 2009; Sanloup et al., 2013), under which circumstances the degree of melt polymerization changes. Thus, the NBO/T parameter as a structural monitor cannot be used with currently available data at high pressure.

Knowledge of NBO/T is useful because a number of melt properties is correlated with NBO/T in a manner simple enough that predictions can be made. For example, in its most basic form, NBO/Si is positively correlated with high-temperature viscosity and conductivity

TABLE 4.2 Procedure for Calculations of NBO/T From Oxide Composition at Low Pressures

Step 1	Convert chemical analyses (in wt%) to atomic proportions
Step 2	$T = Si + Al + Fe^{3+}$. Assign alkalis and alkaline earths to Al^{3+} and Fe^{3+} for charge-balance in tetrahedral coordination (relative stability of aluminate and ferrite complexes known from thermochemical data). The order of charge-balance is: $K > Na > Ca > Fe^{2+}Mg$ and $AlO_2^{-}FeO_2^{-}$[a]
Step 3	Use formal charge of T-cations (4+) and oxygen (2−), which then gives $NBO = (2O - 4T)$ and $NBO/T = (2O - 4T)/T$

[a] *Note that Ti^{4+}, P^{5+}, and B^{3+} are not included in this calculation. See text for discussion of complex and variable structural role of these cations.*

of simple binary metal oxide-SiO_2 melts (Mysen, 1995; Polyakov et al., 2010). This is not surprising because in such simple compositions, NBO/Si and alkali/silicon ratios are effectively equivalent, and melt viscosity depends on the latter ratio (Bockris et al., 1955). Relationships between NBO/T and viscosity may be extended to natural magmatic liquids at pressures and temperatures where the proportion of tetrahedrally coordinated cations can be calculated (Mysen, 1987; see also Chapter 18).

The NBO/T can be a useful parameter in semiquantitatively estimating viscosity, although there is considerable scatter in such relationships because of the number of other composition variables influencing transport properties (Mysen, 1995; Giordano and Dingwell, 2003). Other parameters that seem related to the degree of polymerization include activity-composition relations of major, minor, and trace elements (Mysen, 1995). Therefore, the NBO/T can be used to express composition dependence of mineral-melt element partitioning (Jana and Walker, 1997; Walter and Thibault, 1995; Toplis and Corgne, 2002).

4.4 THE TETRAHEDRAL OXYGEN NETWORK

At low pressure, silicates—whether crystalline, glassy, or molten—consist of a network of SiO_4 tetrahedra in which Si^{4+} may be partially replaced by other cations that have a similar ionic radius, r, and a formal electrical charge, Z, of about 4. Cations of this type are referred to as network-formers.

4.4.1 Bridging Oxygen Bonds

A bridge is formed by oxygens bonded to tetrahedrally coordinated cations shared by adjacent oxygen tetrahedra. Even when Si^{4+} is not the most abundant cation, its oxygen polyhedra constitute an anionic framework whose connectivity depends on the Si/O ratio of the material (Fig. 4.6). For the SiO_2 stoichiometry of pure silica, low-pressure SiO_4 tetrahedra necessarily polymerize to form an open, three-dimensional network in which each oxygen in the crystal structure is bridging (BO). The bridging oxygens are shared by two neighboring tetrahedra. At the other end of the spectrum, the M_2SiO_4 stoichiometry of crystalline olivines gives rise to isolated SiO_4 tetrahedra where all oxygens are nonbridging (NBO).

Bond lengths and bond angles (and, therefore, bond strength) depend not only on pressure and temperature but also on the nature of the tetrahedrally coordinated cations, T. The bond length can vary perhaps by as much as 10%. This variation is often governed by substitution of Si^{4+} by other tetrahedrally coordinated cations such as Al^{3+} whose ideal Al—O length is ~1.71 Å as compared with ~1.60 Å for Si—O (e.g., Navrotsky et al., 1985). Other cations potentially in fourfold coordination with oxygen are Fe^{3+}, B^{3+}, and P^{5+}. Among these cations, $^{[IV]}Fe^{3+}$—O bonds are the longest (Henderson et al., 1984; Holland et al., 1999).

4.4.2 Network-Formers and Si-Based Structural Units

The silicate structural backbone, be it in glasses, melts, or crystals, is the silicate tetrahedron, where anywhere from 0 to 4 of the oxygen anions form bridges across to other silicate tetrahedra (Fig. 4.6). In crystalline silicate structures, typically a single form of silicate interconnectivity exists (e.g., Liebau, 1981). However, in amorphous silicates such as glasses and melts, several different forms of silicate entities typically coexist as originally proposed more than 50 years ago on the basis of property variations of simple silicate melts (MacKenzie, 1947; Bockris et al., 1955). In the original models, from the systematics of viscous flow a small number of discrete silicate polymers was proposed to coexist in this original model. From their studies of trimethylsilyl derivatives of silicate glasses, Smart and Glasser (1978) proposed some time later a polymer model characterized by a continuous change of degree of polymerization as a function of changing metal/silicon ratio. This model was subsequently found unrealistic, however, as a rapidly increasing database, relying on spectroscopic methods and numerical simulations, was found to be consistent with structures that comprise only a small number of specific structural units (Virgo et al., 1980; Stebbins, 1987; Buckermann et al., 1992; Schneider et al., 2003; Polyakov et al., 2010). This principle is illustrated schematically in Fig. 4.6. In this structural arrangement, changing bulk composition is accommodated in the structure by simply changing the proportion of these species. In other words, the equilibrium constants that describe equilibria among various Q-species vary with silicate composition (Stebbins, 1987):

$$2Q^{n} = Q^{n+1} + Q^{n-1}, \tag{4.7}$$

where the superscript, n, which is an integer, denotes the number of bridging oxygens in a Q-species.

4.4.3 Substitution of Si^{+}

The concept of charge-balance of certain tetrahedrally coordinated cations illustrates the dual structural roles played by alkali metals and alkaline earths. One is to serve as network modifiers. In this sense, these cations are linked to terminal oxygens in a tetrahedral network, including, therefore, terminal oxygen in Q-species (Fig. 4.6). The other role is to charge-compensate cations such as B^{3+}, Al^{3+}, and possibly Fe^{3+} in tetrahedral coordination. For trivalent cations, this can be accomplished with alkalis or alkaline earths. For P^{5+} the situation is more complex. In highly polymerized, silica-rich glasses and melts, one oxygen double-bonded to P may serve this purpose (Hoppe et al., 1998; Plotnichenko et al., 2002). Another common charge-compensation for tetrahedrally coordination P^{5+} is via Al-phosphate complexing (Toplis and Schaller, 1998; Cody et al., 2001).

The most prevalent substitution is Al^{3+} for Si^{4+}. Simple charge-balance is obtained when the proportion of charge-balancing cation(s) is equal to, or in excess of, that required for this purpose. When there is an excess of alkali metal or alkaline earth over that required to provide a formal charge of 4+ for Al in tetrahedral coordination, the system is called *peralkaline* (Fig. 4.7) When the proportion of alkali metal or alkaline earth is exactly equal to that required to provide a formal charge of 4+ for Al in tetrahedral coordination, the system is termed *metaaluminous* (Fig. 4.7). When the proportion of Al exceeds that of available cations for charge-balance, the system is called *per-aluminous* (Fig. 4.7)

Experimental evidence exists for this dual structural role of alkali metals and alkaline earths. Results from molecular orbital calculations suggest that the Na-NBO (NBO: nonbridging oxygen) bond is shorter than Na-BO (BO: bridging oxygen) distances and that

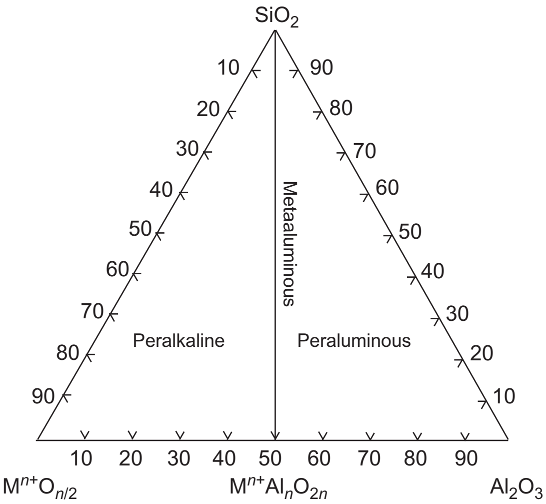

FIG. 4.7 Peralkaline, metaaluminous, and peraluminous fields in aluminosilicate systems.

Ca-NBO distances are shorter than for Ca-BO (Uchino and Yoko, 1998; Cormack and Du, 2001; Ispas et al., 2002; Cormier et al., 2003). For Na^+, for example, such a difference in bond distance is likely to cause more electronic deshielding of the Na nucleus as the proportion of Na-NBO bonds increases. In Al-free glasses, the Na nucleus becomes more deshielded with increasing Na/Si, which would lead to increased Na-NBO distance with increasing Na/Si (Lee and Stebbins, 2003). That prediction agrees with ^{23}Na NMR data and X-ray data for binary Na_2O-SiO_2 glasses and ternary metaaluminosilicate glasses along the alkali and alkaline earth aluminosilicate joins (Xue and Stebbins, 1993; Lee and Stebbins, 2003; Cormier and Neuville, 2004; see also Fig. 4.8). The Na-NBO bond distance might be as much as 10% shorter for Na-NBO than for Na-BO, although the exact relationship to shielding of the Na nucleus also depends on Na/Si and Al/(Al+Si). For glasses with the same Na/Si ratio where Na^+

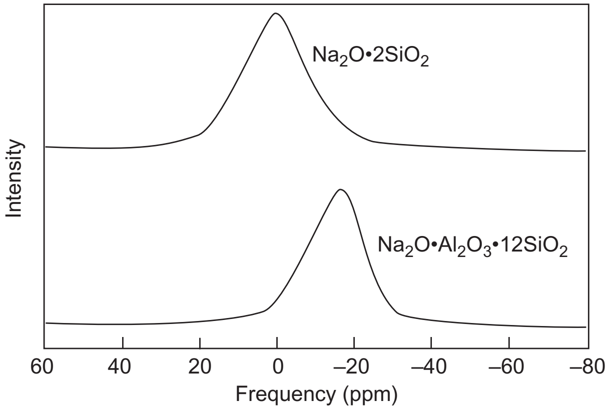

FIG. 4.8 Sodium-23 NMR spectra of $Na_2Si_2O_5$ and $NaAlSi_6O_{14}$ glasses. Data from Lee and Stebbins (2003).

FIG. 4.9 Sodium-23 chemical shift in NMR spectra of glasses along the SiO_2-$NaAlO_2$ join against Al/(Al+Si) (Lee and Stebbins, 2003).

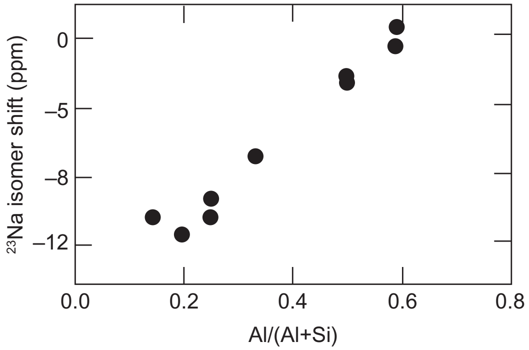

serves to charge-balance Al^{3+}, the ^{23}Na chemical shift increases (Na becomes more deshielded) with increasing Al/(Al+Si) (Fig. 4.9). As far as deshielding is concerned, however, there remains a distinct difference between Na as a charge-balancing cation and as a network-modifier. Whether this difference reflects differences in electrical field gradients or different oxygen coordination numbers, or both (see Gambuzzi et al., 2015), remains open to further study.

4.4.3.1 *Aluminum Substitution*

X-ray radial distribution (XRDF) analysis is useful to determine T—O, T—T, and O—O bond lengths (T = tetrahedrally coordinated cation) and in some cases may be used to map bond lengths to distances reaching several coordination spheres. Such features are well illustrated by X-ray radial distribution functions of metaaluminosilicate glasses. Along the SiO_2-$NaAlO_2$ join, for example, these do show significant similarity to at least 3 Å, which is the approximate distance between the central T-cations to the second nearest neighboring tetrahedron (Taylor and Brown, 1979).

From the X-ray data, the average T—O bond length increases systematically with increasing Al/(Al+Si) (Fig. 4.11). This increase is consistent with the generally slightly longer Al—O bond length compared with Si—O bonds in the oxygen tetrahedra (Brown et al., 1969; Geisinger et al., 1985; Tossell, 1993). Spectroscopic data of glasses on the SiO_2-$NaAlO_2$ join are consistent with random or near substitution of Al^{3+} for Si^{4+} in the structure (Taylor and Brown, 1979; Lee and Stebbins, 1999, 2006). However, for glasses with divalent cations for Al charge balance, the line widths of 29MAS NMR spectra are considerably broader, thus suggesting more structural disorder (Lee and Stebbins, 1999; see also Fig. 4.10).

The ionization potential (as defined by Eq. 2.5) of the charge-balancing cation can affect the extent of Al ⇔ Si ordering (Seifert et al., 1982; Lee and Stebbins, 1999, 2006). For example, whereas Na^+ and Ca^{2+} have similar ionic radii (Whittaker and Muntus, 1970), they charge-balance 2 and 1 tetrahedrally coordinated Al^{3+}, respectively. This effect is seen quite clearly in the electron density around Al—O bonds in crystals like nepheline and anorthite (Tait et al., 2003; Angel, 1988). In anorthite, at least one of the Al—O bonds is severely underbonded, presumably reflecting the steric problems associated with Ca^{2+} charge-compensation of Al^{3+} in the crystal structure.

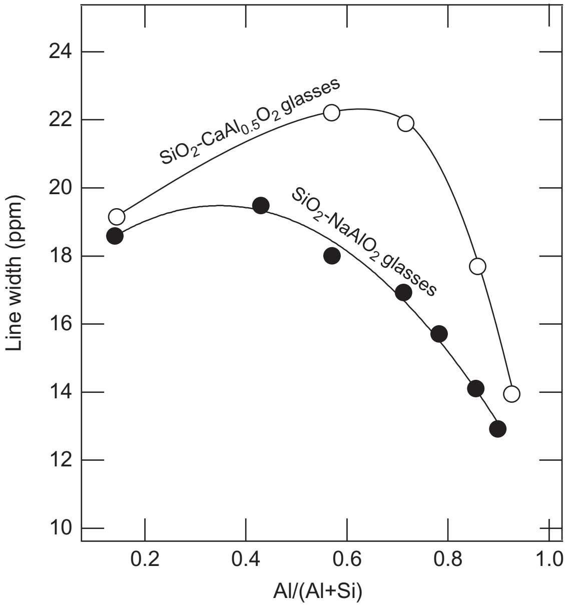

FIG. 4.10 Full width at half height of ^{29}Si peak from fully polymerized aluminosilicate species in ^{29}Si MAS NMR spectra plotted against Al/(Al+Si) of glasses along the joins SiO_2-$NaAlO_2$ and SiO_2-$CaAl_{0.5}O_2$, (Lee and Stebbins, 1999).

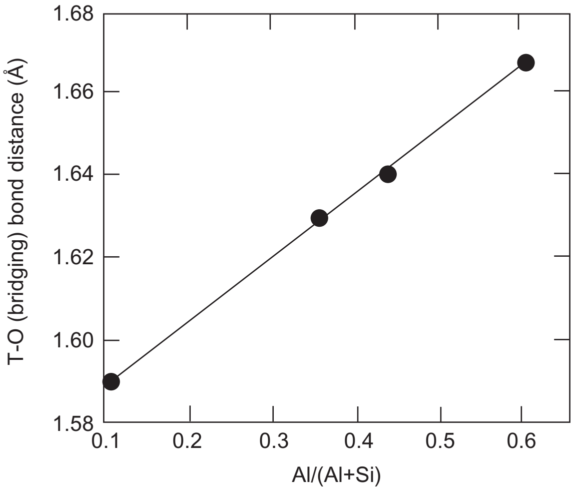

FIG. 4.11 Bridging oxygen distance (T—O—T, T = Al, Si) in glasses along the SiO_2-$NaAlO_2$ join from analysis of the X-ray radial distribution functions of glasses (Taylor and Brown, 1979).

Similar structural restrictions likely exist in aluminosilicate glasses and melts as suggested, for example, by the systematic relationship between ^{29}Si NMR line width and ionization potential of the charge-balancing cation in glasses along the joins SiO_2-$NaAlO_2$, SiO_2-$KAlO_2$, and SiO_2-$CaAl_2O_4$ (Murdoch et al., 1985; Lee and Stebbins, 2003; see also Fig. 4.11). Although this line width depends on Al/(Al+Si), for a given Al/(Al+Si), it increases as the

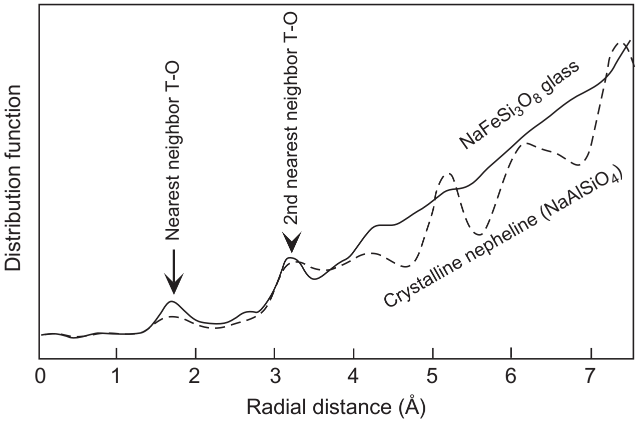

FIG. 4.12 X-ray radial distribution functions of $NaFeSi_3O_8$ glass *(solid line)* and of crystalline nepheline *(dashed line)* (Henderson et al., 1984).

charge-balancing cation becomes more electronegative. These line width relationships are consistent with increasing Si ⇔ Al disorder with increasingly electronegative charge-balancing cations (Lee and Stebbins, 1999, 2006).

The difference in Al ⇔ Si ordering with alkali metal versus alkaline earths may also help explain why the structures of $CaAl_2Si_2O_8$ and $NaAlSiO_4$ glass differ. The T—O radial distance of the first coordination sphere is approximately the same for both compositions. However, the T—O radial distance to the second and third coordination spheres in the X-ray spectrum of $CaAl_2Si_2O_8$ is longer than for $NaAlSiO_4$ (Fig. 4.12). This information suggests that there is longer-range order in $CaAl_2Si_2O_8$ than in $NaAlSiO_4$ glasses and melts (Taylor and Brown, 1979; Marumo and Okuno, 1984). These matters are discussed in more detail in Chapter 9.

4.4.3.2 *Ferric Iron*

Ferric iron often has been suggested to be tetrahedrally coordinated in silicate glasses and melts (Alberto et al., 1996; Giuli et al., 2011; Kim et al., 2016) even though tetrahedrally coordinated Fe^{3+} in silicate crystals is rare. Tetrahedrally coordinated Fe^{3+} is consistent with the hyperfine parameters from Mössbauer spectroscopy of Fe^{3+}-rich silicate glasses (Dingwell and Virgo, 1988). Fourfold coordinated Fe^{3+} is also consistent with the X-ray radial distribution function of $NaFeSi_3O_8$ glass (Henderson et al., 1984; see also Fig. 4.12). In the discussion of these data, however, Henderson et al. (1984) noted that the radial distribution function of $NaFeSi_3O_8$ glass is closer to that of $NaAlSiO_4$ glass than to that of its Al-bearing counterpart, $NaAlSi_3O_8$ (Fig. 4.12). In other words, the T—O bond length in the ferrisilicate glass appears longer than that for an equivalent aluminosilicate and matches the aluminosilicate only when its Al/(Al+Si) exceeds $Fe^{3+}/(Fe^{3+}+Si)$. This observation also is consistent with the longer bond distance found for $^{[4]}Fe^{3+}$—O than for $^{[4]}Al$—O (Okamura et al., 1974; Henderson et al., 1984; Redhammer, 1998). Considerable Si ⇔ Fe^{3+} ordering has been suggested, possibly with clusters of Fe^{3+}—O tetrahedra in which there may not be any substitution of Si^{4+} for Fe^{3+} (Mysen et al., 1984; Alberto et al., 1996). A detailed discussion of the structural role of iron in silicate glasses and melts is found in Chapter 11.

4.4.3.3 *Phosphorus*

Phosphorus is a tetrahedrally coordinated cation in most Al-free silicate glasses or melts, even in the system SiO_2-P_2O_5 where P═O bonding is observed in the phosphate tetrahedra (Shibata et al., 1981). In alkali and alkaline earth silicate glasses and melts, phosphorus forms phosphate complexes with different degrees of polymerization, NBO/P, where the value of NBO/P depends on P-content (Nelson and Tallant, 1984, 1986; Dupree, 1991; Kirkpatrick and Brow, 1995). However, the very narrow bands associated with phosphorus in both the Raman and ^{31}P NMR spectra of P-bearing alkali and alkaline earth silicate glasses suggest that these phosphate complexes form clusters in the structure.

The insertion of phosphorus in aluminosilicate melts may differ from that in Al-free (or Al-poor) melts. The ^{31}P NMR spectra of aluminosilicate glasses are quite broad and resemble those of ^{29}Si in this respect (Fig. 4.13). It has been suggested that Al-phosphate complexes are distributed within the aluminosilicate melt structure (Cody et al., 2001). These and other features of the role of phosphorus in melts and glasses are the subject of Chapter 13.

4.4.3.4 *Titanium*

The structural information on Ti^{4+} in silicate glasses suggests that this cation may be in several different coordination states (Farges, 1997, 1999; Cormier et al., 2001; Henderson et al., 2002; Alderman et al., 2014). Its complex structural behavior is such that systematic relationships between oxygen coordination and intensive and extensive variables have not as yet been developed. Available data do not suggest simple substitution for Si^{4+}, as discussed in Chapter 12.

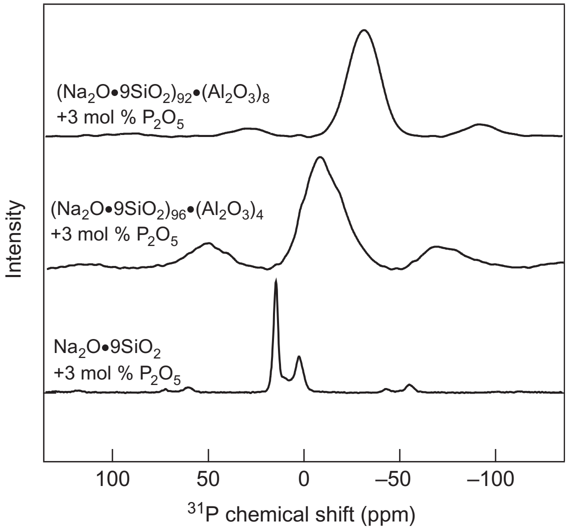

FIG. 4.13 Phosphorus-31 MAS NMR spectra of glasses in the system Na_2O-Al_2O_3-SiO_2 with 3 mol% P_2O_5 added for compositions indicated on individual spectra (Cody et al., 2001).

4.5 LINKAGE BETWEEN TETRAHEDRAL NETWORK UNITS

Network-modifying cations link the silicate or aluminosilicate network units via bonding with nonbridging oxygen (Fig. 4.5). These cations are commonly referred to as network-modifiers. For the most part, they are alkali metals or alkaline earths. It is also possible that Fe^{2+} could be in this category, but some uncertainty exists as to its exact structural role (see Chapter 11).

4.5.1 The Nature of Nonbridging Oxygen Bonds

For illustration purposes, the oxygen polyhedron is represented as an octahedron in Fig. 4.5. However, the number of oxygen ligands varies with the kind of network-modifying cations and probably also depends on the nature of the nonbridging oxygens in question. The coordination number generally increases with increasing ionic radius of the metal cation (Cormier et al., 2001). These polyhedra in addition may be significantly distorted, as seen for CaO_6 polyhedra (e.g., Binsted et al., 1985; Jones et al., 2001). It also appears that the metal-oxygen distances may differ depending on whether or not an alkali metal or alkaline earth is a network-modifier (Cormack and Du, 2001; Lee and Stebbins, 2003).

Both the metal-nonbridging bonds and the Si-nonbridging oxygen bonds are likely affected by the electronic properties of the network-modifying metal cation (Mysen and Shang, 2005; Mysen, 2007). The structure of most melts and glasses consists of several different coexisting units, each with a different number of nonbridging oxygens to which metal cations are bonded (Q^n-species). For a given metal cation, therefore, there may be an effect of melt and glass composition on metal-oxygen bonds. This structural effect, seen in various melt properties, also has been documented for Na—O bonding in Na_2O-SiO_2 glass, for example (Lee and Stebbins, 2003). The ^{23}Na NMR spectrum of $Na_2O{\cdot}SiO_2$ and $Na_2O{\cdot}2SiO_2$ glass contains about 60 and 15 mol% Q^2 and 30 and 85 mol% Q^3 structural units, respectively (Maekawa et al., 1991; Buckermann et al., 1992). There is evidence for two peaks with different chemical shifts (Fig. 4.14). Because the Na nucleus likely is more deshielded the greater the Na/Si ratio

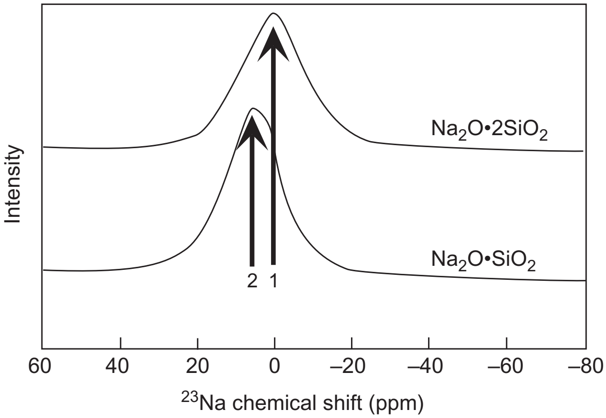

FIG. 4.14 Sodium-23 NMR spectra of $Na_2Si_2O_5$ and Na_2SiO_3 glasses (Lee and Stebbins, 2003).

(Maekawa et al., 1991; Xue and Stebbins, 1993; Lee and Stebbins, 2003), the peak with the greatest chemical shift in the ^{23}Na spectrum can be assigned to Na-nonbridging oxygen bonds involving Q^2 units. The peak with the lower chemical shift is likely assigned to Na-nonbridging oxygen bonds from nonbridging oxygen in Q^3 units.

The properties of Si-nonbridging oxygen bonds are also influenced by the type and proportion of network-modifying cations. This is evident in Raman spectra of alkali and alkaline earth silicate glasses (Mysen and Frantz, 1994; Frantz and Mysen, 1995) indicating correlations between the force constants of Si-nonbridging oxygen bonds and ionization potential of the alkali metal or the alkaline earth. Similar conclusions were drawn by Jones et al. (2001) from ^{29}Si NMR spectroscopy and by Ispas et al. (2002) from numerical simulation of Na_2O-CaO-SiO_2 glass structure. This effect is shown more clearly in the ^{29}Si NMR chemical shift of Na_2O-SiO_2 glasses as a function of Na_2O/SiO_2 abundance ratio (Fig. 4.15). These shifts indicate that the Si nucleus in the Q^4, Q^3, and Q^2 units becomes more deshielded the higher the Na/Si (Lee and Stebbins, 2003). Interestingly, the Na/Si effect on the isomer shifts is greater for more polymerized Q^n units. Analogous relationships may be inferred from the ^{29}Si MAS NMR spectra of Li_2O-SiO_2, Na_2O-SiO_2, and K_2O-SiO_2 glasses (Maekawa et al., 1991).

4.5.2 Steric Hindrance and Ordering of Network-Modifying Cations

Site preference is a common structural feature in crystalline materials. For example, in orthopyroxene [(Mg,Fe)SiO_3] and olivine [$(Mg,Fe)_2SiO_4$], Fe^{2+} and Mg^{2+} are distinctly ordered between the M1 and M2 sites (Finger and Virgo, 1971; Hafner and Virgo, 1970). In other words, the M1 and M2 sites are not energetically equivalent. If there exists energetically nonequivalent nonbridging oxygen in glasses and melts, one might likewise expect that

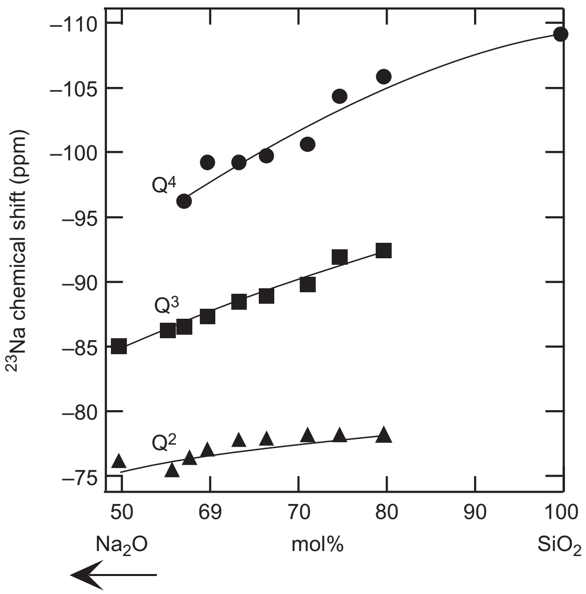

FIG. 4.15 Sodium-23 chemical shifts of peaks in ^{23}Na MAS NMR spectra assigned to Q^4, Q^3, and Q^2 in Na_2O-SiO_2 glasses against composition. Data from Maekawa et al. (1991).

distinct network-modifying cations exhibit a preference for specific nonbridging oxygens. The systematic relationship between ionization potential of metals and the width of liquid immiscibility gaps in metal oxide-SiO_2 melts (Hudon and Baker, 2002) may reflect such ordering phenomena. Nonequivalence also has been inferred from element partitioning between crystals and melts (Mysen, 2007). Among network-modifying cations, ordering would also influence activity-composition relations in silicate melts as inferred from liquidus phase relations, for example, (Kushiro, 1975; Ryerson, 1985) and configurational properties (Richet and Neuville, 1992) of metal oxide-SiO_2 systems.

From a structural perspective, Jones et al. (2001) suggested that, in mixed Na_2O-CaO-SiO_2 glasses the dominant Q^n structural units of which are of Q^3 and Q^2 type, Ca^{2+} shows a tendency to form Ca-oxygen bonds preferentially with nonbridging oxygen in the Q^2 structural units, whereas Na-nonbridging oxygen bonds are formed preferentially in Q^3 structural units. This suggestion has been documented further with results from triple quantum ^{17}O NMR spectroscopy of glasses in the same system by Lee and Stebbins (2003). These latter experiments clearly distinguished oxygen associated only with Si^{4+} (bridging oxygen in Si—O—Si), with Na only (nonbridging Na—O), with Ca only (nonbridging Ca—O), and with a mixed (Na, Ca)-environment [nonbridging (Ca, Na)—O] (Fig. 4.16). Although the ^{17}O data do not offer information on where the various nonbridging oxygens exist in the silicate network, the data of Fig. 4.16 reflect ordering of Na^+ and Ca^{2+} among different nonbridging oxygens in the glasses. In light of the similar ionic radius of Na^+ and Ca^{2+}, it is likely that this ordering results from different electrical charge of Na^+ and Ca^{2+}. Analogous behavior has been observed for Mg^{2+} and Ba^{2+} in MgO-BaO-SiO_2 glasses and melts (Lee et al., 2002). These structural interpretations suggest, therefore, that differences in ionic radius may also result in ordering of the network-modifying cations among energetically nonequivalent nonbridging oxygens in the glasses and melts.

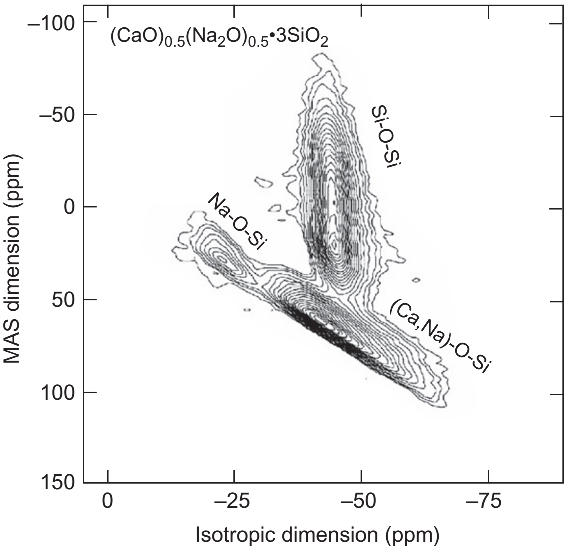

FIG. 4.16 Triple-quantum ^{17}O MAS NMR spectra of glasses in the system Na_2O-CaO-SiO_2 for compositions indicated on individual panels. Data from Lee and Stebbins (2003).

4.6 COMPOSITION, BONDING, AND MELT PROPERTIES

Properties that are determined by bond strength depend on compositional variables such as Si/Al-ratio, for example. Substitution of Si^{4+} by cations such as Al^{3+} weakens the T—O bond and, in turn, affects any property that depends on T—O bond strength.

4.6.1 Transport Properties

Transport properties strongly depend on bond strength (e.g., Bockris and Reddy, 1970). In particular, the energy required to rearrange all oxygen bonds involved in viscous flow finds its measure in activation energy of transport and is related directly to this feature.

Melt viscosity as a function of temperature and composition has been studied extensively. In early high-temperature studies (e.g., Bockris et al., 1955), simple Arrhenius equations were fitted to the observations, viz.

$$\eta = \eta_o \exp\left(\Delta H_\eta / RT\right), \tag{4.8}$$

where η is viscosity, η_o a preexponential term, ΔH_η activation enthalpy, T temperature, and R the gas constant. This activation enthalpy is a systematic function of silica content. For example, the high-temperature activation enthalpy of viscous flow for Na_2O-SiO_2 melts (Fig. 4.17) decreases rapidly from 600 kJ/mol near pure SiO_2—similar to the Si—O bond energy—to a nearly constant value near 200 kJ/mol for melts with Na_2O contents higher than about 15 mol%. Similar relations hold—at least qualitatively—for other alkali and alkaline earth silicate melts (Bockris et al., 1955, 1956). In binary alkali silicates, there is also an effect on ΔH_η,

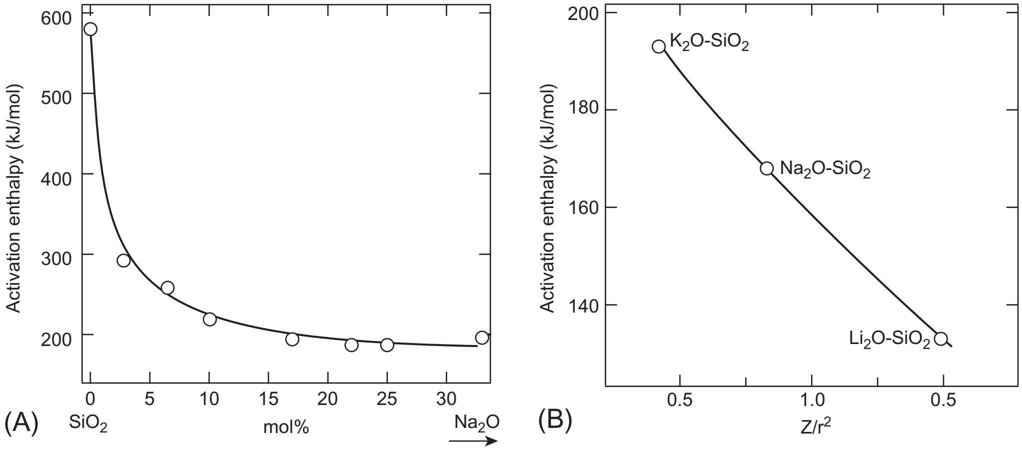

FIG. 4.17 (A) Activation enthalpy of viscous flow, ΔH_η, as a function of Na_2O content for high-temperature viscosity of melts in the system Na_2O-SiO_2 (Bockris et al., 1955). (B) Activation enthalpy of viscous flow, ΔH_η, from high-temperature viscosity of M_2SiO_3 melts (M = K, Na, Li) as a function of ionization potential, Z/r^2, of metal cation (Bockris et al., 1955). Ionization potential calculated for M in sixfold coordination with ionic radii. *From Whittaker and Muntus (1970).*

albeit smaller, of the nature of the metal cation. This ΔH_η decreases by 50 kJ/mol when K is exchanged for Li in simple metal oxide-silica melts.

The relationships in Fig. 4.17 are consistent with breakage of bridging Si—O—Si bonds as an important structural control of viscous flow at high temperature (i.e., well above the glass transition) with a lesser effect of the nature of alkali- or alkaline earth-oxygen bonding on the properties. In fact, this was the assumption made by Bockris and Reddy (1970), when deducing melt structure from physical properties. They built a melt-structure model based on bond strength considerations where they envisioned a small number of coexisting structural units with different Si/O ratios. This concept is consistent with current views of the structure of simple silicate glasses and melts (see also Section 4.3 and Chapter 7).

The Al—O bond strength in silicate crystals with tetrahedrally coordinated Al^{3+} is, on average, between 50% and 75% of that of the Si—O bond (see Table 4.1). The exact value of Al—O bond strength depends on details of the local charge compensation associated with the tetrahedrally coordinated Al^{3+}. That notwithstanding, activation enthalpy of high-temperature viscous flow of metaaluminosilicate melts is a negative function of the Al/(Al+Si) of the melt (Riebling, 1964, 1966; Toplis et al., 1997; Toplis and Dingwell, 2004; Webb, 2011) as illustrated in Fig. 4.18 for SiO_2-$NaAlO_2$ melts at ambient pressure. For metaaluminosilicate melts, their ΔH_η decreases monotonously with increasing Al/(Al+Si). Note, however, that for peralkaline melts with constant M/[Si+(MAl)], the high-temperature activation enthalpy of viscous flow is not only less sensitive to Al/(Al+Si), but may actually have a parabolic form as a function of Al/(Al+Si) (Dingwell, 1986). Further complexity in relationships between viscosity and melt composition is introduced when the ratio of alkalis or alkaline earths relative to Al is varied for melts with constant total SiO_2 content. In the system Na_2O-Al_2O_3-SiO_2, for example, this composition change can be expressed as Na/(Na+Al) at constant total SiO_2 content. As melts along such joins become increasingly aluminous, they also become more viscous with a maximum near, but not necessarily exactly at,

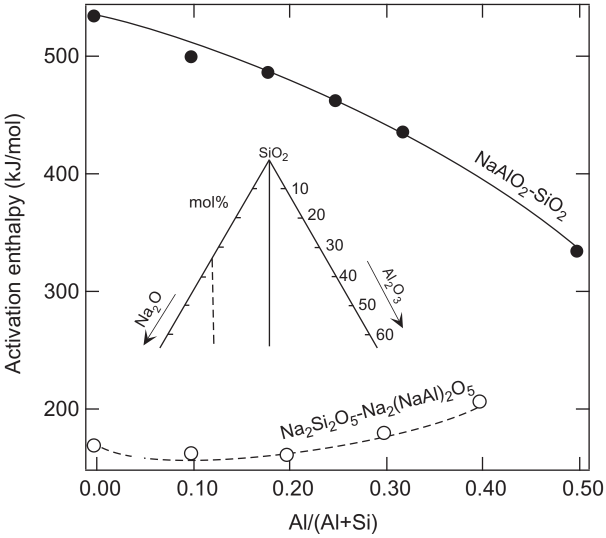

FIG. 4.18 Activation enthalpy of viscous flow, ΔH_η, from high-temperature viscosity of melts at $T/T_g = 1.7$, where T is the actual temperature and T_g the glass transition temperature, along the join $NaAlO_2$-SiO_2 (*solid line* and *symbols*—Toplis et al., 1997) and along the join $Na_2Si_2O_5$-$Na_2(NaAl)_2O_5$ at 1200°C as a function of Al/(Al+Si) of the melts (*dashed line* and *open symbols*—Dingwell, 1986).

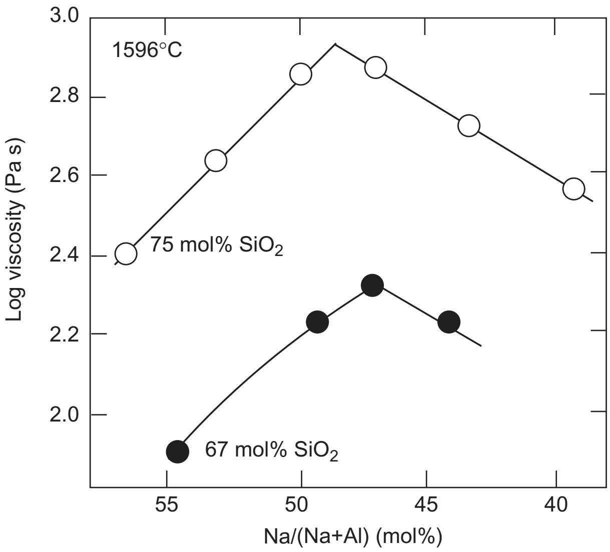

FIG. 4.19 Viscosity of melts in the system Na_2O-Al_2O_3-SiO_2 at constant SiO_2 content (mol%) as a function of Na/(Na+Al) at 1596°C (Toplis et al., 1997).

Na/(Na+Al)=0.5 of the metaaluminosilicate (Fig. 4.19). For highly peraluminous melts, the viscosity actually decreases with decreasing Na/(Na+Al). It appears, therefore, that if viscous flow of aluminosilicate melts reflects relative strength of Si—O and Al—O bonds, the influence of Al^{3+} is considerably more complex than might be expected from simple substitution of Al^{3+} for Si^{4+}. These matters are discussed in more detail in Chapters 8 and 9.

4.6.1.1 *Interrelationships of Transport Properties*

There exist relatively simple functional relationships between viscosity and other transport properties, such as diffusivity and electrical conductivity. For example, the Nernst-Einstein equation may be used to relate conductivity of component λ_i to diffusivity, D_i (Nernst, 1888; Einstein, 1905; see also Mott and Gurney, 1940):

$$\lambda_i = F^2 Z_i D_i / kT, \tag{4.9}$$

where F is Faraday's constant, Z_i the electric charge of ion i, and k Boltzmann's constant. Diffusivity is related to viscosity via the Stokes-Einstein equation (Einstein, 1905):

$$\eta = kT / 6\pi r_i D_i, \tag{4.10}$$

where r_i is the radius of the moving particle. In practical terms, the Eyring equation (Eyring, 1935):

$$\eta = kT / \alpha_i D_i, \tag{4.11}$$

where α_i is the jump distance, is more useful than the Stokes-Einstein equation for silicate melts (Magaritz and Hofmann, 1978; Watson, 1979; Shimizu and Kushiro, 1984, 1991). Its utility is to relate oxygen and silicon diffusion to melt viscosity with the idea that viscous flow of a melt and diffusion of oxygen both require breakage and reformation of oxygen bonds. An

FIG. 4.20 Relationship between viscosity, η, and oxygen diffusion coefficient, D, for $NaAlSi_2O_6$ and $CaMgSi_2O_6$ melts at 1 GPa. *Solid line* shows calculated relationship between viscosity and diffusion coefficient from the Eyring equation (Eq. 4.11) with jump distance, $a = 2.8$ Å (about twice the ionic radius of O^{2-}) (Shimizu and Kushiro, 1984).

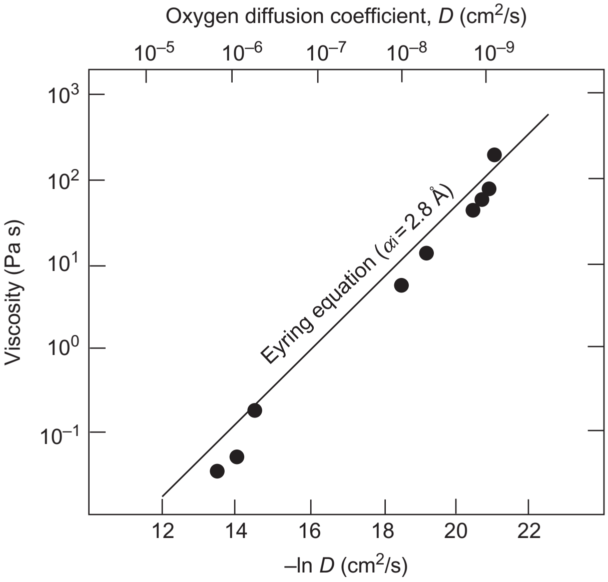

example of the use of the Eyring equation is shown in Fig. 4.20. Here, the jump distance is twice the ionic radius of O^{2-} (2.8 Å) for compositions such as $NaAlSi_2O_6$ and $CaMgSi_2O_6$. Self-diffusion of Si in SiO_2-rich melts also seems to follow the Eyring equation (Watson, 1982; Watson and Baker, 1991; Baker, 1990), which makes intuitive sense because silicon motion in a melt is likely linked to oxygen motion.

4.6.2 Thermal Properties

In solution calorimetry, one measures the change in enthalpy when a material is dissolved under conditions such that its atomic constituents become infinitely diluted in the solvent. Enthalpies of solution in an appropriate solvent, thus, represent a rather direct measure of average bond strength within a glass or a melt. From HF solution calorimetry at 25°C, Tischer (1969) and Hovis et al. (2004) observed that for Na_2O-SiO_2 glasses quenched from 1300°C, the enthalpy of solution decreases as a systematic function of Na_2O content (Fig. 4.21). This decrease may reflect decreasing abundance of Si—O bonds with large bond strength and increasing abundance of Na—O bonds with considerably smaller bond strength. In terms of site potential in crystals, these values are about an order of magnitude greater for Si—O compared with Na—O bonds (Table 4.1). When alkali aluminate components ($KAlO_2$, $NaAlO_2$, and $LiAlO_2$) are mixed with SiO_2 in a glass, the enthalpy of solution at 700°C in molten lead borate is also a systematic function of both the Al/(Al+Si) of the glasses and the electronic properties of the different alkali metals that act as charge-compensators for Al^{3+}, which substitute for Si^{4+} in the glass structure (Fig. 4.21).

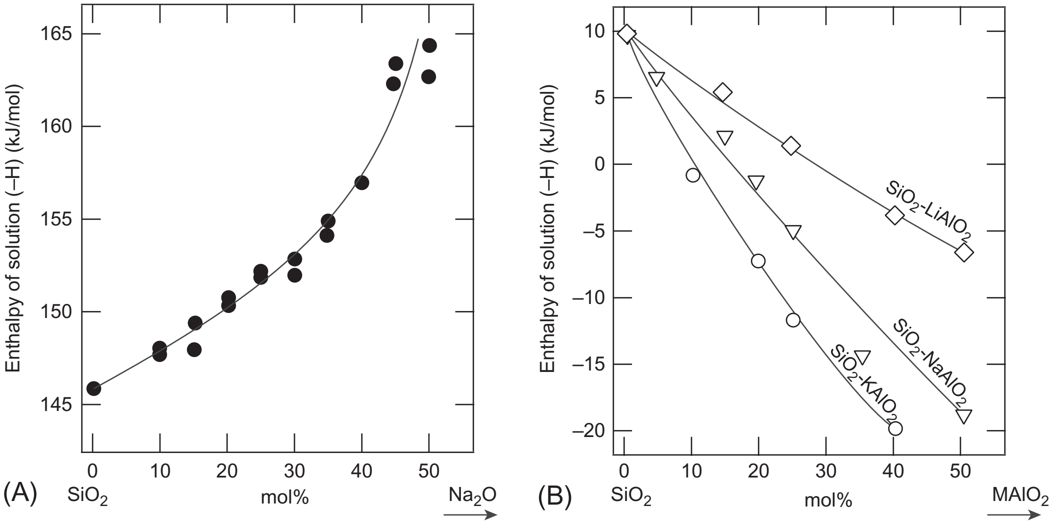

FIG. 4.21 (A) Enthalpy of solution of Na_2O-SiO_2 glasses as a function of composition (data from Hovis et al., 2004). (B) Enthalpy of solution of glasses along the joins SiO_2-$KAlO_2$, SiO_2-$NaAlO_2$, and SiO_2-$LiAlO_2$ as a function of aluminate concentration, $MAlO_2$ (Navrotsky et al., 1982; Roy and Navrotsky, 1984; Navrotsky et al., 1985).

4.7 MIXING, ORDER, AND DISORDER

A number of properties clearly show that silicate glasses and melts are not random mixtures of components, but may be viewed instead as mixtures of structural entities that—at least on a local scale—resemble those of crystalline phases existing at or near their liquidus (see also Chapters 5–7). For example, in a study of compressibility of vitreous SiO_2, Vuckevitch (1972) observed anomalous temperature and pressure relations that he interpreted in terms of two three-dimensionally interconnected SiO_2 structures coexisting. He suggested that such structures were similar to α- and β-polymorphs of crystalline cristobalite.

Likewise, the composition dependence of other properties such as index of refraction and viscosity has been used to suggest that discrete structural units exist in silicate glasses and melts (e.g., Babcock, 1968; Bockris and Reddy, 1970). This concept also found support in the early success of the so-called pseudocrystalline model of melt structure (e.g., Burnham, 1975; Bottinga and Richet, 1978; Nekvasil and Burnham, 1987), and in models of crystal nucleation that assumed entities in the melt with a structure that resemble—at least on a local scale—that of the nucleating phase (Kirkpatrick, 1983). Mixing of two or more structural entities, whatever their structural characteristics may be, affects melt and glass properties.

4.7.1 Transport Properties and Cation Mixing

Application of the Adam and Gibbs (1965) configurational entropy theory of relaxation processes to viscosity is discussed in Chapter 3 where emphasis was put on the effects of temperature and composition through the relevant variations of configurational entropy. Here, we will focus on the connection between bond strength and the potential energy barriers opposing viscous flow. The starting point for this discussion is the expression derived by Adam and Gibbs (1965),

$$B_e/S^{conf}(T_g) = z^*(T_g)\Delta\mu/k, \tag{4.12}$$

where T_g is the glass transition temperature, z^* is the size of the smallest rearranging units in the liquid at the glass transition temperature, and $\Delta\mu$ is the Gibbs free energy barrier opposing configurational rearrangements.

From the rheological data available for simple binary alkali silicate melts, Toplis (1998) observed that $B_e/S^{conf}(T_g)$ decreases rapidly with increasing alkali content and reaches a constant value for melts with ~30 mol% or more Na_2O (Fig. 4.22). He suggested, therefore, that a unique $B_e/S^{conf}(T_g)$-value may be assigned to individual metal oxides. His $B_e/S^{conf}(T_g)$-values for different alkali metals in alkali tetrasilicate ($M_2Si_4O_9$) melts are shown in Fig. 4.22B. It follows from those data that either the Gibbs free energy barrier, $\Delta\mu$, or the size of the smallest rearranging units, $z^*(T_g)$, are negatively correlated with alkali content for compositions less alkali-rich than about 30 mol% oxide (Fig. 4.22; see also Eq. 4.12). For fixed alkali content, either of these two variables [$\Delta\mu$ and $z^*(T_g)$] is positively correlated with the ionic radius of the alkali cation. Most likely, the dominant factor between the two is the energy barrier (Toplis, 1998). The lowering of $\Delta\mu$ is consistent with the observation (Table 4.1) that alkali-oxygen bond strengths are only about 10%–20% of that of Si—O bonds. The relationships between $B_e/S^{conf}(T_g)$ and ionic radius of the alkali metal (Fig. 4.22) may be the result of the larger size of the alkali cation, for which more energy is required to cross the energy barrier.

In a similar study of $NaAlO_2$-SiO_2 glasses and melts, Toplis et al. (1997) found that $B_e/S^{conf}(T_g)$ is negatively correlated with Al/(Al+Si). Therefore, in analogy with the analysis of the variations of $B_e/S^{conf}(T_g)$ in alkali silicate melts, one concludes that the height of the energy barrier, $\Delta\mu$, is lowered as the system becomes more aluminous. This effect is reasonable given the premise that, with Si and Al in fourfold coordination, the bond strength of the Al—O bond is less than that of the Si—O bond (Table 4.1). Thus, the energy barrier associated with cooperative motion during viscous flow will also be lowered.

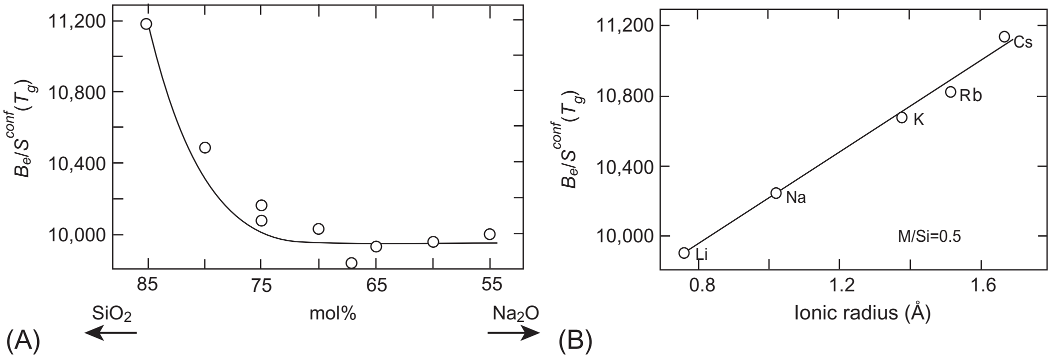

FIG. 4.22 (A) Relationship between $B_e/S^{conf}(T_g)$ and composition in the system Na_2O-SiO_2. (B) Relationship of $B_e/S^{conf}(T_g)$ and ionic radius of alkali metal in the systems Li_2O-SiO_2, Na_2O-SiO_2, K_2O-SiO_2, Rb_2O-SiO_2 (Toplis, 1998). See also text for discussion of the configuration entropy model relevant to these data.

4.7.2 Thermal Properties and Cation Mixing

By mixing two or more components in a silicate glass or melt, many physical properties become nonlinear functions of the mixing ratio (Richet, 1984; Richet and Neuville, 1992; Solvang et al., 2004). Such effects are particularly evident for configurational properties. For example, the configurational entropy of $CaSiO_3$-$MgSiO_3$ melt shows this effect with a very strong entropy maximum at intermediate composition (Neuville and Richet, 1991; see also Fig. 4.23). Analogous variations have been reported for Fe^{2+}-Mg mixtures (Solvang et al., 2004). In this case, a simple mixing model of the silicate endmember compositions mimics the configurational entropy rather well:

$$S^{conf}(T) = \sum X_i S_i^{conf}(T) + S^{mix}, \tag{4.13}$$

where $S^{conf}(T)$ is the configurational entropy at temperature, T, X_i, and S_i^{conf} are the mol fraction and configurational entropy of the endmembers, and S^{mix} is the entropy of mixing, which for ideal mixing simply is:

$$S^{mix} = -nR\sum X_i \ln X_i, \tag{4.14}$$

The solid line in Fig. 4.23 is the result of fitting to Eqs. (4.13), (4.14).

As calculated from Eqs. (4.13), (4.14), the solid line in Fig. 4.23 describes the data rather well because the structures of the Ca- and Mg-metasilicate endmembers are quite similar. It is likely, however, the greater the structural difference between the endmembers of a mixture, the greater will be the configurational entropy and heat capacity. This feature can be seen, for example, in mixed feldspar composition glasses and melts. For example, whereas $NaAlSi_3O_8$-$KAlSi_3O_8$ melts mix nearly ideally (Navrotsky et al., 1985; Fraser and Bottinga, 1985), melts on

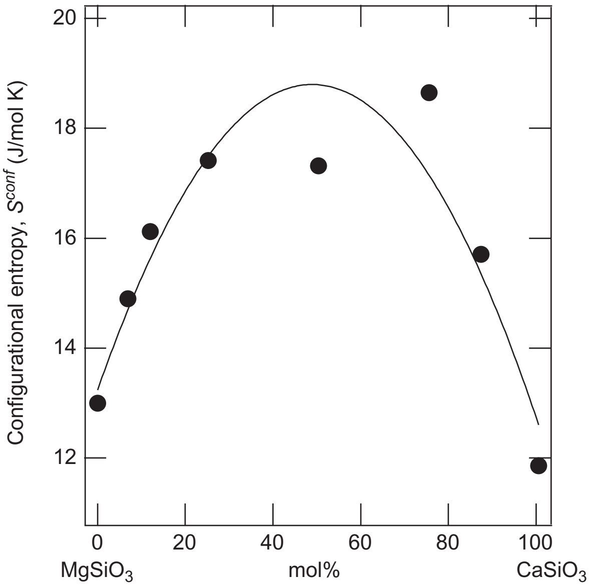

FIG. 4.23 Configurational entropy, S^{conf}, of melts across the $CaSiO_3$-$MgSiO_3$ join at 1100 K (Neuville and Richet, 1991).

the join $NaAlSi_3O_8$-$CaAl_2Si_2O_8$ show significant deviations from ideal mixing. This difference likely reflects the significantly different structure of $CaAl_2Si_2O_8$ melts where a Ca^{2+} charge-balances two Al^{3+} cations, compared with $KAlSi_3O_8$ where Na^+ and K^+ occupy similar structural positions.

References

Adam, G., Gibbs, J.H., 1965. On the temperature dependence of cooperative relation properties in glass-forming liquids. J. Chem. Phys. 43, 139–146.

Alberto, H.V., Pinto da Cunha, J.L., Mysen, B.O., Gil, J.M., de Campos, N.A., 1996. Analysis of Mossbauer spectra of silicate glasses using a two-dimensional Gaussian distribution of hyperfine parameters. J. Non-Cryst. Solids 194, 48–57.

Alderman, O.L.G., Skinner, L.B., Benmore, C.J., Tamalonis, A., Weber, J.K.R., 2014. Structure of molten titanium dioxide. Phys. Rev. B. 90.

Angel, R.J., 1988. High-pressure structure of anorthite. Am. Mineral. 73, 1114–1119.

Babcock, C.L., 1968. Substructures in silicate glasses. J. Am. Ceram. Soc. 51, 163–169.

Baker, D.R., 1990. Chemical interdiffusion in dacite and rhyolite: anhydrous measurements at 1 atm and 10 kbar, application of transition theory, and diffusion in zoned magma chambers. Contrib. Mineral. Petrol. 104, 407–423.

Binsted, N., Greaves, G.N., Henderson, C.M.B., 1985. An EXAFS study of glassy and crystalline phases of compositions $CaAl_2Si_2O_8$ (anorthite) and $CaMgSi_2O_6$ (diopside). Contrib. Mineral. Petrol. 89, 103–109.

Bockris, J.O.'.M., Reddy, A.K.N., 1970. Modern Electrochemistry. Plenum Press, New York.

Bockris, J., Mackenzie, J.O.'.M., Kitchner, J.A., 1955. Viscous flow in silica and binary liquid silicates. Trans. Faraday Soc. 51, 1734–1748.

Bockris, J.O.M., Tomlinson, J.W., White, J.L., 1956. The structure of liquid silicates. Trans. Faraday Soc. 52, 299–311.

Bottinga, Y., Richet, P., 1978. Thermodynamics of liquid silicates, a preliminary report. Earth Planet. Sci. Lett. 40, 382–400.

Brawer, S.A., White, W.B., 1975. Raman spectroscopic investigation of the structure of silicate glasses. I. The binary silicate glasses. J. Chem. Phys. 63, 2421–2432.

Brown, G.E., Gibbs, G.V., Ribbe, P.H., 1969. The nature and variation in length of the Si-O and Al-O bonds in framework silicates. Am. Mineral. 54, 1044–1061.

Buckermann, W.-A., Muller-Warmuth, W., Frischat, G.H., 1992. A further 29Si MAS NMR study on binary alkali silicate glasses. Glasstechn. Ber. 65, 18–21.

Burnham, C.W., 1975. Thermodynamics of melting in experimental silicate-volatile systems. Geochim. Cosmochim. Acta 39, 1077–1084.

Cody, B.O., Mysen, B.O., Saghi-Szabo, G., Tossell, J.A., 2001. Silicate-phosphate interaction in silicate glasses and melts. I. A multinuclear (^{27}Al, ^{29}Si, ^{31}P) MAS NMR and ab initio chemical shielding (31P) study of phosphorus speciation in silicate glasses. Geochim. Cosmochim. Acta 65, 2395–2411.

Cormack, A.N., Du, J., 2001. Molecular dynamics simulations of soda-lime-silicate glasses. J. Non-Cryst. Solids 293, 283–289.

Cormier, L., Neuville, D.R., 2004. Ca and Na environments in Na_2O-CaO-Al_2O_3-SiO_2 glasses: influence of cation mixing and cation-network interactions. Chem. Geol. 213, 103–113.

Cormier, L., Calas, G., Gaskell, P.H., 2001. Cationic environment in silicate glasses studied by neutron diffraction with isotopic substitution. Chem. Geol. 174, 349–363.

Cormier, L., Ghaleb, D., Neuville, D.R., Delaye, J.-M., Calas, G., 2003. Chemical dependence of network topology of calcium aluminosilicate glasses: a computer simulation study. J. Non-Cryst. Solids 332, 255–270.

Dingwell, D.B., 1986. Viscosity-temperature relationships in the system $Na_2Si_2O_5$-$Na_4Al_2O_5$. Geochim. Cosmochim. Acta 50, 1261–1265.

Dingwell, D.B., Virgo, D., 1988. Viscosities of melts in the Na_2O-FeO-Fe_2O_3-SiO_2 systems and factors controlling relative viscosities in fully polymerized melts. Geochim. Cosmochim. Acta 52, 395–404.

Donnay, G., 1969. Further use of the Pauling-bond concept. In: Carnegie Instn. Washington Year Book. vol. 68, pp. 395–404.

Dupree, R., 1991. MAS NMR as a structural probe of silicate glasses and minerals. Trans. Am. Cryst. Soc. 27, 255–269.

Einstein, A., 1905. Über die von der molekular-kinetischen Theorie der Wärme geforderte Bewegung von in ruhenden Flüssigkeiten suspendierten Teilchen. Ann. Phys. 17, 549–560.

Etchepare, J., 1972. Study by Raman spectroscopy of crystalline and glassy diopside. In: Douglas, R.W., Ellis, E. (Eds.), Amorphous Materials. Wiley-Interscience, New York, pp. 337–346.

Eyring, H., 1935. The activated complex and the absolute rate of chemical reactions. Chem. Rev. 17, 65–77.

Farges, F., 1997. Coordination of Ti^{4+} in silicate glasses: a high-resolution XANES spectroscopy study at the Ti K edge. Am. Mineral. 82, 36–43.

Farges, F., 1999. A Ti K-edge EXAFS study of the medium range environment around Ti in oxide glasses. J. Non-Cryst. Solids 244, 25–33.

Finger, L.W., Virgo, D., 1971. Confirmation of Fe/Mg ordering in Olivines. In: Year Book—Carnegie Institution of Washington.vol. 70. pp. 221–225.

Frantz, J.D., Mysen, B.O., 1995. Raman spectra and structure of BaO-SiO_2, SrO-SiO_2, and CaO-SiO_2 melts to 1600°C. Chem. Geol. 121, 155–176.

Fraser, D.G., Bottinga, Y., 1985. The mixing properties of melts and glasses in the system $NaAlSi_3O_8$-$KAlSi_3O_8$: comparison of experimental data obtained by Knudsen cell mass spectrometry and solution calorimetry. Geochim. Cosmochim. Acta 49, 1377–1381.

Fukui, H., Kanzaki, M., Hiraoka, N., Cai, Y.Q., 2009. Coordination environment of silicon in silica glass up to 74 GPa: an x-ray Raman scattering study at the silicon L-edge. Phys. Rev. B. 78.

Furukawa, T., Fox, K.E., White, W.B., 1981. Raman spectroscopic investigation of the structure of silicate glasses. III. Raman intensities and structural units in sodium silicate glasses. J. Chem. Phys. 153, 3226–3237.

Gambuzzi, E., Pedone, A., Menziani, M.C., Angeli, F., Florina, P., Charpentier, T., 2015. Calcium environment in silicate and aluminosilicate glasses probed by ^{43}Ca MQMAS NMR experiments and MD-GIPAW calculations. Solid State Nucl. Reson. 68–69, 31–36.

Geisinger, K.L., Gibbs, G.V., Navrotsky, A., 1985. A molecular orbital study of bond length and bond angle variations in framework structures. Phys. Chem. Miner. 11, 266–283.

Gibbs, G.V., Meagher, E.P., Newton, M.D., Swanson, D.K., 1981. A comparison of experimental and theoretical bond length and angle variations for minerals and inorganic solids, and molecules. In: O'Keefe, M., Navrotsky, A. (Eds.), Structure and Bonding in Crystals. Academic Press, New York (chapter 9).

Gibbs, G.V., Boisen, M.B., Hill, F.C., Tamada, O., 2000. Search for a connection among bond strength, bond length, and electron-density distributions. In: Aoki, H., Syono, Y., Hemley, R.J. (Eds.), Physics Meets Mineralogy: Condensed-Matter Physics in Geoscinecs. Cambridge University Press, Cambrdige, pp. 83–123.

Giordano, D., Dingwell, D.B., 2003. Viscosity of Etna basalt: implications for Plinian-style eruptions. Bull. Volcanol. 65, 8–14.

Giuli, G., Paris, E., Hess, K.-U., Dingwell, D.B., Cicconi, M.R., Eeckhout, S.G., Fehr, K.T., Valenti, P., 2011. XAS determination of the Fe local environment and oxidation state in phonolite glasses. Am. Mineral. 96, 631–636.

Gordy, W., 1946. A new method for determining electronegativity from other atomic properties. Phys. Rev. 69, 604–607.

Hafner, S.S., Virgo, D., 1970. Temperature-dependent cation distribution in lunar and terrestrial pyroxenes .Proc. 3rd Lunar. Sci. Conf, pp. 2183–2198.

Hazen, R.M., Finger, L.W., 1982. Comparative Crystal Chemistry: Temperature, Pressure, Composition, and the Variation of Crystal Structure. Wiley and Sons, New York.

Henderson, G.S., Fleet, M.E., Bancroft, G.M., 1984. An X-ray scattering study of vitreous $KFeSi_3O_8$ and $NaFeSi_3O_8$ and reinvestigation of vitreous SiO_2 using quasicrystalline modelling. J. Non-Cryst. Solids 68, 333–349.

Henderson, G.S., Liu, X., Fleet, M.E., 2002. A Ti-L-edge x-ray absorption study of Ti-silicate glasses. Phys. Chem. Miner. 29, 32–42.

Holland, D., Mekki, A., Gee, I.A., McConville, C.F., Johnson, J.A., Johnson, C.E., Appleyard, P., Thomas, M., 1999. The structure of sodium iron silicate glass—a multi-technique approach. J. Non-Cryst. Solids 253, 192–202.

Hoppe, U., Walter, G., Barz, A., Stachel, D., Hannon, A.C., 1998. The P-O bond lengths in vitreous P_2O_5 probed by neutron diffraction with high real-space resolution. J. Phys. Condens. Matter 10, 261–270.

Hovis, G.L., Toplis, M.J., Richet, P., 2004. Thermodynamic mixing properties of sodium silicate liquids and implications for liquid-liquid immiscibility. Chem. Geol. 213, 173–186.

Hudon, P., Baker, D.R., 2002. The nature of phase separation in binary oxide melts and glasses. I. Silicate systems. J. Non-Cryst. Solids 303, 299–345.

Ispas, S., Benoit, M., Jund, P., Jullien, R., 2002. Structural properties of glassy and liquid sodium tetrasilicate: comparison between ab initio and classical molecular dynamics simulations. J. Non-Cryst. Solids 307, 946–955.

Jana, D., Walker, D., 1997. The influence of silicate melt composition on distribution of siderophile elements among metal and silicate liquids. Earth Planet. Sci. Lett. 150, 463–472.

Jones, A.R., Winter, R., Greaves, G.N., Smith, I.H., 2001. MAS NMR study of soda-lime-silicate glasses with variable degrees of polymerisation. J. Non-Cryst. Solids 293–295, 87–92.

Kelsey, K.E., Stebbins, J.F., Mosenfelder, J.L., Asimow, P.D., 2009. Simultaneous aluminum, silicon, and sodium coordination changes in 6 GPa sodium aluminosilicate glasses. Am. Mineral. 94, 1205–1215.

Kim, H.-I., Sur, J.C., Lee, S.K., 2016. Effect of iron content on the structure and disorder of iron-bearing sodium silicate glasses: a high-resolution Si-29 and O-17 solid-state NMR study. Geochim. Cosmochim. Acta 173, 160–180.

Kirkpatrick, R.J., 1983. Theory of nucleation in silicate melts. Am. Mineral. 68, 66–78.

Kirkpatrick, R.J., Brow, R.K., 1995. Nuclear magnetic resonance investigation of the structures of phosphate and phosphate containing glasses: a review. Solid State Nucl. Magn. Reson. 5, 3–8.

Kohara, S., Akola, J., Morita, H., Suzuya, K., Weber, J.K.R., Wilding, M.C., Benmore, C.J., 2011. Relationship between topological order and glass forming ability in densely packed enstatite and forsterite composition glasses. Proc. Natl. Acad. Sci. U. S. A. 108, 14780–14785.

Kubicki, J.D., Lasaga, A.C., 1987. Molecular dynamics simulation of Mg_2SiO_4 and $MgSiO_3$ melts: structural and diffusivity changes with pressure. Eos 68, 436.

Kushiro, I., 1975. On the nature of silicate melt and its significance in magma genesis: regularities in the shift of liquidus boundaries involving olivine pyroxene, and silica materials. Am. J. Sci. 275, 411–431.

Lee, S.K., Stebbins, J.F., 1999. The degree of aluminum avoidance in aluminum silicate glasses. Am. Mineral. 84, 937–945.

Lee, S.K., Stebbins, J.F., 2003. Nature of cation mixing and ordering in Na-Ca silicate glasses and melts. J. Phys. Chem. B 107, 3141–3148.

Lee, S.K., Stebbins, J.F., 2006. Disorder and the extent of polymerization in calcium silicate and aluminosilicate glasses: O-17NMR results and quantum chemical molecular orbital calculations. Geochim. Cosmochim. Acta 70, 4275–4286.

Lee, S.K., Stebbins, J.F., Mysen, B.O., Cody, G.D., 2002. The nature of polymerization in silicate glasses and melts: solid state NMR, modeling and quantum chemical calculations. Eos Trans. AGU. 83(47).

Lee, S.K., Cody, G.D., Fei, Y.W., Mysen, B.O., 2006. The effect of Na/Si on the structure of sodium silicate and aluminosilicate glasses quenched from melts at high pressure: a multi-nuclear (Al-27, Na-23, O-17) 1D and 2D solid-state NMR study. Chem. Geol. 229, 162–172.

Levien, L., Prewitt, C.T., Weidner, D.J., 1980. Structure and elastic properties of quartz at high pressure. Am. Mineral. 65, 920–930.

Lewis, G.N., 1916. The atom and the molecule. J. Am. Chem. Soc. 38, 762–785.

Liebau, F., 1981. The influence of cation properties on the conformation of silicate and phosphate anions. In: Structure and Bonding in Crystals. Academic Press, New York, pp. 197–232.

MacKenzie, J.D., 1947. The discrete ion theory of viscous flow in liquid silicates. Trans. Faraday Soc. 53, 1488–1494.

Maekawa, H., Maekawa, T., Kawamura, K., Yokokawa, T., 1991. The structural groups of alkali silicate glasses determined from ^{29}Si MAS-NMR. J. Non-Cryst. Solids 127, 53–64.

Magaritz, M., Hofmann, A.W., 1978. Diffusion of Sr, Ba, and Na in obsidian. Geochim. Cosmochim. Acta 42, 595–605.

Marumo, Y., Okuno, M., 1984. X-ray structural studies of molten silicates: anorthite and albite melts. In: Sunagawa, I. (Ed.), Materials Science in the Earth's Interior. Tokyo, Terra Scientific, pp. 25–38.

Mott, N.F., Gurney, R.W., 1940. Electronic Processes in Ionic Crystals. The Clarendon Press, Oxford.

Mulliken, R.S., 1935. Electronic structure of molecules. XI: electroaffinity, molecular orbitals, and dipole moments. J. Chem. Phys. 2, 782–793.

Murdoch, J.B., Stebbins, J.F., Carmichael, I.S.E., 1985. High-resolution ^{29}Si NMR study of silicate and aluminosilicate glasses: the effect of network-modifying cations. Am. Mineral. 70, 332–343.

Mysen, B.O., 1987. Magmatic silicate melts: relations between bulk composition, structure and properties. In: Mysen, B.O. (Ed.), Magmatic Processes: Physicochemical Principles. Elsevier, University Park, PA, pp. 375–400.

Mysen, B.O., 1995. Experimental, in-situ, high-temperature studies of properties and structure of silicate melts relevant to magmatic temperatures. Eur. J. Mineral. 7, 745–766.

Mysen, B.O., 2007. Partitioning of calcium, magnesium, and transition metals between olivine and melt governed by the structure of the silicate melt at ambient pressure. Am. Mineral. 92, 844–862.

Mysen, B.O., Frantz, J.D., 1994. Silicate melts at magmatic temperatures: in-situ structure determination to 1651°C and effect of temperature and bulk composition on the mixing behavior of structural units. Contrib. Mineral. Petrol. 117, 1–14.

Mysen, B.O., Shang, J., 2005. Evidence from olivine/melt element partitioning that nonbridging oxygen in silicate melts are not equivalent. Geochim. Cosmochim. Acta 69, 2861–2876.

Mysen, B.O., Virgo, D., Seifert, F.A., 1984. Redox equilibria of iron in alkaline earth silicate melts: relationships between melt structure, oxygen fugacity, temperature and properties of iron-bearing silicate liquids. Am. Mineral. 69, 834–848.

Navrotsky, A., Hon, R., Weill, D.F., Henry, D.J., 1982. Thermochemistry of glasses and liquids in the system $CaMgSi_2O_6$-$CaAl_2SiO_6$-$NaAlSi_3O_8$, SiO_2-$CaAl_2Si_2O_8$-$NaAlSi_3O_8$ and SiO_2-Al_2O_3-CaO-Na_2O. Geochim. Cosmochim. Acta 44, 1409–1433.

Navrotsky, A., Geisinger, K.L., McMillan, P., Gibbs, G.V., 1985. The tetrahedral framework in glasses and melts—influences from molecular orbital calculations and implications for structure, thermodynamics, and physical properties. Phys. Chem. Miner. 11, 284–298.

Nekvasil, H., Burnham, C.W., 1987. The calculated individual effects of pressure and water content on phase equilibria in the granite system. In: Mysen, B.O. (Ed.), Magmatic Processes: Physicochemical Principles. Geochemical Society of America, University Park, PA, pp. 433–446.

Nelson, C., Tallant, D.R., 1984. Raman studies of sodium silicate glasses with low phosphate contents. Phys. Chem. Glasses 25, 31–39.

Nelson, C., Tallant, D.R., 1986. Raman studies of sodium phosphates with low silica contents. Phys. Chem. Glasses 26, 119–122.

Nernst, W., 1888. Zur Kinetik der in lösung befindtlicher Körper. Erste Abhandlung, Theorie der Diffusion. Z. Phys. Chem. 2, 613–637.

Neuville, D.R., Richet, P., 1991. Viscosity and mixing in (Ca,Mg) molten garnets and pyroxenes. Geochim. Cosmochim. Acta 55, 1011–1019.

Okamura, F.P., Ghose, S., Ohashi, H., 1974. Structure and crystal chemistry of calcium Tschermak's molecule, $CaAlAlSiO_6$. Am. Mineral. 59, 549–557.

Pauling, L., 1929. The principles determining the structure of complex ionic crystals. J. Am. Chem. Soc. 51, 1010–1026.

Pauling, L., 1960. The Nature of the Chemical Bond. Cornell University Press, Cornell.

Phillips, J.C., 1970. Ionicity of the chemical bond in crystals. Rev. Mod. Phys. 42, 317.

Plotnichenko, V.G., Sokolov, V.O., Koltashev, V.V., Dianov, E.M., 2002. On the structure of phosphosilicate glasses. J. Non-Cryst. Solids 306, 209–226.

Polyakov, V.B., Ariskin, A.A., Shil'dt, A.V., 2010. Analysis of disproportionation of Q(n) structons in the simulation of the structure of melts in the Na_2O-SiO_2 system. Glas. Phys. Chem. 36, 579–588.

Poole, P.H., McMillan, P.F., Wolf, G.H., 1995. Computer simulations of silicate melts. In: Stebbins, J.F., McMillan, P.F., Dingwell, D.B. (Eds.), Structure, Dynamics and Properties of Silicate Melts. Mineralogical Society of America, Washington, DC, pp. 563–616.

Redhammer, G.J., 1998. Mossbauer spectroscopy and Rietveld refinement on synthetic ferri-Tschermak's molecule $CaFe^{3+}(Fe^{3+},Si)O_6$ substituted diopside. Eur. J. Mineral. 10, 439–452.

Richet, P., 1984. Viscosity and configurational entropy of silicate melts. Geochim. Cosmochim. Acta 48, 471–483.

Richet, P., Neuville, D.R., 1992. Thermodynamics of silicate melts; configurational properties. In: Saxena, S.K. (Ed.), Thermodynamic Data; Systematics and Estimation. Springer, New York, NY, United States, pp. 132–161.

Riebling, E.F., 1964. Structure of magnesium aluminosilicate liquids at 1700°C. Can. J. Chem. 42, 2811–2821.

Riebling, E.F., 1966. Structure of molten sodium aluminosilicate liquids containing at least 50 mol% SiO_2 at 1500°C. J. Chem. Phys. 44, 2857–2865.

Ross, N.L., Meagher, E.P., 1984. A molecular orbital study of $H_6Si_2O_7$ under simulated compression. Am. Mineral. 69, 1145–1149.

Roy, B.N., Navrotsky, A., 1984. Thermochemistry of charge-coupled substitutions in silicate glasses: The systems $M^{n+}_{1n}AlO_2$ - SiO_2 (M = Li, Na, K, Rb, Cs, Mg, Ca, Sr, Ba, Pb). J. Am. Ceram. Soc. 67, 606–610.

Ryerson, F.J., 1985. Oxide solution mechanisms in silicate melts: systematic variations in the activity coefficient of SiO_2. Geochim. Cosmochim. Acta 49, 637–651.

Sanderson, R.T., 1960. Chemical Periodicity. Reinhold, New York.

Sanloup, C., Drewitt, J.W.E., Crépisson, C., Kono, Y., Park, C., McCammon, C., Hennet, L., Brassamin, S., Bytchkov, A., 2013. Structure and density of molten fayalite at high pressure. Geochim. Cosmochim. Acta 118, 118–128.

Sato, T., Funamori, N., 2010. High-pressure structural transformation of SiO_2 glass up to 100 GPa. Phys. Rev. B 82, 194108.

Schneider, J., Mastelaro, V.R., Zanotto, E.D., Shakhmatkin, B.A., Vedischeva, N.M., Wright, A.C., Panepucci, H., 2003. Qn distribution in stoichiometric silicate glasses: thermodynamic calculations and ^{29}Si high resolution NMR measurements. J. Non-Cryst. Solids 325, 164–178.

Schramm, C.M., DeJong, B.H.W.S., Parziale, V.F., 1984. ^{29}Si magic angle spinning NMR study of local silicon environments in-amorphous and crystalline lithium silicates. J. Am. Chem. Soc. 106, 4396–4402.

Seifert, F.A., Mysen, B.O., Virgo, D., 1982. Three-dimensional network structure in the systems SiO_2-$NaAlO_2$, SiO_2-$CaAl_2O_4$ and SiO_2-$MgAl_2O_4$. Am. Mineral. 67, 696–711.

Seifert, F.A., Mysen, B.O., Virgo, D., 1983. Raman study of densified vitreous silica. Phys. Chem. Glasses 24, 141–145.

Shibata, N., Horigudhi, M., Edahiro, T., 1981. Raman spectra of binary high-silica glasses and fibers containing GeO_2, P_2O_5 and B_2O_3. J. Non-Cryst. Solids 45, 115–126.

Shimizu, N., Kushiro, I., 1984. Diffusivity of oxygen in jadeite and diopside melts at high pressures. Geochim. Cosmochim. Acta 48, 1295–1303.

Shimizu, N., Kushiro, I., 1991. The mobility of Mg, Ca, and Si in diopside-jadeite liquids at high pressures. In: Perchuk, L.L., Kushiro, I. (Eds.), Physical Chemistry of Magmas. Springer, New York, NY, United States, pp. 192–212.

Smart, R.M., Glasser, F.P., 1978. Silicate anion constitution of lead silicate glasses and crystals. Phys. Chem. Glasses 19, 95–102.

Smyth, J.R., Bish, D.L., 1988. Crystal Structures and Cation Sites of the Rock-Forming Minerals. Allen & Unwin, Boston.

Solvang, M., Yue, Y.Z., Jensen, S.L., 2004. The effects of Mg-Ca and Fe-Mg substitution on rheological and thermodynamic properties of aluminosilicate melts. J. Non-Cryst. Solids 345, 782–786.

Soules, T.F., 1979. A molecular dynamics calculation of the structure of sodium silicate glasses. J. Chem. Phys. 71, 4570–4578.

Stebbins, J.F., 1987. Identification of multiple structural species in silicate glasses by ^{29}Si NMR. Nature 330, 465–467.

Tait, K.T., Sokolova, E.V., Hawthorne, F.C., Khomyakov, A.P., 2003. The crystal chemistry of nepheline sample 3: from Monte Somma, Italy. Can. Mineral. 41, 61–70.

Tangney, P., Scandolo, S., 2002. An ab initio parametrized interatomic force field for silica. J. Chem. Phys. 117, 8898–8904.

Tangney, P., Scandolo, S., 2003. A many-body interatomic potential for ionic systems: application to MgO. J. Chem. Phys. 119, 9673–9685.

Taylor, M., Brown, G.E., 1979. Structure of mineral glasses. II. The SiO_2-$NaAlSiO_4$ join. Geochim. Cosmochim. Acta 43, 1467–1475.

Tischer, R.E., 1969. Heat of annealing of simple alkali silicate glasses. J. Am. Ceram. Soc. 52, 499–503.

Toplis, M.J., 1998. Energy barriers associated with viscous flow and the prediction of glass transition temperatures of molten silicates. Am. Mineral. 83, 480–490.

Toplis, M.J., Corgne, A., 2002. An experimental study of element partitioning between magnetite, clinopyroxene and iron-bearing silicate liquids with particular emphasis on vanadium. Contrib. Mineral. Petrol. 144, 22–37.

Toplis, M.J., Dingwell, D.B., 2004. Shear viscosities of CaO-Al_2O_3-SiO_2, and MgO-Al_2O_3-SiO_2 liquids: implications for the structural role of aluminium and the degree of polymerisation of synthetic and natural aluminosilicate melts. Geochim. Cosmochim. Acta 68, 5169–5188.

Toplis, M.J., Schaller, T., 1998. A ^{31}P MAS NMR study of glasses in the system xNa_2O-$(1-x)Al_2O_3$-$2SiO_2$-yP_2O_5. J. Non-Cryst. Solids 224, 57–68.

Toplis, M.J., Dingwell, D.B., Hess, K.-U., Lenci, T., 1997. Viscosity, fragility, and configuration entropy of melts along the join SiO_2-$NaAlO_2$. Am. Mineral. 82, 979–990.

Tossell, J.A., 1993. A theoretical study of the molecular basis of the Al avoidance rule and of the spectra; characteristics of Al-O-Al linkages. Am. Mineral. 78, 911–920.

Uchino, T., Yoko, T., 1998. Structure and vibrational properties of sodium disilicate glass from ab initio molecular orbital calculations. J. Phys. Chem. B 102, 8372–8378.

Virgo, D., Mysen, B.O., Kushiro, I., 1980. Anionic constitution of silicate melts quenched at 1 atm from Raman spectroscopy: implications for the structure of igneous melts. Science 208, 1371–1373.

Vuckevitch, M.R., 1972. A new interpretation of the anomalous properties of vitreous silica. J. Non-Cryst. Solids 11, 25–63.

Walter, M.J., Thibault, Y., 1995. Partitioning of tungsten and molybdenum between metallic liquid and silicate melt. Science 270, 1186–1189.

Warren, B.W., Pincus, A.G., 1940. Atomic considerations of immiscibility in glass systems. J. Am. Ceram. Soc. 23, 301–304.

Watson, E.B., 1979. Calcium diffusion in a simple silicate melt to 30 kbar. Geochim. Cosmochim. Acta 43, 313–323.

Watson, E.B., 1982. Basalt contamination by continental crust: some experiments and models. Contrib. Mineral. Petrol. 80, 73–87.

Watson, E.B., Baker, D.R., 1991. Chemical diffusion in magmas: an overview of experimental results and geochemical implications. In: Perchuk, L.L., Kushiro, I. (Eds.), Crystal Chemistry of Magmas. Springer, New York, pp. 120–151.

Webb, S.L., 2011. Configurational heat capacity and viscosity of (Mg, Ca, Sr, Ba)O-Al_2O_3-SiO_2 melts. Eur. J. Mineral. 23, 487–497.

Whittaker, E.J.W., Muntus, R., 1970. Ionic radii for use in geochemistry. Geochim. Cosmochim. Acta 34, 945–957.

Xue, X., Stebbins, J.F., 1993. 23 Na NMR chemical shifts and local Na coordination environments in silicate crystals, melts and glasses. Phys. Chem. Miner. 20, 297–307.

Zachariassen, W., 1932. The atomic arrangement in glass. J. Am. Chem. Soc. 54, 3841–3851.

CHAPTER

5

Silica

OUTLINE

5.1 INTRODUCTORY COMMENTS

Silica is the most common oxide on earth with a mean abundance of about 37 wt% (Allègre et al., 1995). The silica content increases from 40 to 50 wt% for fresh magma, typically of basaltic composition, forming at depth to about 75 wt% in the earth's crust where magmatic differentiation ends (Yoder, 1976). During cooling of such melts, quartz precipitates when silica saturation is reached, at typical contents of about 65 wt% under low-pressure conditions (Bowen, 1928). It is this silica saturation (together with the high stability of quartz at the earth's surface) that has made the whole glass industry possible, as natural silicates would have required much too high temperatures to be melted homogeneously and not have yielded transparent materials. Hence, quartz sand has been the only source of silica for man-made glasses, except for some recent products such as rock wool, for which minerals or basalt can be used as raw materials.

https://doi.org/10.1016/B978-0-444-63708-6.00005-3

Except for its simple chemical formula, SiO_2, complex properties and structure are its hallmarks. To start with, the rigid SiO_4 tetrahedra that form at low pressure can assemble in a great many ways to build an open three-dimensional network. About 20 crystalline phases of SiO_2 have been identified (e.g., Sosman, 1965) whose mutual relationships are often not clearly understood (see Heaney, 1994). Moreover, amorphous SiO_2 tends to retain a memory of its path of formation because of its high viscosity and low diffusivity, which adds complexity to the problem. Fortunately, only a few SiO_2 variants are relevant to investigations of the structure and properties of SiO_2 glass and melt.

At low pressure, the liquidus phases observed at progressively higher temperatures are β-quartz, tridymite, and β-cristobalite (Fig. 5.1). Tridymite has a very small stability field and its actual existence as an SiO_2 polymorph is still uncertain because its structure might need stabilization by trace amounts of other metal oxides (see Heaney, 1994). When pressure increases, β-quartz becomes the high-temperature liquidus phase. Coesite is then stable between about 4 and 10 GPa (i.e., 40 and 100 kbar), before being succeeded by the denser stishovite and post-stishovite phases at even higher pressures (Jackson, 1976; Zhang et al., 1993; Yi and Lee, 2012).

Numerous attempts have been made to determine which crystalline silica polymorph is the most closely related to amorphous silica. In particular, anomalies in properties observed near the temperatures of the α-β transitions undergone by the low-pressure SiO_2 polymorphs have long been taken as evidence for such similarities (Vuckevitch, 1972; Goodman, 1987; Polian et al., 2002). The sometime doubtful reality of these anomalies notwithstanding, such claims are difficult to sustain because the properties of amorphous silica can depend markedly on the impurity content of the sample (see Fanderlik, 1990).

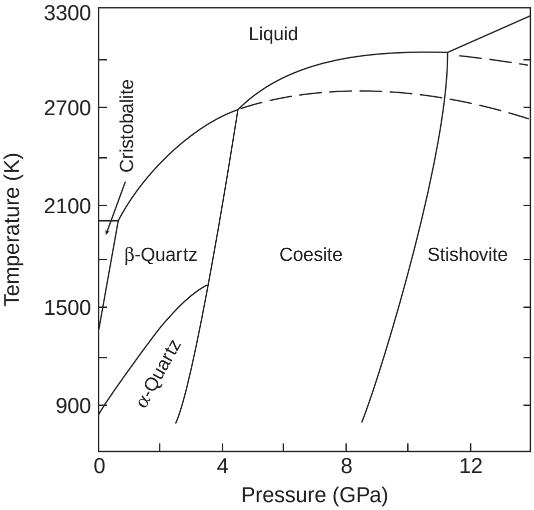

FIG. 5.1 High-temperature and high-pressure phase relations of SiO_2 from calculations of Swamy et al. (1994), which reproduce the melting results of Jackson (1976) and Zhang et al. (1993). Tridymite is not shown (see text). The dashed curves picture the metastable extensions of the melting curves of quartz and coesite.

5.2 AN OUTSTANDING OXIDE

The unusual properties of pure silica have long made melting of quartz quite difficult (see Section 5.3). As a matter of fact, the first measurements made by Volarovich and Leontieva (1936) showed that SiO_2 is the most viscous liquid known (Urbain et al., 1982) and, consequently, has the highest standard glass transition temperature (1200°C; Richet et al., 1982; Cornet et al., 2017). In fact, the viscosity of SiO_2 glass and supercooled liquid is closer to Ahrrenian than any other silicate melt. In this sense, SiO_2 liquid is an archetypical strong liquid in the terminology of Angell (1985).

It follows that investigation of molten and glassy SiO_2 is technically challenging. The intrinsic difficulties caused by high-temperature experiments on a highly viscous melt are compounded by strong reactivity with contaminants present within the experimental setup. Mazurin et al. (1975), for instance, noted that the kinetics of silica crystallization "depend more on the appropriate properties of the furnace refractories and heater material than on the properties of the investigated glass." Amorphous SiO_2 is, in fact, especially sensitive to impurity content as a very small fraction of nonbridging oxygens or other defects can have disproportionate effects on silica properties through breaking up of a fully polymerized structure. Such effects, due to impurity content and method of fabrication of amorphous SiO_2, have been reviewed by Bruckner (1970) and Fanderlik (1990).

5.2.1 A Short Classification

Given the sensitivity of silica glass and melt properties to impurities and the fact that commercially available SiO_2 may contain impurities that depend on the production method, it is useful to classify SiO_2 glass into different types. Depending on synthesis procedure, the most common types of SiO_2 glass can be grouped into four categories (Hetherington and Jack, 1962; Bruckner, 1970, Brückner, 1971). The main distinction is made on the basis of water content (usually expressed as OH) because of markedly different effects of water on optical absorption spectra compared with metal oxides, and because the influence of water on SiO_2 properties is often stronger than that of metal oxides at the same low concentration.

Type I glass is prepared through electric melting of very pure natural quartz under vacuum or an inert atmosphere. The main impurities are aluminum (typically less than 50 ppm) and alkali metals (a few ppm). The OH content is less than 1 ppm. As fusion is generally performed in graphite crucibles, the reducing atmosphere causes silica to be slightly deficient in oxygen with an actual formula of SiO_{2-x}, where x ranges from 10^{-4} to 10^{-5} (Bell et al., 1962). Effects of such a nonstoichiometry on silica properties have been described by Leko and Meshcheryakova (1975).

In type II, the starting material is also natural quartz, but melting is done in a flame as originally described by Gaudin (1839). The main difference between type I and II is an OH content of a few hundred ppm in Type II, as compared with the less than 1 ppm in Type I glass.

The aluminum, alkali metals, and other element contents of type I and II are too high for some applications. These concentrations can be limited to less than 0.1 ppm in type III glasses, which are prepared by vapor-phase hydrolysis or oxidation of $SiCl_4$. The OH content of type III silica glass is still higher than for type II with values of the order of 1000 ppm, whereas the

Cl concentration is about 100 ppm. To limit water intake in type IV glass, $SiCl_4$ is oxidized in a plasma flame free of water vapor. The OH content is less than 1 ppm, but the Cl concentration reaches 200 ppm.

5.2.2 Phase Transitions: Melting and Amorphization

At room pressure, Greig (1927) reported that cristobalite melts at 1713°C on the Geophysical Laboratory temperature scale. This value, which has been confirmed by Wagstaff (1969), translates to 1726°C on later International Temperature Scales (see Richet et al., 1982). Metastable melting of quartz at temperatures below 1726°C can also be observed because of the sluggish kinetics of the quartz-cristobalite transition (MacKenzie, 1960; Ainslie et al., 1961). The metastable room-pressure melting temperature of quartz is about 1400°C (Bourova and Richet, 1998) based on Gibbs-free energy data (Richet et al., 1982) and extrapolation of the high-pressure melting curve to ambient pressure (Jackson, 1976; Zhang et al., 1993).

Cristobalite and quartz are unusual compounds in that both can be superheated significantly. Superheating has been observed over 40°C and 300°C intervals for periods of a few tens of minutes for polycrystalline cristobalite and single-crystal quartz, respectively (Ainslie et al., 1961). Albite ($NaAlSi_3O_8$), which also has a fully polymerized structure, is the only other silicate known to superheat (Dietz et al., 1970). This mineral has been observed 40°C above its melting point of 1118°C, at which the viscosity of the liquid is $10^{6.9}$ Pas (Urbain et al., 1982). At the temperatures of fusion of cristobalite and quartz, the viscosity of Type I molten SiO_2 is $10^{6.2}$ and $10^{8.8}$ Pas, respectively (Urbain et al., 1982). It is suggested that the superheating is related to unusually high melt viscosity at the melting temperatures of these compounds.

The connection between high melt viscosity and glass-forming ability has already been described in Chapter 3, Section 3.4. Viscosity is not, however, the only parameter controlling fusion and crystallization (Roskosz et al., 2005). Whereas $NaAlSi_3O_8$ melt has been kept for 5 years at 100°C below its melting temperature without showing any trace of crystallization (Schairer and Bowen, 1956), cristobalite crystallizes within minutes above 1350°C. Less extensive configurational differences between cristobalite crystals and its melt than between albite ($NaAlSi_3O_8$) and its melt on their liquidii may account for faster crystallization of cristobalite. As has long been known by glassmakers, the kinetics of this process are strongly enhanced by impurities such as water or even finger marks on glass pieces (Dietzel and Wickert, 1956; Wagstaff and Richards, 1966; Mazurin et al., 1975).

Quartz does not form from SiO_2 melt at room pressure. The low temperature of 830°C of the quartz-cristobalite transition (Richet et al., 1982) should indeed prevent quartz from crystallizing from its melt at 1726°C. This lack of quartz crystallization together with the easy crystallization of cristobalite point to greater structural similarity of SiO_2 melt with the structure of cristobalite than with quartz. The same conclusion can be drawn from the fact that transformation of quartz to cristobalite takes place via an intermediate melting stage (MacKenzie, 1960). The reverse should hold true within the stability field of quartz where cristobalite does not form because nucleation and growth of quartz depend on the same factors as described previously for cristobalite in its own stability field (Fratello et al., 1980).

For the high-pressure crystalline SiO_2 polymorphs, coesite and stishovite (Akaogi and Navrotsky, 1984; Ono et al., 2017), their melting temperatures increase with pressure (Fig. 5.1). Both forms can be quenched easily to ambient conditions from their pressure-temperature field of stability. When heated at room pressure, these metastable phases do not transform directly to quartz, the stable polymorph, but first to an amorphous phase (Xu et al., 2005; Huan et al., 2006). Amorphization can begin below 930°C for coesite (Dachille et al., 1963; Gong et al., 1996) and between 300°C and 650°C for stishovite, at temperatures that increase with the quality of the sample (Skinner and Fahey, 1963; Xue et al., 1993; Grimsditch et al., 1994). Thermochemical considerations indicate that coesite should melt near 612°C, i.e., well below the standard glass transition of SiO_2 (Bourova et al., 2000), whereas stishovite is unstable at any temperature with respect to amorphous SiO_2 (Richet, 1988). Clearly, these polymorphs amorphize instead of transforming to quartz because thermal energy at such temperatures is insufficient to overcome the potential energy barriers opposing the cooperative rearrangements needed for a crystal-crystal phase transition.

Alternatively, amorphization can be induced by compression at room temperature. This was first observed for quartz and coesite compressed at a few tens of GPa (Hemley et al., 1988) and subsequently for a number of other silica polymorphs and other silicates (Richet and Gillet, 1997; Cernok et al., 2014; Liang et al., 2015). Again, the basic mechanism is that the kinetics of reconstructive structural transitions are much too slow for Si to change from the fourfold Si coordination of quartz and coesite to the sixfold coordination of stishovite. Instead, progressive amorphization proceeds to phases in which some remnants of crystalline order can still be found. Because any pressure-induced transformation necessarily involves a volume decrease, the amorphous phase is denser than the crystal at the pressure of the experiment. If it is assumed that there is continuity between the volume of the melt, at high temperature, and that of the amorphous phase, it follows that at some high pressure the volume of melting of both quartz and coesite becomes negative and that the melting curve passes through a maximum with increasing pressure (Fig. 5.1).

5.3 PHYSICAL AND THERMAL PROPERTIES

The physical properties of molten silica remain debated in spite of their basic importance. There is, however, more information than often is realized. Here, we will address thermal and volume properties as well as transport properties such as viscosity and diffusion.

This discussion is, in particular, relevant to polyamorphism, a topic that is arousing much theoretical interest (Poole et al., 1997; Saika-Voivod et al., 2000, 2004; Huang et al., 2004; Sonneville et al., 2013; Clark et al., 2014). For molten sulfur and other liquids, polyamorphism is revealed by a first-order liquid-liquid transition. It has not been observed for molten silicates, possibly because it might occur in the supercooled liquid (Clark et al., 2014). If so, the critical point at which the liquid-liquid univariant equilibrium curve ends would be located below the liquidus. Results of computer simulations do suggest that metastable polyamorphism exist in silica (e.g., Roberts and Debenedetti, 1996; Hemmati et al., 2001). Anomalous variations of the heat capacity, thermal expansion coefficient, and

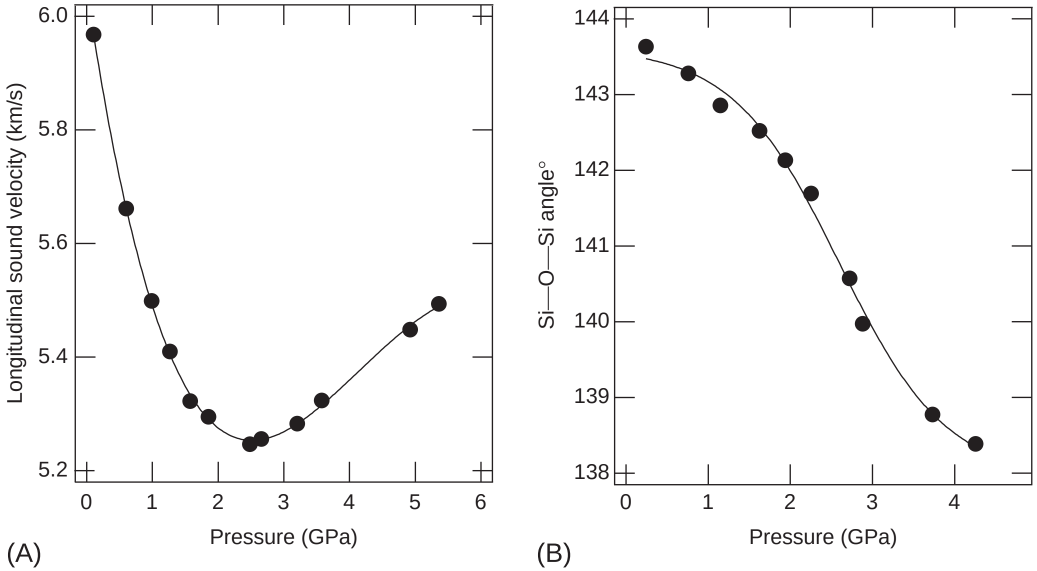

FIG. 5.2 Effects of pressure on silica glass. (A) Longitudinal sound velocity as a function of pressure. (B) Intertetrahedral angle, Si—O—Si, as a function of pressure. *(Data from Sonneville et al., 2013.)*

compressibility of amorphous SiO_2 could be macroscopic evidence of such a transformation (Poole et al., 1997; Sato and Funamori, 2008; Sonneville et al., 2013; Clark et al., 2014; see also Fig. 5.2). An example of this situation is provided by water, which exhibits a sharp transition between two different amorphous phases near 70 K (Mishima et al., 1984; Mishima and Stanley, 1998). Structural analogies between water and silica has long been pointed out (e.g., Angell and Kanno, 1976; Dracinsky et al., 2011).

In this section, attention will be paid to features suggestive of polyamorphism. It should be kept in mind, however, that an almost infinite diversity of quenched silica glasses can be prepared through different temperature and temperature paths, impurity content, and stress conditions. In other words, any difference in a given physical property between different silica glasses, as observed, for instance, in Brillouin scattering experiments (Grimsditch, 1984) and density (Shelby, 2004), does not constitute per se evidence for polyamorphism.

5.3.1 Thermodynamics of Melting

Low values for the enthalpy and entropy of fusion (ΔH_f, ΔS_f) of quartz and cristobalite (Table 5.1) are some unusual features of SiO_2. An enthalpy change of fusion of less than 10 kJ/mol (Richet et al., 1982) confirms that bond breaking is not the essential feature of melting of quartz and cristobalite, because bond breakage during melting or crystallization involves hundreds of kJ/mol and large entropy of fusion similar to what is commonly seen for binary metal oxide silicates and aluminosilicates (Fig. 5.3; see also Chapters 6 and 8, Sections 6.3.1 and 8.3.1). A large increase of the entropy of fusion results from either breakup of the silica network by a network modifier or substitution of Al^{3+} for Si^{4+}. For example, the

TABLE 5.1 Thermodynamic Properties at the Melting Points of β-Cristobalite and β-Quartz (Richet and Bottinga, 1986; Bourova and Richet, 1998)

Property	β-Cristobalite	β-Quartz
T_f(K)	1999	1673
V_l(cm^3/mol)	27.3	27.3
V_c(cm^3/mol)	27.4	23.5
ΔV_f(cm^3/mol)	−0.1	3.8
ΔS_f(J/mol K)	4.61	6.06
ΔH_f(kJ/mol)	8.92	9.10
dT_f/dP(K/GPa)	−21.7	625

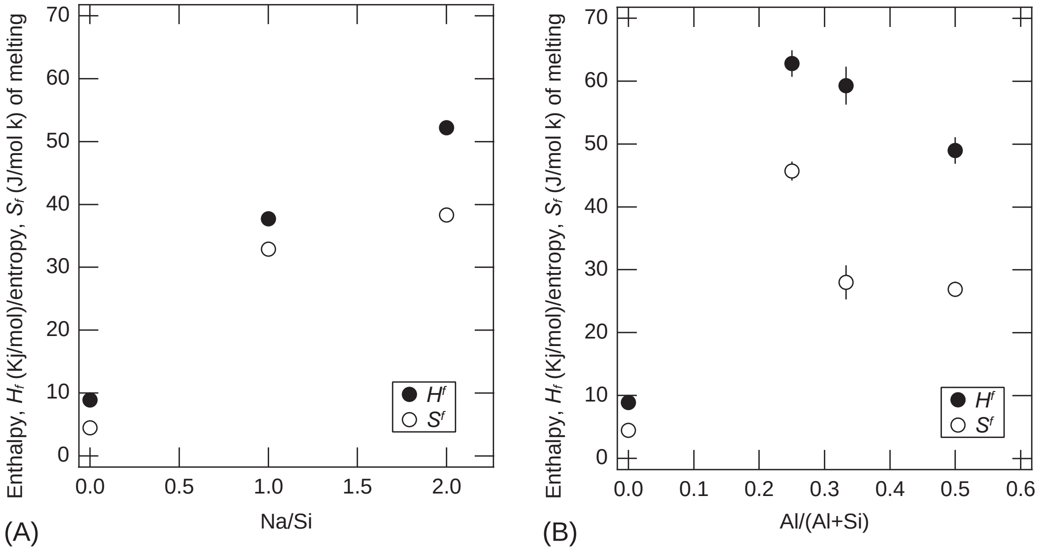

FIG. 5.3 Enthalpy and entropy of fusion, ΔH_f and ΔS_f, as a function of composition. (A) For crystals along the join SiO_2-Na_2O. (B) For crystals along the join SiO_2-$NaAlO_2$. *(Compilation by Richet and Bottinga, 1986.)*

ΔS_f of other tectosilicates, such as albite ($NaAlSi_3O_8$) or nepheline ($NaAlSiO_4$), is 5–10 times greater than that for cristobalite (see data compilation by Richet and Bottinga, 1985). Analogous relationships exist for other systems (e.g., Stebbins et al., 1983), which substantiate further that melting of SiO_2 polymorphs involves less structural rearrangement than any other silicates. More generally, the fusion data of Table 5.1 indicates that molten SiO_2 and cristobalite have similar ordering characteristics than any other silicate (see also Bourova et al., 2000). Enthalpy and entropy of fusion of the high-pressure crystalline phases, coesite and stishovite, seemingly have not been determined. However, from the enthalpy and entropy of the quartz/coesite/stishovite phase transformations (Akaogi and Navrotsky, 1984; Ono et al., 2017), it follows that the enthalpy of fusion of coesite and stishovite at ambient pressure is many times greater than the low-pressure polymorphs, quartz, and cristobalite.

5.3.2 Thermodynamic Properties

The high-temperature heat capacity (C_p) of silica glass is known accurately from many measurements (see review by Richet et al., 1982). No anomaly is found up to the glass transition. The heat capacity change at the glass transition, ΔC_p, is about 10% and is among the lowest of silicate and aluminosilicate glasses (see tabulation by Richet and Bottinga, 1986). Effects of impurities on C_p have not been detected, which is common for solids. A possible exception could be the slight effect of water reported in measurements made on Type I and III SiO_2 glasses (Casey et al., 1976). In the immediate vicinity of 0 K, C_p depends strongly on thermal history and impurity content (e.g., Grosmaire-Vandorpe et al., 1983), but discussion of these effects is beyond our scope.

Heat-capacity data between 0 K and room temperature are scarce. Entropy assessments have generally relied on unpublished measurements made by E.F. Westrum, Jr., which were confirmed by Yamashita et al. (2001). Westrum (1956) also reported a marginally positive C_p difference between two samples annealed at 1340 and 1570 K, a difference that could be real or may simply be the result of the sluggishness of relaxation at these temperatures with 1340 K slightly below and 1570 K somewhat above that of the glass transition of SiO_2 at 1480 K (Richet et al., 1982).

The sensitivity of C_p to short-range order around metal cations below 200 K has been discussed in Chapter 3, Section 3.5. The heat capacity differences between glasses and crystals are small if Si^{4+} is fourfold coordinated by oxygen in both phases, but is much larger when Si^{4+} is sixfold coordinated in the crystal, but not in the glass (Fig. 5.4). This is particularly evident for stishovite (SiO_2 crystals with sixfold coordinate Si^{4+}) and tetragonal GeO_2, which has sixfold coordinated Ge^{4+}, but where the coordination state of Ge^{4+} in its glass is fourfold. For both

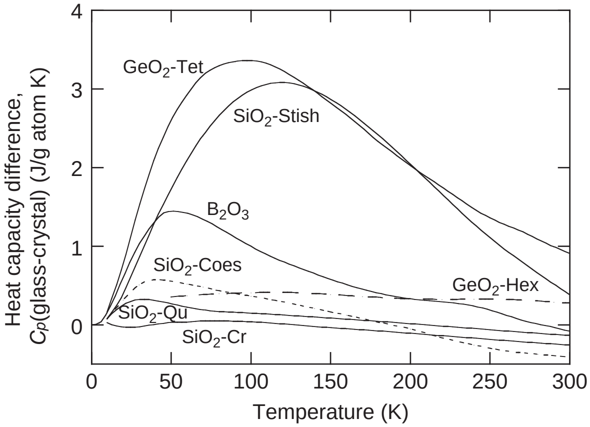

FIG. 5.4 Low-temperature heat capacity differences between glasses and crystals. Coes, coesite; Cr, cristobalite; GeO_2-Tet and -Hex, tetragonal and hexagonal forms of GeO_2; Qu, quartz; St, stishovite. *(See Richet et al., 2003 for data sources and a discussion of the* C_p *difference apparent for* B_2O_3*, which is due to the existence of boroxol rings in only the glass.)*

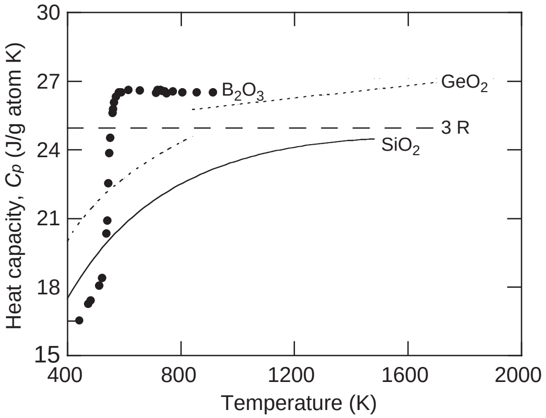

FIG. 5.5 Heat-capacity changes at the glass transition for SiO_2, GeO_2, and B_2O_3. Adiabatic measurements for B_2O_3 (Shmidt, 1966) and values derived from drop calorimetry experiments for GeO_2 (Richet, 1990) and SiO_2 (Richet et al., 1982). The Dulong-and-Petit harmonic limit of 3R/g atom K is shown for comparison.

stishovite and crystalline GeO_2 the heat capacity differences are about five times larger than the difference between glass and SiO_2 and GeO_2 with fourfold coordinated cations (Fig. 5.4).

At the rapid cooling rate of drop-calorimetry experiments, the glass transition of a type I SiO_2 is 1480 K and the associated C_p increase is only 10% (Richet et al., 1982). The similarity of the C_p change for SiO_2 and GeO_2 (Fig. 5.5) might suggest that the heat capacity of SiO_2 liquid increases slightly with temperature as does that of GeO_2. However, other measurements yield a constant partial molar heat capacity for SiO_2 that is equal to the 81.37 J/mol K of the heat capacity of pure SiO_2 liquid (Richet and Bottinga, 1985). These measurements made for a variety of silicate systems include data obtained up to 1800 K (Richet et al., 1984). Hence, evidence is lacking for a significant minimum in heat capacity.

The glass transition range of SiO_2 should depend as strongly on impurity content as viscosity (see the following), but such an effect has not been investigated in calorimetry experiments. There are, however, data for GeO_2 which indicate that the presence of 0.06 mol% Li_2O lowers the glass transition temperature by 200 degrees without influencing the heat capacity of the liquid (Richet, 1990).

Finally, a residual entropy is determined for SiO_2 glass at 0 K of 1.7 J/g atom K from the calorimetric cycle described in Fig. 3.10 (Chapter 3). This is the configurational entropy of the liquid frozen at the glass transition. Its value is one of the smallest for silicates (Table 3.2). Of course, the reason is that this entropy is made up of a single topological contribution, without any contribution of mixing of similar components.

5.3.3 Volume Properties

Silica glass has a low density of 2.20 g/cm^3 at ambient temperature and pressure (molar volume: 27.3 cm^3). Water dissolved in silica glass causes a density decrease as might be expected from its low molecular weight. For trace amounts, however, this decrease is less than 0.001 g/cm^3 for 0.1 wt% OH (Bruckner, 1970; Shackelford et al., 1970) (see Fig. 5.6).

The density of SiO_2 liquid has been discussed extensively because derivation of melt properties from measurements on glasses is fraught with difficulties related to permanent compaction and in view of possible uncontrolled effects during the quench. Because thermal

FIG. 5.6 Relationships between silica density and water content referenced to the open circle marked on the figure (Shelby, 2004).

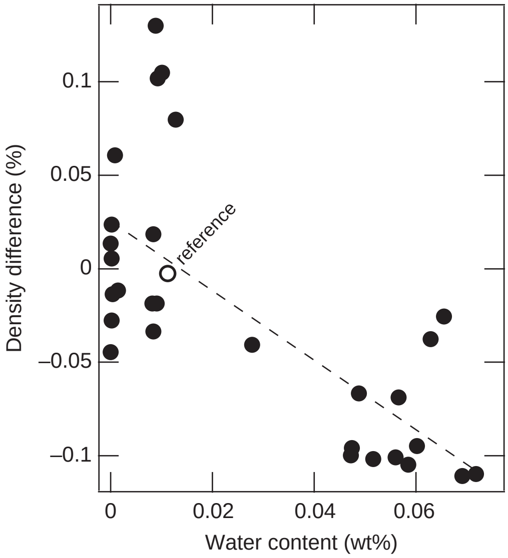

expansion depends on the thermal history of the sample (Douglas and Isard, 1951), dilatometry experiments must be performed on glasses annealed at well-defined temperatures and be terminated before reaching temperatures at which relaxation becomes significant. For example, Douglas and Isard (1951) showed that an equilibrium density of silica glass is reached in 50 h at 1080°C, but cannot be attained in more than 400 h at 903°C. As another example, the existence of the density maximum reported by Bruckner (1970) has been questioned from observed Raman shifts of glasses with fictive temperatures up to 1550°C (Kakiuchida et al., 2003). The only density measurements available have been made between 1930°C and 2170°C by Bacon et al. (1960) where presumably the equilibrium density could be reached rapidly. These yielded a molar volume of 28.87 cm^3/mol at 1730°C and a thermal expansion coefficient of 10^{-4} K^{-1}. If real, both properties would imply a dramatic dilation change somewhere below 1930°C to match the density data on quenched glasses. More recent expansion data show, however, an expansion coefficient between 5 and $6.5 \cdot 10^{-7}$ K^{-1} (Fig. 5.7; see also Kühn and Schadrack, 2009). In the latter case, there is a slight increase in expansion coefficient with increasing fictive temperature. Notably, for expansion measurements over the wider temperature range, the resulting expansion coefficient seems more sensitive to fictive temperature. Interestingly, no effect of dissolved OH on the thermal expansion has been reported, at least to about 1300 ppm OH (Kühn and Schadrack, 2009).

The molar volume of molten SiO_2 can be determined more reliably from the melting curve of cristobalite, which has a very small slope (Jackson, 1976; Zhang et al., 1993). From the Clausius-Clapeyron equation, it follows that the volume difference between molten SiO_2 and cristobalite is also very small (see also Table 5.1). The volume of SiO_2 liquid thus obtained is near the 27.4 cm^3/mol measured for cristobalite at its melting temperature (Fig. 5.8). Support for this value is provided by extrapolations of molar volumes of binary barium and sodium silicate melts to pure SiO_2, which result in molar voume of 27.5 cm^3/mol (Fig. 5.9).

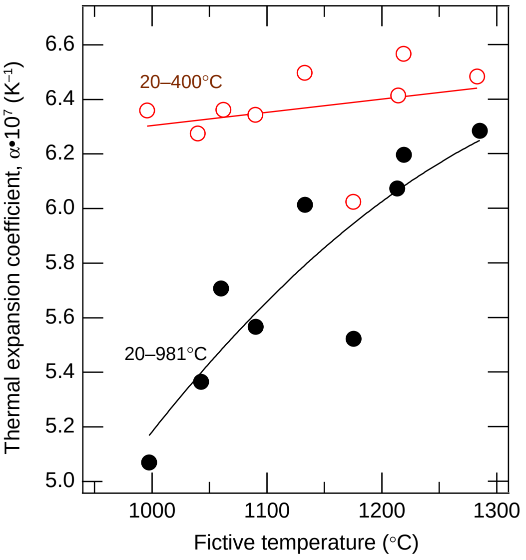

FIG. 5.7 Thermal expansion of SiO_2 glass as a function of their fictive temperature in the two ranges indicated (Kühn and Schadrack, 2009).

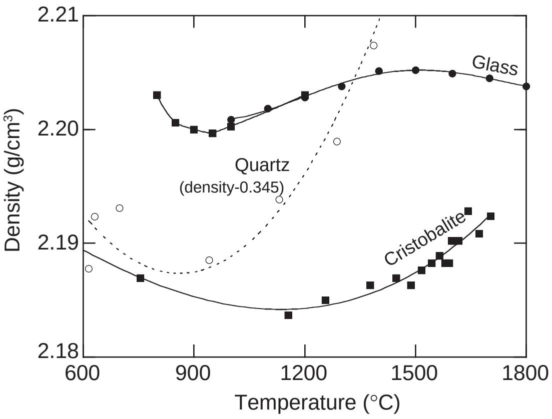

FIG. 5.8 Densities of quartz and cristobalite against temperature and 25°C density of SiO_2 glass against quench temperature, with data from Bruckner (1970), for type I silica (*solid squares*), and Sen et al. (2004) for a type III SiO_2 (*solid circles*) after complete density relaxation (1200°C density assumed to be 2.203 g/cm^3). The data for quartz have been displaced downward by 0.345 g/cm^3 to expand the scale as much as possible. (*Data from Bourova and Richet, 1998.*)

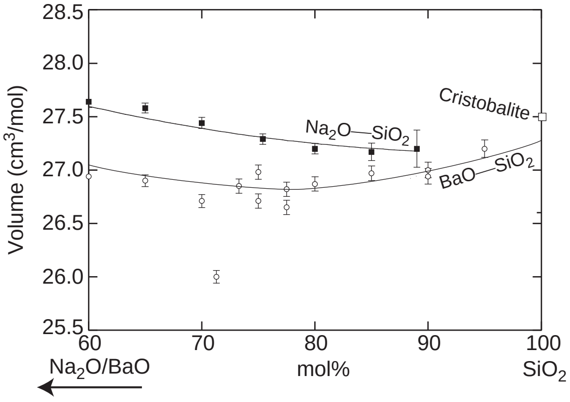

FIG. 5.9 High-temperature molar volumes: cristobalite at 1700°C, Na_2O-SiO_2 melts at 1400°C, and BaO-SiO_2 melts at 1700°C. (*Data from Bourova and Richet, 1998; Bockris et al., 1956; Tomlinson et al., 1958.*)

Of course, it also needs to be kept in mind that in complex melts there are both bridging and nonbridging oxygens and bridging oxygens have a larger partial molar volume than nonbridging oxygens (Bottinga and Richet, 1995). Partial molar volume data from melts with a significant proportion of nonbridging oxygen may, therefore, result in SiO_2 molar volume values that reflect these differences and might not, therefore, be directly comparable to measured molar volume of pure SiO_2 melt.

On the other hand, partial molar volume values of SiO_2 at the melting temperature of cristobalite (1723°C) ranging from 27.03 cm^3/mol (Ghiorso and Kress, 2004) to 29.5 cm^3 (Knoche et al., 1995) have been reported from a comprehensive thermodynamic model of a wide variety of melts of varying chemical complexity and from measurements on granitic melts with oxide additions, repectively. Whether or not these are real differences or resulting from the way the volumes were obtained cannot be ascertained.

Silica glass distinguishes itself by its extremely small thermal expansion. In Type III, dissolved water enhances dilation by about 5% from 0°C to 100°C (Hetherington and Jack, 1962). The effect extends to higher temperatures. The average of mean thermal expansion coefficients, measured between 0°C and 1000°C, for various type I, II, and III glasses are 45.5, 45.8, and 48.9 $10^{-8}\,K^{-1}$, respectively (Oishi and Kimura, 1969), whereas Kühn and Schadrack (2009) reported values in the 50–65·$10^{-8}\,K^{-1}$ range.

By combining effects of OH content and fictive temperature, thermal expansion has been described with the empirical expression (Kühn and Schadrack, 2009):

$$\alpha\left(K^{-1}\right)=\left[0.267+2.88\cdot 10^{-4*}T_f\left({}^{\circ}C\right)-3.26\cdot 10^{-5}\cdot OH(ppm)\right]\cdot 10^{-6} \tag{5.1}$$

In Eq. (5.1), α is the thermal expansion coefficient, T_f the fictive temperature, and OH the concentration of OH.

These thermal expansion coefficients are from 10% to 1% of the values generally determined for silicate glasses. In fact, the volume of SiO_2 melt varies by less than 0.1 cm^3/mol between the glass transition and the melting point of cristobalite. It is also consistent with the low value of $10^{-6}\,K^{-1}$ drawn from extrapolations to pure SiO_2 of measurements made for binary metal oxide systems (Chapter 6, Section 6.4.1). Moreover, the compressional sound velocity of amorphous SiO_2 is a linear function of temperature from the glass transition to more than 2000°C (see the following). In view of the strong sensitivity of sound velocity to density, this linear relationship rules out any significant increase of thermal expansion coefficient at a temperature below 2000°C. Finally, SiO_2 liquid has definite structural similarity with cristobalite (Bourova et al., 2000; Takada et al., 2004), the thermal expansion coefficient of which is also very small near its melting point. In fact, cristobalite, and quartz as well, contract slightly before melting (Bourova and Richet, 1998), consistent with the aforementioned minimum density observed for SiO_2 glasses quenched from 950°C (Sen et al., 2004). This difference probably relates to the fact that in SiO_2 glass, all bonding is bridging Si—O bonds, which are much stiffer and several times stronger than most other bonds found in silicate glass, minerals, and crystals.

Silica glass and melts are highly compressible (Bridgman and Simon, 1953; Della Valle and Venuti, 1996; Huang and Kieffer, 2004; Clark et al., 2014). Silica glass is particularly interesting, however, in that above pressures between about 4 and 6 GPa, it is permanently compacted (Yokoyama et al., 2010; Clark et al., 2014). As a result, density versus pressure

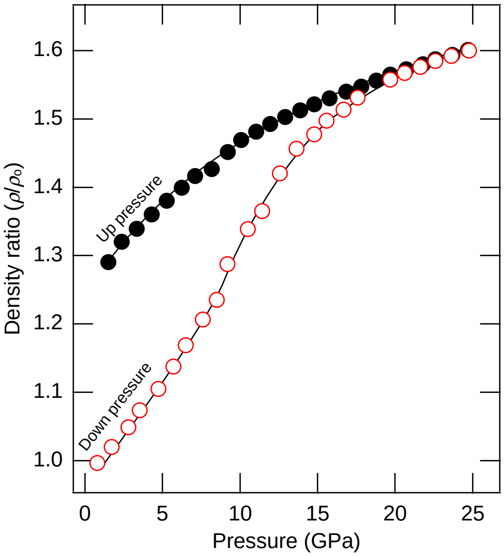

FIG. 5.10 Relative density, ρ/ρ_0, of SiO_2 glass as a function of pressure. Closed symbols are from measurements during increased pressure and open symbols decreased pressure. *(Results of calculations by Della Valle and Venuti, 1996.)*

evolution from compression studies will differ from density evolution during decompression (Fig. 5.10; see also Della Valle and Venuti, 1996).

Sound velocity is the typical means by which density is determined at high pressure and temperature because density, ρ, is related to longitudinal, V_P, and transverse, V_S, sound velocity as (Polian and Grimsditch, 1993; Zha et al., 1994):

$$\rho(P) = \rho(P_0) + \int_{P_0}^{P} \gamma\left(V_P^2 - 4/3V_S^2\right)\partial P, \tag{5.2}$$

where $\rho(P)$ and $\rho(P_0)$ are densities at pressure, P, and at reference pressure, P_0, the γ is the ratio of the isothermal to adiabatic bulk bulk modules and set equal to 1 for SiO_2 glass (Yokoyama et al., 2010). The sound velocities exibit minimum values in the 3–5 GPa-range, a pressure range that depends on temperature (Yokoyama et al., 2010; Fig. 5.11). Transverse velocities are considerably slower than the longitudinal ones in all pressure ranges. The results reproduced in Fig. 5.11 were recorded from measurements made both during up and down pressure experimental series. The profound minima cannot be discerned during down-pressure expriments, a feature that reflects the irreversible compaction that occurred in the 3–5 GPa range during up-pressure experiments.

Irreversible compaction depends on the conditions of the experiment. Its onset is observed at lower pressure either when the temperature is increased or under increasingly nonhydrostatic conditions (Shelby, 2004; Yokoyama et al., 2010). Owing to this sensitivity, it is not possible to predict accurately the density of SiO_2 glass beyond the pressure range where the glass is mechanically elastic. Likewise, the adiabatic bulk and shear moduli are well defined only at low pressure (Fig. 5.12) where they first decrease linearly with increasing pressure (Kondo et al., 1981; Suito et al., 1992; Zha et al., 1994). After passing through a

FIG. 5.11 Longitudinal velocity, V_P, at 800 K during up and down pressure measurements as indicated (Yokoyama et al., 2010).

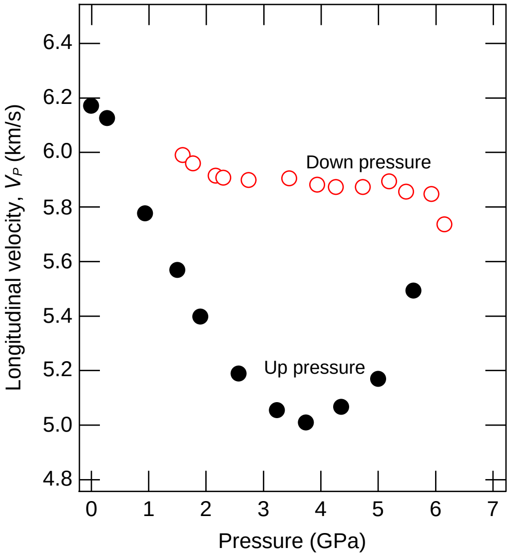

FIG. 5.12 Bulk (K_S) and shear (G) moduli of silica glass against pressure at room temperature. The room-pressure values are 36.9 and 31.1 GPa for K_S and G, respectively. The dashed lines give the pressure dependence of the moduli in the elastic region ($dK_S/dP = -5.12$ and $dG/dP = -3.34$). *(Data from Suito et al., 1992.)*

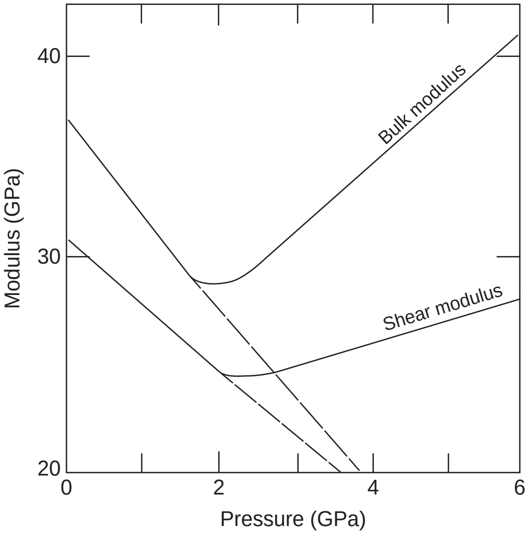

minimum near 2 GPa, both moduli increase as a result of the permanent compaction that begins to take place near this pressure. Interestingly, extrapolation of the low-pressure data indicates that both moduli would vanish at a pressure of about 9 GPa. However, permanent compaction prevents such a mechanical instability from occurring.

The high viscosity of liquid SiO_2 makes determination of its compressibility (β) difficult. In Brillouin scattering experiments (Bucaro and Dardy, 1976; Krol et al., 1986; Zha et al., 1994), relaxation problems were circumvented through determination of the so-called

Landau-Placzek ratio, the intensity ratio of the Rayleigh and Brillouin lines, from which the adiabatic compressibility is obtained. The differences between the two determinations made in this way are probably within the error margins of the technique. Likewise, the temperature dependence of the compressibility is too small to be determined. Finally, the equilibrium compressibility of molten silica cannot be determined by ultrasonic methods but extrapolation of the measurements performed on SiO_2-rich melts may be used to check these results. The observations for binary metal-oxide systems (see Chapter 6, Section 6.4.1) are in best agreement with the datum of Bucaro and Dardy (1976). Interestingly, the partial molar compressibility of SiO_2 in multicomponent melts does not differ significantly from this value (Kress and Carmichael, 1991).

The bulk modulus of SiO_2 melt is greater than that of SiO_2 glass (Polian et al., 2002). This difference illustrates the importance of configurational changes in high-temperature compressibility. Comparison of equilibrium and vibrational compressibility determined by Brillouin scattering enables a more detailed analysis (see Chapter 3, Section 3.3.1). Bucaro and Dardy (1976), for example, reported a constant value of 2×10^{-11} Pa^{-1} for vibrational compressibility in the temperature range between 1200°C and 1700°C. This observation implies that 75% of the compression of molten SiO_2 originates in configurational changes, which was confirmed by Polian et al. (2002). Instead of being constant, however, the vibrational compressibility decreases with increasing temperature from 25°C to 2000°C (Fig. 5.13). The unusual feature is the variation of its temperature dependence was observed not at the glass transition, T_g, but at a lower temperature near 700–750°C. This change is attributable to the shear velocity, which decreases with rising temperatures above T_g, whereas the compressional velocity measured at the highest temperatures extrapolates smoothly down to the glass transition range.

The compressibility of SiO_2 glass decreases with increasing pressure. However, because permanent compaction occurs at several gigapascals during increasing pressure, the pressure

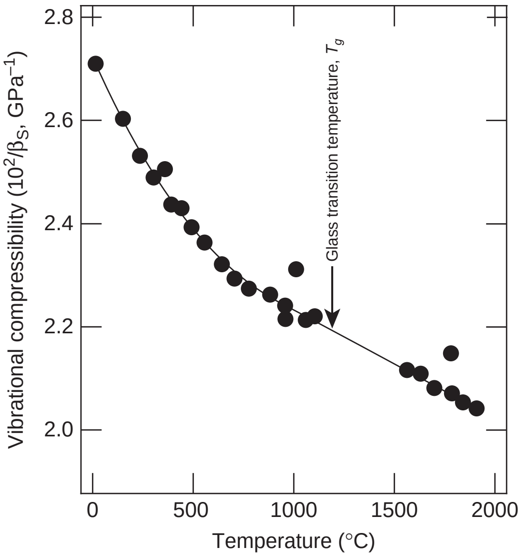

FIG. 5.13 Vibrational compressibility vs. temperature of type I SiO_2 glass and liquid determined from Brillouin scattering. The glass transition temperature (~1200°C) is shown with an arrow (Polian et al., 2002). In these experiments, crystallization of the supercooled SiO_2 liquid prevented measurements from being made between 1100°C and 1550°C.

dependence measured after such compaction differs significantly from that measured during up-pressure (Suito et al., 1992; Huang and Kieffer, 2004; Clark et al., 2014; see also Fig. 5.12). The compressibility of SiO_2 liquid necessarily also decreases with increasing pressure, but the effect cannot be determined from quench experiments because of permanent compaction. As high-pressure measurements are lacking, the compressibility of molten SiO_2 has been determined from thermodynamic analyses of the melting curve of SiO_2 polymorphs (e.g., Bottinga, 1991; Swamy et al., 1994). Such determinations are useful starting points, but they suffer from the fact that pressure and temperature are not independent variables along a melting curve. In addition, the results thus obtained depend on the high-pressure melting properties of the polymorphs, which are much less well known than their equations of state (e.g., Fabrichnaya et al., 2004).

5.3.4 Transport Properties

Transport properties of a three-dimensionally interconnected structure such as SiO_2 melt and glass differ in many ways from other silicates because transport requires availability of adequately sized cavities and the availability of gates between them. As these features likely depend significantly on pressure, pressure-dependent transport properties of this material might also be unusual.

5.3.4.1 Viscosity

A viscosity comparison with molten GeO_2 and B_2O_3, two other glass-forming oxides, illustrates the remarkable properties of SiO_2 liquid (Fig. 5.14A). Not only is there a very large viscosity increase from B_2O_3 to GeO_2 and SiO_2, but the deviation of viscosity from Arrhenian variations decreases markedly in the same order. A result of this evolution is that the activation enthalpies for viscous flow (ΔH_η) of these melts differ by much less near the glass transition than at high temperatures.

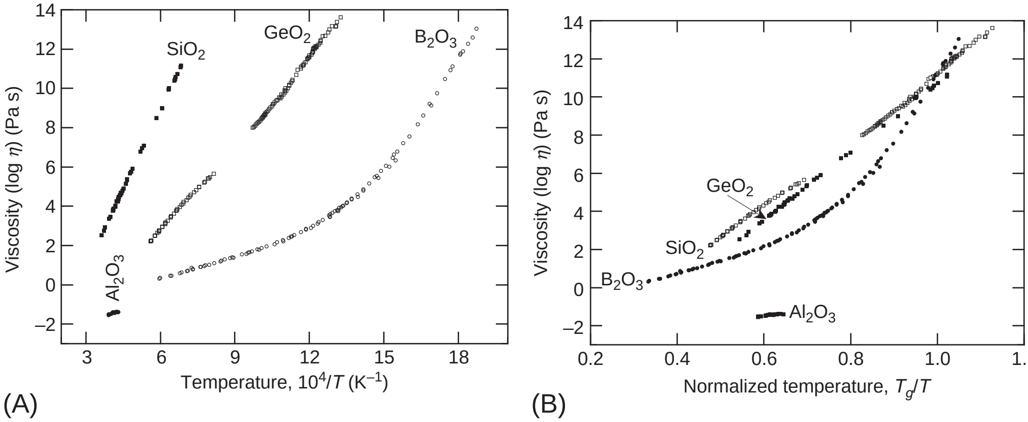

FIG. 5.14 Viscosity of molten glass-forming oxides, and alumina. (A) Viscosity vs reciprocal temperature. (B) Viscosity vs normalized temperature, T/T_g; the extreme fragility of Al_2O_3 liquid is shown by the data plotted with the two arbitrary values; $T_g = 1000$ K (left) and 1500 K (right) which, by definition, join with the other sets at $T_g/T = 1$. *(Data for SiO_2 from Urbain et al., 1982; for GeO_2 from Fontana and Plummer, 1966; for B_2O_3 from Napolitano et al., 1965 and Macedo and Napolitano, 1968; for Al_2O_3 from Urbain, 1982.)*

In the terminology introduced by Angell (1985), molten silica is the archetype of a strong liquid, whereas B_2O_3 has a definite fragile character. In order to compare the viscosities of liquids having widely different standard glass transition temperatures (T_g), Laughlin and Uhlmann (1972) introduced plots of log η against the reduced temperature T_g/T (Fig. 5.14B). In such a representation, the fragility, f, is defined as the viscosity gradient at T_g:

$$f = d\log\eta / d(T_g/T). \tag{5.3}$$

No liquid is known to be stronger (or less fragile) than molten silica.

The other common oxide components of silicate melts either decompose before melting (alkali oxides) or are extremely poor glass formers (e.g., MgO, CaO, Al_2O_3). At best, their viscosity-temperature relationships are known over restricted temperature intervals above their liquidus. As an example, the data for molten Al_2O_3 included in Fig. 5.14 illustrate that other molten metal oxides are much less viscous than SiO_2 and have smaller activation energies for viscous flow. Above 2000 K, the ΔH_η is, for example, 110 ± 5 and 515 ± 3 kJ/mol for Al_2O_3 and SiO_2, respectively (Urbain et al., 1982; Urbain, 1982), whereas extrapolations of measurements made along the CaO-Al_2O_3 join yield a value for CaO of 90 ± 1 kJ/mol (Urbain, 1983). In accordance with these results, one observes that, when mixed with pure SiO_2, other oxides systematically cause viscosity to decrease and fragility to increase (Fig. 5.14; see also Chapters 6 and 8, Sections 6.4.2 and 8.4.1).

For the glass-forming oxides of Fig. 5.14, a correlation between viscosity and melting temperature of the liquidus polymorph seems consistent with the influence of bond strength on both properties (see Chapter 2, Section 2.2.2). Although B—O bonds are very strong and interconnected in glassy B_2O_3 below the glass transition temperature, at higher temperature in the liquid state, isolated BO_3 rings dominate structure (Sakowski and Herms, 2001). The bonding between these rings is weak, which leads to much lower viscosity (see also Mozzi and Warren, 1970). The three-dimensional network of GeO_2 is, by contrast, closely related to that of SiO_2 (Konnert et al., 1973; Price and Saboungi, 1998; Hoang, 2006). The viscosity difference of GeO_2 and SiO_2 stems essentially from lower ionization potential of Ge^{4+} compared with Si^{4+}.

The bond strength-viscosity correlation also holds for predominantly ionic molten oxides such as alumina. There is an apparent anomaly, however, in that, despite weaker bond strength, corundum, lime, and periclase all melt at much higher temperatures than cristobalite (1723°C) (Al_2O_3 melting temperature: ~2020°C; Osborn and Muan, 1960a; CaO melting temperature: ~2500°C; Osborn and Muan, 1960b; MgO melting temperature; ~2800°C; Osborn and Muan, 1960b). The reason is that, despite the strong ionic character of these oxides, bonding lacks directionality so that the configurational rearrangements that cause melting require breaking of M—O bonds. In contrast, the partially covalent nature of Si—O bonds gives rise to a strong directionality within the SiO_4 tetrahedra. This directionality is associated with great flexibility of Si—O—Si angles. Because Si—O bonds do not need to be severed for configurational rearrangements to occur (see Chapter 4, Section 4.3.2), melting takes place at lower temperatures (Richet and Ottonello, 2014).

Among existing data for SiO_2 above the glass transition temperature, the viscosities of Urbain et al. (1982) are generally taken as a reference because they cover a wide temperature interval and are part of an extensive and accurate set performed over a large composition interval. Unfortunately, these data do not establish rigorously the actual Arrhenian nature of the viscosity of SiO_2. At the lowest temperatures, their timescale of a few hours (see the

FIG. 5.15 Viscosity of SiO_2 melt as a function of temperature. Note that the data from Urbain (1990) were from Silica III. (*Data from Volarovich and Leontieva, 1936; Bacon et al., 1960; Fontana and Plummer, 1966; Urbain et al., 1982; Urbain, 1990.*)

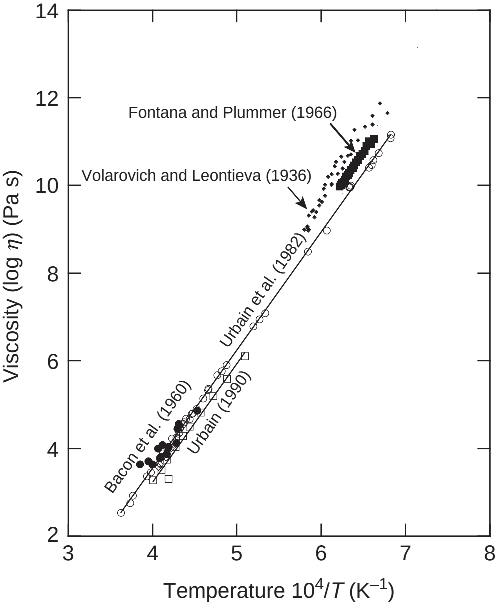

procedure described by Urbain and Auvray, 1969) may have been insufficient to obtain equilibrium viscosities. In other words, the reported viscosity values might be too low. Attainment of equilibrium was checked in the experiments of Hetherington et al. (1964). The fact that they join smoothly with those of Urbain et al. (1982) near 1350°C could, thus, point to the non-Arrhenian character that is apparent in Fig. 5.15 when both data sets are considered (see Richet, 1984). Unfortunately, it is difficult to check this conclusion because only fitted results were published by Hetherington et al. (1964).

It is a general rule that viscosity is a considerably stronger function of composition near the glass transition than at high temperatures (see Richet, 1984). Low concentration of impurities may, therefore, have significant effects on silica viscosity near and below the glass transition. The viscosity decrease resulting from impurities is very large as a result of the breakup of the three-dimensional SiO_2 framework by network-modifying cations (Fig. 5.16). Their effect on viscosity also depends strongly on the nature of the impurity. For Al^{3+} and Ga^{3+}, the influence is moderate because the viscosity decrease reflects the decrease of the strength of T—O—T bonds when Al^{3+} and Ga^{3+} substitute for Si^{4+} on tetrahedral sites of the structure. However, with alkali or water impurities, Si—O—Si bridging bonds are replaced by much weaker O—M (alkali or proton) bonds thus reducing the SiO_2 viscosity more effectively. Interestingly, though, for Na, the results of Leko et al. (1977) join smoothly with measurements on binary silicates made up to 35 mol% Na_2O (Bockris et al., 1955). For OH, good agreement is found between the measurements of Hetherington et al. (1964) and Leko et al. (1977). Both data sets indicate an effect of water intermediate between those of Na and Al. The influence of impurities on the activation enthalpy of viscous flow (ΔH_η) is less well determined although it tends to parallel those on viscosity (Fig. 5.16B). The activation enthalpy drops upon addition of Na_2O but increases by 80 kJ/mol for 6 mol% Al_2O_3.

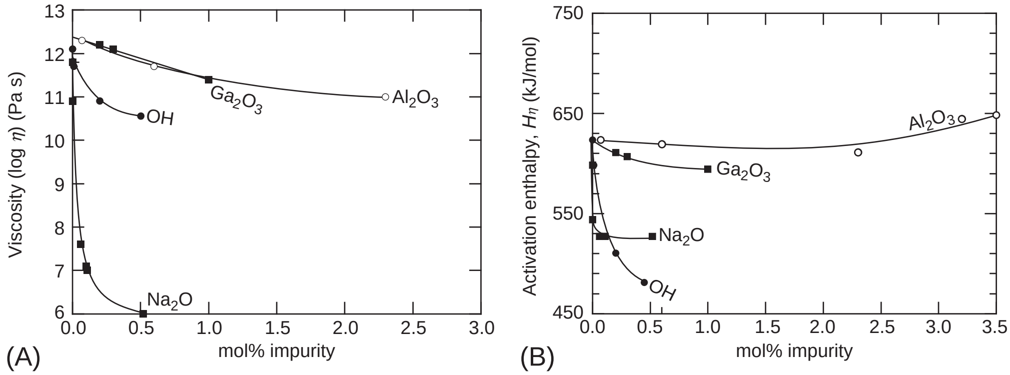

FIG. 5.16 Effects of impurities on the viscosity of SiO_2 near the glass transition range. (A) Viscosity of SiO_2 at 1200°C vs Na_2O, Al_2O_3, Ga_2O_3, and OH contents. (B) Activation enthalpy of viscous flow in the glass transition range. *(Data from Leko et al., 1977 for type I SiO_2, for all impurities.)*

5.3.4.2 *Diffusion*

Noble gas diffusivity and solubility in vitreous and molten SiO_2 have been employed as a probe of the structure and, in particular, cavity distribution and cavity gates (Shen et al., 2011; Kuhtetskiy et al., 2016; Takada et al., 2016; see also Chapter 17, Sections 17.3.1 and 17.4.1). Notably, the noble gas diffusivity in amorphous SiO_2 decreases with increasing size of the gas molecule, whether noble gases or diatomic gases such as O_2 and perhaps Cl_2 (Fig. 5.17). Among the gases (Fig. 5.17), helium diffuses the fastest, as expected from its small size and chemical inertness. It is closely followed by neon, which is bigger, and, rather surprisingly, by sodium, which exhibits very small differences between various types of SiO_2 glasses (Frischat, 1968, 1970). As already noted for viscosity, there is a large difference between the diffusivities of Na and "water," the latter diffusing about four orders of magnitude slower than the former. In turn, "water" diffuses faster than Cl, which suggests that chlorine and hydroxyl ions do not interact in a similar way with bridging oxygens. For alkali elements, the influence of ionic radius is clearly shown by the difference between the diffusivities of Na and Cs, the latter being similar to that of Ca. Modeling of cavity distribution in terms of available intertetrahedral rings can be used to simulate diffusion coefficients with considerable precision (Swets et al., 1961; Kuhtetskiy et al., 2016; see also Fig. 5.18).

Noble gas diffusivity in SiO_2 melt increases not only with increasing temperature (Fig. 5.17) but also with increasing pressure—at least up to the 15–20 GPa range where the diffusivity decreases with further pressure increase (see, e.g., Takada et al., 2016; Fig. 5.19). Hung et al. (2007) also determined minimum diffusivity of oxygen and silicon at high pressure, but placed this pressure slightly below 10 GPa in contrast to the nearly 20 GPa in the simulation study by Takada et al. (2016). Notably, this diffusivity maximum with pressure becomes less distinct at higher temperature and at least in the simulations of Takada et al. (2016) could not be discerned at temperatures above about 3000 K.

A summary of tracer diffusivity measured for a number of elements in amorphous SiO_2 is shown in Fig. 5.20. Although most results do not cover a very wide temperature range, there is no evidence for changes in diffusivity mechanisms at the glass transition (shown as a vertical

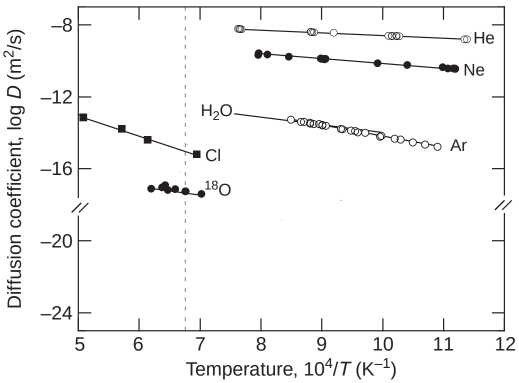

FIG. 5.17 Tracer diffusivity in amorphous SiO_2 of gases against reciprocal temperature. The glass transition of SiO_2 is shown as a dashed line "H_2O" data for a type I glass in an H_2 atmosphere (Bell et al., 1962); Ar data for a SiO_2 thin film deposited on a porous Vycor substrate (Perkins and Begal, 1971); for Cl: Cl-free SiO_2 under a low Cl pressure (Hermann et al., 1985). For ^{20}Ne: type I silica under 0.1 MPa Ne pressure (Frank et al., 1961); for He: similar procedure by Swets et al. (1961). (*^{45}Ca data from Zhabrev et al. (1976) for type III glass. Ar data from Rothman et al., 1982.*)

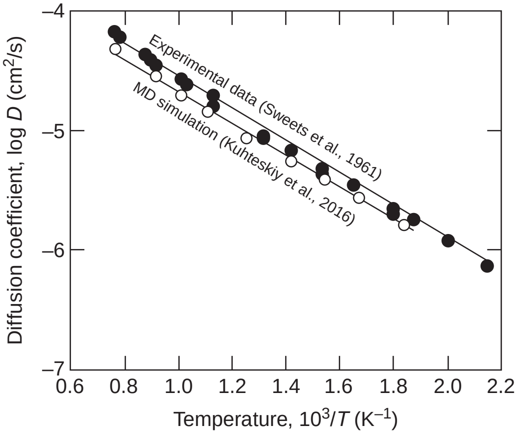

FIG. 5.18 Calculated (MD simulation—Kuhtetskiy et al., 2016) and experimentally measured (Swets et al., 1961) He diffusion coefficient as a function of temperature. The slopes of these lines both are equivalent to an activation energy of 25 kJ/mol.

FIG. 5.19 Pressure dependence of oxygen diffusivity in SiO_2 melt at different temperatures as indicated. (*Results from MD simulations by Takada et al., 2016.*)

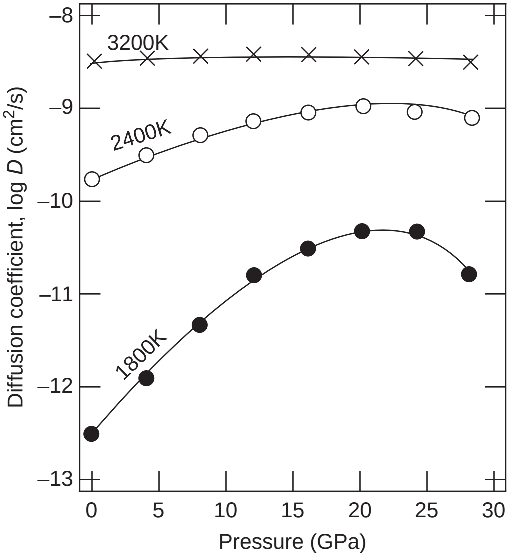

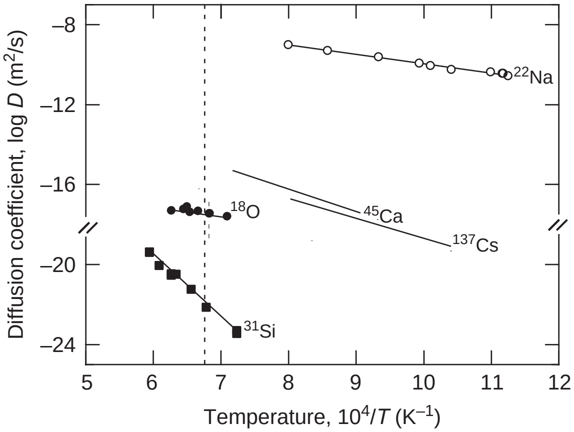

FIG. 5.20 Tracer diffusivity of impurities in SiO_2 glasses and melts. ^{31}Si measurements for a type I silica (Brébec et al., 1980); ^{18}O data for a type II silica at 0.01 MPa O_2 pressure (Muelenbachs and Schaeffer, 1977), and fitted results of Sucov (1963) for an "optical quality" sample heated at 0.1 MPa O_2 pressure; ^{137}Cs data for types I, II, and III; for ^{22}Na: type I silica, probably in air (Frischat, 1968).

dashed line in Fig. 5.17). This observation is consistent with the small extent of temperature-induced structural changes in liquid SiO_2, which is indicated by the small configurational heat capacity across the glass transition (Richet and Bottinga, 1985). The other important feature is the clear correlation between the diffusivity and structural role of the element and, particularly, the strength of its bonding within the silica network. For activation enthalpies, these effects have been discussed by Roselieb and Jambon (2002) to whom we refer for more details.

Given the large difference between oxygen and silicon diffusivities, the question arises as to which one correlates better with the values calculated from viscosity through the Eyring relationship (Chapter 2, Eq. (2.11)). The answer, therefore, is ambiguous (Fig. 5.20), although at high pressures, the relationship seems to hold better (Hung et al., 2007). There is close agreement with silicon diffusivity from either the viscosities of Hetherington et al. (1964) or those of Urbain et al. (1982). The much higher diffusivity measured for ^{18}O indicates that mechanisms other than viscous flow are operating for transporting oxygen. This conclusion suggests that the oxygen dynamics that prevail in SiO_2 polymorphs at high temperatures (see Chapter 4, Section 4.3.2 and Bourova et al., 2004) could also operate in amorphous SiO_2.

5.4 STRUCTURE OF SiO_2 GLASS AND MELT

Structural models proposed for SiO_2 glass and melt may be grouped into three types. (i) The earliest models assumed a random network structure (Zachariassen, 1932; Bell et al., 1980). (ii) In contrast, in pseudocrystalline models some similarity with crystal structure is assumed (Geissberger and Bray, 1983; Grimley et al., 1990; Yuan and Cormack, 2003; Clark et al., 2004). (iii) The coexistence of several distinct structural entities defined by a number of coexisting, three-dimensionally interconnected tetrahedra to form ring structures forms the basis of the third kind of models. This latter group of models has received the most attention in recent years, both from observational (experimental) and simulation perspectives (Hench and West, 1995; Machacek et al., 2007; Yi and Lee, 2012; Sonneville et al., 2013; Takada et al., 2016).

5.4.1 Random Network Structure

The random network model for the structure of vitreous SiO_2 originally was suggested by Zachariassen (1932). This model has four important premises. (i) The structural positions are energetically equivalent for all oxygen atoms as well as for all silicon atoms. (ii) There is no ordering among the SiO_4 tetrahedra. (iii) Oxygen in the corners of SiO_4 tetrahedra are shared between neighboring tetrahedra. (iv) The structure is three-dimensionally interconnected.

The random network model received support in spectroscopic studies by Bell and co-workers (Bell and Dean, 1970; Bell et al., 1980; Bell and Hibbins-Butler, 1976). With some differences, this model allowed these workers to calculate important features of the vibrational and neutron spectra of vitreous SiO_2. The differences between observed and calculated spectra are most notable in the low-frequency end. In this regime, Phillips (1984) noted, for example, that the Raman bands are unusually narrow, which suggests localized vibrations. However, localized vibrations cannot easily be accommodated with the random network model where all O and all Si positions are equivalent.

5.4.2 Pseudocrystalline Structure Model

Because the Si and O positions in vitreous SiO_2 cannot be energetically equivalent (Phillips, 1984), the original random network model has been refined such that, at least on the scale of several angstroms, structural similarities between glass (and melt) and crystalline SiO_2 polymorphs may exist. Such a structure model also found early support in Randall et al. (1930) from an X-ray diffraction study of SiO_2 glass and cristobalite. Structural similarity between these two materials also finds support in the exceptionally small values of enthalpy and entropy of fusion (Table 5.1; Fig. 5.3). Modeling of X-ray diffraction data of vitreous SiO_2 by plausible crystalline models also has met with significant success (Mozzi and Warren, 1969; see also discussion by Taylor and Brown, 1979). This general conclusion is also that which may be drawn from the small volume, entropy, and entropy of melting of cristobalite, for example (see also Table 5.1), as well as the negligible heat-capacity difference between vitreous SiO_2 and cristobalite compared with other silicates. These X-ray data are best displayed in terms of pair distribution functions whereby the obtained Si—O, O—O, and Si—Si distances are compared with distances in appropriate models (Fig. 5.21).

Mozzi and Warren (1969) originally stated that their X-ray data were best interpreted on the basis of the random network model, but that some similarities between the spectra of vitreous SiO_2, tridymite, and cristobalite do exist. Konnert and Karle (1973) and Konnert et al. (1973) concluded that significant similarities persisted between the spectra of vitreous SiO_2 and that of tridymite to distances of perhaps as much as 15–20 Å. Bourova et al. (2000),

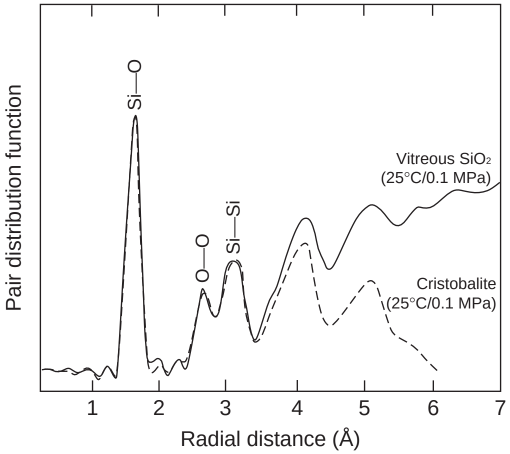

FIG. 5.21 Pair distribution function from X-ray diffraction data of vitreous SiO_2 and cristobalite at ambient pressure and 25°C (Mozzi and Warren, 1969).

from their numerical simulation, found considerable similarity between the structure of β-cristobalite and molten SiO_2 to distances beyond the first Si—O, Si—Si, and O—O distances in these materials. Short- and medium-range structural similarity between molten SiO_2 and silica polymorphs is also consistent with results of numerical simulations and structural interpretations of neutron, X-ray, and NMR data (Geissberger and Bray, 1983; Grimley et al., 1990; Yuan and Cormack, 2003; Clark et al., 2004; Dracinsky et al., 2011). We note that among the possible crystalline SiO_2 model compounds, the β-cristobalite structure shows the greatest similarity to the structure of SiO_2 glass and melt (Hosemann et al., 1991; Huang and Kieffer, 2004; de Ligny et al., 2009). Structural differences between glass and melt, on the one side, and β-cristobalite on the other, however, remain in the medium- and long-range domains (Wright, 1994; Bourova et al., 2000).

5.4.3 Numerical Simulations of Structure

Numerical simulation of SiO_2 glass and melt structure at ambient pressure has focused on Si—O—Si and O—Si—O angle distribution (Benoit et al., 2001; Kuzuu et al., 2004; Dracinsky et al., 2011; Kim et al., 2012), on Si—O bond length, and on ring statistics (Sykes and Kubicki, 1996; Harkless et al., 1996; Hench and West, 1995; Kim et al., 2012). Void size distribution is closely related to the ring statistics (Malavasi et al., 2006). Bond angle distribution and bond distances in glassy and molten SiO_2 have been simulated to temperatures in excess of 9000 K (Kuzuu et al., 2004). However, most simulation studies have been restricted to temperatures below about 4000 K. High-pressure simulations have addressed bond angle compression and changes in oxygen coordination numbers surrounding Si^{4+} (Rustad et al., 1991; Tsuneyuki and Matsui, 1995; Hung et al., 2007; Li et al., 2014; Takada et al., 2016).

For liquid SiO_2, Si—O, O—O, and Si—Si distances from Born-Oppenheimer molecular dynamics simulations are slightly sensitive to temperature (Kim et al., 2012), but in general closely resemble early X-ray diffraction data (Mozzi and Warren, 1969). Here, the Si—O distance was 1.63 Å, O—O between 2.61 and 2.65 Å, and Si—Si distance between 3.05 and 3.15 Å in the 3120–3700 K temperature range. The same computation method yields the respective distances for cristablite at 1.55, 2.53, and 3.09 Å (Kim et al., 2012).

The Si—O—Si and O—Si—O angle distributions in vitreous and molten SiO_2 have been subjected to several simulations (Kuzuu et al., 2004; Hung et al., 2007; Dracinsky et al., 2011; Kim et al., 2012). The O—Si—O angle maximum falls between 107 and 110 degrees at ambient pressure, whereas the Si—O—Si angle maximum occurs between 140 and 150 degrees depending on calculation methods (Fig. 5.22). It shifts to lower values and broadens with increasing temperature (Kuzuu et al., 2004).

The average bond angles of the simulated SiO_2 glass and melt structures decrease with increasing pressure by ~21% between ambient pressure at about 80 GPa (Li et al., 2014; Fig. 5.23). In contrast, the O—Si—O angle is much less compressible with a decrease of only 4.6% in this pressure range according to the same calculations. The Si—O bond distance also decreases from slightly above 1.6 Å near ambient pressure, but with a rapid increase to slightly more than 1.8 Å near 20 GPa and as much as 2.2 Å at near 80 GPa, where the glass density would have increased to 4.8 g/cm^3, which is a nearly 120% density increase (Fig. 5.23B). Eventually there will be coordination transformation of Si^{4+} from dominantly fourfold at and near ambient pressure to sixfold coordination at pressures above 10 GPa (Della Valle and Venuti, 1996; Horbach, 2008; Li et al., 2014).

Calculated Si—O—Si angles have a distinctly asymmetric distribution or even two maxima (Kim et al., 2012) (Fig. 5.22). Such an asymmetry could point to coexisting structures linked into rings having different numbers of tetrahedra (Galeener, 1982; Hench and West, 1995; Harkless et al., 1996; Barmes et al., 2006).

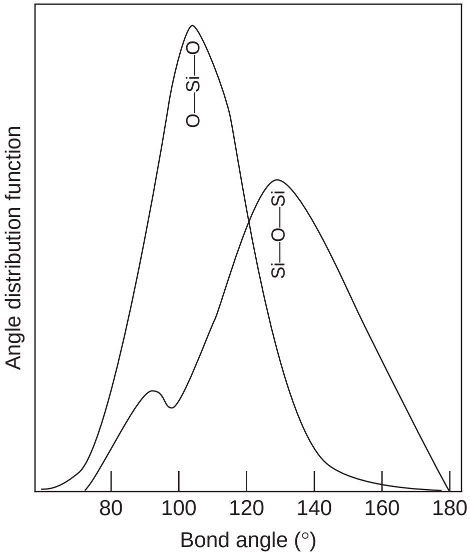

FIG. 5.22 Angle distribution function of liquid SiO_2 calculated with molecular dynamics simulation at 3120 K and ambient pressure. *(Calculation by Kim et al., 2012.)*

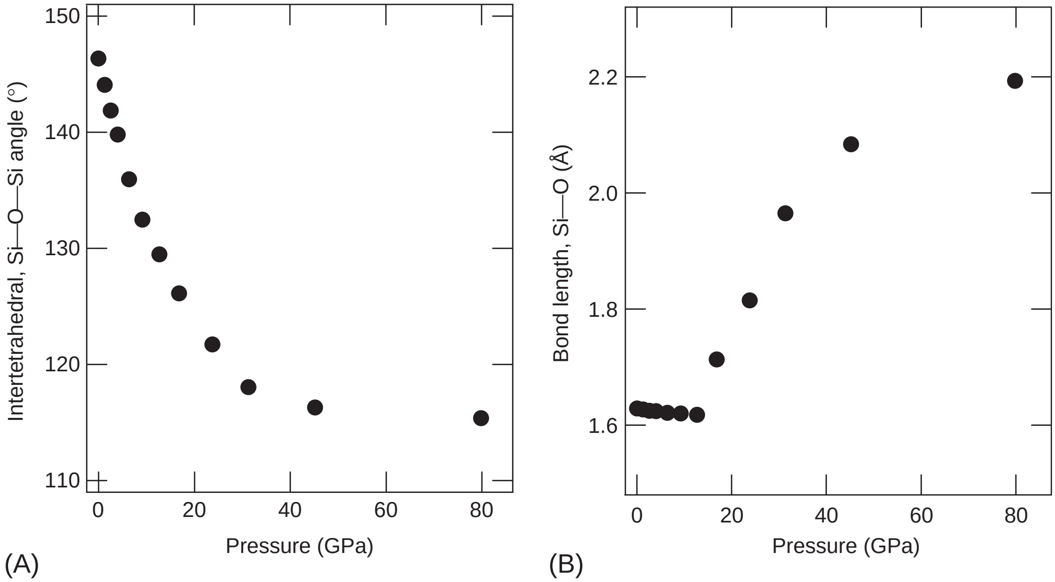

FIG. 5.23 Calculated structural changes in SiO_2 glass with pressure. (A) Si—O—Si angle compression. (B) Si—O bond lengthening. *(Calculation results from Li et al., 2014.)*

The stability of these structures has also been investigated through enthalpy calculations. Whereas Galeener (1982) found a minimum energy for 4-membered rings in early ab initio molecular dynamics simulations, molecular orbital calculations made by Hench and West (1995) with two different methods yielded a very flat minimum between 4- and 6-membered rings (Fig. 5.24) in spite of differences between the obtained bond distances and angles in three-dimensional-interconnected networks of SiO_4 tetrahedra. Interestingly, the results in best agreement with experimental data point to 4- or 5-membered rings (Fig. 5.24B). This conclusion generally is not consistent with the results from Barmes et al. (2006), who concluded that there is an approximately Gaussian distribution of number of rings centered at number 6 at ambient pressure for either the glass or the high-temperature liquid.

At high pressure, however, fourfold coordinated Si^{4+} becomes less important, whereas the proportion of sixfold coordination increases. This evolution can also be seen for the fivefold coordinated Si^{4+}, but there may be a flat abundance maximum near 30 GPa (Hung et al., 2007; Horbach, 2008; see also Fig. 5.25). At high pressure, the abundance of fourfold coordinated Si^{4+} increases with temperature, whereas that of sixfold coordinated Si^{4+} decreases. The $^{[5]}Si^{4+}$ appears less sensitive to temperature at high pressure (Horbach, 2008). We also note that the relative proportions of the calculated coordination states differ from one study to another, although the general trends as a function of temperature and pressure are similar.

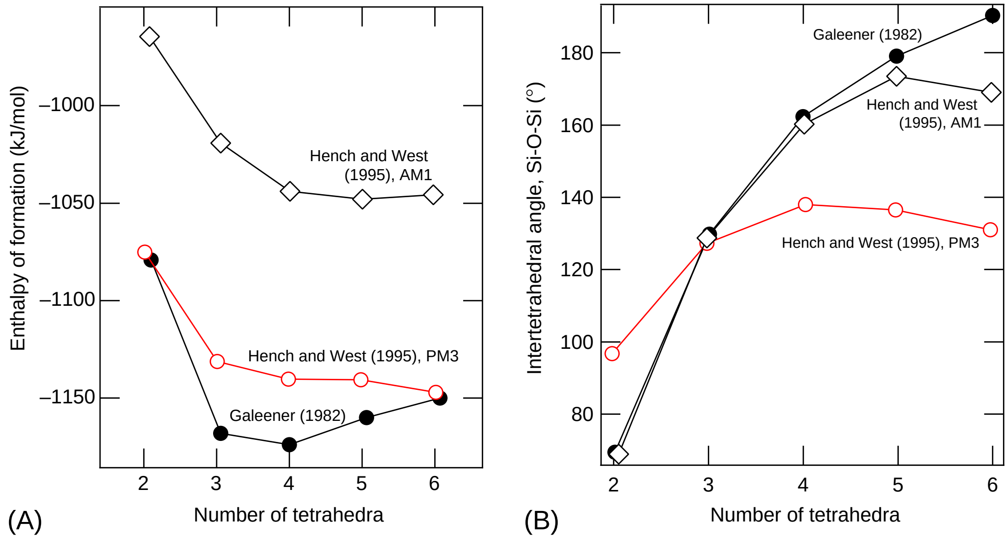

FIG. 5.24 Results of molecular orbital calculations of geometric features of three-dimensionally interconnected rings. (A) Number of tetrahedra versus enthalpy of formation. (B) Intertetrahedral angle versus number of tetrahedral. *(Results from Galeener, 1982; Hench and West, 1995.)*

FIG. 5.25 Evolution of Si^{4+} species of different coordination with oxygen (4, 5, 6) as a function of pressure at 3580 K. *Redrawn from Horbach (2008).*

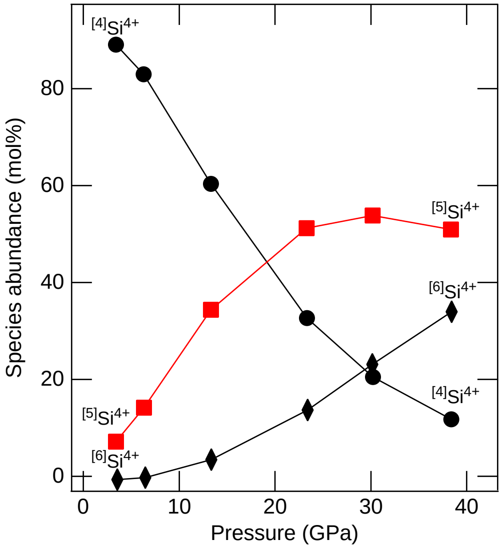

5.4.4 Direct Structure Determination

Thermodynamic data indicate that bond breakage and reassembly do not play major roles in glassy and molten SiO_2 (Table 5.1). However, there are particular problems in studies of glass structure because of very high melt viscosity and low atomic diffusivities, which makes the structure (and properties) of SiO_2 glass difficult to determine, because they may depend not only on time, but also on the pressure-temperature pathways followed to produce a glass.

5.4.5 Bond Angles and Bond Lengths

Together with Si—O bond lengths, the intertetrahedral (Si—O—Si) and torsion angle (O—Si—O) distributions have been investigated for SiO_2 glass by a number of spectroscopic methods (Mauri et al., 2000; Shimada et al., 2002; Tucker et al., 2005; Malfait et al., 2008; Mei et al., 2008; Charpentier et al., 2009). In a review of experimental data for SiO_2 glass, Malfait et al. (2008) found average Si—O—Si angles of 149 ± 6 degrees and 147 ± 4 degrees from X-ray and NMR data, respectively, which compare well with the 149 ± 6 degrees derived from various simulations.

In agreement with these results, Charpentier et al. (2009) derived from their ^{17}O and ^{29}Si NMR data an Si—O—Si angle of 147 ± 11 degrees and an Si—O distance of 1.60 ± 0.01 Å, and in addition reported a broad correlation between increases of these angles and decreases of these distances (Fig. 5.26). In a recent two-dimensional dynamic angle ^{17}O NMR study, Clark et al. (2004) reported the angle maximum at 147 degrees, which, of course, is in complete accord with the Charpentier et al. (2009) angle of 147 ± 11 degrees from oxygen-17 NMR data. From the ^{29}Si chemical shift from NMR spectra, Mauri et al. (2000) suggested two possible models (Fig. 5.27), which they obtained by fitting their ^{29}Si NMR data to an angle distribution function, $p(\theta)$, of two different forms. In particular, one of their models (model 2 in Fig. 5.27) shows a distinct asymmetry toward the higher angles, also with the total angle distribution

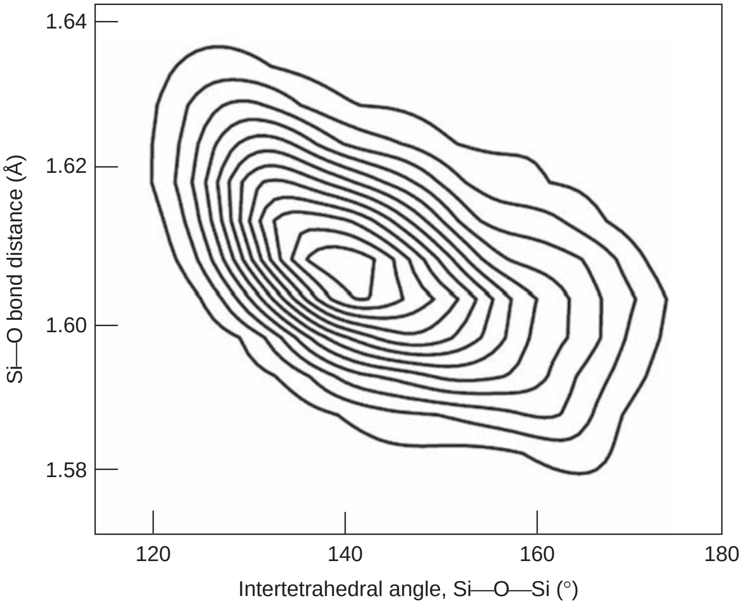

FIG. 5.26 Relationship between intertetrahedral angle, Si—O—Si, and Si—O bond length from NMR data modeling by Charpentier et al. (2009).

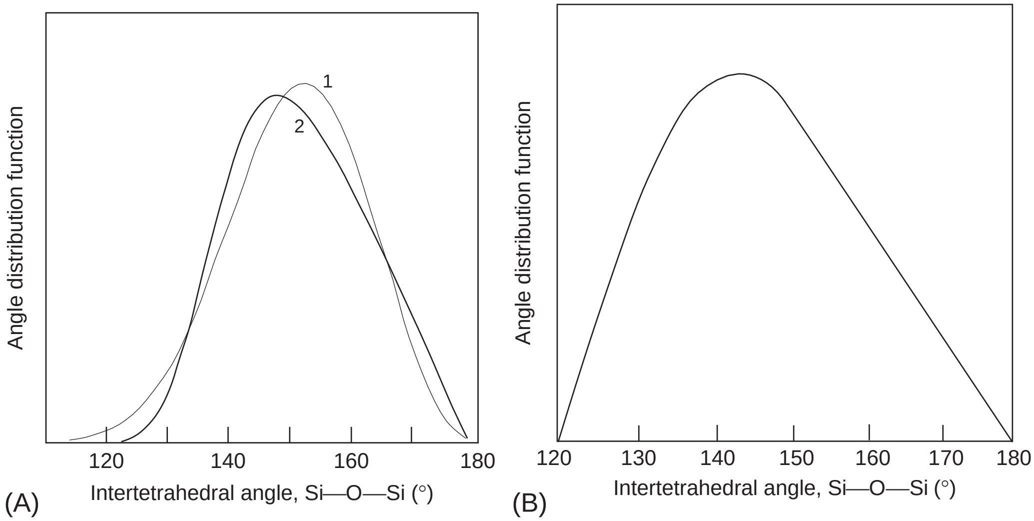

FIG. 5.27 Angle distribution functions from X-ray and ^{29}Si MAS NMR data. (A) X-ray-based angle distribution function. (B) NMR-based angle distribution function (Mozzi and Warren, 1969; Mauri et al., 2000).

between about 120 and 180 degrees, as in the case of the angle distribution from the X-ray data (Fig. 5.27B). This value is quite similar to the maximum in the average Si—O—Si angle distribution from numerical simulation of β-cristobalite at temperatures near its melting point (Bourova et al., 2000) and exactly that in crystalline β-cristobalite (Clark et al., 2004). It is is slightly higher than that typically concluded on the basis of numerical simulations at ambient pressure, which is in the range ~140–150°C (Dracinsky et al., 2011; Kim et al., 2012; Li et al., 2014).

5.4.5.1 *Pressure and Temperature*

McMillan and Wolf (1995) suggested that the three-dimensionally interconnected open network of glassy and molten SiO_2 encounters a deformation limit when the volume reaches about 17 cm^3/mol. At or near this value, the material would reach a state where oxygen is in or near a cubic body-centered packing (see also Hazen et al., 1989), with Si—O—Si angles near 120 degrees, and where the Si atoms would be in or near nonbonding contact. According to the equation-of-state of vitreous SiO_2, the 17 cm^3 molar volume is reached at a pressure of about 15–20 GPa at 25°C (Karki et al., 2007; Wakabayashi et al., 2011). Hence, a further pressure increase should cause a disruption of the SiO_2 network through Si^{4+}coordination changes.

Experimental data support this view. For example, the Raman spectrum of vitreous SiO_2 undergoes dramatic changes between about 8 and 27 GPa (Fig. 5.28). At high pressure, the main peak is a broad band with a maximum near 600 cm^{-1}. Hemley et al. (1986) suggested that this spectrum reflects at least a portion of the Si^{4+} in oxygen coordination polyhedra with more than four oxygens. The infrared spectrum of vitreous SiO_2 above 20 GPa is also consistent with at least a partial coordination transformation of Si^{4+} (Williams et al., 1993).

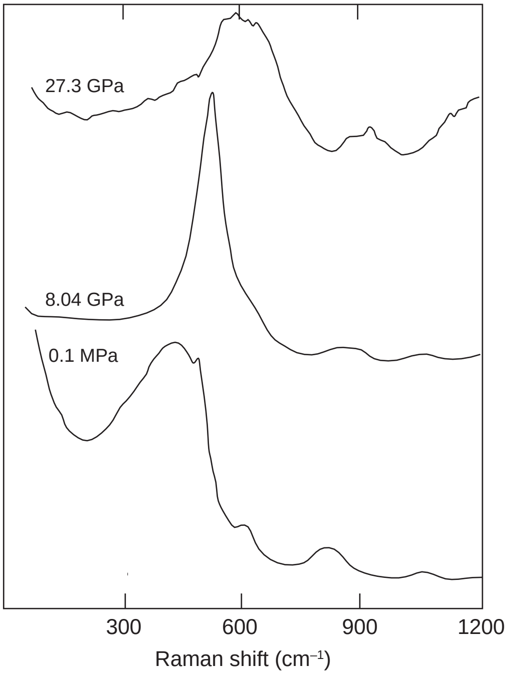

FIG. 5.28 Raman spectra of SiO_2 glass at 25°C at the indicated pressures (Hemley et al., 1986).

Results from X-ray diffraction studies of SiO_2 glass to 42 GPa point to a significant lengthening of the Si—O bond (Meade et al., 1992). Meade et al. (1992) concluded that the Si—O bond length increases from 1.59 to 1.64 Å between ambient pressure and 28 GPa and then to 1.66 Å at 42 GPa. In stishovite, where Si^{4+} is in sixfold coordination, the Si—O bond length is 1.69 Å at 42 GPa (Meade et al., 1992). Thus, the X-ray data are consistent with at least a partial coordination transformation of Si^{4+} at pressures higher than about 15 GPa. These data also agree with the Raman and infrared information (Hemley et al., 1986, 1994; Williams et al., 1993).

Most of the experimental data at high pressure are from X-ray diffraction recorded in diamond-anvil cells at high pressure and room temperature (Benmore et al., 2010; Sato and Funamori, 2010; Wakabayashi et al., 2011). Notably, one study by Inamura et al. (2004), to 19.2 GPa, was made with a multianvil, high-pressure apparatus up to 900°C.

The bond angle distribution and Si—O bond lengths in vitreous and molten SiO_2 change with increasing pressure. Whereas the experimental data suggest only minor variations in the oxygen coordination number for pressures lower than 20 GPa, changes from about four- to sixfold coordination are suggested between 20 and 100 GPa (Devine et al., 1987; Benmore et al., 2010; Sato and Funamori, 2010). In parallel, the maximum of the bond angle distribution shifts to lower values so that ^{29}Si NMR data indicate an approximate 5-degree decrease in the Si—O—Si angle for a glass densified at 7 GPa and 700°C (Devine et al., 1987). As shown in Fig. 5.29, the angle distribution is distinctly asymmetric toward higher values, as previously noted in Fig. 5.26 for X-ray and other NMR data (Mozzi and Warren, 1969; Mauri et al., 2000).

FIG. 5.29 Intertetrahedral angle (Si—O—Si) distribution of vitreous SiO_2 at 0.01 MPa and after permanently densified at 7 GPa/700°C (Devine et al., 1987).

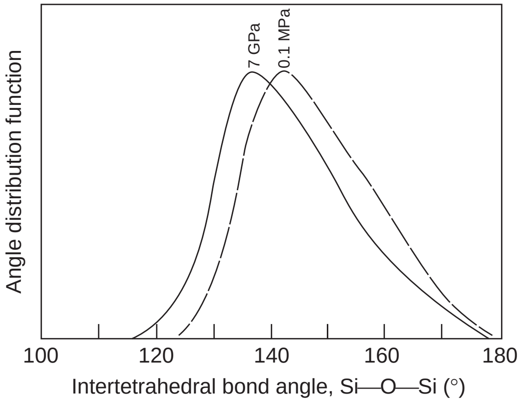

As also discussed elsewhere, decreasing intertetrahedral bond angle is associated with increasing Si—O bond lengths (see Chapter 2, Section 2.2). Such features in the structure of glassy and molten SiO_2 were also discussed previously in the summary of results from numerical simulations (see, e.g., Fig. 5.23), and also are clearly evident in the response of the SiO_2 glass structure to increased pressures (Benmore et al., 2010; Sato and Funamori, 2010; Wakabayashi et al., 2011). The Si—O distance increases from near 1.6 Å at pressures below about 20 GPa, but then reaches more than 1.70 Å in the 30–40 GPa pressure range (Fig. 5.30). A rapid shift of the maximum in the bond angle distribution from 144 to 137 degrees has been noted between 10 and 15 GPa (Sonneville et al., 2013).

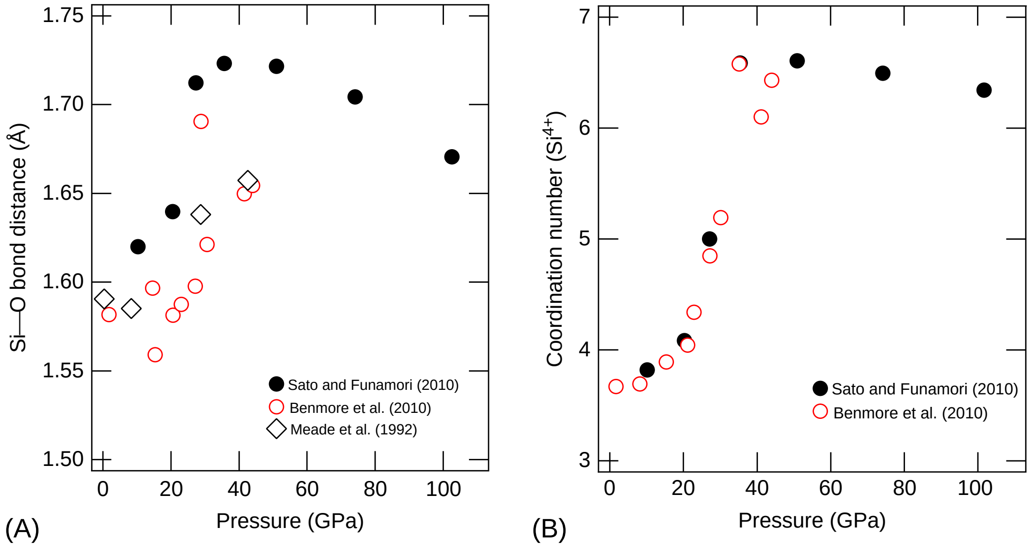

FIG. 5.30 (A) Measured bond length evolution in SiO_2 glass at ambient temperature as a function of pressure. With the summary information on Si—O bond length vs Si^{4+} coordination number, the experimental data from "A" were used to deduce coordination number of Si^{4+} (Sato and Funamori, 2010; Benmore et al., 2010). *(Data from Sato and Funamori, 2010; Benmore et al., 2010; Meade et al., 1992.)*

The unusual temperature dependence of many physical properties of SiO_2 glass and melt suggests that temperature may cause unusual structural changes in these materials. One must determine, therefore, to what extent the structure of the melt differs from that of its glass. The extent to which silicate structures change with increasing temperatures above the glass transition has been addressed by means of high-temperature Raman spectroscopy. Broadly speaking, the Raman spectra of SiO_2 glass and supercooled liquid resemble one another on both sides of the glass transition (Fig. 5.31). Thus, to a first approximation, the structures of SiO_2 melt above the glass transition temperature, T_g, and that of SiO_2 glass below this temperature appear similar. Interestingly, when cristobalite is heated to temperatures near its melting point, its Raman spectrum becomes more similar to that of SiO_2 melt (Fig. 5.32). This observation is also consistent with the numerical simulations of Bourova et al. (2000). These similarities are also in agreement with the concept that the structure of SiO_2 melt shares common traits with that of its liquidus phase, β-cristobalite. Moreover, these conclusions also are in accord with high-temperature Si K-edge XANES spectra to similar temperatures (de Ligny et al., 2009).

Even though the Raman spectra of SiO_2 glass and melt resemble one another (Fig. 5.29), there are subtle but important features that may reflect temperature-induced structural changes as SiO_2 liquid is heated up. For example, the frequency of the 440 cm^{-1} band in the spectra of SiO_2 exhibits a distinct change of slope at a temperature in the glass transition range (McMillan et al., 1994). None of the other bands in the Raman spectrum shows a similar temperature-dependent frequency. McMillan et al. (1994) suggested that the variation of the 440 cm^{-1} band reflects the response to temperature of Si—O—Si angles in the network. The break in the slope of the Raman frequency-temperature relationship in the glass transition range was taken to suggest that there exist entities with small Si—O—Si angles in relaxed

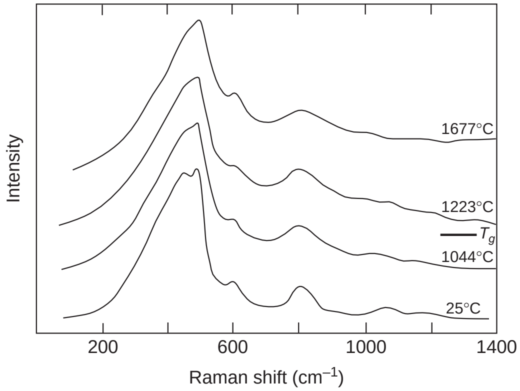

FIG. 5.31 Unpolarized Raman spectra of SiO_2 glass and supercooled melt at temperatures indicated on individual spectra (McMillan et al., 1994). T_g indicates the glass transition temperature of SiO_2 (Richet et al., 1982).

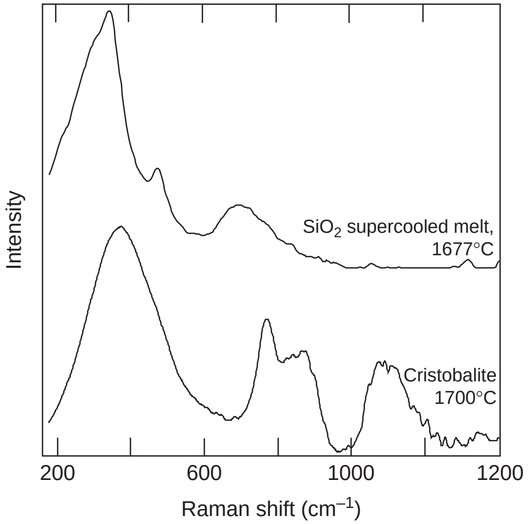

FIG. 5.32 Unpolarized Raman spectra recorded at 1677°C for supercooled SiO_2 melt (McMillan et al., 1994) and at 1700°C for cristobalite. *Redrawn from Richet and Mysen (1999).*

SiO_2 melt but that these entities are less evident in SiO_2 glass. This conclusion indicates that the intertetrahedral angle in molten SiO_2 decreases at a rate of about 1 degree per 100 K temperature increase.

5.4.6 Multiple Structural Units

Interestingly, all structure studies of vitreous SiO_2 are consistent with a maximum in the angle distribution resembling the Si—O—Si angle in silica polymorphs. Clark et al. (2004) pointed out, for example, that the structure of vitreous and molten silica consists predominantly of three-dimensionally interconnected, 6-membered rings. A smaller number of tetrahedra yields Si—O—Si angles that may be too narrow compared with experimental and simulation data (Uchino et al., 1998). Of course, from the calculations of Kim et al. (2012) discussed in Section 5.4.3, a minimum number of four seems more realistisc.

As noted early on by Vuckevitch (1972), two or more average structures may coexist in glassy and molten SiO_2. If SiO_2 melt and glass have more than one average structure, this feature may be reflected in the distribution of average Si—O—Si angles, which is, of course, what is seen in the asymmetric angle distributions in Figs. 5.27–5.29 (Mozzi and Warren, 1969; Devine et al., 1987; Poulsen et al., 1995; Mauri et al., 2000).

The results of the energy calculations summarized in Figs. 5.24 lead to the suggestion that 4-, 5-, and 6-membered rings are likely to dominate the structure of vitreous SiO_2. However, in these calculations, the energy penalty associated with increasing the number of tetrahedra further is quite small. In fact, in the calculations by Harkless et al. (1996), there is essentially no effect on enthalpy of formation by increasing the number of tetrahedra beyond 6. Interestingly, among silicate crystals with three-dimensionally interconnected structure, only 4- and 6-membered rings have been documented (e.g., Zoltai and Buerger, 1960). The β-cristobalite structure consists of 6-membered rings.

A detailed theoretical study led to the conclusion that the 490 and 605 cm^{-1} modes in the Raman spectra of vitreous SiO_2 are indeed essentially decoupled, which most likely reflect the presence of 4- and 3-membered rings, respectively (Barrio et al., 1993). This interpretation is consistent with that of Sykes and Kubicki (1996), which was based on numerical simulations of silicate clusters. In this model, the 3-membered ring would be essentially planar with an intertetrahedral angle near 130 degrees. With the general consensus from spectroscopy and simulation studies that the angle maximum is near 150 degrees, however, rings with such a small number of tetrahedra seems unrealistic (see also Clark et al., 2004).

The Raman spectra of vitreous and molten SiO_2 have been used extensively in the discussion of ring distributions. In analogy with silicate crystals, Mammone et al. (1981) and Sharma et al. (1981) suggested from the Raman spectra of vitreous SiO_2 that there are, on average, two kinds of rings with either 4 or 6 Si. The Raman signals used to document their presence were the 495 and 605 cm^{-1} bands. Seifert et al. (1982) examined the entire Raman spectrum and concluded that the spectra reflect two coexisting, three-dimensionally interconnected structures whose intertetrahedral angles, θ_1 and θ_2, differed, on average, by $5-10$ degrees. This view is in accord with the model of Vuckevitch (1972) who envisioned a structure analogous to that of the α- and β-polymorphs of cristobalite with an Si—O—Si angle difference of 8 degrees. A simple cristobalite-like model is also appealing in that it accounts for the very small or negligible ΔH_f, ΔV_f, and ΔS_f of silica polymorphs (Table 5.1).

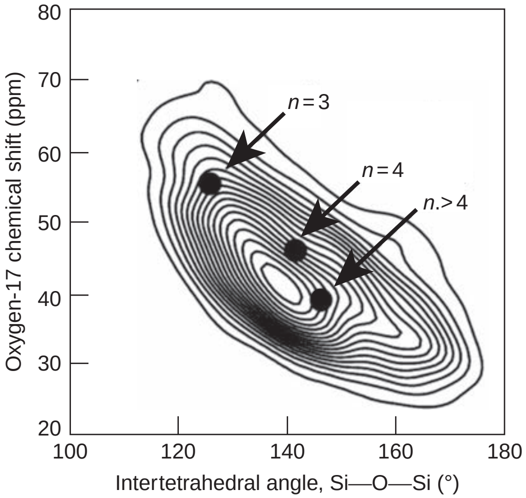

FIG. 5.33 Relationship between bond angle and oxygen-17 isomer shift with locations for SiO_4 rings with three, four, and more than four tetrahedra (Charpentier et al., 2009).

The broad range of ^{17}O NMR shifts with Si—O—Si angle is consistent with multiple coexisting rings made up of at least three and more tetrahedra (Charpentier et al., 2009; see also Fig. 5.33). A change from three to four tetrahedra in a ring results in a ~15% Si—O—Si angle increase (Fig. 5.33), but in an increase of the Si—O bond distance of less than 0.02 Å or ~1% (Charpentier et al., 2009).

5.5 STRUCTURE-PROPERTY RELATIONS

Molten and glassy SiO_2 are unique among silicates in that their differences in thermodynamic properties are so small (Table 5.1) that bond breakage and reformation are unlikely. This suggestion is substantiated by the observation that the high-temperature structure of β-cristobalite closely resembles that of SiO_2 glass and melt to at least medium-range nearest neighbors (Hosemann et al., 1991; Bourova et al., 2000; Kohara and Suzuya, 2005; Bowron, 2008). In other words, thermodynamic data, together with the structural information, lead to the conclusion that melting merely involves changes in the long-range disordering of the crystalline structure.

Configurational entropy is usually ignored in structural models of vitreous silica. An exception is the estimate derived by Bell and Dean (1968) within the framework of random network theory. Their upper bound of 1.9 J/g atom K is slightly higher than the experimental value, but their recommended range of 1.1–1.25 J/g atom K is too low. However, the change in SiO_2 glass and melt structure with temperature is the small, only about 10%, change in heat capacity across the glass transition (Richet et al., 1982). In other words, structural relaxation of SiO_2 supercooled liquid above its glass transition likely involves minor adjustments in long-range order. This could also be the reason for the near Ahrrenian nature of transport properties of SiO_2 (Fig. 5.15).

Multiple ring structures with different numbers of SiO_4 tetrahedra do represent an intuitive problem when considering the thermodynamics of melting of cristobalite or any other SiO_2 polymorphs, because of the very small differences between SiO_2 and the crystalline liquidus phase (Richet et al., 1982; Stebbins et al., 1983; Bourova and Richet, 1998). The cristobalite structure can be viewed as consisting of 6-membered, three-dimensionally interconnected rings (Downs and Palmer, 1994). Thus, the thermochemical data would suggest that SiO_2 melt consists predominantly of ring structures resembling those of cristobalite (six Si atoms per ring) and not rings with a smaller number of SiO_4 tetrahedra. However, the structural data for SiO_2 melt and glass seem to indicate structures dominated by coexisting rings where the number of SiO_4 tetrahedra seem to be between 4 and 6 or perhaps even 3 to 6 or 7 (Sykes and Kubicki, 1996; Harkless et al., 1996; Hench and West, 1995; Kim et al., 2012). If SiO_2 melt and crystals contain different numbers of SiO_4 tetrahedra, melting most likely would result in significant differences in thermodynamic properties, which is not the case (Table 5.1). It may be that the ring systematics depends on temperature leading to more and more structurally open 6-membered rings as SiO_2 liquid is heated up or that the abundance of 4- and 3-membered rings is small compared with the abundance of 6-membered rings.

Volume properties such as compression and expansivity of vitreous SiO_2 have been related to the response of Si—O—Si and O—Si—O angles to pressure. The Si—O—Si angle is particularly compressible, which likely is the explanation for the anomalously high compressibility of amorphous SiO_2 (Della Valle and Venuti, 1996; Huang and Kieffer, 2004; Clark et al., 2014).

References

Ainslie, N.G., Mackenzie, J.D., Turnbull, D., 1961. Melting kinetics of quartz and cristobalite. J. Phys. Chem. 65, 1718–1724.

Akaogi, M., Navrotsky, A., 1984. The quartz-coesite-stishovite transformations: new calorimetric measurements and calculations of phase diagrams. Phys. Earth Planet. Int. 36, 124–134.

Allègre, C.J., Poirier, J.P., Humler, E., Hofmann, A.W., 1995. The chemical composition of the Earth. Earth Planet. Sci. Lett. 134, 515–526.

Angell, C.A., 1985. Strong and fragile liquids. In: Ngai, K.L., Wright, G.B. (Eds.), Relaxation in Complex Systems. U.S. Department of Commerce Technical Information Service, Springfield, VA, pp. 3–11.

Angell, C.A., Kanno, H., 1976. Density maxima in high-pressure supercooled water and liquid silicon dioxide. Science 193, 1121–1122.

Bacon, J.F., Hasapis, A.A., Wholley, J.W., 1960. Viscosity and density of molten silica and high silica content glasses. Phys. Chem. Glasses 1, 90–98.

Barmes, F., Soulard, L., Mareschal, M., 2006. Molecular dynamics of shock-wave indicated structural changes in silicate glass. Phys. Rev. B.. 73224108.

Barrio, R.A., Galeener, F.L., Martinez, E., Elliott, R.J., 1993. Regular ring dynamics in AX2 tetrahedral glasses. Phys. Rev. B 48, 15672–15689.

Bell, R.J., Dean, P., 1968. The configurational entropy of vitreous silica in the random network theory. Phys. Chem. Glasses 9, 125–127.

Bell, R.J., Dean, P., 1970. Atomic vibrations in vitreous silica. Disc. Farady Soc. 50, 55–61.

Bell, R.J., Hibbins-Butler, D.C., 1976. Raman scattering by normal modes in vitreous silica, germania and beryllium fluoride. J. Phys. Chem. 9, 2955–2959.

Bell, T., Hetherington, G., Jack, K.H., 1962. Water in vitreous silica. Part 2: some aspects of hydrogen-water-silica equilibria. Phys. Chem. Glasses 3, 141–146.

Bell, R.J., Carnevale, A., Kurkjian, C.R., Peterson, G.E., 1980. Structure and phonon spectra of SiO_2, B_2O_3 and mixed SiO_2-B_2O_3 glasses. J. Non-Cryst. Solids 35, 1185–1190.

Benmore, C.J., Soignard, E., Amin, S.A., Guthrie, M., Shastri, S.D., Lee, P.L., Yarger, J.L., 2010. Structural and topological changes in silica glass at pressure. Phys. Rev. B. 81.

Benoit, M., Ispas, S., Tuckerman, M.E., 2001. Structural properties of molten silicates from ab initio molecular-dynamics simulations: comparison between CaO-Al_2O_3-SiO_2 and SiO_2. Phys. Rev. B. 64, 224205.

Bockris, J.O.'.M., Mackenzie, J.O., Kitchner, J.A., 1955. Viscous flow in silica and binary liquid silicates. Trans. Farad. Soc. 51, 1734–1748.

Bockris, J.O.M., Tomlinson, J.W., White, J.L., 1956. The structure of the liquid silicates. Partial molar volumes and expansivities. Trans. Farad. Soc. 52, 299–310.

Bottinga, Y., 1991. Thermodynamic properties of silicate liquids at high pressure and their bearing on igneous petrology. In: Perchuk, L., Kushiro, I. (Eds.), Physical Chemistry of Magmas. Springer, New York, pp. 213–232.

Bottinga, Y., Richet, P., 1995. Silicate melts: the "anomalous" pressure dependence of the viscosity. Geochim. Cosmochim. Acta 59, 2725–2732.

Bourova, E., Richet, P., 1998. Quartz and cristobalite: high-temperature cell parameters and volumes of fusion. Geophys. Res. Lett. 25, 2333–2336.

Bourova, E., Parker, S.C., Richet, P., 2000. Atomistic simulation of cristobalite at high temperature. Phys. Rev. B 62, 12052–12061.

Bourova, E., Parker, S.C., Richet, P., 2004. High-temperature structure and dynamics of coesite (SiO_2) from numerical simulations. Phys. Chem. Miner. 31, 569–579.

Bowen, N.L., 1928. The Evolution of the Igneous Rocks. Princeton University Press, Princeton, NJ.

Bowron, D.T., 2008. An experimentally consistent atomistic structural model of silica glass. Mater. Sci. Eng. B 149, 166–170.

Brébec, G., Seguin, R., Sella, C., Bevenot, J., Martin, J.C., 1980. Diffusion du silicium dans la silice amorphe. Acta Metall. 28, 327–333.

Bridgman, P.W., Simon, I., 1953. Effects of very high pressure on glass. J. Appl. Phys. 24, 405–413.

Bruckner, R., 1970. Properties and structure of vitreous silica. II. J. Non-Cryst. Solids 5, 177–216.

Brückner, R., 1971. Metastable equilibrium density of hydroxyl-free synthetic vitreous silica. J. Non-Cryst. Solids 5, 281–285.

Bucaro, J.A., Dardy, H.D., 1976. Equilibrium compressibility of glassy SiO_2 between the transformation and the melting temperature. J. Non-Cryst. Solids 20, 149–151.

Casey, D.N., Hetherington, G., Winterbum, J.A., Yates, B., 1976. The influence of the hydroxyl content upon the specific heat capacity of vitreous silica at elevated temperatures. Phys. Chem. Glasses 17, 77–82.

Cernok, A., Boffa Ballaran, T., Caracas, R., Miyajima, N., Bykova, E., Prakapenka, V., Liermann, H.-P., Dubrovinski, L., 2014. Pressure-induced phase transitions in coesite. Am. Mineral. 99, 755–763.

Charpentier, T., Kroll, P., Mauri, F., 2009. First-principles nuclear magnetic resonance structural analysis of vitreous silica. J. Phys. Chem. C 113, 7917–7929.

Clark, T.M., Grandinetti, P.J., Florian, P., Stebbins, J.F., 2004. Correlated structural distributions in silica glass. Phys. Rev. B 70, 1–8.

Clark, A.N., Lesher, C.E., Jacobsen, S.D., Sen, S., 2014. Mechanisms of anomalous compressibility of vitreous silica. Phys. Rev. B. 90.

Cornet, A., Martinez, V., De Ligny, D., Champagnon, B., Martinet, C., 2017. Relaxation processes of densified silica glass. J. Chem. Phys.. 146.

Dachille, F., Zeto, R.J., Roy, R., 1963. Coesite and stishovite: stepwise reversal transformations. Science 140, 991–993.

de Ligny, D., Neuville, D.R., Cormier, L., Roux, J., Henderson, G.S., Panczer, G., Shoval, S., Flank, A.M., Lagarde, P., 2009. Silica polymorphs, glass and melt: an in situ high temperature XAS study at the Si K-edge. J. Non-Cryst. Solids 355, 1099–1102.

Della Valle, R.G., Venuti, E., 1996. High-pressure densification of silica glass: a molecular-dynamics simulation. Phys. Rev. B 54, 3809–3816.

Devine, R.A., Dupree, R., Farnan, I., Capponi, J.J., 1987. Pressure-induced bond-angle variation in amorphous SiO2. Phys. Rev. B 35, 2560–2562.

Dietz, E.D., Baak, T., Blau, H.H., 1970. The superheating of an albite feldspar. Z. Kristallogr. 132, 340–360.

Dietzel, A., Wickert, H., 1956. Der Verlauf der Glasigkeit im System Na_2O-SiO_2. Glastechn. Ber. 29, 1–4.

Douglas, R.W., Isard, J.O., 1951. Density changes in fused silica. J. Soc. Glas. Technol. 35, 206–225.

Downs, R.T., Palmer, D.C., 1994. The pressure behavior of alpha cristobalite. Am. Mineral. 79, 9–14.

Dracinsky, M., Benda, L., Bour, P., 2011. Ab initio modeling of fused silica, crystal quartz, and water Raman spectra. Chem. Phys. Lett. 512, 54–59.

Fabrichnaya, O., Saxena, S.K., Richet, P., Westrum Jr., E.F., 2004. Thermodynamic Data, Models and Phase Diagrams in Multicomponent Oxide Systems. Springer, Berlin.

Fanderlik, I., 1990. Silica Glass and Its Application. Elsevier, Amsterdam.

Fontana, E.H., Plummer, W.A., 1966. A study of viscosity-temperature relationship in the GeO_2 and SiO_2 systems. Phys. Chem. Glasses 7, 139–146.

Frank, R.C., Swets, D.E., Lee, R.W., 1961. Diffusion of neon isotopes in fused quartz. J. Chem. Phys. 35, 1551–1459.

Fratello, V.J., Hays, J.F., Spaepen, F., Turnbull, D., 1980. The mechanism of growth of quartz crystals into fused silica. J. Appl. Phys. 51, 4718–4728.

Frischat, G.H., 1968. Sodium diffusion in SiO_2 glass. J. Am. Ceram. Soc. 51, 528–530.

Frischat, G.H., 1970. Natriumdiffusion in verschiedenen Kieselgläsern. Glastechn. Ber. 43, 482–488.

Galeener, F.L., 1982. Planar rings in glasses. Solid State Commun. 44, 1037–1040.

Gaudin, M.A., 1839. Sur les propriétés du cristal de roche fondu. C.R. Acad. Sci. 8, 678–679 and 711–713.

Geissberger, A.E., Bray, P.J., 1983. Determination of the structure and bonding in amorphous SiO2 using ^{17}O NMR. J. Non-Cryst. Solids 54, 121–137.

Ghiorso, M.S., Kress, V.C., 2004. An equation of state for silicate melts. II. Calibration of volumetric properties at 105 Pa. Am. J. Sci. 304, 679–751.

Gong, W.L., Wang, L.M., Ewing, R.C., Fei, Y., 1996. Surface and grain-boundary amorphization: thermodynamic melting of coesite below the glass transition temperature. Phys. Rev. B 53, 2155–2158.

Goodman, C.H.L., 1987. A new way of looking at glass. Glass Techn. 28, 19–29.

Greig, J.W., 1927. On liquid immiscibility in the system $FeO\text{-}Fe_2O_3\text{-}Al_2O_3\text{-}SiO_2$. Am. J. Sci. 14, 473–484.

Grimley, D.I., Wright, A.C., Sinclair, R.N., 1990. Neutron scattering from vitreous silica, IV. Time-of-flight diffraction. J. Non-Cryst. Solids 119, 49–64.

Grimsditch, M., 1984. Polymorphism in amorphous SiO2. Phys. Rev. Lett. 52, 2379–2381.

Grimsditch, M., Popova, S., Brazhkin, V.V., Voloshin, R.N., 1994. Temperature-induced amorphization of SiO_2 stishovite. Phys. Rev. B. 50, 12984–12986.

Grosmaire-Vandorpe, M., Lasjaunias, J.C., Penn, G., 1983. Influence of thermal treatments on the low-temperature specific heat of Suprasil-W vitreous silica. J. Non-Cryst. Solids 57, 157–166.

Harkless, J.A.W., Stillinger, D.K., Stillinger, F.H., 1996. Structures and energies of SiO_2 clusters. J. Phys. Chem. 100, 1098–1103.

Hazen, R.M., Finger, L.W., Hemley, R.J., Mao, H.K., 1989. High-pressure crystal chemistry and amorphization of α-quartz. Solid State Commun. 72, 507–511.

Heaney, P.J., 1994. Structure and chemistry of the low-pressure silica polymorphs. In: Heaney, P.J., Prewitt, C.T., Gibbs, G.V. (Eds.), Silica: Physical Behavior, Geochemistry and Materials Applications. Mineralogical Society of America, Washington, DC, pp. 1–40.

Hemley, R.J., Mao, H.K., Bell, P.M., Mysen, B.O., 1986. Raman spectroscopy of SiO_2 glass at high pressure. Phys. Rev. Lett. 57, 747–750.

Hemley, R.J., Jephcoat, A.P., Mao, H.K., Ming, L.C., Manghnani, M.H., 1988. Pressure-induced amorphization of crystalline silica. Nature 334, 52–54.

Hemley, R.J., Prewitt, C.T., Kingma, K.J., 1994. High-pressure behavior of silica. In: Heaney, P.J., Prewitt, C.T., Gibbs, G.V. (Eds.), Slica: Physical Behavior, Geochemistry and Materials Properties. Mineralogical Society of America, Washington, DC, pp. 41–82.

Hemmati, M., Moynihan, C.T., Angell, C.A., 2001. Interpretation of the molten BeF_2 viscosity anomaly in terms of a high temperature density maxium, and other waterlike features. J. Chem. Phys. 115, 6663–6671.

Hench, L.L., West, J.K., 1995. Molecular orbital models of silica. Annu. Rev. Mater. Sci. 25, 37–68.

Hermann, W., Rau, H., Ungelenk, J., 1985. Solubility and diffusion of chlorine in silica glass. Ber. Bunsenges. Phys. Chem. 89, 423–426.

Hetherington, G., Jack, K.H., 1962. Water in vitreous silica. Part I. Influence of "water" content on the properties of vitreous silica. Phys. Chem. Glasses 3, 129–133.

Hetherington, G., Jack, K.H., Kennedy, J.C., 1964. The viscosity of vitreous silica. Phys. Chem. Glasses 5, 130–136.

Hoang, V.V., 2006. Structure and dynamic properties of liquid and amorphous GeO_2. J. Phys. Condensed Matter 18, 777–786.

Horbach, J., 2008. Molecular dynamics computer simulation of amorphous silica under high pressure. J. Phys. Condensed Matter. 20.

Hosemann, R., Hindeleh, A.M., Bruckner, R., 1991. Paracrystalline lattice structure of silica glass, alpha- and beta-crystobalite. Phys. Stat. Sol. Appl. Res. 126, 313–324.

Huan, L., Durandurdu, M., Kieffer, J., 2006. Transformation pathways of silica under pressure. Nat. Mater. 5, 977–981.

Huang, L., Kieffer, J., 2004. Amorphous-amorphous transitions in silica glass. II. Irreversible transitions and densification limit. Phys. Rev. B. 69224204.

Huang, L., Duffrene, L., Kieffer, J., 2004. Structural transitions in silica glass: thermo-mechanical anomalies and polyamorphism. J. Non-Cryst. Solids 349, 1–9.

Hung, P.K., Hong, N.V., Vinh, L.T., 2007. Diffusion and structure in liquid silica: a molecular dynamics simulation. J. Phys. Condensed Matter. 19466103.

Inamura, Y., Katayama, Y., Utsumi, W., Funakoshi, K., 2004. Transformations in the intermediate-range structure of SiO_2 glass under high pressure and temperature. Phys. Rev. Lett. 93, 01550.

Jackson, I., 1976. Melting of the silica isotypes SiO_2, BeF_2 and GeO_2 at elevated pressures. Phys. Earth Planet. Int. 13, 219–231.

Kakiuchida, H., Saito, K., Ikushima, A.J., 2003. Precise determination of fictive temperature of silica glass by infrared absorption spectrum. J. Appl. Phys. 93, 777–779.

Karki, B.B., Bhattarai, D., Stixrude, L., 2007. First-principles simulations of liquid silica: structural and dynamical behavior at high pressure. Phys. Rev. B. 76.

Kim, M., Khoo, K.H., Chellikowski, J.R., 2012. Simulating liquid and amorphous silicon dioxide using real-space pseudopotentials. Phys. Rev. B. 86054104.

Knoche, R., Dingwell, D.B., Webb, S.L., 1995. Leucogranitic and pegmatitic melt densities: partial molar volumes for SiO_2, Al_2O_3, Na_2O, K_2O, Rb_2O, Cs_2O, Li_2O, BaO, SrO, CaO, MgO, TiO_2, B_2O_3, P_2O_5, F_2O_{-1}, Ta_2O_5, Nb_2O_5 and WO_3. Geochim. Cosmochim. Acta 59, 4645–4652.

Kohara, S., Suzuya, K., 2005. Intermediate-range order in vitreous SiO_2 and GeO_2. J. Phys. Condensed Matter 17, 577–586.

Kondo, K.-I., Ito, S., Sawaoka, A., 1981. Nonlinear pressure dependence of the elastic moduli of fused quartz up to 3 GPa. J. Appl. Phys. 52, 2826–2831.

Konnert, J.H., Karle, L., 1973. The computation of radial distribution functions for glassy materials. Acta Cryst. A29, 702–710.

Konnert, J.H., Karle, J., Ferguson, G.A., 1973. Crystalline ordering in silica and germania glasses. Science 179, 177–178.

Kress, V.C., Carmichael, I.S.E., 1991. The compressibility of silicate liquids containing Fe2O3 and the effect of composition, temperature, oxygen fugacity and pressure on their redox states. Contr. Mineral. Petrol. 108, 82–92.

Krol, D.M., Lyons, K.B., Brawer, S.A., Kurkjian, C.R., 1986. High-temperature light scattering and the glass transition in vitreous silica. Phys. Rev. B33, 4196–4201.

Kühn, B., Schadrack, R., 2009. Thermal expansion of synthetic fused silica as a function of OH content and fictive temperature. J. Non-Cryst. Solids 355, 323–326.

Kuhtetskiy, S.V., Fomenko, E.V., Anshits, A.G., 2016. Molecular dynamics simulation of helium diffusion in vitreous silica. J. Non-Cryst. Solids 443, 47–53.

Kuzuu, N., Yoshie, H., Tamai, Y., Wang, C., 2004. Molecular dynamics study of temperature dependence of volume of amorphous silica. J. Non-Cryst. Solids 349, 319–330.

Laughlin, W.T., Uhlmann, D.R., 1972. Viscous flow in simple organic liquids. J. Phys. Chem. 76, 2317–2325.

Leko, V.K., Meshcheryakova, E.V., 1975. Some features of the effect of redox conditions on the viscosity of electromelted vitreous silicas. Sov. J. Glass Phys. Chem. 1, 242–247.

Leko, V.K., Gusakova, N.K., Meshcheryakova, E.V., Prokhorova, T.I., 1977. The effect of impurity alkali oxides, hydroxyl groups, Al_2O_3, and Ga_2O_3 on the viscosity of vitreous silica. Sov. J. Glass Phys. Chem. 3, 204–210.

Li, N., Sakidja, R., Aryal, S., Ching, W.Y., 2014. Densification of a continuous random network model of amorphous SiO_2 glass. Phys. Chem. Chem. Phys. 16, 1500–1514.

Liang, Y.F., Miranda, C.R., Scandolo, S., 2015. Atomistic pathways of the pressure-induced densification of quartz. Phys. Rev. B. 92. https://dx.doi.org/10.1103/PhysRevB.92.134102.

Macedo, P.B., Napolitano, A., 1968. Inadequacies of viscosity theories for B_2O_3. J. Chem. Phys. 49, 1887–1895.

Machacek, J., Gedeon, O., Liska, M., 2007. Molecular approach to the 5-coordinated silicon atoms in silicate glasses. Phys. Chem. Glasses Eur. J. Glass Sci. Technol. B 48, 345–353.

MacKenzie, J.D., 1960. tructure of some inorganic glasses from high temperature studies. Ch. 8, In: MacKenzie, J.D. (Ed.), Modern Aspects of the Vitreous State. Butterworths, Washington, DC.

Malavasi, G., Menziani, M.C., Pedone, A., Segre, U., 2006. Void size distribution in MD-modelled silica glass structures. J. Non-Cryst. Solids 352, 285–296.

Malfait, W.J., Halter, W.E., Verel, R., 2008. 29Si NMR spectroscopy of silica glass: T1 relaxation and constraints on the Si–O–Si bond angle distribution. J. Non-Cryst. Solids 256, 269–277.

Mammone, J.F., Sharma, S.K., Nicol, M.F., 1981. Ring structures in silica glass—a Raman spectroscopic investigation. Eos 62, 425.

Mauri, F., Pasquarello, A., Pfrommer, B.G., Yoon, Y.-G., Louie, S.G., 2000. Si-O-Si bond-angle distribution in vitreous silica from first-principles ^{29}Si NMR analysis. Phys. Rev. B 62, R4786–R4789.

Mazurin, O.V., Leko, V.V., Komarova, L.A., 1975. Crystallization of silica and titanium-oxide silica corning glasses (codes 7940 and 7071). J. Non-Cryst. Solids 18, 1–9.

McMillan, P.F., Wolf, G.H., 1995. Vibrational spectroscopy of silicate liquids. In: Stebbins, J.F., McMillan, P.F., Dingwell, D.B. (Eds.), Melts. Mineralogical Society of Washington, Washington, DC, pp. 247–315.

McMillan, P.F., Poe, B.T., Gillet, P., Reynard, B., 1994. A study of SiO_2 glass and supercooled liquid to 1950 K via high-temperature Raman spectroscopy. Geochim. Cosmochim. Acta 58, 3653–3664.

Meade, C., Hemley, R.J., Mao, H.K., 1992. High-pressure x-ray diffraction of SiO_2 glass. Phys. Rev. Lett. 69, 1387–1390.

Mei, Q., Benmore, C.J., Sen, S., Sharma, R., Yarger, J.L., 2008. Intermediate range order in vitreous silica from partial structure factor analysis. Phys. Rev. B. 78144204.

Mishima, O., Stanley, H.E., 1998. The relationship between liquid, supercooled and glassy water. Nature 396, 329–335.

Mishima, O., Calvert, L.D., Whalley, E., 1984. An apparently first-order transition between two amorphous phases of ice induced by pressure. Nature 314, 76–78.

Mozzi, R.L., Warren, B.E., 1969. Structure of vitreous silica. J. Appl. Crystallogr. 2, 164–172.

Mozzi, R.L., Warren, B.E., 1970. The structure of vireous boron oxide. J. Appl. Crystallogr. 3, 251–257.

Muelenbachs, K., Schaeffer, H.A., 1977. Oxygen diffusion in vitreous silica—utilization of natural isotopic abundances. Can. Mineral. 15, 179–184.

Napolitano, A., Macedo, P.B., Hawkins, E.G., 1965. Viscosity and density of boron trioxide. J. Am. Ceram. Soc. 48, 613–616.

Oishi, J., Kimura, T., 1969. Thermal expansion of fused quartz. Metrologia 5, 50–55.

Ono, S., Kikegawa, T., Higo, Y., Tange, Y., 2017. Precise determination of the phase boundary between coesite and stishovite in SiO_2. Phys. Earth Planet. Int. 264, 1–6.

Osborn, E.F., Muan, A., 1960a. Phase equilibrium diagrams for ceramists. Plate 4. The system Na_2O-Al_2O_3-SiO_2. Am. Ceram. Soc.. .

Osborn, E.F., Muan, A., 1960b. Plate 2. the system CaO-MgO-SiO_2: phase equilibrium diagrams of oxide systems. Am. Ceram. Soc.. .

Perkins, W.G., Begal, D.R., 1971. Diffusion and permation of He, Ne, Kr, and D_2 through silicon dioxide thin films. J. Chem. Phys. 54, 1683–1694.

Phillips, J.C., 1984. Microscopic origin of anomalously narrow Raman lines in network glasses. J. Non-Cryst. Solids 63, 347–355.

Polian, A., Grimsditch, M., 1993. Sound velocities and refractive index of densified α-SiO_2 to 25 GPa. Phys. Rev. B 47, 13979–13982.

Polian, A., Vo-Thanh, D., Richet, P., 2002. Elastic properties of α-SiO_2 up to 2300 K from Brillouin scattering measurements. Europhys. Lett. 57, 375–381.

Poole, P.H., Hemmati, M., Angell, C.A., 1997. Comparison of thermodynamic properties of simulated liquid silica and water. Phys. Rev. Lett. 49, 2281–2284.

Poulsen, H.F., Neuefeind, J., Neumann, H.-B., Schneider, J.R., Zeidler, M.D., 1995. Amorphous silica studied by high energy x-ray diffraction. J. Non-Cryst. Solids 188, 63–74.

Price, D.L., Saboungi, M.-L., 1998. Structure of vitreous germania. Phys. Rev. Lett. 81, 3207–3210.

Randall, J.T., Rooksby, H.P., Cooper, B.S., 1930. X-ray diffraction and the structure of vitreous solids. I. Z. Kristall. 75, 196–214.

Richet, P., 1984. Viscosity and configurational entropy of silicate melts. Geochim. Cosmochim. Acta 48, 471–483.

Richet, P., 1988. Superheating, melting and vitrification through decompression of high-pressure minerals. Nature 331, 56–58.

Richet, P., 1990. Glass transitions and thermodynamic properties of polymorphs. Phys. Chem. Minerals 17, 79–88.

Richet, P., Bottinga, Y., 1985. Heat capacity of aluminum-free liquid silicates. Geochim. Cosmochim. Acta 49, 471–486.

Richet, P., Bottinga, Y., 1986. Thermochemical properties of silicate glasses and liquids: a review. Rev. Geophys. 24, 1–26.

Richet, P., Gillet, P., 1997. Pressure-induced amorphization of minerals: a review. Eur. J. Mineral. 9, 907–933.

Richet, P., Mysen, B.O., 1999. High-temperature dynamics in cristobalite (SiO_2) and carnegieite ($NaA1SiO_4$): a Raman spectroscopy study. Geophys. Res. Lett. 26, 2283.

Richet, P., Ottonello, G., 2014. The Earth as a multiscale quantum-mechanical system. Comp. R. Geosci. 346, 317–325.

Richet, P., Bottinga, Y., Denielou, L., Petitet, J.P., Téqui, C., 1982. Thermodynamic properties of quartz, cristobalite and amorphous SiO_2; drop calorimetry measurements between 1000 and 1800 K and a review from 0 to 2000 K. Geochim. Cosmochim. Acta 46, 2639–2659.

Richet, P., Bottinga, Y., Tequi, C., 1984. Heat capacity of sodium silicate liquids. J. Am. Ceram. Soc. 67, C6–C8.

Richet, P., de Ligny, D., Westrum, E.F., 2003. Low-temperature heat capacity of GeO_2 and B_2O_3 glasses: thermophysical and structural implications. J. Non-Cryst. Solids 315, 20–30.

Roberts, C.J., Debenedetti, P.G., 1996. Polyamorphism and density anomalies in network-forming fluids: zeroth- and first-order approximations. J. Chem. Phys. 105, 658–672.

Roselieb, K., Jambon, A., 2002. Tracer diffusion of Mg, Ca, Sr, and Ba in Na-aluminosilicate melts. Geochim. Cosmochim. Acta 66, 109–123.

Roskosz, M., Toplis, M.J., Besson, P., Richet, P., 2005. Nucleation mechanisms: a crystal-chemical investigation of highly supercooled aluminosilicate liquids. J. Non-Cryst. Solids 351, 1266–1282.

Rothman, S.J., Marcuso, T.L.M., Nowicki, L.J., Baldo, P.M., McCormick, A.W., 1982. Diffusion of alkali ions in vitreous silica. J. Am. Ceram. Soc. 65, 578–583.

Rustad, J.R., Yuen, D.A., Spera, F.J., 1991. Molecular dynamics of amorphous silica at very high pressures (135 GPa): thermodynamics and extraction of structures through analysis of Voronoi polyhedra. Phys. Rev. B 44, 2108–2121.

Saika-Voivod, I., Sciortino, F., Poole, P.H., 2000. Computer simulations of liquid silica: equation of state and liquid-liquid phase transition. Phys. Rev. E. 63011202.

Saika-Voivod, I., Sciortino, F., Poole, P.H., 2004. Fragile-to-strong crossover and polyamorphism in liquid silica: changes in liquid structure. Philos. Mag. 84, 1437–1445.

Sakowski, J., Herms, G., 2001. The structure of vitreous and molten B_2O_3. J. Non-Cryst. Solids 293–295, 304–311.

Sato, T., Funamori, N., 2008. Sixfold-coordinated amorphous polymorph of SiO_2 under high pressure. Phys. Rev. Lett.. 101255502.

Sato, T., Funamori, N., 2010. High-pressure structural transformation of SiO_2 glass up to 100 GPa. Phys. Rev. B. 82184102.

Schairer, J.F., Bowen, N.L., 1956. The system Na_2O-Al_2O_3-SiO_2. Am. J. Sci. 254, 129–195.

Seifert, F.A., Mysen, B.O., Virgo, D., 1982. Three-dimensional network structure in the systems SiO_2-$NaAlO_2$, SiO_2-$CaAl_2O_4$ and SiO_2-$MgAl_2O_4$. Am. Mineral. 67, 696–711.

Sen, S., Andrus, R.L., Baker, D.E., Murtagh, M.T., 2004. Observation of an anomalous density minimum in vitreous silica. Phys. Rev. Lett. 93, 125902–125901—125920-125904.

Shackelford, J.F., Masaryk, J.S., Fulrath, R.M., 1970. Water content, fictive temperature, and density relations for fused silica. J. Am. Ceram. Soc. 53, 417.

Sharma, S.K., Mammone, J.F., Nicol, M.F., 1981. Raman investigation of ring configurations in vitreous silica. Nature 292, 140–141.

Shelby, J.E., 2004. Density of vitreous silica. J. Non-Cryst. Solids 349, 331–336.

Shen, G., Meng, Q., Prakapenka, V.B., Lazor, P., Sinogeikin, S., Men, Y., Park, C., 2011. Effect of helium on the structure and compression behavior of SiO2 glass. Proc. Natl. Acad. Sci. U. S. A. 108, 6004–6007.

Shimada, Y., Okuno, M., Syono, Y., Kikuchi, M., Fukuoka, K., Ishikawa, N., 2002. An x-ray diffraction study of shockwave densified SiO_2 glasses. Phys. Chem. Mineral. 29, 233–239.

Shmidt, N.E., 1966. Heat capacity and heat of fusion of crystalline boron oxide. Russ. J. Inorg. Chem. 11, 241–247.

Skinner, B.J., Fahey, J.J., 1963. Observations of the inversion of stishovite to silica glass. J. Geophys. Res. 68, 5595–5604.

Sonneville, C., Deschamps, T., Martinet, C., de Ligny, D., Mermet, A., Champagnon, B., 2013. Polyamorphic transitions in silica glass. J. Non-Cryst. Solids 382, 133–136.

Sosman, R.B., 1965. The Phases of Silica. Rutgers University Press, Rutgers, MJ.

Stebbins, J.F., Carmichael, I.S.E., Weill, D.F., 1983. The high-temperature liquid and glass heat contents and heats of fusion of diopside, albite, sanidine and nepheline. Am. Mineral. 68, 717–731.

Sucov, E.W., 1963. Diffusion of oxygen in vitreous silica. J. Am. Ceram. Soc. 46, 14–20.

Suito, K., Miyoshi, M., Sakakura, T., Fujisawa, H., 1992. Elastic properties of obsidian, vitreous SiO_2, and vitreous GeO_2. In: Syono, Y., Manghnani, M.H. (Eds.), High-Pressure Research: Application to Earth and Planetary Sciences. American Geophysical Uniion, Washington, DC, pp. 219–225.

Swamy, V., Saxena, S.K., Sundman, B., Zhang, J., 1994. A thermodynamic assessment of silica phase diagram. J. Geophys. Res. 99, 11787–11794.

Swets, D.E., Lee, R.W., Frank, R.C., 1961. Diffusion coefficients of Helium in fused quartz. J. Chem. Phys. 34, 17–22.

Sykes, D., Kubicki, J.D., 1996. Four-membered rings in silica and aluminosilicate. Am. Mineral. 81, 265–272.

Takada, A., Richet, P., Catlow, C.R.A., Price, G.D., 2004. Molecular dynamics simulations of vitreous silica structures. J. Non-Cryst. Solids 345–346, 224–229.

Takada, A., Bell, R.G., Catlow, C.R., 2016. Molecular dynamics study of liquid silica under high pressure. J. Non-Cryst. Solids 451, 124–130.

Taylor, M., Brown, G.E., 1979. Structure of mineral glasses. II. The SiO2-NaAlSiO4 join. Geochim. Cosmochim. Acta 43, 1467–1475.

Tomlinson, J.W., Heynes, M.S.R., Bockris, J.O.M., 1958. The structure of liquid silicates. Part 2. Molar volume and expansivities. Trans. Farad. Soc. 54, 1822–1834.

Tsuneyuki, S., Matsui, Y., 1995. Molecular dynamics study of pressure enhancement of ion mobilities in liquid silica. Phys. Rev. Lett. 74, 3197–3200.

Tucker, M.G., Keen, D.A., Dove, M.T., Trachenko, K., 2005. Refinement of the Si–O–Si bond angle distribution in vitreous silica. J. Phys. Condensed Matter 17, S67–S75.

Uchino, T., Tokuda, Y., Yoko, T., 1998. Vibrational dynamics of defect modes in vitreous silica. Phys. Rev. B 58, 5322–5328.

Urbain, G., 1982. Viscosité de l'alumine liquide. Rev. Int. Hautes Temp. Refract. 19, 55–57.

Urbain, G., 1983. Viscosité de liquides du système CaO-Al_2O_3. Rev. Int. Hautes Temp. Refract. 20, 135–139.

Urbain, G., 1990. The effect of differing water contents on the viscosity of liquids silica. Rev. Int. Hautes Temp. Refract. 26, 193–197.

Urbain, G., Auvray, P., 1969. Mesure de la viscosité d'un verre de silice par une méthode d'écrasement. C. R. Acad. Sci. C298, 8–11.

Urbain, G., Bottinga, Y., Richet, P., 1982. Viscosity of liquid silica, silicates and aluminosilicates. Geochim. Cosmochim. Acta 46, 1061–1072.

Volarovich, M.P., Leontieva, A.A., 1936. Determination of the viscosity of quartz glass within the softening range. J. Soc. Glas. Technol. 20, 139–143.

Vuckevitch, M.R., 1972. A new interpretation of the anomalous properties of vitreous silica. J. Non-Cryst. Solids 11, 25–63.

Wagstaff, F.E., 1969. Crystallization and melting kinetics of cristobalite. J. Am. Ceram. Soc. 52, 650–654.

Wagstaff, F.E., Richards, K.J., 1966. Kinetics of crystallization of stoichiometric SiO_2 glass in H2O atmospheres. J. Am. Ceram. Soc. 49, 118–121.

Wakabayashi, D., Funamori, N., Sato, T., Taniguchi, T., 2011. Compression behavior of densitifed silica. Phys. Rev. B 84, 144103.

Westrum E.F., J. (1956). The Low-Temperature Heat Capacity of Neutron-Irradiated Quartz. Trav. 4ième Congr. Int. Verre, Paris, 396–399.

Williams, Q., Hemley, R.J., Kruger, M.B., Jeanloz, R., 1993. High pressure infrared spectra of a-quartz, coesite, stishovite, and silica glass. J. Geophys. Res. 93, 2280–2288.

Wright, A.C., 1994. Neutron-scattering from vitreous silica. 5. The structure of vitreous silica—what have we learned from 60 years of diffraction studies? J. Non-Cryst. Solids 179, 84–115.

Xu, C.M., Wang, S.W., Huang, X.X., Guo, J.K., 2005. Amorphization of cristobalite at high temperature in vacuum. J. Mater. Res. 20, 1943–1946.

Xue, X., Stebbins, J.F., Kanzaki, M., 1993. A 29-Si MAS NMR study of sub-Tg amorphization of stishovite at ambient pressure. Phys. Chem. Miner. 19, 480–485.

Yamashita, I., Tojo, T., Kawaji, H., Atake, T., Linard, Y., Richet, P., 2001. Low-temperature heat capacity of sodium borosilicate glasses. J. Chem. Therm. 33, 535–553.

Yi, Y.S., Lee, S.K., 2012. Pressure-induced changes in local electronic structures of SiO_2 and MgSiO3 polymorphs: insights from ab initio calculations of O K-edge energy-loss near-edge structure spectroscopy. Am. Mineral. 97, 897–909.

Yoder, H.S., 1976. Generation of Basaltic Magma. National Academy of Science, Washington, DC.

Yokoyama, A., Matsui, M., Higo, Y., Kono, Y., Irifune, T., Funakoshi, K.-i., 2010. Elastic wave velocities of silica glass at high temperatures and high pressures. J. Appl. Phys.. 107123530.

Yuan, X., Cormack, A.N., 2003. Si-O-Si bond angle and torsion angle distribution in vitreous silica and sodium silicate glasses. J. Non-Cryst. Solids 319, 31–43.

Zachariassen, W., 1932. The atomic arrangement in glass. J. Am. Chem. Soc. 54, 3841–3851.

Zha, C.-S., Hemley, R.J., Mao, H.K., Duffy, T.S., Meade, C., 1994. Brillouin scattering of silica glass to 57.5 GPa. Am. Inst. Phys. 93–96.

Zhabrev, V.A., Moiseev, V.V., Sviridov, S.I., Chistoserdov, V.G., 1976. Diffusion of divalent ions in vitreous silica. Sov. J. Glass Phys. Chem. 2, 326–329.

Zhang, J., Liebermann, R.C., Gasparik, T., Herzberg, C.T., 1993. Melting and subsolidus relations of SiO2 at 9-14 GPa. J. Geophys. Res. 98, 19785–19793.

Zoltai, T., Buerger, M.J., 1960. The relative energies of rings of tetrahedra. Z. Kristallog. 114, 1–8.

CHAPTER

6

Properties of Metal Oxide-Silica Systems

OUTLINE

6.1 INTRODUCTORY COMMENTS

There are many practical and fundamental reasons why the physical properties of molten silicates have been most extensively investigated for binary silicate systems with either alkali or alkaline-earth oxides. For example, the low liquidus temperatures and ease of vitrification of alkali silicates make a large variety of experiments feasible over large temperature intervals that span both the stable and metastable states. Besides, such simple MO-SiO_2 melts (M = Li_2, Na_2, Mg, Ca, etc.) represent obvious model systems for industrially important materials, as thousands of factories worldwide produce flat or container glass whose composition is approximately 70 mol% SiO_2, 15% Na_2O and 15% CaO + MgO. Even though alumina is also a major component of magma, alkali and alkaline earth silicates are, in addition, important

https://doi.org/10.1016/B978-0-444-63708-6.00006-5

starting points for modeling the role of melts and melting in geochemistry. Investigations of MO-Al_2O_3 melts generally raise considerable experimental difficulties in view of the high temperatures at which they must be performed. As discussed in later chapters (Chapters 8 and 9), it is then easier to determine the effect of added alumina on the properties of metal oxide-silica systems than that of added metal oxides on the properties of SiO_2-Al_2O_3 melts.

The main goal of this chapter is to present some general conclusions that can be drawn from macroscopic properties and to set the framework for the structural discussion that follows in the next chapter. In passing, we will also give a few glimpses into experimental accuracy and constraints. Because dealing with all important physical properties is beyond our scope, index of refraction, surface tension, and internal friction will not be addressed. A wealth of references on these and other subjects can be found in available compilations (Mazurin et al., 1987; Bansal and Doremus, 1986). Also note that ferrous iron is a divalent cation that exerts an influence on melt properties which, in some respects, is analogous to that of alkaline earths. In view of the complications raised by the existence of two valence states, however, the properties of iron-bearing melts will be mainly dealt with separately in Chapter 10.

6.2 PHASE RELATIONSHIPS

Phase diagrams indicate the pressures and temperatures under which thermodynamic equilibrium is reached between different phases as a function of composition. These diagrams are prerequisites to any practical use of amorphous silicates because liquidus and solidus relations indicate the temperatures at which the first crystal should form and that at which the last droplet of liquid should crystallize, respectively. From a fundamental standpoint, phase diagrams represent an integrated balance of crystal and melt properties that can be subjected to quantitative thermodynamic analyses. These relations can also point to significant structural similarity between amorphous and crystalline phases and, thus, give useful information on mixing in both. Liquidus phase relations have also been employed for quantitative modeling of the melt structure at the liquidus (Babcock, 1968; Bottinga et al., 1981; Nekvasil and Burnham, 1987).

6.2.1 Liquidus and Solvus Relations

Solid-liquid phase relations in silicate systems are usually determined from quenching experiments because, except for transformations involving very fluid SiO_2-poor melts, melting and crystallization near equilibrium are sluggish reactions. For simple systems, most of these experiments were performed during the first half of the 20th century with an unsurpassed care. This activity was closely linked to the Geophysical Laboratory Temperature Scale (Adams, 1914). At the highest reported temperatures, slight adjustments of up to 20 degrees may be needed from the original temperature scale to the current International Practical Temperature Scale (e.g., Sosman, 1952). Of more serious concern is the fact that, owing to the lack of microanalytical methods at that time, the petrographic microscope was the main tool used for mineral characterization. With the exception of well-known continuous solid solutions such as, for example, albite-anorthite, minerals were thus generally assumed to have the nominal stoichiometry and phase diagrams to be eutectic when they actually could have shown narrow solid solutions. These limitations should be kept in mind when examining silicate phase diagrams determined in this manner.

At least in the SiO_2-rich parts of phase diagrams, however, solid solutions are unlikely significant in binary metal oxide-silica systems with alkali and alkaline earth elements (Fig. 6.1). There are several topological similarities among these phase diagrams. The main features are the occurrence of liquid immiscibility at high silica contents and the existence of eutectic-type equilibria at high metal oxide concentrations. For both features, the equilibrium temperatures and SiO_2 content depend systematically on the cation size, r, and charge, Z, such that the positive correlation between those variables and Z/r^2 (ionization potential) of the metal cation obtains for alkalis and alkaline earths (Table 6.1).

Concerning the critical temperature of the miscibility gap, an important distinction must be made depending on whether liquid unmixing takes place at temperatures higher or lower than the liquidus. In the former case (e.g., Ca, Mg), liquid immiscibility is stable and precedes crystallization because of very rapid kinetics at the high temperatures at which it takes place. In the latter case (e.g., Ba, Li, Na, K), phase separation is metastable and may occur at subliquidus temperature. Phase separation in these systems can proceed only if crystallization is bypassed. In view of the low temperatures at which immiscibility may develop, the process is time-dependent and is rarely observed at temperatures below that of the glass transition. As a result, in M_2O-SiO_2 systems the solvus is still controversial for K_2O, whereas its existence for Rb_2O and Cs_2O cannot be observed because the critical temperature, if any, is likely lower than the standard glass transition.

6.2.2 Energetics, Phase Stability, and Immiscibility

The differences in ionization potential or bond strength, discussed in Section 2.2, also manifest themselves in liquid immiscibility and liquidus temperatures (Fig. 6.1). Both stable or metastable solvii reflect directly the differing strength of interactions of oxygens with alkaline earth and alkali cations in the melts in the SiO_2-rich parts of the diagrams. Likewise, melting is associated with configurational rearrangements, which require lower thermal energy when bonding is weak (Nesbitt et al., 2017). Liquidus temperatures thus are systematically lower for alkali than for alkaline earth systems and vary systematically in both series (Fig. 6.1). The differences are especially large at the eutectic points, which can be lower temperatures than 800°C for alkali silicate systems, but higher than 1300°C for alkaline earth silicate systems.

The contrast between alkali and alkaline earth silicate systems extends dramatically toward the pure metal oxide endmembers. Liquidus temperatures rise very steeply toward CaO or MgO, which are among the most refractory compounds known. In this respect, it might seem paradoxical that CaO and MgO melt at a much higher temperature than SiO_2 polymorphs, given the lower strength of M—O compared to Si—O bonds, which should make SiO_2 the most refractory component of magma. This apparent anomaly thus has truly fundamental consequences because it is the root of the silica enrichment that characterizes magma differentiation. As discussed by Richet and Ottonello (2014), it is due to the ready configurational changes in molten SiO_2 that are made possible, without severing of Si—O bonds, by the great flexibility of Si—O—Si angles (see Sections 5.3.1 and 5.5.1).

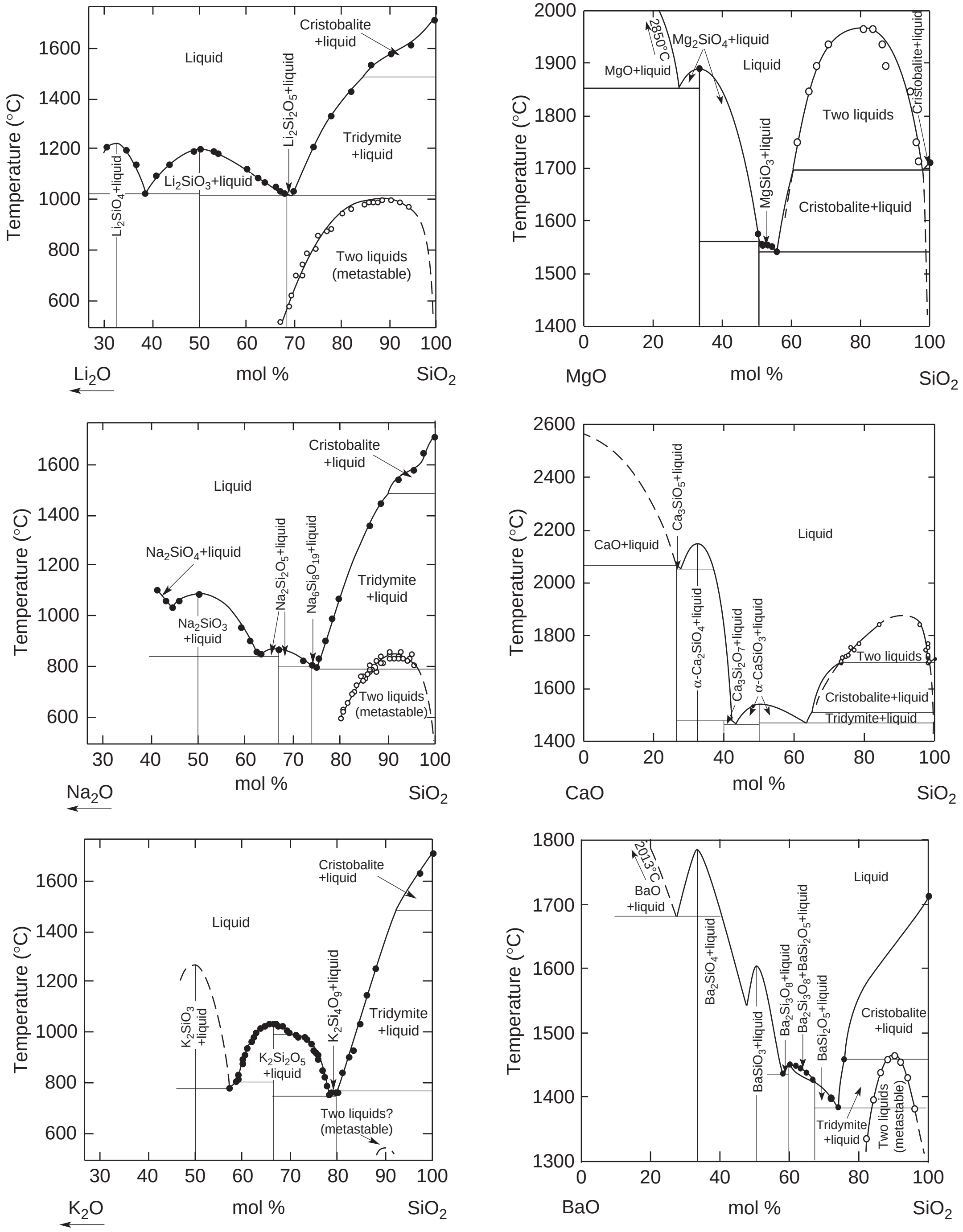

FIG. 6.1 Phase diagrams of binary alkali (*left*) and alkaline earth (*right*) systems. Data for Li_2O-SiO_2 from Kracek (1930a) and Haller et al. (1974); Kracek (1930b), for Na_2O-SiO_2 from Williamson and Glasser (1965) and Haller et al. (1974); for MgO-SiO_2 from Kracek et al. (1929, 1937) and Charles (1967) for K_2O; Bowen and Andersen (1914) and Hageman et al. (1986); for CaO-SiO_2 from Rankin and Wright (1915) and Tewhey and Hess (1979); and for BaO-SiO_2 from Eskola (1922) and Seward et al. (1968). For other determinations or assessments of miscibility gaps, see Levin (1970), Mazurin et al. (1984), and Hudon and Baker (2002a).

TABLE 6.1 Binary Systems: Composition of the Most Silica-Rich Liquidus Phase, Temperature of the Deepest Eutectic, and Critical Temperature and Width at the Monotectic of the Solvus (mol%)[a]

	First compound		First eutectic		Solvus
	mol% SiO_2	**NBO/*T***	**T_{eut}(°C)**	**T_c(°C)**	**Width**
K_2O	80	3.5	742	350	
Na_2O[b]	73	3.25	800	820	
Li_2O	67	3	1000	1000	
BaO	67	3	1370	1460	
SrO	50	2	1358	1642	19
CaO	50	2	1460	1890	28
MgO	50	2	1543	1960	39

[a] *See Fig. 6.1 for references. Data for SrO from Hageman and Oonk (1986).*

[b] *$Na_6Si_8O_{19}$ (N_3S_8): incongruently melting compound (Williamson and Glasser, 1965).*

The solid-liquid phase diagrams of Fig. 6.1 do not show glass-forming regions because vitrification is not an equilibrium but a kinetic process (see Chapter 3, Section 3.3.4). The glass-forming ability of alkaline earth silicate melts is limited to a narrow compositional range near eutectic points. On the SiO_2-rich side, formation of homogeneous glasses is prevented by stable liquid immiscibility. At high M_xO contents, rapid crystallization takes place, because too much configurational entropy is lost on cooling so that ultrafast quenching is required to make glasses with fictive temperatures that are much higher than the standard glass transition temperature would be (Richet et al., 1993). As for alkali-rich crystalline silicates, they do not give rise to glasses because they decompose increasingly readily, in the order of increasing alkali mass, on moderate heating often before melting. An analogous trend is observed for the hygroscopicity of alkali-silicate glasses and crystals, which indicates that protons compete successfully with alkali, but not with alkaline earth cations, to bind with oxygen (Cody et al., 2005). Hygroscopicity is, in fact, such a problem that physical, chemical, or structural information is scarce for binary Rb_2O- and Cs_2O-SiO_2 glass systems.

6.2.3 Steric Hindrance and Polymerized Structures

A general trend apparent in Fig. 6.1 is that the composition of the most silica-rich compound shifts toward the metal oxide when the ionization potential of the cation increases. Whereas potassium fits in the tetrasilicate crystal (80 mol% SiO_2), calcium and magnesium are incorporated only in crystals with at most 50 mol% SiO_2. On the SiO_2-poor side of the diagrams, in contrast, there can be a variety of compounds with M_xO contents higher than the 50 mol% of metasilicates (Table 6.1).

This difference in mixing between the two sides of metal oxide-silica systems also holds for liquids. A single solution exists for SiO_2-poor compositions, but the difficulty of mixing pure SiO_2 with metal oxides is indicated by the prevalence of liquid-liquid unmixing. In fact, Hudon and Baker (2002a, b) proposed a model for liquid immiscibility in which the structure

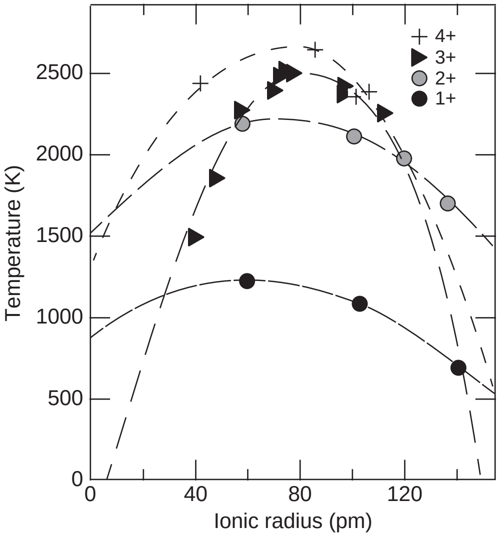

FIG. 6.2 Consolute temperatures in M_xO-SiO_2 melts as a function of ionic radius of the metal cation (data summary by Hudon and Baker (2002a)).

of the SiO_2 component plays an active role by selecting which cations may take on tetrahedral coordination. They proposed that there is, therefore, a critical radius of metal cations below which they may occupy tetrahedral coordination and above which they do not. There is also an intermediate range, where the cation may occupy two different coordination states, of which one is tetrahedral, thus suppressing liquid immiscibility, and one is not and thus promotes liquid immiscibility (Hudon and Baker, 2002a, b; see also Fig. 6.2). The maximum in the consolute temperature distribution in Fig. 6.2 coincides with the ionic radius below which the cations may be in fourfold coordination, whereas above it the metal cations are not.

In all systems, a very SiO_2-rich melt coexists with another phase whose composition becomes increasingly M_xO-rich at lower temperatures and may reach that of the first existing silicate compound and subliquidus temperatures (Fig. 6.1). For the silica-rich phase, the structural mismatch is reduced only near the critical point where the width of the solvus becomes narrower, because the possibility of incorporating some metal oxide becomes effective.

As noted early on by Warren and Pincus (1940) for miscibility gaps, phase diagrams provide valuable information about the competition between silicon and other metal cations for bonding with oxygen. Whether in crystalline or in amorphous phases, it is clearly difficult to form the coordination polyhedra of the network-modifying cations with the oxygens of a silica-rich framework. As discussed further in Chapter 7, Section 7.3, the first nonbridging oxygens formed when metal oxide concentration increases belong to Q^3 species, because the continuous three-dimensional network of pure SiO_2 melt begins to depolymerize. However, bonding to the nonbridging oxygen of a number of Q^3 species meets with serious steric hindrance and thus energetic difficulties, which in melts has profound effects on the composition range within which Q^3 species are stable and also affects their abundance (Frantz and Mysen, 1995; Jones et al., 2001; Lin et al., 2007). This feature not only affects the liquidus phase relations, but also influences a number of other properties of metal oxide–silicate melts and glasses, as discussed further in the following text.

Optimization of coordination polyhedra of metal cations requires a number of perhaps energetically different nonbridging oxygens (Kohn and Schofield, 1994; Jones et al., 2001; Lee et al., 2003). Nonbridging oxygens belonging to smaller entities, to which metal cations can bond more readily, are generated by disproportion reactions of the form $2Q^n \Leftrightarrow Q^{n-1} + Q^{n+1}$ (see Chapter 2, Section 2.4.2 and Chapter 7, Sections 7.3.1 and 7.3.2). When there is a need for a metal cation to bond to several nonbridging oxygens, which is the case for divalent and more highly charged cations, segregation of Q^3 to Q^2 and Q^4 species and eventually formation of two different phases, which both have a narrow Q^n distribution, may occur. Because nonbridging oxygens are scarce, the Q^4-rich phase generally remains close in composition to pure SiO_2, whereas greater flexibility in the more depolymerized phase allows its composition to vary with temperature. Beyond the metasilicate stoichiometry, which is stoichiometrically equivalent to Q^2, Q^1, and Q^0 species become common (Mysen et al., 1982; Meneses et al., 2006; Lin et al., 2010). They represent an abundant resource of nonbridging oxygens to which metal cations can bond readily. Even for alkaline earth orthosilicate stoichiometry (isolated SiO_4 tetrahedra), oxygen occurs in several species, such as Q^1, Q^0, and as "free" metal cations (Mysen et al., 1982; Sen et al., 2009).

Such a description is only a starting point, however, as other factors must be invoked for a more realistic description (see Charles, 1969; Levin, 1970; Hageman et al., 1986; Hudon and Baker, 2002a, b). In particular, the nominal number of nonbridging oxygens is not sufficient to account for metal cation content along the SiO_2-rich branch of the solvus. The effective electrical charge of bridging oxygens, which is not zero (see Chapter 2, Section 2.4.2), should also be considered. As such, it allows these oxygens to contribute to the coordination polyhedra of metal cations, a feature observed in molecular dynamics simulations (Cormack and Du, 2001).

Everything else being equal, large miscibility gaps are produced by small cations with a high ionization potential, which compete the most effectively with silicon for oxygen. For large cations with a low ionization potential, the steric hindrance and energetic problems are less severe so that the solubility of the metal oxide in SiO_2 is more extensive. This interpretation agrees with the observation that, in crystal structures, the more silica-rich the mineral, the greater the steric hindrance associated with bonding of alkali and alkaline earth to oxygen. In other words, the availability of electron donors diminishes with greater SiO_2 content, thus restricting the types of crystal structures that may form. In crystal structures with silicate chains, for example, the chains become less stretched (more buckled) the greater the ionization potential of the metal (Liebau and Pallas, 1981).

6.3 THERMAL PROPERTIES

In multicomponent systems, phase relationships at a given pressure and temperature are determined by the composition dependence of Gibbs free energies of mixing, ΔG_m, which themselves are made up of enthalpy and entropy contributions. When dealing with silicate melts, the basic difficulty is that information on the latter is virtually nonexistent. Although, as described in Chapter 3, Section 3.5.3, entropies of mixing could be obtained from analysis of viscosity data, such results are not always used in discussion of thermodynamic modeling of melts and thermodynamics of melting.

6.3.1 Enthalpy of Mixing

Thermodynamically, two phases unmix if phase separation causes a decrease of the Gibbs free energy of the system. In other words, the Gibbs free energy of mixing must be positive:

$$\Delta G_m = \Delta H_m - T\Delta S_m > 0, \tag{6.1}$$

where ΔH_m and ΔS_m denote the enthalpy and entropy of mixing. Because ΔS_m is positive, phase separation requires a positive enthalpy of mixing of magnitude greater than $T\Delta S_m$ (Fig. 6.3). Unmixing in silicate melts usually tends to disappear at higher temperatures, however, because of the increasing contribution of $T\Delta S_m$ to ΔG_m. In other words, the width of the solvus decreases with increasing temperature and vanishes at the critical point when the entropy term, which favors mixing, takes over the enthalpy term of steric hindrance in the Gibbs free energy of mixing of the system.

Enthalpies of mixing should correlate with critical temperature and extent of liquid immiscibility in the SiO_2-rich parts of the binary systems of Fig. 6.1, and thus with the ionization potential of the cation. Although ΔH_m could be determined from solution calorimetry experiments, such data are lacking. For alkaline earth systems, homogeneous amorphous samples cannot be obtained over sufficiently large composition intervals. For alkali silicates, reliable data are limited to sodium silicates from pure SiO_2 to the metasilicate composition (Fig. 6.4). The data define two distinct composition ranges when referred to isothermal values with

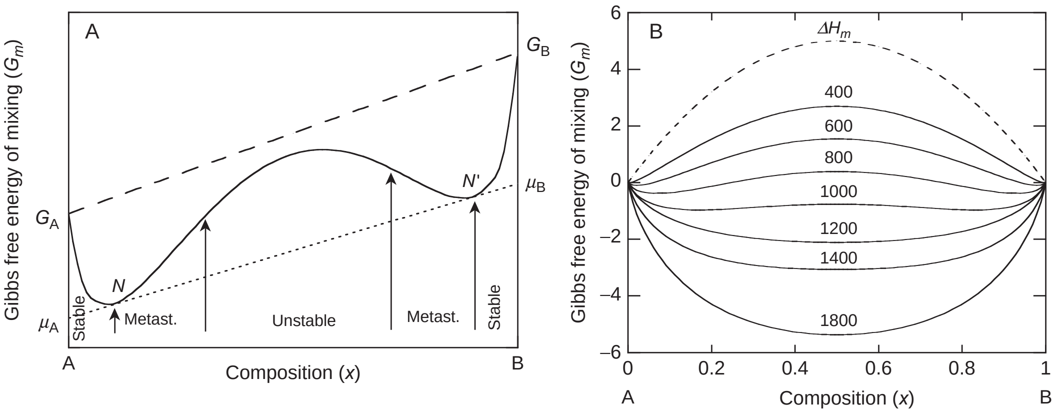

FIG. 6.3 Gibbs free energy in a phase-separating binary system A–B. (A) Gibbs free energy of mixing, ΔG_m, as given by the difference between the Gibbs free energy of the solution (*solid curve*) and that of a mechanical mixture of the components A and B (*dashed line*). In silicate melts, unmixing is a very sensitive probe of the energetics as the associated ΔG_m is only a few hundred joules (see Tewhey and Hess, 1979). In the central part of the diagram, the solution is unstable because any composition fluctuation causes a decrease of ΔG_m. In the metastable range (Cahn and Charles, 1965), unmixing takes place through nucleation and growth as separation in two phases first causes an increase *e* of free energy. At both ends the solution is stable. The compositions N and N' of the coexisting liquids are determined by the two points at which the free energy curve has a common tangent such that the criterion (6.1), see following, is satisfied; the chemical potentials of both components are then given by the intercepts of this tangent on the A and B axes. B. Variation with temperature (in K) of ΔG_m for a symmetric $\Delta H_m = W\,x\,(1-x)$, with $W = 20$ kJ/mol (*dashed curve*), and an ideal entropy of mixing $\Delta S_m = -R \sum x \ln x$ ($R =$ gas constant). In this case, the critical point is $T_c = W/2R = 1200$ K as determined from the criterion $(\partial^3 G/\partial x^3)_{P,T} = 0$.

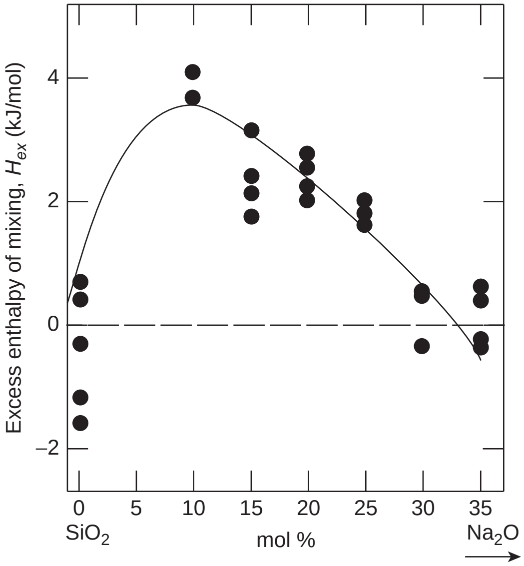

FIG. 6.4 Excess enthalpy of mixing of Na_2O-SiO_2 melt relative to ideal mixing (*horizontal dashed line*) as a function of composition (Hovis et al., 2004).

Eq. (2.15). From 100 to about 70 mol% SiO_2, an excess enthalpy is clearly observed. Within the field of metastable liquid immiscibility, it translates to a positive enthalpy of mixing of about 4 kJ/mol near 10 mol% Na_2O. The asymmetry of the ΔH_m curve indicates that partial molar enthalpies of mixing are much greater near the SiO_2 endmember than on the other side of the solvus of the system. This observation agrees with the fact that the composition of the SiO_2-rich unmixed phase varies much less with temperature than that of the second phase. From about 70 to 50 mol% SiO_2, enthalpies vary linearly with composition, which shows that mixing of silicate entities becomes almost ideal when the amount of Q^4 species vanishes.

6.3.2 Thermodynamics of Melting

The values of thermodynamic parameters associated with melting to a considerable degree reflect the structural differences between a crystalline material and its melt. Disorder in the melts governed by the nature of the metal cation may affect these values further.

Some of these concepts were summarized in Chapter 5, Section 5.3, where it was shown that, as degree of polymerization of the crystalline materials decreases from that of a silica polymorph, ΔH and ΔS of fusion increase systematically (Fig. 5.3). This evolution likely reflects the increasing differences between the structure of the crystalline and molten materials on the liquidus. In other words, the more extensive the bond breakage and formation necessary for melting and crystallization, the greater would be the entropy and enthalpy of fusion (Fig. 5.3).

The nature of the network-modifying cation also affects the ΔS and ΔH of fusion. For crystalline materials of given degree of polymerization, NBO/Si, the more electronegative the metal cation, the larger are the ΔH and ΔS values of fusion (Fig. 6.5). In the summary of

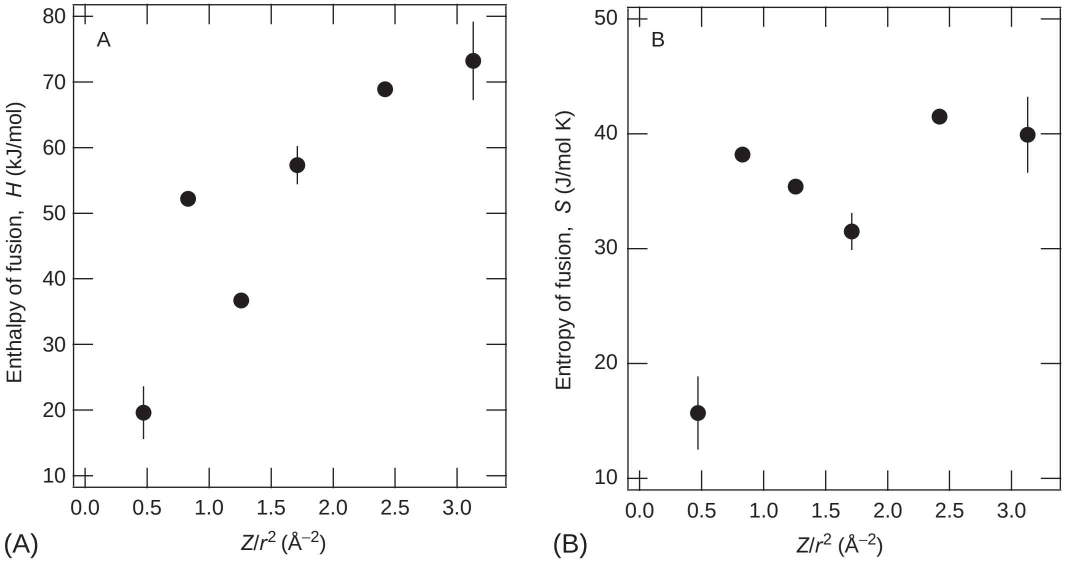

FIG. 6.5 Thermodynamics of fusion of metal oxide-silicate crystalline materials as a function of ionization potential of the metal cation. (A) Enthalpy of fusion. (B) Entropy of fusion. (Thermodynamic data compilation by Richet and Bottinga, 1986.) Ionic radii used are those for sixfold coordination of metal cation from Whittaker and Muntus (1970).

the thermodynamic data in this figure, ionic radii for sixfold coordination of the metal cations were used for convenience. This is a slightly unrealistic assumption as the oxygen coordination numbers tend to increase with increasing ionic radii (see also Section 7.3.2). However, the effects of such adjustments in coordination numbers on the Z/r^2-values are small and the relative trends shown in Fig. 6.5 would not be affected.

Interestingly, the change of configurational heat capacity of glasses across their glass transition is positively correlated with the ΔS and ΔH values of fusion (Beyer et al., 1979; Yageman and Matveev, 1982; Richet and Bottinga, 1985, 1986). This leads to the suggestion, therefore, that the composition effects on thermodynamics of melting to a considerable extent are governed by the properties of the melt.

6.3.3 Activity-Composition Relations

A review of phase diagram calculations is beyond the scope of this chapter. We will limit ourselves to the observed regularities in liquidus branches of the SiO_2-rich parts of the diagrams and to the main factors that determine variations of SiO_2 and M_xO activities.

In a system in thermodynamic equilibrium, the temperature and pressure are constant and the chemical potential (μ) of any component i is the same in all coexisting phases. Equilibrium between two phases α and β (either solid and liquid, or both liquid) thus requires that:

$$\mu_i^\alpha = \mu_i^\beta \tag{6.2}$$

for each independent component of the system. By expressing the chemical composition of the relevant solid or liquid solution in terms of mol fraction, x_i, one writes for the chemical potential of component i in this phase:

$$\mu_i = \mu_i^o + RT \ln a_i = \mu_i^o + RT \ln x_i + RT \ln \gamma_i, \tag{6.3}$$

where R is the gas constant, μ_i^o the standard potential, a_i the activity, and γ_i the activity coefficient of component i. Alternatively, the chemical potential of i can be expressed as:

$$\mu_i = \mu_i^o + \overline{\Delta H}_{mi} - T\overline{\Delta S}_{mi}, \tag{6.4}$$

where $\overline{\Delta H}_{mi}$ and $\overline{\Delta S}_{mi}$ are the partial molar enthalpies and entropies of mixing of i in the relevant solid or liquid solutions.

In both cases, the standard state is usually taken as pure i in the crystalline state at the temperature and pressure of interest. In the absence of solid solution, the chemical potential of the crystalline phase then reduces to:

$$\mu_i^c = \mu_i^{oc} + RT \ln a_i^c = \mu_i^{oc} \tag{6.5}$$

because the activity of i is unity in the crystal. In a two-component system, i–j, one may then extract the chemical potential of component j from the Gibbs-Duhem relation:

$$X_i d \ln \mu_i + X_j d ln \mu_j = 0. \tag{6.6}$$

Ryerson (1985) noted that cristobalite can be considered a pure phase in binary metal oxide-silica systems. When cristobalite is in equilibrium with a melt, Eqs. (6.1) and (6.4) state that the activity of SiO_2 in the liquid ($a_{SiO_2}^{melt}$) is buffered to the unity value of the SiO_2 activity in the crystal. From the known SiO_2 mol fraction of the melt in equilibrium with cristobalite, it is possible to calculate $a_{SiO_2}^{melt}$ and to determine how the activity coefficient of SiO_2 in the melt ($\gamma_{SiO_2}^{melt}$) varies with the network-modifier metal cation. By assuming that the partial molar enthalpy of SiO_2 in a given system is constant, Ryerson (1985) derived the activity coefficients of the form:

$$\ln \gamma_{SiO2} = a/T + \text{constant}, \tag{6.7}$$

which are plotted in Fig. 6.6. These data closely resemble those reported by Romero-Serrano et al. (2005, 2010) obtained with similar methods.

There is a clear hierarchy in these data in that $\gamma_{SiO_2}^{melt}$ is positively correlated with the ionization potential of alkali metal and alkaline earth for any given metal/Si ratio, which is similar to the results reported by Charles (1967) and Morita et al. (2000). This trend is, of course, consistent with the inferences drawn from liquid immiscibility relations in the same systems where the width of immisciobility gaps also increases with increasing ionization potential of the metal cation (Section 6.2.2, Fig. 6.2; see also Hudon and Baker, 2002a, b). In other words, the increase in steric hindrance as the Z/r^2 of the metal cation increases is reflected by increased activity coefficients of SiO_2.

From the data on SiO_2 activity combined with the Gibbs-Duhem equation, activities of the metal oxide components can be calculated (Fig. 6.7; see also Charles, 1967). It follows, therefore, from the activity coefficient of SiO_2 components that here the analogous hierarchical relationship with the activity coefficients is increasing as the metal cation becomes more electronegative.

FIG. 6.6 Activity coefficient of SiO_2 in metal silicate melts at 1550 °C derived from liquidus phase relations of silica polymorphs (after Ryerson, 1985).

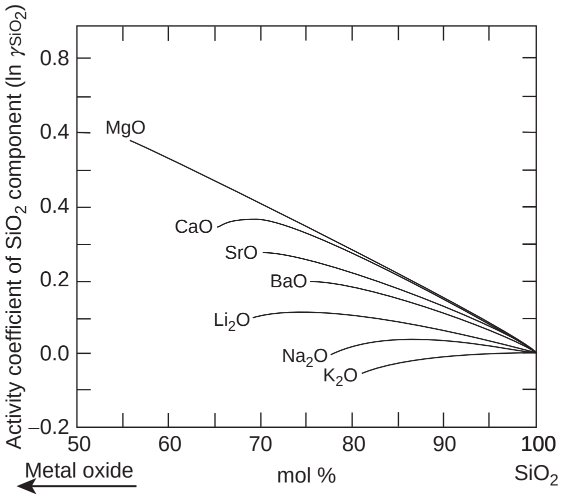

FIG. 6.7 Activity coefficient of alkali oxides, K_2O, Na_2O, and Li_2O in M_2O-SiO_2 melts calculated at 1000°C (calculations by Charles, 1967).

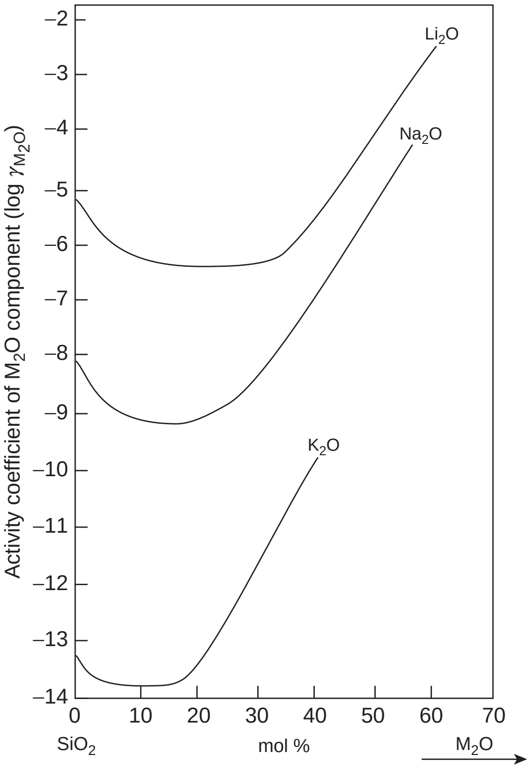

Phase relations could be calculated if either the activity-composition relationships or the enthalpies and entropies of mixing were known independently over the relevant temperature and composition ranges. These data are now available for major solid solutions (see Geiger, 2001; Fabrichnaya et al., 2003). Some entropy and enthalpy data for binary silicate melts are now available (Morishita et al., 2004), which show that partial molar enthalpy and entropy of SiO_2 are very sensitive to the bulk composition of metal oxide-silicate melts. The phase diagram information is available in the form of extensive compilations (Levin et al., 1975).

6.3.4 Oxygen Activity and Acid-Base Reactions

The activity of SiO_2 can change significantly with changes in the NBO/T of the melt. Such determinations can be made through measurements of vapor pressures (e.g., Frohberg et al., 1973; Plante, 1978) and electromotive forces (e.g., Kohsaka et al., 1979), or through studies of equilibration of the melt with another phase for which the activity-composition relationship of the component of interest is known (e.g., Rao and Gskell, 1981; Chamberlin et al., 1994). For alkali silicates, the activity of metal oxides has also been determined from ionic conductivity measurements with the assumption that the number of M^+ carriers is determined by the dissociation equilibrium of metal oxide into M^+ and OM^- ions (Ravaine and Souquet, 1977). Often, the experiments cannot be performed from 0 to 100 mol% SiO_2 with the same method, or the activity of only one component can be measured, in which case that of the second can be determined through integration of the Gibbs-Duhem equation.

Such variations are intimately related to the acid-base character of the oxygen speciation reactions. In this respect, we may recall first that, in the 19th century, it became widely believed that all silicates derived from silicic acid, H_4SiO_4. A reminder of these ideas is the use of the terms *acid* and *basic* applied to igneous rocks to designate what today is more properly denoted by *silicic* and *mafic* (from Mg and Fe) rocks, respectively. Ironically, more recent ideas could be invoked to justify this old nomenclature.

The success of the ionic theories developed by Arrhenius and Brönsted for aqueous solutions has resulted in attempts at transposing analogous concepts to reactions in other kinds of solvents. Adopting Lewis's (1923) definition of acids and bases as acceptors and donors of an electron doublet, respectively, Lux (1939) and Flood et al. (1947), for instance, considered that acid-base reactions take place in molten oxides via exchange of "free" O^{2-} ions. According to this definition, SiO_2 is an acid whereas metal oxides are bases, in accordance with the basic character long attributed to an oxide like CaO. To account for such acid-base reactions, Toop and Samis (1962) started from the equilibrium between the three different kinds of oxygens first considered by Fincham and Richardson (1954):

$$O^0(\text{bridging oxygen}) + O^{2-}(\text{free oxygen}) \Leftrightarrow 2O^-(\text{nonbridging oxygen}). \tag{6.8}$$

Of course, Eq. (6.8) is just a shorthand notation for the various reactions that involve more complex entities with various proportions of bridging and nonbridging oxygens. The equilibrium constant of this reaction is related to the oxygen ion activities by:

$$K = {a_{O^-}}^2 / \left(a_{O^0} a_{O^{2-}}\right). \tag{6.9}$$

Finally, the Gibbs free energy of mixing is given by:

$$\Delta G_m = 0.5 N_{O^-} RT \ln K, \tag{6.10}$$

because $N_{O^-}/2$ oxygens react for 1 mol of melt. By definition, ΔG_m is independent of composition and is proportional to the degree of depolymerization.

Through the very simple Toop and Samis (1962) model, the considerable variations of $a_{SiO_2}^{melt}$ are related in this manner to changes in the concentrations of the three kinds of oxygen ions. Because it distinguishes only three different species, the model could in principle be generalized to multicomponent systems. Agreement with experimental activity data is not excellent, however, because the four basic assumptions are not really valid even for binary systems:

(i) The equilibrium constant K does depend on composition and, thus, on the degree of polymerization of the melt and, in particular, on Q^n-speciation for a given composition (Dron, 1982). As described in Chapter 10, such a simple formalism fails when applied to iron redox reactions because the activity coefficients of the three kinds of oxygens involved depend on the composition of the system.

(ii) The three types of oxygens do not mix ideally, as indicated by the prevalence of stable or metastable miscibility gaps in binary metal oxide-silica systems and by the existence of positive enthalpies of mixing (see Section 6.3.4).

(iii) The assumption that the metal oxide M_xO dissociates entirely is difficult to ascertain, for this would require characterization of all sorts of M—O bonds. However, no significant "free" oxygen ions have, for example, been observed in silicates with more than 50 mol% SiO_2.

(iv) The Gibbs free energy of mixing is not entirely due to mixing of the three kinds of oxygen ions, because their distribution within the Q^n-units and mixing of larger anionic units should also contribute to entropy of mixing.

The success of acid-base theories in aqueous solutions rests primarily on the well-defined nature and extremely small concentration of solutes. This allows activities to be either approximated by mol fractions, or readily calculated from the Debye-Hückel theory of electrolytes for solute concentration of up to about 1 mol%. Although a Debye-Hückel formalism has been used to model liquid immiscibility in binary metal oxide-silica systems (Tomozawa et al., 1990), no further application has been made. As a matter of fact, a general theory of aqueous solutions valid for concentrations of solutes similar to those of M_xO oxides in silicate melts remains to be worked out. Hence, formalisms established for concentrated aqueous solutions are unlikely to be transposable to silicate melts where MO_n complexes are not discrete independent entities dispersed throughout the solvent but rather essential components of the structure.

These differences notwithstanding, there remain definite similarities between the optical spectra of ions in silicate glasses and in aqueous solutions (see Duffy and Ingram, 2002). The similar colors conferred by dissolved ions in both cases are the most obvious manifestation of this kinship. For this reason, Duffy and Ingram (1971) assumed that spectroscopic measurement could provide a measure of the electron donor power of oxygen as a function of the nature of the cation (see also Duffy, 2018). Such a general scale of *optical basicity* relies on ultraviolet spectroscopic measurements made on dissolved ions, such as Tl^+ and Pb^{2+}, whose electron densities are very sensitive probes of the extent to which these ions receive negative charge from oxygen atoms. Duffy and Ingram (1971) thus defined the optical basicity as:

$$\Lambda = \left(v_{\text{free ion}} - v_{\text{glass}}\right) / \left(v_{\text{free ion}} - v_{\text{CaO}}\right), \tag{6.11}$$

where v is the s-p frequency of the probe ion in a free, uncomplexed state (e.g., 60,700 cm^{-1} for Pb^{2+}) in the glass and in crystalline CaO (e.g., 29,700 cm^{-1} for Pb^{2+}), which is taken as a convenient reference state. This parameter ranges from 0.33 (P^{5+}) to 1.7 (Cs^{+}), with values of 0.48 (Si^{4+}), 0.60 (Al^{3+}), 1.0 (Fe^{2+}), 1.15 (Na^{+}), and 1.3 (Mg^{2+}). It can be used for phosphate and other oxidic glass. Hence, it allows basicity to be determined directly for a variety of complex materials and to be related to other measures of basicity such as carbonate or sulfide solubility (e.g., Moretti and Ottonello, 2003). Further work has led to its empirical determination as a function of composition (Duffy, 1993; Mills, 1993).

6.3.5 Energetics of Mixing

Some enthalpy and Gibbs free energy data of mixing for binary melt oxide silica systems exists based on calorimetric observations and numerical modeling (Seo and Tsukihashi, 2004; Morishita et al., 2004; Romero-Serrano et al. 2010; Sugawara et al., 2011). Heat of solution of SiO_2 in alkali-SiO_2 glasses, $\Delta H^{sol}(SiO_2)$, were reported by Morishita et al. (2004). From those data, they derive partial molar enthalpy of SiO_2 in liquids as a function of composition:

$$\Delta\overline{\mathrm{H}}_{\mathrm{SiO2}}(\text{liquid}) = \frac{\Delta \mathrm{H}_{\mathrm{so1}}(\text{liquid})}{\Delta \mathrm{n}_{\mathrm{SiO2}}} \tag{6.12}$$

where Δn_{SiO_2} is the increment of SiO_2 added to the solution at high temperature and ΔH^{sol}(liquid) is the measured enthalpy of solution. The partial molar enthalpy of SiO_2 in these mixtures relative to the molar enthalpy of pure SiO_2 for any SiO_2 content follows the hierarchy of the metal cation properties (Fig. 6.8). Furthermore, the partial molar enthalpy is a strong nonlinear function of metal/Si ratio (Fig. 6.8) in a manner similar to that reported by Charles (1967). The relative partial molar entropy of SiO_2 in these melt systems also is very sensitive to the metal/Si ratio of the melt and very far from an ideal mixture (Morishita et al., 2004). Similar results were calculated for MO-SiO_2 liquids by Seo and Tsukihashi (2004) and Romero-Serrano et al. (2010). For the same systems, the calculated results seem very similar to one another.

Interestingly, in the M_xO-SiO_2 systems there is a systematic correlation between the depth of the minimum and the ionization potential of the divalent cation (Fig. 6.9). It was suggested that this latter correlation reflected a distribution of the divalent cations among free (isolated) oxygen anions and oxygen ions also bonded to the silicate structure (Romero-Serrano et al., 2010).

Experimentally determined enthalpy of mixing for Na_2O-SiO_2 melts shows a profound minimum between 30 and 40 mol% SiO_2 (Sugawara et al., 2011). The minimum also compares well with that computed by Romero-Serrano et al. (2005). Compared with the slope of an enthalpy of ideal mixing line, there is a distinct excess enthalpy with the maximum in quite silica-rich compositions (Hovis et al., 2004; see also Fig. 6.4). This composition corresponds to that of the metastable critical temperature of unmixing in the Na_2O-SiO_2 system

FIG. 6.8 Partial molar enthalpy of SiO_2 in alkali oxide-silica melts relative to the enthalpy of solution of pure SiO_2 (data from Morishita et al., 2004). Dashed lines are from Charles (1967).

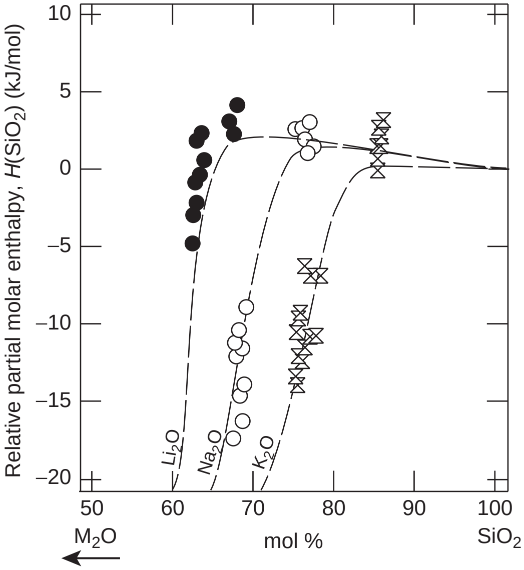

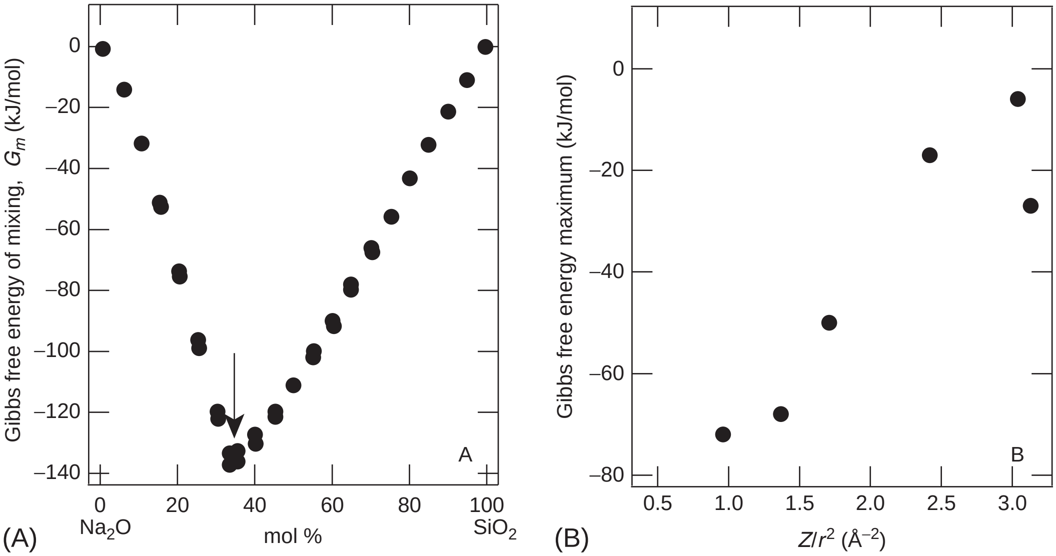

FIG. 6.9 Gibbs free energy of mixing along binary metal oxide-silica joins. (A) Gibbs free energy of mixing, G_m, as a function of Na_2O/SiO_2 abundance ratio (data from Sugawara et al., 2011). (B) Gibbs free energy of mixing maximum value (composition indicated by arrow in A) for various $MO\text{-}SiO_2$ glasses computed at 1600°C by Romero-Serrano et al. (2010). Ionization potential, Z/r^2, was calculated with the radius values from Whittaker and Muntus (1970) assuming sixfold coordinated cations with formal electrical charge, $Z=2$.

(Fig. 6.1). This is also the composition, therefore, with maximum steric hindrance. From about 70 to 50 mol% SiO_2, enthalpies vary linearly with composition. As the ionization potential of the metal cation increases, this effect also becomes more pronounced, which also leads to wider miscibility gaps and higher critical temperatures (Hudon and Baker, 2002a, b; see also Fig. 6.2).

6.3.6 Heat Capacity

The heat capacity, C_p, determines the temperature dependencies of the Gibbs free energy and other thermodynamic functions. To give a specific example, enthalpy of mixing as derived in the previous section from solution calorimetry relies on appropriate C_p data for glasses and liquids. The heat capacity must also be known in solid-liquid phase equilibria calculations. Given the differences between crystal and melt properties discussed in Chapter 4, Section 4.2, and illustrated in Fig. 4.2, the freezing point depressions, which can reach 1000 K in binary alkali silicates, cannot be modeled correctly without heat capacity data. Because the heat capacity can be split into vibrational and configurational parts, the latter can also provide basic information on atomic interactions.

A summary of available C_p measurements for binary metal oxide-silicate melts is given in Fig. 6.10. In most of the systems shown in Fig. 6.10, the heat capacity does not depend on temperature and is a linear function of composition from pure SiO_2 to the highest metal oxide content investigated. Hence, when writing

$$C_p = \sum x_i \overline{C}_{pi} = \sum x_i C_{pi}^{\circ} \qquad (6.13)$$

where x_i is the mol fraction of oxide i, $\overline{C}_{pi}$, the partial molar heat capacity of i does not depend on composition (and also on temperature) and thus is equal to a constant value C_{pi}°. The conclusion is best established for sodium silicates where measurements have been made on temperature intervals reaching 1000 K for the stable and supercooled liquid states. It is more circumstantial for CaO and MgO, in which cases the conclusion has to be drawn from analyses of data for more complicated melts because liquid immiscibility in binary CaO-SiO_2 and

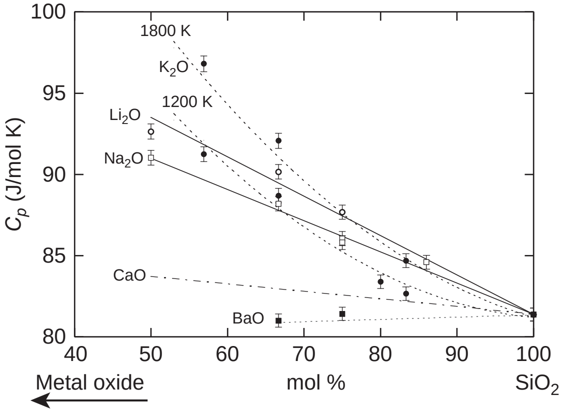

FIG. 6.10 Heat capacity, C_p, of binary silicate liquids. All C_p data are temperature independent, except for the K_2O-SiO_2 system for which C_p is shown at 1200 and 1800 K. Data from Stebbins et al. (1984) for 66 mol% BaO, and from Richet et al. (1984), Richet and Bottinga (1985), Téqui et al. (1992) for other melts.

MgO-SiO_2 restricts measurements in these systems to too narrow composition intervals. The only exceptions to these simple trends are provided by potassium silicates for which C_p increases with temperature and does not vary linearly with composition (Fig. 6.10). Similar variations for the binary systems involving the heavier alkali elements Rb and Cs could be expected, but measurements are lacking for both alkalis to check this assumption.

An important practical consequence of the lack of excess heat capacity embodied in the linear trends of Fig. 6.10 is that both enthalpy and entropy of mixing are independent of temperature. In addition, from the thermodynamic relationship:

$$\overline{C}_{pi} = C_{pi}^{\circ} - 2\,RT(\partial \ln \gamma_i/\partial T)_{P,nj} - RT^2\left(\partial^2 \ln \gamma_i/\partial T^2\right)_{P,nj} \tag{6.14}$$

one concludes that the activity coefficient of any oxide i varies with temperature as:

$$\ln \gamma_i = k_{i1}/T + k_{i2} \tag{6.15}$$

whenever the partial molar heat capacities of oxide components are independent of the composition of the melt.

The configurational heat capacity is approximated by the difference between the measured C_p and the vibrational value of $3R$/g atom K (see Chapter 3, Section 3.5.1). As noted by Stebbins et al. (1984), the configurational heat capacity approximatively increases with the ionization potential of the cation and thus correlates with the extent of liquid immiscibility. In this respect, an important conclusion is that the partial molar heat capacities of SiO_2 and metal oxides do not generally depend on composition, even though the melt structure varies widely between pure SiO_2 and the metasilicate stoichiometry. This feature indicates that temperature-induced structural changes in melts depend mainly on the abundance and abundance change with temperature of basic structural units that do not by themselves change much with composition, and not on the details of the structure (Richet and Bottinga, 1985). Hence, most of the configurational heat capacity is associated with short-range oxygen-cation interactions, which are also at the roots of liquid immiscibility and with coordination changes of network-forming cations (Stebbins, 1991; Stebbins and McMillan, 1993). This view does not mean that medium-range order is not affected but, rather, that the energetics involved in such changes are small, as already stated in Chapter 4, Section 4.2, from an analysis of low-temperature heat capacities.

6.4 VOLUME AND TRANSPORT PROPERTIES

In industry or in the earth sciences, few physical properties of silicate melts match in practical importance volume, or density (cf. Toplis, 2018). Both properties also are of fundamental interest. Whereas volume is a direct measure of ionic radii and atomic packing, the fact that viscosity is a very strong function of composition has been used to derive the early realistic structural models of melts (Bockris et al., 1956; Bockris and Reddy, 1970). In addition to volume and viscosity, electrical conductance must be mentioned because this transport property has provided the most demonstrative evidence for the partially ionic nature of silicate melts (Bockris et al., 1952a, b).

6.4.1 Volume, Thermal Expansion, and Compressibility

In this section, we will thus discuss molar volumes along with their deriviative properties, expansivity, and compressibility. Along with chemical composition, density in particular remains a basic parameter for characterizing a glass because it varies with the fictive temperature, $\overline{T}$, as follows

$$d\rho = \rho\left(\alpha_l - \alpha_g\right) d\overline{T}, \tag{6.16}$$

where α_l and α_g are the thermal expansion coefficients of the liquid and glass, respectively. For a given composition, the effects are small because the range of fictive temperatures that can be achieved with usual laboratory cooling rates is generally a few tens of degrees. In contrast, the effects of fictive temperature differences are not necessarily negligible when dealing with different glasses belonging to the same system. The extreme case is that of binary alkali silicates whose fictive temperatures can be lower than that of pure SiO_2 by 700 K or even more.

With typical values for silicates $\rho = 3\ \mathrm{g/cm^3}$, $\alpha_l = 8\ 10^{-5}$ and $\alpha_v = 10^{-5}\ \mathrm{K^{-1}}$, Eq. (6.15) indicates that a fictive temperature difference of 100 K translates into a density change of $0.02\ \mathrm{g/cm^3}$. This figure, in fact, represents the magnitude of density changes induced by variations in medium-range order. Hence, such simple calculations could be used to constrain models of glass structure. Conversely, slight apparent breaks found near eutectic compositions in density-composition relationships determined for glasses at room temperature have been interpreted in terms of varying substructure (Robinson, 1969; Doweidar, 1996). To be warranted, however, such interpretations should first rule out any bias due to differing thermal histories.

6.4.1.1 Volume and Thermal Expansion

The limitations of glasses as model substances for liquids are particularly clear when one considers the volume-composition relationship of sodium silicates (Fig. 6.11; see also Bockris et al., 1956; Knoche et al., 1994; Megahed, 1999). Not only is the thermal expansion coefficient much smaller for glasses than for liquids, but the volume-composition relationships are markedly different in both kinds of phases, with the thermal expansion coefficient for any Na/Si ratio greater for the melt than for its glass (Fig. 6.12B). Because the thermal expansion coefficient of liquids increases strongly with increasing Na_2O content, the density decreases sympathetically for high-temperature liquids. The effect, of course, reflects the increasingly important configurational changes that take place in the liquid as a result of increasing depolymerization.

For glasses, the density and thermal expansion are readily measured through Archimedean and dilatometric experiments, respectively. However, softening of the sample in the glass transition range and then too-high viscosities, often associated with partial crystallization, prevent dilatometric measurements at higher temperatures. For melts, several methods can be used when the viscosity has become sufficiently low above the liquidus. The most precise is high-temperature Archimedean measurements (see data comparisons by Bottinga et al., 1983). By combining such data with volumes determined by dilatometry at the glass transition, one can determine an average thermal expansion coefficient for the liquid:

$$\alpha = 1/V(\partial V/\partial T)_P, \tag{6.17}$$

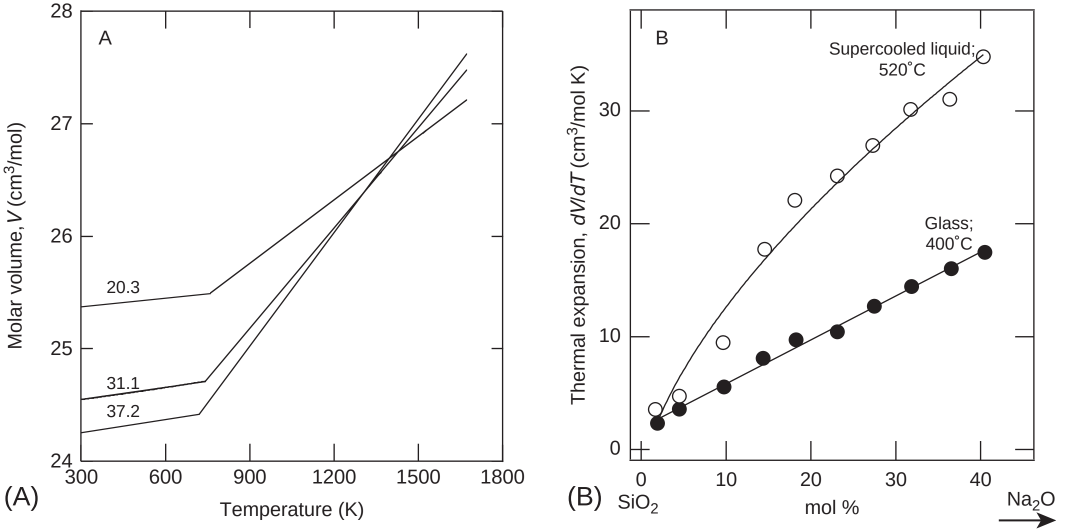

FIG. 6.11 Volume properties of glasses and melts. (A) Molar volumes of Na_2O-SiO_2 glasses and melts for the Na_2O mol% values indicated. Dilatometric data of Shermer (1956) up to the glass transition and Archimedean measurements of Bockris et al. (1956) above the liquidus. (B) Thermal expansivity of Na_2O-SiO_2 glasses and melts at conditions indicated as a function of composition (Knoche et al., 1994).

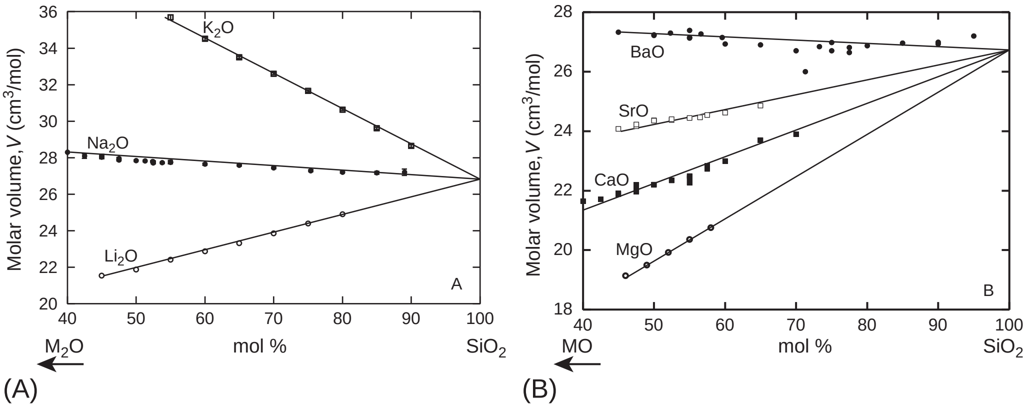

FIG. 6.12 Molar volumes of binary metal oxide-silica melts at 1400°C. (A) Alkali silicates (data from Bockris et al., 1956), and (B) Alkaline earth silicates (Tomlinson et al., 1958).

as shown in Fig. 6.11A for sodium silicate glasses and melts. In this case, the differences in the density-composition relationships between the glass and high-temperature melt illustrate the importance of knowing the changes in thermal expansion coefficient at the glass transition as accurately as possible.

For binary metal oxide-silica systems, the most precise and extensive volume measurements remain those of Bockris et al. (1956) for alkali silicate melts and Tomlinson et al.

(1958) for alkaline earth silicate melts. In all cases (Fig. 6.12), the volume-composition relationships are linear within experimental error. Notably, by mixing different alkalis such as Li and Cs, for example, the volume is a linear function of the proportion of the added component (Li^+) in exchange for another alkali metal, in this case Cs^+ (Fig. 6.13; see also Megahed, 1999). Analogous relations have been reported for Li^+ for K^+ and Na^+ for K^+ exchange (Megahed, 1999). The relationship seems to hold for different SiO_2 concentrations as well. Interestingly, the slope in Fig. 6.13 shows only a very slight decrease as the SiO_2 concentration is increased from 67 to 80 mol% (slope decreases by ~5%).

As originally emphasized by Bottinga and Weill (1970), the partial molar volumes of oxides thus are essentially independent of composition from 40 to 80 mol% SiO_2. For the SiO_2 component, the partial molar volume of about 26.8 cm^3/mol is, in addition, almost temperature independent. If volume is an additive function of composition at any temperature, then additivity also holds true for thermal expansion, $(\partial V/\partial T)_p$, with the consequence that the thermal expansion coefficient, as given by Eq. (6.15), cannot be exact linear functions of composition. But the effect is small so that, in the high-temperature range investigated by Archimedean methods, the thermal expansion coefficient, α, is also an additive function of composition within experimental errors at least for alkali silicate melts (Fig. 6.14). The data for alkaline earth silicate melts are considerably more scattered. However, in all cases, there is a continuous decrease in thermal expansion with increasing SiO_2 concentration (Bockris et al., 1956; Tomlinson et al., 1958; Knoche et al., 1994).

The thermal expansion coefficient of metal oxide-silicate melts, whether from alkali or alkaline earth silicate, decreases as the melts become silica-enriched and as the ionization potential of the metal cation decreases (Figs. 6.11B, 6.14). These trends can be correlated with the average bond strength of the melts. As SiO_2 concentration increases, the thermal expansion

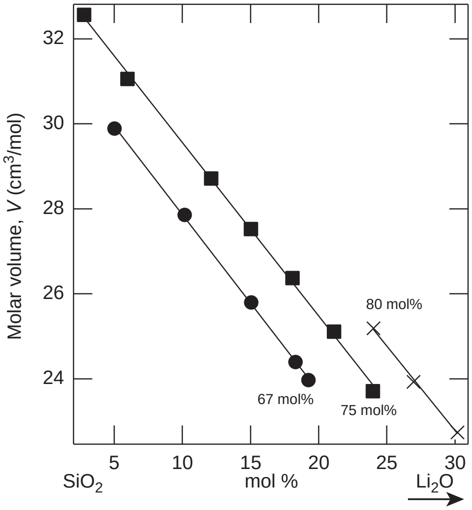

FIG. 6.13 Molar volume of Li_2O-Cs_2O-SiO_2 glasses as a function of their Li_2O and SiO_2 concentrations. *Redrawn from Megahed (1999).*

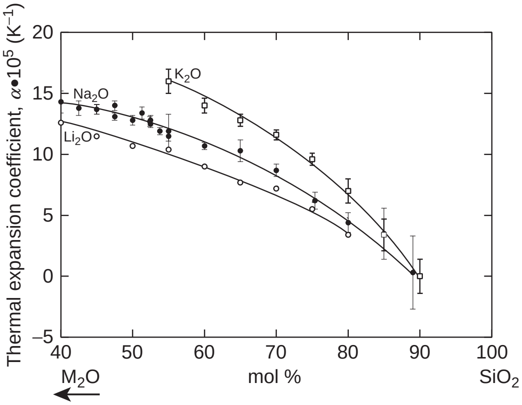

FIG. 6.14 Thermal expansion coefficient of binary alkali oxide-silica melts at 1400°C (Bockris et al., 1956).

becomes increasingly dependent on the strength of bridging Si—O—Si bonds, which are the strongest among the bonds in these structures. Consequently, with increasing SiO_2 concentration the average bond strength increases and the thermal expansion coefficient decreases. The negative correlation between thermal expansion and ionization potential of the metal cation can be rationalized in a similar manner. The curvature of these trends as a function of metal oxide/SiO_2 ratio also explains why extrapolation to pure SiO_2 results in molar volume values of SiO_2 (26.8 cm^3/mol) that differ from those measured for pure SiO_2 (see Chapter 5, Section 5.3.3).

6.4.1.2 *Volume and Compressibility*

It has been suggested that the partial molar volume of bridging oxygen is greater than that of nonbridging oxygen (Bottinga and Richet, 1995). It would follow that high pressure should promote depolymerization of the silicate framework unless this pressure derivative changes with pressure, because volume is the pressure derivative of the Gibbs free energy.

High-pressure volumes can be calculated from the isothermal compressibility:

$$\beta_T = -1/V\,(\partial V/\partial P)_T. \tag{6.18}$$

With ultrasonic or Brillouin scattering methods, it is in principle much less difficult to measure compressional sound velocities, v_p, which yield the adiabatic compressibility:

$$\beta_S = -1/V(\partial V/\partial P)_S = 1/\rho v_p^2, \tag{6.19}$$

where ρ is density.

However, few studies have been made because of the high temperatures required to overcome relaxation problems that clearly beset earlier ultrasonic work (e.g., Bockris and Kojonen, 1960) in view of the 10^{-6} s timescales of these experiments (cf. Section 2.3.2). For alkali silicates, an added difficulty lies in the risk of composition changes caused by sample vaporization during the experiments at such high temperatures.

Results for binary metal oxide-silica melts are plotted in Fig. 6.15. They indicate linear variations of both sound velocity and adiabatic compressibility with composition at least to 90 mol% SiO_2. Relaxation is a problem for SiO_2-rich melts as indicated in Fig. 6.15A by the sound velocities measured at 2070 K for lithium silicates, which become increasingly too high at SiO_2 contents higher than 88 mol%.

For relaxed compressibility data, the effects of metal oxides depend on the nature of the metal cation. The contrast between the influence of K_2O on the one hand, and that of CaO and Li_2O on the other, shows that the compressibility is increased or decreased by addition of metal oxides depending on whether the ionization potential is low or high. This effect reflects in part different average stiffness of the nonbridging oxygen bonds depending on the network-modifying cation with which it forms bonding (see Chapter 2, Section 2.3) and in part on the different distribution of silicate structural units depending on the electronegativity of the metal cation (see also Chapter 7).

For the three binary systems of Fig. 6.16, the adiabatic compressibility converges toward a common value of about 7.5 10^{-11} Pa^{-1} for pure SiO_2, which appears to depend little on temperature in view of the differing temperatures of the experimental data. The precision of these data is insufficient, however, to check whether there could exist a compressibility difference

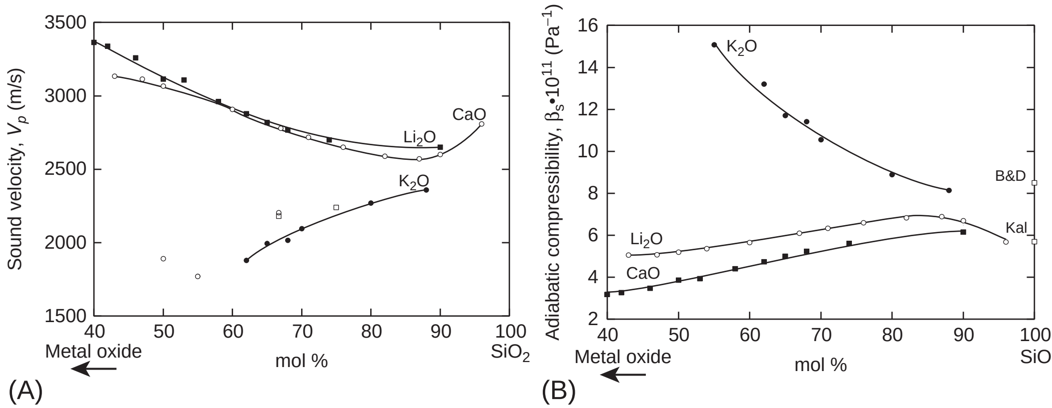

FIG. 6.15 Elastic properties of binary silicate liquids. (A) Sound velocity at 1900 K for CaO-SiO_2, at 1670 K for K_2O-SiO_2, and at 1670 and 2070 K for SiO_2-poor and SiO_2-rich Li_2O-SiO_2 melts, respectively (both sets join smoothly because of a slight temperature dependence in this system). Data of Baidov and Kunin (1968), with measurements of Laberge et al. (1973, *open squares*) and Rivers and Carmichael (1987, *open circles*) near 1700 K for potassium silicates. (B) Adiabatic compressibility derived from the data shown in A and the densities of Bottinga and Weill (1970). The Brillouin results of Bucaro and Dardy, 1976, B and D) and Krol et al., 1986, Kal) are plotted for pure SiO_2.

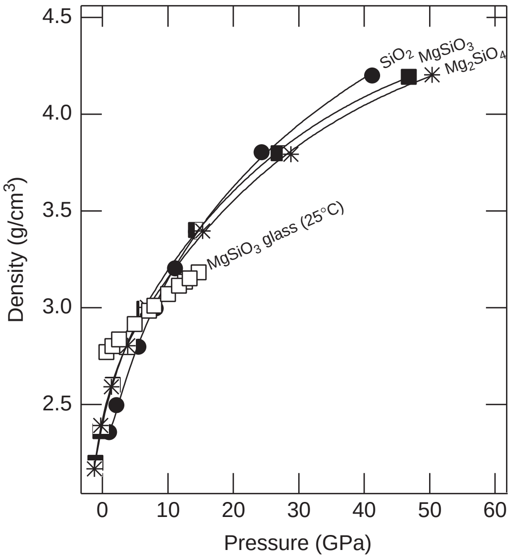

FIG. 6.16 Pressure-dependent melt density as a function of Mg/Si ratio of MgO-SiO_2 melts at 3000 K (Lacks et al., 2007). Also shown are experimentally determined glass densities (from sound velocity measurements) from Sanchez-Valle and Bass (2010).

between bridging and nonbridging oxygens analogous to that discussed for molar volume in the previous section.

Density, volume, and compressibility data for metal oxide-silicate melts and glasses have been recorded both at ambient pressure and as a function of pressure (Laberge et al., 1973; Rivers and Carmichael, 1987; Agee, 1992; Murakami et al., 2007; Sanchez-Valle and Bass, 2010; Sanloup et al., 2013). The high-pressure data are, however, restricted to information for melts and glasses in the system CaO-FeO-MgO-SiO_2, a restriction likely driven by the desire to determine the density of melts and glasses in the interior of the earth and terrestrial planets.

Most of the high-pressure information has been either from ambient-temperature, high-pressure elastic measurements (Murakami et al., 2007; Sanchez-Valle and Bass, 2010) or by numerical simulation at high temperature and pressure (Lacks et al., 2007; Stixrude et al., 2009; Sun et al., 2011; Ghosh et al., 2014). The comparative lack of data recorded for melts at high temperature and pressure reflects the significant experimental challenges associated with such experiments.

For melts along the SiO_2-MgO join at low pressure, results from numerical simulation indicate that density increases with increasing Mg/Si abundance ratio (Lacks et al., 2007). However, these relationships are reversed at pressure above about 15 GPa (Fig. 6.16). That happens because melts are increasingly compressible with decreasing Mg/Si abundance ratio. Also shown in Fig. 6.16 are the experimental density data of $MgSiO_3$ glass as a function of pressure (Sanchez-Valle and Bass, 2010). Notably at low pressure, density is greater for the glass than for its melt. Glass is less compressible than melt, however, so this relationship is reversed at high pressure (Fig. 6.16).

Melt density and compressibility also respond to various solid solutions such as Mg, Fe (Stixrude et al., 2009) and Ca, Mg (Chen et al., 2002; Ghiorso, 2004). For metasilicate compositions, for example, increasing Fe/Mg or Ca/Mg abundance ratios both result in increased density. However, the compressibility is less sensitive to melt and glass composition. The main differences are different pressure-temperature trajectories of the Ca^{2+}, Mg^{2+}, and Fe^{2+} coordination numbers.

6.4.2 Transport Properties

6.4.2.1 *Viscosity*

Viscosity is of particular importance because it controls the rate of transport of matter and thus of energy. For silicate melts, it is usually measured either above the liquidus, in the range 1–10^5 Pas, or near the glass transition in the interval 10^{13}–10^9 Pas (see Deubener (2018) for a review). Crystallization generally prevents measurements from being made at intermediate viscosities.

A great many measurements have been made by glassmakers and metallurgists on binary metal oxide-silica melts (see review by Ryan and Blevins, 1987). Those by Bockris and Lowe (1954) and Bockris et al. (1955a, b) still remain the most extensive data set and are considered the most reliable at high temperature. Owing to the problems raised by poor glass formation, hygroscopicity at low SiO_2 concentration, or liquid immiscibility at high SiO_2 content, measurements are scarce, in contrast, near the glass transition where they are restricted to alkali silicates (e.g., Poole, 1948).

The most conspicuous features are the viscosity variations with both composition and temperature. Probably there is no other property of silicate melts that can vary by more than 8 orders of magnitude at constant temperature along a binary join (Fig. 6.17). The extent of this variation does, however, decrease with increasing temperature.

Likewise, the viscosity can vary by more than 10 orders of magnitude between the glass transition and superliquidus conditions (Fig. 6.18A). In an Arrhenius diagram, it also appears

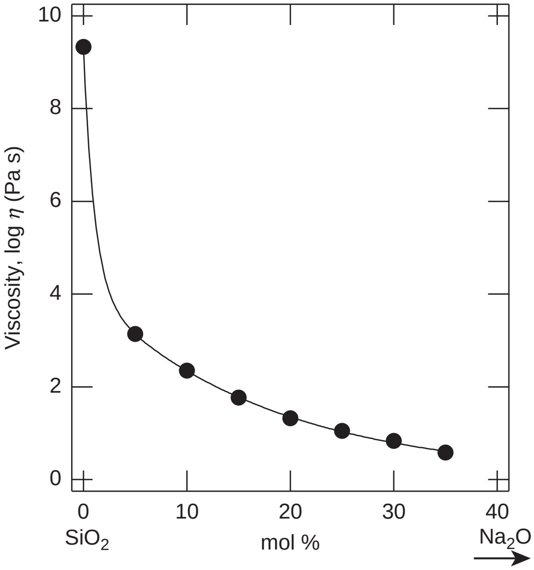

FIG. 6.17 Viscosity of melts (and supercooled melts) along the SiO_2-Na_2O join at 1350°C (data from Urbain et al., 1982; Knoche et al., 1994). Note that the 5 and 10 mol% Na_2O data points were obtained by extrapolating the higher-temperature viscosity data to 1350°C assuming Arrhenian viscosity behavior in this temperature range.

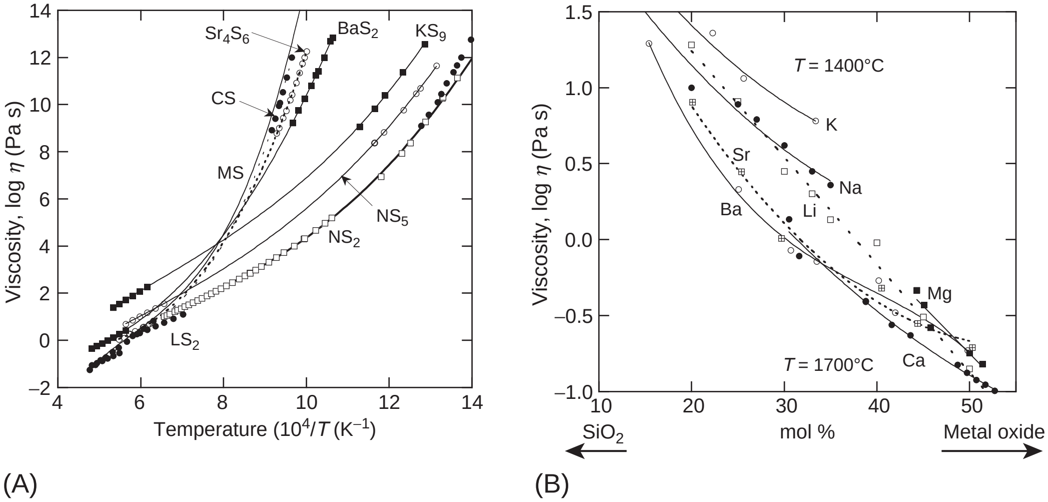

FIG. 6.18 Viscosity of binary metal oxide-silica melts. (A) Against reciprocal temperature. (B) Against SiO_2 content for alkali and alkaline earth melts at 1400°C and 1700°C, respectively. At these temperatures, the log viscosity (Pas) of SiO_2 liquid is 8.9 and 6.4 (Urbain et al., 1982). Abbreviations used in (A): Ba (BaO), C (CaO), K (K_2O), L (Li_2O), M (MgO), N (Na_2O), S(SiO_2), Sr (SrO). Data from Fontana and Plummer (1979) for NS_2; Bockris et al. (1955a, b), Poole (1948), and Sipp and Richet (2002) for other alkali silicate; Bockris et al. (1955a, b) and Neuville (unpub.) for BaS_2; Neuville (2006) for Sr_4S_6; Bockris et al. (1955a, b) and Neuville and Richet (1991) for MS and CS. In B, all data from Bockris and Lowe (1954) and Bockris et al. (1955a, b).

that both viscosity and its temperature dependence depend markedly on composition. The departure from an Arrhenian variation increases with decreasing SiO_2 content and is larger for alkaline earth than for alkali silicates. For a given stoichiometry, the viscosity varies relatively little within both series. Practically, an important consequence of non-Arrhenian viscosity is the crossover observed at around 1200 K (Fig. 6.18A) when alkali silicates, least viscous at low temperatures, become more viscous than alkaline earth melts. As described in Chapter 3, Section 3.4.5, these variations are quantitatively connected to the melt configurational heat capacities through the Adam and Gibbs (1965) theory of relaxation processes (Richet, 1984).

In contrast to the many orders of magnitude viscosity differences that prevail near the glass transition, the viscosity of silicate melts depends relatively weakly on composition at high temperature (Figs. 6.18B). The largest changes are found when metal oxides begin to be added to pure SiO_2 (Fig. 6.17). The associated variations of activation energies follow similar trends. These changes are much greater than the differences observed within both the alkali and alkaline earth series, where the viscosity varies by less than a factor of five at constant temperature for a given stroichiometry. Again, the viscosity varies with the ionization potential of the cation, except for Li melts at high SiO_2 content.

The viscosity of ternary metal oxide-silicate melts is not linear functions of compositions but instead typically deviates negatively from such a mixing trend (Day, 1976; Neuville and Richet, 1991; Le Losq and Neuville, 2017; see also Fig. 6.19). Analogous data have been reported for other alkali and alkaline earth silicate joins and modeled by a combination of configurational entropy theory with structural characterization of the melts (Le Losq and Neuville, 2017).

In metal oxide-silicate systems, the activation energy of viscous flow varies with temperature (Fig. 6.20), which is, of course, a direct consequence of the non-Arrhenian behavior of such melts and glasses. As described in Chapter 3, Section 3.4.5, the Adam and Gibbs (1965) theory of relaxation processes provides an explanation of such behavior in terms of increases of configurational entropy, the energy barriers hindering the cooperative rearrangements of the structure remaining the same at all temperatures (Richet et al., 1986). Specifically, one derives from Eq. (2.24), Section 2.4.5 in Chapter 2:

$$\Delta H_\eta = 2.303 \bullet \mathrm{R} \bullet \mathrm{B_e}\left(S^{conf} + C_p{}^{conf}\right) / \left(S^{conf}\right)^2, \tag{6.20}$$

an equation that accounts quantitatively for the observed variations of activation energies.

In addition, alkali silicate liquids illustrate an important pitfall that can affect activation energies. Viscosity is measured either above the liquidus or near the glass transition. There is commonly a gap at intermediate temperatures because of incipient crystallization, which restricts measurements to temperatures outside this crystallization interval. In both the low- and high-temperature intervals where no crystallization occurs, viscosity may appear Arrhenian if the data cover restricted temperature intervals or experimental accuracy is not high. The comparisons made in Fig. 6.20 for sodium silicate melts between such isothermal activation energies and average "Arrhenian" values show that the latter can be biased to the point that their composition dependence is the opposite of the actual trend. The origin of the bias is that the temperature intervals investigated vary systematically with composition because they are determined by various conditions (glass transition and liquidus

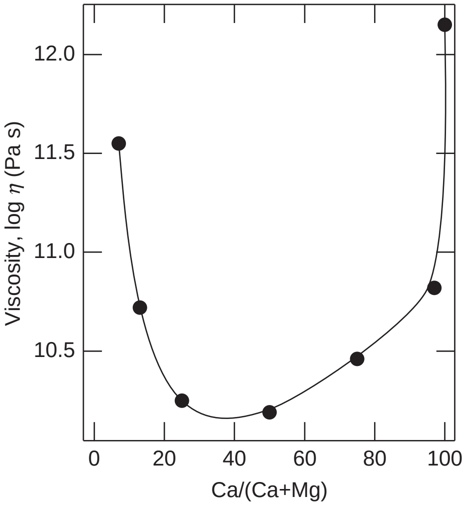

FIG. 6.19 Viscosity of metasilicate melts at 1050°C as a function of Ca/(Ca + Mg) abundance ratio (Neuville and Richet, 1991).

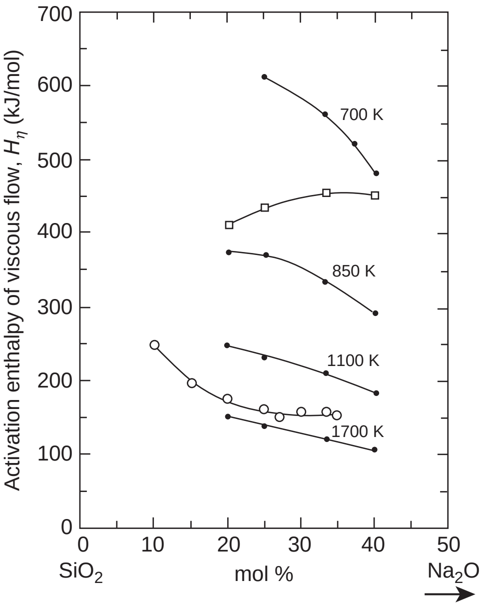

FIG. 6.20 Actual, temperature-dependent activation enthalpies for viscous flow of sodium silicate liquids at the temperatures indicated. Values derived by Richet et al. (1986) from the data of Poole (1948) above the glass transition, and Bockris et al. (1956) above the liquidus. For comparison, the mean activation enthalpies determined from Arrhenius laws for each range of temperatures are plotted as open symbols.

temperatures, high-temperature volatility, etc.), which also vary strongly with composition (see, e.g., Knoche et al., 1994). Identification of breaks in activation energies at eutectic or other fixed points of phase diagrams thus is not warranted unless actual isothermal values have been derived from non-Arrhenian fits made to the experimental data.

Experimental measurements of viscosity of metal oxide–silicate melts for the most part have been restricted to less than 10 GPa (Scarfe et al., 1987; Dickinson et al., 1990; Spice et al., 2015). An exception is the study by Reid et al. (2003), who measured the viscosity of liquid $CAMgSi_2O_6$ to 13 GPa. In these experimental studies, the general conclusion has been that for pressures less than 10 GPa, initial melt polymerization governs whether the viscosity of the melts is a positive or negative function of pressure (Fig. 6.21; see also Scarfe et al., 1987; Dickinson et al., 1990). In an early discussion of these viscosity data, Scarfe et al. (1987) concluded that melts with $NBO/Si \leq 1$ likely would show decreasing viscosity with increasing pressure, whereas for melts with $NBO/Si \geq 1$, their viscosity generally would increase with increasing pressure. Of course, as pressure reached values where coordination transformation of cations takes place, melt viscosity tends to turn to a negative function of pressure (Reid et al., 2003). The pressure at which this viscosity turnover occurs seems dependent on melt composition. In the calculations by Lacks et al. (2007), the viscosity of SiO_2 melt decreases until about 20 GPa pressure, above which it increases with further pressure increase

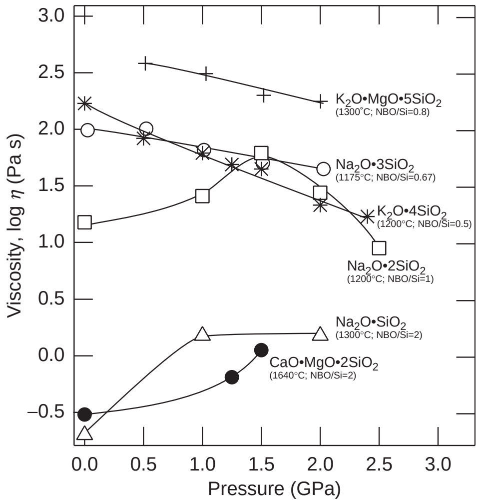

FIG. 6.21 Viscosity of various metal oxide-silicate melts as a function of pressure to about 2.5 GPa. Data sources are Scarfe et al. (1987), Dickinson et al. (1990), Kushiro (1976, 1977).

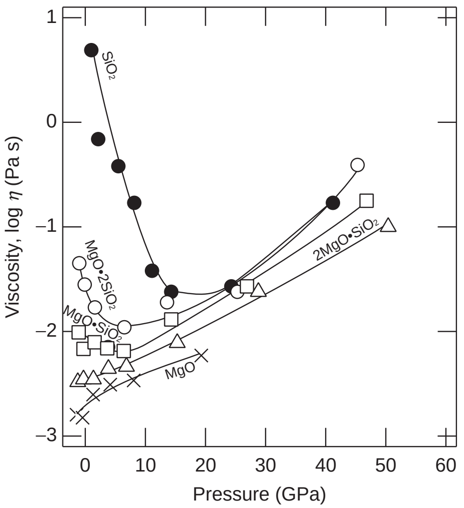

FIG. 6.22 Calculated viscosity of melts along the join MgO-SiO_2 at 3000 K as a function of pressure (Lacks et al., 2007).

(Fig. 6.22). However, for melts with Mg/Si ≤ 2 (MgO·SiO_2), the viscosity minimum seems to be at lower pressure—near 10 GPa, whereas for even more Mg-rich melts, the viscosity increases continuously from ambient pressure. Interestingly, the viscosity above the pressure minimum is much less sensitive to composition than at lower pressures (Fig. 6.22). By exchanging Ca^{2+} for Mg^{2+}, similar trends have been reported from results of numerical simulations, but with a tendency for increased viscosity compared with melts in the simpler system MgO-SiO_2 (Zhang et al., 2010).

An exception to this general rule can be found in recent data by Spice et al. (2015) for Fe_2SiO_4 melts, which was found to decrease with increasing pressure. Although no experimental data exist for other orthosilicate composition melts, results of numerical simulation of high-pressure viscosity of Mg_2SiO_4 indicate increasing viscosity with increasing pressure (Lacks et al., 2007; Adjaoud et al., 2011). The reason for this apparent difference is not clear, but may be related to different coordination number and pressure dependence of Fe^{2+} and Mg^{2+}.

6.4.2.2 *Diffusion*

Although there is a wealth of tracer diffusion data for simple metal oxide-silica systems (see Ni and Koker, 2018), few measurements have been made for different elements in the same composition. Some of these results have already been mentioned in Section 4.6.1 to show the great difference between the diffusivities and associated activation enthalpies observed between network-modifying cations and oxygen. Interesting exceptions are the data gathered at 1600°C for CaO-SiO_2 melts (Fig. 6.23). Consistent with the trends already discussed, no difference is found between oxygen and silicon diffusivities, which are both lower than that of Ca^{2+} by less than an order of magnitude. All diffusivities

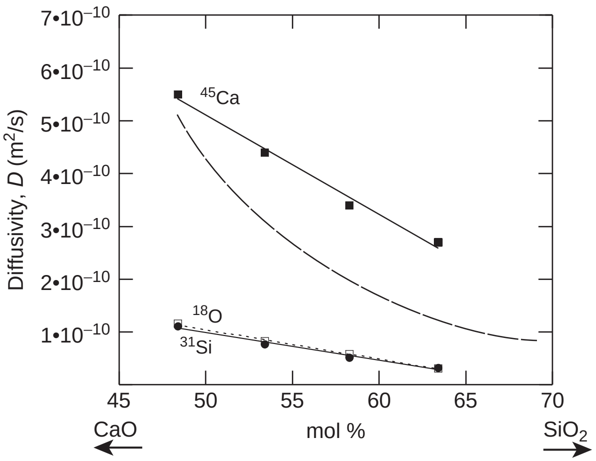

FIG. 6.23 Tracer diffusivities of ^{45}Ca, ^{18}O, and ^{31}Si against SiO_2 content in binary CaO-SiO_2 melts at 1600°C (Keller and Schwerdtfeger, 1979; Keller et al., 1979, 1982). The dashed line represents diffusivities calculated from the Eyring relation and the viscosities of Bockris and Lowe (1954) and Urbain et al. (1982).

are linear functions of composition in the investigated intervals. Interestingly, however, their difference decreases sufficiently rapidly with increasing SiO_2 content so that an extrapolation of these trends would point to faster diffusion for Si and O than for Ca at SiO_2 contents higher than 80 mol%. In view of the data shown in Fig. 5.19, this situation is unlikely. This indicates that, before such a concentration is reached, the linear relationships should break down to match the higher diffusivity of O compared to Si in pure SiO_2. One might expect that information could be derived in this respect from the Eyring relationship in Eq. (4.11), as it relates diffusivities to viscosities which are known up to 100 mol % SiO_2. The Eyring diffusivities are of little help, however, because they match, curiously, the Ca data at low SiO_2 content before tending to the Si diffusivities as described for pure SiO_2 in Chapter 5, Section 5.3.4.2.

In general, the diffusivity and activation enthalpy of diffusion of metal oxide-silicate melts at high temperature decrease with increasing metal/silicon abundance ratio (Seo and Tsukihashi, 2004; see review by Lesher, 2010). For given melt composition, the diffusivity also decreases with increasing electrical charge.

From simple system numerical simulations, one finds that, more often than not, there is at least a semiquantitative link between viscosity and diffusivity (Shimizu and Kushiro, 1984; Reid et al., 2003; Lacks et al., 2007; Zhang et al., 2010). Therefore, the zero-pressure diffusivity of melts in the MgO-SiO_2 system follows a pattern of decreasing values as the proportion of MgO increases (Fig. 6.24). We also see that the diffusivities of O and Si are for all practical purposes identical, while the D_{Mg} is decoupled from the Si and O (Fig. 6.4). Notably, this difference diminishes with increasing Mg/Si abundance ratio. Though present, these relationships become less distinct at high pressure (Zhang et al., 2010). The O and Si diffusivities are for all practical purposes mirror images of the melt viscosity, which is, of course, as would be expected if these properties were linked via the Eyring equation; see Eq. (4.11).

From the limited experimental and simulation data available, it appears that pressure effects on diffusivity also seem to be a mirror image of melt viscosity. For diopside melt, for example, oxygen and silicon diffusivities decrease with pressure until slightly below 10 GPa before both diffusivities increase with further pressure increase (Fig. 6.25; see also

FIG. 6.24 Simulated melt viscosity and diffusivities at 3000 K and ambient pressure for melts along the join MgO-SiO_2 (Lacks et al., 2007).

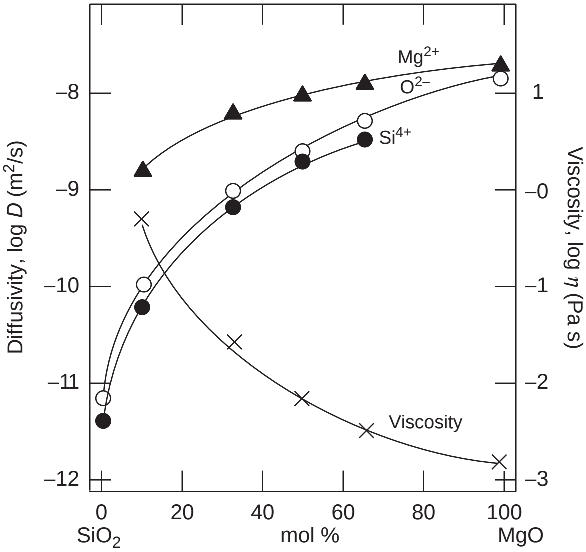

FIG. 6.25 Oxygen and silicon diffusion in CaO·MgO·2SiO_2 melt at 2000°C as a function of pressure (Dunn, 1982; Shimizu and Kushiro, 1984, 1991; Reid et al., 2003).

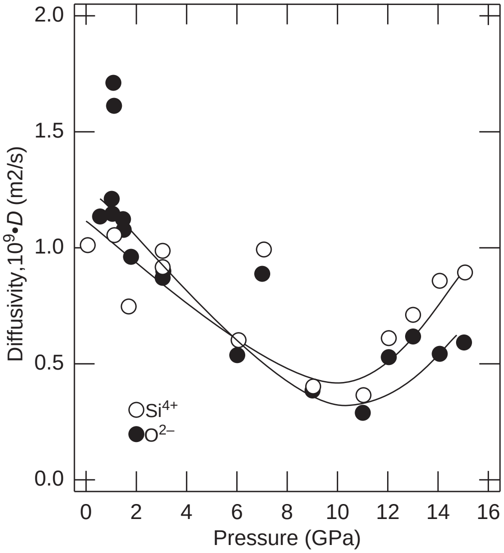

Reid et al., 2001; Verma and Karki, 2012). It may be recalled that the viscosity of diopside melt increases with increasing pressure until a maximum value is reached (Reid et al., 2003).

6.4.2.3 *Electrical Conductivity*

Until the mid-19th century, molten silicates were generally considered to be made up of molecular entities. Following the discovery of ionic dissociation in solutions, the question remained unclear until the classic high-temperature experiments by Bockris et al. (1952a,

b) eventually demonstrated the ionic nature of a variety of binary metal oxide-silica systems (Souquet, 2018). First, Bockris et al. (1952a, b) found that the electrical resistivity of these melts is lower, but of the same order of magnitude, than that of chlorides of the same metals. Second, the resistivity decreases with the proportion of metal oxide and is lowest with oxides of univalent metals with small ionic radii. Over the temperature intervals investigated, the resistivity follows an Arrhenius law

$$\rho_e = \rho_0 \exp\left(-\Delta H_\rho / RT\right). \tag{6.21}$$

The activation enthalpy, ΔH_ρ, increases slightly with increasing metal oxide content, whereas the preexponential parameter, ρ_0, decreases or increases with increasing metal oxide content in alkaline earth and alkali systems, respectively.

Through electrolysis experiments, Bockris et al. (1952a) further showed that electrical current is carried wholly by network-modifying cations. They found no evidence for either "free" oxygen ions O^{2-} or free Si^{4+}, the concentration of the former having later been found to be of the order of 10^{-5} (Semkow and Haskin, 1985). These observations demonstrated that silicate melts are only partially ionic and that anions must be large in size compared to the cations. Bockris et al. (1952b) also made the important observation that the activation energy is from two to four times smaller for electrical conduction than for viscous flow.

Although it has often been assumed that electrical resistivity follows Arrhenian laws, measurements made over sufficiently large temperature intervals show that this is generally not the case (Fig. 6.26). As for viscosity, the observations can be reproduced by the TVF equation:

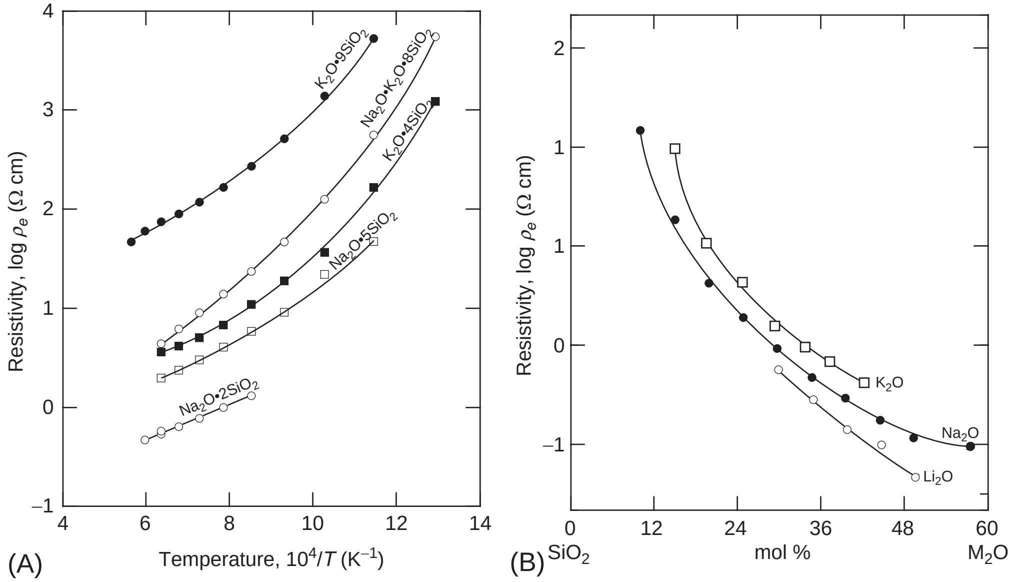

FIG. 6.26 Electrical resistivity of alkali silicate melts. (A) Against reciprocal temperature; (B) Against metal oxide content at 1200°C. *Redrawn from Tickle (1967).*

$$\log \rho_e = A + B/(T - T_1), \tag{6.22}$$

where A, B, and T_1 are fit parameters. In alkali silicates, electrical conductivity is due to the mobility of alkali ions. Because alkali ions remain mobile when viscous flow become vanishingly small, the temperature, T_1, of such equations is lower for electrical resistivity than for viscosity. For instance, the T_1 values are 318 (35) kJ/mol and 427 (11) kJ/mol for $K_2Si_9O_{19}$, and 88 (173) J/mol and 420 (3) J/mol for $Na_2Si_5O_{11}$ for electrical resistivity and viscosity, respectively. The electrical resistivity is a regular function of ionic potential, the order being Li, Na, K (Fig. 6.26B), except at high SiO_2 content where, for reasons that are yet unclear, the order is Na, Li, K (Tickle, 1967).

Another significant feature is the marked nonlinear variation of resistivity when two different alkali cations are mixed and the M_2O/SiO_2 ratio is kept constant (Fig. 6.27). The effect is more pronounced the lower the temperature. It parallels the viscosity extremum described previously for an alkaline earth system (Fig. 6.19), with the important feature that the viscosity minimum is associated with a resistivity maximum. These are two manifestations of the so-called mixed alkali effect, which is also observed in internal friction, electrical conductivity, or alkali diffusion experiments. Although numerous theories have been proposed to account for its various aspects (e.g., Day, 1976; Ngai et al., 2002), no general explanation has been agreed upon.

FIG. 6.27 Mixed alkali effect on electrical resistivity. Data for (Na, K)$_2$Si$_4$O$_9$ liquids at the temperatures indicated. *Redrawn from Tickle (1967).*

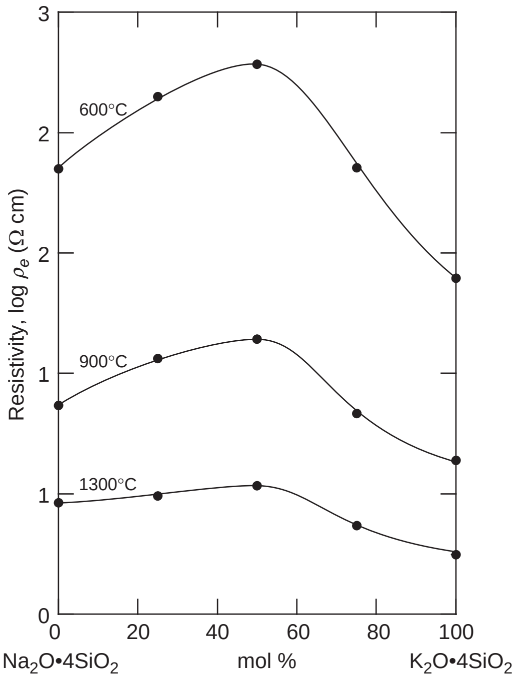

References

Adam, G., Gibbs, J.H., 1965. On the temperature dependence of cooperative relaxation properties in glass-forming liquids. J. Chem. Phys. 43, 139–146.

Adams, L.H., 1914. Calibration tables for copper-constantan and platinum-platinum rhodium thermoelements. J. Am. Chem. Soc. 36, 65–72.

Adjaoud, O., Steinle-Neumann, G., Jahn, S., 2011. Transport properties of Mg_2SiO_4 liquid at high pressure: physical state of a magma ocean. Earth Planet. Sci. Lett. 312, 463–470.

Agee, C.B., 1992. Isothermal compression of molten Fe_2SiO4. Geophys. Res. Lett. 19, 1169–1172.

Babcock, C.L., 1968. Substructures in silicate glasses. J. Am. Ceram. Soc. 51, 163–169.

Baidov, V.V., Kunin, L.L., 1968. Speed of ultrasound and compressibility of molten silica. Soviet. Phys. 13, 64–65.

Bansal, N., Doremus, R., 1986. Handbook of Glass Properties. Academic Press, Orlando.

Beyer, R.P., Ferranta, M.J., Brown, R.R., Daut, G.E., 1979. Thermodynamic properties of potassium metasilicate and disilicate. U.S. Bur. Mines Rep. Invest. 8410, 21.

Bockris, J.O'M., Kojonen, E., 1960. The compressibilities of certain molten alkali silicates and borates. J. Phys. Chem. 82, 4493–4497.

Bockris, J.O.'.M., Lowe, D.C., 1954. Viscosity and the structure of molten silicates. Proc. Roy. Soc. A226, 423–435.

Bockris, J.O'M., Reddy, A.K.N., 1970. Modern Electrochemistry. vol. 1. Plenum, New York.

Bockris, J.O'M., Kitchener, J.A., Davies, A.E., 1952a. Electric transport in liquid silicates. Trans. Farad. Soc. 48, 536–548.

Bockris, J.O'M., Kitchener, J.A., Ignatowicz, S., Tomlinson, J.W., 1952b. Electric conductance in liquid silicates. Trans. Farad. Soc. 48, 75–91.

Bockris, J.O'M., Mackenzie, J.O., Kitchner, J.A., 1955a. Viscous flow in silica and binary liquid silicates. Trans. Faraday Soc. 51, 1734–1748.

Bockris, J.O'M., Mackenzie, J.D., Kitchener, J.A., 1955b. Viscous flow in silica and binary liquid silicates. Trans. Farad. Soc. 51, 1734–1748.

Bockris, J.O'M., Tomlinson, J.W., White, J.L., 1956. The structure of the liquid silicates. Partial molar volumes and expansivities. Trans. Farad. Soc. 52, 299–310.

Bottinga, Y., Richet, P., 1995. Silicate melts: the "anomalous" pressure dependence of the viscosity. Geochim. Cosmochim. Acta 59, 2725–2732.

Bottinga, Y., Weill, D.F., 1970. Densities of liquid silicate systems calculated from partial molar volumes of oxide components. Am. J. Sci. 269, 169–182.

Bottinga, Y., Weill, D.F., Richet, P., 1981. Thermodynamic modeling of silicate melts. In: Newton, R.C., Navrotsky, A., Wood, B.J. (Eds.), Thermodynamics of Minerals and Melts. Springer Verlag, New York, pp. 207–245.

Bottinga, Y., Richet, P., Weill, D.F., 1983. Calculation of the density and thermal expansion coefficient of silicate liquids. Bull. Mineral. 106, 129–138.

Bowen, N.L., Andersen, O., 1914. The binary system MgO-SiO_2. Am. J. Sci. 37, 487–500.

Bucaro, J.A., Dardy, H.D., 1976. Equilibrium compressibility of glassy SiO_2 between the transformation and the melting temperature. J. Non-Cryst. Solids 20, 149–151.

Cahn, J.W., Charles, R.J., 1965. The initial stages of phase separation in glasses. Phys. Chem. Glasses 6, 181–191.

Chamberlin, L., Beckett, J.R., Stolper, E., 1994. Pd-oxide equilibration: a new experimental method for the direct determination of oxide activities in melts and minerals. Contrib. Mineral. Petrol. 116, 169–181.

Charles, R.J., 1967. Activities in Li_2O, Na_2O, and K_2O-SiO_2 solutions. J. Am. Ceram. Soc. 50, 631–641.

Charles, R.J., 1969. The origin of immiscibility in silicate solutions. Phys. Chem. Glasses 10, 169–178.

Chen, G.Q., Ahrens, T.J., Stolper, E.N., 2002. Shock-wave equation of state of molten and solid fayalite. Phys. Earth Planet. Int. 134, 35–52.

Cody, G.D., Mysen, B.O., Lee, S.K., 2005. Structure vs. composition: a solid-state H-1 and Si-29 NMR study of quenched glasses along the Na_2O-SiO_2-H_2O join. Geochim. Cosmochim. Acta 69, 2373–2384.

Cormack, A.N., Du, J., 2001. Molecular dynamics simulations of soda-lime-silicate glasses. J. Non-Cryst. Solids 293, 283–289.

Day, D.E., 1976. Mixed alkali glasses–their properties and uses. J. Non-Cryst. Solids 21, 343–372.

Deubener, J., 2018. Viscosity of glass-forming melts. In: Richet, P. (Ed.), Encyclopedia of Glass Science, Technology, History and Culture. J. Wiley & Sons, Hoboken, NJ.

Dickinson, J.E., Scarfe, C.M., McMillan, P., 1990. Physical properties and structure of K2Si4O9 melt quenched from pressure up to 2.4 GPa. J. Geophys. Res. 95, 15675–15681.

Doweidar, H., 1996. The density of alkali silicate glasses in relation to the microstructure. J. Non-Cryst. Solids 194, 155–162.

Dron, R., 1982. Acid-base reactions is molten silicates. J. Non-Cryst. Solids 53, 267–278.

Duffy, J.A., 1993. A review of optical basicity and its applications to oxidic systems. Geochim. Cosmochim. Acta 57, 3961–3970.

Duffy, J., 2018. Optical basicity. Theory and applications. In: Richet, P. (Ed.), Encyclopedia of Glass Science, Technology, History and Culture. J. Wiley & Sons, Hoboken, NJ.

Duffy, J.A., Ingram, M.D., 1971. Establishment of an optical scale for Lewis basicity in inorganic oxyacids, molten salts, and glasses. J. Am. Ceram. Soc. 93, 6448–6454.

Duffy, J.A., Ingram, M.D., 2002. Solvent properties of glass melts: resemblance to aqueous solutions. C.R. Chimie 5, 797–804.

Dunn, T., 1982. Oxygen diffusion in three silicate melts along the join diopside–anorthite. Geochim. Cosmochim. Acta 46, 2293–2299.

Eskola, P., 1922. The silicates of strontium and barium. Am. J. Sci. 4, 331–375.

Fabrichnaya, O., Saxena, S.K., Richet, P., Westrum Jr., E.F., 2004. Thermodynamic Data, Models and Phase Diagrams in Multicomponent Oxide Systems. Springer, Berlin.

Fincham, F.D., Richardson, F.D., 1954. The behavior of sulphur in silicate and aluminate slags. Proc. Roy. Soc. Lond. A223, 40–62.

Flood, H., Forland, T., Roald, B., 1947. Acidic and basic properties of oxides III. Acta Chem. Scand. 1, 790–798.

Fontana, E.H., Plummer, W.A., 1979. A viscosity-temperature relation for glass. J. Am. Ceram. Soc. 62, 367–369.

Frantz, J.D., Mysen, B.O., 1995. Raman spectra and structure of BaO-SiO_2, SrO-SiO_2, and CaO-SiO_2 melts to 1600^3C. Chem. Geol. 121, 155–176.

Frohberg, M.G., Caune, E., Kappor, M.L., 1973. Messung der Aktivität der Sauerstoffionen in den flüssigen Systemen Na_2O-SiO_2 und K_2O-SiO_2. Arch. Eisenhüttenwes. 44, 585–588.

Geiger, C., 2001. Solid Solutions in Silicate and Oxide Systems. European Mineralogical Union, Budapest.

Ghiorso, M.S., 2004. An equation of state for silicate melts. III. Analysis of stoichiometric liquids at elevated pressure: shock compression data, molecular dynamics simulations and mineral fusion curves. Am. J. Sci. 304, 752–810.

Ghosh, D.B., Karki, B.B., Stixrude, L., 2014. First-principles molecular dynamics simulations of $MgSiO_3$ glass: structure, density, and elasticity at high pressure. Am. Mineral. 99, 1304–1314.

Hageman, V.B.M., Oonk, H.A.J., 1986. Liquid immiscibility in the SiO_2 + MgO, SiO_2 + SrO, SiO_2 + La_2O_3, and SiO_2 + Y_2O_3 systems. Phys. Chem. Glasses 27, 194–198.

Hageman, V. B. M., van der Berg, G. J. K., Janssen, H. J., & Oonk, H. A. J. (1986). A reinvestigation of liquid immiscibility in the SiO_2-CaO system. Phys. Chem. Glasses, 27**,** 100–106.

Haller, W., Blackburn, D.H., Simmons, J.H., 1974. Miscibility gaps in alkali-silicate binaries–data and thermodynamic interpretation. J. Am. Ceram. Soc. 57, 120–126.

Hovis, G.L., Toplis, M.J., Richet, P., 2004. Thermodynamic mixing properties of sodium silicate liquids and implications for liquid-liquid immiscibility. Chem. Geol. 213, 173–186.

Hudon, P., Baker, D.R., 2002a. The nature of phase separation in binary oxide melts and glasses. I. Silicate systems. J. Non-Cryst. Solids 303, 299–345.

Hudon, P., Baker, D.R., 2002b. The nature of phase separation in binary oxide melts and glasses. II. Selective solution mechanisms. J. Non-Cryst. Solids 303, 346–353.

Jones, A.R., Winter, R., Greaves, G.N., Smith, I.H., 2001. MAS NMR study of soda-lime-silicate glasses with variable degrees of polymerisation. J. Non-Cryst. Solids 293–295, 87–92.

Keller, H., Schwerdtfeger, K., 1979. Tracer diffusivity of ^{31}Si in CaO-SiO_2 melts at 1600°C. Metal. Trans. B10, 551–554.

Keller, H., Schwerdtfeger, K., Hennesen, K., 1979. Tracer diffusivity of ^{45} Ca and electrical conductivity in calcium oxide-silica melts. Metal. Trans. B10, 67–70.

Keller, H., Schwerdtfeger, K., Petri, H., Hölzle, R., Hennesen, K., 1982. Tracer diffusivity of ^{18}O in CaO-SiO_2 melts at 1600°C. Metal. Trans. B13, 237–240.

Knoche, R., Dingwell, D.B., Seifert, F.A., Webb, S.L., 1994. Nonlinear properties of supercooled liquids in the system Na_2O-SiO_2. Chem. Geol. 116, 1–16.

Kohn, S.C., Schofield, P.F., 1994. The importance of melt composition in controlling trace-element behaviour: an exprimental study of Mn and Zn partitioning between forsterite and silicate melt. Chem. Geol. 117, 73–87.

Kohsaka, S., Sato, S., Yokokawa, T., 1979. E.m.f. measurements of molten oxide mixtures. III. Sodium oxide + silicon dioxide. J. Chem. Therm. 11, 547–551.

Kracek, F.C., 1930a. The binary system Li_2O-SiO_2. J. Phys. Chem. 34, 2641–2650.

Kracek, F.C., 1930b. The system sodium oxide-silica. J. Phys. Chem. 34, 1583–1598.

Kracek, F.C., Bowen, N.L., Morey, G.W., 1929. The system potassium metasilicate-silica. J. Phys. Chem. 33, 1857–1879.

Kracek, F.C., Bowen, N.L., Morey, G.W., 1937. Equilibrium relations and factors influencing their determination in the system K_2SiO_3-SiO_2. J. Phys. Chem. 41, 1183–1193.

Krol, D.M., Lyons, K.B., Brawer, S.A., Kurkjian, C.R., 1986. High-temperature light scattering and the glass transition in vitreous silica. Phys. Rev. B33, 4196–4201.

Kushiro, I., 1976. Changes in viscosity and structure of melt of $NaAlSi_2O_6$ composition at high pressure. J. Geophys. Res. 81, 6347–6350.

Kushiro, I., 1977. Phase transformations in silicate melts under upper mantle conditions. In: Manghnani, M.H. (Ed.), High Pressure Research: Applications in Geophysics. Academic Press, pp. 25–37.

Laberge, N.L., Vasilescu, V.V., Montrose, C.J., Macedo, P.B., 1973. Equilibrium compressibility and density fluctuations in K_2O-SiO_2 glasses. J. Am. Ceram. Soc. 56, 506–509.

Lacks, D. J., Rear, D. B., & van Orman, J. A. (2007). Molecular dynamics investigation of viscosity, chemical diffusivities and partial molar volumes of liquids along the MgO–SiO_2 join as functions of pressure. Geochim. Cosmochim. Acta, 71, 1313–1323.

Le Losq, C., Neuville, D.R., 2017. Molecular structure, configurational entropy and viscosity of silicate melts: link through the Adam and Gibbs theory of viscous flow. J. Non-Cryst. Solids 463, 175–188.

Lee, S.K., Fei, Y., Cody, G.D., Mysen, B.O., 2003. Order and disorder in sodium silicate glasses & melts at 10 GPa. Geophys. Res. Lett. 30, 1845 1810.1029/2003GL017735.

Lesher, C.E., 2010. Self-diffusion in silicate melts: theory, observations and applications to magmatic systems. Rev. Mineral. Geochem. 72, 269–309.

Levin, E.M., 1970. Liquid immiscibility in oxide systems. In: Phase Diagrams, Materials Science and Technology. Vol. III. Academic Press, New York, pp. 143–236.

Levin, E.M., Robins, C.R., McMurdie, H.F., 1975. Phase Diagrams for Ceramists, second ed. American Ceramic Soc, Columbus, OH.

Lewis, G.N., 1923. Valence and the Structure of Atoms and Molecules. Chemical Catalog Company, New York.

Liebau, F., Pallas, I., 1981. The influence of cation properties on the shape of silicate chains. Z. Kristall. 155, 139–153.

Lin, C.C., Chen, S.F., Liu, L.G., Li, C.C., 2007. Anionic structure and elasticity of Na_2O-MgO-SiO_2 glasses. J. Non-Cryst. Solids 353, 413–425.

Lin, C.C., Chen, S.F., Liu, L.G., Li, C.C., 2010. Size effects of modifying cations on the structure and elastic properties of Na2O-MO-SiO_2 glasses (M = Mg, Ca, Sr, Ba). Mater. Chem. Phys. 123, 569–580.

Lux, H., 1939. "Saüren" und "basen" im Schmelzfluss: Die Bestimmung des Sauerstoffionen-Konzentration. Z. Elektrochem. 45, 303–309.

Mazurin, O.V., Roskovs, G.P., Porai-Koshits, E.A., 1984. Immiscibility diagrams of oxide glass-forming systems. In: Mazurin, O.V., Porai-Koshits, E.A. (Eds.), Phase Separation in Glass. North Holland, Amsterdam, pp. 103–142.

Mazurin, O.V., Streltsina, M.V., Shvaiko-Shvaikovskaya, T.P., 1987. Handbook of Glass Data. Part A. Silica Glass and Binary Silicate GlassesElsevier, Amsterdam.

Megahed, A.A., 1999. Density of mixed alkali silicate glasses. Phys. Chem. Glasses 40, 130–134.

Meneses, D.D., Malki, M., Echegut, P., 2006. Optical and structural properties of calcium silicate glasses. J. Non-Cryst. Solids 352, 5301–5308.

Mills, K.C., 1993. The influence of structure on the physico-chemical properties of slags. ISIJ Int. 33, 148–155.

Moretti, R., Ottonello, G., 2003. A polymeric approach to the sulfide capacity of slags and melts. Metall. Trans. B 34, 399–410.

Morishita, M., Navrotsky, A., Wilding, M.C., 2004. Direct measurement of relative partial molar enthalpy of SiO_2 in SiO_2-M_2O (M=Li, Na, K, Cs) binary and SiO_2-CaO-Al_2O_3 ternary melts. J. Am. Ceram. Soc. 87, 1550–1555.

Morita, K., Kume, K., Sano, N., 2000. A newly developed method of determining SiO_2 activity in silicate slags equilibrated with molten silicon alloys. ISIJ Int. 40, 554–560.

Murakami, M., Sinogeikin, S.V., Hellwig, H., Bass, J.D., Li, J., 2007. Sound velocity of $MgSiO_3$ perovskite to Mbar pressure. Earth Planet. Sci. Lett. 256, 47–54.

Mysen, B.O., Virgo, D., Seifert, F.A., 1982. The structure of silicate melts: implications for chemical and physical properties of natural magma. Rev. Geophys. 20, 353–383.

Nekvasil, H., Burnham, C.W., 1987. The calculated individualeffects of pressure and water content on phase equilibria in the granite system. In: Mysen, B.O. (Ed.), Magmatic Processes: Physicochemical Principles. The Geochemical Society, University Park, pp. 433–446.

Nesbitt, H.W., Bancroft, G.M., Henderson, G.S., Richet, P., O'Shaughnessy, C., 2017. Melting, crystallization, and glass transition: toward a unified description for silicate phase transitions. Am. Mineral. 102, 412–420.

Neuville, D.R., 2006. Viscosity, structure and mixing in (Ca, Na) silicate melts. Chem. Geol. 229, 28–49.

Neuville, D.R., Richet, P., 1991. Viscosity and mixing in molten (Ca,Mg) pyroxenes and garnets. Geochim. Cosmochim. Acta 55, 1011–1020.

Ngai, K.L., Wong, Y., Moynihan, C.T., 2002. The mixed alkali effect revisited: the importance of ion-ion interactions. J. Non-Cryst. Solids 307–310, 999–1011.

Ni, H. and de Koker, N. (2018) Diffusion in oxide glass-forming systems. In Encyclopedia of Glass Science, Technology, History and Culture (ed. P. Richet). J. Wiley & Sons, Hoboken, NJ

Plante, E.R., 1978. Vapor pressure measurements of potassium over K_2O-SiO_2 solutions by a Knudsen effusion, mass spectrometric method. NBS Spec. Pub. 561, 265–281.

Poole, J.P., 1948. Viscosité à basse temperature des verre alcalino-silicaté. Verres Refract. 2, 222–228.

Rankin, G.A., Wright, F.E., 1915. The ternary system CaO-Al_2O_3-SiO_2. Am. J. Sci. 39, 1–79.

Rao, K.D.P., Gskell, D.R., 1981. The thermodynamic properties of melts in the system MnO-SiO2. Metal. Trans. B12, 311–317.

Ravaine, D., Souquet, J.L., 1977. A thermodynamic approach to ionic conductivity in oxide glasses. Part 1. Correlation of the ionic conductivity with the chemical potential of alkali oxide in oxide glasses. Phys. Chem. Glasses 18, 27–31.

Reid, J.E., Poe, B.T., Rubie, R.C., Zotov, N., Wiedenbeck, M., 2001. The self-diffusion of silicon and oxygen in diopside ($CaMgSi_2O_6$) liquid up to 15 GPa. Chem. Geol. 174, 77–86.

Reid, J.E., Suzuki, A., Funakoshi, K., Terasaki, K., Poe, B.T., Rubie, D.C., Ohtani, E., 2003. The viscosity of $CaMgSi_2O_6$ liquid at pressure up to 13 GPa. Phys. Earth Planet. Int. 139, 45–54.

Richet, P., 1984. Viscosity and configurational entropy of silicate melts. Geochim. Cosmochim. Acta 48, 471–483.

Richet, P., Bottinga, Y., 1985. Heat capacity of aluminum-free liquid silicates. Geochim. Cosmochim. Acta 49, 471–486.

Richet, P., Bottinga, Y., 1986. Thermochemical properties of silicate glasses and liquids: a review. Rev. Geophys. 24, 1–25.

Richet, P., Ottonello, G., 2014. The Earth as a multiscale quantum-mechanical system. C.R. Geosci. 346, 317–325.

Richet, P., Bottinga, Y., Téqui, C., 1984. Heat capacity of sodium silicate liquids. J. Am. Ceram. Soc. 67, C6–C8.

Richet, P., Robie, R.A., Hemingway, B.S., 1986. Low-temperature heat capacity of diopside glass: a calorimetric test of the configurational entropy theory as applied to the viscosity of liquid silicates. Geochim. Cosmochim. Acta 50, 1521–1533.

Richet, P., Leclerc, F., Benoist, L., 1993. Melting of forsterite and spinel, with implications for the glass transition of Mg_2SiO_4 liquid. Geophys. Res. Lett. 20, 1675–1678.

Rivers, M.L., Carmichael, I.S.E., 1987. Ultrasonic studies of silicate melts. J. Geophys. Res. 92, 9247–9270.

Robinson, H.A., 1969. Physical properties of alkali silicate glasses. I. Additive relations in alkali binary glasses. J. Am. Ceram. Soc. 53, 392–399.

Romero-Serrano, A., Gomez-Yanez, C., Hallen-Lopez, M., Araujo-Osorlo, J., 2005. Thermodynamic modeling of alkali metal oxide-silica binary melts. J. Am. Ceram. Soc. 88, 141–145.

Romero-Serrano, A., Cruz-Ramirez, A., Zeifert, B., Hallen-Lopez, M., Hernandez-Ramirez, A., 2010. Thermodynamic modeling of the BaO-SiO_2 and SrO-SiO_2 binary melts. Glas. Phys. Chem. 36, 171–178.

Ryan, M.P., Blevins, J.Y.K., 1987. The Viscosity of Synthetic and Natural Silicate Melts and Glasses at High Temperatures and 1 bar (10^5 Pascals) Pressure and at Higher Pressures. Vol. 1764. U.S. Geological Survey, Washington, DC.

Ryerson, F.J., 1985. Oxide solution mechanisms in silicate melts: systematic variations in the activity coefficient of SiO_2. Geochim. Cosmochim. Acta 49, 637–651.

Sanchez-Valle, C., Bass, J.D., 2010. Elasticity and pressure-induced structural changes in vitreous MgSiO3-enstatite to lower mantle pressures. Earth Planet. Sci. Lett. 295, 523–530.

Sanloup, C., Drewitt, J.W.E., Crepisson, C., Kono, Y., Park, C., McCammon, C., Bytchkov, A., 2013. Structure and density of molten fayalite at high pressure. Geochim. Cosmochim. Acta 118, 118–128.

Scarfe, C.M., Mysen, B.O., Virgo, D., 1987. Pressure dependence of the viscosity of silicate melts. In: Mysen, B.O. (Ed.), Magmatic Processes: Physicochemical Principles. In: Vol. Special Publication Number 1. Geochemical Society, pp. 59–68.

Semkow, K.W., Haskin, L.A., 1985. Concentrations and behavior of oxygen and oxide ion in melts of composition CaO.MgO.xSiO_2. Geochim. Cosmochim. Acta 49, 1897–1908.

Sen, S., Maekawa, H., Papatheodorou, G.N., 2009. Short-range structure of invert glasses along the pseudo-binary join $MgSiO_3$-Mg_2SiO_4: results from ^{29}Si and ^{25}Mg MAS NMR spectroscopy. J. Phys. Chem. B 113, 14243–15248.

Seo, W.G., Tsukihashi, F., 2004. Molecular dynamics simulation of the thermodynamic and structural properties for the CaO-SiO_2 system. ISIJ Int. 44, 1817–1825.

Seward III, T.P., Uhlmann, D.R., Turnbull, D., 1968. Phase separation in the system BaO-SiO_2. J. Am. Ceram. Soc. 51, 278–285.

Shermer, H.F., 1956. Thermal expansion of binary alkali silicate glasses. J. Nat. Bureau Stand. 57, 97–101.

Shimizu, N., Kushiro, I., 1984. Diffusivity of oxygen in jadeite and diopside melts at high pressures. Geochim. Cosmochim. Acta 48, 1295–1303.

Shimizu, N., Kushiro, I., 1991. The mobility of Mg, Ca, and Si in diopside-jadeite liquids at high pressures. In: Perchuk, L.L., Kushiro, I. (Eds.), Physical Chemistry of Magmas. In: Vol. 9. Springer, New York, NY, United States, pp. 192–212.

Sipp, A., Richet, P., 2002. Equivalence of volume, enthalpy and viscosity relaxation kinetics in glass-forming silicate liquids. J. Non-Cryst. Solids 298, 202–212.

Sosman, R.B., 1952. Temperature scales and silicate research. Amer. J. Sci. , Bowen vol. 517–528.

Souquet, J.-L., 2018. Ionic and electronic transport. In: Richet, P. (Ed.), Encyclopedia of Glass Science, Technology, History and Culture. J. Wiley & Sons, Hoboken, NJ.

Spice, H., Sanloup, C., Cochain, B., de Grouchy, C., Kono, Y., 2015. Viscosity of liquid fayalite up to 9 GPa. Geochim. Comochim. Acta 148, 219–227.

Stebbins, J.F., 1991. NMR evidence for 5-coordinated silicon in a silicate glass at atmospheric-pressure. Nature 351, 638–639.

Stebbins, J.F., McMillan, P.D., 1993. Compositional and temperature effects on five coordinated silicon in ambient pressure silicate glasses. J. Non-Cryst. Solids 160, 116–125.

Stebbins, J.F., Carmichael, I.S.E., Moret, L.K., 1984. Heat capacities and entropies of silicate liquids and glasses. Contrib. Mineral. Petrol. 86, 131–148.

Stixrude, L., de Koker, N., Sun, N., Mookerjee, M., Karki, B., 2009. Thermodynamics of silicate liquids in the deep Earth. Earth Planet. Sci. Lett. 278, 226–232.

Sugawara, T., Shinoya, K., Yoshida, S., Matsuoka, J., 2011. Thermodynamic mixing properties of liquids in the system Na_2O-SiO_2. J. Non-Cryst. Solids 357, 1390–1398.

Sun, N., Stixrude, L., de Koker, N., Karki, B.B., 2011. First principles molecular dynamics simulations of diopside ($CaMgSi_2O_6$) liquid to high pressure. Geochim. Cosmochim. Acta 75, 3792–3802.

Téqui, C., Grinspan, P., Richet, P., 1992. Thermodynamic properties of alkali silicates: heat capacity of Li_2SiO_3 and lithium-bearing silicate melts. J. Am. Ceram. Soc. 75, 2601–2604.

Tewhey, J.D., Hess, P.C., 1979. The two-phase region in the CaO-SiO_2 system: experimental data and thermodynamic analysis. Phys. Chem. Glasses 20, 41–53.

Tickle, R.E., 1967. The electrical conductance of molten alkali silicates. Phys. Chem. Glasses 8, 101–112.

Tomlinson, J.W., Heynes, M.S.R., Bockris, J.O.M., 1958. The structure of liquid silicates. Part 2. Molar volume and expansivities. Trans. Farad. Soc. 54, 1822–1834.

Tomozawa, M., McGahay, V., Hyde, J.M., 1990. Phase separation of glasses. J. Non-Cryst. Solids 123, 197–207.

Toop, D.W., Samis, C.S., 1962. Some new ionic concepts of silicate slags. Can. Metall. Q. 1, 129–152.

Toplis, M., 2018. Density of amorphous oxides. In: Richet, P. (Ed.), Encyclopedia of Glass Science, Technology, History and Culture. J. Wiley & Sons, Hoboken, NJ.

Urbain, G., Bottinga, Y., Richet, P., 1982. Viscosity of liquid silica, silicates and alumino-silicates. Geochim. Cosmochim. Acta 46, 1061–1072.

Verma, A.K., Karki, B.B., 2012. First-principles study of self-diffusion and viscous flow in diopside ($CaMgSi_2O_6$) liquid. Am. Fortschr. Mineral. 97, 2049–2055.

Warren, B.E., Pincus, A.G., 1940. Atomic considerations of immiscibility in glass systems. J. Am. Ceram. Soc. 23, 301–304.

Whittaker, E.J.W., Muntus, R., 1970. Ionic radii for use in geochemistry. Geochim. Cosmochim. Acta 34, 945–957.

Williamson, J., Glasser, F.P., 1965. Phase relations in the system $Na_2Si_2O_5$-SiO_2. Science 148, 1589–1591.

Yageman, V.D., Matveev, G.M., 1982. Heat capacity of glasses in the system SiO_2-$Na_2O.SiO_2$ (in Russian). Fiz. Khim. Stekla 8, 238–245.

Zhang, L., Van Orman, J.A., Lack, s.D.J., 2010. Molecular dynamics investigation of MgO–CaO–SiO_2 liquids: influence of pressure and composition on density and transport properties. Chem. Geol. 256 (275), 50–57.

CHAPTER

7

Structure of Metal Oxide-Silica Systems

OUTLINE

7.1 INTRODUCTORY COMMENTS

In this chapter, we will discuss the structure of binary alkali and alkaline earth silicate glasses and melts. The principal objective is to further our understanding of how structure relates to the physical and chemical properties of these melts and glasses. However, before doing so, the most important features of the individual models will be summarized.

A number of structure models have been proposed. They can be divided into those obtained by direct determination and by some form of rationalization of property information, including liquidus phase relations and numerical simulation. Sometimes there is considerable accord between such models and the information obtained by direct measurement, but sometimes there is considerable incompatibility. The structural role(s) of tetrahedrally coordinated cations other than Si^{4+} will be the subject of later chapters (Chapters 9, 11–13).

https://doi.org/10.1016/B978-0-444-63708-6.00007-7

7.2 MODELING STRUCTURE

Pseudocrystalline models rely on the assumption that there exist in melts (and glasses) structural entities that resemble, at least on a local scale, those of crystals on or near the liquidus for the same system. Models based on assumptions of how physicochemical properties are governed by structure also use crystal chemical analogies. In thermodynamic modeling, one assumes a specific set of components, which should ideally resemble those in the melts, with which to describe the thermodynamic data. This is not a requirement, however, although the models that do so tend to be the more successful. Numerical simulations based on energy-minimization techniques to calculate bond angles, bond distances, bond strengths, and coordination numbers have been quite useful when following their benchmarking against known structure. In many situations, numerical simulation is the only method by which to develop a sense of the behavior of glasses and melts at very high pressures and temperatures.

7.2.1 Pseudocrystalline and Quasichemical Models

Here, it is assumed that there exist in melts and glasses silicate species resembling those found in crystalline materials. In one group of models, structural similarity of minerals on the liquidus and the melt is assumed (Morey and Bowen, 1924; Burnham, 1975; Bottinga and Richet, 1978; Burnham and Nekvasil, 1986). Melt structure modeled on this basis has been used, for example, to derive liquidus phase relations (Burnham, 1975; Bottinga and Richet, 1978; Bottinga et al., 1981; Burnham and Nekvasil, 1986). Such models also have been used, with some success, to explain nucleation in metal oxide silicate systems (Kirkpatrick, 1983; Davis and Ihinger, 1999, 2002; Zotov and Delaplane, 2000).

Bottinga and Richet (1978) pointed out that the constraints imposed by liquidus phase equilibria and the Gibbs-Duhem equation are not sufficient to calculate the chemical potential of a liquidus phase in multicomponent systems, because all possible structural entities in the melt must be identified and their mixing properties ascertained for a complete description of the melt structure. In light of the paucity of such information, they assumed that the structural entities of a multicomponent melt are produced by melting of the known crystalline materials in the system. For example, in the system MgO-SiO_2, liquidus phases are periclase (MgO), forsterite (Mg_2SiO_4), clinoenstatite ($MgSiO_3$), and silica polymorphs (Bowen and Andersen, 1914; Greig, 1927). In other systems such as alkali silicates, the number of liquidus phases sometimes is greater (Kracek, 1930a,b, 1932; Morey et al., 1930), and the number of assumed species in the liquid must increase correspondingly.

Another group of models relies on inferences from measurements of physical properties. Among these, transport properties have been particularly attractive because these can often be linked to breakage and formation of bonding in the structure. Several models dating back 60 years or more have met with significant success and some have arrived at conclusions surprisingly similar to those derived from much more recent spectroscopic measurements. This includes the models by MacKenzie (1947) and by Bockris and Reddy (1970), which were based on an assumed relationship between activation energy of viscous flow and Si—O bond strength. Another example is the substructure model proposed by Babcock (1968), which relied on refractive index and molar volume data of glasses.

Quasichemical models can incorporate structural information in the formulations of equilibria used for free energy minimizations. For example, Bottinga and Richet (1978) modeled successfully the liquidus phase relations in the MgO-SiO$_2$ system. Their model comprises elements of this approach.

Pelton and coworkers (Blander and Pelton, 1984, 1987; Pelton and Wu, 1999) developed a model based in part on the observation that there is a pronounced free energy minimum near orthosilicate compositions in binary metal oxide-silica systems (see Navrotsky et al., 1985, for compilation of these data). In binary metal oxide (M) silicate (Si) melts, the model considers the formation to M—Si bonds from M—M and Si—Si bonds (Pelton and Wu, 1999) as follows:

$$(\mathrm{M}-\mathrm{M}) + (\mathrm{Si}-\mathrm{Si}) \Leftrightarrow 2(\mathrm{M}-\mathrm{Si}). \tag{7.1}$$

To minimize the energy change of reactions formalized in this equation, equilibria among species in the melts of interest are considered. For example, for the system MgO-SiO$_2$, Blander and Pelton (1987) wrote:

$$\mathrm{MgO}^{\mathrm{liquid}} + \mathrm{SiO_2}^{\mathrm{liquid}} \Leftrightarrow \mathrm{MgSiO_3}^{\mathrm{liquid}}, \tag{7.2}$$

and

$$2\mathrm{MgO}^{\mathrm{liquid}} + \mathrm{SiO_2}^{\mathrm{liquid}} \Leftrightarrow \mathrm{Mg_2SiO_4}^{\mathrm{liquid}}. \tag{7.3}$$

Other reactions could also be written, but those used were obviously chosen in part so that the most reliable thermodynamic data can be brought to bear on the question. By choosing melt components resembling structural species otherwise determined for the melts and glasses of interest, this treatment brings thermodynamic modeling closer to the melt structure.

7.2.2 Polymer Modeling

In polymer models, the formation of silicate melt is considered as chemical interactions between metal oxide (e.g., MO) and silica. There are various versions of this model (e.g., Masson, 1968, 1977). One may view this as a gradually evolving polymerization of silicate complexes as the Si/O ratio is changed:

$$\mathrm{SiO_4}^{4-} + \mathrm{Si}_n\mathrm{O}_{3n+1}^{2(n+1)-} \rightleftharpoons \mathrm{Si}_{n+1}\mathrm{O}_{n+4}^{2(n+2)-} + \mathrm{O}^{2-}. \tag{7.4}$$

This model received experimental support in several experimental studies of structure carried out with the aid of analysis of TMS (trimethylsilyl) derivatives of the silicate glass network. These include those of Smart and Glasser (1978) for glasses in the system PbO-SiO$_2$ and Lentz (1969) for Na$_2$O-SiO$_2$ composition glasses.

There are, however, important problems with the TMS method itself that make the results unreliable. First, it involves formation of a solution from the glass. The chemical process employed to create the solution does not produce 100% yield. Presumably, the residue contains highly polymerized units that cannot be broken down so that chromatographic analysis of solutions of TMS derivatives provides incomplete results. Second, in the data Smart and Glasser (1978) reported for a PbO-SiO$_2$ glass, for example, they calculated the bulk melt polymerization, NBO/Si, by adding up the proportions of the various reported structural units (monomers, dimers, trimers, etc.). This resulted in NBO/Si = 2.4, whereas the bulk composition yields a nominal value of 2.8. In the study by Lentz (1969) on glasses in the system Na_2O-SiO_2, the bulk NBO/Si from the measurements of TMS derivatives was 2.8, yet the bulk composition had a nominal NBO/Si-value of 1.0.

7.2.3 Thermodynamic Modeling

Structures inferred from modeling of thermodynamic properties share a common trait, which is that the thermodynamic data can be described in terms of components that are not necessarily equivalent to actual structural entities in the melt. That notwithstanding, models of this type have been developed to such a level of refinement that these can reproduce properties of the system with considerable accuracy (Ghiorso and Sack, 1995). The use of such models for compositions, temperature, or pressures outside the range where the modeling was carried out is, however, fraught with danger. A better approach to modeling thermodynamic behavior is to incorporate presumed melt species that may resemble, at least in a compositional sense, those of relevant crystalline silicates (Bottinga and Richet, 1978; Pelton and Wu, 1999).

7.2.4 Computational Models

Numerical simulations can yield significant insight into the structure and dynamics of amorphous materials (Horbach et al., 2001; Ispas et al., 2002; Wu et al., 2004, 2015; Polyakov et al., 2010). In fact, in many cases information from computational models is the only source of information on structure and properties of silicate melts at very high temperature and pressure (Ghiorso, 2004; Karki et al., 2006; Adjaoud et al., 2008, 2011; Karki and Stixrude, 2010).

7.2.4.1 Bond Distance and Bond Angle

Computational models often focus on calculating bond angles, bond distances, average coordination numbers, and angle and distance distributions. For example, Ispas et al. (2002) and Huang and Cormack (1990) simulated radial distribution functions for melts in the system Na_2O-SiO_2 and derived Si—O, Si—Si, O—O, and Na—O bond distances and angle distributions as functions of composition (Fig. 7.1). A comparison of the simulated structure (Ispas et al., 2002) with that obtained by neutron diffraction (Zotov and Keppler, 1998) for an Na_2O-SiO_2 glass with 20 mol% Na_2O is shown in Table 7.1. Most simulated and experimentally determined parameters agree within several percent, although exceptions to this conclusion can be found in Si—Si distances, for example.

The first two distances, Si—O and O—O, are clearly identified in the radial distribution function simulated for the SiO_2 and also for Na_2O-SiO_2 glass with 30 mol% Na_2O (Fig. 7.1). Another important feature is the broadening of the Si—O peaks. This peak also becomes distinctly asymmetric when the Na_2O content increases and eventually evolves into two distinct components. One Si—O peak is near or slightly below 1.6 Å and the other near 1.65 Å. These features likely result from overlapping of Si—NBO and Si—BO distances (between Si and nonbridging and bridging oxygen, respectively), as shown more clearly in Fig. 7.1B for a simulated $Na_2Si_4O_9$ melt (Ispas et al., 2002). These results (Fig. 7.1) are consistent with NMR data, which also indicate different bond distances for Si—NBO and Si—BO

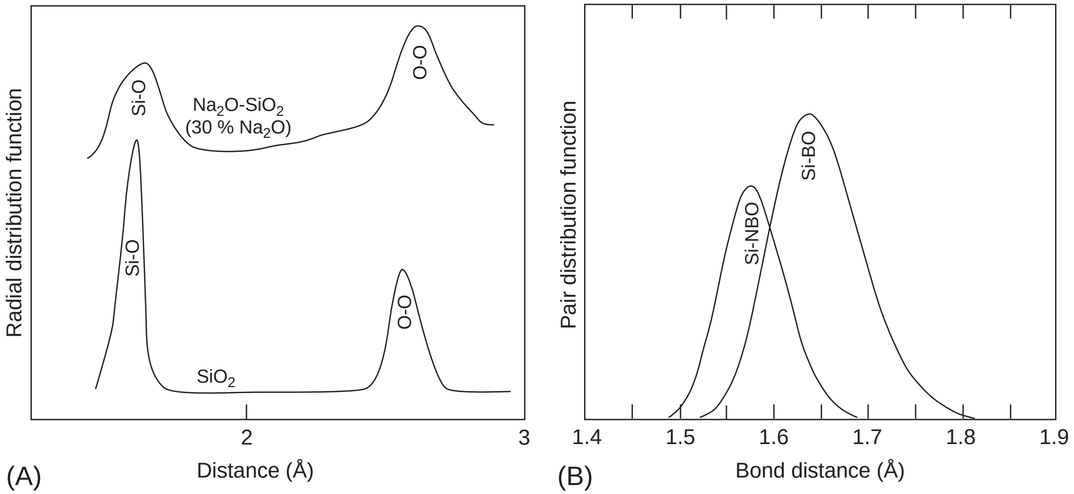

FIG. 7.1 (A) Computed radial distribution function for an SiO_2 glass and a $0.3Na_2O{\cdot}0.7SiO_2$ glass (Huang and Cormack, 1990). (B) Details of the first Si—O distance simulated for $Na_2Si_4O_9$ glass (Ispas et al., 2002).

(Lee and Stebbins, 2003a,b). The Si—NBO bond is several percent shorter than the Si—BO bond. This difference is understandable given the much weaker bonding of Na in the nonbridging Si—O—Na linkages compared with that of Si in the bridging Si—O—Si linkages. The weaker Na—O bond results in the nonbridging oxygen in the Si—O—Na linkage moving closer to the Si atom, which also results in distinctly different spectroscopic signatures of Si—NBO bonds as compared with Si—BO (Furukawa et al., 1981; McMillan, 1984; Lee and Stebbins, 2003a,b).

7.2.4.2 Multiple Silicate Species

From molecular dynamics simulation, Soules (1979) concluded that the Si—O—Si angle distributions of Na_2O-SiO_2 melts with 32 and 22 mol% Na_2O exhibit two maxima, one near 160 degrees and another near 110 degrees. More recent simulation results for $Na_2Si_4O_9$ melt

TABLE 7.1 Band Assignments in the 700–1200 cm^{-1} Frequency Region of Raman Spectra of Silicate Glasses

Band	Assignment
840–860	Si—O^- in Q^0[a]
880–910	Si—O^- in Q^1
940–970	Si—O^- in Q^2
1070–1110	

[a] *Q^0, Q^1, Q^2, and Q^3 denote SiO_4 and AlO_4 species where the superscript is the number of bridging oxygen in the unit. The Raman bands assigned to Si—O stretching in these species have been discussed by Brawer and White (1975), Furukawa et al. (1981), McMillan (1984), McMillan et al. (1992), and Mysen et al. (2003).*

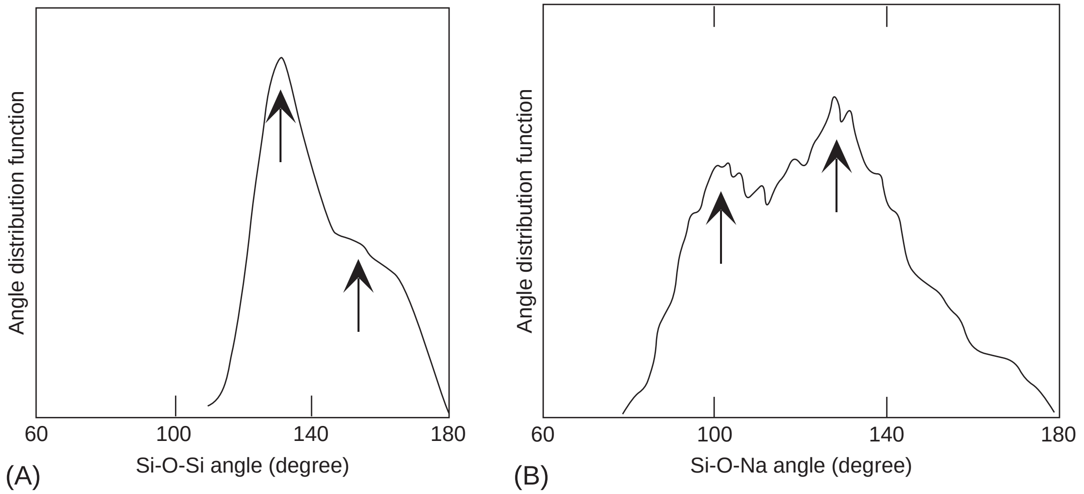

FIG. 7.2 Si—O—Si (A) and Si—O—Na (B) angle distribution functions from molecular dynamics simulations of $Na_2Si_4O_9$ melt by Ispas et al. (2002). The *arrows* in both figures highlight the two maxima in the distributions.

show two clear maxima in the Si—O—Si and Si—O—Na angle distribution functions (Fig. 7.2). In the former, the two clear maxima (marked with arrows in Fig. 7.2A) likely reflect the coexistence of at least two silicate structures with angle distributions around two distinctly different maxima. Such different angles, in turn, would be consistent with structural entities in the melt that differed, for example, in their number of nonbridging oxygens (Furukawa et al., 1981) or, perhaps, are the result of different ring statistics (Kohara et al., 2011).

The Si—O—Na angle distribution (Fig. 7.2B) is the angle between the Si^{4+} in tetrahedra and the central cation in adjacent oxygen ligands surrounding network-modifying cations. The oxygen in this distribution is, therefore, nonbridging. The two distinct angle distributions in Fig. 7.2B would lead to the suggestion, therefore, that there are at least two distinctly different types of nonbridging oxygen in $Na_2Si_4O_9$ melt. In a similar simulation, Newell et al. (1989) inferred that the melt structure of $Na_2Si_3O_7$ consists of two structural units with, on average, 1 and 0 nonbridging oxygen, along with smaller proportions of structural entities that are characterized by different NBO/Si-values. Interestingly, in structure simulations with mixed modifier cations such as Na and Ca, the most electronegative modifier cations tend to favor specific locations in the structure, whereas the other, more positive cation occupies different locations (Cormack and Du, 2001) (see also Fig. 7.3).

More recently, simulations have been expanded to address the nature of the silicate species in silicate glasses and melts (Horbach et al., 2001; Seo and Tsukihashi, 2004; Polyakov and Ariskin, 2008; Polyakov et al., 2010; Wu et al., 2015). It has generally been concluded that five Q^n-species can be used to build the equilibria. In what is perhaps the most comprehensive numerical simulations, Polyakov et al. (2010) found maximum abundance of Q^3, Q^2, Q^1, and Q^0 species in the Na_2O-SiO_2 system at Na/Si ratios of the Si_2O_5, SiO_3, Si_2O_7, and SiO_4 stoichiometries (Fig. 7.4). This model also finds support in early experimental studies (e.g., Etchepare, 1972; Brawer and White, 1975) as well as in numerous recent works (see Section 7.3).

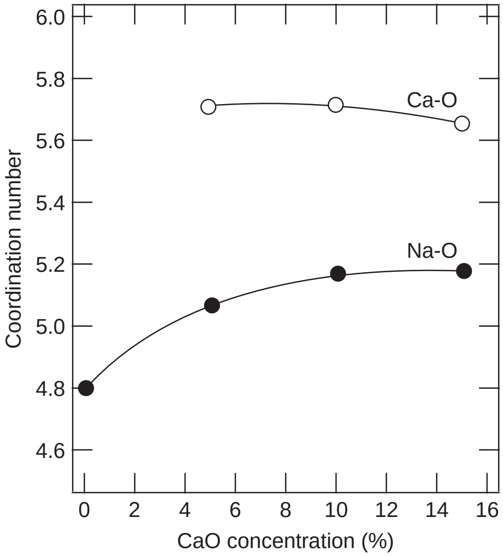

FIG. 7.3 Coordination number of oxygen surrounding Ca and Na (as indicated) as a function of CaO concentration in the system $(25-x)Na_2O$-xCaO-$75SiO_2$ (Cormack and Du, 2001).

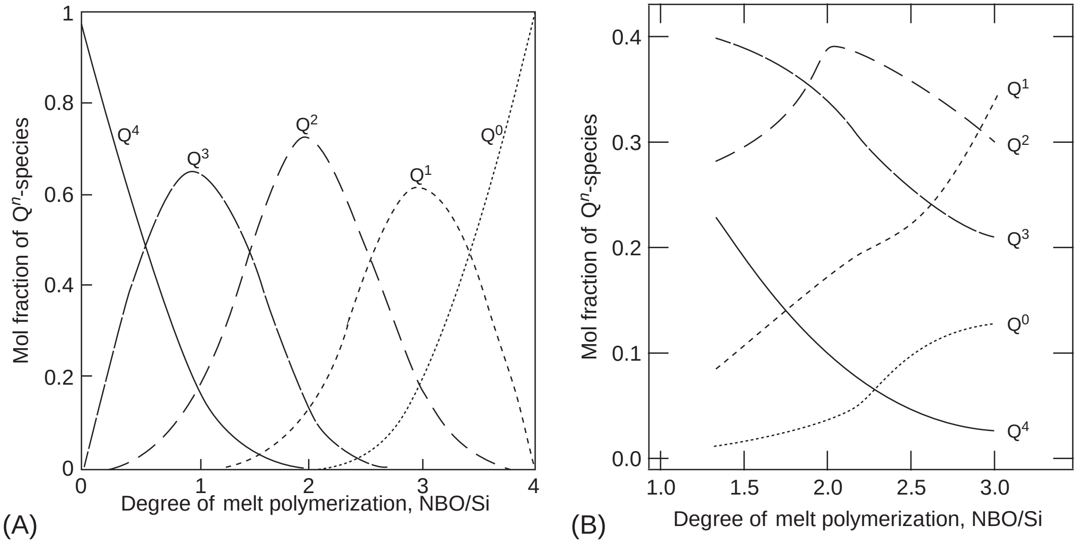

FIG. 7.4 Distribution of Q^n-species as a function of polymerization of melt and glass, NBO/Si (A) Calculated for Na_2O-SiO_2 melts and supercooled liquids at 1200°C. (B) Calculated for melts in the system CaO-SiO_2. *Redrawn from Polyakov et al. (2010) and Seo and Tsukihashi (2004).*

Considering the enthalpy changes of the Q^n-species disproportionation reactions:

$$2Q^n \Leftrightarrow Q^{n-1} + Q^{n+1}, \tag{7.5}$$

Polyakov et al. (2010) calculated values in the 20–30 kJ/mol range, which are within about 50% of the data derived from experimental Q^n-speciations (McMillan et al., 1992; Mysen, 1997). Those Q^n-species trends also resemble those derived for the CaO-SiO_2 system by Wu et al. (2015) (Fig. 7.4). Seo and Tsukihashi (2004) also retained some of the topology of the abundance diagrams from Polyakov et al. (2010). Moreover, in the latter calculations, for a bulk melt NBO/Si = 4, the results in Fig. 7.4 show only Q^0 species (isolated SiO_4 tetrahedra). However, in other calculations and experimental observations, combinations of Q^0, Q^1 and free oxygen were reported for both alkali and alkaline earth silicate melts with bulk NBO/Si = 4 (Umesaki et al., 1988; Sen and Tangeman, 2008). Further discussion of these issues is provided in Section 7.3, where experimental data are brought to bear on this question.

7.2.4.3 *Simulation of High-Pressure Structure*

Experimental characterization of silicate melts at high temperature and pressure (often above 1000°C and >100 GPa) is greatly restricted by experimental limitations that often make it necessary to return the sample to ambient conditions for structural examination. Numerical simulations then are especially valuable (Matsui, 1996; Diefenbacher et al., 1998; Ghosh et al., 2014; Zhao et al., 2014). Much of this work is driven by the desire to gather knowledge of structure and properties relevant to the formation and crystallization of melts in the interior of the earth and other terrestrial planets. This work has, therefore, often been restricted to the systems MgO-SiO_2 (Stixrude and Karki, 2005; Zhao et al., 2014; Ghosh et al., 2014), CaO-MgO-SiO_2 (Shimoda and Okuno, 2006; Sun et al., 2011) and MgO-CaO-Al_2O_3-SiO_2 (Matsui, 1996). Less information exists for alkali silicates, but what has been done offers useful information (Diefenbacher et al., 1998; Noritake et al., 2012).

Pressure effects may be divided into changes in average bond distances, bond angles, and oxygen coordination numbers, on the one hand, and silicate speciation on the other. Numerical simulations lend themselves well to the former group of data. For example, in the $Na_2O \cdot SiO_2$ system, the Si—O—Si angle decreases systematically with increasing pressure, but expands only slightly with increasing temperature and any pressure (Noritake et al., 2012) (see also Fig. 7.5). Interestingly, the O—Si—O angle also decreases systematically with pressure, which suggests that there is significant tetrahedral deformation as pressure is increased (Fig. 7.5B). There is no evidence in those simulation results for coordination transformation, at least up to the maximum pressure investigated (Fig. 7.5). There is merely a slight compression of the Si—O bond distances, which was, of course, as would be expected given the shrinkage of the intertetrahedral angles (Fig. 7.6) The Q^n-speciation also is slightly pressure-dependent with a suggestion of a minor decrease in Q^3 abundance coupled with a small increase in Q^2 and Q^4 abundance (Noritake et al., 2012) (see also Fig. 7.7). In other words, the results from Noritake et al. (2012) for $Na_2O \cdot 3SiO_2$ melt at high temperature and pressure suggest a very minor shift to the right of the disproportionation equilibrium:

$$2Q^3 \Leftrightarrow Q^2 + Q^4. \tag{7.6}$$

However, the increases of Q^2 and Q^4 abundances differ, which means that Eq. (7.6) is better rewritten as:

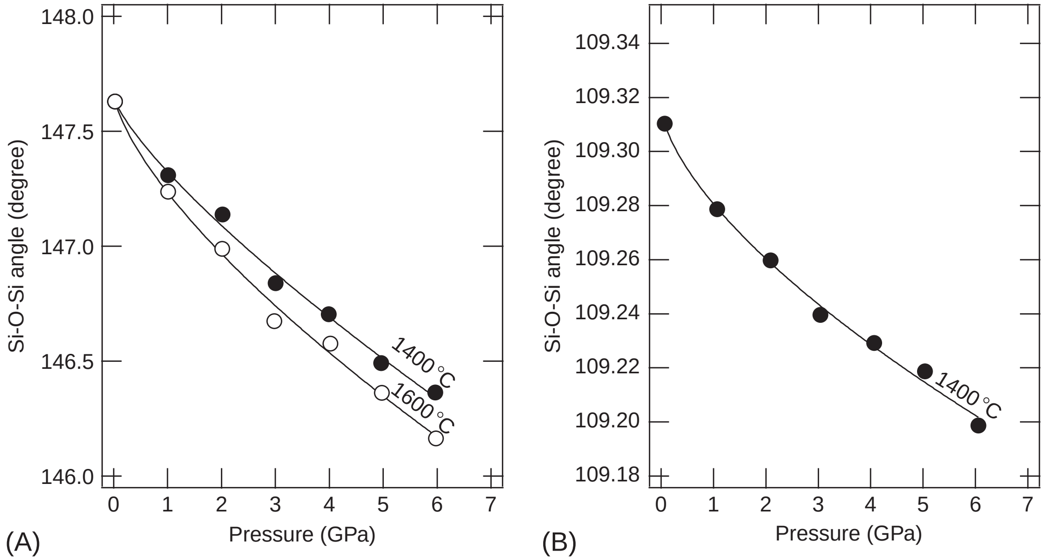

FIG. 7.5 Pressure effects, from molecular dynamics simulation, of $Na_2O{\cdot}3SiO_2$ melt simulated at 1400°C and 1600°C. (A) Si—O—Si angle with pressure and temperature. (B) O—Si—O angle at 1400°C with pressure (Noritake et al., 2012).

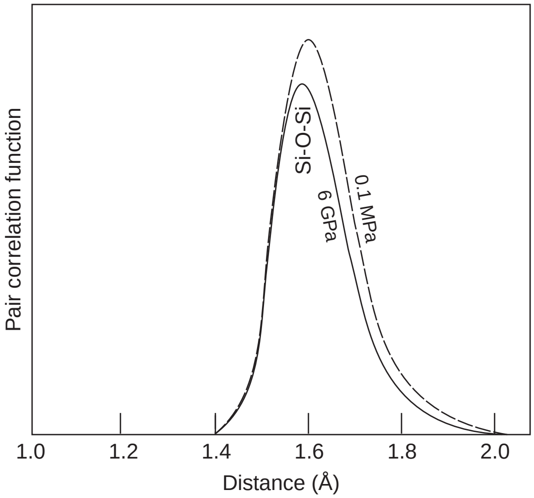

FIG. 7.6 Simulated radial distance as a function of pressure for $NaO{\cdot}3SiO_2$ melt (Noritake et al., 2012).

$$(x+y)Q^3 \Leftrightarrow xQ^2 + yQ^4, \qquad (7.6a)$$

where $x < 7$ (Fig. 7.7). With the data reported by Noritake et al. (2012), this means that the melt gets increasingly polymerized with increasing pressure—at least to the 6 GPa maximum pressure in this study (see insert in Fig. 7.7).

In alkaline earth silicate melts, molecular dynamics simulations have been taken to higher pressures (Matsui, 1996; Adjaoud et al., 2008; Ghosh et al., 2014). This initially results in further compression of Si—O—Si angles, which, at least to about 15 GPa, is a near-linear function of pressure and insensitive to the Ca/Mg ratio (Shimoda and Okuno, 2006) (see also Fig. 7.8).

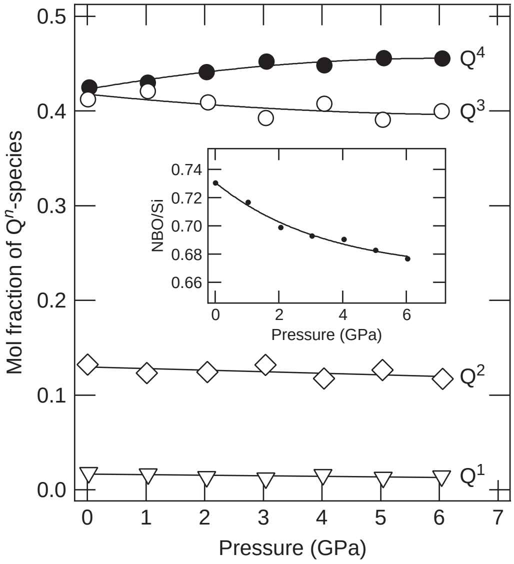

FIG. 7.7 Q^n-species evolution with pressure at 1600° C for $Na_2O{\cdot}3SiO_2$ melt. Inset: evolution of melt NBO/Si based on the species evolution (Noritake et al., 2012).

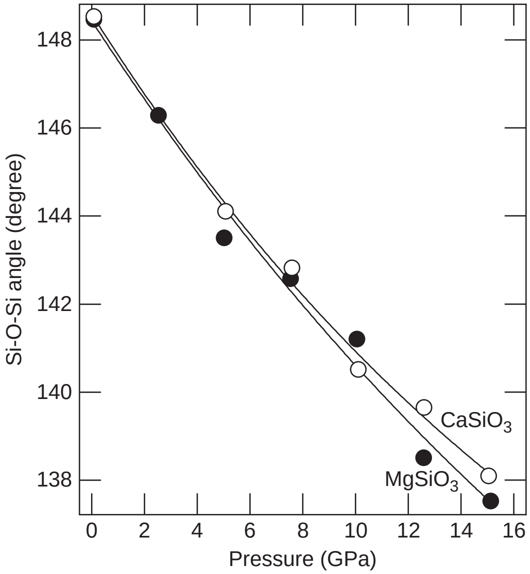

FIG. 7.8 Evolution of average Si—O—Si angle as a function of pressure in melts of $CaSiO_3$ and $MgSiO_3$ as indicated. *Redrawn from Shimoda and Okuno (2006).*

Above this pressure range, molecular dynamics simulations also indicate a coordination transformation of Mg^{2+} (Matsui, 1996; Adjaoud et al., 2008; Ghosh et al., 2014). Analogous evolutions can be seen in Ca^{2+} coordination even though the coordination number of Ca^{2+} is considerably higher than that of Mg^{2+} (and Si^{4+}) (Fig. 7.9). This greater oxygen coordination number around Ca^{2+} can at least qualitatively be ascribed to a greater Ca^{2+} than Mg^{2+} ionic radius. To about 15 GPa, Si^{4+} remains essentially in fourfold coordination (Shimoda and Okuno, 2006; Adjaoud et al., 2008). A further pressure increase results in a gradual and nearly linear increase in coordination numbers, so that for $MgSiO_3$ melt, for example, the Si^{4+} coordination number is near 6 even at 175 GPa, whereas that of Mg^{2+} approaches 8 (Ghosh et al., 2014). By using ab initio molecular dynamics methods, Zhao et al. (2014) extended the pressure range to >450 GPa for cation coordination in $MgSiO_3$ melt at 13,000 K. In the 230–465 GPa range, the coordination number remains essentially constant near 8.2 for Mg^{2+}, whereas that of Si increases gradually from near 6.4 at 230 GPa to 7.2 GPa at 465 GPa (Fig. 7.10).

7.3 DIRECT DETERMINATION

Direct structural examination of metal oxide-silica glasses has been carried out since the 1970s when vibrational spectroscopy, neutron and X-ray diffraction, together with nuclear magnetic resonance techniques began to be applied extensively (Etchepare, 1972; Brawer and White, 1975, 1977; Kawazoe et al., 1981; Greaves et al., 1985; Misawa et al., 1980; Schramm et al., 1984; Schneider et al., 1987; Zhang et al., 1996). Among these methods, neutron and X-ray diffraction probe bond distances and bond angles relevant to short- and medium-range

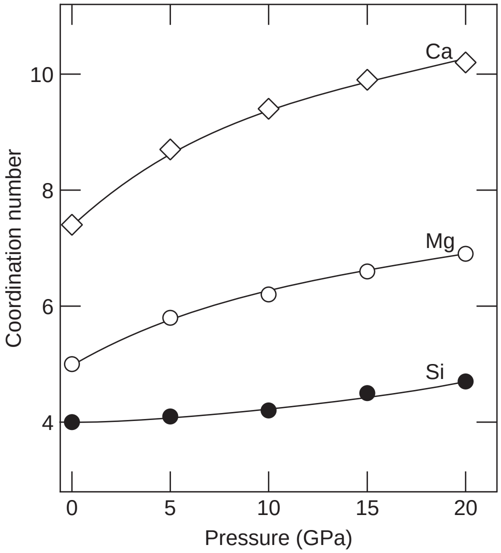

FIG. 7.9 Evolution of Ca, Mg, and coordination numbers with pressure simulated for $CaMgSi_2O_6$ melt (Matsui, 1996).

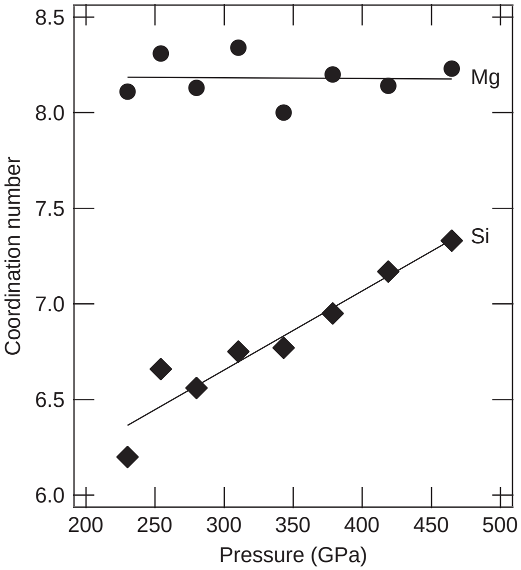

FIG. 7.10 Oxygen coordination around Si and Mg simulated $MgSiO_3$ melt at 13,000 K in the 230–460 GPa pressure range (Zhao et al., 2014).

order, whereas vibrational and nuclear magnetic resonance (NMR) spectroscopy probe local structure in and near individual SiO_4 tetrahedra as well as the extent to which these entities can form extended, more polymerized silicate structures (Henderson, 2018). X-ray-based models also have been used to characterize the environment of network-modifying cations. Beginning at about the same time, vibrational spectroscopy and, to a lesser extent, NMR and diffraction techniques have been applied to probe temperature- and pressure-induced structural changes in liquids (Waseda and Suito, 1977; Seifert et al., 1981; Farnan and Stebbins, 1990a,b; McMillan et al., 1992; Mysen and Frantz, 1993).

7.3.1 Silicate Network

Vibrational spectroscopy was originally used to probe the anionic structure of silicate glasses through the so-called "fingerprinting" technique. With this method, the main features of the spectra of a glass are compared with those of relevant crystalline materials. As an example, Etchepare (1972) suggested that the main anionic entities of $CaMgSi_2O_6$ glass resemble those of diopside crystals because the main Raman peaks in both spectra occur at approximately the same frequency. A comparison of the Raman frequencies in the spectra of $CaMgSi_2O_6$ melt and diopside recorded at the diopside liquidus temperature of 1392°C (Kushiro, 1969) have revealed even greater similarity between spectra of diopside and $CaMgSi_2O_6$ melt at this high temperature (Richet et al., 1994).

Brawer and White (1975, 1977) were among the very first to establish systematic relationships between silicate glass and melt structure and chemical composition through a Raman spectroscopic study of binary M_2O-MO-SiO_2 (M = Li, Na, and K, alkaline earths) glasses and for binary, ternary, and quaternary systems. They also observed that the intense bands assigned to antisymmetric Si—NBO stretching in SiO_3 and Si_2O_5 groups were similar in crystalline and glassy M_2SiO_3 and $M_2Si_2O_5$ (M = alkali metal). Intermediate compositions resulted in Raman spectra with intermediate intensity of Raman bands assigned to vibrations in these silicate entities.

In a further extension of the structural concepts originally advanced by Etchepare (1972) and Brawer and White (1975, 1977), Virgo et al. (1980), Mysen et al. (1982), and McMillan (1984) investigated glasses ranging from pure SiO_2 to nearly as depolymerized compositions as orthosilicate. Not only do SiO_3- and Si_2O_5-like structures exist, but there are additional types of units such as SiO_2, Si_2O_7, and SiO_4 groups. Virgo et al. (1980) suggested that disportionation reactions, such as

$$Si_2O_5 \Leftrightarrow SiO_3 + SiO_2, \tag{7.7}$$

can be used to describe their mutual equilibria. An equation equivalent to (7.7) then can be written with the Q^n-species notation (Stebbins, 1987):

$$2Q^n \Leftrightarrow Q^{n-1} + Q^{n+1}. \tag{7.8}$$

Additional complexity with more than three coexisting Q^n-species also has been reported (Silva et al., 2011), for example, when divalent alkaline earths are introduced in alkali silicates and enhance steric hindrance near nonbridging oxygens, causing additional disproportionation. Another interesting feature of this systematics is that melts of and glasses of orthosilicate composition, with therefore ${SiO_4}^{4-}$ silicate stoichiometry, comprise polymerized species such as Q^1 (Sen et al., 2009; Kohara et al., 2011), a structural feature also predicted by molecular dynamics simulations (Umesaki et al., 1988). Of course, given both Q^0 and Q^1 units, free oxygen forming bonding only with metal cations must also exist in such melts and glasses.

Implicit in the preceding discussion is the conclusion that there exists a small number of discrete silicate structures ($n = 0, 1, 2, 3$, and 4). In other words, the silicate structure cannot be described in terms of a gradually increasing degree of polymerization of individual structural species with decreasing metal/silicon-ratio. This idea finds strong support in results from NMR and Raman spectroscopy (Virgo et al., 1980; Schramm et al., 1984; Stebbins, 1987; Maekawa et al., 1991; Buckermann et al., 1992; Zhang et al., 1996). For example, in a comprehensive ^{29}Si MAS NMR (MAS: magic angle spinning) study of glass structure of alkali disilicates, Maekawa et al. (1991) observed that individual peaks remain at nearly constant frequency but change their relative intensity as a function of the alkali/silicon ratio (Fig. 7.11). These frequencies, indicated by thick lines in Fig. 7.11, are similar to those observed in the ^{29}Si NMR spectra of crystalline alkali silicates of equivalent degree of polymerization (see also Engelhardt and Michel, 1987). As the number of bridging oxygens in a structural entity decreases (the value of n in the Q^n-species decreases), the Si nucleus becomes progressively deshielded, resulting in decreasing values of the chemical shifts. The ^{29}Si MAS NMR data (Fig. 7.11) offer strong support, therefore, for the concepts that a small number of Q^n-species exist in silicate glasses, and that Eq. (7.8) can, indeed, be used to express the equilibria among them.

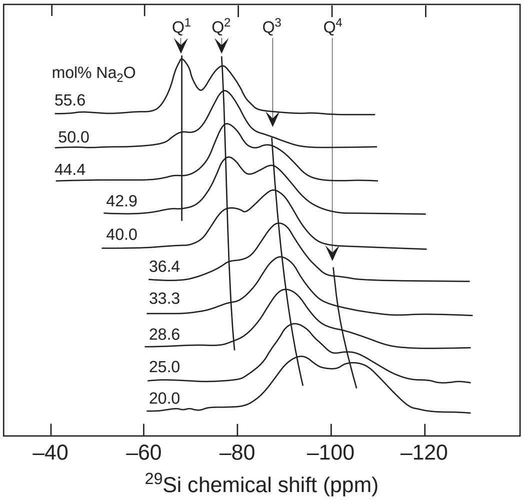

FIG. 7.11 ^{29}Si MAS NMR spectra of glasses in the system Na_2O-SiO_2 for Na_2O content indicated on individual spectra. See text for discussion of assignments and *thick lines* (Maekawa et al., 1991).

The chemical shift of bands assigned to individual Q^n-species (Fig. 7.11) varies slightly because there is a small deshielding effect even for the individual Q^n-species. This effect results from the fact that the extent of deshielding of ^{29}Si nucleus also depends on Si—O bond length, Si—O—Si bridging bond angles, and on changes in second- and third-nearest neighbor environments (Murdoch et al., 1985; Oestrike et al., 1987; Schneider et al., 1987; Engelhardt and Michel, 1987; Xue et al., 1994; Mauri et al., 2000).

The presence of a few well-defined anionic silicate units not only is supported by an extensive ^{29}Si MAS NMR literature, but is also consistent with Raman spectra. In fact, a striking feature of Raman spectra is that, regardless of the metal/silicon ratio, the frequencies assigned to antisymmetric Si—O stretching vibrations (see Table 7.2) in the various Q^n-species are nearly independent of composition for alkali and alkaline earth glasses (Fig. 7.12). Interestingly, the concept of a small number of coexisting silicate structures does have many similarities with pseudocrystalline glass structure models (see Section 7.2.1). These concepts, developed from Raman spectra of metal oxide-silica glasses, are also consistent with results from numerical simulations (Section 7.2.4).

The ^{29}Si NMR spectra can be used to determine the abundance ratios of structural units. The intensity of Raman bands, in contrast, is not a simple function of abundance because their intensity does not depend only on concentration of specific structural units, but also varies as a function of other variables such as (i) the nature of next-nearest neighbors, (ii) the type of cations in tetrahedral coordination, (iii) the number of nonbridging oxygens in the Q^n-species of interest, and (iv) the temperature at which a Raman spectrum is recorded.

The Q^n-species abundance data from ^{29}Si MAS NMR, shown for K_2O-SiO_2 and Na_2O glasses in Fig. 7.13, are consistent with the idea that the principal structural variations in metal oxide silicate glasses are in the abundance of the individual structural units. In pure SiO_2 glass, only Q^4 species are detected (with the possible exception of some bond defects; see also Chapter 5). Upon addition of metal oxides, Q^4 species transform into Q^3 whose abundance reaches a maximum near the disilicate stoichiometry (Si_2O_5). Likewise, that of Q^2 is near

TABLE 7.2 Comparison of Bond Distances (Å) and Coordination Numbers (CN) for $Na_2Si_4O_9$ Glass from MD Numerical Simulation (Ispas et al., 2002) and Neutron Diffraction Experiments (Zotov and Keppler, 1998)

	Simulation		**Neutron Diffraction**	
Bond	**Distance (Å)**	**CN**	**Distance (Å)**	**CN**
Si—O	1.63	4.0	1.63	4
Si—Si	2.06	3.5	3.06	3.6
O—O	2.66	5.5	2.61	5.5
Na—O	2.28	5.4	2.45	4.3

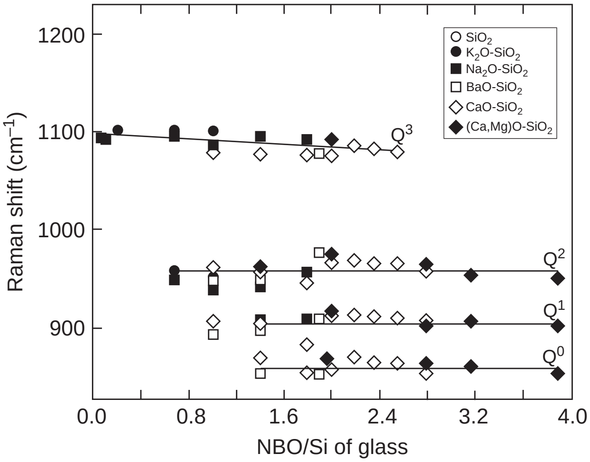

FIG. 7.12 Frequency of Raman bands in spectra of metal oxide glasses assigned to Si—NBO and Si—BO in Q^4, Q^3, Q^2, Q^1, and Q^0 structural units as a function of NBO/Si of glass for compositions identified on the figure (Mysen et al., 1982).

the metasilicate stoichiometry (SiO_3). This evolution is analogous to that observed by Polyakov et al. (2010) from molecular simulation calculations for Na_2O-SiO_2 melts (Fig. 7.4A).

The NMR data in Fig. 7.13A offer a hint that the abundances of Q^n-species also depend on the type of metal cation. This dependence has been further documented by ^{29}Si MAS NMR data for $M_2Si_2O_5$ glasses ($M=K$, Na, and Li) shown in Fig. 7.13B. For a fixed M/Si ratio, the abundance of Q^3 species in a binary metal oxide silicate glass decreases with increasing ionization potential of the alkali metal, whereas those of Q^2 and Q^4 increase. These relationships suggest that Eq. (7.8) shifts to the right, at least with $n=3$, with increasing ionization potential of the metal cation (Mysen, 1997; Lin et al., 2010).

We infer from the observations (Figs. 7.13A and B) that the nonbridging oxygens in the various Q^n-species are not energetically equivalent. This inference has been substantiated via ^{29}Si MAS NMR and ^{17}O triple quantum NMR spectroscopy of glasses in the systems Na_2O-CaO-SiO_2 (Jones et al., 2001; Lee and Stebbins, 2003a,b) and BaO-MgO-SiO_2 (Lee et al., 2003). Other properties also are strong indicators of some ordering of nonbridging oxygens (Kohn and Schofield, 1994; Mysen, 2007). The general rule seems to be that the more electronegative the metal cation, the stronger is its tendency to bond with nonbridging oxygens in the least polymerized Q^n-species available. This steric hindrance is also seen in

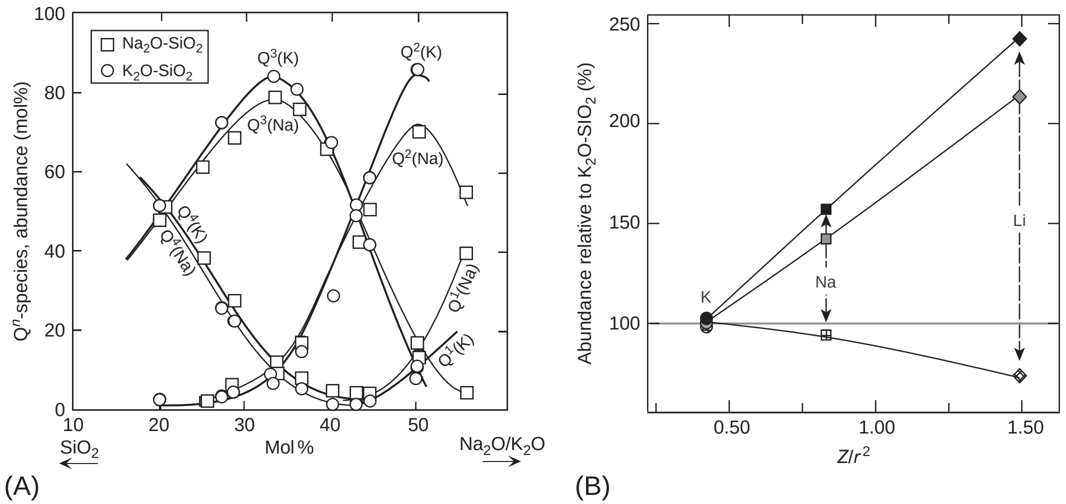

FIG. 7.13 Abundance (mol%) of Q^4, Q^3, Q^2, and Q^1 species. (A) In K_2O-SiO_2 and Na_2O-SiO_2 glasses against glass composition (Maekawa et al., 1991). (B) In $Na_2Si_2O_5$ and $Li_2Si_2O_5$ glass relative to $K_2Si_2O_5$ glass (Mysen, 1997).

the effect of cation size on O—Si—O angles in SiO_3 chains. The chain becomes increasingly buckled the smaller the cation (Table 7.2), although Li-silicate may deviate some from this relationship, as the small cation may actually form mixed bonding with bridging and nonbridging oxygens (Yasui et al., 1983). Similar structural effects have been observed in crystalline metasilicates (Liebau and Pallas, 1981).

7.3.2 Network-Modifiers and Interconnectivity

Energetically nonequivalent nonbridging oxygens in different coexisting Q^n-species in metal oxide-silica glass imply that there is also some ordering of the metal cations that serve to link different Q^n-species. This idea accords with neutron diffraction data of $Li_2Si_2O_5$ glass (Zhao et al., 1998), which yield Li—Li interatomic distances near or slightly below 2 Å. This distance is considerably smaller than that which would be expected if Li^+ were randomly distributed. Lee and Stebbins (2003a,b) reported that ^{23}Na MAS NMR chemical shifts in spectra of Na_2O-SiO_2 could be related to different Na—NBO bonding characteristics in the different Q^n-species. Moreover, in ternary Na_2O-CaO-SiO_2 glasses, Calas et al. (2002) concluded that similar structural features are found in other metal silicate glasses, both for alkali and alkaline earth metals and for transition metals. In general, in multicomponent silicate glasses such as, for example, Na_2O-CaO-SiO_2, K_2O-MgO-SiO_2. In K_2O-BaO-SiO_2 and Na_2O-MgO-SiO_2, the oxygen bonding characteristics differ such that the more electropositive cations (i.e., Na^+ and K^+ rather than Ca^{2+} and Ba^{2+}) would tend to form bonding with nonbridging oxygen in the most polymerized of coexisting silicate structures (Cormack and Du, 2001; Allwardt and Stebbins, 2004; Trcera et al., 2011).

The oxygen polyhedra that surround network-modifying cations in a glass and melt typically show some order perhaps to the second oxygen coordination shell (Eckersley et al., 1988). The oxygen coordination number commonly is smaller than that around crystalline materials with the same chemical composition (Cormier et al., 2001). Moreover, the type and proportion of the metal-oxygen coordination polyhedra are related to both the availability of various types of nonbridging oxygen and to the ionization potential of the network-modifier (Lee et al., 2003; Lee and Stebbins, 2003a,b). Furthermore, the smaller the metal cation, the smaller the coordination number. For example, for Li^+, for glasses such as $Li_2O{\cdot}2SiO_2$, the coordination number seems near 3.2 ± 0.2 (Zhao et al., 1998). In Na-silicate glasses, the number is 6–7 (Angeli et al., 2000), and in Cs-silicate glasses, between 8 and 10 (Hanson and Egami, 1986). Also, in mixed cation silicate environments, the coordination number around given cations varies with the metal-cation abundance ratios and often shows a range of coordination numbers depending on composition (Gambuzzi et al., 2015). In general, such cations have larger oxygen coordination numbers when they have charge-balancing roles than when they are network-modifiers (Angeli et al., 2000, 2007; Gambuzzi et al., 2015). In addition, in mixed cation environments, the individual bond distances, and therefore oxygen coordination numbers, tend to be greater than in single cation systems (Gambuzzi et al., 2015). These differences may be related to different oxygen bond distances depending on the proportion of metal cations in a glass (Angeli et al., 2007; Gambuzzi et al., 2015) (see also Fig. 7.14). The bond distance reflects the oxygen coordination number, which is typically proposed to be 6 or higher (Eckersley et al., 1988). Shimoda et al. (2007), using ^{43}Ca MQMAS NMR, reported an oxygen coordination between 7 and 8 for Ca^{2+}, as did Angeli et al. (2007), whereas Gambuzzi et al. (2015) proposed a wider range of numbers. When bonding to nonbridging oxygen, the smaller Mg^{2+} cation gives rise to Mg—O bond distances significantly shorter than that of Ca—O, for example. It follows that the oxygen coordination number around Mg^{2+} likely also is smaller than that of Ca^{2+}. Waseda and Toguri (1977) suggested 4.8 ± 0.3 as the average coordination number. However, more recent X-ray work by Wilding et al. (2008) is consistent with MgO_n polyhedra with a mixture of $n = 4$, 5, and 6. Kroeker and

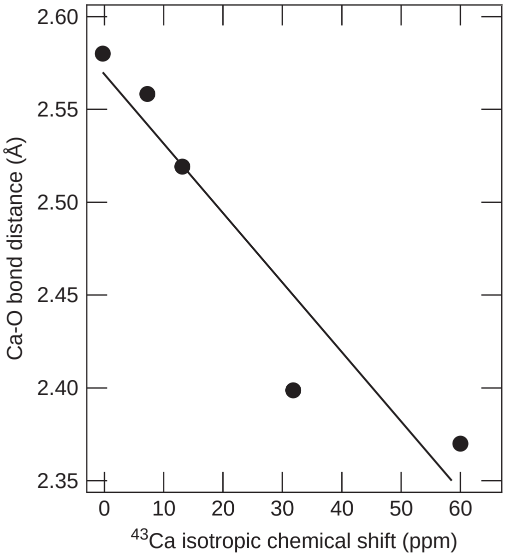

FIG. 7.14 Relationship between Ca—O distance and ^{43}Ca chemical shift for glasses with 60 mol% SiO_2, 20 Mol% CaO and 20 mol% Al_2O_3 (Ca—O distance: 2.58 Å), 60 mol% SiO_2, 20 mol% Al_2O_3 and 10 mol% Na_2O and CaO, respectively (Ca—O distance: 2.47 Å) and 60 mol% SiO_2, 20 mol% CaO and 20 mol% Na_2O (Ca—O distance: 2.36 Å) (Angeli et al., 2007).

Stebbins (2000) from ^{29}Mg MAS NMR concluded that, at least in Mg-bearing alkaline earth silicate glasses, the coordination number is 6 and, in fact, the same as in their crystalline counterparts (e.g., crystalline and glassy $CaMgSi_2O_6$). This conclusion also is in accord with the ^{25}Mg triple quantum MAS results of Shimoda et al. (2007) for $MgSiO_3$ glass.

A cation has different oxygen coordination numbers depending on its network-modifier or charge-balance function (Binsted et al., 1985; Angeli et al., 2007). In the former situation, steric considerations would suggest that the less polymerized a Q^n-species sharing a nonbridging oxygen with a network-modifying cation is, the larger is the oxygen coordination number. Also, the larger the cation, the larger is the oxygen coordination number. These structural characteristics are analogous to those of silicate crystals. This latter structural feature can be seen in both alkali and alkaline earth silicates (Waseda and Toguri, 1977; Angeli et al., 2007; Gambuzzi et al., 2015). The oxygen coordination numbers are influenced by the geometric restrictions on how the charge-balance may be carried out.

7.3.3 Temperature and Pressure

The data discussed so far have been recorded on glasses that were formed with temperature-quenching of melt whose structure was thus frozen in at the glass transition. This conclusion, in turn, implies that structure and property data of glasses cannot be extrapolated with precision to the conditions of a high-temperature melt, because the structure of metal silicate melts is temperature dependent (Seifert et al., 1981; Stebbins et al., 1985; Dingwell and Webb, 1990; McMillan et al., 1992; Mysen and Frantz, 1993). Many properties also depend on temperature, some of which may be related to temperature-dependent melt structure (Mysen, 1995). These can be characterized in structural terms only with data obtained at temperatures above the glass transition.

7.3.3.1 Temperature

Changes in bond angles and bond distances develop progressively with temperature in the supercooled and superliquidus states. This continuity has been observed in neutron diffraction experiments (Zotov and Keppler, 1998; Majérus et al., 2004) and in simulation of structure (Ispas et al., 2002). For the same reason, the glass transition cannot be detected in exchange frequencies of Si and O between coexisting Q^n-species (Farnan and Stebbins, 1990a,b; Maekawa and Yokokawa, 1997; George and Stebbins, 1998). Instead, it has been seen as an abrupt decrease in ^{29}Si NMR spin relaxation time for $K_2Si_2O_5$ (Farnan and Stebbins, 1990a,b).

Notably, oxygen coordination polyhedra in melts with the stronger metal-oxygen bond are less sensitive to temperature. For example, in Na_2O-MgO-SiO_2, ^{25}Mg MAS NMR data indicate a significant decrease of 0.025 ppm/°C in the ^{25}Mg chemical shift with increasing temperature, whereas for the much stronger Si—O bond, the decrease is approximately one order of magnitude less (0.0025 ppm/°C) (Fiske and Stebbins, 1994) (see Fig. 7.15). There is, in fact, a correlation between the ionization potential of the metal cation, Z/r^2, and isotropic chemical shifts (George and Stebbins, 1998) (see Fig. 7.16), which, in turn is consistent with longer oxygen bonds and larger coordination numbers (George and Stebbins, 1998). On the basis of relationships between the ionization potential and ^{25}Mg isotropic chemical shift of crystalline materials, George and Stebbins (1998) concluded that for an average Z/r^2 value near 2.2 and

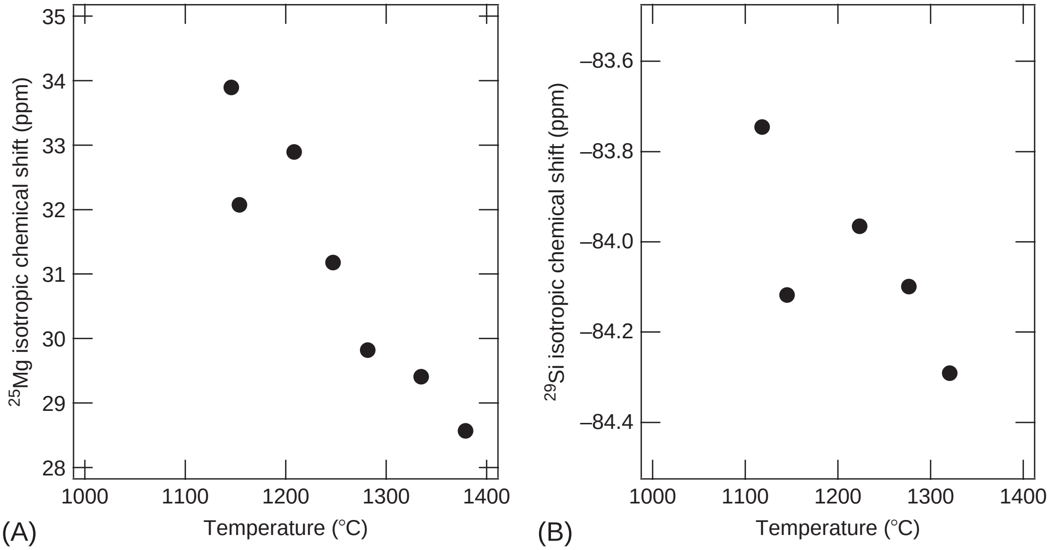

FIG. 7.15 Isotropic chemical shifts from NMR spectra of the composition $(Na_2O)_{0.28}(MgO)_{0.18}(SiO_2)_{0.54}$ as a function of temperature at ambient pressure. (A) ^{25}Mg chemical shift with an average change of 0.025 ppm/°C. (B) ^{29}Si chemical shift with an average change of 0.0025 ppm/°C (Fiske and Stebbins, 1994).

FIG. 7.16 Isotropic chemical shifts of ^{25}Mg in melts at temperatures near 1400°C for melts in the systems K_2O-Na_2O-MgO-SiO_2, Na_2O-MgO-SiO_2, CaO-MgO-Al_2O_3-SiO_2, and CaO-MgO-SiO_2 (George and Stebbins, 1998).

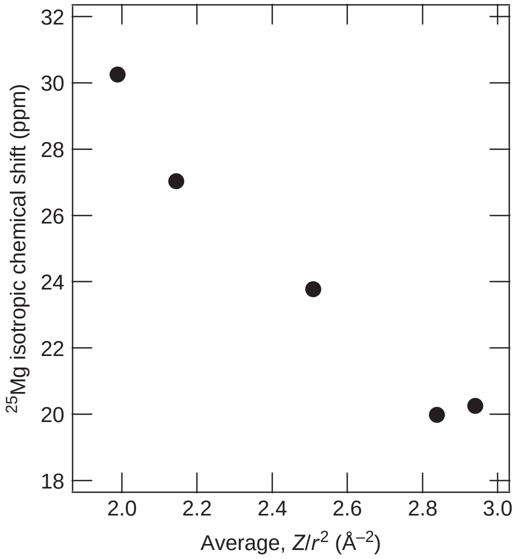

higher, the oxygen coordination number is 6 or higher, whereas for Z/r^2 values near 1.6, the oxygen coordination number for Mg^{2+} would be 4. For the compositions in Fig. 7.16, this means that essentially all Mg^{2+} in these glasses occupy sixfold coordination.

The silicate species in melts and glasses are linked together by various combinations of network-modifying cations. This speciation depends not only on silicate composition, but also on temperature. At the glass transition, at which this Q^n-species abundance such as shown in Fig. 7.13 is frozen in, the Q^n-species abundance varies with both metal/Si ratio and with the type of alkali metal. Therefore, if equilibrium of Eq. (7.8) also depends on temperature, its variations are included in the data summarized in Fig. 7.13. Moreover, a number of temperature-dependent melt properties (e.g., transport properties; see Section 7.4) can be linked to the types and abundance of silicate species. It is therefore necessary to establish the temperature-dependent variations in Q^n-species abundance. This has been accomplished through first-principles simulations and high-temperature spectroscopic identification and quantification of Q^n-species (Stebbins, 1988; McMillan et al., 1992; Mysen and Frantz, 1993, 1994; Mysen, 1995, 1997, 1999; Maekawa and Yokokawa, 1997; Horbach et al., 2001).

Because Q^n-speciation does not vary in the glassy state, the onset of structural relaxation manifests itself at the glass transition as a distinct change in the slope of the temperature versus Q^n abundance relationship (Fig. 7.17). In the example of $K_2Si_2O_5$ (Fig. 7.17), the Q^2 and Q^4 abundance increases by the same amount as a function of temperatures, whereas that of Q^3 decreases. Similar variations of the Q^n-species can be found in other alkali silicate and aluminosilicate glasses and melts (Mysen, 1997; Mysen et al., 2003). Hence, equilibrium (7.8), with $n=3$, shifts to the right with increasing temperature as proposed by Stebbins (1988) and Brandriss and Stebbins (1988), and subsequently documented by in situ, high-temperature studies in a variety of metal oxide silicate melts (McMillan et al., 1992; Mysen and Frantz, 1993). This shift has been examined in terms of the effect of temperature on the constant, K, for this equilibrium:

$$K = \frac{X_{Q^2} \cdot X_{Q^4}}{\left(X_{Q^3}\right)^2}, \tag{7.9}$$

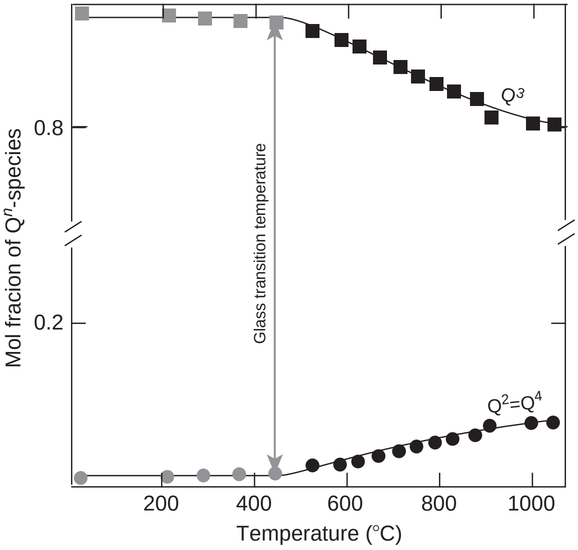

FIG. 7.17 Abundance of Q^n-species in $K_2Si_2O_5$ below and above the glass transition against temperature from in situ Raman spectroscopy (Mysen and Frantz, 1994; Mysen, 1997). Glass transition temperature (*gray line*) from Richet and Bottinga (1986).

where it is assumed that the mol fraction of an individual Q^n-species, X_{Q^n}, is equal to activity. Above the glass transition temperature, T_g, $\ln K$ is a linear function of reciprocal temperature and a positive function of the ionization potential of the metal cation (Fig. 7.18A). Thus, steric hindrance seen in glasses and governed by the electronic properties of the cation also affects melt structure so that equilibrium (7.8) shifts to the right as the cation becomes smaller or more highly charged (Fig. 7.18B). Such a trend is expected because increasingly electronegative metal cations should bond to nonbridging oxygens in increasingly depolymerized Q^n-species (Jones et al., 2001; Lee and Stebbins 2003a,b) and Q^2 is less polymerized than Q^3.

The enthalpy change (ΔH) of reaction (7.8) can be estimated from the slope of the $\ln K$ versus $1/T$ relationship. For Na-disilicate melts, it was originally suggested to be near -30 ± 15 kJ/mol (Stebbins, 1988; Brandriss and Stebbins, 1988) from analysis of ^{29}Si NMR spectra of glasses with different fictive temperatures. This value agrees with the -27 ± 5 kJ/mol found for $Na_2Si_2O_5$ melt by Maekawa and Yokokawa (1997) from high-temperature ^{29}Si NMR spectroscopy. From calibrated, high-temperature Raman spectra of the same $Na_2Si_2O_5$ melt, Mysen (1997) reported ΔH near -36 ± 4 kJ/mol, which compares fairly well with the aforementioned values. We also note that the ΔH of reaction (7.8) also is positively correlated with the ionization potential of the metal cation (Fig. 7.18C). The enthalpy change also increases as the melt becomes more polymerized. Thus, the details of the equilibria among Q^n-species in metal oxide silicate melts depend on both the properties of the metal cation and on the degree of polymerization, NBO/Si, of the melt.

7.3.3.2 Pressure

Compression of metal oxide silicate glass and melts may take three basic forms: (i) Decreased intertetrahedral angles and associated lengthening of Si—O bridging bonds (Xue et al., 1991; Gaudio et al., 2008; Sanchez-Valle and Bass, 2010), (ii) Changes in the disproportionation reactions, such as that described with Eq. (7.8) because of volume differences between Q^n-species (Dickinson et al., 1990; Xue et al., 1991; Bottinga and Richet, 1995), and (iii) Coordination changes of network-forming (Si^{4+} and Al^{3+}) and network-modifying cations (Diefenbacher et al., 1998; Lee et al., 2005; Wilding et al., 2008; Adjaoud et al., 2008; Lee, 2011).

The Si—O—Si angle compression can be observed in a narrowing of the ^{29}Si MAS NMR resonance assigned to Q^4 entities (Gaudio et al., 2008) (see also Fig. 7.19). The full width at half height of the two spectra in Fig. 7.19 is considerably less in the high-pressure glass (21 vs. 24 ppm). Furthermore, the greater width is in the region of the spectra dominated by resonances from the most polymerized species (Q^4 and perhaps Q^3), reflecting therefore the suggestion that the strongest Si—O—Si angle compression takes place in the most polymerized species, such as Q^4.

Angle compression and bond length increase seem to become decreasingly important with increasing metal/Si ratio. This effect likely reflects a decreasing abundance of Q^4 species as the metal/silicon ratio decreases (Xue et al., 1991). That the Q^4 is more compressible than the other species is also reflected by the decreasing compressibility of alkali silicate melts with increasing alkali/silicon ratio (see also Chapter 6, Section 6.4.1).

The second way in which pressure can affect structure concerns the volume change associated with reaction (7.8), whose sign depends primarily on the partial molar volumes of the

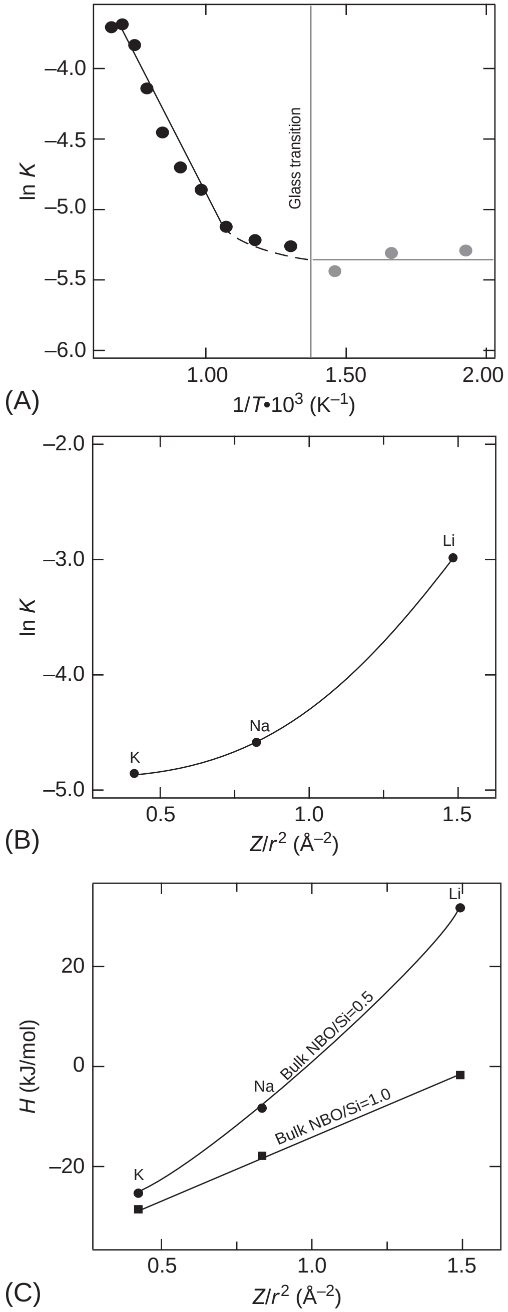

FIG. 7.18 Thermodynamic relations of the equilibrium $2Q^3 \rightleftharpoons Q^2+Q^4$. (A) Equilibrium constant, ln *K*, for the equilibrium, $2Q^3 \Leftrightarrow Q^4+Q^2$ of alkali silicate melts against either reciprocal temperature or the electrical charge, *Z*, and ionic radius, *r* (Å), for sixfold coordination (Whittaker and Muntus, 1970) of the alkali. (A) For $Na_2Si_2O_5$ below and above the glass transition temperature, T_g (Mysen, 1997; T_g from the compilation by Richet and Bottinga, 1986). (B) For metasilicates $K_2Si_2O_5$, $Na_2Si_2O_5$, and $Li_2Si_2O_5$ at 1050°C (Mysen, 1997). (C) For disilicates, $K_2Si_2O_5$, $Na_2Si_2O_5$, and $Li_2Si_2O_5$ (Bulk NBO/Si = 1) and tetrasilicate melts, $K_2Si_4O_9$, $Na_2Si_4O_9$, and $Li_2Si_4O_9$ (Bulk NBO/Si = 0.5), at 1050°C (Mysen, 1997).

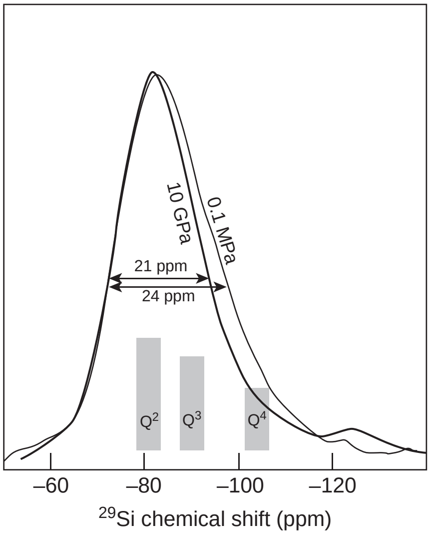

FIG. 7.19 ^{29}Si MAS NMR spectra of $MgSiO_3$ glass at ambient pressure (0.1 MPa, *thin line*) and recovered from 10 GPa and 773°C *(thick line)*. Also marked are the approximate positions of the resonances from Q^4, Q^3, and Q^2 silicate entities. *Double arrows* illustrate FWHH of the spectra (Gaudio et al., 2008).

Q^n-species. This change varies with the proportion of bridging (BO) and nonbridging (NBO) oxygens, with the compressibility of the metal-oxygen polyhedral linking Q^n-species, and with the compressibility of the Q^n structural units. Bottinga and Richet (1995) inferred from molar volume relations that the partial molar volume of bridging oxygen is greater than that of nonbridging oxygen. This is also consistent with a larger Si—BO bond distance compared with Si—NBO (Lee and Stebbins, 2003a,b). The Q^4-species with four bridging oxygen bonds likely has the largest partial molar volume. The Q^2 species with two nonbridging and two bridging oxygens would have a smaller partial molar volume than Q^3 species with only one nonbridging and two bridging oxygens. Thus, the ΔV of reaction (7.8) would be negative. The volume effect probably is further enhanced because of the greater compressibility of Q^4 compared with Q^3 and Q^2. The compressibility of Q^4 units likely resembles that of pure SiO_2 (see Chapter 5).

These volume considerations are consistent with observed changes with pressure of the species abundances that define equilibrium (7.8) (Fig. 7.20) (see also Xue et al., 1991; Dickinson et al., 1990). The Q^2 and Q^4 abundances do increase with pressure, whereas that of Q^3 decreases. This observation also agrees with the results reported by Dickinson et al. (1990), who suggested that the Raman spectra of $K_2Si_4O_9$ glass, quenched at 2.1 GPa, are consistent with a slight increase in Q^4 and Q^2 abundance in $K_2Si_4O_9$ melt with pressure, a conclusion similar to that of Mysen (1990) for $Na_2Si_2O_5$ quenched at 2 GPa.

Pressure can also result in coordination changes of both network-forming cations such as Si^{4+} and Al^{3+} (Ohtani et al., 1985; Xue et al., 1991; Allwardt et al., 2005, 2007; Lee et al., 2006; Sanloup et al., 2013) and alkali and alkaline earth network-modifying cations (Wilding et al., 2008; Sanloup et al., 2013; Ghosh et al., 2014) (see also Fig. 7.21). For network-modifying cations, coordination numbers increase rapidly with pressure, the rate of increase and actual coordination numbers depending on the cation (Sun et al., 2011; Sanloup et al., 2013; Ghosh et al., 2014). For network-formers such as Si^{4+}, there is incontrovertible multinuclear NMR

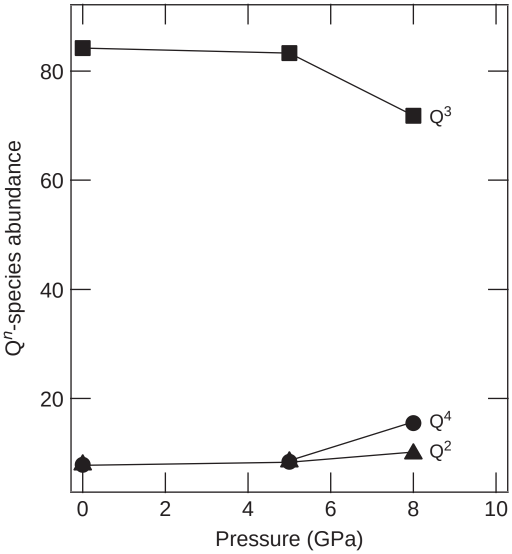

FIG. 7.20 Evolution of Q^n-species abundance on $Na_2Si_2O_5$ quenched melt as a function pressure of equilibration prior to quenching (Xue et al., 1991).

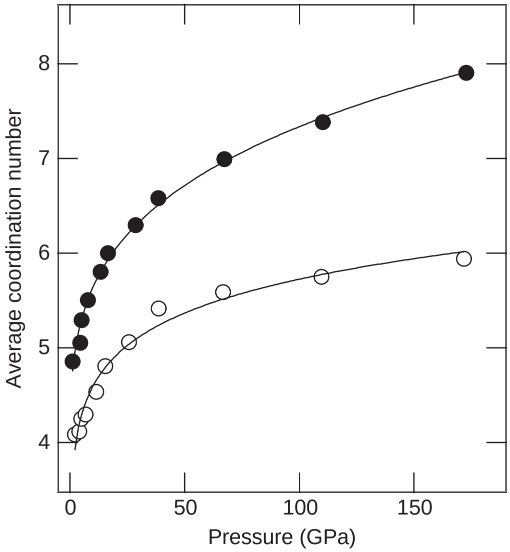

FIG. 7.21 Coordination numbers for Si^{4+} and Mg^{2+} in $MgSiO_3$ melt as a function of pressure calculated by Ghosh et al. (2014).

evidence that $Na_2Si_3O_7$ and $Na_2Si_4O_9$ glasses quenched from melt at pressures up to 10 GPa contain both $^{[4]}Si—O—^{[5,6]}Si$ and $Na—O—^{[5,6]}Si$ bonds (Lee et al., 2003, 2006) (see also Fig. 7.22). The comparatively abrupt abundance changes in the 6–8 GPa range would suggest that it is here that major coordination transformation of Si^{4+} occurs. This conclusion (Lee and Stebbins, 2003a,b) is also supported by results from Xue et al. (1994) from static and MAS NMR studies of other high-pressure Na-silicate glasses. The extent to which

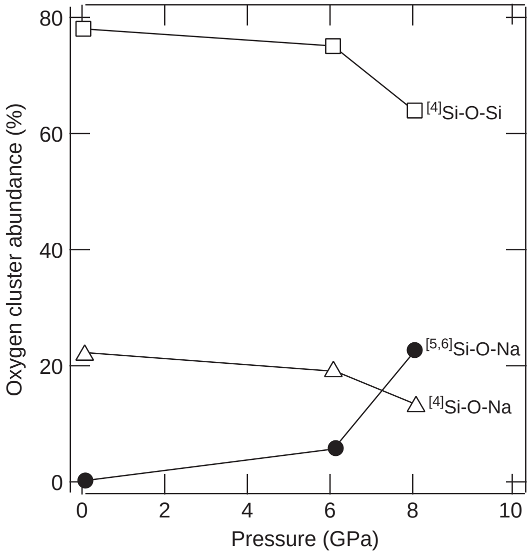

FIG. 7.22 Population of oxygen bonding in $Na_2Si_4O_9$ glass quenched from melt at 1750–1900°C at pressures indicated. The superscripts $^{[4]}$Si and $^{[5,6]}$Si indicate Si^{4+} in fourfold and in five+sixfold coordination with oxygen, respectively. In other words, the oxygen in $^{[4]}$Si—O—Si is a bridging oxygen and in $^{[4]}$S—O—Na a nonbridging oxygen. Note that for the more highly coordinated Si^{4+} the oxygen is linked to another Si^{4+} and Na (Lee et al., 2006).

Si-coordination changes occur with pressure and the pressure range over which it may occur appear dependent on the availability of nonbridging oxygen in the starting materials (Lee et al., 2003).

7.4 STRUCTURE AND MELT PROPERTIES

The variations of properties of silicate melts and glasses in general, and binary metal oxide in particular, reflect structural changes, be they from bulk composition, temperature, or pressure. Some models were derived on the basis of assumed relationships between structure and properties (see, e.g., Sections 7.2.1 and 7.2.3). Some of these models are consistent with the data obtained by direct measurements (Section 7.3), thus lending credence to the assumptions in some of the property-based structure models. In other cases, current understanding of melt structure can be used to decide which ones are consistent with the available data.

The minimum M/Si ratios of stable crystalline phases in various metal oxide silicate crystals reflect the extent to which steric hindrance is associated with accommodation of cations in a crystalline silicate network (Liebau, 1980; Liebau and Pallas, 1981). In silicate glasses and melts, many of the same structural restrictions can be applied in terms of the relative stability of Q^n-species and the response of types and proportions of Q^n-species to changes in the proportions and electronic properties of the network-modifying metal cations (M-cation). The fact that the equilibrium constant for Eq. (7.8) is positively correlated with the ionization potential of the metal cation is a direct consequence of steric restrictions imposed by bonding the metal cations to nonbridging oxygen in Q^3-species (Fig. 7.18).

7.4.1 Thermal Properties

7.4.1.1 Liquidus Surfaces

Several studies have quantified thermodynamic data of silicate melts in terms of oxide components or used liquidus phases as guides of speciation in the melts. However, given current knowledge of the actual structure of silicate melts, such as illustrated in Section 7.3, the structural information may be combined with thermodynamic data. This has been done, for example, by a combination of available structural data for the Na_2O-SiO_2 system and with the assumption of ideal mixing of the Q^n-species together with additive and temperature-independent heat capacities to derive a quantitative thermodynamic model of melts (Halter and Mysen, 2004). In this way, agreement was found between the experimental and calculated liquidus phase relations (Fig. 7.23).

7.4.1.2 Mixing

Liquidus phase diagrams may be used to compute the activities of oxide components. For example, the liquidus surfaces of silica polymorphs in metal oxide-silica systems (see Chapter 6, Figs. 6.1 and 6.6) indicate that as the activity of SiO_2 increases, the more electronegative is the metal cation. Notably, for the system Na_2O-SiO_2, the activity coefficient of SiO_2 is near unity (Ryerson, 1985; Morishita et al., 2004). In other words, the system is near ideal, at least in the composition range of the liquidus surfaces of silica polymorphs. This conclusion accords with that reached by Halter and Mysen (2004) as discussed previously.

In terms of melt structure, the activity of SiO_2 as deduced from the cristobalite/tridymite liquidus trajectory (see Chapter 6, Section 6.3) is particularly interesting, as it is related to the abundance of Q^4 species. The expansion of the cristobalite/tridymite liquidus volume toward

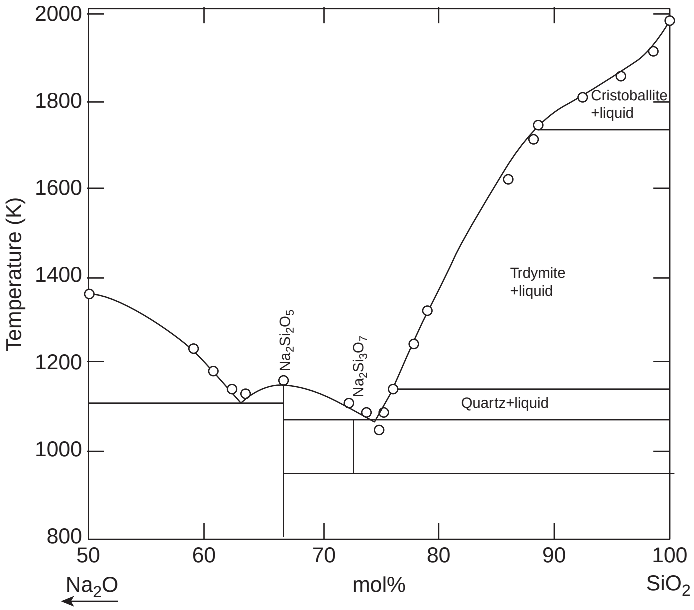

FIG. 7.23 Calculated liquidus diagram for portions of the system Na_2O-SiO_2 at ambient pressure, calculated by Halter and Mysen (2004).

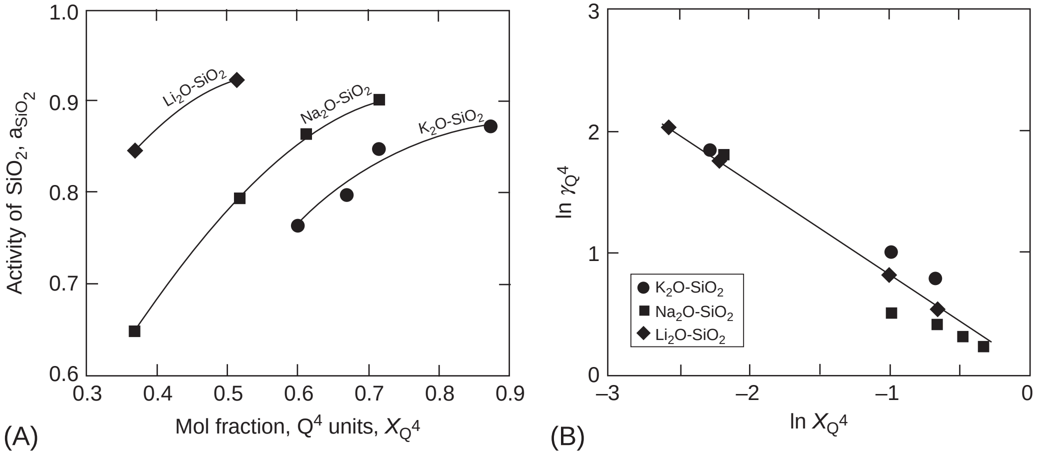

FIG. 7.24 Activity and activity coefficients of silica in Li_2O-SiO_2, Na_2O-SiO_2, and K_2O-SiO_2 melts at their liquidi. (A) Relative to Q^4 abundances (from compilation of Ryerson, 1985 together with melt structure data for these systems from Mysen and Frantz, 1994). (B) Logarithmic relationships between activity coefficients, γ_{Q4}, and mol fraction of Q^4, X_{Q4}, respectively, at the liquidus of silicate polymorphs (for Q^4 relations) (calculations by Mysen and Frantz, 1994).

decreasing silica content with increasing ionization potential of the metal cation (Fig. 7.24) follows naturally from the observation that the disproportionation reaction (7.8) among Q^n-species shifts to the right with increasing ionization potential of the metal cation (Fig. 7.24). Thus, even if the mixing properties between Q^n-species were not affected by the properties of the metal cations, the relationships in Fig. 7.18 are consistent with the liquidus phase relations in Fig. 7.24. In other words, an increase in the activity coefficient of the component, SiO_2, as derived from liquidus relations (see also Ryerson, 1985), at least in part, is the result of increasing concentration of fully polymerized Q^4 species in the melt.

Mixing in binary metal oxide silicate melts has also been determined experimentally (Hovis et al., 2004; Morishita et al., 2004; Sugawara et al., 2011). Molecular dynamics simulation also has been employed for this purpose (Seo and Tsukihashi, 2004; Zhang, 2011). For Na_2O-SiO_2 melts, there is a small excess enthalpy, which reaches about 4 kJ/mol as indicated by a 4th-order polynomial fit (Fig. 7.25), which likely increases with decreasing temperature (Sugawara et al., 2011) and eventually results in metastable immiscibility near the glass transition. Zhang (2011), using first-principles molecular dynamics simulation at 4000 K, also observed a tendency to generate excess heat of mixing in MgO-SiO_2 melts with between 80 and 90 mol% SiO_2, although the compositional extent of this maximum somewhat depends on the methods used for calculation.

Sugawara et al. (2011) found a maximum in the entropy of mixing, and a corresponding configurational entropy maximum, along this join at approximately the same composition (Fig. 7.26). This unmixing likely reflects steric incompatibility of Q^4 and Q^3 structural units, which for all practical purposes are the two coexisting silicate structures in the composition region of the enthalpy of mixing maximum. This incompatibility eventually leads to unmixing as the temperature is decreased. These features have also been observed as variations in the partial molar enthalpies of SiO_2 in Li_2O-SiO_2, Na_2O-SiO_2, and K_2O-SiO_2 melts,

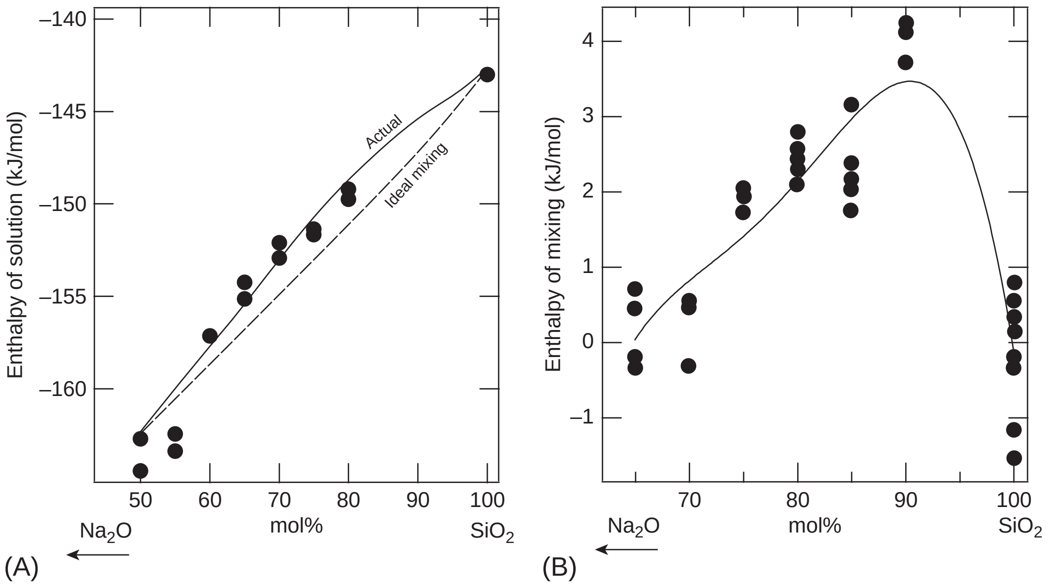

FIG. 7.25 Mixing properties of melts along the Na_2O-SiO_2 join. (A) Enthalpy of solution adjusted to a fictive temperature of 1000 K from Hovis et al. (2004). (B) Calculated enthalpy of mixing (Hovis et al., 2004).

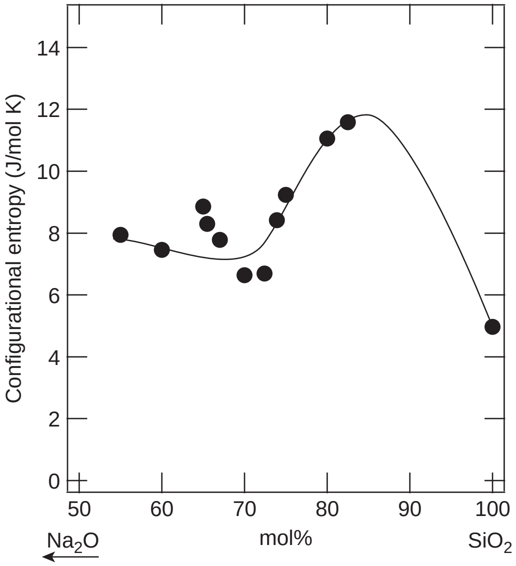

FIG. 7.26 Configurational entropy of supercooled Na_2O-SiO_2 melts at their glass transition temperature (Knoche et al., 1994).

where a change from negative to positive is observed for SiO_2-rich compositions (Morishita et al., 2004). The SiO_2 content where this crossing takes place decreases as the metal cation becomes increasingly electronegative. Of course, the abundance of Q^4 units in metal oxide silicate melts also is positively correlated with the electronic properties of the metal cation. It seems, therefore, that the critical factor governing excess heat of mixing in binary metal oxide silicate melt and glass systems is the abundance of Q^4 structural units relative to units with nonbridging oxygen.

Mixing parameters such as configurational heat capacity, C_p^{conf}, can also be derived from Q^n-speciation, provided that C_p^{conf} values are available for each Q^n-species. This can be done by combining, for example, thermodynamic data by Richet and Neuville (1992) for Na_2O-SiO_2 melts with Q^n-speciation information from the same system (Mysen, 1997). For Q^4, Q^3, and Q^2 species, the individual $C_p^{conf}(Q^n)$ values can be obtained from a set of linear equations of the type:

$$\sum_{n=0}^{n=4} X_{Q^n} C_p^{conf}(Q^n) = C_p^{conf}, \tag{7.10}$$

where X_{Q^n} is the mol fraction of Q^n-species and $C_p^{conf}(Q^n)$ is the configurational heat capacity of individual Q^n-species. We can apply the $C_p^{conf}(Q^n)$ data from Na_2O-SiO_2 melts, together with Q^n-speciation data (Mysen and Frantz, 1993), to other systems by adding a mixing term in which the temperature dependence of Q^n-speciation and glass transition temperature for the composition of interest are known (Mysen, 1995). A comparison of configurational heat capacities calculated in this manner for melts in the systems K_2O-SiO_2 (at 1200°C), Na_2O-SiO_2, and Li_2O-SiO_2 shows a close match with the observed values (Fig. 7.27). This C_p^{conf} information can then be used in conjunction with, for example, the configuration entropy model for melt transport to estimate melt viscosity and, perhaps, diffusion.

7.4.1.3 Mixed Alkali Effect

Addition of a second oxide to binary metal oxide silicate glasses and melts often causes deviation from linearity of properties by up to several orders of magnitude. This effect commonly is referred to as the mixed alkali effect (e.g., Day, 1976).

Recent theoretical and experimental examination of this effect is based on the observation that there often is substantial ordering of network-modifying cations among energetically nonequivalent sites in the structure (Yap and Elliott, 1995; Cormack and Du, 2001; Lee and Stebbins, 2003a,b). In this treatment, the availability of specific sites is diminished by the

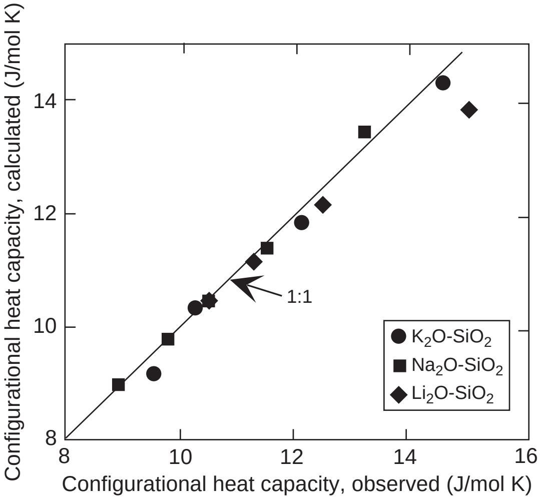

FIG. 7.27 Comparison of measured and calculated configurational heat capacity for melts in the systems K_2O-SiO_2 (at 1200°C), Na_2O-SiO_2, and Li_2O-SiO_2. *Redrawn from Mysen (1995).*

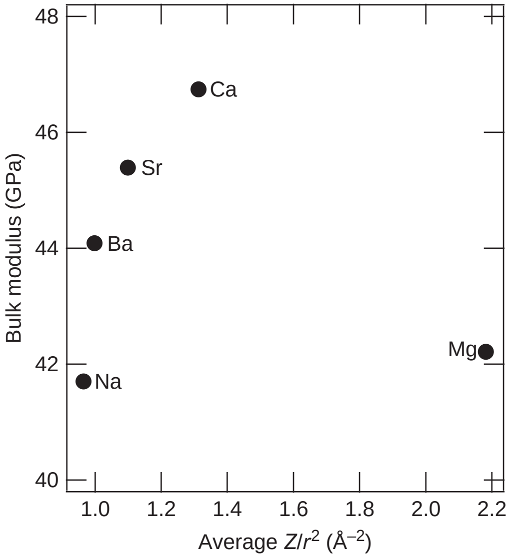

FIG. 7.28 Room-temperature bulk modulus of glasses in the system Na_2O-MO-SiO_2, where M = Ba, Sr, Ca, and Mg, as a function of the average ionization potential, Z/r^2 (Lin et al., 2010).

introduction of a second cation with substantially different ionization potential (different ionic size or electrical charge). Thus, the probability of any one of the other cations being able to move to an energetically equivalent site decreases. In other words, the preference of specific cations for specific oxygen locations in mixed alkali and/or alkaline oxide-silicate melts leads to nonlinear mixing behavior. Elastic properties, for example, likely are quite sensitive to the degree of polymerization of Q^n-species. Therefore, mixing silicate melts with different Q^n-species distributions such as, for example, metals with different ionization potential, will lead to significantly nonlinear evolution of elastic properties as bulk modules, for example (Lin et al., 2010); see also Fig. 7.28. Such mixing will also lead to distinctly nonlinear variations of configurational properties as a function of mixing ratio.

7.4.2 Physical Properties

Physical properties that may be characterized in structural terms include volume and transport properties. Volume properties involve static changes such as bond angles and distances, whereas transport properties involve dynamic processes including bond breakage and reformation.

7.4.2.1 Volume Properties

Density, volume, compressibility, and expansion of silicate glasses and melts vary with silicate composition, temperature, and pressure. At ambient pressure, composition is a major contributor to density and volume changes. As summarized in Chapter 6 (Fig. 6.13), for most melts the molar volume of binary metal-oxide melts increases with SiO_2 content. The general conclusion, however, is that given the linear relationships with SiO_2, the variations in Q^n-species expected over the wide range of SiO_2 concentration do not seem to affect the molar volume. In other words, the partial molar volume of the individual oxides does not vary with composition over broad SiO_2 concentration ranges. It is clear, however, that with large cations, such as K^+ and Ba^{2+}, the opposite trend can be seen. Moreover, for the most SiO_2-rich compositions (e.g., >80% SiO_2), there appears to be a change in partial molar volume of SiO_2 at some compositions, including along the MgO-SiO_2 join (Lacks et al., 2007). If this evolution is viewed in terms of partial molar volume of Q^n-species, then the difference in Si—NBO and Si—BO bond lengths should cause a change in partial molar volume of SiO_2 for Q^4-rich melt compositions, at which this species dominates the structure.

The different volumes of Q^4 and other Q^n-species may also account for the different compressibility of metal oxide silicate melts. Silica glass and melt shows much greater density change than metasilicates (Shimoda et al., 2005) (see also Fig. 7.29). Moreover, it is clear that the cation type also affects compression mechanisms because $CaSiO_3$ glass is more compressible than $MgSiO_3$ glass (Shimoda et al., 2005). This difference probably relates to the larger coordination number for Ca^{2+} as compared with Mg^{2+}, which in turn probably leads to a weakening of Ca—O bonds and more compressible Si—O—Ca angles, as compared with Mg—O bonds. One may also suggest that the different thermal expansion observed for metal oxide silicate melts with different metal cations also relates to the oxygen coordination number, because the larger the cation, the more compressible is the melt (Bockris et al., 1956; Tomlinson et al., 1958) (see also Fig. 6.16; Chapter 6).

Most numerical simulations of metal oxide silicate melt structure and properties have been carried out for the join MgO-SiO_2 (Belonoshko and Dubrovinski, 1996; Wan et al., 2007; Adjaoud et al., 2008; Ghosh et al., 2014). Additional information has been reported for $CaMgSi_2O_6$ (Matsui, 1996; Sun et al., 2011). Little direct experimental data are available,

FIG. 7.29 Density increase of SiO_2 and $CaMgSi_2O_6$ glass with pressure relative to the ambient pressure and temperature values (Shimoda et al., 2005).

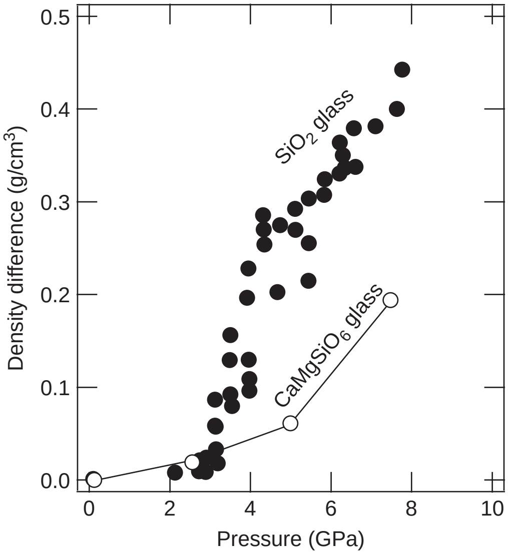

except for Fe_2SiO_4 melt to 8 GPa (Agee, 1992; Chen et al., 2002; Sanloup et al., 2013). As discussed in Chapter 6, all these compositions share common trends of rapidly increasing density (decreasing molar volume) with increasing pressure, features that have been ascribed to a combination of compressing Si—O—Si bonds and coordination changes of network-forming and network-modifying cations with increasing pressure. These results, in turn, were used to compute liquidus melting relations at high temperature and pressure with, generally, good agreement between calculated and experimental curves.

7.4.2.2 Transport Properties

Viscosity, diffusivity, and conductivity are most often related to melt structure via their activation enthalpies. For example, the high-temperature activation enthalpy of viscous flow has long been thought closely related to the energy of oxygen bonds, and more specifically to bonding between oxygen and tetrahedrally coordinated cations (see Chapter 2, Section 2.4). In fact, it was the systematic relationships between metal/silicon ratio of a metal oxide silicate melt and the high-temperature activation enthalpy of viscous flow that led Bockris and Reddy (1970) to propose melt structural models based on the concept of discrete anionic structural units. In this data set involving alkali and alkaline earth silicate melts, the viscosity shows rapid changes at compositions near disilicate (NBO/Si near 1) and metasilicate (NBO/Si near 2) (Bockris and Reddy, 1970; Urbain et al., 1982), a feature also reported by Lacks et al. (2007) and Karki et al. (2013) in their calculations of melt viscosity along the join $MgO\text{-}SiO_2$. These changes are at or near compositions where the abundance of Q^3 and Q^2 species in the melts reach their maximum values (di- and metasilicate, respectively).

These observations lead to the suggestion that the abundance of bridging oxygen bonds in specific structural units contributes significantly to the activation enthalpy of viscous flow, but this is not necessarily the only contribution because, to a considerably lesser extent, there is also a correlation between the ionization potential of the metal cation and the activation energy for any given bulk melt NBO/Si value (see Chapter 6, Fig. 6.19).

An understanding of transport properties at high pressure is of particular importance in the earth sciences. To this end, considerable effort has been devoted to characterizing the response to pressure of the properties and structure of SiO_2 glass and melt (see Chapter 5, Section 5.4). In contrast, similar information is much less abundant for metal oxide-silica melts and glasses. To a major extent, information on very high-pressure viscosity of such melts has relied on numerical simulation (Wan et al., 2007; Lacks et al., 2007; Verma and Karki, 2012; Karki and Stixrude, 2010).

Experimental data on high-pressure melt viscosity of metal oxide-silica melts is relatively scarce, aside from the study by Scarfe et al. (1987), suggesting that the nominal NBO/Si value of a melt is an important factor in determining whether viscosity increases or decreases with increasing pressure from ambient to 2 GPa. There are fewer than a handful of other experimental studies in the same pressure range (Kushiro et al., 1976) and even fewer at higher pressures (Reid et al., 2003).

A change from a negative to a positive pressure dependence of melt viscosity occurs at a nominal NBO/Si near 1 (Scarfe et al., 1987; Lacks et al., 2007) (see also Fig. 7.30). From studies at pressures higher than those summarized by Scarfe et al. (1987), the viscosity of highly

FIG. 7.30 MD simulated viscosities of melts along the $MgO-SiO_2$ join as a function of pressure at 3000 K (Lacks et al., 2007).

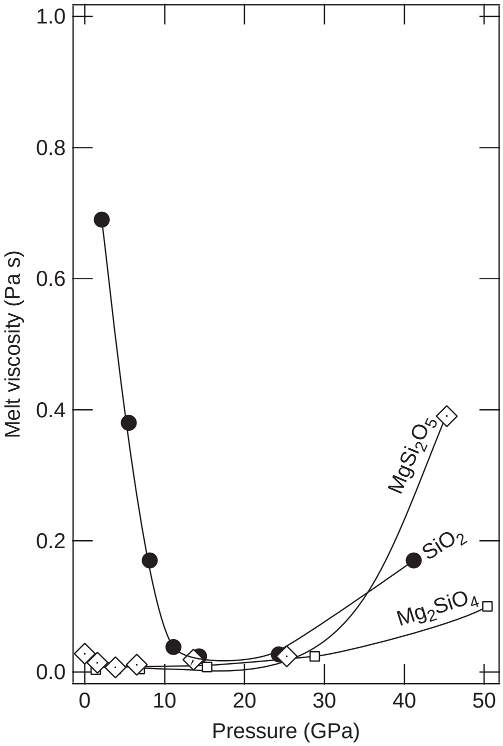

polymerized melts (at low pressure) does in fact begin to increase at pressures near 20 GPa and above that shown in Fig. 7.30. This trend suggests that the abundance of Q^4 units and their response to pressure may be important in the low-pressure regime, as Si—O—Si angle compression is the principal structural response to pressure, thus leading to lower Si—O bond strength. Another question revolves around possibilities to increase the configurational entropy without resorting to changes in abundance of bridging and nonbridging oxygen. This is indeed possible if the volume change of reaction (7.8) ($n=3$) is negative so that this reaction shifts to the right with pressure. Such a change would increase the entropy of mixing. Therefore, within the context of the configurational entropy model, it would also lead to a decrease in viscosity. A shift of reaction (7.8) to the right with pressure, even in the absence of silicon coordination changes, has been proposed on the basis of Raman spectra of metal oxide glasses quenched at pressures to 2.4 GPa (Mysen, 1990; Dickinson et al., 1990).

At much higher pressure, a coordination change of Si^{4+} results in depolymerization of a melt structure, thus causing additional lowering of viscosity. However, after such a coordination transformation has taken place, the compressible Q^4 units no longer exist and the melt viscosity increases with further pressure increase. With $NBO/Si \geq 1$, the abundance of Q^4 units in metal oxide silicate melts is negligible (Maekawa et al., 1991; Mysen, 1999), and the melt viscosity tends to increase across the entire pressure interval.

Diffusion of ions and functional groups that form the anionic structure of the silicate network (oxygen and tetrahedrally coordinated cations) can also be linked to bond strength. Moreover, diffusion of network-forming components (i.e., Si and O) has been linked to melt viscosity via the Eyring equation (Shimizu and Kushiro, 1984, 1991; Rubie et al., 1993; Reid et al., 2001, 2003) (see also Chapter 4, Section 4.6.1). One would expect, therefore, that the activation enthalpy of Si and O self-diffusion would resemble that of viscous flow, as it actually does (Shimizu and Kushiro, 1984, 1991; Reid et al., 2001, 2003). In contrast, the diffusivities and activation enthalpies of network-modifiers do not scale with viscosity (Shimizu and Kushiro, 1991; Watson and Baker, 1991) because of the comparatively small energy contribution (<30 kJ/mol) from the breakage of oxygen-network modifier bonds, compared with Si—O and Al—O bonds (up to nearly 600 kJ/mol for Si—O and about 200 kJ/mol for Al—O in tetrahedral coordination). Interestingly, the activation enthalpy of electrical conductivity (Chapter 6, Section 6.4.2) resembles that of diffusion for network-modifiers. Given the premise that, at least in a simple binary metal-oxide melt, the cation likely is the charge-carrier for the electrical current (Chapter 6, Section 6.4.2), the relationship between the activation energies of diffusion of network-modifying cations and electrical conductivity can be understood.

In light of the relationships between viscosity and self-diffusion of oxygen and tetrahedrally coordinated cations (the network-forming components), it is possible that the pressure-dependent activation energy of diffusion of these components has the same structural explanation as melt viscosity. In other words, the self-diffusion of oxygen in highly polymerized melts (NBO/T < 1; see also the previous discussion), would likely increase with pressure, which it does (Rubie et al., 1993) (see Fig. 7.31), whereas for less polymerized melts, oxygen self diffusion should decrease with increasing pressure, and indeed it does (Reid et al., 2001) (see also Fig. 7.31). Interestingly, in the latter case, for pressures above about 10 GPa, the diffusivity again increases. The pressure-dependent viscosity of a $CaMgSi_2O_6$

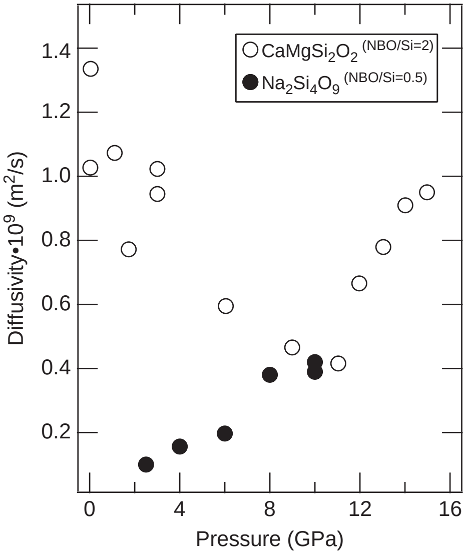

FIG. 7.31 Oxygen diffusivity in polymerized ($Na_2Si_4O_9$) and depolymerized ($CaMgSi_2O_6$) melts as a function of pressure. Data for $Na_2Si_4O_9$ from Rubie et al. (1993) and for $CaMgSi_2O_6$ from Reid et al. (2001), Shimizu and Kushiro (1984, 1991) and Dunn (1982).

melt exhibits the exact opposite trend, with an initial viscosity increase to a maximum near 10 GPa and then a decrease with further pressure increase (Reid et al., 2003). The calculated diffusivities of polymerized melts on the MgO-SiO_2 join increases with increasing pressure, whereas the diffusivity of those less polymerized decreases (Lacks et al., 2007).

These relationships between pressure and diffusivity of network-forming components of melts do not apply to diffusion of network-modifying cations, whose pressure dependence often has the opposite sign as those of network-forming cations (Watson, 1981). This effect is consistent with the decoupling between the mobility of network-forming and network-modifying cations. Similarly, one would expect that electrical conductivity will decrease with increasing pressure.

References

Adjaoud, O., Steinle-Neumann, G., Jahn, S., 2008. Mg_2SiO_4 liquid under high pressure from molecular dynamics. Chem. Geol. 256, 185–192.

Adjaoud, O., Steinle-Neumann, G., Jahn, S., 2011. Transport properties of Mg_2SiO_4 liquid at high pressure: physical state of a magma ocean. Earth Planet. Sci. Lett. 312, 463–470.

Agee, C.B., 1992. Isothermal compression of molten Fe_2SiO_4. Geophys. Res. Lett. 19, 1169–1172.

Allwardt, J.R., Stebbins, J.F., 2004. Ca-Mg and K-Mg mixing around non-bridging O atoms in silicate glasses: an investigation using 17O MAS and 3QMAS NMR. Am. Mineral. 89, 777–784.

Allwardt, J.R., Stebbins, J.F., Schmidt, B.C., Frost, D.J., Withers, A.C., Hirschmann, M.M., 2005. Aluminum coordination and the densification of high-pressure aluminosilicate glasses. Am. Mineral. 90 (7), 1218–1222.

Allwardt, J.R., Stebbins, J.F., Terasaki, H., Du, L.S., Frost, D.J., Withers, A.C., Hirschmann, M.M., Suzuki, A., Ohtani, E., 2007. Effect of structural transitions on properties of high-pressure silicate melts: Al-27 NMR, glass densities, and melt viscosities. Am. Mineral. 92 (7), 1093–1104.

Angeli, F., Delaye, J.-M., Charpentier, T., Petit, J.-C., Ghaleb, D., Faucon, F., 2000. Influence of glass chemical composition on the Na-O bond distance: a 23Na 3Q-MAS NMR and molecular dynamics study. J. Non-Cryst. Solids 276, 132–144.

Angeli, F., Gaillard, M., Jollivet, P., Charpentier, T., 2007. Contribution of 43Ca MAS NMR for probing the structural configuration of calcium in glass. Chem. Phys. Lett. 440, 324–328.

Babcock, C.L., 1968. Substructures in silicate glasses. J. Am. Ceram. Soc. 51, 163–169.

Belonoshko, A.B., Dubrovinski, L.S., 1996. Molecular and lattice dynamics study of the MgO-SiO_2 system using a transferable interatomic potential. Geochim. Cosmochim. Acta 60, 1645–1656.

Binsted, N., Greaves, G.N., Henderson, C.M.B., 1985. An EXAFS study of glassy and crystalline phases of compositions $CaAl_2Si_2O_8$ (anorthite) and $CaMgSi_2O_6$ (diopside). Contrib. Mineral. Petrol. 89, 103–109.

Blander, M., Pelton, A.D., 1984. Analysis and prediction of the thermodynamic properties of multicomponent silicates. Proc. 2nd Internat. Symposium on Metall., Slags, and Fluxes. AIME, Warrendale, PA, pp. 295–304.

Blander, M., Pelton, A.D., 1987. Thermodynamic analysis of binary liquid silicates and prediction of ternary solution properties by modified quasichemical equations. Geochim. Cosmochim. Acta 51, 85–96.

Bockris, J.O.M., Reddy, A.K.N., 1970. Modern Electrochemistry. Plenum Press, New York.

Bockris, J.O.M., Tomlinson, J.W., White, J.L., 1956. The structure of the liquid silicates. Partial molar volumes and expansivities. Trans. Farad. Soc. 52, 299–310.

Bottinga, Y., Richet, P., 1978. Thermodynamics of liquid silicates, a preliminary report. Earth Planet. Sci. Lett. 40, 382–400.

Bottinga, Y., Richet, P., 1995. Silicate melts: the “anomalous” pressure dependence of the viscosity. Geochim. Cosmochim. Acta 59, 2725–2732.

Bottinga, Y., Weill, D.F., Richet, P., 1981. Thermodynamic modeling of silicate melts. In: Newton, R.C., Navrotsky, A., Wood, B.J. (Eds.), Thermodynamics of Minerals and Melts. Springer Verlag, New York, pp. 207–245.

Bowen, N.L., Andersen, O., 1914. The binary system MgO-SiO_2. Am. J. Sci. 37, 487–500.

Brandriss, M.E., Stebbins, J.F., 1988. Effects of temperature on the structures of silicate liquids: 29Si NMR results. Geochim. Cosmochim. Acta 52, 2659–2669.

Brawer, S.A., White, W.B., 1975. Raman spectroscopic investigation of the structure of silicate glasses. I. The binary silicate glasses. J. Chem. Phys. 63, 2421–2432.

Brawer, S.A., White, W.B., 1977. Raman spectroscopic investigation of the structure of silicate glasses. II. The soda-alkaline earth-alumina ternary and quarternary glasses. J. Non-Cryst. Solids 23, 261–278.

Buckermann, W.-A., Muller-Warmuth, W., Frischat, G.H., 1992. A further ^{29}Si MAS NMR study on binary alkali silicate glasses. Glasstechn. Ber. 65, 18–21.

Burnham, C.W., 1975. Thermodynamics of melting in experimental silicate-volatile systems. Geochim. Cosmochim. Acta 39, 1077–1084.

Burnham, C.W., Nekvasil, H., 1986. Equilibrium properties of granite pegmatite compositions. Am. Mineral. 71, 239–263.

Calas, G., Cormier, L., Galoisy, L., Jollivet, P., 2002. Structure-property relationships in multicomponent oxide glasses. C. R. Acad. Sci. 5, 831–843.

Chen, G.Q., Ahrens, T.J., Stolper, E.N., 2002. Shock-wave equation of state of molten and solid fayalite. Phys. Earth Planet. Int. 134, 35–52.

Cormack, A.N., Du, J., 2001. Molecular dynamics simulations of soda-lime-silicate glasses. J. Non-Cryst. Solids 293, 283–289.

Cormier, L., Calas, G., Gaskell, P.H., 2001. Cationic environment in silicate glasses studied by neutron diffraction with isotopic substitution. Chem. Geol. 174, 349–363.

Davis, M.J., Ihinger, P.D., 1999. Influence of hydroxyl on glass transformation kinetics in lithium disilicate melt and re-evaluation of structural relaxation in NBS 710 and 711. J. Non-Cryst. Solids 244, 1–15.

Davis, M.J., Ihinger, P.D., 2002. Effects of thermal history on crystal nucleation in silicate melt: numerical simulations. J. Geophys. Res. 107, 2284.

Day, D.E., 1976. Mixed alkali glasses – their properties and uses. J. Non-Cryst. Solids 21, 343–372.

Dickinson, J.E., Scarfe, C.M., McMillan, P., 1990. Physical properties and structure of K2Si4O9 melt quenched from pressure up to 2.4 GPa. J. Geophys. Res. 95, 15675–15681.

Diefenbacher, J., McMillan, P.F., Wolf, G.H., 1998. Molecular dynamics simulations of $Na_2Si_4O_9$ liquid at high pressure. J. Phys. Chem. B 102, 3003–3008.

Dingwell, D.B., Webb, S.L., 1990. Relaxation in silicate melts. Eur. J. Mineral. 2, 427–449.

Dunn, T., 1982. Oxygen diffusion in three silicate melts along the join diopside–anorthite. Geochim. Cosmochim. Acta 46, 2293–2299.

Eckersley, A.C., Gaskell, P.H., Barnes, A.C., Chieux, P., 1988. The environment of Ca ions in silicate glasses. J. Non-Cryst. Solids 106, 132–136.

Engelhardt, G., Michel, D., 1987. High-Resolution Solid-State NMR of Silicates and Zeolites. Wiley, New York.

Etchepare, J., 1972. Study by Raman Spectroscopy of Crystalline and Glassy Diopside. In: Douglas, R.W., Ellis, E. (Eds.), Amorphous Materials. Wiley-Interscience, New York, pp. 337–346.

Farnan, I., Stebbins, J.F., 1990a. Observation of slow atomic motions close to the glass transition using 2-D ^{29}Si NMR. J. Non-Cryst. Solids 124, 207–215.

Farnan, I., Stebbins, J.F., 1990b. A high temperature ^{29}Si investigation of solid and molten silicates. J. Am. Ceram. Soc. 112, 32–39.

Fiske, P., Stebbins, J.F., 1994. The structural role of Mg in silicate liquids: a high-temperature ^{25}Mg, ^{23}Na, and ^{29}Si NMR study. Am. Mineral. 79, 848–861.

Furukawa, T., Fox, K.E., White, W.B., 1981. Raman spectroscopic investigation of the structure of silicate glasses. III. Raman intensities and structural units in sodium silicate glasses. J. Chem. Phys. 153, 3226–3237.

Gambuzzi, E., Pedone, A., Menziani, M.C., Angeli, F., Florina, P., Charpentier, T., 2015. Calcium environment in silicate and aluminosilicate glasses probed by ^{43}Ca MQMAS NMR experiments and MD-GIPAW calculations. Solid State Nucl. Reson. 68–69, 31–36.

Gaudio, S.J., Sen, S., Lesher, C., 2008. Pressure-induced structural changes and densification of vitreous $MgSiO_3$. Geochim. Cosmochim. Acta 72, 1222–1230.

George, A., Stebbins, J.F., 1998. Structure and dynamics of magnesium in silicate melts: a high-temperature ^{25}Mg NMR study. Am. Mineral. 83, 1022–1029.

Ghiorso, M.S., 2004. An equation of state for silicate melts. III. Analysis of stoichiometric liquids at elevated pressure: shock compression data, molecular dynamics simulations and mineral fusion curves. Am. J. Sci. 304, 752–810.

Ghiorso, M.S., Sack, R.O., 1995. Chemical mass transfer in magmatic processes; IV, a revised and internally consistent thermodynamic model for the interpolation and extrapolation of liquid-solid equilibria in magmatic systems at elevated temperatures and pressures. Contrib. Mineral. Petrol. 119, 197–212.

Ghosh, D.B., Karki, B.B., Stixrude, L., 2014. First-principles molecular dynamics simulations of $MgSiO_3$ glass: structure, density, and elasticity at high pressure. Am. Mineral. 99, 1304–1314.

Greaves, G.N., Fontaine, A., Lagarde, P., Raoux, D., Gurman, S.J., 1985. Local structure of silicate glasses. Nature 293, 611–616.

Greig, J.W., 1927. Immiscibility in silicate melts. Am. J. Sci. 13, 1–44.

Halter, W.E., Mysen, B.O., 2004. Melt speciation in the system Na_2O-SiO_2. Chem. Geol. 213, 115–123.

Hanson, C.D., Egami, T., 1986. Distribution of Cs^+ ions in single and mixed alkali silicate glasses from energy dispersive X-ray diffraction. J. Non-Cryst. Solids 87, 171–184.

Henderson, G.S., 2018. Structural probes of glass. In: Richet, P. (Ed.), Encyclopedia of Glass Science, Technology, History and Culture. J. Wiley & Sons, Hoboken, NJ.

Horbach, J., Kob, W., Binder, K., 2001. Structural and dynamical properties of sodium silicate melts: an investigation by molecular dynamics computer simulation. Chem. Geol. 174, 87–101.

Hovis, G.L., Toplis, M.J., Richet, P., 2004. Thermodynamic mixing properties of sodium silicate liquids and implications for liquid-liquid immiscibility. Chem. Geol. 213, 173–186.

Huang, C., Cormack, A.N., 1990. The structure of sodium silicate glass. J. Chem. Phys. 93, 8180–8186.

Ispas, S., Benoit, M., Jund, P., Jullien, R., 2002. Structural properties of glassy and liquid sodium tetrasilicate: comparison between ab initio and classical molecular dynamics simulations. J. Non-Cryst. Solids 307, 946–955.

Jones, A.R., Winter, R., Greaves, G.N., Smith, I.H., 2001. MAS NMR study of soda-lime-silicate glasses with variable degrees of polymerisation. J. Non-Cryst. Solids 293–295, 87–92.

Karki, B.O., Stixrude, L., 2010. Viscosity of $MgSiO_3$ liquid at Earth's mantle conditions: implications for an early magma ocean. Science 328, 740–742.

Karki, B.B., Bhattarai, D., Stixrude, L., 2006. First principles calculations of the structural, dynamical and electronic properties of liquid MgO. Phys. Rev. B 73, 174208.

Karki, B.B., Zhang, J., Stixrude, L., 2013. First principles viscosity and derived models for MgO-SiO_2 melt system at high temperature. Geophys. Res. Lett. 40, 94–99.

Kawazoe, H., Kokumai, H., Tanazawa, T., Gohshi, Y., 1981. Coordination of Mg^{2+} in oxide glasses determined by X-ray emission spectroscopy. J. Phys. Chem. Solids 42, 579–581.

Kirkpatrick, R.J., 1983. Theory of nucleation in silicate melts. Am. Mineral. 68, 66–78.

Knoche, R., Dingwell, D.B., Seifert, F.A., Webb, S.L., 1994. Nonlinear properties of supercooled liquids in the system Na_2O-SiO_2. Chem. Geol. 116, 1–16.

Kohara, S., Akola, J., Morita, H., Suzuya, K., Weber, J.K.R., Wilding, M.C., Benmore, C.J., 2011. Relationship between topological order and glass forming ability in densely packed enstatite and forsterite composition glasses. Proc. Natl. Acad. Sci. 108, 14780–14785.

Kohn, S.C., Schofield, P.F., 1994. The importance of melt composition in controlling trace-element behaviour: an exprimental study of Mn and Zn partitioning between forsterite and silicate melt. Chem. Geol. 117, 73–87.

Kracek, F.C., 1930a. The binary system Li_2O-SiO_2. J. Chem. Phys. 32, 2641–2650.

Kracek, F.C., 1930b. The system sodium oxide-silica. J. Phys. Chem. Solids 34, 1583–1598.

Kracek, F.C., 1932. The ternary system K_2SiO_3-Na_2SiO_3-SiO_2. J. Phys. Chem. 36, 2529–2542.

Kroeker, S., Stebbins, J.F., 2000. Magnesium coordination environments in glasses and minerals: new insight from high-field magnesium-25 MAS NMR. Am. Mineral. 85, 1459–1464.

Kushiro, I., 1969. The system forsterite-diopside-silica with and without water at high pressures. Am. J. Sci. 267-A, 269–294.

Kushiro, I., Yoder, H.S., Mysen, B.O., 1976. Viscosities of basalt and andesite melts at high pressures. J. Geophys. Res. 81, 6351–6356.

Lacks, D.J., Rear, D.B., van Orman, J.A., 2007. Molecular dynamics investigation of viscosity, chemical diffusivities and partial molar volumes of liquids along the MgO–SiO_2 join as functions of pressure. Geochim. Cosmochim. Acta 71, 1313–1323.

Lee, S.K., 2011. Simplicity in melt densification in multicomponent magmatic reservoirs in Earth's interior revealed by multinuclear magnetic resonance. Proc. Natl. Acad. Sci. 108, 6847–6852.

Lee, S.K., Stebbins, J.F., 2003a. The distribution of sodium ions in aluminosilicate glasses: a high-field Na-23 MAS and 3Q MAS NMR study. Geochim. Cosmochim. Acta 67, 1699–1710.

Lee, S.K., Stebbins, J.F., 2003b. Nature of cation mixing and ordering in Na-Ca silicate glasses and melts. J. Phys. Chem. B 107, 3141–3148.

Lee, S.K., Fei, Y., Cody, G.D., Mysen, B.O., 2003. Disorder in silicate glasses & melts at 10 GPa. Geophys. Res. Lett. **30**, 1845. https://dx.doi.org/10.1029/2003GL017735.

Lee, S.K., Cody, G.D., Mysen, B.O., 2005. Structure and extent of disorder in quaternary (Ca-Mg and Ca-Na) aluminosilicate glasses and melts. Am. Mineral. 90, 1315–1324.

Lee, S.K., Cody, G.D., Fei, Y.W., Mysen, B.O., 2006. The effect of Na/Si on the structure of sodium silicate and aluminosilicate glasses quenched from melts at high pressure: a multi-nuclear (Al-27, Na-23, O-17) 1D and 2D solid-state NMR study. Chem. Geol. 229, 162–172.

Lentz, M., 1969. Silicate minerals as sources of trimethsilyl silicates and silicate structure analysis of sodium silicate solutions. Inorg. Chem. 3, 574–579.

Liebau, F., 1980. The role of cationic hydrogen in pyroxenoid crystal chemistry. Am. Mineral. 65, 981–985.

Liebau, F., Pallas, I., 1981. The influence of cation properties on the shape of silicate chains. Z. Kristall. 155, 139–153.

Lin, C.C., Chen, S.F., Liu, L.G., Li, C.C., 2010. Size effects of modifying cations on the structure and elastic properties of Na_2O-MO-SiO_2 glasses (M = Mg, Ca, Sr, Ba). Mater. Chem. Phys. 123, 569–580.

MacKenzie, J.D., 1947. The discrete ion theory of viscous flow in liquid silicates. Trans. Faraday Soc. 53, 1488–1494.

Maekawa, H., Yokokawa, T., 1997. Effects of temperature on silicate melt structure: a high temperature ^{29}Si NMR study of $Na_2Si_2O_5$. Geochim. Cosmochim. Acta 61, 2569–2575.

Maekawa, H., Maekawa, T., Kawamura, K., Yokokawa, T., 1991. The structural groups of alkali silicate glasses determined from ^{29}Si MAS-NMR. J. Non-Cryst. Solids 127, 53–64.

Majérus, O., Cormier, L., Calas, G., Beuneu, B., 2004. A neutron diffraction study of temperature-induced structural changes in potassium disilicate glass and melt. Chem. Geol. 213, 89–102.

Masson, C.R., 1968. Ionic equilibria in liquid silicates. J. Am. Ceram. Soc. 51, 134–143.

Masson, C.R., 1977. Anionic constitution of glass-forming melts. J. Non-Cryst. Solids 1, 1–42.

Matsui, M., 1996. Molecular dynamics simulation of structures, bulk moduli, and volume thermal expansivities of silicate liquids in the system CaO-MgO-Al_2O_3-SiO_2. Geophys. Res. Lett. 23, 395–398.

Mauri, F., Pasquarello, A., Pfrommer, B.G., Yoon, Y.-G., Louie, S.G., 2000. Si-O-Si bond-angle distribution in vitreous silica from first-principles ^{29}Si NMR analysis. Phys. Rev. B 62, R4786–R4789.

McMillan, P., 1984. Structural studies of silicate glasses and melts – applications and limitations of Raman spectroscopy. Am. Mineral. 69, 622–644.

McMillan, P.F., Wolf, G.H., Poe, B.T., 1992. Vibrational spectroscopy of silicate liquids and glasses. Chem. Geol. 96, 351–366.

Misawa, M., Price, D.L., Suzuki, K., 1980. The short-range structure of alkali disilicates by pulsed neutron scattering. J. Non-Cryst. Solids 37, 85–98.

Morey, G.W., Bowen, N.L., 1924. The binary system sodium metasilicate-silica. J. Phys. Chem. 28, 1167–1179.

Morey, G.W., Kracek, F.C., Bowen, N.L., 1930. The ternary system K_2O-CaO-SiO_2. Trans. Soc. Glass Technol. 14, 149–187.

Morishita, M., Navrotsky, A., Wilding, M.C., 2004. Direct measurement of relative partial molar enthalpy of SiO_2 in SiO_2-M_2O (M=Li, Na, K, Cs) binary and SiO_2-CaO-Al_2O_3 ternary melts. J. Am. Ceram. Soc. 87, 1550–1555.

Murdoch, J.B., Stebbins, J.F., Carmichael, I.S.E., 1985. High-resolution ^{29}Si NMR study of silicate and aluminosilicate glasses: the effect of network-modifying cations. Am. Mineral. 70, 332–343.

Mysen, B.O., 1990. Effect of pressure, temperature, and bulk composition on the structure and species distribution in depolymerized alkali aluminosilicate melts and quenched melts. J. Geophys. Res. 95, 15733–15744.

Mysen, B.O., 1995. Experimental, in-situ, high-temperature studies of properties and structure of silicate melts relevant to magmatic temperatures. Eur. J. Mineral. 7, 745–766.

Mysen, B.O., 1997. Aluminosilicate melts: structure, composition and temperature. Contrib. Mineral. Petrol. 127, 104–118.

Mysen, B.O., 1999. Structure and properties of magmatic liquids: from haplobasalt to haploandesite. Geochim. Cosmochim. Acta 63, 95–112.

Mysen, B.O., 2007. Partitioning of calcium, magnesium, and transition metals between olivine and melt governed by the structure of the silicate melt at ambient pressure. Am. Mineral. 92, 844–862.

Mysen, B.O., Frantz, J.D., 1993. Structure of silicate melts at high temperature: in-situ measurements in the system BaO-SiO_2 to 1669°C. Am. Mineral. 78, 699–1669.

Mysen, B.O., Frantz, J.D., 1994. Alkali silicate glass and melt structure in the temperature range 25–1651°C at atmospheric pressure and implications for mixing behavior of structural units. Contrib. Mineral. Petrol. 117, 1–14.

Mysen, B.O., Virgo, D., Seifert, F.A., 1982. The structure of silicate melts: implications for chemical and physical properties of natural magma. Rev. Geophys. 20, 353–383.

Mysen, B.O., Lucier, A., Cody, G.D., 2003. The structural behavior of Al^{3+} in peralkaline melts and glasses in the system Na_2O-Al_2O_3-SiO_2. Am. Mineral. 88, 1668–1678.

Navrotsky, A., Geisinger, K.L., McMillan, P., Gibbs, G.V., 1985. The tetrahedral framework in glasses and melts–influences from molecular orbital calculations and implications for structure, thermodynamics, and physical properties. Phys. Chem. Miner. 11, 284–298.

Newell, R.G., Feuston, B.P., Garofalini, S.H., 1989. The structure of sodium trisilicate glass via molecular dynamics employing three-body potentials. J. Mater. Res. 4, 434–439.

Noritake, F., Kawamura, K., Yoshino, T., Takahashi, E., 2012. Molecular dynamics simulation and electrical conductivity measurement of $Na_2O \bullet 3SiO_2$ melt under high pressure; relationship between its structure and properties. J. Non-Cryst. Solids 358, 3109–3118.

Oestrike, R., Yang, W.-H., Kirkpatrick, R.J., Hervig, R., Navrotsky, A., Montez, B., 1987. High-resolution ^{23}Na, ^{27}Al and ^{29}Si NMR spectroscopy of framework aluminosilicate glasses. Geochim. Cosmochim. Acta 51, 2199–2210.

Ohtani, E., Taulelle, F., Angell, C., 1985. Al^{3+} coordination changes in liquid aluminosilicates under pressure. Nature 314, 78–81.

Pelton, A.D., Wu, P., 1999. Thermodynamic modeling in glass-forming melts. J. Non-Cryst. Solids 253, 178–191.

Polyakov, V.B., Ariskin, A.A., 2008. Simulation of the composition and proportions of anions in polymerized silicate melts. Glass Phys. Chem. 34, 50–62.

Polyakov, V.B., Ariskin, A.A., Shil'dt, A.V., 2010. Analysis of disproportionation of Q(n) structons in the simulation of the structure of melts in the Na_2O-SiO_2 system. Glass Phys. Chem. 36, 579–588.

Reid, J.E., Poe, B.T., Rubie, R.C., Zotov, N., Wiedenbeck, M., 2001. The self-diffusion of silicon and oxygen in diopside ($CaMgSi_2O_6$) liquid up to 15 GPa. Chem. Geol. 174, 77–86.

Reid, J.E., Suzuki, A., Funakoshi, K., Terasaki, K., Poe, B.T., Rubie, D.C., Ohtani, E., 2003. The viscosity of $CaMgSi_2O_6$ liquid at pressure up to 13 GPa. Phys. Earth Planet. Inter. 139, 45–54.

Richet, P., Bottinga, Y., 1986. Thermochemical properties of silicate glasses and liquids: a review. Rev. Geophys. 24, 1–26.

Richet, P., Neuville, D.R., 1992. Thermodynamics of silicate melts; configurational properties. In: Saxena, S.K. (Ed.), Thermodynamic Data; Systematics and Estimation. Springer, New York, NY, pp. 132–161.

Richet, P., Ingrin, J., Mysen, B.O., Courtial, P., Gillet, P., 1994. Premelting effects in minerals; an experimental study. Earth Planet. Sci. Lett. 121, 589–600.

Rubie, D.C., Ross, R.C., Carol, M.R., Elphick, S.C., 1993. Oxygen self-diffusion in $Na_2Si_4O_9$ liquid up to 10 GPa and estimation of high-pressure viscosities. Am. Mineral. 78, 574–582.

Ryerson, F.J., 1985. Oxide solution mechanisms in silicate melts: systematic variations in the activity coefficient of SiO_2. Geochim. Cosmochim. Acta 49, 637–651.

Sanchez-Valle, C., Bass, J.D., 2010. Elasticity and pressure-induced structural changes in vitreous $MgSiO_3$-enstatite to lower mantle pressures. Earth Planet. Sci. Lett. 295, 523–530.

Sanloup, C., Drewitt, J.W.E., Crepisson, C., Kono, Y., Park, C., McCammon, C., Hennert, L., Brassamin, S., Bytchkov, A., 2013. Structure and density of molten fayalite at high pressure. Geochim. Cosmochim. Acta 118, 118–128.

Scarfe, C.M., Mysen, B.O., Virgo, D., 1987. Pressure dependence of the viscosity of silicate melts. In: Mysen, B.O. (Ed.), Magmatic Processes: Physicochemical Principles. Geochemical Society, University Park, PA, pp. 59–68.

Schneider, E., Stebbins, J.F., Pines, A., 1987. Speciation and local structure in alkali and alkaline earth silicate glasses: constraints from 29-Si NMR spectroscopy. J. Non-Cryst. Solids 89, 371–383.

Schramm, C.M., DeJong, B.H.W.S., Parziale, V.F., 1984. ^{29}Si magic angle spinning NMR study of local silicon environments in-amorphous and crystalline lithium silicates. J. Am. Chem. Soc. 106, 4396–4402.

Seifert, F.A., Mysen, B.O., Virgo, D., 1981. Structural similarity between glasses and melts relevant to petrological processes. Geochim. Cosmochim. Acta 45, 1879–1884.

Sen, S., Tangeman, J., 2008. Evidence for anomalously large degree of polymerization in Mg_2SiO_4 glass and melt. Am. Mineral. 93, 946–949.

Sen, S., Maekawa, H., Papatheodorou, G.N., 2009. Short-range structure of invert glasses along the pseudo-binary join $MgSiO_3$-Mg_2SiO_4: results from 29Si and 25Mg MAS NMR spectroscopy. J. Phys. Chem. B 113, 14243–15248.

Seo, W.G., Tsukihashi, F., 2004. Molecular dynamics simulation of the thermodynamic and structural properties for the CaO-SiO_2 system. ISIJ Int. 44, 1817–1825.

Shimizu, N., Kushiro, I., 1984. Diffusivity of oxygen in jadeite and diopside melts at high pressures. Geochim. Cosmochim. Acta 48, 1295–1303.

Shimizu, N., Kushiro, I., 1991. The mobility of Mg, Ca, and Si in diopside-jadeite liquids at high pressures. In: Perchuk, L.L., Kushiro, I. (Eds.), Physical Chemistry of Magmas. Springer, New York, NY, pp. 192–212.

Shimoda, K., Okuno, M., 2006. Molecular dynamics study of $CaSiO_3$–$MgSiO_3$ glasses under high pressure. J. Phys. Condens. Matter. 18.

Shimoda, K., Miyamoto, H., Kikuchi, A., Kusaba, K., Okuno, M., 2005. Structural evolutions of $CaSiO_3$ and $CaMgSi_2O_6$ metasilicate glasses by static compression. Chem. Geol. 222, 83–93.

Shimoda, K., Tobu, Y., Shimoikeda, Y., Nemoto, T., Saito, K., 2007. Multiple Ca^{2+} environments in silicate glasses by high-resolution ^{43}Ca MQMAS NMR technique at high and ultra-high (21.8 T) magnetic fields. J. Magn. Reson. 186, 156–159.

Silva, A.M.B., Queiroz, C.M., Agathopoulos, S., Correia, R.N., Fernandes, M.H.V., Oliveira, J.M., 2011. Structure of SiO_2-MgO-Na_2O glasses by FTIR, Raman and Si-29 MAS NMR. J. Mol. Struct. 986, 16–21.

Smart, R.M., Glasser, F.P., 1978. Silicate anion constitution of lead silicate glasses and crystals. Phys. Chem. Glasses 19, 95–102.

Soules, T.F., 1979. A molecular dynamics calculation of the structure of sodium silicate glasses. J. Chem. Phys. 71, 4570–4578.

Stebbins, J.F., 1987. Identification of multiple structural species in silicate glasses by ^{29}Si NMR. Nature 330, 465–467.

Stebbins, J.F., 1988. Effects of temperature and composition on silicate glass structure and dynamics: Si-29 NMR results. J. Non-Cryst. Solids 106, 359–369.

Stebbins, J.F., Schneider, E., Murdoch, J.B., 1985. NMR spectroscopy of Na-23 and Si-29 in molten aluminosilicates; molecular motion and relaxation times. AGU 1985 Spring Meeting. American Geophysical Union, Washington, DC, p. 395.

Stixrude, L., Karki, B., 2005. Structure and freezing of $MgSiO_3$ liquid in Earth's lower mantle. Science 310, 297–299.

Sugawara, T., Shinoya, K., Yoshida, S., Matsuoka, J., 2011. Thermodynamic mixing properties of liquids in the system Na_2O-SiO_2. J. Non-Cryst. Solids 357, 1390–1398.

Sun, N., Stixrude, L., de Koker, N., Karki, B.B., 2011. First principles molecular dynamics simulations of diopside ($CaMgSi_2O_6$) liquid to high pressure. Geochim. Cosmochim. Acta 75, 3792–3802.

Tomlinson, J.W., Heynes, M.S.R., Bockris, J.O.M., 1958. The structure of liquid silicates. Part 2. Molar volume and expansivities. Trans. Farad. Soc. 54, 1822–1834.

Trcera, N., Rossano, S., Tarrida, M., 2011. Structural study of Mg-bearing sodosilicate glasses by Raman spectroscopy. J. Raman Spectrosc. 42, 765–772.

Umesaki, N., Iwamoto, N., Takahashi, M., Tatsumisago, M., Minami, T., Matsui, Y., 1988. Molecular dynamics study of Li2O-SiO2 melts and glasses. Trans ISIJ 28, 852–859.

Urbain, G., Bottinga, Y., Richet, P., 1982. Viscosity of liquid silica, silicates and alumino-silicates. Geochim. Cosmochim. Acta 46, 1061–1072.

Verma, A.K., Karki, B.B., 2012. First-principles study of self-diffusion and viscous flow in diopside ($CaMgSi_2O_6$) liquid. Am. Mineral. 97, 2049–2055.

Virgo, D., Mysen, B.O., Kushiro, I., 1980. Anionic constitution of 1-atmosphere silicate melts: implications of the structure of igneous melts. Science 208, 1371–1373.

Wan, J.T.K., Duffy, T.S., Scandolo, S., Car, R., 2007. First-principles study of density, viscosity, and diffusion coefficients of liquid $MgSiO_3$ at conditions of the Earth's deep mantle. J. Geophys. Res.. 112.

Waseda, Y., Suito, H., 1977. The structure of molten alkali metal silicates. Trans. Iron Steel Inst. Jpn. 17, 82–91.

Waseda, Y., Toguri, J.M., 1977. The structure of the molten binary systems CaO-SiO_2 and MgO-SiO_2. Metall. Trans. B 8, 563–568.

Watson, E.B., 1981. Diffusion in magmas at depth in the Earth: the effects of pressure and dissolved H_2O. Earth Planet. Sci. Lett. 52, 291–301.

Watson, E.B., Baker, D.R., 1991. Chemical diffusion in magmas; an overview of experimental results and geochemical applications. In: Percuk, L.L., Kushiro, I. (Eds.), Physical Chemistry of Magmas. Springer, New York, pp. 121–151.

Whittaker, E.J.W., Muntus, R., 1970. Ionic radii for use in geochemistry. Geochim. Cosmochim. Acta 34, 945–957.

Wilding, M.C., Benmore, C.J., Weber, J.K.R., 2008. In situ diffraction studies of magnesium silicate liquids. J. Mater. Sci. 43, 4707–4713.

Wu, Y.Q., Jiang, G.C., You, J.L., Hou, H.Y., Chen, H., Xu, K.D., 2004. Theoretical study of the local structure and Raman spectra of CaO-SiO_2 binary melts. J. Chem. Phys. 121, 7883–7895.

Wu, T., He, S.P., Liang, Y.J., Wang, Q., 2015. Molecular dynamics simulation of the structure and properties for the CaO-SiO_2 and CaO-Al_2O_3 systems. J. Non-Cryst. Solids 411, 145–151.

Xue, X.Y., Stebbins, J.F., Kansazki, M., McMillan, P.D., Poe, B.T., 1991. Pressure-induced silicon coordination and tetrahedral structural changes in alkali oxide–silica melts up to 12 GPa-NMR, Raman, and infrared spectroscopy. Am. Mineral. 76, 8–26.

Xue, X., Stebbins, J.F., Kanzaki, M., 1994. Correlations between ^{17}O parameters and local structure around oxygen in high-pressure silicates: implications for the structure of silicate melts at high pressure. Am. Mineral. 79, 31–42.

Yap, A.T.-W., Elliott, S.R., 1995. A study of mixed alkali effect in disilicate glasses using 7Li nuclear magnetic resonance. J. Non-Cryst. Solids 192&193, 2007–2211.

Yasui, I., Hasegawa, H., Imaoka, M., 1983. X-ray diffraction study of the structure of silicate glasses. Part 1. Alkali metasilicate glasses. Phys. Chem. Glasses 24, 65.

Zhang, L.Q., 2011. Thermodynamic properties calculation for MgO-SiO_2 liquids using both empirical and first-principles molecular simulations. Phys. Chem. Chem. Phys. 13, 21009–21015.

Zhang, P., Dunlap, C., Florian, P., Grandinetti, P.J., Farnan, I., Stebbins, J.F., 1996. Silicon site distributions in an alkali silicate glass derived by two-dimensional Si-29 nuclear magnetic resonance. J. Non-Cryst. Solids 204, 294–300.

Zhao, J., Gaskell, P.H., Cluckie, M.M., Soper, A.K., 1998. A neutron diffraction substitution study of the structure of $Li_2O \bullet 2SiO_2$ glass. J. Non-Cryst. Solids 232-234, 721–727.

Zhao, G., Mu, H.F., Tan, X.M., Wang, D.H., Yang, C.L., 2014. Structural and dynamical properties of $MgSiO_3$ melt over the pressure range 200–500 GPa: Ab initio molecular dynamics. J. Non-Cryst. Solids 385, 169–174.

Zotov, N., Delaplane, R., 2000. Structure and crystallization kinetics of sodium tetrasilicate glass: a high temperature neutron diffraction study. Mater. Sci. Forum 321–324, 535–539.

Zotov, N., Keppler, H., 1998. The structure of sodium tetrasilicate glass from neutron diffraction, reverse Monte Carlo simulations and Raman spectroscopy. Phys. Chem. Miner. 25, 259–267.

CHAPTER

8

Properties of Aluminosilicate Systems

OUTLINE

8.1 INTRODUCTORY COMMENTS

Solution of alumina in glass usually results in increased chemical durability, hardness, tensile and compressive strengths, and thermal endurance. Alumina also reduces devitrification tendency and lowers thermal expansion. This influence is, therefore, of considerable practical interest. Besides, approximately 95% of magma composition can be expressed within the system metal oxide-alumina-silica (Mysen, 1987). In fact, the alumina content can be as high as 15 mol% in magma and still higher in some melts of industrial interest, such as, for example, when used for making insulating stone wool (Yue and Solvang, 2018).

To describe composition effects of alumina on aluminosilicate properties, we will take as a starting point the binary metal oxide silicates discussed in previous chapters. An alternative, adding metal oxides to SiO_2—Al_2O_3 melts and glasses, poses severe experimental challenges because of the very high melting temperatures (see summary review by Osborn and Muan, 1960a, b, c) and such melts tend to devitrify upon cooling (Johnson et al., 2001; Roskosz et al., 2005). Therefore, we will deal mainly with the addition of alumina at constant SiO_2/M_xO

https://doi.org/10.1016/B978-0-444-63708-6.00008-9

ratio, with substitution of Al_2O_3 for M_xO at constant SiO_2 content, or with substitution of Al for Si at constant nominal NBO/T, where M designates an alkali or an alkaline earth cation.

In view of the possible dual role of aluminum as a network-former or network-modifier, we must first recall an important distinction pertaining to charge-compensation of Al^{3+}. Depending on whether or not there are sufficient metal cations to charge-compensate Al^{3+} in tetrahedral coordination, aluminosilicates are said to be peralkaline (even in alkaline earth systems) or peraluminous (see also Section 2.4.3 and Fig. 9.1). The boundary between these two fields is represented by meta-aluminosilicates in which metal cations reach the appropriate proportion needed for charge-compensation of all Al^{3+}.

It has long been reckoned that a change of aluminum from network-former to network-modifier should affect physical and chemical properties. Hence, important questions include how physical properties may change when the meta-aluminous join is crossed, whether or how the nature of the charge-compensating cations affect the properties, and how the nature of this cation affects property changes across the meta-aluminosilicate join. These questions are not at all new. Since the early 1960s, such variations, when observed, have been associated with either coordination changes of aluminum, generally from tetrahedral to octahedral (Day and Rindone, 1962; Riebling, 1964, 1966; Neuville et al., 2006; Mysen and Toplis, 2007), or to incorporation of Al^{3+} in triclusters, i.e., in groups of three $(Si, Al)O_4$ tetrahedra sharing a common bridging oxygen (Lacy, 1963; Osaka et al., 1987; Toplis et al., 1997a).

8.2 PHASE RELATIONSHIPS

Solution of alumina in binary silicate melts has definite effects on glass formation, on liquidus and solidus temperatures, and on the extent of liquid-liquid immiscibility, as simply documented by ternary M_xO-Al_2O_3-SiO_2 phase diagrams (Osborn and Muan, 1960a, b, c, d). This influence of Al_2O_3 is more pronounced in alkali than in alkaline-earth systems. However, the contrasts in physical properties between alkali and alkaline-earth Al-free systems tend to diminish or disappear in aluminosilicate melts when the meta-aluminous join is approached.

8.2.1 Liquidus Relations

Liquidus phase relations are represented on a mol% basis for the Na, K, Ca, and Mg aluminosilicate systems in Fig. 8.1. Most diagrams share a common feature of only two ternary compounds on the liquidus. In the Na, K, and Ca systems, the less silica-rich compound has the same $M_xO\cdot Al_2O_3\cdot 2SiO_2$ stoichiometry, from which that of the magnesian mineral cordierite ($MgO\cdot Al_2O_3\cdot 2.5SiO_2$) does not depart significantly.

The differing topological complexity of the ternary diagrams of Fig. 8.1 is essentially due to differences in the number of compounds stable on the liquidus in the limiting M_xO-SiO_2 and M_xO-Al_2O_3 binary systems, because there is a single compound, mullite ($Al_2O_3\cdot 2SiO_2$), along the common Al_2O_3-SiO_2 join shared by the ternary diagrams. In the limiting binary M_xO-SiO_2 systems, there are two compounds for Mg, three for K, and four for both Na and Ca. But the largest difference is found along the M_xO-Al_2O_3 joins where the calcium system stands apart with its five different compounds. Such a variety of crystalline phases signals a remarkable

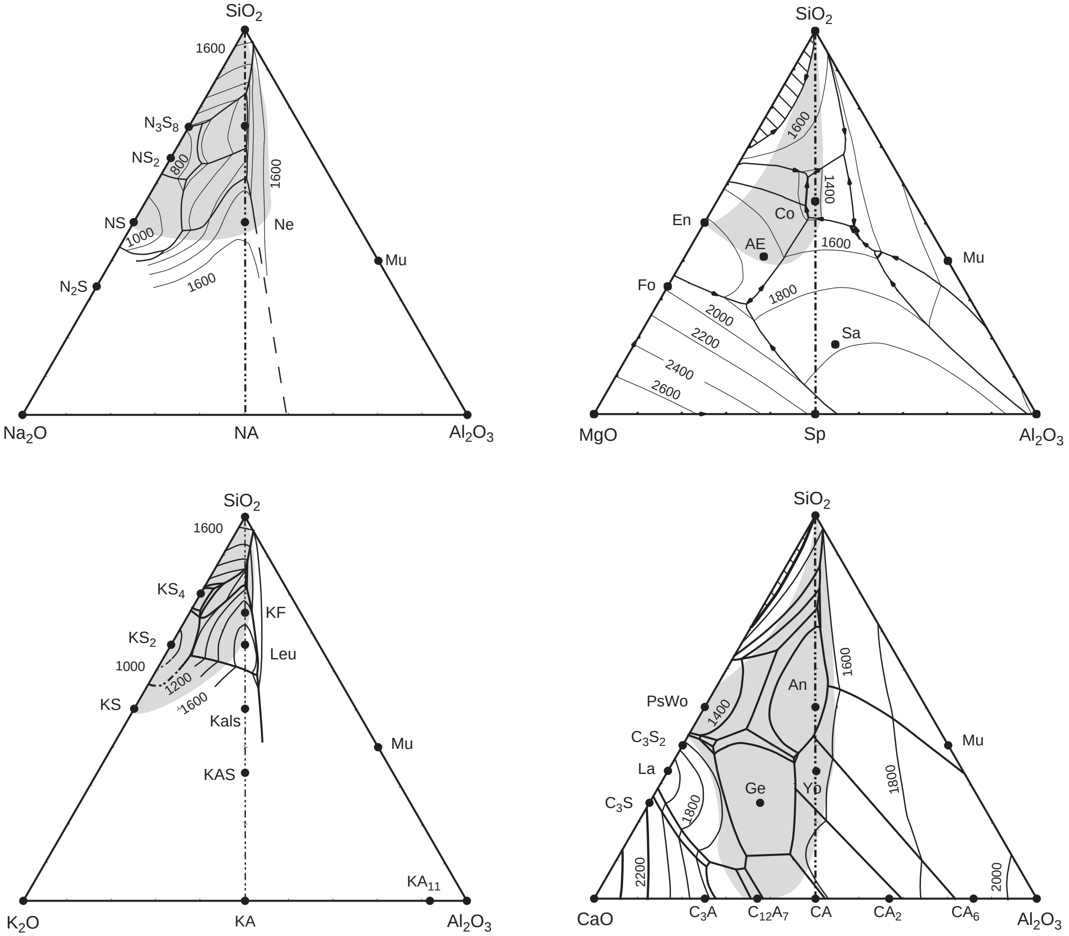

FIG. 8.1 Liquidus surfaces of ternary aluminosilicates redrawn on a mol% oxide basis from Levin et al. (1964). The compounds crystallizing from the melts are shown as solid points, stable miscibility gaps as hachured areas, the domains of glass formation under usual cooling rate conditions as gray areas (data from Schairer and Bowen, 1955, 1956, and from the authors' own observations). Abbreviations: A: Al_2O_3; K: K_2O; N: Na_2O; S: SiO_2; Ab: albite ($NaAlSi_3O_8$); AE: aluminous enstatite ($Mg_3Al_2Si_3O_{12}$); An: anorthite ($CaAl_2Si_2O_8$); Co: cordierite ($Mg_2Al_4Si_5O_{20}$); En: enstatite ($MgSiO_3$); Fo: forsterite (Mg_2SiO_4); Geh: gehlenite ($Ca_2Al_2SiO_7$); Kals: kalsilite ($KAlSiO_4$); KF: K feldspar ($KAlSi_3O_8$); La: larnite (Ca_2SiO_4); Leu: Leucite ($KAlSi_2O_6$); Mu: mullite ($Si_2Al_6O_{13}$); Ne: nepheline ($NaAlSiO_4$); PsWo: pseudowollastonite ($CaSiO_3$); Sa: sapphirine ($Mg_4Al_{10}Si_2O_{23}$); Yo: yoshiokaite (wide solid solution around the composition $CaAl_2SiO_6$). Aluminous enstatite and yoshiokaite form metastably at high degree of supercooling (see Lejeune and Richet, 1995; Roskosz et al., 2005). Other such metastable compounds could exist.

match between the ionic radius of O^{2-} with those of Ca^{2+} and also of Si^{4+} and of Al^{3+} in both four- and sixfold coordination.

Just above the glass transition, a greater number of disordered, nonstoichiometric crystalline phases can nucleate and grow metastably (Longhi and Hays, 1979; Roskosz et al., 2005), but these phases eventually transform to stable phases on moderate heating. Even for

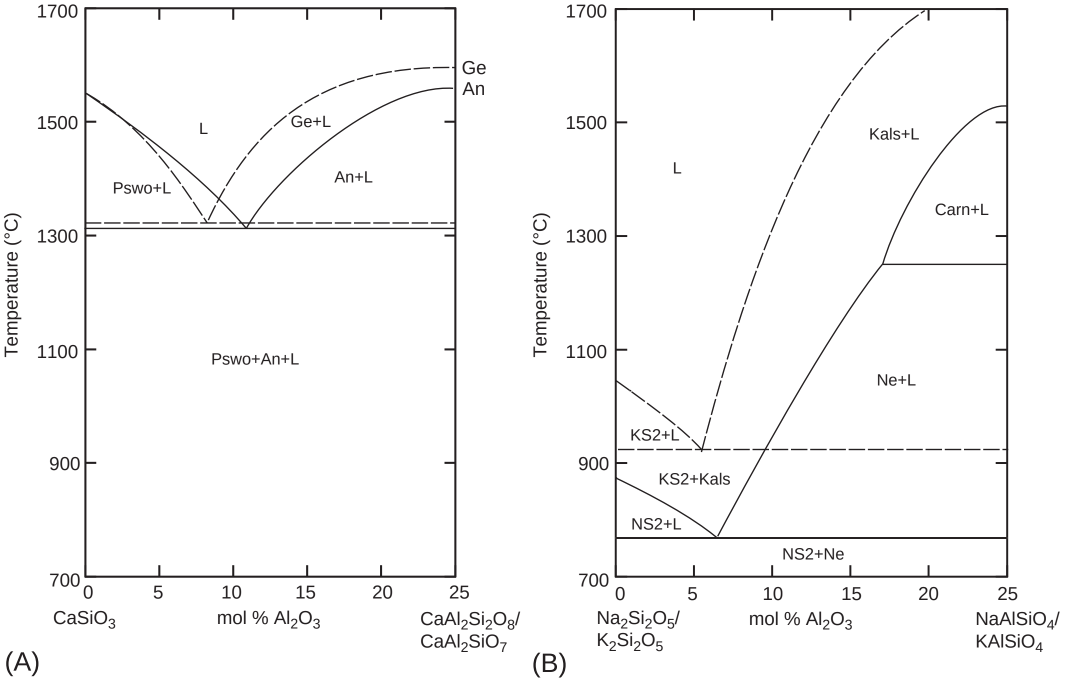

FIG. 8.2 Influence of alumina on liquidus phase relations at constant or near constant M_xO/SiO_2 in alkaline and alkaline earth systems. (A) Phase diagram derived from data in the systems $CaSiO_3$-$CaAl_2Si_2O_8$ (Osborn, 1942) and $CaSiO_3$-$Ca_2Al_2SiO_7$ (Osborn and Schairer, 1941): An: anorthite ($CaAl_2Si_2O_8$); Ge: gehlenite ($CaAl_2SiO_7$); L: liquid; Pswo: pseudowollastonite ($CaSiO_3$). Analogous diagrams are not available for $MgSiO_3$ because of the incongruent melting of enstatite at ambient pressure. (B) Phase diagram derived from data in the systems $K_2Si_2O_5$-$KAlSiO_4$ (Schairer and Bowen, 1955) and $Na_2Si_2O_5$-$NaAlSiO_4$ (Tilley, 1933): Carn: carnegieite ($NaAlSiO_4$); Kals: kalsilite ($KAlSiO_4$); Ne: nepheline ($NaAlSiO_4$).

potassium aluminosilicates, for which four such compounds exist, only a few aluminosilicate configurations are stabilized in the crystalline state at high temperature despite the wide ranges of composition and stoichiometry presented by the ternary systems.

Another important feature of the diagrams of Fig. 8.1 is the markedly differing manner in which liquidus temperatures vary with composition in alkali and alkaline earth systems. Liquidus temperatures in the alkali aluminosilicate systems are much more sensitive to composition than those in the equivalent Ca-aluminosilicate systems. The effect is evident when Al_2O_3 is added at constant M_x/Si ratio, as illustrated in Fig. 8.2 for the pseudobinary joins $M_xO{\cdot}2SiO_2$-$M_xO{\cdot}2SiO_2{\cdot}Al_2O_3$. In the alkaline earth systems (Fig. 8.2A), the differences between the melting temperatures of the endmembers are marginal. In contrast, they are considerable in alkali systems as liquidus temperatures increase by about 600 degrees when the Al_2O_3 content increases from 0 to 25 mol% (Fig. 8.2B). These temperatures eventually become comparable to, or even higher than, those of the alkaline earth melts (Fig. 8.2A). This trend correlates with the increase in coordination number described in Section 4.2.3 for charge-compensating alkali cations. In other words, the average bond strength in alkali and alkaline earth systems becomes at least similar with increasing alumina content. Not only are weak

M—O bonds replaced by stronger Al—O bonds when the melt becomes increasingly polymerized as the Al_2O_3 concentration increases, but the order of liquidus temperatures near the meta-aluminous join confirms that the strength of the association of Al with metal cations increases in the order Mg, Ca, Na, K. Interestingly, the same trend holds in complex melts as concluded, for example, from phase equilibrium experiments on immiscible melts of the system MgO-CaO-TiO_2-Al_2O_3-SiO_2 (Hess and Wood, 1982).

Beyond the meta-aluminous join, the influence of individual M-cations becomes blurred for SiO_2-rich compositions because liquidus temperatures obviously tend to be governed by the SiO_2 and Al_2O_3 components. Likewise, near the M_xO endmember the properties of each oxide predominate. As discussed in Section 6.2.2, the relatively low temperatures at which alkali oxides become unstable contrast markedly with the extremely high temperatures that prevail close to the CaO and MgO endmembers. In both cases, the effect is that glass formation is prevented so that vitrification of such melts is extremely challenging. In alkali systems, however, the strong association of Al with alkali cations also manifests itself by the fact that alkali-rich glasses are stabilized by losing their very high hygroscopic character as soon as a few mol% Al_2O_3 are added.

The Si ⇔ Al substitution is the last factor affecting liquidus temperatures to be mentioned. The effect is most clearly observed between pure SiO_2 and ternary compounds on the meta-aluminous join (Fig. 8.3). For reasons of clarity, phase diagrams are shown only for Ca, Ba, and K aluminosilicates, although a similar contrast would be observed in the analogous Na- and Mg-systems (see Fig. 8.1). The lowest temperature is that of a eutectic point located in the SiO_2-rich part of both diagrams of Fig. 8.3, but this freezing-point depression is considerably greater for alkali than for alkaline earth systems. As will be discussed shortly from a calorimetric standpoint, this contrast reflects a difference between the affinities of SiO_2 and $M_{x/2}AlO_2$ groups, which are stronger for alkali than for alkaline earth M-cations.

8.2.2 Energetics, Phase Stability, and Immiscibility

In alkali silicate melts, the metastable miscibility gaps disappear rapidly when aluminum is introduced (Fig. 8.1; Osborn and Muan, 1960a, b, c). The solvus of the Na_2O-SiO_2 system is lowered below the glass transition, where the kinetics of unmixing are vanishingly slow, upon addition of less than 2 wt% Al_2O_3 (Topping and Murthy, 1973), or even perhaps of less than 1 wt% (Hager et al., 1967). Consistent with the relative extent of miscibility gaps in Al-free melts (Fig. 6.1), a similar effect has been observed for lithium aluminosilicates with the slightly higher alumina addition of 5 mol% (Savva and Newns, 1971) and for Ca-rich melts in the CaO-Na_2O-SiO_2 system where the liquid immiscibility extends to near 10 mol% (Moir and Glasser, 1976).

As originally described by Greig (1927), a large reduction in solvus temperatures near the M_xO-SiO_2 join is also observed for alkaline earth compositions (Fig. 8.4). In the MgO-Al_2O_3-SiO_2 system with more than about 3 mol% Al_2O_3, the solvus crosses the liquidus surface and then becomes metastable. This cross-over occurs at still lower Al_2O_3 contents in the other aluminosilicates of Fig. 8.4. An important feature is that the aluminum oxide does not affect the relative extent of unmixing in the alkaline earth series compared to that in Al-free systems. In both cases, phase separation is favored by high ionization potential of the metal cation.

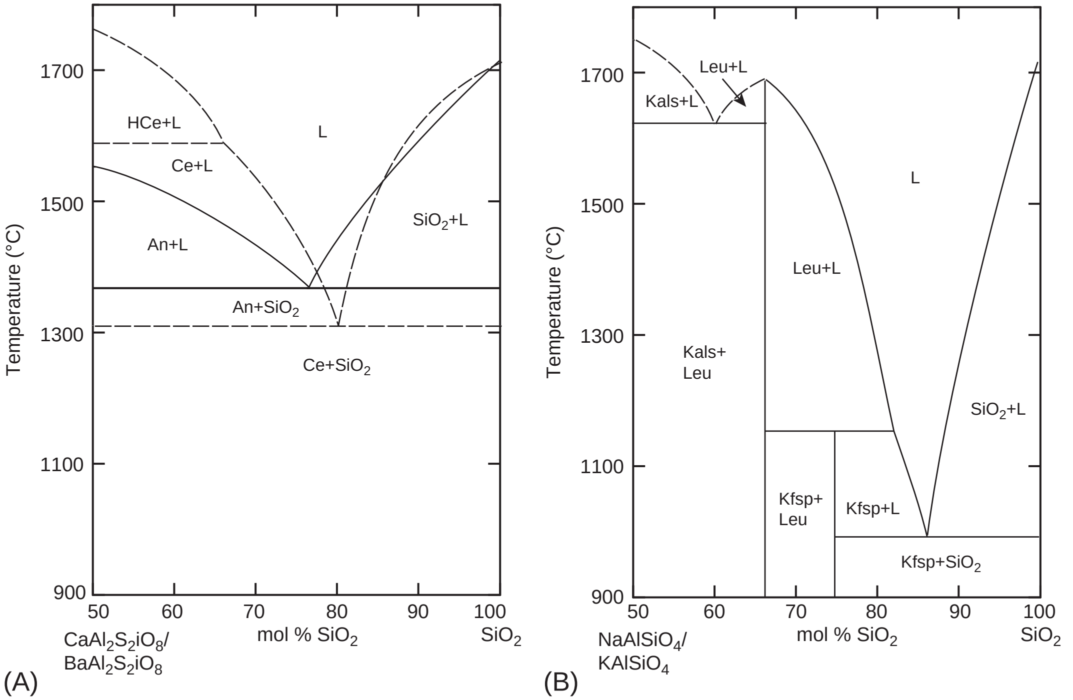

FIG. 8.3 Influence of Al⇔Si substitution on aluminosilicate melting equilibria. (A) Phase diagram derived from data in systems SiO_2-$CaAl_2Si_2O_8$ (Schairer and Bowen, 1947) and SiO_2-$BaAl_2Si_2O_8$ (Foster and Lin, 1969): An: anorthite ($CaAl_2Si_2O_8$); Ce and HCe: celsian and hexacelsian ($BaAl_2Si_2O_8$); L: liquid; SiO_2: cristobalite and tridymite. (B) Phase diagram derived from data in the system SiO_2-$KAlSiO_4$ (Schairer and Bowen, 1955): Kals: kalsilite ($KAlSiO_4$); Kfsp: $KAlSi_3O_8$; Leu: leucite ($KAlSi_2O_6$).

Qualitatively, these trends are readily accounted for. When Al^{3+} substitutes for Si^{4+}, it causes the anionic framework to polymerize through association with the other metal cations that are no longer network-modifiers. As a consequence, the steric hindrance problems discussed in previous chapters for bonding of “free” metal cations with nonbridging oxygens diminishes. Interestingly, however, unmixing vanishes well before the meta-aluminosilicate join is reached (Fig. 8.4). Because Al—O bonds are not as strong as Si—O bonds (see Table 2.1), one may surmise that the proportion of bridging oxygens in the coordination sphere of M-cations not involved in charge compensation for Al^{3+} is higher in Al-bearing than in Al-free systems. Likewise, this proportion is probably higher in alkali than in alkaline-earth aluminosilicates at comparable temperatures and overall stroichiometry or nominal NBO/T.

Other things being equal, the influence of Al^{3+} on immiscibility is the least important in the magnesium system (Fig. 8.4), which indicates that Mg^{2+} is the alkaline earth cation that associates the least strongly with Al^{3+}. The strength of this association increases in order of increasing ionic radius for other cations of the series.

Another metastable miscibility gap exists near the SiO_2-Al_2O_3 join. Its critical temperature and composition have been found at 1630°C and 73 mol% SiO_2 by MacDowell and Beall

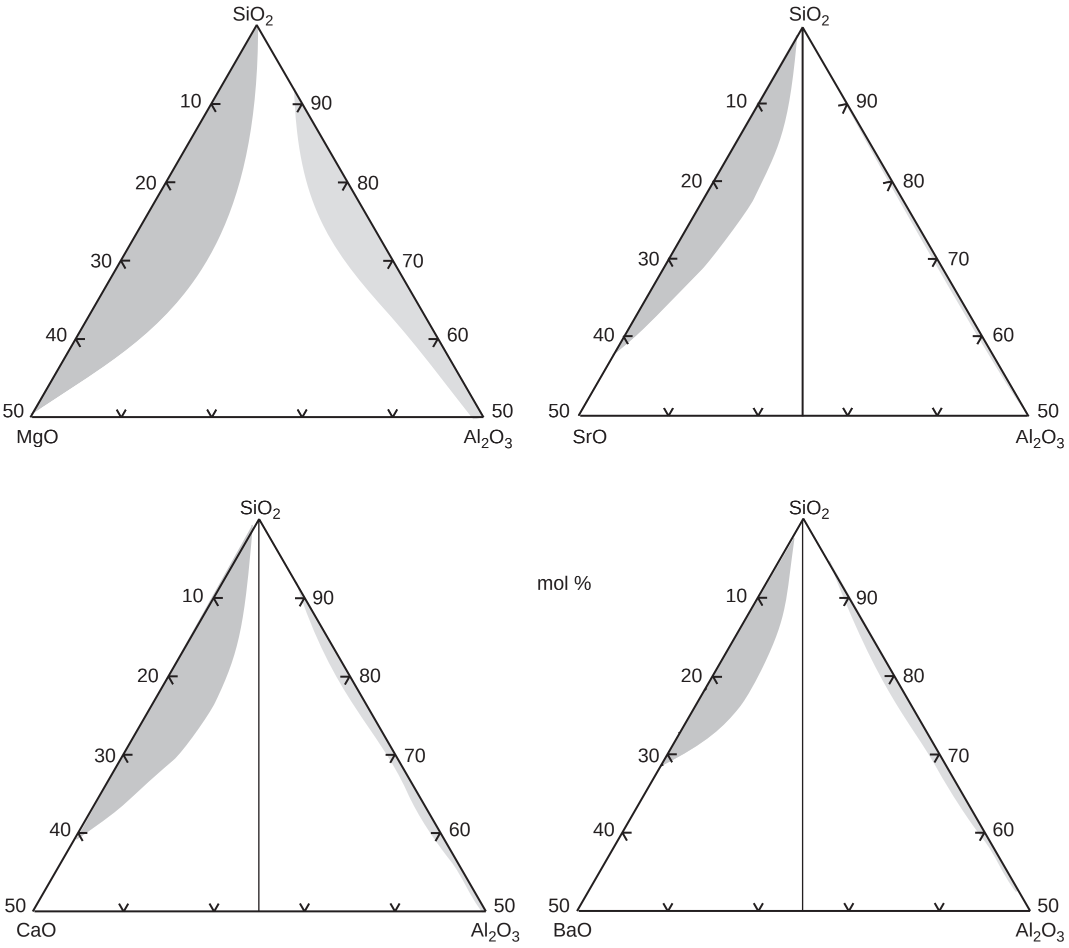

FIG. 8.4 Extent of liquid immiscibility in ternary alkaline earth aluminosilicate systems as summarized by Galakhov et al. (1985). Temperatures of the isotherms indicated in K.

(1969). However, the 1300°C and 80 mol% of Galakhov et al. (1976) are likely more reliable (Mazurin et al., 1984).

According to the diagrams of Fig. 8.4, alkaline earth cations exert the same influence on this gap as on phase separation in the Al_2O_3-poor sides of the systems. Stronger association between Al^{3+} and metal cation favors mixing of silicate and aluminate entities, with the consequence that unmixing near the SiO_2-Al_2O_3 join is marginal for Sr^{2+}, small for both Ba^{2+} and Ca^{2+}, but significant for Mg^{2+}. As a result, immiscibility is prevalent throughout the silica-rich part of the Mg aluminosilicate system. One could then wonder how homogeneous glasses can be prepared in that case. From a practical standpoint, this very wide field of unmixing is not necessarily problematic. Supercooling is intrinsically difficult for Mg compositions, so that crystallization would begin before the onset of phase separation. This is the reason why determination of the SiO_2-Al_2O_3 miscibility gap has proven so difficult. But both processes are bypassed with the high cooling rates needed to quench the melt in the composition range where homogeneous vitrification is possible.

8.2.3 Glass Formation

With usual cooling rates of tens of degrees per minute, the composition range where vitrification of aluminosilicates is possible also depends on the metal cation (Fig. 8.1). As expected from the trends in the Al-free binary melts, glass formation occurs over a wider compositional range in the K and Na than in the Mg system and also in the Cs system (Bollin, 1972).

The CaO-Al_2O_3-SiO_2 system does not fit with this trend because its glass-forming region is anomalously large and even extends to Si-free materials along the CaO-Al_2O_3 join, perhaps reflecting the large number of compounds (six) that are formed along this join (Fig. 8.1) This exceptionally wide glass-forming region makes calcium aluminosilicates particularly well suited for investigating glass and melt properties not only over a wide range of composition, but also over large temperature interval compositions. This system also offers the possibility of performing measurements in the entire supercooled liquid temperature interval down to the glass transition. Calcium aluminosilicates are, therefore, valuable model systems for other alkaline earth aluminosilicates.

As a network-forming cation, aluminum generally improves glass formation because slower crystallization kinetics are ensured by the viscosity increases resulting from polymerization of the anionic framework. This effect is particularly clear along the joins $MSiO_3$-Al_2SiO_5 ($M = Mg$, Ca) where, in contrast to $MSiO_3$ metasilicate compositions, those close to the meta-aluminous joins vitrify readily. As described in Section 3.2, glass formation is easier near eutectic compositions because lower liquidus temperatures of eutectic compositions result in higher melt viscosity. Consistently high liquidus temperatures can account for the poor vitrification ability of peraluminous compositions, regardless of the structural role of Al^3.

The very wide glass-forming region of calcium aluminosilicates, however, cannot be explained in terms of viscosity changes. For example, the SiO_2-free melts that vitrify along the join CaO-Al_2O_3 are extremely fluid (Urbain, 1983) at liquidus temperature that can exceed 1600°C (Fig. 8.1). Hence, other factors must be considered. Compared to Na, K, or Mg compositions, Ca aluminosilicates have an important peculiarity. As a result of the aforementioned match between the ionic radii of Ca^{2+} and other ions in the system, a greater number of compounds are stable on the liquidus of the two limiting CaO-SiO_2 and CaO-Al_2O_3 binaries. As described in Section 3.2, it is tempting to relate their strong glass-forming ability to this feature. In Fig. 8.1, a correlation is indeed observed between the extent of glass formation and the abundance of compounds stable on the liquidus.

8.3 THERMAL PROPERTIES

Thermodynamically, the reduction of the size of miscibility gaps upon addition of alumina to binary metal oxide-silica systems is a clear evidence for decreasing deviations from ideality. But there remain important differences between alkaline and alkaline earth aluminosilicate systems. This is especially so for the influence of "free" and charge-compensating metal cations on melt properties.

8.3.1 Thermodynamics of Melting

The values of enthalpy and entropy of fusion of the SiO_2 endmember is so low (8.92 ± 1 kJ/mol and 4.46 ± 0.5 J/mol K; see Richet et al., 1982) that it is generally concluded that melting and crystallization do not involve bond breaking or bond formation (see Section 5.3.1), with the general conclusion that at least in the short to medium range, the SiO_2 melt structure resembles that of crystalline SiO_2, perhaps cristobalite. Such similarities cannot be observed, however, for the Al_2O_3 endmember, the enthalpy of fusion of which is 112 ± 1 kJ/mol (Jerebtsov and Mikhailov, 2001), which reflects very large structural differences of crystalline Al_2O_3 (corundum) and its melt. The differences have been ascribed to significantly different Al^{3+} coordination number in melt (multiple coordination numbers between 4 and 6) and the crystalline materials (sixfold coordination) (see Section 9.3.1).

In the ternary M_xO-Al_2O_3-SiO_2 systems there are systematic variations in enthalpy and entropy of fusion, which vary with both Al/(Al + Si) and the type of M_xO oxide (see Richet and Bottinga, 1986 for review of most of those data). Regardless of the nature of the metal cation, both enthalpy and entropy of fusion of the aluminosilicate compositions greatly exceed the values for pure SiO_2 (Fig. 8.5).

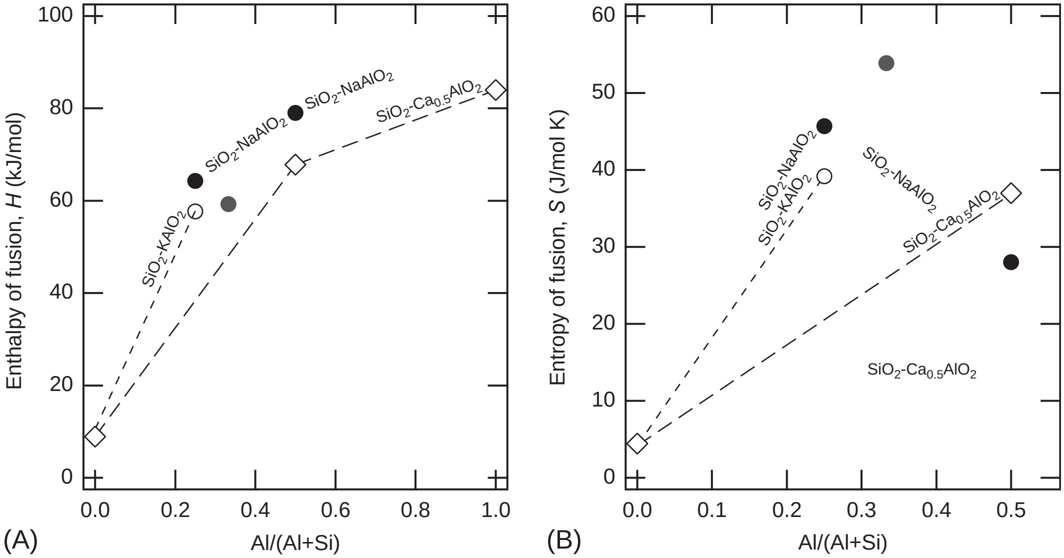

FIG. 8.5 Thermodynamics of melting of aluminosilicate compositions. (A) Enthalphy of fusion along the joins SiO_2-$NaAlO_2$, SiO_2-$KAlO_2$, and SiO_2-$Ca_{0.5}AlO_2$ (review by Richet and Bottinga, 1986 and Jerebtsov and Mikhailov, 2001). (B) Entropy of fusion along the joins SiO_2-$NaAlO_2$, SiO_2-$KAlO_2$, and SiO_2-$Ca_{0.5}AlO_2$ (review by Richet and Bottinga, 1986). Notice that for both Δ*H* and Δ*S* evolution, the values for the composition along the SiO_2-$NaAlO_2$ with Al/(Al + Si) = 0.333 is grayed. This is because the stable crystalline phase, jadeite, has Al^{3+} in sixfold coordination, whereas the coordination number in melt at ambient pressure is 4. The data summaries in this figure represent, therefore, metastable melting.

In the Al/(Al+Si) ranges for which data are available, the enthalpy of fusion increases continuously with increasing Al/(Al+Si) (Fig. 8.5A). It is notable that these values tend to be higher along the SiO_2-$NaAlO_2$ join (where enthalpies of mixing are nearly ideal) than along the SiO_2-$Ca_{0.5}AlO_2$ join (where they are definitely not ideal) (Roy and Navrotsky, 1984). Hence, this difference likely reflects structural similarities between the crystalline and liquid phases on the liquidus. Similar arguments can be made on the basis of the entropy of melting (Fig. 8.5B), but the more limited amount of these data makes the argument a little less firm.

8.3.2 Activity-Composition Relations

Activity measurements for ternary aluminosilicate melts are relatively uncommon for aluminosilicates. Owing to the experimental difficulties due to high liquidus temperatures, the data are sketchy for magnesium aluminosilicates (Henderson and Taylor, 1966), but recent data from the MgO-Al_2O_3-SiO_2 have alleviated this dearth of data somewhat (Stolyarova et al., 2011). They have long been more extensive for the CaO-MgO-Al_2O_3-SiO_2 system (e.g., Rein and Chipman, 1965; Beckett, 2002; Stolyarova, 2008), and particularly for calcium aluminosilicates because of the importance of these melts in desulfurization and dephosphorization of steel through metal-slag equilibria (see Zaitsev et al., 1997; Mills, 2018).

Such data may be extracted from liquidus phase relations (e.g., Ryerson, 1985) or they may be obtained by Knudsen Cell Mass Spectrometry (Fraser et al., 1983, 1985; Zaitsev et al., 1997; Bondar et al., 2005; Stolyarova, 2008). For example, working in the system CaO-Al_2O_3-SiO_2 Stolyarova (2008) found negative deviation of SiO_2 activity along a join from SiO_2 to CaO/Al_2O_3 = 1 (Fig. 8.6). In the MgO-Al_2O_3-SiO_2 system, on the other hand, at similar temperatures (1890 K) and equivalent MgO/Al_2O_3 ratio (unity), the SiO_2 activity deviates positively from ideal mixing (Stolyarova et al., 2011). Interestingly, the only other composition join with an

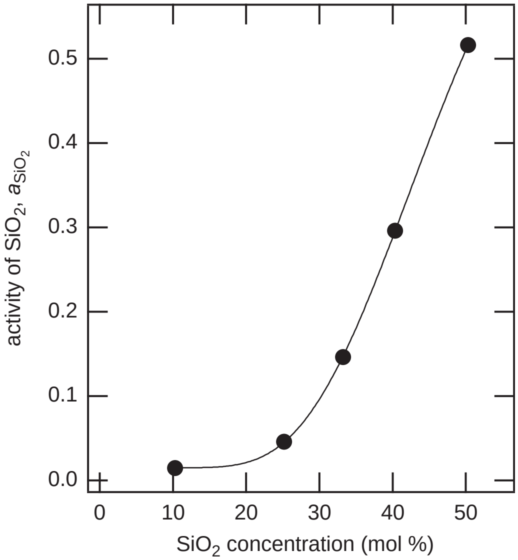

FIG. 8.6 Activity-composition relations in the melt system CaO-Al_2O_3-SiO_2 along a join with CaO/Al_2O_3 = 1 (Stolyarova, 2008).

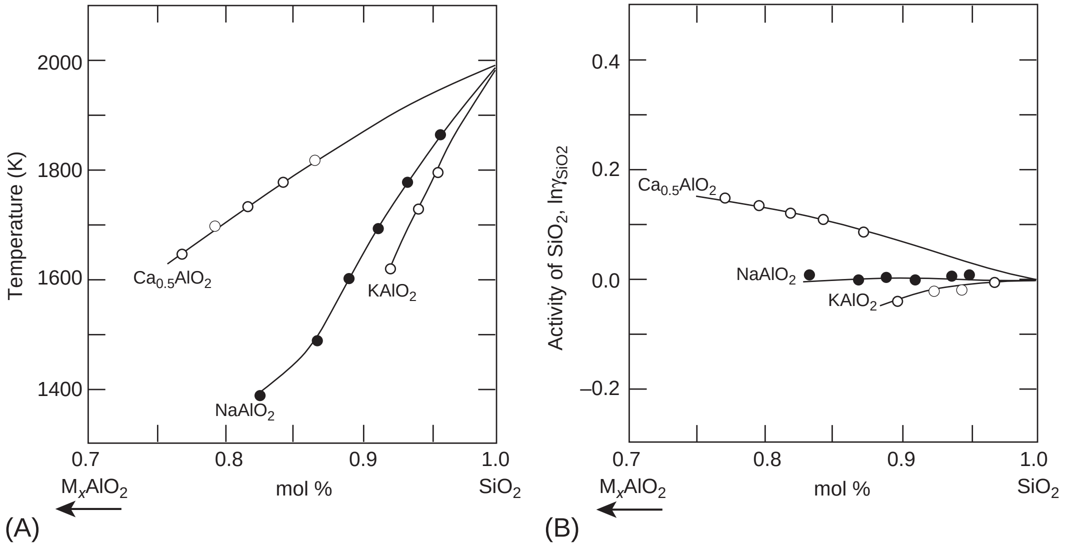

FIG. 8.7 Effects of a variety of oxides and aluminates: (A) On freezing-point depressions near the SiO_2 endmember on meta-aluminous joins. (B) On the activity coefficient of SiO_2 in the same melts (Ryerson, 1985).

analogous positive deviation has been reported along the SiO_2-Al_2O_3 join (Shornikov and Archakov, 2002), for which a_{SiO_2} exceeds 1 for Al-rich compositions. This is the same composition range where there is incipient liquid immiscibility at temperatures above the liquidus (Risbud and Pask, 1977).

The composition dependence of SiO_2 activity in aluminosilicate melts along meta-aluminosilicate joins were determined by Ryerson (1985) from the liquidus phase relations of silica polymorphs. The method has already been described in Section 6.3.2 for binary metal oxide-silica systems. The results are plotted in Fig. 8.7. The activity-composition relationship is nearly ideal for the Na system, whereas negative and positive deviations from ideality are found for the K and Ca systems, respectively. This indicates that departures from ideality mainly result from the enthalpy, and not from the entropy, contribution to the Gibbs free energy.

8.3.3 Energetics of Mixing

Most experimental data address Si⇔Al substitution for a number of alkali and alkaline earth cations (e.g., Navrotsky et al., 1982). As summarized by Roy and Navrotsky (1984), these results are plotted in Fig. 8.8 in the form of negative of enthalpies of solution, because this representation allows the enthalpy scale to be visualized directly.

Depending on whether the standard glass transition temperature is lower or higher than 700°C, the temperature of solution calorimetry, the measurements refer to glasses or to relaxed supercooled liquids. In the former case, samples have different fictive temperatures so that proper isothermal adjustment of the data should be made (Section 3.4.3). Such adjustments typically can amount to 5 kJ/mol or more (Richet and Bottinga, 1984a; Hovis et al., 2004).

FIG. 8.8 Energetics of Si⇔Al substitution in aluminosilicate glasses or supercooled liquids: Enthalpy of solution in molten lead borate at 700°C along the joins SiO_2-M_x, where M is an alkali or alkaline earth element (data compilation by Roy and Navrotsky, 1984).

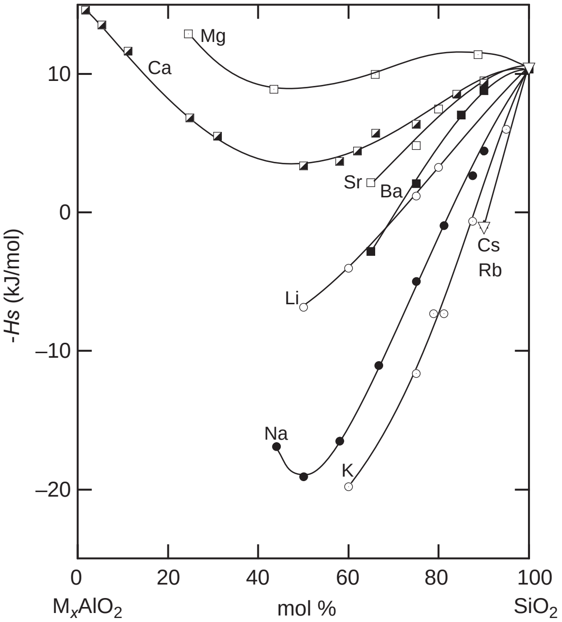

Because of the slight curvature of the enthalpies plotted in Fig. 8.8, these adjustments would be necessary to determine accurately enthalpies of mixing between SiO_2 and the most SiO_2-poor composition investigated for a given system. For our purpose of comparing the effects of different M-cations, however, these adjustments are unnecessary in view of the large differences between the enthalpy trends for each system.

From K to Mg, all enthalpy-composition relationships succeed each other in the order of ionization potential of the metal cation (Fig. 8.8). Only a single measurement exists for Rb and Cs, but both data conform to this order, although they suggest some leveling off of the systematics beyond potassium. Of special interest is the fact that there is no sharp boundary between the alkaline and alkaline earth series, as the data for the Li and Ba compositions fall practically on the same curve.

For all systems, the most evident feature is the negative enthalpy of mixing between SiO_2 and M_xAlO_2, which indicates strong affinity between these components. Moreover, as the Al/(Al+Si) increases, the heat of solution also increases (becomes more negative; see Roy and Navrotsky, 1984). Interestingly, though, it appears that whereas such simple correlations between ΔH_s and Al/(Al+Si) are clear for any group of metal cations with the same formal electrical charge, a separate trend can be seen for each series of differently charged metal cations (Fig. 8.9). When the composition range investigated allows its determination, the enthalpy minimum is found near 50 mol% SiO_2 (Navrotsky, 1994). Its magnitude varies strongly with the nature of the M-cation, occurring near 10 kJ/mol for Mg- and below −20 kJ/mol for K-aluminosilicates. The depths of these minima correlate with the relative extent of freezing-point depressions at eutectics (Fig. 8.1). They also follow the relative stabilization energy trends shown in Fig. 9.10 (Chapter 9). In contrast, the compositions of the eutectics

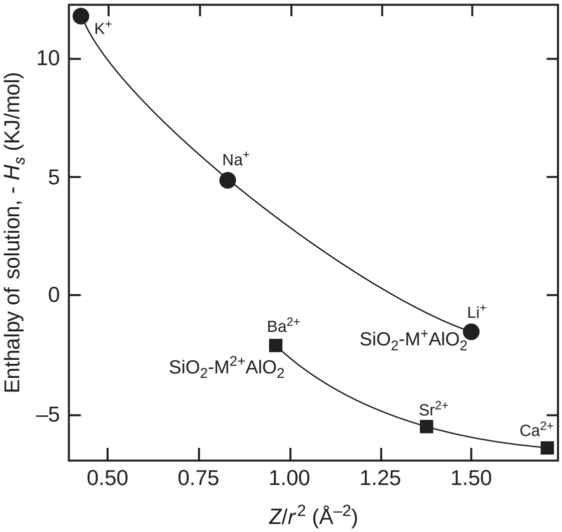

FIG. 8.9 Energetics of Si ⇔ Al substitution in aluminosilicate glasses or supercooled liquids: Enthalpy of solution in molten lead borate at 700°C along the joins SiO_2-M_xAlO_2 as a function of their Al/(Al+Si), where M is an alkali or alkaline earth element (data compilation by Roy and Navrotsky, 1984). The type of metal cation is expressed in terms of their ionization potential, Z/r^2, where Z is formal electrical charge and r is ionic radius obtained by assuming sixfold coordination and using the data of Whittaker and Muntus (1970).

do not match those of the enthalpy minima of Fig. 8.8. The reason is, of course, that enthalpy is not the only factor determining phase equilibria. Finally, we note that only Mg-aluminosilicates unmix at very high SiO_2 content along the meta-aluminous join (Fig. 8.1). Consistent with this observation, the Mg meta-aluminate join is the only one for which the enthalpy-composition relationship in Fig. 8.8 shows an initial maximum and where the SiO_2 deviates positively from ideal mixing (Stolyarova et al., 2011), i.e., the positive enthalpy of mixing that is generally associated with phase separation.

8.3.4 Heat Capacity

In liquids, the heat capacity (C_p) is made up of vibrational and configurational contributions. The former has been extensively discussed in Section 4.2.3 in relation to short-range order and oxygen coordination of cations in glasses. It suffices here to recall that the vibrational density of states is a sensitive function of oxygen coordination of every cation (Section 3.2.2). In particular, low-temperature heat capacity conveys information on the environment of cations whether free, network-modifying or acting as charge compensators (Richet et al., 1993). At least for peralkaline compositions, analysis of the available data indicates that association with aluminum entails major changes in short-range order around alkali cations. Their oxygen coordination number increases from about 5 to the higher values found in tectosilicate crystals. In contrast, the oxygen environment of alkaline earth cations does not change significantly.

It follows that network-modifying and charge-compensating alkali cations must be distinguished when evaluating the vibrational entropy of silicate glasses, whereas such a distinction is unnecessary for alkaline earth cations. Beyond the meta-aluminous joins, vitrification becomes difficult so that data are generally lacking. The exception concerns calcium aluminosilicates for which extensive measurements could be made (Richet et al., 2009). The original

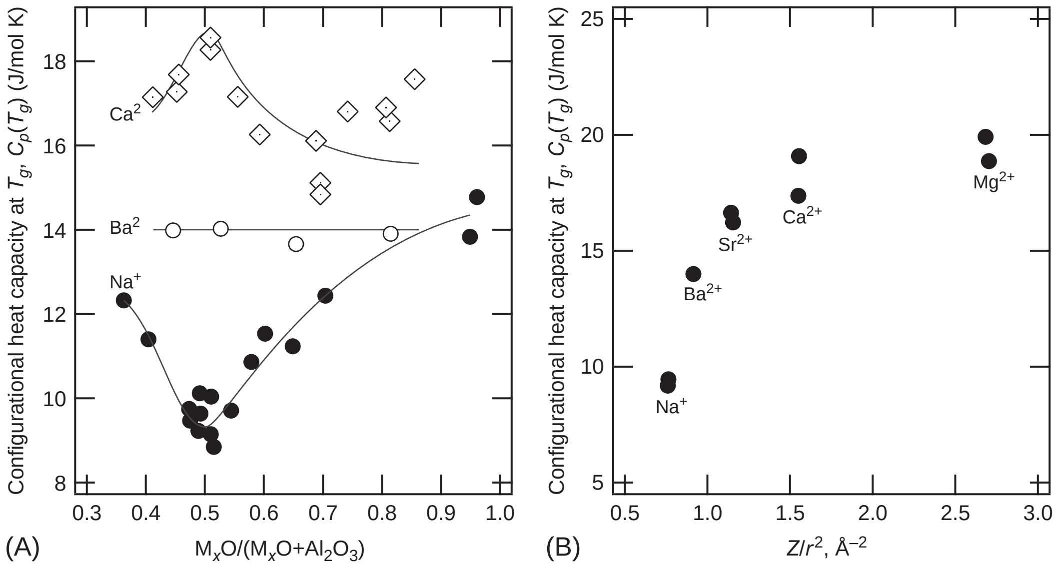

FIG. 8.10 Variations in configuration heat capacity at the glass transition temperature, $C_p(T_g)$. (A) As a function of $M_xO/(M_xO+Al_2O_3)$ at 67 mol% SiO_2. (B) As a function of ionization potential of charge-balancing cation at $M_xO/(M_xO+Al_2O_3)=0.45–0.5$. *Redrawn from Webb (2008, 2011).*

feature has been the determination of partial molar heat capacities and entropies of Al_2O_3 species, which decrease with increasing four-, five-, and sixfold coordination of Al (Fig. 3.7), but no effect of Al speciation on the coordination of calcium has been detected.

Above room temperature, heat capacity has been measured over a wide range of compositions in M_xO-Al_2O_3-SiO_2 melt and glass (Richet and Bottinga, 1984a,b; Courtial and Richet, 1993; Toplis et al., 1997a, b; Tangeman and Lange, 1998; Bouhifd et al., 1998; Webb, 2008, 2011). For both peralkaline and peraluminous compositions, analysis of the data again points to major changes in short-range order around alkali cations caused by association with tetrahedral Al^{3+} (Fig. 8.10; see also Webb, 2008, 2011). For alkaline earth aluminosilicates, C_p increases to a maximum near the meta-aluminate join that increases systematically with Z/r^2 of the metal cation. For alkali aluminosilicates, there is a decrease on both sides of the meta-aluminate-silica join to a minimum value at the meta-aluminosilicate join (Fig. 8.10). Notably, the configurational heat capacity becomes less sensitive to the type of metal cation the more electronegative it is. Presumably, this change reflects greater similarity of the M—O and Al—O bond strength—a feature that also is evident in other properties such as viscosity and activation enthalpy of viscous flow (see Section 8.4.1).

We must also recall that the heat capacity of glasses is nearly additive with respect to chemical composition. Addition of Al_2O_3 to a binary metal oxide system tends to cause a very minor temperature-dependent decrease (Tangeman and Lange, 1998), but this tendency, which is on the order of 1%–2%, may well be within experimental uncertainty.

The heat capacity at the standard glass transition is close to the Dulong-and-Petit limit of $3\ R/g$ atom K. The configurational heat capacity (C_p^{conf}) is approximated by the difference between the measured heat capacity of the liquid (C_{pl}) and this limit. Because the

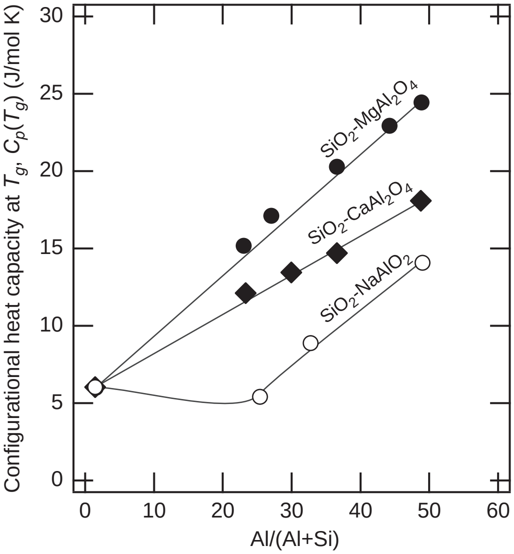

FIG. 8.11 Configuration heat capacity of glasses along the meta-aluminosilicate joins indicated (data compilation by Richet and Neuville, 1992).

Dulong-and-Petit limit is determined by the number of atoms in the formula unit, the composition dependences of C_{pl} and C_p^{conf} are the same. For analogous melt compositions, C_p^{conf} increases in the order Mg, Ca, Na (Fig. 8.11; see also Webb, 2011). We also note that, whereas for the Mg- and Ca-meta-aluminosilicate melts the configurational heat capacity is essentially a linear function of Al/(Al+Si), this is not so for the SiO_2-$NaAlO_2$ melts. These effects likely relate to the fact that in the alkaline earth aluminosilicates, two Al^{3+} cations are charge-compensated for each metal cation, whereas only one Al^{3+} is charge-compensated by the monovalent Na^+ cation. There is therefore less flexibility and probably longer range order in the alkaline earth aluminosilicate glasses and melts, thus leading to an apparent linear relationship between C_p^{conf} and Al/(Al+Si) for these compositions.

As the temperature-derivative of configurational entropy (S^{conf}), configurational heat capacity, C_p^{conf}, is an expression of temperature-induced structural changes. More precisely, C_p^{conf} mainly reflects short-range interactions as discussed in Section 6.3.5. Hence, its variations with decreasing ionization potential of the charge-compensating cation are consistent with the increasingly strong association between Al- and M-cation. From Mg to K, this association restricts the number of configurations available to alkali compared to alkaline earth melts. On the other hand, the rate at which new configurations become accessible increases faster with temperature in alkali than in alkaline earth systems because, due to increasing thermal energy, high enthalpy barriers can be overcome to maximize the entropy.

The C_p^{conf} contrasts between Al-free melts and their fully polymerized Al-bearing counterparts are small except for the two potassium-bearing compositions, $K_2Si_3O_7$ and $KAlSi_3O_8$ (Fig. 8.12). On average, such differences might seem insignificant over wide temperature intervals. This slight effect could be misleading, however, if one were not heeding the large differences in polymerization between the various series of melts shown in Fig. 8.12. This is because, as discussed in Section 6.3.5 for binary M_xO-SiO_2 systems, the configurational heat capacity decreases with increasing degree of polymerization and reaches a minimum value

FIG. 8.12 Heat capacity comparison between fully polymerized aluminosilicates liquids and their Al-free counterparts (*shown in italics*) with the same SiO_2 content (Richet and Bottinga, 1984a, b, Richet and Bottinga, 1995; Richet et al., 1984).

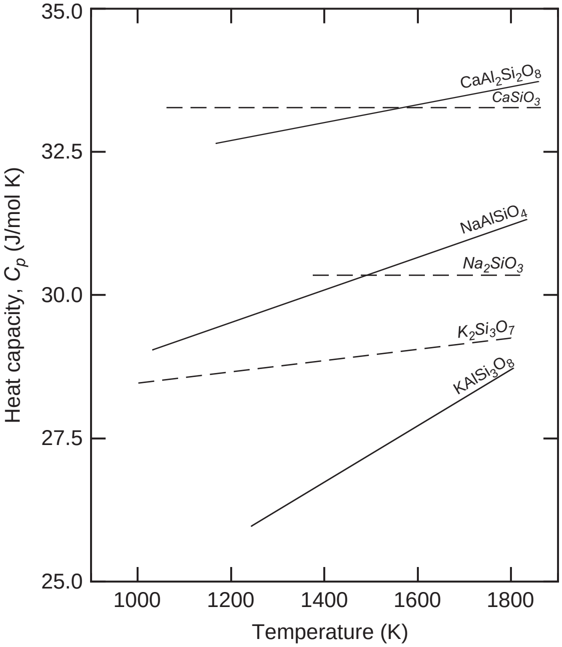

for pure SiO_2. For a given NBO/T, the data of Fig. 8.12 thus point to a marked increase of C_p^{conf} when Al^{3+} substitutes for Si^{4+}. As a network-forming cation, Al^{3+} causes configurational heat capacity to increase to values of the Al-free melt with a much higher NBO/T.

A detailed examination of the relationships between heat capacity and composition indicates that these effects depend on the nature of the M-cation. For the system $MgO\text{-}Al_2O_3\text{-}SiO_2$, at constant Mg/Al along two different joins (Fig. 8.13A), C_p varies linearly with SiO_2 concentration. It is independent of temperature. By linear extrapolation with MgO concentration at constant SiO_2 content (Fig. 8.13B), these trends again show a linear variation with composition. When extrapolated to the $MgO\text{-}Al_2O_3$ join, the trends for different temperatures converge to the temperature-independent partial molar heat capacity of MgO derived for Al-free silicates (Fig. 8.13C). These trends also extrapolate to values consistent with the heat capacity measured for pure Al_2O_3 liquid (Barkhatov et al., 1973). This observation implies, therefore, that the temperature-dependence of the heat capacity of $MgO\text{-}Al_2O_3\text{-}SiO_2$ liquids is entirely attributable to the partial molar heat capacity of the Al_2O_3 component in Mg aluminosilicate melts.

Even though Mg aluminosilicates are thermodynamically strongly nonideal solutions (Roy and Navrotsky, 1984; Stolyarova et al., 2011), they do not show excess heat capacity at least up to the meta-aluminous join. By denoting the mol fraction of oxide i by x_i, we can write:

$$C_p = \sum x_i \overline{C}_{pi}, \tag{8.1}$$

and find that the partial molar heat capacity of oxide i, $\overline{C}_{pi}$, does not vary significantly with composition (Richet and Bottinga, 1995; Tangeman and Lange, 1998). It varies with

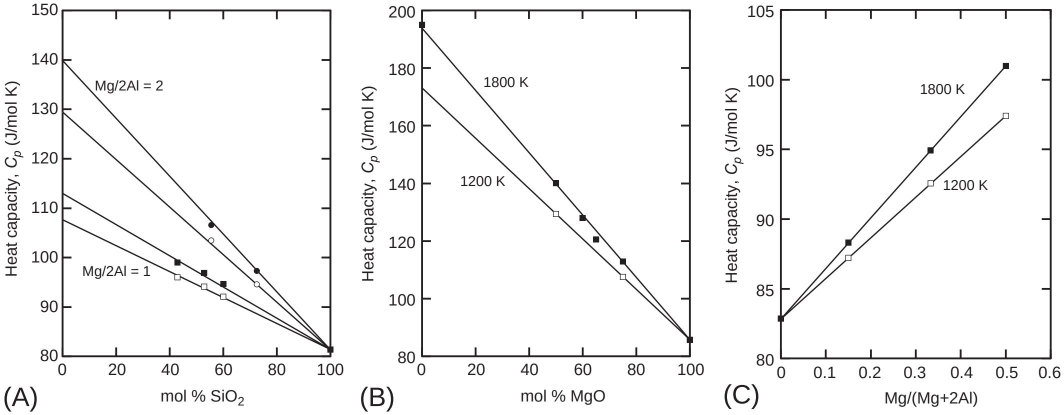

FIG. 8.13 Heat capacity of magnesium aluminosilicate melts at 1200 K (open symbols) and 1800 K (solid symbols): (A) When the SiO_2 content varies at constant Mg/Al. (B) When MgO substitutes for Al_2O_3 at constant SiO_2 content. (C) When data are extrapolated along the join MgO-Al_2O_3. Courtial and Richet (1993) with the value derived for pure MgO in Al-free melts (Richet and Bottinga, 1995) and that reported for pure Al_2O_3 liquid (Barkhatov et al., 1973). The solid lines are calculated with the assumption of composition-independent partial molar heat capacities.

temperature only for Al_2O_3. Again, no inference can be made for compositions lying on the Al-excess side of the meta-aluminous join because high liquidus temperatures and problems with quenching crystal-free glasses have prevented measurements from being made.

The simplicity expressed in Eq. (8.1) is lost, however, if the coordination of the M-cation changes through charge compensation of tetrahedrally coordinated Al^{3+}. This is the case for sodium aluminosilicates for which the heat capacity is not a linear function of either SiO_2 content at constant Na/Al (Fig. 8.14A) or of Na/(Na + Al) at constant SiO_2 content (Fig. 8.14B). Here, it is known from structural studies that the coordination environment around Na^+ differs in Al-free and Al-bearing glasses and melts (Lee and Stebbins, 2003; Gambuzzi et al., 2015).

The temperature dependence of the heat capacity is also a complex function of composition (Fig. 8.14). It is significant only near the meta-aluminous join and causes the C_p vs composition relationships to become linear at high temperature along the meta-aluminous join (upper curve in Fig. 8.14A). Conversely, at constant SiO_2 content this relationship becomes increasingly nonlinear with increasing temperatures (Fig. 8.14B). To rationalize such complicated variations, one needs to distinguish in Eq. (8.1) partial molar heat capacities of sodium oxides with either free or charge-compensating Na^+, and, therefore, that the partial molar heat capacity of Na^{2+} in these two different environments has different relationships to temperature. Finally, it appears that C_p varies smoothly when the meta-aluminous join is crossed, at least for SiO_2-rich compositions (Fig. 8.14B). We note, however, that Webb (2008), in her study of less SiO_2-rich compositions, reported a distinct minimum on the configurational heat capacity near the sodium meta-aluminosilicate join (Fig. 8.10).

Heat capacity data for other systems are less comprehensive. From Mg to K systems they do conform to the trends already described in this chapter. Along the meta-aluminous join, calcium aluminosilicates have slight excess heat capacities (Richet and Neuville, 1992), which

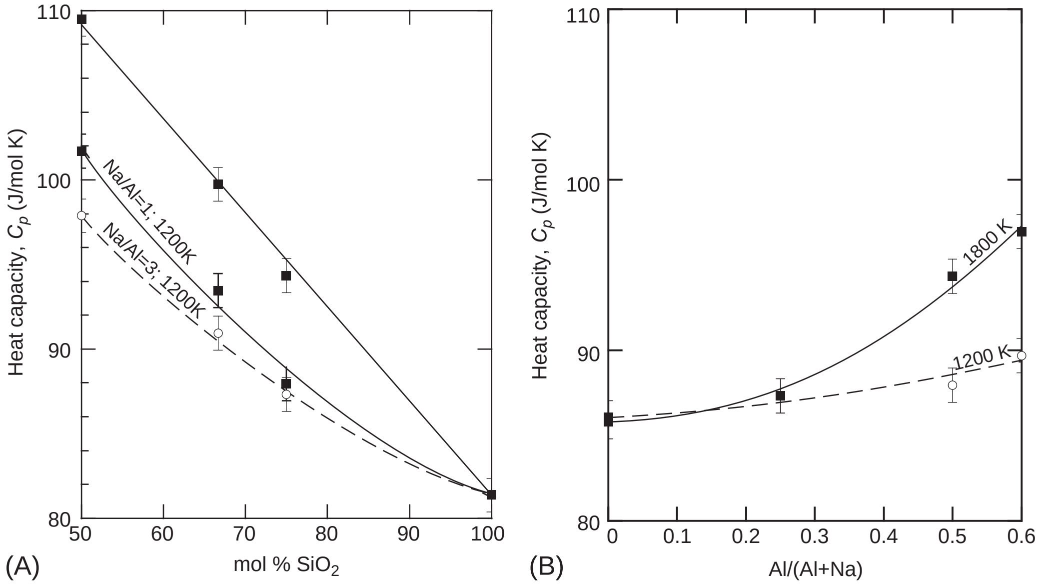

FIG. 8.14 Heat capacity, C_p, of sodium aluminosilicate liquids. (A) Against SiO_2 content at constant Na/Al ratio. (B) Against Al/(Al+Na) at 75 mol% SiO_2. For Al-free and Al-poor melts, the temperature dependence of C_p is too small to be detected even when the calorimetric measurements span intervals of almost 1000°. Data from Richet and Bottinga (1984b) and Richet (unpub).

appear as a maximum in their configurational heat capacities near the meta-aluminosilicate composition (Webb, 2011). Finally, the heat capacity of potassium aluminosilicates shows a stronger temperature dependence than that of their sodium counterparts (Richet and Bottinga, 1984b). The reason is that, among Al-free melts, only potassium silicate liquids have a temperature-dependent C_p (see Chapter 6), which enhances this feature in K-bearing aluminosilicates.

8.4 PHYSICAL PROPERTIES

8.4.1 Transport Properties

8.4.1.1 Viscosity

Melt and glass viscosity at ambient pressure varies with degree of polymerization, the nature of network-modifying cations, the nature of cations serving to charge-balance tetrahedral coordination of Al^{3+}, and Al/Si abundance ratio (Bockris et al., 1955; Urbain et al., 1982; Richet 1984; Richet and Neuville, 1992; Toplis et al., 1997a, b; Sukenaga et al., 2006; Le Losq and Neuville, 2013). The influence of composition on the viscosity of aluminosilicate melts varies from several to many orders of magnitude, depending on melt and glass composition, as illustrated with a few examples in Fig. 8.15. The viscosity range tends to increase with decreasing temperature. The data for $Na_2Si_4O_9$ and $CaSiO_3$ are included as a reminder of the differences between Al-free alkali and alkaline earth melts. Consistent with the effects

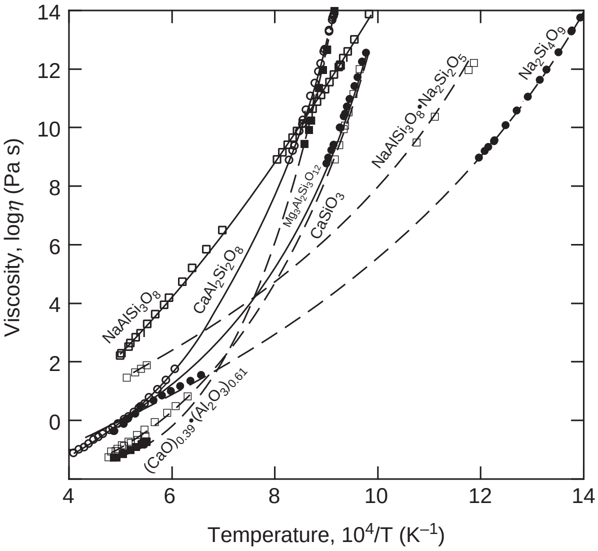

FIG. 8.15 Viscosity of silicate and aluminosilicate melts against reciprocal temperature: $NaAlSi_3O_8$ (Urbain et al., 1982; Taylor and Rindone, 1970); $CaAl_2Si_2O_8$ (Urbain et al., 1982; Neuville, 1992); $(CaO)_{0.39}{\cdot}(Al_2O_3)_{0.61}$ (Urbain, 1983; Sipp and Richet, 2002); $Mg_3Al_2Si_3O_{12}$ and $CaSiO_3$ (Neuville and Richet, 1991); $NaAlSi_3O_8{\cdot}Na_2Si_2O_5$ (Riebling, 1966; Taylor and Rindone, 1970); $Na_2Si_4O_9$ (Bockris et al., 1955; Sipp and Richet, 2002).

described in previous sections, the viscosity differences between various Al-free melts and glasses reduce gradually when Al^{3+} is introduced.

From Al-free compositions to the meta-aluminous join or beyond, these changes will be described in more detail in following text. They are, in fact, so large that comparisons of isothermal values require unwarranted extrapolation of the data when these have been gathered only at high or low viscosities for a given composition. To avoid these problems, it is preferable to compare the temperature of a given isokom (i.e., of isoviscosity values). This will mainly be made near the glass transition because the sensitivity of viscosity to composition and structure is much greater in this temperature range than above the liquidus, where the data tend to converge (Fig. 8.15).

The effects of the addition of alumina at constant M/Si ratio are to increase the viscosity near the temperature of the glass transition until compositions are near those of the meta-aluminosilicate joins (Fig. 8.16; see also Riebling, 1964, 1966; Taylor and Rindone, 1970; Webb et al., 2004). Once more, the differences between alkali and alkaline earth systems are borne out by the temperature of the 10^{12} Pa s isokom. This temperature does not vary much for Mg liquids, rises gently for Ca melts, and increases by nearly 400 K for the Na system from a composition without Al_2O_3 until reaching the meta-aluminosilicate join, before decreasing slightly beyond this join (Fig. 8.16). Webb et al. (2004) reported that a similar viscosity plateau can be observed under isothermal conditions.

The sensitivity of viscosity to melt and glass structure has long been used to address whether or not structural changes occur across the meta-aluminous join. For sodium aluminosilicates, the observations made at constant SiO_2 content close to the glass transition range (Taylor and Rindone, 1970; Webb et al., 2004) and at high temperature (Riebling, 1966) show either a plateau or a decrease in viscosity when the Na/Al atomic ratio is close to unity (Fig. 8.17). The effects of such a change have also been observed in electrochemical

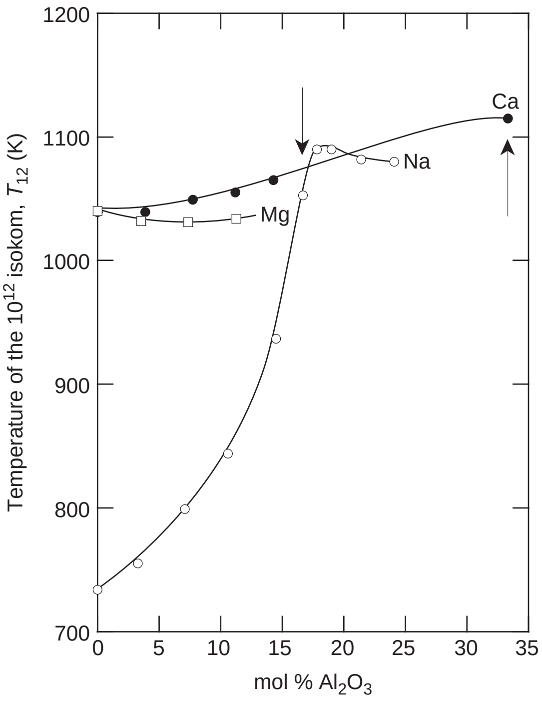

FIG. 8.16 Composition dependence of viscosity near the glass transition as given by the temperature of the 10^{12} Pa s isokom against mol% alumina along the joins $Na_2Si_3O_7$-Al_2O_3 (Na), $MgSiO_3$-Al_2O_3 (Mg), and $CaSiO_3$-Al_2O_3 (Ca). The arrows indicate the position of the meta-aluminous join. Data from Shelby (1978), Taylor and Rindone (1970), and Neuville (1992).

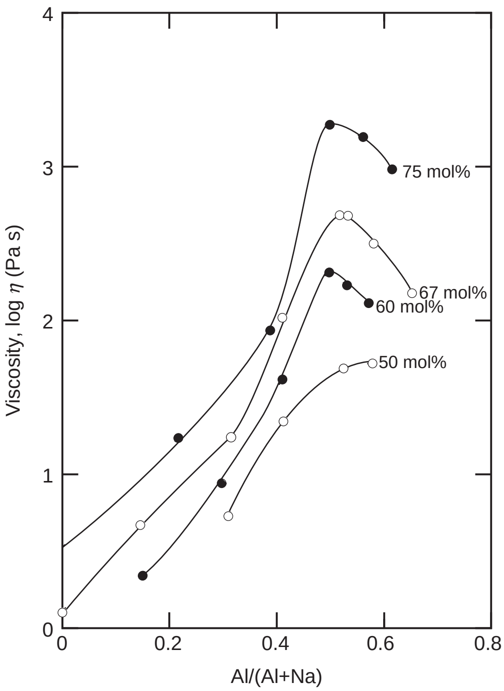

FIG. 8.17 Viscosity at 1800 K for the four SiO_2 mol % indicated (Riebling, 1966, with data of Bockris et al., 1955 for the Al-free endmembers).

measurements performed on the same series of sodium-bearing glasses (Graham and Rindone, 1964). More recent observations by Toplis et al. (1997b) agree with Riebling's (1966) results, although they do not locate the viscosity maximum on the meta-aluminous join but at values of Na/(Na + Al) slightly lower than 0.5. The deviation from this value varies with SiO_2 content and increases with decreasing temperatures. These features have been interpreted in terms of triclusters by Toplis et al. (1997b). A similar plateau has been observed in the dilatometric glass transition temperatures of lithium aluminosilicates at Li/(Li + Al) of about 0.48 (Shelby, 1978).

In view of the differing effects of alkaline and alkaline earth elements on viscosity, the existence and position of this maximum should indeed depend on the nature of the M-cation. For Ca and Mg aluminosilicates, the results subsequently obtained at low and high temperature by Toplis and Dingwell (2004) do show important differences, since a viscosity maximum is observed only for the former (Fig. 8.18).

For charge-compensating cations, the viscosity values of Fig. 8.15 illustrate the more general fact that the strength of the association with aluminum decreases in the familiar

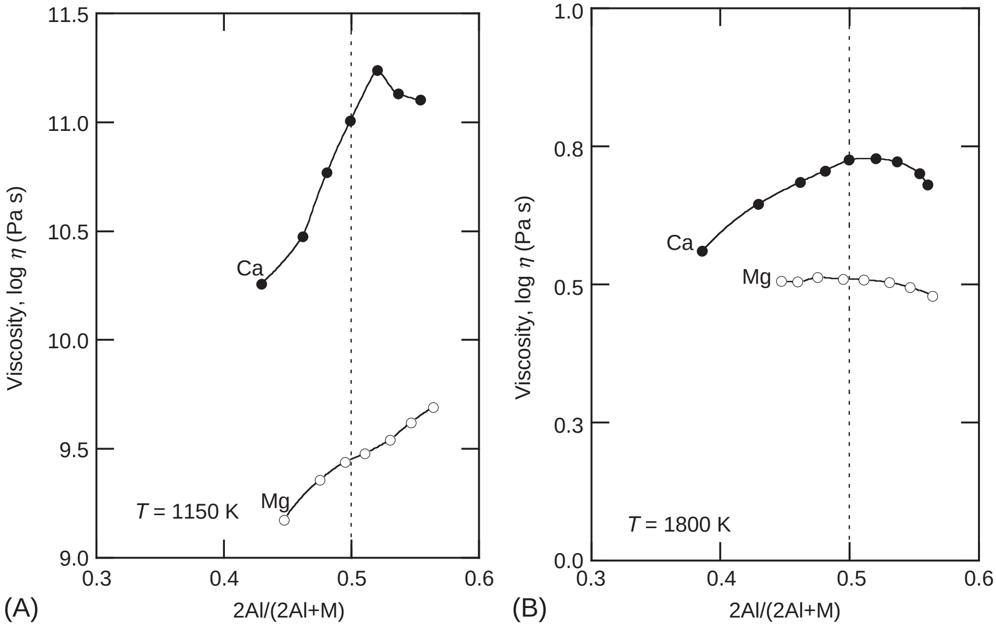

FIG. 8.18 Viscosity variations across the meta-aluminous join for Ca and Mg aluminosilicates with 50 mol% SiO_2 at 1150 K (A) and 1800 K (B). Data from Toplis and Dingwell (2004).

order Na, Ca, Mg. Liquidus temperatures and melt viscosity depend on bond strength. Hence, there is similarity between the variations of both kinds of properties (Figs. 8.2 and 8.15). The main difference, of course, deals with the existence of minima at eutectic points for liquidus temperatures, which cannot have any counterpart in viscosity. This difference accounts for the basic unreliability of the various empirical relationships, such as the rule $T_g/T_l=2/3$ (T_l=liquidus temperature) proposed by Kauzmann (1948), which aim at relating liquidus and standard glass transition temperatures.

Regarding Si ⇔ Al substitution, the difference in Si—O and Al—O bond strength is evident in the temperature T_{12} of the 10^{12} Pa s isokom (Fig. 8.19), in composition-dependent high-temperature viscosity along the meta-aluminous join (Fig. 8.20), and in changes in fragility as a function of metal cation type and Al/(Al+Si) (Fig. 8.21). From pure SiO_2, the decrease amounts to more than 300 K for T_{12} and to more than four orders of magnitude for viscosity. Because association of Al with the charge-compensating cation is weaker in Mg than in Ca melts, viscosity is lower within the former than the latter system such that the order of increasing viscosity becomes Mg, Ca, Na, Li. This is confirmed and complemented by high-temperature viscosities, which are extensive along the meta-aluminous join (Fig. 8.20).

Recognition of such a systematic relationship among charge-compensating cations was, in fact, the basis of the successful model of prediction of high-temperature viscosity proposed by Bottinga and Weill (1972), which relied on correct identification of the metal cation-aluminate species present in the melt. The systematics in viscosity (Fig. 8.16) and enthalpy (Fig. 8.9) are remarkably similar. This is also indicated by the dilatometric glass transition temperatures

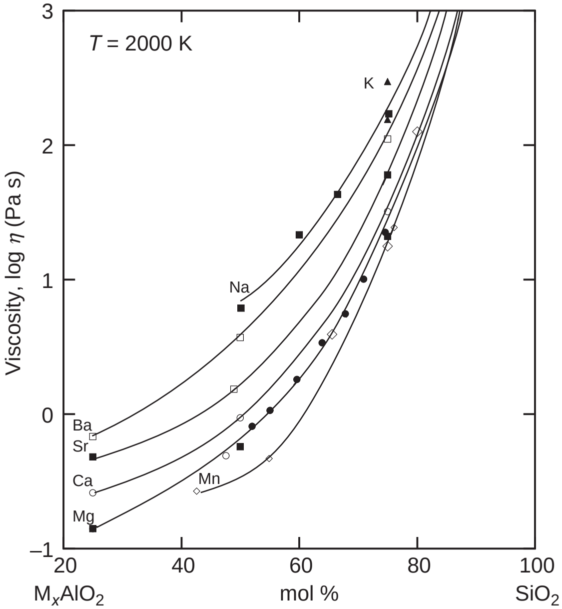

FIG. 8.19 Effects of the charge-compensating cation of Al^{3+} on viscosity along the meta-aluminous join at 2000 K. Data from Riebling (1964, 1966) for Mg and Na systems and from Arrhenian fits made to the measurements of Urbain et al. (1982) and Boiret and Urbain (1987) for the other joins.

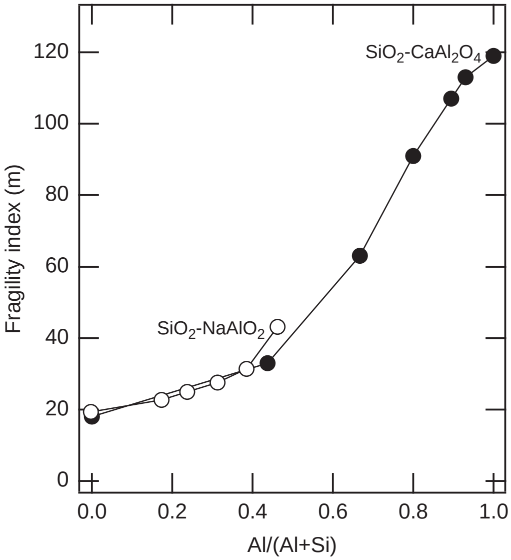

FIG. 8.20 Fragility index along the joins SiO_2-$NaAlO_2$ and SiO_2-$CaAl_2O_4$ as a function of Al/(A + Si) (data and calculations from Toplis et al., 1997b; Bouhadja et al., 2014).

measured by Hasegawa (1986) for Mg, Ca, Sr, and Ba aluminosilicates, which define trends that may depend on M_xO content.

The viscosity-composition relationships of the aluminosilicate melts are markedly nonlinear at high temperature and especially near the glass transition (Toplis et al., 1997b; Bouhadja et al., 2014). Because they originate from the same datum for SiO_2 liquid, their order

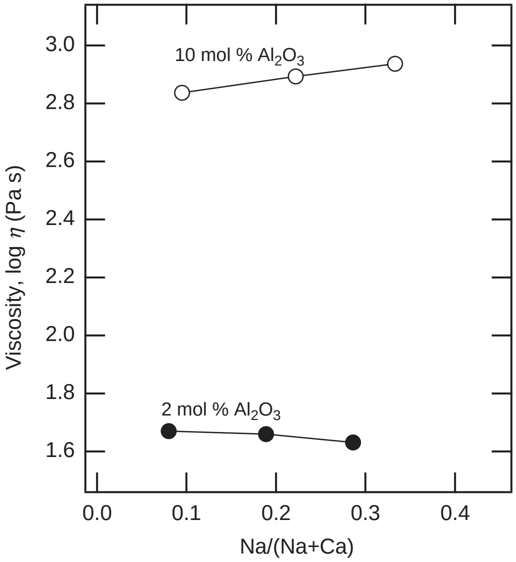

FIG. 8.21 Viscosity of peralkaline melts in the Na_2O-CaO-Al_2O_3-SiO_2 system (50 mol% SiO_2) at 1514°C as a function of Na/(Na + Ca) abundance ratio and for 2 and 10 mol% Al_2O_3 (Zhen et al., 2014).

is that of increasing deviations from Arrhenian laws or of increasing fragility (Fig. 8.16). This order is also that of increasing configurational heat capacity (see Fig. 8.7). As described in Chapter 4, Section 4.6.1, for mixed alkaline earth melts, these features are readily interpreted within the framework of configurational entropy theory according to which the temperature dependence of viscosity is inversely related to that of configurational entropy (Adam and Gibbs, 1965; Richet, 1984). Consistent with the contribution of Si ⇔ Al mixing to chemical entropy, the viscosity-composition relationship is still more nonlinear near the glass transition than at high temperatures (Fig. 8.19).

The fragility not only varies with the nature of the charge-balancing cation, but it also can be correlated with the Al/(Al + Si) along any of the silica-aluminate composition joins (Fig. 8.20). Such features often are expressed in terms of variations in the fragility index, *m*:

$$m = \partial(\log \eta)\partial/(T_g/T)\ (\text{at the glass transition temperature}). \tag{8.2}$$

The viscosity of aluminosilicate melts as a function of pressure has been a subject of study in Ca- and Na-aluminosilicate systems (Kushiro, 1976, 1981; Suzuku et al., 2002, Suzuki et al., 2005; Mori et al., 2000; Allwardt et al., 2007). As mentioned in Section 6.4.1, highly polymerized, Al-free melts exhibit decreasing viscosity with increasing pressure until reaching pressures corresponding to that where Si^{4+} coordination transformation is reached. The data in Fig. 8.22 indicate, however, relationships between pressure and melt viscosity that are more complex. In meta-aluminosilicate melts, which are highly polymerized, the nature of the charge-balancing cation clearly also plays a role. With increasing Al/(Al + Si), the viscosity in Na systems suggests an approximately constant pressure dependence. However, for melts with Ca^{2+} serving to charge-balance Al^{3+}, the pressure dependence actually becomes less pronounced with increasing Al/(Al + Si) (Fig. 8.22). Furthermore, for two compositions with the same Al/(Al + Si), the viscosity is more sensitive to pressure for Na^+ than for Ca^{2+} as a charge-balancing cation for tetrahedral Al^{3+} through an effect on the strength of the Al—O bond.

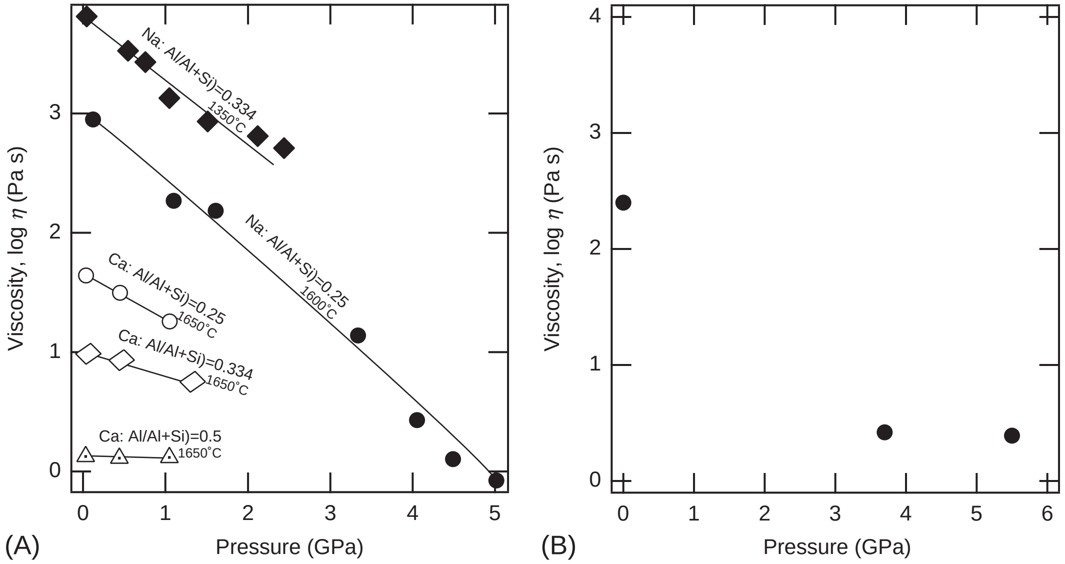

FIG. 8.22 (A) Viscosity of melts a function of pressure along the joins SiO_2-$CaAl_2O_4$ at 1650°C for different Al/(Al+Si) ratios as indicated (Kushiro, 1981) and SiO_2-$NaAlO_2$, also at different Al/(Al+Si) at the two different temperatures indicated (Brearley et al., 1986; Suzuku et al., 2002; Mori et al., 2000). (B) Viscosity in the CaO-Al_2O_3-SiO_2 system as a function of pressure at NBO/T=0.25 and 1640°C (Allwardt et al., 2007).

The viscosity data from a slightly depolymerized (NBO/T=0.25) CaO-Al_2O_3-SiO_2 melt exhibit a small decrease with pressure and reach a minimum viscosity value near 3.5 GPa and 1640°C (Fig. 8.23; see also Allwardt et al., 2007). The initial slight viscosity decrease with increasing pressure resembles that of the fully polymerized SiO_2-$CaAl_2O_4$ melt with Al/(Al+Si)=0.25. Mixed $NaAl_2O_6$-$CaMgSi_2O_6$ melts exhibit somewhat similar variations, although they show a viscosity minimum near a few GPa pressure (Suzuki et al., 2005). This decreasing effect with pressure suggests that the Al—O bonds become decreasingly compressible with increasing pressure or the Al distribution of the coexisting structural units may be pressure dependent. Current data do not permit further assessment of this situation.

8.4.1.2 Diffusion

It is commonly assumed that melt viscosity and self-diffusion of network-building ions (Si^{4+}, Al^{3+}, O^{2-}) are linked via the Eyring expression (Eq. (4.11)), as for example made by Shimizu and Kushiro (1984) in their examination of viscosity and self-diffusion in liquid $CaMgSi_2O_6$ (Fig. 4.20). However, for aluminosilicate melts, this relationship may not show the same quantitative precision. For example, in a molecular dynamics simulation study of melts along the SiO_2-$CaAl_2O_4$ join, Bouhadja et al. (2014) found significant deviations from the Eyring relations, which were more pronounced the less aluminous the melt. According to the Eyring expression, the diffusivity is proportional to the viscosity/temperature (η/T), when in fact it is commonly a power function relationship. There remains a correlation, but the relationship is not linear, as demanded by the Eyring equation.

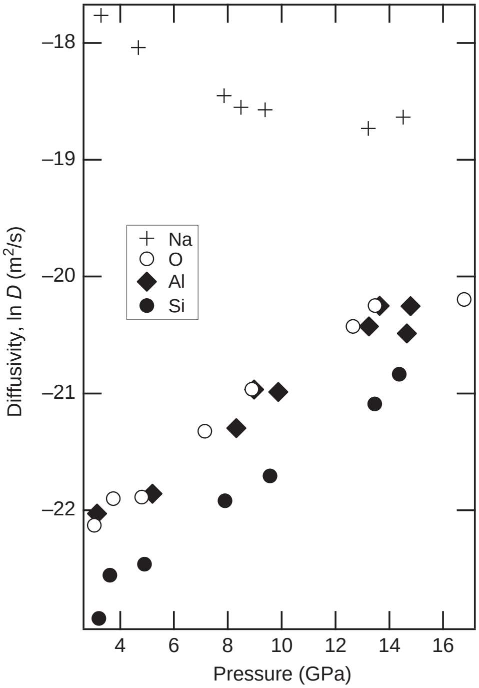

FIG. 8.23 Diffusivity as identified in $NaAlSi_2O_6$ melt simulated by molecular dynamics at 5000 K (results from Bryce et al., 1997).

Viscosity/diffusivity correlations can be seen when comparing pressure-dependent melt viscosity with self-diffusion, for example (Figs. 8.22 and 8.23). Where the viscosity of $NaAlSi_2O_6$ decreases isothermally with increasing pressure (Fig. 8.22), the diffusivity of Si, Al, and O increases (Fig. 8.23). Interestingly, though, the diffusivities of these three components are not quite the same. So, if in fact the Eyring equation holds, the jump distance of these three components must differ. It is not so clear how this can be accomplished. The Na^+ cations, on the other hand, do not follow this relationship at all, as there is a continuous sodium diffusivity decrease with increasing pressure (Fig. 8.23). This is in some ways surprising, because in these melts, all Na^{2+} is in a charge-compensating role for Al^{3+}, which would lead to a suggestion of coupling between Na^+ and Al^{3+} diffusion.

The geochemical importance of aluminosilicates has motivated numerous diffusion studies. In particular, the extensive data available for $NaAlSi_3O_8$ throw interesting light on the factors that determine atomic mobility, at least along the meta-aluminous join where diffusivities can vary by more more than 10 orders of magnitude, depending on size and electrical charge (Fig. 8.24). Weakly bonded noble gases diffuse the fastest, with a diffusivity that decreases in the order of increasing atomic size (see also Chapter 18, Section 18.3). Tracer diffusion is in general faster for alkali than for alkali earth cations (Fig. 8.24). The slowest diffusing species are Si and Ga. In these three series, the activation enthalpy for diffusion increases when the diffusivity decreases, so that the linear relationships of Fig. 8.24 tend to converge at very high temperature. For network-modifier cations, diffusivity is not affected by the glass transition but continues smoothly across this temperature (dashed line in Fig. 8.24), which indicates that relaxation of the aluminosilicate network is not a governing factor (see also Fig. 8.23).

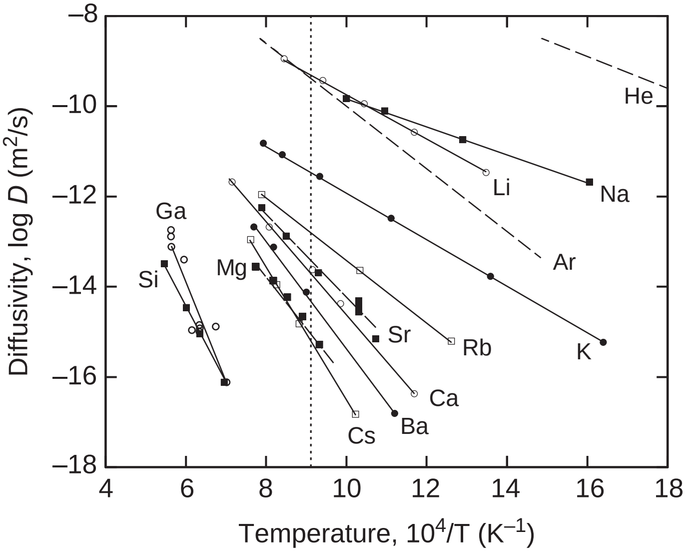

FIG. 8.24 Tracer diffusivity in glassy and molten $NaAlSi_3O_8$ against reciprocal temperature. Roselieb et al. (1992) for He and Ar; Jambon and Semet (1978) for Li; Jambon and Carron (1976) for Na, K, Rb, and Cs; Roselieb and Jambon (2002) for Mg, Sr, and Ba; Jambon and Delbove (1977) for Ca; and Baker (1995) for Si and Ga. The vertical dashed line indicates the location of the glass transition temperature for $NaAlSi_3O_8$.

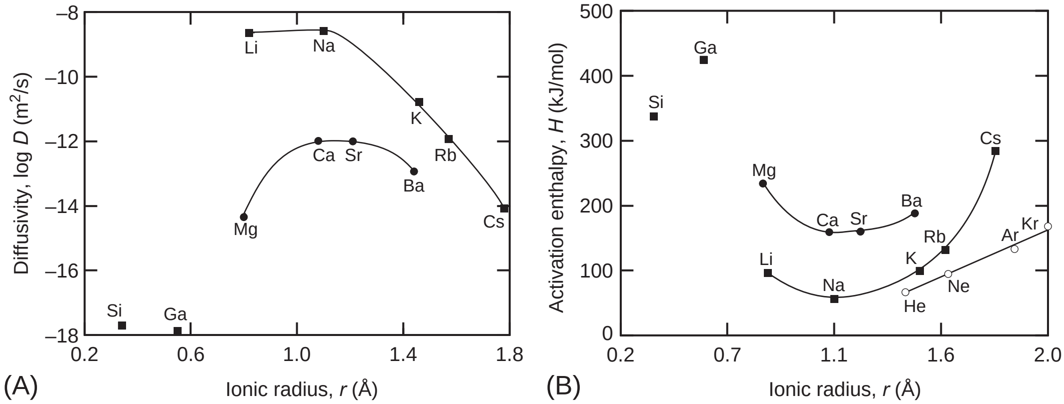

FIG. 8.25 Influence of ionic radius on diffusivity in amorphous $NaAlSi_3O_8$. (A) Tracer diffusivity at 1000°C from the data of Fig. 8.24. (B) Activation enthalpy for diffusion. Ionic radii of Whittaker and Muntus (1970).

As reviewed by Roselieb and Jambon (2002), there is a clear control of both tracer diffusivity and activation enthalpy for diffusion by the ionic radius and charge of the cation (Fig. 8.25). The simple influence of size is illustrated by noble gases, for which electrical charge does not need to be considered. For other elements, an optimum is reached for a certain ionic radius for a given charge. In a structure tailored for Na^+, the larger ionic radius of heavier alkali elements or the 2+ charge of alkaline earths lowers diffusion considerably through steric hindrance or electrostatic interactions, which is quantified by the enthalpy of diffusion (Fig. 8.25B). Because the relevant parameters are the size and especially the charge differences with Na +, diffusivities and activation energies do not vary monotonously with the ionization potential of the cation. Given the existence of the plagioclase solid solution, it is not fortuitous that Ca is the alkaline earth with the highest diffusivity and lowest activation energy for diffusion. As for Ga^{3+}, it is probably fortuitous that its data plot in Fig. 8.25 on the alkaline earth trends.

8.4.2 Volume, Expansion, and Compressibility

The volume of glasses and melts is sensitive to composition, temperature, and pressure. As a direct measure of atomic packing, volume and related properties are a sensitive probe of oxygen coordination around cations. For example, decades before NMR demonstrated the point at a microscopic scale, density and refractivity measurements by Safford and Silverman (1947) indicated that most Al^{3+} is in tetrahedral coordination because the partial molar volume of 40 cm^3/mol found for Al_2O_3 is much greater than the 25 cm^3/mol of the molar volume of corundum.

8.4.2.1 Volume and Thermal Expansion

The volume and thermal expansion of aluminosilicate melts and glasses differ. Examples are provided by data in systems such as $CaO\text{-}Al_2O_3\text{-}SiO_2$ and $Na_2O\text{-}Al_2O_3\text{-}SiO_2$ showing the distinctly different thermal expansion of the glass up to the glass transition and its melt and supercooled liquid above the glass transition temperature (Fig. 8.26; see also Lange, 1996, 1997). This large difference reflects the large configurational contribution to thermal expansivity of the melt compared to its glass. Moreover, it is again notable that expansivity of the partial molar volume of individual oxide components increases in the order $K_2O > Na_2O > CaO > MgO$ (Lange and Carmichael, 1987; Knoche et al., 1995; Lange, 1997; see also Fig. 8.27).

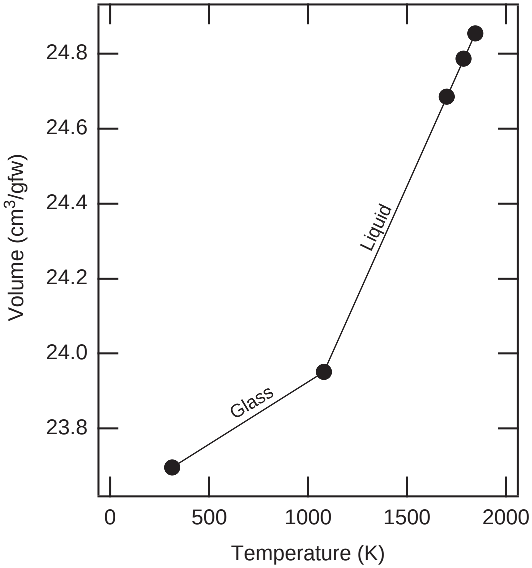

FIG. 8.26 Volume of $CaO\text{-}Al_2O_3\text{-}SiO_2$ glass and melt as a function of temperature (Lange and Carmichael, 1987).

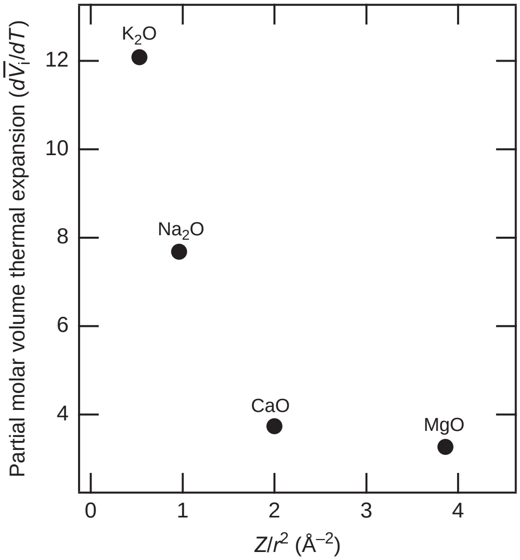

FIG. 8.27 Thermal expansion of partial molar volume of K_2O, Na_2O, CaO, and MgO in the system $K_2O\text{-}Na_2O\text{-}CaO\text{-}MgO\text{-}Al_2O_3\text{-}SiO_2$ at 1500°C (Lange, 1997).

In the early study of Bottinga and Weill (1970), it was concluded that both partial molar volume and expansivities of aluminosilicate melts could be considered as additive functions of composition. Since then, empirical models have been improved to predict density with greater accuracy or over wider temperature and composition ranges (Bottinga et al., 1982, 1983; Lange and Carmichael, 1987; Knoche et al., 1995; Lange, 1997). For this purpose, new measurements have been made on compositions scattered throughout a variety of systems (e.g., Stein et al., 1986; Lange and Carmichael, 1987; Lange, 1996). Since it is difficult to draw structural inferences from multiparameter analyses of measurements, we will consider instead data along well-defined joins. Particular attention will be paid to the circumstances under which the additive nature of molar volume could break down, and in particular to the aluminum environment in peraluminous melts.

With peraluminous melts, there is a departure from volume additivity (Bottinga et al., 1982; Takahashi et al., 2015). This departure results from the fact that the molar volume of liquid alumina (about 33 cm^3/mol above 2000°C) is lower than the 38–39 cm^3/mol derived for the partial molar volume of Al_2O_3 in peralkaline melts (Fig. 8.28). Later models have not addressed this question, however, probably because nonlinear effects are relatively small and of limited implications, at least within the composition range of geochemical interest. This means that later models have yielded lines closely resembling that of Bottinga and Weill (1970) shown in Fig. 8.28. These will all be off the real molar volumes in the peralkaline portions of aluminosilicate systems, however, because they do not consider the changing structural roles and partial molar volumes of Al_2O_3 in this region (Bottinga et al., 1982; Lange and Carmichael, 1987; Webb and Courtial, 1996; Lange, 1997).

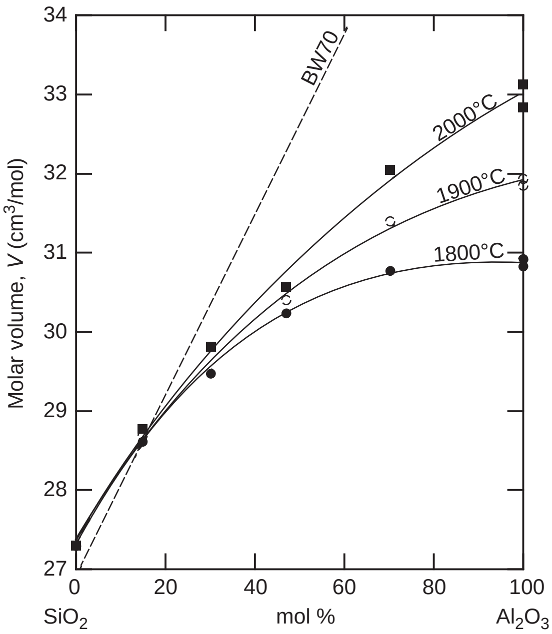

FIG. 8.28 Molar volume of binary SiO_2-Al_2O_3 melts at the temperatures indicated. Data of Aksay et al. (1979) for binary compositions, Mitin and Nagibin (1970) and Shpil'rain et al. (1973) for pure Al_2O_3, and Bottinga and Richet (1995) for SiO_2 (see also Chapter 5). The dashed curve BW70 shows the 1800°C model values of Bottinga and Weill (1970).

Reliable measurements are available for binary SiO_2-Al_2O_3 liquids in spite of technical difficulties caused by very high temperatures (Aksay et al., 1979). The data join smoothly with the data for pure Al_2O_3 and SiO_2 (Fig. 8.28). Although the thermal expansion coefficients of liquid Al_2O_3 and of the most Al_2O_3-rich melt are not well constrained, a definite nonlinearity is observed beyond about 60 mol% Al_2O_3 at 1900–2000°C, the interval where Al_2O_3 and all binary compositions could be investigated.

The manner in which the density of binary Al_2O_3-SiO_2 melts is approached from ternary metal aluminosilicate systems should depend on the nature of the M-cation. For Na^+ and Mg^{2+}, this hypothesis can be checked with the measurements made by Riebling (1964, 1966) for a series of joins at constant SiO_2 content. For the sodium system, additivity of molar volume with respect to chemical composition breaks down as soon as the meta-aluminous join is crossed (Fig. 8.29A). The extent of deviation from linearity increases with decreasing SiO_2 content and, therefore, with increasing Al_2O_3 concentration. For 50 mol% SiO_2, there is even a clear maximum in molar volume that probably lies between Al/(Al + Na) values of 0.6 and 0.8, i.e., between 30 and 40 mol% Al_2O_3. With a same SiO_2 content of 50 mol%, the single join investigated in the Mg system shows less deviation from linearity (Fig. 8.29B) than the sodium aluminosilicate system (Fig. 8.29A). The data extrapolate to a volume of 31 cm^3/mol for pure Al_2O_3 (compared with 32.5 cm^3/mol for the analogous Na join at 1800°C at which these data were extrapolated). This value is essentially the same as that of liquid Al_2O_3 on its liquidus (2073°C; see Shpil'rain et al., 1973).

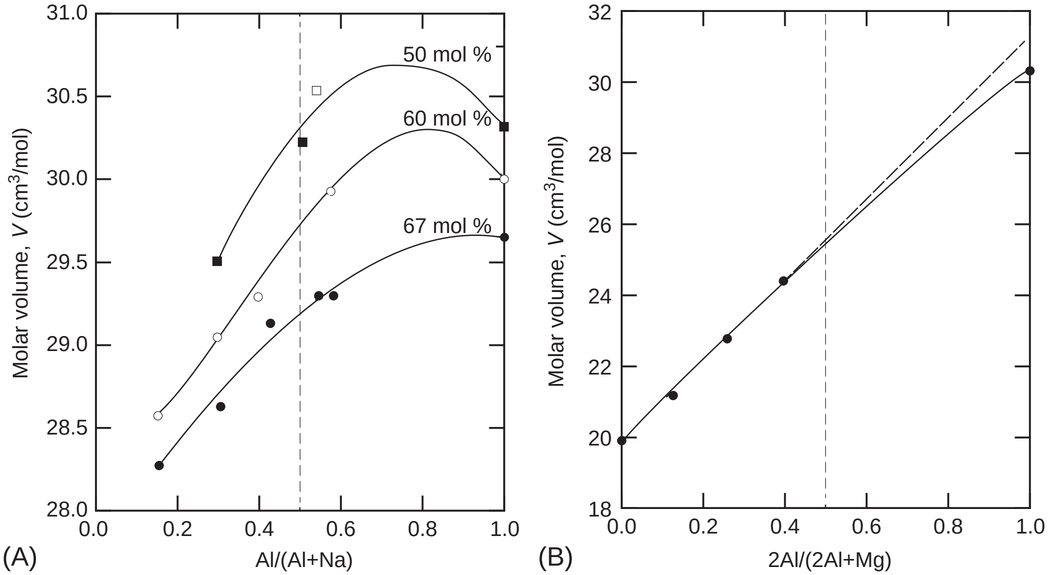

FIG. 8.29 Molar volume of alumosilicate melts at 1800°C at constant SiO_2 content. (A) Sodium aluminosilicates for the SiO_2 mol fractions indicated (Riebling, 1966). (B) Magnesium aluminosilicates at 50 mol% SiO_2; data from Riebling (1964) and Tomlinson et al. (1958) for the Al-free endmember. Note the scale difference between both diagrams, where the data for SiO_2-Al_2O_3 melts are the interpolated values of Aksay et al. (1979) in Fig. 8.28.

In summary, additive models of prediction of density break down for peraluminous melts, because the partial molar volume of alumina then depends on composition. As might be expected, the density of peralkaline melts also bears witness to the less strong association of Al^{3+} with Mg^{2+} than with Na^+. Clearly, Al^{3+} is present in a denser state in peraluminous than in peralkaline melts. But volume data cannot help to discriminate between various structural models in which Al^{3+} has a coordination higher than tetrahedral or achieves a dense arrangement through the existence of oxygen triclusters.

8.4.2.2 Pressure and Compressibility

The response of melt density to pressure typically is a combination of bond angle compression and torsion (at lower pressures) and coordination changes (at high pressures). The bond angles in aluminosilicates are somewhat more compressible than in Al-free silicates, because the Al—O bond is longer and weaker than the Si—O (see Chapter 2, Section 2.2.2). Moreover, in peralkaline aluminosilicate melts, pressure may also affect Al^{3+} distribution among the coexisting Q^n-species, which may, in turn, affect volume and compressibility (Section 9.4.2). This would be expected because compressibility is the highest for the most polymerized melts (Fig. 8.30; see also Kuryaeva and Dmitrieva, 2014) and therefore for Q^4 species, which would tend to enhance Al^{3+} partitioning into such structural units. In this environment, the nature of the charge-compensating cation is important as Al—O bonds are stiffer with divalent (e.g., alkaline earths) than with monovalent charge compensation (e.g., alkali metals). This effect is seen in the compression of meta-aluminosilicate glasses (Fig. 8.31), where the density change is greater with alkalis than with Ca^{2+} (Allwardt et al., 2005).

More attention will be paid in this section to sound velocities than to adiabatic compressibilities, because it is not possible to accurately determine densities over the whole composition range investigated, which extends to peraluminous melts. With ultrasonic methods, the

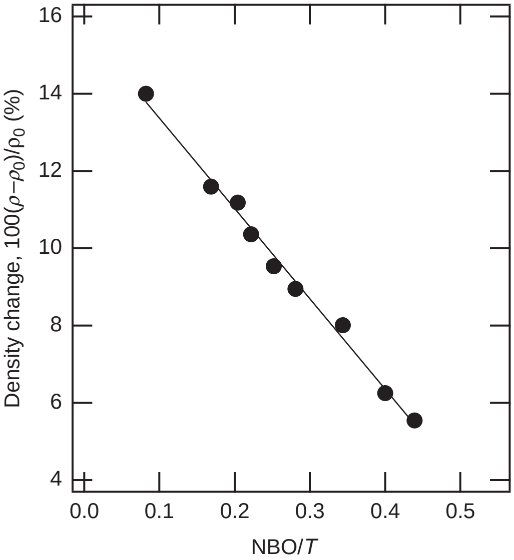

FIG. 8.30 Relative density change of Na_2O-CaO-MgO-Al_2O_3-SiO_2 glasses between ambient pressure (ρ_0) and density at 4 GPa, ρ (Kuryaeva and Dmitrieva, 2014).

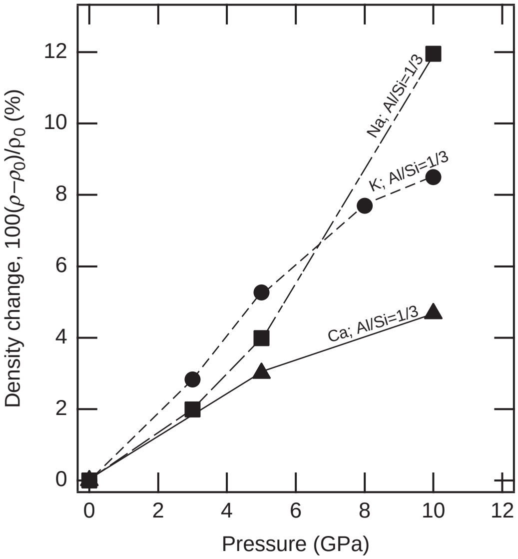

FIG. 8.31 Relative density change of aluminosilicate glasses formed by temperature-quenching of melts from above their liquidus temperature at given pressure compressed to 10 GPa. Glasses were on the meta-aluminosilicate joins with fixed Al/Si = 1/3. The K, Na, and Ca identifiers indicate the charge-compensating cation (Allwardt et al., 2005).

adiabatic compressibility (β_S) is determined from the density (ρ) and the longitudinal sound velocity (v_p) by Eq. (6.19), $\beta_S = 1/\rho v_p^2$. For aluminosilicates, the high viscosity of which can translate into long relaxation times, determination of compressibility is made difficult by the high temperatures at which measurements must be performed to achieve complete relaxation (see Section 3.4.3). At such high temperatures, composition changes induced by partial volatilization in addition become a serious concern. For alkali systems, this is why measurements are available for few compositions over narrow temperature intervals (Rivers and Carmichael, 1987; Kress et al., 1988; Ai and Lange, 2008). From an analysis of their measurements for sodium aluminosilicates, Kress et al. (1988) did, nevertheless, conclude that sound velocity is insensitive to Na/Si and increases linearly with Al_2O_3 content in peralkaline compositions, from 2450 m/s for molten sodium metasilicate to 2900 m/s for a melt with 20 mol% Al_2O_3.

These trends are not followed in calcium aluminosilicates, which have been the subject of comprehensive studies by Sokolov et al. (1970). Their results are, however, generally consistent with the less comprehensive observations of Rivers and Carmichael (1987) and Webb and Courtial (1996) in similar composition glasses and melts.

A continuous decrease in sound velocity is observed when Al^{3+} is substituted for Si^{4+} along two different joins (Fig. 8.32). As might be expected from weaker Al—O compared with Si—O bonds, in both cases these variations are offset by those of density, so that the adiabatic bulk modulus ($K_S = 1/\beta_S$) derived by Webb and Courtial (1996) actually increases with decreasing SiO_2 concentration (and increasing $Ca_{0.5}AlO_2$ content) (Fig. 8.33). The variations are not as simple when Al_2O_3 is added at constant Si/Ca (Fig. 8.32B). For Si/Ca = 2, little attention should be paid to the complex variation of sound velocity, which is due to the stable miscibility gap existing close to the limiting binary SiO_2-Al_2O_3 (Fig. 8.4; see also Galakhov et al., 1985). No such bias affects the measurements for the join at constant Si/Ca = 1. There, the

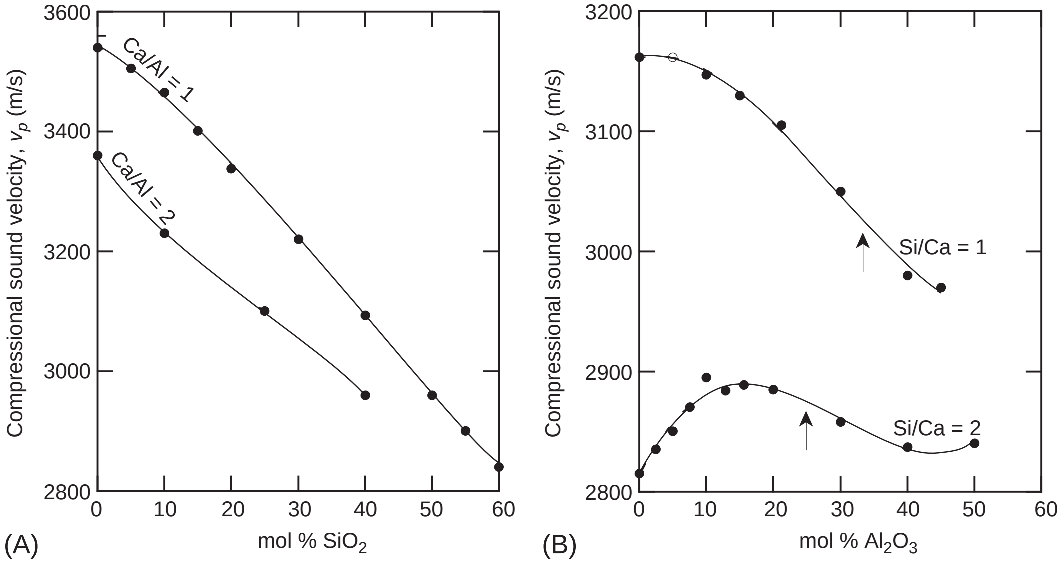

FIG. 8.32 Compressional sound velocity in calcium aluminosilicate melts at 2000 K. (A) Against SiO_2 content at constant Ca/Al. (B) Against Al_2O_3 content at constant Si/Ca; the arrows indicate the position of the meta-aluminous join. Data from Sokolov et al. (1970).

FIG. 8.33 Adiabatic bulk modulus, $K_S = 1/\beta_S$, of calcium aluminosilicates at constant Ca/Al and 1600°C. From Webb and Courtial (1996), with data of Sokolov et al. (1970), Rivers and Carmichael, (1987) and, for SiO_2, the result of Table 5.1.

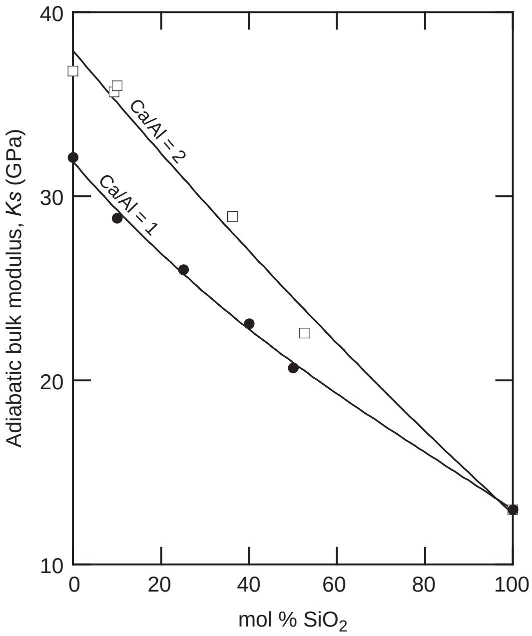

speed of sound decreases continuously with increasing Al_2O_3 content from the metasilicate composition to beyond the meta-aluminous join.

This trend should not be followed at higher alumina content, however, because the speed of sound must increase markedly to match that of pure alumina, which is about 3000 m/s (Slagle and Nelson, 1970). Actually, such an increase is suggested by the results or the most Al_2O_3-rich melts along the join $Si/Ca = 2$ (Fig. 8.32B), where an upswing toward greater sound velocity in Al-rich compositions is indicated. Combined with a marked rise in density, indicated by the plots of Figs. 8.30 and 8.31, this increase will result in a strong decrease in compressibility when the alumina endmember is approached. This effect conforms to the general trend according to which compressibility decreases with increasing density and, thus, with more compact atomic arrangement.

Like the heat capacity, the compressibility of liquids is made up of vibrational and configurational contributions. A more detailed analysis of compressibility must deal separately with both aspects. When made with Brillouin scattering, the timescale of sound velocity measurements is so short that, even above 2000 K, only the solid-like response of the liquid is probed (Section 3.4.3). The relative importance of vibrational and configurational compressibility thus can be ascertained through a combination of unrelaxed and fully relaxed measurements of sound velocity. The information obtained in this way is still very sketchy (Askarpour et al., 1993). For calcium aluminosilicates, both contributions to compressibility vary strongly with composition. The total compressibility is 4.83×10^{11} and $3.84 \times 10^{11}\,Pa^{-1}$ for molten $CaAl_2Si_2O_8$ and $Ca_3Al_2Si_3O_{12}$, of which the configurational part represents 58% and 32%, respectively. Clearly, compression and rotation of bonds represent only a fraction of the compressibility of the open, three-dimensional network of $CaAl_2Si_2O_8$. In this case, configurational changes give rise to additional compression mechanisms that are more restricted in the less polymerized structure of $Ca_3Al_2Si_3O_{12}$.

References

Adam, G., Gibbs, J.H., 1965. On the temperature dependence of cooperative relaxation properties in glass-forming liquids. J. Chem. Phys. 43, 139–146.

Ai, Y., Lange, R.A., 2008. New acoustic velocity measurements on CaO-MgO-Al_2O_3-SiO_2 liquids: reevaluation of the volume and compressibility of $CaMgSi_2O_6$-$CaAl_2Si_2O_8$ liquids to 25 GPa. J. Geophys. Res. 113, B04203. https://dx.doi.org/10.1029/2007JB005010.

Aksay, I.A., Pask, J.A., Davis, R.F., 1979. Densities of SiO_2-Al_2O_3 melts. J. Am. Ceram. Soc. 62, 332–336.

Allwardt, J.R., Stebbins, J.F., Schmidt, B.C., Frost, D.J., Withers, A.C., Hirschmann, M.M., 2005. Aluminum coordination and the densification of high-pressure aluminosilicate glasses. Am. Mineral. 90, 1218–1222.

Allwardt, J.R., Stebbins, J.F., Terasaki, H., Du, L.S., Frost, D.J., Withers, A.C., Hirschmann, M.M., Suzuki, A., Ohtani, E., 2007. Effect of structural transitions on properties of high-pressure silicate melts: Al-27 NMR, glass densities, and melt viscosities. Am. Mineral. 92, 1093–1104.

Askarpour, V., Manghnani, M.H., Richet, P., 1993. Elastic properties of diopside, anorthite, and grossular glasses and liquids: a Brillouin scattering study up to 1400 K. J. Geophys. Res. 98, 17683–17689.

Baker, D.R., 1995. Diffusion of silicon and gallium (as an analogue for aluminium) network-forming cations and their relationship to viscosity in albite melt. Geochim. Cosmochim. Acta 59, 3561–3571.

Barkhatov, L.S., Kagan, D.N., Tsytsarkin, A.F., Shpil'rain, E.E., Yakimovich, K.A., 1973. Investigation of the thermodynamic properties of molten aluminum oxide. Teplofiz. Vys. Temper. 11, 1188–1191.

Beckett, J.R., 2002. Role of basicity and tetrahedral speciation in controlling the thermodynamic properties of silicate liquids, part 1: the system CaO-MgO-Al_2O_3-SiO_2. Geochim. Cosmochim. Acta 66, 93–107.

Bockris, J.O.M., Mackenzie, J.D., Kitchener, J.A., 1955. Viscous flow in silica and binary liquid silicates. Trans. Farad. Soc. 51, 1734–1748.

Boiret, M., Urbain, G., 1987. Mesures de viscosités d'aluminosilicates de lithium. C.R. Acad. Sci. II 305, 167–169.

Bollin, P.L., 1972. Glass formation in the system Cs_2O-Al_2O_3-SiO_2. J. Am. Ceram. Soc. 55, 483.

Bondar, V.V., Lopatin, S.I., Stolyarova, V.L., 2005. High-temperature thermodynamic properties of the Al_2O_3-SiO_2 system. Inorg. Mater. 41, 362–369.

Bottinga, Y., Richet, P., 1995. Silicate melts: the "anomalous" pressure dependence of the viscosity. Geochim. Cosmochim. Acta 59, 2725–2731.

Bottinga, Y., Weill, D.F., 1970. Densities of liquid silicate systems calculated from partial molar volumes of oxide components. Am. J. Sci. 269, 169–182.

Bottinga, Y., Weill, D.F., 1972. The viscosity of magmatic silicate liquids: a model for calculation. Am. J. Sci. 272, 438–475.

Bottinga, Y., Weill, D.F., Richet, P., 1982. Density calculations for silicate liquids. I. Revised method for aluminosilicate compositions. Gechim. Cosmochim. Acta 46, 909–919.

Bottinga, Y., Richet, P., Weill, D.F., 1983. Calculation of the density and thermal expansion coefficient of silicate liquids. Bull. Mineral. 106, 129–138.

Bouhadja, M., Jakse, N., Pasturel, A., 2014. Stokes-Einstein violation and fragility in calcium aluminosilicate glass formers: a molecular dynamics study. Mol. Simul. 40, 251–259.

Bouhifd, M.A., Courtial, P., Richet, P., 1998. Configurational heat capacities: alkali vs. alkaline-earth aluminosilicate liquids. J. Non-Cryst. Solids 231, 169–177.

Brearley, M., Dickinson, J.E., Scarfe, C.M., 1986. Pressure dependence of melt viscosities on the join diopside-albite. Geochim. Cosmochim. Acta 50, 2563–2570.

Bryce, J.G., Spera, F.J., Stein, D.J., 1997. Dependence of self diffusivity on P and T in molten $NaAlSi_2O_6$: comparison of laboratory and molecular dynamics experiments. Geophys. Res. Lett. 24, 711–714.

Courtial, P., Richet, P., 1993. Heat capacity of magnesium aluminosilicate melts. Geochim. Cosmochim. Acta 57, 1267–1276.

Day, D.E., Rindone, G.E., 1962. Properties of soda aluminosilicate glasses: I, refractive index, density, molar refractivity, and infrared absorption spectra. J. Am. Ceram. Soc. 45, 489–496.

Foster, W.R., Lin, H.C., 1969. Studies in the system BaO-Al_2O_3-SiO_2 II. The binary system celsian ($BaAl_2Si_2O_8$)-silica (SiO_2). Am. J. Sci. 267A, 134–144.

Fraser, D.G., Rammensee, W., Jones, R.H., 1983. The mixing properties of melts in the system $NaAlSi_2O_6$-$KAlSi_2O_6$ as determined by Knudsen cell mass spectrometry. Bull. Mineral. 106, 111–117.

Fraser, D.G., Rammensee, W., Hardwick, A., 1985. Determination of the mixing properties of molten silicates by Knudsen cell mass specgrometry II. The systems (Na-K)$AlSi_4O_{10}$ and (Na-K)$AlSi_5O_{12}$. Geochim. Cosmochim. Acta, 349–359.

Galakhov, F.Y., Aver'yanov, V.I., Vavilonova, V.T., Areshev, M.P., 1976. The metastable liquid phase separation region in the MgO-Al_2O_3-SiO_2 system. Fiz. Khim. Stekla 2, 412–416.

Galakhov, F.Y., Aver'yanov, V.I., Vavilonova, V.T., Areshev, M.P., 1985. Liquation in the systems SrO (BaO)-Al_2O_3-SiO_2. Fiz. Khim. Stekla 11, 712–716.

Gambuzzi, E., Charpentier, T., Menziani, M.C., Pedone, A., 2015. Computational interpretation of ^{23}Na MQMAS NMR spectra: a comprehensive investigation of the Na environment in silicate glasses. Chem. Phys. Lett. 612, 56–61.

Graham, P.W.L., Rindone, G.E., 1964. Properties of soda aluminosilicate glasses: IV. Relative acidities and some thermodynamic properties. J. Am. Ceram. Soc. 47, 19–24.

Greig, J.W., 1927. On liquid immiscibility in the system FeO-Fe_2O_3-Al_2O_3-SiO_2. Am. J. Sci. 14, 473–484.

Hager, I., Hähnert, M., Hinz, W., 1967. Beitrag zur Phasentrennung in Gläsern des Systeme Na_2O-SiO_2-B_2O_3 und Na_2O-Al_2O_3-SiO_2. Silikattechnik 18, 360.

Hasegawa, Y., 1986. The influence of composition on some physical properties of glasses in the RO-Al_2O_3-SiO_2 system. Glastech. Ber. 59, 53–58.

Henderson, D., Taylor, J., 1966. Thermodynamic properties in the CaO-MgO-SiO_2 and MgO-Al_2O_3-SiO_2 systems. J. Iron Steel Inst. 204, 39–43.

Hess, P. C. & Wood, M. I. (1982). Aluminum coordination in meta aluminous and peralkaline silicate melts. Contrib. Mineral. Petrol. 81, 103–112.

Hovis, G.L., Toplis, M.J., Richet, P., 2004. Thermodynamic mixing properties of sodium silicate liquids and implications for liquid-liquid immiscibility. Chem. Geol. 213, 173–186.

Jambon, A., Carron, J.-P., 1976. Diffusion of Na, K, Rb and Cs in glasses of albite and orthoclase composition. Geochim. Cosmochim. Acta 40, 897–903.

Jambon, A., Delbove, F., 1977. Etude, à 1 bar, de la diffusion du calcium dans les verres feldspathiques. C.R. Acad. Sci. D284, 2191–2194.

Jambon, A., Semet, M., 1978. Lithium diffusion in silicate glasses of albite, orthoclase, and obsidian composition: an ion microprobe determination. Earth Planet. Sci. Lett. 37, 445–450.

Jerebtsov, D.A., Mikhailov, G.G., 2001. Phase diagram of the CaO-Al_2O_3 system. Ceram. Int. 27, 25–28.

Johnson, B.R., Kriven, W.M., Schneider, J., 2001. Crystal structure development during devitrification of quenched mullite. J. Eur. Ceram. Soc. 21, 2541–2562.

Kauzmann, W., 1948. The nature of the glassy state and the behavior of liquids at low temperatures. Chem. Rev. 43, 219–256.

Knoche, R., Dingwell, D.B., Webb, S.L., 1995. Melt densities for leucogranites and granitic pegmatites: partial molar volumes for SiO_2, Al_2O_3, Na_2O, K_2O, Li_2O, Rb_2O, Cs_2O, MgO, CaO, SrO, BaO, B_2O_3, P_2O_5, F_2O_{-1}, TiO_2, Nb_2O_5, Ta_2O_5, and WO_3. Geochim. Cosmochim. Acta 59, 4645–4652.

Kress, V.C., Williams, Q., Carmichael, I.S.E., 1988. Ultrasonic investigation of melts in the system Na_2O-Al_2O_3-SiO_2. Geochim. Cosmochim. Acta 52, 283–293.

Kuryaeva, R.G., Dmitrieva, N.V., 2014. Effect of the replacement of sodium by calcium on compressibility in the CaO(Na_2O)- Al_2O_3-SiO_2 glass system. Phys. Chem. Glasses Part B 55, 253–260.

Kushiro, I., 1976. Changes in viscosity and structure of melt of $NaAlSi_2O_6$ composition at high pressures. J. Geophys. Res. 81, 6347–6350.

Kushiro, I., 1981. Viscosity change with pressure of melts in the system CaO-Al_2O_3-SiO_2. Carnegie Instn. Washington Year Book 80, 339–341.

Lacy, E.D., 1963. Aluminium in glasses and melts. Phys. Chem. Glasses 4, 234–238.

Lange, R.A., 1996. Temperature independent thermal expansivities of sodium aluminosilicate melts between 713 and 1835 K. Geochim. Cosmochim. Acta 60, 4989–4996.

Lange, R.A., 1997. A revised model for the density and thermal expansivity of K_2O-Na_2O-CaO-MgO-Al_2O_3-SiO_2 liquids from 700 to 1900 K: extension to crustal magmatic temperatures. Contrib. Mineral. Petrol. 130, 1–11.

Lange, R.A., Carmichael, I.S.E., 1987. Densities of Na_2O-K_2O-CaO-MgO-Fe_2O_3-Al_2O_3-TiO_2-SiO_2 liquids: new measurements and derived partial molar properties. Geochim. Cosmochim. Acta 51, 2931–2946.

Le Losq, C., Neuville, D.R., 2013. Effect of the Na/K mixing on the structure and the rheology of tectosilicate silica-rich melts. Chem. Geol. 346, 57–71.

Lee, S.K., Stebbins, J.F., 2003. The distribution of sodium ions in aluminosilicate glasses: a high-field Na-23 MAS and 3Q MAS NMR study. Geochim. Cosmochim. Acta 67, 1699–1709.

Lejeune, A.M., Richet, P., 1995. Rheology of crystal-bearing silicate melts; an experimental study at high viscosities. J. Geophys. Res. B 100, 4215–4229.

Levin, E.M., Robbins, C.R., McMurdie, H.F., 1964. Phase Diagrams for Ceramists, second ed. Am. Ceram. Soc., Columbus.

Longhi, J., Hays, J.F., 1979. Phase equilibria and solid solution along the join $CaAl_2Si_2O_8$-SiO_2. Am. J. Sci. 279, 876–890.

MacDowell, J.F., Beall, G.H., 1969. Immiscibility and crystallization in Al_2O_3-SiO_2 glasses. J. Am. Ceram. Soc. 52, 17–25.

Mazurin, O.V., Roskova, G.P., Porai-Koshits, E.A., 1984. Immiscibility diagrams of oxide glass-forming systems. In: Mazruin, O.V., Porai-Koshits, E.A. (Eds.), In Phase Separation in Glass, pp. 103–142. North Holland.

Mills, K.C., 2018. Metallurgical slags. In: Richet, P. (Ed.), Encyclopedia of Glass Science, Technology, History and Culture. J. Wiley & Sons, Hoboken, NJ.

Mitin, B.S., Nagibin, Y.A., 1970. Density of molten aluminum oxide. Russ. J. Phys. Chem. 44, 741–742.

Moir, G.K., Glasser, F.P., 1976. Phase equilibria in the glass-forming region of the system Na_2O-CaO-Al_2O_3-SiO_2. Phys. Chem. Glasses 17, 45–53.

Mori, S., Ohtani, E., Suzuki, A., 2000. Viscosity of albite melt to 7 GPa at 2000K. Earth Planet. Sci. Lett. 175, 87–92.

Mysen, B.O., 1987. Magmatic silicate melts: relations between bulk composition, structure and properties. In: Mysen, B.O. (Ed.), Magmatic Processes: Physicochemical Principles. Elsevier, pp. 375–400.

Mysen, B.O., Toplis, M.J., 2007. Structural behavior of Al^{3+} in peralkaline, meta-aluminous, and peraluminous silicate melts and glasses at ambient pressure. Am. Mineral. 92, 933–946.

Navrotsky, A., 1994. Physics and Chemistry of Earth Materials. Cambridge University Press, Cambridge.

Navrotsky, A., Peraudeau, G., McMillan, P., Coutures, J.P., 1982. A thermochemical study of glasses and crystals along the joins silica-calcium aluminate and silica-sodium aluminate. Gechim. Cosmochim. Acta 46, 2039–2047.

Neuville, D.R., 1992. Etude des propriétés thermodynamiques et rhéologiques des silicates fondus. Ph. D. Thesis, Université Paris 7.

Neuville, D.R., Richet, P., 1991. Viscosity and mixing in molten (Ca,Mg) pyroxenes and garnets. Geochim. Cosmochim. Acta 55, 1011–1019.

Neuville, D.R., Cormier, L., Massiot, D., 2006. Al coordination and speciation in calcium aluminosilicate glasses: effects of composition determined by Al-27 MQ-MAS NMR and Raman spectroscopy. Chem. Geol. 229, 173–185.

Osaka, A., Ono, M., Takahashi, K., 1987. Aluminum oxide anomaly and structure model of alkali aluminosilicate glasses. J. Am. Ceram. Soc. 70, 242–245.

Osborn, E.F., 1942. The system $CaSiO_3$-diopside-anorthite. Am. J. Sci. 240, 751–788.

Osborn, E.F., Muan, A., 1960a. Phase Equilibrium Diagrams for Ceramists. Plate 4. The System Na_2O-Al_2O_3-SiO_2. American Ceramic Society, Columbus, OH.

Osborn, E.F., Muan, A., 1960b. Phase Equilibrium Diagrams of Oxide Systems. Plate 2. The System CaO-Al_2O_3-SiO_2. American Ceramic Society, Columbus, OH.

Osborn, E.F., Muan, A., 1960c. Phase Equilibrium Diagrams of Oxide Systems. Plate 3. The System MgO-Al_2O_3-SiO_2. American Ceramic Society, Columbus, OH.

Osborn, E.F., Muan, A., 1960d. Phase Equilibrium Diagrams of Oxide Systems. Plate 5. The System K_2O-Al_2O_3-SiO_2. American Ceramic Society, Columbus, OH.

Osborn, E.F., Schairer, J.F., 1941. The ternary system pseudo-wollastonite-akermanite-gehlenite. Am. J. Sci. 239, 715–763.

Rein, R.H., Chipman, J., 1965. Activities in the liquid solution SiO_2-CaO-MgO at 1600°C. Trans. AIME 233, 415–425.

Richet, P., 1984. Viscosity and configurational entropy of silicate melts. Geochim. Cosmochim. Acta 48, 471–483.

Richet, P., Bottinga, Y., 1984a. Anorthite, andesine, wollastonite, diopside, cordierite and pyrope: thermodynamics of melting, glass transitions, and properties of the amorphous phases. Earth Planet. Sci. Lett. 67, 415–432.

Richet, P., Bottinga, Y., 1984b. Glass transitions and thermodynamic properties of amorphous SiO_2, $NaAlSi_nO_{2n+1}$ and $KAlSi_3O_8$. Geochim. Cosmochim. Acta 48, 453–470.

Richet, P., Bottinga, Y., 1986. Thermochemical properties of silicate glasses and liquids: a review. Rev. Geophys. 24, 1–25.

Richet, P., Bottinga, Y., 1995. Rheology and configurational properties of silicate melts. In: Stebbins, J.F., McMillan, P.F., Dingweel, D.B. (Eds.), Rev. Mineral. Mineralogical Society of America, Washington, DC, pp. 67–93.

Richet, P., Neuville, D.R., 1992. Thermodynamics of silicate melts; configurational properties. In: Saxena, S.K. (Ed.), Thermodynamic Data; Systematics and Estimation. Vol. 10.Springer, New York, NY, United States, pp. 132–161.

Richet, P., Bottinga, Y., Denielou, L., Petitet, J.P., Téqui, C., 1982. Thermodynamic properties of quartz, cristobalite and amorphous SiO_2: drop calorimetry measurements between 1000 and 1800K and a review from 0 to 2000K. Geochim. Cosmochim. Acta 46, 2639–2658.

Richet, P., Bottinga, Y., Tequi, C., 1984. Heat capacity of sodium silicate liquids. J. Am. Ceram. Soc. 67, C6–C8.

Richet, P., Robie, P.A., Hemingway, B.S., 1993. Entropy and structure of silicate glasses and melts. Geochim. Cosmochim. Acta 57, 2751–2766.

Richet, P., Nidaira, A., Neuville, D.R., Atake, T., 2009. Aluminum speciation, vibrational entropy and short-range order in calcium aluminosilicate glasses. Geochim. Cosmochim. Acta 73, 3894–3904.

Riebling, E.F., 1964. Structure of magnesium aluminosilicate liquids at 1700°C. Can. J. Chem. 42, 2811–2821.

Riebling, E.F., 1966. Structure of sodium aluminosilicate melts containing at least 50 mole % SiO_2 at 1500°C. J. Chem. Phys. 44, 2857–2865.

Risbud, S.H., Pask, J.A., 1977. Calculated thermodynamic data and metastable immiscibility in system SiO_2-Al_2O_3. J. Am. Ceram. Soc. 60, 418–424.

Rivers, M., Carmichael, I.S.E., 1987. Ultrasonic studies of silicate melts. J. Geophys. Res. 92, 9247–9270.

Roselieb, K., Jambon, A., 2002. Tracer diffusion of Mg, Ca, Sr, and Ba in Na-aluminosilicate melts. Geochim. Cosmochim. Acta 66, 109–123.

Roselieb, K., Rammensee, W., Büttner, H., Rosenhauer, M., 1992. Solubility and diffusion of noble gases in vitreous albite. Chem. Geol. 96, 241–266.

Roskosz, M., Toplis, M.J., Richet, P., 2005. Experimental determination of crystal growth rates in highly supercooled aluminosilicate liquids: implications for rate-controlling processes. Am. Mineral. 90, 1146–1155.

Roy, B.N., Navrotsky, A., 1984. Thermochemistry of charge-coupled substitutions in silicate glasses: the systems $M^{n+}_{1/n}AlO_2$-SiO_2 (M = Li, Na, K, Rb, Cs, Mg, Ca, Sr, Ba, Pb). J. Am. Ceram. Soc. 67, 606–610.

Ryerson, F.J., 1985. Oxide solution mechanisms in silicate melts: systematic variations in the activity coefficient of SiO_2. Geochim. Cosmochim. Acta 49, 637–651.

Safford, H.W., Silverman, A., 1947. Alumina-silica relationship in glass. J. Am. Ceram. Soc. 30, 203–211.

Savva, M.A., Newns, G.R., 1971. Metastable liquid-liquid immiscibility in the lithium aluminium silicate system. IXthInternational Congress on Glass. Institut du verre, Paris, pp. 419–424.

Schairer, J.F., Bowen, N.L., 1947. The system anorthite-leucite-silica. Bull. Commun. Géol. Finl. 20, 67–87.

Schairer, J.F., Bowen, N.L., 1955. The system K_2O-Al_2O_3-SiO_2. Am. J. Sci. 253, 681–746.

Schairer, J.F., Bowen, N.L., 1956. The system Na_2O-Al_2O_3-SiO_2. Am. J. Sci. 254, 129–195.

Shelby, J.E., 1978. Viscosity and thermal expansion of lithium aluminosilicate glasses. J. Appl. Phys. 49, 5885–5891.

Shimizu, N., Kushiro, I., 1984. Diffusivity of oxygen in jadeite and diopside melts at high pressures. Geochim. Cosmochim. Acta 48, 1295–1303.

Shornikov, S.I., Archakov, I.Y., 2002. A mass spectrometric determination of the enthalpies and entropies of Al_2O_3-SiO_2 melts. Russ. J. Phys. Chem. 76, 1054–1060.

Shpil'rain, E.E., Yakimovich, K.A., Tsitsarkin, A.F., 1973. Experimental study of the density of liquid alumina up to 2750°C. High Temp. High Press. 5, 191–198.

Sipp, A., Richet, P., 2002. Equivalence of volume, enthalpy and viscosity relaxation kinetics in glass-forming silicate liquids. J. Non-Cryst. Solids 298, 202–212.

Slagle, O.D., Nelson, R.P., 1970. Adiabatic compressibility of molten alumina. J. Am. Ceram. Soc. 53, 637–638.

Sokolov, L.N., Baidov, V.V., Kunin, L.L., 1970. Ultrasonic study of melts of the calcium oxide-aluminum oxide-silicon dioxide ternary system. Svoista Strukt. Shlakovykh Rasplatov, 94–100.

Stein, D.J., Stebbins, J.F., Carmichael, I.S.E., 1986. Density of molten aluminosilicates. J. Am. Ceram. Soc. 69, 396–399.

Stolyarova, V.L., 2008. Thermodynamic properties and structure of ternary silicate glass-forming melts: experimental studies and modeling. J. Non-Cryst. Solids 354, 1373–1377.

Stolyarova, V.L., Lopatin, S.I., Fabrichnaya, O.B., 2011. Thermodynamic properties of silicate glasses and melts: VIII system MgO-Al_2O_3-SiO_2. Russ. J. Gen. Chem. 81, 2051–2061.

Sukenaga, S., Saito, N., Kawakami, K., Nakashima, K., 2006. Viscosities of CaO-SiO_2-Al_2O_3 (R_2O or RO) melts. ISIJ Int. 46, 352–358.

Suzuki, A., Ohtani, E., Terasaki, H., Funakoshi, K., 2005. Viscosity of silicate melts in $CaMgSi_2O_6$–$NaAlSi_2O_6$ system at high pressure. Phys. Chem. Minerals 32, 140–145.

Suzuku, A., Ohtani, E., Funakoshi, K., Terasaki, H., Kubo, T., 2002. Viscosity of albite melt at high pressure and high temperature. Phys. Chem. Mineral. 29, 159–165.

Takahashi, S., Neuville, D.R., Takebe, H., 2015. Thermal properties, density and structure of percalcic and peraluminus CaO-Al_2O_3-SiO_2 glasses. J. Non-Cryst. Solids 411, 5–12.

Tangeman, J.A., Lange, R.A., 1998. The effect of Al^{3+}, Fe^{3+}, and Ti^{4+} on the configurational heat capacities of sodium silicate liquids. Phys. Chem. Minerals 26, 83–99.

Taylor, T.D., Rindone, G.E., 1970. Properties of soda aluminosilicate glasses: V, low-temperature viscosities. J. Am. Ceram. Soc. 53, 692–695.

Tilley, C.E., 1933. The ternary system Na_2SiO_3-$Na_2Si_2O_5$-$NaAlSiO_4$. Mineral. Petr. Mitt. 43, 406–421.

Tomlinson, J.W., Heynes, M.S.R., Bockris, J.O.M., 1958. The structure of liquid silicates. Part 2. Molar volume and expansivities. Trans. Farad. Soc. 54, 1822–1834.

Toplis, M.J., Dingwell, D.B., 2004. Shear viscosities of CaO-Al_2O_3-SiO2, and MgO-Al_2O_3-Si_{O2} liquids: implications for the structural role of aluminium and the degree of polymerisation of synthetic and natural aluminosilicate melts. Geochim. Cosmochim. Acta 68, 5169–5188.

Toplis, M.J., Dingwell, D.B., Hess, K.-U., Lenci, T., 1997a. Viscosity, fragility, and configuration entropy of melts along the join SiO_2-$NaAlO_2$. Am. Mineral. 82, 979–990.

Toplis, M.J., Dingwell, D.B., Lenci, T., 1997b. Peraluminous viscosity maxima in Na_2O-Al_2O_3-SiO_2 liquids: the role of triclusters in tectosilicate melts. Gechim. Cosmochim. Acta 61, 2605–2612.

Topping, J.A., Murthy, M.K., 1973. Effect of small additions of Al_2O_3 and Ga_2O_3 on the immiscibility temperature of Na_2O-SiO_2 glasses. J. Am. Ceram. Soc. 56, 270–275.

Urbain, G., 1983. Viscosité de liquides du système CaO-Al_2O_3. Rev. Int. Hautes Temp. Réfract. 20, 135–139.

Urbain, G., Bottinga, Y., Richet, P., 1982. Viscosity of liquid silica, silicates and aluminosilicates. Geochim. Cosmochim. Acta 46, 1061–1072.

Webb, S.L., 2008. Configurational heat capacity of Na2O–CaO–Al_2O_3–SiO_2 melts. Chem. Geol. 256, 92–101.

Webb, S.L., 2011. Configurational heat capacity and viscosity of (Mg, Ca, Sr, Ba)O-Al_2O_3-SiO_2 melts. Eur. J. Mineral. 23, 487–497.

Webb, S., Courtial, P., 1996. Compressibility of melts in the CaO-Al_2O_3-SiO_2 system. Geochim. Cosmochim. Acta 60, 75–86.

Webb, S.L., Muller, E., Buttner, H., 2004. Anomalous rheology of peraluminous melts. Am. Mineral. 89, 812–818.

Whittaker, E.J.W., Muntus, R., 1970. Ionic radii for use in geochemistry. Geochim. Cosmochim. Acta 34, 945–957.

Yue, Y., Solvang, M., 2018. Stone and glass wool. In: Richet, P. (Ed.), Encyclopedia of Glass Science, Technology, History and Culture. J. Wiley & Sons, Hoboken, NJ.

Zaitsev, A.I., Litvina, A.D., Lyakishev, N.P., Mogutnov, B.M., 1997. Thermodynamics of CaO-Al_2O_3-SiO_2 and CaF_2-CaO-Al_2O_3-SiO_2 melts. J. Chem. Soc. Faraday T. 93, 3089–3098.

Zhen, Y.L., Zhang, G.H., Tang, X.L., Chou, K.C., 2014. Influences of Al_2O_3/CaO and Na_2O/CaO ratios on viscosities of CaO-Al_2O_3-SiO_2-Na_2O melts. Metall. Mater. Trans. B Process Metall. Mater. Process. Sci. 45, 123–130.

CHAPTER

9

Structure of Aluminosilicate Glass and Melt

OUTLINE

9.1 INTRODUCTORY COMMENTS

Aluminosilicate melts and glasses are defined as peralkaline or peraluminous depending on whether or not there are sufficient metal cations to charge-compensate Al^{3+} in tetrahedral coordination. The term *charge-balance* sometimes is used as synonymous with *charge-compensation*. In ternary metal oxide aluminosilicates, meta-aluminosilicate joins, SiO_2-$M^{n+}Al_nO_{2n}$, where M is the metal cation serving to charge-compensate tetrahedrally coordinated Al^{3+}, separates peraluminous from peralkaline compositions (Fig. 9.1). Hence, peralkaline, meta-aluminous, and peraluminous compositions are discussed separately in this chapter.

https://doi.org/10.1016/B978-0-444-63708-6.00009-0

FIG. 9.1 Compositional relations between peralkaline, peraluminous, and meta-aluminous compositions in the system $M^{n+}O_{n/2}$-Al_2O_3-SiO_2 where M is an alkali and alkaline earth oxide.

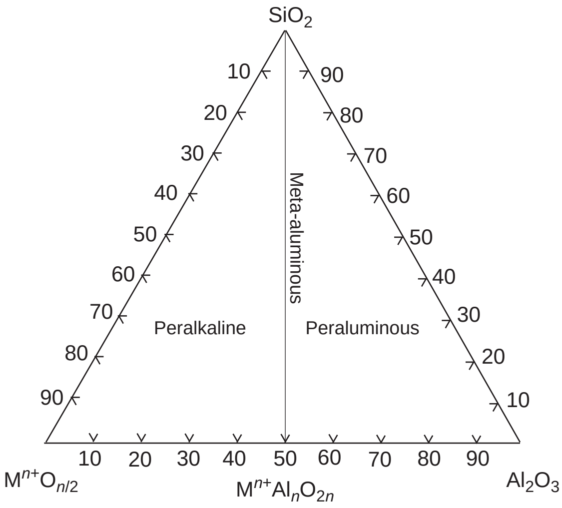

9.2 NUMERICAL SIMULATION OF STRUCTURE

In aluminosilicate systems, as for other compositions, numerical simulation can be quite helpful to deduce structure and structural trends with compositions that cannot readily be examined experimentally. Such limitations may include problems associated with quenching a melt to a glass as seen along SiO_2-Al_2O_3 joins (Sato et al., 1991), or where melting temperatures are so high that controlled laboratory experimentation becomes excessively challenging.

9.2.1 Compositions Without Charge-Balance

Compositions without or with insufficient metal cations for charge-balance of Al^{3+} define the peraluminous field outlined in Fig. 9.1. Compositions without any charge-balance lay along the join SiO_2-Al_2O_3. The endmember SiO_2 was discussed in Chapter 5. Here we will discuss simulations of amorphous Al_2O_3 (Ahuja et al., 1998; Hemmati et al., 1999; Gutierrez and Johansson, 2002) and structural simulations of melt and glass compositions along the join Al_2O_3-SiO_2 (Belashchenko and Fedko, 1992; Pfleiderer et al., 2006; Hoang et al., 2007).

9.2.1.1 Al_2O_3 Simulations

The ultimate Al-bearing melt is pure Al_2O_3. The average Al—O distance from molecular simulation is in the range 1.71–1.79 Å, which is that expected for Al^{3+} in tetrahedral coordination forming an AlO_4 tetrahedron (Ahuja et al., 1998; Gutierrez and Johansson, 2002). In comparison, the Al—O distance in crystal structures with sixfold coordination, such as jadeite, averages about 1.9 Å (Prewitt and Burnham, 1966).

The simulated Al—O—Al bond-angle distribution is asymmetric or may even exhibt two distinct peaks (Fig. 9.2). The angle distribution maxima, near 100 degrees and about 120 degrees, have led to different interpretations. For example, Hemmati et al. (1999)

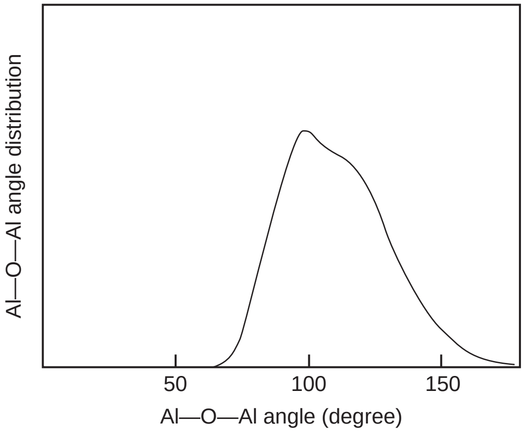

FIG. 9.2 Al—O—Al angle distribution computed at 2390°C and ambient pressure (after Hemmati et al., 1999).

proposed that this distribution reflects coexisting four-, five-, and sixfold coordination of Al^{3+}, with fivefold coordination dominating. Belashchenko and Fedko (1992) concluded that five- and fourfold coordinated Al^{3+} exist in about equal proportions in molten Al_2O_3. Gutierrez and Johansson (2002), on the other hand, concluded from analogous data that the average oxygen coordination around Al^{3+} is slightly higher than 4 (4.25), where about 85% of the Al^{3+} exists in fourfold coordination. This conclusion also is in accord with that of Ahuja et al. (1998), who found that Al^{3+} is in fourfold coordination, based on the good agreement between the calculated and experimental (Ansell et al., 1997) melting temperature of Al_2O_3.

9.2.1.2 Al_2O_3-SiO_2 Simulations

Simulated Al_2O_3-SiO_2 melt and glass structures reveal some environmental similarities for Al^{3+} compared with that of the pure Al_2O_3 endmember. However, differences also exist, which tend to grow as the compositions become more SiO_2-rich. For example, oxygen triclusters have been reported to be quite common in SiO_2-Al_2O_3 melts and glasses (Winkler et al., 2004; Tossell and Horbach, 2005; Pfleiderer et al., 2006). Moreover, the AlO_4 tetrahedra that coexist with SiO_4 tetrahedra seem quite different, in that edge-sharing is common for AlO_4 but has not been reported for SiO_4 tetrahedra, at least not at ambient pressure.

There is also a distribution of Al—O polyhedra with different oxygen coordination. For example, Hoang et al. (2007) computed angle distributions in relaxed melt and in Al_2O_3-SiO_2 glass and found evidence for multiple average angles for a composition such as $Al_2O_3{\cdot}2SiO_2$ (Fig. 9.3). Those data were interpreted to suggest Si—O and Al—O coordination numbers. The average oxygen coordination number from this and similar calculations for Al_2O_3-SiO_2 glasses and melts ranges between about 4.5 and 5 (Winkler et al., 2004; Pfleiderer et al., 2006; Hoang et al., 2007). These coordination numbers also appear to depend on temperature as Pfleiderer et al. (2006) found that the abundance of three- and fivefold coordinated Al^{3+} diminishes with increasing temperature, whereas fourfold coordinated Al^{3+} becomes increasingly abundant (Fig. 9.4). Such a general trend seems independent of the Si/Al ratio, although this ratio will affect the relative abundances of these different structural forms of Al^{3+} (Winkler et al., 2004; Pfleiderer et al., 2006).

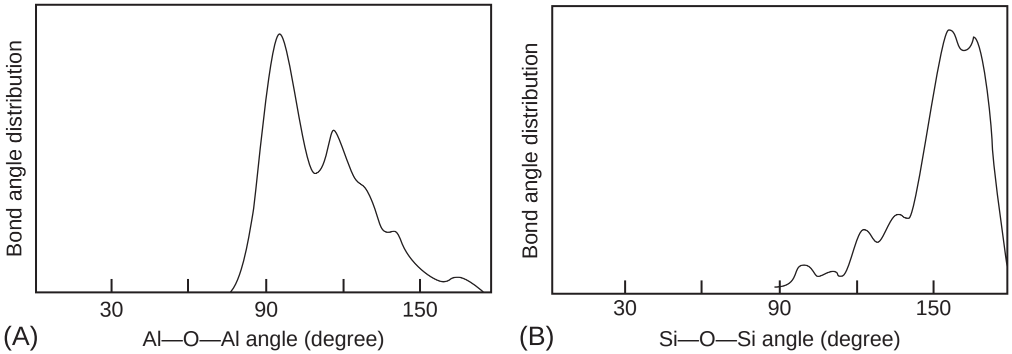

FIG. 9.3 Simulated angle distributions of $Al_2O_3{\cdot}2SiO_2$ glass (relaxed at 350 K). (A) Al—O—Al angle distribution. (B) Si—O—Si angle distribution. *(B) Redrawn from Hoang et al. (2007).*

FIG. 9.4 Simulated Al coordination number for Al^{3+} in Al_2O_3-SiO_2 melt (13 mol% Al_2O_3=) at $T > 2000$ K (calculations by Pfleiderer et al., 2006).

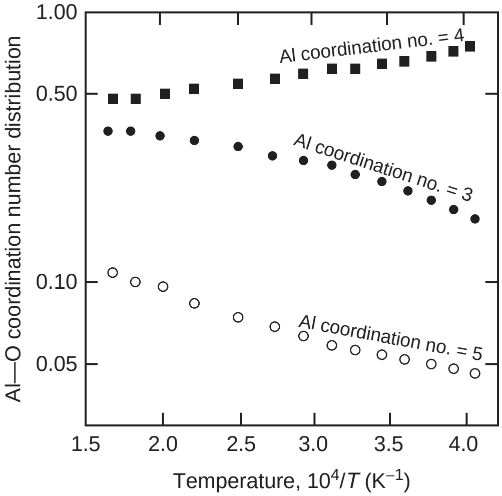

9.2.2 Composition With Charge-Balanced Al^{3+}

Charge-balance or charge-compensation for tetrahedrally coordinated cations with formal charge different from 4 was discussed in Chapter 4, Section 4.4. Among cations requiring charge-balance, Al^{3+} is the most common and likely also the most stable (Connelly et al., 2011). The relative stability and properties of aluminate complexes thus formed vary with the electronic properties of the charge-compensating cation. It has been shown from melt viscosities (Bottinga and Weill, 1972) and thermochemical measurements of glasses (Navrotsky et al., 1985) that there is a simple hierarchy of relative stability of the order $K^+ > Na^+ > Li^+ > Ca^{2+} > Mg^{2+}$ and so on.

Aluminum-bearing glasses and melts where all or some of the Al^{3+} is charge-compensated can be divided into those with and without SiO_2. Most of the results of such calculations have been for compositions of the type $M^{n+}{}_{2/n}O\text{-}Al_2O_3$ (Kang et al., 2006; Jahn, 2008; Wu et al., 2015) and compositions along meta-aluminosilicate joins, $SiO_2\text{-}M^{n+}Al_nO_{2n}$ (Kubicki and Sykes, 1993; Benoit et al., 2001; Morgan and Spera, 2001; Kubicki and Toplis, 2002; Bouhadja et al., 2013), with fewer simulations for peralkaline and peraluminous compositions (Angeli et al., 2000; Cormier et al., 2003; Benoit et al., 2005; Pedone et al., 2012).

9.2.2.1 $M^{n+}{}_{2/n}O\text{-}Al_2O_3$ Simulations

Numerical simulation of metal oxide-alumina glasses and melts has focused on Ca and Mg aluminates (Cormier et al., 2003; Poe et al., 1994; McMillan et al., 1996a, b; Kang et al., 2006; Jahn, 2008; Wu et al., 2015). Along this join, the average Al—O distance in glasses and melts is near 1.76 Å, as expected for tetrahedrally coordinated Al^{3+} (Kang et al., 2006). However, the average Al—O and Ca—O coordination numbers increase from about 5.5 to near 6 with increasing Al^{3+} in simulated $CaO\text{-}Al_2O_3$ melt structures (Table 9.1; see also Kang et al., 2006). There is a range of oxygen coordination numbers around Ca^{2+}. The maximum is near 6 with, however, a broad distribution around this value (Benoit et al., 2005).

Along both $MgO\text{-}Al_2O_3$ and $CaO\text{-}Al_2O_3$ joins, numerical simulation results show that the degree of depolymerization, here defined as NBO/Al, is positively correlated with the M/Al ratio ($0.5\ M^{2+} > Al^{3+}$) (Cormier et al., 2003; Jahn, 2008; Wu et al., 2015; see also Fig. 9.5). If we assume that bridging and nonbridging oxygens are the only contributors to polymerization, these melts, be they Mg- or Ca-aluminates, become increasingly depolymerized as the metal cation abundance increases. Notably, in the $MgO\text{-}Al_2O_3$ system, the proportion of nonbridging oxygen increases continuously beginning from near pure Al_2O_3 melt (Jahn, 2008). There is a significant proportion of oxygen triclusters, the abundance of which diminishes with increasing Ca/Al as well as Mg/Al ratios. In addition, the abundance of bridging oxygen in the $MgO\text{-}Al_2O_3$ glasses from these simulations is more than 50% lower than in the equivalent $CaO\text{-}Al_2O_3$ system, and the abundance of nonbridging oxygens much higher. Moreover, the proportions of free oxygens and triclusters are also higher in the $MgO\text{-}Al_2O_3$ system (see Jahn, 2008; Wu et al., 2015).

In their simulations of melts along the $CaO\text{-}Al_2O_3$ join, Cormier et al. (2003) concluded that Q^n-species, conceptually analogous to those in silicate systems but with Al^{3+} as the tetrahedrally coordinated cation, replace Si^{4+}. This concept was expanded further by Wu et al. (2015), who computed Q^n-species abundances along the join $CaO\text{-}Al_2O_3$ (Fig. 9.6). Here, increasing the CaO abundance leads to a decrease in Q^4 and an increase in Q^3 and Q^2 as in the analogous

TABLE 9.1 Structure Parameters for Glasses Along the Join $CaO\text{-}Al_2O_3$ Simulated at 300 K and 0.1 MPa (data from Kang et al., 2006)

	30 mol% Al_2O_3	38 mol% Al_2O_3	50 mol% Al_2O_3	60 mol% Al_2O_3
CN (Al—O)	4.05	4.14	4.44	4.53
Al—O distance (Å)	1.76	1.76	1.76	1.78
CN (Ca—O)	5.59	5.57	5.87	5.89
Ca—O distance (Å)	2.32	2.32	2.34	2.34

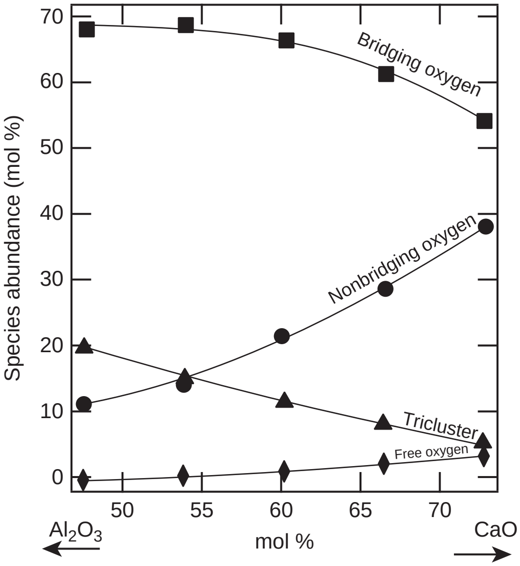

FIG. 9.5 Abundance evolution of oxygen species in glasses at 300 K/0.1 MPa simulated for compositions along the CaO-Al_2O_3 join as a function of CaO concentration (Wu et al., 2015).

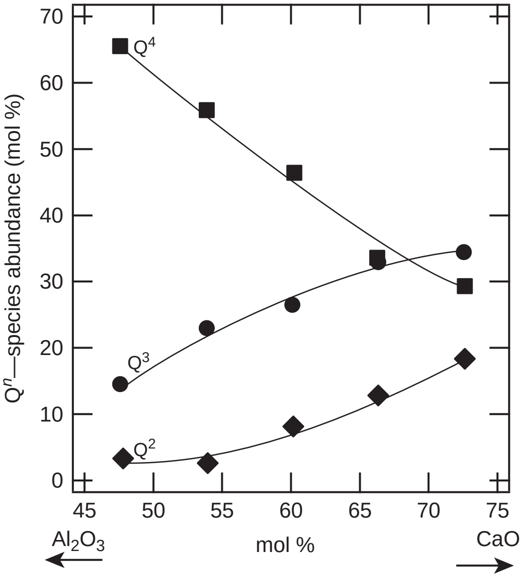

FIG. 9.6 Computed abundance of Q^n-species in CaO-Al_2O_3 melts at 1600°C and ambient pressures (results from computations by Wu et al., 2015).

CaO-SiO_2 system (see Chapter 7). There are quantitative differences between CaO-SiO_2 and CaO-Al_2O_3, in that the abundance of polymerized species for a given CaO content is greater in the aluminate compared with the silicate system. This difference likely reflects the longer Al—O bonds compared with Si—O bonds, which in turn would tend to lead to Al^{3+} forming more polymerized species than Si^{4+}.

9.2.2.2 SiO_2-$M^{n+}_{n/2}O$-M^{n+} Al_nO_{2n} Simulations

Melt and glass compositions from the peralkaline compositions (Fig. 9.1) have been subject to a number of simulations, at least in part because these compositions provide the simplest expression of exchange of charge-compensated Al^{3+} for Si^{4+} in tetrahedral coordination (Kubicki and Sykes, 1993; Stein and Spera, 1995; Benoit et al., 2001, 2005; Ganster et al., 2007; Pedone et al., 2012; Xiang et al., 2013). In this composition region, results of computations agree that about 90% or more of Al^{3+} and Si^{4+} exist in tetrahedral coordination, most of the remainder being in fivefold coordination (Stein and Spera, 1995; Xiang et al., 2013).

The average (Al,Si)—O—(Al,Si) bond angle decreases with increasing Al/(Al+Si), as would be expected because of the longer Al—O compared with the Si—O bond length (Stein and Spera, 1995). Interestingly, however, the Al—O—Al bond-angle distribution shows two or more distinct maxima, indicating therefore possibly multiple Al-bearing sites (Fig. 9.7). The distribution of Si—O—Al angles shows much less variation. The Al—O and Si—O bond distances are insensitive to parameters such as Al/(Al+Si). They are consistent with essentially all Al^{3+} and Si^{4+} in tetrahedral coordination because the calculated Si—O and Al—O bond distances vary by less than 2% from the nominal values for tetrahedral Al^{3+} and

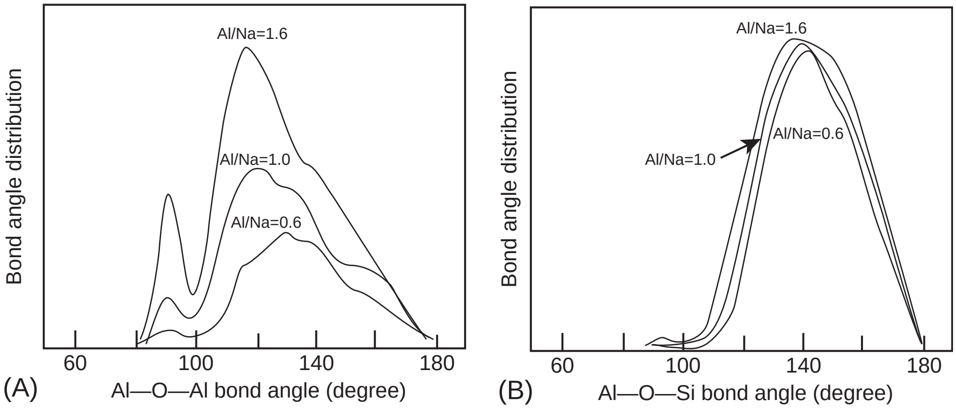

FIG. 9.7 Intertetrahedral angle distribution simulation of Na-aluminosilicate glasses calculated as a function of Al/Na ratio so that Al/Na=0.5 is peralkaline, Al/Na=1 is meta-aluminous, and Al/Na=1.5 peraluminous. (A) Al—O—Al angle distribution. (B) Si—O—Al angle distribution (calculations by Xiang et al., 2013).

Si^{4+} (Benoit et al., 2005; Xiang et al., 2013). The Al—NBO bonds are a few percent shorter than Al—BO (Benoit et al., 2005).

9.3 DIRECT DETERMINATION

9.3.1 Aluminate and Aluminosilicate Without Al^{3+} Charge-Balance

Binary Al_2O_3-SiO_2 melts are important because they offer information on the structural role of Al^{3+} when there is no metal cation for charge-compensation. There are, however, experimental complexities associated with experiments on such compositions because melts along the Al_2O_3-SiO_2 do not quench easily to homogeneous glasses. It is often necessary, therefore, to conduct structural measurements while the material is molten, which commonly requires temperatures in excess of 2000°C. Such thermal requirements limit experimental tools available for structural examination.

9.3.1.1 Al_2O_3 Data

Less structural information is available for pure Al_2O_3 than for SiO_2 because Al_2O_3, which is an extremely poor glass former, has to be investigated near and above 2071°C, the melting point of corundum. The large volume change and heat of fusion upon melting (Mitin and Nagibin, 1970; Richet et al., 1993) indicate very significant structural differences between crystalline corundum and its corresponding melt on its liquidus (see also Chapter 8). Results from ^{27}Al NMR spectroscopy of molten Al_2O_3 to temperatures near 2450°C are consistent with an Al^{3+} coordination number greater than 4, but mostly less than 6, perhaps mostly 4 (Florian et al., 1995; Bessada et al., 1999). This conclusion is also consistent with the Al—O bond distance of about 1.76 Å derived from the X-ray radial distribution function of Al_2O_3 near and above the melting temperature (Ansell et al., 1997). This distance points to a largely fourfold Al^{3+} coordination. Landron et al. (2001), using neutron diffraction, also found fourfold Al^{3+} to

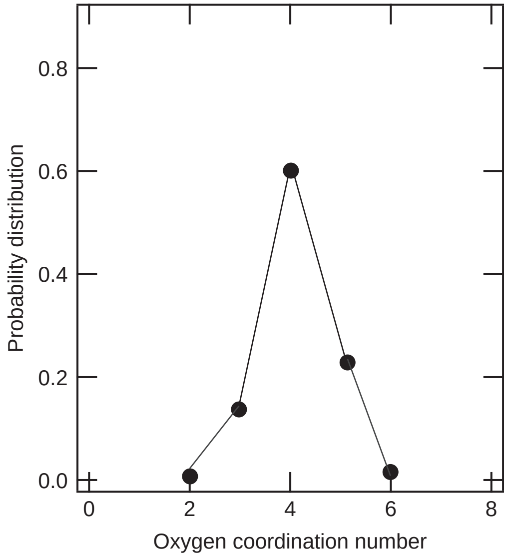

FIG. 9.8 Probability distribution of oxygen coordination number surrounding Al^{3+} in Al_2O_3 while laser-heated in a gas levitation device at 2500K (Landron et al., 2001).

dominate (~60%), with significant contributions from both higher and lower coordination numbers (Fig. 9.8). Large structural differences between molten and crystalline Al_2O_3 also have been reported from ^{27}Al NMR spectroscopy from 2300°C to 2450°C (Florian et al., 1995). In this case, fivefold coordination of Al^{3+} was proposed to dominate the structure, but in all cases a distribution of oxygen coordination was proposed. The average Al^{3+} coordination number, therefore, is less than for crystalline Al_2O_3. These experimental results in the main also accord with the numerical simulations discussed in Section 9.2 (see also Winkler et al., 2004; Pfleiderer et al., 2006; Hoang et al., 2007).

9.3.1.2 Al_2O_3-SiO_2 Data

For binary glasses with up to 6wt% Al_2O_3, the Raman spectra of quenched glasses resemble the spectrum of pure SiO_2. It has been proposed therefore that at least to this amount of Al_2O_3, the dissolved Al_2O_3 does not disrupt the SiO_2 structure significantly (Kato, 1976). Those early data formed the basis for a more comprehensive Raman spectroscopic study of SiO_2-Al_2O_3 glass with up to 59 mol% Al_2O_3 (McMillan and Piriou, 1982). Even though rapid splat cooling was used (~10^6–10^7°C/s), phase separation or crystal nucleation developed in many of the glasses (McMillan and Piriou, 1982; Sato et al., 1991). That problem notwithstanding, it was found that the structure of silica-rich (>70 mol% SiO_2) glasses along the SiO_2-Al_2O_3 join resembles that of pure SiO_2 with, however, a small number of nonbridging oxygens, because some Si—O—Al linkages between oxygen tetrahedra were observed (McMillan and Piriou, 1982). This conclusion differs somewhat, though, from those of a multinuclear NMR study of Al_2O_3-SiO_2 glasses with Al_2O_3 contents between 0.4 and 12wt%. In this composition range, Sen and Youngman (2004) reported four-, five-, and sixfold coordinated Al^{3+}. For higher alumina contents, McMillan and Piriou (1982) suggested that a significant portion of the Al^{3+} occurs in some form of aluminate clusters, whereas at low Al_2O_3 content, Al^{3+} is an integral part of the Al_2O_3-SiO_2 structure. These clusters, examined more recently with X-ray diffractional and vibrational spectroscopy, comprise ${}^{[4]}$A, ${}^{[5]}$Al, and ${}^{[6]}$Al (Okuno et al., 2005; Wilding et al., 2010).

Additional structural information has been obtained from ^{27}Al MAS NMR spectra of Al_2O_3-SiO_2 glasses that, however, had experienced incipient phase separation (Risbud et al., 1987; Okuno et al., 2005). The latter authors concluded that ^{27}Al MAS NMR spectra indicate multiple oxygen coordination states and proposed, in accord with the X-ray data of Okuno et al. (2005) and Wilding et al. (2010), that these are four-, five-, and sixfold coordinated Al^{3+} (Fig. 9.9). Therefore, even with several tens of mol% SiO_2 added to Al_2O_3, the Al^{3+} structural role may not differ greatly from that in pure Al_2O_3 melt with an average oxygen coordination number for Al^{3+} slightly below 5, but with significant proportions of four- and sixfold coordinated Al^{3+}. When investigating the same series of glass samples as McMillan and Piriou (1982) (up to 59 mol% Al_2O_3), Sato et al. (1991) confirmed this conclusion and added that the proportions of these different Al-complexes vary with Al_2O_3 content and also, interestingly, with the rate at which the glasses had been quenched. These conclusions also accord with those from numerical simulation discussed in Section 9.2 (see also Hemmati et al., 1999).

The difficulties associated with quenching of melts to homogeneous glass and the observation that Al-speciation in SiO_2-Al_2O_3 glasses may depend on quenching rate make structural interpretation difficult and prevent ready application of glass data to melts. It would also be difficult to compare results from Al_2O_3 glasses quenched at different rates whose effects might partly explain some of the different structural interpretations summarized immediately earlier.

Quenching problems were avoided by Poe et al. (1992), however, who coupled high-temperature 27Al NMR spectroscopy with molecular dynamics simulation of SiO_2-Al_2O_3 melts to temperatures above 2000°C. The 27Al isotropic shift is broadly correlated with the Al_2O_3/SiO_2 abundance ratio (Poe et al., 1992), which could be correlated with an increase in Al^{3+} coordination number (Bessada et al., 1999). Further, this average Al coordination

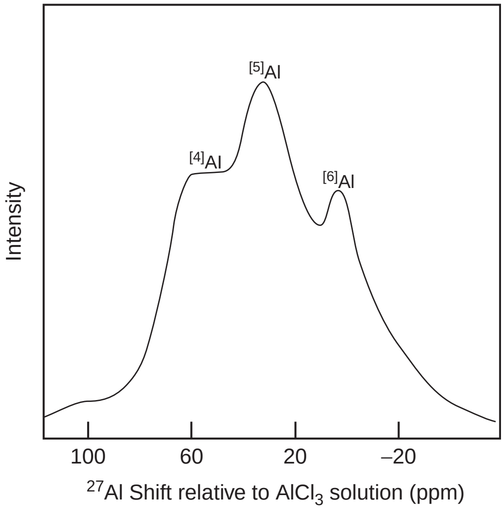

FIG. 9.9 ^{27}Al MAS NMR spectrum of Al_2O_3-SiO_2 glass with 30 wt% Al_2O_3 (Risbud et al., 1987) and 70 wt% SiO_2.

number was thought to reflect the presence of Al^{3+} in several different aluminate complexes whose coordination numbers range between 4 and 6. This observation is at least qualitatively in accord with other interpretations of Raman and NMR spectra of SiO_2-Al_2O_3 glasses (McMillan and Piriou, 1982; Risbud et al., 1987; Sato et al., 1991; Schmücker et al., 1997; Okuno et al., 2005) as well as results from simulations of Al_2O_3-SiO_2 melt and glass structure (Winkler et al., 2004; Hoang et al., 2007; see also Section 9.2.1.2).

There is a significant fraction of fourfold coordinated Al^{3+} even in the most aluminous SiO_2-Al_2O_3 glasses and melts, including pure Al_2O_3, which implies that some of the Al^{3+} may be in fourfold coordination with oxygen without metal cations for charge-compensation. Lacy (1963) proposed aluminum triclusters as a means to accomplish electrical neutrality under such circumstances. The tricluster concept subsequently was used to rationalize a number of features of Al-containing silicate melts that do not contain metal cations in sufficient quantity to provide formal charge-compensation of Al^{3+} in tetrahedral coordination (Stebbins et al., 2001; Landron et al., 2001; Kubicki and Toplis, 2002; Tossell and Horbach, 2005; Pfleiderer et al., 2006).

9.3.2 Charge-Balanced Al^{3+}

As was illustrated previously when discussing simulation of aluminosilicate structures, the substitution of Al^{3+} for Si^{4+} in tetrahedral coordination in a glass and melt (and crystalline materials, for that matter: see Angel et al., 1991; Prewitt et al., 1976; Phillips and Ribbe, 1973) is not simply an exchange of Al^{3+} for Si^{4+}, but also requires some form of charge-compensation to reach local charge balance. This can be accomplished with the aid of a metal cation such as an alkali metal or an alkaline earth;

$$Si^{4+} \Leftrightarrow Al^{3+} + 1/nM^{n+}. \tag{9.1}$$

The electronic properties of the M^{n+}-cations affect the aluminosilicate structure and physical and chemical properties, because the bond strength and bond angle distribution are affected by how Al^{3+} is charge-compensated (Navrotsky et al., 1985; Lee and Stebbins, 1999, 2002, 2006). The perturbation, $\Delta(TO)_{aver}$, of the T—O bond resulting from the nature of Al^{3+} charge-compensation can be expressed as a deviation from ideal Si—O and Al—O bond lengths and their mixing as a function of $X = Al/(Al+Si)$ (Navrotsky et al., 1985):

$$\Delta(TO)_{aver} = X \bullet \Delta(AlO) + (1 - X) \bullet \Delta(SiO), \tag{9.2}$$

where $\Delta(Al)$ and $\Delta(SiO)$ are expressions of the difference of Si—O and Al—O bond lengths from ideal values, 1.712 and 1.581 Å, respectively.

The perturbation of the T—O bond lengths resulting from different forms of charge-compensation of tetrahedral Al^{3+} affects the stability of mixed aluminosilicates and can be expressed as a function of cation type. For example, the stabilization enthalpy, ΔH_{stab}, relative to the enthalpies of solution of SiO_2 and aluminosilicate, ΔH_{soln}, has been expressed as (Navrotsky et al., 1985):

$$H_{stab} = \left[\Delta H_{soln}\left(M_{X/n}Al_XSi_{1-x}O_2\right) - \Delta H_{soln}(SiO_2)\right]/X. \tag{9.3}$$

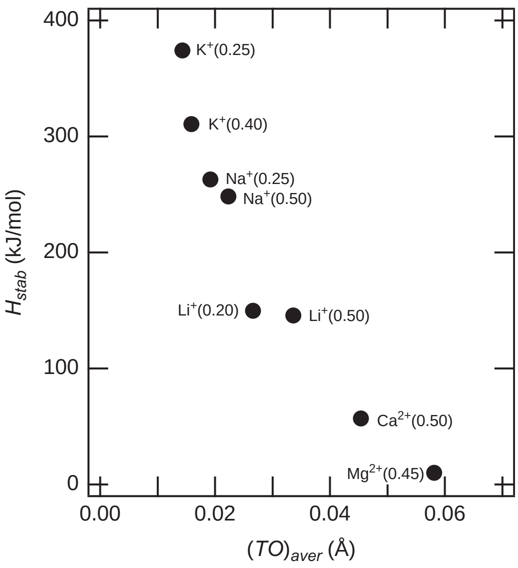

FIG. 9.10 Stabilization enthalpy, ΔH_{stab}, as a function of perturbation of the T—O bond, $\Delta(TO)_{aver}$ for charge-compensated Al^{3+} of glasses in SiO_2-aluminate glasses. The numbers in perentheses indicate the Al/(Al+Si) ratio of the material (Navrotsky et al., 1985).

As seen in Fig. 9.10, the perturbation of the T—O bond length is negatively correlated with the stabilization enthapy. In other words, the more perturbed (weakened) the T—O bond by various charge-compensating cations, the less stable is the alumnosilicate complex.

9.3.2.1 *Modifier Cation Data*

For all compositions except those along the join AlO_3-SiO_2, metal cations, typically alkalis and alkaline earths, can serve to charge-compensate Al^{3+} in tetrahedral coordination. In addition, for compositions to the left of the SiO_2-$M^{n+}Al_nO_{2n}$ join, (Fig. 9.1), metal cations may also serve as network-modifiers. Typically, the M—O bond length and coordination number when serving as a charge-compensating cation are slightly greater than when serving as a network-modifier (Creux et al., 1995; George and Stebbins, 1996; Cormier and Neuville, 2004; Gambuzzi et al., 2015). This can be discerned in ^{23}Na and ^{43}Ca MAS NMR (George and Stebbins, 1996; Maekawa et al., 1999; Henderson et al., 2009; Gambuzzi et al., 2015; see also Fig. 9.11). In Fig. 9.11, the chemical shifts are calibrated with Ca—O bond distance in various crystalline materials, which yield a Ca—O bond longer by more than 5% when Ca^{2+} charge-compensates Al^{3+} as compared with network-modifying Ca^{2+}. In Na_2O-Al_2O_3-SiO_2 glasses analogous relations have been recorded in relationships between ^{23}Na MAS NMR shift and Na-O oxygen coordination (Maekawa et al., 1999).

Increasing coordination number means increasing bond length (Tossell, 1999; Xue and Stebbins, 1993; see also Chapter 2, Section 2.2.2). However, in the latter case, there are also systematic changes in ^{23}Na chemical shifts with melt polymerization and Al/(Al+Si). The relationship with melt polymerization (Fig. 9.12) probably reflects the fact that in these glasses Na^+ serves both as a charge-compensating cation for Al^{3+} and as a network-modifier. The more depolymerized melt (higher NBO/*T*), the longer is the Na—O bond distance (Lee and Stebbins, 2003).

FIG. 9.11 Correlation between ^{42}Ca chemical shift in spectra of crystals and their Ca—O average distance. Arrows indicate chemical shifts in the glass systems (Gambuzzi et al., 2015).

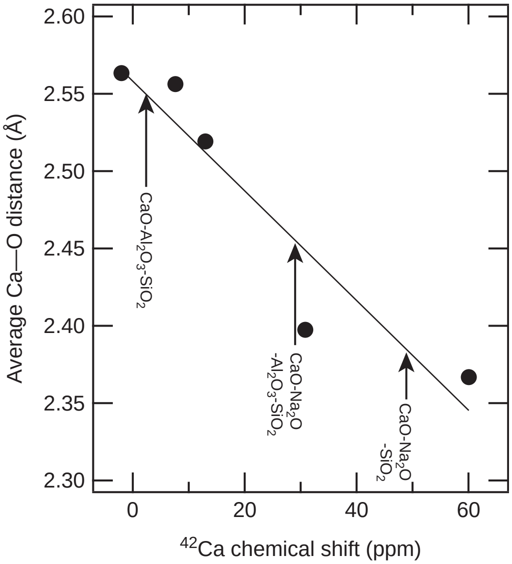

FIG. 9.12 Relationship between ^{23}Na chemical shift of crystals and their Na coordination numbers for different NBO/*T*-values in the system Na_2O-Al_2O_3-SiO_2 (Maekawa et al., 1999).

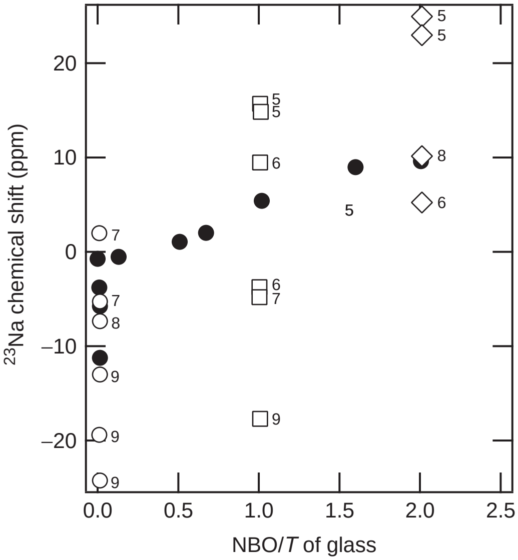

In mixed metal-oxide alumiosilicate melts and glasses, the different structural behavior of metal cations as network modifiers and as charge-compensating cations also leads to preferences of metal cations for charge-compensation versus network-modifying behavior. This can be seen in Na_2O-CaO-Al_2O_3-SiO_2 glasses and melts where Ca^{2+} tends to form Ca—O bonds with nonbridging oxygens, whereas Na^+ tends to act to charge-compensate Al^{3+} (Cormier and Neuville 2004). In the CaO-MgO-Al_2O_3-SiO_2 system, Mg^{2+} shows a preference for

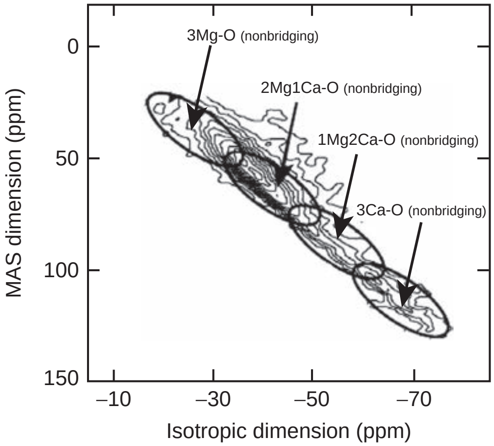

FIG. 9.13 Oxygen-17 3QMAS NMR spectra of glass with composition $Mg_{0.25}Ca_{0.75}Al_2Si_3O_{12}$. Contours mark signal intensity between 6% and 95% (Kelsey et al., 2009).

nonbridging oxygens over Ca^{2+} (Kelsey et al., 2009; see also Fig. 9.13). This behavior of metal cations in mixed aluminosilicate glasses (and melts) is, of course, as expected from the relative stabilities, ΔH_{stab}, of aluminate complexes (Fig. 9.9). In the case of Mg^{2+}, there is less convincing evidence for different structural characteristics of MgO as charge-compensator and network-modifying cation with an average coordination number near 5.1 and Mg—O bond distance between 1.98 amd 2.05 Å (Guignard and Cormier, 2008).

9.3.2.2 $M^{n+}{}_{2/n}O$-Al_2O_3 Data

Compositions along this join (lower horizontal join in Fig. 9.1) range from $M^{n+}O_{n/2}$-$M^{n+}Al_nO_{2n}$, which have excess metal cations over that needed to charge-balance Al^{3+} in tetrahedral coordination, to composition on the peraluminous side of $M^{n+}Al_nO_{2n}$-SiO_2, where there are insufficient metal cations to charge-compensate Al^{3+}. The former portion is, therefore, peralkaline, whereas the latter portion is peraluminous.

It appears that structural data along $M^{n+}{}_{2/n}O$-Al_2O_3 joins for the most part are limited to CaO-$CaAl_2O_4$ and MgO-$MgAl_2O_4$ (Engelhardt and Michel, 1987; Poe et al., 1994; McMillan et al., 1996a, b; Stebbins et al., 1999, 2001; Allwardt et al., 2003; Cormier et al., 2003; Hennet et al., 2007; Neuville et al., 2010). An exception is the study of Licheron et al. (2011), who also addressed the structure of Ba- and Sr peralkaline aluminate glasses. This comparative paucity of data is in part because of practical difficulties. Not only are these melts notoriously poor glass formers but, for alkali systems, they are in addition prone to alkali metal loss during high-temperature experiments.

The ^{27}Al isotropic chemical shift in spectra of Al_2O_3-$CaAl_2O_4$ melts, recorded near 2300°C, decreases systematically with increasing Al_2O_3 (Poe et al., 1993, 1994; Fig. 9.14). By comparing such data with results from molecular dynamics simulations, Poe et al. (1993, 1994) suggested that an increase in Al_2O_3 content along those joins is correlated with a higher average oxygen coordination around Al^{3+}, a trend that actually continues from the peralkaline to the peraluminous side of the $M^{n+}Al_nO_{2n}$ composition. This trend leads to the suggestion of a gradual coordination change of Al^{3+} extending into the peralkaline portion of these joins.

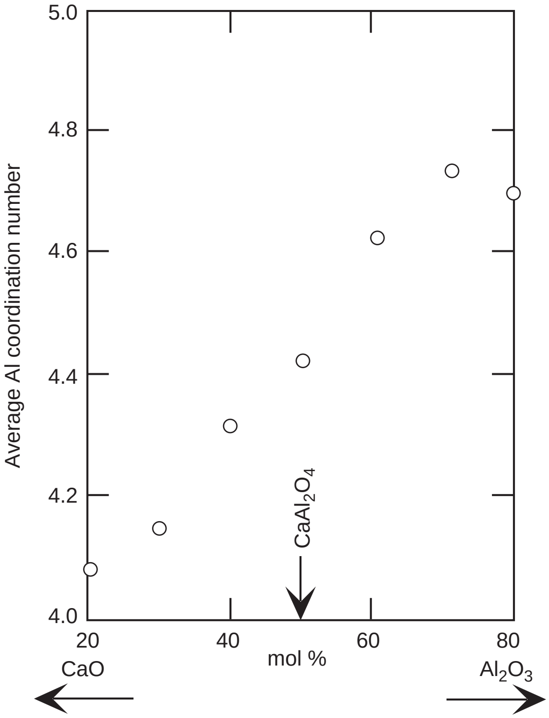

FIG. 9.14 Average coordination number of Al^{3+} as a function of composition in melts (at 2300°C and ambient pressure) along the CaO-Al_2O_3 join. The information was obtained by combining simulation methods with ^{27}Al MAS NMR (Poe et al., 1994).

The average coordination number of Al^{3+} is slightly higher in Al_2O_3-$MgAl_2O_4$ than in Al_2O_3-$CaAl_2O_4$ melts. As concluded for the SiO_2-Al_2O_3 structure (Poe et al., 1992), the increased number of oxygens coordinated to Al^{3+} was assigned to composition-dependent changes in the proportions of four-, five-, and sixfold coordinated Al^{3+} in both CaO-$CaAl_2O_4$ and MgO-Mg Al_2O_4 melts, the proportion of Al^{3+} with the highest coordination number increasing with the Al_2O_3 content. This interpretation of the ^{27}Al NMR data may be an oversimplification of the structure, however, because there was no consideration of other parameters that could affect the ^{27}Al shifts. For example, McMillan et al. (1996a, b) noted that, in crystalline Ca-aluminates, Al—O bond lengths, which are affected by Al coordination changes, do not correlate well with ^{27}Al chemical shift (see also Engelhardt and Michel, 1987; Skibsted et al., 1993). Moreover, in the ^{27}Al NMR study of Ca-, Sr-, and Ba-aluminate glasses by Licheron et al. (2011), an increasing chemical shift of ^{27}Al with increasing M_xO/Al_2O_3 ratio was actually observed (Fig. 9.15). Licheron et al. (2011) concluded that, this shift notwithstanding, there were no changes in Al^{3+} coordination.

The ^{17}O MAS NMR spectrum of a CaO-$CaAl_2O_4$ glass with nominal NBO/Al = 0.62 (Fig. 9.8) shows clear evidence of nonbridging oxygen. The Al^{3+} remains in tetrahedral coordination (Allwardt et al., 2003). The NBO/Al calculated from the relative integrated area of the peak assigned to nonbridging oxygen in the ^{27}Al MAS NMR spectrum of this glass is 0.6, thus suggesting that the nominal and actual NBO/Al-values for all practical purposes are

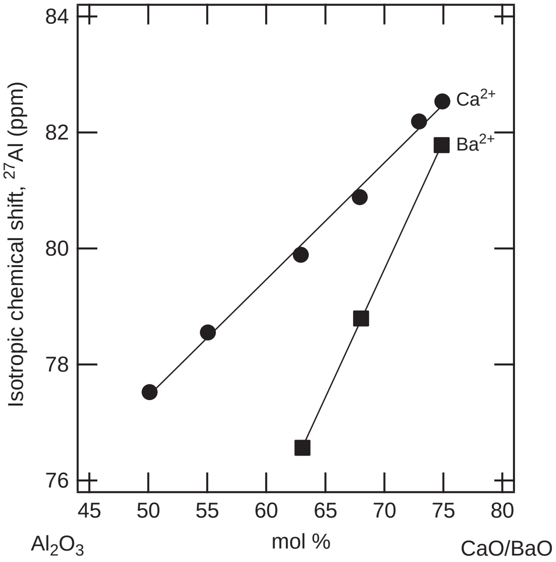

FIG. 9.15 Variation in the isotropic chemical shift from ^{27}Al MAS NMR spectra of glasses on the joins Al_2O_3-CaO and Al_2O_3-BaO (Licheron et al., 2011).

identical. Hence, at least for such a peralkaline composition, all the oxygens in the glass are either bridging or nonbridging and there is no need for more exotic aluminate structures. The ^{27}Al NMR results of Fig. 9.8 also agree with the molecular dynamics simulation made for a composition with nominal NBO/Al = 0.7 by Cormier et al. (2003) in which all Al—O bonds involved only bridging and nonbridging oxygens (Fig. 9.15). The Al—NBO bonds are shorter than the Al—BO bonds, just as observed in metal oxide-silica systems where Si—NBO bonds are shorter than Si—BO bonds (Ispas et al., 2002).

The results by Allwardt et al. (2003) and Cormier et al. (2003) accord with the interpretation of Raman spectra of glasses (McMillan and Piriou, 1982) and ^{27}Al NMR data by McMillan et al. (1996a, b), but cannot be easily integrated into the CaO-$CaAl_2O_4$ melt structure model of Poe et al. (1994). Whereas McMillan et al. (1996a, b) derived from their ^{27}Al MAS NMR data for glasses a structural model similar to that subsequently proposed by Cormier et al. (2003), Poe et al. (1994) concluded from molecular dynamics simulations that the ^{27}Al isotropic chemical shifts (open symbols in Fig. 9.14) reflect changes in the proportion of four-, five-, and sixfold coordination of Al^{3+} with oxygen. These changes, in turn, would cause the variations of the average Al coordination numbers.

On the peraluminous side of the Al_2O_3-$M^{n+}Al_nO_{2n}$ join, aluminum triclusters could also exist in addition to Al^{3+} with oxygen coordination number exceeding 4. Supporting evidence for triclusters was reported by Stebbins et al. (1999, 2001) in combined ^{27}Al and ^{17}O MAS NMR studies of $CaAl_2O_4$ and $CaAl_4O_7$ glasses. Triclusters would also be consistent with the presence of nonbridging oxygens in the ^{17}O 3Q MAS NMR spectrum of nominally fully polymerized $CaAl_2O_4$ (Stebbins et al., 2001). This information notwithstanding, alternative structural interpretations of the ^{17}O 3Q MAS NMR data have been advanced (Kubicki and Toplis, 2002).

9.3.2.3 *Meta-Aluminosilicate Compositions*

Existing data on the structure of melt and glass along meta-aluminosilicate joins, SiO_2-$M^{n+}Al_nO_{2n}$, are considerably more comprehensive, detailed, and systematic (Neuville and Mysen, 1996; Lee and Stebbins, 1999, 2003, 2006; Maekawa et al., 1999; Neuville et al., 2006; Dubinsky and Stebbins, 2006; Guignard and Cormier, 2008). This is probably due to the relevance of compositions along SiO_2-$M^{n+}Al_nO_{2n}$ joins to both industrial and geological processes, and also to the fact that experiments are often technically more tractable than examination of glasses and melts along binary aluminate joins (lower temperatures, better glass-formers, and so forth).

The structural data for SiO_2-$NaAlO_2$ glasses and melts are considerably more comprehensive than for those with other metal cations for charge-compensation (Taylor and Brown, 1979a, b; Matson et al., 1986; Neuville and Mysen, 1996; Lee and Stebbins, 2000; Maekawa et al., 1999). Some structural data, however, also have been reported for Cs, Rb, K, and Li systems (Matson et al., 1986; McMillan et al., 1998; Dubinsky and Stebbins, 2006; Thompson and Stebbins, 2011) as well as SiO_2-$CaAl_2O_4$ and SiO_2-$MgAl_2O_4$ glass and melt (Stebbins and Xu, 1997; Toplis et al., 2000; Neuville et al., 2004; Lee and Stebbins, 2006; Guignard and Cormier, 2008).

In a radial distribution analysis of SiO_2-$NaAlO_2$ glasses (see Fig. 9.16), Taylor and Brown (1979a, b) found that there are only subtle structural variations with Al/(Al + Si), which points to a simple network structure that varies smoothly between pure SiO_2 to at least the $NaAlSiO_4$ composition. This systematic and gradual evolution in the radial distribution functions with Al/(Al + Si) suggests that glasses along the SiO_2-$NaAlO_2$ join have considerable structural resemblance with pure SiO_2 (see also Chapter 5). Moreover, this similarity extends to at least 5 Å, which would, therefore, suggest medium-range order in this type of glass. In addition, from ^{17}O MQMS NMR, these structures seem built by mixing Si—O and mixed Si,Al—O bonds, with aluminum avoidance being essentially fully obeyed, at least to $NaAlSi_3O_8$ (Dirken et al., 1997; Lee and Stebbins, 1999). However, some ordering exists before the $NaAlSiO_4$ composition is reached where Al—O—Al bonding was detected (Dubinsky and Stebbins, 2006; see also Fig. 9.17). Furthermore, the abundance of Al—O—Al bonding increases with the electronegativity of the alkali metal (resulting, e.g., from Li^+ charge-balance)

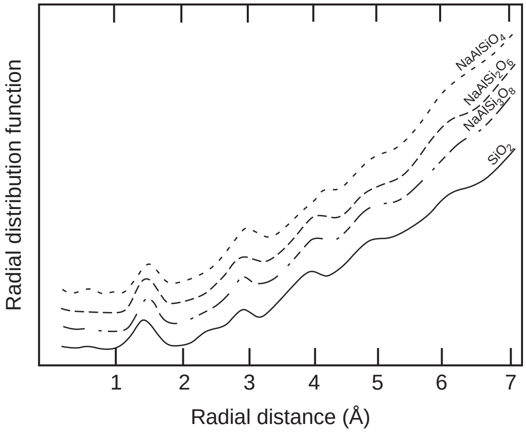

FIG. 9.16 X-ray radial distribution functions of glasses along the join SiO_2-$NaAlSiO_4$ (Taylor and Brown, 1979a, b).

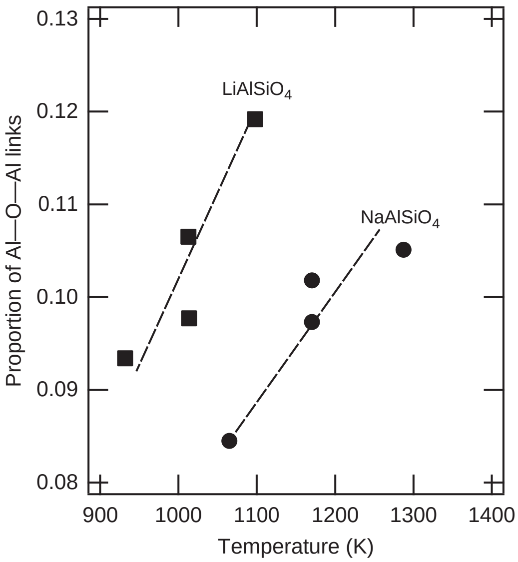

FIG. 9.17 Proportion of Al—O—Al linkages in MAlSiO$_4$ melts (M = Na and Li) as a function of temperature (Lee and Stebbins, 1999, 2000; Dubinsky and Stebbins, 2006).

(Dubinsky and Stebbins, 2006), more than in glasses with less electronegative charge-compensators (Lee and Stebbins, 1999).

The structure of SiO_2 glass and melt likely is made up of distribution of a small number of three-dimensionally interconnected rings of SiO_4 tetrahedra (see Chapter 5). From the X-ray data, one may infer that the SiO_2-$NaAlO_2$ glass structure resembles that of SiO_2. Although there are many differences in detail, molecular dynamics simulations are also consistent with this view (Zirl and Garofalini, 1990). However, as the Al/(Al+Si) of the glasses increases, ^{29}MAS NMR and ^{27}Al MAS NMR data indicate a gradual increase in (Si,Al)—O bond length, as reflected in the decreasing ^{29}Si and ^{27}Al NMR chemical shifts (Lee and Stebbins, 1999; see also Fig. 9.18), which is consistent with the earler interpretation of the X-ray radial distribution functions of SiO_2-$NaAlSiO_4$ glasses (Taylor and Brown, 1979a, b). Interestingly, the ^{23}Na chemical shift also follows such trends, which suggests therefore that the Na—O bond lengths also expand with increasing Al/(Al+Si) (Maekawa et al., 1999). The ^{29}Si and ^{27}Al chemical shifts in the spectra of SiO_2-$NaAlO_2$ glasses, for all practical purposes, are duplicated in NMR spectra of other alkali meta-aluminosilicate glasses such as those of Rb^+ and Cs^+ (McMillan et al., 1998). Neither the ^{27}Al nor the ^{29}Si chemical shifts appear sensitive to metal cation properties.

The high-frequency region of Raman spectra of SiO_2-$NaAlO_2$ glasses and melts provides information on Al,Si substitution in Q^4-type positions, as the frequencies of these Raman bands decrease systematically with increasing Al/(Al+Si) (Seifert et al., 1982; Neuville and Mysen, 1996; see also Fig. 9.19). This decrease, reflecting decreasing force constants, at least in part was interpreted as due to decreasing bond strength as Al^{3+} is substituted for Si^{4+}. By using a simple central force model (Sen and Thorpe, 1977; Galeener, 1979) similar to that employed to interpret the Raman spectrum of vitreous SiO2 (see Chapter 5), Seifert et al. (1982) concluded that the doublets of Raman bands seen in this frequency range

FIG. 9.18 Evolution of ^{29}Si chemical shift from NMR spectra of SiO_2-$NaAlO_2$ glasses as a function of Al/(Al+Si) (Lee and Stebbins, 1999).

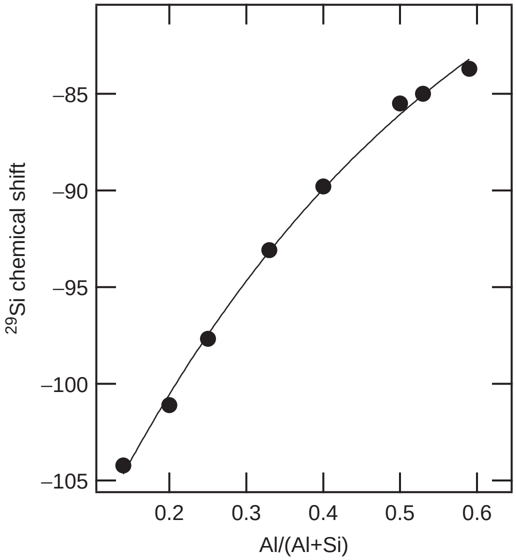

FIG. 9.19 Shift of Raman bands assigned to (Si, Al)—BO stretching of glasses on the join SiO_2-$NaAlO_2$ as a function of Al/(Al+Si) (after Neuville and Mysen, 1996).

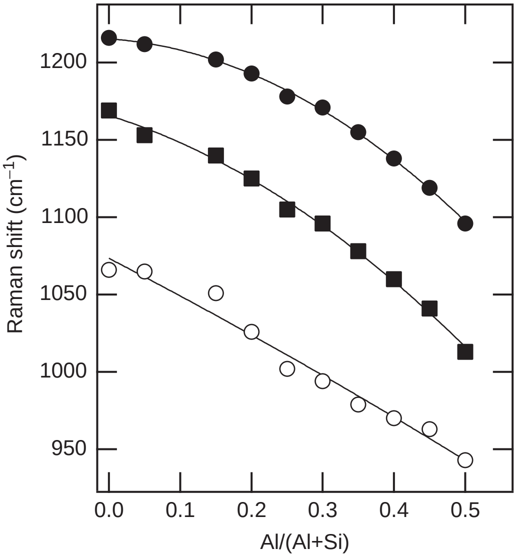

reflect, on average, two coexisting, three-dimensionally interconnected structures whose intertetrahedral angles differ by 5–10 degrees. The actual values of these angles were difficult to determine with precision, but the average T—O—T angle decreases by about 6–7 degrees from SiO_2 to $NaAlSiO_4$ glass. The ring with the smaller angle probably is the most aluminous of the two (Seifert et al., 1982; Neuville and Mysen, 1996).

There is considerably more disorder in the glass (and melt) than in the crystal structure. For glasses and melts on meta-aluminosilicate joins, SiO_2-$M^{n+}Al_nO_{2n}$, the extent of disorder depends on both Al/Si and on the nature of the charge-compensating metal cation (e.g., Taylor and Brown, 1979a, b; Navrotsky et al., 1985; Stebbins et al., 1999; Lee and Stebbins, 1999, 2002; Neuville et al., 2004; Neuville et al., 2008; Thompson and Stebbins, 2011). The extent to which there is Al,Si ordering in glasses and melts along meta-aluminosilicate joins can be quantified by the proportion of Al—O—Al bonding via the behavior of an equilibrium such as (Lee and Stebbins, 1999):

$$\mathrm{SiOSi} + \mathrm{AlOAl} = 2\mathrm{SiOAl}, \tag{9.4}$$

where SiOSi, etc., denote bridging oxygen bonds with the indicated cations (Al^{3+} or Si^{4+}) linking to the bridging oxygen. Lee and Stebbins (1999) defined a lattice energy difference, E_w, for reaction (9.4) as:

$E_w = z[W_{\mathrm{SiOAl}} - 0.5(W_{\mathrm{SiOSi}} + W_{\mathrm{AlOAl}})]$. (9.5)

Here the W_{SiOSi}, etc., are the lattice energies of the cation pairs across the bridging oxygen and z is the number of neighboring tetrahedra. The degree of Al avoidance, Q, was defined as:

$$Q = 1 - \mu^2, \tag{9.6}$$

where

$$\mu = \exp(2E_W/zKT), \tag{9.7}$$

where K is Bolzman's constant and T is absolute temperature. When $Q = 1$, there is perfect agreement with the Al avoidance rule, whereas $Q = 0$ means completely random avoidance. In this study, Lee and Stebbins (1999) concluded that Na-aluminosilicate glasses have nearly perfect Al-avoidance ($Q = 0.93$–0.99), whereas for the equivalent Ca-aluminosilicate glasses, the Q-range is 0.8–0.87, which implies less perfect Al-avoidance.

The different Q values (Al-avoidance) result in differently integrated line widths in ^{29}Si MAS NMR spectra (Fig. 9.20), because the number and distribution of nearest AlO_4 neighbor, n, governs the ^{29}Si chemical shift (Engelhardt et al., 1985). These relationships are shown as population of Q^4n) versus energy penalty from the calculations of Lee and Stebbins (1999) (Fig. 9.21).

Different Al,Si ordering as a function of the nature of charge-compensating metal cations can be seen in the distribution of T—O—T angles as a function of metal cation type (Scamehorn and Angell, 1991). The wider the angle range and the more maxima, indicating perhaps specific, average angle distributions, most likely the more disordered is the aluminosilicate structure (Fig. 9.22). For all three materials, Na, Ca, and Mg, meta-aluminosilicate melts at $Al/(Al+Si) = 0.5$, the T—O—T angle maxima range between about 120 and 180 degrees. However, both the maxima in the angle distribution function and the distribution around this maximum depend on the metal cation properties.

The data summarized here, mostly from NMR spectroscopy of the glasses, address local structural phenomena such as Al,Si subsitutions and Al,Si ordering in (Al,Si)—O—(Al,Si) and (Al,Si)—O—M bonds. However, those data do not offer information on the aluminosilicate entities that presumably comprise the meta-aluminosilicate glasses. Such

FIG. 9.20 Integrated line width in ^{29}Si MAS NMR spectra of glasses along the joins SiO_2-$NaAlO_2$ (NAS) and SiO_2-$CaAl_2O_4$ (CAS) as a function of Al/(Al+Si) (Lee and Stebbins, 1999).

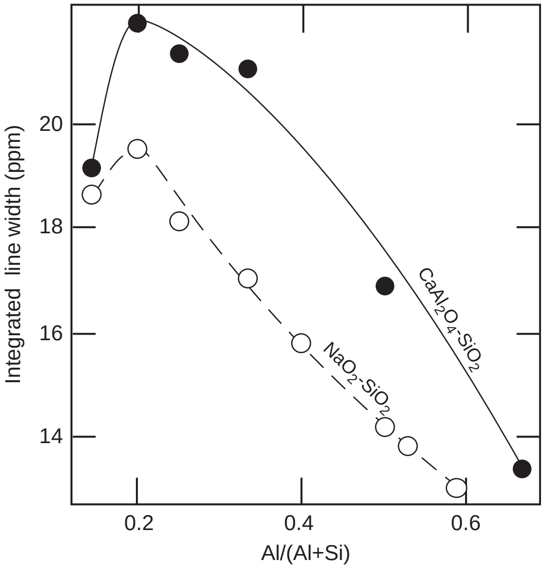

FIG. 9.21 Variations of $Q^4(n)$ species abundance (n = mol fraction Al component) as function of energy penalty (extent of ordering for glasses along the meta-aluminosilicate joins, $NaAlO_2$-SiO_2 and $CaAl_2O_4$-SiO_2). Shaded regions illustrate the energy penalty range calculated for Q-range (see text) for melts along the two joins indicated (data and results from Lee and Stebbins, 1999).

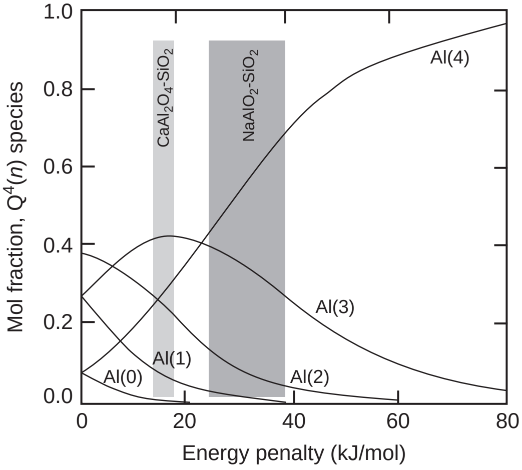

information may be gained from X-ray, neutron and Raman studies (Taylor and Brown, 1979a, b; Seifert et al., 1982; Marumo and Okuno, 1984; Himmel et al., 1991; Zotov et al., 1995; Daniel et al., 1995; Mysen et al., 2003).

The X-ray radial distrubution function of anorthite crystals resembles that of anorthite glass to perhaps 5 Å or slightly more (Taylor and Brown, 1979a, b), which has been interpreted as medium-range order of $CaAl_2Si_2O_6$ glass with a structure resembling that of anorthite crystals. This conclusion also found support in a wide-angle X-ray study of the same glass (Himmel et al., 1991). However, Himmel et al. (1991) also suggested that the X-ray spectrum of a more SiO_2-rich glass on the same join ($CaO{\cdot}Al_2O_3{\cdot}4SiO_2$) could be treated as a mixture of

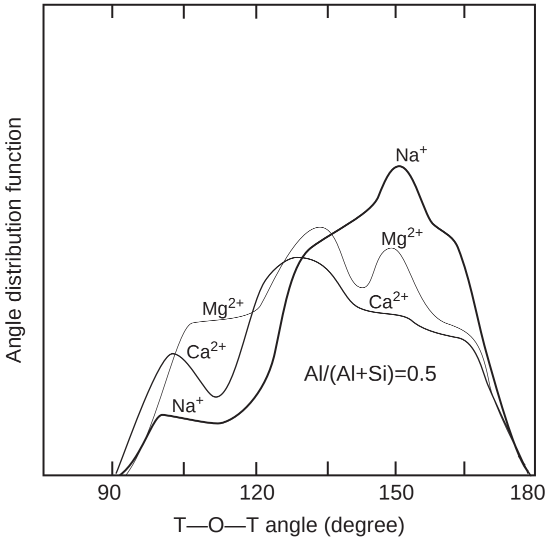

FIG. 9.22 Results from numerical simulation of the distribution of the intertetrahedral angle, (Si,Al)—O—(Si,Al) in $Mg_{0.5}AlSiO_4$, $Ca_{0.5}AlSiO_4$, and $NaAlSiO_4$ melt (after Scamehorn and Angell, 1991).

anorthite-like and SiO_2-like structures, because of a significant mismatch of the X-ray intensity function of a 4-membered three-dimensional structure and that of the $CaAl_2O_8$ glass. This structural model also resembles that of Daniel et al. (1995) from their interpretation of Raman spectra of $CaAl_2Si_2O_8$ melt at high temperature.

In detail, tetrahedrally coordinated Al^{3+} depends on the electronic properties of its charge-compensating metal cation. For example, the frequencies of Raman bands in the spectra of SiO_2-$CaAl_2O_4$ glass assigned to (Si,Al)—O stretch vibrations do not vary with Al/(Al+Si) (Fig. 9.23A), whereas those of SiO_2-$NaAlO_2$ glasses do (Fig. 19.19). These observations suggest that for the $NaAlO_2$-SiO_2 glasses, the Al/(Al+Si) ratio of the three-dimensional entities changes with changes in bulk Al/(Al+Si), whereas this is not the case for glasses on on the $CaAl_2O_4$-SiO_2 join and perhaps also on other $MAlO_4$-SiO_2 joins. In fact, it has been suggested that distinct structural entities coexist in SiO_2-$CaAl_2O_4$ glasses (Seifert et al., 1982; Himmel et al., 1991). With a constant composition, they resemble Al-unit (without Si) together with $Al_{0.5}Si_{0.5}$- and Al-free SiO_2-like structure (denoted Si-unit in Fig. 9.24). Their abundance varies with Al/(Al+Si) (Fig. 9.23B), but not their individual Al/(Al+Si) ratios. Analogous entities may exist in SiO_2-$MgAl_2O_4$ glasses (Seifert et al., 1982). This structural interpretation was based on the observation that the frequencies of Raman bands assigned to the various Si—BO and Al—BO stretch vibrations in the spectra of $CaAl_2O_4$-SiO_2 glasses not only seem independent of bulk Al/(Al+Si) but that, when extrapolated to Al/(Al+Si) = 0 (silica glass), those frequencies are the same as those of SiO_2 glass at ambient temperature and pressure (Seifert et al., 1982).

The description so far has not addressed whether or not glasses and melts along the meta-aluminosilicate joins are fully polymerized. Ideally, one might expect that they are. However, spectroscopic data, relying almost completely on NMR spectroscopy with ^{29}Si and ^{27}Al as the principal structural tools, indicate that this assumption is not entirely correct (Stebbins and Xu, 1997; Neuville et al., 2004, 2008; Thompson and Stebbins, 2011). The extent

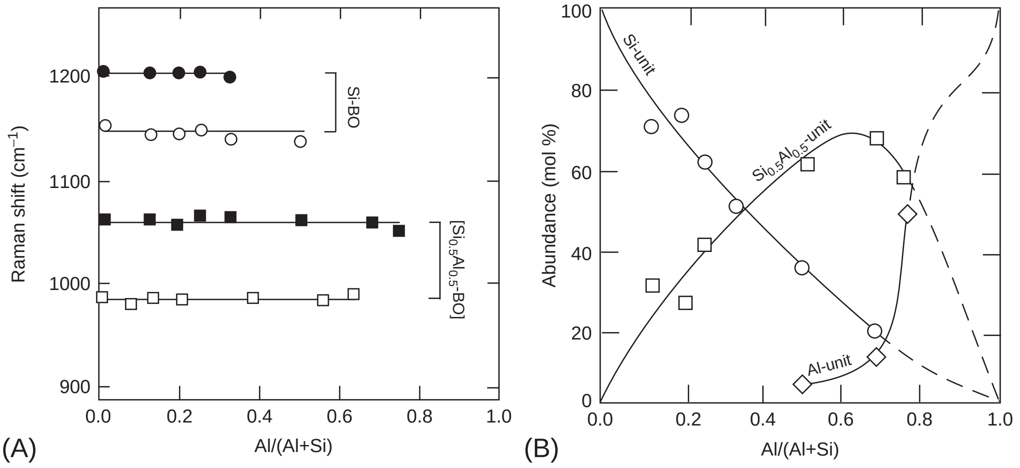

FIG. 9.23 Spectroscopy and structure of SiO_2-$CaAl_2O_4$ glasses as a function of bulk Al/(Al+Si). (A) Shift of Raman bands assigned to (Si,Al)—BO stretching of glasses on the join SiO_2-$CaAl_2O_4$ as a function of Al/(Al+Si) (Seifert et al., 1982). (B) Structure model for glasses and melts along the join SiO_2-$CaAl_2O_4$.

FIG. 9.24 Proportion of Al^{3+} in fivefold coordination in CaO-Al_2O_3-SiO_2 and MgO-Al_2O_3-SiO_2 glasses with 50 mol% SiO_2 (quenched from melt) at ambient pressure as a function of Al_2O_3/CaO and Al_2O_3/MgO. The dashed line denotes the meta-aluminosilicate compositions. Compositions to the left of this line are peralkaline and those to the right are peraluminous (Neuville et al., 2007).

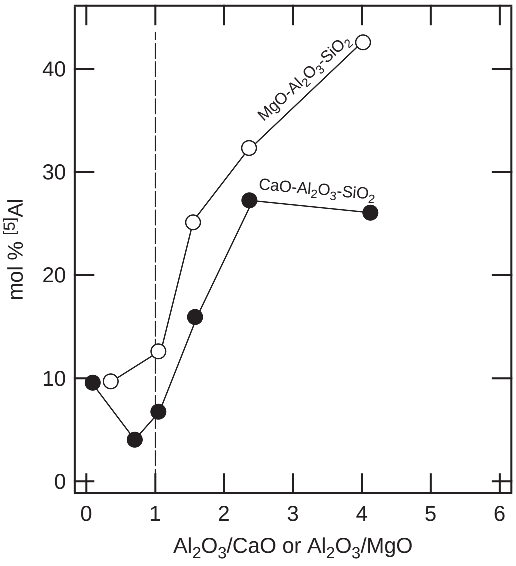

to which such deviations occur appears dependent on the nature of the charge-balancing metal cation. In addition, for meta-aluminosilicate glasses with given M-cation, the Al/(Al+Si) ratio also affects the abundance of fivefold coordinated Al^{3+} and, by implication, the proportion of nonbridging oxygen (Thompson and Stebbins, 2011). Notably, at least in the SiO_2-$CaAl_2O_4$ glasses examined by Thompson and Stebbins (2011), the glasses with the highest Al content have the greatest abundance of nonbridging oxygens (~5%) and remain at this level until Al/Al+Si)~0.75, and then decrease slowly as the Al/(Al+Si) decreases further.

9.3.2.4 Peralkaline and Peraluminous Compositions

Compositions on the left side of the SiO_2-$M^{n+}Al_nO_{2n}$ joins are peralkaline and those on the right are peraluminous (Fig. 9.1). Interestingly, a number of properties and structural features of melts and glasses tend to reach maximum or minimum values at or near the SiO_2-$M^{n+}Al_nO_{2n}$ compositions, whether arriving from the peraluminous or the peralkaline side. An example is the abundance of higher coordination numbers of Al^{3+} (Neuville et al., 2007; Takahashi et al., 2015) or the formation of triclusters (Thompson and Stebbins, 2011), both of which reach a maximum near the meta-aluminosilicate join.

The abundance of fivefold coordinated Al^{3+} increases as the composition moves into the peraluminous region, $^{[5]}Al$ in Mg-aluminosilicates being slightly more abundant than in Ca-aluminosilicates (Fig. 9.24). With the fivefold coordination of Al^{3+}, this means that the proportion of nonbridging oxygen follows an analogous trend. However, if this species were triclusters with Al^{3+} instead, the proportion of nonbridging oxygens would decrease, as concluded from ^{17}O and ^{27}Al MAS NMR by Thompson and Stebbins (2011). Whether triclusters or fivefold Al^{3+}, the abundance of this species decreases further when exchanging alkalis for alkaline earths (Thompson and Stebbins, 2011).

Peralkaline alkali aluminosilicate melts and glasses have been the subject of numerous experimental studies both at ambient conditions (Merzbacher et al., 1990; Mysen et al., 2003; Angeli et al., 2000, 2007; Guignard and Cormier, 2008; Moesgaard et al., 2010; Park and Lee, 2014) and at high temperature (Mysen, 1997, 1999; Maekawa et al., 1999; Kanehashi and Stebbins, 2007; Stebbins et al., 2008) and pressure (Yarger et al., 1995; Allwardt et al., 2005, 2007; Kelsey et al., 2007; Lee and Stebbins, 2006; Lee et al., 2012; Sakamaki et al., 2012; Drewitt et al., 2011, 2015). As discussed in more detail previously (Section 9.3.2.1), regardless of conditions, the alkali or alkaline earth cations in peralkaline melts and glasses serve in at least two, principally different structural roles, namely as charge-compensating cations for Al^{3+} and as network-modifier. Depending on the nature of this cation or these cations, the response of the structure to temperature and pressure will differ.

The role of Si,Al substitution in meta-aluminosilicate glass and melt structures, discussed in Section 9.3.2.3, provides an overall sense of structural environments surrounding Al^{3+} in tetrahedral coordination. However, in perakaline glasses and melts, which are depolymerized ($NBO/T > 0$) and where multiple Q^n-species coexist (see Chapter 7), further structural complexity affecting Al,Si substitution is encountered. This is so because the bond length is about 6% greater for $^{[4]}Al$—O than for ^4Si—O. As a result, from crystal chemical considerations and observations alone, if given the choice Al^{3+} would likely tend to favor substitution for Si^{4+} where the greater bond length can be accommodated and where, therefore, the (Si,Al)—O—(Si,Al) bond angle is the smallest, as discussed in some detail in Chapter 2, Section 2.4.3. Among the Q^n-species, ideally, the (Si,Al)—O—(Si,Al) bond angle is smaller, the more polymerized the Q-species (see Furukawa et al., 1981, for simple discussions of the principles governing these structural features).

In an early structural study of depolymerized, peralkaline aluminosilicate glasses and melts, aided by ^{29}Si and ^{27}Al, Merzbacher et al. (1990) concluded that Al^{3+} is dominantly in Q^4 units in the CaO-Al_2O_3-SiO_2 system, at least for compositions with less than about 15 mol% SiO_2. This conclusion is consistent with other results from ^{29}Si and ^{27}Al MAS NMR as well as results from molecular dynamics simulations of peralkaline, low-Si glasses and melts in this system (Engelhardt et al., 1985; Cormier et al., 2003; Allwardt et al., 2003; Mysen et al., 2003).

An implication of Al-preference for Q^4 structural units in peralkaline aluminosilicate melts and glasses is that the equilibrium originally proposed for Al-free alkali silicate glasses and melts (see Chapters 2 and 7):

$$2Q^3 \Leftrightarrow Q^4 + Q^2, \tag{9.8}$$

likely depends on the bulk melt Al/(Al+Si).

Systematic relationships between Al/(Al+Si) and Q^n-speciation have been observed for glasses and melts in Li_2O-Al_2O_3-SiO_2, Na_2O-Al_2O_3-SiO_2, and K_2O-Al_2O_3-SiO_2 systems (Maekawa et al., 1991; Mysen, 1999; Le Losq et al., 2014). Some data are also available for CaO-Al_2O_3-SiO_2 and MgO-Al_2O_3-SiO_2 melts (quenched from high temperature) (Mysen et al., 1981; Merzbacher and White, 1991). Compared to alkali aluminosilicates, the structural role of Al^{3+} in alkaline earth aluminosilicates is less well known because the presence of liquid immiscibility limits the compositional range that can be examined (Osborn and Muan, 1960b, c). Further, rapid nucleation of supercooled liquids at the timescale of spectroscopic measurements of supercooled melts tends to restrict the temperature range over which the structure of peralkaline melts can be studied (see also Chapter 8).

Solution of Al_2O_3 in polymerized alkali aluminosilicate glasses and melts results in essentially all the Al^{3+} entering Q^4 species (Mysen et al., 2003; see also Fig. 9.25). Thus, as Al/(Al+Si) increases in systems in which the nominal NBO/T (T=Si+Al) is constant, the abundance of Q^2 and Q^4 structural units increases, whereas Q^3 units become less abundant (Fig. 9.26). Further, because Al^{3+} substitutes for Si^{4+} preferentially in Q^4 units, the

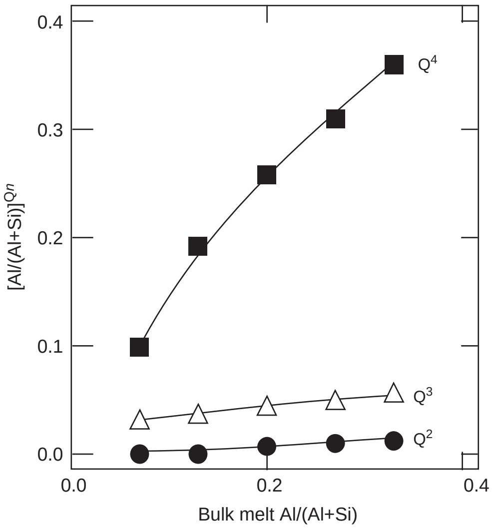

FIG. 9.25 Al/(Al+Si) of coexisting Q^n-species in glasses along the join $Na_2Si_3O_7$-$Na_2(NaAl)_3O_7$ as a function of bulk melt Al/(Al+Si) (Mysen et al., 2003).

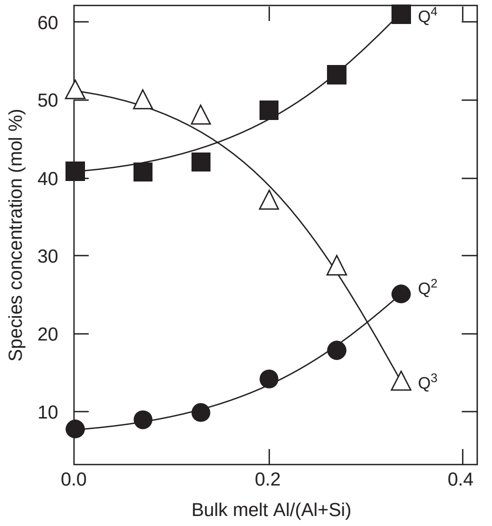

FIG. 9.26 Concentration of Q^4, Q^3, and Q^2 species in glasses along the join $Na_2Si_3O_7$-$Na_2(NaAl)_3O_7$ as a function of bulk melt Al/6(Al+Si). The Q^n-species abundance calculated with Si^{4+} and Al^{3+} incorporated in the individual Q^n-species (Mysen et al., 2003).

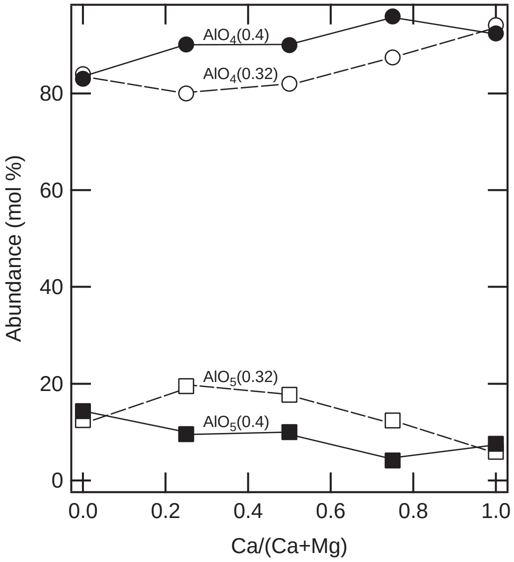

FIG. 9.27 Evolution of four- and fivefold coordinated Al^{3+} in peralkaline Ca,Mg aluminosilicate glasses formed by quenching from melt as a function of their Ca/(Ca+Mg) for two different Al/(Al+Si) ratios (0.4 and 0.3), marked as AlO_4(0.4) and AlO_4(0.32), AlO_5(0.4), and AlO_5(0.32). There are also 3% or fewer of AlO_6 groups, but these are not shown (Neuville et al., 2008).

Al/(Al+Si) of the latter units increases rapidly with Al/(Al+Si) (Fig. 9.25). However, in peralkaline alkaline earth aluminosilicate glasses and melts, some of the Al^{3+} also is in five- and sixfold coordination, where the proportion of the Al-species are functions of both Ca/Mg and Al/(Al+Si) (Fig. 9.27; see also Neuville et al., 2008). The proportion of higher-coordinated species generally decreases with increasing Ca/(Ca+Mg) ratio of these melts. This proportion also increases as a glass and melt becomes less aluminous. Finally, in the mixed Ca,Mg aluminosilicate glasses and melts, there is ordering of Ca^{2+} and Mg^{2+} among the oxygen anions with which they bond so that the local nonbridging oxygen environment is enriched in Mg^{2+} over the average Ca/Mg abundance ratio, whereas Ca^{2+} preferentially serves to charge-balance tetrahedral Al^{3+} (Kelsey et al., 2008).

9.4 TEMPERATURE AND PRESSURE

The structural data hitherto discussed have been obtained at ambient temperature and thus deal with the structure of the melt frozen in at the glass transition of each composition (see Chapter 3). The structure, and in particular the environment of network-formers such as Si^{4+} and Al^{3+} in aluminum silicates, can vary significantly with pressure, thus affecting both the structure and properties of the materials.

9.4.1 Temperature

In certain cases, the difference between the structures of a glass and its melt may be minimal or not detectable. This was the case in an early X-ray study of $NaAlSi_3O_8$ and $CaAl_2Si_2O_8$ (Marumo and Okuno, 1984), for which the data were recorded to 1200°C and 1600°C, respectively. However, more recent and detailed examinations of individual nuclei of both network-modifying and charge-balancing cations do indeed show systematic temperature effects. Such effects can be seen in NMR and vibrational spectra. For instance, relaxation of melt structure as the glass transforms to a supercooled liquid manifests itself by changes in the spin-lattice relaxation time from NMR spectroscopy. This feature has been correlated with transport behavior of cations in silicate melts (Farnan and Stebbins, 1990a; Fiske et al., 1994; George and Stebbins, 1996; Maekawa et al., 1997).

The spin-lattice time, T_1, of various nuclei in silicate and aluminosilicates decreases to a minimum value with increasing temperature, typically below the liquidus, but not necessarily coincident with the glass transition (Farnan and Stebbins, 1990a,b; George and Stebbins, 1996; Kanehashi and Stebbins, 2007). At temperatures above that of this minimum, an Arrhenius fit to the data for individual cations in melts yields an activation energy that tends to be near that of transport properties such as viscosity and diffusion of the same materials (Farnan and Stebbins, 1990a; Fiske et al., 1994; George and Stebbins, 1996; Kanehashi and Stebbins, 2007).

The frequency shifts of NMR from various metal nuclei depend on temperature whether in meta-aluminosilicates or peralkaline aluminosilicate melts and glasses (Liu et al., 1987; Maekawa et al., 1997; Kanehashi and Stebbins, 2007). An example can be seen in the ^{23}Na MAS NMR spectra of peralkaline Na_2O-Al_2O_3-SiO_2 melts (Maekawa et al., 1997). Here, the chemical shift decreases with increasing temperature (Fig. 9.28), which could reflect lengthening of Na—O bonds. Lengthening of these bonds would be consistent with increased coordination of Na^+ in alkali silicate and alkali aluminosilicate melts as the temperature is increased (Xue and Stebbins, 1993; Maekawa et al., 1997; Tossell, 1999).

The (Al,Si)-ordering and Al^{3+} coordination in an aluminosilicate network also depends on temperature (Neuville and Mysen, 1996; Stebbins et al., 2008). Neuville and Mysen (1996) concluded that there is a small temperature effect on the proportion of two coexisting, three-dimensionally connected structural units in Na-metaaluminosilicate melts (Fig. 9.29),

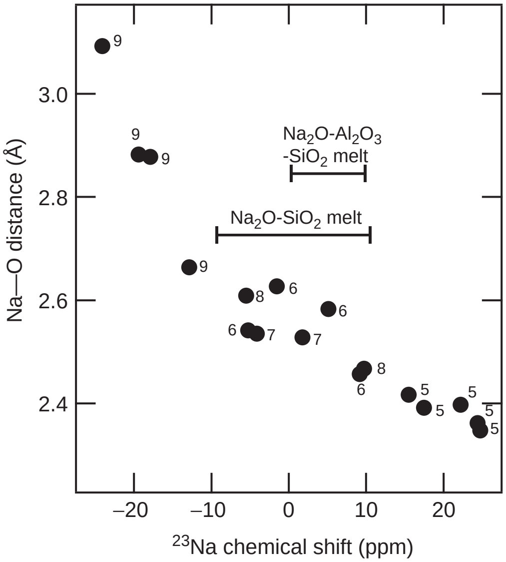

FIG. 9.28 Relationship between sodium-23 chemical shift and Na—O bond length in crystalline materials where the numbers associated with each data point reflect the Na^+ coordination number. The ^{23}Na chemical shift range in melts in silicate and aluminosilicate are also shown to indicate, therefore, that there likely is a wide range of coordination numbers in melts as well (data and data compilations by Maekawa et al., 1997).

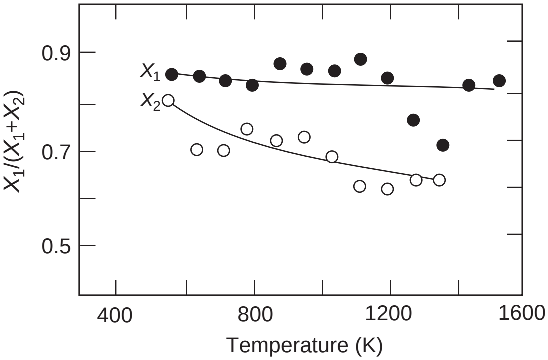

FIG. 9.29 Proportion of three-dimensionally interconnected unit 1, with the largest Al/(Al+Si), as given by the structure model of Seifert et al. (1982) along the join SiO_2-$NaAlO_2$ for glasses and melts with two different bulks Al/(Al+Si) as a function of temperature (Neuville and Mysen, 1996).

and that this temperature-dependence also varies with Al/(Al+Si). From this analysis, the abundance of the unit with the highest Al/(Al+Si) (denoted unit "1" in Fig. 9.29) decreases slightly with increasing temperature. The distribution of Al^{3+} among the coexisting, fully polymerized $(Si,Al)O_4$ tetrahedra in SiO_2-$NaAlO_2$ melts appears, therefore, to depend on temperature.

It has also been demonstrated that the proportion of high-coordinate Al^{3+} in melts such as those in the CaO-Al_2O_3-SiO_2 system depends on the fictive temperature (Stebbins et al., 2008). Here, the abundance ratio, $^{[5]}Al$/total Al, increases with increasing temperature. The enthalpy of the reaction between the two coordination states, $^{[5]}Al$ and $^{[4]}Al$, ranges between 26 ± 10 kJ/mol and 11 ± 10 kJ/mol. This enthalpy change varies with both Al/(Al+Si) and CaO/Al_2O_3 (Stebbins et al., 2008).

The relationships between Q^n-abundance and temperature in peralkaline aluminosilicates qualitatively resemble those observed for the Al-free alkali silicate endmembers (McMillan et al., 1992; Mysen and Frantz, 1992, 1994; Mysen, 1995, 1997, 1999). The concentration of Q^2, Q^3, and Q^4 species initially remain insensitive to temperature over several hundred degrees (Fig. 9.25). Near the glass transition, the abundances of Q^4 and Q^2 species then increase and that of Q^3 decreases (Mysen et al., 2003).

Although the temperature-dependent Q^n-speciation resembles that of Al-free alkali silicate melts, the speciation is somewhat more sensitive to temperature than in the absence of alumina (Fig. 9.30). This means that the enthalpy for the disproportion reaction, Eq. (9.8), depends on the Al/(Al+Si). This effect of Al/(Al+Si) relates back to the strong preference of Al^{3+} for occupation of Q^4 species in the melts and glasses (see Section 9.3.2.4). In addition, this enthalpy generally is a positive function of the bulk Al/(Al+Si) (Fig. 9.30A) and a negative function of the nominal NBO/T of the melt (Mysen, 1999). It also depends on the electronic properties of the alkali metal as it is higher the more electronegative the alkali metal that serves to charge-compensate Al^{3+} (Fig. 9.30B).

9.4.2 Pressure

By subjecting silicate and aluminosilicate glasses and melts to high pressure (often multiple GPa to tens of GPa), whether via experiment or numerical simulation, the material can respond by changing bond angles, bond lengths, and coordination numbers. Large bond

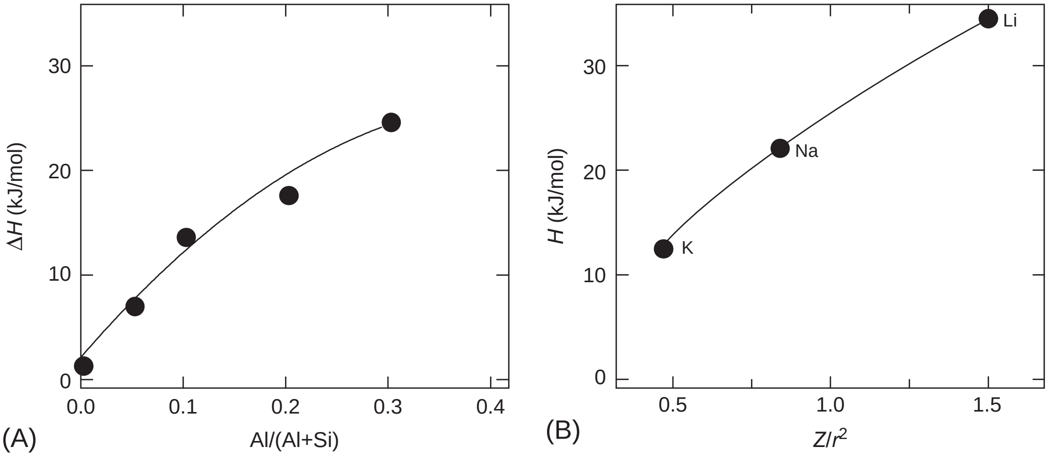

FIG. 9.30 Enthalpy of reaction (9.8) calculated from the abundance of Q^4, Q^3, and Q^2 structural units at temperatures above the glass transition range for tetrasilicate melts (after Mysen, 1999). (A) ΔH for melts along the join $Na_2Si_4O_9$-$Na_2(NaAl)_4O_9$ as a function of bulk melt Al/(Al+Si). (B) ΔH for melts along the joins $K_2Si_4O_9$-$K_2(KAl)_4O_9$, $Na_2Si_4O_9$-$Na_2(NaAl)_4O_9$, and $Li_2Si_4O_9$-$Li_2(LiAl)_4O_9$ at bulk melt $Al/(Al+Si)=0.2$ as a function of ionization potential, Z/r^2, for cation in sixfold coordination with oxygen (radii from Whittaker and Muntus, 1970).

length and bond angle changes generally take place at lower pressures than those where major coordination changes can be observed (Seifert et al., 1982; Sykes et al., 1993; Poe et al., 2001; Sakamaki et al., 2012). Coordination changes, which involve network-formers, network-modifers, and charge-balancing cations typically take place at higher pressure (Ohtani et al., 1985; Yarger et al., 1995; Bryce et al., 1999; Lee and Stebbins, 2006; Allwardt et al., 2007; Ni and De Kroker, 2011; Karki et al., 2011; Drewitt et al., 2011). Any and all of these effects depend not only on pressure itself but also on composition and temperature. In spite of considerable difficulties, some X-ray experiments have been performed (Funamori et al., 2004; Yamada et al., 2011; Sakamaki et al., 2012; Drewitt et al., 2015). However, in most cases, and in particular when information other than simply bond length and bond angles is required, most measurements have been conducted on glasses quenched from high-pressure melts. Of course, in addition, numerical simulations methods allow computations for high pressure at temperatures at which CPU time does not become excessive or unrealistically long (Matsui, 1996; Bryce et al., 1999; Adjaouda et al., 2008; Ni and De Kroker, 2011).

At pressures of up to a few gigapascals, the aluminosilicate melt structure responds by (Si, Al)—O—(Si,Al) and O—(Si,Al)—O angle compression (Fig. 9.32). In fact, the strength of the (Si,Al)—O bond is such that, instead of extending the bond length, the aluminosilicate tetrahedra adjust by changing O—(Si,Al)—O angles, which in addition results in a decrease of the distance between tetrahedrally coordinated cations (Fig. 9.31). These structural features are seen clearly in the experimental data for $NaAlSi_2O_6$ melt (Fig. 9.30). They have also been recorded in Al-free silicates, such as SiO_2 melt (see Chapter 5). They also have been proposed to occur in $KAlSi_3O_8$ and $CaAl_2Si_2O_8$ composition melts (Sykes et al., 1993; Poe et al., 2001).

The compressibility of (Si,Al)—O—(Si,Al) angles should be related to both Al/(Al+Si) and ~~to~~ the nature of the cations that serve to charge-compensate tetrahedral Al^{3+}. For example, the

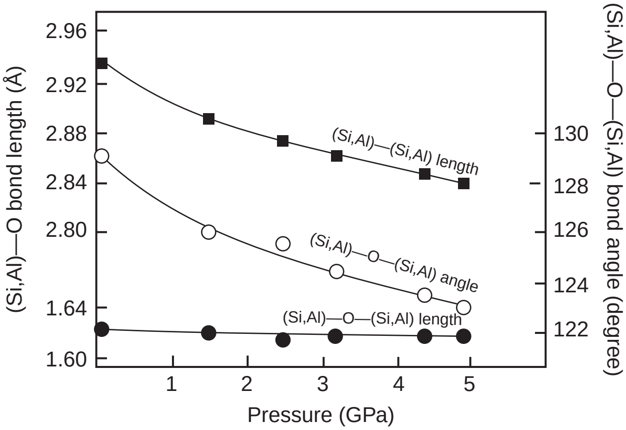

FIG. 9.31 Evolution of bond angles and bond lengths as identified on figure for $NaAlSi_2O_6$ melt at 1700°C as a function of pressure (Sakamaki et al., 2012).

intertetrahedral angle is more sensitive to pressure in SiO_2-$NaAlO_2$ than in SiO_2-$CaAl_2O_4$ melts (Mysen et al., 1983; see also Fig. 9.31). Furthermore, whereas the decrease of intertetrahedral is positively correlated with Al/(Al+Si) in SiO_2-$NaAlO_2$ melts, the intertetrahedral angle in the SiO_2-$CaAl_2O_4$ melts becomes less compressible with increasing Al/(Al+Si) (Fig. 9.32). The explanation of this different response to pressure lies in how the electronic environment of Al^{3+} is linked to the charge-compensating metal cation. In the SiO_2-$NaAlO_2$ system, substitution of Al^{3+} for Si^{4+} results in increasing Al/Si in the three-dimensionally interconnected rings. Because replacement of Si^{4+} with Al^{3+} results in weakening of the (Si,Al)—O bonds (see Chapter 2, Table 2.1), these bonds become more flexible

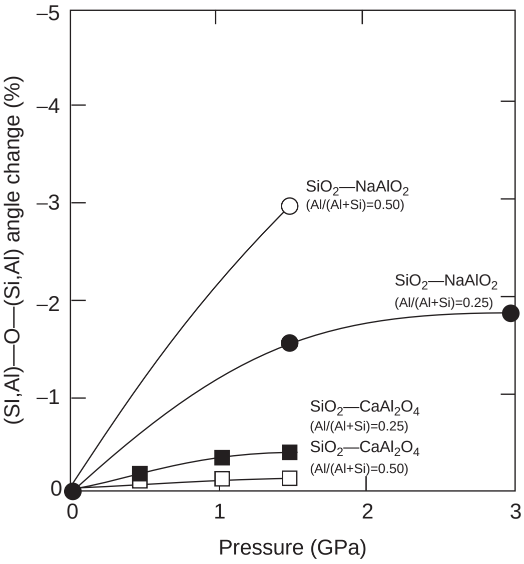

FIG. 9.32 Relative change of angle, (Si,Al)—O—(Si,Al) angle (percent relative to angle at ambient pressure) as a function of pressure for temperature-quenched melts along the joins SiO_2-$NaAlO_2$ and SiO_2-$CaAl_2O_4$ of the bulk melt Al/(Al+Si), which is indicated on individual lines (Mysen et al., 1983).

and the (Si,Al)—O—(Si,Al) angles more compressible with increasing bulk Al/(Al+Si), because this ratio within the units also increases (Fig. 9.29). In SiO_2-$CaAl_2O_4$ melts, on the other hand, these ratios in the coexisting three-dimensionally interconnected structural units do not vary with the bulk Al/(Al+Si). Only their proportions do. Therefore, the changes in average intertetrahedral angles merely reflect variations of these proportions and the compressibility of these units. Among these, the more open Al-deficient or Al-free unit likely is the most compressible (Fig. 9.24). As the abundance of these latter structural entities decreases with increasing Al/(Al+Si), bulk compressibility is also likely to decrease. This structural effect is evident in the decreasing sensitivity to pressure of the intertetrahedral angle as Al/(Al+Si) of SiO_2-$CaAl_2O_4$ melts increases (Fig. 9.32).

Whether in numerical simulation or experimental determination, as pressure is increased to 10GPa or more, there is a gradual increase in oxygen coordination numbers surrounding the metal cations in aluminosilicate melts (Yarger et al., 1995; Bryce et al., 1999; Lee and Stebbins, 2006; Lee et al., 2012; Allwardt et al., 2005, 2007; Kelsey et al., 2009; Ni and De Kroker, 2011; Drewitt et al., 2011). The bond lengths also vary in part because of changes in coordination and in part by simple deformation. Interestingly, the M—O bond length of charge-balancing and network-modifying cations is considerably more sensitive to pressure than are Al—O and Si—O bond lengths (Drewitt et al., 2011; see also Fig. 9.33). Changes in coordination numbers around Al^{3+} and Si^{4+} in silicate melts also are more sensitive to pressure than for network-modifying and charge-compensating cations (Fig. 9.33B; see also Ni and De Kroker, 2011; Drewitt et al., 2015). These differences appear greater in alkaline

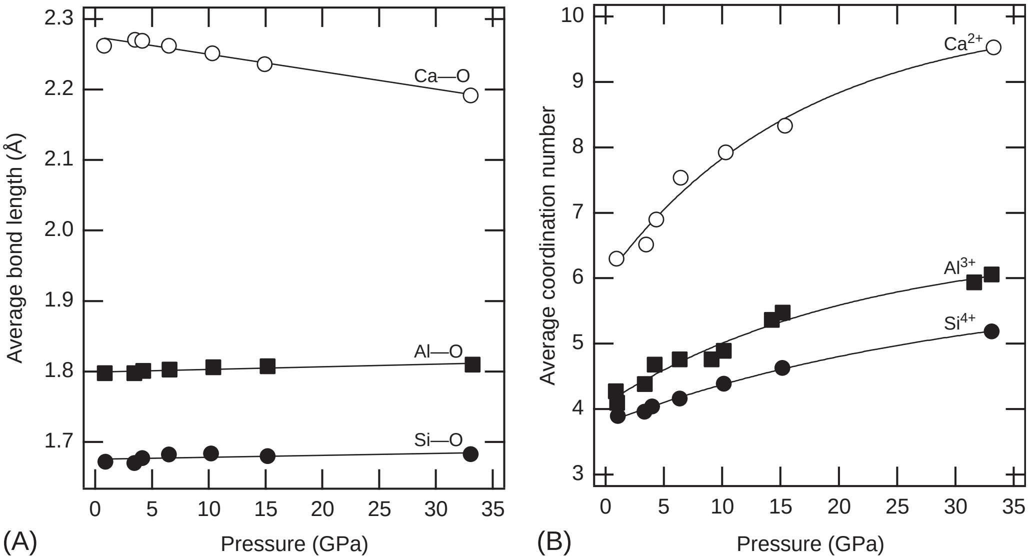

FIG. 9.33 Bond lengths and coordination numbers in $CaAl_2Si_2O_8$ composition melt near 3000K as a function of pressure. (A) Bond lengths for cation-oxygen distances as indicated on individual curves. (B) Average oxygen coordination numbers of cations as indicated on individual curves. *Redrawn from* Drewitt et al. (2011).

earth than in alkali aluminosilicate melts (Ni and De Kroker, 2011; Drewitt et al., 2015), perhaps again because of the softer (Si,Al)—O bonding in the latter systems.

The results shown in Fig. 9.33 are average values reflecting a distribution of angles, often with a Gaussian distribution, as well as a distribution of different coordination numbers. In aluminosilicate glasses and melts, Al^{3+} has attracted the most attention. In numerical simulations, four-, five-, and sixfold coordinated Al^{3+} are found in high-pressure alkali aluminosilicate melts. The proportions of $^{[4]}Al$ decrease; that of $^{[5]}Al$ initially increases but passes through a maximum at a few GPa pressure; whereas $^{[6]}Al$ increases gradually with increasing pressure (Bryce et al., 1999; Ni and De Kroker, 2011). In an ^{27}Al evidence for partial coordination transformation of Al^{3+} in a $(NaAlSi_3O_8)50(Na_2Si_4O_9)50$ sample at ≥6 GPa, Lee et al. (2006) reported ^{27}Al, ^{23}Na, and ^{17}O NMR spectra for pure $NaAlSi_3O_8$ and a composition between $NaAlSi_3O_8$ and $Na_2Si_3O_7$ $[(Na_2O)0.75(Al_2O_3)0.25{\cdot}3SiO_2]$ quenched from 8 GPa (Fig. 9.34). Five- and sixfold coordinated Al^{3+} are evident in the NMR data of these glasses from both studies. It is also clear that the proportion of both five- and sixfold coordinated Al^{3+} is positively correlated with pressure, but that the pressure at which higher oxygen-coordination numbers can be detected is considerably less than that where minerals with Al^{3+} in sixfold coordination become stable (Fig. 9.35; see also Lee et al., 2006, 2012). Moreover, the pressure at which any coordination change begins to take place and finishes is sensitive to Al/(Al + Si). It also decreases as a melt becomes increasingly depeolymerized (Lee et al., 2012).

Finally, the extent to which cations undergo coordination changes with pressure also depends on the electronic properties of the metal cation itself. This is illustrated in Fig. 9.36 for peralkaline melt compositions in the system K_2O-CaO-MgO-Al_2O_3-SiO_2, where Allwardt et al. (2007) found that average Al^{3+} coordination increases the greater

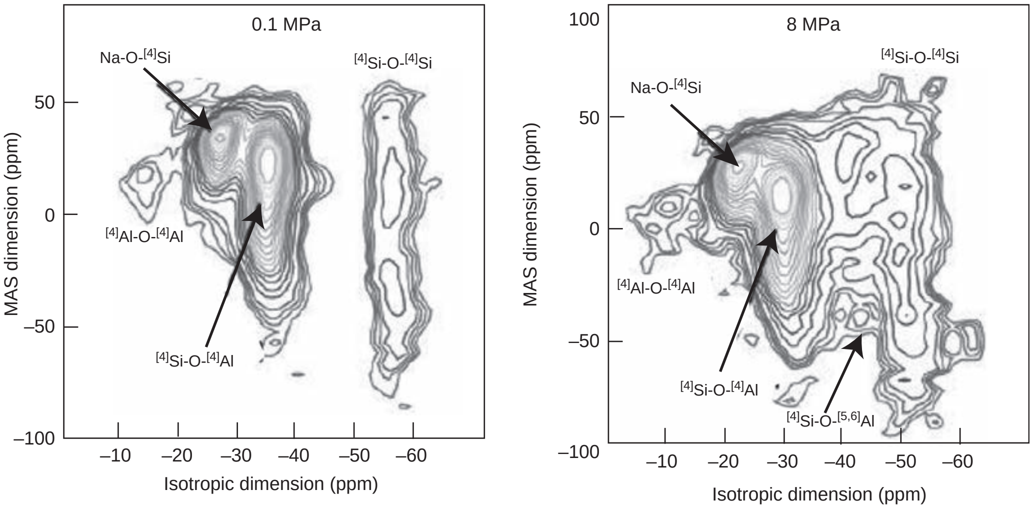

FIG. 9.34 Oxygen-17 3QMAS NMR spectra of $Na_6Al_2O_{10}$ quenched melt, quenched from superliquidus temperatures at ambient pressure (0.1 MPa) and 8 GPa (Lee et al., 2012).

FIG. 9.35 Population of Al^{3+} in different coordination states as indicated on each curve for $Na_3Al_2Si_{12}O_{30}$ quenched from temperatures above its liquidus at high pressure as a function of pressure (Lee et al., 2012).

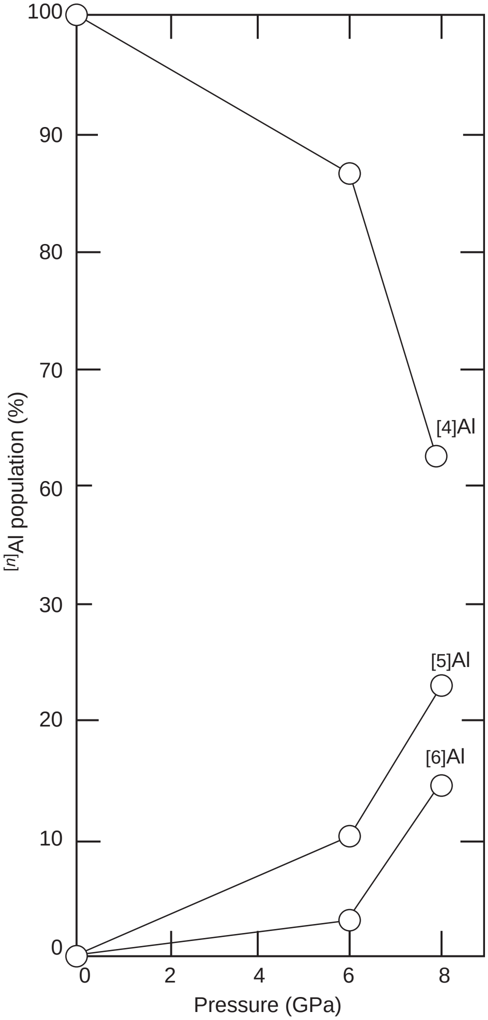

the ionization potential of the metal cations used for charge-compensation. In the latter case, variations in Z/r^2 were accomplished by combining two cations in various proportions. It warrants notice, though, that these melts also are peralkaline with different degree polymerization at ambient pressure (NBO/T differences). As discussed previously, the response of Al coordination to pressure also depends on peralkalinity (Lee et al., 2003, 2006). Finally, the treatment summarized in Fig. 9.36 does not take into account the tendency of the more electronegative (higher Z/r^2 value) metal cations to associate with nonbridging oxygens, whereas the more electropositive cation serves to charge-compensate Al^{3+} when in tetrahedral coordination (see, e.g., Neuville et al., 2008). Further details are provided in Section 9.3.2.4.

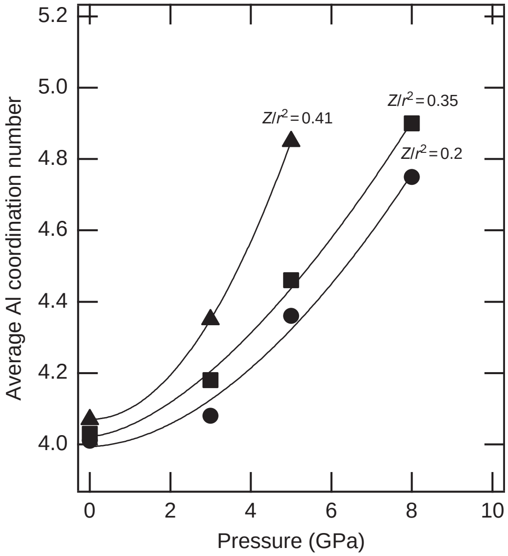

FIG. 9.36 Average Al^{3+} coordination number in quenched melts as a function of pressure and ionization potential, Z/r^2, of the metal cations in the systems $CaO\text{-}K_2O\text{-}Al_2O_3\text{-}SiO_2$ ($Z/r^2=0.2$, $NBO/T=0.35$), $CaO\text{-}MgO\text{-}K_2O\text{-}Al_2O_3\text{-}SiO_2$ ($Z/r^2=0.35$, $NBO/T=0.5$), and $CaO\text{-}MgO\text{-}Al_2O_3\text{-}SiO_2$ ($Z/r^2=0.41$, $NBO/T=0.7$). Note that NBO/T-values were calculated with the assumption that any metal cation in excess of that required to charge-compensate Al^{3+} in tetrahedral coordination at ambient pressure would serve as a network-modifier. The glasses were formed by temperature-quenching from above their liquidii at rates exceeding 100°C/s (Allwardt et al., 2007).

9.5 STRUCTURE AND PROPERTIES OF ALUMINOSILICATE MELTS

Physical and chemical properties of aluminosilicate glasses and melts vary systematically with composition. The main factors to be considered are the extent of Al^{3+} charge-compensation, the nature of the charge-compensating cation (or cations), and the silicate polymerization as characterized by the Q^n distribution.

9.5.1 Thermal Properties

Configurational properties of aluminosilicate melts and glasses are sensitive to structure in much the same manner as in binary metal oxide silicates glasses and melts (Courtial and Richet, 1993; Bouhifd et al., 1998; Solvang et al., 2004, Webb, 2008). As investigated by various authors (Barkhatov et al., 1973; Stolyarova et al., 1996; Wilding and Navrotsky, 1998; Shornikov and Archakov, 2002), the solution thermodynamics of the silicate components are, of course, the driving force for these structural changes as a function of composition. For example, the gradual changes in activity of Al_2O_3 in melts along the $SiO_2\text{-}Al_2O_3$ join (Shornikov and Archakov, 2002) likely is the cause of the gradual structural changes of Al^{3+} in melts along this join as the Al/Si abundance ratio of the melts decreases (Figs. 9.2–9.4). Moreover, the different structure of crystalline Al_2O_3 with Al^{3+} in sixfold coordination and that of its melts with four-, five-, and sixfold Al^{3+} coexisting (Landron et al., 2001) is reflected in the large heat of fusion of Al_2O_3 (~22 kJ/mol) and large volume change upon melting (Mitin and Nagibin, 1970; Barkhatov et al., 1973; Richet et al., 1993).

The environment of Al^{3+} in meta-aluminosilicate melts depends on the charge-compensating cation (Lee and Stebbins, 2000; Maekawa et al., 1999; McMillan et al., 1998;

Dubinsky and Stebbins, 2006; Thompson and Stebbins, 2011; Stebbins and Xu, 1997; Toplis et al., 2000; Neuville et al., 2004; Lee and Stebbins, 2006; Guignard and Cormier, 2008). These differences in general terms can be related to the varying strength of Al—O bonds. That strength, in turn, is expressed in enthalpy of solution of SiO_2-$M^{n+}Al_2O_{2n}$ glasses, which decreases systematically with increasing ionization potential of the metal cation (Roy and Navrotsky, 1984; see also Fig. 8.8). In fact, here there is a distinctive difference between the evolution of enthalpy of solution and metal cation properties, depending on the effective charge of the metal (Fig. 8.8). Moreover, the overall (Al,Si) ordering in these melts varies systematically with metal cation type (Seifert et al., 1982; Lee and Stebbins, 1999, 2000; Dubinsky and Stebbins, 2006; Neuville et al., 2007). The positive correlation of configurational heat capacity with the ionization potential of the charge-compensating cation of SiO_2-$M^{n+}Al_2O_{2n}$ melts (Richet and Neuville, 1992; Courtial and Richet, 1993; see Chapter 8, Fig. 8.10) is consistent with the structural evolution as the entropy and heat capacity of mixing increases as the structures become more disordered when the ionization potential of the charge-balancing cation increases.

Structure-property relationships in peralkaline aluminosilicate melts often are affected by the observation that Al^{3+} tends to partition strongly into Q^4 units compared with depolymerized structural units such as Q^3 and Q^2, and the fact that increasing Al/(Al+Si) tends therefore to drive equilibrium (Eq. 9.8) to the right.

In more polymerized portions of aluminosilicate melt compositional range, where tridymite is a liquidus phase, the temperature-composition trajectory of the SiO_2 polymorph liquidus surface can be used to calculate with the Van't Hoff relation the activity of SiO_2 in the melt and then to extract the activity coefficient of SiO_2, γSiO_2^{melt}. In such calculations, the trajectory of γSiO2melt differs significantly depending on whether we consider meta-aluminosilicate compositions with nearly all Q^4 species, and peralkaline, depolymerized aluminosilicate melts where Q^4-species coexist with Q^3 and Q^2 species (Fig. 9.37). In the latter,

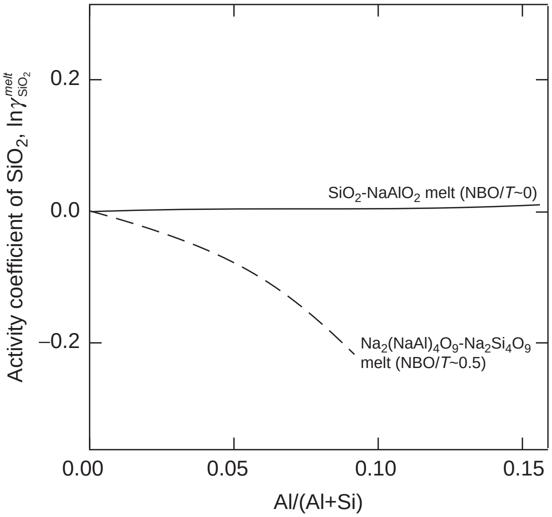

FIG. 9.37 Activity coefficient of SiO_2 in melts in the Na_2O-Al_2O_3-SiO_2 system, γSiO_2^{melt}, for compositions along the meta-aluminosilicate join, SiO_2-$NaAlO_2$ (*solid line*), and along the peralkaline composition join, $Na_2Si_4O_9$-$Na_2(NaAl)_4O_9$ (*dashed line*) from the temperature-composition trajectories of silica polymorphs on the liquidus. Calculations are based on ambient-pressure liquidus phase equilibrium data by Osborn and Muan (1960a).

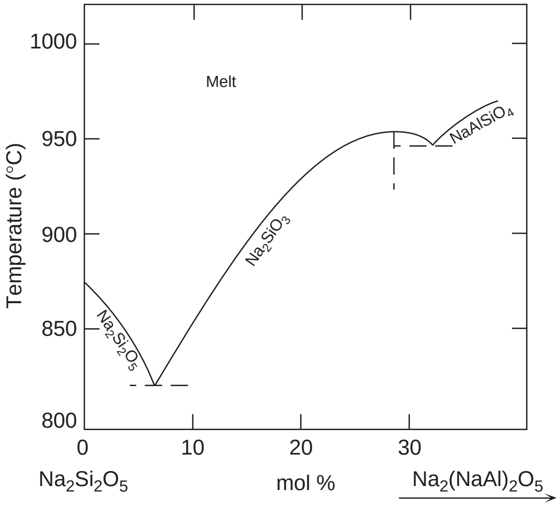

FIG. 9.38 Liquidus phase relations, at ambient pressure along the join $Na_2Si_2O_5$-$Na_2(NaAl)_2O_5$ (after Osborn and Muan, 1960a). Chemical formula denote crystalline phase on the liquidus in the composition range indicated.

γSiO_2^{melt} is profoundly dependent on the fact that the Al^{3+} preferentially substitutes for Si^{4+} in Q^4 units. In fact, with essentially all Al^{3+} in the Q^4 unit in depolymerized melts and the expectation that activity of SiO_2 in other Q species is less than unity, a decrease in the activity coefficient of SiO_2 in peralkaline Na-aluminosilicate melts with increasing bulk Al/(Al+Si) would be expected.

The nonrandom Al^{3+} distribution among structural units also is reflected in changes in liquidus phase relations along composition joins with constant nominal NBO/*T* but varying Al/(Al+Si). An example is the join $Na_2Si_2O_5$-$Na_2(NaAl)_2O_5$ where increasing Al/(Al+Si) results in disappearance of $Na_2Si_2O_5$ as the liquidus phase. However, instead of the appearance of an aluminous crystal, Na-metasilicate (Na_2SiO_3) is the liquidus phase over a wide Al/(Al+Si) range (Fig. 9.38). Although liquidus phase relations obviously depend on the properties of both melts and solids, this change is certainly consistent with increasing abundance of Q^2 units in the melts as the Al/(Al+Si) increases.

Element partitioning between melt and liquidus crystals can also reflect the melt structure in general (Jaeger and Drake, 2000; Toplis and Corgne, 2002) and the effect of Al^{3+} on speciation in the melt in particular (Mysen, 2007). Such effects have been recorded for transition metal partitioning between melt and olivine (Mg_2SiO_4) crystals on the liquidus (Mysen, 2007; see Fig. 9.39). In situations where melts retain constant bulk NBO/*T* (*T*=Al+Si) at constant temperature, but where the Al/(Al+Si) is allowed to vary, transition metal partition coefficients are very sensitive to the bulk Al/(Al+Si) of the melts. This sensitivity is a reflection of how Al^{3+} causes changes in proportion of different nonbridging oxygens, and therefore changes in activity coefficients of transition metals and, in the present example, Mg^{2+}. This happens because Al^{3+} governs the equilibrium coefficient for Eq. (9.8) and because different metal cations exhibit preference for nonbridging oxygens in different depolymerized Q^n-species in the melt (Mysen, 2007).

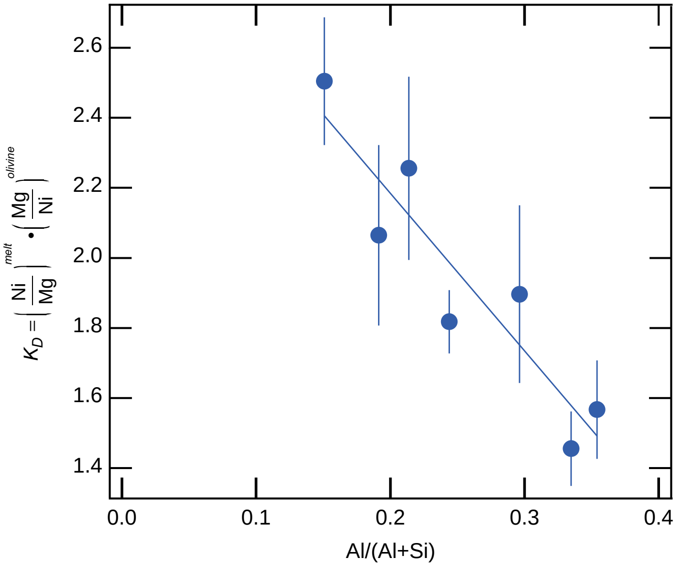

FIG. 9.39 Exchange equilibium coefficient (Ni, Mg) for an equilibrium, $Ni^{olivine}+Mg^{melt}=Mg^{olivine}+Ni^{melt}$, between olivine, Mg_2SiO_4, and coexisting melts in the system $NaAlSiO_4$-Mg_2SiO_4-SiO_2 at 145°C and ambient pressure as a function of Al/(ASi) (Mysen, 2007).

9.5.2 Physical Properties

Transport, volume and other physical properties are sensitive to the melt structure. In all cases, an important structural control lies in the strength of Al—O bonds in aluminosilicate tetrahedra. This strength, in turn, is governed by the form of charge-compensation of tetrahedrally coordinated Al^{3+} and in the response of (Si,Al)—O—(Si,Al) angles to substitution of Si^{4+} by Al^{3+} with different forms of charge-compensation.

9.5.2.1 Transport Properties

The main transport properties to be discussed are viscosity and diffusion. In Chapter 4, it was pointed out that for network-forming components (oxygen and tetrahedrally coordinated cations), these two types of properties may be linked, sometimes quantitatively, via the Stokes-Einstein or Eyring equations (see Chapter 4, Eqs. (4.10) and (4.11), respectively). The most useful treatment of complex systems such as aluminosilicate melts with multiple forms of charge-compensation and network-modification is the Eyring equation (Eyring, 1935), where melt viscosity and diffusivity are inversely related. The Stokes-Einstein relation commonly does not work well (Bouhadja et al., 2014).

The viscosity of Al_2O_3 melt, in contrast to that of SiO_2, is non-Ahrrenian (Urbain, 1982; Urbain et al., 1982; Langstaff et al., 2013). The curvature (Fig. 9.40) would be consistent with multiple AlO_n-species in Al_2O_3 melt, where the abundance of these species likely depends on temperature. That structural effect is reflected in the temperature-dependent average coordination number for Al^{3+} in Al_2O_3 above its liquidus temperature (Florian et al., 1995; Bessada et al., 1999; Winkler et al., 2004; Pfleiderer et al., 2006; Hoang et al., 2007). There is no evidence for a change in curvature across the melting point (Fig. 9.41), which would be consistent with the structure of supercooled Al_2O_3 liquid being in continuum with the superliquidus structure. Of course, the Ahrrenian nature of the viscosity of stable and supercooled liquid SiO_2 is

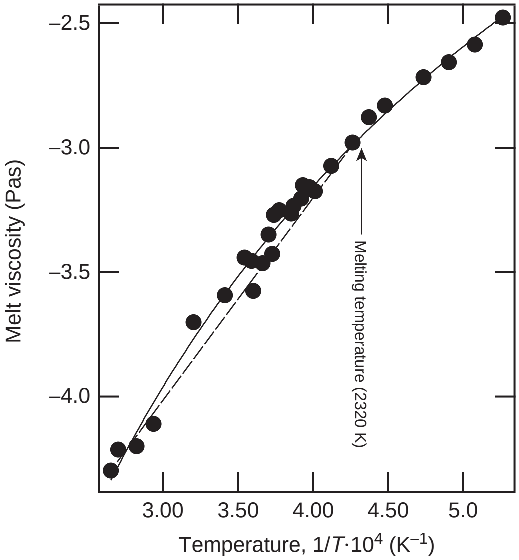

FIG. 9.40 Viscosity of Al_2O_3 melt from above to below its melting temperature (marked with arrow). A straight line fit to the data from the melting temperature and above is shown as a dashed line with a slope equivalent to 55±1J/mol. *Redrawn from Urbain (1982) and Langstaff et al. (2013).*

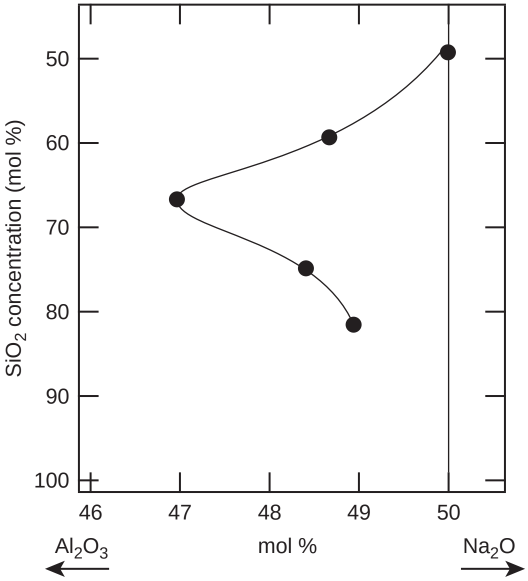

FIG. 9.41 Position of the viscosity maximum in Na_2O-Al_2O_3-SiO_2 melt at 1600°C as a function of composition (Toplis et al., 1997).

consistent with little or no structural change with temperature (see further discussion of SiO_2 melt in Chapter 5).

Transport properties of SiO_2-Al_2O_3 melts differ significantly from those of Al_2O_3 (Urbain et al., 1982). The viscous flow of molten Al_2O_3 is non-Ahrrenian. A rapid increase of viscosity and activation enthalpy of viscous flow attests to an important effect of the SiO_2 component. Moreover, the viscosities of SiO_2-Al_2O_3 melts are Ahrrenian above their liquidus temperatures with a rapid increase in activation enthalpies as Al/(Al+Si) decreases (Urbain et al., 1982). One might surmise from these differences that there is a close connection between structure and viscosity because, even for SiO_2-rich melts, there are multiple AlO_n polyhedra, the proportions of which likely are temperature dependent (Poe et al., 1992; Winkler et al., 2004). Interestingly, the diffusion constants for Si^{4+}, Al^{3+}, and O^{2+}, are non-Ahrrenian, at least in molecular dynamics simulations (Winkler et al., 2004; Pfleiderer et al., 2006; Hoang et al., 2007). Clearly, at least for aluminosilicate melts without charge-compensation, the Eyring relationship between melt viscosity and diffusivity fails.

Transport properties of aluminosilicate melts with partial or complete charge-compensation of Al^{3+} tend to show viscosity maxima and diffusivity minima near the meta-aluminosilicate joins. For example, in Na-aluminosilicate melts, isothermal viscosity reaches a maximum value near the SiO_2-$NaAlO_2$ join (Riebling, 1964, 1966; Toplis et al., 1997; Le Losq et al., 2014), a feature that led Riebling (1966) to suggest that as Na-aluminosilicate melts entered the peraluminous field, there may be a coordination transformation of the fraction of Al^{3+} for which Na is no longer available for charge-compensation. That simple model is consistent with the structural data in Fig. 9.2, which indicate that an increase in Al content from peralkaline to peraluminous is associated with a minimum in degree of polymerization, NBO/T, near the meta-aluminosilicate join. In Ca- and Mg-aluminosilicate melts, the viscosity maximum is much less pronounced. In fact, for Mg-aluminosilicates, the viscosities of Toplis and Dingwell (2004) do not show any maximum near the meta-aluminosilicate join (see also Chapter 8, Fig. 8.16). This smearing out and eventual disappearance of the viscosity maximum near the meta-aluminosilicate join likely is a reflection of three factors. These are: (i) the strength of the Al—O bond diminishes as the Z/r^2 of the charge-compensating cation increases (becomes more electronegative), (ii) the strength of the M—O bond increases with Z/r^2 (see Chapter 2, Table 2.1) so that the bond strengths of M—O and Al—O bonds approach one another, and, finally, (iii) the proportion of nonbridging oxygen in meta-aluminosilicate melts increases as the Z/r^2 of the charge-balancing cation increases (see Section 9.3.2.3).

The well-defined viscosity maximum of SiO_2-$NaAlO_2$ stable and supercooled melts (Riebling, 1966; Toplis et al., 1997) corresponds rather well to the minima in polymerization (Mysen and Cody, 2001). There is, however, a tendency of the maximum to shift slightly to the peraluminous side of the join (Fig. 9.41; see also Toplis et al., 1997). At least for peraluminous compositions near the meta-aluminosilicate join, most recent models have invoked Al-triclusters, the formation of which involves release of charge-compensating Na^+ cation, and, therefore, the shift of the viscosity maximum to the peraluminous side of the SiO_2-$NaAlO_2$ join (Mysen and Toplis, 2007). As noted previously, the greater abundance of triclusters in SiO_2-$CaAl_2O_4$ and SiO_2-$MgAl_2O_4$ melts (Neuville et al., 2008; Thompson and Stebbins, 2011) compared with SiO_2-$NaAlO_2$ may be at least partly responsible for the diminished expression of viscosity maxima in melts in the CaO-Al_2O_3-SiO_2 and MgO-Al_2O_3-SiO_2, as the CaO/Al_2O_3 and MgO/Al_2O_3 abundance ratio decreases from peralkaline across the meta-aluminous join to peraluminous melts (Chapter 8, Fig. 8.16).

Another interesting feature of the viscosity of melts along $SiO_2=M^{n+}Al_nO_{2n}$ is that by exchanging Ca^{2+} for Na^+ (two dissimilar charge-compensating cations resulting in some structural differences), the activation energy of viscous flow is a linear function of Na/(Na+Ca). In addition, the linearity remains whether the melts are peralkaline or peraluminous, although the slopes of these straight lines differ (Webb, 2008). In other words, there is no apparent "mixed alkalii effect." This observation implies that the nonlinear mixing effects seen in the viscosities of $NaAlSiO_8$-$CaAl_2Si_2O_8$ melts (Cranmer and Uhlmann, 1981) are probably more related to the variations in Al/(Al+Si) of the melts than to exchange of Ca^{2+} (as in $CaAl_2Si_2O_8$) for Na^+ (as in $NaAlSi_3O_8$). Interestingly, electrical conductivity, which likely is governed by metal cation mobility, does show a significant mixed alkali effect (Lapp and Shelby, 1987).

Substitution of Al^{3+} for Si^{4+} results in weakening of the (Si,Al)—O bridging oxygen bonds. In its simplest form this means that any property that depends on (Si,Al)—O bond strength reflects this substitution. This is evident in decreasing viscosity and activation energy of viscous flow of meta-aluminosilicate melts with increasing Al/(Al+Si) (Riebling, 1966; Toplis et al., 1997; Sukenaga et al., 2006). The magnitude of this viscosity change does, however, depend on the metal cation that serves to charge-compensate for Al^{3+} (Riebling, 1964, 1966; Stein and Spera, 1993; Toplis et al., 1997; Sukenaga et al., 2006). This is in part because the strength of bridging Al—O bonds is likely negatively correlated with the ionization potential of the charge-compensating metal cation. The latter structural differences may also account for the much greater compressibility of SiO_2-$NaAlO_2$ compared with SiO_2-$CaAl_2O_4$ melts (Kushiro, 1980, 1981; see also Fig. 9.32).

This difference in bond strength and flexibility of Al—O bonds may also explain why the negative pressure-dependence of viscosity of SiO_2-$NaAlO_2$ melts differs from that of SiO_2-$CaAl_2O_4$ melts (Mori et al., 2000; Suzuki et al., 2005; Allwardt et al., 2007). For the former, a negative pressure effect increases with increasing Al/(Al+Si) (Kushiro, 1976, 1978, 1980), whereas along the latter join, the viscosity becomes less dependent on pressure the higher the Al/(Al+Si) of the melt (Kushiro, 1981). This effect is related to differences in the flexibility of (Si,Al)—O—(Si,Al) angles depending on the nature of the charge-compensating cation. Interestingly, the O, Al, and Si diffusivities follow the opposite trend with pressure. At least for SiO_2-$NaAlO_2$ melts, these diffusion coenstants increase with pressure in the same pressure regime (Bryce et al., 1999), whereas for a Ca-aluminosilicate melt such as $CaAl_2Si_2O_8$, the O, Al, and Si dffusion constants decrease with increasing pressure (Karki et al., 2011).

It is notable, however, that in the 15–10 GPa pressure range, Al, Si, and O diffusivities reach maximum values before decreasing with further pressure increase (Bryce et al., 1999). Very likely, the melt viscosities in this system will reach minimum values in the same pressure range and then show viscosity increase with further pressure increase. This turnover likely reflects A^{3+} and Si^{4+} coordination changes in the melt, which lead to depolymerization and, therefore, different responses of transport properties to pressure (see also Chapters 6 and 7).

Structure-property relationships as a function of Al/(Al+Si) differ in peralkaline aluminosilicate and meta-aluminosilicate melts. For example, the activation energies of viscous flow in Na-dialuminosilicate decrease only slightly with Al/(Al+Si) and pass through minimum values at intermediate Al/(Al+Si) (Dingwell, 1986). This trend reflects the fact that Al^{3+} tends to partition strongly into Q^4 units compared with depolymerized structural units such as Q^3 and Q^2 and that increasing Al/(Al+Si) tends, therefore, to drive equilibrium (Eq. 9.8) to the right. This, in turn affects the activation energy of viscous flow and, therefore, the viscosity of these melts. The extent to which such effects will be encountered clearly depends on polymerization as well as on the way in which Al^{3+} is partitioned between coexisting structural units.

9.5.2.2 *Volume Properties*

The ambient-pressure partial molar volumes of SiO_2, alkali and alkaline earth oxides in silicate melts appear essentially independent of composition, and therefore melt structure (Bottinga et al., 1983; Lange and Carmichael, 1987; Lange, 1997). This simplicity does not hold true, however, for the partial molar volume of Al_2O_3 in molten Al_2O_3 and aluminum silicate melts (see Chapter 8 for details). In addition, thermal expansion and compressibility vary significantly with structure, and in particular the Al/Al+Si and metal/Al ratios as well as the nature of the metal cation (Aksay et al., 1979; Hunold and Bruckner, 1980; Courtial and Dingwell, 1995, 1999; Webb and Courtial, 1996; Sukenaga et al., 2011; Kuryaeva and Dmitrieva, 2014). These compositional effects relate back to the strength of the Al—O bond as a function of the type of charge-compensating cation. Compressibility and thermal expansion also are directly related to the Al—O bond strength, which in turn reflects the Al/(Al+Si) ratio and charge-compensating cation. Even in the absence of Al-charge compensation, for instance along the SiO_2-Al_2O_3 join, the molar volume of Al_2O_3 changes with Al/(Al+Si) (Aksay et al., 1979) because the average coordination number for Al^{3+} varies with Al/(Al+Si) (Bessada et al., 1999; Landron et al., 2001; Sen and Youngman, 2004; Pfleiderer et al., 2006). This evolution also changes with increasing temperature and becomes more pronounced the higher the temperature (see Fig. 8.26 in Chapter 8), which may reflect temperature-dependent Al^{3+} coordination in Al_2O_3 and perhap Al_2O_3-rich SiO_2-Al_2O_3 melts.

Finally, it follows from the structural and property summaries given previously and in Chapter 8 that the partial molar volume of Al_2O_3 in peralkaline aluminosilicate melts differs substantially from the molar volume of liquid Al_2O_3 (see Fig. 8.26). The structure of melts along meta-aluminosilicate joins, where nominally all Al^{3+} is charge-compensated with either alkali metals or alkaline earths, is nearly fully polymerized. These structural features change gradually on the peraluminous side of the meta-aluminosilicate join as high-coordinate Al^{3+} together with Al triclusters become more important.

References

Adjaouda, O., Steinle-Neumann, G., Jahn, S., 2008. Mg_2SiO_4 liquid under high pressure from molecular dynamics. Chem. Geol. 256, 185–192.

Ahuja, R., Belonoshko, A.B., Johansson, B., 1998. Melting and liquid structure of aluminum oxide using a molecular-dynamics simulation. Phys. Rev. E 57, 1673–1676.

Aksay, I.A., Pask, J.A., Davis, R.F., 1979. Densities of SiO_2-Al_2O_3 melts. J. Am. Ceram. Soc. 62, 332–336.

Allwardt, J.R., Lee, S.K., Stebbins, J.F., 2003. Bonding preference of non-bridging O atoms: evidence from ^{17}O MAS and 3QMAS NMR on calcium aluminate and low-silica Ca-aluminosilicate glasses. Am. Mineral. 88, 949–954.

Allwardt, J.R., Stebbins, J.F., Schmidt, B.C., Frost, D.J., Withers, A.C., Hirschmann, M.M., 2005. Aluminum coordination and the densification of high-pressure aluminosilicate glasses. Am. Mineral. 90, 1218–1222.

Allwardt, J.R., Stebbins, J.F., Terasaki, H., Du, L.S., Frost, D.J., Withers, A.C., Hirschmann, M.M., Suzuki, A., Ohtani, E., 2007. Effect of structural transitions on properties of high-pressure silicate melts: Al-27 NMR, glass densities, and melt viscosities. Am. Mineral. 92, 1093–1104.

Angel, R.J., McMullan, R.K., Prewitt, C.T., 1991. Substructure and superstructure of mullite by neutron diffraction. Am. Mineral. 76, 332–342.

Angeli, F., Delaye, J.M., Charpentier, T., Petit, J.-C., Ghaleb, D., Faucon, P., 2000. Investigation of Si-O-Al bond angle in glass by ^{27}Al 3Q-MAS NMR and molecular dynamics. Chem. Phys. Lett. 320, 681–687.

Angeli, F., Gaillard, M., Jollivet, P., Charpentier, T., 2007. Contribution of ^{43}Ca MAS NMR for probing the structural configuration of calcium in glass. Phys. Chem. Lett. 440, 324–328.

Ansell, S., Krishnan, S., Weber, R.K., Felten, J.J., Nordine, P.C., Bena, M.A., Price, D.L., Saboungi, M.L., 1997. Structure of liquid aluminum oxide. Phys. Rev. Lett. 78, 464–466.

Barkhatov, L.S., Kagan, D.N., Tsytsarkin, A.F., Shpil'rain, E.E., Yakimovich, K.A., 1973. Investigation of the thermodynamic properties of molten aluminum oxide. Teplofiz. Vys. Temper. 11, 1188–1191.

Belashchenko, D.K., Fedko, A.D., 1992. Computer study of the structure and properties of Al_2O_3-SiO_2 oxide systems. Inorg. Mater. 28, 85–94.

Benoit, M., Ispas, S., Tuckerman, M.E., 2001. Structural properties of molten silicates from ab initio molecular-dynamics simulations: comparison between CaO-Al_2O_3-SiO_2 and SiO_2. Phys. Rev. B 64, 224205. https://dx.doi.org/10.1103/PhysRevB.64.224205.

Benoit, M., Profeta, M., Mauri, F., Pickard, C.J., Tuckerman, M.E., 2005. First-principles calculation of the O-17 NMR parameters of a calcium aluminosilicate glass. J. Phys. Chem. B 109, 6052–6060.

Bessada, C., Lacassagne, V., Massiot, D., Florian, P., Coutures, J.-P., Robert, E., Gilbert, B., 1999. Structural and dynamic approaches of molten salts by high temperature spectroscopies. Z. Naturforschung Teil A 54, 162–166.

Bottinga, Y., Weill, D.F., 1972. The viscosity of magmatic silicate liquids: a model for calculation. Am. J. Sci. 272, 438–475.

Bottinga, Y., Richet, P., Weill, D.F., 1983. Calculation of the density and thermal expansion coefficient of silicate liquids. In: Anonymous, (Ed.), Conference on Liquid Silicates. Masson, Paris, France, pp. 129–138.

Bouhadja, M., Jakse, N., Pasturel, A., 2013. Structural and dynamic properties of calcium aluminosilicate melts: a molecular dynamics study. J. Chem. Phys. 138. https://dx.doi.org/10.1063/1.4809523.

Bouhadja, M., Jakse, N., Pasturel, A., 2014. Stokes-Einstein violation and fragility in calcium aluminosilicate glass formers: a molecular dynamics study. Mol. Simul. 40, 251–259.

Bouhifd, M.A., Courtial, P., Richet, P., 1998. Configurational heat capacities: alkali vs. alkaline-earth aluminosilicate liquids. J. Non-Cryst. Solids 231, 169–177.

Bryce, J.G., Spera, F.J., Stein, D.J., 1999. Pressure dependence of self-diffusion in the $NaAlO_2$-SiO_2 system: compositional effects and mechanisms. Am. Mineral. 84, 345–356.

Connelly, A.J., Hyatt, N.C., Travis, K.P., Hand, R.J., Maddrell, E.R., 2011. Predicting the preference for charge compensation in silicate glasses. Phys. Chem. Glasses-B 52, 64–67.

Cormier, L., Neuville, D.R., 2004. Ca and Na environments in Na_2O-CaO-Al_2O_3-SiO_2 glasses: influence of cation mixing and cation-network interactions. Chem. Geol. 213, 103–113.

Cormier, L., Ghaleb, D., Neuville, D.R., Delaye, J.-M., Calas, G., 2003. Chemical dependence of network topology of calcium aluminosilicate glasses: a computer simulation study. J. Non-Cryst. Solids 332, 255–270.

Courtial, P., Dingwell, D.B., 1995. Nonlinear composition dependence of molar volume of melts in the CaO-Al_2O_3-SiO_2 system. Geochim. Cosmochim. Acta 59, 3685–3695.

Courtial, P., Dingwell, D.B., 1999. Densities of melts in the CaO-MgO-Al_2O_3-SiO_2 system. Am. Mineral. 84, 465–476.

Courtial, P., Richet, P., 1993. Heat capacity of magnesium aluminosilicate melts. Geochim. Cosmochim. Acta 57, 1267–1276.

Cranmer, D., Uhlmann, D.R., 1981. Viscosities in the system albite-anorthite. J. Geophys. Res. 86, 7951–7957.

Creux, S., Bouchetfabre, B., Gaskell, P.H., 1995. Anomalous wide-angle x-ray scattering study of strontium silicate and aluminosilicate glasses. J. Non-Cryst. Solids 193, 360–363.

Daniel, I., Gillet, P., McMillan, P.F., Richet, P., 1995. An in-situ high-temperature structural study of stable and metastable $CaAl_2Si_2O_8$ polymorphs. Mineral. Mag. 59, 25–33.

Dingwell, D.B., 1986. Viscosity-temperature relationships in the system $Na_2Si_2O_5$-$Na_4Al_2O_5$. Geochim. Cosmochim. Acta 50, 1261–1265.

Dirken, P.J., Kohn, S.C., Smith, M.E., van Eck, E.R.H., 1997. Complete resolution of Si-O-Si and Si-O-Al fragments in an aluminosilicate glass by O-17 multiple quantum magic angle spinning NMR spectroscopy. Chem. Phys. Lett. 266, 568–574.

Drewitt, J.W.E., Jahn, S., Cristiglio, V., Bytchov, A., Leydier, M., Brassamin, S., Fisher, H.E., Hennet, L., 2011. The structure of liquid calcium aluminates as investigated using neutron and high energy x-ray diffraction in combination with molecular dynamics simulation methods. J. Phys. Condensed Matter 23, 155101.

Drewitt, J.W.E., Jahn, S., Sanloup, C., de Grouchy, C., Garbariono, G., Hennet, L., 2015. Development of chemical and topological structure in aluminosilicate liquids and glasses at high pressure. J. Phys. Condensed Matter 27, 105103.

Dubinsky, E.V., Stebbins, J.F., 2006. Quench rate and temperature effects on framework ordering in aluminosilicate melts. Amer. Mineral. 91, 753–761.

Engelhardt, G., Michel, D., 1987. High-Resolution Solid-State NMR of Silicates and Zeolites. Wiley, New York.

Engelhardt, G., Nofz, M., Forkel, K., Wishmann, F.G., Magi, M., Samoson, A., Lippmaa, E., 1985. Structural studies of calcium aluminosilicate glasses by high resolution solid state ^{29}Si and ^{27}Al magic angle spinning nuclear magnetic resonance. Phys. Chem. Glasses 26, 157–165.

Eyring, H., 1935. The activated complex and the absolute rate of chemical reactions. Chem. Rev. 17, 65–77.

Farnan, I., Stebbins, J.F., 1990a. The relationship between atomic scale dynamics and the bulk macroscopic properties of silicate liquids; results from high temperature NMR. In: Anonymous, (Ed.), V. M. Goldschmidt Conference; Program and Abstract. Soc., United States: Geochem, 45.

Farnan, I., Stebbins, J.F., 1990b. A high temperature ^{29}Si investigation of solid and molten silicates. J. Amer. Ceram. Soc. 112, 32–39.

Fiske, P.S., Stebbins, J.F., Farnan, I., 1994. Bonding and dynamical phenomena in MgO; a high temperature 17-O and 25-Mg NMR study. Phys. Chem. Minerals 20, 587–593.

Florian, P., Massiot, D., Poe, B., Farnan, I., Coutures, J.-P., 1995. A time resolved ^{27}Al study of the cooling process of liquid alumina from 2450°C to crystallization. Solid State Magn. Res. 5, 233–238.

Funamori, N., Ymamaoto, S., Yagi, T., Kikegawa, T., 2004. Exploratory studies of silicate melt structure at high pressures and temperatures by in situ X-ray diffraction. J. Geophys. Res. 109. https://dx.doi.org/10.1029/2003JB002650.

Furukawa, T., Fox, K.E., White, W.B., 1981. Raman spectroscopic investigation of the structure of silicate glasses. III. Raman intensities and structural units in sodium silicate glasses. J. Chem. Phys. 153, 3226–3237.

Galeener, F.L., 1979. Band limits and the vibrational spectra of tetrahedral glasses. Phys. Rev. B19, 4292–4298.

Gambuzzi, E., Pedone, A., Menziani, M.C., Angeli, F., Florina, P., Charpentier, T., 2015. Calcium environment in silicate and aluminosilicate glasses probed by ^{43}Ca MQMAS NMR experiments and MD-GIPAW calculations. Solid State Nucl. Reson. 68–69, 31–36.

Ganster, P., Benoit, M., Delaye, J.M., Kob, W., 2007. Structural and vibrational properties of a calcium aluminosilicate glass: classical force-fields vs. first-principles. Mol. Simul. 33, 1093–1103.

George, A.M., Stebbins, J.F., 1996. Dynamics of Na in sodium aluminosilicate glasses and liquids. Phys. Chem. Minerals 23, 526–534.

Guignard, M., Cormier, L., 2008. Environments of Mg and Al in MgO-Al_2O_3-SiO_2 glasses: a study coupling neutron and X-ray diffraction and Reverse Monte Carlo modeling. Chem. Geol. 256, 111–118.

Gutierrez, G., Johansson, B., 2002. Molecular dynamics study of structural properties of amorphous Al_2O_3. Phys. Rev. B. 65. https://dx.doi.org/10.1103/PhysRevB.65.104202.

Hemmati, M., Wilson, M., Madden, P.A., 1999. Structure of liquid Al_2O_3 from a computer simulation model. J. Phys. Chem. B 103, 4023–4028.

Henderson, G.S., Neuville, D.R., Cormier, L., 2009. An O K-edge XANES study of glasses and crystals in the CaO-Al_2O_3-SiO_2 (CAS) system. Chem. Geol. 259, 54–62.

Hennet, L., Pozdnyakova, I., Cristiglio, V., Krishnan, S., Bytchkov, A., Albergamo, F., Cuello, G.J., Brun, J.F., Fischer, H.E., Zanghi, D., Brassamin, S., Saboungi, M.L., Price, D.L., 2007. Structure and dynamics of levitated liquid aluminates. J. Non-Cryst. Solids 353, 1705–1712.

Himmel, B., Weigelt, J., Gerber, T., Nofz, M., 1991. Structure of calcium aluminosilicate glasses—wide-angle x-ray scattering and computer simulation. J. Non-Cryst. Solids 136, 27–36.

Hoang, V.V., Linh, N.N., Hung, N.H., 2007. Structure and dynamics of liquid and amorphous $Al_2O_3 \bullet 2SiO_2$. Eur. Phys. J. Appl. Phys. 37, 111–118.

Hunold, K., Bruckner, R., 1980. Physikalische Eigenschaften und struktureller Feinbau von Natrium-Alumosilicatgläsern und -schmelzen. Glastechn. Ber. 53, 149–161.

Ispas, S., Benoit, M., Jund, P., Jullien, R., 2002. Structural properties of glassy and liquid sodium tetrasilicate: comparison between ab initio and classical molecular dynamics simulations. J. Non-Cryst. Solids 307, 946–955.

Jaeger, W.L., Drake, M.J., 2000. Metal-silicate partitioning of Co, Ga, and W; dependence on silicate melt composition. Geochim. Cosmochim. Acta 64, 3887–3895.

Jahn, S., 2008. Atomic structure and transport properties of MgO-Al_2O_3 melts: a molecular dynamics simulation study. Am. Mineral. 93, 1486–1492.

Kanehashi, K., Stebbins, J.F., 2007. In situ high temperature Al-27 NMR study of structure and dynamics in a calcium aluminosilicate glass and melt. J. Non-Cryst. Solids 353, 4001–4010.

Kang, E.T., Lee, S.J., Hannon, A.C., 2006. Molecular dynamics simulations of calcium aluminate glasses. J. Non-Cryst. Solids 352, 725–736.

Karki, B.B., Bohara, B., Stixrude, L., 2011. First-principles study of diffusion and viscosity of anorthite ($CaAl_2Si_2O_8$) liquid at high pressure. Am. Mineral. 96, 744–751.

Kato, D., 1976. Raman spectrum and refractive index behavior of Al_2O_3 added high-silica-content glass. J. Appl. Phys. 47, 5344–5348.

Kelsey, K.E., Stebbins, J.F., Du, L.S., Hankins, B., 2007. Constraining O-17 and Al-27 NMR spectra of high-pressure crystals and glasses: new data for jadeite, pyrope, grossular, and mullite. Am. Mineral. 92, 210–216.

Kelsey, K.E., Allwardt, J.R., Stebbins, J.F., 2008. Ca-Mg mixing in aluminosilicate glasses: an investigation using O-17 MAS and 3QMAS and Al-27 MAS NMR. J. Non-Cryst. Solids 354, 4644–4653.

Kelsey, K.E., Stebbins, J.F., Mosenfelder, J.L., Asimow, P.D., 2009. Simultaneous aluminum, silicon, and sodium coordination changes in 6 GPa sodium aluminosilicate glasses. Am. Mineral. 94, 1205–1215.

Kubicki, J.D., Sykes, D., 1993. Molecular orbiatal calculations on $H_6Si_2O_7$ with a variable Si-O-Si angle: implications for the high-pressure vibrational spectra of silicate glasses. Am. Mineral. 78, 253–259.

Kubicki, J.D., Toplis, M.J., 2002. Molecular orbital calculations on aluminosilicate tricluster molecules: implications for the structure of aluminosilicate glasses. Am. Mineral. 87, 668–678.

Kuryaeva, R.G., Dmitrieva, N.V., 2014. Effect of the replacement of sodium by calcium on compressibility in the $CaO(Na_2O)$-Al_2O_3-SiO_2 glass system. Phys. Chem. Glasses-B 55, 253–260.

Kushiro, I., 1976. Changes in viscosity and structure of melt of $NaAlSi_2O_6$ composition at high pressures. J. Geophys. Res. 81, 6347–6350.

Kushiro, I., 1978. Viscosity and structural changes of albite ($NaAlSi_3O_8$) melt at high pressures. Earth Planet. Sci. Lett. 41, 87–91.

Kushiro, I., 1980. Viscosity, density, and structure of silicate melts at high pressures, and their petrological applications. In: Hargraves, R.B. (Ed.), Physics of Magmatic Processes. Princeton University Press, Princeton, NJ, pp. 93–120.

Kushiro, I., 1981. Viscosity change with pressure of melts in the system CaO-Al_2O_3-SiO_2. Carnegie Instn. Washington Year Book 80, 339–341.

Lacy, E.D., 1963. Aluminum in glasses and melts. Phys. Chem. Glasses 4, 234–238.

Landron, C., Hennet, L., Jenkins, T.E., Greaves, G.N., Coutures, J.-P., Soper, A.K., 2001. Liquid alumina: detailed atomic coordination determined from neutron diffraction data using empirical potential structure refinement. Phys. Rev. Lett. 86, 4839–4842.

Lange, R.A., 1997. A revised model for the density and thermal expansivity of K_2O-Na_2O-CaO-MgO-Al_2O_3-SiO_2 liquids from 700 to 1900 K: extension to crustal magmatic temperatures. Contrib. Mineral. Petrol. 130, 1–11.

Lange, R.A., Carmichael, I.S.E., 1987. Densities of Na_2O-K_2O-CaO-MgO-Fe_2O_3-Al_2O_3-TiO_2-SiO_2 liquids: new-measurements and derived partial molar properties. Geochim. Cosmochim. Acta 51, 2931–2946.

Langstaff, D., Gunn, M., Greaves, G.N., Marsing, A., Kargl, F., 2013. Aerodynamic levitator furnace for measuring thermophysical properties of refractory liquids. Rev. Sci. Instr. 84. https://doi.org/10.1063/1.4832115.

Lapp, J.C., Shelby, J.E., 1987. The mixed alkali effect in lithoum-sdium aluminosilicate glasses. J. Non-Cryst. Solids 95–96, 889–896.

Le Losq, C., Neuville, D.R., Florian, P., Henderson, G.S., Massiot, D., 2014. The role of Al3+ on rheology and structural changes in sodium silicate and aluminosilicate glasses and melts. Geochim. Cosmochim. Acta 126, 495–517.

Lee, S.K., Stebbins, J.F., 1999. The degree of aluminum avoidance in aluminum silicate glasses. Am. Mineral. 84, 937–945.

Lee, S.K., Stebbins, J.F., 2000. The structure of aluminosilicate glasses: high-resolution O-17 and Al-27 MAS and 3QMAS. J. Phys. Chem. B 104, 4091–4100.

Lee, S.K., Stebbins, J.F., 2002. Extent of intermixing among framework units in silicate glasses and melts. Geochim. Cosmochim. Acta 66, 303–309.

Lee, S.K., Stebbins, J.F., 2003. The distribution of sodium ions in aluminosilicate glasses: a high-field Na-23 MAS and 3Q MAS NMR study. Geochim. Cosmochim. Acta 67, 1699–1709.

Lee, S.K., Stebbins, J.F., 2006. Disorder and the extent of polymerization in calcium silicate and aluminosilicate glasses: O-17 NMR results and quantum chemical molecular orbital calculations. Geochim. Cosmochim. Acta 70, 4275–4286.

Lee, S.K., Fei, Y., Cody, G.D., Mysen, B.O., 2003. Structure and disorder of silicate melts at high pressure: ^{17}O 3Q MAS NMR, quantum calculations and thermodynamic modeling. Geochim. Cosmochim. Acta 67 (S1), A248.

Lee, S.K., Cody, G.D., Fei, Y.W., Mysen, B.O., 2006. The effect of Na/Si on the structure of sodium silicate and aluminosilicate glasses quenched from melts at high pressure: a multi-nuclear (Al-27, Na-23, O-17) 1D and 2D solid-state NMR study. Chem. Geol. 229, 162–172.

Lee, S.K., Yi, Y.S., Cody, G.D., Mibe, K., Fei, Y.W., Mysen, B.O., 2012. Effect of network polymerization on the pressure-induced structural changes in sodium aluminosilicate glasses and melts: Al-27 and O-17 solid-state NMR Study. J. Phys. Chem. C 116, 2183–2191.

Licheron, M., Montouillout, V., Millot, F., Neuville, D.R., 2011. Raman and 27Al NMR structure investigations of aluminate glasses: (1–x)Al_2O_{3-}x MO, with M = Ca, Sr, Ba and ($0.5<x<0.75$). J. Non-Cryst. Solids 357, 2796–2801.

Liu, S.B., Pines, A., Brandriss, M., Stebbins, J.F., 1987. Relaxation mechanisms and effects of motion in albite ($NaAlSi_3O_8$) liquid and glass: a high temperature NMR study. Phys. Chem. Minerals 15, 155–162.

Maekawa, H., Maekawa, T., Kawamura, K., Yokokawa, T., 1991. ^{29}Si MAS NMR investigation of the Na2O-Al_2O_3-SiO_2 glasses. J. Phys. Chem. 95, 6822–6827.

Maekawa, H., Nakao, T., Shimokawa, S., Yokokawa, T., 1997. Coordination of sodium ions in $NaAlO_2$-SiO_2 melts: a high temperature Na-23 NMR study. Phys. Chem. Mineral. 24, 53–65.

Maekawa, H., Nakao, T., Shimokawa, S., Yokokawa, T., 1999. Coordination of sodium ions in $NaAlO_2$–SiO_2 melts: a high temperature ^{23}Na NMR study. Phys. Chem. Minerals 24, 53–65.

Marumo, Y., Okuno, M., 1984. X-ray structural studies of molten silicates: anorthite and albite melts. In: Sunagawa, I. (Ed.), Materials Science in the Earth's Interior. Tokyo, Terra Scientific, pp. 25–38.

Matson, D.W., Sharma, S., Philpotts, J.A., 1986. Raman spectra of some tectosilicates and glasses along the orthoclase-anorthite and nepheline-anorthite joins. Am. Mineral. 71, 694–704.

Matsui, M., 1996. Molecular dynamics simulation of structures, bulk moduli, and volume thermal expansivities of silicate liquids in the system CaO-MgO-Al_2O_3-SiO_2. Geophys. Res. Lett. 23, 395–398.

McMillan, P., Piriou, B., 1982. The structures and vibrational spectra of crystals and glasses in the silica-alumina system. J. Non-Cryst. Solids 279–298.

McMillan, P.F., Wolf, G.H., Poe, B.T., 1992. Vibrational spectroscopy of silicate liquids and glasses. Chem. Geol. 96, 351–366.

McMillan, P., Petusky, W.T., Coté, B., Massiot, D., Landron, C., Coutoures, J.P., 1996a. A structural investigation of CaO-Al_2O_3 glasses via ^{27}Al MAS-NMR. J. Non-Cryst. Solids 195, 261–271.

McMillan, P.F., Petuskey, W.T., Cote, B., Massiot, D., Landron, C., Coutures, J.P., 1996b. A structural investigation of CaO-Al_2O_4 glasses via Al-27 MAS-NMR. J. Non-Cryst. Solids 195, 261–271.

McMillan, P.F., Grzechnik, A., Chotalla, H., 1998. Structural characterization of SiO_2-$CsAlO_2$ and SiO_2-$RbAlO_2$ glasses. J. Non-Cryst. Solids 226, 239–248.

Merzbacher, C.I., White, W.B., 1991. The structure of alkaline earth aluminosilicate glasses as determined by vibrational spectroscopy. J. Non-Cryst. Solids 130, 18–34.

Merzbacher, C.I., Sherriff, B.L., Hartman, J.S., White, W.B., 1990. A high-resolution ^{29}Si and ^{27}Al NMR study of alkaline earth aluminosilicate glasses. J. Non-Cryst. Solids 124, 194–206.

Mitin, B.S., Nagibin, Y.A., 1970. Density of molten aluminum oxide. Russ. J. Phys. Chem. 44, 741–742.

Moesgaard, M., Keding, R., Skibsted, J., Yue, Y.Z., 2010. Evidence of intermediate-range order heterogeneity in calcium aluminosilicate glasses. Chem. Mater. 22, 4471–4483.

Morgan, N.A., Spera, F.J., 2001. A molecular dynamics study of the glass transition in $CaAl_2Si_2O_8$: thermodynamics and tracer diffusion. Am. Mineral. 86, 915–926.

Mori, S., Ohtani, E., Suzuki, A., 2000. Viscosity of albite melt to 7 GPa at 2000K. Earth Planet. Sci. Lett. 175, 87–92.

Mysen, B.O., 1995. Structural behavior of Al^{3+} in silicate melts: In-situ, high-temperature measurements as a function of bulk chemical composition. Geochim. Cosmochim. Acta 59, 455–474.

Mysen, B.O., 1997. Aluminosilicate melts: structure, composition and temperature. Contrib. Mineral. Petrol. 127, 104–118.

Mysen, B.O., 1999. Structure and properties of magmatic liquids: from haplobasalt to haploandesite. Geochim. Cosmochim. Acta 63, 95–112.

Mysen, B.O., 2007. Olivine/melt transition metal partitioning, melt composition, and melt structure—influence of $Si^{4+,}$ Al^{3+} substitution in the tetrahedral network. Geochim. Cosmochim. Acta 71, 5500–5513.

Mysen, B.O., Cody, G.D., 2001. Silicate-phosphate interaction in silicate glasses and melts. II. Quantitative, high-temperature structure of P-bearing alkali aluminosilicate melts. Geochim. Cosmochim. Acta 65, 2413–2431.

Mysen, B.O., Frantz, J.D., 1992. Raman spectroscopy of silicate melts at magmatic temperatures: Na_2O-SiO_2, K_2O-SiO_2, and Li_2O-SiO_2 binary compositions in the temperature range 25°-1475°C. Chem. Geol. 96, 321–332.

Mysen, B.O., Frantz, J.D., 1994. Structure of haplobasaltic liquids at magmatic temperatures: in-situ, high-temperature study of melts on the join $Na_2Si_2O_5$-$Na_2(NaAl)_2O_5$. Geochim. Cosmochim. Acta 58, 1711–1733.

Mysen, B.O., Toplis, M.J., 2007. Structural behavior of Al^{3+} in peralkaline, metaluminous, and peraluminous silicate melts and glasses at ambient pressure. Am. Mineral. 92, 933–946.

Mysen, B.O., Virgo, D., Kushiro, I., 1981. The structural role of aluminum in silicate melts—a Raman spectroscopic study at 1 atmosphere. Am. Mineral. 66, 678–701.

Mysen, B.O., Virgo, D., Danckwerth, P., Seifert, F.A., Kushiro, I., 1983. Influence of pressure on the structure of melts on the joins $NaAlO_2$-SiO_2, $CaAl_2O_4$-SiO_2 and $MgAl_2O_4$-SiO_2. N. Jb. Mineral. Abh. 147, 281–303.

Mysen, B.O., Lucier, A., Cody, G.D., 2003. The structural behavior of Al^{3+} in peralkaline melts and glasses in the system Na_2O-Al_2O_3-SiO_2. Am. Mineral. 88, 1668–1678.

Navrotsky, A., Geisinger, K.L., McMillan, P., Gibbs, G.V., 1985. The tetrahedral framework in glasses and melts—influences from molecular orbital calculations and implications for structure, thermodynamics, and physical properties. Phys. Chem. Minerals 11, 284–298.

Neuville, D.R., Mysen, B.O., 1996. Role of aluminum in the silicate network: in-situ, high-temperature study of glasses and melts on the join SiO_2-$NaAlO_2$. Geochim. Cosmochim. Acta 60, 1727–1738.

Neuville, D.R., Cormier, L., Massiot, D., 2004. Al environment in tectosilicate and peraluminous glasses: an Al-27 MQ-MAS NMR, Raman, and XANES investigation. Geochim. Cosmochim. Acta 68, 5071–5079.

Neuville, D.R., Cormier, L., Massiot, D., 2006. Al coordination and speciation in calcium aluminosilicate glasses: effects of composition determined by Al-27 MQ-MAS NMR and Raman spectroscopy. Chem. Geol. 229, 173–185.

Neuville, D.R., Cormier, L., Montouillout, V., Massiot, D., 2007. Local Al site distribution in aluminosilicate glasses by Al-27 MQMAS NMR. J. Non-Cryst. Solids 353, 180–184.

Neuville, D.R., Cormier, L., Montouillout, V., Florian, P., Millot, F., Rifflet, J.C., Massiot, D., 2008. Structure of Mg- and Mg/Ca aluminosilicate glasses: Al-27 NMR and Raman spectroscopy investigations. Am. Mineral. 93, 1721–1731.

Neuville, D.R., Henderson, G.S., Cormier, L., Massiot, D., 2010. The structure of crystals, glasses, and melts along the CaO-Al_2O_3 join: results from Raman, Al L- and K-edge X-ray absorption, and Al-27 NMR spectroscopy. Am. Mineral. 95, 1580–1589.

Ni, H., De Kroker, N., 2011. Thermodynamics, diffusion and structure of $NaAlSi_2O_6$ liquid at mantle conditions: a first-principles molecular dynamics investigation. J. Geophys. Res. 116. https://dx.doi.org/10.1029/2010JB008072.

Ohtani, E., Taulelle, F., Angell, C.A., 1985. Al^{3+} coordination changes in liquid silicates under pressure. Nature 314, 78–81.

Okuno, M., Zotov, N., Schmucker, M., Schneider, H., 2005. Structure of SiO_2-Al_2O_3 glasses: combined X-ray diffraction, IR and Raman studies. J. Non-Cryst. Solids 351, 1032–1038.

Osborn, E.F., Muan, A., 1960a. Phase equilibrium diagrams for ceramists. Plate 4. The system Na_2O-Al_2O_3-SiO_2. Amer. Ceram. Soc. Columbus OH.

Osborn, E.F., Muan, A., 1960b. Phase equilibrium diagrams of oxide systems. Plate 3. The System MgO-Al_2O_3-SiO_2. Amer. Ceram. Soc. Columbus OH.

Osborn, E.F., Muan, A., 1960c. Phase equilibrium diagrams of oxide systems. Plate 2. The System CaO-Al_2O_3-SiO_2. Amer. Ceram. Soc. Columbus OH.

Park, S.Y., Lee, S.K., 2014. High-resolution solid-state NMR study of the effect of composition on network connectivity and structural disorder in multi-component glasses in the diopside and jadeite join: implications for structure of andesitic melts. Geochim. Cosmochim. Acta 147, 26–42.

Pedone, A., Gambuzzi, E., Malavasi, G., Menziani, M.C., 2012. First-principles simulations of the Al-27 and O-17 solid-state NMR spectra of the $CaAl_2Si_3O_{10}$ glass. Theor. Chem. Acct. 131. https://dx.doi.org/10.1007/s00214-012-1147-5.

Pfleiderer, P., Horbach, J., Binder, K., 2006. Structure and transport properties of amorphous aluminium silicates: computer simulation studies. Chem. Geol. 229, 186–197.

Phillips, M.W., Ribbe, P.H., 1973. The structures of monoclinic potassium-rich feldspars. Am. Mineral. 58, 263–270.

Poe, B.T., McMillan, P.F., Coté, B., Massiot, D., Coutoures, J.-P., 1992. SiO_2- Al_2O_3 liquids: in-situ study by high-temperature ^{27}Al NMR spectroscopy and molecular dynamics simulations. J. Phys. Chem. 96, 8220–8224.

Poe, B., McMillan, P.F., Coté, B., Massiot, D., Coutures, J.-P., 1993. Magnesium and calcium aluminate liquids: in situ high-temperature ^{27}Al NMR spectroscopy. Science 259, 786–788.

Poe, B., McMillan, P.F., Coté, B., Massiot, D., Coutoures, J.P., 1994. Structure and dynamics of calcium aluminate liquids: high-temperature 27Al NMR and Raman spectroscopy. J. Am. Ceram. Soc. 77, 1832–1838.

Poe, B.T., Romano, C., Zotov, N., Cibin, G., Marcelli, A., 2001. Compression mechanisms in aluminosilicate melts: Raman and XANES spectroscopy of glasses quenched from pressures up to 10 GPa. Chem. Geol. 174, 21–31.

Prewitt, C.T., Burnham, C.W., 1966. The crystal structure of jadeite, $NaAlSi_2O_6$. Am. Mineral. 51, 956–975.

Prewitt, C.T., Sueno, S., Papike, J.J., 1976. The crystal structures of high albite and monalbite at high temperatures. Am. Mineral. 61, 1213–1225.

Richet, P., Neuville, D.R., 1992. Thermodynamics of silicate melts: configurational properties. In: Saxena, S.K. (Ed.), Thermodynamic Data: Systematics and Estimation. Springer, New York, NY, pp. 132–161.

Richet, P., Leclerc, F., Benoit, L., 1993. Melting of forsterite and spinel, with implications for the glass transition of Mg_2SiO_4 liquid. Geophys. Res. Lett. 20, 1675–1678.

Riebling, E.F., 1964. Structure of magnesium aluminosilicate liquids at 1700°C. Can. J. Chem. 42, 2811–2821.

Riebling, E.F., 1966. Structure of molten sodium aluminosilicate liquids containing at least 50 mol% SiO_2 at 1500°C. J. Chem. Phys. 44, 2857–2865.

Risbud, S.H., Kirkpatrick, R.J., Taglialavore, A.P., Montez, B., 1987. Solid-state NMR evidence of 4-, 5-, and 6-fold aluminum sites in roller-quenched SiO_2-Al_2O_3 glasses. J. Am. Ceram. Soc. 70, C10–C12.

Roy, B.N., Navrotsky, A., 1984. Thermochemistry of charge-coupled substitutions in silicate glasses: the systems $M^{n+}_{1/n}AlO_2$- SiO_2 (M = Li, Na, K, Rb, Cs, Mg, Ca, Sr, Ba, Pb). J. Am. Ceram. Soc. 67, 606–610.

Sakamaki, T., Wang, Y.B., Park, C., Yu, T., Shen, G.Y., 2012. Structure of jadeite melt at high pressures up to 4.9 GPa. J. Appl. Phys. 111. https://dx.doi.org/10.1063/1.4726246.

Sato, R.K., McMillan, P.F., Dennison, P., Dupree, R., 1991. A structural investigation of high alumina glasses in the CaO-Al_2O_3-SiO_2 system via Raman and magic angle spinning nuclear magnetic resonance spectroscopy. Phys. Chem. Glasses 32, 149–160.

Scamehorn, C.A., Angell, C.A., 1991. Viscosity-temperature relations and structure in fully polymerized aluminosilicate melts from ion dynamics simulations. Geochim. Cosmochim. Acta 55, 721–730.

Schmücker, M., MacKenzie, J.J.D., Schneider, H., Meinhold, R., 1997. NMR studies on rapidly solidified SIO_2-Al_2O_3 and SiO_2-Al_2O_3-Na_2O-glasses. J. Non-Cryst. Solids 217, 95–105.

Seifert, F.A., Mysen, B.O., Virgo, D., 1982. Three-dimensional network structure in the systems SiO_2-$NaAlO_2$, SiO_2-$CaAl_2O_4$ and SiO_2-$MgAl_2O_4$. Am. Mineral. 67, 696–711.

Sen, N., Thorpe, M.F., 1977. Phonons in AX2 glasses: from molecular to band-like modes. Phys. Rev. Lett. B15, 4030–4038.

Sen, S., Youngman, R.E., 2004. High-resolution multinuclear NMR structural study of binary aluminosilicate and other related glasses. J. Phys. Chem. B 108, 7557–7564.

Shornikov, S.I., Archakov, I.Y., 2002. A mass spectrometric determination of the enthalpies and entropies of Al_2O_3-SiO_2 melts. Russ. J. Phys. Chem. 76, 1054–1060.

Skibsted, J., Henderson, E., Jakobsen, H.J., 1993. Characterization of calcium aluminate phases in cements by high-performance ^{27}Al MAS NMR spectroscopy. Inorg. Chem. 32, 1013–1027.

Solvang, M., Yue, Y.Z., Jensen, S.L., 2004. The effects of Mg-Ca and Fe-Mg substitution on rheological and thermodynamic properties of aluminosilicate melts. J. Non-Cryst. Solids 345, 782–786.

Stebbins, J.F., Xu, X., 1997. NMR evidence for excess non-bridging oxygen in an aluminosilicate glass. Nature 390, 60–62.

Stebbins, J.F., Lee, S.K., Oglesby, J.V., 1999. Al-O-Al oxygen sites in crystalline aluminates and aluminosilicate glasses: high-resolution oxygen-17 NMR results. Am. Mineral. 84, 983–986.

Stebbins, J.F., Oglesby, J.V., Kroeker, S., 2001. Oxygen triclusters in crystalline $CaAl_4O_7$ (grossite) and in calcium aluminosilicate glasses: ^{17}O NMR. Am. Mineral. 86, 1307–1311.

Stebbins, J.F., Dubinsky, E.V., Kanehashi, K., Kelsey, K.E., 2008. Temperature effects on non-bridging oxygen and aluminum coordination number in calcium aluminosilicate glasses and melts. Geochim. Cosmochim. Acta 72, 910–925.

Stein, D., Spera, F.J., 1993. Experimental rheometry of melts and supercooled liquids in the system $NaAlSiO_4$-SiO_2: implications for structure and dynamics. Am. Mineral. 78, 710–723.

Stein, D.F., Spera, F.J., 1995. Molecular dynamics simulations of liquids and glasses in the system $NaAlSiO_4$-SiO_2: methodology and melt structures. Am. Mineral. 80, 417–431.

Stolyarova, V.L., Shornikov, S.I., Shultz, M.M., 1996. High-temperature mass spectrometric study of the thermodynamic properties of the CaO-Al_2O_3-SiO_2 system. High Temp. Mat. Sci. 36, 15–35.

Sukenaga, S., Saito, N., Kawakami, K., Nakashima, K., 2006. Viscosities of CaO-SiO_2-Al_2O_3 (R_2O or RO) melts. ISIJ Int. 46, 352–358.

Sukenaga, S., Haruki, S., Nomoto, Y., Saito, N., Nakashima, K., 2011. Density and surface tension of CaO-SiO_2-Al_2O_3-R_2O (R = Li, Na, K) melts. ISIJ Int. 51, 1285–1289.

Suzuki, A., Ohtani, E., Terasaki, H., Funakoshi, K., 2005. Viscosity of silicate melts in $CaMgSi_2O_6$-$NaAlSi_2O_6$ system at high pressure. Phys. Chem. Minerals 32, 140–145.

Sykes, D., Poe, B.T., McMillan, P.F., Luth, R.W., Sato, R.K., 1993. A spectroscopic investigation of anhydrous $KAlSi_3O_8$ and $NaAlSi_3O_8$ glasses quenched from high-pressure. Geochim. Cosmochim. Acta 57, 1753–1759.

Takahashi, S., Neuville, D.R., Takebe, H., 2015. Thermal properties, density and structure of percalcic and peraluminus CaO-Al_2O_3-SiO_2 glasses. J. Non-Cryst. Solids 411, 5–12.

Taylor, M., Brown, G.E., 1979a. Structure of mineral glasses. I. The feldspar glasses $NaAlSi_3O_8$, $KAlSi_3O_8$, $CaAl_2Si_2O_8$. Geochim. Cosmochim. Acta 43, 61–77.

Taylor, M., Brown, G.E., 1979b. Structure of mineral glasses. II. The SiO_2-$NaAlSiO_4$ join. Geochim. Cosmochim. Acta 43, 1467–1475.

Thompson, L.M., Stebbins, J.F., 2011. Non-bridging oxygen and high-coordinated aluminum in metaluminous and peraluminous calcium and potassium aluminosilicate glasses: high-resolution O-17 and Al-27 MAS NMR results. Am. Mineral. 96, 841–853.

Toplis, M.J., Corgne, A., 2002. An experimental study of element partitioning between magmetite, clinopyroxene, and iron-bearing silicate liquids with particular emphasis on vanadium. Contrib. Mineral. Petrol. 144, 22–37.

Toplis, M.J., Dingwell, D.B., 2004. Shear viscosities of CaO-Al_2O_3-SiO_2 and MgO-Al_2O_3-SiO_2 liquids: implications for the structural role of aluminium and the degree of polymerisation of synthetic and natural aluminosilicate melts. Geochim. Cosmochim. Acta 68, 5169–5188.

Toplis, M.J., Dingwell, D.B., Lenci, T., 1997. Peraluminous viscosity maxima in Na_2O-Al_2O_3-SiO_2 liquids: the role of triclusters in tectosilicate melts. Geochim. Cosmochim. Acta 61, 2605–2612.

Toplis, M.J., Kohn, S.C., Smith, M.E., Poplett, I.J.F., 2000. Fivefold-coordinated aluminum in tectosilicate glasses observed by triple quantum MAS NMR. Am. Mineral. 85, 1556–1560.

Tossell, J.A., 1999. Quantum mechanical calculation of ^{23}Na NMR shieldings in silicates and aluminosilicates. Phys. Chem. Minerals 27, 70–80.

Tossell, J.A., Horbach, J., 2005. O triclusters revisited: classical MD and quantum cluster results for glasses of composition $(Al_2O_3)_2(SiO_2)$. J. Phys. Chem. B. 109, 1794–1797.

Urbain, G., 1982. Viscosité de l'alumine liquide. Rev. Int. Hautes Temp. Refract. 19, 55–57.

Urbain, G., Bottinga, Y., Richet, P., 1982. Viscosity of liquid silica, silicates and aluminosilicates. Geochim. Cosmochim. Acta 46, 1061–1072.

Webb, S.L., 2008. Configurational heat capacity of Na_2O–CaO–Al_2O_3–SiO_2 melts. Chem. Geol. 256, 92–101.

Webb, S., Courtial, P., 1996. Compressibility of melts in the CaO-Al_2O_3-SiO_2 system. Geochim. Cosmochim. Acta 60, 75–86.

Whittaker, E.J.W., Muntus, R., 1970. Ionic radii for use in geochemistry. Geochim. Cosmochim. Acta 34, 945–957.

Wilding, M.C., Navrotsky, A., 1998. The dissolution of silica and alumina in silicate melts: in situ high temperature calorimetric studies. N. Jb. Mineral. Abh. 172, 177–201.

Wilding, M.C., Benmore, C.J., Weber, J.K.R., 2010. High-energy X-ray diffraction from aluminosilicate liquids. J. Phys. Chem. B 114, 5742–5746.

Winkler, A., Horbach, J., Kob, W., Binder, K., 2004. Structure and diffusion in amorphous aluminum silicate: a molecular dynamics computer simulation. J. Chem. Phys. 120, 384–393.

Wu, T., He, S.P., Liang, Y.J., Wang, Q., 2015. Molecular dynamics simulation of the structure and properties for the CaO-SiO_2 and CaO-Al_2O_3 systems. J. Non-Cryst. Solids 411, 145–151.

Xiang, Y., Du, J.C., Smedskjaer, M.M., Mauro, J.C., 2013. Structure and properties of sodium aluminosilicate glasses from molecular dynamics simulations. J. Chem. Phys. 139 https://dx.doi.org/10.1063/1.4816378.

Xue, X.Y., Stebbins, J.F., 1993. Na-23 NMR chemical shifts and local Na coordination environments in silicate crystals, melts and glasses. Phys. Chem. Minerals 20, 297–307.

Yamada, A., Wang, Y., Inoue, T., Yang, W., Park, C., Yu, T., Shen, G., 2011. High-pressure x-ray diffraction studies on the structure of liquid silicate using a Paris–Edinburgh type large volume press. Rev. Sci. Instr. 82, 015103.

Yarger, J.L., Smith, K.H., Nieman, R.A., Diefenbacher, J., Wolf, G.H., Poe, B.T., McMillan, P.F., 1995. Al coordination changes in high-pressure aluminosilicate liquids. Science 270, 1964–1966.

Zirl, S.M., Garofalini, S.H., 1990. Structure of aluminosilicate glasses. J. Am. Ceram. Soc. 73, 2848–2856.

Zotov, N., Boysen, H., Romano, C., Dingwell, D., Yanev, Y., 1995. Neutron-diffraction study of feldspar glasses—mixed alkali effect. J. Non-Cryst. Solids 191, 124–131.

CHAPTER

10

Properties of Iron-Silicate Glasses and Melts

OUTLINE

10.1 INTRODUCTORY COMMENTS

Iron is ubiquitous in igneous rocks. Its abundance generally decreases with magmatic differentiation and increasing SiO_2 content (Bowen, 1928), but it remains present in amounts that have significant effects on physical properties of melts. Even at low concentration, iron signals

https://doi.org/10.1016/B978-0-444-63708-6.00010-7

its presence by the dark hue it confers to minerals and glasses (cf. Calas et al., 2018). Clear, transparent glass requires less than a few wt‰ iron oxides in the raw materials, which has long made work difficult for glassmakers.

Optical transitions in the visible part of the electromagnetic spectrum are indeed a common feature of transition metals, among which iron is by far the most abundant in nature. Another characteristic feature of transition metals, of greater geological importance, is the existence of several oxidation states. For iron, the metal (Fe^0) can coexist with the ferric (Fe^{2+}) and ferrous (Fe^{3+}) states. The latter two valences affect melt structure and properties in specific and often complex ways, because their relative abundances vary not only with temperature, pressure, and chemical composition but also with the oxygen fugacity of the system. These complexities set iron apart from aluminum or alkali and alkaline earth elements. They make it useful to distinguish the compositions in which Fe^{2+} and Fe^{3+} predominate by the terms ferro- and ferrisilicates, respectively.

The first studies of iron redox reactions were made by glass scientists as early as in the 1930s. In petrology, interest in the redox state of iron came later. Following Kennedy (1948) and Fudali (1965), the iron redox ratio of igneous rocks is a probe of redox conditions within the earth and terrestrial planets. As a result, understanding how Fe^{3+}/Fe^{2+} ratio is determined by intensive thermodynamic parameters has motivated numerous experimental studies with applications that include the evolution of oxygen in the earth in time and space (Kasting et al., 1993; Frost and McCammon, 2008). These studies have been complemented by determinations of the influence of iron content and redox state on density, viscosity, and other physical properties of melts. Many, perhaps most, of the latter properties also have commercial applications. Iron-bearing glasses, for instance, have useful optical and insulating properties (Calas et al., 2002; Smedskjaer et al., 2010; Yue and Solvang, 2018), whereas the SiO_2-poor slags play a critical role in metallurgy by controlling in particular the impurity content of the molten metal (Meadowcroft et al., 1996; Mills, 2018).

Before reviewing these features, a basic difference between oxidation and reduction reactions must be pointed out. When changes in an intensive property induce reduction, the reaction cannot be prevented because oxygen can eventually be released and form bubbles which separate from the melt. In contrast, oxidation cannot proceed without a source of oxygen. This is why the kinetics and mechanisms of redox reactions have been mainly investigated for oxidation.

10.2 FERROUS AND FERRIC IRON

In this chapter, we will deal mostly with redox reactions between ferrous and ferric iron. Metallic iron will be paid little attention because its solubility in silicate melts is quite low (Ariskin et al., 1992). Under sufficiently reducing conditions, it precipitates and forms solid solutions of its own. Under such circumstances, its main effect is to induce changes in the melt composition.

As is usually done, we will denote by $\sum Fe$ the total atomic $Fe^{2+}+Fe^{3+}$ or the total wt% $FeO+Fe_2O_3$. In the literature, the iron redox ratio is expressed either as $Fe^{2+}/\sum Fe$ or $Fe^{3+}/\sum Fe$. On an atomic or weight percentage basis, the latter definition will be used consistently in the following. In addition, we will use the notations "FeO" or "Fe_2O_3" to report total iron content in the form of either Fe^{2+} or Fe^{3+}.

10.2.1 Redox States

In the metallic state, the 3*d* electronic shell of iron is partially filled so that the electronic configuration is $4s^2\,3d^6$. Without the two electrons of the outer 4*s* shell of Fe^0, the configurations of Fe^{2+} and Fe^{3+} are $3d^6$ and $3d^5$, respectively. Because they are generally present in a high-spin state, both ions have a magnetic moment that makes them very sensitive to their local environment in solid solutions (see Harrison and Becker, 2001).

The differing electronic configurations of Fe^{2+} and Fe^{3+} are associated with relatively small differences in ionic radii (Whittaker and Muntus, 1970); see Table 10.1. Of special interest is the fact that the spin configuration and the oxygen coordination number exert a comparable influence on the ionic radius of both ions. It is this narrow range of radii that results in multiple structural states and makes diverse coupled substitutions with di-, tri- and tetravalent cations possible.

As a starting point to an analysis of redox reactions, consider the solid-state formation of wüstite (FeO) and hematite (Fe_2O_3) from metallic iron:

$$Fe + {}^{1}/_{2}\,O_2 \Leftrightarrow FeO, \tag{10.1}$$

$$2\,Fe + {}^{3}/_{2}\,O_2 \Leftrightarrow Fe_2O_3. \tag{10.2}$$

From the mass action law and the reported Gibbs free energies of formation of the oxides (Robie et al., 1979), the oxygen fugacity (f_{O_2}) is readily calculated as a function of temperature for both equilibria (Fig. 10.1). One finds that high temperature induces iron reduction. This trend is a direct consequence of Le Chatelier's principle in that reduction implies production of gaseous oxygen, which causes a large entropy increase and, correlatively, a decrease of the Gibbs free energy of the Fe—O system.

In contrast to other major elements, for which a single valence has to be considered, iron has the peculiarity that two of its valence states are energetically similar. This similarity is evident in Fig. 10.1 when one compares the positions of the two Fe oxidation reactions to that of Ni, which forms a continuous solid solution with Fe, whose 2+ state is indeed closely related to Fe^{2+}. Hence, another important feature is that slight variations of temperature or oxygen fugacity can induce definite changes in the iron redox ratio.

A noteworthy consequence of the similar energetics of Fe^{2+} and Fe^{3+} in oxides is the nonstoichiometry of wüstite, a mineral whose actual formula is $Fe_{1-x}O$. As a matter of fact, wüstite has a defect rocksalt (NaCl) structure in which $1-3x$ Fe^{2+} ions coexist with vacancies and $2x$ Fe^{3+} ions, the value of x ($0.04 < x < 0.12$) depending on synthesis conditions (see Hazen

TABLE 10.1 Ionic Radii (Å) for Iron in Four- and Sixfold Oxygen Coordination

	IV	VI (High Spin)	VI (Low Spin)
Fe^{2+}	0.71	0.69	0.86
Fe^{3+}	0.57	0.63	0.73

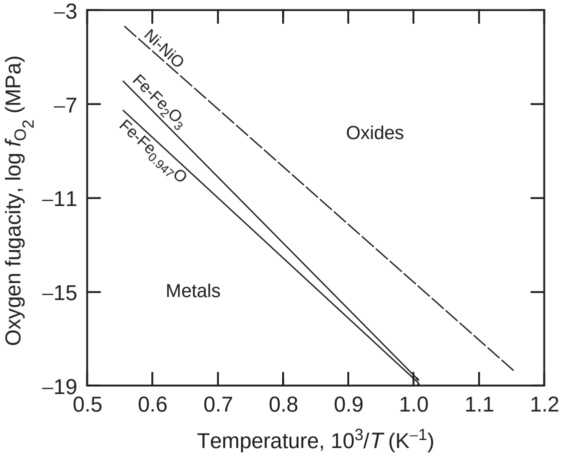

FIG. 10.1 Oxygen buffers: oxygen fugacity for iron and nickel oxidation equilibria. Metals are stable at high temperature and low oxygen fugacity, oxides at low temperature and high oxygen fugacity. Calculations made with the data of Robie et al. (1979). Data are for nonstoichiometric wüstite.

and Jeanloz, 1984). Not only is the stoichiometric $x = 1$ value not reached below 10 GPa, but Fe^{2+} occupies either octahedral sites or tetrahedral interstices of the structure. Wüstite, the simplest iron-bearing oxide compound, thus summarizes the complex structural and physical problems raised by the commonest transition element.

10.2.2 Oxygen Fugacity

For any melt, the temperature dependence of the redox reaction causes Fe^{3+}/Fe^{2+} to be the highest near the glass transition and the lowest at superliquidus temperatures. The changes in the relative abundances of ferrous and ferric iron are simply described by the reaction:

$$2\,FeO + 1/2\,O_2 \Leftrightarrow Fe_2O_3. \qquad (10.3)$$

At constant temperature and pressure, the equilibrium constant of this reaction depends on the activities of FeO and Fe_2O_3 in the melt, which are both complex functions of composition, and oxygen fugacity. In experimental studies, care is thus taken to achieve equilibrium under well-defined redox conditions.

In general, oxygen fugacity is controlled with buffers (see Huebner, 1971; Nafziger et al., 1971; Myers and Eugster, 1983; O'Neill and Pownceby, 1993). In a system where Ni and NiO coexist (NNO buffer), for example, the f_{O_2} is fixed and given by the value shown in Fig. 10.1 for the temperature of interest. The same applies to the coexistence of iron and wüstite (IW buffer), of magnetite (Fe_3O_4) and hematite (MH buffer), or of quartz, fayalite (Fe_2SiO_4) and magnetite (QFM buffer). At low pressure, however, there is no need for these solid phases to be physically present in the system. The oxygen fugacity of a given buffer can be reproduced through equilibration, at the temperature of the experiment, of the right proportions of gases (CO and CO_2, or H_2 and CO_2) that make up the experimental atmosphere at ambient pressure conditions. In this case, redox conditions nevertheless remain frequently referred to such buffers. Because the f_{O_2}-temperature relationships of different buffers have similar slopes (Fig. 10.1), this is a simple means of using a relative redox scale that depends little on temperature.

In experimental studies, particular attention must be paid to the fact that the redox conditions can be affected via interaction with many materials commonly used for sample containers. For example, an oxygen buffer approaching iron-wüstite conditions is realized when an iron crucible is used (Bowen and Schairer, 1932; Thornber and Huebner, 1982a). The oxygen fugacity is not determined only by temperature, however, because the activity of FeO in the melt depends on chemical composition and also because that of Fe in the metal can be affected by impurity content.

Platinum is the most inert material for containing liquid silicates, but it has long been known that it forms a continuous solid solution with Fe, especially under reducing conditions (Isaac and Tammann, 1907). The alloying between these two metals causes equilibrium (10.1) in the melt to be displaced to the left and oxygen to be lost. The resulting changes in chemical composition can be significant (Bowen and Schairer, 1932). These can be minimized through saturation of Pt with iron in preliminary experiments (e.g., Darken and Gurry, 1946) or the use of FePt alloys instead of pure platinum (Presnall and Brenner, 1974; Grove, 1981). Alternatively, platinum can exert an oxidizing influence on iron. The effect has been described for alkali silicates with >70 mol% SiO_2 by Paul and Douglas (1965) who assigned it to the reaction:

$$1/4Pt^{4+} + Fe^{2+} \Leftrightarrow 1/4Pt + Fe^{3+}, \tag{10.4}$$

which involves initial formation of platinum oxide (PtO_2).

Finally, note that the concept of oxygen fugacity takes a different meaning in experimental studies, on the one hand, and in natural or industrial processes on the other. In the latter cases, equilibrium between a melt and a gaseous phase is generally irrelevant. Either heterogeneous redox reactions are too sluggish or, more simply, a gaseous phase is lacking. Then, the redox state is entirely determined by the chemical composition of the system and the temperature and pressure of interest. An oxygen fugacity can nonetheless be defined. Without making reference to an actual gaseous phase, it just represents a convenient parameter to specify the redox state of the system. As noted by Fudali (1965), this is why the term fugacity is to be preferred over partial pressure, although both are numerically equivalent at the low values appropriate for redox reactions of practical interest. An important example is that of industrial glasses whose oxygen fugacity is determined by the starting materials and added fining agents like sulfates, but not by the furnace atmosphere with which equilibration would be much too slow (Conradt, 2018).

10.2.3 Analysis of Redox Ratio

Description of experimental methods in general is beyond the scope of this book, but some details are in order for iron redox analyses because proper interpretation of the results reviewed in this chapter depend directly on accurate determinations of ferrous and ferric iron contents. It is necessary, therefore, to appreciate the precision and accuracy of the methods being used.

In preamble, one should be aware of the practical problem that the redox ratio of a glass can differ markedly from that of its parent melt if partial crystallization takes place during the quench (Bowen and Schairer, 1932). Along with decreasing precision of the analyses, an apparent decrease from 6 to 2 wt% of the Fe^{2+} content of a calcium ferrosilicate glass was observed by Kress and Carmichael (1989). Both effects were perhaps due to preferential partitioning of Fe^{2+} into the quench crystals and, then, to lack of dissolution of these crystals during the wet chemical analyses. In other words, determinations of redox ratios have been restricted to liquids that could be quenched, often in small amounts, which introduces bias as to the composition ranges investigated. For example, data are more extensive for the system CaO-"FeO"-SiO_2 (Mysen et al., 1984; Kress and Carmichael, 1989) than for MgO-"FeO"-SiO_2 compositions (Mysen and Virgo, 1989).

Wet-chemical analysis of the redox ratio of iron has been for a long time the only available method. The concentrations of total iron and Fe^{2+} are derived from titrations made with a potassium dichromate solution after about 500 mg of glass has been dissolved in HF and in $HF + H_2SO_4$ solutions, respectively (Wilson, 1960). Uncertainties of ± 0.02 in $Fe^{3+}/\sum Fe$ are usually reported. Because the Fe^{3+} concentration is given by the difference between these two figures, the relative errors are higher for oxidized samples.

Alternatively, iron redox ratios can be determined by Mössbauer spectroscopy because glass structure is sufficiently rigid to allow recoilless absorption of gamma photons by ^{57}Fe nuclei (see Kurkjian, 1970; Bancroft, 1973). As resonant absorption takes place at different energies for Fe^{2+} and Fe^{3+}, the relative abundances of the two cations are determined from the areas of the two peaks that form a broad doublet in the spectra (see Section 11.4 for an example). These areas are strictly proportional to concentrations only at cryogenic temperatures, but proper calibration taking into account differences in recoilless fractions, this allows measurements to be performed under ambient conditions (see Alberto et al., 1996).

The Mössbauer resonant-absorption method has several advantages over wet-chemical methods. It is nondestructive, less time consuming, requires smaller samples of about 50–100 mg with standard techniques, and can sometimes be used at the scale of 50 μm (McCammon, 1994). In addition, Mössbauer spectroscopy provides direct information on the structural environments of Fe^{3+} and Fe^{2+} in the sample because the hyperfine parameters of both ferrous and ferric iron depend on oxygen coordination and geometry of coordination polyhedra.

Comparisons made between Mössbauer and wet-chemical analyses performed on the same samples do not reveal systematic differences (Fig. 10.2) (see also Mysen et al., 1985c; Dingwell, 1991). The precision of redox ratios derived from both methods is similar. This is especially true when adequate fitting procedures of hyperfine parameter distributions are applied to Mössbauer spectra. Such fitting protocols also yield more detailed structural information than conventional curve-fitting of the absorption envelope (Alberto et al., 1996). According to Lange and Carmichael (1989) and Ottonello et al. (2001), Mössbauer spectroscopy would underestimate Fe^{3+}/Fe^{2+} for total iron oxide content higher than 14 wt%. Such an effect is not demonstrated by the results of both techniques when their differences are plotted against total iron content (Fig. 10.3). More important, the existence of systematic bias has not been confirmed by further analyses (Partzsch et al., 2004), in accordance with the fact that there are no practical or theoretical reasons why Mössbauer analyses would be unreliable at high iron contents (see also Jayasuriya et al., 2004).

Redox ratios can be determined on still smaller samples than those used in Mössbauer spectroscopy from the preedge feature of X-ray absorption spectra, which is sensitive to the redox state and local environment of iron (Waychunas et al., 1983). The errors are now about ± 0.02 in the Fe^{3+}/Fe^{2+} ratio (Cottrell et al., 2009). The X-ray absorption near edge

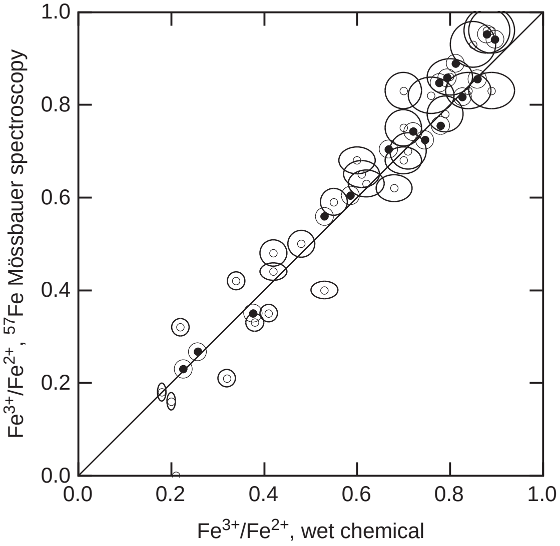

FIG. 10.2 Comparison between redox ratios determined from Mössbauer spectroscopy experiments and wet chemical analyses; *open circles*: Mysen et al. (1985a,b); *solid circles*: Dingwell (1991). The combined error margins of the measurements are shown as *ovals* around the data points.

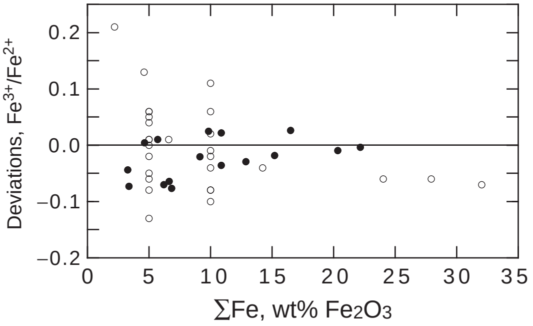

FIG. 10.3 Difference between redox ratios determined from Mössbauer and wet chemical analyses against total iron, expressed as Fe_2O_3. Same *symbols* and data sources as in Fig. 10.1.

structure (XANES) measurements have the important advantages of being very rapid and feasible at high temperatures, so as to make in situ kinetic studies possible (Berry et al., 2003; Magnien et al., 2004, 2008; Cochain et al., 2012). Moreover, the beam can be collimated to $<10 \times 10\,\mu m$, which permits detailed spot analyses of samples (Cottrell et al., 2009). A related technique is electron energy-loss spectroscopy (EELS), which is practiced in a transmission electron microscope at room temperature. This method used for minerals (e.g., Garvie and Buseck, 1994) could also be applied to glasses.

In the latter two methods, however, beam damage can be caused by highly energetic X-ray or electron beams. Analysis of redox ratios on the same spatial scale has thus been attempted by microRaman techniques (Magnien et al., 2008; Cochain et al., 2012; Di Genova et al., 2016). The method is very quick and convenient, for example in studies of the kinetics of redox reactions. Its applicability is restricted to continuous solutions, however, for which the redox ratios of the endmembers must be known independently.

Electron microprobe analyses must also be mentioned in view of their widespread use. Only total iron is usually reported in the form of FeO. For minerals, the iron redox state may then be estimated from stoichiometric considerations (Droop, 1987), but such methods are not valid for glasses for which there are few or no stoichiometric constraints. However, the shifts of the Lα peaks recorded with an electron microprobe may also be employed. The abundance of both valences can be determined directly with errors of about 5% (Fialin et al., 2004).

Finally, a few words must be devoted to electrochemical methods. High-temperature linear- and square-wave voltammetry are the most common, differing by the shape of the current pulse used (see Sasahira and Yokokawa, 1985; Gerlach et al., 1998; Medlin et al., 1998; Rüssel, 2018). The reduction potential of an element, with reference to an oxygen electrode, is determined from the observed current versus tension relationship. These measurements can be made difficult by electrode corrosion and background corrections. They do not give redox ratios directly, but yield the enthalpy and entropy of the redox reaction when standard potentials are measured as a function of temperature. In addition, the potentials of several valences of the same multivalent element or of the valences of different elements can be measured in the same experiment. Another advantage is that the diffusion coefficients of the redox couples can also be estimated from the peak height of the current signal (Claussen et al., 1999; Wiedenroth and Rüssel, 2003; Rüssel, 2018).

10.3 PHASE EQUILIBRIA

10.3.1 Ferrosilicate Phase Relations

The “FeO”-SiO_2 phase diagram illustrates the actual ternary nature of binary iron-bearing melts (Fig. 10.4). In view of increasing liquidus temperatures with “FeO” content, one might expect a correlative decrease of the redox ratio. The opposite trend is actually observed (Fig. 10.4A), thus reflecting the dominant effect of structural changes of the melt with increasing “FeO”/SiO_2 ratio. At temperatures sufficiently high for all iron to be essentially in the ferrous state, a large stable miscibility gap is observed in the SiO_2-rich part of the FeO-SiO_2 diagram. This gap is similar to those observed for binary alkaline earth silicates (compare with Fig. 6.1). Likewise, a eutectic point occurs at a higher SiO_2 content, similar to those seen in alkaline earth systems. As for the deeper freezing-point depression apparent in Fig. 10.4, it simply results from the much lower melting point of FeO (1339°C) compared with those of CaO or MgO, which are both higher than 2500°C.

This kinship of Fe^{2+} with alkaline earth cations is borne out by the phase diagrams of ternary systems (Fig. 10.5). The similarity is greatest between Fe^{2+} and Mg^{2+}, which is perhaps analogous to the continuous (Fe, Mg) solid solutions of magnesiowüstite, olivine, and pyroxene. In the “FeO”-MgO-SiO_2 system, those three mineral solutions are the only liquidus phases. The liquidus temperatures are generally high except in the FeO-rich part of the system. Along with the incongruent melting of ferrosilite ($FeSiO_3$), this trend points to weaker bonding in structures that could also be weakened further by the presence of some Fe^{3+}. The glass-forming ability is poor throughout most of the Mg-bearing system.

The CaO-“FeO”-SiO_2 phase diagram is more complicated (Fig. 10.5). The inadequate match between the ionic radii of Ca^{2+} and Fe^{2+} is illustrated by the lack of (Ca, Fe) solid

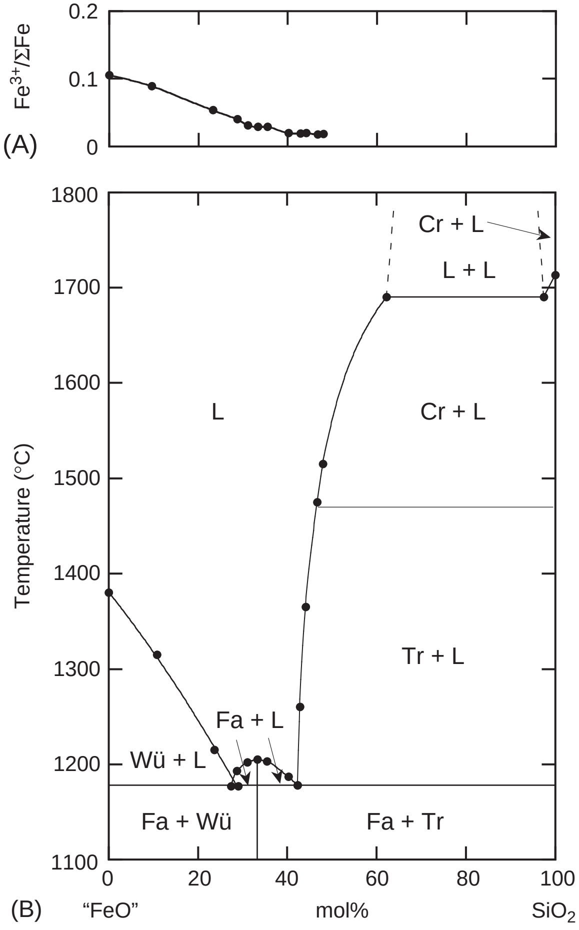

FIG. 10.4 Phase diagram of the "FeO"-SiO_2 system (Greig, 1927a; Bowen and Schairer, 1932). (A) Atomic redox ratio of charges quenched from the liquidus in the experiments made on Fe-rich melts. (B) Liquidus relationships determined for melts heated in iron crucibles under a nitrogen atmosphere. Cr: cristobalite and Tr: tridymite (SiO_2); Fa: fayalite (Fe_2SiO_4); L: liquid; Wü: wüstite.

solutions in the pyroxene and olivine structures. Liquidus temperatures remain high, however, with the exception of the valley that runs from $CaSiO_3$ to $FeSiO_3$. As for Mg, there are no new ternary compounds. When liquidus temperatures are low, glasses can be prepared only via rapid quenching of small charges.

Liquidus temperatures are markedly lower for alkali than for alkaline earth ferrosilicates. The phase relations are known for the "FeO"-K_2O-SiO_2 system (Roedder, 1952), where two ternary compounds exist and vitrification is possible over a wide composition range. Phase relations are less well known for the "FeO"-Na_2O-SiO_2 system in which, however, the Fe_2O_3 contents of melts on the liquidus are lower than 2.5 wt% (Schairer et al., 1954). The existence of at least one ternary compound has been described without having been identified (Schairer et al., 1954), but the stability field of this phase (or these phases) does not encompass the composition of the Na_2FeSiO_4 compound reported by Carter and Ibrahim (1952). In both Na and K systems, vitrification is not too difficult, as judged by the rather wide composition ranges where the refraction indices of glasses were measured successfully.

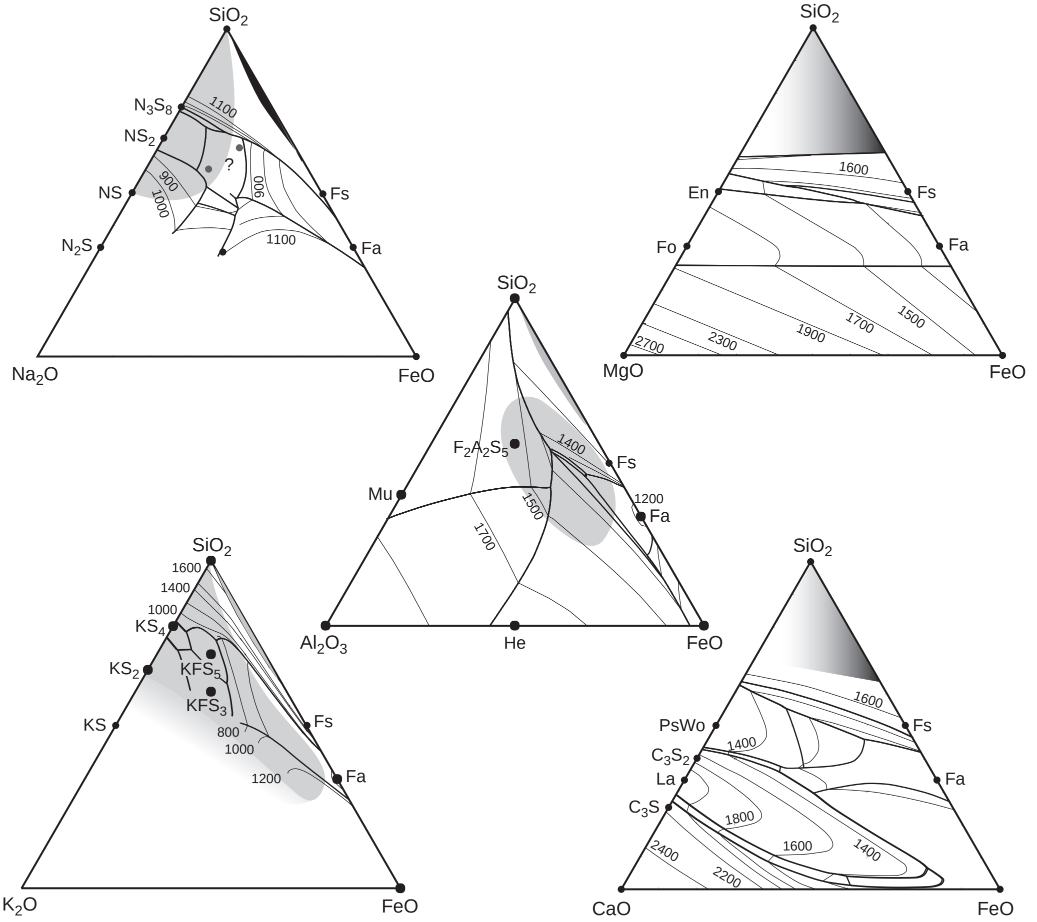

FIG. 10.5 Phase diagrams of ternary ferrosilicates redrawn on a mol% oxide basis. Fields of liquid immiscibility and glass formation (from the reported isofracts) indicated by *gray areas*, respectively. Abbreviations: A: Al_2O_3; F: FeO; K: K_2O; S: SiO_2; Fa: fayalite (Fe_2SiO_4); Fo: forsterite (Mg_2SiO_4); Fs: ferrosilite (Fe_2SiO_3); En: enstatite ($MgSiO_3$); He: hercynite ($FeAl_2O_4$); La: larnite (Ca_2SiO_4); Mu: mullite ($3Al_2O_3{\cdot}2SiO_2$). Data from Schairer et al. (1954) for the system NFS, Roedder (1952) for KFS, Levin et al. (1964) for CFS and MFS, and Schairer and Yagi (1952) for AFS.

Schairer et al. (1954) pointed out that there are clear analogies between the topologies of the MgO-Na_2O-SiO_2 and "FeO"-Na_2O-SiO_2 liquidus phase diagrams. This similarity, which also can be seen in the "FeO"-K_2O-SiO_2 phase diagram, applies in particular to liquid unmixing, which rapidly becomes metastable when Na_2O and K_2O are added to FeO-SiO_2 melts. Another similarity exists between the "FeO"-Al_2O_3-SiO_2 and MgO-Al_2O_3-SiO_2 phase relations (compare Fig. 10.5 with Fig. 8.1). In the former, the single ternary compound, $Fe_2Al_4Si_5O_{18}$, has the same stoichiometry as cordierite, with which it forms a solid solution. These observations thus confirm the conclusion drawn at the beginning of this section from the "FeO"-MgO-SiO_2 system, namely that Fe^{2+} is a weak analog of Mg^{2+}.

10.3.2 Ferrisilicate Phase Relations

Phase relations under oxidizing conditions have been less extensively studied (Fig. 10.6). In view of the wealth of information gathered for aluminosilicates (Chapters 8 and 9), an important question is the relative kinship of Fe^{3+} and Al^{3+}. With respect to physical properties, attention must, in particular, be paid to the influence of possible association of iron with a charge-compensating cation. In analogy with aluminosilicates, the meta-ferric join will designate the SiO_2-$M_{2/x}$ FeO_2 compositions where the metal cation M might charge-compensate all Fe^{3+} in tetrahedral coordination.

If bond strength were depending only on charge and ionic radius, one would expect bonding with oxygen to be weaker for Fe^{3+} ($r = 0.57$ Å) than for Al^{3+} ($r = 0.47$ Å). Actually, weaker bonding in Fe_2O_3 compared to Al_2O_3 manifests itself by the fact that, when heated in air, hematite decomposes to oxygen and an Fe_2O_3-Fe_3O_4 solid solution well before reaching its hypothetical congruent melting point of about 1895 K (see Muan and Osborn, 1965). This feature translates into ternary ferric iron-containing systems, since the phase diagrams of Fig. 10.6 share the common feature that liquidus temperatures are systematically lower for ferri- than for aluminosilicates.

The system "Fe_2O_3"-SiO_2 would be an obvious starting point but its melting relations cannot be investigated because reduction of significant amounts of Fe^{3+} to Fe^{2+} cannot be

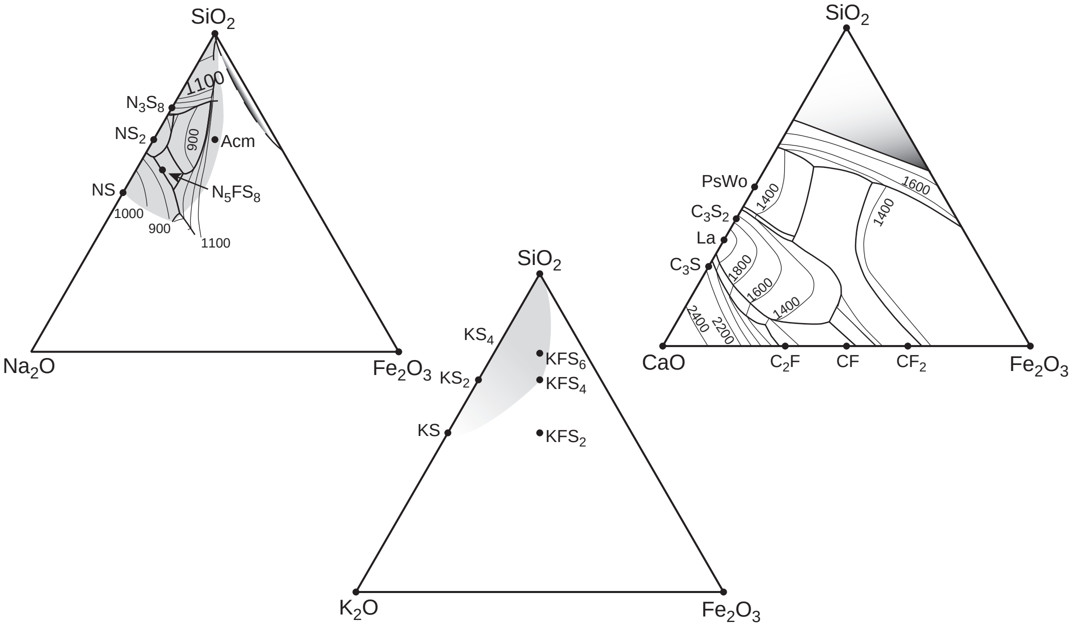

FIG. 10.6 Phase diagrams of ternary ferrisilicates redrawn on a mol% oxide basis. The fields of liquid immiscibility and glass formation (from the reported isofracts) are indicated by the *gray gradient* and *gray areas*, respectively. Abbreviations: F: Fe_2O_3; K: K_2O; N: Na_2O; S: SiO_2; Acm: acmite ($NaFeSi_2O_6$); La: larnite (Ca_2SiO_4); PsWo: pseudowollastonite ($CaSiO_3$). Data from Bowen et al. (1930) for the system Na_2O-Fe_2O_3-SiO_2, Faust (1936) and Faust and Peck (1938) for K_2O-Fe_2O_3-SiO_2, and Levin et al. (1964) for CaO-Fe_2O_3-SiO_2.

prevented at high temperatures. From extrapolation of data in ternary systems, Bowen et al. (1930) did nevertheless assert that binary SiO_2-Fe_2O_3 compounds do not exist. From these and other results by Greig (1927a), they also concluded that the SiO_2-Fe_2O_3 eutectic should be very close to SiO_2 because of the existence of a large stable miscibility gap between the two molten oxides. It appears, therefore, that Fe^{3+} substitutes much less readily for Si^{4+} than does Al^{3+} in melts (Section 8.2).

For calcium-containing systems, another difference with aluminosilicates is the number of mixed compounds. There are three along the CaO-Fe_2O_3 join, compared with five along the CaO-Al_2O_3 join. No ternary compound exists in the CaO-Fe_2O_3-SiO_2 system in contrast with the two calcium aluminosilicates, anorthite and gehlenite (Fig. 8.1). Although there is definite affinity between CaO and Fe_2O_3, no clear specific association is induced by the presence of SiO_2. Another significant feature is the similar trends seen in the FeO-poor parts of the Ca diagrams in the ferrosilicate systems of Figs. 10.4 and 10.5. This similarity could, however, reflect the fact that, at temperatures of about 1400°C, the actual iron redox ratios in ferro- and ferrisilicates differ less than indicated by the nominal melt compositions.

The difference between ferri- and aluminosilicate systems is even clearer for sodium ferrisilicates. Four compounds in the Na_2O-FeO_3-SiO_2 system were described by Bowen et al. (1930), although only two, acmite ($NaFeSi_2O_6$, also named aegirine) and $(Na_2O)_5{\cdot}F_2O_3{\cdot}(SiO_2)_8$, have been adequately identified. None of these compounds suggests an association between Na^+ and Fe $^{+}$ of a strength comparable to that of Na^+ with Al^{3+}. Acmite, in particular, has a pyroxene structure where Fe^{3+} is in octahedral coordination, in which the structural role of Na^+ is quite different. In this respect, the variations of liquidus temperatures between acmite and the $Na_2Si_4O_9$ composition (Fig. 10.7) differ considerably from those of the analogous aluminosilicate systems (Fig. 8.4). Although the eutectic compositions and temperatures are similar in both kinds of systems, acmite itself melts incongruently to hematite plus liquid at the low temperature of 1000°C.

Existing information for potassium ferrisilicates is incomplete. The important feature of the "Fe_2O_3"-K_2O-SiO_2 system is the presence of three compounds that have the same stoichiometry as K-feldspar, leucite, and kalsilite (Faust, 1936) and thus lie on the meta-ferric join (SiO_2-$NaFeO_2$). Here, clear evidence for alkali charge compensation is provided by the existence of these compounds along with the limited solid solutions that these compounds form with their aluminosilicate counterparts. Finally, Na and K ferrisilicates share two common points. Owing to low liquidus temperatures, melts heated in air just above the liquidus have very low Fe^{2+} contents in both systems. In addition, the area of glass formation is rather large.

From this brief review of solid-liquid equilibria, it appears that the strength of the association with network-modifying cations varies in the same order for Fe^{3+} and Al^{3+}. Although association is strongest with potassium, lower liquidus temperatures and decomposition or incongruent melting indicate that Fe^{3+} is at most a weak analog of Al^{3+}.

10.3.3 Phase Relations in Complex Systems

The strong influence of the iron redox state on ternary phase equilibria translates to more complex systems. Osborn (1959), for example, emphasized that crystallization paths depend markedly on whether or not iron participates in olivine, pyroxene, and magnetite solid

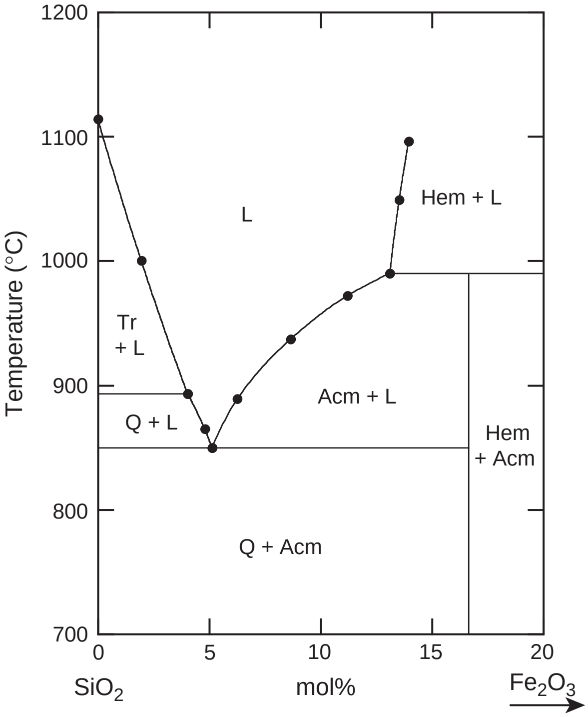

FIG. 10.7 Silica-rich part of the phase diagram of the system $Na_{0.4}Si_{0.8}O_{1.8}$-"Fe_2O_3" (Bowen and Schairer, 1929). Acm: acmite ($NaFeSi_2O_6$); Hem: hematite (Fe_2O_3); L: liquid; Q: quartz, and Tr: tridymite. Similar liquidus relationships are observed for the sodium disilicate-acmite system, with a eutectic point at 810°C and 4.2 mol% Fe_2O_3 (Bowen et al., 1930).

solutions. Although crystallization and melting paths can be complicated in multicomponent systems, they can be determined from equilibrium phase relations. By contrast, the effects of iron redox on the kinetics of crystal nucleation and growth in melts are less predictable.

As described for alkaline earth silicate systems in Section 8.2.1, the high-temperature miscibility gaps of iron-bearing systems (Figs. 10.4–10.6) disappear rapidly upon addition of alumina or alkali oxides. Following Greig's (1927b) work, it was widely thought, for this reason, that liquid immiscibility could not be relevant to the composition range of igneous rocks. That liquid unmixing is nevertheless of interest was pointed out by Roedder (1951), who discovered a rather large field of liquid unmixing in the system Fe_2SiO_4-$KAlSi_2O_6$-SiO_2 (Fig. 10.8). Under reducing conditions, the gap occurs at temperatures between 1100°C and 1270°C for compositions whose alkali content is higher than 16 wt%. This gap owes its importance to the fact that it subsists in more complex chemical compositions such as tholeiitic basalts (Roedder, 1978; Philpotts and Doyle, 1983).

The miscibility gap tends to expand with increasing total iron content and oxygen fugacity (Naslund, 1983). Both of those variables tend to increase Fe^{3+}/Fe^{2+} of melts. In these situations, Fe^{3+} thus enhances liquid immiscibility. The size of the miscibility gap shrinks with increasing pressure and could vanish near 1.5 GPa (Nakamura, 1974), an effect of pressure well described for the MgO-SiO_2 system (Dalton and Presnall, 1997; Hudon et al., 2004). However, it is not clear whether this shrinkage reflects increasing monotectic temperature with pressure or some other effect.

FIG. 10.8 Schematic liquid unmixing (in *gray*) and phase boundaries of the system leucite ($KalSi_2O_6$)-fayalite (Fe_2SiO_4)-silica (Roedder, 1951, 1978). The *solid line* within the ternary miscibility gap represents the 1180°C isotherm. Melts heated in iron crucible under an N_2 pressure of 1 atm.

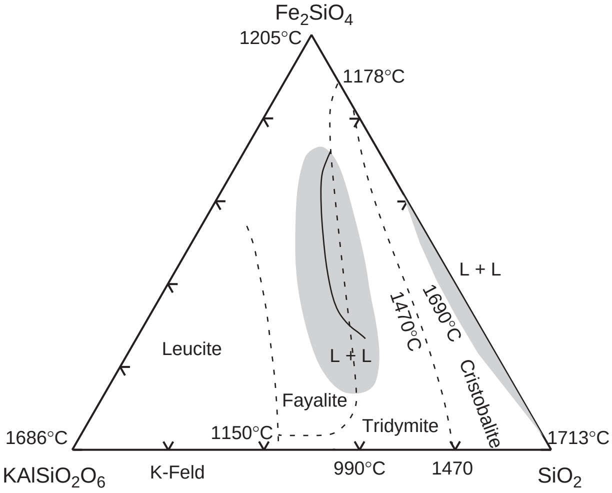

Unmixing also develops upon addition of TiO_2 and P_2O_5, two oxides that generally foster phase separation in silicate melts (see Chapters 12 and 13). Miscibility gaps originate in steric hindrance problems experienced by network-modifying cations when bonding to nonbridging oxygens in highly polymerized melts (see Section 6.2.2). The Al^{3+} ion causes unmixing to disappear through its association with network modifiers and the ensuing network polymerization. That Fe^{3+} does not have this effect is clear evidence for different structural roles of Fe^{3+} and Al^{3+} in silicate melts and glasses. Contrary to what might be assumed, however, the presence of iron is not a prerequisite for liquid unmixing to occur in complex systems. For example, an analogous effect has been described by Kingery et al. (1983) for the system CaO-K_2O-Al_2O_3-SiO_2. The main difference is that unmixing often is metastable, and not stable as observed for the gap of Fig. 10.8.

Regardless of the chemical complexity of a melt, crystallization typically is enhanced by oxidizing conditions. Rogers and Williamson (1969) found that Fe^{3+} acts as a nucleating agent in CaO-MgO-Al_2O_3-SiO_2 glasses. This observation was also made by Cukierman and Uhlmann (1974) for a Fe-rich lunar composition. Beall and Rittler (1976) even claimed that oxidation of iron is the main factor controlling crystallization of basalt. Crystallization is fast only for oxidized samples, magnetite forming first between 650°C and 700°C, followed by pyroxene, which nucleates on magnetite nuclei and grows between 750°C and 900°C. Similar results have been reported by Karamanov and Pelino (2001) for various glasses with SiO_2 contents ranging from 4 to 72 wt%, and by Bouhifd et al. (2004) and Villeneuve et al. (2008) for other basalts. The effect might be related to weakening of the silicate network by tetrahedral Fe^{3+}, such as, for example, formation of Fe^{3+} clusters (Bingham et al., 1999). Surprisingly, however, the Fe^{3+} concentration can be much lower in the nucleating spinel than in the melt itself (Rogers and Williamson, 1969; Bouhifd et al., 2004). Interestingly, Jurado-Egea et al. (1987) related magnetite crystallization to electronic conduction, but more work is needed to picture consistently nucleation and growth in iron-bearing systems.

10.4 IRON REDOX REACTIONS

The basic features of redox reactions were deciphered in the 1960s through experiments made mostly on alkali silicate melts. With proper adjustment for differing valence states, the phenomenology described here for iron applies to other multivalent elements that are important for practical applications (Mn, Ti, Cr, As, etc.) or for tracing geochemical processes (Eu, Ce, etc.). More recently, measurements on a variety of model melts have aimed at determining the variations of the iron redox ratio over wide ranges of temperature, pressure, oxygen fugacity, and chemical composition.

10.4.1 Temperature and Oxygen Fugacity

When written as Eq. (10.3), the iron redox reaction does not lend itself to ready thermodynamic or structural interpretations, because the activities of both FeO and Fe_2O_3 are generally known only for limited composition ranges. In terms of ionic species, a more detailed representation of the redox reaction is provided by the equations:

$$Fe^{2+} + 1/4\,O_2 \Leftrightarrow Fe^{3+} + 1/2\,O^{2-}, \tag{10.5}$$

$$K_{3/2} = \left(a_{Fe^{3+}}/a_{Fe^{2+}}\right)\left(a_{O^{2-}}\right)^{1/2}/{f_{O_2}}^{1/4}, \tag{10.6}$$

where $K_{3/2}$, the equilibrium constant of the reaction, is determined by the oxygen fugacity and the activity (a) of iron and oxygen ions. Activity is replaced by concentration if the silicate solution is assumed thermodynamically ideal. If the activity of the oxygen ion can further be assumed not to depend on the iron redox state, then a plot of log Fe^{3+}/Fe^{2+} against $-\log f_{O_2}$ at constant temperature should have a slope of 1/4.

The enthalpy and entropy changes of reaction (10.5) have been estimated from calorimetric measurements to be 106–134 kJ/mol and 49–67 J/mol K, respectively (Tangeman et al., 2001; Sugawara and Akaogi, 2004), defining rather wide ranges of values that can simply reflect the influence of differing silicate composition. Interestingly, Kress and Carmichael (1991) reported $\triangle H$ and $\triangle S$ values for natural basaltic compositions similar to those based by Sugawara and Akaogi (2004) on their data for iron oxide and acmite compositions.

At low iron concentrations (Fig. 10.9), the data for molten sodium disilicate refer to a wide range of oxygen fugacities achieved with air, CO-CO_2, and H_2-CO_2 atmospheres (Johnston, 1965). Between log $f_{O_2} = -0.7$ (air) and -13, the experimental slope differs little from the expected 0.25 value. Similar results are shown in Fig. 10.10 for a $(CaMgSi_2O_6)_{68}\cdot(CaAl_2Si_2O_8)_{32}$ melt. In both cases, the assumed constancy of the oxygen ion activity is justified by the dilute nature of the iron solution, whereas the ratio of the activity coefficients of iron ions should differ less from unity than the individual coefficients. The errors due to both assumptions cannot be separated, but the differences of the slopes of Fig. 10.9 with the 0.25 nominal value are insignificant. For concentrated iron solutions, a mean value of 0.207 (7) has in contrast been reported (e.g., Kress and Carmichael, 1988). Such a value represents an apparently simple means to account for the actual nonideality of the melt.

Another important point shown by the NS_2 data in Fig. 10.9 is the constant Fe^{3+}/Fe^{2+} values at very low f_{O_2}. This feature signals precipitation of iron metal (Johnston, 1965).

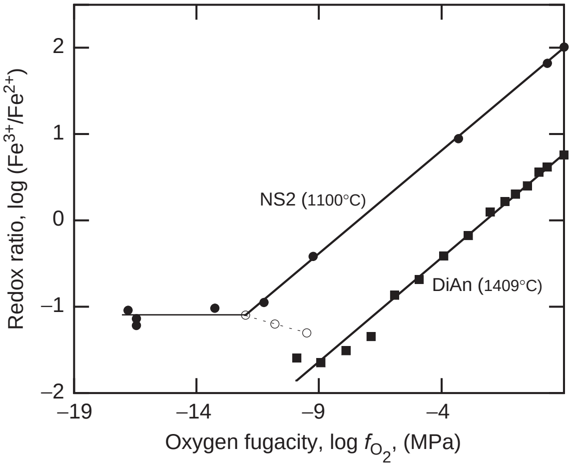

FIG. 10.9 Iron redox equilibrium at 1100°C for $Na_2Si_2O_5$ (NS_2) with 2.5 wt% Fe_2O_3 (Johnston, 1965). The slope of the *solid line* is 0.239 ± 0.002. The *open circles* indicate the conditions for metallic iron saturation at the temperatures indicated. For comparison, a slope of 0.245 ± 0.004 is shown at 1409°C for the diopside-anorthite eutectic composition (DiAn) with 1 wt% Fe_2O_3 (Jayasuriya et al., 2004).

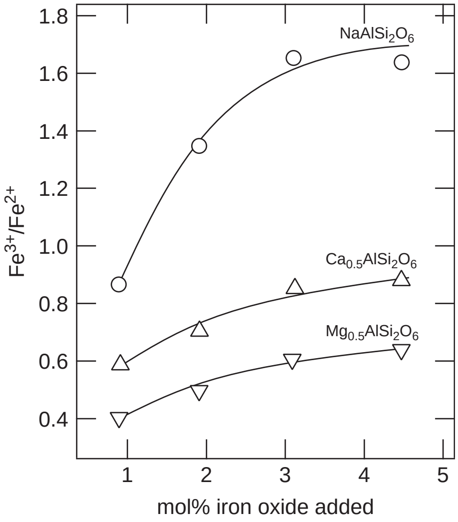

FIG. 10.10 Redox ratio of iron, Fe^{3+}/Fe^{2+}, in glasses of compositions indicated as a function of total iron oxide content added as Fe_2O_3. Samples quenched after equilibration with air at 1400°C at ambient pressure (Mysen, 2006).

Saturation is attained at higher oxygen fugacity and lower redox ratio when the temperature increases. It can be described in terms of dismutation of ferrous iron according to:

$$3Fe^{2+} \Leftrightarrow Fe^0 + 2Fe^{3+}, \tag{10.7}$$

$$K_{2/03} = \left(a_{Fe^{3+}}\right)^2 / \left(a_{Fe^{2+}}\right)^3. \tag{10.8}$$

When the oxygen fugacity is sufficiently low for iron to precipitate, the simplest manner for $K_{2/03}$ to remain constant is that the redox ratio of the melt also remains constant. This constancy is borne out by the iron saturation data, which provide another justification for the use of concentration ratios in place of activity ratios for iron ions in Eq. (10.4). The Fe^{3+}/Fe^{2+} ratio at which Fe^0 precipitates is low, near 0.1 in Fig. 10.9, but such that the concentration of Fe^{3+} remains significant. It is, in fact, a general observation that the three redox states of iron coexist in a system under highly reduced conditions (e.g., Fig. 10.4A).

Finally, the dependence of the iron redox ratio on iron concentration at constant temperature and redox conditions reflects the nonideal nature of the solution of ferric and/or ferrous iron in silicate melts (Larson and Chipman, 1953; Mysen et al., 1984; Mysen, 2006). This effect depends on silicate composition and in particular on Al/(Al+Si) and the nature of the alkali and alkaline earths (Mysen, 2006). The result is that the slope of the iron redox ratio versus oxygen fugacity yields an activation coefficient ratio that differs from unity. With a slope, x, the activity coefficient ratio $\gamma(Fe^{3+})/\gamma(Fe^{2+})$ then becomes:

$$\gamma\left(Fe^{3+}\right)/\gamma\left(Fe^{2+}\right) = 10^{(X+0.25)}. \tag{10.9}$$

This ratio clearly depends on silicate composition, i.e., on the extent of melt polymerization, expressed as NBO/T (Fig. 10.11) (see also Mysen et al., 1985a,b). Everything else being equal, both the Al/(Al+Si) ratio and the nature of the charge-balancing cation in addition play important roles.

10.4.2 Temperature and Pressure

Over temperature intervals of a few hundred degrees, the logarithm of the Fe^{3+}/Fe^{2+} ratio varies linearly with reciprocal temperature (Fig. 10.12). The slope of this relationship also depends on melt composition (Mysen and Virgo, 1989; Jayasuriya et al., 2004; Borisov and McCammon, 2010; Borisov et al., 2015). The enthalpy of the iron redox reaction is readily determined from these plots with the Van't Hoff relation. As expected for an oxidation reaction,

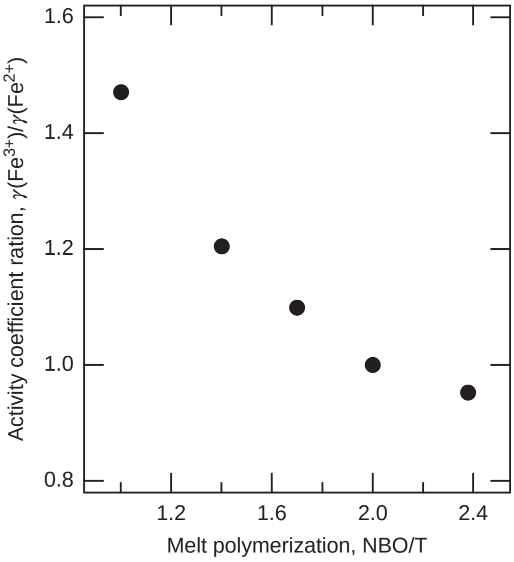

FIG. 10.11 Activity coefficient ratio, $\gamma(Fe^{3+})/\gamma(Fe^{2+})$, in $CaO\text{-}SiO_2$ glasses quenched from 1600°C at ambient pressure as a function of the NBO/T of the melt (Mysen et al., 1985a,b).

FIG. 10.12 Temperature dependence of the iron redox ratio in air. Data of Johnston (1965) for the sodium disilicate of Fig. 10.10 in either platinum *(open circles)* or alumina *(solid circles)* crucibles, with >15 wt% Al_2O_3 contamination in the latter case. NAS (Mysen and Virgo, 1989) and CAS (Mysen et al., 1985c) are Na and Ca aluminosilicates with 5 wt% Fe_2O_3. The results of Baak and Hornyak (1961) for 2.9 wt% Fe_2O_3 in NS_2 (B & H) illustrate departure from equilibrium at lower temperatures when run duration is too short.

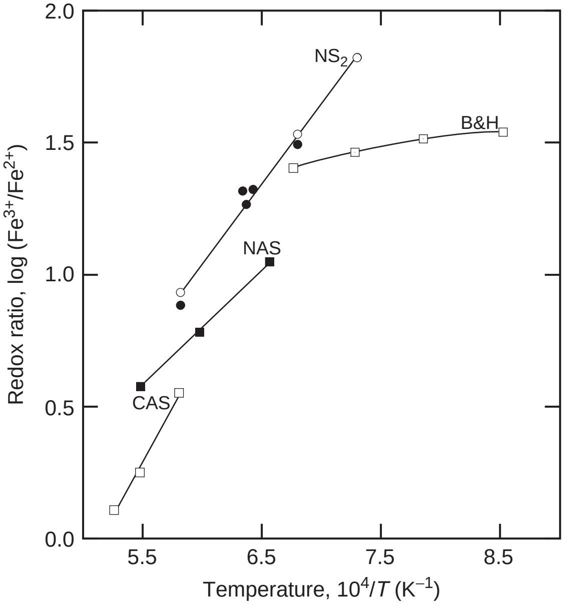

it is exothermic with an enthalpy change of about 40 kJ/mol (Borisov et al., 2015), but varies with silicate composition. In Fig. 10.12, the slope of the linear relationship is, for example, twice as high for CAS than for NAS. At least in aluminosilicate melts, this enthalpy becomes increasingly negative as the ionization potential of the charge-balancing cation for Al^{3+} increases (Mysen et al., 1985b; Mysen and Virgo, 1989). How or whether other compositional variables such as SiO_2 content may affect this enthalpy change is less clear. For example, Borisov and McCammon (2010) concluded that there is no effect of SiO_2 in their study of melts along the join $CaMgSi_2O_6$-$CaAl_2Si_2O_8$. In this system, however, one could argue that a complex chemistry, in particular in regard to Al^{3+}, makes it possible to assume that SiO_2 is no longer an independent variable.

Efforts to determine the partial molar volume of Fe_2O_3 have also been motivated by the close connection of this volume with the pressure dependence of the iron redox ratio. At constant temperature, the condition for univariant thermodynamic equilibrium boils down to $\Delta G = \Delta V\, dP = 0$. In view of the relationship

$$RT\, d\, \ln f_{O_2} = \overline{V}_{O_2} dP, \tag{10.10}$$

where $\overline{V}_{O_2}$ is the partial molar volume of O_2 dissolved in the melt, Mo et al. (1982) pointed out that the variation of the oxygen fugacity for Fe^{3+}-Fe^{2+} equilibrium is related to the partial molar volumes of Fe_2O_3 and FeO by:

$$RT \int_{P_0}^{P} d\, \ln f_{O_2} = \int_{P_0}^{P} \left(2\, \overline{V}_{Fe_2O_3} - 4\, \overline{V}_{FeO}\right) dP = \int_{P_0}^{P} \Delta\overline{V}\, dP. \tag{10.11}$$

Integration of Eq. (10.11) from the reference pressure P_0 is straightforward if one assumes that $\Delta\overline{V}$ is constant. At ambient pressure, the volume difference, ΔV, in Eq. (10.7) is about 30 cm^3/mol (partial molar volume data from Lange and Carmichael, 1987). It follows that Fe^{2+} is stabilized at high pressure at the expense of Fe^{3+}, as will be discussed in more detail following.

The compressibility difference between Fe^{2+}- and Fe^{3+}-bearing melts should be known for more detailed analyses of pressure effects. For both valences, transformation from tetrahedral to octahedral coordination ensures greater density increases than compression of FeO_6 octahedra. The coordination contrast between Fe^{2+} and Fe^{3+} at low pressure should thus result in a greater compressibility for Fe_2O_3 than for FeO. This prediction is borne out by available ultrasonic measurements on Fe-bearing melts. Although the data are too scarce to allow detection of possible effects of melt composition, the analysis made by Kress and Carmichael (1991) indicates that the average compressibility of Fe_2O_3 is about twice that of FeO. Curiously, however, compressibility appears to be 50% higher for FeO than for either MgO or CaO, whereas it is similar for Fe_2O_3 and Al_2O_3. In fact, ultrasonic data indicate that the presence of Fe_2O_3 may even increase the stiffness of glasses (Burkhard, 2000) whereas another complication is that the compressibility of FeO strongly depends on Fe^{2+} coordination (Guo et al., 2013).

As noted by Kress and Carmichael (1991), the difference in compressibility between Fe_2O_3 and FeO in melts is too small to change the sign of the volume difference in Eq. (10.7) below pressures of at least 3 GPa. In other words, the Fe^{3+}/Fe^{2+} ratio of melts should decrease continuously with increasing pressure in this pressure interval. For the opposite trend to occur at still higher pressure, the pressure derivative of the bulk modulus (K_S) should be much higher for the FeO than for the Fe_2O_3 component. Such a contrast is unlikely in view of the "normal" value $\partial K_S/\partial P = 10.1$ determined for molten Fe_2SiO_4 from compression experiments up to 55 GPa (Agee, 1992).

This volume discussion implies that, at constant temperature and oxygen fugacity, the Fe^{3+}/Fe^{2+} of silicate melts should decrease with increasing pressure. This has indeed been observed experimentally for molten $NaAlSi_2O_6$ and $Na_2O{\cdot}2SiO_2$ as well as for natural melts, with a rapid decrease of Fe^{3+} concentration as the pressure is increased (Mysen and Virgo, 1978, 1985; O'Neill et al., 2006; Zhang et al., 2017) (see also Fig. 10.13). Using methods similar

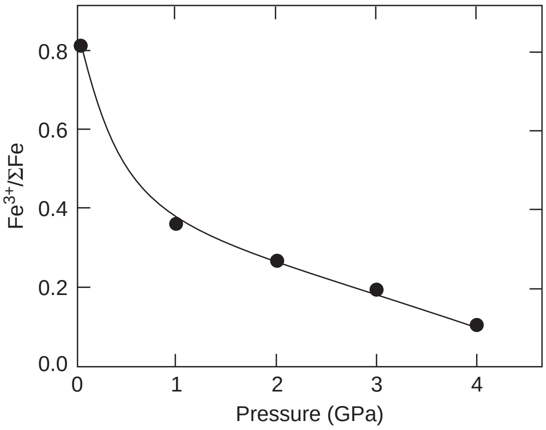

FIG. 10.13 Pressure-dependence of the redox ratio of iron at 1400°C for NS_2 melt with 5 mol% iron oxide added (Mysen and Virgo, 1985).

to those of Mysen and Virgo, Brearley (1990) in contrast concluded that all iron of NS_2 melt to 4 GPa at 1700°C remains Fe^{3+}, but undergoes a coordination change with pressure. This statement is somewhat surprising in light of the common observation that, at such temperatures, significant fractions of iron in silicate melts occurs as Fe^{2+} even when equilibrated under oxidizing conditions. In chemically more complex melts, O'Neill et al. (2006) observed that $Fe^{3+}/\Sigma Fe$ does indeed decrease with pressure by about 10% between ambient and 1.5 GPa for an andesitic melt, a result that agrees with recent data to >6 GPa (Zhang et al., 2017).

10.4.3 Oxygen Activity and Glass Basicity

Measurements on binary alkali melts have long been made to determine the influence of melt basicity on redox ratios of multivalent elements. For low values of $\sum Fe$, one observes that log Fe^{3+}/Fe^{2+} is a linear function of SiO_2 content (Fig. 10.14). At the same silica content, iron is more oxidized in the order K, Na, Li. Because the linear relationships converge toward pure SiO_2, they become less steep in the same order K, Na, Li. The redox reaction (10.8) should provide a simple means to interpret these effects of chemical composition on the redox state of a multivalent element. With the assumption of an ideal solution, Paul and Douglas (1965) wrote the equilibrium constant (10.9) as:

$$\log\left(Fe^{3+}/Fe^{2+}\right) = \log K_{3/2} + 1/4 \log f_{O_2} - 1/2 \log aO^{2-} = A - 1/2 \log aO^{2-}, \qquad (10.12)$$

where A is a constant if the oxygen fugacity is constant.

Other things being equal, this equation indicates that the redox ratio should decrease with increasing oxygen activity and thus with increasing melt basicity and alkali oxide content. For a given alkali element, the experimental results clearly contradict this prediction (Fig. 10.14). According to Eq. (10.12), the trends of Fig. 10.14 would then suggest that melt basicity increases in the order K, Na, Li for a given SiO_2 content. This prediction has been checked against experimental data. The basicity can be determined by various methods such as e.m.f. measurements or determinations of CO_2 solubility from the equilibrium constant of

FIG. 10.14 Iron redox ratio of alkali silicate melts at 1400°C in air against SiO_2 concentration (Paul and Douglas, 1965). Total iron content of 0.41 wt%.

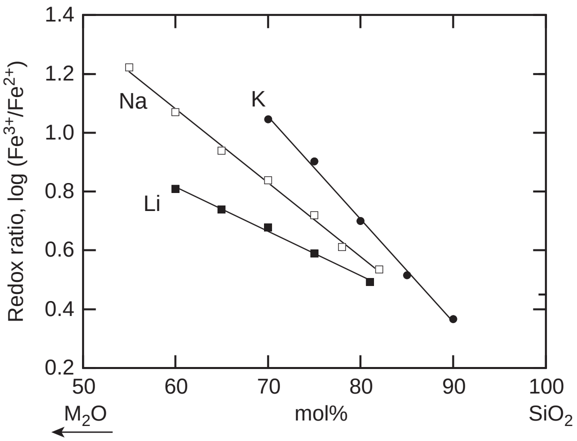

the solution reaction $CO_2 + O^{2-} \Leftrightarrow CO_3{}^{2-}$ (see Chapter 16). The results obtained in these different ways are not necessarily in quantitative agreement, but the trends are mutually consistent (Douglas et al., 1965). For alkali systems, they indicate that melt basicity increases in the order Li, Na, K, a trend which is opposite to that expected from the redox data.

Douglas et al. (1965) invoked variations of aO^{2-} with composition to account for this failure. More specifically, Holmquist (1966) pointed out that the amphoteric nature of Fe_2O_3 prevented the change in the activity of the oxygen ion from being estimated if the coordination of Fe^{3+} were not known. In addition, Jeddeloh (1984) noted that Eq. (10.12) suffers from loosely defined standard states for the ionic species involved. When writing Eq. (10.7), the two kinds of oxygen ions that bond with Fe^{2+} and Fe^{3+} are implicitly assumed to be the same. But their standard states cannot be considered identical because pure FeO and Fe_2O_3 liquids are of course not equivalent either structurally or energetically. When this assumption is denied explicitly, the equilibrium constant $K_{3/2}$ is written as:

$$K_{3/2} = \left(a\mathrm{Fe}^{3+}/a\mathrm{Fe}^{2+}\right)\left[\left(a\mathrm{OII}^{2-}\right)/\left(a\mathrm{OIII}^{2-}\right)^{3/2}\right] f_{O_2}{}^{1/2}, \tag{10.13}$$

where the indices II and III refer to oxygen ions bonding to Fe_2O_3 and Fe^{3+}, respectively. Hence, relating redox ratio to average melt basicity is much less straightforward than suggested by Eq. (10.12). As an additional practical difficulty, standard-state thermochemical calculations involving Fe_2O_3 suffer from the high-temperature decomposition of hematite that hampers direct determinations of the melting properties of this oxide. The enthalpy and entropy of fusion of hematite estimated by Sugawara and Akaogi (2004) should thus prove useful in this respect.

10.4.4 Composition and Redox State

The relative variations of the proportions of all oxides in melts and glasses can induce changes in redox ratio at constant temperature, pressure, and oxygen fugacity (Kress and Carmichael, 1988, 1991; Borisov and Shapkin, 1989; Jayasuriya et al., 2004; Borisov et al., 2015). The first composition effect to be examined is that of total iron content. In the "FeO"-SiO_2 system, a fivefold increase of $Fe^{3+}/\sum Fe$ ratio was observed by Bowen and Schairer (1932) between 60 and 100 mol% "FeO." According to other early experiments by Densem and Turner (1938) on a window glass composition, the redox ratio is a complex function of total iron at very low iron concentrations, before leveling off to a constant value above 2 wt% Fe_2O_3 (Fig. 10.15).

More recently, Borisov et al. (2015) also reported a positive correlation between $Fe^{3+}/\Sigma Fe$ and total iron content in basaltic compositions (Fig. 10.16). In their study, however, a continuous linear increase of $Fe^{3+}/\Sigma Fe$ with increasing total iron content was observed, which contrasts somewhat with the results by Densem and Turner (1938) and Mysen et al. (1984), who reported major variations at low total iron content, but much less so as the iron content increased further. Moreover, the rate of increase is greater for the more oxidized composition (equilibrated in air).

For higher iron content, an initial increase of the Fe^{3+}/Fe^{2+} ratio has also been observed for sodium disilicate (Larson and Chipman, 1953), Li, Na, and K silicates with 70 mol% SiO_2 (Paul and Douglas, 1965), sodium borosilicates (Dunn et al., 1978), sodium silicates (Lange and

FIG. 10.15 Effect of total iron content on redox ratio of iron for a window glass (W75 wt% SiO_2, 10 CaO, 15 Na_2O) melted in air at 1400°C in Pt crucibles (Densem and Turner, 1938) and for calcium metasilicate ($CaO{\cdot}SiO_2$) heated at 1725°C in a Pt loop (Mysen et al., 1984).

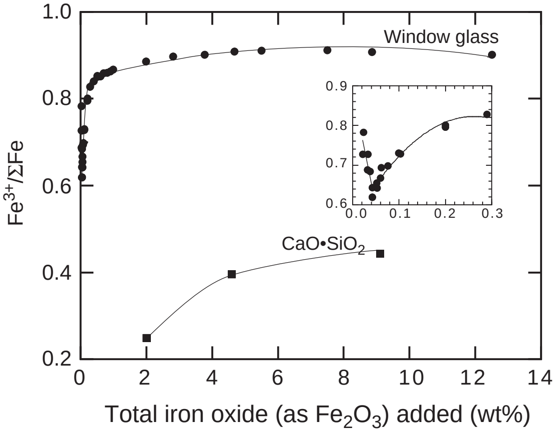

FIG. 10.16 Effects of total iron content on redox ratio of iron in haplobasaltic composition equilibrated at 1500°C in air ($\log f_{O_2} = -0.68$; *closed symbols*) and at $\log f_{O_2} = -2.75$ *(open symbols)* (Borisov et al., 2015).

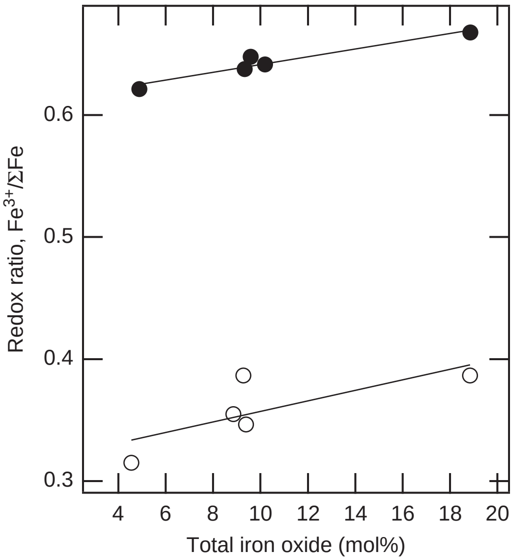

Carmichael, 1989), and calcium silicates (Mysen et al., 1984). For potassium silicates, in contrast, the redox ratio generally decreases (Tangeman et al., 2001), although in the latter study there were problems with maintaining the chemical composition during the high-temperature experiments. Goldman (1983) did not observe any dependence on total iron content for two industrial borosilicate compositions to which he added from 0.09 to 0.5 wt% Fe_2O.

Because of the constraint of glass formation, available measurements in binary systems are the most abundant for alkali silicates. In such melts, the Fe^{3+}/Fe^{2+} ratio decreases with increasing SiO_2 content (Paul and Douglas, 1965; Virgo et al., 1981) (see also Fig. 10.15). As concluded previously from liquid immiscibility data, this transformation of ferric into ferrous iron does not conform to the trend expected if Fe^{3+} were substituting for Si^{4+}. If this were the case, the opposite transformation would represent a simple way to solve the steric hindrance problems raised by bonding of metal cations with nonbridging oxygens. Of course, it is not clear from these data whether the change is driven by the changes in SiO_2 content, which affects the oxygen ion activity in Eq. (10.3), or by the decrease of alkali concentration as the melts become more SiO_2 rich. In fact, Dickenson and Hess (1986), Tangeman et al. (2001), and Giuli et al. (2012) all noted that increasing peralkalinity leads to increased $Fe^{3+}/\Sigma Fe$ even at essentially the same SiO_2 concentration.

For a given stoichiometry, these results indicate that the redox ratio increases in the order Li, Na, K. There is, in fact, a clear correlation between the redox state and the ionization potential of the metal cation (Fig. 10.17). Although available data for alkaline earth obey the same relationship, the linear trend in Fig. 10.17 is probably coincidental in view of differing temperature and total iron contents in both series of experiments. Everything else being equal, the presence of cations with a low ionization potential favors the ferric state of iron. From the results discussed for Al^{3+} in previous chapters, one might account for this effect in terms of more efficient charge compensation of Fe^{3+} in tetrahedral sites by such cations.

The dissimilarity between alkalis and alkaline earths is reflected in the lines of constant redox ratios determined by Kress and Carmichael (1989) and Lange and Carmichael (1989) for the calcium and sodium systems, respectively (Fig. 10.18). In the former, the redox state is essentially determined by the Ca/Si ratio, with little influence of total iron content (except, as shown in Fig. 10.15, at very low Fe concentration). In the latter, increasing the Fe content at constant Na/Si results in a more oxidized state. Extensive measurements have also been made for the K_2O-"Fe_2O_3"-SiO_2 system (Tangeman et al., 2001). A more complex composition dependence is observed in that increasing K_2O content causes the redox ratio to decrease in peralkaline melts.

These effects determined in simple compositions are also observed in more complicated systems. In basaltic and other complex melts, the oxidizing power of cations increases in the order Ca, Na, K (Thornber et al., 1980; Kilinc et al., 1983; Dickenson and Hess, 1986). Likewise, the redox ratio increases systematically with melt depolymerization as expressed by the

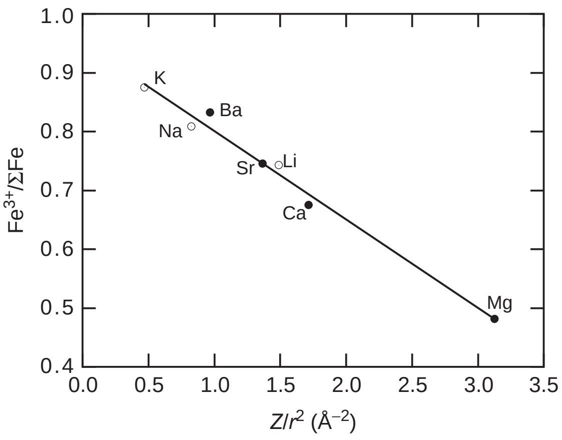

FIG. 10.17 Iron redox ratio against the ionization potential of the cation in alkali trisilicates with 0.4 wt% in air at 1400°C (Paul and Douglas, 1965) and in alkaline earth metasilicate melts with 5 wt% Fe_2O_3 heated in air at 1550°C (Mysen et al., 1984). For Mg, the sample composition is slightly off the $MgSiO_3$ stoichiometry.

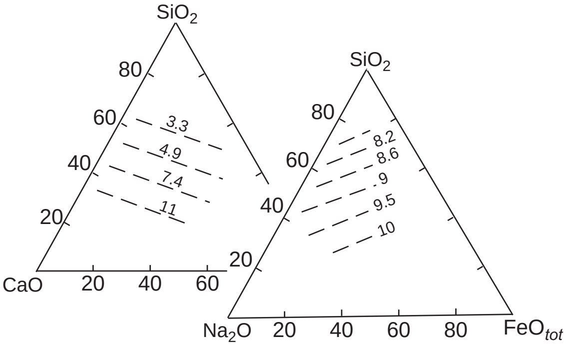

FIG. 10.18 Contours of equal Fe^{3+}/Fe^{2+} ratios in the systems CaO-"FeO"-SiO$_2$ and Na$_2$O-"FeO"-SiO$_2$ as drawn by Kress and Carmichael (1989) from their data and those of Lange and Carmichael (1989). These trends are consistent with the results of Mysen et al. (1985c) for Ca and those of Mysen and Virgo (1989) for Na systems.

parameter NBO/T. In this respect, the influences of Al and Si are analogous in the quaternary system CaO-MgO-Al$_2$O$_3$-SiO$_2$ (Mysen et al., 1985c) as well as in natural melts (Sack et al., 1980; Kilinc et al., 1983).

As indicated by phase equilibria data, the association of tetrahedral Fe^{3+} with charge-compensating cations is strongest for K^+. Attention has thus been paid to the competition between Fe^{3+} and Al^{3+} to associate with this cation. In potassium aluminosilicates, the variations of the iron redox state observed as a function of Al/(Al+K) show two different regimes (Fig. 10.19). The redox ratio first increases weakly in the peralkaline domain, and then decreases markedly after the meta-aluminous join has been crossed. Dickenson and Hess (1981) thus concluded that K^+ does associate with Al^{3+} in peralkaline melts, but not in peraluminous compositions, where it partly reduces to Fe^{2+}, which may in turn serve as a charge-compensator for the remaining Fe^{3+}, perhaps in the form of Fe$_3$O$_4$-like clusters (O'Horo and Levy, 1978; Virgo and Mysen, 1985). On the other hand, the weaker association of Ca^{2+} with Fe^{3+} is attested to by the insensitivity of the redox ratio with respect to substitution of Ca^{2+} for K^+ in peralkaline melts, and its decreases in peraluminous melts (Dickenson and Hess, 1986).

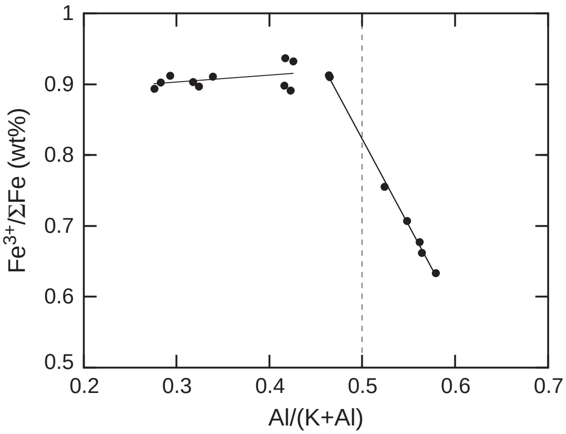

FIG. 10.19 Iron redox ratio against K/(K+Al) for potassium aluminosilicates at constant 78 mol% SiO$_2$ (Dickenson and Hess, 1981). Experiments made in air at 1400°C with a total of 2 wt% FeO.

10.4.5 Water and Minor Components

Minor oxide components and volatiles in the C—O—H system may have profound effects on the redox ratio of iron (Baker and Rutherford, 1996; Gaillard et al., 2001; Botcharnikov et al., 2005; Maia and Russel, 2006; Borisov et al., 2013). Among volatiles, dissolved H_2O has attracted the most attention. In most experimental studies the redox ratio of iron did indeed vary with water activity in the melt whether in rhyolitic or basaltic compositions (Baker and Rutherford, 1996; Gaillard et al., 2001, 2003; Botcharnikov et al., 2005; Schuessler et al., 2008). The one exception to this conclusion is that of Moore et al. (1995), who reported that water does not have an effect on the redox ratio of hydrous basaltic melts at pressures up to 300 MPa. The reason for this divergent result is not clear.

Baker and Rutherford (1996) concluded that the effects of water on $Fe^{3+}/\Sigma Fe$ are similar to those of alkali metal oxides and thus result in an increase in $Fe^{3+}/\Sigma Fe$. For peraluminous rhyolites, however, $Fe^{3+}/\Sigma Fe$ decreases greatly with hydroxyl content at high temperature under redox conditions near the nickel-nickel oxide (NNO) buffer (Baker and Rutherford, 1996). A similar conclusion has been arrived at by Gaillard et al. (2001) for other silicic metaaluminous melts. The apparent disagreement between these studies suggests that the influence of water on iron redox state depends on silicate composition and oxygen fugacity. Indeed, Gaillard et al. (2003) have concluded that this influence is smallest for peralkaline compositions and oxidizing conditions. But the complex nature of the compositions investigated have prevented the main factors that determine these variations from being identified. Substitution of Ca for Na causes a decrease of the redox ratio in hydrous melts.

In hydrous basalt melt at fixed temperature and pressure, the redox ratio increases with increasing water concentration (Fig. 10.20), but the rate of this increase depends on redox

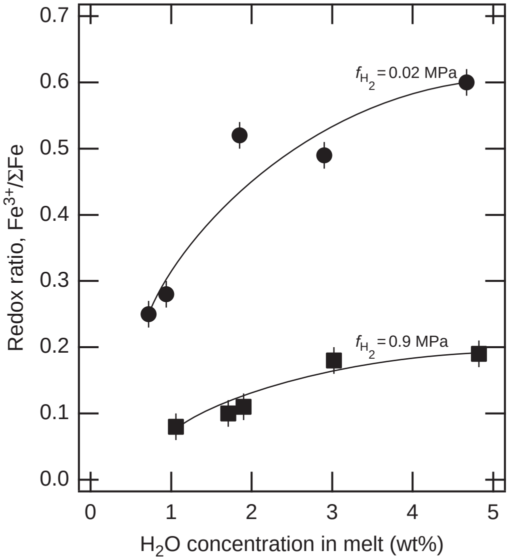

FIG. 10.20 Iron redox ratio of iron, $Fe^{3+}/\Sigma Fe$ as a function of H_2O concentration in melt and redox conditions (defined by the fugacity of hydrogen f_{H_2}). Because the total H_2O concentration is a variable, the oxygen fugacity at fixed hydrogen fugacity also varies (Botcharnikov et al., 2005).

conditions (Botcharnikov et al., 2005). The redox ratio is less sensitive to water concentration under reducing conditions, perhaps because the structural environment of iron is a function of the redox ratio (see Section 11.4.1), which in turn is governed by redox conditions (hydrogen fugacity). Notice that the oxygen fugacity is a variable dependent on the water fugacity because the water concentration varies as:

$$\mathrm{Log}\, f_{O_2} = \left(\log\left(f_{H_2O}/f_{H_2}\right) - \log K_{H_2O}\right)/0.5, \tag{10.14}$$

where f_{O_2}, f_{H_2}, and f_{H_2O} are the fugacities of oxygen, hydrogen, and water, and K_{H_2O} is the dissociation constant of H_2O.

Data on the effect of other volatile components on the redox state of iron in silicate glasses and melts are scarce. Fluorine qualitatively seems to have the same effect as H_2O, as it results in increased $Fe^{3+}/\Sigma Fe$ of melts at high temperature (Maia and Russel, 2006), but otherwise the literature seems mute on this topic.

Concerning the effects of other minor oxides, those of TiO_2 and P_2O_5 have been subjected to a small number of experimental studies (Mysen, 1992; Toplis et al., 1994; Borisov et al., 2013). For both oxides, an increasing concentration tends to result in a lowering of the $Fe^{3+}/\Sigma Fe$ of the melt at constant temperature, pressure, and oxygen fugacity. This effect probably indicates that both TiO_2 and P_2O_5 increase the silicate polymerization (see Sections 12.6 and 13.4), which in turn would result in iron reduction.

10.4.6 Prediction of Iron Redox Ratio

Ever since the first experiments of Kennedy (1948) and Fudali (1965), the importance of knowing iron redox ratio has motivated efforts to predict it as a function of temperature and composition. The first model seems to be that of Lauer (1977) and Lauer and Morris (1977) not only for Fe, but also for Ce and Cr. The composition dependence of the activity coefficient of oxygen ions in simple silicate liquids was related empirically to the ionization potential of network-modifying cations. However, no attempt has since then been made to extend such a formalism to more complex compositions.

A purely empirical approach was followed by Sack et al. (1980) and pursued with additional data by Kilinc et al. (1983), who assumed that the effects of oxygen fugacity and temperature on the redox ratio do not depend on composition and that, at constant T and f_{O_2}, the redox ratio is an additive function of oxide concentration. The expression they fitted to available and new redox data for melts of geochemical interest ranging from mafic to felsic was thus:

$$\ln\ (x_{Fe_2O_3}/x_{FeO}) = a\ \ln f_{O_2} + b/T + c + \Sigma d_i x_i, \tag{10.15}$$

where x designates an oxide mol fraction; a, b, and c are constants; and the d_i are specific parameters for SiO_2, Al_2O_3, "FeO," MgO, CaO, Na_2O, and K_2O. There are, however, objections to the assumptions made in these models. These are, for example, inconsistent with the nonlinear dependence of redox ratio on total iron content (Fig. 10.15). Besides, network formers and modifiers should influence the redox state in differing ways. These problems were accommodated in the symmetric regular solution model proposed by Borisov et al. (2015).

Here, the interaction parameters between Fe^{3+}, Fe^{2+}, and the remaining components account for these deviations. When the "FeO" content is not small, variations of the redox state are in addition synonymous with changes in melt polymerization, oxygen activity, and energetics of the redox reaction. All such factors make it difficult to neglect the influence of composition on the variation of redox state with temperature and oxygen fugacity.

To distinguish the effects of network-forming and modifying cations, Mysen (1987) modified Eq. (10.15) as follows:

$$\ln\left(x_{\mathrm{Fe}^{3+}}/x_{\mathrm{Fe}^{2+}}\right) = a\ \ln f_{\mathrm{O}_2} + b/T + c + d\left(\mathrm{Al}/(\mathrm{Al}+\mathrm{Si})\right) + e\left(\mathrm{Fe}^{3+}/\mathrm{Fe}^{3+}+\mathrm{Si}\right) + \Sigma f_i x_i, \tag{10.16}$$

where x_i designates the NBO/T value pertaining to the network-modifying cation i. Although a better fit to the input data base of Kilinc et al. (1983) was obtained in this way by Mysen (1987), this model has not been extensively used in the petrological literature. Probable reasons are the need for structural information and the iterative nature of the calculation due to the fact that the structural components are functions of both FeO and Fe_2O_3 contents.

A less empirical method was adopted by Kress and Carmichael (1988). As described in Section 10.4.2, deviations from the nominal 0.25 value of the stoichiometry coefficient of the redox reaction are a measure of nonideal mixing of Fe^{2+} and Fe^{3+}. Conversely, one may try to cope with thermodynamic nonideality via the choice of components such that the stoichiometry coefficient remains close to 0.25. Kress and Carmichael (1988) used in this fashion FeO and $FeO_{1.464}$ components, the latter being thought to reflect a fundamental aspect of the structure of natural melts. They then fitted the equation:

$$\ln\left(x_{\mathrm{FeO}_{1.464}}/x_{\mathrm{FeO}}\right) = 0.232\ \ln f_{\mathrm{O}_2} - (\Delta H + \Sigma W_i x_i)/RT + \Delta S/R, \tag{10.17}$$

to a data set complemented by new measurements made at very low oxygen fugacity. In this equation, note that the actual enthalpy of the redox reaction differs from the fit parameter, ΔH, because it depends on composition via the term involving the adjustable W_i variables.

Subsequently, the effects of pressure on redox ratio were incorporated by Kress and Carmichael (1991) as part of a study of the compressibility of Fe-bearing melts. They reverted to Eq. (10.15), to which they added pressure-dependent terms, viz.:

$$\begin{aligned} \ln\left(x_{\mathrm{Fe}_2\mathrm{O}_3}/x_{\mathrm{FeO}}\right) &= a\ \ln f_{\mathrm{O}_2} + b/T + c + \Sigma d_i x_i \\ &+ e\left[1 - T_0/T - \ln T/T_0\right] + f\ P/T + g(T - T_0)P/T + hP^2/T, \end{aligned} \tag{10.18}$$

where e, f, g, and h are fit parameters and T_0 (1673 K) a reference temperature.

These various models have been tested by Nikolaev et al. (1996). In spite of their differences, they were found to give similar results, with typical deviations of 0.03–0.05 from the measured redox ratios. The less reliable predictions were for felsic melts of the andesite-rhyolite series. To improve predictions, Nikolaev et al. (1996) finally split the available data base into four different domains of temperature, oxygen fugacity, and redox ratio, for which they fitted distinct sets of Eq. (10.9) parameters.

As tested by Partzsch et al. (2004) with new measurements, the models of Kress and Carmichael (1991) and Nikolaev et al. (1996) generally reproduce the observed Fe^{3+}/Fe^{2+} ratios to within 0.05. Deviations of up to 0.1 are nonetheless observed, particularly for felsic compositions or strongly oxidizing conditions. Interestingly, the models can also be extrapolated to subliquidus temperatures, where they are most useful, although they were necessarily calibrated with superliquidus data. The fact that composition effects are averaged out in chemically complex systems such as magmatic liquids ensures the interest of the predictions, but at the same time prevents them from being made outside the composition range on which they were calibrated. The paradox is that further progress will require better understanding of basic mechanisms to be achieved from the study of simple systems to which current models cannot be applied.

The Mössbauer study of an aluminosilicate melt by Jayasuriya et al. (2004) illustrates this point. In agreement with results of Virgo and Mysen (1985) and Mysen (2006), a definite interaction was detected between Fe^{2+} and Fe^{3+} whereby Fe^{3+}—Fe^{2+} bond distances vary with the $Fe^{3+}/\Sigma Fe$ ratio (Fig. 10.21). The neglect of such interactions is the reason why available models do not work well at low iron content. Jayasuriya et al. (2004) also pointed out that deviations from the nominal 0.25 stoichiometry coefficient of the redox reaction (10.3) at low Fe concentration are indeed negligible if, consistent with Eq. (10.3), $FeO_{1.5}$, instead of Fe_2O_3, is chosen along with FeO as a component. Hence, the proper way to account for Fe^{2+}—Fe^{3+} interactions is not to adjust the stoichiometry coefficient of the reaction, but to add a specific term in the expression of the redox ratio. Jayasuriya et al. (2004) thus included a regular-like interaction term derived from their results.

Another way to account for Fe^{2+}—Fe^{3+} interactions is not to adjust the stoichiometry coefficient of the reaction, but to add a specific term in the expression of the redox ratio. Jayasuriya et al. (2004) included a regular-like term derived from their results, $W_{Fe^{3+},j}$, $W_{Fe^{2+},j}$ and $W_{Fe^{2+}\text{-}Fe^{3+}}$, so that:

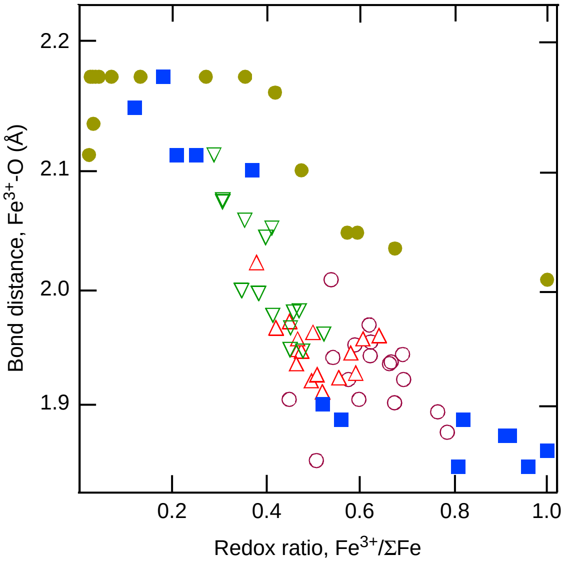

FIG. 10.21 Bond distance, Fe^{3+}—O, in silicate melts as a function of their redox ratio, $Fe^{3+}/\Sigma Fe$. Bond distance was calculated from Eq. (11.1) in Chapter 11 where the isomer shift from ^{57}Fe resonant Mössbauer spectroscopy is related to bond length. Data: *closed squares*, Dingwell and Virgo (1987); *closed circles*, Jayasuriya et al. (2004); *open symbols*, Mysen (2006).

$$1\mathrm{n}\left(\frac{X_{\mathrm{Fe}^{3+}\mathrm{O}_{1.5}}}{X_{\mathrm{Fe}^{2+}\mathrm{O}}}\right) = 0.25 \ln f_{\mathrm{O}_2} - \frac{-\Delta G}{RT} - \left(\sum_{j}^{n} X_j \left(W_{\mathrm{Fe}^{3+}-j} - W_{\mathrm{Fe}^{2+}-j}\right)/RT + \left(X_{\mathrm{Fe}^{2+}\mathrm{O}} - X_{\mathrm{Fe}^{3+}\mathrm{O}_{1.5}}\right) W_{\mathrm{Fe}^{3+}-\mathrm{Fe}^{2+}}/RT\right). \qquad (10.19)$$

In this very simple way, they showed how models could account for the dependence of redox ratio on total iron content (Fig. 10.22). Among the models summarized previously, that of Kress and Carmichael (1991) results in redox ratios that nearly coincide with the Jayasuriya et al. (2004) data, whereas other models differ by up to >25% (see also Jayasuriya et al., 2004, for a detailed discussion of these differences and similarities).

Along different lines, the acid-base approach followed by Ottonello et al. (2001) is also of interest. The starting point is the model of Toop and Samis (1962) for the oxygen speciation reactions (6.6) whose equilibrium constants are determined from optical basicity data (see Section 6.3.4). The activities of iron oxides are then obtained from the Temkin model (Temkin, 1945), with proper allowance for the network-forming or network-modifying character of Fe and other cations. In this respect, the main difference between iron oxides is the amphoteric character of Fe_2O_3 that gives rise to two dissociation reactions instead of the single one that applies to FeO.

The fact that oxygen ions can thus appear either as reactants or products in the redox reaction explains why addition of metal oxides at constant oxygen fugacity can cause either oxidation or reduction. Although Ottonello et al. (2001) assumed that Fe^{2+} and Fe^{3+} mix ideally over the cation sublattice, the ratio of the activity coefficients of $FeO_{1.5}$ and FeO differs from unity as a result of the contribution of these dissociation reactions to mixing in the anionic

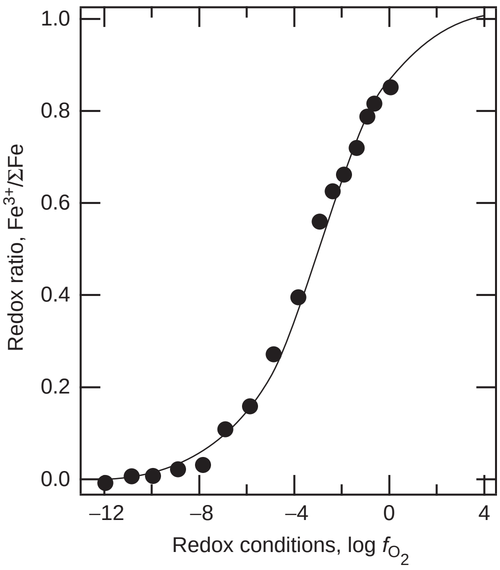

FIG. 10.22 Redox data from Jayasuriya et al. (2004) fitted to their model reproduced as Eq. (10.19) in the text.

matrix. Making use of relevant thermochemical data, Ottonello et al. (2001) proceeded to calculate the activity of FeO as a function of composition and, finally, equilibrium redox ratios for the same database as used by Kilinc et al. (1983). The advantage of such a thermodynamically based approach is obvious if one considers that a precision similar to that of the model of Kilinc et al. (1983) was achieved with less than half the number of adjustable parameters.

10.4.7 Mechanisms of Redox Reactions

Thermodynamic measurements are of little help in understanding the mechanisms of redox reactions. Insights have been gained instead from kinetic studies, because these allow the rate-limiting parameters of the reactions to be determined (cf. Cooper, 2018). Although the majority of studies have been devoted to oxidation reactions, experiments described in the following text have shown that oxidation and reduction reactions have basically the same kinetics and obey the same mechanisms.

The simplest assumption is that the redox rate is controlled by diffusion of oxygen in either molecular or ionic form. In both cases, the relevant half reactions would be:

$$O_2 + 4e^- \Leftrightarrow 2O^{2-}, \tag{10.20}$$

and

$$4Fe^{2+} \Leftrightarrow 4Fe^{3+} + 4e^-. \tag{10.21}$$

With diffusion of physically dissolved molecular oxygen, the redox and diffusion fronts coincide. By starting from the surface, they move together inside the melt (Fig. 10.23). With (chemical) diffusion of O^{2-}, the oxidation mechanism is more complicated because the oxygen ionization reaction (10.20) occurs at the melt-atmosphere interface, whereas the iron oxidation reaction (10.21) takes place at progressively greater depths within the melt so that a counterflux of electrons is needed to ensure local electroneutrality.

Without distinguishing physical and chemical diffusion, Goldman and Gupta (1983) calculated the effective oxygen diffusivity needed to account for the rate of change of the redox ratio measured in air for a Ca—Al borosilicate. By assuming instantaneous local equilibrium between iron and oxygen ions, they derived from their kinetic measurements an oxygen diffusivity of $3.7 \times 10^{-11}\,\mathrm{m^2/s}$ at 1260°C, which is similar to tracer diffusivities measured for other silicate melts (Oishi et al., 1975; Yinnon and Cooper, 1980; Dunn, 1983). Goldman and Gupta (1983) thus concluded that oxygen diffusion is controlling the redox kinetics. Notably, Goldman (1983) found that the reaction rate is slower for reduction than for oxidation.

Schreiber et al. (1986) reached a similar conclusion from a more detailed analysis. They stated that in a chemical gradient the chemical diffusion of oxygen determined in redox studies is several orders of magnitude faster than the diffusion of oxygen belonging to the silicate framework (Fig. 10.24). For the latter process, activation enthalpies are, in addition, twice as great as for the former. Schreiber et al. (1986) also stressed that only oxygen ions, in equilibrium with dissolved O_2 (whose concentration is related to oxygen partial pressure via Henry's law), participate in the redox reaction.

An intriguing fact is that both diffusivities and activation enthalpies for chemical diffusion of oxygen seem similar to the values determined for tracer diffusion of divalent

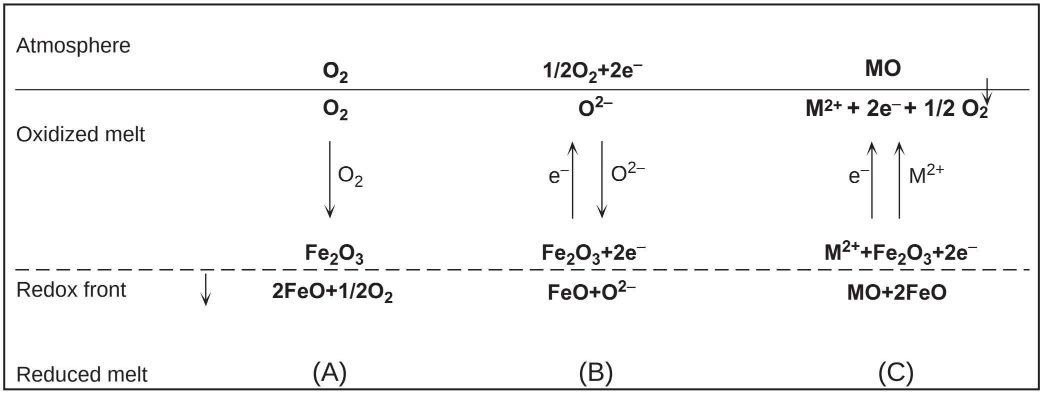

FIG. 10.23 Reactions at the moving redox front and at the fixed melt-atmosphere interface, along with the associated fluxes of species, for rate-controlled oxidation by diffusion of molecular oxygen (A), oxygen ions (B), and divalent cations (C). In (C), crystallization at the surface can be more complicated when several divalent cations are present (see text). In an ionic medium, an electron and the surrounding region in which it induces strong polarization are called a polaron. *Small* polarons are of atomic size, have an effective mass much higher than that of the electron, and hop from one site to another with the assistance of phonons. It is often stated that they ensure electrical conductivity in glasses (e.g., Jurado-Egea et al., 1987). Alternatively, electrical conduction in crystals indicates that electroneutrality can be achieved through a counterflux of electron holes in the valence band. These are also designated as small polarons because of the structural distortion they induce. In Fe-bearing olivines, electrical conductivity indeed results from small polaron hopping of holes from Fe^{3+} to Fe^{2+} on the Mg sublattice, which is a faster mechanism than electron hopping (Hirsch et al., 1993). Because of their more familiar nature, electron fluxes are shown above but they could be readily replaced by opposite fluxes of electron holes. In (B), it follows that the electrical conductivity of the melt could be the rate-limiting factor.

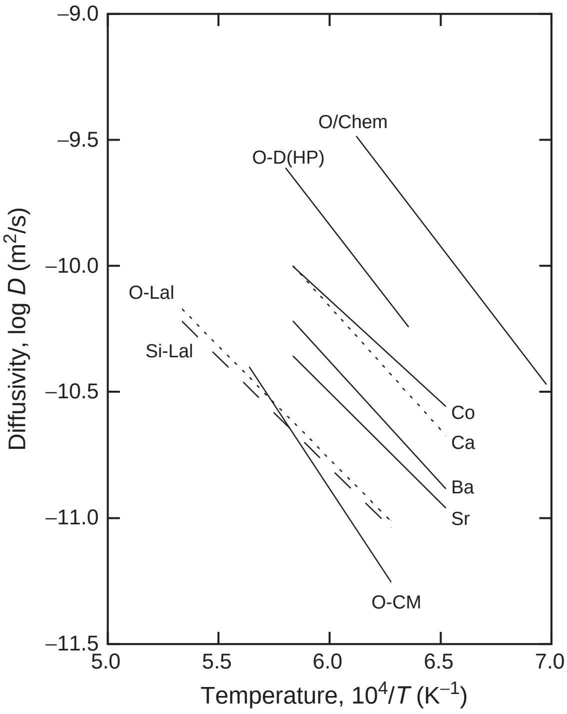

FIG. 10.24 Tracer diffusivities in tholeiitic basalt melts. Data for divalent cations from Magaritz and Hoffmann (1978); for silicon and oxygen (Lal) from Lesher et al. (1996); for oxygen (CM) from Canil and Muelenbachs (1990) (same results under an O_2 or CO atmosphere); for oxygen (D-HP) from Dunn (1983) at 1.2GPa (with a pressure effect of about −0.3 log units compared with room-pressure values). For oxygen (O/Chem), the chemical diffusivity of Wendlandt (1991) has been included.

network-modifying cations (Dunn, 1982; Dunn and Scarfe, 1986). This led Cook et al. (1990) to determine whether the redox reaction was controlled instead by diffusion of Ca^{2+} or Mg^{2+}. In a variety of ionic solids, including oxides and silicates such as magnesiowüstites and $(Mg, Fe)_2SiO_4$ olivines (Luecke and Kohlstedt, 1988; Wu and Kohlstedt, 1988), oxidation occurs via the removal of divalent cations rather than by addition of oxygen. With this mechanism, oxygen is not transported at all. At the redox front, it is released by alkaline earth cations that migrate toward the vapor-melt interface where they react with gaseous oxygen to form a thin oxide layer. Electroneutrality can be achieved through a simultaneous flux of electrons or a counterflux of electron holes from the surface to the redox front. The fact that Fe ions are involved in these processes make the kinetics of the reaction dependent on total iron concentration.

Extensive study of this mechanism was made by Cook et al. (1990) for an Fe-bearing Mg aluminosilicate oxidized at 700–800°C in air. A crystalline layer made up of MgO and $(Mg, Fe)_3O_4$ was detected at the glass surface. With Rutherford backscattering spectroscopy, Cook et al. (1990) correlatively observed a depletion of divalent cations near the glass surface, which followed a parabolic law characteristic of a diffusive process. These experiments have been complemented by observations made on a reduced nepheline normative olivine basalt glass heated in air at 550–600°C (Cooper et al., 1996). At the surface, precipitation of CaO and MgO was observed. As a result, Mg and Ca were depleted near the surface of the glass where Na was, in contrast, enriched because it charge-compensated Fe^{3+} and, doing so, prevented spinel from crystallizing. Consistent results have been described for a tholeiitic basalt by Burkhard (2001) heated in air and in argon between 850°C and 940°C.

Internal oxidation does not necessarily yield the lowest energy state. Such a process takes place when it dissipates the gradient of oxygen chemical potential between the melt and the external atmosphere faster than oxygen diffusion. Because it is the flux that matters, this mechanism is generally the most efficient near, or even below, the glass transition as decoupling between bulk and local relaxation makes diffusion much faster for network-modifying cations than for oxygen (see Section 2.2.5). For Fe-bearing pyroxene compositions, this has been confirmed by in situ XANES measurements made just above the glass transition range where the observed oxidation kinetics were orders of magnitude too fast to have been caused by oxygen diffusion (Magnien et al., 2004, 2008).

The mechanisms of internal oxidation depend on the silicate composition. For example, in a study of Na aluminosilicate melt (Barton et al., 1992; Barton and Caurant, 1993), iron oxidation at 800°C again took place through diffusion of Na^+. No crystalline precipitate was observed at the surface, however, whereas there was some evidence for back-diffusion of Na within the glass.

In the other glasses investigated by Cooper and coworkers, crystalline precipitates formed at the surface. For Mg aluminosilicate glasses with Fe contents lower than 0.54 wt% heated at 700–850°C in air, oxidation occurred via diffusion of Fe^{2+} and a counterflux of electron holes (Cook and Cooper, 2000). Interestingly, this mechanism did not operate below 800°C in glasses with <0.19 wt% because the Fe concentration was then too low to ensure a sufficient conductive flux. Transport of oxygen species was assumed to have taken place instead. In another study, part of the Mg^{2+} ions were replaced by bigger Ca^{2+} ions to determine whether expansion of the structure would affect the oxidation mechanisms (Smith and Cooper, 2000). The reaction remained dominated by diffusion of divalent cations, but the rate of the reaction was 100 times faster in the presence of Ca^{2+}. Although the nature of crystalline precipitates differed in air and in argon, in both cases the morphology was suggestive of cation diffusion through the interconnected channels of the structure assumed in the modified random network model of Greaves (1985). Under extremely reducing conditions, different observations were made by Cooper et al. (2010) for the reduction of Fe-bearing Ca,Mg aluminosilicate, in that the phase precipitating at the melt surface was a (Fe,Si,C) alloy, whereas the kinetics of the redox reaction was controlled by diffusion of CO.

As a matter of fact, differences in high-temperature diffusivities could perhaps not be as clear-cut as has been concluded from measurements made on different melt compositions. This is suggested by the data available for molten tholeiitic basalts, which are the most extensive (Fig. 10.25). Only the diffusivity of iron (Dunn and Ratliffe, 1990) is several orders of magnitude lower than that of the elements considered in this figure. For hydrous melts, note finally that Gaillard et al. (2002) have described a two-step reaction mechanism whereby very fast hydrogen diffusion is followed by slow reorganization around iron ions.

Support for this view is provided by a similar contrast in reduction mechanisms. In a study of reduction of a Mg aluminosilicate between 1300°C and 1400°C, Everman and Cooper (2003) observed the formation of nanometer-scale iron metal precipitates at an internal surface, which they assigned to flux of electron holes and Mg^{2+} with a diffusivity of 10^{-10} m^2/s. Simultaneously, ionic oxygen was released at the surface where it transformed to molecular oxygen. It is common experience, however, that oxygen bubbles rapidly escape out of oxidized melts heated in air at sufficiently high temperatures. In this case, there is no evidence for precipitates when oxygen is released within the melt. Instead, oxygen bubbles nucleate very rapidly and grow while moving to the surface.

The question arises as to whether internal oxidation can remain the dominant mechanism at high temperature where element diffusivities tend to converge. A positive answer has been given by observations made on droplets of molten basalt levitated in air at 1400°C (Cooper et al., 1996). Although quench reactions could have complicated the situation, precipitation of magnetite was observed at the redox front and precipitation of hematite (Fe_2O_3) and

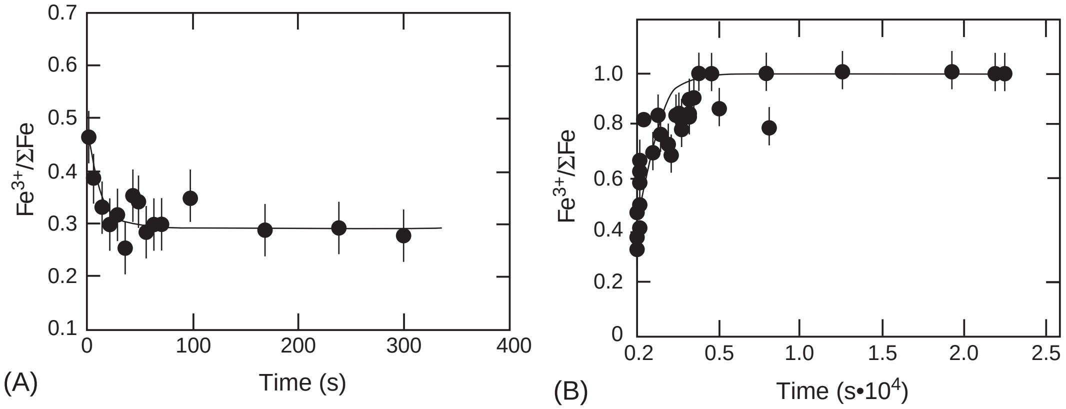

FIG. 10.25 Time dependence of the iron redox ratio of an Fe-bearing pyroxene melt (Pyrox). (A) Upon reduction from 1723 to 2058 K. (B) Upon oxidation from 1923 to 1280 K (Magnien et al., 2008).

pseudowollastonite ($CaSiO_3$) near the sample surface. In this case, oxidation clearly caused an increase of liquidus temperature that made crystallization of these phases possible.

10.4.8 Kinetics of Redox Reactions

The fact that crystallization cannot be observed above the liquidus indicates that internal oxidation could no longer be the dominant mechanism at sufficiently high temperatures. When superliquidus conditions prevent crystallite precipitation at the surface, a possibility of lowering the Gibbs free energy of the melt disappears and thus a driving force for cation diffusion. Oxygen diffusion then becomes the dominant mechanism as asserted by Goldman and Gupta (1983) and ascertained by kinetic experiments performed on a variety of iron-bearing silicates (Magnien et al., 2004, 2008) and borosilicates (Cochain et al., 2013a,b) with different iron and alkali oxide contents. The evolution of $Fe^{3+}/\sum Fe$ with time, observed with XANES experiments made at the K-edge of iron at a given temperature (Fig. 10.26), can then be reproduced by the expression (2.2) used for relaxation times:

$$\left(F_t - F_{eq}\right) = \left(F_0 - F_{eq}\right) \exp\left(-t/\tau\right), \tag{10.22}$$

where F_t is the redox ratio at time t, F_0 the initial ratio, F_{eq} the equilibrium value and τ a characteristic time (Magnien et al., 2006). As determined from a least-squares fit of Eq. (10.22) to the experimental redox data with a relative uncertainty of 10%, this parameter depends primarily on temperature and not on the initial redox state. In accordance with the diffusion-controlled nature of the process, it is a linear function of the square root of time. At high temperatures, where both kinds of reactions could be investigated, these times are in addition similar for oxidation and reduction, thus indicating similar kinetics for both reactions.

At a given temperature, each kinetic experiment can further be characterized by the time (t_{eq}) required to reach equilibrium, which is arbitrarily considered to be achieved when the redox ratio reaches 99% of the new equilibrium value. In all experiments, however, the

FIG. 10.26 Differences of redox mechanisms at high temperatures and above the glass transition range evidenced by the changes in redox diffusivities for iron-bearing pyroxene melts to which Li_2O or Na_2O have been added (Magnien et al., 2008).

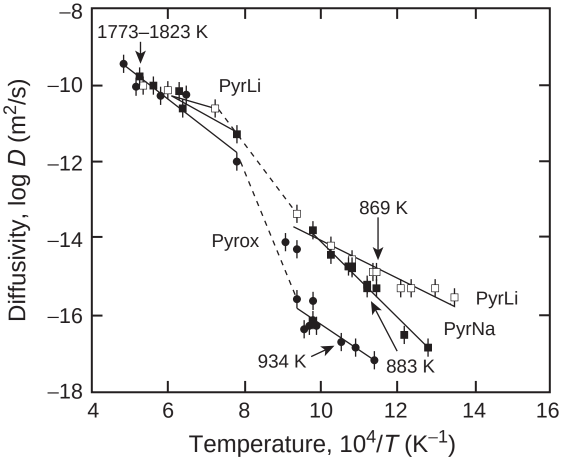

kinetics of course depends on the size of the sample investigated. With the assumption that samples are spheres of radius r, the concept of redox diffusivity D_{red} has thus been introduced to eliminate this effect with the simple relation:

$$D_{red} = r^2/4t_{eq}, \tag{10.23}$$

so that direct comparisons with measured diffusivities can be made (Magnien et al., 2008). Either above the glass transition range or between 1300 and 2100 K, redox diffusivity follows an Arrhenius law:

$$D = D_0 \exp(-E_a/RT), \tag{10.24}$$

where R is the ideal gas constant, D_0 a preexponential factor, and E_a an activation enthalpy. That the redox mechanisms are different at low and high temperatures is clearly shown by the very rapid change in redox diffusivities between the two regimes (Fig. 10.27). As is now well

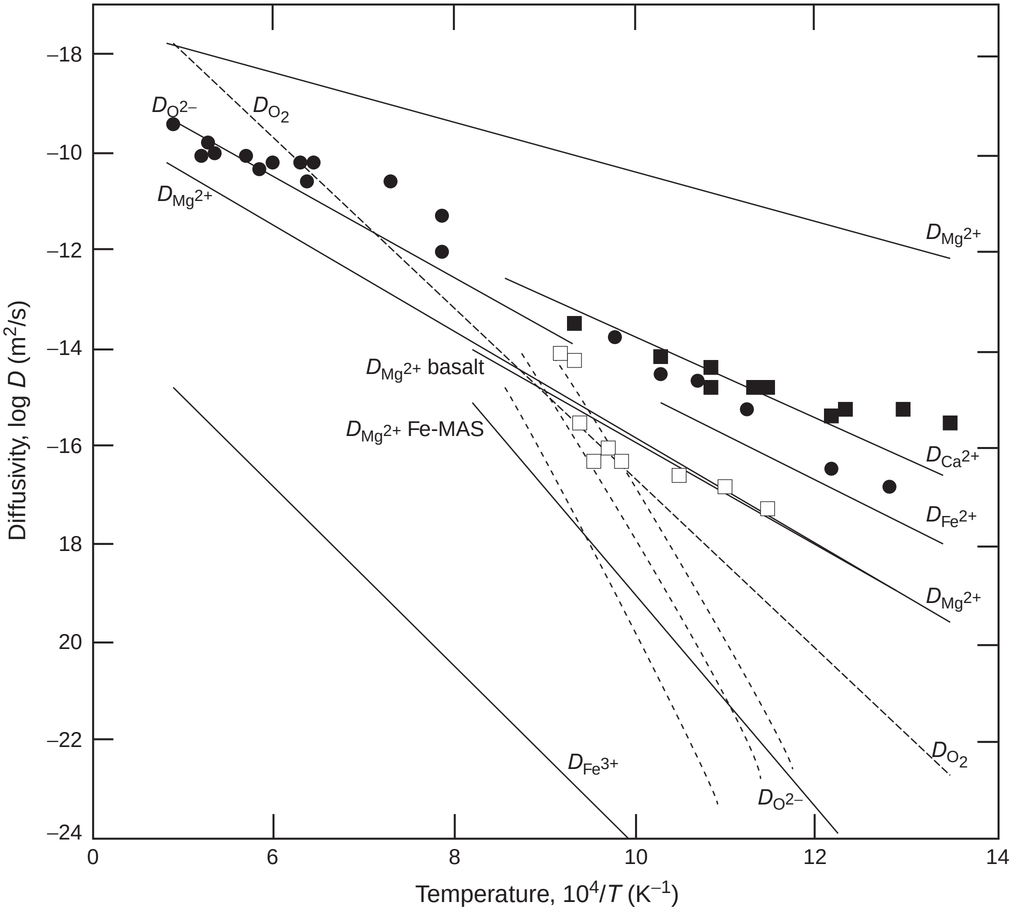

FIG. 10.27 Comparisons between the redox diffusivities of the Pyr samples and the diffusion coefficients of various elements in related melts (Magnien et al., 2008).

FIG. 10.28 Comparisons of redox diffusivities *(solid symbols)* with oxygen diffusivities derived from the Eyring relationship (O^{2-}) and the diffusivities deduced from electrical conductivities ("divalent cations") on both sides of the glass transition (Malki et al., 2015).

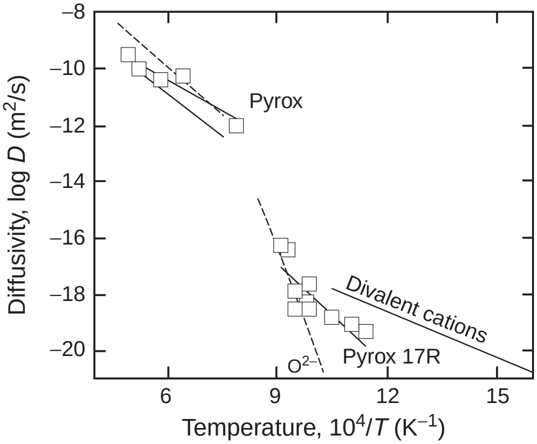

established, diffusion of divalent cations is the dominant mechanism at low temperatures but the enhanced kinetics observed for alkali-bearing melts indicate that Li^+ and Na^+ also participate in ionic transport. At superliquidus temperatures, in contrast, diffusion of oxygen represents the dominant mechanism (Fig. 10.28). Interestingly, such kinetics can be predicted without any fit parameter. From viscosity and electrical conductivity measurements, Malki et al. (2015) determined the diffusivity of oxygen and divalent cations of the same samples through the Eyring and Nernst-Einstein relationships, respectively. Excellent agreement with the redox diffusivities was found in this way (Fig. 10.29), illustrating that describing melt properties in an integrated manner is becoming possible.

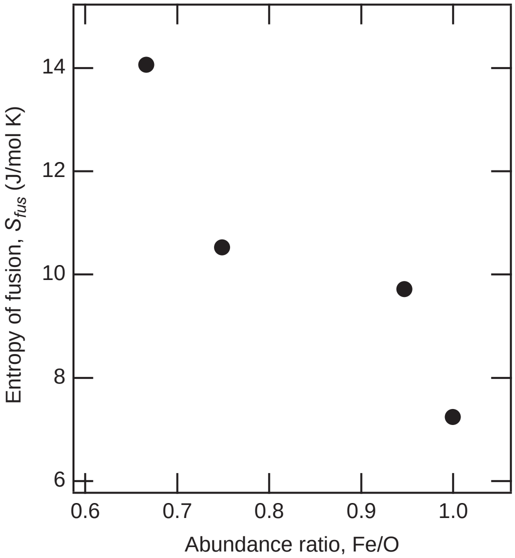

FIG. 10.29 Entropy of fusion of iron oxides as a function of their Fe/O ratio (Sugawara and Akaogi, 2004).

Similar results have been obtained on a series of iron-bearing sodium borosilicate melts (Cochain et al., 2013a). Substitution of sodium for boron at constant SiO_2 content first causes transformation of BO_3 triangles into BO_4 tetrahedra until an excess of sodium induces instead melt depolymerization (e.g., Youngman, 2018). These changes in the degree of polymerization and boron coordination lead to a maximum in oxygen diffusivity at around 18 mol% B_2O_3, and correlatively, to a viscosity minimum. Because this change of trigonal into tetrahedral boron requires charge compensation of B^{3+} by cations such as Na^+ ions, the mobility of Na^+ decreases and reduces the rate of oxidation. In addition, the decreasing fraction of Na^+ ions and their change from a free to a charge-compensating role explain the decreasing redox diffusivities and electrical conductivities of the samples. Whereas the redox kinetics are again controlled near the glass transition range by the diffusion of network-modifying cations toward the surface of the melt, the original feature is that it is limited at superliquidus temperatures by the diffusion of free Na^+ ions to charge-compensate Fe^{3+} in tetrahedral coordination, along with the diffusion of oxygen (Cochain et al., 2013a).

10.5 THERMAL PROPERTIES

The set of available thermodynamic properties is considerably less comprehensive for iron-bearing than for aluminosilicate melts. This relative scarcity is partly due to the high temperatures required to form iron-bearing silicate melts, since the pure Fe^{3+} endmember melts cannot be synthesized even when equilibrated under oxidizing conditions such as that of air. Moreover, crystallization during calorimetric measurements often can be a serious obstacle to accurate determination above the glass transition. Exceptions to those observations are activity-composition relations, which have been extensively determined for the SiO_2-pour compositions of slags because of their fundamental importance in steel making.

10.5.1 Thermodynamics of Melting

The enthalpy and entropy of fusion of several iron oxides (FeO, Fe_3O_4, and Fe_2O_3) have been reported by Sugawara and Akaogi (2004). Strikingly, as the bulk Fe/O abundance ratio decreases, the entropy of fusion increases (Fig. 10.30). Notably, the entropy of fusion of FeO is only several J/mol K, and resembles that of SiO_2 (see Section 5.3.1), which suggests that melting of FeO does not involve bond breakage and reformation. However, as soon as iron is oxidized and Fe/O decreases, the entropy of fusion increases rapidly (Fig. 10.30). Whether this is because of redox differences in melts and crystalline materials, forming and rupturing of bonds, or both, is not known.

Among iron silicates, the enthalpy of fusion of acmite, $NaFe^{3+}Si_2O_6$, has been reported to be 70.5 ± 9.4 kJ/mol (Sugawara and Akaogi, 2004), which is not greatly different from that of jadeite, $NaAlSi_2O_6$ (59.3 ± 3 kJ/mol) (see Richet and Bottinga, 1984). Similarly, the entropies of fusion of acmite and jadeite also resemble each other and are quite high, at 51.3 ± 6.8 and 53.9 ± 2.7 J/mol K, respectively (Sugawara and Akaogi, 2004; Richet and Bottinga, 1984). These high, and relatively similar, values may be related to the fact that for those two

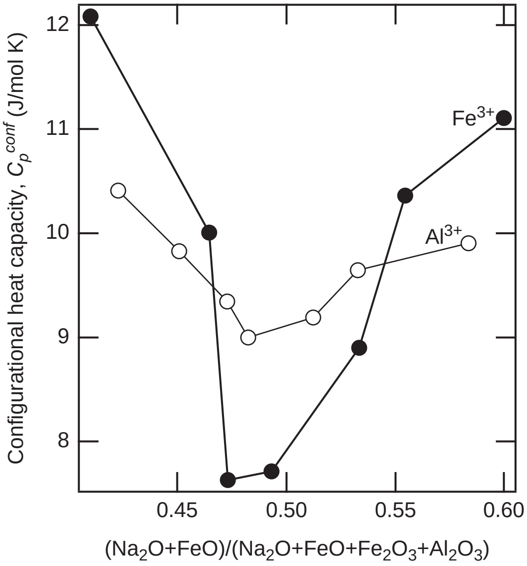

FIG. 10.30 Configurational heat capacity in Al- and Fe-bearing systems from peralkaline to peraluminous side. *Redrawn from Falenty and Webb (2010).*

crystalline materials, Fe^{3+} and Al^{3+} are in octahedral coordination, whereas in their molten state, these cations occur predominantly in fourfold coordination (see Sections 9.3.2 and 11.2.1).

10.5.2 Activity-Composition Relations

The activities measured for iron-bearing melts are too numerous to be reviewed in any detail. Here, the salient point to be emphasized is that, in accordance with Richardson's (1956) proposition and the kinship of Fe^{2+} and Mg^{2+} noted earlier in this chapter, mixing of FeO and MgO can be considered nearly ideal in simple as well as in complex mafic systems (Doyle and Naldrett, 1986; Doyle, 1988). At the other end of the composition range of geochemical interest, it is also of note that the effects of water on the activities of FeO and Fe_2O_3 have been determined for hydrous silicic melts (Gaillard et al., 2003). Under reducing conditions, water increases the activity of FeO and decreases that of Fe_2O_3, and both of them increase with oxygen.

10.5.3 Enthalpy of Mixing

Sugawara and Akaogi (2004) also measured the enthalpy of mixing for melts on the join Na_2SiO_3-Fe_2O_3 and found slight negative excess values of −2.5 to −6.1 kJ/mol. These small enthalpies are considerably less negative than in equivalent Na-aluminosilicate systems, for example, where excess enthalpies range from 10 to 20 kJ/mol (Navrotsky et al., 1989).

A different approach was followed by Bouhifd et al. (2007) in a calorimetric study of basalt melting. By a combination of solution and drop calorimetry made on the crystalline and amorphous phases of an alkali basalt, they found that the enthalpy of fusion (in J/g) could be simply expressed as $\triangle H_f(T) = -118.48 + 0.36311\,T\,(K)$ between 1000 and 1800 K. The close agreement with these values obtained from the weighted enthalpies of fusion of the seven mineral components of the basalt (albite, K-feldspar, anorthite, diopside, forsterite, fayalite, and ilmenite) then indicated that mixing is nearly ideal from an enthalpy standpoint.

10.5.4 Heat Capacity

Calorimetric measurements on iron-bearing glasses and melts are scarce. From their low-temperature C_p measurements on sodium-disilicate and calcium-aluminosilicate based glasses, Sipowska et al. (2009) derived $S_{298} - S_0$ values of 56.7 and 116 J/mol K for FeO and Fe_2O_3 (respectively). Contrary to the observation made for aluminosilicates, association with tetrahedral Fe^{3+} does not imply significant changes to the coordination of Na^+. In all samples, however, an original feature is the unusually strong excess deviations from Debye law observed below 20 K. Owing to these very low temperatures, these anomalies do not have any thermochemical consequences, but their origin remains to be determined.

From literature data, Stebbins et al. (1984) calculated partial molar heat capacities of 79 ± 6 and 229 ± 18 J/mol K for FeO and Fe_2O_3, respectively. The results derived by Richet and Bottinga (1985) obtained in a similar way were 79 and 200 J/mol K for FeO and Fe_2O_3. They compare with the values of 86 J/mol K for both MgO and CaO, and with an average value of 187 J/mol K at 1700 K for the partial molar C_p of Al_2O_3, which is actually temperature and composition dependent. On a g atom basis, the values for FeO and Fe_2O_3 are thus the same. Richet and Bottinga (1985) suggested configurational heat capacities that are similar for both oxides and higher than for Al_2O_3.

The earliest heat capacity measurements specifically devoted to Fe_2O_3-bearing melts were made between 1000°C and 1400°C in air on a series of molten lavas and Na and Ca ferrisilicates (Lange and Navrotsky, 1992). With a constant value of 241 ± 8 J/mol K, no composition dependence was found for the partial molar heat capacity of Fe_2O_3. For sodium ferrisilicates, other measurements have been made by differential scanning calorimetry just above the glass transition (Tangeman and Lange, 1998), with a decrease of C_p with increasing temperature similar to that observed for titanosilicates (Section 12.4.2). Agreement with the high-temperature data of Lange and Navrotsky (1992) was generally poor, however, with the result that the influence of Fe^{3+} on heat capacity remains to be determined as a function of temperature and composition.

A comparison of heat capacity in alumino- and ferrisilicate melt systems was reported by Falenty and Webb (2010). Whether for Al^{3+} or Fe^{3+}, the heat capacity decreases from peralkaline and peraluminous compositions toward minimum values at or near the meta-alumino and meta-ferrisilicate joins (Fig. 10.31). The configurational heat capacity of ferrisilicate melts is not, however, sensitive to temperature.

10.6 OTHER PHYSICAL PROPERTIES

As for thermal properties, measurements of other physical properties of iron-bearing melts are made difficult by the intrinsic variations of the redox ratio with temperature, pressure,

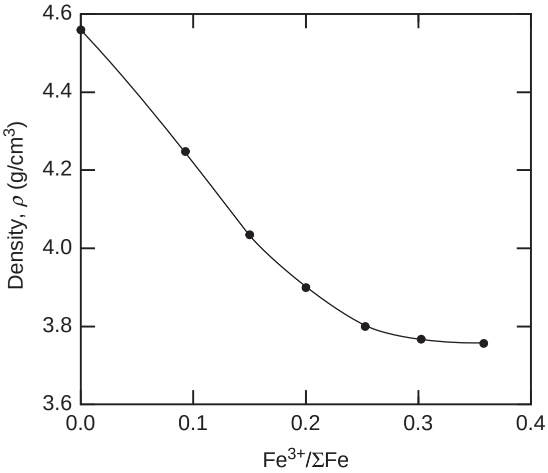

FIG. 10.31 Density of "FeO" at 1500°C against the atomic redox ratio of the melt in experiments made under varying CO-CO_2 atmospheres. The data shown for pure FeO are for a nearly stoichiometric FeO melt contained at 1410°C in iron crucibles, with argon as a bubbling gas. *Redrawn from Mori and Susuki (1968).*

and bulk chemical composition. Attainment of redox equilibrium must not only be checked, but the sample often has to be quenched for analysis because it is usually not possible to determine simultaneously its redox state and the property of interest while the melt is at high temperature. In data analysis, proper allowance must then be made for the variations of the redox ratio with temperature. This represents a serious hindrance, as inferences about the composition dependence of properties cannot be made from direct representations of the experimental data along simple joins. They have to be drawn instead from multivariate analyses of the data, which often do not yield unequivocal solutions. And although metallurgical slags have been investigated extensively (e.g., Mills, 2018), use of these measurements can be made difficult by the need to disentangle the specific influence of FeO and Fe_2O_3 from that of SiO_2-poor contents and resulting melt depolymerization.

10.6.1 Density

Volume properties exemplify the difficulties raised by measurements on iron-bearing melts. Although density can be measured regardless of the actual redox state, determination of molar volume and subsequent analysis in terms of partial molar volumes cannot. For molten "FeO," the large range of redox ratio induced by changes in oxygen fugacity yields a density decrease from 4.6 to 3.8 g/cm^3 under increasingly oxidizing conditions (Fig. 10.32). Under the most reducing conditions, the density of 4.57 g/cm^3 measured by Gaskell and Ward (1967) gives a molar volume of 15.8 cm^3/mol for pure "FeO."

For the pseudobinary "FeO"-SiO_2 system, measurements have been made by various methods (see Henderson, 1964; Shiraishi et al., 1978). Under reducing conditions, the molar volume is a linear function of SiO_2 content (Fig. 10.33). A partial molar volume of 23.6 cm^3/mol is obtained for SiO_2, which is lower than the 26.8 cm^3/mol derived in Section 6.4.1 from measurements on binary alkali and alkaline earth systems. These two volumes are not directly comparable, however, because they refer to markedly different ranges

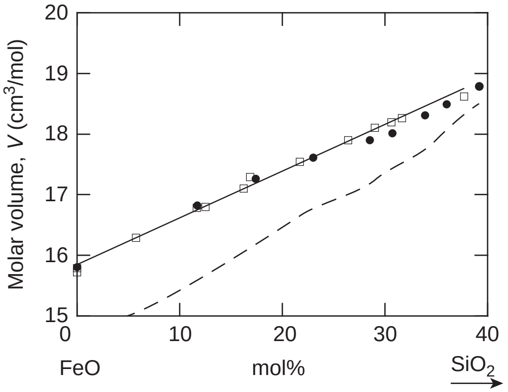

FIG. 10.32 Molar volume of "FeO"-SiO_2 melts at 1410° C (*solid squares*: Gaskell and Ward, 1967) or 1400°C (*open circles*: Shiraishi et al., 1978). The *dashed wavy curve* represents the volumes calculated from the ternary compositions reported by Shiraishi et al. (1978) with the partial molar volumes of Bottinga and Weill (1970).

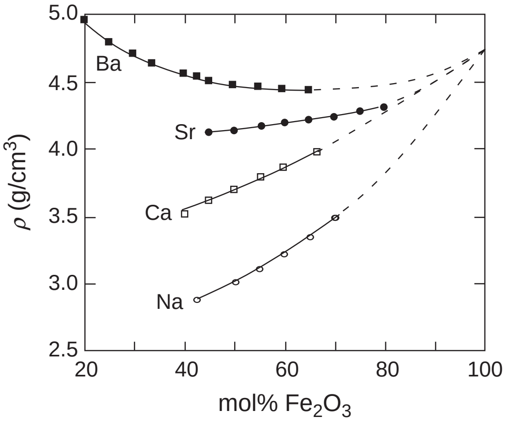

FIG. 10.33 Molar volume of molten ferrites against Fe_2O_3 content. Redrawn from Sumita et al. (1983) at 1400°C for $Na_2O{\cdot}Fe_2O_3$, and at 1500°C for the alkaline earth systems.

of SiO_2 contents. In accordance with the positive difference between the volumes of bridging and nonbridging oxygens noted in Section 6.2.1, the lower partial molar volume found for the SiO_2-poor melts of Fig. 10.33 could simply reflect a lower volume for SiO_2 in Q^0- than in Q^n-species with a smaller number of nonbridging oxygens.

The partial molar volume of FeO also depends on composition. The linear relationship of Fig. 10.33 yields a value of 15.8 cm^3/mol, which is higher than the volumes ranging from 12.8 to 13.8 cm^3/mol derived at 1400°C from measurements made on iron-bearing SiO_2-rich melts (Bottinga and Weill, 1970; Mo et al., 1982; Bottinga et al., 1983; Dingwell et al., 1988; Lange and Carmichael, 1989). That these models do not apply to slags and other Fe-rich melts is illustrated in Fig. 10.33 by the differences between their predictions and the experimental data for the "FeO"-SiO_2 system, even when actual Fe_2O_3 contents are accounted for. Likewise, the agreement is not good between such model values and the volumes measured for ternary CaO-FeO-SiO_2 melts by Henderson (1964) and Lee and Gaskell (1974).

In their study of SiO_2-poor calcium ferrosilicate melts in equilibrium with iron, Lee and Gaskell (1974) reported that the partial molar volume of both FeO and CaO depends on composition. They assigned these variations to preferred association of Ca^{2+} with the silicate anionic framework, and of Fe^{2+} with "free" oxygen ions. At higher silica contents, however, the partial molar volumes of these oxides are not a strong function of composition. Hence, possible changes in the structural state of Fe^{2+} seem to affect the density only at low SiO_2 contents. In contrast, the 12.8–13.8 cm^3/mol partial molar volume of FeO quoted previously in silica-rich melts is closer to that of MgO (11.6 cm^3/mol) than to that of CaO (16.5 cm^3/mol), and is similar to the molar volume of wüstite (12.8 cm^3 at 1400°C). These figures indicate essentially octahedral coordination for ferrous iron. They are, in addition, consistent with the greater similarity of Fe^{2+} with Mg^{2+} than with Ca^{2+} noted in previous sections.

The variations of the partial molar volume of Fe_2O_3 with composition could be more problematic. For pure Fe_2O_3, the density measured for molten ferrites (Fig. 10.34) converges at 1400–1500°C to a value of 4.7 g/cm^3, which is similar to the density of FeO melt (Fig. 10.32). The resulting molar volume of 34.0 cm^3 is marginally higher than that of hematite (32.8 cm^3) at the same temperature, which suggests that Fe^{3+} would be primarily in octahedral coordination in pure metastable Fe_2O_3 melt. On the other hand, the presence of ferric iron lowers markedly the density of molten "FeO" (Fig. 10.32). That this effect could be due to tetrahedral coordination is indicated by the high partial molar volume of about 41 cm^3/mol consistently determined for Fe_2O_3 in silicate melts (see the following). Hence, the question arises as to how the partial molar volume of Fe_2O_3 varies between such low and high values when other oxides are introduced.

In simple systems, two cases must be distinguished, depending on the strength of the association between tetrahedral Fe^{3+} and its charge-compensating cation. For sodium ferrisilicates, the existence of slight excess volumes asserted by Dingwell et al. (1988) has been questioned by Lange and Carmichael (1989) on the basis of their alleged systematic bias affecting redox analyses by Mössbauer spectroscopy (see Section 10.2.3). This disagreement is minor, however, compared to the main conclusion reached in both studies that Na^+ clearly stabilizes Fe^{3+} in tetrahedral coordination in the investigated peralkaline compositions. At

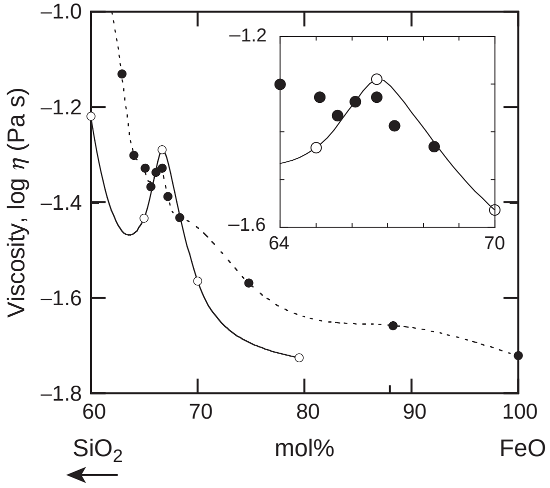

FIG. 10.34 Viscosity of FeO-SiO_2 melts at 1400°C in equilibrium with iron. *Solid circles*: Shiraishi et al. (1978); *open circles*: Urbain et al. (1982). In the experiments of Shiraishi et al. (1978), the Fe_2O_3 content decreased from 12 to 0.7 wt% from 100 to 61 wt% "FeO."

1400°C, for instance, the partial molar volume of Fe_2O_3 is 40.7 and 41.8 cm^3/mol according to Dingwell et al. (1988) and Lange and Carmichael (1989), respectively. For calcium ferrisilicates, composition-independent partial molar volumes were found inadequate by Dingwell and Brearley (1988). These authors dealt with excess volumes primarily in terms of a large positive interaction between Ca^{2+} and Fe^{3+} in tetrahedral coordination. The nonlinear variations of molar volume were then assigned to the coexistence of octahedral and tetrahedral Fe^{3+} whose proportions would vary with temperature and melt composition. Finally, Dingwell and Brearley (1988) suggested that the partial molar volume of FeO might also depend on composition in calcium systems.

10.6.2 Transport Properties

Transport properties of mixed-valence iron silicate melts are particularly interesting because of the different structural roles of Fe^{3+} and Fe^{2+}. In addition, as transport properties are sensitive to melt structure, these likely also are sensitive to the redox ratio of iron (Dingwell and Virgo, 1988; Harizanova et al., 2008; Falenty and Webb, 2010; Kim and Kwon, 2010; Osugi et al., 2013).

10.6.2.1 Viscosity

For obvious metallurgical reasons, the viscosity of SiO_2-poor ferrosilicate melts has long been investigated (see Bottinga and Weill, 1972). As for the density, assessment of the specific effects of FeO are made difficult by the lower ranges of SiO_2 content investigated compared with those reviewed in previous chapters for other metal oxides. In addition, viscosity data generally are lacking near the glass transition because of the difficulties of quenching iron-rich glasses in simple systems. Hence, viscosity-temperature relationships are generally known over only restricted intervals, and the connections made in other chapters between rheological and thermodynamic properties remain to be established for Fe-bearing melts.

Under reducing conditions, it appears that iron, in the form of FeO, does not induce any peculiar anomaly. Analogies between the effects of FeO, MgO, and BaO on viscosity were, for instance, noted by Bills (1963). Accordingly, Bottinga and Weill (1972) assumed in their empirical model of prediction of high-temperature viscosities that, like those of other metal oxides, the effects of FeO are a monotonous function of concentration. Good agreement with experimental data on FeO-rich melts has been achieved in this way (e.g., Cukierman et al., 1972; Cukierman and Uhlmann, 1974). Even though Fe^{2+} may also be in tetrahedral coordination (see Section 11.3.1), data are lacking to document the influence that this coordination state might have on viscosity. In this section, this is why attention will be paid instead to changes in iron redox ratio and to the coordination state of Fe^{3+}, whose effects have been more extensively investigated.

In the binary "FeO"-SiO_2 system, the only anomalous feature is the intriguing viscosity maximum that has been repeatedly observed near the fayalite composition (Fig. 10.35). Although its magnitude differs from one study to another, this maximum has been interpreted as indicating some kind of clustering at the orthosilicate composition (see Shiraishi et al., 1978). Unfortunately, it is not known whether an analogous maximum would also be found for other binary metal oxide-silica melts.

FIG. 10.35 Viscosity of "FeO"-SiO_2 melts against oxygen fugacity. Redrawn from Toguri et al. (1976) for three series whose Fe/Si atomic ratios is indicated. For each series (same *symbols*), the lower data refer to 1250°C and the upper data to 1350°C. The steeper slope of the results for Fe/Si = 1.95 at low f_{O_2} signals the Fe_2SiO_4 anomaly. The iron redox ratios were not determined.

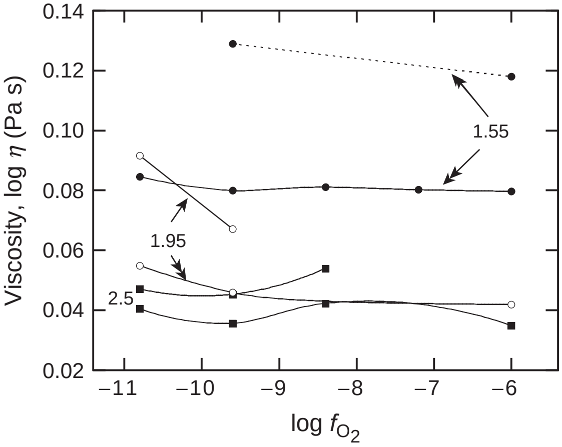

Of interest is also the slight influence of the iron redox state on the viscosity of "FeO"-SiO_2 melts (Fig. 10.36). At these high temperatures and low SiO_2 contents, Fe_2O_3 causes the viscosity to decrease. This influence is much lower than that of decreasing silica concentration, however, as also indicated by the measurements of Fig. 10.36 where the Fe_2O_3 content becomes significant near pure "FeO."

Without any complication from Si^{4+}, molten ferrites represent a natural starting point to investigate the effects of changing Fe^{3+} coordination on viscosity. In all systems of Fig. 10.37, the viscosity increases with increasing metal oxide content. A sharp maximum is observed near the equimolar M_xO/Fe_2O_3 ratio for Na^+, and at a slightly higher value for Ba^{2+}, whereas the increase is continuous for both Ca^{2+} and Sr^{2+}. These variations clearly

FIG. 10.36 Viscosity of molten binary ferrites against Fe_2O_3 content. Data at 1400°C for sodium and 1500°C for alkaline earth ferrites. *Redrawn from Sumita et al. (1983).*

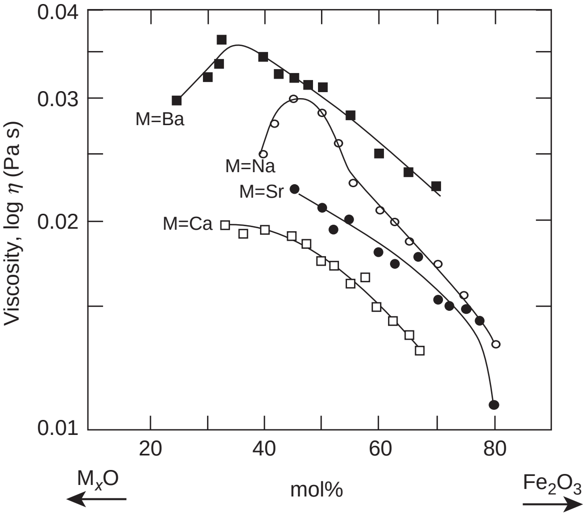

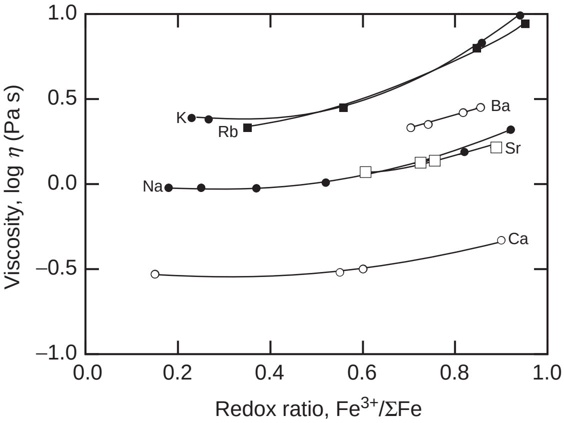

FIG. 10.37 Iron redox state and viscosity of melts with the stoichiometry $M_{x/2}FeSi_2O_6$ (nominal). Results from Dingwell and Virgo (1987) for Na and Na_2, another Na melt with a high Fe_2O_3 content of 34 wt% (1430°C); Dingwell and Virgo (1988) for Ca (1400°C, two data points for reduced compositions discarded), and Dingwell (1991) for K (1380°C), Rb (1470°C), Ba (1345°C), and Sr (1350°C).

correlate with the specific affinity of Fe^{3+} with the various charge-compensating cations. Most Na^+ and a high fraction of Ba^{2+} probably associate with Fe^{3+}, but only part of Ca^{2+} and Sr^{2+}. It follows that the proportion of tetrahedral Fe^{3+} seems to pass through a clear maximum for Na^+ and Ba^{2+}, but to increase almost continuously for Ca^{2+} and Sr^{2+}. Compared to those described in Chapter 8 for Al^{3+}, these viscosity increases due to coordination changes of Fe^{3+} are extremely small. In particular, they are not much greater for Na^+ than for alkaline earth cations.

Such extensive viscosity data cannot be gathered for Fe-bearing silicates. For these melts, the investigated changes in Fe^{3+} coordination have resulted from variations of the iron redox ratio. This restriction notwithstanding, the measurements available for a variety of systems indicate that viscosity consistently increases upon iron oxidation (Fig. 10.38). The variations are larger with increasing iron content (Dingwell and Virgo, 1987). Consistent with the relative strength of association with Fe^{3+}, they are greater in alkali than in alkaline earth systems (Dingwell, 1991). From primarily Fe^{2+} to essentially pure Fe^{3+}, however, the increase is less than one order of magnitude at high temperature. Likewise, viscosity increases have been observed near the glass transition. They increase with iron content, reaching more than an order of magnitude for about 10 wt% FeO in sodium aluminosilicates (Klein et al., 1983) as well as for a molten basalt (Bouhifd et al., 2004).

At high temperature, the influence of redox ratio on the viscosity of silicate melts is of the same magnitude as the intrinsic effects of iron, whether ferrous or ferric. For Ca ferrisilicates, Mysen et al. (1985b) showed that substitution of Fe^{3+} for Si^{4+} lowers the viscosity by less than one order of magnitude. For Na systems, interesting comparisons have been made by Dingwell and Virgo (1988) with aluminosilicates of the same stoichiometry (Fig. 10.39). In agreement with all the information reviewed in preceding sections, the bonding contrast between Fe^{3+} and Al^{3+} manifests itself in the systematically lower viscosities of ferrisilicates compared to aluminosilicates. As pointed out by Dingwell and Virgo (1988), the viscosity of ferrisilicates is, in fact, similar to those of borosilicates. The depressing effect of iron should be much greater near the glass transition but, as already noted, data are unfortunately lacking.

A final comparison with aluminosilicates can be made through the systematic measurements made by Dingwell (1989) for alkali and alkaline earth melts along the silicate-ferrite

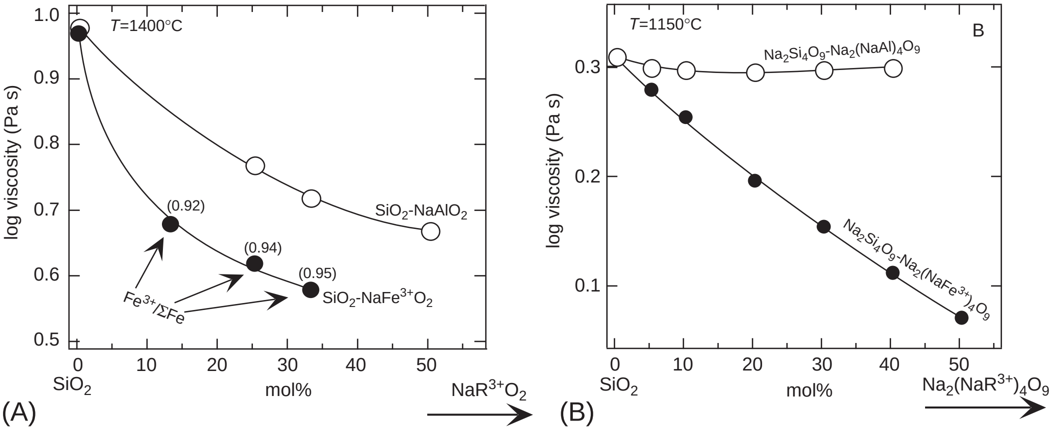

FIG. 10.38 Comparison between the viscosity of sodium alumino- and ferri silicates. (A) Along the meta-aluminous and meta-ferric joins SiO_2-$NaRO_2$ (R=Al, Fe) at 1400°C, the numbers near the data points indicating the redox ratios of the samples. (B) Along the joins $Na_2Si_4O_9$-$Na_2(NaR)_4O_9$ at 1150°C. Data from Dingwell and Virgo (1988).

FIG. 10.39 Viscosity of ferrisilicates with 67 mol% SiO_2 along the meta-ferric join against reciprocal temperature. Data from Dingwell and Virgo (1988) for Na and from Dingwell (1989) for the other systems. Similar trends are observed for melts with 50 and 75 mol% SiO_2.

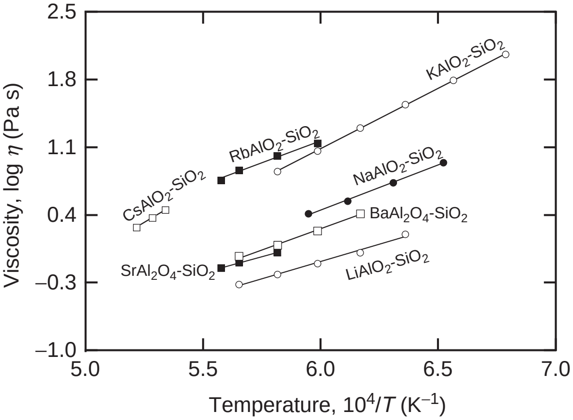

join SiO_2-$M_{2/x}FeO_4$ (M=alkali or alkaline earth). The trends determined for 50, 67, and 75 mol% SiO_2 are similar. At constant SiO_2, the viscosity decreases in the order Cs, Rb, K, Na, Ba, Sr, Ca, Mg, Li. The order is the same as determined for aluminosilicates (see Fig. 8.18). There is some bias because of the systematic variations of the actual redox ratio from one system to another. In view of the rather weak influence of the iron redox state on viscosity, the effect is sufficiently small that it does not affect the reported trend. From Li^+ to Rb^+, the variation is about one order of magnitude, and thus is similar to the effects shown in Fig. 8.18 for the high-temperature viscosity of aluminosilicates.

10.6.2.2 *Diffusion*

Iron and associated oxygen diffusion were discussed in some detail in Section 10.4.6. Here, we will therefore only briefly note that, among experimental studies on iron diffusion, (Rüssel and Wiedenroth, 2004; Magnien et al., 2008; Kim and Kwon, 2010), it is generally found that there is no distinction between Fe^{3+} and Fe^{2+} with activation enthalpies of viscous flow in the 100–200 kJ/mol range, depending on melt composition (Rüssel and Wiedenroth, 2004; Magnien et al., 2008). Notably, though, in alkali-alkaline earth aluminosilicate melts, there is a clear correlation between the diffusivity or iron and Na_2O concentration (Rüssel and Wiedenroth, 2004) and a much less pronounced correlation with MgO content. This difference likely reflects the much weaker bonding between Fe^{3+} and Mg^{2+} than between Fe^{3+} and Na^+, perhaps in a manner resembling analogous associations in aluminosilicate melts (Sections 8.4.1 and 9.5.2).

We also note that the relationship between melt viscosity and iron self diffusion is distinctly nonlinear and deviates therefore from Eyring's Law (Kim and Kwon, 2010). In other words, iron diffusion is not linked directly to network motion, defined by diffusion of network oxygen (see also previous discussion on oxygen diffusion in Section 10.4.6).

References

Agee, C., 1992. Isothermal compression of molten Fe_2SiO_4. Geophys. Res. Lett. 19, 1169–1172.

Alberto, H.V., Pinto da Cunha, J.L., Mysen, B.O., Gil, J.M., de Campos, N.A., 1996. Analysis of Mossbauer spectra of silicate glasses using a two-dimensional Gaussian distribution of hyperfine parameters. J. Non-Cryst. Solids 194, 48–57.

Ariskin, A.A., Borisov, A.A., Barmina, G.S., 1992. Simulating iron-melt equilibrium for silicate systems.Proc. Lunar Planet. Sci., XXII, pp. 35–36.

Baak, T., Hornyak, E.R., 1961. The iron-oxygen equilibrium in glass: effect of platinum on Fe^{2+}/Fe^{3+} equilibrium. J. Am. Ceram. Soc. 44, 541–544.

Baker, L.L., Rutherford, M.J., 1996. The effect of dissolved water on the oxidation state of silicic melts. Geochim. Cosmochim. Acta 60, 2179–2187.

Bancroft, G.M., 1973. Mössbauer Spectroscopy: An Introduction for Inorganic Chemists and Geochemists. McGraw-Hill, New York.

Barton, J.L., Caurant, D., 1993. The oxidation of ferrous iron in glass at high temperatures. Riv. Staz. Sperim. Vetro 23, 193–198.

Barton, J.L., Banner, D., Caurant, D., Pincemin, F., 1992. The oxidation of ferrous iron in glass at high temperature. Bull. Soc. Esp. Ceram. Vid. 31C-6, 215–220.

Beall, G.H., Rittler, H.L., 1976. Basalt glass ceramics. Ceram. Bull. 55, 579–582.

Berry, A.J., Shelley, J.M.G., Foran, G.J., O'Neill, H.S.C., Scott, D.R., 2003. A furnace design for XANES spectroscopy of silicate melts under controlled oxygen fugacities and temperatures to 1773 K. J. Synchrotron Radiat. 10, 332–336.

Bills, P., 1963. Viscosities in silicate slags systems. J. Iron Steel Inst. 201, 133–140.

Bingham, P.A., Parker, J.M., Searle, T., Williams, J.M., Fykes, K., 1999. Redox and clusterig of iron in silicate glasses. J. Non-Cryst. Solids 253, 203–209.

Borisov, A., McCammon, C., 2010. The effect of silica on ferric/ferrous ratio in silicate melts: an experimental study using Mössbauer spectroscopy. Am. Mineral. 95, 545–555.

Borisov, A.A., Shapkin, A.I., 1989. A new empirical equation relating Fe^{3+}/Fe^{2+} in magmas to their composition, oxygen fugacity, and temperature. Geochem. Int. 27, 111–116.

Borisov, A., Behrens, H., Holtz, F., 2013. The effect of titanium and phosphorus on ferric/ferrous ratio in silicate melts: an experimental study. Contrib. Mineral. Petrol. 166, 1577–1591.

Borisov, A., Behrens, H., Holtz, F., 2015. Effects of melt composition on Fe^{2+}/Fe^{3+} in silicate melts: a step to model ferric/ferrous ratio in multicomponent systems. Contrib. Mineral. Petrol. 169. https://dx.doi.org/10.1007/s00410-015-1119-6.

Botcharnikov, R.E., Koepke, J., Holtz, F., McCammon, C., Wilke, M., 2005. The effect of water activity on the oxidation and structural state of Fe in a ferro-basaltic melt. Geochim. Cosmochim. Acta 69, 5071–5085.

Bottinga, Y., Weill, D.F., 1970. Densities of liquid silicate systems calculated from partial molar volumes of oxide components. Am. J. Sci. 269, 169–182.

Bottinga, Y., Weill, D.F., 1972. The viscosity of magmatic silicate liquids: a model for calculation. Am. J. Sci. 272, 438–475.

Bottinga, Y., Richet, P., Weill, D.F., 1983. Calculation of the density and thermal expansion coefficient of silicate liquids. Bull. Mineral. 106, 129–138.

Bouhifd, M.A., Richet, P., Besson, P., Roskosz, M., Ingrin, J., 2004. Redox state, microstructure and viscosity of partially crystallized basalt. Earth Planet. Sci. Lett. 218, 31–44.

Bouhifd, M.A., Besson, P., Courtial, P., Gérardin, C., Navrotsky, A., Richet, P., 2007. Thermochemistry and melting properties of basalt. Contrib. Mineral. Petrol. 153, 689–698.

Bowen, N.L., 1928. The Evolution of the Igneous Rocks. Princeton University Press, Princeton, NJ.

Bowen, N.L., Schairer, J.F., 1929. The fusion relations of acmite. Am. J. Sci. 18, 365–374.

Bowen, N.L., Schairer, J.F., 1932. The system SiO_2-FeO. Am. J. Sci. 24, 177–213.

Bowen, N.L., Schairer, J.F., Willems, H.W.V., 1930. The ternary system Na_2SiO_3-Fe_2O_3-SiO_2. Am. J. Sci. 20, 405–455.

Brearley, M., 1990. Ferric iron in silicate melts in the system Na_2O-Fe_2O_3-SiO_2 at high pressure. J. Geophys. Res. 95, 15703–15716.

Burkhard, D.J.M., 2000. Iron-bearing silicate glasses at ambient conditions. J. Non-Cryst. Solids 275, 175–188.

Burkhard, D.J.M., 2001. Crystallization and oxidation of Kilauea basalt glass: processes during reheating experiments. J. Petrol. 42, 507–527.

Calas, G., Cormier, L., Galoisy, L., Jollivet, P., 2002. Structure-property relationships in multicomponent oxide glasses. C. R. Chimie 5, 831–843.

Calas, G., Cormier, L., Galoisy, L., 2018. The color of glass. In: Richet, P. (Ed.), Encyclopedia of Glass Science, Technology, History and Culture. J. Wiley & Sons, Hoboken, NJ.

Canil, D., Muelenbachs, K., 1990. Oxygen diffusion in an Fe-rich basalt melt. Geochim. Cosmochim. Acta 54, 2947–2951.

Carter, P.T., Ibrahim, M., 1952. The ternary system Na_2O-FeO-SiO_2. J. Soc. Glas. Technol. 36, 156.

Claussen, O., Gerlach, S., Russel, C., 1999. Self-diffusivity of polyvalent ions in silicate liquids. J. Non-Cryst. Solids 253, 76–83.

Cochain, B., Neuville, D.R., Henderson, G.S., McCammon, C.A., Pinet, O., Richet, P., 2012. Effects of the iron content and redox state on the structure of sodium borosilicate glasses: a Raman, Mössbauer and Boron K-Edge XANES Spectroscopy Study. J. Am. Ceram. Soc. 95, 962–971.

Cochain, B., Pinet, O., Richet, P., 2013a. Diffusion of charge-compensating cations as the rate-limiting step of internal redox reactions. J. Non-Cryst. Solids 365, 23–26.

Cochain, B., Neuville, D.R., de Ligny, D., Malki, M., Testemale, D., Baudelet, F., Pinet, O., Richet, P., 2013b. Dynamics of iron-bearing borosilicate melts: effects of melt structure and composition on viscosity, electrical conductivity and kinetics of redox reactions. J. Non-Cryst. Solids 373–374, 18–27.

Conradt, R., 2018. Fusion of glass. In: Richet, P. (Ed.), Encyclopedia of Glass Science, Technology, History and Culture. Wiley & Sons, Hoboken.

Cook, G.B., Cooper, R.F., 2000. Iron concentration and the physical processes of dynamic oxidation in alkaline earth aluminosilicate glasses. Am. Mineral. 85, 397–406.

Cook, G.B., Cooper, R.F., Wu, T., 1990. Chemical diffusion and crystalline nucleation during oxidation of ferrous iron-bearing magnesium aluminosilicate glass. J. Non-Cryst. Solids 120, 207–222.

Cooper, R.F., 2018. Redox thermodynamics and kinetics in silicate melts and glasses (and related morphology/texture). In: Richet, P. (Ed.), Encyclopedia of Glass Science, Technology, History and Culture. Wiley & Sons, Hoboken.

Cooper, F.R., Fanselow, J.B., Poker, D.B., 1996. The mechanism of oxidation of a basaltic glass: chemical diffusion and network-modifying cations. Geochim. Cosmochim. Acta 60, 3253–3266.

Cooper, R., Everman, R.L.A., Hustoft, J.W., Dan Shin, S.-H., 2010. Mechanisms and kinetics of reduction of a FeO-Fe_2O_3-CaO-MgO aluminosilicate melt in a high-CO activity environment. Am. Mineral. 95, 810–824.

Cottrell, E., Kelley, K.A., Lanzirotti, A., Fischer, R.A., 2009. High-precision determination of iron oxidation state in silicate glasses using XANES. Chem. Geol. 268, 167–179.

Cukierman, M., Uhlmann, D.R., 1974. Effect of iron oxidation state on viscosity, lunar composition 1555. J. Geophys. Res. 79, 1594–1598.

Cukierman, M., Tutts, P.M., Uhlmann, D.R., 1972. Viscous flow behavior of lunar composition 14259 and 14310. Geochim. Cosmochim. Acta Suppl. 3, 2619–2625.

Dalton, J.A., Presnall, D.C., 1997. No liquid immiscibility in the system $MgSiO_3$-SiO_2 at 5.0 GPa. Geochim. Cosmochim. Acta 61, 2367–2373.

Darken, L.S., Gurry, R.W., 1946. The system iron-oxygen. II Equilibrium and thermodynamics of liquid oxide. J. Am. Chem. Soc. 68, 798–816.

Densem, N.E., Turner, W.E.S., 1938. The equilibrium between ferrous and ferric oxides in glasses. J. Soc. Glass Technol. 22, 372–389.

Di Genova, D., Hess, K.-U., Chevrel, M.O., Dingwell, D.B., 2016. Models for the estimation of Fe^{3+}/Fe_{tot} ratio in terrestrial and extraterrestrial alkali- and iron-rich silicate glasses using Raman spectroscopy. Am. Mineral. 101, 943–952.

Dickenson, M.P., Hess, P.C., 1981. Redox equilibria and the structural role of iron in aluminosilicate melts. Contrib. Mineral. Petrol. 78, 352–358.

Dickenson, M.P., Hess, P.C., 1986. The structural role and homogeneous redox equilibria of iron in peraluminous, metaluminous and peralkaline silicate melts. Contrib. Mineral. Petrol. 92, 207–217.

Dingwell, D.B., 1989. Shear viscosities of ferrosilicate liquids. Am. Mineral. 74, 1038–1044.

Dingwell, D.B., 1991. Redox viscometry of some Fe-bearing silicate melts. Am. Mineral. 76, 1560–1562.

Dingwell, D.B., Brearley, M., 1988. Melt densities in the CaO-FeO-Fe_2O_3-SiO_2 system and the compositional dependence of the partial molar volume of ferric iron in silicate melts. Geochim. Cosmochim. Acta 52, 2815–2825.

Dingwell, D.B., Virgo, D., 1987. The effect of oxidation state on the viscosity of melts in the system Na_2O-FeO-Fe_2O_3-SiO_2. Geochim. Cosmochim. Acta 51, 195–205.

Dingwell, D.B., Virgo, D., 1988. Viscosities of melts in the Na_2O-FeO-Fe_2O_3-SiO_2 systems and factors-controlling relative viscosities in fully polymerized melts. Geochim. Cosmochim. Acta 52, 395–404.

Dingwell, D.B., Brearley, M., Dickinson Jr. J.E., 1988. Melt densities in the Na_2O-FeO-Fe_2O_3-SiO_2 system and the partial molar volume of tetrahedrally-coordinated ferric iron in silicate melts. Geochim. Cosmochim. Acta 52, 2467–2475.

Douglas, R.W., Nath, P., Paul, A., 1965. Oxygen ion activity and its influence on the redox equilibrium in glasses. Phys. Chem. Glasses 6, 216–223.

Doyle, C., 1988. Prediction of the activity of FeO in multicomponent magma from known values in [SiO_2-$KAlO_2$-$CaAl_2Si_2O_8$]-FeO liquids. Geochim. Cosmochim. Acta 52, 1827–1834.

Doyle, C., Naldrett, A.J., 1986. Ideal mixing of divalent cations in mafic magma and its effect on the solution of ferrous oxide. Gechim. Cosmochim. Acta 50, 435–443.

Droop, G.T.R., 1987. A general equation for estimating Fe^{3+} concentrations in ferromagnesian silicates and oxides from microprobe analyses, using stoichiometric criteria. Mineral. Mag. 51, 431–435.

Dunn, T., 1982. Oxygen diffusion in three silicate melts along the join diopside-anorthite. Geochim. Cosmochim. Acta 47, 2292–2299.

Dunn, T., 1983. Oxygen chemical diffusion in three basaltic liquids at elevated temperatures and pressures. Geochim. Cosmochim. Acta 47, 1923–1933.

Dunn, T., Ratliffe, W.A., 1990. Chemical diffusion of ferrous iron in a peraluminous sodium aluminosilicate melt: 0.1 MPa to 2.0 GPa. J. Geophys. Res. 95, 15665–15673.

Dunn, T., Scarfe, C.M., 1986. Variation in the chemical diffusivity of oxygen and viscosity of an andesite melt with pressure at constant temperature. Chem. Geol. 54, 203–216.

Dunn, A.G., Beales, K.J., Newns, G.R., Wilson, J.L., 1978. Near infrared optical absorption of iron(II) in some sodium borosilicate glasses. Phys. Chem. Glasses 19, 1–4.

Everman, R.L.A., Cooper, R.F., 2003. Internal reduction of an iron-doped magnesian aluminosilicate melt. J. Am. Ceram. Soc. 86, 487–494.

Falenty, K., Webb, S.L., 2010. Shear modulus, heat capacity, viscosity and structural relaxation time of Na_2O-Al_2O_3-SiO_2 and Na_2O-Fe_2O_3-Al_2O_3-SiO_2 melts. Phys. Chem. Miner. 37, 613–634.

Faust, G.T., 1936. The fusion relations of iron-orthoclase, with a discussion of the evidence of an iron-orthoclase molecule in feldspar. Am. Mineral. 21, 735–763.

Faust, G.T., Peck, A.B., 1938. Refractive indices of some glasses in the ternary system $K_2O\cdot4SiO_2$-Fe_2O_3-SiO_2. J. Am. Ceram. Soc. 21, 320–324.

Fialin, M., Bézos, A., Wagner, C., Magnien, V., Humler, E., 2004. Quantitative electron microprobe analysis of $Fe^{3+}/\Sigma Fe$: Basic concepts and experimental protocol for glasses. Am. Mineral. 89, 654–662.

Frost, D.J., McCammon, C.A., 2008. The redox state of the Earth's mantle. Annu. Rev. Earth Planet. Sci. 36, 389–420.

Fudali, F., 1965. Oxygen fugacity of basaltic and andesitic magmas. Geochim. Cosmochim. Acta 29, 1063–1075.

Gaillard, F., Scaillet, B., Pichavant, M., Beny, J.M., 2001. The effect of water and *f*O2 on the ferric-ferrous ratio of silicic melts. Chem. Geol. 174, 255–273.

Gaillard, F., Scaillet, B., Pichavant, M., 2002. Kinetics of iron oxidation-reduction in hydrous silicic melts. Am. Mineral. 87, 829–837.

Gaillard, F., Pichavant, M., Scaillet, B., 2003. Experimental determination of activities of FeO and Fe_2O_3 components in hydrous silicic melts under oxidizing conditions. Geochim. Cosmochim. Acta 67, 4389–4409.

Garvie, L.A.J., Buseck, P.R., 1994. Ratios of ferrous to ferric iron from nanometre-sized areas in minerals. Nature 396, 667–670.

Gaskell, D.R., Ward, R.G., 1967. Density of iron oxide-silica melts. Trans. Met. Soc. AIME 239, 249–252.

Gerlach, S., Claussen, O., Rüssel, C., 1998. Thermodynamics of iron in alkali-magnesia-silica glasses. J. Non-Cryst. Solids 238, 75–82.

Giuli, G., Alonso-Mori, R., Cicconi, M.R., Paris, E., Glatzel, P., Eeckhout, S.G., Scaillet, B., 2012. Effect of alkalis on the Fe oxidation state and local environment in peralkaline rhyolitic glasses. Am. Mineral. 97, 468–475.

Goldman, D.S., 1983. Oxidation equilibrium of iron in borosilicate glass. J. Am. Ceram. Soc. 66, 205–209.

Goldman, D.S., Gupta, P.K., 1983. Diffusion-controlled redox kinetics in a glass melt. J. Am. Ceram. Soc. 66, 188–190.

Greaves, G.N., 1985. EXAFS and the structure of glass. J. Non-Cryst. Solids 71, 204–217.

Greig, J.W., 1927a. Immiscibility in silicate melts, Part II. Am. J. Sci. 13, 133–154.

Greig, J.W., 1927b. On liquid immiscibility in the system FeO-Fe_2O_3-Al_2O_3-SiO_2. Am. J. Sci. 14, 473–484.

Grove, T.L., 1981. Use of FePt alloys to eliminate the iron loss problem in 1 atmosphere gas mixing experiments: theoretical and practical considerations. Contrib. Mineral. Petrol. 78, 298–304.

Guo, X., Lange, R.A., Ai, Y., 2013. The density and compressibility of CaO-FeO-SiO_2 liquids at one bar: evidence for four-coordinated Fe^{2+} in the $CaFeO_2$ component. Geochim. Cosmochim. Acta 120, 206–219.

Harizanova, R., Keding, R., Ruessel, C., 2008. Electric conductivity of glasses in the system $Na_2O/CaO/SiO_2/Fe_2O_3$. J. Non-Cryst. Solid. 354, 65–71.

Harrison, R.J., Becker, U., 2001. Magnetic ordering in solid solutions. In: Geiger, C.A. (Ed.), Solid Solutions in Silicate and Oxide Systems. Eötvös University Press, Budapest, pp. 349–383.

Hazen, R.M., Jeanloz, R., 1984. Wustite ($Fe_{1-x}O$): a review of its defect structure and physical properties. Rev. Geophys. Space Phys. 22, 37–46.

Henderson, J., 1964. Density of lime-iron oxide-silica melts. Trans. Met. Soc. AIME 230, 501–504.

Hirsch, L.M., Shankland, T.J., Duba, A.G., 1993. Electrical conduction and polaron mobility in Fe-bearing olivine. Geophys. J. Int. 114, 36–44.

Holmquist, S.B., 1966. Ionic formulation of redox equilibria in glass melts. J. Am. Ceram. Soc. 49, 228–229.

Hudon, P., Jung, I.H., Baker, D.R., 2004. Effect of pressure on liquid-liquid miscibility gaps: a case study of the systems CaO-SiO_2, MgO-SiO_2, and $CaMgSi_2O_6$-SiO_2. J. Geophys. Res. Solid Earth, B03207. https://dx.doi.org/10.1029/2003JB002659.

Huebner, J.S., 1971. Buffering techniques for hydrostatic systems at elevated pressures. In: Ulmer, G.C. (Ed.), Research Techniques for High Pressure and High Temperature. Springer Verlag, New York. (chapter 15).

Isaac, E., Tammann, G., 1907. Über die Legierungen des Eisens mit Platin. Z. Anorg. Chem. 55, 63–71.

Jayasuriya, K., O'Neill, H.S.C., Berry, A.J., Campbell, S.J., 2004. A Mossbauer study of the oxidation state of Fe in silicate melts. Am. Mineral. 89, 1597–1609.

Jeddeloh, G., 1984. The redox equilibrium in silicate melts. Phys. Chem. Glasses 25, 163–164.

Johnston, W.D., 1965. Oxidation-reduction equilibria in molten $Na_2O \cdot SiO_2$ glass. J. Am. Ceram. Soc. 48, 184–190.

Jurado-Egea, J.R., Owen, A.E., Bandyopadhyay, A.K., 1987. Electronic conduction in basalt glass and glass-ceramics—correlation with magnetite crystallization. J. Mater. Sci. 22, 3602–3606.

Karamanov, A., Pelino, M., 2001. Crystallization phenomena in iron-rich glasses. J. Non-Cryst. Solids 281, 139–151.

Kasting, J.F., Eggler, D.H., Raeburn, S.P., 1993. Mantle redox evolution and the oxidation state of the Archean atmosphere. J. Geol. 101, 245–257.

Kennedy, G.C., 1948. Equilibrium between volatiles and iron oxides in rocks. Am. J. Sci. 246, 529–549.

Kilinc, A., Carmichael, I.S.E., Rivers, M.L., Sack, R.O., 1983. The ferric-ferrous ratio of natural silicate liquids equilibrated in air. Contrib. Mineral. Petrol. 83, 136–141.

Kim, K.D., Kwon, S.K., 2010. Redox equilibrium of Fe^{3+}/Fe^{2+} and diffusivity of iron in alkali-alkaline earth-silicate glass melts. J. Ceram. Process. Res. 11, 460–464.

Kingery, W.D., Vandiver, P.B., Huang, I.W., Chiang, Y.M., 1983. Liquid-liquid immiscibility and phase separation in the quaternary systems K_2O-Al_2O_3-CaO-SiO_2 and Na_2O-Al_2O_3-CaO-SiO_2. J. Non-Cryst. Solids 54, 163–171.

Klein, L.C., Fasano, B.V., Wu, J.M., 1983. Viscous flow behavior of four iron-containing silicates with alumina: effects of composition and oxidation condition. J. Geophys. Res. 88, A880–A886.

Kress, V.C., Carmichael, I.S.E., 1988. Stoichiometry of the iron oxidation reaction in silicate melts. Am. Mineral. 73, 1267–1274.

Kress, V.C., Carmichael, I.S.E., 1989. The lime-iron-silicate system: redox and volume systematics. Geochim. Cosmochim. Acta 53, 2883–2892.

Kress, V.C., Carmichael, I.S.E., 1991. The compressibility of silicate liquids containing Fe_2O_3 and the effect of composition, temperature, oxygen fugacity and pressure on their redox states. Contrib. Mineral. Petrol. 108, 82–92.

Kurkjian, C.R., 1970. Mössbauer spectroscopy in inorganic glasses. J. Non-Cryst. Solids 3, 1579194.

Lange, R.A., Carmichael, I.S.E., 1987. Densities of Na_2O-K_2O-CaO-MgO-Fe_2O_3-Al_2O_3-TiO_2-SiO_2 liquids: new-measurements and derived partial molar properties. Geochim. Cosmochim. Acta 51, 2931–2946.

Lange, R.A., Carmichael, I.S.E., 1989. Ferric-ferrous equilibria in Na_2O-FeO-Fe_2O_3-SiO_2 melts: effects of analytical techniques on derived partial molar volumes. Geochim. Cosmochim. Acta 53, 2195–2204.

Lange, R.A., Navrotsky, A., 1992. Heat-capacities of Fe_2O_3-bearing silicate liquids. Contrib. Mineral. Petrol. 110, 311–320.

Larson, H., Chipman, J., 1953. Oxygen activity in iron oxide slags. Trans. AIME 196, 1089–1096.

Lauer, H.V., 1977. Effect of glass composition on major element redox equilibria: Fe^{2+}–Fe^{3+}. Phys. Chem. Glasses 18, 49–52.

Lauer, H.V., Morris, R.V., 1977. Redox equilibria of multivalent ions in silicate glasses. J. Am. Ceram. Soc. 60, 443–451.

Lee, Y.E., Gaskell, D.R., 1974. The densities and structures of melts in the system CaO-FeO-SiO_2. Am. Inst. Min. Metall. Pet. Eng. Trans. 5, 853.

Lesher, C.E., Hervig, R.L., Tinker, D., 1996. Self-diffusion of network-formers (silicon and oxygen) in naturally occurring basaltic liquids. Geochim. Cosmochim. Acta 60, 405–413.

Levin, E.M., Robbins, C.R., McMurdie, H.F., 1964. Phase Diagrams for Ceramists, second ed. Amer. Ceram. Soc, Columbus.

Luecke, W., Kohlstedt, D.L., 1988. Kinetics of the internal oxidation of (Mg,Fe)O solid solutions. J. Am. Ceram. Soc. 71, 189–196.

Magaritz, M., Hoffmann, A., 1978. Diffusion of Sr, Ba and Na in obsidian. Geochim. Cosmochim. Acta 42, 595–605.

Magnien, V., Neuville, D.R., Cormier, L., Mysen, B.O., Briois, V., Belin, S., Pinet, O., Richet, P., 2004. Kinetics of iron oxidation in silicate melts: a preliminary XANES study. Chem. Geol. 213, 253–263.

Magnien, V., Neuville, D.R., Cormier, L., Roux, J., Hazemann, J.-L., Pinet, O., Richet, P., 2006. Kinetics of iron redox reactions: a high-temperature XANES and Raman spectroscopy study. J. Nucl. Mater. 352, 190–195.

Magnien, V., Neuville, D.R., Cormier, L., Roux, J., Hazemann, J.-I., de Ligny, D., Pascarelli, S., Vickridge, I., Pinet, O., Richet, P., 2008. Kinetics and mechanisms of iron redox reactions in silicate melts: the effects of temperature and alkali cations. Geochim. Cosmochim. Acta 72, 2157–2168.

Maia, L., Russel, C., 2006. The effect of fluoride on the Fe^{2+}/Fe^{3+}-redox equilibrium in glass melts in the system Na_2O/NaF/CaO/Al_2O_3/SiO_2. J. Non-Cryst. Solids Solids 352, 4082–4087.

Malki, M., Magnien, V., Pinet, O., Richet, P., 2015. Electrical conductivity in iron-bearing silicate glasses and melts. Implications for the mechanisms of iron redox reactions. Geochim. Cosmochim. Acta 165, 137–147.

McCammon, C.A., 1994. A Mössbauer microprobe: practical considerations. Hyperfine Interact. 92, 1235–1239.

Meadowcroft, T.R., Ionescu, D., Barr, P.V., Murphy, J.N., 1996. Physical chemistry of some slag and glass systems useful in recycling. Mater. Trans. Jpn. Inst. Metal. 37, 532–539.

Medlin, M.W., Sienerth, K.D., Schreiber, H.D., 1998. Electrochemical determination of reduction potentials in glass-forming liquids. J. Non-Cryst. Solids 240, 193–201.

Mills, K.C., 2018. Metallurgical slags. In: Richet, P. (Ed.), Encyclopedia of Glass Science, Technology, History and Culture. J. Wiley & Sons, Hoboken, NJ.

Mo, X.X., Carmichael, I.S.E., Rivers, M., Stebbins, J., 1982. The partial molar volume of Fe_2O_3 in multicomponent silicate liquids and the pressure dependence of oxygen fugacity in magmas. Mineral. Mag. 45, 237–245.

Moore, G., Righter, K., Carmichael, I.S.E., 1995. The effect of water on the oxidation state of iron in natural silicate liquids. Contrib. Mineral. Petrol. 120, 170–179.

Mori, K., Susuki, K., 1968. Density of iron oxide melts in equilibrium with CO_2-CO gas mixtures. Tetsu to Hagane 54, 1123–1127.

Muan, A., Osborn, E.F., 1965. Phase Equilibria Among Oxides in Steelmaking. Addison-Wesley, Reading.

Myers, J., Eugster, H.P., 1983. The system Fe-Si-O: oxygen buffer calibrations to 1,500 K. Contrib. Mineral. Petrol. 82, 75–90.

Mysen, B.O., 1987. Magmatic silicate melts: Relations between bulk composition, structure and properties. In: Magmatic Processes: Physiochemical Principles. The Geochemical Society, University Park, pp. 375–399 (special publication).

Mysen, B.O., 1992. Iron and phosphorus in calcium silicate quenched melts. Chem. Geol. 98, 175–202.

Mysen, B.O., 2006. Redox equilibria of iron and silicate melt structure: implications for olivine/melt element partitioning. Geochim. Cosmochim. Acta 70, 3121–3138.

Mysen, B.O., Virgo, D., 1978. Influence of pressure, temperature, and bulk composition on melt structures in the system $NaAlSi_2O_6$ - $NaFe^{3+}Si_2O_6$. Am. J. Sci. 278, 1307–1322.

Mysen, B.O., Virgo, D., 1985. Iron-bearing silicate melts: relations between pressure and redox equilibria. Phys. Chem. Miner. 12, 191–200.

Mysen, B.O., Virgo, D., 1989. Redox equilibria, structure, and properties of Fe-bearing aluminosilicate melts: relationships between temperature, composition, and oxygen fugacity in the system Na_2O-Al_2O_3-SiO_2-Fe-O. Am. Mineral. 74, 58–76.

Mysen, B.O., Virgo, D., Seifert, F.A., 1984. Redox equilibria of iron in alkaline earth silicate melts: relationships between melt structure, oxygen fugacity, temperature and properties of iron-bearing silicate liquids. Am. Mineral. 69, 834–848.

Mysen, B.O., Virgo, D., Neumann, E.R., Seifert, F.A., 1985a. Redox equilibria and the structural states of ferric and ferrous iron in melts in the system CaO-MgO-Al_2O_3-SiO_2: relations between redox equilibria, melt structure and liquidus phase equilibria. Am. Mineral. 70, 317–322.

Mysen, B.O., Virgo, D., Scarfe, C.N., Cronin, D.J., 1985b. Viscosity and structure of iron- and aluminum-bearing silicate melts at 1 atm. Am. Mineral. 70, 487–498.

Mysen, B.O., Carmichael, I.S.E., Virgo, D., 1985c. Comparison of ferric/ferrous obtained by wet chemical and 57Fe Mossbauer spectroscopic methods. Contrib. Mineral. Petrol. 90, 101–106.

Nafziger, R.H., Ulmer, G.C., Woermann, E., 1971. Gaseous buffering for the control of oxygen fugacity at one atmosphere. In: Ulmer, G.C. (Ed.), Research Techniques for High Pressure and High Temperature. Springer, New York.

Nakamura, Y., 1974. The system Fe_2SiO_4-$KAlSi_2O_6$-SiO_2 at 15 kbar. In: Carnegie Instn. Washington Year Book.vol. 73. pp. 352–354.

Naslund, H.R., 1983. The effect of oxygen fugacity on liquid immiscibility in iron-bearing silicate melts. Am. J. Sci. 283, 1034–1059.

Navrotsky, A., Ziegler, D., Oestrike, R., Maniar, P., 1989. Calorimetry of silicate melts at 1773 K: measurement of enthalpies of fusion and of mixing in the systems diopside-anorthite-albite and anorthite-forsterite. Contrib. Mineral. Petrol. 101, 122–130.

Nikolaev, G.S., Borisov, A.A., Ariskin, A.A., 1996. Calculation of the ferric-ferrous ratio in magmatic melts: testing and additional calibration of empirical equations for various magmatic series. Geochem. Int. 34, 641–649.

O'Horo, M.P., Levy, R.A., 1978. Effect of melt atmosphere on the magnetic properties of a $[(SiO_2)_{45}\ (CaO)_{55}]_{65}\ [Fe_2O_3]_{35}$ glass. J. Appl. Phys. 49, 1635–1637.

O'Neill, H.S., Pownceby, M.I., 1993. Thermodynamic data from redox reactions at high temperatures. I. An experimental and theoretical assessment of the electrochemical method using stabilized electrolytes, with revised values for the Fe-"FeO", Co-CoO, Ni-NiO, and Cu-Cu_2O oxygen buffers, and new data for the W-WO2 buffer. Contrib. Mineral. Petrol. 114, 296–314.

O'Neill, H.S.C., Berry, A.J., McCammon, C., Jayasuriya, K.D., Campbell, S.J., Foran, G., 2006. An experimental determination of the effect of pressure on the $Fe^{3+}/\Sigma Fe$ ratio of an anhydrous silicate melt to 3.0 GPa. Am. Mineral. 91, 404–412.

Oishi, R., Terai, R., Ueda, H., 1975. Oxygen diffusion in liquid silicates and relation to their viscosity. In: Cooper, A.R., Heuer, A.R. (Eds.), Mass Transport Phenomena in Ceramics. Plenum Press, New York.

Osborn, E.F., 1959. Role of oxygen pressure in the crystallization and differentiation of basaltic magmas. Am. J. Sci. 257, 609–647.

Osugi, T., Sukenaga, S., Inatomi, Y., Gonda, Y., Saito, N., Nakashima, K., 2013. Effect of oxidation state of iron ions on the viscosity of alkali silicate melts. ISIJ Int. 53, 185–190.

Ottonello, G., Moretti, R., Marini, L., Zuccolini, M.V., 2001. Oxidation state of iron in silicate glasses and melts: a thermochemical model. Chem. Geol. 174, 157–179.

Partzsch, G.M., Lattard, D., McCammon, C., 2004. Mössbauer spectroscopic determination of Fe^{3+}/Fe^{2+} in synthetic basaltic glass: a test of empirical f_{O2} equations under superliquidus and subliquidus conditions. Contrib. Mineral. Petrol. 147, 565–580.

Paul, A., Douglas, R.W., 1965. Ferrous-ferric equilibrium in binary alkali silicate glasses. Phys. Chem. Glasses 6, 207–211.

Philpotts, A.R., Doyle, C.D., 1983. Effect of magma oxidation state on the extent of silicate liquid immiscibility in a tholeiitic basalt. Am. J. Sci. 283, 966–986.

Presnall, D.C., Brenner, N.L., 1974. A method for studying iron silicate liquids under reducing conditions with negligible iron-loss. Geochim. Cosmochim. Acta 38, 1785–1788.

Richardson, F.D., 1956. Activities in ternary silicate melts. Trans. Faraday Soc. 52, 1312–1324.

Richet, P., Bottinga, Y., 1984. Anorthite, andesine, wollastonite, diopside, cordierite and pyrope: thermodynamics of melting, glass transitions, and properties of the amorphous phases. Earth Planet. Sci. Lett. 67, 415–432.

Richet, P., Bottinga, Y., 1985. Heat capacity of aluminum-free liquid silicates. Geochim. Cosmochim. Acta 49, 471–486.

Robie, R.A., Hemingway, B.S., Fisher, J.R., 1979. Thermodynamic properties of minerals and related substances at 298.15 K and 1 bar (105 pascals) pressure and at higher temperatures. U.S. Geol. Surv. Bull. 1452.

Roedder, E., 1951. Low-temperature liquid immiscibility in the system K_2O-FeO-SiO_2. Am. Mineral. 36, 282–286.

Roedder, E., 1952. A reconnaissance study of liquid relations in the system $K_2O{\cdot}SiO_2$-FeO-SiO_2. Am. J. Sci. 250-A, 435–456.

Roedder, E., 1978. Silicate liquid immiscibility in magmas and in the system K_2O-FeO-Al_2O_3-SiO_2: an example of serendipity. Geochim. Cosmochim. Acta 42, 1597–1617.

Rogers, P.S., Williamson, J., 1969. The nucleation of crystalline phases in silicate glasses containing iron oxides. Glass Technol. 10, 128–133.

Rüssel, C., 2018. Electrochemistry of oxide melts. In: Richet, P. (Ed.), Encyclopedia of Glass Science, Technology, History and Culture. J. Wiley & Sons, Hoboken, NJ.

Rüssel, C., Wiedenroth, A., 2004. The effect of glass composition on the thermodynamics of the Fe^{3+}/Fe^{2+} equilibrium and the iron diffusivity in $Na_2O/MgO/CaO/Al_2O_3/SiO_2$ melts. Chem. Geol. 213, 125–135.

Sack, R.O., Carmichael, I.S.E., Rivers, M., Ghiorso, M.S., 1980. Ferric-ferrous equilibria in natural silicate liquids at 1 bar. Contrib. Mineral. Petrol. 75, 369–377.

Sasahira, A., Yokokawa, T., 1985. Fe^{3+}/Fe^{2+} + redox equilibrium in the molten Na_2O-B_2O_3 system by linear sweep voltametry. Electrochim. Acta 30, 441–448.

Schairer, J.F., Yagi, K., 1952. The system FeO-Al_2O_3-SiO_2. Am. J. Sci. 252A, 471–512.

Schairer, J.F., Yoder, H.S., Keene, A.G., 1954. Anhydrous silicate systems. In: Carnegie Instn. Washington Year Book. vol. 53. pp. 123–128.

Schreiber, H.D., Kozak, S.J., Merkel, R.C., Balazs, G.B., Jones, P.W., 1986. Redox equilibria and kinetics of iron in a borosilicate glass-forming melt. J. Non-Cryst. Solids 84, 186–195.

Schuessler, J.A., Botcharnikov, R.E., Behrens, H., Misiti, V., Freda, C., 2008. Oxidation state of iron in hydrous phonotephritic melts. Am. Mineral. 93, 1493–1504.

Shiraishi, Y., Ikeda, K., Tamura, A., Saito, T., 1978. On the viscosity and density of the molten FeO-SiO_2 system. Trans. Jpn. Inst. Metals 19, 264–274.

Sipowska, J.T., Atake, T., Mysen, B.O., Richet, P., 2009. Entropy and structure of oxidized and reduced iron-bearing silicate glasses. Geochim. Cosmochim. Acta 73, 3905–3913.

Smedskjaer, M.M., Solvang, M., Yue, Y., 2010. Crystallisation behaviour and high-temperature stability of stone wool fibres. J. Eur. Ceram. Soc. 30, 1287–1295.

Smith, D.R., Cooper, R.F., 2000. Dynamic oxidation of a Fe^{2+}-bearing calcium-magnesium-aluminosilicate glass: the effect of molecular structure on chemical diffusion and reaction morphology. J. Non-Cryst. Solids 278, 145–163.

Stebbins, J.F., Carmichael, I.S.E., Moret, L.K., 1984. Heat capacities and entropies of silicate liquids and glasses. Contrib. Mineral. Petrol. 86, 131–148.

Sugawara, T., Akaogi, M., 2004. Calorimetry of liquids in the system Na_2O-Fe_2O_3-SiO_2. Am. Mineral. 89, 1586–1596.

Sumita, S., Morinaga, K.J., Yanagase, T., 1983. Physical properties and structure of binary ferrite melts. Trans. Jpn. Inst. Metals 24, 35–41.

Tangeman, J.A., Lange, R.A., 1998. The effect of Al^{3+}, Fe^{3+}, and Ti^{4+} on the configurational heat capacities of sodium silicate liquids. Phys. Chem. Miner. 26, 83–99.

Tangeman, J.A., Lange, R., Forman, L., 2001. Ferric-ferrous equilibria in K_2O-FeO-Fe_2O_3-SiO_2 melts. Geochim. Cosmchim. Acta 65, 1809–1819.

Temkin, M., 1985. Mixtures of fused salts as ionic solutions. Acta Phys. Chim. URSS 20, 411–420.

Thornber, C.R., Huebner, J.S., 1982. Techniques for using iron crucibles in experimental igneous petrology. Am. Mineral. 67, 1144–1154.

Toguri, J.M., Kaiura, G.H., Marchant, G., 1976. The viscosity of the molten FeO-Fe_2O_3-SiO_2 system. In: Extraction of Metallurgy of Copper. Physical Chemistry of Copper Smelting, vol. 1. Metall. Soc. AIME, New York, pp. 259–273.

Toop, D.W., Samis, C.S., 1962. Some new ionic concepts of silicate slags. Can. Metall. Q. 1, 129–152.

Toplis, N.J., Libourel, G., Carroll, M.R., 1994. The role of phosphorus in crystallization processes of basalt: an experimental study. Geochim. Cosmochim. Acta 58, 797–810.

Urbain, G., Bottinga, Y., Richet, P., 1982. Viscosity of liquid silica, silicates and aluminosilicates. Geochim. Cosmochim. Acta 46, 1061–1072.

Villeneuve, N., Neuville, D.R., Boivin, P., Bachèlery, P., Richet, P., 2008. Magma crystallization and viscosity: a study of molten basalts from the Piton de la Fournaise volcano (La Réunion island). Chem. Geol. 256, 242–251.

Virgo, D., Mysen, B.O., 1985. The structural state of iron in oxidized vs. reduced glasses at 1 atm: A ^{57}Fe Mossbauer study. Phys. Chem. Miner. 12, 65–76.

Virgo, D., Mysen, B.O., Seifert, F.A., 1981. Relationship between the oxidation state of iron and structure of silicate melts. In: Carnegie Instn. Washington Year Book.vol. 80. pp. 308–311.

Waychunas, G.A., Apted, M.J., Brown, G.E., 1983. X-ray K-edge absorption spectra of Fe minerals and model compounds: near-edge structure. Phys. Chem. Miner. 10, 1–9.

Wendlandt, R.F., 1991. Oxygen diffusion in basalt and andesite melts: experimental results and discussion of chemical versus tracer diffusion. Contrib. Mineral. Petrol. 108, 463–471.

Whittaker, E.J.W., Muntus, R., 1970. Ionic radii for use in geochemistry. Geochim. Cosmochim. Acta 34, 945–957.

Wiedenroth, A., Rüssel, C., 2003. The effect of mixed alkaline earths on the diffusivity and the incorporation of iron in $5Na_2O$•xMgO•(15-x)CaO•yAl_2O_3• (80-y)SiO_2 melts. J. Non-Cryst. Solids 330, 90–98.

Wilson, A.D., 1960. The micro-determination of ferrous iron in silicate minerals by volumetric and colorimetric method. Analyst 85, 823–827.

Wu, T., Kohlstedt, D.L., 1988. Rutherford backscattering spectroscopy study of the kinetics of oxidation of $(Mg,Fe)_2SiO_4$. J. Am. Ceram. Soc. 71, 540–545.

Yinnon, H., Cooper, A.R., 1980. Oxygen diffusion in multicomponent glass forming silicates. Phys. Chem. Glasses 21, 204–211.

Youngman, R., 2018. Borosilicate glasses. In: Richet, P. (Ed.), Encyclopedia of Glass Science, Technology, History and Culture. J. Wiley & Sons, Hoboken, NJ.

Yue, Y., Solvang, M., 2018. Stone and glass wool. In: Richet, P. (Ed.), Encyclopedia of Glass Science, Technology, History and Culture. J. Wiley & Sons, Hoboken, NJ.

Zhang, H.L., Hirschmann, M.M., Cottrell, E., Withers, A.C., 2017. Effect of pressure on $Fe^{3+}/\Sigma Fe$ ratio in a mafic magma and consequences for magma ocean redox gradients. Geochim. Cosmochim. Acta 204, 83–103.

CHAPTER

11

Structure of Iron Silicate Glasses and Melts

OUTLINE

11.1 INTRODUCTORY COMMENTS

Iron is the only major component of natural and industrial silicate melts and glasses that is present in several oxidation states. Despite the importance and abundance of Fe^{3+} and Fe^{2+}, however, our knowledge of their structural environment is less complete than for other major components as, for example, Al^{3+}. Equilibria between Fe^{3+} and Fe^{2+} require interaction with oxygen, which implies close connections between structure and redox relations that themselves depend on temperature, pressure, and oxygen fugacity. In this chapter, we will thus discuss aspects relevant to the iron-oxygen coordination polyhedra before integrating that information with our understanding of the overall silicate melt structure. These relationships will, in turn, be linked to physical and chemical properties of iron-bearing silicate glasses and melts.

https://doi.org/10.1016/B978-0-444-63708-6.00011-9

11.2 FE^{3+} DISTRIBUTION IN FERRISILICATE SYSTEMS

The ionic radii of Fe^{3+} (0.49 Å) and Al^{3+} (0.39 Å) are not greatly different (Whittaker and Muntus, 1970), which occasionally has led to the use of Fe^{3+} as a proxy for Al^{3+} in silicate melts and glasses (Waff, 1977; Mysen and Virgo, 1978). This analogy is not, however, borne out by the roles of these cations in silicate crystals, where Al^{3+} commonly is in fourfold coordination with oxygen, whereas Fe^{3+} nearly always occurs in sixfold coordination. Tetrahedrally coordinated Fe^{3+} in crystals is rare (Burns, 1994; Burkhard, 2000).

Alumino- and ferrisilicate glasses are not structurally similar either. The X-ray radial distribution functions of analogous glasses such as $NaAlSi_3O_8$ and $NaFeSi_3O_8$ (Henderson et al., 1984) reveal differences in average bond distances and angles (Table 11.1). The T—O bond lengths (T = Al, Si) in aluminosilicate glasses (Taylor and Brown, 1979) are shorter than those ($T = Fe^{3+}$, Si) in ferrisilicate glasses, while the T—T distances and T—O—T angles are larger (Henderson et al., 1984). These differences can be related back to the different ionic radii and Fe^{3+} and Al^{3+} in an oxygen structure environment.

11.2.1 Ferric Iron Bond Length and Oxygen Coordination

The Fe^{3+}—O bond length is a sensitive indicator of the oxygen coordination number, just as seen for Al—O and other metal-oxygen bond lengths (Chapter 9, Section 9.3). The $^{[4]}Fe^{3+}$—O bond length in crystals is ~1.90 Å, whereas the $^{[6]}Fe^{3+}$—O distance varies from near 2.0 Å to as much as 2.1 Å. It must be noted, however, that these bond lengths depend somewhat on the ionization potential of the alkali and alkaline earth cations in the crystalline materials (Menil, 1985; Johnson et al., 1999; Burkhard, 2000).

In iron silicate glasses and melts, the Fe^{3+}—O bond length in addition depends on Si^{4+}—O so that the average (Si,Fe^{3+})—O increases with $Fe^{3+}/(Fe^{3+}+Si)$. This feature can be seen in the data for $NaFeSi_3O_8$ and $KFeSi_3O_8$ glasses where the bond length is 1.7 Å (see also Table 11.1). This value is, nevertheless, consistent with Fe^{3+} in tetrahedral coordination because a 1.60 Å Si—O bond length and a 1.91 Å $^{[4]}Fe^{3+}$—O bond length (Brese and O'Keefe, 1991) yield an average of 1.68 Å for a glass or melt with $Fe^{3+}/(Fe^{3+}+Si) = 0.25$, such as in the feldspar stoichiometry.

Additional information on Si—O and Fe^{3+}—O bond distances in ferrisilicate glasses and melts (Figs. 11.1 and 11.2) has been obtained with more detailed X-ray and neutron diffraction measurements, Mössbauer spectroscopy, electron spin resonance (ESR), and molecular

TABLE 11.1 Characteristics of T^a—O and T—T Bonds Together With T—O—T Angle in Glasses as a Function of the Nature of Tetrahedrally Coordinated Cations (Data From Taylor and Brown, 1979; Henderson et al., 1984)

Composition	T—O Bond Length (Å)	T—T Distance (Å)	T—O—T Angle (Degrees)
SiO_2 glass	1.60	3.10	151
$NaAlSi_3O_8$ glass	1.63	3.12	146
$NaFeSi_3O_8$ glass	1.70	3.20	140

[a] *T-cations are Si^{4+}, Al^{3+}, and Fe^{3+}.*

dynamics simulations (Hannoyer et al., 1992; Hayashi et al., 2000; Farges et al., 2004; Weigel et al., 2008; Giuli et al., 2011, 2012). Along the join $(Na_2O)_{0.3}\cdot(SiO_2)_{0.7}$-$(Na_2O)_{0.3}\cdot(Fe_2O_3)_{0.7}$, the correlation function for a glass with 13 mol% of the $(Na_2O)_{0.3}\cdot(Fe_2O_3)_{0.7}$ component may be compared with a simulated function for a $NaFe^{3+}Si_2O_6$ glass with sixfold coordinated

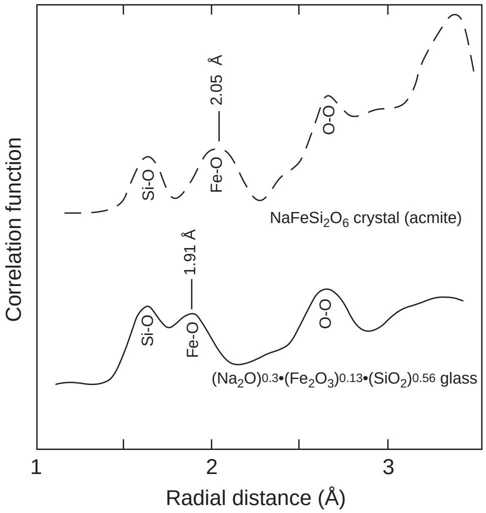

FIG. 11.1 Correlation functions from neutron diffraction spectra of $(Na_2O)_{0.3}\cdot(Fe_2O_3)_{0.13}\cdot(SiO_2)_{0.57}$ glass and from simulated acmite ($NaFeSi_2O_6$) with Fe^{3+} in sixfold coordination with oxygen (Holland et al., 1999; Johnson et al., 1999).

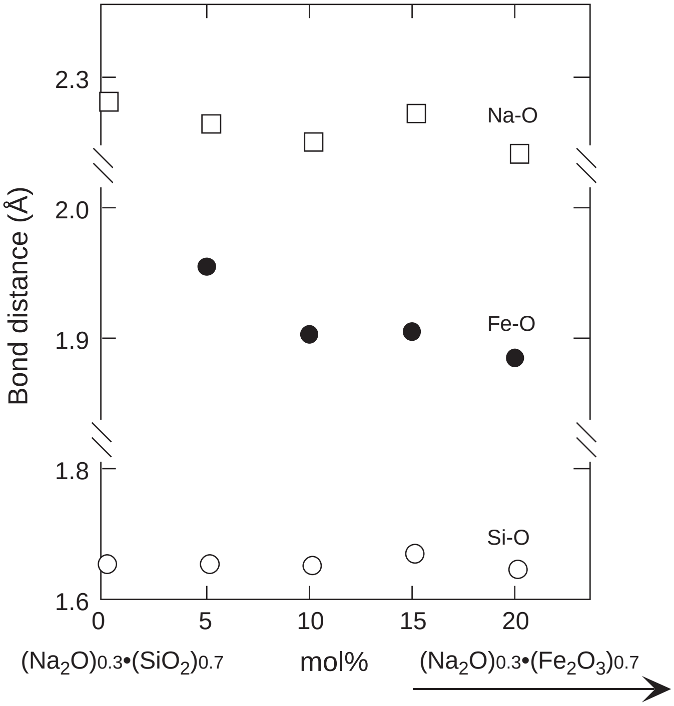

FIG. 11.2 Si—O, Na—O, and Fe—O distances in glasses along the join $(Na_2O)_{0.3}\cdot(SiO_2)_{0.7}$-$(Na_2O)_{0.3}\cdot(Fe_2O_3)_{0.7}$ as a function of $(Na_2O)_{0.3}\cdot(Fe_2O_3)_{0.7}$ content (Holland et al., 1999).

Fe^{3+} (Fig. 11.1). The Fe—O distance in the actual glass is considerably shorter (~1.91 Å) than in the simulated $NaFe^{3+}Si_2O_6$ material (2.05 Å) and is in fact consistent with Fe^{3+} in fourfold coordination (Holland et al., 1999).

The Fe^{3+}—O bond length may vary with total iron content, which, in turn, may be due to variations in Fe^{3+} coordination (Holland et al., 1999; Weigel et al., 2008). For example, this distance in glasses and melts along the $(Na_2O)_{0.3}\cdot(SiO_2)_{0.7}$-$(Na_2O)_{0.3}\cdot(Fe_2O_3)_{0.7}$ join decreases with increasing Fe^{3+} content (Fig. 11.2). Even linear extrapolation of these data to lower Fe^{3+} concentrations suggests distances near or above 2 Å at small iron concentrations (1–2 mol%). Such a decrease may in fact lead to bond distances similar to those of Fe^{3+} coordination polyhedra with more than four oxygens, as reported for $CaO\cdot 2SiO_2$ glasses with total iron oxide concentrations as low as 2.6 mol% (Mysen et al., 1984). Weigel et al. (2008), on the other hand, with the aid of neutron diffraction of $NaFeSi_2O_6$, concluded from the asymmetry of the structure refinements (Fig. 11.3) that the Fe^{3+}—O bond length is best interpreted as mixed four- and fivefold coordination, with about 60% of the former. In this case, the reported distances were 1.87 and 2.0 Å for four- and fivefold coordinated Fe^{3+}, respectively. This difference may well indicate that the coordination polyhedron of Fe^{3+} depends on whether alkalis or alkaline earths are the dominant metal cations. It is notable, however, that from the X-ray absorption K and pre-edge of various $(Na_2O)_{0.3}(Fe_2O_3)_x(SiO_2)_{0.7-x}$ with $x = 0.2$, Faiz et al. (2011) concluded that Fe^{3+} is in sixfold coordination, whereas a dominantly fivefold coordinated Fe^{3+} was deduced by Lukanin et al. (2002) for a basaltic glass quenched from 1350°C at 0.5 GPa. From volume measurements on Fe_2O_3-bearing alkali silicate melts, Liu and Lange (2006) concluded that Fe^{3+} is in fivefold coordination because of differences between the partial molar volume of Fe_2O_3 and those of Fe_2O_3 in four- and sixfold coordination in crystals.

Variable Fe^{3+}—O bond distance can also be inferred from changes in the isomer shift of Fe^{3+} from ^{57}Fe resonant absorption Mössbauer spectroscopy of glasses and melts, $IS_{Fe^{3+}}$ (Menil, 1985; Jackson et al., 1993; Johnson et al., 1999). An approximately linear relationship between bond length, $d_{Fe^{3+}\text{—}O}$, and $IS_{Fe^{3+}}$ has been reported (Johnson et al., 1999):

$$d_{Fe^{3+}-O} = 1.58 + 1.30 IS_{Fe^{3+}}. \tag{11.1}$$

The isomer shifts of Fe^{3+} are negatively correlated with the iron content of highly oxidized glasses (Fig. 11.3) (see also Dingwell and Virgo, 1988). From the expression (11.1), we may infer that a number of compositional variables affect the average Fe^{3+}—O bond length in silicate glasses and melts.

From Eq. (11.1), the isomer shift range in Fig. 11.4 corresponds to $d_{Fe^{3+}\text{—}O}$-values ranging from about 1.99 Å, for the lowest iron oxide content (2.2 mol% as Fe_2O_3) in $Na_2Si_2O_5$ glass, to 1.89 Å for the $Na_2Si_2O_5$ sample with the highest iron oxide content (13.4 mol%). For glasses and melts along the nominal SiO_2-$NaFeO_2$ join, the average bond distance ranges between 1.99 and 1.86 Å. Then increased Fe^{3+}—O distance with decreasing total iron content may imply coordination increases. In this low iron oxide concentration range, Farges et al. (2004), from K-edge XANES spectra, concluded that, regardless of silicate stoichiometry, the average Fe^{3+} coordination number is between 4.5 and 5, which would agree qualitatively with the interpretation of Mössbauer data of low-Fe silicate glasses.

We note that the Fe^{3+}—O bond length is considerably more sensitive to total iron oxide content in the absence of charge-compensating cations for tetrahedral Fe^{3+} than in the

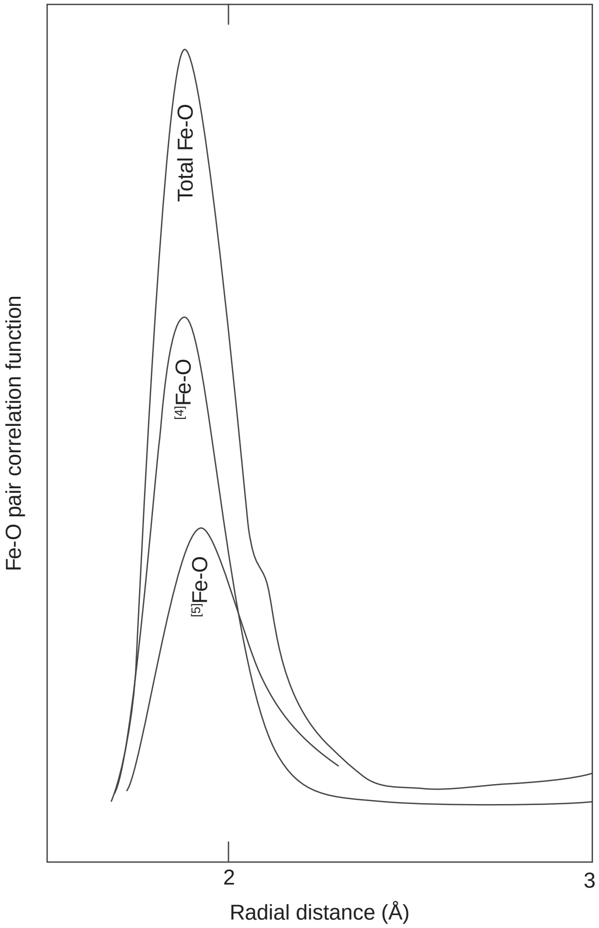

FIG. 11.3 Partial pair distribution function for Fe—O based on EPSR simulations. Four- and fivefold coordinated Fe^{3+} partial functions are identified (Weigel et al., 2008).

presence of an alkali metal such as Na$^+$ (Fig. 11.4). This difference may reflect either variations in average coordination state and/or variations in the distortion of Fe^{3+}—O polyhedra, depending on the presence of absence of charge-compensation. The quadrupole splitting for Fe^{3+} from the Mössbauer spectra of these glasses seems rather insensitive to total iron content (Dingwell and Virgo, 1988), which leads to the suggestion that the Fe^{3+}-oxygen polyhedra are not significantly distorted. One suggests, therefore, that a small fraction of the Fe^{3+} in the glasses, for which data are shown in Fig. 11.4A, may be coordinated with more than four oxygens. A similar conclusion may be drawn for the decrease of the isomer shift of Fe^{3+} with increasing Al/(Al+Si). From Fig. 11.4B and Eq. (11.1), there is not only a decrease of ~5% of the Fe^{3+}—O bond length in the Al/(Al+Si) range between 0 and about 0.4 (Fig. 11.4B), but also the Q^n-speciation in peralkaline aluminosilicate melts may be affected by Al/(Al+Si) (Mysen et al., 2003).

The coordination number of Fe^{3+} in silicate melts and glasses also may vary as a function of the electronic properties of the network-modifying cations (Fox et al., 1982; Mysen et al., 1984,

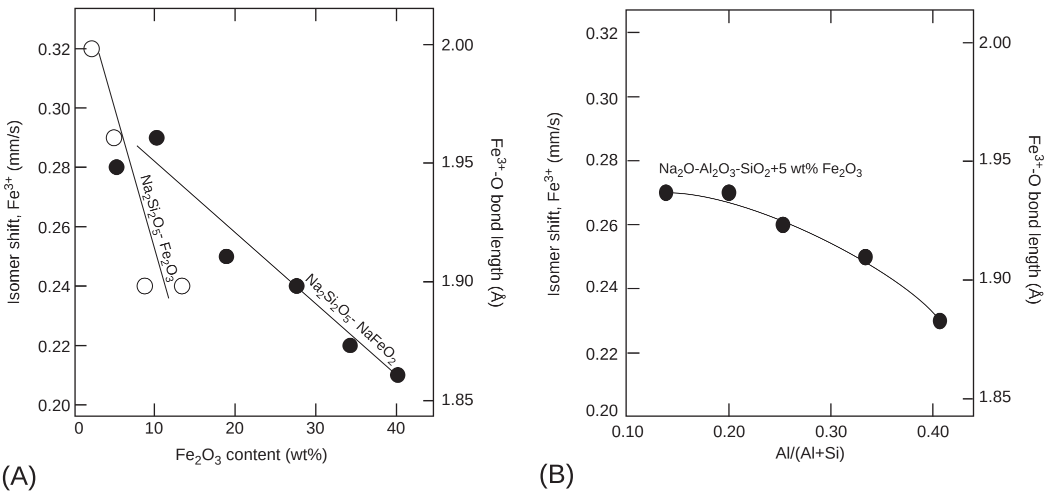

FIG. 11.4 Isomer shift of Fe^{3+}, $IS_{Fe^{3+}}$, relative of Fe metal at 298 K, from Mössbauer spectra of glasses equilibrated with air at 1550°C. (A) Along the nominal joins $Na_2Si_2O_5$-Fe_2O_3 *(open symbols)* and SiO_2-$NaFeO_2$ *(closed symbols)* as a function of iron oxide (Fe_2O_3) added. (B) As a function of Al/(Al+Si) of Na_2O-Al_2O_3-SiO_2 glasses (quenched from 1550°C after equilibration in air) containing 5 wt% iron oxide as Fe_2O_3. The nominal NBO/T of the Fe-free glasses is 0.65 (Virgo et al., 1983; Dingwell and Virgo, 1988; Mysen and Virgo, 1989).

1985; Hayashi et al., 2000; Burkhard, 2000; Bingham et al., 2002, 2007; Giuli et al., 2012). In particular, alkali/alkaline earth abundance ratios as well as Al/(Al+Si) are important variables affecting Fe^{3+}—O bond length and, therefore, the Fe^{3+} coordination state (Fig. 11.5) (see also Mysen et al., 1985; Giuli et al., 2012). Moreover, there is a >15% increase in the isomer shift and >30% increase in quadrupole splitting of Fe^{3+} with alkaline earths changing from Ba^{2+} to Mg^{2+} in the Mössbauer spectra of metasilicate ($MSiO_3$) glasses and melts with divalent network-modifying cations (Fig. 11.5). From Eq. (11.1), the isomer shift increase corresponds to an Fe^{3+}—O bond length change from 1.97 to 2.04 Å. These changes alone would suggest an increase in highly coordinated Fe^{3+} as the alkaline earth becomes more electronegative. The increase of $IS_{Fe^{3+}}$ with the Z/r^2 of the metal cation is well known in crystalline iron silicates (Burns, 1994) and could reflect an increasing fraction of Fe^{3+} in sixfold coordination, a concept consistent with results from other iron-bearing alkaline earth and mixed alkali/alkaline earth silicate melts (Dingwell and Brearley, 1988; Hannoyer et al., 1992; Nagata and Hayashi, 2001; Burkhard, 2000). Furthermore, the $IS_{Fe^{3+}}$ (at 298 K) of Fe-bearing $MgSiO_3$ glass (~0.35 mm/s relative to metallic Fe) is near the lower end of the range observed in minerals with octahedral Fe^{3+} (Burns, 1994). From bond-valence calculations (Brese and O'Keefe, 1991), the value $d_{Fe^{3+}\text{—}O} = 2.03$ Å derived from the spectrum of $MgSiO_3$ glass, would point to Fe^{3+} dominantly in sixfold coordination, whereas the 1.96 Å value recorded for $BaSiO_3$ glass is near or slightly higher than expected for Fe^{3+} in fourfold coordination. A mixture of four- and sixfold coordinated Fe^{3+} might yield average $d_{Fe^{3+}\text{—}O}$-values in between. In analogy with other transition metals (e.g., Calas et al., 2002), one might also surmise that a fivefold coordination exists.

However, the increase in quadrupole splitting with Z/r^2 of the metal cation also could indicate considerable increases in polyhedral distortion, which may imply that structural factors other than simple coordination transformation of Fe^{3+} are involved. Similar conclusions

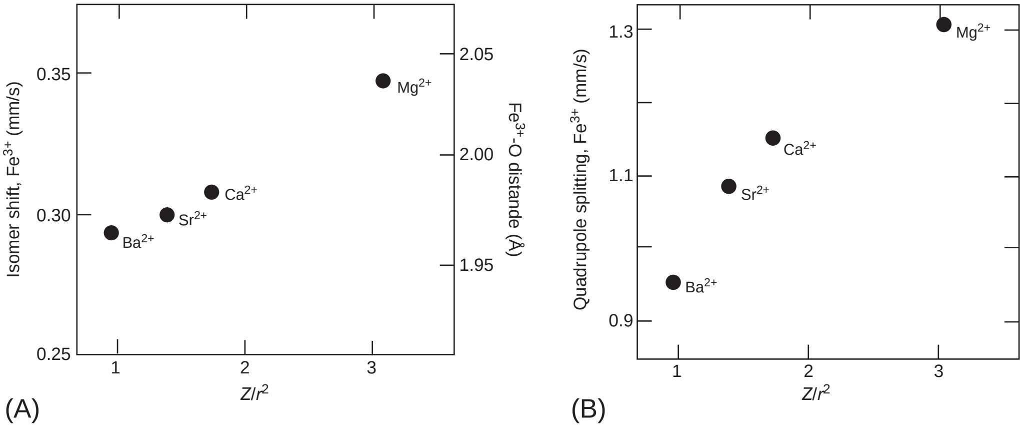

FIG. 11.5 (A) Isomer shift and (B) quadrupole splitting of Fe^{3+} (relative to Fe metal at 298 K) from Mössbauer spectra of metasilicate ($MSiO_3$) glasses with divalent M-cations. Each sample contains 5 wt% iron oxide as Fe_2O_3. Glasses were formed by quenching of melts equilibrated with air at 1550–1625°C (Mysen et al., 1984). The Fe^{3+}—O distance in (A) was calculated from Eq. (11.1) (Johnson et al., 1999).

have been drawn from Mössbauer spectra of other alkali and alkaline earth silicate glasses (Bingham et al., 2002). Furthermore, in mixed alkali-alkaline earth silicate glasses, the relative abundance of tetrahedral Fe^{3+} increases as the alkali/alkaline earth abundance ratio increases (Bingham et al., 2002). That there may be more than one coordination state of Fe^{3+} has also been proposed for mixed alkali/alkaline earth silicate glasses (Levy et al., 1976; Nagata and Hayashi, 2001).

By using Mössbauer spectroscopy to characterize a $(CaO)_{0.4}\cdot(SiO_2)_{0.4}\cdot(Fe_2O_3)_{0.2}$ glass formed from a melt equilibrated with air between 1608 and 1858 K, Nagata and Hayashi (2001) concluded that the $^{[4]}$Fe^{3+}/$^{[6]}$Fe^{3+} ratio is negatively correlated with temperature (Fig. 11.6). The temperature-dependence thus recorded yields an enthalpy of 68 kJ/mol for this coordination change, but it is not clear whether this transformation is actually governed by temperature or distortion of the Fe^{3+}—O_4 tetrahedra.

Variable Fe^{3+}—O bond lengths in FeO_4 tetrahedra may, in fact, result from the existence of more than one type of tetrahedra. Different tetrahedra have been documented in silicate glasses and melts (Fox et al., 1982; Giuli et al., 2012) from changes in Raman and in luminescence spectroscopic data with changes in composition of the silicate glass. The relative abundance of these tetrahedra appears to be a function of the Na/Si-ratio and likely also of the nature of the metal cation(s) (Fox et al., 1982; Bingham et al., 2007). The existence of two different FeO_4 tetrahedra is also consistent with interpretations of the ^{57}Fe Mössbauer spectra of glasses in the same system (Burkhard, 2000). Whether such a structural situation exists in alkaline earth silicate glasses is not known, but it seems a reasonable assumption.

11.2.2 Fe^{3+} Distribution Versus Clustering

Given the large bond length difference between $^{[4]}$Fe^{3+}—O (1.91 Å) and [4]Si—O (1.61 Å) (Brese and O'Keefe, 1991), it is not surprising that there is either clustering of FeO_4 tetrahedra,

FIG. 11.6 Relationship between the proportion of four- and sixfold coordinated Fe^{3+} and the temperature of equilibration for a $(CaO)_{0.4}\cdot(SiO_2)_{0.4}\cdot(Fe_2O_3)_{0.2}$ (nominal) glass after equilibration with air at the temperatures indicated (as proposed by Nagata and Hayashi, 2001).

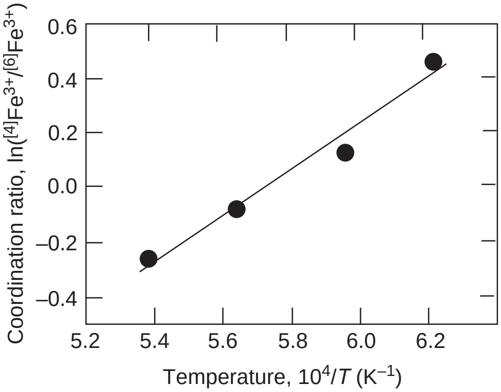

or at the very least very considerable Fe^{3+},Si ordering. From measurements of Mössbauer spectra, magnetic properties, and thermodynamic data, it has been suggested the Fe^{3+} in silicate glasses (and perhaps melts) forms clusters, because the hyperfine parameters seem independent of the type of charge-balancing cation and degree of melt polymerization (Burkhard, 2000). In fact, it has been suggested that such clusters might have a spinel-like stoichiometry (O'Horo and Levy, 1978; Virgo and Mysen, 1985; Hayashi et al., 1999).

The existence of clusters or of isolated FeO_4 tetrahedra has also been inferred from Raman bands assigned to Fe^{3+}—O stretching near 900 and 980 cm^{-1} in Ca- and Na-silicate glasses whose intensities increase with iron content (Alberto et al., 1993; Magnien et al., 2006; Roskosz et al., 2008; Belova et al., 2015). These frequencies are independent of iron content, which means that Fe^{3+} cannot be occupying structural positions where the $Fe^{3+}/(Fe^{3+}+Si)$ changes with total iron content. Such a structural situation would be consistent, however, with Fe^{3+},Si ordering or clustering of Fe^{3+} cations.

The fact that the isomer shift of $^{[4]}Fe^{3+}$ decreases with increasing total iron content (Fig. 11.4) would be better interpreted as resulting from Fe^{3+}—O bond contraction, which would be expected if the degree of Fe^{3+},Si ordering became more pronounced with increasing iron content. Hyperfine splitting from Mössbauer spectra of Na,Ca-silicate glasses with $\leq$2 wt% Fe_2O_3 has been interpreted to reflect isolated Fe^{3+} groups in the structure (Bingham et al., 1999). From optical absorption near 15,000 cm^{-1}, Bingham et al. (1999) proposed that this absorption should be assigned to Fe^{3+}—O—Fe^{3+} and Fe^{2+}—O—Fe^{3} linkages. Bingham et al. (2002), with subsequent concurrence by Dunaeva et al. (2014) and Vercamer et al. (2015), interpreted ESR data similarly. In other words, clustering of Fe^{3+} in silicate glass structure is common. Moreover, from the ESR spectra, Bingham et al. (2002) concluded that clustering becomes more prevalent as the cation or cations serving to charge-balance tetrahedrally coordinated Fe^{3+} become more electropositive. This conclusion is supported by the increased intensity of the $g=2$ resonance (clustered Fe^{3+}) relative to $g=4.3$ (isolated Fe^{3+}) (see also Fig. 11.7). That conclusion differs, however, from that of Vercamer et al. (2015) who, also employing ESR methods, suggested that the $g=2$ resonance becomes more intense as the metal cations become increasingly electronegative (i.e., Mg^{2+} vs Ca^{2+}), which according to Bingham et al. (2002) would suggest a decreasing abundance of Fe^{3+} clusters.

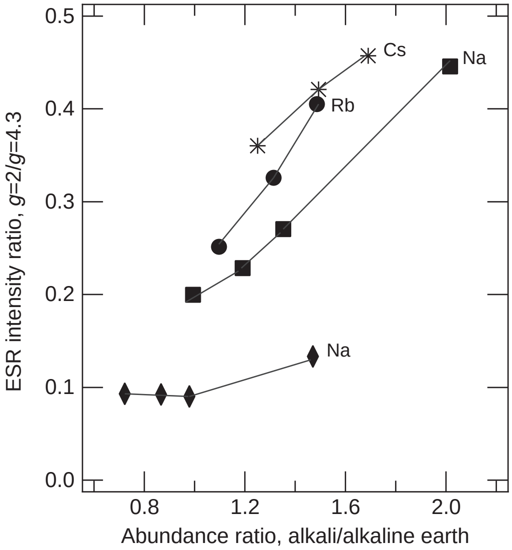

FIG. 11.7 Intensity ratio of resonances $g = 2$ and $g = 4.3$ from electron spin resonance (ESR) measurements as a function of alkali/alkaline earth abundance ratio in the system $(SiO_2)_{0.7}(M_2O)_{0.15}(M'O)_{0.15}$, where M is an alkali metal and M′ is alkaline earth. In this diagram, the alkali is unidentified and the alkaline earth is CaO. The $g = 2$ resonance is assigned to clustered Fe^{3+}, whereas the $g = 4.3$ resonance is assigned to isolated Fe^{3+} ions. *Redrawn from Bingham et al. (2002).*

11.3 FE^{2+} IN SILICATE SYSTEMS

In analogy with the crystal chemistry of crystalline ferromagnesian materials, it has sometimes been assumed that Fe^{2+} occupies structural positions similar to that of Mg^{2+} in silicate melts and glasses. From this reasoning Fe^{2+} is a network-modifying cation perhaps in octahedral coordination with oxygen. Because Mg^{2+} does not always occupy sixfold coordination (see Chapter 7), this analogy then implies that there may also be other coordination states of Fe^{2+}. Structural data that address the coordination of Fe^{2+} are the primary objective of this section (Calas and Petiau, 1983; Bingham et al., 1999, 2002, 2007; Rossano et al., 2000; Lukanin et al., 2002; Farges et al., 2004; Waychunas et al., 1988; Weigel et al., 2008; Giuli et al., 2011, 2012).

11.3.1 Ferrous Iron Bond Length and Oxygen Coordination

The Fe^{2+}—O bond lengths and coordination numbers of ferrous iron in silicate glasses and melts have been the focus of a number of studies conducted with a variety of structural tools. For example, for Fe^{3+}—O, X-ray and neutron-based methods have provided Fe^{2+}—O distances (Waseda and Toguri, 1978; Calas and Petiau, 1983; Waychunas et al., 1988; Holland et al., 1999; Rossano et al., 2000; Farges et al., 2004; Jackson et al., 2005; Weigel et al., 2008; Giuli et al., 2012). In peralkaline, iron-bearing alkali silicate glasses, the Fe—O distance (which combined both Fe^{3+} and Fe^{2+} and the Fe^{2+}/Fe^{3+} ratio varying with total iron content) (see Holland et al., 1999) and Na—O distances decrease slightly with increasing iron oxide content (Holland et al., 1999) (see also Fig. 11.8). The Fe^{2+}—O bond-length decrease was correlated with a decrease of the Fe^{2+} coordination numbers from about 5 to about 4 with increasing iron content. The latter numbers are in close agreement with those reported more recently by Weigel et al.

(2008), also obtained by an analysis of neutron diffraction data. However, from EXAFS and molecular dynamics simulation of iron-rich alkaline earth silicate glass ($CaFeSi_2O_6$), Rossano et al. (2000) reported Fe^{2+}—O distances between 1.99 and 2.00 Å (Fig. 11.9). Such distances would correspond to Fe^{2+} coordination numbers near or slightly below 6 (Brese and O'Keefe, 1991). Rossano et al. (2000) suggested an average coordination number of 4.3 through a combination of 70% $^{[4]}Fe^{2+}$ and 30% $^{[5]}Fe^{2+}$. Interestingly, in a study of peralkaline silicate glasses, Jackson et al. (2005), from EXAFS information, reported Fe^{2+}—O bond lengths between 1.94 and 2.07 Å with a corresponding evolution of Fe^{2+} coordination numbers from 4 to 5.7, these values varying with the type and proportion of alkali and alkaline earths present.

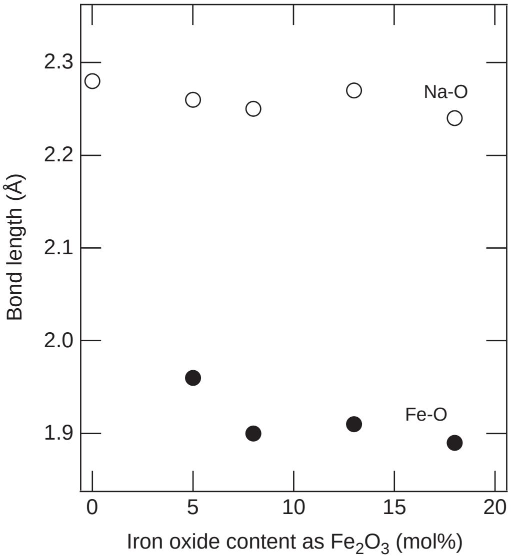

FIG. 11.8 Fe—O and Na—O bond lengths in Fe-bearing alkali silicate glasses as a function of their iron oxide content from neutron diffraction data by Holland et al. (1999).

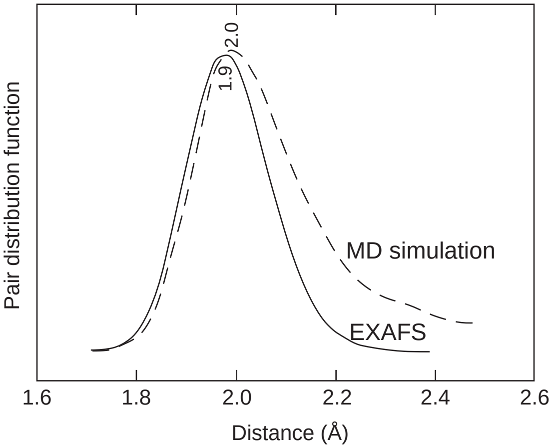

FIG. 11.9 Pair distribution function for FeO in a $CaFeSi_2O_6$ glass, quenched from a melt equilibrated at $f_{O_2} = 10^{-7}$ bar at 1075 K, from molecular dynamics (MD) simulation and EXAFS analysis (Rossano et al., 2000).

Notably, Waseda and coworkers (Waseda and Toguri, 1978; Waseda et al., 1980) in their early in situ, high-temperature X-ray work, interpreted Fe^{2+}—O bond lengths of 2.05–2.10 Å, as indicating fourfold coordination of Fe^{2+}. However, more recent work on the relationship between Fe^{2+}—O bond length and coordination numbers (Brese and O'Keefe, 1991) would rather lead to the conclusion that a 2.05–2.10 Å bond length is consistent with sixfold coordination of Fe^{2+}.

Optical spectroscopy is another method suited for examination of the structural role of transition metals in silicate melts (Wong and Angell, 1976; Fox et al., 1982; Calas and Petiau, 1983; Keppler, 1992; Bingham et al., 2002, 2007). In spectra of Fe^{2+}-bearing glasses of $NaAlSi_3O_8 + 3$ wt% FeO and $(NaAlSi_3O_8)_{0.5}(CaMgSi_2O_6)_{0.5} + 2$ wt% FeO composition (Keppler, 1992), there is a broad peak maximum near 9000 cm^{-1} that was assigned to Fe^{2+} in sixfold coordination, from comparisons with optical absorption spectra of Fe^{2+}-bearing minerals. Similar assignments of Fe^{2+} from optical spectra of other Fe^{2+}-rich glasses have been made by Bell and Mao (1974) and Nolet et al. (1979). More recent studies have led to the conclusion, however, that the frequencies of the bands in these spectra are quite sensitive to the electronic properties of the network-modifying metal cations such as alkalis and alkaline earths (Bingham et al., 2002, 2007). In fact, the luminescence spectra of alkali oxide-CaO-SiO_2 glasses show a systematically increasing wavenumber with increasing alkali/CaO ratio (Fig. 11.10). This increase, which is associated with decreasing wavelength with increasing alkali/CaO ratio, might be interpreted as a reflection of decreasing Fe^{2+} coordination number as the glasses become increasingly alkali-enriched.

The hyperfine parameters (isomer shift and quadrupole splitting) of Fe^{2+} from ^{57}Fe Mössbauer resonant absorption spectroscopy have also been used to distinguish between the possible 4, 5, and 6 oxygen coordination numbers for Fe^{2+}. In crystalline ferromagnesian silicates there is not much overlap of isomer shifts for four- and sixfold coordinated Fe^{2+}, with

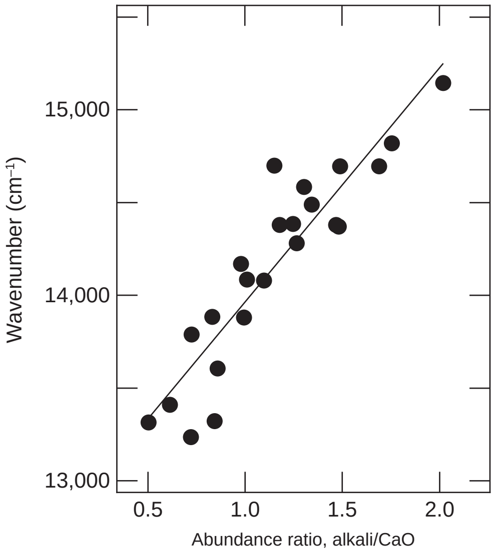

FIG. 11.10 Fe luminescence peak frequency as a function of alkali/CaO abundance ratio. *Redrawn from Bingham et al. (2002).*

values higher and lower than 1 mm/s, respectively, for those two coordination states. It is not difficult, therefore, to distinguish between fourfold and sixfold or higher coordination of Fe^{2+} in silicate glasses. The interpretation of the isomer shift becomes more difficult when the possibility of Fe^{2+} in fivefold coordination is included, because variations in hyperfine parameters for four- and fivefold coordination of Fe^{2+} are not necessarily large (Fig. 11.11). The underlying problem in Mössbauer spectroscopy of glasses is that, rather than modeling the line shape of the absorption envelope (Mysen et al., 1985; Waychunas et al., 1988; Lukanin et al., 2002), we should model the distribution of the hyperfine fields that are in the direct responses of the structure around the Fe nucleus. Such fitting procedures are more appropriate approaches to the deconvolution of the Mössbauer absorption envelope (Alberto et al., 1996; Rossano et al., 1999; Galoisy et al., 2000; Wilke et al., 2002).

In reduced Fe-bearing Ca-silicate glasses, fitting the Fe^{2+} hyperfine parameter distribution (Fig. 11.12) yields maximum $IS_{Fe^{2+}}$ values between 1.1 and 1.2 mm/s (marked "$^{[6]}Fe^{2+}$" in Fig. 11.12), which would be consistent with Fe^{2+} in sixfold coordination. However, the nature of the alkali metals and alkaline earths also affects the hyperfine parameters of Fe^{2+} (Mysen, 2006a,b). In Fig. 11.13 are Mössbauer data for $NaAlSi_2O_6$ and $Mg_{0.5}AlSi_2O_6$ glasses, to which were added $NaFeO_2$ and $MgFe_2O_6$, fitted in the same manner as in Fig. 11.12. An immediately notable feature is that the Fe^{2+} isomer shift in the $NaAlSi_2O_6$ glass is near or below 1.00 mm/s, whereas it is near 1.1 mm/s and above in the $Mg_{0.5}AlSi_2O_6$ glass, regardless of how the iron oxide was added. There is only a small effect of cation type on $IS_{Fe^{2+}}$. These features reflect an

FIG. 11.11 Isomer shift of Fe^{2+} for Fe-bearing silicate crystals with *symbols* use for identification of oxygen coordination numbers (Burns, 1994).

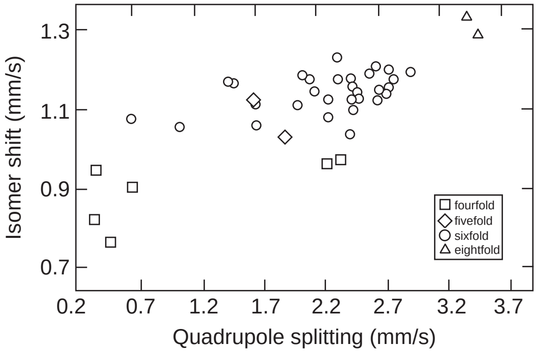

FIG. 11.12 Example of isomer shift and quadrupole splitting distribution in Fe-bearing $CaO\text{-}SiO_2$ glass (Alberto et al., 1996).

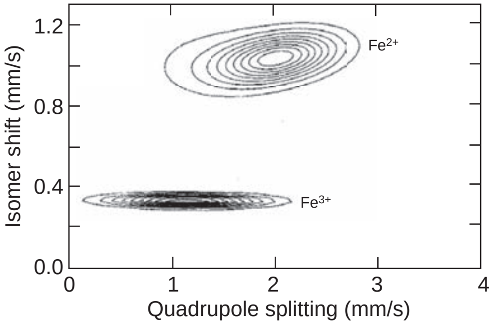

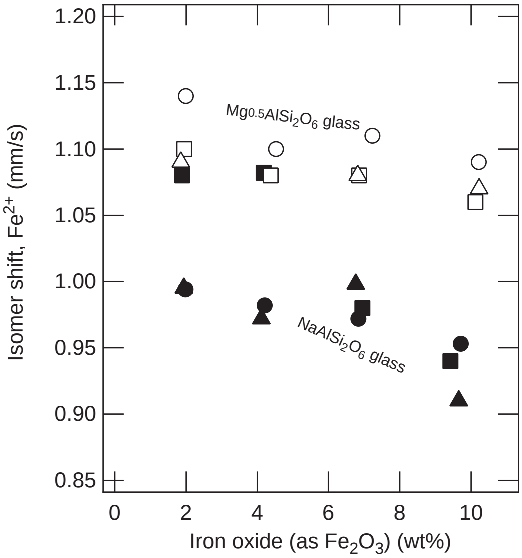

FIG. 11.13 Evolution of Fe^{2+} isomer shift (relative to Fe metal at 298K) from aluminosilicate glasses quenched from their melts as a function of the form and concentration of the iron oxide added. *Closed symbols* are $NaAlSi_2O_6$ and *open symbols* $Mg_{0.5}AlSi_2O_6$. *Circles* are data with iron oxide added to the starting compositions as Fe_2O_3, *squares* as $NaFeO_2$, and *triangles* as $MgFe_2O_6$. Samples were equilibrated at 1500°C in air, from which the melts were quenched to glass. The Fe^{2+} proportions in the $NaAlSi_2O_6$ glasses ranged from 0.35 to 0.45, whereas for the $Mg_{0.5}AlSi_2O_6$ glasses the Fe^{2+} proportion of the total iron content was between 0.6 and 0.7 (Mysen, 2006a,b).

exchange of cations in the precursor melt between the base glass and the added iron oxide component. For $NaAlSi_2O_6$, the structural role of Fe^{2+} is governed by the exchanged Na^+, whereas for $Mg_{0.5}AlSi_2O_6$, this role is governed by Mg^{2+}. In the case of alkali metal control, the hyperfine parameter data indicate that Fe^{2+} probably exists in four- and fivefold coordination, whereas it appears predominantly in sixfold coordination for the Mg system. When $Ca_{0.5}AlSi_2O_6$ is employed as a base glass, intermediate coordination numbers of Fe^{2+} have been inferred from the Mössbauer data (Mysen, 2006a,b).

11.4 MIXED VALENCE STATES

Iron occurs as ferrous and ferric iron under most conditions. Under highly reducing circumstances, Fe° also exists. Most commonly, Fe^{2+} and Fe^{3+} occur together. Changes in redox ratio may affect the structural state of Fe^{3+} and Fe^{2+} as well as that of a silicate solvent.

11.4.1 Redox Ratio and Oxygen Coordination

In an experimental study of relationships between the redox ratio of iron oxides, silicate melt structure, temperature, and oxygen fugacity, Kress and Carmichael (1988) best modeled the redox data by assuming that two oxide components, FeO and $FeO_{1.464}$, coexisted in the melts and that those oxides could then be described as an ideal mixture (Fig. 11.14), which was not the case with ideal mixing of a mixture of FeO and Fe_2O_3.

With the two components FeO and $FeO_{1.464}$, the equilibrium expression is (Kress and Carmichael, 1988):

FIG. 11.14 Relationship between the redox ratio of iron oxides and oxygen fugacity at 1360°C and ambient pressure (Kress and Carmichael, 1988).

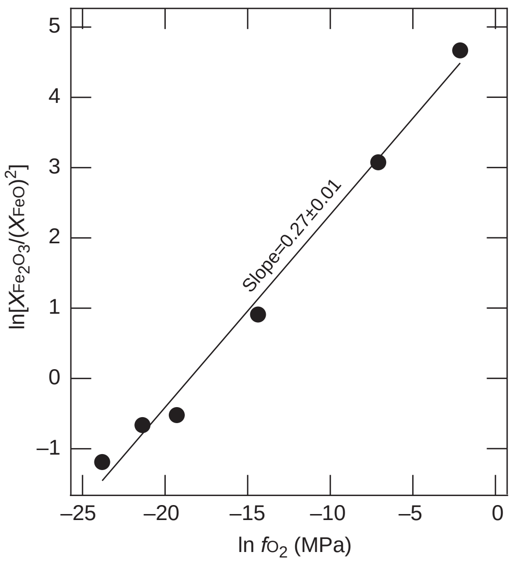

$$FeO + 0.232O_2 = FeO_{1.464}, \tag{11.2}$$

so that with ideal mixing of the two iron oxide components, the redox ratio of iron at constant temperature T is related to the oxygen fugacity as:

$$\ln(X_{FeO1.464}/X_{FeO}) = 0.232\ \ln f_{O_2} - \triangle H/RT + \triangle S/R. \tag{11.3}$$

The actual slope is 0.27 ± 0.01 (Fig. 11.14), or nearly that which would be expected from ideal mixing.

A change of the isomer shift of Fe^{3+} in melts and glasses as a function of their redox ratio, $Fe^{3+}/\sum Fe$ (Fig. 11.15) (see also Virgo and Mysen, 1985; Dingwell and Virgo, 1987; Jayasuriya et al., 2004; Mysen, 2006a,b; Sipowska et al., 2009), leads to the suggestion that some form of complexing that involves the ferrous and ferric iron takes place at intermediate redox ratio values. Most likely, as the redox ratio changes, the proportion of such species changes, with other possible species being Fe^{2+} serving, for example, as a network-modifier, at low $Fe^{3+}/\sum Fe$-values. At $Fe^{3+}/\sum Fe$ above the $IS_{Fe^{3+}}$ transition interval, Fe^{3+} in some form coexists with this species. Given that the $Fe^{3+}/\sum Fe$ interval corresponding to changing $IS_{Fe^{3+}}$ seems comparatively insensitive to the composition (structure) of the silicate and apparently also insensitive to total iron content, the conclusion is that it is the $Fe^{3+}/\sum Fe$ ratio that governs this complex formation.

11.4.2 Iron-Silicate Interaction

Reduction of network-forming Fe^{3+} to network-modifying Fe^{2+} may be expressed as (Holmquist, 1966):

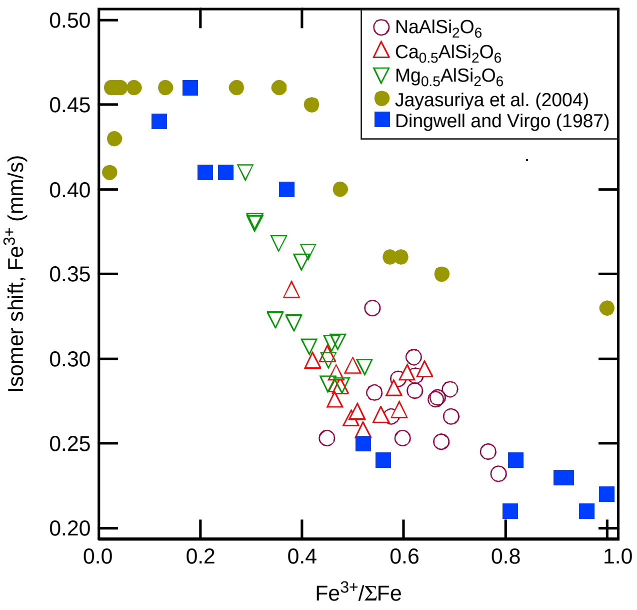

FIG. 11.15 Isomer shift of Fe^{3+} in melts as a function of redox ratio of iron, $Fe^{3+}/\sum Fe$, for compositions indicated (Mysen, 2006a,b; Jayasuriya et al., 2004; Dingwell and Virgo, 1987).

$$4\,FeO_2{}^{-} = 4\,Fe^{2+} + O_2 + 6\,O^{2-}. \tag{11.4}$$

In this equation, the oxygen anion, O^{2-}, is the link between the redox relations and the silicate network. The link can be expanded with a schematic reaction of the type:

$$2Q^4 + O^{2-} = 2Q^3. \tag{11.5}$$

In Eq. (11.5), the NBO/Si of Q^4 structural units equals 0, and that of Q^3 equals 1. Reduction of tetrahedral Fe^{3+} to octahedral Fe^{2+} does, therefore, result in depolymerization of the melt:

$$4FeO_2{}^{-} + 12Q^4 = 12Q^3 + 4Fe^{2+} + O_2. \tag{11.6}$$

It follows from Eq. (11.6) that parameters affecting the iron redox ratio also influence extent of melt polymerization, NBO/T, as well as silicate speciation. Upon dissolution of Fe_2O_3 in a silicate melt to form a ferri-complex with tetrahedrally coordinated Fe^{3+}, for example, silicate polymerization increases:

$$Fe_2O_3 + 2Q^3 = 2FeO_2{}^{-} + 2Q^4. \tag{11.7}$$

An example of how much of such an effect would be expected is shown in Fig. 11.16. An approximately 1.5% decrease in NBO/T of a melt per mol% Fe_2O_3 dissolved as $FeO_2{}^{-}$ is the result.

11.4.3 Temperature and Pressure

Application of glass structure data to characterization of Fe-bearing melts relies on the assumption that temperature-quenching of a melt to a glass does not significantly affect the

FIG. 11.16 Change in melt polymerization (expressed as percent change in NBO/T) with dissolution of Fe_2O_3 to form FeO_2^- complexes relative to a melt without Fe_2O_3.

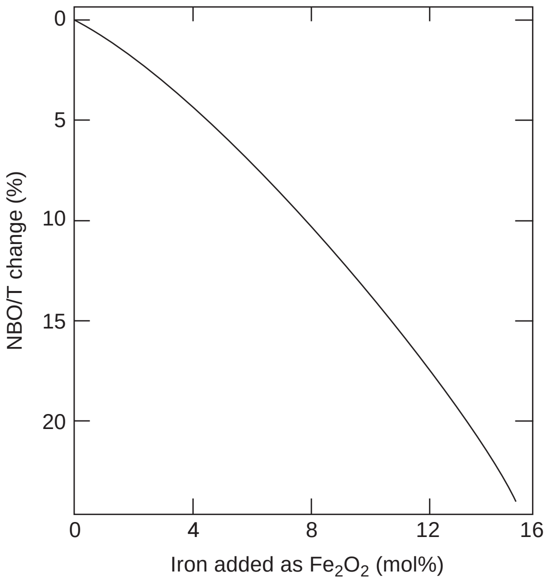

structural position of Fe^{3+} or Fe^{2+}. It is also assumed that the redox ratio of iron from equilibration of melt at high temperature can be quenched in the glass. Current experimental data indicate that for any melt composition there is a limiting quench rate beyond which Fe^{3+} and Fe^{2+} are no longer affected (Dyar et al., 1987; Metrich et al., 2006). However, the extent to which these issues could be a problem is known only for a limited set of samples under a limited number of conditions. Resolution of this question requires examination of relations between quenching rate and redox relations or, even better, structural studies of melts at high temperature.

11.4.3.1 Temperature

X-ray techniques and vibrational spectroscopy have been used to examine the structure of Fe-bearing melts at high temperature. Wilke et al. (2007) examined the structure of iron-bearing alkali silicate glasses and melts with X-ray techniques to near 750°C and found that the Fe^{3+}—O bond length at ambient temperature is slightly below 2 Å, and increases by 2%–3% up to 750°C. The bond length range was found consistent with Fe^{3+} in a coordination slightly greater than fivefold in all the alkali silicate compositions examined.

Along with $NaFeSi_2O_6$, Wang et al. (1993) investigated oxidized and reduced samples of an Fe-bearing sodium trisilicate glass and melt, namely $Na_2O{\cdot}3SiO_2{\cdot}0.5Fe_2O_3$ and $Na_2O{\cdot}3SiO_2{\cdot}FeO$. From Mössbauer analysis of the $Na_2O{\cdot}3SiO_2{\cdot}0.5Fe_2O_3$ glass formed from a melt equilibrated in air at 771°C, they found all iron to be oxidized and hyperfine Mössbauer parameters consistent with fourfold coordination of Fe^{3+}. The Raman spectra of this glass at 25°C and of the supercooled liquid at 771°C show considerable similarity (Fig. 11.17). Wang et al. (1993) concluded that Fe^{3+} is in fourfold coordination in both glass and melt. They also observed, however, an intensity growth near 1060–1070 cm^{-1} in the high-temperature Raman

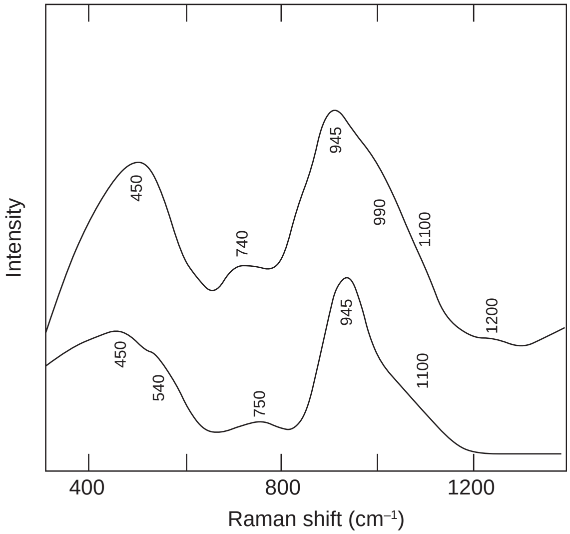

FIG. 11.17 Unpolarized Raman spectra of glass (25°C) and supercooled melt (771°C) of $Na_2O{\cdot}3SiO_2{\cdot}0.5Fe_2O_3$ (after Wang et al., 1993).

spectrum of this sample, but could not determine whether it was due to some changes in Q^n-abundance as the temperature was increased across the glass transition or, more simply, to temperature-dependent Raman cross-sections. In light of more recent experimental studies of the temperature-dependence of Q^n-species in silicate melts (see Chapter 7, Section 7.3.3), the changes in the 771°C spectrum likely reflects a growth in Q^4 abundance. Moreover, growth near 990 cm^{-1} at high temperature could reflect an increased abundance of Fe^{3+}—O vibrons with a Raman band in this frequency regime.

By annealing the same material under a hydrogen atmosphere, Wang et al. (1993) obtained a glass of composition $Na_2O{\cdot}3SiO_2{\cdot}FeO$ with all the iron as FeO. Its NBO/Si would be 1.3 with the assumption that all Fe^{2+} is a network-modifier. The Raman spectra at room temperature (glass) and at 676°C (supercooled liquid under a hydrogen atmosphere) are nearly identical to that of Fe-free $Na_2O{\cdot}1.5SiO_2$ glass, a glass whose NBO/Si is also 1.3 (Furukawa et al., 1981). Hence, it was concluded that the Raman spectra of the reduced glass and melt are consistent with Fe^{2+} serving in a network-modifying role.

In a study by Waychunas et al. (1988), Mössbauer spectra of glasses were recorded to 850°C on glasses and supercooled melts that were compositionally similar to those examined by Wang et al. (1993). However, Waychunas et al. (1988) interpreted their XANES spectra of melts at 850°C in terms of Fe^{2+} in fourfold coordination, whereas Wilke et al. (2007) concluded that the coordination number was between 4 and 5 for alkali silicate glasses and melts, with a slight decrease as temperatures were increased. This general conclusion would agree with that of Waseda and Toguri (1978) and Waseda et al. (1980) who reported, from X-ray absorption studies of FeO-SiO_2 and FeO-Fe_2O_3-SiO_2 melts, that the Fe—O bond lengths (between 2.04 and 2.08 Å) are those expected for Fe^{2+} in fourfold coordination (Fig. 11.18). However, as also noted in Section 11.2.1, by using the bond valence treatment of Brese and O'Keefe (1991), Fe—O bond lengths in this 2.05–2.1 Å range should be considered consistent with those expected for Fe^{2+} in a coordination state higher than 4.

FIG. 11.18 Si—O and Fe—O distances in FeO-SiO_2 melts at 1250–1400°C from X-ray diffraction (Waseda and Toguri, 1978).

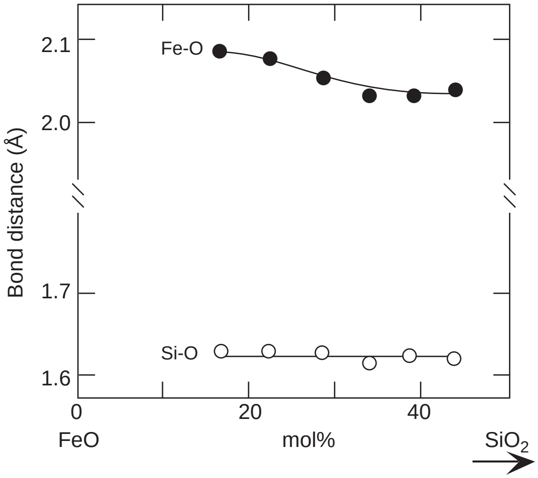

The Raman spectra of $Na_2O{\cdot}3SiO_2{\cdot}FeO$ glass and melts are similar to Raman spectra of $Na_2O{\cdot}1.5SiO_2$ glass, which suggests that Fe^{2+} is indeed a network-modifying cation. The Fe^{2+}—O bond lengths from the high-temperature FeO-SiO_2 melt X-ray data (Fig. 11.18) are consistent with sixfold coordinated Fe^{2+}. However, from the high-temperature X-ray absorption study of $FeO{\cdot}2SiO_2$ supercooled melt to 850°C, Jackson et al. (2005) found that the Fe—O bond length is 1.98 ± 0.02 Å as compared with 2.20 Å in crystalline Fe_2SiO_4 (fayalite). They concluded, therefore, that Fe^{2+} in these materials is in fourfold coordination, consistent with Waseda and Toguri's (1978) interpretation of their X-ray data, but not with the relationships between Fe—O bond length and Fe coordination state by Brese and O'Keefe (1991).

11.4.3.2 Pressure

Pressure effects on of Fe^{2+} and Fe^{3+} in silicate glasses and melts include coordination changes and, at very high pressure, possible high-spin/low-spin transitions (Mysen and Virgo, 1985; Nomura et al., 2011; Sanloup et al., 2013). Notably, the coordination numbers of Fe^{2+} in melt compositions that have been examined to high pressures strongly depend on pressure and increased from about 4.8 to slightly above 7 in the 0.001–7.5 GPa range (Fig. 11.19) (see also Sanloup et al., 2013). In comparison, the coordination number of Mg^{2+} in analogous $MgO{\cdot}2SiO_2$ melt as well as in basalt melt also increases with pressure, but at a slower rate than that of Fe^{2+} (Fig. 11.19) (see also Guillot and Sator, 2007; de Koker et al., 2009). At low pressure, the coordination numbers of Fe^{2+} and Mg^{2+} are indistinguishable, but as pressure increases Fe^{2+} undergoes more significant coordination changes than does Mg^{2+}.

Ferric iron also undergoes coordination changes with pressure, which likely is in response to changing $Fe^{3+}/\sum Fe$ with pressure, because of the different molar volumes of FeO and $FeO_{1.5}$ in melts (Mysen and Virgo, 1978, 1985; Lange and Carmichael, 1987). Mysen and Virgo (1985) and Brearley (1990) reported ^{57}Fe Mössbauer spectroscopic data of glasses formed by temperature-quenching melts in equilibrium with air at pressures of up to 4 GPa. In these two studies, the $Fe^{3+}/\sum Fe$ decreased with increasing pressure (Fig. 11.20A), a feature that correlated with pressure sensitive $IS_{Fe^{3+}}$ (Fig. 11.20B). The rapid increase in isomer shift

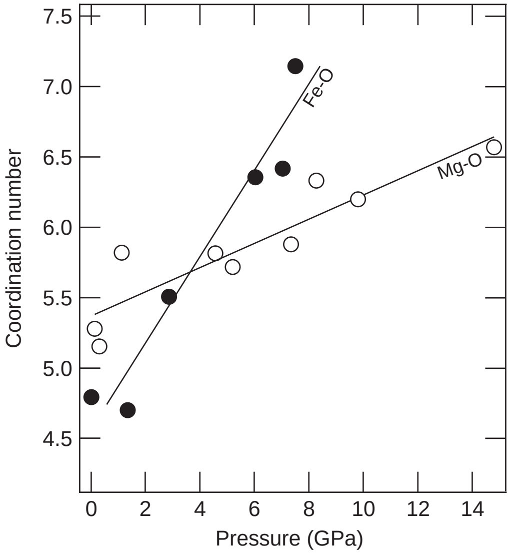

FIG. 11.19 Pressure dependence of Fe^{2+} coordination number in $FeO{\cdot}2SiO_2$ glass quenched from melt at high pressure (Sanloup et al., 2013) compared with the coordination number of Mg^{2+} calculated for $MgO{\cdot}2SiO_2$ and basalt melts (de Koker et al., 2009; Guillot and Sator, 2007).

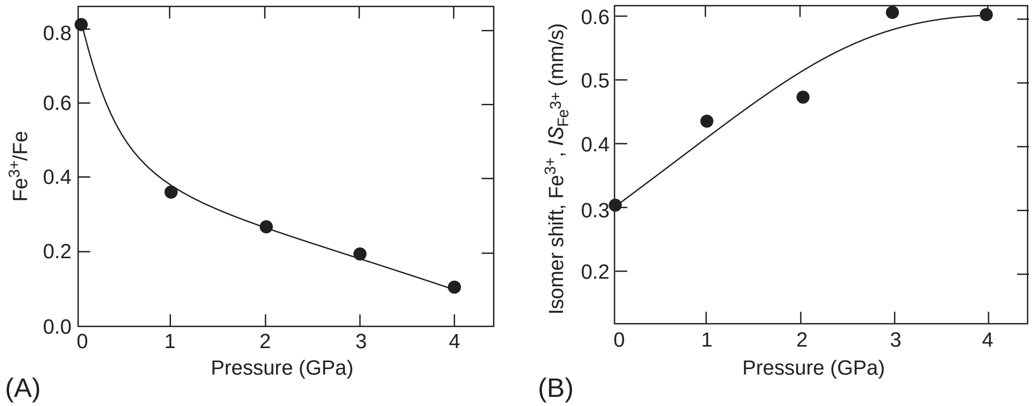

FIG. 11.20 (A) Redox ratio of iron and (B) isomer shift of Fe^{3+} from Mössbauer spectra (relative to Fe metal at 298 K) of $Na_2Si_2O_5$ + 7.5 mol% (nominal) Fe_2O_3 quenched from 1400°C at the pressures indicated (Mysen and Virgo, 1985).

from about 0.3 mm/s at ambient pressure and 298 K, to slightly <0.6 mm/s for glasses formed at 3 and 4 GPa, points to a transformation of Fe^{3+} from tetrahedral to perhaps octahedral coordination. It was suggested that this coordination change was in response to decreasing $Fe^{3+}/\sum Fe$ as the pressure increased. There is no evidence in the Mössbauer spectra of these glasses to suggest that the structural role of Fe^{2+} varies with pressure, at least in the pressure range up to 4 GPa where such measurements have been made. However, in a study of slightly hydrous basalt melt to 0.5 GPa, Lukanin et al. (2002) did not report analogous pressure effects. Whether this is the result of greatly different melt compositions or different experimental protocol cannot be assessed.

11.5 STRUCTURE AND MELT PROPERTIES

The $Fe^3/\sum Fe$ ratio together with the coordination numbers of Fe^{3+} and Fe^{2+} in melts and glasses can control the silicate polymerization and speciation, as seen in Eqs. (11.6), (11.7), and therefore a range of physical and chemical properties (see also Chapter 10). The redox ratio of iron, in turn, varies with temperature, pressure, oxygen fugacity, and melt composition. These parameters will therefore also affect polymerization of Fe-bearing silicate melts. At constant iron content and oxygen fugacity, increasing temperature results in decreasing $Fe^3/\sum Fe$ (see Chapter 10, Fig. 10.11). Increasing temperature will therefore cause equilibrium in Eq. (11.6) to shift to the right, thus depolymerizing Fe^{3+}-containing silicate melts (Fig. 11.21). Two trends are shown, however, in Fig. 11.21. The dashed line is NBO/T trajectory with Fe^{3+} in fourfold coordination at all temperatures ($^{[4]}Fe^{3+}$). The "actual" trend depicts an NBO/T trend that incorporates a gradual transformation of $^{[4]}Fe^{3+}$ to $^{[6]}Fe^{3+}$ caused by increasing temperature, and a resultant decrease in $Fe^{3+}/\sum Fe$, which in turn induces the coordination change of ferric iron; see Section 11.4.1. As a result of the coordination transformation of Fe^{3+}, depolymerization of the melt occurs because:

$$^{[4]}FeO_2{}^- + 2Q^4 = {}^{[6]}Fe^{3+} + 2Q^3. \qquad (11.8)$$

A pressure increase also causes reduction of Fe^{3+} to Fe^{2+} (Chapter 10, Fig. 10.12), and therefore depolymerization of the melt structure (Fig. 11.21B). NBO/T is more sensitive to pressure ("actual" curve) than expected if the coordination state of Fe^{3+} were not affected by pressure (dashed line in Fig. 11.21B). However, as pressure can also induce coordination transformation of Fe^{3+} from fourfold to sixfold, Eqs. (11.6), (11.8) describe the circumstances.

Decreasing oxygen fugacity results in decreasing $Fe^{3+}/\sum Fe$ (Chapter 10, Fig. 10.19) and therefore affects the degree of polymerization in the same manner as pressure and temperature (Fig. 11.21C). Changes in melt polymerization, NBO/T, obviously also affect Q^n-speciation, but experimental data are lacking to determine the relationships between iron content, redox ratio of iron, structural roles of Fe^{2+} and Fe^{3+}, and Q^n-speciation, although some data were proposed by Belova et al. (2015), who assumed that Fe^{3+} serves as a network-modifying cation, a conclusion that has found little support elsewhere in the literature.

Relationships between redox ratio, iron coordination, and Q^n-speciation will depend on whether tetrahedrally coordinated Fe^{3+} substitutes for Si^{4+} in the structure or it forms instead isolated complexes. In the former case, partitioning of Fe^{3+} between individual Q^n-species may affect speciation in a manner conceptually similar to that observed for Al^{3+} in peralkaline aluminosilicate melts (Chapter 9, Section 9.3.2.4; see also Fig. 9.26), thus possibly driving the general Q^n-speciation reaction (Stebbins, 1987):

$$2Q^n \Leftrightarrow Q^{n+1} + Q^{n-1}, \qquad (11.9)$$

to the right. The situation is, however, likely more complicated because Fe^{2+}, with its large ionization potential, tends to favor bonding with oxygen in the least polymerized of available Q^n-species (Q^{n-1} in Eq. 11.8). This tendency would tend to drive equilibrium in Eq. (11.8) to the right with increasing pressure for Fe-bearing silicate melts, because $Fe^{3+}/\Sigma Fe$ decreases with increasing pressure.

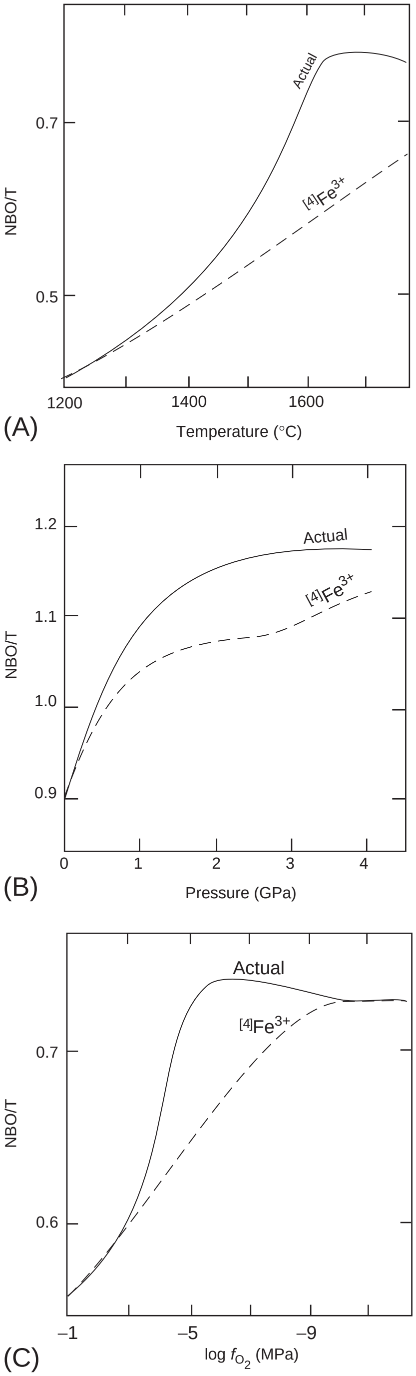

FIG. 11.21 Relationships between degree of polymerization of silicate network, NBO/T, and the structure and redox relations of iron. (A) Sodium aluminosilicate glass with Al/(Al+Si)=0.334, Na/(Na+Al)=0.65 and 5wt% iron oxide added as Fe_2O_3 quenched from melt equilibrated with air at the temperatures indicated (Mysen and Virgo, 1989). (B) Glass of nominal composition $Na_2Si_2O_5$+7.5mol% Fe_2O_3, quenched from 1400°C at the pressure indicated (Mysen and Virgo, 1985). (C) Same glass as in (A) quenched from melt equilibrated with CO-CO_2 gas mixture to control f_{O_2} at 1550°C (Mysen and Virgo, 1989).

Given the complex relationships between redox relations of iron, the iron coordination, and their effects on melt structure, it follows that essentially all properties of iron-bearing silicate melts will show significant dependence on the same parameters. Many of those have been discussed in the previous chapter (Chapter 10). Here, we will highlight how some of those properties can be linked to the structural variations governed by ferric and ferrous iron.

11.5.1 Thermal Properties

Existing thermal data include scattered information on heat capacity, molar volume, and composition-activity relations (Lange and Navrotsky, 1992; Tangeman et al., 2001; Gaillard et al., 2003; Fredriksson and Seetharaman, 2004; Sugawara and Akaogi, 2004; Liu and Lange, 2006; Sipowska et al., 2009; Falenty and Webb, 2010). Among these data, configurational properties seem the most commonly addressed, perhaps because of their close relationships to transport properties (see also Chapter 4, Section 4.6.1).

11.5.1.1 Configurational Properties

Configurational properties of melts, such as configurational heat capacity, incorporate a mixing term resulting from abundance variations of individual species, including iron-species (see Chapter 7, Eq. 7.10). The abundance of these species, in turn, governs the overall degree of polymerization of the melt, NBO/T:

$$\mathrm{NBO/T} = \sum (\mathrm{nbo/t})_i \cdot x_i, \tag{11.10}$$

where $(\mathrm{nbo/t})_i$ is the contribution of a species, i, to the overall polymerization and x_i is its mol fraction. In simple binary metal oxide silicate melts, there is a positive correlation between configurational heat capacity and melt NBO/Si, as seen for the Na_2O-SiO_2 system in Fig. 11.22. The scatter in that figure likely results from the fact that the NBO/T parameter does not take into account the variations in the Q^n-species and that the Q^n-species themselves also carry a specific configurational heat capacity (Mysen, 1995). That limitation notwithstanding, the correlation is much better than the one obtained, whether or not Fe^{3+} is included in the NBO/T calculation, when Fe_2O_3 is dissolved in melt. There is at best a very poor correlation between configurational heat capacity and NBO/T (Fig. 11.22). This situation very likely reflects the fact that Fe-bearing species contribute to the configurational heat capacity, but details of such contributions are not known and could not therefore be taken into account in Fig. 11.22.

The configurational heat capacities define clear minima (Fig. 11.22, dashed line) slightly on the left side of the meta-alumina/meta-ferric join in ternary and quaternary melt systems such as Na_2O-Al_2O_3-SiO_2 and Na_2O-FeO-Fe_2O_3-SiO_2, along joins from peralkaline to compositions with Al_2O_3 or Fe_2O_3 in excess of the charge-compensation capacity of Na^+ (Falenty and Webb, 2010); see also Fig. 11.23. Such minima are primarily a result of minimum entropy of mixing and therefore configurational heat capacity, in melts near the meta-joins where the number of structural units is minimal. Furthermore, the minimum is deeper and the slope toward the minimum steeper for Na_2O-FeO-Fe_2O_3-SiO_2 compared with Na_2O-Al_2O_3-SiO_2 melts. This difference reflects greater disorder in the iron-bearing melts, because Fe^{3+} forms isolated tetrahedra (see Section 11.2.2).

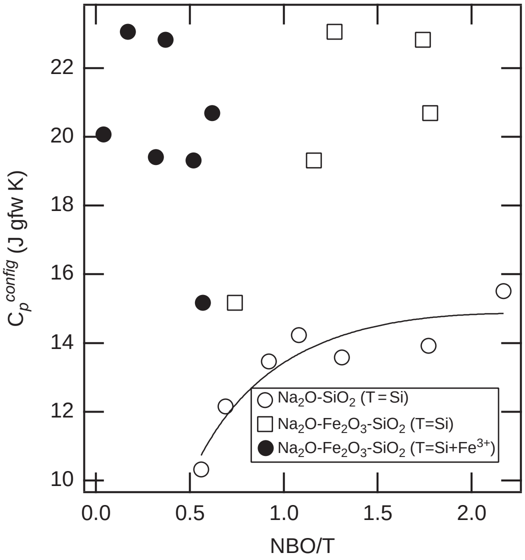

FIG. 11.22 Configurational heat capacity at the glass transition in the system Na_2O-Fe_2O_3-SiO_2. The symbols are identified in the figure (Tangeman and Lange, 1998).

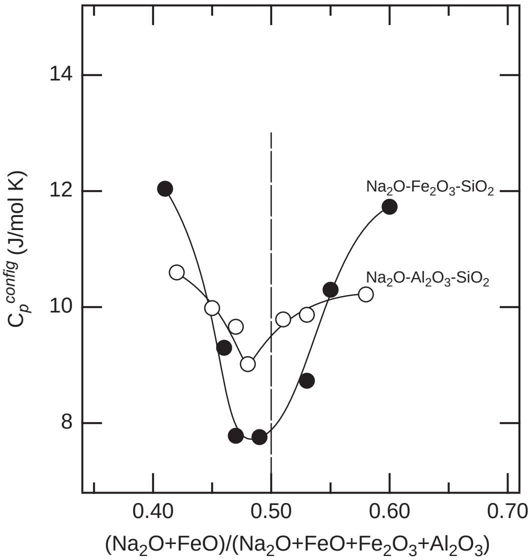

FIG. 11.23 Evolution of configurational heat capacity, C_p^{config}, of $NaAl_2O_3$-SiO_2 and Na_2O-FeO-FeO_3-SiO_2 melts as a function of composition shown at ambient pressure and quenched from melts (Falenty and Webb, 2010).

11.5.2 Physical Properties

11.5.2.1 Transport Properties

The principal transport properties of iron-bearing melts and glasses are viscosity and diffusion. The former has been most extensively investigated, typically as a function of iron content, redox ratio, and alkalinity of the melts (Mysen et al., 1985; Dingwell and Virgo, 1988; Falenty and Webb, 2010; Osugi et al., 2013; Chevrel et al., 2013). From these data, it is immediately evident that the effect of Fe^{3+} on melt viscosity differs dramatically from that of Al^{3+}, even though both cations may be tetrahedrally coordinated in the melt structure and may be charge-balanced with the same cations, be they alkalis or alkaline earths. Along Na meta-aluminosilicate (SiO_2-$NaAlO_2$) and meta-ferrisilicate (SiO_2-$NaFeO_2$) joins, for example, the viscosity evolution from increasing Fe^{3+} is much greater than with equivalent portions of Al^{3+} (Dingwell and Virgo, 1988); see also Chapter 10, Fig. 10.24A. Moreover, whereas the activation enthalpy of viscous flow along Na-meta-ferrisilicate melt joins is independent of $Fe^{3+}/(Fe^{3+}+Si)$, it decreases rapidly with increasing $Al/(Al+Si)$ (Dingwell and Virgo, 1988; Toplis et al., 1997); see Chapter 10, Fig. 10.24B. These large differences result from the fact that, whereas Al^{3+} in SiO_2-$NaAlO_2$ melts substitutes for Si^{4+} in a near random manner (see Chapter 9, Section 9.3.2), Fe^{3+} does not, but instead forms clusters of FeO_4 tetrahedra and isolated FeO_4 tetrahedra. The latter structural environment differs greatly from that of Al^{3+}, and evidently is responsible for the quite different transport behavior of meta-ferrisilicate melts. However, it may be speculated that the transport properties of the two types of systems will be less dissimilar with other charge-balancing cations such as Ca^{2+} and Mg^{2+}, with which Fe^{3+} clustering is much less prevalent (e.g., Bingham et al., 2002) and Al^{3+} is much more ordered (Lee and Stebbins, 1999, 2006).

The difference between Fe^{3+} and Al^{3+} in alkali aluminosilicate and alkali ferrisilicate melts is also evident in peralkaline melts. Along peralkaline aluminosilicate joins, the $Si^{4+} \Leftrightarrow (NaAl)^{4+}$ substitution has only a minor effect on viscous flow (Chapter 8, Section 8.4.2) (see also Dingwell, 1986), whereas the equivalent $Si^{4+} \Leftrightarrow (NaFe)^{4+}$ substitution results in a significant viscosity decrease and a lowering of the activation enthalpy of viscous flow (Chapter 10, Section 10.5.2) (see also Dingwell and Virgo, 1988; Falenty and Webb, 2010; Osugi et al., 2013). These differences again reflect those between tetrahedrally coordinated Al^{3+} and Fe^{3+}. As discussed in Chapters 8 and 9, Al^{3+} in depolymerized aluminosilicate melts substitutes for Si^{4+} in Q^4 species and drives the disproportion reaction (11.9) to the right (Merzbacher et al., 1990; Allwardt et al., 2003; Mysen et al., 2003). However, it would seem that clustered Fe^{3+} in the equivalent peralkaline ferrisilicate melts does not have this effect on the structure, as it does not substitute for Si^{4+} and does not therefore affect the silicate speciation equilibrium in the same manner as Al^{3+}.

The activation enthalpy for diffusion of iron in ferrisilicate melts is near 150 kJ/mol for alkali + alkaline earth silicate melts (Kim and Kwon, 2010), which is considerably less than for Fe-free melts. This difference may testify to the unique structural role of Fe^{3+} as it clusters in the melts. Furthermore, the relationship between melt viscosity and self-diffusion is strongly nonlinear (Chapter 10, Fig. 10.30) (see also Kim and Kwon, 2010), which contrasts with that of Al^{3+} in similar melts and again therefore highlights the different structural behavior of Fe^{3+} and Al^{3+}. It is noted, however, that in a study of interdiffusivity of FeO and CaO in CaO-FeO-SiO_2 melts, Ueda and Doi (1995), using methods similar to those of Kim and Kwon (2010), found a range of activation energies from 138 to 247 kJ/mol with increasing enthalpy values as melts became more polymerized. Ueda and Doi (1995) also noted that the inverse relation between diffusion and viscosity was consistent with an Eyring-type relationship (see also Chapter 4, Section 4.6.1). Existing experimental data necessary to resolve these differences do not appear available.

11.5.2.2 *Volume Properties*

Liu and Lange (2006) derived a composition-independent partial molar volume of Fe_2O_3 of $41.52 \pm 0.34\,cm^3/mol$ in a study of melts in the systems Na_2O-FeO-Fe_2O_3-SiO_2 and K_2O-FeO-Fe_2O_3-SiO_2 equilibrated with air to 1534°C (where generally $Fe^{3+} > Fe^{2+}$, except for the highest temperatures). In contrast, Dingwell and Brearley (1988) did find a significant composition dependence for CaO-FeO-Fe_2O_3-SiO_2 melts. One may resolve this difference by recognizing that clustering of Fe^{3+} is much more pronounced in alkali-silicate than in alkaline earth-silicate systems (Bingham et al., 2002) (see also Fig. 11.7). The constant partial molar volume of Fe_2O_3 would then result from Fe^{3+} clustering. However, Dingwell and Brearley (1988) also reported that there is a small excess volume term from linear fits to the Fe_2O_3 volume data, a conclusion that also differs from that of Liu and Lange (2006). The difference is not large (<2%), but the underlying cause is not clear.

References

Alberto, H.V., Gil, J.M., Ayres DeCampos, N., Mysen, B.O., 1993. Redox equilibria of iron in Ti-bearing calcium silicate quenched glasses. J. Non-Cryst. Solids 151, 39–50.

Alberto, H.V., Pinto da Cunha, J.L., Mysen, B.O., Gil, J.M., de Campos, N.A., 1996. Analysis of Mössbauer spectra of silicate glasses using a two-dimensional Gaussian distribution of hyperfine parameters. J. Non-Cryst. Solids 194, 48–57.

Allwardt, J.R., Lee, S.K., Stebbins, J.F., 2003. Bonding preference of non-bridging O atoms: Evidence from ^{17}O MAS and 3QMAS NMR on calcium aluminate and low-silica Ca-aluminosilicate glasses. Am. Mineral. 88, 949–954.

Bell, P.M., Mao, H.K., 1974. Crystal-field spectra of Fe^{2+} and Fe^{3+} in synthetic basalt glass as a function of oxygen fugacity. In: Carnegie Instn. Washington Year Book.vol. 73. pp. 496–497.

Belova, E.V., Kolyagin, Y.A., Uspenskaya, I.A., 2015. Structure and glass transition temperature of sodium-silicate glasses doped with iron. J. Non-Cryst. Solids 423, 50–57.

Bingham, P.A., Parker, J.M., Searle, T., Williams, J.M., Fyles, K., 1999. Redox and clustering of iron in silicate glasses. J. Non-Cryst. Solids 253, 203–209.

Bingham, P.A., Parker, J.M., Searle, T., Williams, J.M., Smith, I., 2002. Novel structural behaviour of iron in alkali-alkaline-earth-silica glasses. C. R. Chimie 5, 787–796.

Bingham, P.A., Parker, J.M., Searle, T.M., Smith, I., 2007. Local structure and medium range ordering of tetrahedrally coordinated Fe^{3+} ions in alkali-alkaline earth-silica glasses. J. Non-Cryst. Solids 353, 2479–2494.

Brearley, M., 1990. Ferric iron in silicate melts in the system Na_2O-Fe_2O_3-SiO_2 at high pressure. J. Geophys. Res. 95, 15703–15716.

Brese, N.E., O'Keefe, M., 1991. Bond-valence parameters for solids. Acta Cryst. B47, 192–197.

Burkhard, D.J.M., 2000. Iron-bearing silicate glasses at ambient conditions. J. Non-Cryst. Solids 275, 175–188.

Burns, R.G., 1994. Mineral Mössbauer spectroscopy: correlations between chemical shift and quadrupole splitting parameters. Hyperfine Interact. 91, 739–745.

Calas, G., Petiau, J., 1983. Coordination state of iron in oxide glasses through high-resolution K-edge spectra: information from pre-edge. Solid State Commun. 48, 625–629.

Calas, G., Cormier, L., Galoisy, L., Jollivet, P., 2002. Structure-property relationships in multicomponent oxide glasses. C. R. Chimie 5, 831–843.

Chevrel, M.O., Giordano, D., Potuzak, M., Courtial, P., Dingwell, D.B., 2013. Physical properties of $CaAl_2Si_2O_8$-$CaMgSi_2O_6$-FeO-Fe_2O_3 melts: analogues for extra-terrestrial basalt. Chem. Geol. 346, 93–105.

de Koker, N.P., Stixrude, L., Kakrki, B.B., 2009. Thermodynamics, structure, dynamics, and freezing of Mg_2SiO_4 liquid at high pressure. Geochim. Cosmochim. Acta 72, 1427–1441.

Dingwell, D.B., 1986. Viscosity-temperature relationships in the system $Na_2Si_2O_5$-$Na_4Al_2O_5$. Geochim. Cosmochim. Acta 50, 1261–1265.

Dingwell, D.B., Brearley, M., 1988. Melt densities in the CaO-FeO-Fe_2O_3-SiO_2 system and the compositional dependence of the partial molar volume of ferric iron in silicate melts. Geochim. Cosmochim. Acta 52, 2815–2825.

Dingwell, D.B., Virgo, D., 1987. The effect of oxidation state on the viscosity of melts in the system Na2O-FeO-Fe_2O_3-SiO_2. Geochim. Cosmochim. Acta 51, 195–205.

Dingwell, D.B., Virgo, D., 1988. Viscosities of melts in the Na_2O-FeO-Fe_2O_3-SiO_2 systems and factors-controlling relative viscosities in fully polymerized melts. Geochim. Cosmochim. Acta 52, 395–404.

Dunaeva, E.S., Ugolkova, E.A., Efimov, N.N., Minin, V.V., Novotortsev, V.M., 2014. ESR spectroscopy of Fe-III ions in sodium silicate glasses. Russ. Chem. Bull. 63 (1), 60–63.

Dyar, M.D., Naney, M.T., Swanson, S.E., 1987. Effect of quench methods on Fe^{3+}/Fe^{2+} ratios: a Mössbauer and wet chemical study. Am. Mineral. 72, 792–800.

Faiz, M., Mekki, A., Kariapper, M.S., Mun, B.S., Hussain, Z., 2011. X-ray absorption near edge structure investigation of iron-sodium silicate glasses. J. Non-Cryst. Solids 357, 3803–3806.

Falenty, K., Webb, S.L., 2010. Shear modulus, heat capacity, viscosity and structural relaxation time of Na_2O-Al_2O_3-SiO_2 and Na_2O-Fe_2O_3-Al_2O_3-SiO_2 melts. Phys. Chem. Miner. 37, 613–634.

Farges, F., Lefrere, Y., Rossano, S., Berthereau, A., Calas, G., Brown, G.E., 2004. The effect of redox state on the local structural environment of iron in silicate glasses: a molecular dynamics, combined XAFS spectroscopy, and bond valence study. J. Non-Cryst. Solids 344, 176–188.

Fox, K.E., Furukawa, Y., White, W.B., 1982. Transition metal ions in silicate melts. Part 2. Iron in sodium silicate glasses. Phys. Chem. Glasses 23, 169–178.

Fredriksson, P., Seetharaman, S., 2004. Thermodynamic activities of "FeO" in some ternary "FeO"-containing slags. Steel Res. Int. 75, 357–365.

Furukawa, T., Fox, K.E., White, W.B., 1981. Raman spectroscopic investigation of the structure of silicate glasses. III. Raman intensities and structural units in sodium silicate glasses. J. Chem. Phys. 153, 3226–3237.

Gaillard, F., Pichavant, M., Scaillet, B., 2003. Experimental determination of activities of FeO and Fe_2O_3 components in hydrous silicic melts under oxidizing conditions. Geochim. Cosmochim. Acta 67, 4389–4409.

Galoisy, L., Cormier, L., Rossano, S., Ramos, A., Calas, G., Gaskell, P., Le Grand, M., 2000. Cationic ordering in oxide glasses: the example of transition elements. Mineral. Mag. 64, 409–424.

Giuli, G., Paris, E., Hess, K.-U., Dingwell, D.B., Cicconi, M.R., Eeckhout, S.G., Fehr, K.T., Valenti, P., 2011. XAS determination of the Fe local environment and oxidation state in phonolite glasses. Am. Mineral. 96, 631–636.

Giuli, G., Alonso-Mori, R., Cicconi, M.R., Paris, E., Glatzel, P., Eeckhout, S.G., Scaillet, B., 2012. Effect of alkalis on the Fe oxidation state and local environment in peralkaline rhyolitic glasses. Am. Mineral. 97, 468–475.

Guillot, B., Sator, N., 2007. A computer simulation study of natural silicate melts. Part II: high pressure properties. Geochim. Cosmochim. Acta 71, 4538–4556.

Hannoyer, B., Lenglet, M., Dürr, J., Cortes, J., 1992. Spectroscopic evidence of octahedral iron (III) in soda-lime silicate glasses and crystals. J. Non-Cryst. Solids 151, 209–216.

Hayashi, M., Susa, M., Nagata, K., 1999. Magnetic structure of as-quenched silicate glasses containing iron oxides. J. Appl. Phys. 85, 2257–2263.

Hayashi, M., Hori, M., Susa, M., Fukuyama, H., Nagata, K., 2000. Oxidation states and coordination structures of iron ions in silicate melts during relaxation process and at equilibrium. Phys. Chem. Miner. 41, 49–54.

Henderson, G.S., Fleet, M.E., Bancroft, G.M., 1984. An X-ray scattering study of vitreous $KFeSi_3O_8$ and $NaFeSi_3O_8$ and reinvestigation of vitreous SiO_2 using quasicrystalline modelling. J. Non-Cryst. Solids 68, 333–349.

Holland, D., Mekki, A., Gee, I.A., McConville, C.F., Johnson, J.A., Johnson, C.E., Appleyard, P., Thomas, M., 1999. The structure of sodium iron silicate glass – a multi-technique approach. J. Non-Cryst. Solids 253, 192–202.

Holmquist, S., 1966. Ionic formulation of redox equilibria in glass melts. J. Am. Ceram. Soc. 49, 228–229.

Jackson, W.E., Mustre de Leon, J., Brown, G.E., Waychunas, G.A., Conradson, S.D., Combes, J.-M., 1993. High-temperature XAS study of Fe_2SiO_4 liquid: reduced coordination of ferrous iron. Science 262, 229–232.

Jackson, W.E., Farges, F., Yeager, M., Mabrouk, P.A., Rossano, S., Waychunas, G.A., Solomon, E.I., Brown, G.E., 2005. Multi-spectroscopic study of Fe(II) in silicate glasses: Implications for the coordination environment of Fe(II) in silicate melts. Geochim. Cosmochim. Acta 69, 4315–4332.

Jayasuriya, K., O'Neill, H.S.C., Berry, A.J., Campbell, S.J., 2004. A Mössbauer study of the oxidation state of Fe in silicate melts. Am. Mineral. 89, 1597–1609.

Johnson, J.A., Johnson, C.E., Holland, D., Mekki, A., Appleyard, P., Thomas, M.F., 1999. Transition metal ions in ternary sodium silicate glasses: a Mössbauer and neutron study. J. Non-Cryst. Solids 246, 104–114.

Keppler, H., 1992. Crystal field spectra and geochemistry of transition metal ions in silicate melts and glasses. Am. Mineral. 77, 62–75.

Kim, K.D., Kwon, S.K., 2010. Redox equilibrium of Fe^{3+}/Fe^{2+} and diffusivity of iron in alkali-alkaline earth-silicate glass melts. J. Ceram. Process. Res. 11, 460–464.

Kress, V.C., Carmichael, I.S.E., 1988. Stoichiometry of the iron oxidation reaction in silicate melts. Am. Mineral. 73, 1267–1274.

Lange, R.A., Carmichael, I.S.E., 1987. Densities of Na_2O-K_2O-CaO-MgO-Fe_2O_3-Al_2O_3-TiO_2-SiO_2 liquids: new-measurements and derived partial molar properties. Geochim. Cosmochim. Acta 51, 2931–2946.

Lange, R.A., Navrotsky, A., 1992. Heat-capacities of Fe_2O_3-bearing silicate liquids. Contrib. Mineral. Petrol. 110, 311–320.

Lee, S.K., Stebbins, J.F., 1999. The degree of aluminum avoidance in aluminosilicate glasses. Am. Mineral. 84 (5–6), 937–945.

Lee, S.K., Stebbins, J.F., 2006. Disorder and the extent of polymerization in calcium silicate and aluminosilicate glasses: O-17 NMR results and quantum chemical molecular orbital calculations. Geochim. Cosmochim. Acta 70, 4275–4286.

Levy, R.A., Lupis, C.H., Flinn, P.A., 1976. Mössbauer analysis of the valence and coordination of iron cations in SiO_2-Na_2O-CaO glasses. Phys. Chem. Glasses 17, 94–103.

Liu, Q., Lange, R.A., 2006. The partial molar volume of Fe_2O_3 in alkali silicate melts: Evidence for an average Fe3+ coordination number near five. Am. Mineral. 91, 385–393.

Lukanin, O.A., Rusakov, V.S., Kotel'nikova, A.A., Kadik, A.A., 2002. Valence and structural state of iron in basaltic melts at pressures up to 5 kbar. Petrology 10, 299–320.

Magnien, V., Neuville, D.R., Cormier, L., Roux, J., Hazemann, J.L., Pinet, O., Richet, P., 2006. Kinetics of iron redox reactions in silicate liquids: a high-temperature X-ray absorption and Raman spectroscopy study. J. Nucl. Mater. 352, 190–195.

Menil, G., 1985. Systematic trends of the ^{57}Fe Mössbauer isomer shifts in (FeO) and FeF polyhedra. Evidence of new correlation between the isomer shift and the inductive effect of the bond T-X (*Fe) where X is 0 or F and T any element with a formal positive charge. J. Phys. Chem. Solids 46, 663–789.

Merzbacher, C.I., Sherriff, B.L., Hartman, J.S., White, W.B., 1990. A high-resolution ^{29}Si and ^{27}Al NMR study of alkaline earth aluminosilicate glasses. J. Non-Cryst. Solids 124, 194–206.

Metrich, N., Susini, J., Foy, F., Farges, F., Massare, D., Sylla, L., Lequin, S., Bonnin-Mosbah, M., 2006. Redox state of iron in peralkaline rhyolitic glass/melt: X-ray absorption micro-spectroscopy experiments at high temperature. Chem. Geol. 231, 350–363.

Mysen, B.O., 1995. Experimental, in-situ, high-temperature studies of properties and structure of silicate melts relevant to magmatic processes. Eur. J. Mineral. 7, 7459766.

Mysen, B.O., 2006a. The structural behavior of ferric and ferrous iron in aluminosilicate glass near meta-aluminosilicate joins. Geochim. Cosmochim. Acta 70, 2337–2353.

Mysen, B.O., 2006b. Redox equilibria and melt structure: implications for olivine/melt element partitioning. Geochim. Cosmochim. Acta. 70.

Mysen, B.O., Virgo, D., 1978. Influence of pressure, temperature, and bulk composition on melt structures in the system $NaAlSi_2O_6$- $NaFe^{3+}Si_2O_6$. Am. J. Sci. 278, 1307–1322.

Mysen, B.O., Virgo, D., 1985. Iron-bearing silicate melts: relations between pressure and redox equilibria. Phys. Chem. Miner. 12, 191–200.

Mysen, B.O., Virgo, D., 1989. Redox equilibria, structure, and properties of Fe-bearing aluminosilicate melts: relationships between temperature, composition, and oxygen fugacity in the system Na_2O-Al_2O_3-SiO_2-Fe-O. Am. Mineral. 74, 58–76.

Mysen, B.O., Virgo, D., Seifert, F.A., 1984. Redox equilibria of iron in alkaline earth silicate melts: relationships between melt structure, oxygen fugacity, temperature and properties of iron-bearing silicate liquids. Am. Mineral. 69, 834–848.

Mysen, B.O., Virgo, D., Neumann, E.R., Seifert, F.A., 1985. Redox equilibria and the structural states of ferric and ferrous iron in melts in the system CaO-MgO-Al_2O_3-SiO_2: relations between redox equilibria, melt structure and liquidus phase equilibria. Am. Mineral. 70, 317–322.

Mysen, B.O., Lucier, A., Cody, G.D., 2003. The structural behavior of Al^{3+} in peralkaline melts and glasses in the system Na_2O-Al_2O_3-SiO_2. Am. Mineral. 88, 1668–1678.

Nagata, K., Hayashi, M., 2001. Structural relaxation of silicate melts containing iron oxide. J. Non-Cryst. Solids 282, 1–6.

Nolet, D.A., Burns, R.G., Flamm, S.L., Besancon, J.R., 1979. Spectra of Fe-Ti silicate glasses: implications to remote-sensing of planetary surfaces.Proc. 10th Lun. Planet. Sci. Confpp. 1775–1786.

Nomura, R., Ozawa, H., Tateno, S., Hirose, K., Hernlund, J., Muto, S., Isjii, H., Hiraoka, N., 2011. Spin crossover and iron-rich silicate melt in the Earth's deep mantle. Nature 473, 199–202.

O'Horo, M.P., Levy, R.A., 1978. Effect of melt atmosphere on the magnetic properties of a $[(SiO_2)_{45}\ (CaO)_{55}]_{65}$ $[Fe_2O_3]_{35}$ glass. J. Appl. Phys. 49, 1635–1637.

Osugi, T., Sukenaga, S., Inatomi, Y., Gonda, Y., Saito, N., Nakashima, K., 2013. Effect of oxidation state of iron ions on the viscosity of alkali silicate melts. ISIJ Int. 53, 185–190.

Roskosz, M., Toplis, M.J., Neuville, D.R., Mysen, B.O., 2008. Quantification of the kinetics of iron oxidation in silicate melts using Raman spectroscopy: what role of oxygen diffusion. Am. Mineral. 93, 1749–1759.

Rossano, S., Balan, E., Morin, G., Bauer, J.-P., Calas, G., Brouder, C., 1999. ^{57}Fe Mössbauer spectroscopy of tektites. Phys. Chem. Miner. 26, 530–538.

Rossano, S., Ramos, A.Y., Delaye, J.M., 2000. Environment of ferrous iron in $CaFeSi_2O_6$ glass: contributions of EXAFS and molecular dynamics. J. Non-Cryst. Solids 273, 48–52.

Sanloup, C., Drewitt, J.W.E., Crépisson, C., Kono, Y., Park, C., McCammon, C., Hennet, L., Brassamin, S., Bytchkov, A., 2013. Structure and density of molten fayalite at high pressure. Geochim. Cosmochim. Acta 118, 118–128.

Sipowska, J.T., Atake, T., Mysen, B.O., Richet, P., 2009. Entropy and structure of oxidized and reduced iron-bearing silicate glasses. Geochim. Cosmochim. Acta 73, 3905–3913.

Stebbins, J.F., 1987. Identification of multiple structural species in silicate glasses by ^{29}Si NMR. Nature 330, 465–467.

Sugawara, T., Akaogi, M., 2004. Calorimetry of liquids in the system Na_2O-Fe_2O_3-SiO_2. Am. Mineral. 89, 1586–1596.

Tangeman, J.A., Lange, R.A., 1998. The effect of Al^{3+}, Fe^{3+}, and T^{i4+} on the configurational heat capacities of sodium silicate liquids. Phys. Chem. Miner. 26, 83–99.

Tangeman, J.A., Lange, R., Forman, L., 2001. Ferric-ferrous equilibria in K_2O-FeO-Fe_2O_3-SiO_2 melts. Geochim. Cosmochim. Acta 65, 1809–1819.

Taylor, M., Brown, G.E., 1979. Structure of mineral glasses. II. The SiO_2-$NaAlSiO_4$ join. Geochim. Cosmochim. Acta 43, 1467–1475.

Toplis, M.J., Dingwell, D.B., Hess, K.-U., Lenci, T., 1997. Viscosity, fragility, and configuration entropy of melts along the join SiO_2-$NaAlO_2$. Am. Mineral. 82, 979–990.

Ueda, K., Doi, S., 1995. Interdiffusivity of FeO-CaO in FeO-CaO-SiO_2 melts by means of electrochemical method. J. Jap. Inst. Met. 59, 164–168.

Vercamer, V., Lelong, G., Hijiya, H., Kondo, Y., Galoisy, L., Calas, G., 2015. Diluted Fe^{3+} in silicate glasses: structural effects of Fe-redox state and matrix composition. An optical absorption and X-band/Q-band EPR study. J. Non-Cryst. Solids 428, 138–145.

Virgo, D., Mysen, B.O., 1985. The structural state of iron in oxidized vs. reduced glasses at 1 atm: A ^{57}Fe Mössbauer study. Phys. Chem. Miner. 12, 65–76.

Virgo, D., Mysen, B.O., Danckwerth, P.D., 1983. Redox equilibria and the anionic structure of $Na_2O.xSiO_2$-Fe-O melts: effects of oxygen fugacity. In: Carnegie Instn. Washington Year Book.vol. 82. pp. 305–308.

Waff, H.S., 1977. The structural role of ferric iron in silicate melts. Can. Mineral. 15, 198–199.

Wang, Z., Cooney, T.F., Sharma, S.K., 1993. High temperature structural investigation of $Na_2O\bullet 0.5Fe_2O_3\bullet 3SiO_2$ and $Na_2O\bullet FeO\bullet 3SiO_2$ melts and glasses. Contrib. Mineral. Petrol. 115, 112–122.

Waseda, Y., Toguri, J.M., 1978. The structure of the molten FeO-SiO_2 system. Metall. Trans. B 9, 595–601.

Waseda, Y., Shiraishi, Y., Toguri, J.M., 1980. The structure of the molten FeO-Fe_2O_3-SiO_2 system by X-ray diffraction. Trans. Jpn. Inst. Metall. 21, 51–62.

Waychunas, G.A., Brown, G.E., Ponader, C.W., Jackson, W.E., 1988. Evidence from x-ray absorption for network-forming Fe^{2+} in molten alkali silicates. Nature 332, 251–253.

Weigel, C., Cormier, L., Calas, G., Galoisy, L., Bowron, D.T., 2008. Nature and distribution of iron sites in a sodium silicate glass investigated by neutron diffraction and EPSR simulation. J. Non-Cryst. Solids 354, 5378–5385.

Whittaker, E.J.W., Muntus, R., 1970. Ionic radii for use in geochemistry. Geochim. Cosmochim. Acta 34, 945–957.

Wilke, M., Behrens, H., Burkhard, D.J.M., Rossano, S., 2002. The oxidation state of iron in silicic melt at 500 MPa water pressure. Earth Planet. Sci. Lett. 189, 55–67.

Wilke, M., Farges, F., Partzsch, G.M., Schmidt, C., Behrens, H., 2007. Speciation of Fe in silicate glasses and melts by in-situ XANES spectroscopy. Am. Mineral. 92, 44–56.

Wong, J., Angell, C.A., 1976. Glass Structure by Spectroscopy. Marcel Dekker Inc., New York.

CHAPTER

12

Titanium-Bearing Systems

OUTLINE

12.1 INTRODUCTORY REMARKS

Under oxidizing conditions, titanium has the same 4+ electrical charge as silicon. Its ionic radius (fourfold coordinated, 0.42 Å; sixfold coordinated, 0.61 Å), is 60% greater than that of fourfold Si^{4+}, so that Ti^{4+} might not be expected to substitute for Si^{4+} in SiO_4 tetrahedra, at least at low pressure. Umixing occurs in TiO-SiO_2 melts and glasses at comparatively low TiO_2 concentrations because of structural incompatibilities of Si^{4+} and Ti^{4+} (DeVries and Roy, 1954; Kirschen et al., 1999). It is not surprising, therefore, that Ti^{4+} in crystalline materials often occurs in sixfold coordination with oxygen as exemplified by rutile (TiO_2)

https://doi.org/10.1016/B978-0-444-63708-6.00012-0

(Howard et al., 1991). However, titanium can also be found in four- and fivefold coordination in crystalline materials such as Mg_2TiO_4 and $Ba_2TiSi_2O_8$ (Wechsler and Von Dreele, 1989; Moore and Louisnathan, 1969).

In glasses and melts, the situation is perhaps even more complex. Titanium may be a network former on its own, at least under some circumstances, or may perhaps exist in the form of oxy-titanate complexes, analogous to silicate and phosphate complexes (see Chapters 7, 9, and 13). Titanate complexing seems to rely on some form of association with metal cations where the properties of the metal cations themselves have an impact on titanate formation (Farges, 1999; Henderson and St-Amour, 2004). Titanium also may exist in fivefold coordination in molten TiO_2 and TiO_2-SiO_2 (Henderson and Fleet, 1997; Alderman et al., 2014). As a result, physical properties of Ti-bearing silicate glasses and melts can be complex functions of temperature, titanium concentration, and chemical composition.

These complex relationships have a direct bearing on properties of Ti-bearing silicates both for commercial purposes and in magma in the earth. For example, TiO_2 has long been used as a nucleating agent in glass ceramics (e.g., Strnad, 1986), where crystallization often develops after liquid unmixing induced by small amounts of Ti^{4+}, which results in a poor glass-forming melt (Maurer, 1962). Titanosilicate glasses are also of interest because of their unusual physical and chemical properties. A striking example is provided by Ti-bearing silica glasses, the thermal expansion of which is lower than that of pure SiO_2 (Nordberg, 1942; Schultz, 1976). Other glass properties that can be controlled by TiO_2 include tensile strength, refractive index, compressibility, and resistance to corrosion (Morsi and El-Shennawi, 1984; Shelby, 2005; Duffy, 2006; Liu and Lange, 2001; Scannell et al., 2015). TiO_2 is ubiquitous in igneous rocks with a typical abundance up to 2–3 wt%. Even at such contents, the presence of Ti affects important features such as liquidus phase relations (DeVries and Roy, 1954; Duan et al., 1998; Danek and Nerad, 2002) and liquid immiscibility (Visser and Van Groos, 1979; Kirschen et al., 1999; Hudon and Baker, 2002). Of course, the influence of TiO_2 is still stronger when its abundance reaches 10 wt%, as observed in some lunar glasses (Reid et al., 1973; Van der Kaaden et al., 2015) and in some alkali-rich, silica-poor igneous rocks (Mitchell, 1991).

12.2 TITANIUM REDOX REACTIONS

It is customary to deal solely with titanium in its 4+ oxidation state, although titanium is a transition element the 3+ valence of which can be stabilized under moderately reducing conditions. This neglect of Ti^{3+} is reflected in the scarcity of studies devoted to determining the temperature, composition, and pressure dependences of Ti^{3+}/Ti^{4+} ratios. However, for circumstances under which the redox state of Ti has been examined experimentally, there are many features that resemble those of other redox pairs (Johnson, 1965; Schreiber et al., 1978; Tranell et al., 2002).

The simple redox reaction:

$$4Ti^{4+} + 2O^{2-} \Leftrightarrow 4Ti^{3+} + O_2, \tag{12.1}$$

can be employed to examine the redox relations of titanium. This reaction is a function of both temperature and redox conditions (oxygen fugacity) (Johnson, 1965; Schreiber, 1977; Schreiber et al., 1978; Iwamoto et al., 1983; Morinaga et al., 1994; Ehrt et al., 2001; Tranell et al., 2002). There are also systematic relationships between redox ratio, silicate composition, and total Ti concentration (Tranell et al., 2002). For example, there are linear relationships between log Ti^{3+}/Ti^{4+} and log (oxygen fugacity) with a slope of 4 at constant temperature and silicate composition (Fig. 12.1) (see also Johnson, 1965; Schreiber, 1977; Schreiber et al., 1978; Iwamoto et al., 1983). A slope of 4 would suggest that the activity coefficient ratio of Ti^{3+} and Ti^{4+} is near unity because mol fractions rather than activity were used in Fig. 12.1. This activity coefficient ratio, $\gamma Ti^{3+}/\gamma Ti^{4+}$, depends somewhat on total Ti concentration and increases with titanium concentration (Tranell et al., 2002). However, the redox state varies in a rather unusual fashion with a minimum redox ratio value as a function of increasing Ti concentration, at least in the CaO-SiO_2-TiO_2 system where such experimental data are available (Fig. 12.2A). Titanium is increasingly oxidized (at fixed temperature and oxygen fugacity) the more depolymerized (higher NBO/Si) the silicate melt structure (Fig. 12.2B).

The strong composition and temperature dependences of the equilibrium constant of reaction (12.1) are apparent in Fig. 12.1. The Ti^{3+}/Ti^{4+} ratio increases by nearly a factor of 10 for a temperature rise of 50°C (Schreiber et al., 1978). Under the same conditions, the equilibrium constant differs by nearly two orders of magnitude for the two alkaline earth aluminosilicate

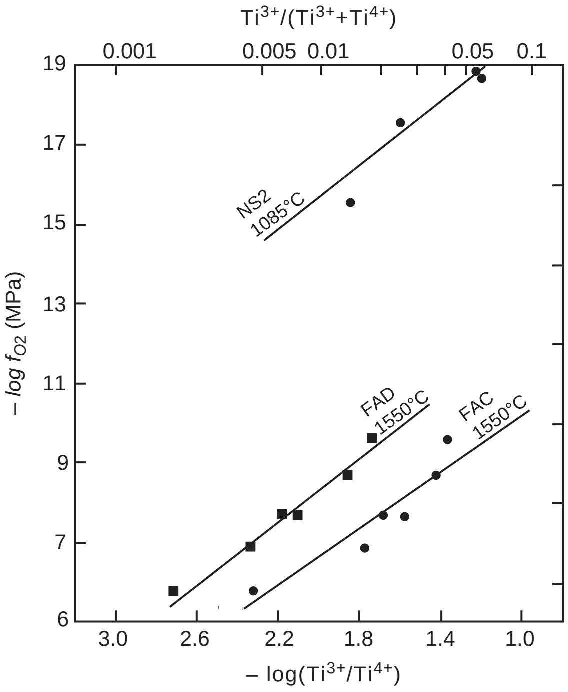

FIG. 12.1 Redox equilibrium of titanium against oxygen fugacity at the indicated temperatures in sodium disilicate (Johnson, 1965) and in two aluminosilicate melts (Schreiber et al., 1978). In the latter cases 1.3 wt% was added to FAD (54.2 SiO_2, 9.9 Al_2O_3, 5.6 CaO, and 30.3 wt% MgO) and to FAC (51.6 SiO_2, 2.3 Al_2O_3, 19.2 CaO, and 26.9 wt% MgO).

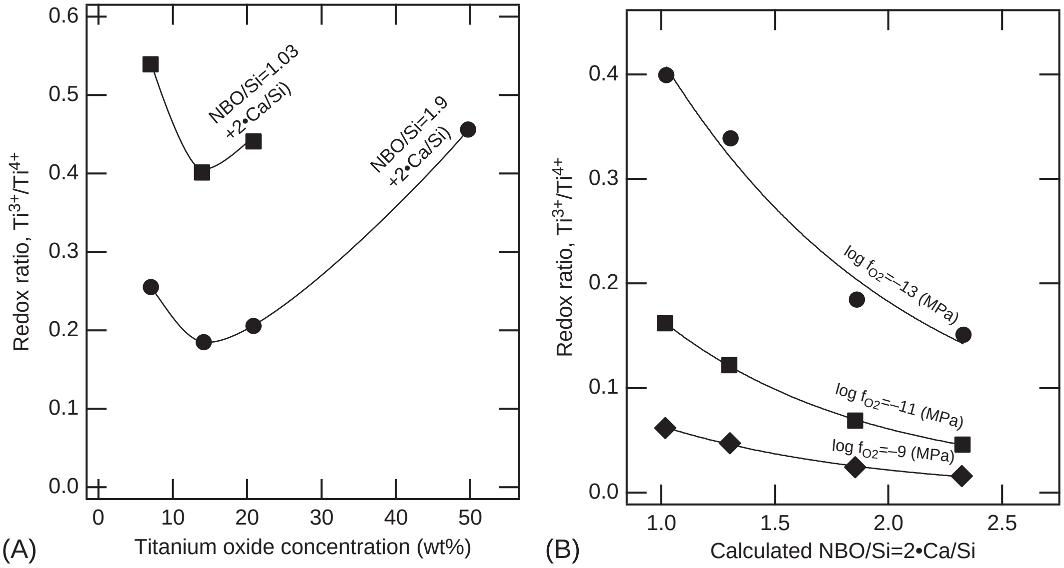

FIG. 12.2 Redox ratio of titanium as a function of silicate composition. (A) Redox ratio as a function of total titanium oxide concentration for two different Ca/Si-ratios (as indicated). The NBO/Si-value for the Ca-silicate was calculated from silicate composition as indicated on individual curves. (B) Redox ratio of titanium as a function of melt composition, Ca/Si, and melt polymerization, NBO/Si, calculated as indicated for redox conditions (oxygen fugacity, f_{O2}) as indicated on individual curves (Tranell et al., 2002).

melts considered. The Ca-aluminosilicate melts are considerably more oxidized than those where both Ca^{2+} and Mg^{2+} are network-modifiers. This simple relationship between electronic properties and the redox ratio of Ti is also analogous to that of other redox pairs such as Fe^{2+}/Fe^{3+} (Chapter 10, Section 10.4.1).

As for any redox reaction, the most reduced valence is favored by higher temperatures, with the result that the abundance of Ti^{3+} could become significant in melts equilibrated in air at temperatures above about 2000°C. Moreover, there is a simple linear relationship between the logarithm and the titanium redox ratio and $1/T$ (K) (Fig. 12.3), which is again analogous to the observation for redox relations in iron-bearing silicate glasses and melts (Chapter 10, Section 10.4.2).

There is a simple linear relationship between the log of the redox ratio of Ti and the reciprocal temperature, $1/T$ (Fig. 12.3). For the $Na_2O{\cdot}2SiO_2$ melt in Fig. 12.3, a linear fit to the datapoints yields an enthalpy change of 86 ± 2 kJ/mol for reaction (12.1), which compares well with the $\triangle H$ for an analogous redox equilibrium of iron in the same melt composition (Chapter 10, Fig. 10.11).

All experimental work mentioned in the rest of this chapter has been performed in air at temperatures that were not extremely high. This will justify the assumption that titanium was essentially in the form of Ti^{4+} ions. Possible effects of Ti^{3+} can be important, however, when dealing with titanosilicates with oxygen fugacity lower than 10^{-6} to 10^{-7} MPa.

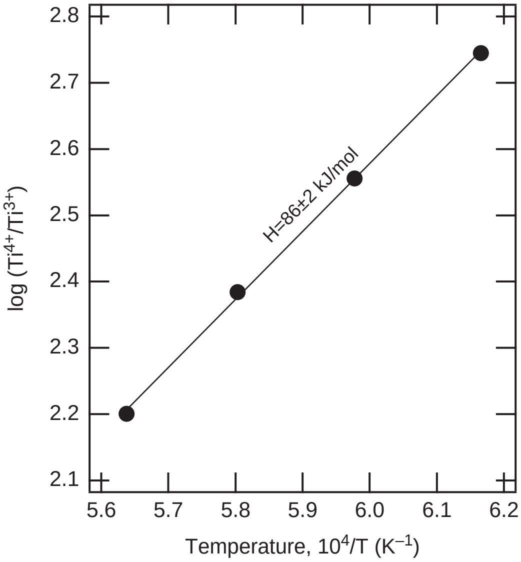

FIG. 12.3 Redox ratio of titanium as a function of temperature (1/*T*, Kelvin) of $Na_2O{\cdot}2SiO_2$ melt (Ehrt et al., 2001).

12.3 MELTING RELATIONS

12.3.1 Liquidus Relations in Binary, Ternary, and More Complex Systems

The melting temperatures of crystalline TiO_2 polymorphs range between 1825°C and 1855°C. Melting and crystallization phase relations in binary TiO_2-SiO_2 and in ternary alkali and/or alkaline earth-TiO_2-SiO_2 systems may highlight the similarities and differences between Ti^{4+} associated with these two different groups of metal cations.

12.3.1.1 TiO_2-SiO_2

Phase relations in the binary system TiO_2-SiO_2 characteristically are quite simple, as there are no intermediate compounds between the SiO_2 and TiO_2 endmembers (Fig. 12.4). Moreover, it is only within the 0–15 mol% TiO_2 concentration range in SiO_2 melt that homogenous glasses can be quenched. Liquid miscibility is restricted to narrow composition intervals at both ends of the diagram with a wide immiscibility gap in between. As noted by DeVries and Roy (1954), this immiscibility is not only stable but is such that "two liquids separate almost immediately owing to the difference in physical properties." From their own experiments and thermodynamic modeling of the miscibility gap, Kirschen et al. (1999) suggested that the critical point of the solvus is near 2600 K.

A freezing point depression of 170°C is found for cristobalite at the eutectic point near 1550°C and 10 mol% TiO_2. This decrease contrasts with the lesser 50°C depression of rutile at the other end of the system. Compared with binary silicate systems, the solvus has the peculiarity of being displaced away from SiO_2 instead of being located near SiO_2.

FIG. 12.4 The TiO_2-SiO_2 phase diagram. Solid-liquid equilibrium (DeVries and Roy, 1954), which is consistent with the observations of McTaggart and Andrews (1957), and solvus from Kirschen et al. (1999), with an estimated critical temperature of 2612±25 K.

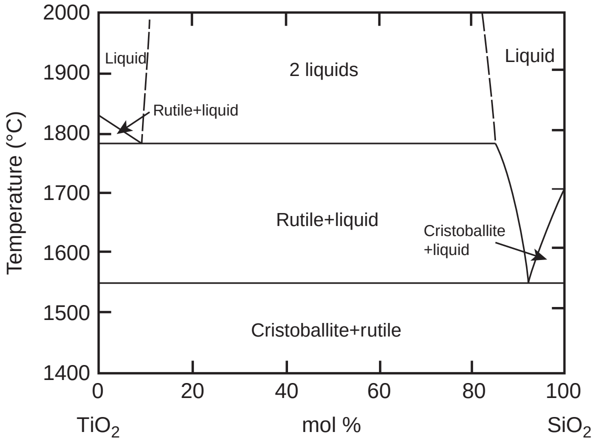

An analogous contrast exists for the solid phases of SiO_2 and TiO_2. There is no significant solid solution of SiO_2 in rutile, which is isostructural with stishovite (the high-pressure structural form of silica with Si^{4+} in sixfold coordination—see Chapter 5—similar to Ti^{4+} in the rutile structure). In contrast, up to about 10 mol% TiO_2 can dissolve in crystalline cristobalite when TiO_2-SiO_2 glasses crystallize at 1450°C. The lattice parameters of the cristobalite increase linearly with TiO_2 content (Evans, 1982). In spite of its strong preference for octahedral coordination, Ti^{4+} can thus enter in significant amounts in the open three-dimensional tetrahedral networks of the solid and liquid phases of SiO_2.

12.3.1.2 TiO_2-Al_2O_3-SiO_2

No complete phase diagram of the system TiO_2-Al_2O_3-SiO_2 has been published, but the melting relationships should be represented reasonably well with the calculations of Kirschen et al. (1999), shown in Fig. 12.5. The phase diagram is extremely simple because there are no ternary compounds on the liquidus. In contrast to the wide miscibility gap along the TiO_2-SiO_2 join (Fig. 12.4), there is a mixed compound and two eutectics points along both limiting Al_2O_3-bearing binary joins (Fig. 12.5). This observation suggests that Al^{3+} can act as linkage between Si^{4+} and Ti^{4+}. Accordingly, Al_2O_3 causes the miscibility gap seen in the limiting TiO_2-SiO_2 system to shrink. The ternary miscibility gap is, in fact, slightly asymmetric, such that Al_2O_3 partitions preferentially into the TiO_2-rich melt (or, conversely, such that Ti^{4+} partitions preferentially into the Al-rich phase). This observation is consistent with a stronger affinity of Al^{3+} for Ti^{4+} than for Si^{4+}, at least in the TiO_2-Al_2O_3-SiO_2 system, where metals are lacking for charge compensation of Al^{3+} in tetrahedral coordination with oxygen. This effect may also be seen in the enhanced Ti^{4+} solubility compared with that along meta-aluminosilicate joins where metal cations are available for charge-compensation of tetrahedral Al^{3+}. This affinity is also suggested by larger freezing-point depressions in the TiO_2-Al_2O_3 than in the SiO_2-Al_2O_3 system bounding systems (Kirschen et al., 1999). The major effect, however, is the shrinkage of the miscibility gap upon addition of Al_2O_3. With 2.5 mol%, the critical temperature decreases from 2600 to 1800 K and the gap eventually disappears at a slightly higher Al_2O_3 content (Fig. 12.5).

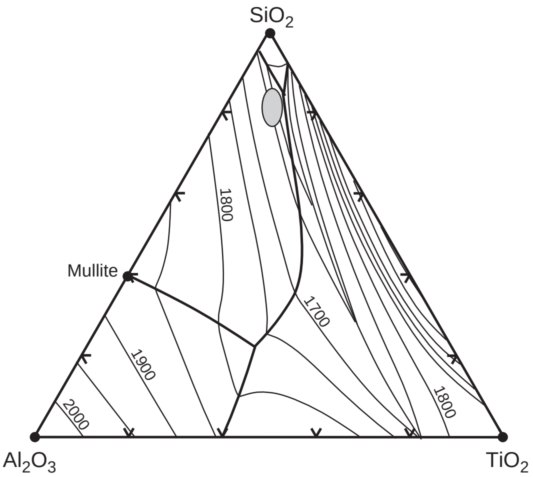

FIG. 12.5 Liquidus phase relations of the TiO_2-Al_2O_3-SiO_2 system (from calculations by Kirschen et al. (1999)). The $TiAl_2O_5$ binary compound melts at 2127 K. Its eutectic with TiO_2 is at 1971 K and 82 mol% TiO_2. Stable liquid unmixing near the TiO_2-SiO_2 join where isotherms are narrowly spaced. Glass formation in the gray area (Kajiwara, 1988). See Kirschen et al. (1999) for sources of experimental data used in the calculations.

12.3.1.3 $M^{n+}_{n/2}$-TiO_2-SiO_2

By substituting for Si^{4+} in tetrahedral coordination, Ti^{4+} would differ markedly from Al^{3+} because it does not need to associate with a charge-compensating cation. Hence, no analogies are to be drawn between the properties of alkali or alkaline earth titanosilicate melts and their aluminosilicate counterparts, save for regular variations induced by differences in the ionization potential of the M-cation. As for Al^{3+} in aluminosilicates, however, one does observe that Ti^{4+} has a greater affinity for alkali than for alkaline earth cations, an affinity that may relate to formation of titanate complexes, be it in molten, glassy, or crystalline form (Wechsler and Von Dreele, 1989; Moore and Louisnathan, 1969; Dickinson and Hess, 1985; Gwinn and Hess, 1989)

Marked contrasts in liquidus temperatures, ternary compounds, and extent of glass formation between alkali and alkaline earth systems are evident in the ternary metal oxide–TiO_2 SiO_2 phase diagrams (Fig. 12.6). There is less of an effect of metal cation on miscibility gaps because the single shared feature is the field of liquid immiscibility that develops near the TiO_2 endmember. The width of the miscibility gap increases only marginally in the order $Na < Ca < Mg$. The real differences in the extent of liquid immiscibility seen in Fig. 12.6 originate in unmixing in the silica-rich parts of the diagrams.

For alkaline earth titanosilicates, the liquidus temperatures are higher in the MgO-SiO_2-TiO_2 than in the CaO-SiO_2-TiO_2 system. Interestingly, ternary crystalline phases on the liquidus in these two systems are scarce, with only a single ternary compound in the Ca system (titanite, $CaTiSiO_5$) and none in the Mg system (Fig. 12.6). Only along the CaO-TiO_2 and MgO-TiO_2 binaries do we find two Ca titanates—perovskite ($CaTiO_3$) and $Ca_3Ti_2O_7$—and three Mg titanates ($MgTi_2O_5$, $MgTiO_3$, and Mg_2TiO_4), whose melting temperatures range from 1550°C to 1970°C. Solid solutions in crystalline materials are lacking. The only known exception is the solubility of a few wt% of $CaTiO_3$ in $CaSiO_3$ which, curiously, has been observed, not in the liquidus phase, pseudowollastonite, but in the subliquidus phase, wollastonite (DeVries et al., 1955). Consistent with the relationship noted in Chapter 3 between

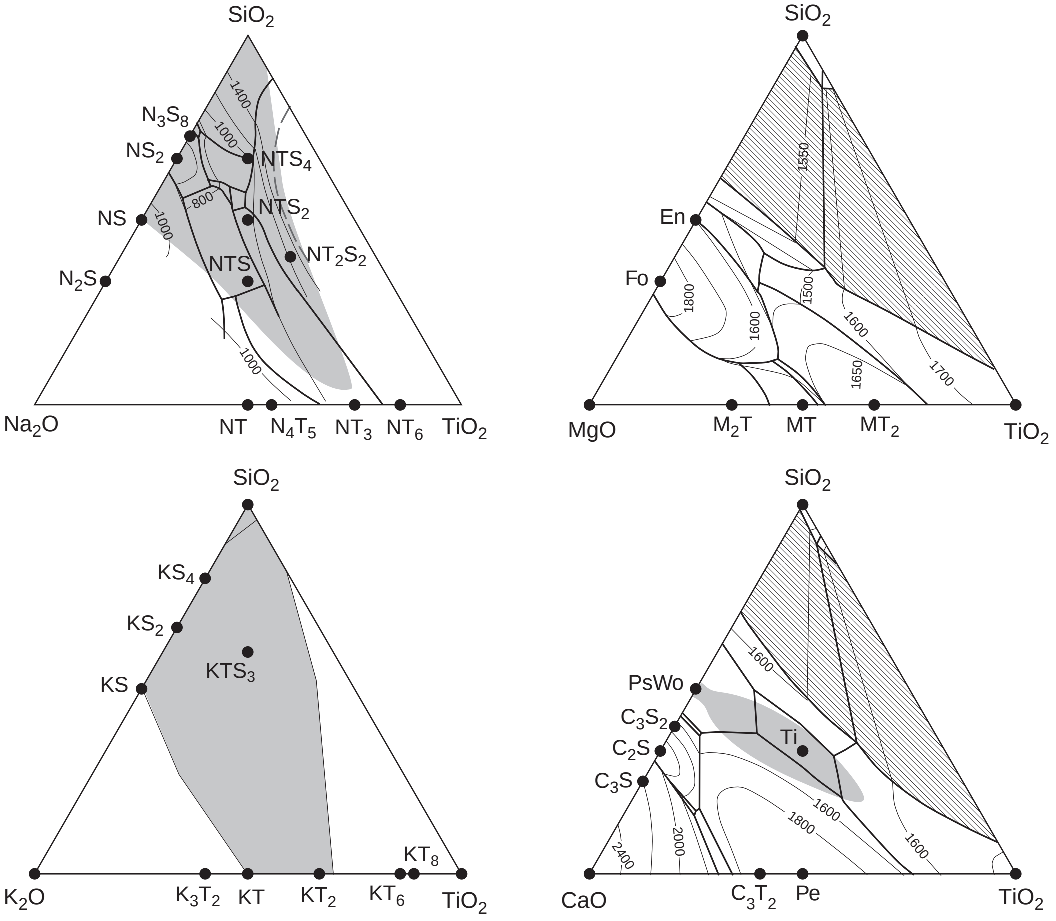

FIG. 12.6 Liquidus phase relations of ternary titanosilicate systems, including stable miscibility gaps (as hachured areas) and glass formation (as gray areas). Data sources: Na-system: Glasser and Maar (1979) and Hamilton and Cleek (1958), K-system: Rao (1963) for K, Mg-system: Massazza and Sirchia (1958), Ca-system: DeVries et al. (1955). All diagrams are shown in mol%.

difficulty of vitrification and scarcity of liquidus compounds, glass formation requires unusually rapid quenching, particularly for the Mg system. Glass formation is restricted to the eutectic valleys that runs from the metal oxide-silica systems toward the center of the diagrams (Fig. 12.6), a feature that is also observed for barium titanosilicates (Cleek and Hamilton, 1956). Under similar quenching conditions, the compositional extent of vitrification increases in the order Mg < Ca < Ba.

Less information is available for alkali titanosilicates. Liquidus data seem to be lacking for the potassium system. Potassium-bearing titanosilicate glasses can, nonetheless, be quenched from 1100°C in a large composition range (Rao, 1963). This observation leads to the suggestion that liquidus temperatures should not be higher than those determined by Glasser and Maar (1979) for the sodium system outside of the miscibility gap (Fig. 12.6), where liquidus temperatures do not vary much with Ti content.

The important difference with alkaline earth systems lies in a large number of binary and ternary compounds in alkali titanosilicate systems. There are four sodium titanates (Na_2TiO_3, $Na_8Ti_5O_{14}$, $Na_2Ti_3O_7$, and $Na_2Ti_6O_{13}$) with melting points between 1030°C and 1300°C. There are also four ternary compounds (Na_2TiSiO_5, $Na_2TiSi_2O_7$, $Na_2Ti_2Si_2O_9$, and $Na_2TiSi_4O_{11}$), which begin to melt, incongruently for three of them, at temperatures lower than 965°C. Therefore, the affinity between TiO_2 and alkali oxides in crystalline materials likely is not coupled with very strong bonding. Finally, vitrification is easy not only for the K but also for the Na system and takes place throughout most of the composition ranges where melts can be prepared (Glasser and Maar, 1979; Rao, 1963). Glass formation even extends to the binary K_2O-TiO_2 join near the 1:1 oxide ratio. This topology would be consistent with a dual structural role of Ti^{4+} in the latter system. Not only can Ti be a network-modifier but, as stressed by Rao (1963), its glass-forming ability implies that it can also be a network-former in the sense discussed in Chapter 4.

12.3.1.4 *Multicomponent Systems*

Titanosilicates are good model systems to determine whether information gathered on binary and ternary simple melts can be extrapolated to more complicated compositions. In chemically more complex melts, the presence of TiO_2 also causes an expansion of liquid miscibility gaps (Hudon and Baker, 2002), as observed in the K_2O-FeO-Al_2O_3-SiO_2 system (Visser and Van Groos, 1979). In this system, TiO_2 partitions preferentially into the less SiO_2-rich melt (Fig. 12.7). Conversely, Al^{3+} very effectively suppresses liquid immiscibility in quaternary titanoaluminosilicates. In the CaO-MgO-TiO_2SiO_2 system, Ti^{4+} also partitions into the SiO_2-poor melt but it does so less efficiently than the other cations (Wood and Hess, 1980). The result is that TiO_2 is the most abundant oxide, after SiO_2, in the SiO_2-rich phase. As for the network-forming character of Ti, it also manifests itself by the presence of 2 wt% TiO_2 in cristobalite on the liquidus

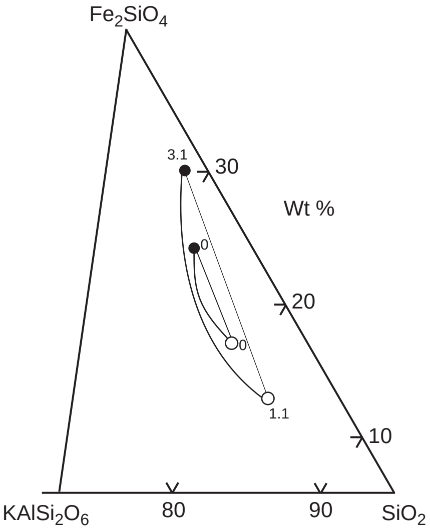

FIG. 12.7 Variation of the extent of miscibility gap with TiO_2 content in the system $KAlSi_2O_6$-Fe_2SiO_4-SiO_2-TiO_2: composition of SiO_2-rich (*open circles*) and mafic (*solid circles*) liquids, the numbers denote wt% TiO_2. *Redrawn from Visser and Koster Van Groos (1979).*

12.3.2 Titanium Solubility in Silicate Melts and Glasses

Some solubility information can be derived from the liquidus surfaces discussed in the previous section. As seen in the binary TiO-SiO_2 diagram (e.g., Fig. 12.4) (see also DeVries and Roy, 1954), the TiO_2 solubility maximum in SiO_2 melt in equilibrium with rutile is near 15 mol% near 1800°C and decreases to less than 10 mol% at the eutectic near 1560°C. Increasing solubility with increasing temperature also has been reported for chemically more complex systems (Ryerson and Watson, 1987; Green and Adam, 2000; Gaetani et al., 2008). In addition, the two last studies reported a decreasing solubility with increasing pressure. Furthermore, the solubility increases and the pressure effects decrease as the silicate melt becomes depolymerized (Figs. 12.8 and 12.9). Interestingly, the temperature dependence of TiO_2 solubility is more pronounced in depolymerized melts.

Rutile solubility determinations also have been used to investigate the competition of Ti^{4+} and Al^{3+} for association with K^+ and Ca^{2+} in aluminosilicate melts (Dickinson and Hess, 1985). The saturation concentration of TiO_2 varies little with the $CaO/(CaO+Al_2O_3)$ ratio (open symbols in Fig. 12.8), which illustrates the nonspecificity of the interaction between Ti^{4+} and Ca^{2+} whether Al^{3+} is present or not. In contrast, the TiO_2 saturation concentration increases markedly with $K_2O/(K_2O+Al_2O_3)$, but it does so only after the meta-aluminous join has been crossed and composition shifts into the peralkaline composition range (closed symbols in Fig. 12.8). Hence, there appears to be a definite affinity of Ti^{4+} for K^+ in the melt, which may outcompete Al^{3+} for charge-balance.

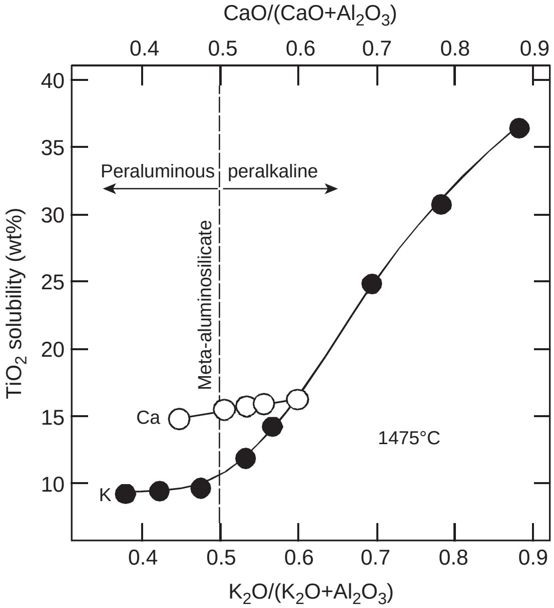

FIG. 12.8 Solubility of rutile in M-aluminosilicates against $M^{n+}_{n/2}O/(M^{n+}_{n/2}O+Al_2O_3)$ at 1475°C with $M=K^+$ and Ca^{2+} as indicated (Dickinson and Hess, 1985).

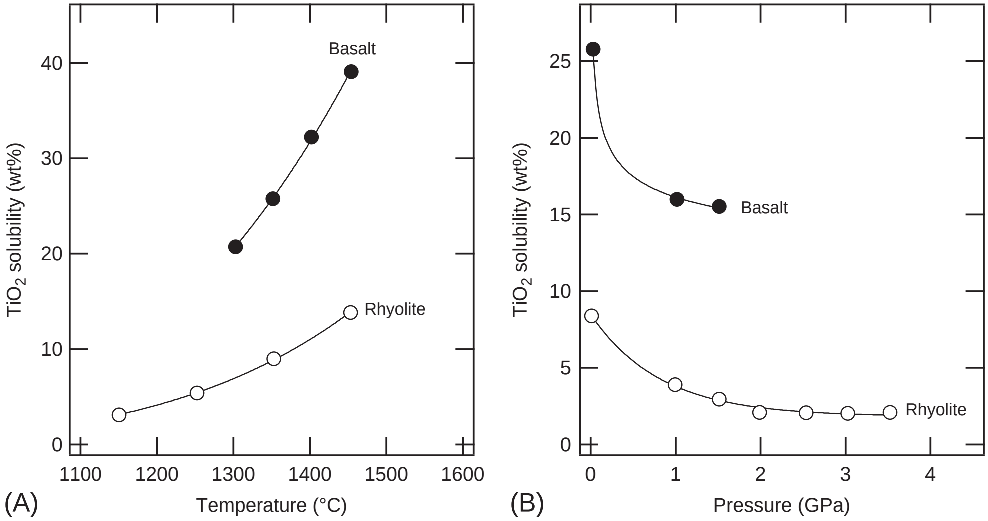

FIG. 12.9 TiO_2 solubility in rhyolite and basalt melt. (A) As a function of temperature at ambient pressure. (B) As a function of pressure at 1350°C (Gaetani et al., 2008).

12.4 THERMAL PROPERTIES

12.4.1 Activity-Composition Relations

Activity-composition relations may be extracted from liquidus phase relations as a function of TiO_2 and also from the redox relations under reducing conditions where both Ti^{3+} and Ti^{4+} are present in measurable abundances (Ryerson, 1985; Tranell et al., 2002). Calorimetric measurements can be used to extract mixing properties as well as to shed light on stability relationships among various Ti-bearing complexes (Gan et al., 1996; Linard et al., 2008). Configurational properties also can be related to mixing and other dynamic properties (Tangeman and Lange, 1998; Bouhifd et al., 1999).

Analysis of liquidus surfaces can be used to obtain information on the thermodynamic activity of a given melt component. The activity of SiO_2, a_{SiO2}, in a melt as a function of proportion of dissolved TiO_2 (or any other component) is given by the temperature depression of the liquidus surface of a silica polymorph and the enthalpy of fusion of the silica polymorph:

$$\ln a_{SiO2}(\text{melt}) = \left(\Delta H_{sio2}{}^{fusion}/R\right) \bullet (1/T_o - 1/T), \qquad (12.2)$$

where R is the gas constant, T_o is the melting point of pure SiO_2 (in kelvins) and T is the liquidus temperature of the mixture.

In the system TiO_2-SiO_2, Ryerson (1985) found values higher than unity for the activity coefficient of SiO_2, γ_{SiO_2}, determined from an analysis of the silica liquidus surface (see Chapter 8, Fig. 8.7). An increase of the activity coefficient of TiO_2 with SiO_2 content has been deduced from the saturation surface of TiO_2 in high-silica alkaline aluminosilicate melts (Ellison and Hess, 1986). A positive deviation from ideality is consistent with the unmixing observed at slightly higher TiO_2 content. The trend opposes that found for $KAlO_2$ and $NaAlO_2$, where the deviations from ideality are much smaller or slightly negative.

The activity coefficient ratio of Ti^{3+} and Ti^{4+} can be extracted from the redox data and the standard free energy for the reaction (Tranell et al., 2002):

$$TiO_2(\text{solid}) \Leftrightarrow TiO_{1.5}(\text{solid}) + 0.25O_2\,(\text{gas}). \tag{12.3}$$

From this treatment, the activity coefficient ratio of reduced and oxidized titanium in calcium silicate melts, $\gamma_{TiO_{1.5}}/\gamma_{TiO_2}$, has been found essentially independent of temperature but increasing with increasing titanium concentration (Tranell et al., 2002). There is also some $\gamma_{TiO_{1.5}}/\gamma_{TiO_2}$ variations as a function of melt structure so that $\gamma_{TiO_{1.5}}/\gamma_{TiO_2}$ is positively correlated with increasing NBO/Si of melt (Fig. 12.10).

12.4.2 Enthalpy, Entropy, and Heat Capacity

An enthalpy of reduction of Ti^{4+} to Ti^{3+} has been extracted from titanium redox data via the temperature-dependence of the redox equilibria (Schreiber et al., 1978; Tanabe and Suito, 1992; Tranell et al., 2002). From these rather limited redox data, the ΔH of reduction is between 152 ± 25 kJ/mol and 293 ± 96 kJ/mol. The ΔH range likely reflects the observation that the redox ratio of titanium depends on melt composition and, therefore, on structure (Tranell et al., 2002; see also Fig. 12.2).

The enthalpy of solution of rutile in silicate melts, ΔH_{sol}, can be used as a measure of the stability of Ti-bearing complexes (Gan et al., 1996; Linard et al., 2008). The enthalpy of solution

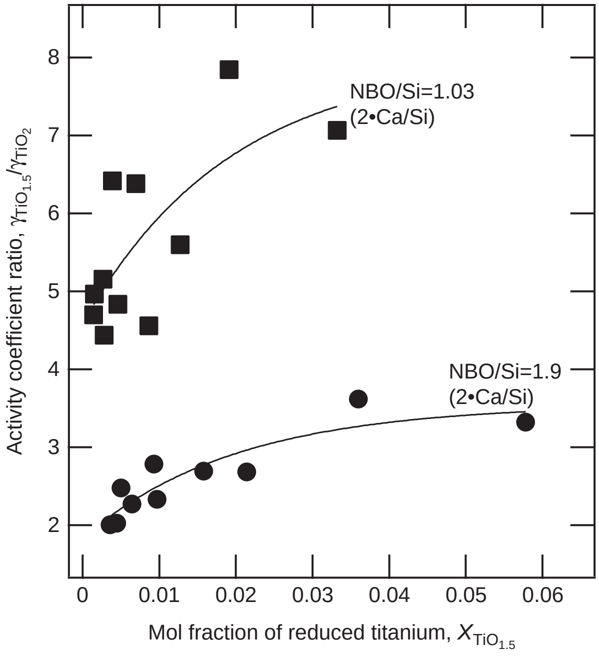

FIG. 12.10 Activity coefficient ratio of $TiO_{1.5}/TiO_2$ as a function of NBO/Si (=2·Ca/Si) of $CaO\text{-}SiO_2\text{-}TiO_2$ melt (Tranell et al., 2002).

generally is endothermic and, at least for alkali silicate melts, is insensitive to alkali metal type, but it does increase with increasing TiO_2 concentration. In addition, it increases when the alkali metal is replaced by an alkaline earth such as Ca^{2+} (Fig. 12.11), thus highlighting the important roles of metal cations in controlling the solution of TiO_2 in silicate melts. In mixed Ca,K melts, the ΔH_{sol} is a nonlinear function of endmember composition (Gan et al., 1996).

The influence of TiO_2 on heat capacity (C_p) was investigated by Richet and Bottinga (1985) to model the C_p of silicate melts as a function of temperature and composition. Two alkali titanosilicates ($M_2TiSi_2O_7$, M = Na, K) were selected because of the wide temperature intervals over which they could be studied. For both melts, the heat capacity decreases markedly with increasing temperature after an unusually large jump of about 50% at the glass transition (Fig. 12.12). At the highest temperatures investigated, the heat capacity of these melts tends to the values of their Ti-free counterparts. These variations are due only to the presence of TiO_2, as borne out by the fact that the same temperature-dependent partial molar heat capacity derived for TiO_2 can account for the experimental results. This applies not only to the two titanosilicates studied by Richet and Bottinga (1985), but also to the heat capacity of liquid $CaTiSiO_5$ (King et al., 1954). The anomalous temperature dependence of C_p thus appears independent of the nature of the M-cation.

Further experiments have confirmed not only the negative temperature dependence of C_p for titanosilicate melts (Lange and Navrotsky, 1993; Tangeman and Lange, 1998; Bouhifd et al., 1999), but also the lack of composition dependence for the partial molar heat capacity of TiO_2, at least for alkali systems (Bouhifd et al., 1999). Investigation of alkaline earth compositions in more detail would be interesting, but measurements on such compositions are made difficult by high liquidus temperatures and the mediocre glass-forming ability of alkaline earth titanosilicates. It is possible, however, to study the effect of TiO_2 in aluminosilicate liquids (Roskosz et al., 2004). Similar decreases of C_p with increasing temperatures were

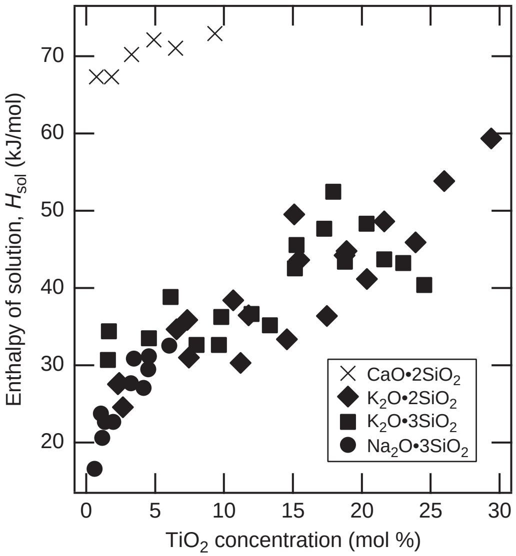

FIG. 12.11 Enthalpy of solution H_{sol} of rutile in melt compositions as indicated (Gan et al., 1996; Linard et al., 2008).

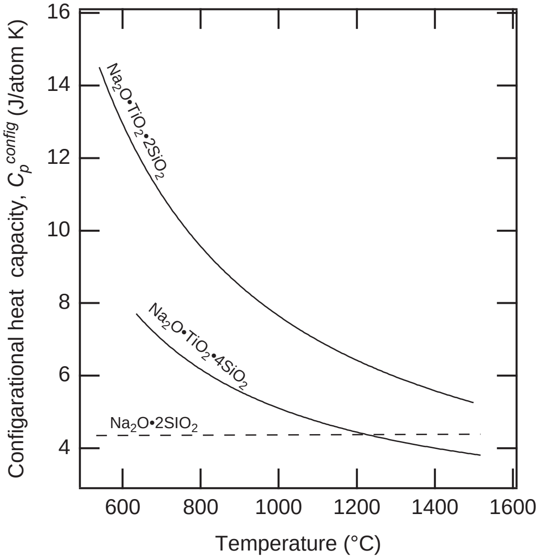

FIG. 12.12 Configurational heat capacity of Na titanosilicates and one of their Ti-free counterparts ($Na_2O·2SiO_2$). For comparison, the heat capacity at the glass transition is 25 J/g atom K (Richet and Bottinga, 1985; Bouhifd et al., 1999).

observed for several series of Ti-bearing sodium aluminosilicates. The C_p anomaly remains proportional to TiO_2 content.

As for other silicates, the glass transition of titanosilicates occurs when the glass heat capacity is near 3 R/g atom K (Lange and Navrotsky, 1993; Tangeman and Lange, 1998; Bouhifd et al., 1999; Roskosz et al., 2004). The entire C_p anomaly thus is clearly configurational in origin. This anomaly depends only on TiO_2 content in both Al-free and Al-bearing titanosilicates, even when all alkali cations serve as charge-compensators for Al^{3+}. As noted in Chapters 6 and 8 for Ti-free melts, this observation implies that the configurational heat capacity originates in interactions between structural entities that exist throughout the whole composition range of interest. Consistent with the fact that energy lies in short-range interactions, not in medium-range order (see Section 12.6.2), we thus conclude that the C_p anomaly of titanosilicates is due to short-range interactions of Ti with oxygen, and that the anomaly is affected little by possible changes of Ti^{4+} coordination with composition.

12.5 PHYSICAL PROPERTIES

Transport and other physical properties of Ti-silicate melts highlight significant effects of TiO_2 in solution. Several properties, including viscosity, fragility, diffusivity, glass transition temperature, volume, compressibility, and expansion, are quite sensitive to TiO_2 concentrations (Dingwell, 1992a, b; Knoche et al., 1995; Bouhifd et al., 1999; Liu and Lange, 2001; Roskosz et al., 2004; Shelby, 2005; Liu et al., 2007; Zhang et al., 2014; Dong et al., 2014). Among these properties, viscosity and volume properties have attracted the most attention.

12.5.1 Transport Properties

The principal transport properties of interest are conductivity, diffusion, and viscosity. As discussed in Chapter 4, Section 4.6.1, these properties are linked via a simple network of relationships.

For TiO_2, available transport property data, except for viscosity, are somewhat limited. Essentially the only data on TiO_2 diffusion are for TiO_2-SiO_2 melt between 1700°C and 2000°C (Kirchhof et al., 2014).

Interestingly, there is a positive correlation between melt viscosity and TiO_2 content at fixed temperature. Moreover, the activation enthalpy of viscous flow also is positively correlated with TiO_2 content, increasing from about 470 kJ/mol for pure SiO_2 to more than 550 kJ/mol for TiO_2-SiO_2 with 7 mol% TiO_2 (Kirchhof et al., 2014). This increase is unusual in that for other binary SiO_2-X melts, the viscosity decreases with increasing concentration of "X" components such as GeO_2, B_2O_3, and Al_2O_3 (Hoang et al., 2007; Kirchhof et al., 2007, 2012; Unger et al., 2011).

Titanosilicate melt viscosity (Fig. 12.13) provides a dramatic illustration of the quantitative link between configurational properties such as entropy, S^{conf}, and viscosity, η. Lange and Navrotsky (1993) pointed out that alkali titanosilicate melts undergo extensive structural rearrangements when the glass transition is approached in view of the anomalously high rate at which these liquids lose configurational entropy. The configurational entropy thus is exceptionally sensitive to both temperature and TiO_2 concentration (Bouhifd et al., 1999). It follows that the activation enthalpy for viscous flow must increase markedly at high viscosity, as predicted from the equation:

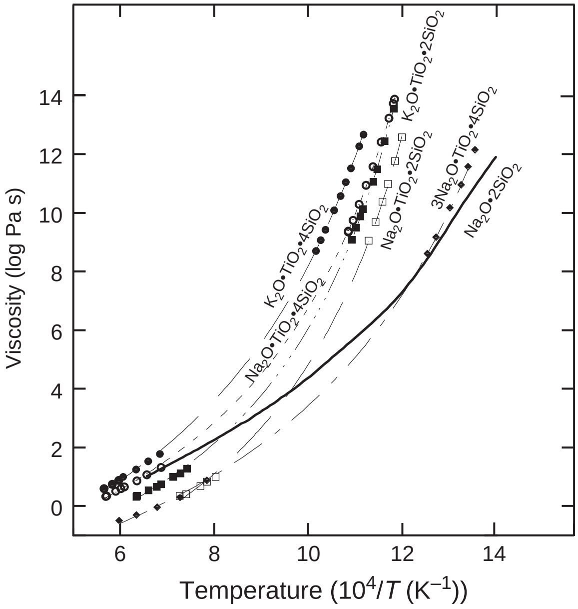

FIG. 12.13 Viscosity of alkali titanosilicate glasses and melts and one of their Ti-free counterparts (Bouhifd et al., 1999).

$$\text{Log}\,\eta = A_e + B_e/TS^{conf}, \tag{12.4}$$

where A_e and B_e are constants.

The viscosities measured by Bouhifd et al. (1999) for a series of alkali titanosilicate melts (Fig. 12.13) conform quantitatively to Eq. (12.4), where the temperature dependence of configurational entropy is calculated from the experimental C_p^{conf} data as illustrated in Fig. 12.12. The unusually steep increases in the viscosity of titanosilicate melts when the glass transition is approached are underscored by the comparison made in Fig. 12.13 with sodium disilicate melt. Moreover, there is a striking increase in fragility with increasing TiO_2 concentration in Ti silicate melts (Roskosz et al., 2004; see also Fig. 12.14). Interestingly, the high-temperature activation enthalpy of viscous flow does not depend on TiO_2 concentration (Dingwell, 1992a). Notably, increasing Al_2O_3 concentration in Ti-bearing Na_2O-Al_2O_3-SiO_2 melts reduces the fragility, perhaps because of association between Ti^{4+} and Al^{3+} in solution, as already suggested previously to explain the relationships between peraluminocity and TiO_2 solubility (Section 12.3.3 and Fig. 12.8). We remember that for melts in the Ti-free Na_2O-Al_2O_3-SiO_2 system, their viscosity is nearly Arrhenian (Chapter 8, Section 8.4.1). Clearly, dissolved Ti^{4+} profoundly affects viscous flow.

Whereas the viscosity of the Ti-free and Ti-bearing liquids is similar near 1600 K, it differs by more than six orders of magnitude at 800 K (e.g., Fig. 12.13). What remains to be determined is whether titanosilicate melts have a higher entropy than their Ti-free counterparts at high temperatures, or a lower entropy at low temperatures. Inspection of the configurational entropies derived with Eq. (12.4) from the viscosity data of Bouhifd et al. (1999)

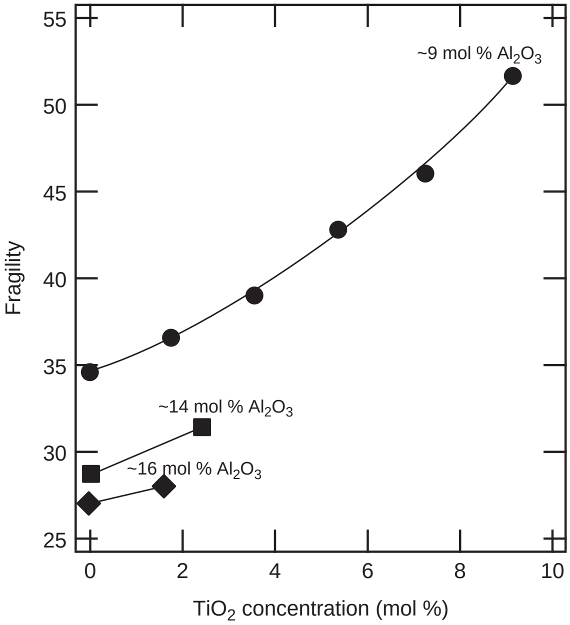

FIG. 12.14 Fragility of Ti-bearing Na_2O-Al_2O_3-SiO_2 melts as a function of their Al_2O_3 and TiO_2 contents (Roskosz et al., 2004).

indicates that the second alternative is correct. Hence, the presence of TiO_2 in a melt gives rise to additional mixing mechanisms compared to Ti-free melts.

The viscosity and its temperature derivative of Ti-bearing silicate melts are also quite sensitive to TiO_2 content (Dingwell, 1992a; Liska et al., 1997; Dong et al., 2014). At high temperatures, the effect of TiO_2 on melt viscosity, whether with alkali metals or alkaline earths, is large, but approximately the same with a viscosity change of about 0.01 log units per mol% TiO_2 dissolved in the melts. This variation also appears insensitive to temperature (Dingwell, 1992a). The activation energy of viscous flow also varies with TiO_2 content, but this variation depends on the nature of the metal cation and total TiO_2 concentration (Fig. 12.15). For alkali metasilicate melt such as Na_2SiO_3, the activation enthalpy passes through to a minimum value with increasing TiO_2, thus suggesting multiple transport mechanisms and, therefore, likely multiple solution mechanisms of TiO_2. For alkaline earth metasilicate melts, on the other hand, such minima cannot be detected. The activation enthalpy decreases with increasing TiO_2, and furthermore for any TiO_2 concentration it is greater (by as much as 30%) than for Na_2SiO_3-TiO_2 melt. These differences must be related to differences of the dissolved TiO_2 component because, in the absence of TiO_2, the activation enthalpy of viscous flow of $CaSiO_3$ melt is less than that of Na_2SiO_3 melt (Bockris et al., 1955).

Titanium effects on melt viscosity also are quite sensitive to temperature. For example, substitution of TiO_2 for SiO_2 in Na_2O-SiO_2 melts at high temperature results in a viscosity decrease, but in an increase at lower temperature, (Fig. 12.16). Hence, the viscosity increases with decreasing temperature caused by the heat capacity anomalies are so sharp that the composition dependence differs considerably at low and high temperatures. Near the glass transition, substitution of Ti^{4+} for Si^{4+} results in the viscosity decreasing by more than four orders of magnitude (Fig. 12.16).

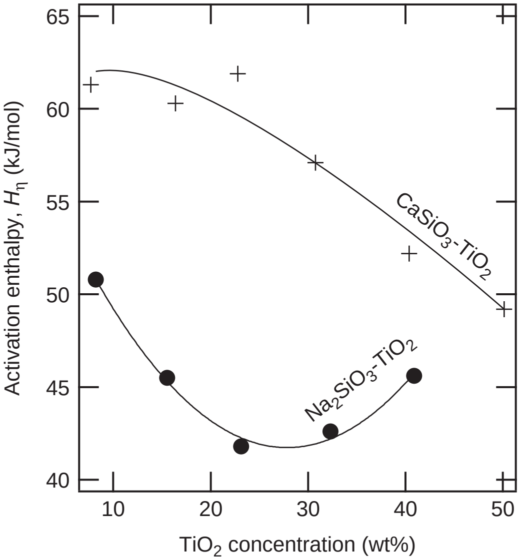

FIG. 12.15 Activation enthalpy of viscous flow of melts along the two joins, Na_2SiO_3-TiO_2 and $CaSiO_3$-TiO_2, as a function of TiO_2 concentration (Dingwell, 1992a).

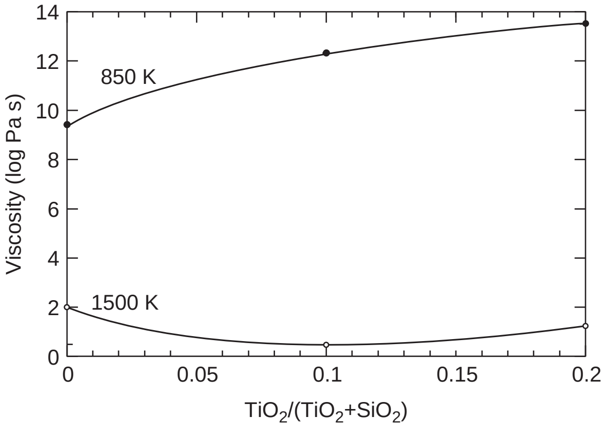

FIG. 12.16 Contrasting effects of Ti on the viscosity of sodium silicates at high and low temperatures at constant 17 mol% Na_2O content (Poole, 1948; Bockris et al. 1955; Bouhifd et al., 1999).

12.5.2 Volume, Expansion, and Compressibility

Volume-compressibility relationships in melts can be sensitive indicators of the nature of the oxygen ligands surrounding the metal cations. Volume relationships of Ti-bearing silicate are, therefore, of considerable interest.

12.5.2.1 Molar Volume

In an early study, Nelson and Carmichael (1979) concluded that in Ti-silicate melts with up to eight oxide components, the partial molar volume of TiO_2 has a constant value of 24.9 cm^3/mol at 1500°C. Lange and Carmichael (1987) found this value too low to account for their own observations on sodium titanosilicate melts, which instead yielded a volume of 28.3 cm^3/mol at 1500°C. This conclusion does not, however, find support in more recent and compositionally more extensive melt and glass systems where metal cation type, metal/silicon proportion, and TiO_2 concentration have been varied. All those compositional variables affect the partial molar volume of TiO_2 in the melts (Lange and Carmichael, 1987; Dingwell, 1991, 1992b; Knoche et al., 1995; Liu and Lange, 2001, Liu et al., 2007). Some of these effects are seen in Fig. 12.17 from volume measurements on melts along the joins Na_2SiO_3-TiO_2 and $CaSiO_3$-TiO_2 (Dingwell, 1992b). If thermal expansion were accounted for, the difference would be even greater between the partial molar volume values of TiO_2 in melts of 27.6 and 24.3 cm^3/mol found at 1150°C and 1600°C for the Na and Ca systems, respectively. However, because the volume versus TiO_2 relations differ, at the same temperatures, the partial molar volume of TiO_2 in $CaSiO_3$ and Na_2SiO_3 melts would become more similar with increasing TiO_2 concentration (Dingwell, 1992b). Of course, for glasses the partial molar volumes of TiO_2 are greater than in melts of the same composition by 1%–3% (Knoche et al., 1995).

The TiO_2 partial molar volume value of 24.3 cm^3/mol for $CaSiO_3$-TiO_2 melt fits very well with the volume of molten TiO_2 measured at higher temperatures (24.11 cm^3/mol at 1600°C, e.g.; see Dingwell, 1991). At room temperature, the molar volume of rutile is 18.9 cm^3/mol, that of anatase (the other TiO_2 form with sixfold coordinated Ti) is 20.5 cm^3/mol, whereas the entropy-volume relationships (see Chapter 3, Fig. 3.10) suggest a volume of about 25 cm^3/mol

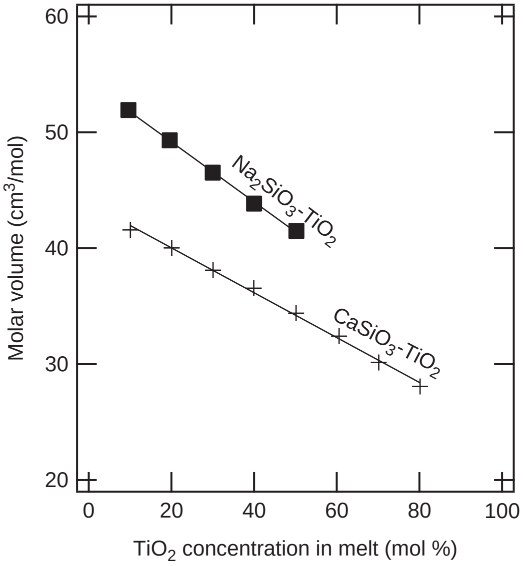

FIG. 12.17 Molar volume of Na_2SiO_3-TiO_2 (NTS) and $CaSiO_3$-TiO_2 (CTS) melts. The partial molar volume of TiO_2 is given by the intercept of linear relationships with the 100 mol% TiO_2 axis at the temperatures indicated (Dingwell, 1992b).

for hypothetical TiO_2 glass with fourfold coordinated Ti^{4+}. Even if one considers thermal expansion, it seems difficult to account for the TiO_2 melt volume of 24.3 cm^3/mol in terms of only sixfold coordinated Ti^{4+}. The density data, thus, suggest an average coordination lower than 6 in alkaline earth titanosilicates. The situation could be more complicated, however, as suggested by data published only in a graphical form that indicate a composition-dependent partial molar volume of TiO_2 in calcium titanosilicate melts (Morinaga et al., 1974).

A complicated volume dependence on chemical composition is well established for alkali titanosilicate glasses and melts. The values range from 25.8 ± 0.5 (for Cs) to 31.3 ± 0.5 (for K) cm^3/mol (Dingwell, 1992b). From other measurements on Na and K titanosilicates, Liu and Lange (2001) found that both the partial molar volume of TiO_2 and its temperature derivative depend on alkali content, the volume being more sensitive to K_2O than Na_2O concentration (Fig. 12.18A). Moreover, the volume also is positively correlated with the metal/Si ratio (Liu and Lange, 2001; Liu et al., 2007; see also Fig. 12.18). Note that in these systems, the Na/Si ratio equals the NBO/Si of the silicate melt solvent (effects of TiO_2 are not considered in such a calculation). Notably, at least in the Na_2O-TiO_2-SiO_2 melts, the partial molar volume of TiO_2 does not seem dependent on total TiO_2 concentration (Liu et al., 2007).

The more extensive density datasets available for Ti-bearing glasses indicate that the actual picture should be more complex. In a study of the density changes induced by replacement of Na_2O by TiO_2 at constant TiO_2 content, Hamilton and Cleek (1958) found that the relationships of molar volume with alkali oxide concentration in Na_2O-TiO_2-SiO_2 and K_2O-TiO_2-SiO_2 glasses become increasingly nonlinear as the TiO_2 content increases (Fig. 12.19). Hence, the partial molar volume of both Na_2O and SiO_2 becomes increasingly composition dependent. Ironically, that of TiO_2 varies little, being consistent with the determinations made from the measurements of Turnbull and Lawrence (1952) as well as with the data of the melts in the same systems at high temperature (Liu et al., 2007). An analogous conclusion is drawn from

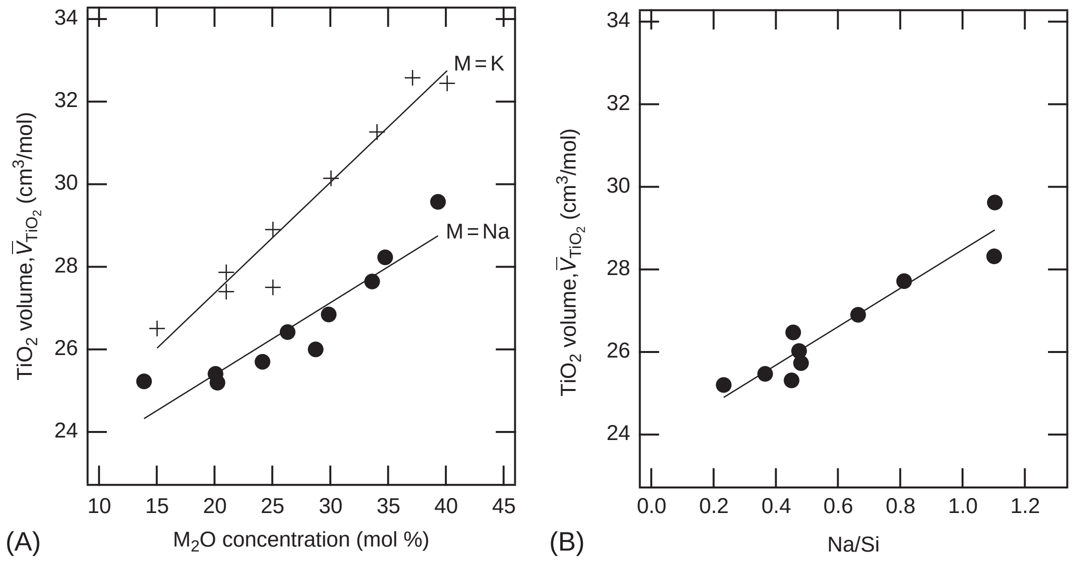

FIG. 12.18 Partial molar volume of TiO_2 and silicate melt composition. (A) Partial molar volume of TiO_2 in Na_2O-TiO_2-SiO_2 and K_2O-TiO_2-SiO_2 melts as a function of alkali oxide concentration (as identified on individual curves). (B) Partial molar volume of TiO_2 in Na_2O-TiO_2-SiO_2 melts as a function of Na/Si. Note that in this system the Na/Si-abundance ratio equals the NBO/Si of the Ti-free silicate melt (Liu and Lange, 2001; Liu et al., 2007).

the density for potassium titanosilicate glasses (Rao, 1963). Although they do not refer to really constant TiO_2 contents, the molar volumes also show strong curvature when K_2O replaces SiO_2. In this case, however, the partial molar volume of K_2O does not vary, whereas that of SiO_2 does. From the Gibbs-Duhem equation, it follows that the partial molar volume of TiO_2 must also depend on composition.

12.5.2.2 Expansion and Compressibility

A comparison of ambient-pressure thermal expansion and isothermal compressibility of Ti-bearing silicate glasses and melts reveals systematic effects of silicate composition and TiO_2 contents (Webb and Dingwell, 1994; Liu and Lange, 2001; Shelby, 2005; Liu et al., 2007; Kaaden et al., 2015). The electronic properties of the metal cations appear to be a predominant factor.

A limited number of thermal expansion measurements have been reported for alkali titanosilicate glasses and melts (Manghnani, 1972; Liu and Lange, 2001). These studies have revealed an unusual thermal expansivity, which for TiO_2-SiO_2 glasses varies with annealing temperature and time (Schultz, 1976; Shelby, 2005). Moreover, the thermal expansion coefficient of alkali silicate glasses varies slightly with the nature of the metal cation in ternary M_2O-TiO_2-SiO_2 glasses from $3.46 \times 10^{-5}\ K^{-1}$ for Li-titanosilicate to values as high as $3.76 \times 10^{-5}\ K^{-1}$ for the analogous K titanosilicate, Na-titanosilicate glasses having intermediate values (Liu and Lange, 2001). There might be a very minor increase of expansion coefficients of these glasses with increasing Ti concentration (by about 5% between 12 and 40 mol% TiO_2 (Liu and Lange, 2001).

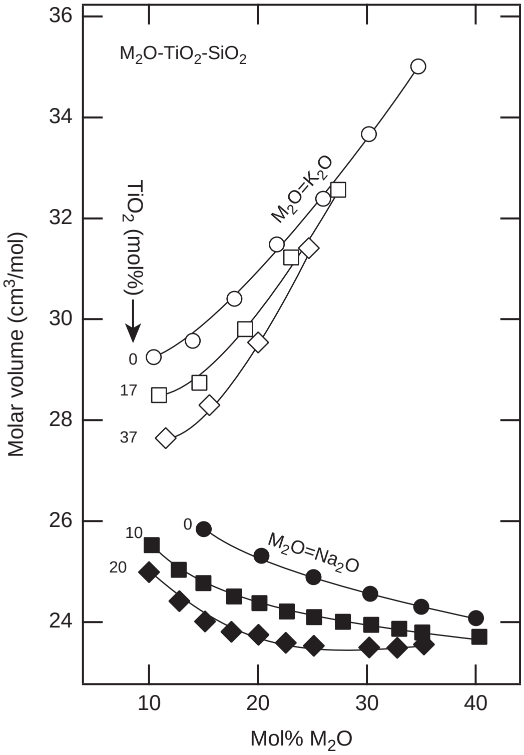

FIG. 12.19 Ambient-temperature molar volumes of alkali titanosilicate glasses with TiO_2 concentrations for individual curves identified by number (mol%) (Hamilton and Cleek, 1958; Rao, 1963).

The thermal expansion coefficients for melts are smaller than those of the equivalent glasses (2.02×10^{-5} K^{-1} for Na titanosilicates at 1100°C, compared with 3.7×10^{-5} K^{-1}; Liu and Lange, 2001). Moreover, for K- and Na-titanosilicate melts, the thermal expansion coefficient of TiO_2 remains poorly correlated with silicate composition (e.g., polymerization) with average values of $2.0 \pm 0.7 \times 10^{-5}$ and $1.5 \pm 0.6 \times 10^{-5}$ K^{-1}, respectively (Liu and Lange, 2001).

Melt compressibility and derivatives thereof typically are correlated with molar volumes (Webb and Dingwell, 1994; Liu et al., 2007), which themselves are correlated with the electronic properties of metal cations and metal/silicon abundance ratios (or NBO/Si) (Webb and Dingwell, 1994; Liu et al., 2007; see also Fig. 12.20). The compressibility also is temperature dependent, a relationship that becomes more profound the greater the ionization potential (Z/r^2) of the metal cation (Webb and Dingwell, 1994). As would be intuitively expected, the compressibility increases with temperature. Moreover, the compressibility is positively correlated with ionic radius, but the electric charge of the metal cation also plays a role (Webb and Dingwell, 1994).

12.6 STRUCTURE

The properties reviewed previously indicate that the solution mechanisms of TiO_2 in silicate melts depend on composition, which, in turn, means structure. Both the nature of

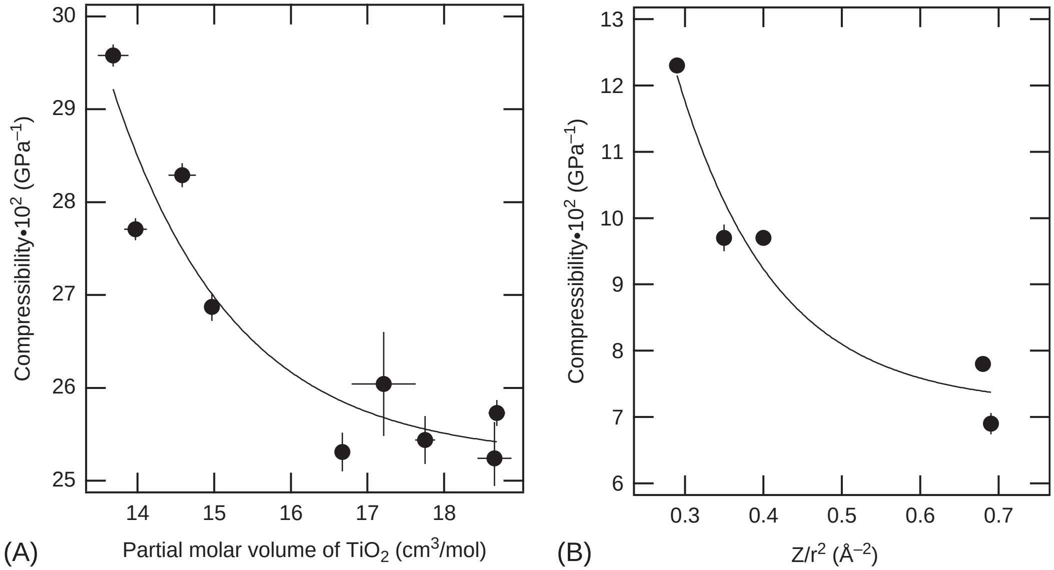

FIG. 12.20 Compressibility of titanosilicate melts. (A) As a function of partial molar volume of TiO_2 in Na-titanosilicate melts (Liu et al., 2007). (B) As a function of ionization potential of metal cation in metal-titanosilicate melts at 1150°C, except for Li^+, which was measured at 1375°C (Webb and Dingwell, 1994).

the metal cations and the TiO_2 content of the melt are important. To unravel the structural role of Ti^{4+} and determine structure-property relationships, isolating individual composition effects on the Ti^{4+} solution mechanisms has been the main goal of studies made on series of compositionally simple systems.

12.6.1 Oxygen Coordination, Ti^{4+} Concentration, and Composition

Cation-oxygen bond length in crystalline materials correlates well with the coordination number of the cation (see, e.g., discussion in Chapters 2, 7, 9, and 11). Such relationships also exist, therefore, for Ti—O bond lengths and Ti^{4+} coordination number (Sandstrom et al., 1980; Sakka et al., 1989). Those relationships also have been translated to linkage between coordination number of frequencies of specific vibrational bands in spectra of Ti-bearing crystalline and glassy materials (Sakka et al., 1989).

12.6.1.1 TiO_2

The simplest Ti-bearing melt obviously is TiO_2, whose structure has been determined through combinations of X-ray diffraction and molecular dynamics simulations (Petkov et al., 1998; Alderman et al., 2014). On a local scale, Petkov et al. (1998) concluded that the structure of amorphous TiO_2 resembles that of brookite, which comprises chains of Ti—O octahedra with Ti—O bond length near 1.95 Å. However, they also noted that the Ti^{4+} coordination number varies with manufacturing methods. It is not clear, therefore, how useful the information is for our understanding of the structure of TiO_2-bearing glass and melt.

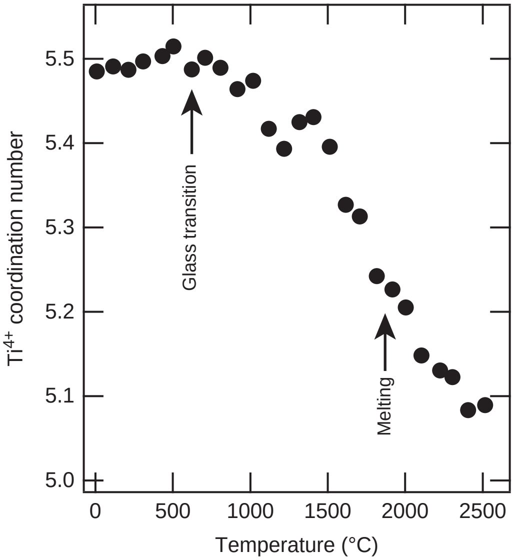

FIG. 12.21 Average coordination number of liquid and amorphous TiO_2 calculated via MD simulations (results from Alderman et al., 2014).

Experimental (X-ray scattering) and MD simulation data relevant to TiO_2 melts were obtained to temperatures as high as near 2000°C (Alderman et al., 2014). From that information, the Ti—O bond length is 1.87 Å compared with 1.95 Å, for crystalline rutile. The average Ti—O—Ti bond angle is near 120 degrees, but with a broad and asymmetric distribution of the Ti—O—Ti angles (Alderman et al., 2014).

The average Ti^{4+} coordination number in molten TiO_2 is slightly above 5, but this value decreases with increasing temperature (Fig. 12.21). It represents a mixture of four- and sixfold coordinated Ti^{4+}, the proportions of which obviously depend on temperature (Alderman et al., 2014). Such a structural contrast resembles that of Al_2O_3, where the coordination number is higher for the crystal (corundum) than for the melt, which is the average of several discrete numbers (see Chapter 9, Section 9.3.1).

12.6.1.2 TiO_2-SiO_2

Solution mechanisms of TiO_2 in SiO_2 glass and melt is a complex function of TiO_2 concentration (Greegor et al., 1983; Knight et al., 1989; Chmel et al., 1992; Henderson et al., 2002). For glass and other amorphous forms of TiO_2-SiO_2, the methods used for sample preparation can also be an issue (Dirken et al., 1995).

Structural information has been derived from XANES spectra made at the L near-edge of titanium. From comparisons between minerals and glasses, Henderson et al. (2002) concluded that at low TiO_2 contents (<2.8 mol% TiO_2), the Ti L-edge spectrum of TiO_2-SiO_2 glass most closely resembles that of fresnoite ($Ba_2TiSi_2O_8$), where Ti^{4+} is in fivefold coordination with oxygen ($^{[5]}Ti$). At higher TiO_2 concentration, the Ti L-edge spectrum is similar to that of Ba_2TiO_4, where Ti^{4+} is in fourfold coordination. Such a coordination change is consistent with the results of earlier X-ray absorption studies of TiO_2-SiO_2 glasses (e.g., Sandstrom et al., 1980; Greegor et al., 1983), although Greegor et al. (1983) favored Ti^{4+} in sixfold coordination at low TiO_2 content. Henderson et al. (2002) also concluded that the Si—O bond distance in TiO_2-SiO_2 glasses is not affected by TiO_2. However, earlier work (Greegor et al., 1983) reported a slight expansion of the Si—O—Si angle from the 152 degrees of glassy SiO_2 to 159 degrees.

The Raman spectra of TiO_2-SiO_2 homogeneous glasses by Henderson and Fleet (1995) are similar to those reported previously (Chakraborty and Condrate, 1985; Kusabiraki, 1986; Knight et al., 1989; Bihuniak and Condrate, 1981). Two bands, near 945 and 1100 cm^{-1}, are of special interest because their intensity grows with TiO_2 concentration. Henderson and Fleet (1995) suggested that these bands should be assigned to Si—O vibrations and reflect depolymerization of the silicate network caused by dissolution of Ti^{4+}. Alternatively, these two bands could be assigned to Ti—O vibrations (Tobin and Baak, 1968; Bihuniak and Condrate, 1981; Knight et al., 1989).

12.6.1.3 Ti-Bearing Multicomponent Glasses and Melts

A relatively comprehensive experimental database exists for ternary and more complex silicate and aluminosilicate glasses and melts containing Ti^{4+} (Kusabiraki, 1986; Alberto et al., 1995; Mysen and Neuville, 1995; Ponader et al., 1996; Cormier et al., 1997, 2001; Reynard and Webb, 1998; Farges, 1997, 1999; Romano et al., 2000; Henderson et al., 2002; Henderson and St-Amour, 2004; Larsen et al., 2007; Osipov et al., 2012; Zhang et al., 2014). It is clear from those data that the structural role of Ti^{4+} in silicate glasses and melts is highly variable and depends on TiO_2 concentration (Alberto et al., 1995; Farges, 1997; Henderson and St-Amour, 2004), the nature of the metal cation(s) (i.e., alkalis versus alkaline earths (Farges, 1997, 1999; Henderson et al., 2002), degree of silicate polymerization (Ponader et al., 1996), and Al/Si ratio (Ponader et al., 1996; Romano et al., 2000).

Increasing TiO_2 concentration in alkali silicate glasses and melts results in an increasing abundance of more highly coordinated Ti^{4+} (Farges, 1997; Henderson et al., 2002); see also Fig. 12.22. In Fig. 12.22, the coordination numbers are defined in terms of n and $n+1$ because there is significant discussion about its value, but general agreement that the higher coordination number tends to increase with increasing total TiO_2 concentration. Farges (1997) concluded from XANES spectra of alkali silicate glasses that $n=5$ and $n+1=6$ and that these numbers are not sensitive to the type and proportion of alkali metals, as also supported by neutron diffraction (Cormier et al., 2001; Osipov et al., 2012). However, Henderson et al. (2002), also using XANES, concluded that $n=4$ and $n+1=5$ in Na-silicate glasses, but that the $^{[n+1]}Ti/^{[n]}Ti$ total TiO_2 concentration, in agreement with the conclusion of Farges (1997). Reynard and Webb (1998), using Raman spectroscopy, concluded that high-Ti abundance Na-silicate melts have fivefold coordinated Ti^{4+}, which may accord with the high-TiO_2 abundance data of Henderson et al. (2002). Larsen et al. (2007) using oxygen-17 NMR spectroscopy of potassium titanosilicate glasses, concluded that the dominant coordination number for Ti^{4+} was 4, and with a lesser amount of fivefold coordination of Ti^{4+}. Notably, the abundance of fourfold coordinated Ti^{4+} increases as the radius of the alkali metal increases (Farges, 1997).

Titanosilicate glasses and melts with alkaline earths, on the other hand, tend to be different (Henderson et al., 2002; Henderson and St-Amour, 2004) with a lower Ti^{4+} coordination number. In another Ti XANES study, Farges et al. (1996) and Farges (1997) concluded that titanyl groups with fivefold coordinated Ti^{4+} predominate in Ca and K silicate and aluminosilicate glasses, with minor proportions of four- and sixfold coordination, and that the proportion of

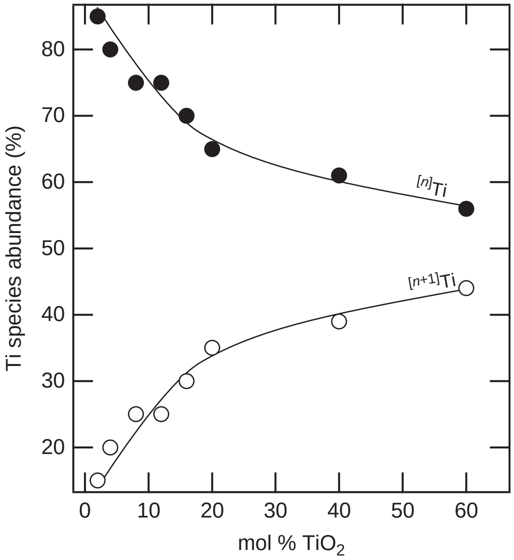

FIG. 12.22 Evolution of Ti coordination numbers with increasing TiO_2 concentration in melts in the Na_2O-TiO_2-SiO_2 system where $TiO_2 + SiO_2 = 60\%$ and increasing TiO_2 concentration is coupled to decreasing SiO_2. Here, the coordination numbers are given as n and $n+1$, because there is some discussion in the literature whether the value of n is 4 or 5 (see text). The data actually are from Farges (1999), who from XANES concluded that $n = 5$.

$^{[4]}Ti$ is slightly higher in alkaline earth than in alkali systems. From a Ti L-near edge XANES study of Na, K, and Ca titanosilicate glasses, Henderson et al. (2002) found instead that (i) the Ti^{4+} coordination number in the Ca-system is lower, on average, than in the K and Na-systems, (ii) the average coordination numbers differ even in the Na- and K-systems, and (iii) the Ti coordination numbers in all three systems depend on TiO_2 content. In both Na and K systems, Henderson et al. (2002) asserted that low-Ti glasses are dominated with fourfold coordinated Ti^{4+} and that the proportion of Ti^{4+} in fivefold coordination increases with increasing TiO_2 content, a conclusion that is in qualitative accord with both neutron diffraction data (Yarker et al., 1986; Cormier et al., 2001) and the early Raman spectroscopic investigation of Bobovich (1962). From a ^{17}O NMR examination of $CaTiSiO_5$ glass, Krocker et al. (2002) found that the NMR data are consistent with all of the structural environments suggested previously.

The interpretation of Raman data is considerably less clear-cut. The spectra characteristically show one or more strong bands between 800 and 900 cm^{-1}, the relative intensities of which depend on TiO_2 content (Fig. 12.23). These bands have sometimes been assigned to Ti^{4+} in some form of four- or fivefold fold coordination (Mysen and Neuville, 1995; Reynard and Webb, 1998). Another Raman band near 950 cm^{-1}, which grows with increasing TiO_2 content, has been assigned to Ti—O vibrations in a structural entity where the Ti^{4+} coordination number is higher (Alberto et al., 1995; Henderson and Fleet, 1995).

Many of the interpretations of Raman data do not depend directly on assignments of Ti—O vibrational modes, but rather on the response to dissolved TiO_2 of the silicate network structure whose Raman signals are well established (see Chapter 7, Section 7.3.1). Mysen and Neuville (1995) determined the degree of silicate polymerization, NBO/T, from the abundance of the individual Q^n-units in $Na_2Si_2O_5$-$Na_2Ti_2O_5$ glasses (Fig. 12.23). They derived the effect of dissolved TiO_2 on the degree of silicate polymerization, NBO/T, from the expression:

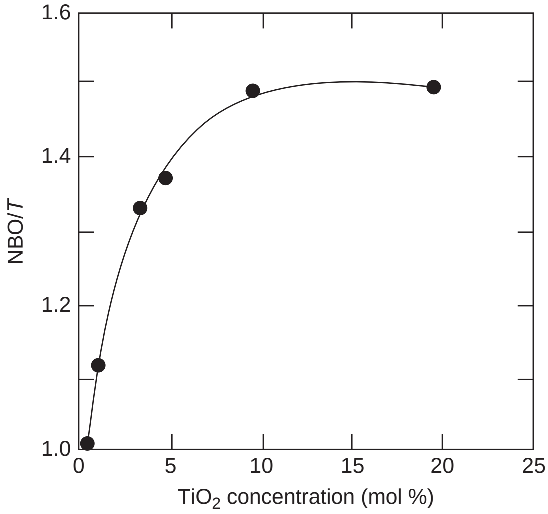

FIG. 12.23 Change in melt polymerization, NBO/*T*, as a function of TiO_2 concentration in glasses along the join $Na_2Si_2O_5$-$Na_2Ti_2O_5$ (Mysen and Neuville, 1995).

$$\mathrm{NOB}/T = \sum_{n-0}^{n-3} (4-n)\mathrm{Q}^n \qquad (12.5)$$

The strongly nonlinear relationship between the NBO/*T* and TiO_2 content of glasses indicates variations of Ti coordination as a function of TiO_2 concentration. At low TiO_2 content, the rapid increase in NBO/*T* with TiO_2 content indicates that Ti^{4+} serves predominantly as a network-modifier, whereas Ti^{4+} may be predominantly a network-former at high TiO_2 content where NBO/*T* varies much less with increasing TiO_2 concentration. These conclusions differ, however, from that which would be expected from the X-ray and Raman-derived structural information, where, as discussed previously, Ti^{4+} shifts to high coordination numbers with increasing TiO_2 content (Fig. 12.22), which intuitively should lead to an increased rate of NBO/*T* with TiO_2 concentration.

In comparison, information on the structural role of Ti^{4+} in aluminosilicate glasses and melts is rare (Romano et al., 2000). In a XANES study of potassium aluminosilicates, Romano et al. (2000) found that the Ti-coordination number decreases when the Al content increases. As the aluminum and silicon K-edge spectra show little or no effects of dissolved Ti^{4+}, this cation has no significant influence on the local environment of Al^{3+} and Si^{4+}. This conclusion agrees with the marginal effect of Al content on the rutile solubility in similar melt compositions (Dickinson and Hess, 1985).

12.6.2 Ti, Si Substitution Vs Ti Clustering

Whether incorporation of Ti^{4+} in the structure of vitreous SiO_2 and other silicate melts and glasses takes place via substitution for Si^{4+} or via formation of Ti—O clusters has been addressed in a number of studies (Farges, 1999; Kim et al., 2000; Gervais et al., 2001; Krocker et al., 2002; Henderson and St-Amour, 2004; Larsen et al., 2007). From vibrational spectra of titanosilicate glasses and melts, Henderson and Fleet (1995) suggested that there is a gradual frequency shift of bands assigned to Ti—O vibrations, which led them to conclude that there is no clustering. Alberto et al. (1995) and Mysen and Neuville (1995) found, however, that the Raman frequencies did not change with TiO_2 content. Only the intensities did. Those observations were considered consistent with considerable Ti,Si ordering of the structure in Ca- and Na-titanosilicate melts.

Ordering or perhaps clustering also was inferred from ^{17}O NMR spectra (Gervais et al., 2001; Krocker et al., 2002). Interestingly, in another ^{17}O NMR study, Larsen et al. (2007), concluded that in spectra K_2O-TiO_2-SiO_2 glasses, there was no evidence for Si,Ti ordering. From Ti EXAFS studies of both TiO_2-SiO_2 and K_2O-TiO_2-SiO_2 glasses, it has been found, however, that there is very significant clustering of Ti—O complexes, as evidenced by the existence of Ti—O—Ti bonds (Farges, 1999; Kim et al., 2000). The proportion of clusters increases with TiO_2 concentration (Fig. 12.24) in both situations. Farges (1999) also concluded that the cluster or domain size in the glasses he studied was on the order of 20 Å across, but that this dimension was a positive function of total TiO_2 content. This conclusion accords with that of Kim et al. (2000), who also found that the number of Ti—O—Ti bonds increased with increasing total TiO_2 concentration.

12.6.3 Temperature and Pressure

Experimental studies of the structural differences between Ti-bearing glasses and melts are relatively limited (Mysen and Neuville, 1995; Farges et al., 1996; Reynard and Webb, 1998; Cormier et al., 2001). In general, these seem small for bond lengths and Ti^{4+} coordination.

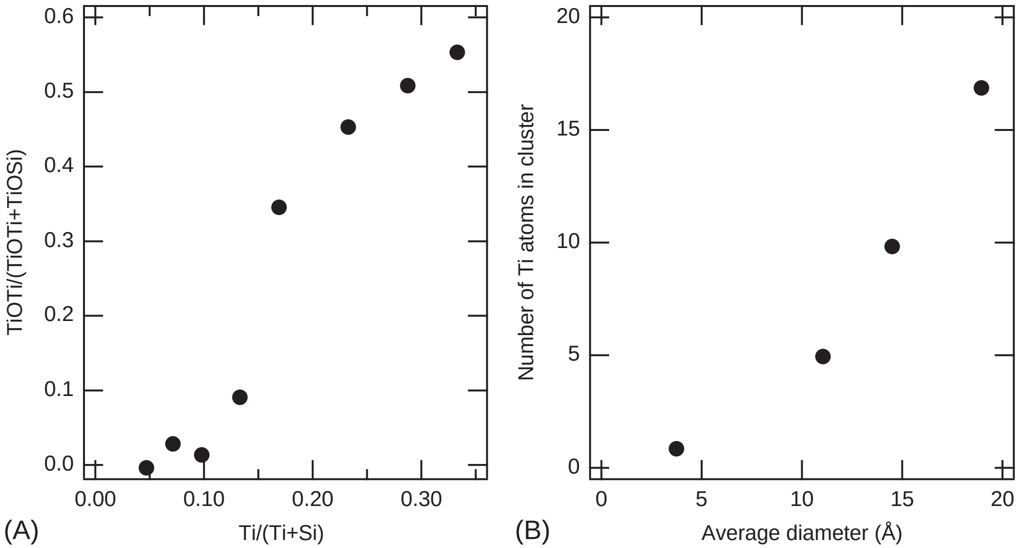

FIG. 12.24 Ti clustering in titanosilicate melts and glasses. (A) Fractions of Ti—O bonds with oxygen shared by neighboring Ti^{4+}, TiOTi, relative to total number of Ti—O bonds in TiO_2-SiO_2 glass (Kim et al., 2000). (B) Number of Ti^{4+} cations as a function of cluster size in alkali titanosilicate glasses (Farges, 1999).

When examining K, Na, and Ca titanosilicate melts to 1650 K by X-ray absorption fine structure (XAFS) spectroscopy, Farges et al. (1996) did not see any temperature effects on the titanium K-edge. In contrast, Cormier et al. (2001) detected relative changes in bond lengths with temperature in a neutron scattering study of Ti-bearing potassium silicate melts to 1360 K. Without finding evidence for temperature-induced changes in Ti^{4+} coordination, they observed variations of bond distances in the dominant TiO_5 polyhedra. Four Ti—O bond lengths were near 1.96 Å at ambient temperature. These expand by about 0.03 Å when the temperature is raised to 1360 K (Cormier et al., 2001; see Fig. 12.25). Such small variations could easily be accommodated without significant structural reorganization of Ti—O polyhedra in the melts. On the other hand, Si—O bond lengths do not change with temperature, whereas the K—O lengths do, by as much as 0.1 Å between room temperature and 1360 K.

In their Raman study of $Na_2TiSi_2O_7$ glass and melt, Reynard and Webb (1998) found no evidence for changes in Ti^{4+} coordination with temperature. The spectra showed, however, an intensity decrease near 700 cm^{-1}, which was attributed to temperature-induced breakage of Si—O—Si and Ti—O—Ti bonds. This interpretation is doubtful because the NBO/Si of this material is such that there likely would not be any Si—O—Si vibrations near 700 cm^{-1} (see also Chapter 7). However, if Ti—O—Ti vibrations are involved, it is more likely that these spectroscopic features reflect breakup of TiO_4 clusters.

Mysen and Neuville (1995) monitored the evolution of the silicate Q^n-species in Ti-bearing silicate glasses and melts as a function of temperature by Raman spectroscopy. The deduced NBO/*T* of $Na_2Si_2O_5$-$Na_2Ti_2O_5$ melts remains constant at low temperature, but varies slightly above temperatures that are close to the glass transition, which is shown with arrows in Fig. 12.26. The effect is greater the higher the TiO_2 content of the melt and reflects, most likely, small but distinct changes in the structure governed by the temperature-dependent environment of Ti^{4+}. We note, however, that the changes in NBO/*T* with temperature seem to begin at

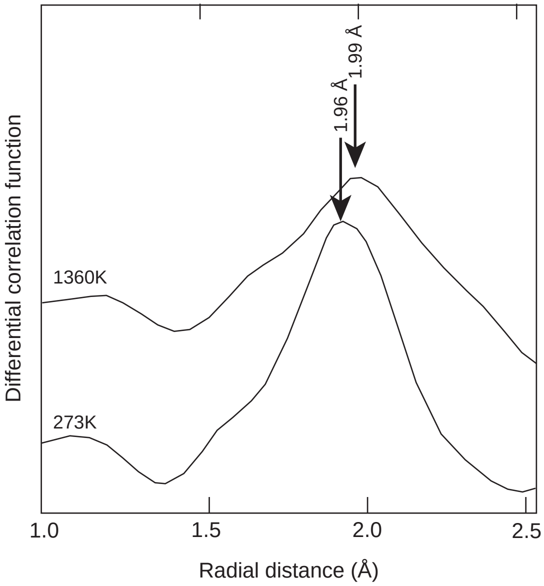

FIG. 12.25 Differential correlation function of $K_2O{\cdot}2SiO_2{\cdot}TiO_2$ glass at 273 K and melt at 1360 K, obtained after subtracting contributions from Si—O, O—O, and K—O (Cormier et al., 2001).

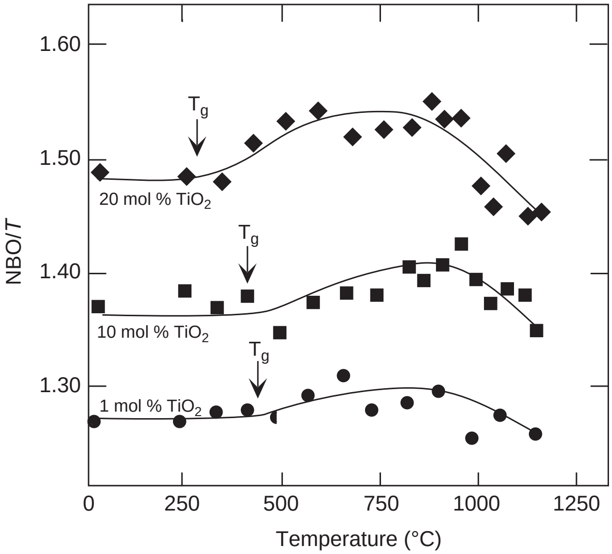

FIG. 12.26 Change in melt polymerization, NBO/*T*, as a function of temperature as calculated with Eq. (12.5) along the join $Na_2Si_2O_5$-$Na_2Ti_2O_5$ for various TiO_2 contents. The glass transition temperatures, T_g, are marked with arrows (Mysen and Neuville, 1995).

temperatures near the glass transition, and may therefore be related to structural changes as a glass transformed to a melt.

At pressure above ambient, a small number of experimentally determined properties, coupled with an even smaller number of structural determinations, indicate that some structural changes may take place in Ti-bearing silicate systems as pressure is increased (Circone and Agee, 1995; Webb and Dingwell, 1994; Paris et al., 1994). In the TiO_2-SiO_2 system, the liquidus phase relations on the Ti-rich side of the diagram change as the eutectic shifts to increasingly Ti-rich compositions and the eutectic temperature decreases between ambient pressure and 3 GPa (Circone and Agee, 1995), thus suggesting changes in the environment of Ti^{4+} in the melt in this compositional range. The bulk modulus of alkali and alkaline earth titanosilicate glasses and melts also changes with increasing pressure without, however, pointing to a single trend independent of silicate composition. In a XANES study of K-titanosilicate glasses quenched at high pressure, Paris et al. (1994), derived the following relationship from the XANES data:

$$IP\,(\text{intensity}, \%) = -28.6\,CN\,(\text{coordination number}) + 194.9. \tag{12.6}$$

From this information, there is evidence for pressure-induced coordination changes (Fig. 12.27), the average number changing from about 4.8 at ambient pressure to about 5.8 at 3 GPa (Paris et al., 1994).

12.7 STRUCTURE AND PROPERTIES OF TI-BEARING MELTS

Titanosilicate glasses and melts often exhibit unusual thermal and physical properties (see Sections 12.2–12.5). These likely reflect the multiple coordination numbers of Ti^{4+}, which are governed by silicate composition and TiO_2 content, together with the apparent

FIG. 12.27 Relationship between pre-edge intensity (from XANES spectra) and Ti^{4+} coordination at the various pressures (in GPa) indicated. "A" means ambient pressure (Paris et al., 1994).

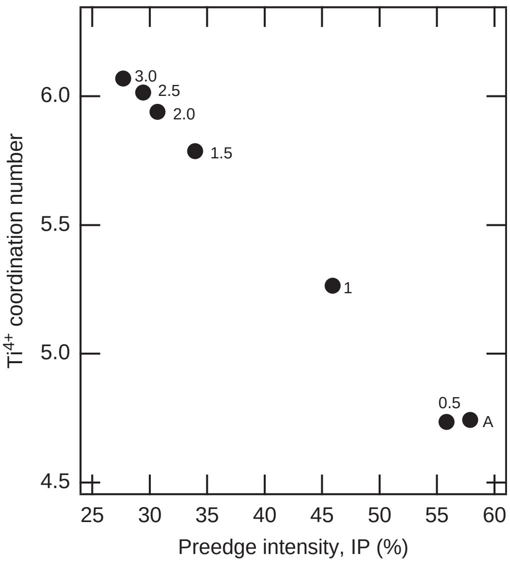

tendency to form Ti-bearing clusters or domains within the structure of these materials. In general terms, these features are common with those already described for Fe^{3+} in melts (see Chapters 10 and 11).

12.7.1 Thermal Properties

Thermal properties include titanium solubility in silicates, activity-composition relations, enthalpy, entropy, and heat capacity. At ambient pressure, the TiO_2 solubility in SiO_2 melts extends only to several mol% before a wide miscibility gap is encountered (DeVries and Roy, 1954; see also Fig. 12.4). These features reflect the clustering effects of Ti-bearing complexes as determined, for example, by Kim et al. (2000) and highlighted in Fig. 12.24. The TiO_2 clusters in TiO_2-SiO_2 melts appear to comprise combinations of four- and fivefold coordinated Ti^{4+}, the relative abundance of which changes with TiO_2 content and where the Ti—O bond lengths of fourfold coordinated polyhedra (near 2 Å) do not match well the Si—O bond length in SiO_4 tetrahedra (near 1.6 Å). Moroever, in fivefold coordinated situations, the mismatch with the geometry of the SiO_4 tetrahedra is even more pronounced. Given that the properties of the SiO_4 tetrahedra (including Si—O bond length) do not vary with TiO_2 concentration, the very limited TiO_2 solubility in SiO_2 melt is understandable.

The activity-composition relations of SiO_2 in silicate melts can be linked to TiO_2 solubility (Kushiro, 1975; Ryerson, 1985) via the Van't Hoff relation (Eq. 12.2). TiO_2 clustering in SiO_2 melts may account for the observation that the activity coefficient of SiO_2 (γ_{SiO_2}) in silica-rich portions of the SiO_2-TiO_2 system is not very sensitive to TiO_2 content and resembles, in fact, that of SiO_2 in SiO_2-aluminate melts. In depolymerized melts, on the other hand, the γ_{SiO_2} increases rapidly with increasing TiO_2 content. This effect presumably is a reflection of the dissolved TiO_2, which shifts liquidus boundaries of silica polymorphs to less SiO_2-rich composition and, therefore, results in increased activity coefficient of SiO_2. This interpretation is also in agreement with Si XANES spectra of Ti-bearing alkali and alkaline earth metasilicate glasses (Henderson and St-Amour, 2004).

The enthalpy of solution of rutile (TiO_2) in melts at high temperature always is endothermic, which likely reflects the relative instability of the titanate complexes that are formed (see also Fig. 12.11). Moreover, the nature of the metal cation has a profound effect, because the TiO_2 solubility is much greater in alkaline earth than in alkali titanosilicate melts, which results from the smaller average Ti^{4+} coordination number of the former compared to the latter (Fig. 12.22; see also Farges, 1999; Henderson et al., 2002). Furthermore, the enthalpy of solution of rutile in melts increases as melts become more polymerized (Fig. 12.11), which likely also reflects the fact that the ratio of Ti-coordinated species, $^{[n+1]}Ti/^{[n]}Ti$, is sensitive to the silicate polymerization.

A number of structural explanations have been proposed to rationalize the anomalous temperature dependence of configurational properties of Ti-bearing silicate melts (Figs. 12.12 and 12.13). Farges et al. (1996) may have come near an explanation when they suggested that the decreasing C_p^{config} with temperature above the glass transition is due to changes in medium-range order. This explanation was advanced because they did not detect any changes in the Ti—O polyhedra as a glass transformed to a melt. Because temperature-dependent changes in configurational properties are governed by local variations in cation and anion ordering and/or other local topological changes (e.g., Richet and Neuville, 1992; Lee and Stebbins, 1999; Roskosz et al., 2004), such changes in medium-range order should rather be a consequence of reorganization near individual Ti—O environments. This interpretation is consistent with XANES neutron diffraction data (Farges, 1999; Kim et al., 2000; Cormier et al., 2001) indicating an important role of Ti-clustering in glasses and melts. Given that the NBO/*T* of melts vary with temperature (Mysen and Neuville, 1995), one may suggest that the extent of clustering of Ti^{4+} varies with temperature as does, therefore, configurational heat capacity. It is also consistent with the observation that NBO/*T* of Ti-bearing alkali silicate melts is slightly temperature-dependent above the glass transition range (Mysen and Neuville, 1995).

12.7.2 Physical Properties

Transport properties often are related successfully to configurational properties (see Chapter 4, Section 4.6.1). In titanosilicate melts, there is a very large change in configurational heat capacity across the glass transition (e.g., Bouhifd et al., 1999), which is an expression of the large deviation from linearity of the log viscosity vs $1/T$ relationships when high and low temperature viscosity are incorporated (Fig. 12.16). Such an anomaly, including the variations in activation enthalpy of viscous flow (Fig. 12.14), tends to take place because the clustering of Ti-complexes leads to enhanced contribution from entropy of mixing to the configurational entropy, and thus the enhanced fragility as TiO_2 is dissolved in silicate melts. The fact that the activation enthalpy of viscous flow of titanosilicate melts at high temperature does not vary much with TiO_2 concentration also is a consequence of the clustering of the Ti—O complexes in the melts.

The partial molar volume of TiO_2 in alkali titanosilicate melts varies systematically with alkali content and also changes (increases) as the ionization potential of the metal cation increases (Fig. 12.18). The compressibility increases with alkali content (Liu et al., 2007). These variations reflect the forms of complexing of the Ti^{4+}, most likely forming some sort of titanate complexes that involve the alkali metal. As a result, the silicate portion of the melts becomes increasingly polymerized. Given that the compressibility of silicate melts increase with the extent of silicate polymerization (see Chapter 6, Section 6.4), it follows that increasing alkali content of titanosilicate melts leads to increased melt compressibility. The positive correlation between the partial molar volume and TiO_2 content (Liu and Lange, 2001) is related to the fact that, as the TiO_2 concentration in a titanosilicate melt increases, the average coordination number of Ti^{4+} also increases (Fig. 12.22). It follows, therefore, that whatever structural changes occur in a melt as a function of its composition, whatever is the result for the coordination of Ti^{4+} governs its volume.

References

Alberto, H.V., Mysen, B.O., DeCampos, N.A., 1995. The structural role of titanium in silicate glasses: a Raman spectroscopic study of the system $CaO\text{-}SiO_2\text{-}TiO_2$. Phys. Chem. Glasses 36, 114–122.

Alderman, O.L.G., Skinner, L.B., Benmore, C.J., Tamalonis, A., Weber, J.K.R., 2014. Structure of molten titanium dioxide. Phys. Rev. B. 90, https://dx.doi.org/10.1103/PhysRevB.90.094204.

Bihuniak, P.P., Condrate, R.A., 1981. Structures, spectra and related properties of group IV B-doped vitreous silica. J. Non-Cryst. Solids 44, 331–344.

Bobovich, Y.S., 1962. An investigation of the structure of glassy phosphates using Raman spectra. Opt. Spect. (Engl. Transl.) 13, 274–277.

Bockris, J.O.M., Mackenzie, J.D., Kitchener, J.A., 1955. Viscous flow in silica and binary liquid silicates. Trans. Farad. Soc. 51, 1734–1748.

Bouhifd, M.A., Sipp, A., Richet, P., 1999. Heat capacity, viscosity, and configurational entropy of alkali titanosilicate melts. Geochim. Cosmochim. Acta 63, 2429–2438.

Chakraborty, I.N., Condrate, R.A., 1985. The vibrational spectra of glasses in the $Na2O\text{-}SiO2\text{-}P_2O_5$ system with a 1:1 SiO_2:P_2O_5 molar ratio. Phys. Chem. Glasses 26, 68–74.

Chmel, A., Eranosyan, G.M., Kharshak, A.A., 1992. Vibrational spectroscopic study of Ti-substituted SiO_2. J. Non-Cryst. Solids 146, 213–217.

Circone, S., Agee, C.B., 1995. Effect of pressure on cation partitioning between immiscible liquids in the system $TiO_2\text{-}SiO_2$. Geochim. Cosmochim. Acta 59, 895–907.

Cleek, G.W., Hamilton, E.H., 1956. Properties of barium titanium silicates. J. Res. N.B.S. 57, 317–323.

Cormier, L., Gaskell, P.H., Calas, G., Zhao, J., Soper, A.K., 1997. The titanium environments in potassium silicate glass measured by neutron scattering with isotopic substitution. Phys. B 234, 393–395.

Cormier, L., Calas, G., Neuville, D.R., Bellisent, R., 2001. A high temperature neutron diffraction study of a titanosilicate glass. J. Non-Cryst. Solids 293–295, 510–516.

Danek, V., Nerad, I., 2002. Phase diagram and structure of melts of the system $CaO\text{-}TiO_2\text{-}SiO_2$. Chem. Pap. Chem. Zvesti 56, 241–246.

DeVries, R.C., Roy, R.F.O.E., 1954. The system $TiO_2\text{-}SiO_2$. Trans. Brit. Ceram. Soc. 53, 525–540.

DeVries, R.C., Roy, R., Osborn, E.F., 1955. Phase equilibria in the system $CaO\text{-}TiO_2\text{-}SiO_2$. J. Am. Ceram. Soc. 38, 158–171.

Dickinson, J.E., Hess, P.C., 1985. Rutile solubility and titanium coordination in silicate melts. Geochim. Cosmochim. Acta 49, 2289–2296.

Dingwell, D.B., 1991. The density of titanium(IV) oxide liquid. J. Am. Ceram. Soc. 74, 2718–2719.

Dingwell, D.B., 1992a. Density of some titanium-bearing silicate liquids and the compositional-dependence of the partial molar volume of TiO_2. Geochim. Cosmochim. Acta 56, 3403–3408.

Dingwell, D.B., 1992b. Shear viscosity of alkali and alkaline earth titanium silicate liquids. Am. Mineral. 77, 270–274.

Dirken, P.J., Smith, M.E., Whitfield, H.J., 1995. 17O and ^{29}Si solid state NMR study of atomic scale structure in sol-gel-prepared TiO_2-SiO_2 materials. J. Phys. Chem. 99, 395–401.

Dong, X.J., Sun, H.Y., She, X.F., Xue, Q.G., Wang, J.S., 2014. Viscosity and viscosity estimation model of fully liquid slags in TiO_2-Al_2O_3-CaO-SiO_2 and TiO_2-Al_2O_3-CaO-SiO_2-MgO systems with high TiO_2 concentration and low mass ratio of CaO to SiO_2. Ironmak. Steelmak. 41, 99–106.

Duan, R.G., Liang, K.M., Gu, S.R., 1998. Effect of changing TiO_2 content on structure and crystallization of CaO-Al_2O_3-SiO_2 system glasses. J. Eur. Ceram. Soc. 18, 1729–1735.

Duffy, J.A., 2006. Refractivity and coordination number changes of the Ti^{4+} ion in glass. Phys. Chem. Glasses B 47, 582–587.

Ehrt, D., Leister, M., Matthai, A., 2001. Polyvalent elements iron, tin and titanium in silicate, phosphate and fluoride glasses and melts. Phys. Chem. Glasses 42, 231–239.

Ellison, A.J., Hess, P.C., 1986. Solution behavior of +4 cations in high silica melts; petrologic and geochemical implications. Contrib. Mineral. Petrol. 94, 343–351.

Evans, D.L., 1982. Glass structure: the bridge between the molten and crystalline states. J. Non-Cryst. Solids 52, 115–128.

Farges, D., 1997. Coordination of Ti^{4+} in silicate glasses: a high-resolution XANES spectroscopy study at the Ti K edge. Am. Mineral. 82, 36–43.

Farges, F., 1999. A Ti K-edge EXAFS study of the medium range environment around Ti in oxide glasses. J. Non-Cryst. Solids 244, 25–33.

Farges, F., Brown, G.E., Navrotsky, A., Gan, H., Rehr, J.J., 1996. Coordination chemistry of Ti(IV) in silicate glasses and melts. II. Glasses at ambient temperature and pressure. Geochim. Cosmochim. Acta 60, 3039–3054.

Gaetani, G.A., Asimow, P.D., Stolper, E.M., 2008. A model for rutile saturation in silicate melts with applications to eclogite partial melting in subduction zones and mantle plumes. Earth Planet. Sci. Lett. 272, 720–729.

Gan, H., Wilding, M.C., Navrotsky, A., 1996. Ti^{4+} in silicate melts: energetics from high temperature calorimetric studies and implications for melt structure. Geochim. Cosmochim. Acta 60, 4123–4131.

Gervais, C., Babonneau, F., Smith, M.E., 2001. Detection, quantification, and magnetic field dependence of solid-state O-17 NMR of X-O-Y (X,Y = Si,Ti) linkages: implications for characterizing amorphous titania-silica-based materials. J. Phys. Chem. B 105, 1971–1977.

Glasser, F.P., Maar, J., 1979. Phase relations in the system Na_2O-TiO_2-SiO_2. J. Am. Ceram. Soc. 62, 42–47.

Greegor, R.B., Lytle, W.B., Sandstrom, D.R., Wong, J., Schultz, P., 1983. Investigation of TiO_2-SiO_2 glasses by X-ray absorption spectroscopy. J. Non-Cryst. Solids 55, 27–43.

Green, T.H., Adam, J., 2000. Pressure effect on Ti- or P-rich accessory mineral saturation in evolved granitic melts with differing K_2O/Na_2O ratios. Lithos 61, 271–282.

Gwinn, R., Hess, P.C., 1989. Iron and titanium solution properties in peraluminous and peralkaline rhyolitic liquids. Contrib. Mineral. Petrol. 101, 326–338.

Hamilton, E.H., Cleek, G.W., 1958. Properties of sodium-titanium silicate glasses. J. Res. N.B.S. 61, 89–94.

Henderson, G.S., Fleet, M.E., 1995. The structure of Ti-silicate glasses by microRaman spectroscopy. Can. Mineral. 33, 399–408.

Henderson, G.S., Fleet, M.E., 1997. The structure of titanium glasses investigated by K-edge X-ray absorption spectroscopy. J. Non-Cryst. Solids 211, 214–221.

Henderson, G.S., St-Amour, J.C., 2004. A Si K-edge XANES study of Ti containing alkali/alkaline-earth silicate glasses. Chem. Geol. 213, 31–40.

Henderson, G.S., Liu, X., Fleet, M.E., 2002. A Ti-L-edge x-ray absorption study of Ti-silicate glasses. Phys. Chem. Mineral. 29, 32–42.

Hoang, V.V., Linh, N.N., Hung, N.H., 2007. Structure and dynamics of liquid and amorphous $Al_2O_3 \bullet 2SiO_2$. Eur. Phys. J. Appl. Phys. 37, 111–118.

Howard, C.J., Sabine, T.M., Dickson, F., 1991. Structural and thermal parameters for rutile and anatase. Acta Cryst. B47, 462–467.

Hudon, P., Baker, D.R., 2002. The nature of phase separation in binary oxide melts and glasses. I. Silicate systems. J. Non-Cryst. Solids 303, 299–345.

Iwamoto, N., Hidaka, H., Makino, Y., 1983. State of Ti^{3+} ion and Ti^{3+}-Ti^{4+} redox reaction in reduced sodium silicate glasses. J. Non-Cryst. Solids 58, 131–142.

Johnson, W.D., 1965. Oxidation-reduction equilibria in molten Na_2O•SiO_2 glass. J. Am. Ceram. Soc. 48, 184–190.

Kajiwara, M., 1988. Formation and crystallization of Al_2O_3-SiO_2-TiO_2 glasses. Glass Ind. 29, 188–192.

Kim, W.B., Choi, S.H., Lee, J.S., 2000. Quantitative analysis of Ti-O-Si and Ti-O-Ti bonds in Ti-Si binary oxides by the linear combination of XANES. J. Phys. Chem. B 104, 8670–8678.

King, E.G., Orr, R.L., Bonnickson, K.R., 1954. Low-temperature heat capacity, entropy at 298.16 K and high temperature heat content of sphene ($CaTiSiO_5$). J. Am. Chem. Soc. 76, 4320–4321.

Kirchhof, J., Unger, S., Knappe, B., Dellith, J., 2007. Diffusion in binary GeO_2-SiO_2 glasses. Eur. J. Glass Technol. B 48, 129–133.

Kirchhof, J., Unger, S., Dellith, J., Scheffel, A., Teichmann, C., 2012. Diffusion coefficients of boron in vitreous silica at high temperatures. Apt. Mater. Express 2, 534–547.

Kirchhof, J., Unger, S., Dellith, J., Scheffel, A., 2014. Diffusion in binary TiO_2-SiO_2 glasses. Opt. Mater. Express 4, 672–680.

Kirschen, M., DeCapitani, C., Millot, F., Rifflet, J.C., Coutures, J.P., 1999. Immiscible silicate liquids in the system SiO_2-TiO_2-Al_2O_3. Eur. J. Mineral. 11, 427–440.

Knight, D.S., Pantano, C.G., White, W.B., 1989. Raman spectra of gel-prepared titania-silica glasses. Mater. Sci. Lett. 8, 156–160.

Knoche, R., Dingwell, D.B., Webb, S.L., 1995. Melt densities for leucogranites and granitic pegmatites: Partial molar volumes for SiO_2, Al_2O_3, Na_2O, K_2O, Li_2O, Rb_2O, Cs_2O, MgO, CaO, SrO, BaO, B_2O_3, P_2O_5, F_2O_{-1}, TiO_2, Nb_2O_5, Ta_2O_5, and WO_3. Geochim. Cosmochim. Acta 59, 4645–4652.

Krocker, S., Rice, D., Stebbins, J.F., 2002. Disordering during melting: an oxygen-17 NMR study of crystalline and glassy $CaTiSiO_5$ (titanite). Am. Mineral. 87, 572–579.

Kusabiraki, K., 1986. Infrared and Raman spectra of vitreous silica and sodium silicates containing titanium. J. Non-Cryst. Solids 79, 208–212.

Kushiro, I., 1975. On the nature of silicate melt and its significance in magma genesis: regularities in the shift of liquidus boundaries involving olivine pyroxene, and silica materials. Am. J. Sci. 275, 411–431.

Lange, R.A., Carmichael, I.S.E., 1987. Densities of Na_2O-K_2O-CaO-MgO-Fe_2O_3-Al_2O_3-TiO_2-SiO_2 liquids: New-measurements and derived partial molar properties. Geochim. Cosmochim. Acta 51, 2931–2946.

Lange, R.A., Navrotsky, A., 1993. Heat capacities of TiO_2-bearing silicate liquids: evidence for anomalous changes in configurational entropy with temperature. Geochim. Cosmochim. Acta 57, 3001–3012.

Larsen, F.H., Rossano, S., Farnan, I., 2007. Order and disorder in titanosilicate glass by O-17 MAS, off-MAS, and 3Q-QCPMG-MAS solid-state NMR. J. Phys. Chem. B 111, 8014–8019.

Lee, S.K., Stebbins, J.F., 1999. The degree of aluminum avoidance in aluminum silicate glasses. Am. Mineral. 84, 937–945.

Linard, Y., Wilding, M.C., Navrotsky, A., 2008. High temperature calorimetric studies of heat of solution of NiO, CuO, La_2O_3, TiO_2, HfO_2 in sodium silicate liquids. Geochim. Cosmochim. Acta 72, 590–601.

Liska, M., Klyuev, V.P., Antalik, J., Stubna, I., 1997. Viscosity of $Na_2O.2(TiO_2, SiO_2)$ glasses. Phys. Chem. Glasses 38, 6–10.

Liu, Q., Lange, R.A., 2001. The partial molar volume and thermal expansivity of TiO_2 in alkali silicate melts: systematic variation with Ti coordination. Geochim. Cosmochim. Acta 65, 2379–2394.

Liu, Q., Lange, R.A., Ai, Y., 2007. Acoustic velocity measurements on Na_2O-TiO_2-SiO_2 liquids: evidence for a highly compressible TiO_2 component related to five-coordinated Ti. Geochim. Cosmochim. Acta 71, 4314–4326.

Manghnani, M.H., 1972. Pressure and temperature dependence of the elastic moduli of Na_2O-TiO_2-SiO_2 glasses. J. Am. Ceram. Sco. 55, 360–365.

Massazza, F., Sirchia, E., 1958. IL sistema MgO-SiO_2-TiO_2, II. Gli equilibri allo stato solido e alia fusione. Chim. Ind. (Milan) 40, 460–467.

Maurer, R.D., 1962. Crystal nucleation in a glass containing titania. J. Appl. Phys. 33, 2132–2135.

McTaggart, G.D., Andrews, A.I., 1957. Immiscibility area in the system TiO_2-ZrO_2-SiO_2. J. Am. Ceram. Soc. 40, 167–170.

Mitchell, R.H., 1991. Coexisting glasses occurring as inclusions in leucite from lamproites: examples of silicate liquid immiscibility in ultrapotassic magmas. Mineral. Mag. 55, 197–202.

Moore, P.B., Louisnathan, S.J., 1969. The crystal structure of fresnoite, $Ba_2(TiO)Si_2O_7$. Z. Kristall. 130, 438–448.

Morinaga, K., Ito, T., Suginohara, Y., Yanagase, T., 1974. Density of the molten CaO-SiO_2-TiO_2 system and infrared absorption spectra of its glasses. J. Jap. Inst. Met. 38, 1065–1070.

Morinaga, K., Yoshida, H., Takebe, H., 1994. Compositional dependence of absorption spectra of Ti^{3+} in silicate, borate, and phosphate glasses. J. Am. Ceram. Soc. 77, 3113–3118.

Morsi, M.M., El-Shennawi, A.W.A., 1984. Some physical properties of silicate glasses containing TiO_2 in relation to their structure. Phys. Chem. Glasses 25, 64–68.

Mysen, B., Neuville, D., 1995. Effect of temperature and TiO_2 content on the structure of $Na_2Si_2O_5$-$Na_2Ti_2O_5$ melts and glasses. Geochim. Cosmochim. Acta 59, 325–342.

Nelson, S.A., Carmichael, I.S.E., 1979. Partial molar volume of oxide components in silicate liquids. Contrib. Mineral. Petrol. 71, 117–124.

Nordberg, N.E., 1942. Glass having an expansion lower than silica. US Patent Office, ver. no. 2,236,059.

Osipov, A.A., Korinevskaya, G.G., Osipova, L.M., Muftakhov, V.A., 2012. Titanium coordination in TiO_2-Na_2O-SiO_2 glasses of $xTiO_2 \bullet (100 - x)[2Na_2O \bullet 3SiO_2]$ $(0 \leq x \leq 30)$ composition based on Raman spectroscopy. Glas. Phys. Chem. 38, 357–360.

Paris, E., Dingwell, D.B., Seifert, F.A., Mottana, A., Romano, C., 1994. Pressure-induced coordination change of Ti on silicate glass: a XANES study. Phys. Chem. Minerals 21, 510–515.

Petkov, V., Holzhuter, G., Troge, U., Gerber, T., Himmel, B., 1998. Atomic-scale structure of amorphous TiO_2 by electron, x-ray diffraction and reverse Monte Carlo simulations. J. Non-Cryst. Solids 231, 17–30.

Ponader, C.W., Boek, H., Dickinson, J.E., 1996. X-ray absorption study of the coordination of titanium in sodium-titanium-silicate glasses. J. Non-Cryst. Solids 201, 81–94.

Poole, J.P., 1948. Viscosite a basse temperature des verre alcalino-silicates. Ver. Refract. 2, 222.

Rao, B.V.J., 1963. Dual role of titanium in the system K_2O - SiO_2 - TiO_2. Phys. Chem. Glasses 4, 22–34.

Reid, A.M., Ridly, W.I., Donaldson, C., Brown, R.W., 1973. Glass compositions in the orange and gray soils from shorty crater, Apollo 17. Eos, Trans. Am. Geophys. Union 54, 607–609.

Reynard, B., Webb, S.L., 1998. High-temperature Raman spectroscopy of $Na_2TiSi_2O_7$ glass and melt: coordination of Ti^{4+} and nature of the configurational changes in the liquid. Eur. J. Mineral. 10, 49–58.

Richet, P., Bottinga, Y., 1985. Heat capacity of aluminum-free liquid silicates. Geochim. Cosmochim. Acta 49, 471–486.

Richet, P., Neuville, D.R., 1992. Thermodynamics of silicate melts: configurational properties. In: Saxena, S.K. (Ed.), Thermodynamic Data: Systematics and Estimation. Springer, New York, NY, United States, pp. 132–161.

Romano, C., Paris, E., Poe, B.T., Giuli, G., Dingwell, D.B., Mottana, A., 2000. Effect of aluminum on Ti-coordination in silicate glasses: a XANES study. Am. Mineral. 85, 108–117.

Roskosz, M., Toplis, M.J., Richet, P., 2004. The strucural role of Ti in aluminosilicate liquids in the glass transition range: Insights from heat capacity and shear viscosity measurements. Geochim. Cosmochim. Acta 68, 591–606.

Ryerson, F.J., 1985. Oxide solution mechanisms in silicate melts: systematic variations in the activity coefficient of SiO_2. Geochim. Cosmochim. Acta 49, 637–651.

Ryerson, F.J., Watson, E.B., 1987. Rutile saturation in magmas; implications for Ti-Nb-Ta depletion in island-arc basalts. Earth Planet. Sci. Lett. 86, 225–239.

Sakka, S., Miyaji, F., Fukumi, K., 1989. Structure of binary K_2O-TiO_2 and Cs_2O-TiO_2 glasses. J. Non-Cryst. Solids 112, 64–68.

Sandstrom, D.R., Lytle, F.W., Wei, P., Greegor, R.B., Wong, J., Schultz, P., 1980. Coordination of Ti in TiO_2-SiO_2 glasses by X-ray absorption spectroscopy. J. Non-Cryst. Solids 41, 201–207.

Scannell, G., Huang, L.P., Rouxel, T., 2015. Elastic properties and indentation cracking behavior of Na_2O-TiO_2-SiO_2 glasses. J. Non-Cryst. Solids 429, 129–142.

Schreiber, H.D., 1977. Redox States of Ti, Zr, Hf, Cr and Eu in Basaltic Magmas: An Experimental Study.Eight Lunar Science Conference, Houston, Texaspp. 1785–1809.

Schreiber, H.D., Thanyashiri, T., Lach, J.J., Legere, R.A., 1978. Redox equilibria of Ti, Cr and Eu in silicate melts: reduction potentials and mutual interactions. Phys. Chem. Glasses 19, 126–140.

Schultz, P.C., 1976. Binary titania-silica glasses containing 10-20 wt% TiO_2. J. Am. Ceram. Sco. 59, 214–218.

Shelby, J.E., 2005. Density of TiO_2-doped vitreous silica. Phys. Chem. Glasses 46, 494–499.

Strnad, Z., 1986. Glass-Ceramic Materials. In: Liquid Phase Separation, Nucleation, and Crystallization in Glasses. Elsevier, New York.

Tanabe, J., Suito, H., 1992. Thermodynamics of nitrogen in CaO-TiO_2-$TiO_{1.5}$ slags. Steel Res. Int. 63, 515–521.

Tangeman, J.A., Lange, R.A., 1998. The effect of Al^{3+}, Fe^{3+}, and T^{i4+} on the configurational heat capacities of sodium silicate liquids. Phys. Chem. Minerals 26, 83–99.

Tobin, M.C., Baak, T., 1968. Raman spectra of some low-expansion glasses. J. Am. Opt. Soc. 58, 1459–1460.

Tranell, G., Ostrovski, O., Johanshahi, S., 2002. The equilibrium partitioning of titanium between Ti^{3+} and Ti^{4+} valency states in $CaO-SiO_2-TiO_x$ slags. Metall. Mater. Trans. B Process Metall. Mater. Process. Sci. 33, 61–67.

Turnbull, R.C., Lawrence, W.G., 1952. The role of titania in silica glasses. J. Am. Ceram. Sco. 35, 48–53.

Unger, S., Dellith, J., Scheffel, A., Kirchhof, J., 2011. Diffusion in $Yb_2O_3-Al_2O_3-SiO_2$ glass. Eur. J. Glass Tech. B 52, 41–46.

Van der Kaaden, K.E., Agee, C.B., McCubbin, F.M., 2015. Density and compressibility of the molten lunar picritic glasses: implications for the roles of Ti and Fe in the structures of silicate melts. Geochim. Cosmochim. Acta 149, 1–20.

Visser, W. & Koster Van Groos, A. F. (1979). Effects of P_2 O_5 and TiO_2 on liquid-liquid equilibria in the system $K_2O-FeO-Al_2O_3$ $-SiO_2$. Am. J. Sci. 279, 970–983.

Webb, S.L., Dingwell, D.B., 1994. Compressibility of titanosilicate melts. Contrib. Mineral. Petrol. 118, 157–168.

Wechsler, B.A., Von Dreele, R.B., 1989. Structure refinement of Mg_2TiO_4, $MgTiO_3$ and $MgTi_2O_5$ by time-of-flight neutron powder diffraction. Acta Cryst. B45, 542–549.

Wood, M.I., Hess, P.C., 1980. The structural role of Al_2O_3 and TiO_2 in immiscible silicate liquids in the system $SiO_2-MgO-CaO-FeO-TiO_2-Al_2O_3$. Contrib. Mineral. Petrol. 72, 319–328.

Yarker, C.A., Johnson, P.A.V., Wright, A.C., Wong, J., Greegor, R.B., Lytle, F.W., Sinclair, R.N., 1986. Neutron diffraction and EXAFS evidence for TiO_5 units in vitreous $K_2O{\bullet}TiO_2{\bullet}2SiO_2$. J. Non-Cryst.Solids 79, 7–136.

Zhang, G.H., Chou, K.C., Zhang, J.L., 2014. Influence of TiO_2 on viscosity of aluminosilicate melts. Ironmak. Steelmak. 41, 47–50.

CHAPTER

13

Phosphorus in Silicate Systems

OUTLINE

13.1 INTRODUCTORY COMMENTS

Phosphorus-bearing silicate glasses have a range of commercial applications. They are used in optical communications systems (Li et al., 1995; Brow, 2000). Phosphorus also plays a role in the development of ceramics and glasses (Chakraborty and Condrate, 1985; Kosinski et al., 1988) and particularly in bioceramics and bioglass technology (Grussaute et al., 2000; Elgayar et al., 2005; Mathew et al., 2015; Brauer and Jones, 2018).

In natural silicate melts such as magmatic liquid and volcanic producs, P_2O_5 can reach concentrations near 1 wt% (Pichavant et al., 1987; London et al., 1993). Even at this comparatively low concentration P_2O_5 can have profound effects on liquidus phase relations and transport properties (Wyllie and Tuttle, 1964; Kushiro, 1975; Toplis et al., 1994; Dingwell et al., 1993; Wolf and London, 1994). Redox equilibria of multivalent components such as Fe^{3+}/Fe^{2+}, Cr^{3+}/Cr^{2+}, and Ti^{4+}/Ti^{3+} can also be affected by phosphorus in silicate melts (Toplis et al., 1994; Ehrt et al., 2001; Borisov et al., 2013). Crystallization of apatite may affect trace element evolution of magmatic systems (Watson and Capobianco, 1981; Montel, 1986). The tendency

https://doi.org/10.1016/B978-0-444-63708-6.00013-2

of P_2O_5 to promote liquid immiscibility in silicate systems can result in unusual magmatic processes (Visser and Van Groos, 1979).

13.2 PROPERTIES OF PHOSPHORUS-BEARING GLASSES AND MELTS

Solution of P_2O_5 in silicate glasses and melts affect their physical and chemical properties. These include activity-composition relations of silicate components, liquidus phase relations, glass transition temperatures, transport and volume behavior (Levien et al., 1964; Ryerson, 1985; O'Donnell et al., 2008; Toplis and Dingwell, 1996; Doweidar, 2009).

13.2.1 Phase Relations

Phase equilibria among P-bearing melts and coexisting crystalline phases reflects activity composition relations in silicate melts, which of course depend on P_2O_5 content and also on temperature.

13.2.1.1 Melting Relations in Chemically Simple Systems

Liquidus phase relations in P-bearing silicate and aluminosilicate systems depend on the absence or presence alkalis or alkaline earths. The electronic properties of the metal cation(s) can also have an effect.

In the systems P_2O_5-SiO_2 (Tien and Hummel, 1962) and P_2O_5-Al_2O_3 (Stone et al., 1956), for example, there are only two crystalline phases on the liquidus (Fig. 13.1). Aside from this small number, which tends to suggest that that the ionic radius mismatch of Si^{4+} (0.26 Å) and P^{5+} (0.17 Å) and Al^{3+} (0.37 Å) could be a governing factor, there are, nevertheless significant mutual solubilities in the melts at the eutectic for these two systems (Fig. 13.1). The very large tempeature depressions of several hundred °C would suggest, however, that the activity-composition relations in these systems deviate from ideal mixing.

The phase relations in metal oxide phosphate systems on the joins P_2O_5-CaO, P_2O_5-MgO, P_2O_5-K2O, and P_2O_5-Na_2O, differ from those of Fig. 13.1 by their much larger number of liquidus phases and greater mutual solubility (Levien et al., 1964). The liquidus temperature depression from the P_2O_5 endmembers also is considerably less pronounced than in the former systems, which leads to the suggestion that these melts show considerably less deviations from ideality. As SiO_2 is added to the P_2O_5-containing alkali and alkaline earth systems, the resulting complex phase relations make vitrification considerably easier.

13.2.1.2 Melting Relations in Chemically Complex Systems

In all systems, including magmatic liquids, solution of P_2O_5 also results in liquidus temperature depressions. Moreover, liquidus phase relations in P-bearing silicate and aluminosilicate systems exhibit cconsiderable changes of liquidus volume of polymerized crystalline phases compared with P_2O_5-free systems (i.e., silica polymorphs rather than metasilicates and metasilicates rather than orthosilicates) (Fig. 13.2; see also Kushiro, 1975 and Ryerson, 1985, for discussion of such phase equilbrium data and their consequences for the solution

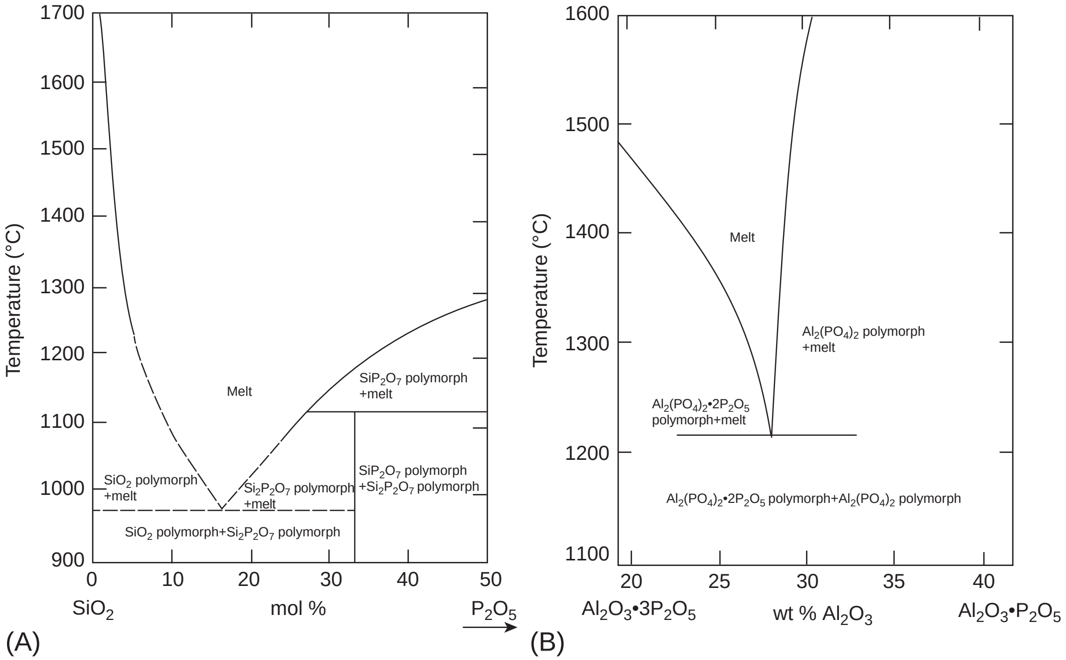

FIG. 13.1 Liquidus phase relations in binary P_2O_5-bearing systems. (A) The system P_2O_5-SiO_2 (Tien and Hummel, 1962). (B) The system P_2O_5-Al_2O_3 (Stone et al., 1956).

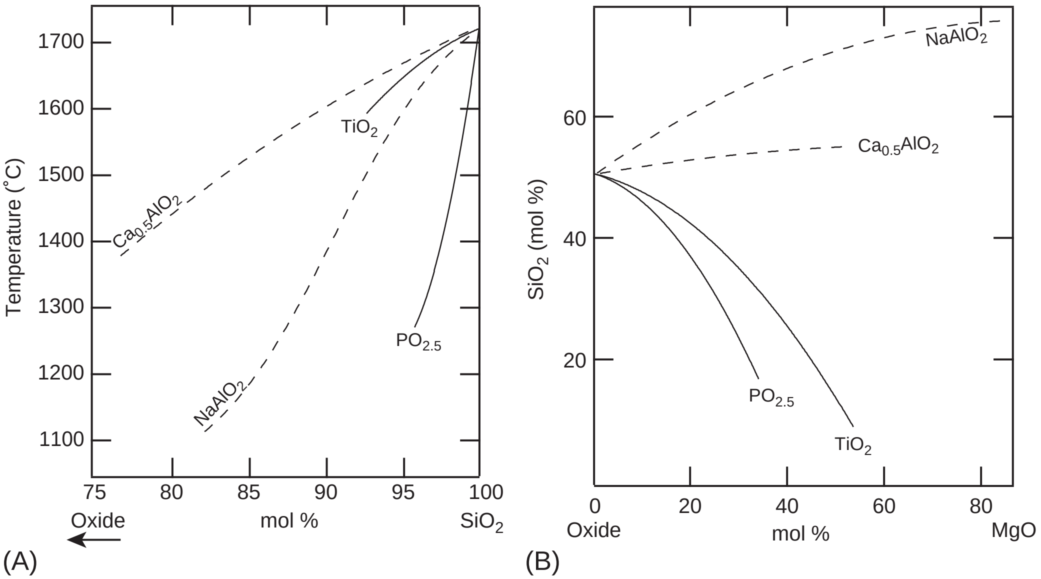

FIG. 13.2 (A) Temperature-composition trajectory of the liquidus surface of SiO_2 polymorphs (cristobalite and tridymite, depending on temperature) as a function of oxide component added to SiO_2 (modified from compilation of phase equilibrium data by Ryerson, 1985). (B) Composition trajectories for the enstatite-forsterite liquidus boundary in the MgO-SiO_2-oxide system as a function of oxide type and concentration relative to MgO (modified from compilation of phase equilibrium data by Ryerson, 1985).

thermodynamics in melts). Compared with TiO_2 (Chapter 12) and Al_2O_3 (Chapter 8), P_2O_5 has a greater effect on the liquidus temperature than any of the other components.

Also shown in Fig. 13.2 is the position of the enstatite-forsterite liquidus boundary in ternary MgO-SiO_2-oxide systems where, of course, enstatite ($MgSiO_3$) is more polymerized than forsterite (Mg_2SiO_4) (Fig. 13.2B). The expansion of the enstatite ($MgSiO_2$) liquidus volume relative to that of forsterite (Mg_2SiO_4) is shown clearly where phosphorus has a stronger effect than TiO_2 and aluminate complexes. The implications for activity-composition relations of melts in these types of system is the subject of Section 13.3.1.

The enhanced activity coefficient of SiO_2 indicated by the phase equilibrium data (Fig. 13.2) ultimately leads to liquid immiscibility not only in simple binary systems (e.g., Fig. 13.1), but also in more complex systems such as Fe_2SiO_4-$KAlSi_2O_6$-SiO_2 (Visser and Van Groos, 1979), where the extent of immiscibility increases systematically with increasing P_2O_5 concentration (Fig. 13.3). That solution of P^{5+} in silica-rich melts is energetically unfavorable is also indicated by the fact that nearly all phosphorus is dissolved in the silica-poor melt of the miscibility gap.

Phosphorus dissolved in hydrous aluminosilicate melts also has a profound influence of the melting relations of aluminosilicates. This can be seen in the liquidus phase relations of the system $NaAlSi_3O_8$-$KAlSi_3O_8$-SiO_2-P_2O_5-H_2O (London et al., 1993) where the so-called granite minimum (Tuttle and Bowen, 1958) shifts away from the SiO_2 apex toward the $NaAlSi_3O_8$-$KAlSi_3O_8$ join with increasing P_2O_5 content (Fig. 13.4). London et al. (1993) suggested that this shift of the granite minimum, which signals a decrease in the activity coefficient of SiO_2 in the system, might be because of formation of some form of Al-phosphate complex. Such changes may also help to account for the effect of P_2O_5 on H_2O solubility in haplogranitic melts

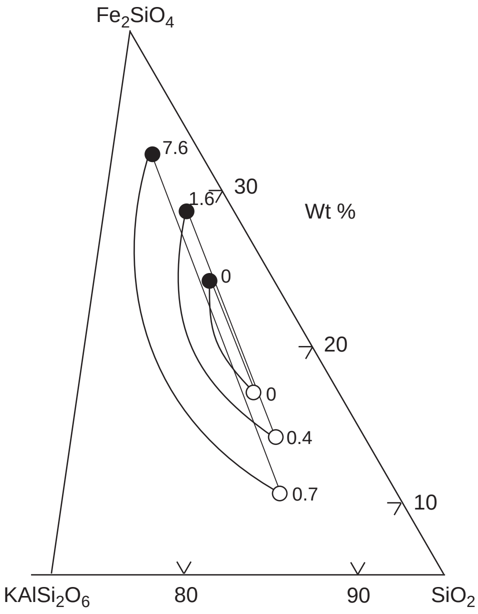

FIG. 13.3 Relationships between liquid miscibility gap and P-content in the system Fe_2SiO_4-$KAlSi_2O_6$-SiO_2. Open symbols: silica-rich melts; closed symbols: silica-poor melt. Numbers next to individual symbols are P_2O_5 contents (wt%) of melts. *Redrawn from Visser and Koster Van Groos (1979).*

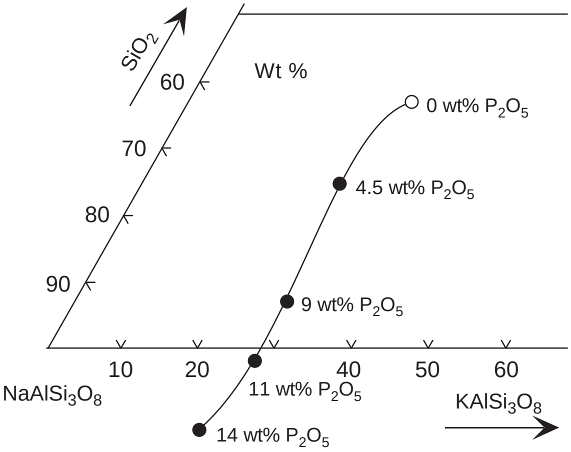

FIG. 13.4 Effect of P_2O_5 on composition of "granite minimum" (melt coexisting with feldspar and quartz) in the system $NaAlSiO_4$-$KAlSiO_4$-SiO_2-H_2O. Numbers next to data point represent P_2O_5 content of melt (London et al., 1993).

($NaAlSi_3O_8$-$KAlSi_3O_8$-SiO_2), more H_2O dissolving in P_2O_5-bearing than in P_2O_5-free melts (Holtz et al., 1993; see also Fig. 13.5). Such enhanced water solubility might also be behind the changes in pressure-temperature trajectories of hydrous $NaAlSi_3O_8$ composition melt when P_2O_5 is dissolved (Fig. 13.6; see also Wyllie and Tuttle, 1964). In the latter case, a temperature depression of up to 150 °C compared with that of H_2O alone might suggest interaction between P_2O_5 and hydrous aluminosilicates, perhaps along the same lines as that which gives rise to the changes in the granite minimum and the H_2O solubility in the melt itself (Figs. 13.4 and 13.5).

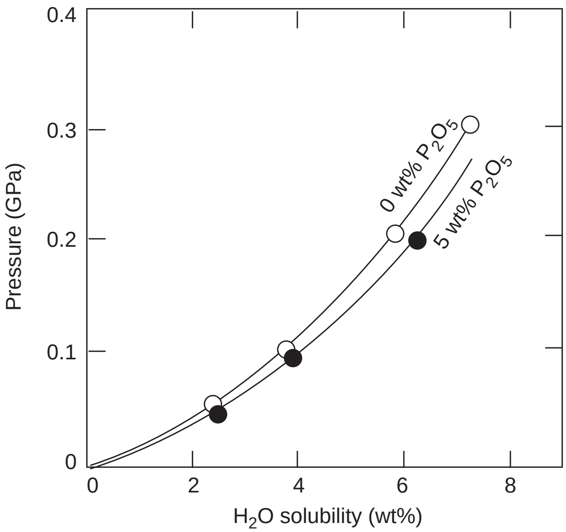

FIG. 13.5 Effect of P_2O_5 on the H_2O-solubility in a haplogranite melt (Holtz et al., 1993).

FIG. 13.6 Effect of P_2O_5 on the H_2O-saturated solidus of $NaAlSi_3O_8$. *Redrawn from Wyllie and Tuttle (1964).*

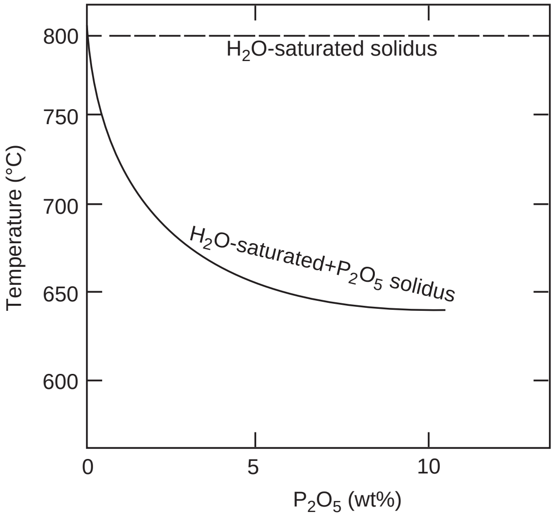

13.2.1.3 *Phosphorus Solubility in Silicate Glasses and Melts*

Phosphorus solubility in melts depends on silicate composition. This is evident in the widths of liquid immiscibility gaps (Tien and Hummel, 1962; Visser and Van Groos, 1979) shown, for example, in the system Fe_2SiO_4-$KAlSi_2O_6$-SiO_2 with various amounts of P_2O_5 added. Aside from the increased width of the gap with phosphorus content (Fig. 13.3), it is clear that most of the phosphorus enters the mafic melt with mafic/felsic melt partition coefficients between 8 and 13 (Watson, 1976; Visser and Koster Van Groos, 1979). Solution of P^{5+} in silica-rich melts thus is energetically unfavorable.

A pronounced dependence of phosphorus solubility on silica content and, therefore, melt polymerization, also is evident in P-partitioning beeween F-apatite and magmatic liquids (Harrison and Watson, 1984). The partition coefficient, $D_p{}^{\text{apatite/melt}}$ (= P_2O_5 in apatite/ P_2O_5 in melt), increases with increasing SiO_2 content and is a linear function of reciprocal temperature (Fig. 13.7). In addition to these two factors, the Al_2O_3 content of melts also affects P_2O_5 solubility as well as P-diffusion (Montel, 1986; Pichavant et al., 1992; Wolf and London, 1994). This effect is particularly clear in the rapidly increasing P_2O_5 solubility with Al_2O_3 content in peraluminous silicate melts (Fig. 13.8).

Phosphate complexing could also be relevant in hydrous aluminosilicate melts. Although Harrison and Watson (1984) concluded that H_2O content does not affect P-partitioning between apatite and magmatic liquids, other properties seem to reveal an interplay between H_2O and phosphorus. For example, the pressure-temperature trajectory of the albite-H_2O-P_2O_5 solidus depends on P_2O_5 content (Fig. 13.6). Holtz et al. (1993) found that addition of P_2O_5 to $KAlSi_3O_8$-$NaAlSi_3O_8$-H_2O melts lowers H_2O solubility in such felsic aluminosilicates (Fig. 13.6). It is not clear, however, whether the relations in Fig. 13.6 reflect interaction between dissolved P_2O_5 and H_2O or whether solution of P_2O_5 affects the aluminosilicate network structure and, therefore, H_2O solubility.

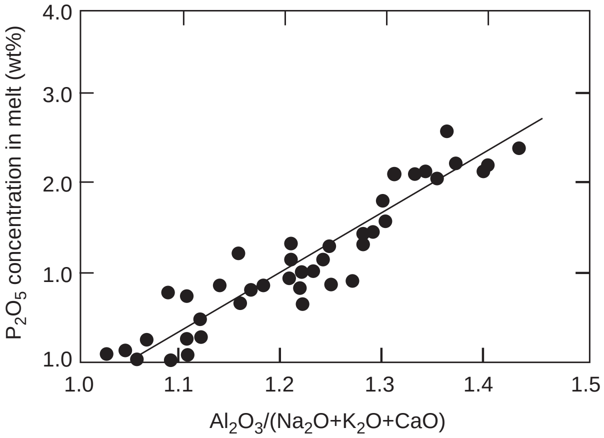

FIG. 13.7 Phosphorus partitioning between coexisting silicate melt and F-apatite as a function temperature for the SiO_2 contents indicated (Harrison and Watson, 1984).

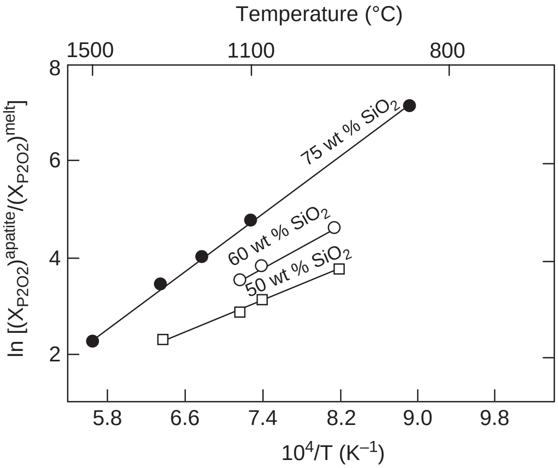

FIG. 13.8 P_2O_5 solubility in peraluminous silicate melts in equilibrium with apatite as a function of per-aluminosity, $Al_2O_3/(Na_2O+K_2O+CaO)$, of the melt (Wolf and London, 1994).

In the presence of mulivalent elements like iron, the P_2O_5 solubility depends on the Fe^{3+}/Fe^{2+} ratio at constant temperature and redox conditions. For example, a correlation between the P_2O_5 content and Fe^{3+}/Fe^{2+}-ratio of silicate melts was noted by Gwinn and Hess (1993) and Toplis et al. (1994). In their study of a basalt composition, Toplis et al. (1994) found clear evidence for decreasing Fe^{3+}/Fe^{2+} as a function of increasing P_2O_5 concentrations when melts were equilibrated in air at high temperature. This conclusion is qualitatively the same as that of Borisov et al. (2013) (Fig. 13.9) although the quantitiative relationships differ. These features may well reflect the wide compositional ranges studied (Al_2O_3 and SiO_2 contents, metal oxide concentrations, and so forth). Such complications are evident from redox vs P_2O_5 data of melts in the CaO-P_2O_5-SiO_2 system (Mysen, 1992) where the Fe^{3+}/Fe^{2+} ratio decreased with increasing P_2O_5 concentration in melts of constant overall CaO/SiO_2 ratio, whereas the Fe^{3+}/Fe^{2+} ratio exhibited a slight increase in melts where both the CaO/SiO_2 and P_2O_5 abundance ratios increased.

FIG. 13.9 Redox ratio of iron, Fe^{3+}/Fe^{2+}, in $CaMgSi_2O_6$-$CaAl_2Si_2O_8$ melt as a function P_2O_5 dissolved in the melt at 1500°C and in equilibrium with air (Borisov et al., 2013).

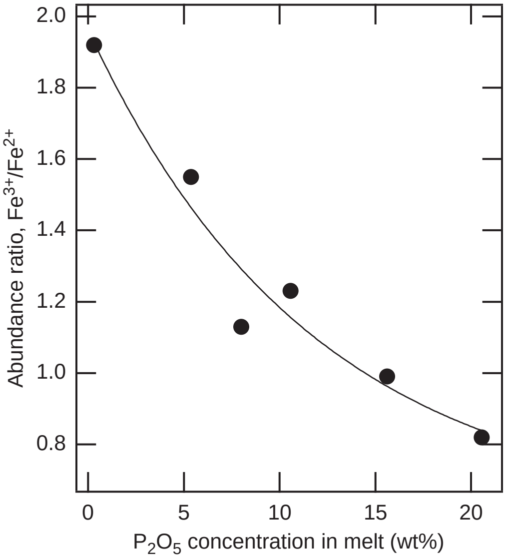

13.2.2 Thermal Properties

Activity-composition information can be extracted from liquidus phase relations combined with Van't Hoff equation (see, e.g., Eq. (12.2), Chapter 12). Here, the activity of SiO_2 as a function of the P-content of the melt can be determined from the temperature-composition trajectory of cristobalite/tridymite liquidus (Ryerson, 1985; see also Fig. 13.2). Interestingly, the activity coefficient of SiO_2 deduced in this way for the system SiO_2-P_2O_5 decreases with increasing P_2O_5 content much faster, on an equimolar basis, than when adding TiO_2 or aluminate components. This feature follows, of course, from the dramatic liquidus temperature depression resulting from dissolved P_2O_5 (Fig. 13.2A). On the other hand, the activity coefficient of SiO_2 increases with increasing phosphorus content in less silica-rich melts, for instance, for compositions corresponding to the olivine/protoenstatite liquidus boundary in the system MgO-SiO_2-P_2O_5 (Fig. 13.10). The complex activity-composition relations of P_2O_5 suggests that phosphorus is not simply either a network former or a network modifier in silicate melts, but that its role depends on the melt composition.

The heat capacity change across the glass transition has been determined for a few compositions in the Na_2O-SiO_2-P_2O_5 system (Hermansen et al., 2015). In the latter study, the ΔC_p-value increases to a maximum approximately halfway between the $0.3Na_2O{\cdot}0.7SiO_2$ and $0.3Na_2O{\cdot}0.7P_2O_5$ endmembers.

13.2.3 Physical Properties

13.2.3.1 Transport Properties

Complicated structural interactions between dissolved phosphorus and silicate components are evident in the relationships between viscosity and composition. For example, in haplogranite, a highly polymerized melt in the system $KAlSi_3O_8$-$NaAlSi_3O_8$-SiO_2 with

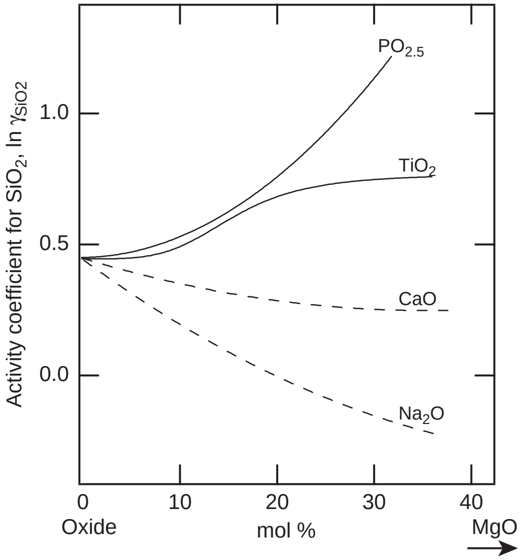

FIG. 13.10 Evolution of the activity coefficient of SiO_2 in melts calculated from the enstatite-forsterite liquidus boundary in the MgO-SiO_2-oxide system as a function of oxide type and concentration relative to MgO (modified from compilation of phase equilibrium data by Ryerson, 1985).

nominal NBO/$T=0$, Dingwell et al. (1993) observed that at constant temperature (1000°C in this case), increasing P_2O_5 melt content results in decreasing melt viscosity (Fig. 13.11A), whereas there is the opposite effect of increasing P_2O_5 concentration on viscosity of a depolymerized natural ferrobasalt melt with P-free NBO/$T=0.75$ (Fig. 13.11B). Thus, both viscosity and the activity coefficient of SiO_2 appears to depend in an analogous way on phosphorous content. In polymerized melts (i.e., haplogranite), both decrease with increasing P_2O_5 concentration (Figs. 13.10 and 13.11A), whereas the opposite holds true for depolymerized melts such as a basalt (Figs. 13.10 and 13.11B).

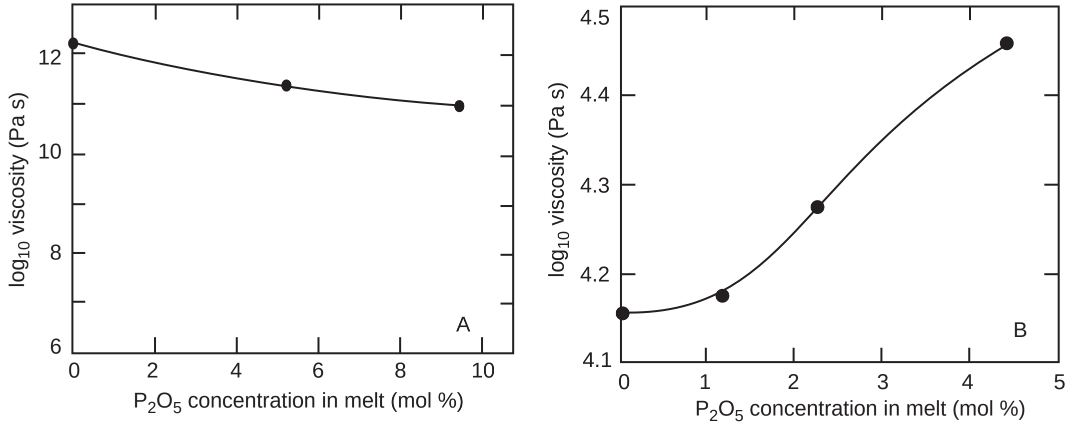

FIG. 13.11 Viscosity of (A) haplogranite melt at 1000°C and (B) Basalt melt at 1250°C as a function of the P_2O_5 content (mol%) (Dingwell et al., 1993; Toplis et al., 1994).

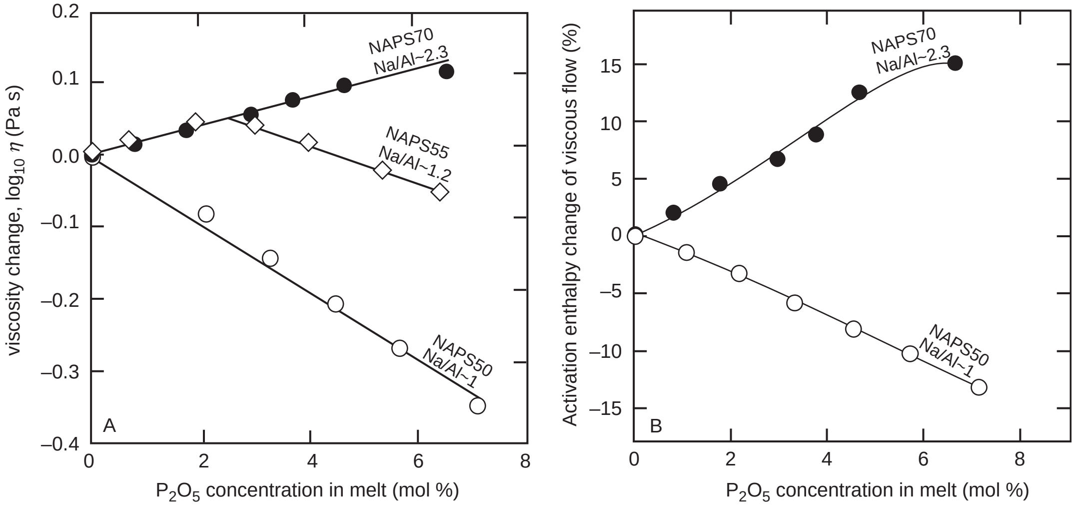

FIG. 13.12 Viscosity relations at high temperature in the system Na_2O-Al_2O_3-SiO_2-P_2O_5 as a function of P_2O_5 concentration. (A) Change in melt viscosity with P_2O_5 content relative to that of P-free melt at 1446°C. (B) Change in high-temperature activation energy of viscous flow with P_2O_5 content relative to that of P-free melts. NAPS50: meta-aluminosilicate melt with 50 mol% SiO_2 and Na/Al ~ 1 (*open circles*); NAPS70: peralkaline aluminosilicate melt with 70 mol% SiO_2 and Na/Al ~ 2.3 (*closed circles*); NAPS55: peralkaline aluminosilicate melt with 55 mol% SiO_2 and Na/Al ~ 1.2. See also text for further discussion of these compositions (Toplis and Dingwell, 1996).

For a better understanding of these relationships, Toplis and Dingwell (1996) determined melt viscosity in a series of compositions in the system xNa$_2$O-$(1-x)$Al$_2$O$_3$-2SiO$_2$ with P_2O_5 contents ranging from 0 to about 7 mol% (Fig. 13.12). For the most alkaline series, NAPS70, both viscosity and high-temperature activation enthalpy of viscous flow increase systematically with increasing P_2O_5. In this series (Na/Al ~ 2.37), Na^+ was in excess of that needed to charge-balance Al^{3+} in fourfold coordination so that formation of Na-phosphate complexes was possible in the entire P_2O_5 concentration range investigated. In contrast, for meta-aluminosilicate melts with nominal $NBO/T = 0$, both viscosity and high-temperature activation enthalpy decrease, whereas the series with Na/Al between 2.3 and 1.0, show an initial viscosity increase followed by a decrease at higher phosphorus content. Hence, it appears that the metal/alumina ratio plays a central role in the control of melt viscosity wherein there is competition for Al^{3+} and/or its charge-balancing cation between aluminate and phosphate complexes.

At least two mechansisms may be at play. According to Toplis and Dingwell (1996), the viscosities shown in Fig. 13.12 reflect interaction between phosphorus, metal cations, and aluminum. For a depolymerized, peralkaline aluminosilicate melt such as NPS70, the effect is described by a simple polymerization reaction,

$$2\mathrm{Si-O-Na} + \mathrm{P-O-P} \Leftrightarrow 2\mathrm{P-O-Na} + \mathrm{Si-O-Si}, \qquad (13.1)$$

which would also take place in the ferrobasalt series for which viscosity data are summarized in Fig. 13.11.

The reason for the viscosity trend of meta-aluminosilicate melts is less clear. Toplis and Dingwell (1996) suggested that the viscosity decrease of NAPS50 melt with P_2O_5 results from formation of alkali and aluminum phosphate complexes through interaction between P_2O_5 and charge-balanced $NaAlO_2$ via an equilibrium along the lines of (see also Gan and Hess, 1992):

$$NaAlO_2 + P_2O_5 \Leftrightarrow AlPO_4 + NaPO_3. \tag{13.2}$$

In melts of the series NAPS55, with intermediate Na/Al, some of the dissolved P_2O_5 might first interact with Na as suggested by Eq. (13.1). After exhaustion of the Na^+ left after completion of Al-charge balance, the mechanism of Eq. (13.2) might then operate. These relationships will be addressed in more details in Section 13.3.1.

13.2.3.2 *Density, Volume, Compressibility, and Expansion*

Density, volume, expansion and compressibility relationships reflect complex solution of P_2O_5 in silicate and aluminosilicate melts. To a cconsiderable extent, the complexity arises from the requirement that both Al^{3+} and P^{5+} require some form of charge compensation (see also Chapter 4, Section 4.4.3).

Solution of P_2O_5 in peralkaline silicate melts results in decreasing density and, therefore, increasing molar volume whether for basalt compositions or simple model systems (Toplis et al., 1994; Webb and Courtial, 1996; Doweidar, 2009; see also Fig. 13.13). However, the molar volume of molten basalt is more sensitive to P_2O_5 concentration (with a rate of increase of $0.35 \pm 0.1\,cm^3/mol$ per mol of P_2O_5 for basalt, compared with 0.25 ± 00 for Na_2O-CaO-SiO_2

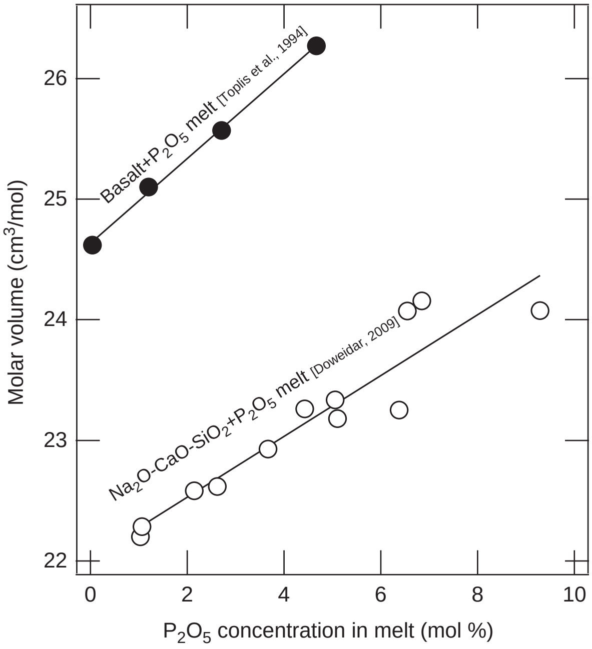

FIG. 13.13 Molar volume of basalt and Na_2O-$CaO+SiO_2$ melts as a function of P_2O_5 dissolved (Toplis et al., 1994; Doweidar, 2009).

FIG. 13.14 Bulk modulus of P-bearing melts with and without Al_2O_3 as a function of temperature and Al_2O_3 contents. The two compositions have, on average, 14 and 16 mol% P_2O_5 (Webb and Courtial, 1996).

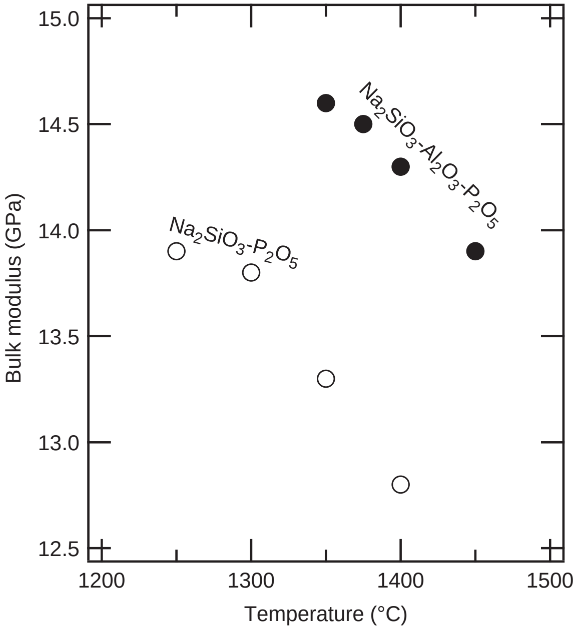

melts). Increasing P_2O_5 concentration causes melts to become more compressible than expected from simple polymerization of the silicate network (Webb and Courtial, 1996). Solution of P_2O_5 in Al-bearing melts causes them to become stiffer and their density to increase. The thermal expansion coefficients decrease for Al-bearing melts (Webb and Courtial, 1996; see also Fig. 13.14). These observations also imply complicated interaction between dissolved phosphorus, alkali metals and aluminum, features that are analogous to those observed for other properties of P-bearing silicate and aluminosilicate melts (Fig. 13.12; see also discussion in Section 13.2.3.1).

13.3 STRUCTURE OF PHOSPHORUS-BEARING GLASSES AND MELTS

The complex relationships between phosphorus content and properties of silicate melts and glasses suggest a variety of solution mechanisms for P^{5+}. Moreover, given the 5+ formal charge of phosphorus, some charge-compensation is necessary to attain a 4+ formal charge commonly needed if P^{5+} were to occupy structural positions similar to Si^{4+}. Exceptions to this general rule can be found in very P-rich glasses, where coordination numbers in excess of 4 may be encountered (Ide et al., 2007; Hermansen et al., 2015).

In crystalline posphosilicates, attainment of an effective 4+ charge around the P^{5+} cation is accomplished by various coupled substitutions,

$$Si^{4+}Si^{4+} \Leftrightarrow P^{5+}Al^{3+} \text{ (berlinite)}$$

$$Si^{4+}Al^{3+} \Leftrightarrow P^{5+}Mg^{2+}\ (\text{ellenbergerite})$$

$$Si^{4+}Al^{3+} \Leftrightarrow P^{5+}\ Be^{2+}\ (\text{hurlbutite})$$

$$Si^{4+}Fe^{2+} \Leftrightarrow P^{5+}\ Li\ (\text{triphyllite})$$

$$Si^{4+}Mg^{2+}{}_{0.5} \Leftrightarrow P^{5+}\square^{+}\ (\text{triphyllite})$$

$$Si^{4+}\ (Fe^{2+})_2 \Leftrightarrow P^{5+}Fe^{3+}\ (\text{heterosite}),$$

where □ denotes a vacancy. In addition, in crystalline P_2O_5, local charge neutrality is accomlished via one oxygen double-bonded to phosphorus.

Similar mechanisms may be envisioned for tetrahedrally coordinated P^{5+} in silicate glasses and melts. The properties summarized above have often be explained, for example, with the aid of AlP and M_xP functionality for charge-compensation. Double-bonded oxygen has also been proposed.

13.3.1 Oxygen Coordination, P^{5+} Concentration, and Composition

Phosphorus may exist as P_2O_5 in glass and melt structures. It may also occur as separate phosphate complexes, or as integral part of P-bearing silicate and aluminosilicate structures (Galeener and Mikkelsen, 1979; Hoppe et al., 1998; Brow, 2000). In this section, we will discuss these structures in terms of increasing chemical complexity.

13.3.1.1 P_2O_5

Glasses and melts of P_2O_5 composition form a three-dimensional network of phosphate tetrahedra comprising three bridging oxygens (BO) and a single terminal oxygen that is double bonded to P^{5+} (Galeener and Mikkelsen, 1979; Plotnichenko et al., 2002). The correlation functions derived from neutron scattering data reveals three P—BO bond lengths at 1.58 Å (Plotnichenko et al., 2002), which is quite similar to the 1.60–1.61 Å bond length is vitreous SiO_2 (see Chapter 5). The double-bonded terminal oxygen (OT) is shorter (1.43 Å) than the bridging oxygen bonds (Hoppe et al., 1998; see also Fig. 13.15). On the short- and median-range scales, this structure resembles that found in crystalline P_2O_5 (Arbib et al., 1996).The P—O—P angle (131 degrees; Plotnichenko et al., 2002) is noticably and perhaps surprisingly smaller than the Si—O—Si angle in vitreous SiO_2 (near 150°; see Chapter 5) given the P—O bridging oxygen bond length around 1.57 Å, which is, of course, near that in SiO_2 glass (1.61 Å).

13.3.1.2 Binary Phosphate Systems

Binary phosphate glasses and melts include compositions with one or more alkali metals or alkaline earths ($M^{n+}{}_{n/2}O$-P_2O_5) (Zeyer et al., 2002; Alam et al., 2000; Brow, 2000; Mathew et al., 2015) as well as compositions such as SiO_2-P_2O_5 and Al_2O_3-P_2O_5 (Kosinski et al., 1988; Li et al., 1995; van Wullen et al., 2007).

The Raman spectra of SiO_2-P_2O_5 glasses suggest that many of the structural features of the P_2O_5 and SiO_2 endmembers remain in mixed SiO_2-P_2O_5 glasses (Fig. 13.16). Additional features near 1100 cm^{-1} in the spectra of these glasses have been assigned to vibrations of

FIG. 13.15 Correlation function from neutron diffraction of P_2O_5 glass. P-OT and P-OB denote phosphorus-oxygen distances for terminal and bridging oxygen, respectively, and OB-OT and OB-OB oxygen-oxygen distances from bridging to terminal and bridging to bridging oxygen, respectively. *Redrawn from Hoppe et al. (1998).*

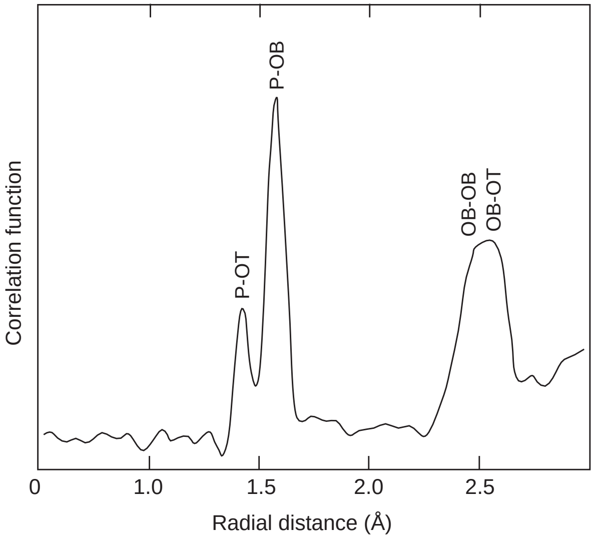

FIG. 13.16 Comparison of the Raman spectra of glasses P_2O_5, SiO_2, and SiO_2+ 14 mol% P_2O_5. Bands assigned to stretching of double bonded O near 1380 cm^{-1} and P—O bonds near 1150 cm^{-1} are marked (Shibata et al., 1981; Meyer, 1997).

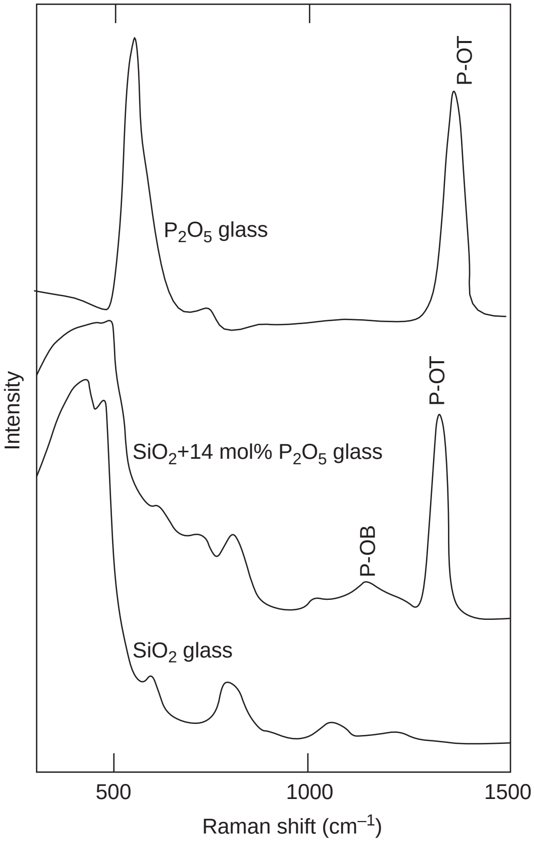

Si—O—P bridges. Phosphorus in this configuration might be referred to as a $Q^n(P)$ entity, where n denotes the number of Si—O—P bridges (Meyer, 1997). Silicon K- and L-edge and phosphorus L-edge X-ray absorption spectra of SiO_2-P_2O_5 glass with less than about 30 mol% P_2O_5 are also consistent with this interpretation (Li et al., 1995). For higher phosphorus contents, Li et al. (1995) suggested that there is evidence for coordination transformation of some of the Si^{4+} from four- to sixfold coordination through, perhaps, formation of complexes with a structure resembling that of crystalline SiP_2O_7.

Phosphate complexes may polymerize to form entities conceptually similar to the Q^n-species described for silicates. In phosphate species less polymerized than $Q^3(P)$ [$Q^2(P)$, $Q^1(P)$, and $Q^0(P)$] there are two or fewer Si—O—P bridges and one or more nonbridging oxygens (Kirkpatrick and Brow, 1995; Brow, 2000). In these less polymerized phosphate species, the nonbridging oxygens bond to other metal cations. In such cases, charge-compensation of P^{5+} is accomplished with a neighboring metal cation. In depolymerized phosphate glasses, there is no evidence of the doubly bonded oxygen found in structures of P_2O_5 glass. Evidently, as metals are dissolved in P_2O_5, the P═O bond is replaced by a nonbridging P—O bond where alkalis or alkaline earths form bonding with the oxygen.

In the metal oxide-phosphate systems, PO_4 groups with different degrees of polymerization coexist in a manner resembling that observed in metal oxide-silicate systems (see Chapter 4, Section 4.4.2 and Chapter 7, Section 7.3)). By using $Q^n(P)$ as a notation analogous to the Q^n of silicate systems, we may write a simple disproportionation equilibrium (Brow, 2000):

$$2Q^n(P) = Q^{n+1}(P) + Q^{n-1}(P), \tag{13.3}$$

where n cannot exceed 2 by the fact that $Q^4(P)$ species as three-dimensionally interconnected vitreous P_2O_5 comprise only three bridging oxygens (Kirkpatrick and Brow, 1995).

The equilibrium constant for equilibrium (13.3) depends on metal/P ratio, which leads to an evolution of species abundances resembling that in metal oxide-silicate systems as a function of metal/Si ratio (Brow et al., 1994; Fig. 13.17, but see also Chapter 7, Fig. 7.13, for another example in a metal oxide-silicate system).

13.3.1.3 *Phosphosilicate Glasses and Melts*

Solution of P_2O_5 in metal oxide-silica melt and glass occurs through formation of phosphate species (Nelson and Tallant, 1984, 1986; Dupree et al., 1989; Li et al., 1995; Mysen, 1998; Toplis and Reynard, 2000; Cody et al., 2001; O'Donnell et al., 2008; Watts et al., 2010; Mathew et al., 2015). There are systematic relationships between ^{31}P NMR shift and phosphate polymerization, as well as between Raman shifts and phosphate speciation (Dupree, 1991; Nelson and Tallant, 1984, 1986; Yamashita et al., 2000; O'Donnell et al., 2008). Increasing phosphate polymerization results in increasingly negative ^{31}P shifts (Fig. 13.18A) and in increasing frequencies of P—O stretch vibrations (Fig. 13.18B). These spectroscopic trends resemble the relationships between degree of polymerization and either Raman frequencies or ^{29}Si NMR chemical shifts described for silicates (see Chapter 7). Moreover, the average ^{31}P and ^{29}Si chemical shifts decrease (become more negative) as the P_2O_5 concentration of alkali silicate glasses increases (O'Donnell et al., 2008).

FIG. 13.17 $Q^n(P)$ species evolution in quenched melts in the system ZnO-SiO_2 from ^{31}P MAS NMR data (Brow et al., 1994).

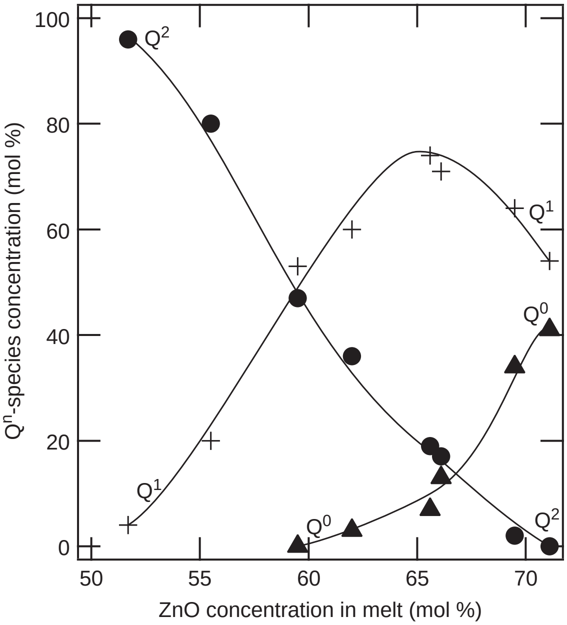

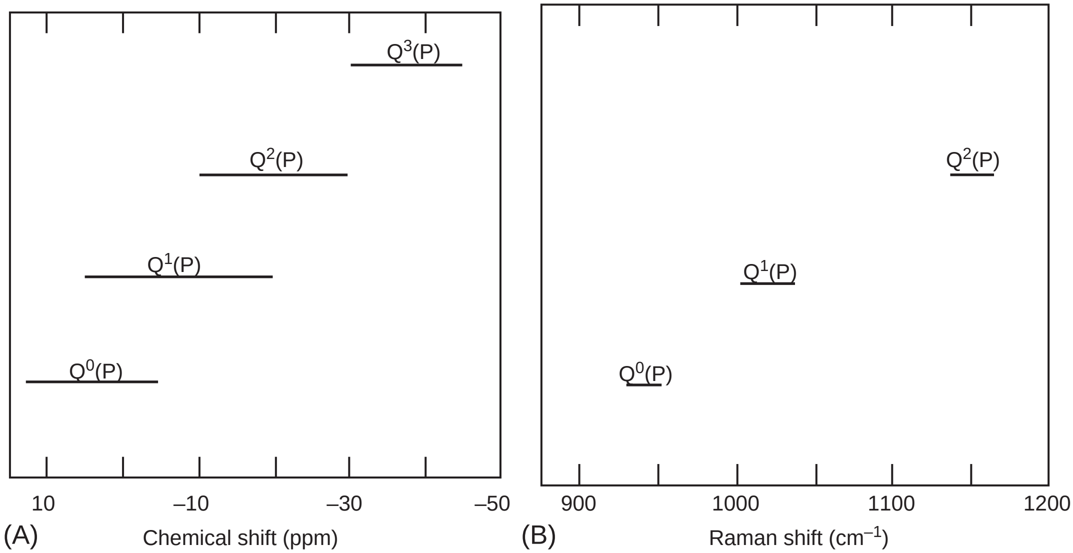

FIG. 13.18 Summary of (A) ^{31}P MAS NMR shifts for different Q^n-species in phosphate systems. The superscript, *n*, is number of bridging oxygens in the phosphate species. (B) Raman shifts for different Q^n-species in phosphate systems. The *n* represents the number of bridging oxygens. *Redrawn from Dupree (1991).*

Nelson and Tallant (1984, 1986) pointed out that the extent of phosphate polymerization in the silicate melts and glasses increases with phosphorus content. Enhanced silicate polymerization of metal oxide-silicate melts have also been suggested from liquidus phase relationships following solution of P_2O_5 in silicate melts (Kushiro, 1975). These polymerization features are evident in the Raman and ^{31}P MAS NMR spectra of metal oxide-$SiO_2-P_2O_5$ glasses (Lockyer et al., 1995; Bykov et al., 2001; O'Donnell et al., 2008; Ding et al., 2012). Polymerization is also consistent with results from near-edge X-ray absorption spectra (Li et al., 1995). Interestingly, in phosphosilicate glasses and melts with more than one type of metal oxide (e.g., Ca and Mg, Ca, and Na, and Na, Mg), there is some uncertainty whether or not different metal cations exhibit preference for specific types of phosphate units (Grussaute et al., 2000) and whether or not, for phosphosilicate glasses, there is ordering of network-modifying metal cations among silicate and phosphate entities in the structures (Watts et al., 2010; Mathew et al., 2015).

The extent to which PO_4-groups are interconnected with the silicate network has been studied by X-ray absorption and NMR spectroscopy (Li et al., 1995; Lockyer et al., 1995; Cody et al., 2001). For Na_2O-SiO_2-P_2O_5 glasses, Li et al. (1995) found that increasing phosphorus contents results in increased energy of the K-edge. As this shift was higher than the energy of the K-edge in fully polymerized SiO_2 glass, Li et al. (1995) concluded that it results from interconnectivity between SiO_4 and PO_4 groups. In other words, Si—O—P bridges were inferred to exist in these materials. However, in more recent NMR studies by Cody et al. (2001) and Watts et al. (2010), little or no evidence for Si—O—P bridges in silicophosphate glasses was reported. If, in fact, P—O—Si bridges exist in the glass and melt structure, an implication of the preceding observation is that the number of such bridges should also correlate with the isomer shift from ^{31}P NMR spectroscopy. The effect is similar to the shielding of Si nuclei by next-nearest Al^{3+} in aluminosilicates (Engelhardt and Michel, 1987; see also Chapter 9, Section 9.3.2).

To address this question in more detail, Cody et al. (2001) employed ab initio shielding calculations to estimate how the number of P—O—Si bridges likely would affect the chemical shift of ^{31}P in sodium phosphosilicate glasses (Fig. 13.19). This shift of a species with one Si—O—P bridge is similar to that resulting from a P—O—P bridge in a phosphate dimer, P_2O_7. However, ^{31}P chemical shifts in a given phosphate complex also shift with the electronic properties of the metal cation (Grussaute et al., 2000; Watts et al., 2010; see also Fig. 13.20). The trend is such that it might be difficult to distinguish between chemical shifts because of polymerization of phosphate species and simply changing the ionization potential of the network-modifying cation (e.g., Na^+ vs Ca^{2+}; see Figs. 13.18 and 13.20). Interestingly, in an exchange of Ca^{2+} with Mg^{2+} in Na_2O-CaO-SiO_2-P_2O_5 glasses, the ^{31}P chemical shift actually increases with increasing MgO/CaO abundance ratio (Fig. 13.21: see Watts et al., 2010). However, this effect could partly originate in the fact that a portion of the Mg^{2+} may be tetrahedrally incorporated in the silicate network (Watts et al., 2010).

In the Raman spectrum the Raman bands assigned to P—O stretch vibrations are distinct because of mass differences between Si and P and also because the P—O force constant depends on the next-nearest cation Si or P (Mysen and Cody, 2001). For a given Si—O or P—O vibration, the Raman shift is insensitive to the nature of the network-modifying cation (see Chapter 7, Section 7.3.1). Taken together, the X-ray absorption, ^{31}P NMR spectroscopy, Raman spectroscopy, and numerical simulation thus indicate that, at least to some extent, phosphate species can be connected to the silicate network via oxygen bridges.

FIG. 13.19 Calculated ^{31}P MAS NMR shift as a function of the number of bridging oxygen (Cody et al., 2001).

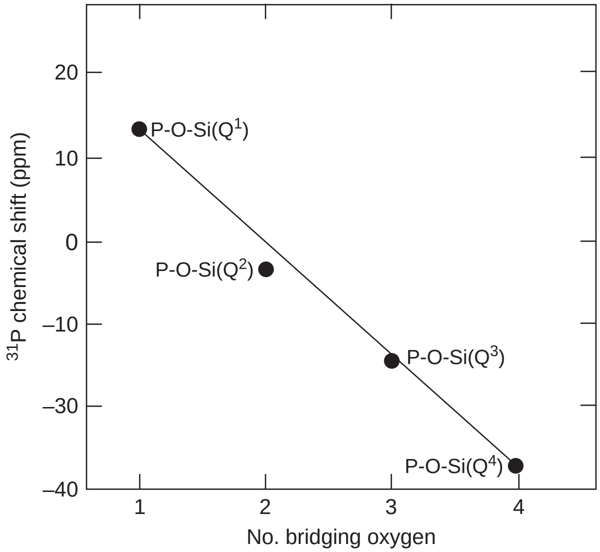

FIG. 13.20 ^{31}P chemical shift from isolated PO_4 (orthophosphate) complexes as a function of CaO/Na_2O abundance ratio of the glass (Grussaute et al., 2000).

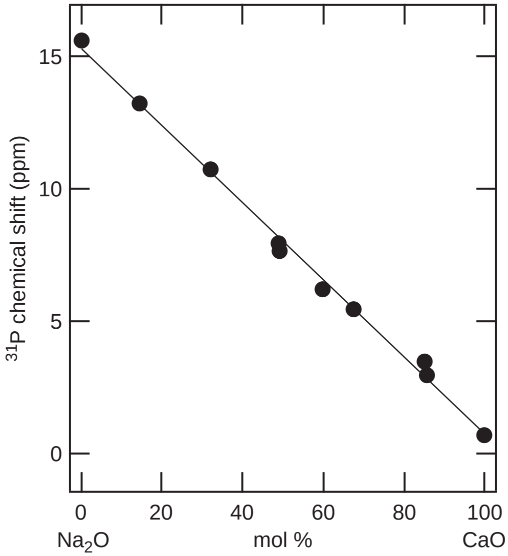

Formation of PO_4-complexes upon solution of P_2O_5 in metal oxide-silica melts is associated with an increase in silicate polymerization (Nelson and Tallant, 1984; Dupree et al., 1988; Li et al., 1995; Toplis and Schaller, 1998; Cody et al., 2001; Toplis and Reynard, 2000). This is evident in the relative abundance of Q^3 and Q^4 structural units from ^{29}Si MAS NMR spectra of quenched melts in the systems Na_2O-SiO_2-P_2O_5 (Dupree et al., 1988, 1989; Toplis and Schaller, 1998), and K_2O-SiO_2-P_2O_5 (Lockeyer et al., 1991) as well as in other P-bearing alkali silicate

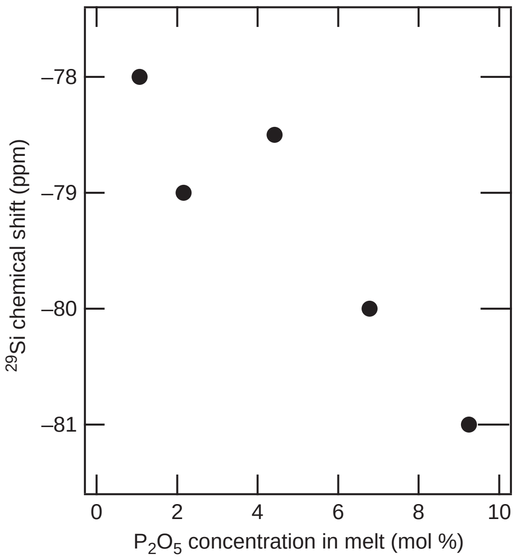

FIG. 13.21 Evolution of ^{31}P chemical shift in NMR spectra of Na_2O-CaO-SiO_2-P_2O_5 glasses as a function of P_2O_5 concentration where increasing P_2O_5 is in exchange for decreasing SiO_2 content (O'Donnell et al., 2008).

and alkaline earth silicate glasses and melts (Yang et al., 1986; Grussaute et al., 2000). Silicon-29 MAS NMR spectra of glasses demonstrating this effect are shown in Fig. 13.22, which illustrates how the abundance ratio, Q^4/Q^3, increases with increasing P_2O_5 concentration. In other words, the glasses and melts become increasingly polymerized as the P concentration increases. Notably, the ^{31}P chemical shift from these same samples does not seem to vary with P_2O_5 concentration (Dupree et al., 1988).

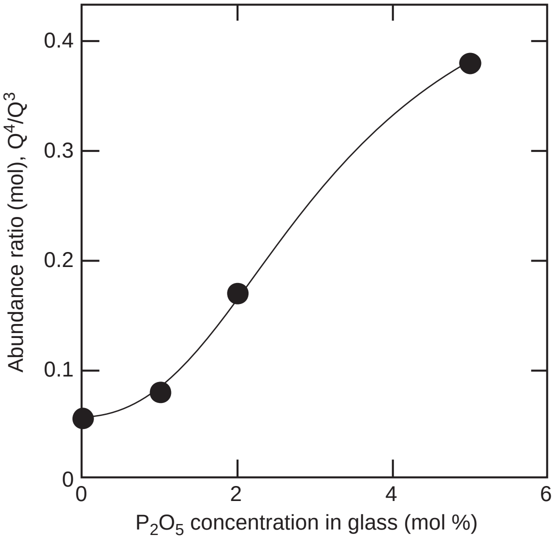

FIG. 13.22 Evolution of molar ratio of Q^4/Q^3 from the ^{29}Si MAS NMR spectra (Dupree et al., 1988).

The schematic solution mechanism of P_2O_5 in binary metal oxide-silicate glass and melts is described by Eq. (13.1). However, the actual process is more complicated than scavenging of metal oxide from the silicate to form metal-phosphate complexes. This is so because there exist at least three different phosphate complexes, even in compositionally simple systems such as binary metal oxide-SiO_2 melts and glasses with P_2O_5; these are PO_4, P_2O_7, and possibly one that comprises one P—O—Si bridge. We will denote this structural entity as $Q^1(P)$ for short. Thus, one may express solution of P_2O_5 in these melts with three equations that involve interactions between the silicate network and the phosphate complexes:

$$6Q^3 + P_2O_5 \Leftrightarrow 6Q^4 + 2PO_4, \tag{13.4}$$

$$4Q^3 + P_2O_5 \Leftrightarrow 4Q^4 + P_2O_7, \tag{13.5}$$

and

$$10Q^3 + P_2O_5 \Leftrightarrow 8Q^4 + 2Q^1(P). \tag{13.6}$$

All three solution mechanisms result in polymerization of the silicate network. However, the production of PO_4 groups is a more efficient polymerization process than formation of P_2O_7 groups. The reaction (13.6) forming $Q^1(P)$ is even less efficient than either reaction (13.4) or (13.5).

13.3.1.4 Phosphate in Metal Oxide-Alumina-Silica Systems

In silica-free alkali phosphate glasses, there are at least two different P—O bond lengths (1.56 Å for P—O—P bonds and 1.53 Å for P—O—Al bonds**)** and a single Na—O length (2.46 Å) in the structure as derived from combinations of NMR, X-ray diffraction measurements, and molecular dynamics simulations. The Al—O bond length varies with total Al_2O_3 concentration. It also differs depending on the next-neighbor environment (Al—O—Al: 1.68–174 Å, Al—O—P: 1.69–1.74 Å, Al—O—Na: 1.64–1.68 Å) (Inoue et al., 1995). This means that Al^{3+} likely exists in four-, five-, and sixfold coordination in these materials. It is not just a simple $AlPO_4$ or equivalent environment. Of course, these bond lengths and coordination numbers not only vary with Al/P ratio, but the type of alkali metal also affects the structural role of P^{5+} and Al^{3+} (Faivre et al., 2005; Viviani et al., 2006).

The structural complexity in P^{5+} in aluminate melts becomes even more difficult in P-bearing aluminosilicate glasses and melts (Dupree et al., 1989; Schaller et al., 1999; Toplis and Schaller, 1998). In this environment, the structure is influenced both by interactions between Al^{3+} and P^{5+} and by the competition for charge-compensation of tetrahedral Al^{3+} and P^{5+} (Toplis and Schaller, 1998; Faivre et al., 2005; Viviani et al., 2006; Ding et al., 2012). Moreover, the phosphate groups occur in different degrees of polymerization and surrounded by different numbers of Na^+ and Al^{3+} depending on the Na/Al ratio (Toplis and Schaller, 1998; see also Fig. 13.23). It is clear that with Al/(Na + Na), the abundances of both PO_4 and P_2O_7 groups bonding only to Na^+ diminishes, whereas PO_4 groups become associated with an increasing proportion of next-neighbor Al^{3+}.

The structural concepts outlined in Toplis and Schaller (1998) were pursued further by Cody et al. (2001), who simulated numerically shielding effects on the P nucleus by neighboring Si and/or Al to help interpret ^{31}MAS NMR spectra of Na_2O-Al_2O_3-SiO_2 glasses with 3 mol

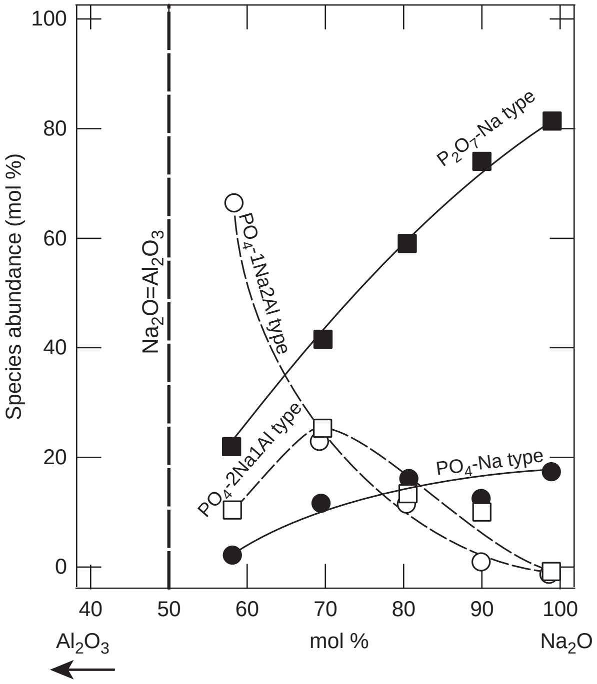

FIG. 13.23 Relative abundance of phosphate species in peralkaline-Al_2O_3-SiO_2 glasses with ~3 mol% P_2O_5 dissolved with Na/Al abundance ratio changing from Al-free to the meta-aluminosilicate join ($Na_2O{=}Al_2O_4$). The data were obtained from ^{31}P MAS NMR spectra. The types of species are indicated on individual lines (Toplis and Schaller, 1998).

% P_2O_5. It was focused, in particular on P—O—Al linkages, which become increasingly important when the Na/Al-ratio of peralkaline aluminosilicate melts decreases (Cody et al., 2001). This is in agreement with the structural interpretations of Schaller et al. (1999) and Toplis and Schaller (1998). Therefore, in P-bearing aluminosilicate glasses and melts, charge-balance is via neighboring Al^{3+}.

Increasingly polymerized phosphate complexes linked to the aluminosilicate network dominate the structure as their Na/Al decreases (Fig. 13.24). Isolated PO_4 and P_2O_7 complexes can be detected only in peralkaline silicate and aluminosilicate melts. The most polymerized Al-phosphate species, $Q^4(P)$, with four P—O—Al bridges that link the PO_4 group to the aluminosilicate network, appears for compositions slightly more aluminous than meta-aluminosilicate. As the PO_4, P_2O_7, and $Q^1(P)$ species become less abundant when the Na/Al-ratio decreases (Fig. 13.24), solution of phosphorus via mechanisms analogous to reactions (13.4–13.6) become less important. (For the join in Fig. 13.24, 5 mol% Al_2O_3 correspond to meta-aluminosilicate composition, Na=Al.) The other species, $Q^1(P)$, $Q^2(P)$, and $Q^3(P)$, have 3, 2, and 1 nonbridging oxygens, respectively. These nonbridging oxygens are bonded to Na as summarized in the legend to that figure. We note that, compared with the results from Toplis and Schaller (1998) in Fig. 13.22, their PO_4-2Na1Al type is equivalent to $Q^1(P)$ and the PO_4-1Na2Al type is equivalent to $Q^2(P)$.

The structural relationship between dissolved P_2O_5 and the aluminosilicate network can be generalized with the expression:

$$10Q^3 + P_2O_5 \Leftrightarrow 2Q^n(P) + (10-n)Q^4. \qquad (13.7)$$

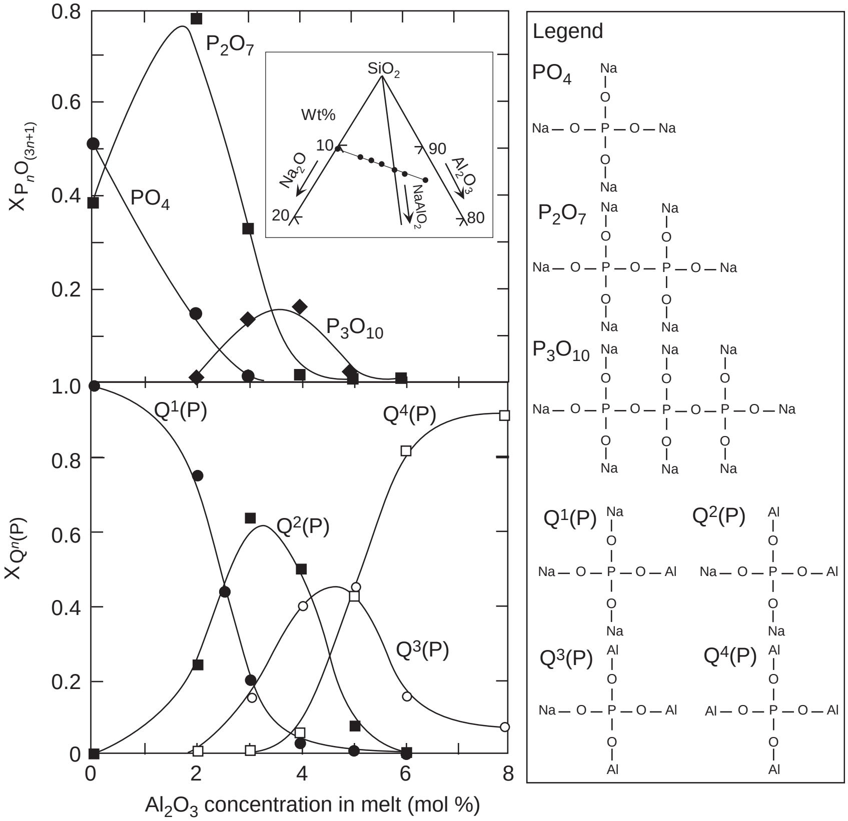

FIG. 13.24 Evolution of phosphate species abundances for glasses (quenched from high-temperature melt) in the Na_2O-Al_2O_3-SiO_2 system at 80 mol% SiO_2 and 3 mol% P_2O_5 as a function of Al_2O_3 concentration, where bulk NBO/T is constant via exchange of charge-balanced Al^{3+} (as NaAl) exchanged with Si^{4+}. Notice the legend, which shows schematic representation of the structural features (Cody et al., 2001). Compared with the results from Toplis and Schaller (1998) in Fig. 13.23, their PO_4-2Na1Al type is equivalent to Q^1(P) and PO_4-1Na2Al type is equivalent to Q^2(P).

This equation cannot, however, completely describe solution of P_2O_5 in fully polymerized aluminosilicates, such as melts along silica-meta-aluminate joins (SiO_2-$NaAlO_2$). Gan and Hess (1992) suggested a mechanism that results in formation of both Al-phosphate and metal-metaphosphate complexes without aluminosilicate depolymerization. However, there is no evidence for the presence of metaphosphate (PO_3) groups in the ^{31}P MAS NMR spectra of these glasses (Toplis and Schaller, 1998; Cody et al., 2001). Toplis and Schaller (1998) proposed, therefore, an alternative whereby three of the oxygens in Q^3(P) species link across either to Al^{3+} or to Si^{4+} in the aluminosilicate network. The fourth oxygen in the phosphate complexes could then be linked to metal cations. This solution mechanism also is in accord with the results summarized in Fig. 13.24.

Finally, Q^4(P) groups dominate when P_2O_5 dissolves in peraluminous melts (>5 mol% Al_2O_3 in Fig. 13.24). We surmise that the proportion of Q^n(P) species with nonbridging oxygen bonded to metal cations (Q^3(P) species) then decreases and that the dominant phosphate species is of Q^4(P) type with its bridging oxygens linked to the aluminosilicate framework via Al^{3+} and Si^{4+}.

13.3.1.5 P^{5+} in Higher Coordination States

The properties of P-bearing metal oxide silicate melts and glasses tend to show discontinuities when the P_2O_5 concentration exceeds about 10 mol% (see, e.g., density and molar volume, Nelson and Tallant, 1984; Dupree et al., 1989; Lockyer et al. 1995; Li et al., 1996; Yamashita et al., 2000; Ide et al., 2007). Such effects can be seen in Si K-edge XANES spectra even of simple SiO_2-P_2O_5 glasses (Li et al., 1996; see also Fig. 13.25). It should be noted that in the data of Li et al. (1995) there are a few samples with >32 mol% P_2O_5 without any sign of sixfold coordinated Si^{4+}. These are not shown in Fig. 13.25 because Li et al. (1996) suggested, as also proposed earlier by Dupree et al. (1989) for other P_2O_5-rich silicate glasses, that for those samples not showing any sixfold coordinated Si^{4+}, there were technical problems associated with the glass formation.

Coordination changes of Si^{4+} also seem to depend on the nature of alkali or alkaline earths in P_2O_5-bearing alkali and alkaline earth silicate glasses (Ide et al., 2007). In a series of alkali silicate glasses with 25 mol% alkali oxide and a mixture of SiO_2 and P_2O_5, the proportion of Si^{4+} in sixfold coordination increases with increasing P_2O_5 concentration, but there appears to be some control on this by the properties of the metal cation (Fig. 13.25B). Substitution of Al_2O_3 for P_2O_5 reduces or destroys the sixfold coordinated Si^{4+} coordination sites (Dupree et al., 1989). From the ^{29}Si, ^{27}Al, and ^{31}P MAS NMR spectra, Dupree et al. (1989) mapped out the effect of Al_2O_3 concentration on both Si^{4+} and Al^{3+} in sixfold coordination in a Na aluminosilicate glass system with variable amounts of Al_2O_3 and P_2O_5 compositionally interconnected by the formula $Na_2O\cdot 2SiO_2\cdot(3-x)PO_5\cdot xAl_2O_3$. These glasses were formed by rapid quenching of melt formed at 1100–1600°C depending on composition. The results in Fig. 13.25C show only the decrease in $^{[6]}$Si with increasing Al_2O_3 replacement of P_2O_5. However, the abundance of sixfold coordinated Al^{3+} forming both Al—O—P and Al—O—Al bonding also decreases in the same manner, but at a lower rate than does $^{[6]}$Si (Dupree et al., 1989).

13.3.2 (P, Si) Substitution Versus P Clustering

The extent of experimental work focused on clustering and ordering of P^{5+} in silicate glasses and melts is quite limited (Chakraborty and Condrate, 1985; Bykov et al., 2001; Ding et al., 2012). This contrasts with other potentially tetrahedrally coordinated cations such as Al^{3+} (Chapter 9), Fe^{3+} (Chapter 11), and Ti^{4+} (Chapter 12) where significant bodies of experimental data are available. The observation that the vibrational modes assigned to P—O stretching in the various phosphate units do not shift in frequency with increasing P_2O_5 concentration in a melt or a glass (Chakraborty an Condrate, 1985; Mysen and Cody, 2001) would suggest some form of ordering, because random substitution likely would lead to next-neighbor effects that would cause a vibrational frequency to shift. This argument resembles that from vibrational spectra of Fe^{3+}—O, and Ti^{4+}—O complexes, where the vibrational frequencies also remain independent of concentration and other spectroscopic methods, indicating with some confidence that clustering and ordering take place.

FIG. 13.25 Sixfold coordinated Si^{4+} with P_2O_5 and Al_2O_3 content. (A) Proportion of Si^{4+} in sixfold coordination (atom %) relative to total amount of Si^{4+} in SiO_2-P_2O_5 (*open circles*) and Na_2O-SiO_2-P_2O_5 glasses as a function of P_2O_5 concentration obtained from the Si K-edge in XANES spectra (Li et al., 1995, 1996). (B) Proportion of sixfold coordinated Si^{4+} in alkali silicate glasses of composition $25M_2O{\cdot}75[(1-x)SiO_2\text{-}xP_2O_5]$, where "$x$" is the mol fraction shown in the figure and M is Li, Na, and *K* as indicated on figure (Ide et al., 2007). (C). Proportion of sixfold coordinated Si^{4+} in $Na_2O{\cdot}2SiO_2{\cdot}(3-x)P_2O_5{\cdot}xAl_2O_3$ glasses (quenched from melt) as a function of fraction of Al_2O_3 in replacement for P_2O_3 as defined by mol fraction, x (Dupree et al., 1989).

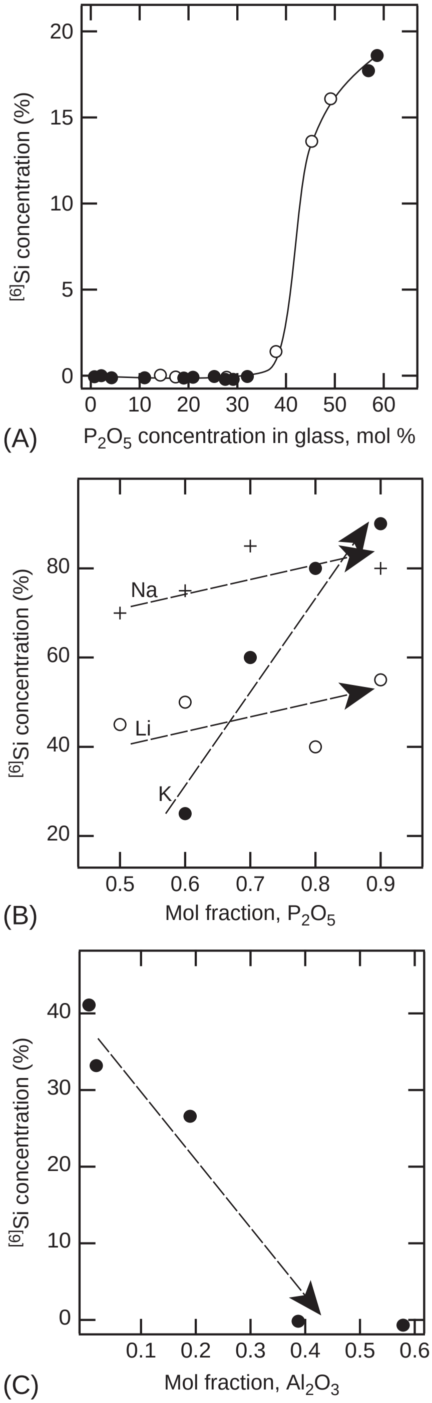

13.3.3 Stucture and Temperature

The aforementioned structural information has been derived from examination of glasses. The extent to which information on glass structure can be extrapolated to P-bearing melts depends on the assumption that quenching of melts to form glasses does not involve significant rearrangements of either the phosphate or the silicate portion of the structure. A few Raman spectroscopy studies of P-bearing glasses and melts carried out to temperatures above 1200°C have addressed the extent to which this hypothesis is justified (Dupree et al., 1989; Mysen, 1998; Toplis and Reynard, 2000; Mysen and Cody, 2001; Bykov et al., 2001; van Wullen et al., 2007). In Al-free, silica-rich melts (Na_2O-SiO_2-P_2O_5 compositions with nominal $NBO/Si < 1$), the two dominant silicate species are Q^3 and Q^4, whereas the main phosphate species are PO_4, P_2O_7, and $Q^1(P)$:

$$2PO_4 + Q^4 \Leftrightarrow P_2O_7 + Q^3, \tag{13.8}$$

and

$$P_2O_7 + 5Q^4 \Leftrightarrow 2Q^1(P) + 3Q^3. \tag{13.9}$$

Equilibrium (13.8) describes the situation where phosphate and silicate groups are not linked across oxygen (no Si—O—P bonding), whereas equilibrium (13.9) describes an equilibrium between species where at least some of the P—O bonds are linked across to the silicate (Si—O—P). As discussed previously, in principle the number of such bonds could then be anywhere between 1 and 4.

A question is whether, or the extent to which, equilibria describing relationships between different structural entities depend on temperature. Moreover, for melts and glasses that comprise sixfold coordinated Si^{4+}, the $^{[4]}Si^{4+}/^{[6]}Si^{4+}$ abundance ratio could depend on temperature. From ^{29}Si MAS NMR spectra of glasses with different fictive temperatures above T_g (Fig. 13.26), Dupree et al. (1989) observed a significant temperature effect of the coordination ratio, which yields an enthalpy change near 18 ± 1.2 kJ/mol for the transformation of sixfold to fourfold Si^{4+} from the slope of ln (concentration ratio) vs 1/T.

Several high-temperature studies of equilibrium (13.8) have been accomplished with Raman spectroscopy (Toplis and Reynard, 2000; Mysen and Cody, 2001; Bykov et al., 2001). Their results are in accord to the extent that this equilibrium shifts to the right with increasing temperature above the glass transition temperature, T_g. As an example, the spectra from a SiO_2-rich Na-silicate with 2 mol% P_2O_5 show a clear intensity increase of a Raman band near 1020 cm^{-1} assigned to P—O vibrations in P_2O_7 units, and of another near 940 cm^{-1}, which is assigned to P—O stretch vibrations in PO_4 units (Fig. 13.27). Qualitatively, it is evident that the intensity ratio of the 1020 and 940 cm^{-1} bands increases with increasing temperature, consistent also with the results of Toplis and Reynard (2000) and Mysen and Cody (2001).

Raman intensity ratios are not equivalent to abundance ratio, as these can depend on a number of other factors (see, e.g., Long, 1977). Intensity ratios, however, have been calibrated with ^{31}P and ^{29}Si MAS NMR (Cody et al., 2001). From such calibration of the Raman data, the abundance ratios of phosphate and silicate species are found independent of temperature from ambient the glass transition, above which the intensity ratios change rapidly (Fig. 13.28A and B). The abundances of the two most polymerized phosphate species

FIG. 13.26 Variations in four- and sixfold coordinated Si^{4+} as a function of temperature for supercooled liquids of $Na_2O{\cdot}2SiO_2{\cdot}4P_2O_5$ composition based on their various fictive temperatures (Dupree et al., 1989).

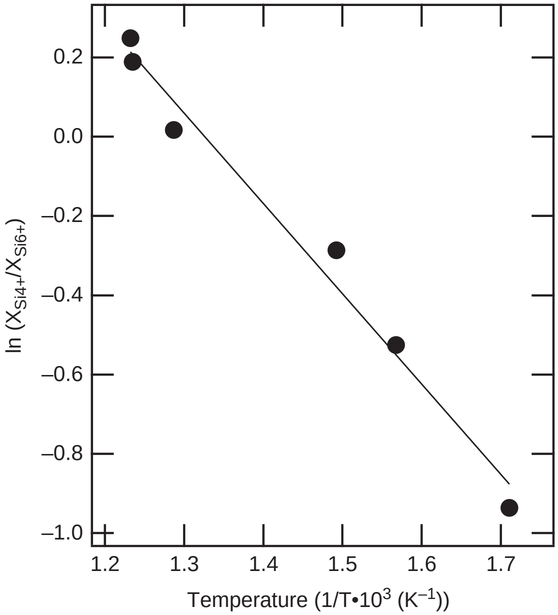

FIG. 13.27 Examples of Raman spectra of glass (at 25°C) and melt (at 795°C) of Na-silicate (10 wt% Na_2O, 90 wt% SiO_2) with 2 mol% P_2O_5 dissolved (Bykov et al., 2001).

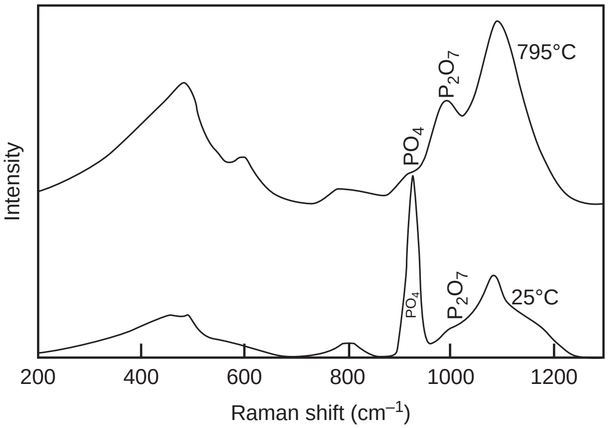

[P_2O_7 and Q^1(P)] increase at higher temperature and that of the orthophosphate, PO_4, decreases (Fig. 13.28A). Smaller but distinct changes also affect the abundance of the silicate species (Fig. 13.28B).

The temperature dependence of the equilibrium constants of these two reactions, $K_{13.8}$ and $K_{13.9}$, indicate that P-bearing metal oxide-silicates become slightly depolymerized as the temperature increases (Mysen, 1998; Mysen and Cody, 2001). Moreover, the variations of these equilibrium constants with temperature yield enthalpy changes of these two equilibria of −-193 ± 43 and −65 ± 23 kJ/mol (Fig. 13.29). The $K_{13.8}$-value is somewhat greater than that reported by Bykov et al. (2001). The different enthalpy values likely result from the reliance

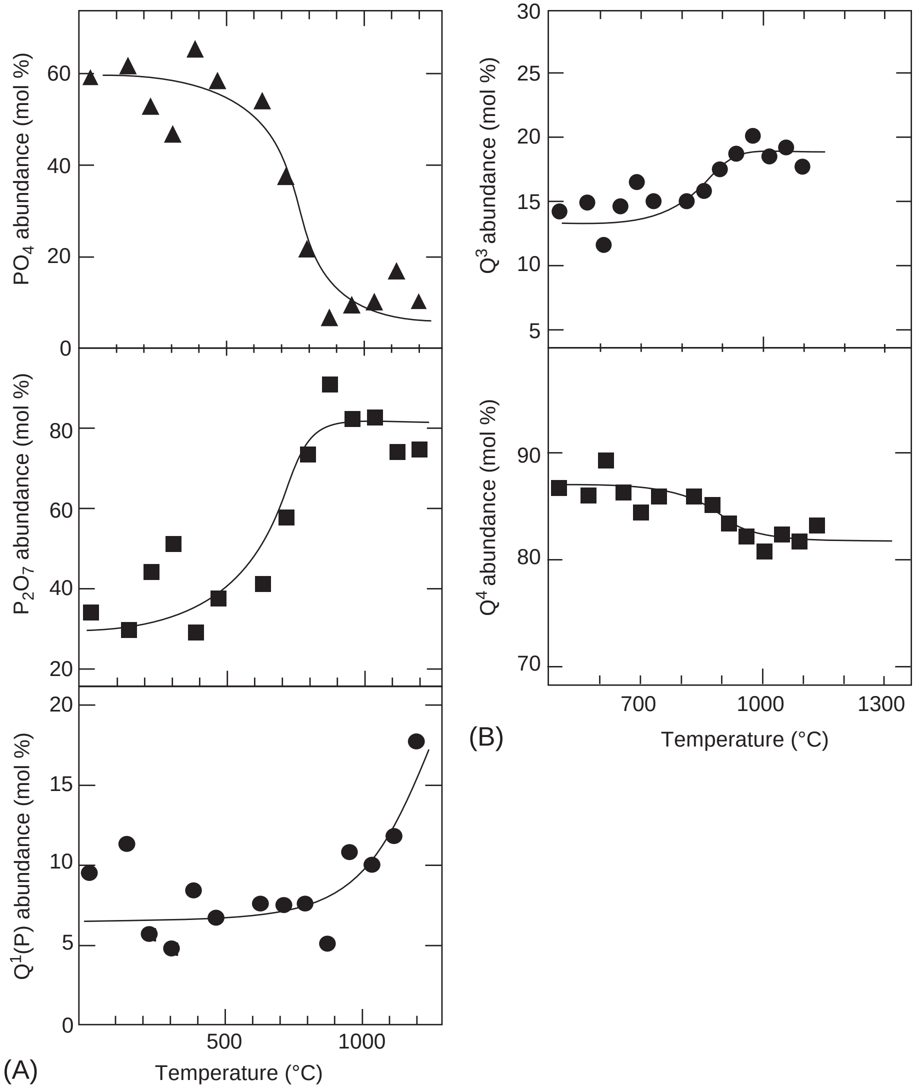

FIG. 13.28 Effect of temperature on phosphate (A) and silicate (B) species abundance in $Na_2O{\cdot}9SiO_2$ glass and melt with 2 mol% P_2O_5 (Mysen and Cody, 2001).

of Bykov et al. (2001) on ratios of integrated Raman intensities as measures of abundance ratios of the relevant species, whereas Mysen and Cody (2001) used calibration of the Raman intensities against intensities from ^{31}P MAS NMR of the glasses at 25°C with the assumption that the glass calibration also could be used for high-temperature melts.

For alkali aluminophosphate melts (without SiO_2), heating to temperatures above the glass transition results in a decrease in Al^{3+} coordination together with a breakage of P—O—Al bonds (van Wullen et al., 2007). For Al-bearing phosphosilicate melts, the structural environment is considerably more complex. Here, the interaction between dissolved phosphorus and

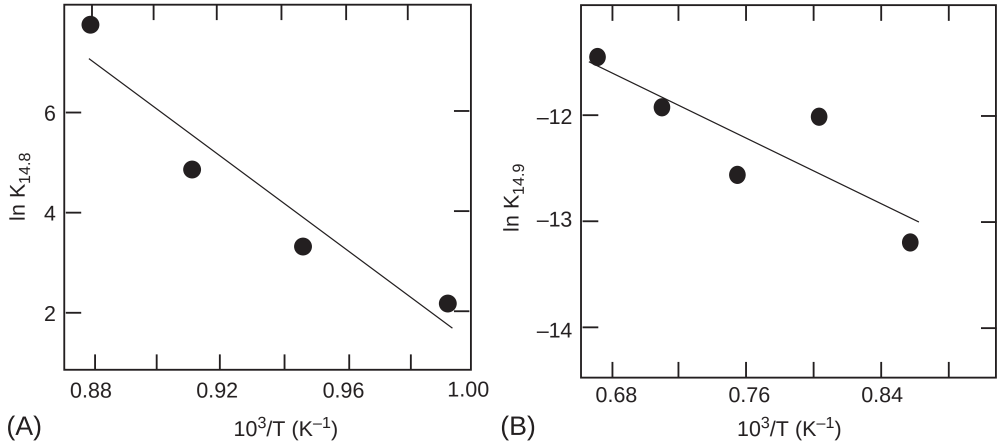

FIG. 13.29 Equilibrium constants for reactions (13.8) and (13.9), $K_{13.8}$ and $K_{13.9}$, at temperatures above the glass transition in the same system as in Fig. 13.27 (Mysen and Cody, 2001).

the aluminosilicate network involves not only reactions (13.8) and (13.9), but also complicated interactions between the Q^n(P)-species themselves and the aluminosilicate network (Toplis and Reynard, 2000; Mysen and Cody, 2001). This development is seen in two more equilibria in addition to (13.8) and (13.9) (Mysen and Cody, 2001):

$$2Q^3(P) \Leftrightarrow Q^2(P) + Q^4(P), \tag{13.10}$$

and

$$Q^4(P) + Q^3 \Leftrightarrow Q^3(P) + 2Q^4. \tag{13.11}$$

Equilibrium (13.10) is conceptually similar to (7.6) (Chapter 7) for silicate species, except that it does not affect the silicate structure. Its ΔH value is only slightly negative (-13 ± 11 kJ/mol; see Fig. 13.30) implying, therefore, that the equilibrium shifts slightly to the right at temperatures above the glass transition.

Near the meta-aluminosilicate join, and for more aluminous melts, equilibrium (13.11) dominates (Mysen and Cody, 2001). This equilibrium does affect the aluminosilicate structure because transformation to a more polymerizing Q^n(P) units is accompanied by an opposite transformation for silicate units. In other words, oxygen is exchanged between phosphate and silicate frameworks. The $K_{13.11}$ is positively correlated with temperature (Fig. 13.30), with an enthalpy of reaction of -23 ± 4 kJ/mol. Thus, interactions between highly polymerizing Q^n(P)-species and Q^n-species in aluminosilicate melts imply high-temperature depolymerization of the structure.

13.4 STRUCTURE AND PROPERTIES

The multiple positions of P^{5+} in silicate and aluminosilicate melts and glasses have profound effects of silicate structure, including the proportions of Q^n-species and overall polymerization changes. The temperature dependence of the phosphate-silicate equilibria implies

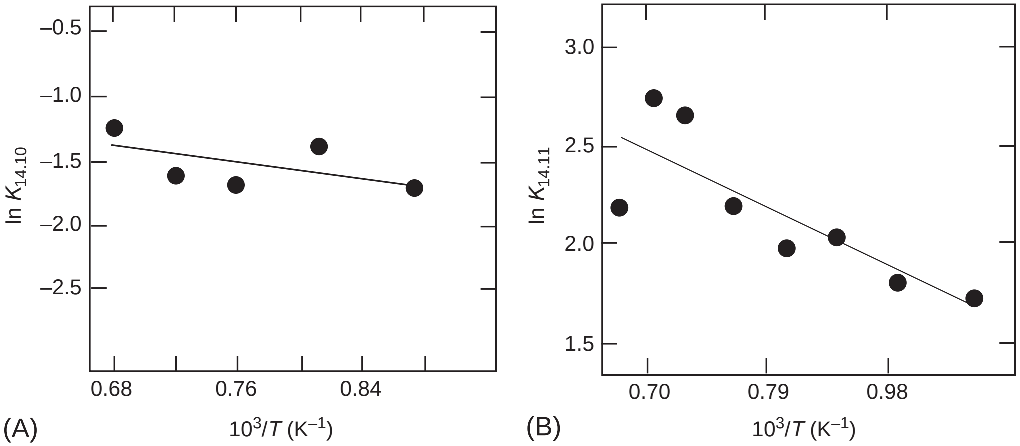

FIG. 13.30 Equilibrium constants for reactions (13.10) and (13.11), $K_{13.10}$ and $K_{13.11}$, at temperatures above the glass transition in the same system as in Fig. 13.27 (Mysen and Cody, 2001).

that the silicate framework, including degree of polymerization, also becomes temperature dependent. This conclusion differs from that reached for P-free silicate and aluminosilicate melts, where temperature affects the proportions of silicate species, whereas the overall degree of silicate polymerization remains unaffected (see Chapters 7 and 9, Sections 7.3.3 and 9.4.1, respectively).

13.4.1 Thermal Properties

The relationships between phosphate and silicate speciation (Eqs. 13.4–13.6) illustrate the sensitivity of the properties of P-bearing silicate melts to P content. For example, the increase of the activity coefficient of SiO_2 in depolymerized melts with P_2O_5 content as reflected in the liquidus boundary shifts (Figs. 13.2 and 13.10) is due to the higher abundance of Q^4-species. It is perhaps less obvious, however, from the structural data why solution of P_2O_5 in SiO_2 melt causes a decrease in the SiO_2 activity coefficient in such melts. Possibly, this decrease is related to the linkage between Si^{4+} in Q^4 species and P^{5+} on Q^3(P) groups with one terminal P=O bond. This process effectively disrupts the three-dimensionally interconnected silicate network structure, thus lowering the concentration of Q^4-species.

The effect of dissolved phosphorus on silicate speciation (Q^n) and therefore overall extent of silicate polymerization probably also explains why the redox ratio of iron, Fe^{3+}/Fe^{2+}, decreases with increasing P_2O_5 concentration (Fig. 13.9). This is so because in silicate melts, the Fe^{3+}/Fe^{2+} at fixed temperature and redox conditions decreases as the melt becomes more polymerized (see Chapter 11, Section 11.4).

The negative correlation between phosphorus solubility and SiO_2 contents of silicate melts in equilibrium with apatite crystalline materials (Fig. 13.7) is probably not related directly to the Q^n-speciation relationships, but instead to the associated changes in metal-cation content of the silicate network. As the SiO_2 content decreases, the abundance of depolymerized Q^n-species increases. The nonbridging oxygens in these Q^n-species are linked via these metal cations. However, the same metal cations also bond with oxygen in depolymerizing phosphate species such as PO_4, P_2O_7, and more complicated phosphosilicate units (Schaller et al., 1999). With decreasing SiO_2 content, the melt becomes less polymerized and the activity of metal cations increases. Phosphate-forming reactions are then favored and therefore a negative correlation between phosphorus solubility and SiO_2 content of melts can be observed.

An analogous reasoning can explain the positive correlation between phosphorus solubility and alumina content of silicate melts (Fig. 13.8). In this case, the phosphate speciation is associated with formation of P—O—Al bridges in the melt structure, as illustrated by reaction (13.7). Thus, as the Al_2O_3 contents of melts increase, the phosphorus solubility also increases.

13.4.2 Physical Properties

Many physical properties of P-bearing silicate glasses and melts show complex relationships to P_2O_5 concentration. For example, both melt density and thermal expansivity are strongly nonlinear functions of P_2O_5 content (O'Donnell et al., 2008), which probably reflects the structural changes observed for such melts.

There are complicated relationships between viscosity (and probably other transport properties), polymerization, and Na/Al content (Figs. 13.11 and 13.12) of P-bearing melts. These variations probably are related to at least three structural factors, as follows. (i) Solution of phosphorus in depolymerized silicate melts causes polymerization, which qualitatively results in viscosity increases (e.g., Urbain et al., 1982). (ii) In highly polymerized silicate melts, the linkage between Si^{4+} in Q^4 species and P^{5+} in $Q^3(P)$ groups with one terminal P=O bond effectively breaks up the silicate network. Thus, this mechanism should cause viscosity decreases as phosphorus is dissolved in highly polymerized melts. (iii) In aluminosilicate melts, formation of $Q^n(P)$ complexes with P—O—Al bridging between phosphate and silicate structures causes depolymerization of the aluminosilicate. However, the more polymerized this aluminosilicate, the smaller is the effect of dissolved P_2O_5 on aluminosilicate polymerization. Thus, for depolymerized aluminosilicate melts, formation of $Q^n(P)$ species tends to drive the system toward greater aluminosilicate polymerization and, thus, higher melt viscosity. For highly polymerized aluminosilicate melts, this effect is greatly diminished or perhaps eliminated.

References

Alam, T.M., McLaughlin, J., Click, C.C., Conzone, S., Brow, R.K., Boyle, T.J., Zwanziger, J.W., 2000. Investigation of sodium distribution in phosphate glasses using spin-echo Na-23 NMR. J. Phys. Chem. B 104, 1464–1472.

Arbib, E.H., Elouadi, B., Chaminade, J.P., Darriet, J., 1996. New refinement of the crystal structure of o-P_2O_5. J. Solid State Chem. 127, 350–353.

Borisov, A., Behrens, H., Holtz, F., 2013. The effect of titanium and phosphorus on ferric/ferrous ratio in silicate melts: an experimental study. Contrib. Mineral. Petrol. 166, 1577–1591.

Brauer, D., Jones, J., 2018. Bioactive glasses. In: Richet, P. (Ed.), Encyclopedia of Glass Science, Technology, History and Culture. J. Wiley & Sons, Hoboken, NJ.

Brow, R.K., 2000. Review: the structure of simple phosphate glasses. J. Non-Cryst. Solids 263–264, 1–28.

Brow, R.K., Tallant, D.R., Myers, S.T., Phifer, C.C., 1994. The short-range structure of zinc polyphosphate glass. J. Non-Cryst. Solids 191, 45–55.

Bykov, V.N., Osipov, A.A., Anfilogov, V.N., 2001. Raman spectra and the structure of melts in the Na_2O-P_2O_5-SiO_2 system. Glas. Phys. Chem. 27, 204–208.

Chakraborty, I.N., Condrate, R.A., 1985. The vibrational spectra of glasses in the Na_2O-SiO_2-P_2O_5 system with a 1:1 SiO_2:P_2O_5 molar ratio. Phys. Chem. Glasses 26, 68–74.

Cody, B.O., Mysen, B.O., Saghi-Szabo, G., Tossell, J.A., 2001. Silicate-phosphate interaction in silicate glasses and melts. I. A multinuclear (^{27}Al, ^{29}Si, ^{31}P) MAS NMR and ab initio chemical shielding (^{31}P) study of phosphorus speciation in silicate glasses. Geochim. Cosmochim. Acta. 65, 2395–2312.

Ding, J., Chen, Y.K., Chen, W., Hu, L.L., Boulon, G., 2012. Effect of P_2O_5 addition on the structural and spectroscopic properties of sodium aluminosilicate glass. Chin. Opt. Lett. 10. https://dx.doi.org/10.3788/col201210.071602.

Dingwell, D.B., Knoche, R., Webb, S.L., 1993. The effect of P_2O_5 on the viscosity of haplogranitic liquid. Eur. J. Mineral. 5, 133–140.

Doweidar, H., 2009. Density-structure correlations in Na_2O-CaO-P_2O_5-SiO_2 bioactive glasses. J. Non-Cryst. Solids 355, 577–580.

Dupree, R., 1991. MAS NMR as a structural probe of silicate glasses and minerals. Trans. Am. Cryst. Soc. 27, 255–269.

Dupree, R., Holland, D., Mortuza, M.G., 1988. The role of small amounts of P_2O_5 in the structure of alkali disilicate glassses. Phys. Chem. Glasses 29, 18–21.

Dupree, R., Holland, D., Mortuza, J.A., Collins, J.A., Lockyer, M.W.G., 1989. Magic angle spinning NMR of alkali phospho-alumino-silicate glasses. J. Non-Cryst. Solids 112, 111–119.

Ehrt, D., Leister, M., Matthai, A., 2001. Polyvalent elements iron, tin, and titanium in silicate, phosphate, and fluoride glasses and melts. Phys. Chem. Glasses 42, 231–239.

Elgayar, I., Aliev, A.E., Boccaccini, A.R., Hill, R.G., 2005. Structural analysis of bioactive glasses. J. Non-Cryst. Solids 351, 173–183.

Engelhardt, G., Michel, D., 1987. High-Resolution Solid-State NMR of Silicates and Zeolites. Wiley, New York, p. 485.

Faivre, A., Viviani, D., Phalippou, J., 2005. Mixed alkali effect in Li and Na aluminophosphate glasses: influence of the cation environment. Solid State Ionics 176, 325–332.

Gan, H., Hess, P.C., 1992. Phosphate speciation in potassium aluminosilicate glasses. Am. Mineral. 77, 495–506.

Galeener, F.L., Mikkelsen, J.C., 1979. The Raman spectra and structure of pure vitreous P_2O_5. Solid State Commun. 20, 505–510.

Grussaute, H., Montagne, L., Palavit, G., Bernard, J.L., 2000. Phosphate speciation in Na_2O-CaO- P_2O_5-SiO_2 and Na_2O-TiO_2- P_2O_5-SiO_2 glasses. J. Non-Cryst. Solids 263–264, 312–317.

Gwinn, R., Hess, P.C., 1993. The role of phosphorus in rhyolitic liquids as determined from the homogeneous iron redox equilibrium. Contrib. Mineral. Petrol. 113, 424–435.

Harrison, T.M., Watson, E.B., 1984. The behavior of apatite during crustal anatexis; equilibrium and kinetic considerations. Geochim. Cosmochim. Acta 48, 1467–1477.

Hermansen, C., Guo, X., Youngman, R.E., Mauro, J.C., Smedskjaer, M.M., Yue, Y., 2015. Structure-topology-property correlations of sodium phosphosilicate glasses. J. Chem. Phys. 143. https://doi.org/10.1063/1.4928330.

Holtz, F., Dingwell, D.B., Behrens, H., 1993. Effects of F, B_2O_3, and P_2O_5 on the solubility of water in haplogranitic melts compared to natural silicate melts. Contrib. Mineral. Petrol. 113, 492–501.

Hoppe, U., Walter, G., Barz, A., Stachel, D., Hannon, A.C., 1998. The P-O bond lengths in vitreous P_2O_5 probed by neutron diffraction with high real-space resolution. J. Phys. Condens. Matter 10, 261–270.

Ide, J., Ozutsumi, K., Kageyama, H., Handa, K., Umesaki, N., 2007. XAFS study of six-coordinated silicon in R_2O-SiO_2-P_2O_5 (R = Li, Na, K) glasses. J. Non-Cryst. Solids 353, 1966–1969.

Inoue, H., Makishima, A., Kanazawa, T., Nanba, T., Yasui, I., 1995. Structure of $50Na_2O \bullet xAl_2O_3 \bullet (50-x) \bullet P_2O_5$ and $(50-x/2)Na_2O \bullet xAl_2O_3 \bullet (50-x/2)P_2O_5$ glasses. Phys. Chem. Glasses 36, 37–43.

Kirkpatrick, R.J., Brow, R.K., 1995. Nuclear magnetic resonance investigation of the structures of phosphate and phosphate containing glasses: a review. Solid State Nucl. Magn. Reson. 5, 3–8.

Kosinski, S.G., Krol, D.M., Duncan, T.M., Douglass, D.C., MacChesney, J.B., Simpson, J.R., 1988. Raman and NMR spectroscopy of SiO_2 glasses co-doped with Al_2O_3 and P_2O_5. J. Non-Cryst. Solids 105, 45–52.

Kushiro, I., 1975. On the nature of silicate melt and its significance in magma genesis: regularities in the shift of liquidus boundaries involving olivine pyroxene, and silica materials. Am. J. Sci. 275, 411–431.

Levien, E.M., Robbins, C.R., McMurdie, H.F. (Eds.), 1964. Phase Diagrams for Ceramists. The American Ceramic Society, Columbus.

Li, D., Fleet, M.E., Bancroft, G.M., Kasrai, M., Pan, Y., 1995. Local structure of Si and P in SiO_2-P_2O_5 and Na_2O-SiO_2-P_2O_5 glasses: a XANES study. J. Non-Cryst. Solids 188, 181–189.

Li, D., Bancroft, G.M., Fleet, M.E., 1996. Coordination of Si in Na_2O-SiO_2-P_2O_5 glasses using Si K- and L-edge XANES. Am. Mineral. 81, 111–118.

Lockeyer, M.W.G., Dupree, R., Holland, D., 1991. MAS NMR applied to potassium phosphosilicate glasses. Trans. Am. Cryst. Soc. 27, 285–292.

Lockyer, M.W.G., Holland, D., Dupree, R., 1995. The structure of $(5x)P_2O_5 \bullet (1\text{-}x)K_2O \bullet 4(1\text{-}x)SiO_2$ glasses. Phys. Chem. Glasses 36, 22–30.

London, D., Morgan, G.B., Babb, H.A., Loomis, J.L., 1993. Behavior and effects of phosphorus in the system Na_2O-K_2O-Al_2O_3-SiO_2-P_2O_5-H_2O at 200 MPa (H_2O). Contrib. Mineral. Petrol. 113, 450–465.

Long, D., 1977. Raman Spectroscopy. McGraw-Hill, New York.

Mathew, R., Stevensson, B., Eden, M., 2015. Na/Ca intermixing around silicate and phosphate groups in bioactive phosphosilicate glasses revealed by heteronuclear solid-state NMR and molecular dynamics simulations. J. Phys. Chem. B 119, 5701–5715.

Meyer, K., 1997. Characterization of the structure of binary zinc ultraphosphate glasses by infrared and Raman spectroscopy. J. Non-Cryst. Solids 209, 227–239.

Montel, J.-M., 1986. Experimental determination of the solubility of Ce-monazite in SiO_2-Al_2O_3-K_2O-Na_2O melts at 800°C, 2 kbar, under H_2-O-saturated conditions. Geology 14, 659–662.

Mysen, B.O., 1992. Iron and phosphorus and in calcium silicate quenched melts. Chem. Geol. 98, 175–202.

Mysen, B.O., 1998. Phosphorus solubility mechanisms in haplogranitic aluminosilicate glass and melt: Effect of temperature and aluminum content. Contrib. Mineral. Petrol. 133, 38–50.

Mysen, B.O., Cody, G.D., 2001. Silicate-phosphate interaction in silicate glasses and melts. II. Quantitative, high-temperature structure of P-bearing alkali aluminosilicate melts. Geochim. Cosmochim. Acta 65, 2413–2431.

Nelson, C., Tallant, D.R., 1984. Raman studies of sodium silicate glasses with low phosphate contents. Phys. Chem. Glasses 25, 31–39.

Nelson, C., Tallant, D.R., 1986. Raman studies of sodium phosphates with low silica contents. Phys. Chem. Glasses 26, 119–122.

O'Donnell, M.D., Watts, S.J., Law, R.V., Hill, R.G., 2008. Effect of P_2O_5 content in two series of soda lime phosphosilicate glasses on structure and properties—Part I: NMR. J. Non-Cryst. Solids 354, 3554–3560.

Pichavant, M., Herrera, J.V., Boulmier, S., Brigueu, L., Joron, J.-L., Juteau, L.M., Michard, A., Sheppard, S.M.F., Treuil, M., Vernet, M., 1987. The Macusani glasses, SE Peru: evidence of chemical fractionation of peraluminous magmas. In: Mysen, B.O. (Ed.), Magmatic Processes: Physicochemical Principles. Geochemical Society, University Park, PA, pp. 359–374.

Pichavant, M., Montel, J.-M., Richard, L.R., 1992. Apatite solubility in peraluminous liquids: experimental data and an extension of the Harrison model. Geochim. Cosmochim. Acta 56, 3855–3861.

Plotnichenko, V.G., Sokolov, V.O., Koltashev, V.V., Dianov, E.M., 2002. On the structure of phosphosilicate glasses. J. Non-Cryst. Solids 306, 209–226.

Ryerson, F.J., 1985. Oxide solution mechanisms in silicate melts: systematic variations in the activity coefficient of SiO_2. Geochim. Cosmochim. Acta 49, 637–651.

Schaller, T., Ring, C., Toplis, M.J., Cho, H., 1999. TRAPDOR NMR investigations of phosphorus-bearing aluminosilicate glasses. J. Non-Cryst. Solids 248, 19–27.

Shibata, N., Horigudhi, M., Edahiro, T., 1981. Raman spectra of binary high-silica glasses and fibers containing GeO_2, P_2O_5 and B_2O_3. J. Non-Cryst. Solids 45, 115–126.

Stone, P.E., Egan, E.P., Lehr, J.R., 1956. Phase relationships in the system CaO-Al_2O_3-P_2O_5. J. Am. Ceram. Soc. 39, 89–98.

Tien, T.-Y., Hummel, F.A., 1962. The system SiO_2-P_2O_5. J. Am. Ceram. Soc. 45, 422–424.

Toplis, M.J., Dingwell, D.W., 1996. The variable influence of P_2O_5 on the viscosity of melts of differing alkali/aluminum ratio: implications for the structural role of phosphorus in silicate melts. Geochim. Cosmochim. Acta 60, 4107–4121.

Toplis, M.J., Reynard, B., 2000. Temperature and time-dependent changes of structure in phosphorus containing aluminosilicate liquids and glasses: in situ Raman spectroscopy at high temperature. J. Non-Cryst. Solids 263–264, 123–131.

Toplis, M.J., Schaller, T., 1998. A 31P MAS NMR study of glasses in the system xNa_2O-$(1\text{-}x)Al_2O_3$-$2SiO_2$-yP_2O_5. J. Non-Cryst. Solids 224, 57–68.

Toplis, M.J., Dingwell, D.B., Libourel, G., 1994. The effect of phosphorus on the iron redox ratio, viscosity, and density of an evolved ferro-basalt. Contrib. Mineral. Petrol. 117, 293–304.

Tuttle, O.F., Bowen, N.L., 1958. Origin of granite in light of experimental studies in the system $NaAlSi_3O_8$-$KAlSi_3O_8$-SiO_2-H_2O. Geol. Soc. Am. Mem. 74, 1–153.

Urbain, G., Bottinga, Y., Richet, P., 1982. Viscosity of liquid silica, silicates and alumino-silicates. Geochim. Cosmochim. Acta 46, 1061–1072.

Visser, W., Koster Van Groos, A.F., 1979. Effects of P_2 O_5 and TiO_2 on liquid-liquid equilibria in the system K_2O-FeO-Al_2O_3-SiO_2. Am. J. Sci. 279, 970–983.

Viviani, D., Faivre, A., Levelut, C., Smdihi, M., 2006. Structural change in Li and Na aluminophosphate glasses: evidence of a "structural mixed alkali effect" J. Phys. Chem. B 110, 7281–7288.

Watson, E.B., 1976. Two-liquid partition coefficients: experimental data and geochemical implications. Contrib. Mineral. Petrol. 56, 119–134.

Watson, E.B., Capobianco, C.J., 1981. Phosphorous and rare earth elements in felsic magmas: an assessment of the role of apatite. Geochim. Cosmochim. Acta 45, 2349–2358.

Watts, S.J., Hill, R.G., O'Donnell, M.D., Law, R.V., 2010. Influence of magnesia on the structure and properties of bioactive glasses. J. Non-Cryst. Solids 356, 517–524.

Webb, S., Courtial, P., 1996. Compressibility of P_2O_5-Al_2O_3-Na_2SiO_3 melts. Phys. Chem. Miner. 23, 205–211.

Wolf, M.B., London, D., 1994. Apatite dissolution into peraluminous haplogranitic melts: an experimental study of solubilities and mechanisms. Geochim. Cosmochim. Acta 58, 4127–4145.

van Wullen, L., Wegner, S., Tricot, G., 2007. Structural changes above the glass transition and crystallization in aluminophosphate glasses: an in situ high-temperature MAS NMR study. J. Phys. Chem. B 111, 7529–7534.

Wyllie, P.J., Tuttle, O.F., 1964. Experimental investigation of silicate systems containing two volatile components. III. The effects of SO_3, P_2O_5, HCl, and Li_2O in addition to H_2O on the melting temperatures of albite and granite. Am. J. Sci. 262, 930–939.

Yamashita, H., Yoshino, H., Nagata, K., Inoue, H., Nakajin, T., Maekawa, T., 2000. Nuclear magnetic resonance studies of alkaline earth phosphosilicate and aluminoborosilicate glasses. J. Non-Cryst. Solids 270, 48–59.

Yang, W.-H., Kirkpatrick, R.J., Turner, G., 1986. ^{31}P and ^{29}Si magic-angle sample-spinning NMR investigation of the structural environment of phosphorous in alkaline-earth silicate glasses. J. Am. Ceram. Soc. 69, C222–C223.

Zeyer, M., Montagne, L., Kostoj, V., Palavit, G., Prochnow, D., Jaeger, C., 2002. O-17 nuclear magnetic resonance study of Na_2O-P_2O_5 glasses. J. Non-Cryst. Solids 311, 223–232.

CHAPTER

14

Properties of Hydrous Melt and Glass

OUTLINE

14.1 INTRODUCTORY COMMENTS

As a component of silicate glasses and melts, water owes its importance to the dramatic influence it exerts, even at very low concentrations, on a variety of physical and chemical properties. This influence is particularly strong for silica-rich compositions. Water also affects phase equilibria (e.g., Kushiro, 1972, 1974), reaction kinetics, and volume properties. The rate of phase separation increases in water-bearing sodium-silicate liquids (McGinnis and Shelby, 1995). Melt crystallization is favored because of enhanced fluidity and element diffusivity (Métrich et al., 2001). In fact, there is probably not a single oxide that influences the properties of silicate melts more.

All these effects depend markedly on both water content and silicate composition. Their study, however, is made experimentally difficult by a number of factors, as follows. (i) The range of water contents relevant to natural magma is wide. Owing to the low molar mass of water compared to that of other oxides, an apparently not so high concentration of 5 wt% translates into about 15 mol% H_2O on an oxide basis. (ii) The dissolution mechanisms

Silicate Glasses and Melts
https://doi.org/10.1016/B978-0-444-63708-6.00014-4

depend on both water content and silicate composition. Moreover, water is not a real one-component oxide because it dissolves in at least two forms, hydroxyl ions (OH^-) and molecular H_2O, whose respective influence on melt properties must be distinguished. (iii) Considerable problems are encountered when measuring physical properties at the high pressures needed to dissolve significant amounts of water. Furthermore, hydrous melts are quite fluid and diffusion is therefore rapid, so that upon quenching changes of sample composition, structure, and properties can take place (Zhang et al., 2000; Whittington et al., 2009; Kreisberg, 2015), along with phase separation and crystallization (Yoder et al., 1957; Mysen et al., 1974; Eggler and Burnham, 1984). (iv) The difficulty of quenching depolymerized melts is as serious in hydrous as in dry systems. Hence, most of the results obtained deal with melts that can be quenched easily, i.e., with aluminosilicate compositions near the meta-aluminous join. Of course, this domain represents only a small part of the composition range of actual interest.

How water content and speciation affect the physical properties of hydrous melts is an important question that has thus long remained poorly known. The viscosity and density of hydrous melts could be measured by the falling sphere method either in internally heated vessels (Shaw, 1963; Persikov et al., 1990) or in piston cylinder apparatus (Kushiro et al., 1976; Fujii and Kushiro, 1977). Such measurements are tedious, however, and they can be performed only over restricted temperature intervals above the liquidus. However, because of the slowness of water exsolution near the glass transition, water can be kept dissolved metastably at room pressure in the supercooled liquid state at concentrations close to saturation (Lejeune et al., 1994; Richet et al., 1996). It is this feature that allows accurate measurements to be performed at room pressure on water-bearing liquids. In this way, a wealth of data could begin to be gathered not only for viscosity but also for thermal expansion (Bouhifd et al., 2001), heat capacity (Bouhifd et al., 2006), and enthalpy of mixing (Richet et al., 2004). In parallel, recent technological breakthroughs have made it possible to examine more conveniently and accurately at least some properties while the sample is at the temperatures and pressures of interest (Bassett et al., 1996; Nowak and Behrens, 1995; Zotov and Keppler, 2000).

14.2 PHASE RELATIONS

Melting phase relations and solubility of water in silicate melts are linked via the Van't Hoff equation. This equation can be used to describe melting in silicate-H_2O systems:

$$\ln a_{\mathrm{H2O}} = \left[\Delta H^{fusion}/R\right] \bullet \left[(1/T) - (1/T_o)\right], \tag{14.1}$$

where a_{H2O} is the activity of water in melt solution, ΔH^{fusion} the enthalpy of fusion of the silicate phase, T_o is the melting temperature of the pure phase, and T the liquidus temperature in the silicate-H_2O mixture. We will first discuss the influence of H_2O on melting and crystallization phase relations, including solidus and liquidus temperature depressions caused by dissolved water (Section 14.2.1). Water in melts and glasses is the subject of Sections 14.2.3 and 14.2.4.

14.2.1 Melting and Crystallization

At pressures above ambient, any amount of H_2O results in large reductions in melting temperatures. The extent of this effect depends on silicate composition and is largest for silica-rich and aluminosilicate-rich systems (Fig. 14.1). The melting temperature of quartz (SiO_2) is lowered by about 900°C by a 1 GPa water pressure (Kennedy et al., 1962; Jackson, 1976), whereas the temperature change is about 400°C for enstatite at similar pressures (Kushiro et al., 1968). An analogous effect can be seen in chemically complex natural silicate systems (Fig. 14.1B). The felsic silicate melt, granite, shows a freezing point depression of near 400°C or more at 1 GPa (Stern et al., 1975), whereas that of the silica-poor peridotite composition shows a depression near 250°C at this pressure (Kushiro et al., 1968; Till et al., 2012; see also Medard and Grove, 2008).

Phase relations that involve equilibria between melt and crystalline materials also are affected by water. For example, enstatite ($MgSiO_3$) melts congruently above about 0.5 GPa under dry conditions (Boyd et al., 1964). However, in the presence of H_2O, it melts incongruently to forsterite + liquid (Kushiro et al., 1968). Such effects can also be seen in phase relations of chemically more complex systems, such as Mg_2SiO_4-$CaMgSi_2O_6$-SiO_2H_2O where melts at the forsterite-pyroxene liquidus are olivine-normative under dry high-pressure conditions but quartz-normative when water saturated (Fig. 14.2). Such changes in melting relationships are the result of decreasing activity of silicate component (s) when H_2O is dissolved. Notably, when pressure exceeds 10–15 GPa, the liquidus volume of forsterite shrinks (Presnall and Gasparik, 1990), which is consistent with changes in the water solution mechanism at very high pressure (Mookherjee et al., 2008; Karki et al., 2010).

Aluminosilicate liquidus phase relations also change under hydrous conditions. For example, with increasing water saturation pressure in the $NaAlSi_3O_8$-$KAlSi_3O_8$-SiO_2 system, the

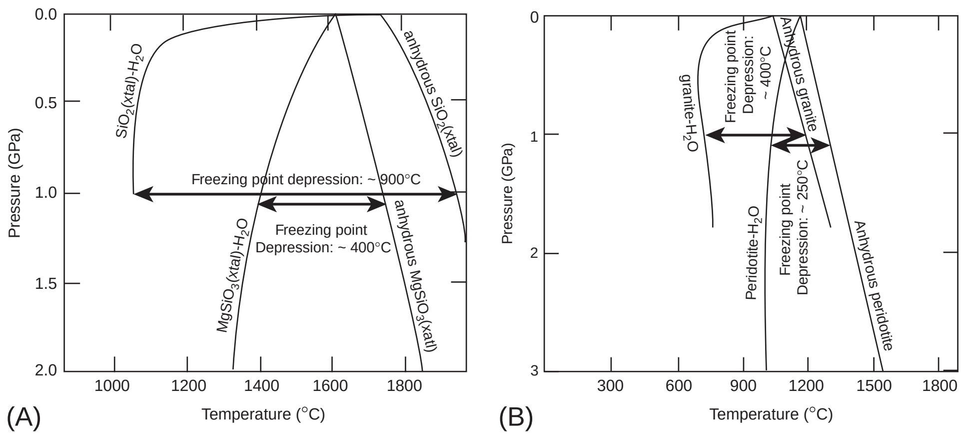

FIG. 14.1 Pressure/temperature trajectories of (A) granite with and without H_2O (granite-H_2O and anhydrous granite) and peridotite with and without H_2O (peridotite-H_2O and anhydrous peridotite) solidi (Stern et al., 1975; Kushiro et al., 1968) and (B) of silica polymorphs and of enstatite with and without H_2O (cristobalite-H_2O, enstatite-H_2O, anhydrous cristobalite and anhydrous enstatite) (Boyd et al., 1964; Kushiro et al., 1968; Jackson, 1976; Boettcher, 1984).

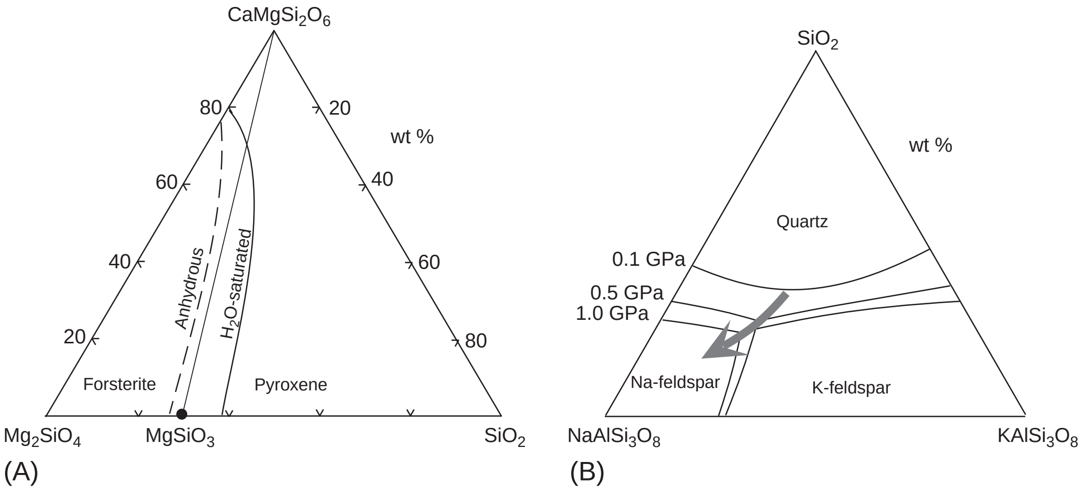

FIG. 14.2 (A) Liquidus phase relations at 2 GPa in the system Mg_2SiO_4-$CaMgSi_2O_6$-SiO_2 with and without excess H_2O as indicated on diagram. (B) Shift of phase boundaries in the haplogranite system, $NaAlSi_3O_8$-$KAlSi_3O_8$-SiO_2-H_2O with increasing water pressure (Tuttle and Bowen, 1958; Luth et al., 1964). (A) Redrawn from Kushiro (1969).

liquidus volume of quartz expands relative to Na- and K-feldspar (Bowen, 1948; Tuttle and Bowen, 1958; Luth et al., 1964); see also Fig. 14.2B. Further, as the water pressure is increased the trajectory of the temperature minimum (shown with a shaded arrow in Fig. 14.2B) is toward the $NaAlSi_3O_8$ corner of the system. Qualitatively, one might infer from these relations that not only does the activity coefficient of SiO_2 decrease more than those of the other components needed to form feldspar, but that there is also an effect of dissolved H_2O on the activity of Na_2O and K_2O in the melt.

The principles that govern melting phase relations in hydrous chemically simple silicate systems also apply to systems of greater chemical complexity, including natural rock systems such as peridotite-H_2O, basalt/gabbro-H_2O, and rhyolite/granite-H_2O. In basalt and peridotite systems, the presence of water in the partial melt again expands the olivine liquidus volume and result in melts becoming increasingly enriched in silica and aluminosilicate components (Mysen and Boettcher, 1975; Sisson and Grove, 1993; Hirose, 1997; Medard and Grove, 2008).

14.2.2 Silicate-H_2O Miscibility

At low pressures and temperatures, silicate melts and water-rich fluids are immiscible. However, as temperature and pressure increase, the water content of silicate melt increases, as does the silicate content of coexisting aqueous fluid, which eventually leads to complete miscibility between silicate and H_2O. Such features were first observed in the SiO_2-H_2O system where the melting curve terminated in a second critical endpoint near 970 MPa and 1080°C (Kennedy et al., 1962; see also Fig. 14.3).

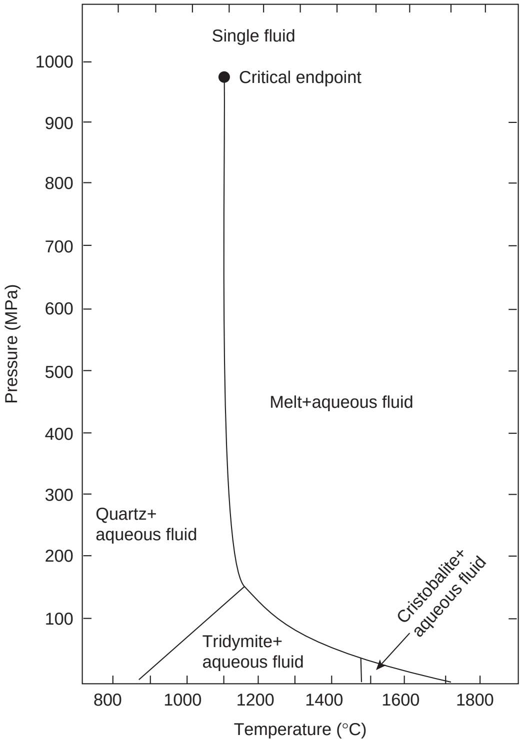

FIG. 14.3 Second critical endpoint in SiO_2-H_2O system. *Redrawn from Kennedy et al. (1962).*

It is difficult, however, to identify complete miscibility between silicate melt and aqueous fluid by examination of experimental charges after returning the sample to ambient temperature and pressure. This is because both the quenched melt (hydrous glass) and the quenched fluid commonly change their composition during quenching and decompression from temperature often above 1000°C and pressures above 1 GPa (Mysen and Acton, 1999). However, this experimental complexity is overcome when experimental charges can be characterized optically, by X-ray absorption, and by vibrational spectroscopic methods while the hydrous melt and coexisting fluid are at the temperature and pressure of interest (Shen and Keppler, 1997; Zotov and Keppler, 2000; Mibe et al., 2004).

The mutual solubility of silicate in fluid and H_2O in melt increases with increasing temperature and pressure (Fig. 14.4). The solvus, which is defined by the composition of coexisting melt and fluid, ends at a critical point beyond which a single supercritical fluid obtains. The temperature/pressure coordinates of this point depend on silicate composition (Shen and Keppler, 1997; Bureau and Keppler, 1999; Sowerby and Keppler, 2002); see also Fig. 14.5. Along the SiO_2-$NaAlO_2$ join, for example, the temperature of the critical point decreases isobarically with increasing Al/(Al+Si) (Fig. 14.5).

In chemically more complex systems, the topology of the solvus depends on other composition variables. For example, an increasing abundance of components that cause silicate

FIG. 14.4 Schematic representation of solvus relations in silicate-H_2O systems at two different pressures, P_1 and P_2, where $P_1 < P_2$.

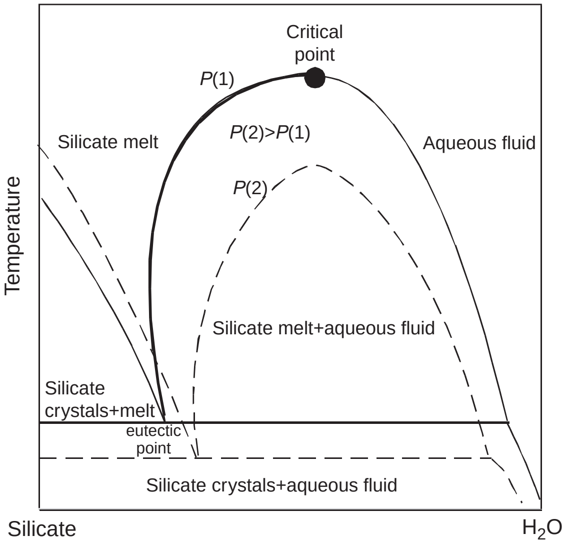

FIG. 14.5 Examples of pressure/temperature trajectories of critical endpoints for systems indicated on individual curves (Bureau and Keppler, 1999).

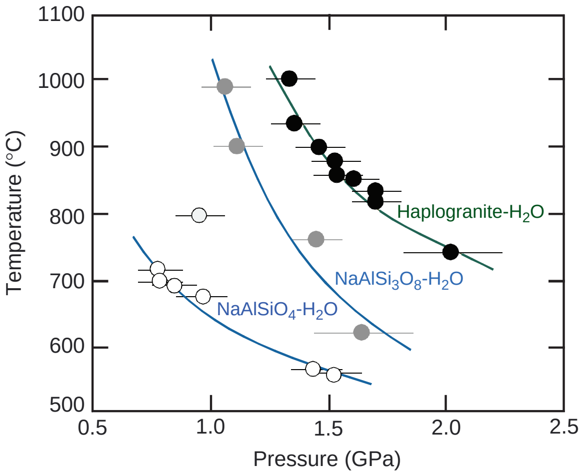

depolymerization tends to reduce temperatures and pressures of the critical point (Sowerby and Keppler, 2002; Mysen, 2013). The solvus itself also changes when the silicate composition varies. When Al_2O_3 is added to a hydrous Na silicate system, the melt limb of the solvus shifts to considerably more polymerized compositions (Fig. 14.6). Moreover, it appears that both the solvus and pressure/temperature coordinates of the critical point are sensitive to the abundance ratios of alkaline earths vs alkalis. In alkali-rich systems such as rhyolite and granite, the critical point tends to be in the 1–2 GPa range at temperatures less than 1000°C, whereas in

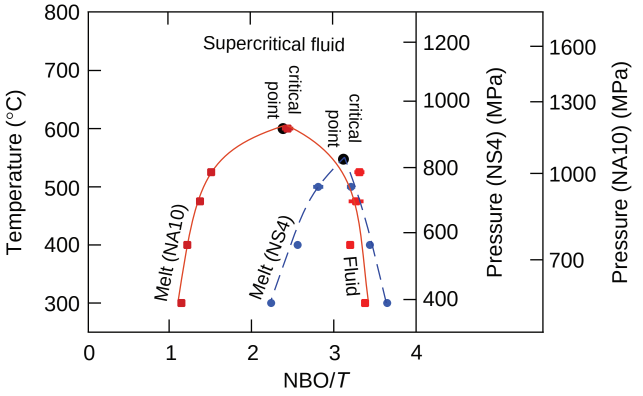

FIG. 14.6 Solvus and critical point for compositions $Na_2Si_4O_9$ (NS4) and $[Na_2Si_4O_9]\cdot[Na_2(NaAl)_4O_9]_{10}$ (NA10) as a function of temperature and pressure when expressed in terms of degree of polymerization of the silicate in melt and fluid (NBO/T, T=Si+Al) (Mysen, 2013).

alkaline earth systems the critical point appears to occur at pressures in excess of 5 GPa and 1000°C (Bureau and Keppler, 1999; Stalder et al., 2001; Mibe et al., 2007).

14.2.3 Water Solubility

Water solubility studies date back to Spallanzani's unsuccessful attempts at measuring water contents in basalt in the late 18th century (Spallanzani, 1792–1797). Following that very early attempt, the first modern results were obtained by Goranson (1936) on H_2O solubility in molten $NaAlSi_3O_8$.

To understand water solubility in silicate melts, it is instructive first to examine the principles that govern phase relations in hydrous silicates at superliquidus temperatures (Fig. 14.4; see also Paillat et al., 1992; Mibe et al., 2007). Water solubility is then defined by the univariant curve that separates the phase field of melt from that of melt + fluid. Therefore, at a given pressure, the slope of this univariant curve defines how solubility varies with temperature. This slope can change from negative to positive with increasing temperature. It can also change from negative to positive with increasing pressure (Holtz et al., 1995). The change in slope also can be affected by silicate composition (Behrens et al., 2001).

14.2.3.1 SiO_2-H_2O

Early studies on water solubility in silicate systems were conducted at low partial pressure of H_2O and total pressure near ambient (e.g., Tomlinson, 1956; Kurkjian and Russell, 1958; Moulson and Roberts, 1961; Shackleford and Masaryk, 1976). Under these conditions, the solubility is proportional to the square root of the H_2O pressure (Fig. 14.7A). That relationship points to a simple solution mechanism whereby oxygen bridges in the three-dimensionally interconnected network of vitreous SiO_2 are replaced by OH-groups, as summarized in Eq. (15.5) (Chapter 15).

The H_2O solubility in SiO_2 melt increases with increasing pressure, but the relationship no longer is a linear function of $\sqrt{P_{H_2O}}$ (Fig. 14.7B; see also Kennedy et al., 1962; Holtz et al., 2000), where therefore the solution mechanism(s) of H_2O must change. The rate of water

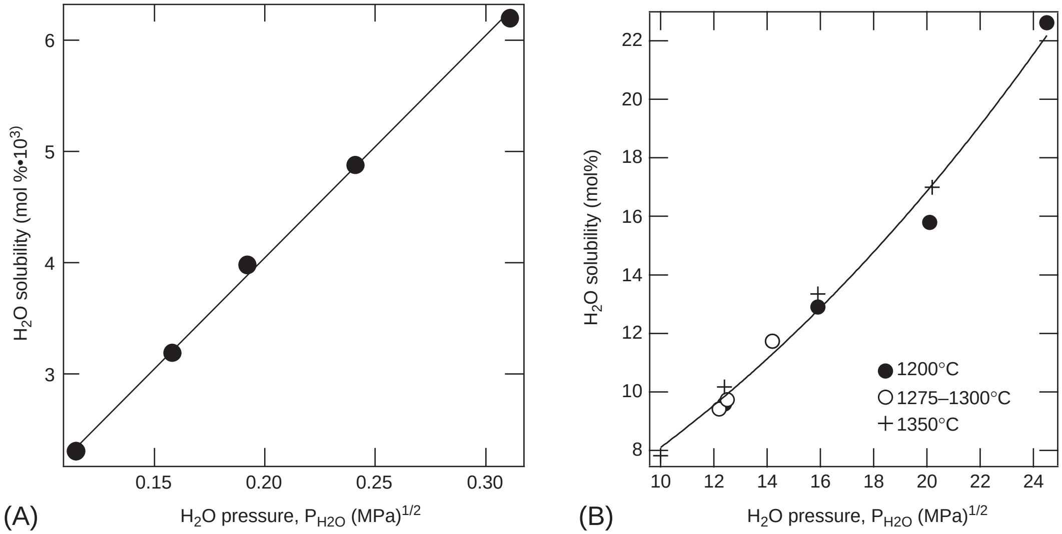

FIG. 14.7 (A) Solubility of H_2O in SiO_2 melt at 1000°C as a function of $\sqrt{P_{H_2O}}$ at pressures below ambient (Moulson and Roberts, 1961). (B) Solubility of H_2O at high pressure (Holtz et al., 2000).

solubility increase is itself pressure dependent. This feature may indicate that the ΔV of equilibrium (15.5) actually is positive and increasingly so with increasing pressure, because the partial molar volume of H_2O in silicate melts decreases with increasing pressure (Sakamaki et al., 2009; Agee, 2008; Malfait et al., 2014). That supposition, in turn, might be expected if the cavity volume in which molecular H_2O is dissolved decreases with increasing pressure (Zhang et al., 2010; see also Section 14.4.1).

Insights into the manner in which such cavities form and influence the physics of the SiO_2-H_2O system have been gained from first-principles calculations (Ottonello et al., 2015). Although focused on the wet solidus of silica, the investigation also aimed at reproducing the observed solubility of water (expressed as OH_2 units) over wide pressures and temperatures and the entire composition range from pure molten silica to pure water. A notable result is that the solution energy is indeed dominated by cavitation terms, mainly entropic in nature, which cause a large negative solution entropy and a consequent marked increase of the gas phase fugacity with increasing temperatures. Besides, the solution enthalpy is negative and dominated by electrostatic terms that depict a pseudopotential well whose minimum occurs at a low water fraction (X_{H_2O}) of about 6 mol%.

14.2.3.2 *Metal Oxide-SiO_2-H_2O*

The metal/silicon ratio and type and proportion of metal cation of metal oxide silicate melts affect water solubility (Kurkjian and Russell, 1958; Uys and King, 1963; Coutures and Péraudeau, 1981). The H_2O solubility decreases with increasing metal/Si ratio and reaches a minimum value at some intermediate ratio before again increasing when equilibrated with water steam at 0.1 MPa (Fig. 14.8A). The water solubility and the location of the solubility minimum vary with the electron properties of the metal cation so that the

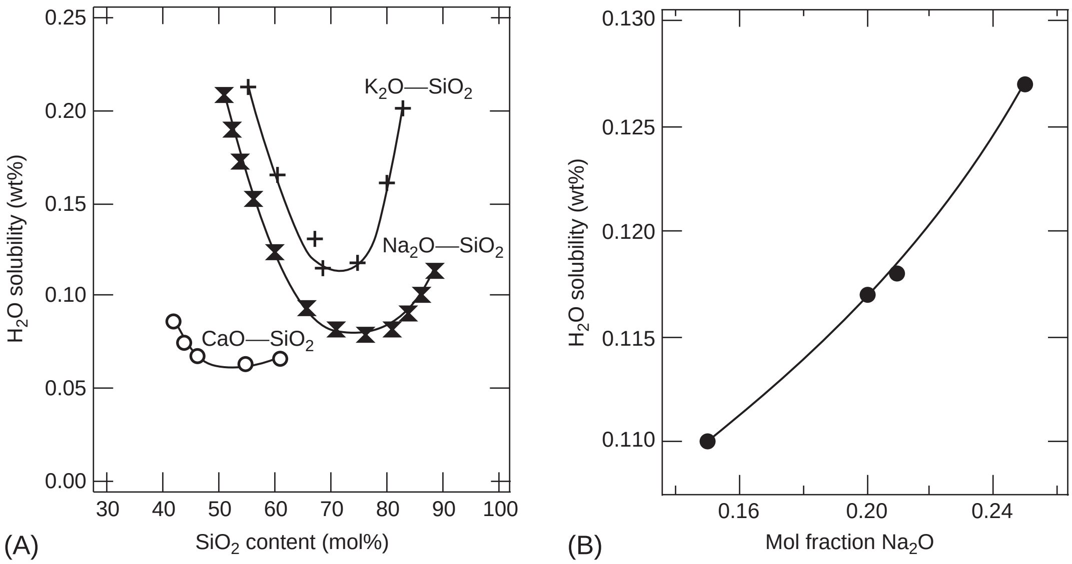

FIG. 14.8 Solubility of H_2O in metal oxide-SiO_2 melts equilibrated with water vapor at $P_{H2O} = 0.1$ MPa. (A) Solubility as a function of metal oxide/SiO_2 for Na_2O and K_2O (Kurkjian and Russell, 1958). (B) Water solubility in melts at $P_{H_2O} = 0.1$ MPa as a function of mol fraction, x, of Na_2O in the system $(Na_2O)_x - (CaO)_{0.05} - (SiO_2)_{1-x-0.05}$. *Redrawn from* *Coutures and Peraudeau (1981).*

solubility increases with increasing cation radius and decreasing electrical charge (Kurkjian and Russell, 1958; Coutures and Péraudeau, 1981). In mixed metal oxide silicate melts, the solubility is positively correlated with the abundance of the most electropositive cation (e.g., increasing Na/Ca ratio; see Fig. 14.8B).

Many of the solubility features observed at ambient pressure qualitatively can also be observed at high pressure. For example, decreasing water solubility with increasing metal oxide/SiO_2 ratio was also reported in the ranges 0.8–2 GPa and 1000°C–1300°C for Na_2O-SiO_2 melts (Fig. 14.9). In other words, as a melt becomes increasingly polymerized, the H_2O solubility increases and the silicate melt structure becomes less polymerized. This increase is temperature dependent.

It follows from the schematic illustration of melt/fluid phase relations (Fig. 14.4) that H_2O solubility should vary with pressure and temperature, as it does (Fig. 14.10). Increasing pressure shifts the silicate-rich limb in Fig. 14.4 toward more water-rich values. In other words, the H_2O solubility should, and does, increase with pressure (Fig. 14.10). Interestingly, though, it seems that this pressure increase also depends on melt composition (structure) and that the more polymerized the silicate, the more sensitive is its H_2O saturation level to pressure (Fig. 14.10A). Furthermore, the slope of the silicate-rich limb of the solvus in Fig. 14.4 changes from negative toward positive with increasing pressure, which is what one also sees by comparing, for example, the solubility in $Na_2O \cdot 4SiO_2$ quenched melt with temperature at 0.8 GPa, where the solubility decreases temperature and at 1.65 GPa where it does not. A further pressure increase results in a positive temperature dependence (Mysen and Cody, 2004).

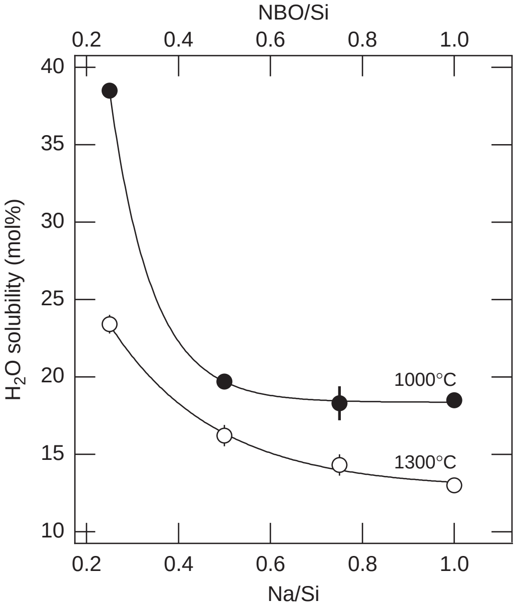

FIG. 14.9 Water solubility in $Na_2O{\cdot}2SiO_2$ glass quenched from melt after equilibration at 1000°C and 1300°C, respectively (as indicated on figure) at 0.8GPa as a function of Na/Si of the melt. For anhydrous melts in this system, the degree of silicate polymerization, NBO/Si, equals the Na/Si ratio (Mysen and Cody, 2004).

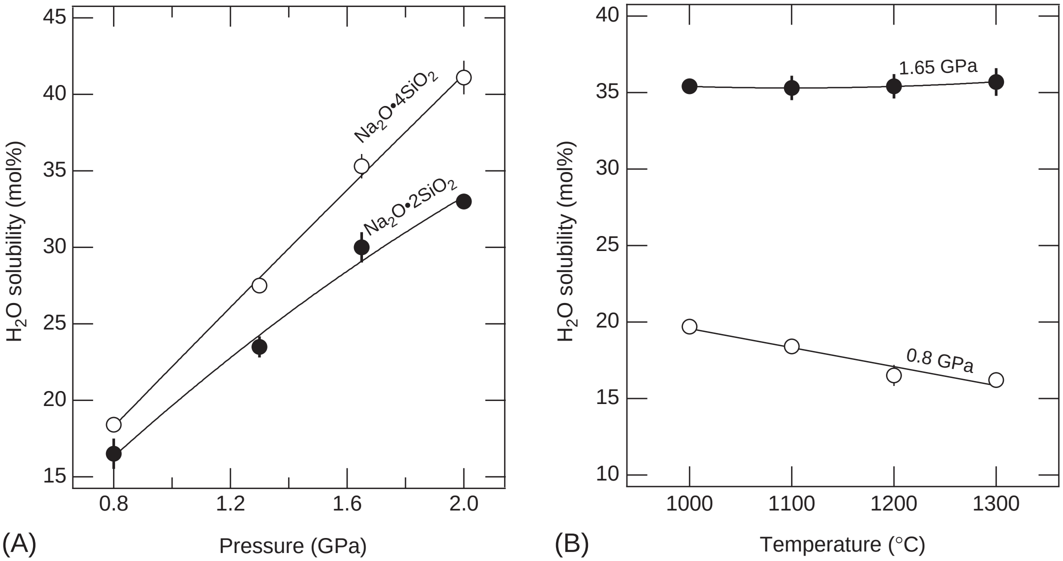

FIG. 14.10 Solubility of H_2O in Na_2-SiO_2 glasses formed by quenched from high temperature at high pressure. (A) Solubility of two compositions indicated, as a function of pressure (P_{H_2O}) equilibrated at 1100°C at pressures indicated (Mysen and Cody, 2004). (B) Temperature dependence of H_2O solubility at two different water pressures, $P_{H_2O}=0.8$ and 1.65GPa (Mysen and Cody, 2004).

14.2.3.3 Aluminosilicate-H_2O

In general, the rules that govern temperature and pressure-dependent solubility variations in silicate melts also apply, at least qualitatively, to the solubility of H_2O in aluminosilicate melts (Behrens, 1995; Behrens et al., 2001). That notwithstanding, water solubility in aluminosilicate melts is influenced by reactions involving Al^{3+} as suggested, for example, by the decreased feldspar liquidus volume relative to that of quartz with increasing water pressure in the system $NaAlSi_3O_8$-$KAlSi_3O_8$-SiO_2-H_2O (Fig. 14.2B). This inference is consistent with the negative correlation, at least at high pressure, between water solubility and Al_2O_3-content, whether in peralkaline (Mysen and Wheeler, 2000; Mysen, 2002) or peraluminous melts (Dingwell et al., 1997). For melts along meta-aluminous joins, in contrast, water solubility *increases* with increasing Al_2O_3 (McMillan and Holloway, 1987; Holtz et al., 2000). In addition, the nature of the metal cation or cations serving to charge-balance Al^{3+} in aluminosilicate melts also affects H_2O solubility (Behrens et al., 2001; Romano et al., 1996; Mysen, 2002).

The water solubility on the peraluminous and peralkaline side of alkali meta-aluminosilicate melts is greater than at the meta-aluminosilicate stoichiometry (Mysen, 2002; Dingwell et al., 1997). Excess Al^{3+} [Al-(K + Na) > 0] has a much greater effect than excess alkalis (Fig. 14.11). From limited data in Ca-aluminosilicate melts (excess Ca over Al), similar relations have been reported, but with Ca-charge-balance of Al^{3+} in tetrahedral cordination, the water solubility is less than for peralkaline alkali aluminosilicate melts (Mysen and Cody, 2004). For peralkaline Li-aluminosilicate compositions, qualitatively similar relationships have been observed with the solubility decreasing as Li substitutes for Na and K (Dingwell et al., 1997). In fact, there seems to be a general trend for aluminosilicate melts that solubility is negatively correlated with the ionic radius of the metal (Behrens et al., 2001; see also Fig. 14.12).

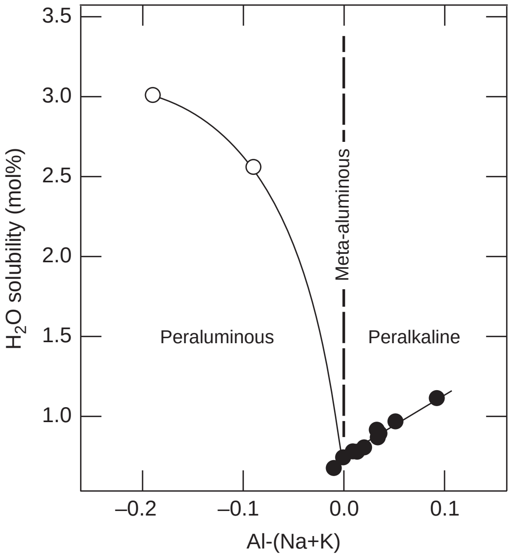

FIG. 14.11 Solubility of H_2O on peraluminous and peralkaline side of haplogranite, HPG8 (Knoche et al., 1995) from analyses of glasses formed by quenching of hydrous melts from 1000°C at 50 MPa (Dingwell et al., 1997).

FIG. 14.12 Solubility of water in $MAlSi_3O_8$ melts as a function of charge-balancing cation, M at pressures indicated (Behrens et al., 2001).

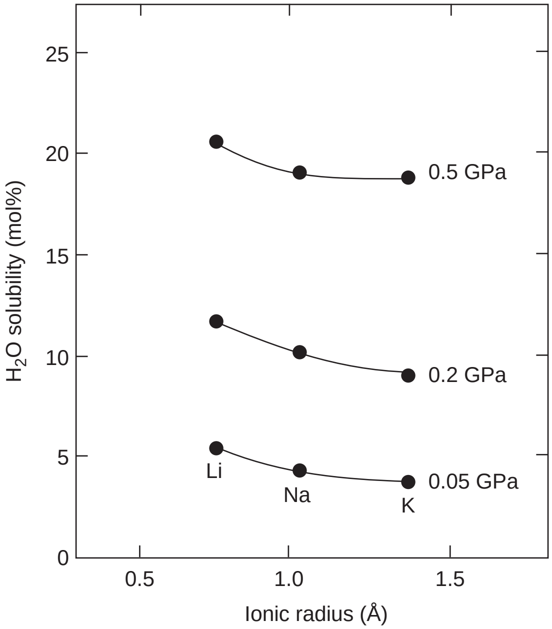

Water solubility and solution mechanisms for compositions along meta-aluminosilicate joins, $SiO_2 - M^{n+}{}_{1/n}AlO_2$, have attracted considerable attention because of the relevance of such melts to our understanding of the role of H_2O in natural magmatic liquids (Goranson, 1938; Burnham, 1975; Silver and Stolper, 1989; Holtz et al., 2000; Kirschen and Pichavant, 2001; Behrens et al., 2001; Benne and Behrens, 2003). The water solubility of melts $SiO_2 - M^{n+}{}_{1/n}AlO_2$ joins varies with compositional variables such as Al/(Al + Si) (Holtz et al., 2000) and with the type of alkali metal or alkaline earth that serves to charge-balance in tetrahedral coordination (Romano et al., 1996; Holtz et al., 2000; Fig. 14.13). Increasingly electronegative charge-balancing cations lead to greater solubility, which may relate to the reactivity of the Al—O bonds being sensitive to this cation (Bouyer et al., 2010).

An alternative to describing water solubility in terms of specific interactions between a melt and dissolved water is the first-principles based models by Ottonello et al. (2014, 2018). As described in more detail in Section 17.2.2.1 for noble gases, the details of the structure do not necessarily need to be considered in the wide composition range for which measurements are available (Papale, 1997; Papale et al., 2006). In such models, the dielectric properties of the medium are the key factor (Ottonello et al., 2018) governing the interaction between the silicate solvent and the volatile solute. For molecular water (expressed as OH_2), the solubility is mainly determined by its cavitation energy as noted previously (Ottonello et al., 2014). Application of the Silver-Stolper ideal homogeneous speciation model (Stolper, 1982) together with consideration of hydrogen bonding then allowed the extensive solubility set available to be reproduced with a mean accuracy of ~2.1 kJ/mol in terms of energy and ~1.7% in terms of the mol fraction of H_2O under saturation conditions (X_{H_2O}).

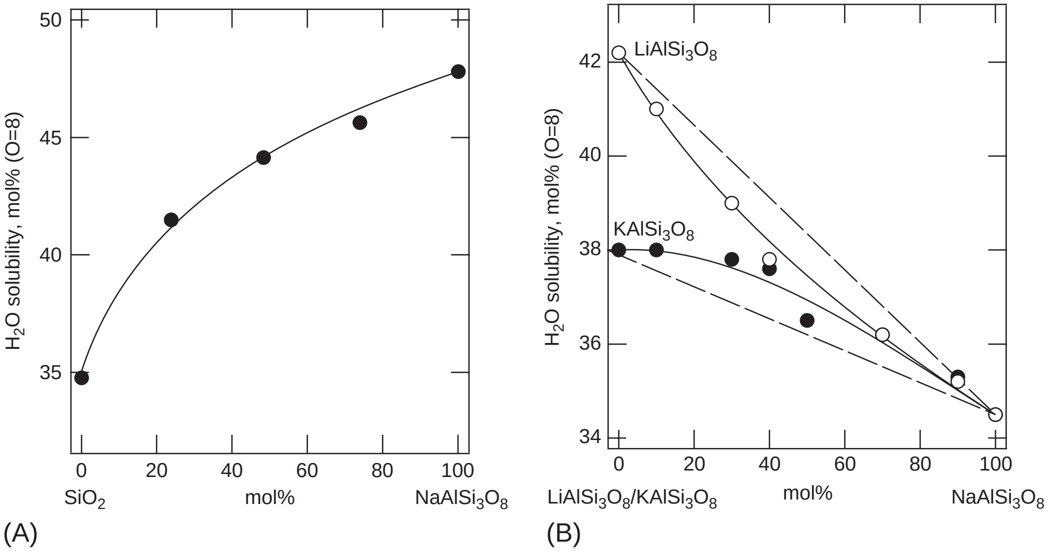

FIG. 14.13 Solubility of water in meta-aluminosilicate melts. (A) Solubility along the join $SiO_2-M^{n+}{}_{1/n}AlO_2$ in glass formed by temperature-quenching from 1200°C at 200 MPa (Holtz et al., 2000). (B) Solubility in glasses along $MAlSi_3O_8$ joins as indicated formed by temperature quenching from 1040°C at 200 MPa (Romano et al., 1996). Mol% calculated with no. of oxygen equal to 8.

14.2.4 Water Solubility and Mixed Volatiles

Limited experimental data exist for situations where H_2O is part of a mixture of fluids with two or more components. The most common mixture is H_2O+CO_2 (for the solubility of CO_2, see Chapter 17, Section 17.3.1) (Mysen, 1976; Holtz et al., 1993; Tamic et al., 2001; Behrens et al., 2009; Shishkina et al., 2010). In such mixtures, the H_2O solubility is a positive function of the ratio, $H_2O/(H_2O+CO_2)$. Data to 500 MPa indicate that for mafic compositions such as basalt, there is a near linear relationship between water solubility and $H_2O/(H_2O+CO_2)$ for values of this ratio higher than 0.2. This may suggest that activity-composition relations in the fluids coexisting with the melts do not change much as a function of the $H_2O/(H_2O+CO_2)$ ratio. However, for more felsic compositions, this linearity breaks down (Fig. 14.14). The different solubilities of water in silica-rich melts in the same $H_2O/(H_2O+CO_2)$ region indicate that CO_2 solubility then changes the silicate structure sufficiently that the solution mechanism(s) of water is affected.

The effects of H_2O+H_2 mixtures on water solubility are different (Schmidt et al., 1999; Bezmen et al., 2011). Bezmen et al. (2011) observed that there is a maximum in total water solubility with ≤10 mol% H_2 (Fig. 14.15). Moreover, there appears to be a strong effect of silicate composition because the solubility of H_2O+H_2 fluid increases as the melt becomes less silicate-rich (Bezmen et al., 2011). The solubility maximum near $H_2/(H_2+H_2O)=0.1$ makes it clear that the H_2O+H_2 mixture cannot be treated as an ideal solution in the melt, a feature also noted by Luth and Boettcher (1986) in their study of freezing point depression at high pressure for various silicate compounds (see also Chapter 18, Section 18.3). In other words, the

FIG. 14.14 Water solubility in basalt melt and rhyolite melt as a function of $H_2O/(H_2O+CO_2)$ of the fluid at pressures indicated (Tamic et al., 2001; Shishkina et al., 2010).

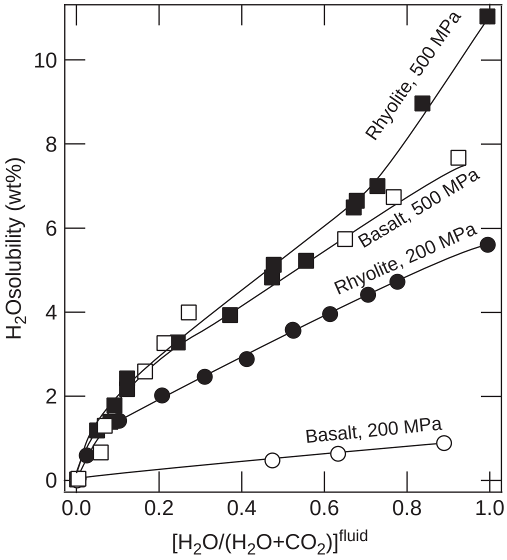

FIG. 14.15 Water solubility in melts as a function of $H_2/(H_2+H_2O)$ of the fluid at 200 MPa total pressure at 950–1200°C (Bezmen et al., 1991, 2011).

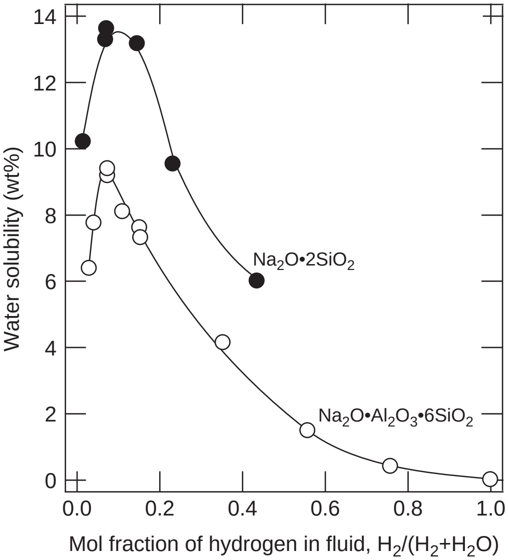

H_2O+H_2 fluid being nearly ideal, hydrogen must interact with the silicate structure to cause such large effects on total water solubility.

The profound effect of dissolved fluorine on water solubility increases with increasing water content (Fig. 14.16; Sorapure and Hamilton, 1984; Holtz et al., 1993). It is not clear, however, whether this effect results from changes in melt structure by dissolved fluorine, thus

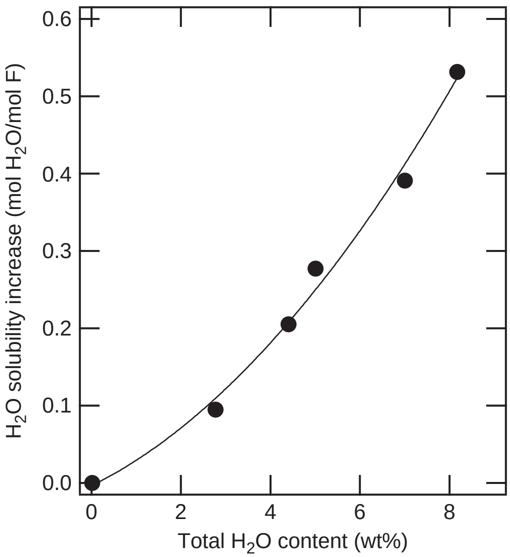

FIG. 14.16 Water solubility increase by dissolved fluorine as a function of total water content (Holtz et al., 1993).

causing increased water solubility, or from changes in the fluid speciation. This effect differs from that of Cl on water solubility. Here, the solubility is insensitive to Cl content until several wt% Cl are dissolved, at which point water solubility decreases dramatically (Webster et al., 1999). The chlorine content where this water solubility drop occurs is quite sensitive to silicate composition.

14.3 THERMAL PROPERTIES

Determination of thermodynamic properties of hydrous silicate melts is hampered by the fact that glasses quenched from temperatures above their liquidi at high pressure necessary to dissolve water commonly exsolve some of this water when heated up to the glass transition range at the ambient pressure often needed for property measurements. Information, therefore, often has been obtained from thermodynamic analysis of phase equilibria data together with equations of state for hydrous silicate systems.

14.3.1 Activity-Composition Relations

An early example of this approach was the experimental study of mixing properties of H_2O in hydrous $Na_2O{\cdot}Al_2O_3{\cdot}6SiO_2$ melt. Here, Burnham and Davis (1974) employed volume data for pure H_2O and H_2O in silicate melt solution to derive a mixing model for H_2O in melts. For mol fraction of H_2O in solution up to 0.5, a simple relationship with fugacity is:

$$f^{melt}{}_{\mathrm{H2O}} = k\left(X^{melt}{}_{\mathrm{H2O}}\right)^2, \tag{14.2}$$

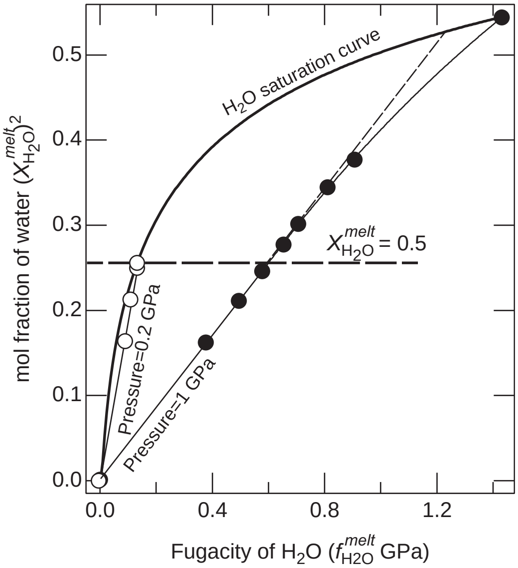

FIG. 14.17 Relationship between mol fraction of dissolved water (squared) and the fugacity of water in hydrous $Na_2O{\cdot}Al_2O_3{\cdot}6SiO_2$ melt at 700°C and 1 GPa pressure, The horizontal dashed line represents the maximum water content below which dissolved H_2O follows Henry's Law (ideal mixture). Curves at 0.2 and 1 GPa total pressure are shown. The bold curve denoted H_2O saturated curve represents the solubility of H_2O in this melt. The extended dashed line shows how the fugacity curve for water deviates from linearity with more than 50 mol% H_2O in solution. *Redrawn from Burnham and Davis (1974).*

where $f^{melt}{}_{H_2O}$ is the fugacity of H_2O in melt and $X^{melt}{}_{H_2O}$ its mol fraction, and k a constant. At higher water concentrations, a more complex relationship was proposed:

$$f^{melt}{}_{H2O} = 0.25k\exp\left(96.52 - 2667\right)/T)\left(X^{melt}{}_{H2O} - 0.5\right). \tag{14.3}$$

In other words, Burnham and coworkers concluded that the silicate melt-H_2O solution could be treated as ideal for water concentrations up to 50 mol%, before deviating from ideality at higher concentrations (Fig. 14.17). This means that at any pressure equal to or lower than that where the $f^{melt}{}_{H2O}$ curve reaches the solubility curve before 50 mol% dissolved water is obtained, the solution is ideal and can be described with Eq. (14.2). For the results in Fig. 14.17, this maximum pressure is near 0.2 GPa (Burnham and Davis, 1974). At higher pressures, the water fugacity relationship is curved and the relationship is described with Eq. (14.3).

14.3.2 Heat Capacity and Enthalpy

It turns out that at least for some glass composition and water contents, it is possible to measure accurately the heat capacity, C_p, of hydrous glasses at room pressure, and up to temperatures of supercooled liquids over a narrow interval above the glass transition (Bouhifd et al., 2006, 2013; Robert et al., 2014, 2015). From such measurements, there is a number of systematic changes as a function of silicate composition and water content (Fig. 14.18). The heat capacity change at the glass transition increases with increasing water content. This increase is essentially due to the fact that the heat capacity of the glass at the transition becomes increasingly smaller than the Dulong-and-Petit limit of $3R$ g/atom K with increasing water concentration. Furthermore, the rate of change of C_p as a function of water concentration increases as a melt becomes more polymerized (NBO/T of phonolite is ~0.2, whereas NBO/T is

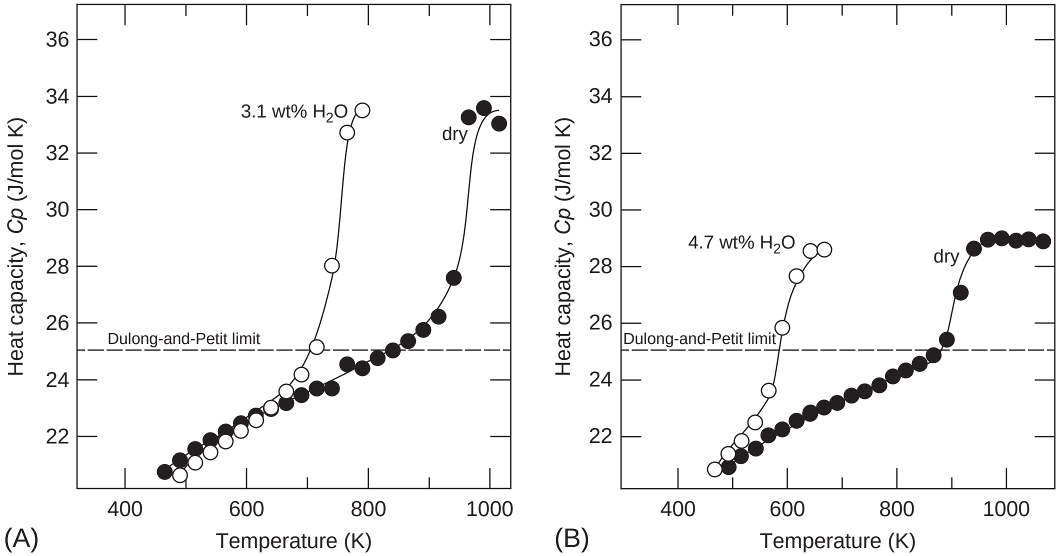

FIG. 14.18 Heat capacity of glass and melt across their glass transition range as a function of water in solution (A) Basalt melt with 3.1 wt% H_2O and dry (Robert et al., 2014). (B) Phonolite melt with 4.7 wt% H_2O and dry (Bouhifd et al., 2006).

~0.6 for the basalt melt in Fig. 14.18). Interestingly, the heat capacity change across the glass transition interval is much greater for depolymerized than polymerized melts, whether these are hydrous or anhydrous (Bouhifd et al., 2013; Robert et al., 2014, 2015).

The partial molar heat capacity of H_2O in melts varies with silicate composition, water content, and temperature (Bouhifd et al., 2006; Robert et al., 2014). It also increases with temperature (Fig. 14.19). When silicate compositions are recast in terms of NBO/*T* values, the

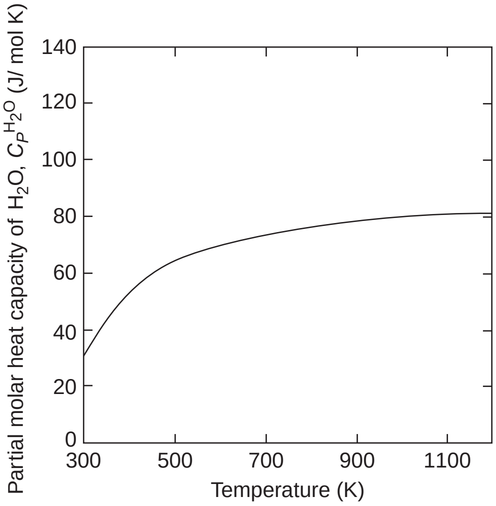

FIG. 14.19 Partial molar heat capacity of water in silicate glasses as derived from a global fit made to 971 measurements on hydrous samples (Robert et al., 2014).

configurational heat capacity increases as melts become increasingly depolymerized (for NBO/T increases, see Di Genova et al., 2014).

From the partial molar heat capacities of dissolved H_2O and of the anhydrous glass and melt, the heat capacity of hydrous glasses and melt may be expressed as:

$$C_{H_2O}^{hydrous\,melt} = X_{H_2O}^{melt} \cdot \overline{C}_P^{H_2O} + \left(1 - X_{H_2O}^{melt}\right) \cdot C_P^{anhydrous\,melt}. \tag{14.4}$$

In general, the heat capacity increases the more depolymerized the silicate, from ~220–240 kJ/mol for greatly depolymerized melts to less than 100 kJ/mol for highly polymerized samples. By combining these data with water speciation models (see Chapter 15, Section 15.2), Bouhifd et al. (2013) found the partial molar heat capacity of molecular H_2O in silicate melts to be 30 ± 15 kJ/mol, whereas for structurally bound OH-groups, the partial molar heat capacity is 281 ± 47 kJ/mol. Di Genova et al. (2014) also observed much greater C_p values for OH groups than for molecular H_2O dissolved in melt. Their values typically were at least 50% lower than those reported by Bouhifd et al. (2013), the narrow temperature intervals over which the measurements can be done likely accounting for at least part of the discrepancy.

Heat capacity data can be used to calculate the temperature dependence of enthalpies of mixing (ΔH_m). Solution calorimetry experiments in lead borate solvent at 700°C have, for instance, been made by Clemens and Navrotsky (1986) on albite and haplogranite compositions (Fig. 14.20). Because pure water could not be investigated, it is difficult to determine the actual ΔH_m from these results. For this reason, Sahagian and Proussevitch (1996) and Zhang (1999) chose to reanalyze the equation-of-state data of Burnham and Davis (1971) to determine the temperature and pressure dependence of ΔH_m. Zhang also incorporated the influence of water speciation.

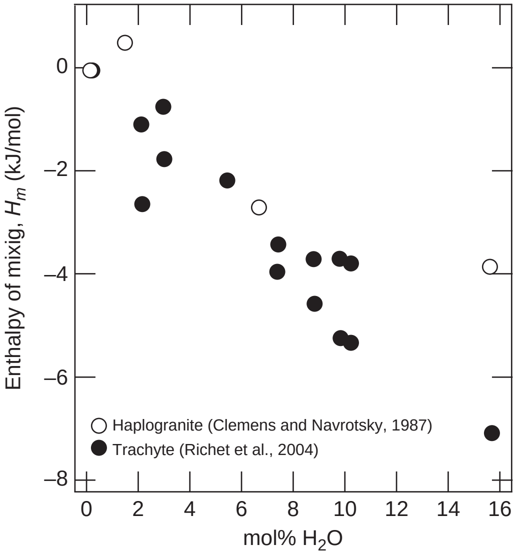

FIG. 14.20 Enthalpy of mixing, ΔH_m, for hydrous glasses of haplogranite ($NaAlSi_3O_8$-$KAlSi_3O_8$-SiO_2) and trachyte composition (Clemens and Navrotsky, 1986; Richet et al., 2004).

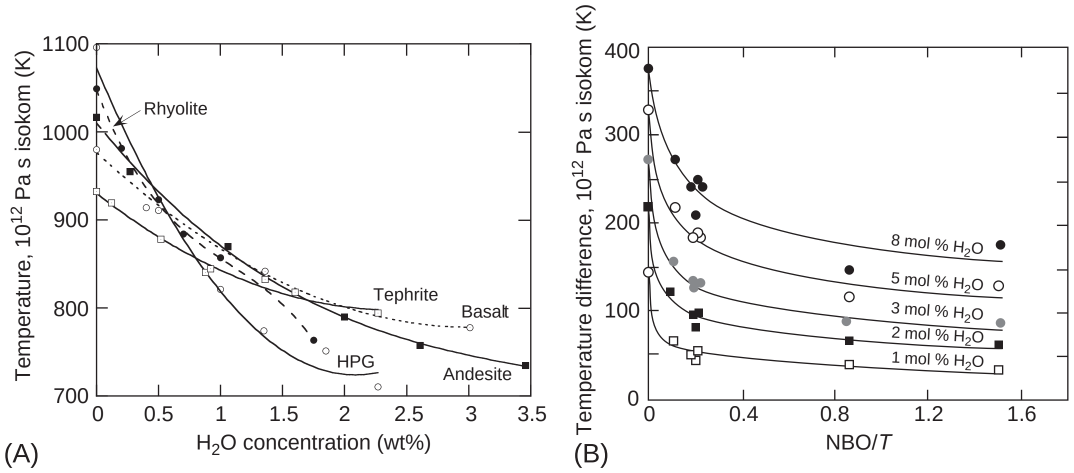

FIG. 14.21 (A) Temperature of the glass transition temperature defined by the 10^{12}Pa s isokom as a function of water content for glass and melt compositions as indicated. Sample HPG as a haplogranite composition of $NaAlSi_3O_8$-$KAlSi_3O_8$-SiO_2 composition. (B) Temperature changes of the glass transition temperature defined by the 10^{12}Pa s isokom as a function of water content for melts of different degrees of polymerization (from data compilation by Whittington et al., 2000).

More accurate values can be obtained from solution calorimetry experiments made in hydrofluoric acid solutions for silicic compositions thanks to easy silicate dissolution and the possibility of extending the measurements up to pure water (Richet et al., 2004, 2006). The results obtained indicate an enthalpy of mixing of about 10 kJ/mol at the highest water contents investigated (Fig. 14.21). Such a determination would be inconsistent, however, because the data do not refer to the same structural state (glass for silicates and liquid for water). Truly isothermal values for a given high temperature, T, can be obtained readily, however, provided that C_p data are available for the glass and supercooled liquid phases, on the one hand, and that the enthalpy of water and steam is known as a function of temperature (Haar et al., 1984), on the other. When these enthalpy adjustments are made, it appears that ΔH_m is basically zero at temperatures higher than 1000 K, and also at a few hundred MPa if enthalpies are adjusted for the effect of pressure (Richet, 2005). In other words, as far as enthalpy is concerned, Burnham's suggestion (Burnham, 1975) that mixing of H_2O and silicate melt is ideal or nearly ideal has been vindicated, at least for SiO_2-rich aluminosilicate compositions.

14.4 OTHER PHYSICAL PROPERTIES

Transport and volume properties will now be considered along with glass transition temperatures. All of them are strongly influenced by water content. Viscvosity will be dealt with in some more detail than other properties not only in view of its fundamental importance, but also because it illustrates particularly well how a rather complete description can be obtained from a combination of extensive measurements performed at room pressure just above the glass transition range with a few high-pressure data obtained above the liquidus.

14.4.1 Transport Properties

Transport properties such as diffusivity, electrical conductivity, and viscosity are sensitive to water content (Saucier, 1952; Shaw, 1963; Dingwell, 1987; Jewell et al., 1993; Zhang and Behrens, 2000; Giordano et al., 2004; Baker et al., 2005; Poe et al., 2006; Ni and Zhang, 2008; Whittington et al., 2009; Ni et al., 2011). However, the extent of change with dissolved water depends on the silicate composition (Whittington et al., 2001, 2009; Behrens et al., 2009). Transport properties of hydrous silicate melts can also vary with pressure (Saucier, 1952; Shaw, 1963; Kushiro, 1978; Dingwell, 1987).

14.4.1.1 Viscosity

Viscosity of hydrous melts decreases by many orders of magnitude even for water concentration levels in the few percent range (Jewell and Shelby, 1988; Richet et al., 1996; Whittington et al., 2000, 2009). The effect of dissolved water on melt viscosity decreases with decreasingly polymerized melts. This is evident, for example, in the results for the temperature of the 10^{12} Pa s isokom as a function of H_2O content, summarized in Fig. 14.21B. The fact that this temperature decreases more rapidly with increasing water content for polymerized melts (e.g., HPG in Fig. 14.21B) compared to depolymerized melts (e.g., basalt in this figure) is a different way of stating that the effect of dissolved water on melt viscosiy diminishes, the less polymerized the anhydrous silicate melt structure. For given melt composition, the rate of viscosity decrease with H_2O concentration is also reduced as total water content is increased (Richet et al., 1996; Whittington et al., 2000, 2009; Fig. 14.22). As H_2O concentration increases, the viscosity evolution of the more polymerized andesite melt approaches that of the less polymerized tehprite composition melt. Interestingly, the effect of increasing alkali content on the viscosity of highly polymerized melts is slightly less (~1 order of magnitude) than that of dissolved H_2O (Schulze et al., 1996).

Because obsidian generally is hydrous, it was an obvious starting material to determine profound effects of water on viscosity (Leonteva, 1940; Sabatier, 1956). Then, measurements under water pressure were pioneered by Saucier (1952) and Shaw (1963). The latter observations, made with the falling sphere method, and the compaction experiments of Friedman et al. (1963) showed that the presence of 4 wt% water in a molten obsidian reduces the viscosity by six orders of magnitude near the glass transition. Other information on these effects was provided by determination of the influence of water on the glass transition temperature of simple silicates (Acocella et al., 1984), which suggested depressions of viscosity by orders of magnitude through addition of a few weight percent of water. Likewise, Jewell and Shelby (1988) and Jewell et al. (1993) found that the activation energy for viscous flow of alkali silicates and aluminosilicates is a significant function of water content at the level of a few hundred ppm (Fig. 14.22). In contrast, for larger water concentrations at high pressure, the effects of dissolved water were much smaller. For andesite melts, Kushiro et al. (1976), for instance, reported only a 20-fold decrease of viscosity with 4 wt% water at 2 GPa, which was nonetheless about five times larger than that observed for the viscosity of the dry melt between room pressure and 2 GPa.

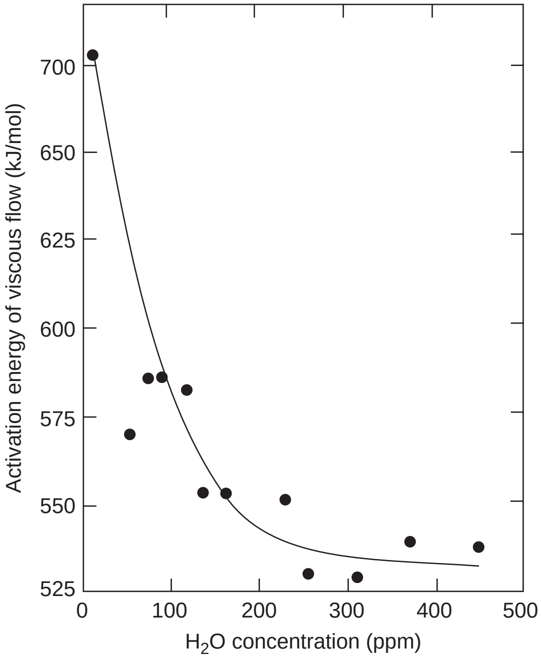

FIG. 14.22 Activation energy of viscous flow of $Na_2O{\cdot}3SiO_2$ melt as a function of water concentration (Jewell and Shelby, 1988).

Measurements above the glass transition have allowed the differing effects of water at low and high temperatures to be determined (Lejeune et al., 1994: Richet et al., 1996). To illustrate the usefulness of the method, the observations made at room pressure for a series of hydrous andesite supercooled liquids over nearly four orders of magnitude are shown in Fig. 14.23. By itself, the strong sensitivity to volatile content demonstrates that no water was lost during the experiments, as any such loss would have been signaled by a departure from the trend set by measurements made at lower temperatures. Significant variation of water content throughout the investigated samples would have caused heterogeneous water distribution. Moreover, infrared analyses made to determine water speciation did not reveal variations of water contents at a small scale. The influence of water is, in fact, so strong that considerable extrapolations would be required to compare isothermal viscosities from 0 to 4 wt% water. Of particular interest is the increasing departure from Arrhenian variation of viscosity with increasing water content apparent in Fig. 14.23.

The complementary nature of high- and room-pressure measurements is apparent in Fig. 14.24. Owing to the slight intrinsic pressure dependence of viscosity, the low-temperature, room-pressure data join smoothly with the high-pressure experiments. Consistent with the trends generally observed for silicates, another important feature apparent in Fig. 14.29 is the convergence of the viscosity data at high temperatures.

FIG. 14.23 Viscosity of hydrous andesite supercooled liquids against reciprocal temperature for the water contents indicated (wt%) (Richet et al., 1996).

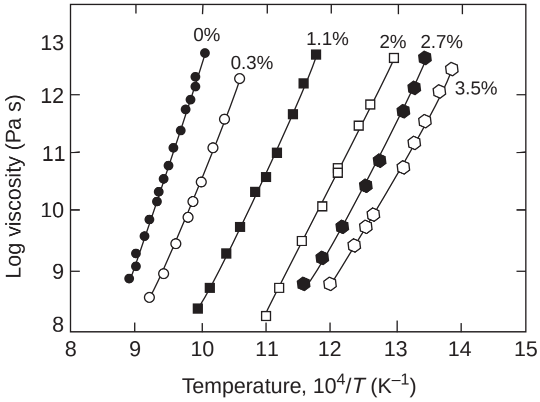

FIG. 14.24 Viscosity of hydrous andesite liquids for the water contents indicated. Measurements made at room pressure at high viscosity and for the water-free sample at low viscosity (Richet et al., 1996), and at high pressure for the other measurements (Kushiro et al., 1976).

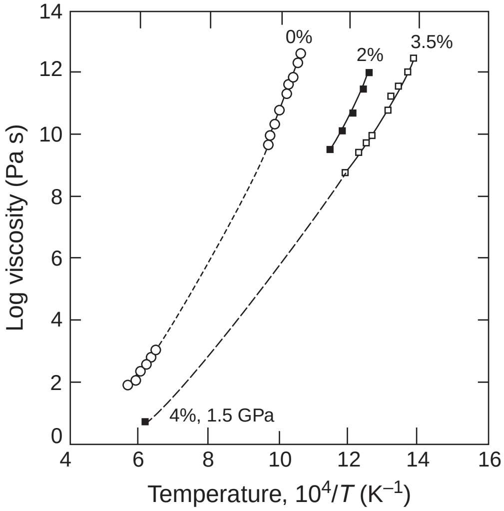

When fitting empirical TVF equations to these measurements:

$$\ln \eta = A + B/(T - T_1), \tag{14.4}$$

one finds that the preexponential parameter, A, can be considered constant, at least for a given series of liquids (Richet et al., 1996). An important consequence is that high-temperature viscosity measurements can be made for the single anhydrous endmember at ambient pressure to determine this parameter for any hydrous silicate series.

The complete viscosity-water content relationships obtained in this way are represented in Fig. 14.25 for a few temperatures. This plot shows more clearly how the tremendous depressing effects of water on viscosity observed near the glass transition tend to level off at higher contents and higher temperatures. In addition, the data of Fig. 14.25 illustrates that the so-called crystallization curtain does not prevent viscosity from being determined between

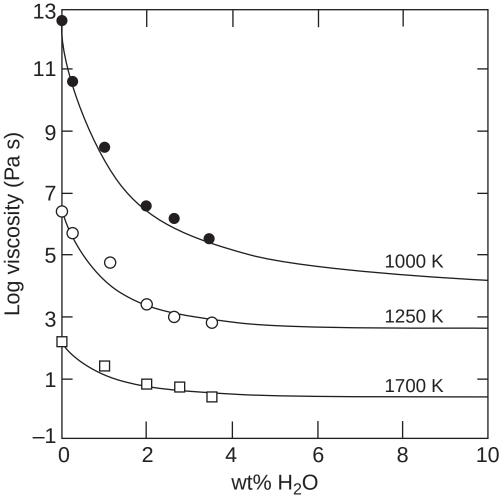

FIG. 14.25 Viscosity of andesite liquids against water content at the temperatures indicated (Richet et al., 1996).

the liquidus temperature and the glass transition. When determined from such a minimum amount of data, these relationships agree with measurements made on hydrous andesites both at high (Kushiro et al., 1976) and at low (Liebske et al., 2003) temperatures.

With the same method, the viscosity of a number of other hydrous melts has been measured. Silicic compositions have received particular attention, with studies devoted to haplogranite (Dingwell et al., 1996), leucogranite (Hess and Dingwell, 1996), rhyolite (Richet et al., 1997; Dingwell et al., 1996; Stevenson et al., 1998), and albite composition melts (Whittington et al., 2005). Less polymerized compositions have also been investigated with tephrite (Whittington et al., 2000), basalt (Richet et al., 1997; Giordano and Dingwell, 2003), phonolite (Giordano and Dingwell, 2003; Whittington et al., 2001; Romano et al., 2003), and trachyte (Whittington et al., 2001; Romano et al., 2003). A surprising consequence of these trends is that hydrous rhyolite becomes less viscous than hydrous basalt at water contents higher than about 2 wt%.

Effects of the M-cation have been investigated by Romano et al. (2003) in alkali and alkaline earth meta-aluminosilicate melts (Fig. 14.26). From at least about 0.5 wt% H_2O to higher water content, the dependence on water content of the 10^{12} Pa s isokom for Li-, Na-, and K-meta-aluminosilicate melts is similar (Fig. 14.26). This dependence differs from that observed for peralkaline and alkaline earth aluminosilicate melts. These observations cannot be readily explained in terms of different degree of depolymerization of the melt (Romano et al., 2003; Jewell et al., 1993). Rather, they could be due to different solution mechanisms of water, for example, to differences in Al$\Leftrightarrow$Si ordering, depending on whether an alkali or an alkaline earth is needed for charge-balance of Al^{3+} in tetrahedral coordination.

As for anhydrous melts, the deviations of viscosity from Arrhenian laws result from the temperature dependence of configurational entropy, S^{conf}, which is itself determined by the configurational heat capacity (C_p^{conf}). The increasing fragility of melts with water content is apparent in Fig. 14.25, which are partly due, as described previously, to dissociation of molecular water into hydroxyl ions. Here, we will not discuss further quantitative applications of

FIG. 14.26 Temperature of the 10^{12} Pa s isokom as a function of water content for the melt compositions indicated (Romano et al., 2003).

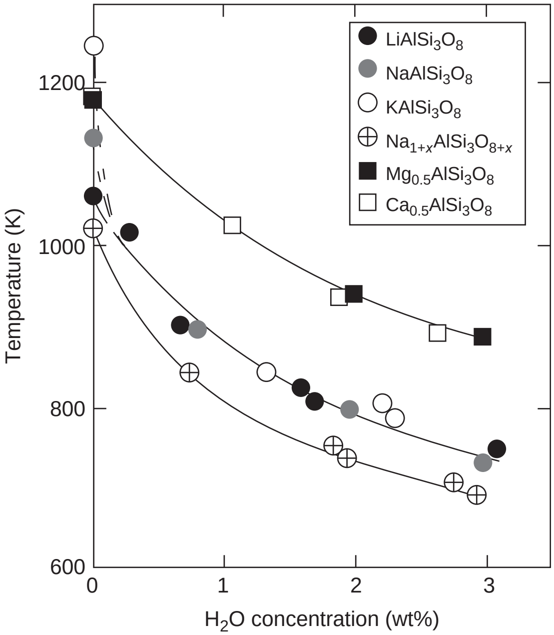

Adam-Gibbs theory. We will just note that, as made for dry melts (Richet, 1984), configurational entropies could be determined from viscosity and be used in thermodynamic modeling of phase equilibria involving hydrous melts.

Notably, the activation energy for viscous flow of aluminosilicate melts is a function of water content even at the level of a few hundred ppm (Fig. 14.27). For the haplogranite composition AOQ ($NaAlSi_3O_8$-$KAlSi_3O_8$-SiO_2), the activation energy decreases as a near linear function of water content for water concentrations in the melt in excess of about 4 wt% (Schulze et al., 1996; see Fig. 14.27). We also note that the activation energy of viscous flow for the $NaAlSi_3O_8$-$KAlSi_3O_8$-SiO_2 composition, which is essentially fully polymerized in the absence of H_2O, is much less than that of the less polymerized $Na_2O{\cdot}3SiO_2$ composition (NBO/Si = 0.67). This difference is the result of the Al-subsitution for Si^{4+} in the $NaAlSi_3O_8$-$KAlSi_3O_8$-SiO_2 composition, which results in significant lowering of melt viscosity and activation energy of viscous flow (see also Chapter 8, Section 8.4.2).

The temperature dependence of melt viscosity of highly polymerized melts deviates more and more from Arrhenian variations as the water concentration in a melt and glass increases (Richet et al., 1996, 1997; Hess and Dingwell, 1996; Whittington et al., 2009; see also Fig. 14.28). In other words, the highly polymerized melts become increasingly fragile as their H_2O content increases (Angell, 1991). However, there seem to be suggestions that highly polymerized alkali aluminosilicate melts, such as rhyolite and granite compositions, differ in this respect from less silica-rich basaltic compositions (Di Genova et al., 2014). These differences may relate to differences in water solution mechanisms in highly polymerized and in depolymerized melts (see Chapter 15, Section 15.4.1).

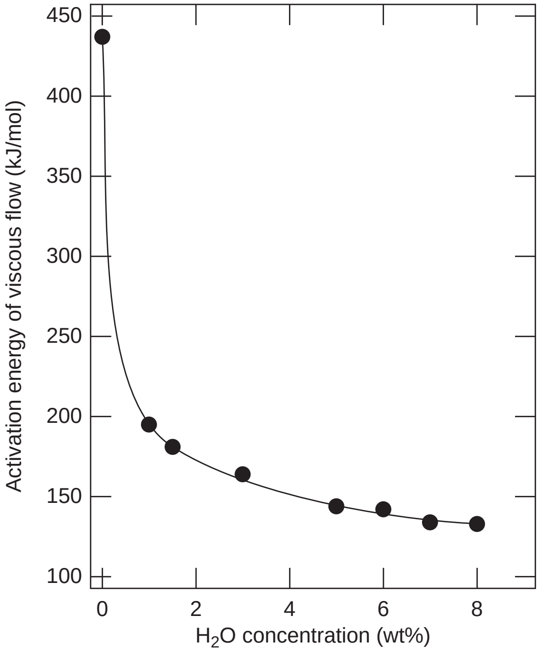

FIG. 14.27 Activation energy of viscous flow as a function of water concentration for $NaAlSi_3O_8$-$KAlSi_3O_8$-SiO_2 melt from Schulze et al. (1996).

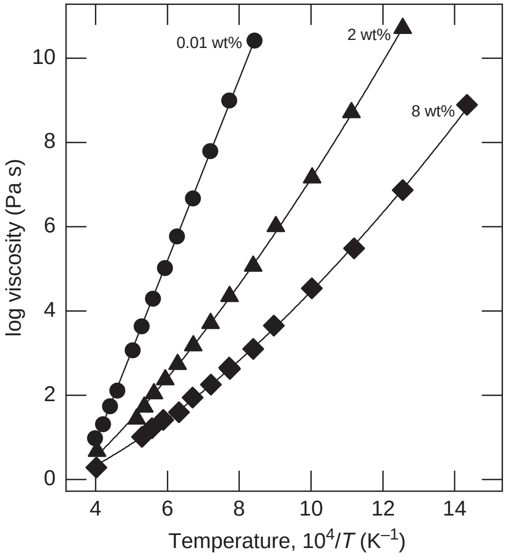

FIG. 14.28 Temperature dependence of melt viscosity of increasingly hydrous $NaAlSi_3O_8$-$KAlSi_3O_8$-SiO_2 melts for H_2O contents (in wt%) indicated on individual curves (data from Hess and Dingwell, 1996).

A number of experimental studies have addressed the effects of pressure on viscosity as a function of water content (Dingwell, 1987; Schulze et al., 1999; Liebske et al., 2003). For anhydrous melts, the viscosities of compositions with NBO/*T* near 1 and less exhibit a negative pressure dependence, whereas more depolymerized melts show a positive pressure dependence (Scarfe, 1987). However, upon solution of water the viscosity becomes less sensitive to pressure. Furthermore, the viscosity of only highly polymerized dry melts, such as those with NBO/*T*∼0, exhibit the same negative pressure dependence as hydrous liquids (Dingwell, 1987; Liebske et al., 2003). In contrast, the vicosity of andesite melts decreases with pressure under dry conditions but increases in the presence of 1 wt% H_2O or more (Liebske et al., 2003).

14.4.1.2 *Diffusivity*

The diffusivity of water in silicate melts depends on water content (Lapham et al., 1984; Chekhmir et al., 1988; Zhang et al., 1991a,b; Doremus, 1995; Behrens and Nowak, 1997). At contents lower than about 2 wt%, the diffusivity is an exponential function of water content and then becomes approximately linear as the H_2O concentration increases further (Fig. 14.29). These variations qualitatively agree with the observations of Chekhmir et al. (1988), Zhang et al. (1991a,b), and Behrens (2010) that the water profiles in silicate melts cannot be modeled with a single diffusion coefficient. In fact, in their study of water diffusion in andesitic melts at 1 GPa, Ni et al. (2009) concluded that the difffusion coefficient is about two orders of magnitude greater for molecular H_2O than for OH. However, the activation energy of diffusion of the two water species, at least at 1 GPa total pressure in the water concentration range of those experiments (3.8–5.8 wt% H_2O) is approximately the same (see also Fig. 14.30). How potentially multiple water species might diffuse at different rates in silicate glasses and melts is discussed further in Chapter 15, Section 15.4.1.

FIG. 14.29 Diffusion coefficient of total water, D_{water}, in $NaAlSi_3O_8$ melt as a function of total water content of melt (data from Behrens and Nowak, 1997).

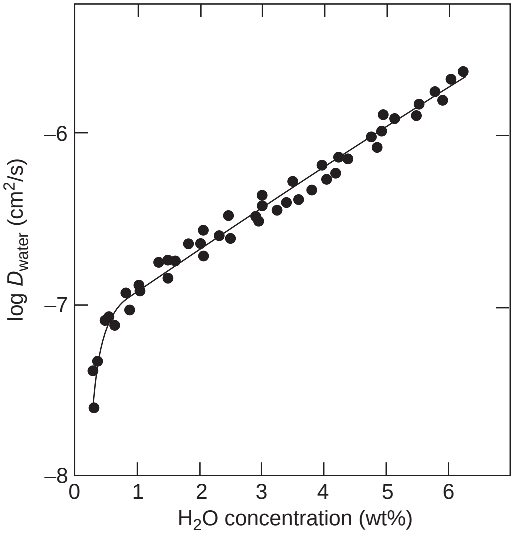

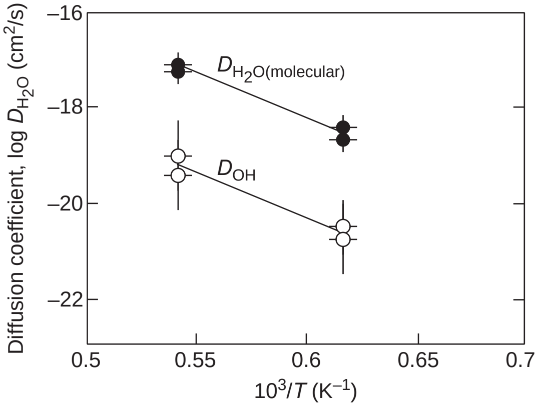

FIG. 14.30 Diffusion coefficient for molecular H_2O and OH-groups in andesitic melts at 1 GPa pressure (Ni et al., 2013).

Nowak and Behrens (1997) observed that the diffusivity of H_2O is approximately the same in pure and hydrous $NaAlSi_3O_8$, $(SiO_2)_{29}(KAlSi_3O_8)_{71}$, and $(SiO_2)_{28}(NaAlSi_3O_8)_{38}(KAlSi_3O_8)_{34}$ melts. They proposed that, at least in these highly polymerized aluminosilicates, the diffusivity of water is nearly independent of composition. Because of the good agreement of their data with results for rhyolitic compositions by Karsten et al. (1982), Shaw (1974), and Lapham et al. (1984), they further assumed that this statement could be generalized to all felsic melts, with the provision that predictions of D_{water} to within 200% of experimental data were indicating "good" agreement. At least for total water contents less than 1 wt%, however, D_{water} could be two orders of magnitude higher in a more mafic composition such as basalt (Zhang and Stolper, 1991; Nowak and Behrens, 1997). For tracer diffusion, there is also a negative correlation between D_{water} and the degree of polymerization. For example, D_{water} is about three orders of magnitude smaller for SiO_2 supercooled melt (nominal NBO/Si = 0) than for $Na_2Si_3O_7$ (nominal NBO/Si = 0.67) near 1300°C with ~0.02 wt% H_2O (Scholze and Mulfinger, 1959; Moulson and Roberts, 1961).

The water diffusivity in hydrous melts retains a systematic relationship with melt polymerization (Ni and Zhang, 2008; Okumura and Nakashima, 2004, 2006; see also Fig. 14.31). Moreover, not only does the water diffusivity decrease as the extent of silicate depolymerization increases, but the activation energy for water diffusion increases, which probably reflects the greater ease with which H_2O molecules migrate to the more open structure of highly polymerized silicate structures.

Dissolved H_2O also affects the diffusion coefficient of other melt components (Watson, 1979, Watson and Green, 1981; Harrison and Watson, 1983, Harrison et al., 1984; Baker, 1991; Mungall and Dingwell, 1994). The increase is larger for a network-former such as Si^{4+} than for a network-modifying cation like Na^+ (Fig. 14.32). The difference between D_{Si} and D_{Na} decreases with increasing water content, especially at low solubility. However, the former remains orders of magnitude smaller than the latter. Similar relationships between network-formers and network-modifiers have been reported for other cations (Baker, 1991; Acosta-Vigil et al., 2005; Indris et al., 2012).

FIG. 14.31 Diffusion coefficient of H_2O in rhyolite, andesite, and basalt melt with 1 wt% H_2O (rhyolite and andesite) and 0.2 wt% H_2O (basalt). Data from Okumura and Nakashima (2004, 2006).

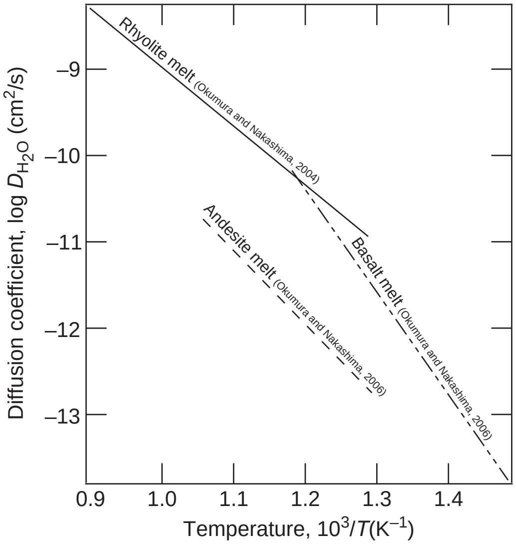

FIG. 14.32 Diffusion coefficient, *D*, of Si and Na in granitic melt as a function of water content at temperatures indicated (Watson, 1994).

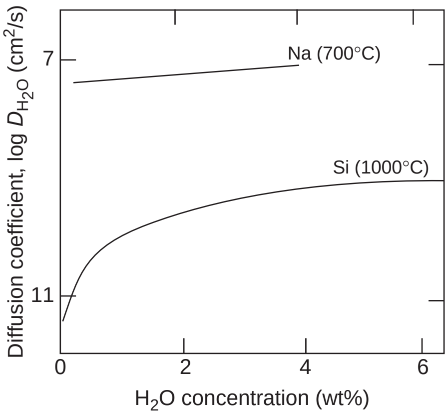

14.4.1.3 Conductivity

Cation diffusion is closely related to electrical conductivity (see Chapter 2, Section 2.6.1). Intriguing observations have been made in this respect by Takata et al. (1981, 1984), who reported that both sodium diffusivity and electrical conductivity in sodium trisilicate melts markedly depend on water content, with minimum values near 3–4 wt% water. These observations are analogous to those observed in the mixed alkali effect. Similarities and differences between the effects of water and alkali oxides on the volume and transport properties of melts have been discussed by Richet et al. (2000). A depressing effect of water on electrical conductivity has also been described for a variety of simple compositions (Satherley and Smedley, 1985; Ni et al., 2011).

14.4.2 Volume, Compressibility, and Expansion

14.4.2.1 Density and Volume

A complication to be mentioned from the outset is that, owing to the high pressure of their synthesis, hydrous glasses are permanently compacted with respect to samples synthesized at room pressure. The hydration pressure generally increases with the water content of samples. Hence, glasses from a given composition series are not strictly comparable when their configurations have been frozen in at different pressures. The effect is illustrated in Fig. 14.33 for a series of phonolite glasses. Because density is the simplest macroscopic measure of structure, this effect should be taken into account in structural studies. A potentially more problematic effect results from the fact that, on heating, a compacted sample will relax to its 1-bar volume, as already shown in Fig. 2.22 (Chapter 2) for hydrous phonolite glasses. Thermal expansion is made up of two different contributions: a relaxational and an isoconfigurational part. For the hydrous glass of Fig. 2.22, the former is approximately half the latter so that an unbiased thermal expansion coefficient can be determined only for samples that have previously been fully relaxed at room pressure (Bouhifd et al., 2001; see also Fig. 14.34). Such a volume relaxation begins more than 100 degrees below the standard glass transition temperature, i.e., its onset is at temperatures at which structural relaxation induced by temperature changes is practically nonexistent under similar heating rates.

As a light oxide, water is expected to lower the density of silicate glasses. A rather extensive set of density data exists for hydrous silicate glasses at room temperature to check this assumption. Interestingly, from the volume data for 40 series of hydrous glasses, these can be extrapolated linearly to the same partial molar volume of pure H_2O ($\overline{V}_{H_2O}$) of $12.0 \pm 0.5\,\mathrm{cm}^3/\mathrm{mol}$ (Richet et al., 2000; see Fig. 14.35). This value, which translates into a density near $1.5\,\mathrm{g/cm}^3$, is essentially the same as the molar volume of Ice VII (Hemley et al., 1987).

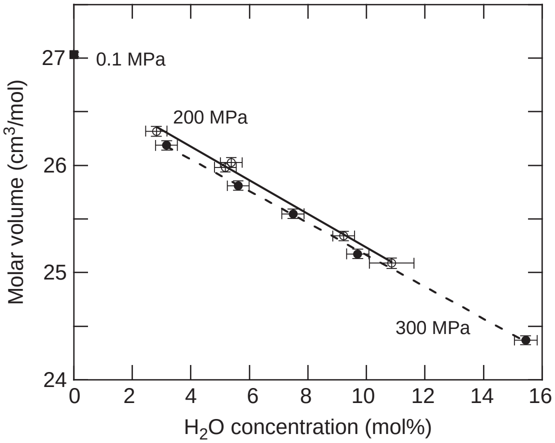

FIG. 14.33 Influence of the pressure of synthesis on the molar volume of hydrous phonolite glasses at room temperature and pressures indicated (open symbols, 200 Mpa; closed symbols, 300 MPa) The dry sample was prepared at room pressure (0.1 MPa), the hydrous glasses under the water pressure indicated. Data from Richet et al. (2000).

FIG. 14.34 Room temperature and pressure molar volume of hydrous glasses against water concentration. Data from Silver et al. (1990), Schulze et al., (1996), and Dingwell et al. (1996) for rhyolite and haplogranite glasses; from Richet et al. (1996) for andesite, and Richet et al. (2000) for basalt.

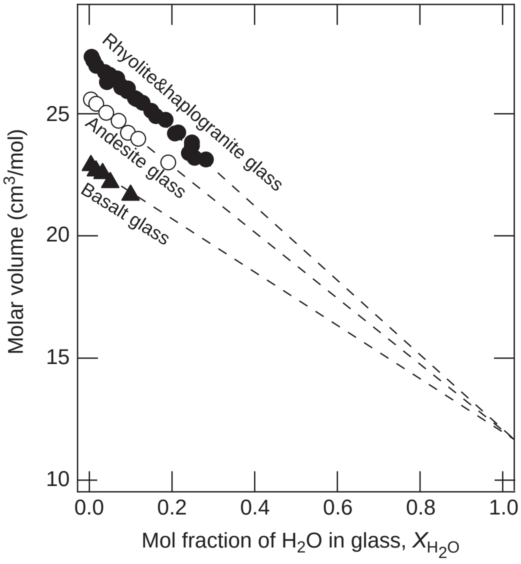

FIG. 14.35 Partial molar volume of H_2O in silicate melts as indicated on individual curves derived from H_2O solubility and calculated with Eq. (14.6). It is assumed in this calculation that the activity coefficient of dissolved H_2O is unity (Mysen, 2002).

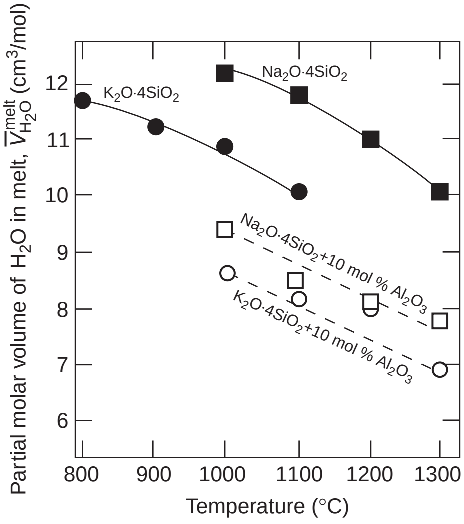

Another noteworthy feature is that $\overline{V}_{H_2O}$ does not depend on water speciation because it remains constant regardless of the relative abundances of hydroxyl ions and molecular water (Ochs and Lange, 1999; Richet et al., 2000; Bouhifd et al., 2015). However, for hydrous silicate melts at temperatures above the glass transition, this suggestion may not be accurate. This feature may be illustrated with the composition-dependent water solubility in melts. Given

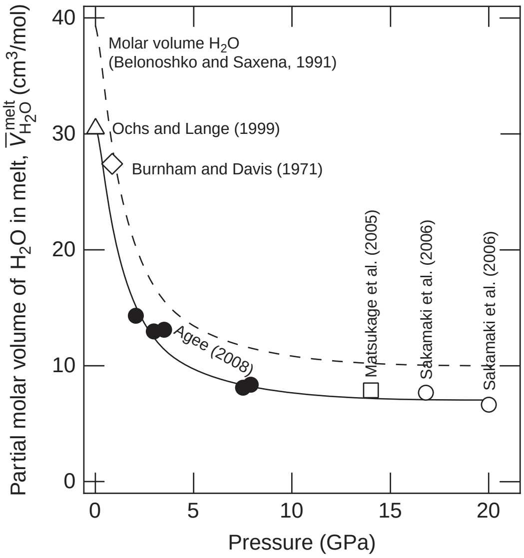

FIG. 14.36 Partial molar volume of H_2O in silicate melts, normalized to 1800°C, as a function of pressure and fitted to the function in Eq. (14.7). Ochs and Lange (1999), Burnham and Davis (1971), Agee (2008), Matsukage et al. (2005), and Sakamaki et al. (2006) were compiled by Agee (2008). The dashed line shows the compression curve of the molar volume of pure H_2O after Belonoshko and Saxena (1991).

that silicate-H_2O solutions are near ideal mixtures (Burnham, 1975; Clemens and Navrotsky, 1986; Richet et al., 2006), water solubility data for melts as a function of pressure can be used to extract partial molar volume from an expression such as:

$$\Delta G_T^{0.1\text{MPa}} + RT \ln \frac{\gamma_{H_2O}^{melt} \cdot X_{H_2O}^{melt}}{f_{H_2O}^{0}} + \int_{0.1\text{MPa}}^{P} \overline{V}_{H_2O}^{melt} \partial P = 0, \tag{14.6}$$

where $\Delta G_T^{0.1\text{MPa}}$ is free energy of solution of H_2O, $X_{H_2O}{}^{melt}$ and $\gamma_{H_2O}{}^{melt}$ are solubility and activity coefficient of H_2O in the melt, $f_{H_2O}{}^{0}$ is the fugacity of H_2O at conditions of experiment, P is pressure, T is temperature (Kelvin), and R is the gas constant.

The partial molar volume of H_2O in alkali tetrasilicate melts with and without Al^{3+}, linked to solubility via Eq. (14.6), depends on composition, both the ionic radius of the alkali metal and the Al_2O_3 content affecting the volume (Fig. 14.36). Moreover, the principal structural variable controlling the volume is the availability of proton sites in the structure, and this availability depends on melt composition (Le Losq et al., 2015).

14.4.2.2 Compressibility

We finally turn to compressibility, which is needed to determine high-pressure densities. In this instance, the difficulty is that the relevant properties, the adiabatic compressibility, β_S, or its reciprocal, the adiabatic bulk modulus, K_S, have been measured either by ultrasonic or Brillouin scattering methods under very short experimental timescales (see Chapter 3) (Whittington et al., 2012). It follows that measurements on fully relaxed liquids are possible only at very high temperatures where the viscosity is so low that it is impossible to keep any

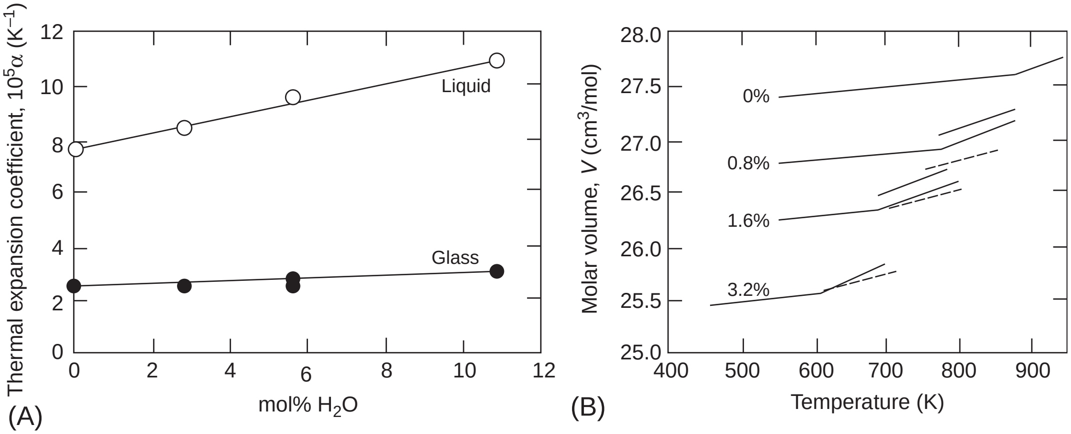

FIG. 14.37 (A) Thermal expansion coefficient of hydrous phonolite glass and supercooled liquid against water concentration. (B) Comparison between the measured molar volume of hydrous phonolite glasses and supercooled liquids with the model predictions of Ochs and Lange (1999), shown as dashed lines, for the wt% water indicated. Data from Bouhifd et al. (2001).

water dissolved in a melt at room pressure. Such measurements have not yet been performed on silicate melts at simultaneously high pressures and temperatures.

The only available information, thus, deals with hydrous glasses at room pressure. As expected, the less dense relaxed glasses are more compressible than the compacted samples (Fig. 14.37). The difference is slight, however, and in both cases a linear variation of the bulk modulus is observed with water content, indicating that water speciation does not influence the compressibility of hydrous glasses. For andesite glasses, this trend extrapolates to a value, $K_S = 18$ (3) GPa, which is close to the bulk modulus of ice VII, $K_S = 23.9$ (9) GPa (Richet and Polian, 1998). As the high compressibility of Ice VII primarily results from the existence of weak hydrogen bonds, this similarity suggests that hydrogen bonding plays an important role in water solubility, as confirmed by aforementioned first-principles calculations (Ottonello et al., 2014).

An alternative is measuring melt density at high temperature and pressure, which has been accomplished with a few melt compositions (Burnham and Davis, 1971; Matsukage et al., 2005; Sakamaki et al., 2006, 2009; Agee, 2008; Malfait et al., 2014). These compositions, which range from that of hydrous $NaAlSi_3O_8$ (Burnham and Davis, 1971) to basalt (Sakamaki et al., 2006) and komatiite melt composition (Agee, 2008), when normalized to a single temperature, fall on a single compression line (Fig. 14.38):

$$\overline{V}_{H_2O}^{melt} = 3.904 + \frac{49.219}{1.764 + P(\text{GPa})}(\text{Agee, 2008}), \tag{14.7}$$

Notably, the partial molar volume of H_2O in solution is comparatively insensitive to silicate melt composition. Moreover, the partial molar volume is always smaller than the molar volume of pure H_2O at the same temperature and pressure.

Finally, measurements on hydrous glasses at ambient temperature show that the partial molar bulk modulus of water in glass also is a strong function of silicate composition

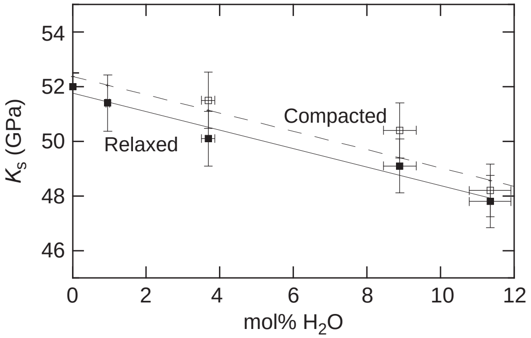

FIG. 14.38 Bulk modulus of hydrous andesite glasses against water concentration. The "compacted" data refer to glasses synthesized at 0.2 or 0.3 GPa, the "relaxed" data to samples annealed at room pressure (Richet and Polian, 1998).

(Whittington et al., 2012). The compressibility of glasses is purely vibrational in origin. As such, it depends less sensitively on structure than the configurational part of the compressibility of liquids, which can represent the major contribution to β_S (Askarpour et al., 1993). Hence, the compressibility of water in hydrous liquids should also be a strong function of silicate composition, with the consequence that early model values of partial molar volume of water (Ochs and Lange, 1999) should be used with some caution at high pressure. In any case, the compressibility data for hydrous glasses demonstrate that bonding between the silicate framework and water, either as hydroxyl ions or as molecular H_2O, varies widely.

References

Acosta-Vigil, A., London, D., Morgan, G.B., 2005. Contrasting interactions of sodium and potassium with H2O in haplogranitic liquids and glasses at 200 MPa from hydration-diffusion experiments. Contrib. Mineral. Petrol. 149 (3), 276–287.

Acocella, J., Tomazawa, M., Watson, B., 1984. The nature of dissolved water in sodium silicate glasses and its effect on various properties. J. Non-Cryst. Solids 65, 355–372.

Agee, C.B., 2008. Compressibility of water in magma and the prediction of density crossovers in mantle differentiation. Philos. T. Roy. Soc. A 366, 4239–4252.

Angell, C.A., 1991. Relaxation in liquids, polymers and plastic crystals—strong/fragile patterns and problems. J. Non-Cryst. Solids 131–133, 13–31.

Askarpour, V., Manghnani, M.H., Richet, P., 1993. Elastic properties of diopside, anorthite, and grossular glasses and liquids: a Brillouin scattering study up to 1400 K. J. Geophys. Res. 98, 17683–17689.

Baker, D.R., 1991. Interdiffusion of hydrous dacitic and rhyolitic melts and the efficacy of rhyolite contamination of dacitic enclaves. Contrib. Mineral. Petrol. 106, 462–473.

Baker, D.R., Freda, C., Brooker, R.A., Scarlato, P., 2005. Volatile diffusion in silicate melts and its effects on melt inclusions. Ann. Geophys. 48, 699–717.

Bassett, W.A., Wu, T.-C., Chou, I.-M., Haselton, T., Frantz, J.D., Mysen, B.O., Huang, W.-L., Sharma, S.K., Schiferl, D., 1996. The hydrothermal diamond anvil cell (DAC) and its applications. In: Dyar, M.D., McCammon, C.A., Schaefer, M. (Eds.), Mineral Spectroscopy: A Tribute to Roger G. Burns. The Geochemical Society, Houston, pp. 261–272.

Behrens, H., 1995. Determination of water solubilitites in high-viscosity melts—an experimental study on $NaAlSi_3O_8$ and $KAlSi_3O_8$ melts. Eur. J. Mineral. 7, 905–920.

Behrens, H., 2010. Ar, CO_2 and H_2O diffusion in silica glasses at 2 kbar pressure. Chem. Geol. 272, 40–48.

Behrens, H., Nowak, M., 1997. The mechanisms of water diffusion in polymerized silicate melts. Contrib. Mineral. Petrol. 126, 377–385.

Behrens, H., Meyer, M., Holtz, F., Benne, D., Nowak, M., 2001. The effect of alkali ionic radius, temperature, and pressure on the solubility of water in $MAlSi_3O_8$ melts (M = Li, Na, K, Rb). Chem. Geol. 174, 275–289.

Behrens, H., Misiti, V., Freda, C., Vetere, F., Botcharnikov, R.E., Scarlato, P., 2009. Solubility of H_2O and CO_2 in ultrapotassic melts at 1200 and 1250 degrees C and pressure from 50 to 500 MPa. Am. Mineral. 94, 105–120.

Belonoshko, A., Saxena, S.K., 1991. A molecular dynamics study of the pressure-volume-temperature properties of supercritical fluids. I. H_2O. Geochim. Cosmochim. Acta 55, 381–389.

Benne, D., Behrens, H., 2003. Water solubility in haplobasaltic melts. Eur. J. Mineral. 15, 803–814.

Bezmen, N.I., Zharikov, V.A., Epelbaum, M.B., Zavelsky, V.O., Dikov, Y.P., Suk, N.I., Koshemchuk, S.K., 1991. The system $NaAlSi_3O_8$-H_2O-H_2 (1200 degrees C, 2 kbar)—the solubility and interaction mechanism of fluid species with melt. Contrib. Mineral. Petrol. 109, 89–97.

Bezmen, N.I., Zavel'sky, V.O., Salova, T.P., 2011. Solubility of water-hydrogen fluid in haplogranite, albite, and sodium disilicate melts. Petrology 19, 183–197.

Boettcher, A.L., 1984. The system SiO_2-H_2O-CO_2: melting solubility mechanisms of carbon and liquid structure to high pressures. Am. Mineral. 69, 823–834.

Bouhifd, M.A., Whittington, A., Richet, P., 2001. Partial molar volume of water in phonolitic glasses and liquids. Contrib. Mineral. Petrol. 142, 235–243.

Bouhifd, M.A., Whittington, A., Roux, J., Richet, P., 2006. Effect of water on the heat capacity of polymerized aluminosilicate glasses and melts. Geochim. Cosmochim. Acta 70, 711–722.

Bouhifd, M.A., Whittington, A.G., Withers, A.C., Richet, P., 2013. Heat capacities of hydrous silicate glasses and liquids. Chem. Geol. 346, 125–134.

Bouhifd, M.A., Whittington, A.G., Richet, P., 2015. Densities and volumes of hydrous silicate melts: new measurements and predictions. Chem. Geol. 418, 40–50.

Bouyer, F., Geneste, G., Ispas, S., Kob, W., Ganster, P., 2010. Water solubility in calcium aluminosilicate glasses investigated by first principles techniques. J. Solid State Chem. 183, 2786–2796.

Bowen, N.L., 1948. The Granite Problem and the Method of Multiple Prejudices. Origin of Granite, Geol. Soc. Am. Memoir: Geological Society of America, pp. 79–90.

Boyd, F.R., England, J.L., Davis, B.C.T., 1964. Effect of pressure and polymorphism of enstatite, $MgSiO_3$. J. Geophys. Res. 69, 2101–2109.

Bureau, H., Keppler, H., 1999. Complete miscibility between silicate melts and hydrous fluids in the upper mantle; experimental evidence and geochemical implications. Earth Planet. Sci. Lett. 165, 187–196.

Burnham, C.W., 1975. Thermodynamics of melting in experimental silicate-volatile systems. Geochim. Cosmochim. Acta 39, 1077–1084.

Burnham, C.W., Davis, N.F., 1971. The role of H_2O in silicate melts. I. P-V-T relations in the system $NaAlSi_3O_8$-H_2O to 10 kilobars and 1000C. Am. J. Sci. 270, 54–79.

Burnham, C.W., Davis, N.F., 1974. The role of H_2O in silicate melts: II. Thermodynamic and phase relations in the system NaAl Si_3O_8-H_2O to 10 kilobars, 700C to 1100C. Am. J. Sci. 274, 902–940.

Chekhmir, A.S., Epel'baum, M.B., Simakin, A.G., 1988. Water transport in magmas. Geochem. Int. 26, 125–127.

Clemens, J.D., Navrotsky, A., 1986. Mixing properties of NaAlSi3O8 melt-H2O: new calorimetric data and some geological implications. J. Geol. 95, 173–186.

Coutures, J.-P., Péraudeau, G., 1981. Examen de la dissolution de l'eau dans les silicates liquides ($P_{H2O} \leq 1$ atm). Rev. Int. Hautes Temp. Réfract. 18, 321–346.

Di Genova, D., Romano, C., Giordano, D., Alletti, M., 2014. Heat capacity, configurational heat capacity and fragility of hydrous magmas. Geochim. Cosmochim. Acta 142, 314–333.

Dingwell, D., Romano, C., Hess, K.U., 1996. The effect of water on haplogranitic melt under P-T-X conditions relevant to silicic volcanism. Contrib. Mineral. Petrol. 124, 19–28.

Dingwell, D.B., 1987. Melt viscosities in the system $NaAlSi_3O_8$-H_2O-F_2O_{-1}. In: Mysen, B.O. (Ed.), Magmatic Processes: Physicochemical Principles. Geochemical Society of America, University Park, PA, pp. 423–432.

Dingwell, D.B., Holtz, F., Behrens, H., 1997. The solubility of H_2O in peralkaline and peraluminous granitic melts. Am. Mineral. 82, 434–437.

Doremus, R.H., 1995. Water diffusion in silica glass. J. Mater. Res. 10, 41–69.

Eggler, D.H., Burnham, C.W., 1984. Solution of H_2O in diopside melts: a thermodynamic model. Contrib. Miner. Perolt. 85, 58–66.

Friedman, I., Long, W., Smith, R.W., 1963. Viscosity and water content of rhyolitic glass. J. Geophys. Res. 68, 6523–6535.

Fujii, T., Kushiro, I., 1977. Density, viscosity and compressibility of basaltic liquid at high pressures. Carnegie Instn. Wash Year Book 76, 419–424.

Giordano, D., Dingwell, D.B., 2003. Viscosity of hydrous Etna basalt: implications for Plinian-style basaltic eruptions. Bull. Volcan. 65, 8–14.

Giordano, D., Romano, C., Dingwell, D.B., Poe, B., Behrens, H., 2004. The combined effects of water and fluorine on the viscosity of silicic magmas. Geochim. Cosmochim. Acta 68, 5159–5168.

Goranson, R.W., 1936. Silicate-water systems: the solubility of water in albite-melt. Trans. Am. Geophys. Union 17, 257–259.

Goranson, R.W., 1938. Silicate-water systems: phase equilibria in the $NaAlSi_3O_8$-H_2O and $KAlSi_3O_8$-H_2O systems at high temperatures and pressures. Am. J. Sci. 35A, 71–93.

Haar, L., Gallagher, J.S., Kell, G.S., 1984. Steam Tables. Thermodynamic and Transport Properties and Computer Programs for Vapor and Liquid States of Water in SI Units. Hemisphere Publishing Corporation, New York.

Harrison, T.M., Watson, E.B., 1983. The Behavior of Apatite during Crustal Anatexis. AGU Fall Meeting. Vol. 1983. American Geophysical Union, Washington, DC, p. 878.

Harrison, T.M., Watson, E.B., Davis, K.E., 1984. What can Accessory Minerals Tell us about Melting Events in the Lower Crust? AGU 1984 Spring Meeting. American Geophysical Union, Washington, DC, United States, p. 231.

Hemley, R.J., Jephcoat, A.P., Mao, H.K., Zha, C.S., Finger, L.W., Cox, D.E., 1987. Static compression of H_2O-ice to 128 GPa. Nature 330, 737–739.

Hess, K.-U. & Dingwell, D. B. (1996). Viscosities of hydrous leucogranitic melts: a non-Arrhenian model. Am. Mineral. 81, 1297–1300.

Hirose, K., 1997. Melting experiments on lherzolite KLB-1 under hydrous conditions and generation of high magnesian andesitic melts. Geology 25, 42–44.

Holtz, F., Dingwell, D.B., Behrens, H., 1993. Effects of F, B_2O_3, and P_2O_5 on the solubility of water in haplogranitic melts compared to natural silicate melts. Contrib. Mineral. Petrol. 113, 492–501.

Holtz, F., Behrens, H., Dingwell, D.B., Johannes, W., 1995. H_2O solubility in haplogranitic melts: composition, pressure, and temperature dependence. Am. Mineral. 80, 94–108.

Holtz, F., Roux, J., Behrens, H., Pichavant, M., 2000. Water solubility in silica and quartzofeldspathic melts. Am. Mineral. 85, 682–686.

Indris, S., Heitjans, P., Grey, C.P., 2012. Multinuclear NMR spectroscopic studies of structure and dynamics in hydrous $NaAlSi_3O_8$ and $Ca_{0.5}AlSi_3O_8$ glasses. J. Non-Cryst. Solids 358, 2862–2867.

Jackson, I., 1976. Melting of the silica isotypes SiO_2, BeF_2 and GeO_2 at elevated pressures. Phys. Earth Planet. Int. 13, 218–231.

Jewell, J.M., Shelby, J.E., 1988. Effect of water content and alumina additions on the transformation range properties of Na_2O-$3SiO_2$ glass. J. Non-Cryst. Solids 102, 24–29.

Jewell, J.M., Shaw, C.M., Shelby, J.E., 1993. Effect of water content on aluminosilicate glasses and the relation to strong/fragile liquid theory. J. Non-Cryst. Solids 152, 32–41.

Karki, B.B., Bhattarai, D., Mookherjee, M., Stixrude, L., 2010. Visualization-based analysis of structural and dynamical properties of simulated hydrous silicate melt. Phys. Chem. Mineral. 37, 103–117.

Karsten, J.L., Holloway, J.R., Delaney, J.R., 1982. Ion microprobe studies of water in silicate melts: temperature-dependent water diffusion in obsidian. Earth Planet. Sci. Lett. 59, 420–428.

Kennedy, G.C., Wasserburgh, G.J., Heard, H.C., Newton, R.C., 1962. The upper three-phase region in the system SiO_2-H_2O. Am. J. Sci. 260, 501–521.

Kirschen, M., Pichavant, M., 2001. A thermodynamic model for hydrous silicate melts in the system $NaAlSi_3O_8$-$KAlSi_3O_8$-Si_4O_8-H_2O. Chem. Geol. 174, 103–114.

Knoche, R., Dingwell, D.B., Webb, S.L., 1995. Leucogranitic and pegmatitic melt densities: partial molar volumes for SiO_2, Al_2O_3, Na_2O, K_2O, Rb_2O, Cs_2O, Li_2O, BaO, SrO, CaO, MgO, TiO_2, B_2O_3, P_2O_5, F_2O_{-1}, Ta_2O_5, Nb_2O_5 and WO_3. Geochim. Cosmochim. Acta 59, 4645–4652.

Kreisberg, V.A., 2015. Diffusion of water and carbon dioxide in some multicomponent silicate glasses. Glas. Phys. Chem. 41, 59–63.

Kurkjian, C.R., Russell, L.E., 1958. Solubility of water in molten alkali silicates. J. Soc. Glass. tech. 42, 130T–144T.

Kushiro, I., 1969. The System Forsterite-Diopside-Silica With and Without Water at High Pressures: The Schairer Volume. Kline Geology Laboratory, Yale University, New Haven, CT, pp. 269–294.

Kushiro, I., 1972. Effect of water on the composition of magmas formed at high pressures. J. Petrol. 13, 311–334.

Kushiro, I., 1974. Melting of hydrous upper mantle and possible generation of andesitic magma: an approach from synthetic systems. Earth Planet. Sci. Lett. 22, 294–299.

Kushiro, I., 1978. Density and viscosity of hydrous calc-alkalic andesite magma at high pressure. Carnegie Inst. Washington Year Book 77, 675–678.

Kushiro, I., Syono, Y., Akimoto, S.I., 1968. Melting of a peridotite nodule at high pressures and high water pressures. J. Geophys. Res. 73, 6023–6029.

Kushiro, I., Yoder, H.S., Mysen, B.O., 1976. Viscosities of basalt and andesite melts at high pressures. J. Geophys. Res. 81, 6351–6356.

Lapham, K.E., Holloway, J.R., Delaney, J.R., 1984. Diffusion of H_2O and D_2O in obsidian at elevated temperatures and pressures. J. Non-Cryst. Solids 67, 179–191.

Le Losq, C., Cody, C.D., Mysen, B.O., 2015. Alkali influence on the water speciation and the environment of protons in silicate glasses revealed by ^{1}H MAS NMR spectroscopy. Am. Mineral. 100, 466–482.

Lejeune, A.M., Holtz, F., Roux, J., Richet, P., 1994. Rheology of a hydrous andesite: an experimental study at high viscosities. Eos 74, 724.

Leonteva, A.A., 1940. Measurements of the viscosity of obsidian and of hydrated glasses. Acad. Sci USSR Ser Geol. 44–54.

Liebske, C., Behrens, H., Holtz, F., Lange, R.A., 2003. The effect of pressure and composition on the viscosity of andesitic melts. Geochim. Cosmochim. Acta 67, 473–486.

Luth, R.W., Boettcher, A.L., 1986. Hydrogen and the melting of silicates. Am. Miner. 71, 264–276.

Luth, W.C., Jahns, R.H., Tuttle, O.F., 1964. The granite system at pressures of 4 to 10 kilobars. J. Geophys. Res. 69, 759–773.

Malfait, W.J., Seifert, R., Petitgirard, S., Mezouar, M., Sanchez-Valle, C., 2014. The density of andesitic melts and the compressibility of dissolved water in silicate melts at crustal and upper mantle conditions. Earth Planet. Sci. Lett. 393, 31–38.

Matsukage, K.N., Jing, Z., Karato, S., 2005. Density of hydrous silicate melt at the conditions of Earth's deep upper mantle. Nature 438, 488–491.

McGinnis, P.B., Shelby, J.E., 1995. Effect of hydroxyl content on phase separation in sodium silicate glasses. Phys. Chem. Glasses 36, 44–49.

McMillan, P.F., Holloway, J.R., 1987. Water solubility in aluminosilicate melts. Contr. Mineral. Petrol. 97, 320–332.

Medard, E., Grove, T.L., 2008. The effect of H_2O on the olivine liquidus of basaltic melts: experiments and thermodynamic models. Contrib. Mineral. Petrol. 155, 417–432.

Métrich, N., Bertagnini, A., Landi, P., Rosi, M., 2001. Crystallization driven by decompresion and water loss at Stromboli volcano (Aeolian islands, Italy). J. Petrol. 42, 1471–1490.

Mibe, K., Kanzaki, M., Kawamoto, T., Matsukage, K.N., Fei, Y., Ono, S., 2004. Determination of the second critical end point in silicate-H_2O systems using high-pressure and high-temperature X-ray radiography. Geochim. Cosmochim. Acta 68, 5189–5195.

Mibe, K., Kanzaki, M., Kawamoto, T., Matsukage, K.N., Fei, Y., Ono, S., 2007. Second critical endpoint in the peridotite-H_2O system. J. Geophys. Res.-Solid Earth. 112. https://dx.doi.org/10.1029/2005jb004125.

Mookherjee, M., Stixrude, L., Karki, B., 2008. Hydrous silicate melt at high pressure. Nature 452, 983–986.

Moulson, A.J., Roberts, J.P., 1961. Water in silica glass. Trans. Faraday Soc. 57, 1208–1216.

Mungall, J.E., Dingwell, D.B., 1994. Einflusse von temperature, Druck und Wassergehalt aud die diffusion von AktinideTracern in Schmelzen haplogranitischer Zussamensetzug. Annu. Rep. Bayreisches Forschungsinstitut fur Exp. Geochem. Geophys. Universitat Beyreuth 91–92.

Mysen, B., 2002. Water in peralkaline aluminosilicate melts to 2 GPa and 1400 degrees C. Geochim. Cosmochim. Acta 66, 2915–2928.

Mysen, B., 2013. Effects of fluid and melt density and structure on high-pressure and high-temperature experimental studies of hydrogen isotope partitioning between coexisting melt and aqueous fluid. Am. Mineral. 98, 1754–1764.

Mysen, B.O., 1976. The role of volatiles in silicate melts: solubility of carbon dioxide and water in feldspar, pyroxene, feldspathoid melts to 30 kb and 1625 degrees C. Am. J. Sci. 276, 969–996.

Mysen, B.O., Acton, M., 1999. Water in H_2O-saturated magma-fluid systems: solubility behavior in K_2O-Al_2O_3-SiO_2-H_2O to 2.0 GPa and 1300 degrees C. Geochim. Cosmochim. Acta 63, 3799–3815.

Mysen, B.O., Boettcher, A.L., 1975. Melting of a hydrous mantle. II. Geochemistry of crystals and liquids formed by anatexis of mantle peridotite at high pressures and high temperatures as a function of controlled activities of water, hydrogen and carbon dioxide. J. Petrol. 16, 549–590.

Mysen, B.O., Cody, G.D., 2004. Solubility and solution mechanism of H_2O in alkali silicate melts and glasses at high pressure and temperature. Geochim. Cosmochim. Acta 68, 5113–5126.

Mysen, B.O., Wheeler, K., 2000. Solubility behavior of water in haploandesitic melts at high pressure and high temperature. Am. Mineral. 85, 1128–1142.

Mysen, B.O., Kushiro, I., Nicholls, I.A., Ringwood, A.E., 1974. A possible mantle origin for andesitic magmas: discussion of a paper by Nicholls and Ringwood. Earth Planet. Sci. Lett. 21, 221–230.

Ni, H., Zhang, Y., 2008. H_2O diffusion models in rhyolitic melt with new high pressure data. Chem. Geol. 250, 68–78.

Ni, H., Liu, Y., Wang, L., Zhang, Y., 2009. Water speciation and diffusion in haploandesitic melts at 743-873 K and 100 MPa. Geochim. Cosmochim. Acta 73, 3630–3641.

Ni, H., Keppler, H., Behrens, H., 2011. Electrical conductivity of hydrous basaltic melts: implications for partial melting in the upper mantle. Contrib. Mineral. Petrol. 162, 637–650.

Ni, H., Xu, Z., Zhang, Y., 2013. Hydroxyl and molecular H_2O diffusivity in a haploandesitic melt. Geochim. Cosmochim. Acta 103, 36–48.

Nowak, M., Behrens, H., 1995. The speciation of water in haplogranitic glasses and melts determined by in-situ near infrared spectroscopy. Geochim. Cosmochim. Acta 59, 3445–3450.

Nowak, M., Behrens, H., 1997. An experimental investigation on diffusion of water in haplogranitic melts. Contrib. Mineral. Petrol. 126, 365–376.

Ochs, F.A., Lange, R.A., 1999. The density of hydrous magmatic liquids. Science 283, 1314–1317.

Okumura, S., Nakashima, S., 2004. Water diffusivity in rhyolitic glasses as determined by in situ IR spectroscopy. Phys. Chem. Minerals 31, 183–189.

Okumura, S., Nakashima, S., 2006. Water diffusion in basaltic to dacitic glasses. Chem. Geol. 227, 70–82.

Ottonello, G., Richet, P., Vetuschi Zuccolini, M., 2015. The wet solidus of silica: predictions from the scaled particle theory and polarized continuum model. J. Chem. Phys.. 142054503.

Ottonello, G., Richet, P., Papale, P., 2018. Bulk solubility and speciation of H_2O in silicate melts. Chem. Geol. 479, 176–187.

Paillat, O., Elphick, E.C., Brown, W.L., 1992. The solubility behavior of H_2O in $NaAlSi_3O_8$ melts: a re-examination of Ab-H_2O phase relationships and critical behavior at high pressure. Contrib. Mineral. Petrol. 112, 490–500.

Papale, P., 1997. Modeling of the solubility of a one-component H_2O or CO_2 fluid in silicate liquids. Contrib. Mineral. Petrol. 126, 237–251.

Papale, P., Moretti, R., Barbato, D., 2006. The compositional dependence of the saturation surface of $H_2O + CO_2$ fluids in silicate melts. Chem. Geol. 229, 78–95.

Persikov, E.S., Zharikov, V.A., Bukhtiyarov, P.G., Pol'skoy, S.F., 1990. The effect of volatiles on the properties of magmatic melts. Eur. J. Mineral. 2, 621–642.

Poe, B.T., Romano, C., Liebske, C., Rubie, D.C., Terasaki, H., Suzuki, A., Funakoshi, K., 2006. High-temperature viscosity measurements of hydrous albite liquid using in-situ falling-sphere viscometry at 2.5 GPa. Chem. Geol. 229, 2–9.

Presnall, D.C., Gasparik, T., 1990. Melting of enstatite ($MgSiO_3$) from 10 to 16.5 GPa, and the forsterite (Mg_2SiO_4)—majorite ($MgSiO_3$) eutectic at 16.5 GPa: implications for the origin of the mantle. J. Geophys. Res. 95, 15771–15778.

Richet, P., 1984. Viscosity and configurational entropy of silicate melts. Geochim. Cosmochim. Acta 48, 471–483.

Richet, P., 2005. Water: an elusive component of silicate melts. Phys. Chem. Glasses 46, 333–339.

Richet, P., Neuville, D.R., Holtz, F., 1997. Viscosity of water-bearing melts. Terra Nova 9, 480. Abstracts Suppl. 1.

Richet, P., Polian, A., 1998. Water as a dense icelike component in silicate glasses. Science 281, 396–398.

Richet, P., Lejeune, A.-M., Holtz, F., Roux, J., 1996. Water and the viscosity of andesite melts. Chem. Geol. 128, 185–197.

Richet, P., Whittington, A., Holtz, F., Behrens, H., Ohlhorst, S., Wilke, M., 2000. Water and the density of silicate glasses. Contrib. Mineral. Petrol. 138, 337–347.

Richet, P., Hovis, G., Whittington, A., Roux, J., 2004. Energetics of water dissolution in trachyte glasses and liquids. Geochim. Cosmochim. Acta 68, 5151–5158.

Richet, P., Hovis, G., Whittington, A., 2006. Water and magmas: thermal effects of exsolution. Earth Planet. Sci. Lett. 241, 972–977.

Robert, G., Whittington, A.G., Stechem, A., Behrens, H., 2014. Heat capacity of hydrous basaltic glasses and liquids. J. Non-Cryst. Solids 390, 19–30.

Robert, G., Knipping, J.L., Scherbarth, S., Robertson, T.E., Stechern, A., Behrens, H., Whittington, A.G., 2015. Heat capacity and viscosity of basaltic melts with H_2O +/- F +/- CO_2. Chem. Geol. 418, 51–65.

Romano, C., Dingwell, D.B., Behrens, H., Dolfi, D., 1996. Compositional dependence of H_2O solubility along the joins $NaAlSi_3O_8$-$KAlSi_3O_8$, $NaAlSi_3O_8$-$LiAlSi_3O_8$, and $KAlSi_3O_8$-$LiAlS_{i3}O_8$. Am. Mineral. 81, 452–461.

Romano, C., Giordano, D., Papale, P., Mincione, V., Dingwell, D.B., Rosi, M., 2003. The dry and hydrous viscosities of alkaline melts from Vesuvius and Phlegrean fields. Chem. Geol. 202, 23–38.

Sabatier, G., 1956. Influence de la teneur en eau sur la viscosité d'une rétinite, verre ayant la composition chimique d'un granite. C.R. Acad. Sci 242, 1340–1342.

Sahagian, D.L., Proussevitch, A.A., 1996. Thermal effects of magma degassing. J. Volc. Geotherm. Res. 74, 19–38.

Sakamaki, T., Suzuki, A., Ohtani, E., 2006. Stability of hydrous melt at the base of the Earth's upper mantle. Nature 439, 192–194.

Sakamaki, T., Ohtani, E., Urakawa, S., Suzuki, A., Katayama, Y., 2009. Measurement of hydrous peridotite magma density at high pressure using the X-ray absorption method. Earth Planet. Sci. Lett. 287, 293–297.

Satherley, K., Smedley, S.I., 1985. The electrical conductivity of some hydrous and anhydrous molten silicates as a function of temperature and pressure. Geochim. Cosmochim. Acta 49, 769–777.

Saucier, P.H., 1952. Quelques expériences sur la viscosité à haute température de verres ayant la composition d'un granite. Influence de la vapeur d'eau sous pression. Bull. Soc. Fr. Mineral. Crystallogr. 75, 1–45 and 245–296.

Scarfe, C.M., Virgo, D., 1987. Pressure-dependence of the viscosity of silicate melts. In: Mysen, B.O., Mysen, B.O. (Eds.), Magmatic Processes: Physicochemical Principles. Geochemical Society, University Park, PA.

Schmidt, B.C., Holtz, F., Pichavant, M., 1999. Water solubility in haplogranitic melts coexisting with H_2O-H_2 fluids. Contrib. Mineral. Petrol. 136, 213–224.

Scholze, H., Mulfinger, H.O., 1959. Einbau des Wqssers in Glaser. V. Die diffusion des Wassers in Glasern bei Hohen temperatured. Glasstechn. Ber. 32, 381–385.

Schulze, F., Behrens, H., Holtz, F., Roux, J., Johannes, W., 1996. The influence of H_2O on the viscosity of a haplogranitic melt. Am. Mineral. 81, 1155–1165.

Schulze, F., Behrens, H., Hurkuck, W., 1999. Determination of the influence of pressure and dissolved water on the viscosity of highly viscous melts: application of a new parallel-plate viscometer. Am. Mineral. 84, 1512–1520.

Shackleford, J.F., Masaryk, J.S., 1976. The thermodynamics of water and hydrogen solubility in fused silica. J. Non-Cryst. Solids 21, 55–64.

Shaw, H.R., 1963. Obsidian-H_2O viscosities at 1000 and 2000 bars in the temperature range 700° and 900°C. J. Geophys. Res. 68, 6337–6343.

Shaw, H.R., 1974. Diffusion of H_2O in granitic liquids. I. Experimental data. In: Hoffman, A.W. (Ed.), Geochemical Transport and Kinetics. Carnegie Instn. Washington, Washington, DC, pp. 139–170.

Shen, A.H., Keppler, H., 1997. Direct observation of complete miscibility the albite-H_2O system. Nature 385, 710–712.

Shishkina, T.A., Botcharnikov, R.E., Holtz, F., Almeev, R.R., Portnyagin, M.V., 2010. Solubility of H_2O- and CO_2-bearing fluids in tholeiitic basalts at pressures up to 500 MPa. Chem. Geol. 277, 115–125.

Silver, L., Stolper, E., 1989. Water in albitic glasses. J. Petrol. 30, 667–710.

Silver, L., Ihinger, P.D., Stolper, E., 1990. The influence of bulk composition on the speciation of water in silicate glasses. Contrib. Mineral. Petrol. 104, 142–162.

Sisson, T.W., Grove, T.L., 1993. Temperature and H_2O contents of low-MgO high alumina basalts. Contrib. Mineral. Petrol. 113, 167–184.

Sorapure, R., Hamilton, D.L., 1984. The solubility of water in melts of albite composition with varying additions of fluorine. In: Henderson, C.M.B. (Ed.), NERC Progress Rept. National Research Council, UK.

Sowerby, J.R., Keppler, H., 2002. The effect of fluorine, boron and excess sodium on the critical curve in the albite- H_2O system. Contrib. Mineral. Petrol. 143, 32–37.

Spallanzani, L., 1792–1797. Viaggi alle Due Sicilie e in alcune parti dell' Appennino, transl. as Travels in the Two Sicilies and Some Parts of the Appenines, J. Robinson, London. Stamperia di B. Comini, Pavia.

Stalder, R., Ulmer, P., Thompson, A.B., Guenther, D., 2001. High pressure fluids in the system MgO-SiO_2-H_2O under upper mantle conditions. Contrib. Mineral. Petrol. 140, 607–618.

Stern, C.R., Huang, W.-L., Wyllie, P.J., 1975. Basalt-andesite-rhyolite- H_2O: crystallization intervals with excess H_2O and H_2O-undersaturated liquidus surfaces to 35 kilobars, with implications for magma genesis. Earth Planet. Sci. Lett. 28, 189–196.

Stevenson, R.J., Bagdassarov, N.S., Dingwell, D.B., Romano, C., 1998. The influence of trace amounts of water on the viscosity of rhyolites. Bull. Volcanol. 60, 89–97.

Stolper, E.M., 1982. The speciation of water in silicate melts. Geochim. Cosmochim. Acta 46, 2609–2620.

Takata, M., Acocella, J., Tomozawa, M., Watson, E.B., 1981. Effect of water content on the electrical conductivity of $Na_2O{\bullet}3SiO_2$ glass. J. Am. Ceram. Soc. 64, 719–724.

Takata, M., Molinelli, J.E., Tomozawa, M., Watson, E.B., 1984. Dielectric characteristics of $Na_2O.3SiO_2$ glasses with high water contents. J. Am. Ceram. Soc. 67, 106–109.

Tamic, N., Behrens, H., Holtz, F., 2001. The solubility of H_2O and CO_2 in rhyolitic melts in equilibrium with a mixed CO_2-H_2O fluid phase. Chem. Geol. 174, 333–347.

Till, C.B., Grove, T.L., Withers, A.C., 2012. The beginnings of hydrous mantle wedge melting. Contrib. Mineral. Petrol. 163, 669–688.

Tomlinson, J.W., 1956. A note on the solubility of water in molten sodium silicate. J. Soc. Glass Techn. 4, 25T–31T.

Tuttle, O.F., Bowen, N.L., 1958. Origin of granite in light of experimental studies in the system $NaAlSi_3O_8$-$KAlSi_3O_8$-SiO_2-H_2O. Geol. Soc. Am. Mem. 74, 1–153.

Uys, J.M., King, T.B., 1963. The effect of basicity on the solubility of water in silicate melts. Trans. AIME 227, 492–500.

Watson, E.B., 1979. Diffusion of Cesium ions in H_2O-saturated granitic melt. Science 205, 1259–1260.

Watson, E.B., 1994. Diffusion in volatile-bearing magmas. In: Carroll, M.R., Holloway, J.R. (Eds.), Volatiles in Magmas. Washington, DC, Mineralogical Society of America, pp. 371–411.

Watson, E.B., Green, T.H., 1981. Apatite/liquid partition coefficients for the rare earth elements and strontium. Earth Planet. Sci. Lett. 56, 405–421.

Webster, J.D., Kinzler, R.J., Mathez, E.A., 1999. Chloride and water solubility in basalt and andesite melts and implications for magma degassing. Geochim. Cosmochim. Acta 63, 729–738.

Whittington, A., Richet, P., Holtz, F., 2000. Water and the viscosity of depolymerized aluminosilicate melts. Geochim. Cosmochim. Acta 64, 3725–3736.

Whittington, A., Richet, P., Behrens, H., Holtz, F., Scaillet, B., 2005. The viscosity of hydrous silicic melts: comparison between real and model compositions. Philos. Trans. Roy. Soc. Edinb. 95, 59–72.

Whittington, A.C., Richet, P., Polian, A., 2012. Water and the compressibility of silicate glasses: a Brillouin spectroscopic study. Am. Mineral. 97, 455–467.

Whittington, A.G., Richet, P., Linard, Y., Holtz, F.O., 2001. The viscosity of hydrous phonolites and trachytes. Chem. Geol. 174, 209–223.

Whittington, A.G., Bouhifd, M.A., Richet, P., 2009. The viscosity of hydrous $NaAlSi_3O_8$ and granitic melts: configurational entropy models. Am. Mineral. 94, 1–16.

Yoder, H.S., Stewart, D.B., Smith, J.R., 1957. Ternary feldspars. Carnegie Instn. Washington Year Book 56, 206–214.

Zhang, C., Duan, Z., Li, M., 2010. Interstitial voids in silica melts and implication for argon solubility under high pressures. Geochim. Cosmochim. Acta 74, 4140–4149.

Zhang, Y., Stolper, E.M., 1991. Water diffusion in a basaltic melt. Nature 351, 306–309.

Zhang, Y., Stolper, E.M., Wasserburg, G.J., 1991a. Diffusion of water in rhyolitic glasses. Geochim. Cosmochim. Acta 55, 441–456.

Zhang, Y.X., 1999. H_2O in rhyolitic glasses and melts: measurements, speciation, solubility, and diffusion. Rev. Geophys. 37, 493–516.

Zhang, Y.X., Behrens, H., 2000. H_2O diffusion in rhyolitic melts and glasses. Chem. Geol. 169, 243–262.

Zhang, Y.X., Stolper, E.M., Wasserburg, G.J., 1991b. Diffusion of a multispecies component and its role in oxygen and water transport in silicates. Earth Planet. Sci. Lett. 103, 228–240.

Zhang, Y.X., Xu, Z.J., Behrens, H., 2000. Hydrous species geospeedometer in rhyolite: improved calibration and application. Geochim. Cosmochim. Acta 64, 3347–3355.

Zotov, N., Keppler, H., 2000. In-situ Raman spectra of dissolved silica species in aqueous fluid to 900°C and 14 kbar. Am. Mineral. 85, 600–603.

CHAPTER

15

Water Solution Mechanisms and Structure

OUTLINE

15.1 INTRODUCTORY COMMENTS

The pronounced effects of dissolved H_2O on chemical and physical properties of silicate glasses and melts (Chapter 14) lead to the suggestion that H_2O is an efficient depolymerizing agent of silicate melt and glass structure. The structural response commonly proposed is formation of OH-groups through cleavage of bridging oxygen bonds. However, OH-groups can also form bonding with network-modifying cations such as alkalis and alkaline earths. These interactions depend on bulk silicate compositions, water concentration, temperature, and pressure. In this chapter, we discuss these solution mechanisms.

Silicate Glasses and Melts
https://doi.org/10.1016/B978-0-444-63708-6.00015-6

15.2 WATER SPECIATION

The extent of depolymerization of silicate structure varies with water concentration. In most silicate melts H^+ bonds with the nonbridging oxygen to form Si—OH functional groups, perhaps analogous to Si—ONa groups, as well as Al—OH and alkali and alkaline earth-OH (Kummerlen et al., 1992; Zotov and Keppler, 1998; Zavelsky and Salova, 2002; Cody et al., 2005). Water is, however, a less efficient depolymerization agent than alkali oxides (Zotov and Keppler, 1998; Mysen, 2007). That and the distinctly nonlinear evolution NBO/Si of a melt with increasing water content (Fig. 15.1) can be related to the existence of several types of water species.

The OH-groups, both in hydrous SiO_2 and in chemically more complex melts and glasses, have been well documented by a variety of spectroscopic and simulation methods (Moulson and Roberts, 1961; Ni et al., 2009; Bouyer et al., 2010). For example, infrared spectra of hydrous silicate glasses, originally reported more than 50 years ago, showed evidence for water solution to form OH-groups and that these groups seemed to coexist with molecular water (Scholze, 1960). This structural concept, schematically illustrated in Fig. 15.2 with Si^{4+} and Al^{3+} as tetrahedrally coordinated cations, subsequently was supported by a variety of experimental and computational studies with various silicate compositions (Hodges, 1974;

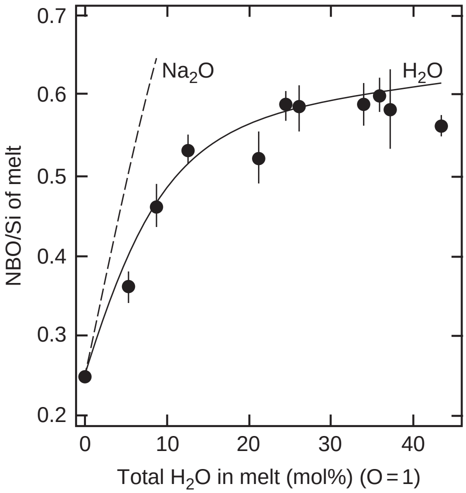

FIG. 15.1 Effect of dissolved water on the extent of depolymerization, NBO/Si of Na-silicate melt ($Na_2O{\cdot}8SiO_2$) from Mysen and Cody (2005). Also shown, as dashed line, is the NBO/Si evolution of the same silicate composition melt with equivalent increase of Na_2O content (data from Maekawa et al., 1991). Note how the NBO/Si of the melt increases much more rapidly with increasing Na_2O content than with H_2O and that the difference between the two trends increases with increasing H_2O concentration. In this diagram, the mol% H_2O in the melt was calculated on the basis of 1 oxygen.

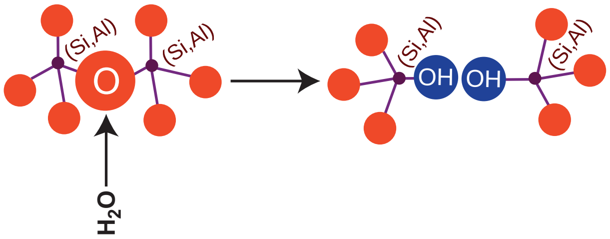

FIG. 15.2 Schematic illustration how H_2O cleaves oxygen bridges connecting adjacent alumnosilicate tetrahedra to form two separate tetrahedra and thus create depolymerized aluminosilicate structure (Eqs. 15.1 and 15.5).

Stolper, 1982; Eckert et al., 1988; Kubicki et al., 1993; Scaller and Sebald, 1995; Cody et al., 2005; Behrens and Yamashita, 2008; Xue and Kanzaki, 2008; Mookherjee et al., 2008; Simakin et al., 2010; Wang et al., 2015).

In its simplest form, a solution mechanism of water in silicate melts may be described as (Stolper, 1982):

$$H_2O\,(\text{molecular}) + O\,(\text{melt}) \Leftrightarrow 2OH\,(\text{melt}), \tag{15.1}$$

with the equilibrium constant:

$$K_{15.1} = [a_{OH}(\text{melt})]^2 / a_{H2O}(\text{molecular})] \bullet a_O(\text{melt}), \tag{15.2}$$

where a_{OH}(melt), etc., is the activity of the species in the subscript. In most treatments of this equilibrium, the activities are replaced with mol fractions. Justification of such an assumption can be found in relatively small values of heat mixing of silicate glass-H_2O solutions (Clemens and Navrotsky, 1987; Richet et al., 2004; see also Chapter 14) and agreement between calculated and experimentally observed liquidus phase relations in calculations where aluminosilicate-H_2O melts were assumed to be ideal solutions (Wen and Nekvasil, 1994).

15.2.1 Composition, Temperature, and Pressure

The water solution model originally proposed by Stolper (1982) (see Eq. 15.1) subsequently has been examined as a function of silicate water concentration, bulk composition, temperature, and pressure. The influence of silicate composition would be reflected in variations in oxygen activity, a_O(melt), in Eq. (15.2). The concentration of water as OH-groups [X_{OH}(melt)] and as molecular H_2O [X_{H_2O}(molecular)] in melts evolves as a function of total water concentration (Fig. 15.3). We note that the OH-groups in this case are only those that form bonding with tetrahedrally coordinated cations such as Si^{4+} and Al^{3+}. It does not, therefore, consider OH-groups that form bonding with network-modifying cations. This definitely takes place (Xue and Kanzaki, 2004; Cody et al., 2005), but the extent to which this occurs is uncertain. That notwithstanding, it should be kept in mind that a diagram such as that in Fig. 15.3 will need significant revision when M—OH bonding is incorporated into the structural model (Ackerson et al., 2017).

The trends of (Si,Al)—OH/H_2O abundance ratio ((Si,Al)-OH denotes OH-groups bonding only to Si or Al) depend on silicate composition and therefore on melt and glass structure (Fig. 15.3A). For example, Deubner et al. (2003) found that the OH/H_2O ratio evolution not only depends on total water content, but also seems to increase with increasing degree of polymerization of the silicate (Fig. 15.3B). However, the Al/(Al+Si) also must play a role, because in the data sets in Fig. 15.3A, where Zotov and Keppler (1998) reported OH/H_2O from composition $Na_2O{\cdot}4SiO_2$ (with NBO/Si=0.5) and Silver and Stolper (1989) data from composition $NaAlSi_3O_8$ (NBO/T=0), the OH/H_2O relations follow the NBO/T trends that are opposite to those suggested by Deubner et al. (2003). Here, OH/H_2O of the most polymerized, but aluminous, melt, $NaAlSi_3O_8$, is less than that of the less polymerized, but Al-free, $Na_2O{\cdot}4SiO_2$.

Various suggestions have been offered to explain such composition effects recorded in the OH/H_2O ratio glasses formed by temperature quenching of melts from temperatures above

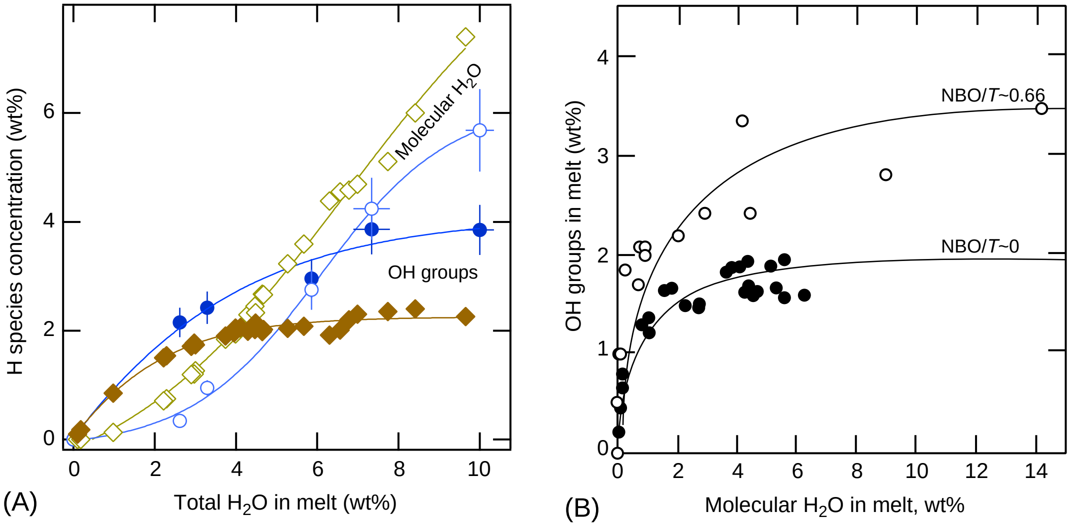

FIG. 15.3 Evolution of OH groups and molecular H_2O in silicate melts as a function of total water concentration in melt. (A) Evolution in quenched $Na_2O{\cdot}4SiO_2$ (*circles*) (data from Zotov and Keppler, 1998) and $NaAlSi_3O_8$ (*diamonds*) (data from Silver and Stolper, 1989). Closed symbols denote OH groups forming bonding with the silicate structure and open circles molecular H_2O. (B) Proportion of OH groups (wt%) of dissolved in $Na_2O{\cdot}3SiO_2$, andesite and rhyolite quenched melts as a function of total water content in melts from experiments conducted with quenching rates from ~0.2 K/s to ~50 K/s (data from Deubner et al., 2003). The $Na_2O{\cdot}3SiO_2$ and andesite data form the curve with average NBO/*T* ~ 0.66 (*open circles*), whereas the rhyolite data form the curve with the NBO/*T* ~ 0 data (*closed circles*).

their liquidii. One factor is that the water speciation is temperature dependent. In fact, Dingwell and Webb (1990) estimated a Gibbs free energy change of -25 ± 5 kJ/mol for reaction (15.1) in rhyolite melt, which of course means that the OH/H_2O ratio decreases as a hydrous melt cools and eventually transforms to a hydrous glass. Another complicating factor is hydrogen bonding, which affects both infrared and Raman band intensities as well as molar extinction coefficients (Mysen, 2012; Valyashko et al.,1981). Hydrogen bonding also can result in a shift of the frequency to lower values of the OH-stretch vibrations in the vibrational spectra. For example, the infrared absorption centered near 4500 cm^{-1} and considered an expression of (Si,Al)—OH-groups (Fig. 15.4), also shifts to lower values when hydrogen bonding is important. Under such circumstances, the 4500 cm^{-1} intensity may not be resolved from the high-frequency shoulder intensity of the O—H stretching centered near 3600 cm^{-1} (Zotov and Keppler, 1998; Le Losq et al., 2015). The 5200 cm^{-1} combination band, considered an expression of molecular H_2O (Fig. 15.4), also will shift to lower frequency because of the hydrogen bond effect.

We also need to evaluate how molecular H_2O may be dissolved in a silicate melt and glass. In general, it seems that three-dimensional cavities in the structure such as those that contain noble gases and other molecular species (see Chapter 17, Section 17.3.1.1), would be the most likely structural location. In that case, the availability and accessibility of such locations govern the proportion of water dissolved in molecular form. The cavity abundance and access likely would increase as a melt becomes more polymerized, for example. This concept implies

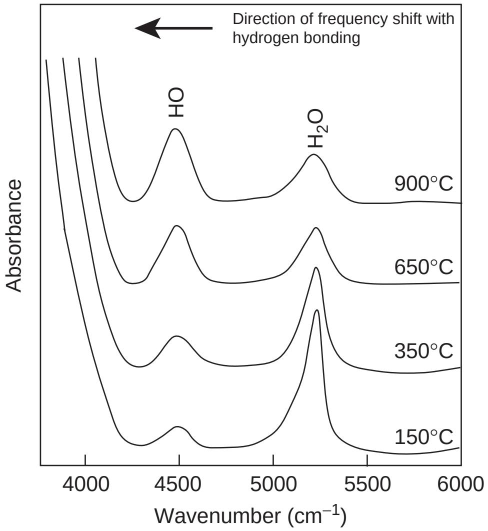

FIG. 15.4 Examples of infrared absorption spectra of rhyolite melt (3.93 wt% total water in solution) recorded in situ at the temperatures indicated on individual diagrams (Sowerby and Keppler, 1999). Arrow shows direction of frequency shifts of the bands assigned to OH and H_2O with increasing extent of hydrogen bonding (see also text for further discussion of this frequency shift).

that there likely would be a maximum concentration of molecular H_2O that could be dissolved in a given melt and glass.

The latter additional considerations notwithstanding, for the OH/H_2O concentration determined in a few quenched glasses of SiO_2 and feldspar composition by FTIR and by ^1H NMR, there is good agreement between the data obtained with the two different methods (Eckert et al., 1988; Schmidt et al., 2001). Finally, the quenching rate to form a hydrous glass from a high-temperature hydrous melt can be a factor, as this rate causes changes in fictive temperature (Silver et al., 1990; Behrens and Nowak, 2003) (see also Chapter 3, Section 3.4, for discussion of fictive temperature), which will result in different OH/H_2O ratios depending on quenching rate. In fact, the quenching rate and fictive temperature have sometimes been varied to deduce temperature-dependent structural changes in silicate melts (see, e.g., Stebbins, 1988). It then follows that the differing OH/H_2O evolutions found as a function of glass composition could simply originate in the fact that water speciations were then frozen in at different temperatures.

Given the complications resulting from quenching a melt to a glass, a better understanding of the interaction between dissolved water and silicate melt structure is gained through measurements of water speciation while a hydrous melt is in equilibrium with an aqueous fluid at temperatures above that of the glass transition. Such experiments also eliminate concerns that arise from hydrogen bonding, because hydrogen bonding that involves molecular H_2O and/or structurally bound OH-groups diminishes with temperature with a $\Delta H = 10 \pm 2$ kJ/mol (Mysen, 2010). Hydrogen bonding cannot be detected in vibrational spectra of hydrous melts or glass above about 600°C (Fig. 15.5).

Water speciation in melts at temperatures above ambient has been investigated via high-temperature and high-pressure infrared (IR) absorption spectroscopy (Keppler and Bagdassarov, 1993; Nowak and Behrens, 1995, Behrens and Schmidt, 1998; Sowerby and Keppler, 1999; Behrens and Yamashita, 2008; Mysen, 2010). This method relies on the relative

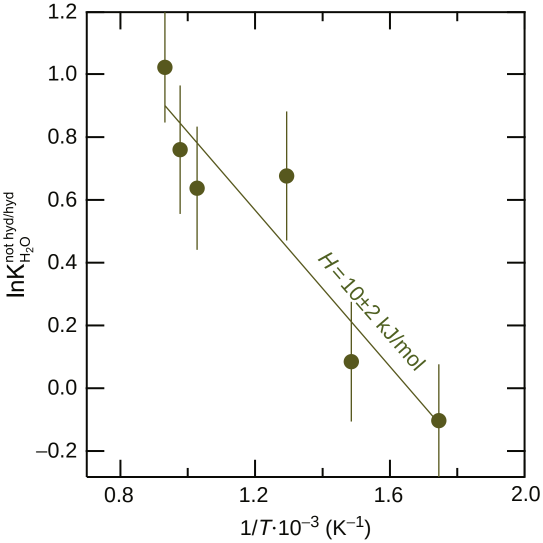

FIG. 15.5 Equilibrium between water dissolved without hydrogen bonding (no hyd) and with hydrogen bonding (hyd) as a function of temperature, from Raman spectra of hydrous melts recorded in situ at high temperature and pressure (data from Mysen, 2010).

variations in intensity of infrared absorption bands. There is some discussion, however, as to pressure and temperature dependence of the molar absorption coefficients needed to quantify these IR results (e.g., Withers et al., 1999; Withers and Behrens, 1999; Mandeville et al., 2002; Behrens and Yamashita, 2008). Those uncertainties notwithstanding, if one assumes that only (Si,Al)-OH boding is operative, then the OH/H_2O ratio increases with temperature (Fig. 15.6) as originally concluded the OH/H_2O ratio, assuming that only (Si,Al)—OH bonding is operative, increases with increasing temperature.

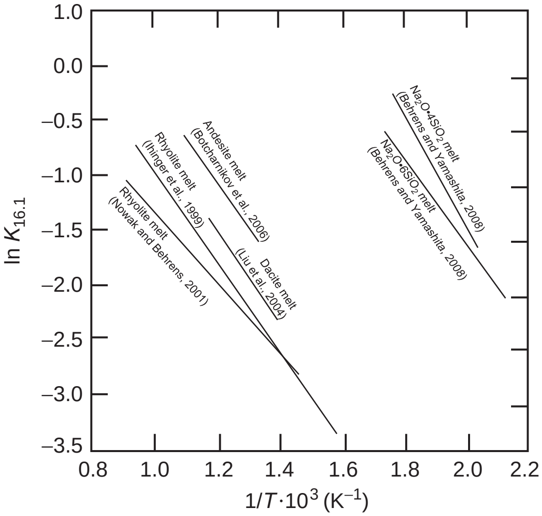

FIG. 15.6 Equilibrium constant for Eq. (15.1), $K_{15.1}$, as a function of temperature ($1/T$, kelvins) for compositions indicated on individual lines. Exact chemical compositions of the melts are provided in the sources.

The equilibrium constant for reaction (15.1) as a function of temperature follows a linear relationship of the type:

$$\ln K_{15.1} = a/T + b, \tag{15.3}$$

at temperatures above glass transition (Fig. 15.6). The temperature dependence depends on silicate composition with the ΔH for reaction (15.1) ranging between ~25 and ~42 kJ/mol. There is a tendency toward increased ΔH values with increasing silicate content. One might surmise therefore that among hydrous silicate melts, ΔH for SiO_2-H_2O melt would be the largest. However, high-temperature, experimental data for melts of the system SiO_2-H_2O do not appear to exist. That lack of experimental data notwithstanding, results from first-principles molecular dynamics simulation indicate for SiO_2 melt with 3.8 wt% H_2O in solution, all water would exist as OH-groups at temperatures near or above 3000 K (Pohlmann et al., 2004).

At total water concentration above about 3 wt%, the ΔH of reaction (15.1) is a function of water content (Sowerby and Keppler, 1999; Hui et al., 2008). A concentration-dependent ΔH (and therefore $K_{15.1}$) has been accommodated with a regular solution model for water in silicate melts (Silver and Stolper, 1989). An alternative, advocated by Doremus (2000), is to employ the Langmuir model whereby the speciation equilibrium constant, Eq. (15.2), can be replaced by an expression of the form:

$$K = S^2/C(R - S), \tag{15.4}$$

In Eq. (15.4), C replaces the concentration of H_2O groups, S is equivalent to the concentration of OH-groups, and R is the concentration of reactive sites. With this model, the solubility and speciation of water in felsic melt determined by Sowerby and Keppler (1999) and Holtz et al. (1995) were modeled quite accurately.

Whether, or the extent to which, pressure affects the water speciation equilibrium (15.1) has been addressed only in a handful of experimental sudies. Sowerby and Keppler (1999) concluded that with different total water contents and pressures from ambient to 1 GPa, the ΔH of reaction (15.1) was not sensitive to pressure, as did Zhang and Behrens (2000) for pressures ≤0.5 GPa. However, Hui et al. (2008) observed that ΔH did indeed decrease with pressure and that the rate of ΔH increase increased with increasing pressure to 3.8 GPa (Fig. 15.7).

There appear not to be experimental data on water speciation in silicate melts at pressures higher than the 3.8-GPa data reported by Hui et al. (2008). First-principles molecular dynamics simulations of hydrous SiO_2 and $MgSiO_3$ melts at ≥2000 K have, however, been carried out to pressures near 90 GPa (Anderson et al., 2008; Mookherjee et al., 2008; Karki et al., 2010). From such calculations, the proportion of both isolated H_2O molecules and of OH-groups decreases with increasing pressure. However, the proportion of molecular H_2O decreases much more rapidly than that of OH-groups, which leads to increased OH/H_2O with increasing pressure (Karki et al., 2010). However, additional, H-species that are more polymerized than isolated OH-groups and single H_2O molecules also are formed (Fig. 15.8). In this process, the O—H bond distance increases as does the fraction of protons bonded to oxygen. It follows that at these higher pressures the oxygen coordination number around H also increases from a value slightly above 1 at ambient pressure to more than 2 above 80 GPa (Fig. 15.8).

FIG. 15.7 Pressure dependence of the enthalpy change associated with the water solution equilibrium (15.1) (Hui et al., 2008).

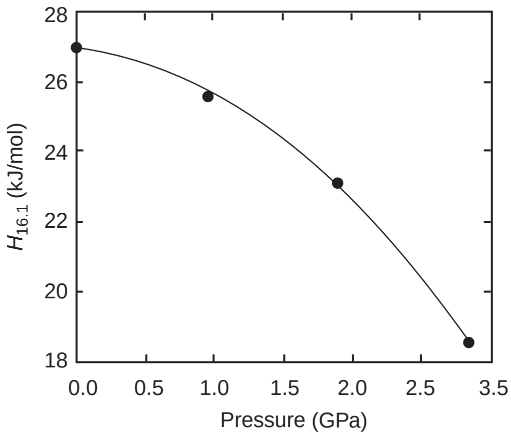

FIG. 15.8 Fraction of hydrogen (total = 2) bonded to 1, 2, and 3 oxygen in a hydrous $MgSiO_3$ melt system as a function of pressure. First-principles molecular dynamics simulations from Mookherjee et al. (2008). Note how the OH groups polymerize with pressure and take on the character of molecular water.

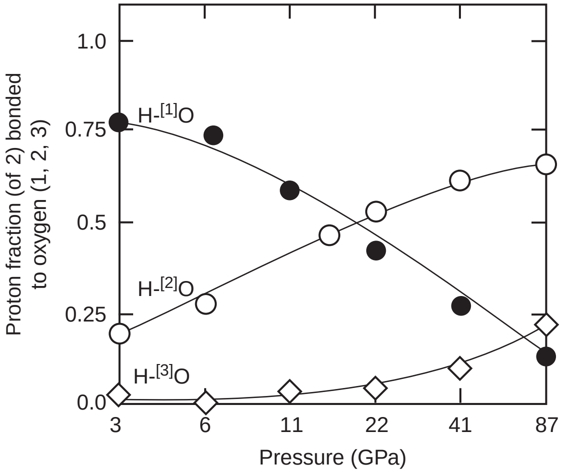

15.3 HYDROUS MELT AND GLASS STRUCTURE

Most experimental data on solution mechanisms of water dissolved in silicate melts actually were obtained on glasses formed by temperature quenching of hydrous melts equilibrated above their liquidii. In an application of such data to hydrous melts, possible effects on structure resulting from cooling the melt to a glass must be kept in mind.

The interaction between silicate structure and dissolved water in its simplest form (Fig. 15.2), as proposed early on by Wasserburg (1957), has an H_2O molecule cleaving an oxygen bridge that links two silicate tetrahedra to form two Si—OH bonds. This is also the most thermodynamically stable Si—OH functional group configuration among those possible in hydrous silicate melts and glasses (Buhler, 1999). The other forms of OH bonding, in addition to Si—OH, can be Al—OH, and alkali—OH and alkaline earth—OH. Their relative abundance depends on the cation properties and their abundance (Cody et al., 2005; Xue and Kanzaki, 2004, 2008; Malfait et al., 2014).

15.3.1 SiO_2-H_2O

Information on water interaction with the structure of hydrous SiO_2 melt has been gained from ^{29}Si MAS NMR, ^{17}O MAS NMR, ^{1}H MAS NMR, and cross-polarization (CP) MAS NMR (Farnan et al., 1987; Maekawa et al., 1998; Cody et al., 2005). The ^{29}Si MAS NMR data provide details on the structural response of the three-dimensionally interconnected network of SiO_2 melt to interaction with H_2O. The ^{1}H MAS NMR data provide information on the local environment surrounding the protons.

The ^{1}H MAS NMR spectra of $SiO_2 + 14$ mol% H_2O melt show evidence for both molecular H_2O and for Si—OH bonds (Fig. 15.9). Silicon-29 CP MAS NMR spectra of hydrous SiO_2 glass with 2.5 and 8.7 wt% H_2O show protons occupying structural positions near Q^2-, Q^3-, and Q^4-species (Farnan et al., 1987). From the single-pulse ^{29}Si MAS NMR, the Q^3/Q^4 abundance ratio increases with increasing water content (Farnan et al., 1987; see also Table 15.1). The OH/H_2O ratio was calculated from these NMR data under the assumption that all OH existed in the

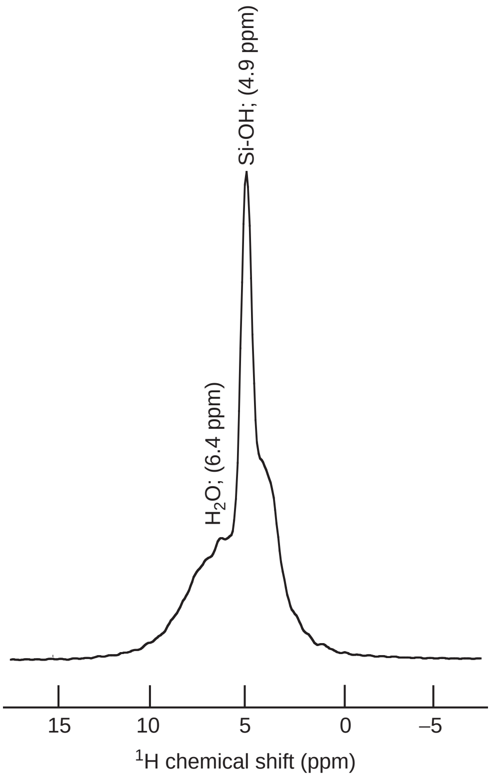

FIG. 15.9 ^{1}H MAS NMR spectrum hydrous SiO_2 glass (14 mol% H_2O) to show the chemical shift of OH groups that form bonding to Si^{4+} and of molecular H_2O (Cody et al., 2005).

TABLE 15.1 Concentration of Si and H Species in SiO_2-H_2O Melts (Farnan et al., 1987)

Water conc. (wt%)	$Q^3/(Q^3+Q^4)$	OH conc. (wt%)	Molecular H_2O (wt%)
2.5	0.086	1.26	1.24
8.7	0.235	3.21	5.49

form of Si—OH groups. There is increasing abundance of both OH-groups and molecular H_2O with increasing total water content.

Farnan et al. (1987) saw no NMR evidence for silicate species less polymerized than Q^3, which leads to a simple solution mechanism for water in SiO_2 melt:

$$2Q^4 + H_2O \Leftrightarrow Q^3(OH). \qquad (15.5)$$

In this expression, Q^3(OH) denotes one OH-group per Si in the Q^3 species.

Additional details on the nature of the dissolved OH-groups and molecular H_2O in silicate glasses and melts have been obtained from vibrational spectroscopy, neutron diffraction, and ^{1}H MAS NMR (Stolper, 1982; Silver and Stolper, 1989; Mysen and Virgo, 1986a, b; McMillan and Remmele, 1986; Eckert et al., 1988; Zavelsky and Salova, 2002; Xue and Kanzaki, 2004; Cody et al., 2005). These data offer information on cation-OH interaction and distances and the extent to which hydrogen bonding plays a role. For example, in the Raman spectra of hydrous silica glass, the pronounced band near 970 cm^{-1} (Fig. 15.10) has been assigned to Si—OH stretch vibrations in the SiO_2-H_2O glasses (Stolen and Walrafen, 1976; McMillan and Remmele, 1986). Its growth with increasing water content in the melts is consistent with increasing abundance of Si—OH bonds as the total water content increases. A band near 1600 cm^{-1} is commonly assigned to H—O—H bending motions and thus attests to the existence of molecular H_2O (Paterson, 1982; Reimers and Watts, 1984). These interpretations accord with those advanced by Farnan et al. (1987) from their ^{29}Si MAS NMR spectra of SiO_2-H_2O glasses.

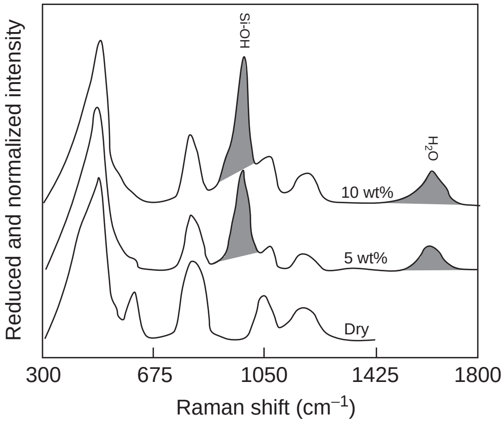

FIG. 15.10 Raman spectra of hydrous SiO_2 glass (temperature-quenched melt) with water contents as indicated on individual spectra. The shaded band marked Si—OH is an Si—O stretch vibration of Si—OH bond and that marked H_2O is a H—O—H bending mode in H_2O molecules (spectra modified from Mysen and Virgo, 1986a, b).

Experimental data that describe the SiO_2-H_2O melt structure at high temperatures and pressures do not appear to exist. However, there are results from first-principles molecular dynamics modeling (Anderson et al., 2008). The OH/H_2O increases with temperature and pressure (Anderson et al., 2008). This observation is, of course, analogous to experimental observations at lower pressures and temperatures discussed previously (Figs. 15.3 and 15.4).

Silicon remains in tetrahedral coordination in SiO_2-H_2O melts to at least 10 GPa pressure (Anderson et al., 2008) as also observed in anhydrous SiO_2 glass (Bridgman and Simon, 1953; Sato and Funamori, 2008; Fukui et al., 2009). The main evidence for this conclusion is the fixed position of first peak of the X-ray Si—O radial distribution function to 10 GPa (Fig. 15.11A).

There also are other pressure-dependent changes of the distribution function. For example, the second Si—O peak broadens significantly with an asymmetry toward shorter distances. Changes can also be seen in the Si—O angular distribution, which broadens and becomes asymmetric toward larger Si—O—Si angles with increasing pressure (Fig. 15.11B). The broadening and asymmetry development of the Si—O—Si angle (Fig. 15.11) reflect in part a decrease in Si—O—Si angles in the three-dimensional network and in part the formation of increasingly abundant less polymerized Q^n-species, which are formed as H_2O is dissolved. Depolymerized silicate species would have larger Si—O—Si angles than the Q^4 species. These pressure-dependent structural developments also are reflected in decreased proportions of corner-shared Q^4 tetrahedra (Fig. 15.12A). At any temperature and pressure, the abundance of Q^4 units also decreases with increasing water content (Fig. 15.12B).

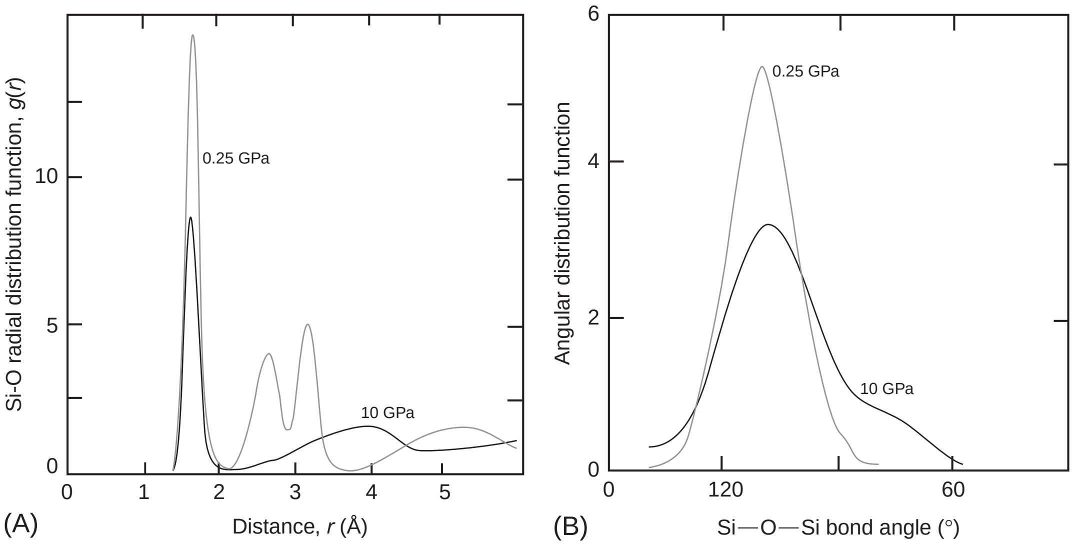

FIG. 15.11 Properties of hydrous SiO_2 melt at different pressures from first-principles MD simulations (Anderson et al., 2008). (A) Si-O radial distribution function at pressures indicated. (B) Si-O-Si angle distribution function at pressures indicated.

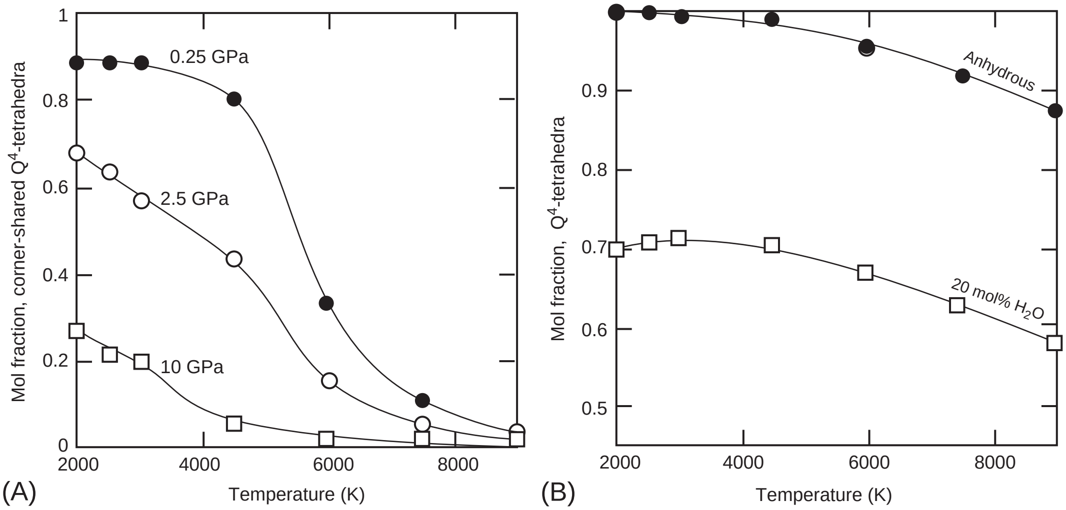

FIG. 15.12 Structural behavior of Q^4-species in hydrous SiO_2 melt from first-principles MD calculations (Anderson et al., 2008). (A) Evolution of corner-shared Q^4 tetrahedra with temperature and pressure. (B) Fraction of Q^4 as a function of temperature at 10 GPa for anhydrous melt and melt with 20 mol% H_2O.

15.3.2 Metal Oxide-Silica-H_2O

Solution of water in metal oxide-silicate melts at least in part can be described with Eq. (15.1) to form more depolymerized silicate species (Zotov and Keppler, 1998; Robert et al., 2001; Cody et al., 2005). By incorporating a role of metal cations, M^{m+}, in such an interaction, the principal solution mechanism with which to break Si—O—Si bridges in metal oxide-SiO_2 melts can be expressed as:

$$Q^n(M^{m+}) + H_2O \Leftrightarrow Q^{n-1}(OH) + 2/mM^{m+}. \tag{15.6}$$

In Eq. (15.6), $Q^n(M^{m+})$ denotes a Q-species with a metal cation, M, with a positive charge, $m+$, serving as a network-modifying cation, $Q^{n-1}(OH)$ denotes a Q-species with a $n-1$ bridging oxygen and where OH-groups form a part of the silicate tetrahedra (Fig. 15.2), so in a way H^+ serves a structural role resembling that of the M^{m+} cations.

Several different Q^n-species coexist in both anhydrous and hydrous metal oxide-silicate melts (Zotov and Keppler, 1998; Robert et al., 2001; Cody et al., 2005). The single-pulse ^{29}Si MAS NMR data of quenched hydrous Na_2O-SiO_2 melts show how the proportion of depolymerized species is increasingly abundant with increasing water content (Fig. 15.13).

Ordering of H^+ and metal cations among nonbridging oxygen in different Q^n-species in melt and glass structures is also likely. In such circumstances, H^+ tends to react with nonbridging oxygens to form OH-groups in the least polymerized among coexisting Q^n-species (Mysen and Cody, 2005).

The rate of silicate depolymerization with increasing water concentration of hydrous melt and therefore the rate of change of Q^n-species concentration, decreases with increasing NBO/Si-values of the anhydrous base glass melt (Figs. 15.1 and 15.14). This evolution is a partly a

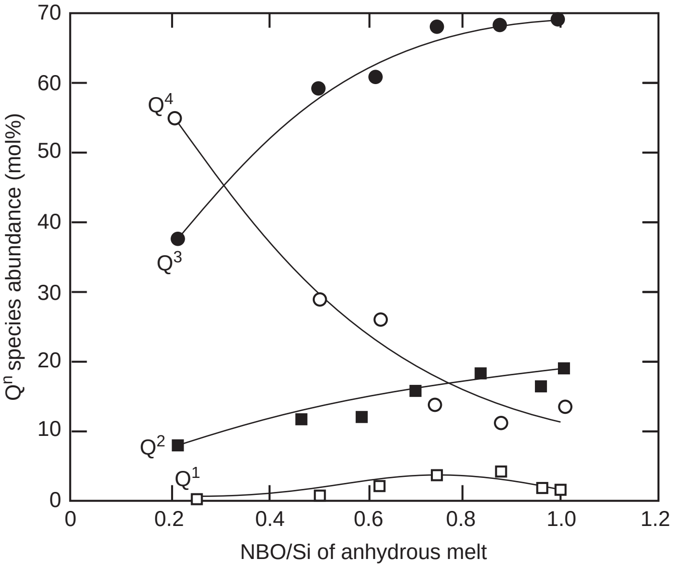

FIG. 15.13 Evolution of Q-species in hydrous melts along the join Na_2O-SiO_2 with 14 mol% H_2O. Note how the Q^4-species abundance diminishes, whereas the abundance of all other species increases. This means that dissolution of water to form OH groups predominantly occurs via reaction with bridging oxygen in the Q^4-species (Cody et al., 2005).

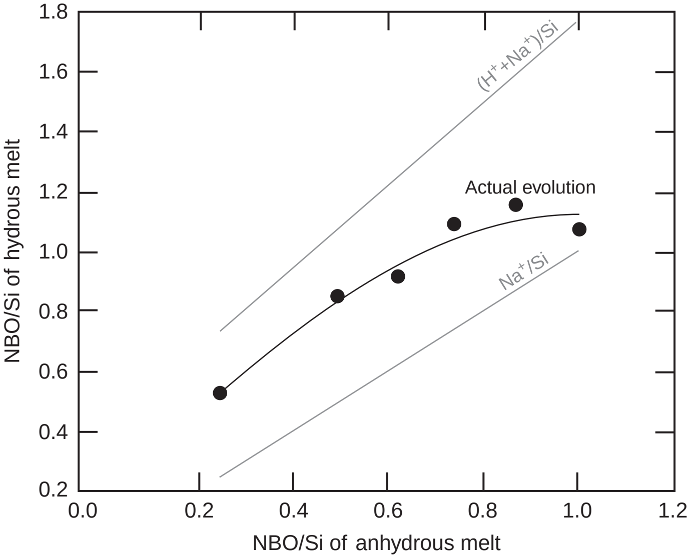

FIG. 15.14 Evolution of NBO/Si of hydrous (14 mol% H_2O) melts along the join Na_2O-SiO_2 as a function of their anhydrous equivalent NBO/Si-values (shown as "actual evolution"). Also shown in grayscale are the hydrous NBO/Si melt values, calculated under the assumption that all protons serve the same structural role as Na^+ and are therefore linked exclusively to Si as Si-OH bonds (gray line marked $(H^+ + Na^+)/Si$) or none of the H^+ forms such bonding, but instead for Na—OH bonds (gray line marked Na^+/Si) (Cody et al., 2005).

reflection of decreasing Si—OH/H_2O abundance ratio with increasing water content and partly because in addition to Si—OH groups (depolymerization), isolated M—OH groups also may form in water-bearing metal oxide silicate melts and their glasses. Their abundance increases as the anhydrous melt becomes increasingly depolymerized (Cody et al., 2005). The NBO/Si of hydrous melts as a function of the NBO/Si of the anhydrous equivalent evolves at a rate between that which would be expected if all H^+ and Na^+ acted as network-modifiers (line $(H^++Na^+)/Si$ in Fig. 15.14) and that where none of the H^+ serve as network-modifier. The actual values of NBO/Si of hydrous melt mean that some of the OH-group formation is through isolated Na-OH complexes. A general expression of such a solution mechanism is (Cody et al., 2005; Xue and Kanzaki, 2001, 2004; Le Losq et al., 2015):

$$(\mathrm{MO})_n + \mathrm{H_2O} = [\mathrm{M(OH)_2}]_m. \tag{15.7}$$

This equilibrium shifts to the right with decreasing M^{n+}-cation radius (Xue and Kanzaki, 2004). Isolated $[M(OH)_2]_m$ groups in melts also become increasingly important as the M-cation becomes more electronegative and as the abundance ratio, $[M(OH)_2]/SiO_2$, increases.

Formation of isolated M—OH groups transforms some of the network-modifying M-cations from a network-modifying role to form these complexes. A reaction with which to form isolated M—OH groups via interaction with the silicate structure is:

$$2\mathrm{Q}^3(\mathrm{M}^{m+}) + \mathrm{H_2O} \Leftrightarrow [\mathrm{M(OH)_2}]_m + 2\mathrm{Q}^4. \tag{15.8}$$

Here $Q^3(M^{m+})$ denotes a Q^3-species with a metal cation, M^{m+}, forming bonds with its nonbridging oxygen. In other words, formation of isolated $[M(OH)_2]_m$ complexes results in polymerization of the silicate network (Cody et al., 2005; Xue and Kanzaki, 2004; Xue, 2009). This reaction mechanism becomes increasingly important as the extent of silicate depolymerization of the anhydrous silicate component, NBO/Si (anhydr), increases (Fig. 15.13B).

The equilibrium constant for equilibrium (15.1), $K_{15.1}$, not only is a function of total water content and degree of polymerization of the anhydrous silicate melt, it also varies systematically with the ionization potential of the metal cation which correlates positively with the abundance ratio OH/H_2O (Le Losq et al., 2015). In other words, the larger the metal cation, the more effectively does dissolved water depolymerize the silicate melt structure (Fig. 15.16).

The cation control on water speciation is further illustrated in the ^1H MAS NMR (Fig. 15.17A). These NMR data, in turn, can be used to estimate the O—H⋯O distance among the water species by using the expression from Eckert et al. (1988):

$$\delta^1\mathrm{H}\,(\mathrm{ppm}) = 79.05 - 2.55\mathrm{d}_{\mathrm{O-H\cdots O}}(\mathrm{pm}). \tag{15.9}$$

Here, δ^1H is the chemical shift and $d_{O\text{-}H\cdots O}$ the oxygen distance in pm. In other words, the differences in silicate melt and glass structure, governed by the electronic properties of the M-cation, also control the distribution of OH and H_2O species in the melt and the extent to which these species cause changes in silicate polymerization. Moreover, if we assume, as did Le Losq et al. (2015), that a mean volume of dissolved water is assumed to be a sphere with the O—H⋯O distances derived from the ^1H MAS NMR spectra and Eq. (15.9), a mean volume of H_2O in the melts can be calculated and compared with the measured partial molar volume of H_2O at similar pressures and temperature. The mean volume of H_2O this calculated is within 10% of the same as a partial molar volume of H_2O in these melts (Fig. 15.18).

Given that the ΔH for equilibrium (15.1) ranges between about 26 and 43 kJ/mol for different melt compositions (Table 15.2), one would expect that the OH/H_2O abundance ratio of temperature-quenched melts (to form glasses) would be lower than their equivalent melts

TABLE 15.2 ΔH for Eq. (15.1) Derived From Temperature-Dependent Data Such as in Fig. 15.6

Composition	ΔH (kJ/mol)	Source
Rhyolite	26.0	Ihinger et al. (1999)
Dacite	29.7	Liu et al. (2004)
Andesite	30.4	Botcharnikov et al. (2006)
QA[a]	25.2	Ohlhorst et al. (2001)
QtzAbAn[b]	43.2	Ohlhorst et al. (2001)
$Na_2O{\cdot}4SiO_2$	28.5	Behrens and Yamashita (2008)
$Na_2O{\cdot}6SiO_2$	31.0	Behrens and Yamashita (2008)

[a] $(SiO_2)_{50}(CaAl_2Si_2O_8)_{50}$.

[b] $(SiO_2)_{33}(NaAlSi_3O_8)_{33}(CaAl_2Si_2O_8)_{33}$.

at high temperature because of back-reaction during cooling from high temperature to that of the glass transition. The reader also is reminded that this OH/H_2O ratio does not include M—OH groups because the necessary details of how M—OH group abundance is governed by pressure is not yet available.

Results of one of the few experimental studies of water speciation of a glass and at temperatures above the glass transition are shown in Fig. 15.19 for hydrous $Na_2Si_2O_5$ composition glass and melt (Chertkova and Yamashita, 2015). By assuming the activity and mol fraction of oxygen to be constant, this yields a ΔH value of 18 ± 2 kJ/mol. Clearly, this ΔH, reflecting the temperature dependence on the OH/H_2O ratio, explains the significant difference in OH-groups vs molecular H_2O evolution measured in a melt at high temperature and its glass at room temperature as well as the influence of quenching rate (Deubner et al., 2003).

In their study, Chertkova and Yamashita (2015) did not observe an effect of water content on the equilibrium constant for reaction (15.1), thus concluding that this silicate-H_2O melt mixture might be treated as ideal. Moreover, by comparing the $K_{15.1}$ vs temperature data with those of $Na_2Si_4O_9$ and $Na_2Si_6O_{13}$ melt to temperatures barely above that of the glass transition of these samples from Behrens and Yamashita (2008), the Chertkova and Yamashita (2015) data show considerably less temperature dependence. This difference may reflect the lower temperatures (<450°C) of the Behrens and Yamashita (2008) experiments where hydrogen bonding played a more significant role. Hydrogen bonding affects the infrared absorption intensity (Valyashko et al., 1981). Another data set for water-saturated $Na_2Si_4O_9$ melt between 400°C and 800°C in the 180–700 MPa pressure range (Mysen, 2009; see also Fig. 15.20) obtained in the same manner as the data reported by Chertkova and Yamashita (2015) closely resemble their data. Indeed, from the least-squares fit of the data as shown in the figure, $\ln[(X_{OH})^2/X_{H2O}] = 5.1 \pm 0.3 – 2170 \pm 282/T$ ($R^2 = 0.95$), which yields $\Delta H = 18$ kJ/mol. The similarity of this ΔH value with that derived for $K_{15.1}$ vs temperature data from the Chertkova and Yamashita (2015) data would suggest that, at least in the pressure/temperature range of these experiments, the activity of oxygen in the melt does not vary significantly.

In the data in Figs. 15.19 and 15.20, it is assumed that the volume change of reaction (15.1), $\Delta V_{15.1}$, equals 0 because in Fig. 15.19 the pressure range employed at 900°C actually is between 0.2 and 2.5 GPa. For the data in Fig. 15.20, the range is 180–700 MPa. In the pressure range of these latter data there appears to be no pressure effect on equilibrium (15.1). However, at much higher pressures (to as much as 150 GPa and between 2000 and 6000 K), results from first-principles molecular dynamics methods have been reported (Mookherjee et al., 2008; Karki et al., 2010). There also exists at least one experimental study of (Mg,Fe)SiO_3 glass at ambient temperatures and high pressure, as well as one for hydrous $MgSiO_3$ melt (Closman and Williams, 1995; Yamada et al., 2007). Those data all indicate that the OH/H_2O increases with pressure.

The results from first-principles molecular dynamics simulation of $MgSiO_3$-H_2O melt structure indicate that water dissolved in such melt at pressures near 10 GPa and above dissolves as OH groups, as single H_2O molecules, and as more extended (O⋯H)-structures (Fig. 15.21). The OH/H_2O abundance ratio increases with increasing pressure in this higher pressure range. In principle, this conclusion is similar to the calculated behavior of dissolved water in SiO_2 melt under similar conditions (Anderson et al., 2008). Formation of extended (O⋯H) structures results in a lengthening of the H—O bonds (Fig. 15.21B). The increasing average bond length (Fig. 15.21B), also seen for Si—O and Mg—O in these calculations (Karki et al., 2010), reflects the increased average oxygen coordination number of H, Mg, and Si with increasing pressure. This behavior of Mg and Si is similar to that reported for anhydrous melts as a function of increased pressure (see Chapters 7 and 9).

A schematic water speciation equilibrium that describes this situation is:

$$nH_2O + O^{2-} = 2OH^- + (H_2O)_{n-1}, \tag{15.10}$$

where $(H_2O)_{n-1}$ denotes a polymerized water structure and the OH-group forms bonding to the silicate structure. Equilibrium (15.10) shifts to the right with pressure (Karki et al., 2010). The OH^- and $(H_2O)_{n-1}$ structures dominate to the extent that at simulated pressures near 80 GPa, for example, only polymerized H_2O molecules are detected in the MD calculations.

Closman and Williams (1995), from the pressure-dependent changes in infrared spectra of their (Mg,Fe)SiO_3 hydrous glasses, suggested that hydrogen bonding also becomes more important with increasing pressure, which could also explain the lengthening O⋯H distance (Fig. 15.21B). It should be remembered, however, that those results are for glasses subjected to pressure at ambient temperature. Other experimental data indicate that hydrogen bonding in hydrous melt does not play a significant role at temperatures above about 600°C (Fig. 15.5) so it seems less likely that the >2000 K simulation results from Karki et al. (2010) could not be ascribed to hydrogen bonding.

Some of the OH-groups in $MgSiO_3$-H_2O melts at high pressure are formed by H^+ reacting with the nonbridging oxygens in the silicate network to form Si—OH groups and some H_2O reacts with Mg^{2+} to form Mg⋯OH complexes (Yamada et al., 2007; Karki et al., 2010). This would be the solution mechanism indicated in Eq. (15.7). This suggestion for high-pressure $MgSiO_3$-H_2O melt resembles that reported from low-pressure experiments with (Ca,Mg) silicate glasses with similar bulk NBO/Si-values (near 2).

The proportion of isolated Mg⋯OH groups is greater in hydrous Mg_2SiO_4 melt than in hydrous $MgSiO_3$ melt (Yamada et al., 2007). Moreover, in (Ca,Mg)-SiO_2-H_2O melt, the abundance ratio, Mg..OH/Ca⋯OH, is greater than 1 (Xue and Kanzaki, 2004), suggesting therefore that these OH-bearing complexes become increasingly stable as the metal cation becomes more electronegative. Evidence for OH-groups that form bonding with cations other than tetrahedrally coordinated Si^{4+} and Al^{3+} also has been reported from MAS NMR measurements of Na_2O-SiO_2 glasses (see Fig. 15.14).

The Mg—O, Si—O, and H—O distances and oxygen coordination numbers around Mg, Si, and H in the simulated $MgSiO_3$-H_2O melt structure increase with increasing pressure (Fig. 15.22A; see also Karki et al., 2010). The data in Fig. 15.22A are average coordination numbers that reflect coexistence of silicate structures with differet numbers of oxygens in the coordination sphere (Fig. 15.22B). In all cases, the average coordination number increases with pressure. Similar structural behavior has been reported from first-principles molecular dyanamics simulations of Mg and Si in anhydrous $MgSiO_3$ and Mg_2SiO_4 melt in the pressure range from <10 GPa to 170 GPa (Ghosh et al., 2014; see also Chapter 7, Section 7.2.4). However, an experimental study of ambient-temperature anhydrous $MgSiO_3$ glass to about 40 GPa does not show evidence of Si coordination transformations (Kubicki et al., 1992). The latter conclusion differs, however, from that of Lee and Stebbins (2003) and Lee et al. (2012)) who, from examination of alkali aluminosilicate glasses formed by temperature quenching of melt at more than 10 GPa and from Sanloup et al. (2013) for molten basalt to 35 GPa. Those authors found that sixfold coordinated Si^{4+} plays a major structural role in silicate melts at these pressures. The difference with the data of Kubicki et al. (1992) and the other data on glass formed by temperature-quenching melt at its liquidus temperature at high pressure likely is because the behavior of ambient-pressure glass cannot be compared with that of melt quenched from or modeled at several thousand kelvins and high pressure (Lee and Stebbins, 2003; Lee et al., 2012; Sanloup et al., 2013; Karki et al., 2010). An ambient-temperature glass is in a nonequilibrium state and does not reach equilibrium conditions simply by compression. High-temperature melt quenched to glass at high pressure, on the other hand, leads to a glass reflecting the equilibrium structure at the fictive temperature at the pressure of quenching.

15.3.3 Aluminosilicate-H_2O

Most studies of water solution mechanisms in silicate melts have focused on feldspar-rich glasses near meta-aluminosilicate joins (Silver and Stolper, 1989; Sykes and Kubicki, 1993; Shen and Keppler, 1995; Behrens et al., 1996; Schmidt et al., 2000, 2001; Xue and Kanzaki, 2007; Malfait and Xue, 2010). There are also a few studies of the solution of water in peralkaline aluminosilicate melts (Mysen, 1992, Mysen and Armstrong, 2002; Benne and Behrens, 2003; Ni et al., 2009; Wang et al., 2015).

Replacement of Si^{4+} in SiO_2 glass and melt with Al^{3+} requires charge-balance of Al^{3+} either with the aid of an alkali metal or an alkaline earth (see Chapters 4 and 9, for discussion of charge-balance). In hydrous aluminosilicate melts and glasses, those alkalis and alkaline earths not only may serve to charge-balance tetrahedrally coordinated Al^{3+}, but could also behave as network-modifiers. Some portions of those alkalis and alkaline earths may also be associated with OH-groups (Maekawa et al., 1998; Xue and Kanzaki, 2004; Cody et al., 2005; Xue, 2009). This is evident, for example, in systematic relationships in NMR spectra of hydrous $NaAlSi_3O_8$-$KASi_3O_8$-SiO_2 composition melts where the ^{23}Na chemical shift decreases systematically with H/(Na + K) of the sample (Fig. 15.23). Increasing chemical shift is correlated with decreasing Na—O bond distance (Tossell, 1999). For the correlation in

Fig. 15.23, this trend might be consistent either with increasing number of H_2O molecules in a hydration shell surrounding Na^+ with increasing water content of the glasses (Schmidt et al., 2001), or there might be Na⋯OH complexes forming in the glasses and melts. Because of such structural features, dissolution of water may lead to major redistribution of the cations forming the hydrous aluminosilicate network compared with their anhydrous equivalent (Mysen and Virgo, 1986a, b; Acosta-Vigil et al., 2005; Malfait and Xue, 2014).

In highly polymerized aluminosilicate melts, an important form of OH formation is Si—OH and Al—OH bonding resulting from breakage of Si—O—Si and Si—O—Al bonds (Bouyer et al., 2010; Malfait and Xue, 2014). One of the ^1H NMR peak positions chemical shift between 1 and 3 ppm in spectra of K-, Na-, and Ca-aluminosilicate glasses has been assigned to protons in Al—OH functional groups (Malfait and Xue, 2014). The shift increases slightly with increasing bulk Al/(Al+Si) (Fig. 15.24A). In spectra of hydrous K- and Na-aluminosilicate melts, the Al/Si-dependence of this shift coincides in the 1–2 ppm range, whereas in NMR spectra of hydrous Ca-aluminosilicate glasses it occurs in the 2.5–3 ppm range (Fig. 15.24A). These NMR data suggest, therefore, similar structural environments of H^+ in the K- and Na-meta-aluminosilicate melts. In the Al—OH environment charge-balanced with Ca^{2+} this environment differs because of the greater chemical shift of the ^1H spectra from those glasses (2.5–3 ppm). The resonance near 1–2 ppm in ^1H MAS NMR spectra reflects a proton environment with large rotational freedom, but with this freedom being more restricted when the chemical shift increases (Wang et al., 2015).

Regardless of the nature of the charge-balancing cation, in these melts the proportion of OH as Al⋯OH relative to total abundance of OH-groups increases with bulk melt Al/(Al+Si) of the melt (Mysen and Virgo, 1986a, b; Padro et al., 2003; Malfait and Xue, 2014; see also Fig. 15.24B). Notably, this evolution also depends on the nature of the charge-balancing cation with the apparent largest preference for Al—OH bonding in K-aluminosilicate melts. In fact, in the K-system at Al/(Al+Si) > 0.3, the Al—OH/OH_{total} exceeds the bulk Al/(Al+Si) of the melt (Fig. 15.24C). In other words, there is ordering of the H^+ among the hydrous Al-species and the degree of ordering varies with type of charge-balancing cation.

The interaction between dissolved water and Si—O—Al bridges in aluminosilicate melts leads to a depolymerization mechanism with a general form:

$$2MAlSi_xO_{2x+1} + 3H_2O \Leftrightarrow 2(Al\cdots OH) + Q^{n-2}(M) + (2x-1)Q^n. \tag{15.11}$$

In Eq. (15.11), the Al⋯OH implies that the Al⋯OH complex comprises three OH-groups per Al^{3+}. According to this solution mechanism, an equivalent portion of M-cations serving as charge-balancers in the anhydrous melt becomes network-modifying in the hydrous melts, which leads to stabilization of the depolymerized $Q^2(M)$ structures.

The OH/H_2O ratio in a given aluminosilicate system does not seem to vary greatly with bulk melt Al/(Al+Si) (Simakin et al., 2010). The type of charge-balancing cation does not seem to have a big effect on OH/H_2O either (Table 15.3; see also Schmidt et al., 2001) at least for melts with Al/(Al+Si) = 0.25 and temperature quenched to a glass at a few hundred megapascals. Given, however, that the reactivity of the Si—O—Al bonds likely is dependent on the charge-balancing cation as seen, for example, in the data of Malfait and Xue (2014), the data in Table 15.3 should not be extrapolated to other Al/Si ratios.

TABLE 15.3 Abundance Ratio, $OH/(OH+H_2O)$ as a Function of Charge-Balancing Cation Type, $MAlSi_3O_8$-H_2O Quenched Melts (Glass) for M = Li, Na, and K, and Total H_2O Content at 2 and 4 wt% (Data From Schmidt et al., 2001)

M-Cation	**$OH/(OH+H_2O)$**	
	2 wt% H_2O	**4 wt% H_2O**
Li		0.40 ± 0.01
Na	0.57 ± 0.01	0.41 ± 0.01
K	0.59 ± 0.02	0.42 ± 0.02

An effect of the metal cation type on the OH/H_2O ratio has, in fact, been reported (Benne and Behrens, 2003). For example, in the system $(CaAl_2Si_2O_8)_{54}(CaMgSi_2O_6)_{46}$, the OH/H_2O ratio is considerably greater than in pure $NAlSi_3O_8$ composition melt (Fig. 15.25). Interestingly, by adding $CaMgSi_2O_6$ components to $NaAlSi_3O_8$, the OH/H_2O actually decreases (Fig. 15.25). It should be noted, however, that the OH-component in Fig. 15.25 was obtained from the 4500 cm^{-1} combination band in the infrared absorption spectra. The OH abundance thus obtained is that which forms bonding of Si—OH and perhaps Al—OH in the aluminosilicate network (Simakin et al., 2010; Malfait and Xue, 2010). This could result in an underestimate of the total OH abundance because Xue and Kanzaki (2008), from MAS NMR spectroscopy, demonstrated that free OH-groups (i.e., groups formed by bonding to Mg or Ca) exist in many of the $(CaAl_2Si_2O_8)$-$(CaMgSi_2O_6)$ melts. The infrared combination signal from OH groups from such complexes together with the fundamental O—H stretching near 3600 cm^{-1} most likely does not appear near 4500 cm^{-1}. Instead, in analogy with infrared and signals from Ca—O and MgO in silicate glasses near 400 cm^{-1} (Gervais et al., 1990), one might expect a combination of fundamental OH stretch vibrations and the Ca—OH/Mg—OH near 400 cm^{-1} to result in a combination band near 4000 cm^{-1}, which is near that reported by Ackerson et al. (2017). The intensity of such a band would be very difficult to extract quantitatively because of interferences from the high-frequency tail of the broad 3600 cm^{-1} band from OH stretching. In short, the OH/H_2O from $CaMgSi_2O_6$-rich compositions such as those shown in Fig. 15.25 likely is underestimated. This disclaimer may also apply to other melt compositions, but detailed information is yet to be published.

Silicate speciation of hydrous aluminosilicate melts varies with both total water content and with $Al/(Al+Si)$ of the system (Xu et al., 1998; Liu et al., 2002; Mysen, 2007, 2011; Malfait and Xue, 2014). The extent to which aluminosilicate melts become depolymerized as water is dissolved increases with $Al/(Al+Si)$ of the melt (Fig. 15.26), because of the changes in Q^n-species abundance of anhydrous aluminosilicate melt with $Al/(Al+Si)$. The Al^{3+} preferentially occupies the Q^4 species, which means that the $Al/(Al+Si)$ of Q^4 is greater than the bulk $Al/(Al+Si)$-value (Mysen et al., 2003; see also Chapter 9, Section 9.3.2.4). This also means that the proportion of Q^4-species in a melt increases with $Al/(Al+Si)$ (Mysen et al., 2003). Therefore, given that H_2O seems to show preference for interaction with bridging oxygen in Q^4-species (Zotov and Keppler, 1998; Mysen and Cody, 2005), and finally that interaction of water with aluminous Q^4-species more effectively depolymerizes a silicate melt, the more rapid build-up of Q^2- and Q^3-species abundance, the more that $Al/(Al+Si)$ would be the result (Fig. 15.27). This effect, in turn, results in more rapid overall depolymerization of the aluminosilicate melts, the greater their bulk Al/(Al+Si).

There is some variation in how OH/H_2O of aluminosilicate melts may vary with temperature based on examination of glass formed by temperature quenching of their melt from temperatures above their melting point. However, these variations may at least in part reflect different quenching rates, different fictive temperatures, and so forth that result in OH/H_2O abundance ratio variations with water content (see also Fig. 15.28). As the quenching rate decreases, the OH/H_2O ratio also decreases. In other words, the equilibria that describe solution mechanism (e.g., Eqs. 15.1, 15.5–15.7) shift in favor of molecular water with decreasing quenching rate. This is simply another way of saying that the hydrous system backreacts during cooling and that examination of glass samples quenched to ambient temperature before structural analysis may not offer an accurate view of the water speciation in hydrous melts.

Results of studies of water speciation in aluminosilicate melts, recorded in situ while the sample was at the pressure and temperature of interest, seems limited to only several experiments along meta-aluminosilicate joins, such as $NaAlSi_3O_8$-H_2O and $KAlSi_3O_8$-$NaAlSi_3O_8$-SiO_2-H_2O (Nowak and Behrens, 1995; Behrens and Schmidt, 1998 Sowerby and Keppler, 2002; Behrens and Nowak, 2003) and a few experimental data on multicomponent rhyolite-H_2O systems (Keppler and Bagdassarov, 1993; Sowerby and Keppler, 1999). In general, the structure data of hydrous melts recorded at high temperature and pressure show slightly different ΔH values for reaction (15.1) than values derived from hydrous glasses quenched from various high temperatures above the glass transition. For example, for the haplogranitic system, $KAlSi_3O_8$-$NaAlSi_3O_8$-SiO_2-H_2O, Nowak and Behrens (2001) found that when the melt was characterized at temperatures above the melting temperatures, the $\Delta H = 35 \pm 1.2$ kJ/mol and $\Delta S = 27.7 \pm 1.3$ J/mol K (Fig. 15.29), whereas these values for the same sample quenched to ambient-pressure glass from various temperatures resulted in $\Delta H = 25.8$ kJ/mol and $\Delta S = 15.6$ J/mol K. In other words, data from glasses formed by temperature quenching will not yield precise equilibrium information on water speciation. The kinetic information that may be derived from such experiments may be used, however, as a geospeedometer, for example (Zhang et al., 1995; Zhang and Behrens, 2000).

The main structural changes of hydrous aluminosilicate melts with increasing pressure involve changes in bond lengths, bond angles, bond angle distribitions, and Al-coordination changes (Sykes et al., 1993; Malfait et al., 2012; Anderson et al., 2014). Qualitatively, these types of changes are similar to those observed in anhydrous glasses and melts (Yarger et al., 1995; Allwardt et al., 2005; Lee et al., 2006; Sakamaki et al., 2012). Anderson et al. (2014), using X-ray diffraction to examine hydrous aluminosilicate melts at 700°C, concluded that the main structural effect in the pressure range from ambient to 600 MPa was a lengthening of the Si—O(H) bonds (by about 5%, or 0.09 Å). Increasing bond length and Al disorder in alkali aluminosilicate melts were reported by Malfait et al. (2012) to 3.5 GPa from their ^{27}Al MAS NMR study of glasses formed by qenching at 175°C/s from ~450°C to ~850°C. There was, furthermore, a small increase of fivefold coordinated Al^{3+} with increasing pressure, but the pressure effect diminishes with increasing total water content (Fig. 15.30). This latter change also was found to take place with increasing peralkalinity. In other words, increasing pressure results in less depolymerization of a hydrous melt than in its anhydrous equivalent.

15.3.4 H_2O and Other Oxide Components

The solution behavior of water in melts with tetrahedrally coordinated cations other than Si^{4+} or Al^{3+} can be affected by those components, the most important of which are Fe^{3+}, P^{5+}, and possibly Ti^{4+} (see Chapters 11–14). Among those cations, iron is of particular interest as water not only may affect the structural behavior of Fe^{2+} and Fe^{3+}, but dissolved water may also cause changes in activity-composition relations (Gaillard et al., 2003) and the redox ratio of iron (Baker and Rutherford, 1996; Wilke et al., 2002; Botcharnikov et al., 2005)

The activity of FeO in basalt melt increases and that of Fe_2O_3 decreases with increasing water concentration (Gaillard et al., 2003; see Fig. 15.31). From Mössbauer spectroscopy of hydrous, iron-bearing glasses quenched from high-temperature melt, there is no evidence to suggest changes in the structural roles of Fe^{2+} and Fe^{3+} as water is dissolved (Botcharnikov et al., 2005). It follows, therefore, that changes in activity-composition relations are in response to water-induced structural changes, such as depolymerization of the silicate melt structure by solution of H_2O (see, e.g., Eqs. 15.5, 15.6, 15.11). That structural change, in turn, likely changes the extent of steric hindrance near oxygens needed to form Fe^{2+}–O and Fe^{3+}–O ligands. As a result, the activity coefficients of FeO and Fe_2O_3, and therefore the $Fe^{3+}/\Sigma Fe$, vary with water content.

The redox ratio of iron of melts responds to dissolved water. For both a basalt and a rhyolite melt, the $Fe^{3+}/\Sigma Fe$ increases with increasing water content (Baker and Rutherford, 1996; Botcharnikov et al., 2005; see also Fig. 15.32). Such an evolution is to be expected from other experimental data, which show that the ferric/ferrous ratio increases with increasing NBO/Si of silicate melts at constant temperature and pressure (Levy et al., 1976; Virgo et al., 1981; Mysen and Virgo, 1989; Russel and Gerlach, 1999). Dissolved water in general also results in increased NBO/Si of a melt, so that positive correlation of $Fe^{3+}/\Sigma Fe$ with increasing water content of a melt would be expected.

Boron may occopy tetrahedral coordination in the form of BO_4 units in a manner resembling the structural behavior of Al^{3+} in aluminosilicate melts (Fleet and Muthupari, 1999; Du and Stebbins, 2003; Schmidt et al., 2004; Koroleva et al., 2011). Structural association of OH-groups with B^{3+} is also possible (Schmidt et al., 2004). Evidence for B—OH groups can be seen in infrared absoprtion spectra of B-bearing aluminosilicate glasses. There is, in fact, a strong positive correlation between OH/H_2O abundance ratio and boron concentration, whereas the total solubility seems insensitive to B_2O_3 content of the melt (Fig. 15.33). The temperature dependence of Eq. (15.1) from in-situ, high-temperature/-pressure experiments yields $\Delta H = 19.9$ kJ/mol and $\Delta S = 15.5$ J/mol·K (Schmidt et al., 2004). These values are about 20% smaller than those reported for water speciation in similar aluminosilicate melts without boron oxide (Nowak and Behrens, 2001), also suggesting, therefore, an active participation of boron on the solubility behavior of water.

The role of P^{5+} in hydrous systems is not well known. A neutron diffraction study of the system Na_2O-P_2O_5-H_2O (Hoppe et al., 2004) revealed an important role of P—OH functional groups, perhaps, therefore, analogous to Si—OH in hydrous silicate systems (see Section 15.3.2). However, no evidence was found for molecular water in the phosphorus system. The rather significant increase in water solubility in $NaAlSi_3O_8$-$KAlSi_3O_8$-SiO_2-H_2O melt by addition of P_2O_5 (Holtz et al., 1993) and shifts in the granite minimum (London et al., 1993) would be consistent with a P—OH structural role of P^{5+} in P-bearing silicate melts.

15.4 STRUCTURE AND PROPERTIES

Bowen (1928) referred to water in magmatic systems as a "Maxwell's Demon" because, as he described it, H_2O can do whatever one wants it to. Bowen's opinions notwithstanding, solution of water in silicate melts and their glasses has profound effects on their properties (see Chapter 14). At its most basic level, property changes can be related to the effect of dissolved water on the degree of silicate polymerization combined with the fact that, for all practical purposes, nearly all silicate melt properties depend on silicate polymerization.

15.4.1 Transport Properties and Structure

The major transport properties are viscosity, diffusion, and conductivity. The principles that govern their interrelationships were described in Chapter 4, Section 4.6. Among transport properties, viscosity and diffusion have attracted the most attention.

Dissolved water results in greatly increased diffusion coefficients of silicate components (Baker, 1991; Watson, 1994; Mungall and Dingwell, 1994). Diffusion of water itself also depends on water concentration (Karsten et al., 1982; Nowak and Behrens, 1997; Behrens et al., 2004; Okumura and Nakashima, 2004, 2006; Ni et al., 2009; see also Chapter 14, Fig. 14.29). This water concentration dependence is understandable in light of the water species equilibrium (15.1) and the evolution of OH/H_2O abundance ratio with total water content (e.g., Fig. 15.3).

Diffusion of water as OH groups may require some form of Si—OH and/or Al—OH bond breakage unless the diffusing species is the proton, in which case much weaker O—H bonds must be broken and reformed, or the diffusing species is isolated M—OH complexes. By assuming activation energy of diffusion resembles the Si—OH and Al—OH bond strength and Si—O and Al—O bond strengths (which are known) can be used as analogues for Si—OH and Al—OH, the activation energies are in the 200–400 kJ/mol range (Bryce et al., 1999; Morgan and Spera, 2001). The activation energy of water diffusion is significantly dependent on Al/Si ratio, which is consistent with this notion because the Al—O bonds are considerably weaker than Si—O bonds (Smyth and Bish, 1988; see also Chapter 4, Section 4.2). As total water concentration increases, the water diffusivity is increasingly governed by motion of H_2O molecules and isolated M—OH complexes through the melt structure, a process likely associated with considerably smaller activation energy than breakage of Si—OH and Al—OH bonds.

Zhang et al. (1991) combined the water speciation model shown in Eq. (15.1) with diffusion data for water content between 0.2 and 1.7 wt% in a dacitic melt. They modeled the diffusion with the expression:

$$\frac{\partial[\mathrm{water}]}{dt} = \frac{\partial}{\partial X}\left[D_{\mathrm{H2O}}\frac{\partial[\mathrm{H_2O}]}{\partial X} + 1/2 \cdot D_{\mathrm{oH}}\frac{\partial[\mathrm{OH}]}{\partial X}\right], \tag{15.12}$$

where t = time, x = diffusion distance, D_{H2O} and D_{OH} are diffusion constants for molecular H_2O and OH groups, and $[H_2O]$, [OH], and [water] are concentrations of molecular H_2O, OH groups, and total water. As the activation energy of water diffusion at high water content is much less than at low water concentrations, under such high water concentration conditions, the first term in Eq. (15.12) dominates and water diffusion is much faster. At low water content, the second term dominates and because of the likely need to break Si,Al—OH bonds, activation energy and diffusion itself are much smaller. This water diffusion behavior is consistent with the results reported by Zhang et al. (1991).

Given that the OH/H_2O evolution with total water content depends on silicate composition (Figs. 15.3 and 15.15), the implication is that relationships between water diffusion and water concentration also depend on silicate composition. For example, decreasing ionization potential of network-modifying cations or increasing NBO/*T* of the melt will result in a wider water concentration range, where water diffusivity is controlled by OH transport. Temperature-dependent OH/H_2O abundance ratio also leads to the suggestion that such an abundance evolution affects the water diffusion.

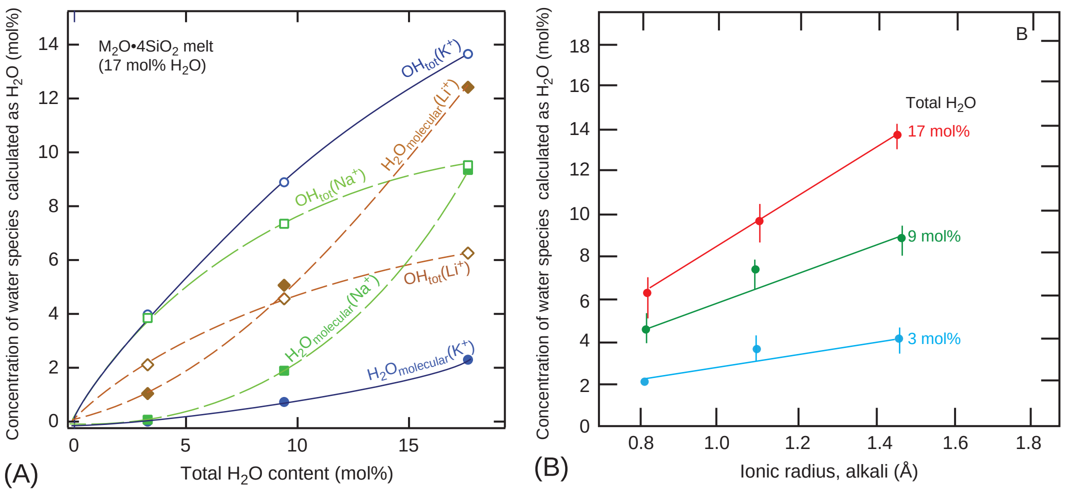

FIG. 15.15 Evolution of water species in alkali silicate melts as a function of total water content and alkali metal type. (A) Evolution of water as OH groups, OH_{tot}, and molecular water, $H_2O_{molecular}$ for tetrasilicate melts of Li, Na, and K. (B) Concentration of OH-species in alkali tetrasilicate melts as a function of ionic radius of alkali metal and total water content as indicated on individual lines (Le Losq et al., 2015).

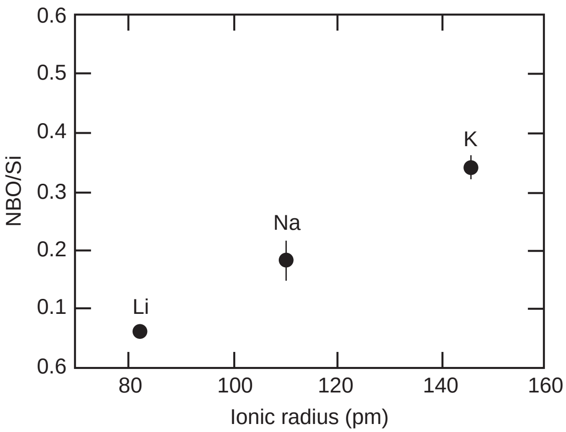

FIG. 15.16 Change in degree of silicate polymerization, ΔNBO/Si, of hydrous (17.6 mol% H_2O) alkali tetrasilicate melts ($M_2O·4SiO_2$) relative to their anhydrous NBO/Si values as a function of ionic radius of the alkali metal (Le Losq et al., 2015).

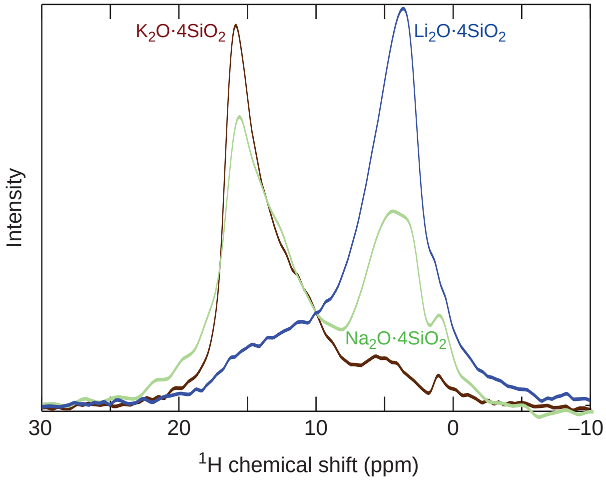

FIG. 15.17 ^{1}H MAS NMR spectra of hydrous (17.6mol 5H_2O) alkali tetrasilicate melts ($M_2O·4SiO_2$) to illustrate how water speciation and abundance depend on the electron properties of the alkali metal (Cody et al., 2005).

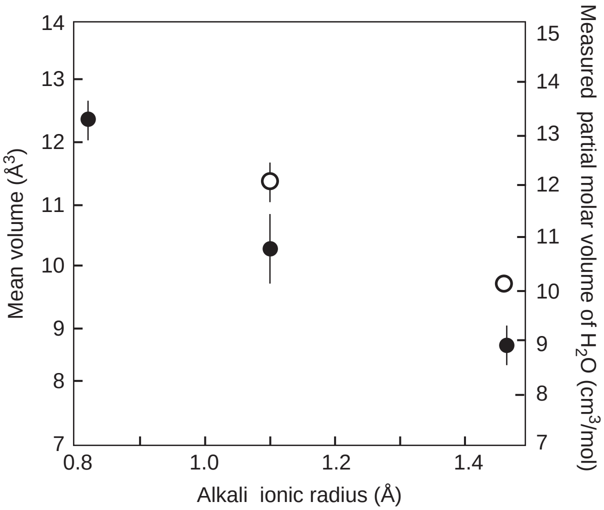

FIG. 15.18 Calculated mean volume for H_2O in $Na_2O·4SiO_2$ melt by using O···H distances from Eq. (15.9) and ^{1}H MAS NMR data (as illustrated in Fig. 15.17) from Le Losq et al. (2015) (*solid symbols*) and measured partial molar volume of H_2O in $Na_2O·4SiO_2$ melt (*open symbols*) from Mysen and Armstrong (2002).

Transport properties of silicate melts are positively correlated with melt polymerization, which in simple aluminosilicate melts and glasses, at least, translates to predominantly an effect of $Al_2O_3+SiO_2$ concentration (Bockris et al., 1955; Ben Martin et al., 2012; Bouhadja et al., 2013). From silicate depolymerization reactions such as Eq. (15.5), formation of OH groups implies silicate depolymerization. That means that the diffusivity of tetrahedrally coordinated cations such as Si^{4+} would show water concentration dependence that qualitatively may resemble that of the OH/H_2O of a melt. This is exactly what happens (Chekhmir et al., 1988).

The viscosity and activation energy of viscous flow as a function of increasing water content also follow a pattern of rapid decrease with the initial 0–2wt% water concentration in melts,

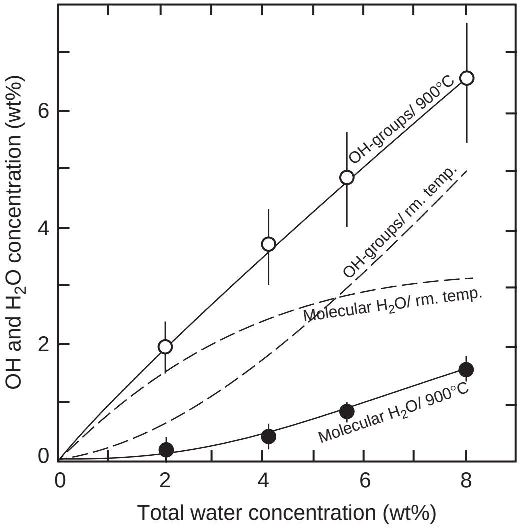

FIG. 15.19 Evolution of OH groups and molecular H_2O in hydrous $Na_2O{\cdot}4SiO_2$ melt (at 900°C) and its glass (ambient temperature—dashed lines) as a function of total water concentration in glass and melt (data from Chertkova and Yamashita, 2015).

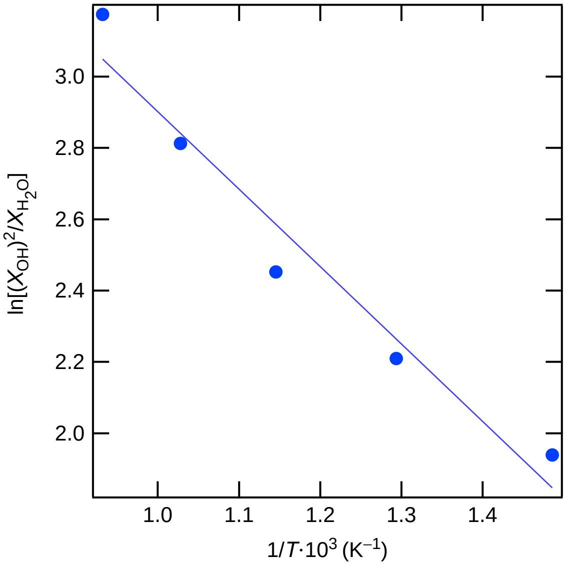

FIG. 15.20 OH/H_2O abundance ratio vs $1/T$ (K^{-1}) of water-saturated $Na_2Si_4O_9$ melt in the 400–800°C temperature and 180–700 MPa pressure range (data from Mysen, 2009). Note that the form OH^2/H_2O is used. This is because in the data set from Mysen (2009), the actual water solubility was not known. The concentration of O^{2-}, needed to compute an equilibrium constant, $K_{15.1}$, could not therefore be carried out. The value of the ratio, OH^2/H_2O, is therefore offset relative to the equivalent $K_{15.1}$. In addition, this offset will change with temperature and pressure because the water solubility changes.

followed by a gradually diminishing dependence on water content (Jewell and Shelby, 1988; Baker, 1996; Liebske et al., 2003). Given the equivalent dependence on water content on melt viscosity and Si^{4+} diffusion, this similarity follows from the decreasing rate of NBO/Si increase with increasing water content of the melt (Fig. 15.1). Notably, the pressure dependence of viscosity of hydrous aluminosilicate melts decreases with increasing water content (Ardia et al., 2008). This evolution also follows from the effect of melt polymerization and pressure-dependent melt viscosity, which decreases as melts become more depolymerized (Scarfe et al., 1987).

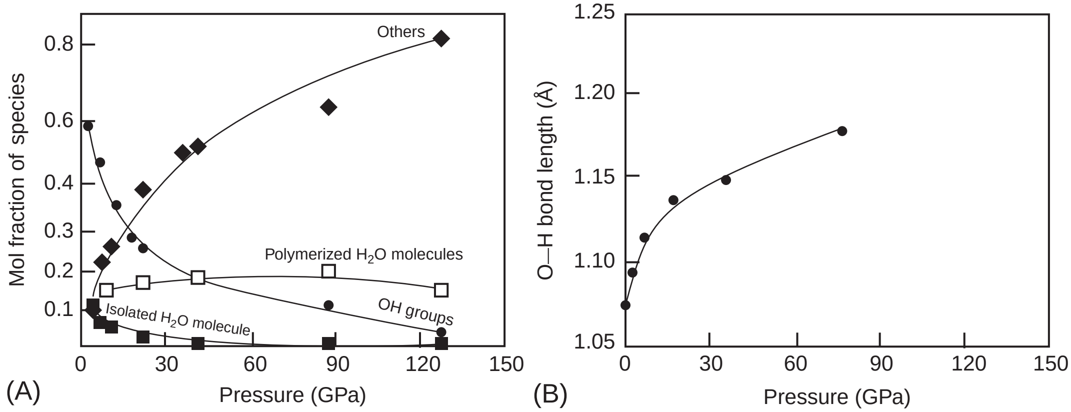

FIG. 15.21 Pressure dependence of water behavior in $MgSiO_3$ melt at 4000 K from first-principles molecular dynamics simulations by Karki et al. (2010). (A) Abundance evolution of individual water species as indicated calculated on the basis of 16H. "Others" means hydrogen that forms two-, three- and even more coordination. This coordination number tends to increase with increasing pressure. (B) Average O—H distance in the hydrous melts as a function of pressure. Si-O and Mg-O distances (not shown) also increase with increasing pressure (Karki et al., 2010).

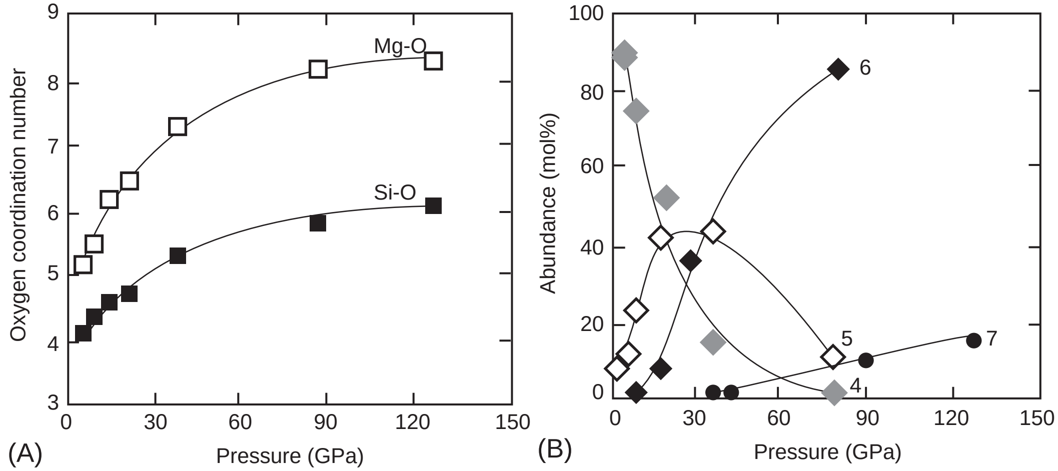

FIG. 15.22 Oxygen coordination environment in hydrous $MgSiO_3$ melts from the first-principles MD simulations of Karki et al. (2010). (A) Pressure evolution of average oxygen coordination numbers for Mg and Si at 4000 K. (B) Pressure evolution of species with 4, 5, 6, and 7 oxygen surrounding Si^{4+}. Numbers on individual curves indicate the oxygen coordination number.

15.4.2 Volume Properties and Structure

The partial molar volume of H_2O in silicate glasses formed by temperature quenching of hydrous melts and measured at ambient temperature and pressure has been reported to be independent of silicate composition (Richet and Polian, 1998; Richet et al., 2000; Ochs and

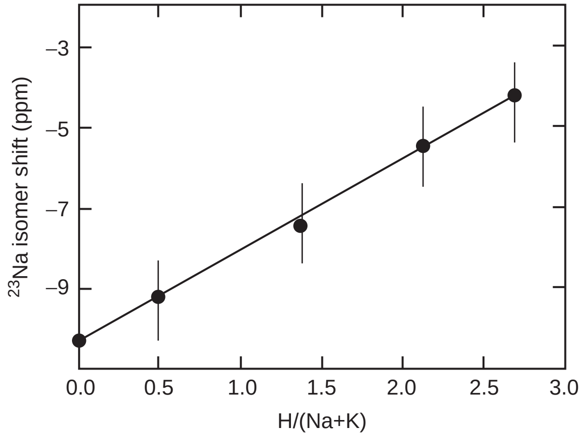

FIG. 15.23 Evolution of the ^{23}Na chemical shift as a function of water content for melts of composition $Na_{0.58}K_{0.43}AlSi_{4.81}O_{11.63}$ as a function of total water content expressed as atomic proportion, H/(Na+K) (data from Schmidt et al., 2001).

Lange, 1999). However, it is clear that volume data obtained on glasses cannot be extrapolated to melts because the thermal expansion coefficients of silicate glasses and melts differ (Bouhifd et al., 2001) and partly because there is extensive hydrogen bonding in hydrous glasses quenched from high temperature, whereas there is no evidence of hydrogen bonding in hydrous melts at temperatures above their liquidus (Section 15.2.1, Fig. 15.5; see also Mysen, 2010).

The thermal expansion difference between a glass and its melt was taken into account by Bouhifd et al. (2015) for some glasses and melts (albite composition, and iron-free tephrite and foidite melts). With this correction, they concluded that partial molar volume of water agreed with the values of hydrous $NaAlSi_3O_8$ melt from Ochs and Lange (1999) to within about 1%. However, the correction of hydrogen bonding is less straightforward. Hydrogen bonding cannot be detected in hydrous melts above about 600°C (Fig. 15.5). It follows that a contribution from hydrogen bonded H_2O and/or OH diminishes gradually with temperature and so will the influence of hydrogen bonding on partial molar volume. High-temperature volume measurements in situ, therefore, are needed. However, such measurements at ambient pressure are challenging because water solubility in silicate melts at ambient pressure is on the order of fractions of a percent. Thus, water exsolves as hydrous glass is heated above its glass transition temperature (Holtz et al., 1996).

Le Losq et al. (2015) proposed an alternative to measuring glass and melt density. They used the NMR results such as in Fig. 15.17 together with Eq. (15.9) to derive a volume of water in the melts by assuming that it can be described as a sphere with radius equal to the sum of the O⋯O distances shown in that figure. This volume is, within <10%, the same as the partial molar volume of H_2O in the same melt composition derived from water solubility measurements (Mysen and Armstrong, 2002). The mean volume of dissolved water in melt thus obtained increases with alkali ionic radius (Fig. 15.18). This volume increase reflects differences of available space in the melt structure within which water species can be located as a function of the size of the alkali metal. Furthermore, if the volume difference for the water solution mchanism differs from 0 (Eq. 15.1), composition-dependent variations of OH/H_2O could result in composition-dependent partial molar volume of water in the melt.

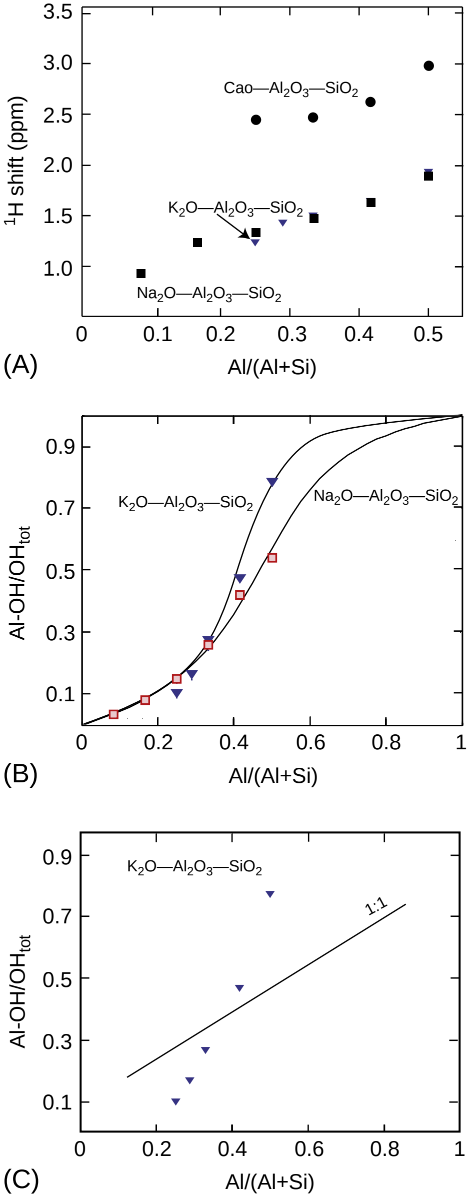

FIG. 15.24 OH speciation in aluminosilicate glasses (quenched melts) as a function of their bulk Al/(Al+Si) (data from Malfait and Xue, 2014). (A) Evolution of the ^{1}H shift near 1–2 ppm (assigned to H resonance in Al—OH bonds) for meta-aluminosilicates along the joins indicated. (B) Abundance evolution of OH groups associated with Al as a function of bulk Al/(Al+Si) for alkali meta-aluminosilicates. (C) Abundance evolution of OH groups associated with Al as a function of bulk Al/(Al+Si) in hydrous K_2O-Al_2O_3-SiO_2 compared with the 1:1 line where the Al/(Al+Si) evolution is identical to the bulk Al/(Al+Si) evolution.

The molar volume of pure H_2O is always greater than the partial molar volume of water in silicate melt at similar temperatures and pressures (Belonoshko and Saxena. 1991; Mysen and Armstrong, 2002; Agee, 2008). Moreover, the pressure dependence of the partial molar volume of water in silicate melts indicates a decrease from values near 29 cm^3/mol at high

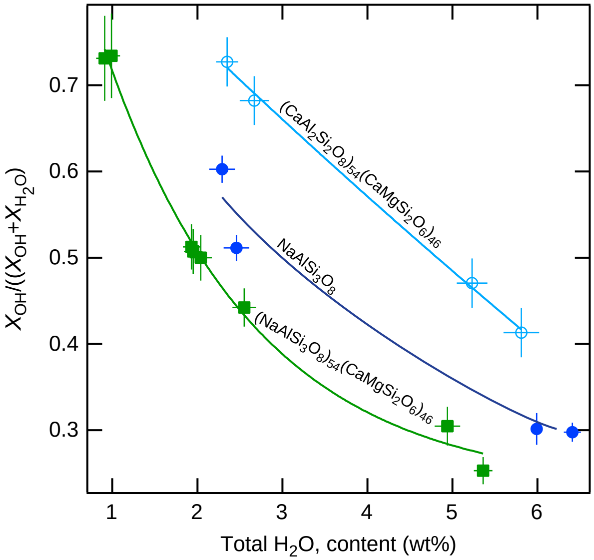

FIG. 15.25 Proportion of OH groups relative to total amount of water as a function of total water content in glasses formed by temperature quenching from 1250°C at 500 MPa pressure for compositions indicated on individual curves. *Redrawn from* Benne and Behrens (2003).

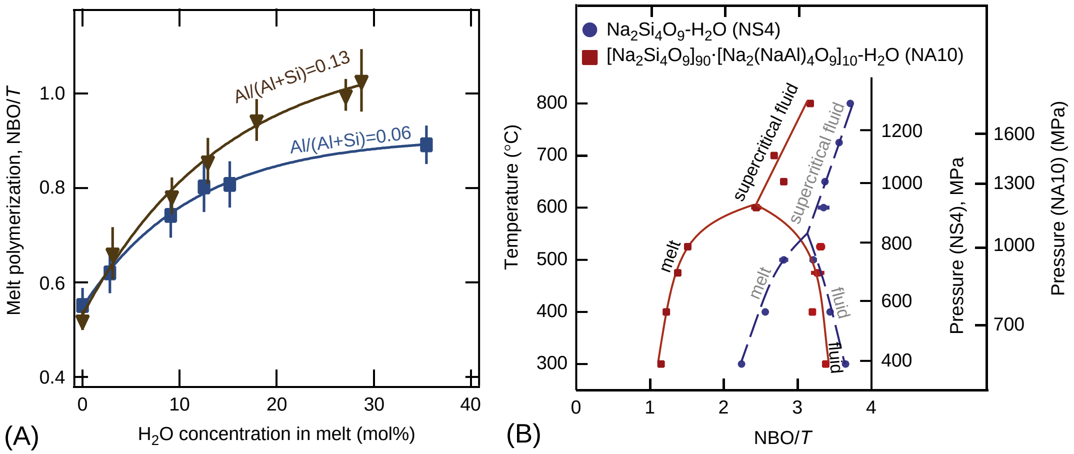

FIG. 15.26 Effect of Al/(Al + Si) on relationship between dissolved water and melt polymerization. (A) Evolution of NBO/*T* (*T* = Si + Al) of hydrous $[Na_2Si_4O_9]_{90}[Na_2(NaAl)_4O_9]_{10}$ melt quenched from 1400°C at 1.5 GPa pressure (data from Mysen, 2007). (B) Evolution of NBO/*T* of coexisting hydrous melt and silicate-saturated aqueous fluid recorded in situ at high temperature and pressure for Al-free melt and NA10 melt (equivalent to $Na_2Si_4O_9$ and $[Na_2Si_4O_9]_{90}[Na_2(NaAl)_4O_9]_{10}$, respectively) (Mysen, 2011).

temperature and ambient pressure to <10 cm^3/mol at pressures >10 GPa pressure (Sakamaki et al., 2012; Agee, 2008; Malfait et al., 2014). This evolution is quite similar to results from first-principles molecular simulations (Anderson et al., 2008; Mookherjee et al., 2008). It is also similar to the evolution of the overall molar volume of the hydrous melt, which suggests that the compressibility of the silicate structure governs the pressure dependence of the partial molar

FIG. 15.27 An example of effects of bulk melt Al/(Al+Si) on Q^n-speciation of melt. The effect is shown as abundance differences for individual species in melts of two different Al/(Al+Si) (data from Mysen et al., 2003). The data are from glasses that were temperature quenched from 1400°C at ~100°C/s while at 1.5 GPa.

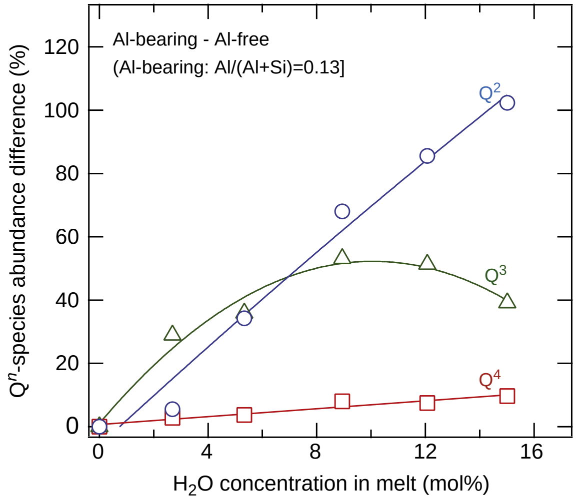

FIG. 15.28 Concentration (wt%) of OH groups of dissolved water in $KAlSi_3O_8$-$NaAlSi_3O_8$-SiO_2-H_2O melt as a function of cooling rate as shown on individual curves. Samples were cooled while kept at high pressures between 500 and 800 MPa (Behrens and Nowak, 2003).

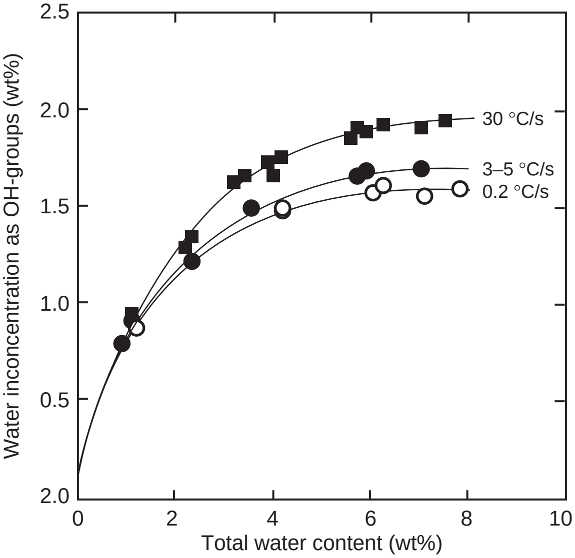

volume of dissolved water, at least in the pressure range up to that where coordination change of Al^{3+} and Si^{4+} takes place (Whittington et al., 2012). After such coordination transformation, melt compressibility and likely the pressure dependence of partial molar volume of dissolved H_2O may change. However, no effect on the coordination change can be seen in the limited information on this subject from numerical simulations of metasilicate melt structures (Adjaouda et al., 2008; Sun et al., 2011).

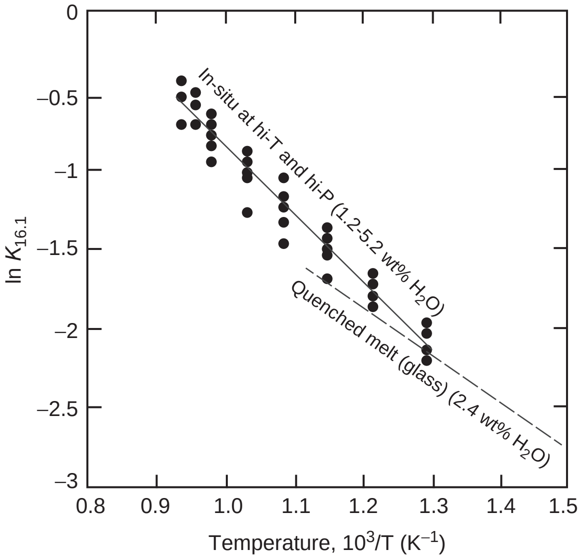

FIG. 15.29 Comparison of temperature-dependent $K_{15.1}$ based on measurements recorded in situ while the samples are at the temperatures and pressures of interest (*filled circles*, data from Nowak and Behrens, 2001), compared with regression curve from hyolite melt equilibrated 500 MPa and 1400°C followed by annealing near glass transition temperature (from Zhang et al., 1995).

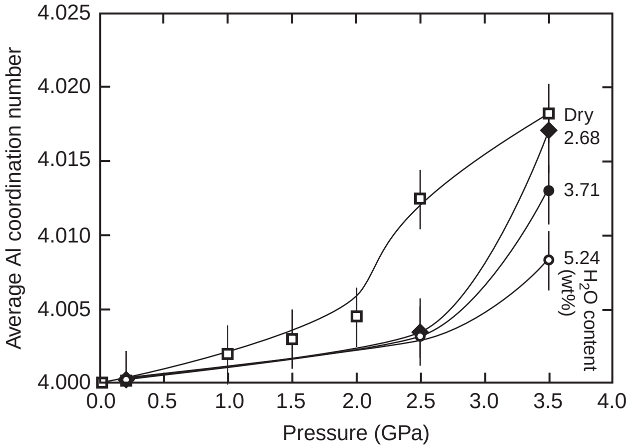

FIG. 15.30 Averaged coordination change of Al^{3+} from ^{27}MAS NMR spectroscopy of glasses in $KAlSi_3O_8$-$NaAlSi_3O_8$-SiO_2-H_2O quenched from high temperature (900–1200°C) with quenching rate of 175 ± 25°C/s. Water concentration of each series of glass is indicated on the individual curves in the figure (data from Malfait et al., 2012).

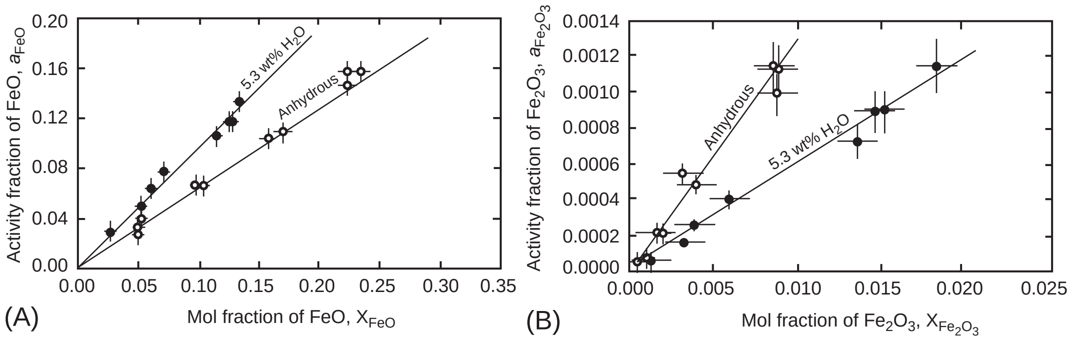

FIG. 15.31 Activity-composition relations of FeO and Fe_2O_3 in hydrous (5.3 wt% H_2O) and anhydrous quenched melts (quenched from 1150–1200°C) at ambient pressure and at 200 MPa (data from Gaillard et al., 2003). (A) Activity-composition relations for FeO. (B) Activity-composition relations for Fe_2O_3.

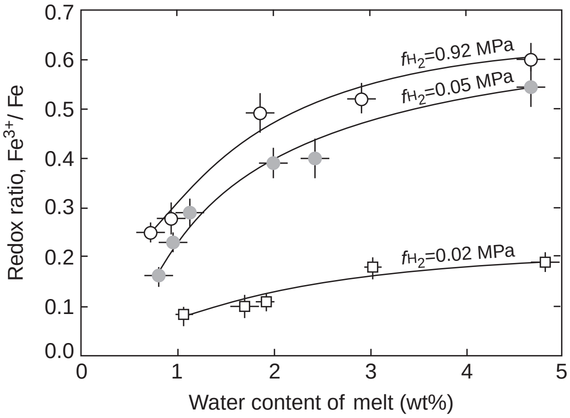

FIG. 15.32 Redox ratio of iron in silicate melts as a function of water content and hydrogen fugacity (as indicated on individual curves). The samples were analyzed by Mössbauer and by Fe K-edge X-ray near edge structure (XANES) spectrometry. Samples were equilibrated at 1200°C and 200 MPa before quenching to a glass (Botcharnikov et al., 2005).

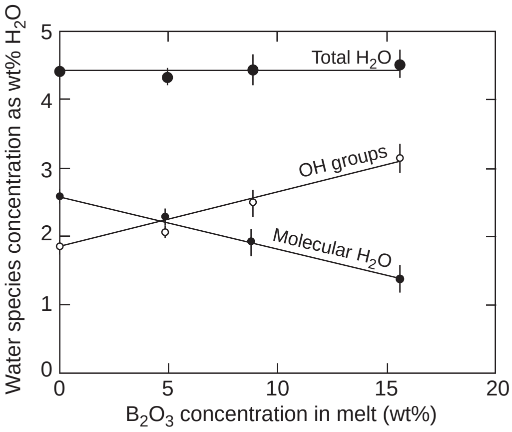

FIG. 15.33 Water speciation in hydrous (4.4 wt% total water content) $NaAlSi_3O_8$-$NaBSi_3O_8$ glass quenched from melt at 1000°C at 200 MP expressed as a function of B_2O_3 content. Water speciation was determined from low-temperature ^{1}NMR spectroscopy (Schmidt et al., 2004).

15.4.3 Crystallization, Melting, and Structure

The solidus temperature decrease of silicates caused by dissolved water is in part because of the dilution of the silicate solution by dissolved water, and in part because of the nature of the interaction between dissolved water and the silicate structure. Notably, water causes a larger depression of the solidus temperature of highly polymerized melt systems compared with depolymerized silicate systems (see Chapter 14, Fig. 14.1). This difference probably results from the fact that depolymerized melts are less prone to further fragmentation than highly polymerized melts in the absence of H_2O (see also Fig. 14.16). Moreover, in highly depolymerized melts, free M—OH complexes become important and increasingly so with increasing M/Si-abundance ratio of the melt (Xue and Kanzaki, 2004; Cody et al., 2005). This mechanism has an overall effect of reducing the degreee of polymerization of the melt, which also explains why the enstatite + forsterite eutectic in the MgO-SiO_2-H_2O system shifts to more silica-rich compositions at very high pressure (Luth, 1993; Xue and Kanzaki, 2008; Yamada et al., 2007).

Depolymerization of a melt via solution of water also leads to a decrease of the activity of SiO_2 because the interconnected silicate network of an anhydrous melt is broken up to form less polymerized entities and OH groups (Eq. 15.1). As a result of the decreased silicate activity, liquidus volumes of polymerized silicate minerals shrink relative to less polymerized minerals. A classic example of this effect is the observation that at high pressure, enstatite ($MgSiO_3$) melts congruently at least to 3 GPa pressure (Boyd et al., 1964), whereas in the presence of excess H_2O, enstatite melts incongruently to form olivine + melt (Kushiro et al., 1968).

An implication of these features is that the effect of dissolved water on the activity of SiO_2 in a silicate melt is positively correlated with the OH/H_2O abundance ratio. This, in turn, implies not only more reduction of a_{SiO2} with increasing water content of a given melt composition (Fig. 15.1), it also implies that any other melt compositional variable affecting the OH/H_2O will affect the extent to which water affects the a_{SiO2}. One might expect, for example, that with decreasing ionization potential of a network-modifying cation, the influence of H_2O on a_{SiO2} would decrease because of the positive correlation between OH/H_2O and the ionization potential.

Related to the behavior of OH groups in aluminosilicate melts is the shift in the "granite minimum" (Tuttle and Bowen, 1958; Luth et al., 1964) away from the SiO_2 apex toward more feldspar-rich compositions with increasing water pressure, P_{H2O}. This shift, in turn, is related to interaction between dissolved water and the alkali aluminate components in the melt. For compositions as aluminous as those corresponding to the granite minimum, structural data summarized previously (Mysen and Virgo, 1986b; Schmidt et al., 2000; Malfait and Xue, 2014) indicate that dissolved water interacts increasingly with Al^{3+}. As a result, the activity of feldspar components in the system decreases relative to that of SiO_2, thus leading to the expansion of the liquidus volume of quartz relative to feldspar.

15.4.4 Water Solubility, Solution Mechanisms, and Structure

Water solubility in silicate melts is a complex function of the silicate composition (see Chapter 14). This behavior reflects relative stabilities of Si—OH, Al—OH, and M—OH complexes in the melt. Such information is not readily available except for some of the M—OH complexes, where Kurkjian and Russell (1958) and Pohlmann et al. (2004) reported that the relative stabilities are Li-OH < Na-OH < K-OH. Increased water solubility in alkali silicate melts with increasing ionization potential of the alkali metal (Kurkjian and Russell, 1958) is, therefore, understandable. Interestingly, when alkali metals serve to charge-balance tetrahedrally coordinated Al^{3+} in meta-aluminosilicate melts, the opposite solubility trend can be seen (Behrens et al., 2001; see also Fig. 14.12). In this case, the reactivity of the (Si, Al)—O bond, which governs reactivity to produce Al—OH, probably governs the solubility. This reactivity increases with increasing ionization potential of the charge-balancing cation (Bouyer et al., 2010).

Relative stability of Al—OH and Si—OH complexes is not established. However, from the increased water solubility with Al/(Al + Si) along SiO_2-aluminate joins (Holtz et al., 2000), one may infer that, at least for alkali meta-aluminosilicate systems, water interaction with Al—O bonds to form Al—OH is preferred over that of Si—O bonds to produce Si—OH. This conclusion is also supported by the observation from Malfait and Xue (2014) that the fraction, Al—OH/total OH, is greater than the bulk Al/(Al+Si) of meta-aluminosilicate melts. Notably, this trend differs from that seen in peralkaline aluminosilicate melts, where the water solubility decreases with increasing peralkalinity (Mysen and Armstrong, 2002), but in this respect resembles that where solubility decreases along SiO_2-alkali oxide joins with increasing alkali/silicon ratio (Mysen and Cody, 2004). Evidently, the effect of increasing peralkalinity dominates over the effect of increased Al/(Al+Si).

References

Ackerson, M.R., Mysen, B., Cody, G., 2017. Speciation of water in basaltic and thyolitic glasses investigated through ^{1}H MAS NMR. In: Abstract SIT26-10, JPGU-AUG Joint Meeting 2017. Japan Geoscience Union, Makuhari, Japan.

Acosta-Vigil, A., London, D., Morgan, G.B., 2005. Contrasting interactions of sodium and potassium with H_2O in haplogranitic liquids and glasses at 200 MPa from hydration-diffusion experiments. Contrib. Mineral. Petrol. 149, 276–287.

Adjaouda, O., Steinle-Neumann, G., Jahn, S., 2008. Mg_2SiO_4 liquid under high pressure from molecular dynamics. Chem. Geol. 256, 185–192.

Agee, C.B., 2008. Compressibility of water in magma and the prediction of density crossovers in mantle differentiation. Philos. Trans. Roy. Soc. A 366, 4239–4252.

Allwardt, J.R., Poe, B.T., Stebbins, J.F., 2005. The effect of fictive temperature on Al coordination in high-pressure (10 GPa) sodium aluminosilicate glasses. Am. Mineral. 90, 1453–1457.

Anderson, K.E., Grauvilardi, L.C., Hirschmann, M.M., 2008. Structure and speciation in hydrous silica melts. 2. Pressure effects. J. Phys. Chem. 112, 13015–13021.

Anderson, A.J., Yan, H., Mayanovic, R.A., Solferino, G., Benmore, C.J., 2014. High-energy X-ray diffraction of a hydrous silicate liquid under conditions of high pressure and temperature in a modified hydrothermal diamond anvil cell. High Press. Res. 34, 100–109.

Ardia, P., Giordano, D., Schmidt, M.W., 2008. A model for the viscosity of rhyolite as a function of H_2O-content and pressure: a calibration based on centrifuge piston cylinder experiments. Geochim. Cosmochim. Acta 72, 6103–6123.

Baker, D.R., 1991. Interdiffusion of hydrous dacitic and rhyolitic melts and the efficacy of rhyolite contamination of dacitic enclaves. Contrib. Mineral. Petrol. 106, 462–473.

Baker, D.R., 1996. Granitic melt viscosities: empirical and configurational entropy models for their calculation. Am. Mineral. 81, 126–134.

Baker, L.L., Rutherford, M.J., 1996. The effect of dissolved water on the oxidation state of silicic melts. Geochim. Cosmochim. Acta 60, 2179–2187.

Behrens, H., Nowak, M., 2003. Quantification of H_2O speciation in silicate glasses and melts by IR spectroscopy—in situ versus quench techniques. Phase Trans. 76, 45–61.

Behrens, H., Schmidt, M.O., 1998. Infrared spectroscopy of hydrous silicic glasses at temperatures up to 600 degrees C and implications for the incorporation and dynamics of water in glasses. Neues JB Miner. Abh. 172, 203–226.

Behrens, H., Yamashita, S., 2008. Water speciation in hydrous sodium tetrasilicate and hexasilicate melts: constraint from high temperature NIR spectroscopy. Chem. Geol. 256, 306–315.

Behrens, H., Romano, C., Nowak, M., Holtz, F., Dingwell, D.B., 1996. Near-infrared spectroscopic determination of water species in glasses in the system $MAlSi_3O_8$ (M=Li, Na, K): in interlaboratory study. Chem. Geol. 128, 41–63.

Behrens, H., Meyer, M., Holtz, F., Benne, D., Nowak, M., 2001. The effect of alkali ionic radius, temperature, and pressure on the solubility of water in $MAlSi_3O_8$ melts (M = Li, Na, K, Rb). Chem. Geol. 174, 275–289.

Behrens, H., Zhang, Y.X., Xu, Z.G., 2004. H_2O diffusion in dacitic and andesitic melts. Geochim. Cosmochim. Acta 68, 5139–5150.

Belonoshko, A., Saxena, S.K., 1991. A molecular dynamics study of the pressure-volume-temperature properties of super-critical fluids: I. H_2O. Geochim. Cosmochim. Acta 55, 381–387.

Ben Martin, G., Ghiorso, M., Spera, F.J., 2012. Transport properties and equation of state of 1-bar eutectic melt in the system $CaAl_2Si_2O_8$-$CaMgSi_2O_6$ by molecular dynamics simulation. Am. Mineral. 97, 1155–1164.

Benne, D., Behrens, H., 2003. Water solubility in haplobasaltic melts. Eur. J. Mineral. 15, 803–814.

Bockris, J.O.'.M., Mackenzie, J.O., Kitchner, J.A., 1955. Viscous flow in silica and binary liquid silicates. Trans. Faraday Soc. 51, 1734–1748.

Botcharnikov, R.E., Koepke, J., Holtz, F., McCammon, C., Wilke, M., 2005. The effect of water activity on the oxidation and structural state of Fe in a ferro-basaltic melt. Geochim. Cosmochim. Acta 69, 5071–5085.

Botcharnikov, R., Behrens, H., Holtz, F., 2006. Solubility and speciation of C–O–H fluids in andesitic melt at $T = 1100$–1300 °C and $P = 200$ and 500 MPa. Chem. Geol. 229, 125–143.

Bouhadja, M., Jakse, N., Pasturel, A., 2013. Structural and dynamic properties of calcium aluminosilicate melts: a molecular dynamics study. J. Chem. Phys. 138 https://dx.doi.org/10.1063/1.4809523.

Bouhifd, M.A., Whittington, A., Richet, P., 2001. Partial molar volume of water in phonolitic glasses and liquids. Contrib. Mineral. Petrol. 142, 235–243.

Bouhifd, M.A., Whittington, A.G., Richet, P., 2015. Densities and volumes of hydrous silicate melts: new measurements and predictions. Chem. Geol. 418, 40–50.

Bouyer, F., Geneste, G., Ispas, S., Kob, W., Ganster, P., 2010. Water solubility in calcium aluminosilicate glasses investigated by first principles techniques. J. Solid State Chem. 183, 2786–2796.

Bowen, N.L., 1928. The Evolution of the Igneous Rocks. Princeton University Press, Princeton.

Boyd, F.R., England, J.L., Davis, B.C.T., 1964. Effect of pressure on the melting and polymorphism of enstatite, $MgSiO_3$. J. Geophys. Res. 69, 2101–2109.

Bridgman, P.W., Simon, I., 1953. Effects of very high pressure on glass. J. Appl. Phys. 24, 405–413.

Bryce, J.G., Spera, F.J., Stein, D.J., 1999. Pressure dependence of self-diffusion in the $NaAlO_2$-SiO_2 system: compositional effects and mechanisms. Am. Fortschr. Mineral. 84, 345–356.

Buhler, P., 1999. Thermodynamics of reactions between oxide glass melts and gases: I. Solubility of water vapor. Glass Phys. Chem. 25, 427–433.

Chekhmir, A.S., Epel'baum, M.B., Simakin, A.G., 1988. Water transport in magmas. Geochem. Int. 26, 125–127.

Chertkova, N., Yamashita, S., 2015. In situ spectroscopic study of water speciation in the depolymerized $Na_2Si_2O_5$ melt. Chem. Geol. 409, 149–156.

Clemens, J.D., Navrotsky, A., 1987. Mixing properties of $NaAlSi_3O_8$ melt-H_2O: new calorimetric data and some geological implications. J. Geol. 95, 173–186.

Closman, C., Williams, Q., 1995. In-situ spectroscopic investigation of high-pressure hydrated (Mg,Fe)SiO_3 glasses: OH vibrations as a probe of glass structure. Am. Mineral. 80, 201–212.

Cody, G.D., Mysen, B.O., Lee, S.K., 2005. Structure vs. composition: a solid state ^1H and ^{29}Si NMR study of quenched glasses along the Na_2O-SiO_2-H_2O join. Geochim. Cosmochim. Acta 69, 2373–2384.

Deubner, J., Müller, R., Behrens, H., Heide, G., 2003. Water and the glass transition temperature of silicate melts. J. Non-Cryst. Solids 330, 268–273.

Dingwell, D.B., Webb, S.L., 1990. Relaxation in silicate melts. Eur. J. Mineral. 2, 427–449.

Doremus, R.H., 2000. Diffusion of water in rhyolite glass: diffusion-reaction model. J. Non-Cryst. Solids 261, 101–107.

Du, L.S., Stebbins, J.F., 2003. Nature of silicon-boron mixing in sodium borosilicate glasses: a high-resolution ^{11}B and ^{17}O NMR study. J. Phys. Chem. 107, 10063–10076.

Eckert, H., Yesinowski, J.P., Silver, L.A., Stolper, E.M., 1988. Water in silicate glasses: quantification and structural studies by ^1H solid echo and MAS NMR methods. J. Phys. Chem. 92, 2055–2064.

Farnan, I., Kohn, S.C., Dupree, R., 1987. A study of the structural role of water in hydrous silica using cross-polarisation magic angle NMR. Geochim. Cosmochim. Acta 51, 2869–2874.

Fleet, M.E., Muthupari, S., 1999. Coordination of boron in alkali borosilicate glasses using XANES. J. Non-Cryst. Solids 255, 233–241.

Fukui, H., Kanzaki, M., Hiraoka, N., Cai, Y.Q., 2009. Coordination environment of silicon in silica glass up to 74 GPa: an x-ray Raman scattering study at the silicon L-edge. Phys. Rev. B. 78 https://dx.doi.org/10.1103/PhysRevB.78.012203.

Gaillard, F., Pichavant, M., Scaillet, B., 2003. Experimental determination of activities of FeO and Fe2O3 components in hydrous silicic melts under oxidizing conditions. Geochim. Cosmochim. Acta 67, 4389–4409.

Gervais, F., Lagrange, C., Blin, A., Aliari, M., Hauret, G., Coutoures, J.P., Leroux, M., 1990. Comparison of dielectric response deduced from infrared reflectivity and Raman spectra of silicate glasses. J. Non-Cryst. Solids 119, 79–88.

Ghosh, D.B., Karki, B.B., Stuxrude, L., 2014. First-principles molecular dynamics simulations of $MgSiO_3$ glass: structure, density, and elasticity at high pressure. Am. Mineral. 99, 1304–1314.

Hodges, F.N., 1974. The solubility of H_2O in silicate melts. Carnegie Instn. Wash Year Book 73, 251–255.

Holtz, F., Dingwell, D.B., Behrens, H., 1993. Effects of F, B_2O_3, and P_2O_5 on the solubility of water in haplogranitic melts compared to natural silicate melts. Contrib. Mineral. Petrol. 113, 492–501.

Holtz, F., Behrens, H., Dingwell, D.B., Johannes, W., 1995. H_2O solubility in haplogranitic melts: compositional, pressure, and temperature dependence. Am. Mineral. 80, 94–108.

Holtz, F., Beny, J.M., Mysen, B.O., Pichavant, M., 1996. High-temperature Raman spectroscopy of silicate and aluminosilicate hydrous glasses: implications for water speciation. Chem. Geol. 128, 25–39.

Holtz, F., Roux, J., Behrens, H., Pichavant, M., 2000. Water solubility in silica and quartzofeldspathic melts. Am. Mineral. 85, 682–686.

Hoppe, U., Kranold, R., Stachel, D., Barz, A., Benmore, C.J., 2004. Structural role of water in a sodium phosphate glass by neutron diffraction. Z. Naturforsch. A 59, 879–887.

Hui, H., Zhang, Y., Xu, Z., Behrens, H., 2008. Pressure dependence of the speciation of dissolved water in rhyolitic melts. Geochim. Cosmochim. Acta 72 (13), 3229–3240.

Ihinger, P.D., Zhang, Y.X., Stolper, E.M., 1999. The speciation of dissolved water in rhyolitic melt. Geochim. Cosmochim. Acta 63, 3567–3578.

Jewell, J.M., Shelby, J.E., 1988. Effect of water content and alumina additions on the transformation range properties of Na_2O-$3SiO_2$ glass. J. Non-Cryst. Solids 102, 24–29.

Karki, B.B., Bhattarai, D., Mookherjee, M., Stixrude, L., 2010. Visualization-based analysis of structural and dynamical properties of simulated hydrous silicate melt. Phys. Chem. Mineral. 37, 103–117.

Karsten, J.L., Holloway, J.R., Delaney, J.R., 1982. Ion microprobe studies of water in silicate melts; temperature-dependent water diffusion in obsidian. Earth Planet. Sci. Lett. 59, 420–428.

Keppler, H., Bagdassarov, N.S., 1993. High-temperature FTIR spectra of H_2O in rhyolite melt to 1300 degrees C. Am. Mineral. 78, 1324–1327.

Koroleva, O.N., Shabunina, L.A., Bykov, V.N., 2011. Structure of borosilicate glasses according to Raman spectroscopic data. Glas. Ceram. 67, 340–342.

Kubicki, J.D., Hemley, R.J., Hofmeister, A.M., 1992. Raman and infrared study of pressure-induced structural changes in $MgSiO_3$, $CaMgSi_2O_6$, and $CaSiO_3$ glasses. Am. Mineral. 77, 258–269.

Kubicki, J.D., Sykes, D., Rossman, G.R., 1993. Calculated trends of OH infrared stretching vibrations with composition and structure in aluminosilicate molecules. Phys. Chem. Minerals 20, 425–432.

Kummerlen, J., Merwin, L.H., Sebald, A., Keppler, H., 1992. The structural role of H_2O in sodium-silicate glasses—results from Si-29 and H-1 NMR spectroscopy. J. Phys. Chem. A 96, 6405–6410.

Kurkjian, C.R., Russell, L.E., 1958. Solubility of water in molten alkali silicates. J. Soc. Glass Technol. 42, 130T–144T.

Kushiro, I., Yoder Jr., H.S., Nishikawa, M., 1968. Effect of water on the melting of enstatite. Geol. Soc. Am. Bul. 79, 1685–1692.

Le Losq, C., Cody, C.D., Mysen, B.O., 2015. Alkali influence on the water speciation and the environment of protons in silicate glasses revealed by ^1H MAS NMR spectroscopy. Am. Mineral. 100, 466–482.

Lee, S.K., Stebbins, J.F., 2003. The distribution of sodium ions in aluminosilicate glasses: a high-field Na-23 MAS and 3Q MAS NMR study. Geochim. Cosmochim. Acta 67, 1699–1709.

Lee, S.K., Cody, G.D., Fei, Y.W., Mysen, B.O., 2006. The effect of Na/Si on the structure of sodium silicate and aluminosilicate glasses quenched from melts at high pressure: a multi-nuclear (Al-27, Na-23, O-17) 1D and 2D solid-state NMR study. Chem. Geol. 229, 162–172.

Lee, S.K., Yi, Y.S., Cody, G.D., Mibe, K., Fei, Y.W., Mysen, B.O., 2012. Effect of network polymerization on the pressure-induced structural changes in sodium aluminosilicate glasses and melts: Al-27 and O-17 solid-state NMR study. J. Phys. Chem. C 116, 2183–2191.

Levy, R.A., Lupis, C.H., Flinn, P.A., 1976. Mössbauer analysis of the valence and coordination of iron cations in SiO_2-Na_2O-CaO glasses. Phys. Chem. Glasses 17, 94–103.

Liebske, C., Behrens, H., Holtz, F., Lange, R.A., 2003. The effect of pressure and composition on the viscosity of andesitic melts. Geochim. Cosmochim. Acta 67, 473–486.

Liu, Y., Nekvasil, H., Long, H., 2002. Water dissolution in albite melts: constraints from ab initio NMR calculations. Geochim. Cosmochim. Acta 66, 4149–4163.

Liu, Y., Behrens, H., Zhang, X., 2004. The speciation of dissolved H_2O in dacitic melt. Am. Mineral. 89, 277–284.

London, D., Morgan, G.B., Babb, H.A., Loomis, J.L., 1993. Behavior and effects of phosphorus in the system Na_2O-K_2O-Al_2O_3-SiO_2-P_2O_5-H_2O at 200 MPa (H_2O). Contrib. Mineral. Petrol. 113, 450–465.

Luth, R.W., 1993. Melting in the Mg_2SiO_4-H_2O system at 3 to 12 GPa. Geophys. Res. Lett. 20, 233–235.

Luth, W.C., Jahns, R.H., Tuttle, O.F., 1964. The granite system at pressures of 4 to 10 kilobars. J. Geophys. Res. 69, 759–773.

Maekawa, H., Maekawa, T., Kawamura, K., Yokokawa, T., 1991. The structural groups of alkali silicate glasses determined from ^{29}Si MAS-NMR. J. Non-Cryst. Solids 127, 53–64.

Maekawa, H., Saito, T., Yokokawa, T., 1998. Water in silicate glass: O-17 NMR of hydrous silica, albite, and $Na_2Si_4O_9$ glasses. J. Phys. Chem. B 102, 7523–7529.

Malfait, W.J., Xue, X., 2010. The nature of hydroxyl groups in aluminosilicate glasses: quantifying Si-OH and Al-OH abundances along the SiO2-NaAlSiO4 join by H-1, Al-27-H-1 and Si-29-H-1 NMR spectroscopy. Geochim. Cosmochim. Acta 74 (2), 719–737.

Malfait, W.J., Xue, X., 2014. Hydroxyl speciation in felsic magmas. Geochim. Cosmochim. Acta 140, 606–620.

Malfait, W.J., Verel, R., Ardia, P., Sanchez-Valle, C., 2012. Aluminum coordination in rhyolite and andesite glasses and melts: effect of temperature, pressure, composition and water content. Geochim. Cosmochim. Acta 77, 11–26.

Malfait, W.J., Seifert, R., Petitgirard, S., Mezouar, M., Sanchez-Valle, C., 2014. The density of andesitic melts and the compressibility of dissolved water in silicate melts at crustal and upper mantle conditions. Earth Planet. Sci. Lett. 393, 31–38.

Mandeville, C.W., Webster, J.D., Rutherford, M.J., Taylor, B.E., Timbal, A., Faure, K., 2002. Determination of molar absorptivities for infrared absorption bands of H_2O in andesitic glasses. Am. Mineral. 87, 813–821.

McMillan, P.F., Remmele, R.L., 1986. Hydroxyl sites in SiO_2 glass: a note on infrared and Raman spectra. Am. Mineral. 71, 772–778.

Mookherjee, M., Stixrude, L., Karki, B., 2008. Hydrous silicate melt at high pressure. Nature 452, 983–986.

Morgan, N.A., Spera, F.J., 2001. Glass transition, structural relaxation, and theories of viscosity: a molecular dynamics study of amorphous $CaAl_2Si_2O_8$. Geochim. Cosmochim. Acta 65, 4019–4041.

Moulson, A.J., Roberts, J.P., 1961. Water in silica glass. Trans. Faraday Soc. 57, 1208–1216.

Mungall, J.E., Dingwell, D.B., 1994. Einflusse von Temperature, Druck und Wassergehalt aud die Diffusion von AktinideTracern in Schmelzen haplogranitischer Zussamensetzug. Annual Report. Bayreisches Forschungsinstitut fur Experimentelle Geochemie und Geophysik Universitat Beyreuth, Bayreuth, pp. 91–92.

Mysen, B., 1992. Peralkalinitt, Al-Si substitution, and solubility mechanisms of H_2O in aluminosilicate melts. J. Petrol. 33, 347–375.

Mysen, B.O., 2007. The solution behavior of H_2O in peralkaline aluminosilicate melts at high pressure with implications for properties of hydrous melts. Geochim. Cosmochim. Acta 71, 1820–1834.

Mysen, B.O., 2009. Solution mechanisms of silicate in aqueous fluid and H_2O in coexisting silicate melts determined in-situ at high pressure and high temperature. Geochim. Cosmochim. Acta 73, 5748–5763.

Mysen, B., 2010. Structure of H_2O-saturated peralkaline aluminosilicate melt and coexisting aluminosilicate-saturated aqueous fluid determined in-situ to 800C and 800 MPa. Geochim. Cosmochim. Acta 74, 4123–4139.

Mysen, B.O., 2011. An experimental study of phosphorous and aluminosilicate speciation in and partitioning between aqueous fluids and silicate melts determined in-situ at high temperature and pressure. Am. Mineral. 96, 1636–1649.

Mysen, B.O., 2012. Silicate-COH melt and fluid structure, their physicochemical properties, and partitioning of nominally refractory oxides between melts and fluids. Lithos 148, 228–246.

Mysen, B.O., Armstrong, L., 2002. Solubility behavior of alkali aluminosilicate components in aqueous fluids and silicate melts at high pressure and temperature. Geochim. Cosmochim. Acta 66, 2287–2298.

Mysen, B.O., Cody, G.D., 2004. Solubility and solution mechanism of H_2O in alkali silicate melts and glasses at high pressure and temperature. Geochim. Cosmochim. Acta 68, 5113–5126.

Mysen, B.O., Cody, G.D., 2005. Solution mechanisms of H_2O in depolymerized peralkaline melts. Geochim. Cosmochim. Acta 69, 5557–5566.

Mysen, B.O., Virgo, D., 1986a. Volatiles in silicate melts at high pressure and temperature. 1. Interaction between OH-groups and Si^{4+}, Al^{3+}, Ca^{2+}, Na^+, and H^+. Chem. Geol. 57, 303–331.

Mysen, B.O., Virgo, D., 1986b. The structure of melts in the system Na_2O-CaO-Al_2O_3-SiO_2-H_2O quenched from high temperature at high pressure. Chem. Geol. 57, 333–358.

Mysen, B.O., Virgo, D., 1989. Redox equilibria, structure, and properties of Fe-bearing aluminosilicate melts: relationships between temperature, composition, and oxygen fugacity in the system Na_2O-Al_2O_3-SiO_2-Fe-O. Am. Mineral. 74, 58–76.

Mysen, B.O., Lucier, A., Cody, G.D., 2003. The structural behavior of Al^{3+} in peralkaline melts and glasses in the system Na_2O-Al_2O_3-SiO_2. Am. Mineral. 88, 1668–1678.

Ni, H., Behrens, H., Zhang, Y., 2009. Water diffusion in dacitic melt. Geochim. Cosmochim. Acta 73, 3642–3655.

Nowak, M., Behrens, H., 1995. The speciation of water in haplogranitic glasses and melts determined by in-situ near infrared spectroscopy. Geochim. Cosmochim. Acta 59, 3445–3450.

Nowak, M., Behrens, H., 1997. An experimental investigation on diffusion of water in haplogranitic melts. Contrib. Mineral. Petrol. 126, 365–376.

Nowak, M., Behrens, H., 2001. Water in rhyolitic magmas: getting a grip on a slippery problem. Earth Planet. Sci. Lett. 184, 515–522.

Ochs, F.A., Lange, R.A., 1999. The density of hydrous magmatic liquids. Science 283, 1314–1317.

Ohlhorst, S., Behrens, H., Holtz, F., 2001. Compositional dependence of molar absorptivities of near-infrared OH- and H_2O bands in rhyolitic to basaltic glasses. Chem. Geol. 174, 5–20.

Okumura, S., Nakashima, S., 2004. Water diffusivity in rhyolitic glasses as determined by in situ IR spectroscopy. Phys. Chem. Minerals 31, 183–189.

Okumura, S., Nakashima, S., 2006. Water diffusion in basaltic to dacitic glasses. Chem. Geol. 227, 70–82.

Padro, D., Schmidt, B.C., Dupree, R., 2003. Water solubility mechanism in hydrous aluminosilicate glass: information from ^{27}Al MAS and MQMAS NMR. Geochim. Cosmochim. Acta 67, 1543–1552.

Paterson, M.S., 1982. The determination of hydroxyl by infrared absorption in quartz, silicate glasses and similar materials. Bull. Mineral. 105, 20–29.

Pohlmann, M., Benoit, M., Kob, W., 2004. First-principles molecular-dynamics simulations of a hydrous silica melt: structural properties and hydrogen diffusion mechanism. Phys. Rev. B. 70 https://dx.doi.org/10.1103/PhysRevB.70.184209.

Reimers, J.R., Watts, R.O., 1984. The structure and vibrational spectra of small clusters of water molecules. J. Phys. Chem. 85, 83–112.

Richet, P., Polian, A., 1998. Water as a dense icelike component in silicate glasses. Science 281, 396–398.

Richet, P., Whittington, A., Holtz, F., Behrens, H., Ohlhorst, S., Wilke, M., 2000. Water and the density of silicate glasses. Contrib. Mineral. Petrol. 138, 337–347.

Richet, P., Hovis, G., Whittington, A., Roux, J., 2004. Energetics of water dissolution in trachyte glasses and liquids. Geochim. Cosmochim. Acta 68, 5151–5158.

Robert, E., Whittington, A., Fayon, F., Pichavant, M., Massiot, D., 2001. Structural characterization of water-bearing silicate and aluminosilicate glasses by high-resolution solid-state NMR. Chem. Geol. 174, 291–305.

Russel, C., Gerlach, S., 1999. The effect of glass composition on the Fe^{2+}/Fe^{3+} equilibrium. Ceramics-Silikaty 43, 165–168.

Sakamaki, T., Wang, Y.B., Park, C., Yu, T., Shen, G.Y., 2012. Structure of jadeite melt at high pressures up to 4.9 GPa. J. Appl. Phys. 111 https://dx.doi.org/10.1063/1.4726246.

Sanloup, C., Drewitt, J.W.E., Konopkova, Z., Dallady-Simpson, P., Morton, D.M., Rai, N., van Westrenen, W., Morgenroth, W., 2013. Structural change in molten basalt at deep mantle conditions. Nature 503, 104–107.

Sato, T., Funamori, N., 2008. Sixfold-coordinated amorphous polymorph of SiO_2 under high pressure. Phys. Rev. Lett. 101, 255–502.

Scaller, T., Sebald, A., 1995. One- and two-dimensional ^1H magic-angle spinning experiments on hydrous silicate glasses. Solid State Nucl. Magn. Reson. 5, 89–102.

Scarfe, C.M., Mysen, B.O., Virgo, D., 1987. Pressure-dependence of the viscosity of silicate melts. In: Mysen, B.O. (Ed.), Magmatic Processes: Physicochemical Principles. Geochemical Society, University Park, PA.

Schmidt, B.C., Riemer, T., Kohn, S.C., Behrens, H., Dupree, R., 2000. Different water solubility mechanisms in hydrous glasses along the Qz-Ab join: evidence from NMR spectroscopy. Geochim. Cosmochim. Acta 64, 513–526.

Schmidt, B.C., Riemer, T., Kohn, S.C., Holtz, F., Dupree, R., 2001. Structural implications of water dissolution in haplogranitic glasses from NMR spectroscopy: influence of total water content and mixed alkali effect. Geochim. Cosmochim. Acta 65, 2949–2964.

Schmidt, B.C., Zotov, N., Dupree, R., 2004. Structural implications of water and boron dissolution in albite glass. J. Non-Cryst. Solids 337, 207–219.

Scholze, H., 1960. Über die quantitative IR-Spektrosskopische Wasser-Bestimmung in Sillicaten. Fortschr. Mineral. 38, 122–123.

Shen, A., Keppler, H., 1995. Infrared spectroscopy of hydrous silicate melts to 1000 degrees C and 10 kbar: Direct observation of H_2O speciation in a diamond-anvil cell. Am. Mineral. 80, 1335–1338.

Silver, L., Stolper, E., 1989. Water in albitic glasses. J. Petrol. 30, 667–710.

Silver, L., Ihinger, P.D., Stolper, E., 1990. The influence of bulk composition on the speciation of water in silicate glasses. Contrib. Mineral. Petrol. 104, 142–162.

Simakin, A.G., Salova, T.P., Eremyashev, V.E., 2010. Mechanism of water solubility in silicate melts of the albite-nepheline system. Mineral. Petrol. 99, 279–285.

Smyth, J.R., Bish, D.L., 1988. Crystal Structures and Cation Sites of the Rock-Forming Minerals. Allen & Unwin, Boston.

Sowerby, J.R., Keppler, H., 1999. Water speciation in rhyolitic melt determined by in-situ infrared spectroscopy. Am. Mineral. 84, 1843–1849.

Sowerby, J.R., Keppler, H., 2002. The effect of fluorine, boron and excess sodium on the critical curve in the albite-H_2O system. Contrib. Mineral. Petrol. 143, 32–37.

Stebbins, J.F., 1988. Effects of temperature and composition on silicate glass structure and dynamics: Si-29 NMR results. J. Non-Cryst. Solids 106, 359–369.

Stolen, R.H., Walrafen, G.E., 1976. Water and its relation to broken bond defects in fused silica. J. Chem. Phys. 64, 2623–2631.

Stolper, E., 1982. The speciation of water in silicate melts. Geochim. Cosmochim. Acta 46, 2609–2620.

Sun, N., Stixrude, L., De Koker, N., Kakrki, B.B., 2011. First principles molecular dynamics simulations of diopside ($CaMgSi_2O_6$) liquid to high pressure. Geochim. Cosmochim. Acta 75, 3792–3802.

Sykes, D., Kubicki, J.D., 1993. A model of H_2O solubility mechanisms in albite melts from infrared spectroscopy and molecular orbital calculations. Geochim. Cosmochim. Acta 57, 1039–1052.

Sykes, D., Sato, R., Luth, R.W., McMillan, P., Poe, B., 1993. Water solubility mechanisms in $KAlSi_3O_8$ melts at high pressure. Geochim. Cosmochim. Acta 57, 3575–3584.

Tossell, J.A., 1999. Quantum mechanical calculation of ^{23}Na NMR shieldings in silicates and aluminosilicates. Phys. Chem. Mineral. 27, 70–80.

Tuttle, O.F., Bowen, N.L., 1958. Origin of granite in light of experimental studies in the system $NaAlSi_3O_8$-$KAlSi_3O_8$-SiO_2-H_2O. Geol. Soc. Amer. Mem. 74, 1–153.

Valyashko, V.M., Buback, M., Franck, E.U., 1981. Infrared absorption of concentrated aqueous $NaClO_4$ solutions to high pressures and temperatures. Z. Nat. A 36, 1169–1176.

Virgo, D., Mysen, B.O., Seifert, F.A., 1981. Relationship between the oxidation state of iron and structure of silicate melts. Carnegie Instn. Washington Year Book 80, 308–311.

Wang, Y., Cody, S.X., Foustoukos, D., Mysen, B.O., Cody, G.D., 2015. Very large differences in intramolecular D-H partitioning in hydrated silicate melts synthesized at upper mantle pressures and temperatures. Am. Mineral. 100, 1182–1189.

Wasserburg, G.J., 1957. The effects of H_2O in silicate systems. J. Geol. 65, 15–23.

Watson, E.B., 1994. Diffusion in volatile-bearing magmas. In: Carroll, M.R., Holloway, J.R. (Eds.), Volatiles in Magmas. Washington, DC, Mineralogical Society of America, pp. 371–411.

Wen, S.X., Nekvasil, H., 1994. Ideal associated solutions—application to the system albite-quartz-H_2O. Am. Mineral. 79, 316–331.

Whittington, A.C., Richet, P., Polian, A., 2012. Water and the compressibility of silicate glasses: a Brillouin spectroscopic study. Am. Mineral. 97, 455–467.

Wilke, M., Behrens, H., Burkhard, D.J.M., Rossano, S., 2002. The oxidation state of iron in silicic melt at 500 MPa water pressure. Chem. Geol. 189, 55–67.

Withers, A.C., Behrens, H., 1999. Temperature-induced changes in the NIR spectra of hydrous albitic and rhyolitic glasses between 300 and 1000 K. Phys. Chem. Minerals 27, 119–132.

Withers, A.C., Zhang, Y., Behrens, H., 1999. Reconciliation of experimental results on H_2O speciation in rhyolitic glass using in-situ and quenching techniques. Earth Planet. Sci. Lett. 173, 343–349.

Xu, Z., Maekawa, H., Oglesby, J.V., Stebbins, J.F., 1998. Oxygen speciation in hydrous silicate glasses—an oxygen-17 NMR study. J. Am. Chem. Soc. 20, 9894–9901.

Xue, X., 2009. Water speciation in hydrous silicate and aluminosilicate glasses: direct evidence from Si-29-H-1 and Al-27-H-1 double-resonance NMR. Am. Mineral. 94, 395–398.

Xue, X.Y., Kanzaki, M., 2001. Ab initio calculation of the O-17 and H-1 NMR parameters for various OH groups: implications to the speciation and dynamics of dissolved water in silicate glasses. J. Phys. Chem. B 105, 3422–3434.

Xue, X.Y., Kanzaki, M., 2004. Dissolution mechanisms of water in depolymerized silicate melts: constraints from H-1 and Si-29 NMR spectroscopy and ab initio calculations. Geochim. Cosmochim. Acta 68, 5027–5057.

Xue, X., Kanzaki, M., 2007. Al coordination and water speciation in hydrous aluminosilicate glasses: direct evidence from high-resolution heteronuclear H-1-Al-27 correlation NMR. Solid State Nucl. Magn. Reson. 31, 10–27.

Xue, X., Kanzaki, M., 2008. Structure of hydrous aluminosilicate glasses along the diopside-anorthite join: a comprehensive one- and two-dimensional H-1 and Al-27 NMR study. Geochim. Cosmochim. Acta 72, 2331–2348.

Yamada, A., OInoue, T., Urakawa, S., Funakoshi, K.-i., Funamori, N., Kikegawa, T., Ohfuji, H., Irifune, T., 2007. In situ X-ray experiment on the structure of hydrous Mg-silicate melt under high pressure and high temperature. Geophys. Res. Lett. 34L10303.

Yarger, J.L., Smith, K.H., Nieman, R.A., Diefenbacher, J., Wolf, G.H., Poe, B.T., McMillan, P.F., 1995. Al coordination changes in high-pressure aluminosilicate liquids. Science 270, 1964–1966.

Zavelsky, V.O., Salova, T.P., 2002. Dissolution mechanism and speciation of water in glasses of the system Na_2O-Al_2O_3-SiO_2: an NMR study. Geochem. Int. 40, S34–S45.

Zhang, Y.X., Behrens, H., 2000. H_2O diffusion in rhyolitic melts and glasses. Chem. Geol. 169, 243–262.

Zhang, Y., Stolper, E.M., Wasserburg, G.J., 1991. Diffusion of water in rhyolitic glasses. Geochim. Cosmochim. Acta 55, 441–456.

Zhang, Y., Stolper, E.M., Ihinger, P.D., 1995. Kinetics of the reaction $H_2O+O=2OH$ in rhyolitic and albitic glasses: preliminary results. Am. Mineral. 80, 593–612.

Zotov, N., Keppler, H., 1998. The influence of water on the structure of hydrous sodium tetrasilicate glasses. Am. Mineral. 83, 823–834.

CHAPTER

16

Reactive Silicate-C-O-H-N-S Systems

OUTLINE

16.1 INTRODUCTORY COMMENTS

Most experimental studies of volatile components in the C-O-H-N-S system have been performed on melts, often at high pressure, which subsequently were quenched to ambient temperature to form a glass prior to chemical and structural characterization. During the last decade, methods have also become available to characterize melt structure while the sample is at high temperature and usually also high pressure. This method commonly is used in part because reaction rates are much faster at the high temperatures of melts and in part because

https://doi.org/10.1016/B978-0-444-63708-6.00016-8

the solubility of volatile components in melts typically is pressure dependent, so that pressure variations may be used to obtain melts and glasses with different concentrations. In this chapter, we therefore mostly discuss melts and glasses formed in this manner.

16.2 CONCEPTS

The volatile species to be discussed in this and Chapter 17 are compounds and single-component volatile species within the system C-O-H-N-S except for H_2O, which is discussed in Chapters 14 and 15. Among these species, those that interact with the silicate structural components will be referred to as reactive (Fig. 16.1). These can have significant impact on structure and properties of melts and glasses in which they are dissolved. Under certain circumstances, oxygen in the melt and glass silicate network may be replaced by one of these components (e.g., oxycarbides, oxysulfides, and oxynitrides). Other volatiles dissolve in their elemental (noble gases) or molecular form (e.g., N_2) where these species may occupy cavities in the melt and glass structure. These are the nonreactive volatiles, which will be discussed in Chapter 17.

The solubility in melts of species of the C-O-H-N-S system and their effects on silicate structure depend on the compositions of both volatiles and silicate together with temperature, pressure, and redox conditions (as generally specified by oxygen or hydrogen fugacity). Under reducing conditions, species such as CH_4 together with CH_3-groups, and NH_3, together with NH_2-groups can be stabilized (Eggler and Baker, 1982; Kadik et al., 2004; Mysen and Fogel, 2010; Ardia et al., 2013). Oxygen in the silicate structure can then be replaced with functional groups such as CH_3 from methane, or NH_2 from ammonia together with molecular CH_4 and NH_3 (Fig. 16.1).

In the absence of hydrogen, elemental carbon, carbides, nitrides, and chalcogenides may be the reduced species in glasses under which conditions oxygen in silicate tetrahedra may be replaced by sulfide, carbide, or nitride (Renlund et al., 1991; Sakka, 1995; Tokuda et al., 2003; Kadik et al., 2004; Sharafat et al., 2009). Under oxidizing conditions, oxygen often is a part of the volatiles species (e.g., CO_3, N_2O, SO_4) or both oxygen and hydrogen are involved as in HCO_3 and HSO_4 (Mysen and Popp, 1980; Brooker et al., 2001; Mysen, 2015). Carbon dioxide can form CO_3 groups where one or more oxygens can be shared with the silicate network or carbon may form isolated carbonate complexes through bonding with oxygen in isolated

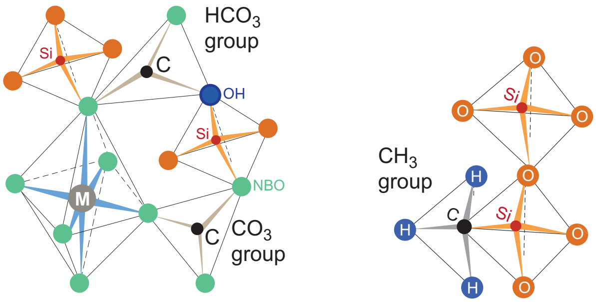

FIG. 16.1 Schematic structural representation of reactive C-bearing groups in silicate-C-O-H systems under oxidizing (CO_3 and HCO_3 groups) and reducing (CH_3 groups) conditions.

oxides (i.e., MgO, CaO, etc.). Oxidized sulfur forms SO_4 groups by sharing oxygen with the silicate. Under rare circumstances, nitrosyl groups may be stabilized in silicate glasses and melts (Roskosz et al., 2006). Here, nitrogen effectively functions as a network-modifier. All these features are discussed in this chapter.

16.3 CARBON IN C-O-H SYSTEMS

The main volatiles of interest in the C-O-H system are H_2O, H_2, CO_2, CO, and hydrocarbons. Fluid compositions in this system most relevant to igneous processes in the earth are those limited by the graphite saturation surface and the join CO_2-H_2O-H_2 (Fig. 16.2).

Even under the most reducing of conditions, the dominant C-bearing species in C-O-H fluids at high temperatures and pressures is CH_4 (see, e.g., Holloway and Blank, 1994; Ni and Keppler, 2013, for calculations of speciation as a function of redox conditions). There is also a very small stability field for CO. As already noted, carbide complexes may form under highly reducing conditions (Renlund et al., 1991; Yurkov and Polyak, 1996). Under oxidizing conditions, the only C-bearing species in C-O-H and C-O fluids is CO_2 (Fig. 16.2).

The nature of the carbon species in (C-O-H)-bearing silicate melts varies with redox conditions, temperature, pressure, and silicate composition (Eggler et al., 1979; Eggler and Baker, 1982; Behrens and Gaillard, 2006; Morizet et al., 2010; Stanley et al., 2011; Mysen et al., 2011). The presence of other volatiles, such as H_2O, will also influence the speciation and solubility of C-bearing species (Mysen, 1976; King and Holloway, 2002; Tamic et al., 2001; Botcharnikov et al., 2006).

16.3.1 Solubility and Solution Mechanisms of Oxidized Carbon

Oxidized carbon in C-O fluids exists as CO_2. However, in C-O-H systems, CO_3^{2-} and HCO_3^- species also can exist where their abundance depends on the pH, fluid composition, temperature, and pressure (French, 1966; Zhang and Duan, 2009). In silicate melt

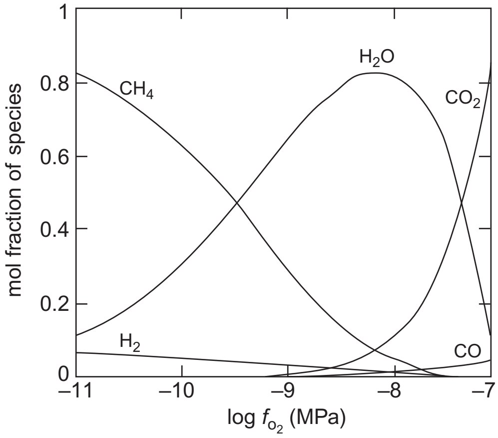

FIG. 16.2 COH speciation in fluid in equilibrium with graphite as a function of oxygen fugacity, f_{O_2}, at 1200°C and 2GPa (modified after Ni and Keppler, 2013).

solution, these relations can be complicated further because of interaction between the C-O-H and the silicate structural components (Mysen, 1976; Nowak et al., 2003; Guillot and Sator, 2011).

16.3.1.1 *Carbon Dioxide*

Carbon dioxide solubility in silicate melts depends on silicate composition, temperature, and pressure (Mysen, 1976; Holloway et al., 1976; Fine and Stolper, 1985; Brooker et al., 2001; Duncan and Dasgupta, 2014). In mixed fluid environments such as CO_2-H_2O, the CO_2 solubility also varies with the CO_2/H_2O ratio (Mysen, 1976; Botcharnikov et al., 2006; Behrens et al., 2009; Shishkina et al., 2010; Iacono-Marziano et al., 2012).

The CO_2 solubility in melt is positively correlated with pressure and for the most part negatively correlated with temperature whether in simple model systems such as $NaAlSi_3O_8$ and $CaMgSi_2O_6$ or in chemically more complex natural melt compositions (Eggler and Kadik, 1979; Eggler and Rosenhauer, 1978; Guillot and Sator, 2011; Iacono-Marziano et al., 2012; Morizet et al., 2013; Duncan and Dasgupta, 2014; see also Fig. 16.3). Regardless of chemical complexity, the silicate composition plays an important role in determining the CO_2 solubility. This influence can be subdivided into several effects. First, it is positively correlated with the overall degree of melt polymerization, typically expressed as NBO/T (see Chapter 4, Section 4.3, for discussion of NBO/T and aluminosilicate structure) (Holloway et al., 1976; Brooker et al., 2001; Iacono-Marziano et al., 2012). This relationship alone does, however, result in significant scatter in the data (Fig. 16.4). This scatter may, in part, be the result of interactions between CO_2 and the type and proportions of network-modifying alkalis and alkaline earths. Such features are seen in the positive correlation between CO_2 solubility and peralkalinity of a melt (Pearce, 1964; Vetere et al., 2014; Fig. 16.4B). Furthermore, the CO_2 solubility in aluminosilicate melts is positively correlated with the Al/(Al+Si) (Mysen, 1976; Fine and Stolper, 1985; see also Fig. 16.4C). Finally, the type of alkali metal or alkaline earth also is important with an apparent negative correlation between solubility and the electronegativity of the metal cation (Holloway et al., 1976; See Fig. 16.4D).

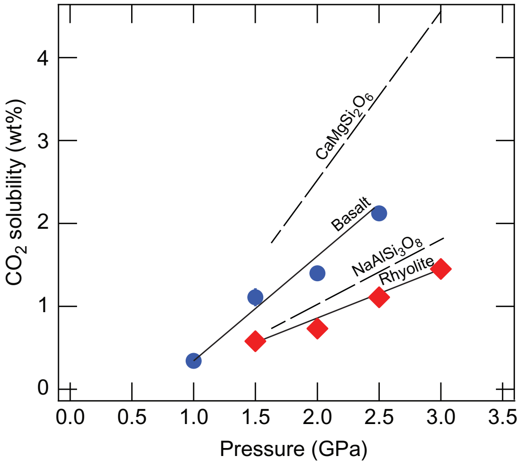

FIG. 16.3 CO_2 solubility with pressure. Solubility data for $NaAlSi_3O_8$ and $CaMgSi_2O_6$ melts from Eggler et al. (1979), basalt (Stanley et al., 2011) with composition (wt %): SiO_2: 46.91, TiO_2: 0.53, Al_2O_3: 10.52, FeO (total): 19.87, MnO: 0.32, MgO: 10.79, CaO: 7.99, Na_2O: 2.40, K_2O: 0.11, P_2O_5: 0.52. Rhyolite (Duncan and Dasgupta, 2014) with composition (wt%): SiO_2: 68.81, TiO_2: 0.50, Al_2O_3: 15.72, FeO (total): 0.99, MnO: 0.50, MgO: 0.19, CaO: 1.47, Na_2O: 4.19, K_2O: 7.33, P_2O_5: 0.29.

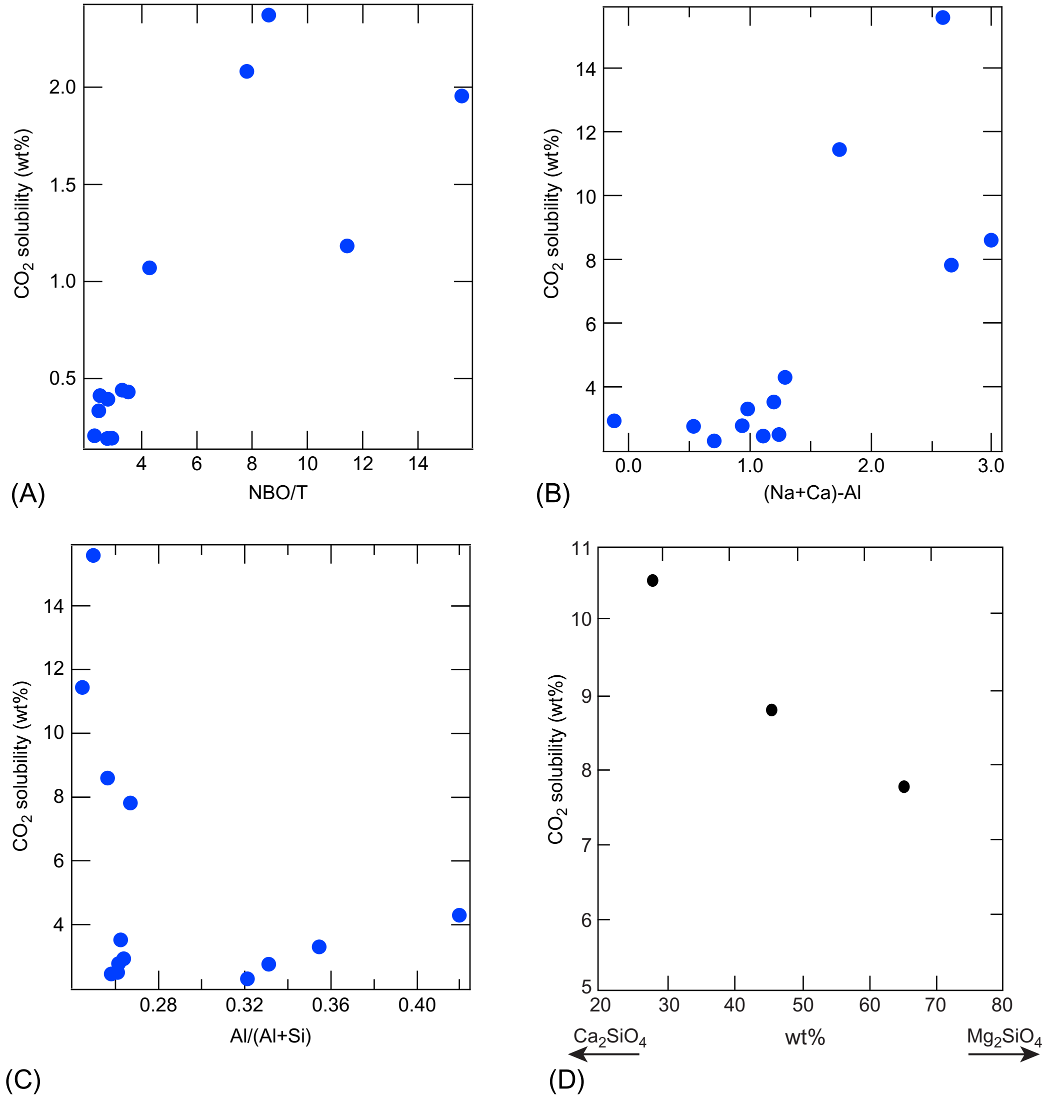

FIG. 16.4 (A) CO_2 solubility as a function of melt NBO/T in the systems Na_2O-CaO-Al_2O_3-SiO_2 and Na_2O-CaO-MgO-Al_2O_3-SiO_2 as a function of NOB/T of the melt. (B) CO_2 solubility and peralkalinity, [((Na+Ca)-Al)]. (C) CO_2 solubility with Al/Al+Si peralkaline compositions (Brooker et al., 2001). (D) Solubility along the join Ca_2SiO_4-Mg_2SiO_4 quenched from melts at 1500°C and 3GPa. *(D) Redrawn from Holloway et al. (1976).*

With mixed volatiles such as CO_2-H_2O mixtures, the CO_2 solubility in a melt will be affected by the proportion of H_2O (King and Holloway, 2002; Behrens et al., 2009; Shishkina et al., 2010; Vetere et al., 2014; see also Fig. 16.5). Such effects reflect two phenomena. Water dissolved in silicate melt results in melt depolymerization (see Section 16.3) and in increased CO_2 solubility, which is positively correlated with NBO/T (as illustrated in Fig. 16.4) and,

FIG. 16.5 CO_2 solubility in melt as a function of $CO_2/(H_2O+CO_2)$ abundance ratio from quenched melts equilibrated at 500 MPa and 1250°C. Melt composition (wt%): SiO_2: 49.89, TiO_2: 0.89, Al_2O_3: 15.57, FeO (total): 7.82, MnO: 0.02, MgO: 5.75, CaO: 11.40, Na_2O: 1.95, K_2O: 0.11, P_2O_5: 0.52. Rhyolite (Duncan and Dasgupta, 2014) with composition (wt %): SiO_2: 68.81, TiO_2: 0.50, Al_2O_3: 15.72, FeO (total): 0.99, MnO: 0.50, MgO: 0.19, CaO: 1.47, Na_2O: 4.19, K_2O: 7.52 (Behrens et al., 2009).

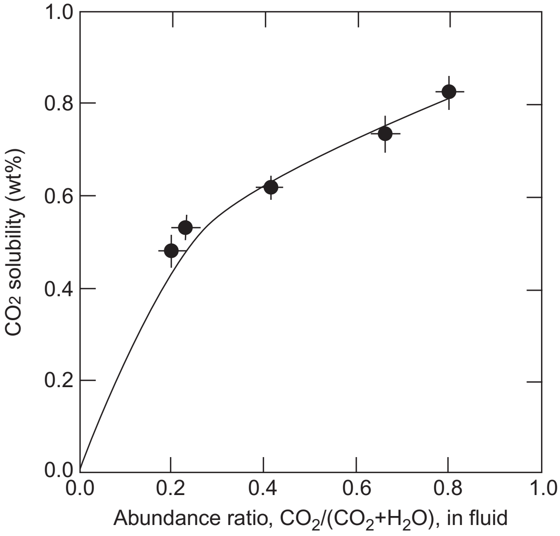

thus, water content. The second effect, which tends to oppose melt depolymerization, is the reduction of CO_2 activity by mixing H_2O and CO_2 in a fluid coexisting with CO_2+H_2O-bearing melt (Fig. 16.5).

A portion of the CO_2 in melt interacts with the silicate structure whereby $CO_3{}^{2-}$ complexes are formed (Pearce, 1964; Mysen, 1976; Fine and Stolper, 1985; Guillot and Sator, 2011; Konschak and Keppler, 2014; Morizet et al., 2015). A simple equilibrium between molecular CO_2 and carbonate, $CO_3{}^{2-}$, is (Fine and Stolper, 1985; Nowak et al., 2003; Stanley et al., 2011):

$$CO_2 + O^{2-} \Leftrightarrow CO_3{}^{2-}, \tag{16.1a}$$

with

$$K_{16.1} = X_{CO_3}/f_{CO_2} \cdot X_{O^{2-}}, \tag{16.1b}$$

where it is assumed that mol fractions, X, can be used in place of activities. The O^{2-} in these equations is the proportion of oxygen anions in the melt structure.

From the temperature and pressure dependences of this equilibrium (Fig. 16.6), Stanley et al. (2014) reported standard enthalpy and volume changes for reaction (16.1a) near -14 ± 14 kJ/mol and 23 ± 2 cm^3/mol, respectively, derived from their own and other experimental data (Pan et al., 1991; Holloway and Blank, 1994; Thibault and Holloway, 1994). We should note here that the very large uncertainty in the average enthalpy change is due to the widely discrepant nature of one data set (Pan et al., 1991). Without those data, the average enthalpy change is -20 ± 8 kJ/mol. In other words, from the data summarized in Fig. 16.6, equilibrium (16.1a) and (16.1b) shifts to the left with increasing temperature, thus favoring molecular CO_2 over $CO_3{}^{2-}$ groups, and to the right with increasing pressure thus favoring the $CO_3{}^{2-}$ groups over molecular CO_2. This conclusion is also consistent with the molecular simulations of Guillot and Sator (2011) to 10 GPa. The data also accord

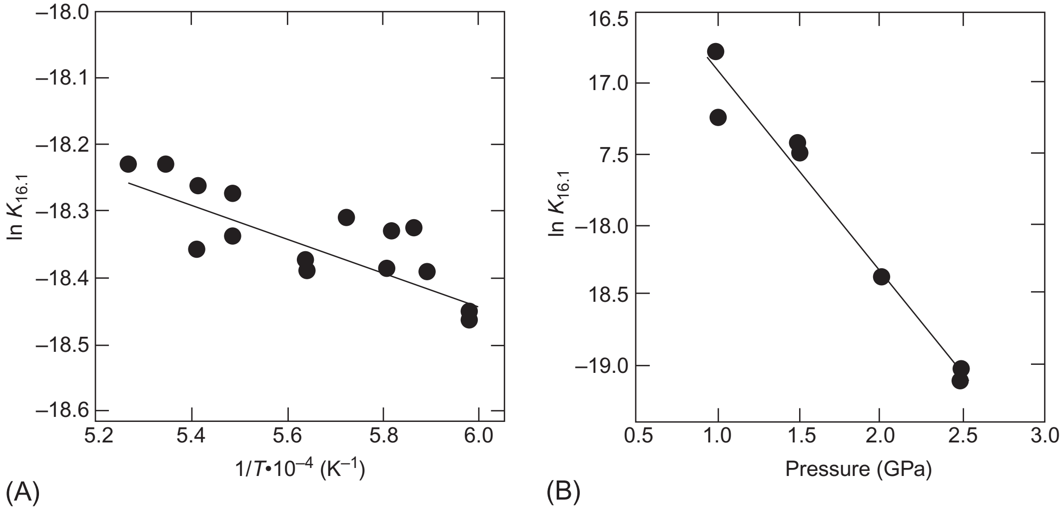

FIG. 16.6 Temperature (A) and pressure (B) dependence of the $CO_2 + O^{2-} \Leftrightarrow CO_3{}^{2-}$ equilibrium constant, $K_{16.1}$, in basalt melts after Stanley et al. (2011). Basalt melt composition (wt%): SiO_2: 46.96, TiO_2: 0.56, Al_2O_3: 10.93, Na_2O: 10.7, K_2O: 5.5. Dacite melt composition (wt%): SiO_2: 70.7, TiO_2: 0.52, Al_2O_3: 15.5, MgO: 2.33, CaO: 3.08, Na_2O: 4.51, K_2O: 3.05.

semiquantitatively with the experimental results from Nowak et al. (2003) who found $\Delta H = -12 \pm 2\,\mathrm{kJ/mol}$ for a $NaAlSi_3O_8$ melt and $-29 \pm 2\,\mathrm{kJ/mol}$ for a complex melt of dacitic composition.

Formation of $CO_3{}^{2-}$-complexes may be accomplished either through a reaction whereby nonbridging oxygens from the silicate network is also altered. The process involves the release their network-modifying cation(s) and one of the nonbridging oxygen to form $CO_3{}^{2-}$ complexes that form bonding with the released network-modifying cation. Another nonbridging cation is converted to a bridging oxygen. In other words, the silicate structure becomes polymerized via a schematic solution mechanism that combines Eqs. (16.1a), (16.1b) with a silicate polymerization reaction;

$$2Q^{n-1} \Leftrightarrow 2Q^{n} + O^{2-}, \tag{16.2}$$

to yield:

$$2Q^{n-1} + CO_2 \Leftrightarrow 2Q^{n} + CO_3{}^{2-}. \tag{16.3}$$

Given, for example, that CO_2 solubility in melts increases with increasing pressure, Eq. (16.3) would suggest that at CO_2-saturation, increasing pressure will result in increasing silicate polymerization. This exactly what has been observed (Morizet et al., 2015; see Fig. 16.7).

The equilibrium constant of Eq. (16.3) and its temperature-dependence varies with the type of metal cation ceasing to be a network-modifier to associate with $CO_3{}^{2-}$-complexes. A positive correlation between ionization potential of the metal cation and degree of

FIG. 16.7 Degree of polymerization with pressure, under oxidizing conditions from glass quenched from melt equilibrated at 1500°C and from melt derived by first-principles molecular dynamics simulation (Morizet et al., 2009). Composition (wt%): SiO_2: 48.87, Al_2O_3: 16.40, CaO: 16.33, MgO: 16.40.

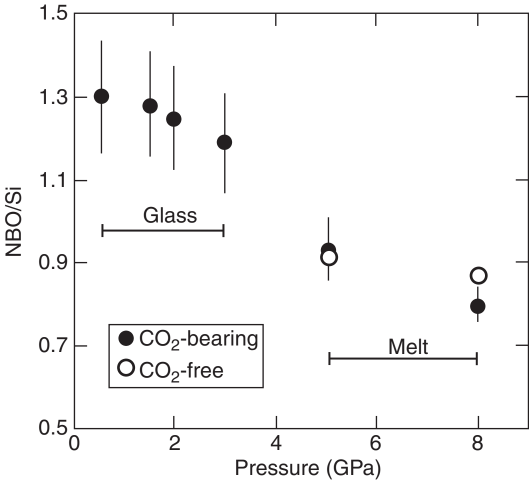

deformation of the carbonate group, well known in crystalline carbonate structures (White, 1974), has also been observed in CO_2-saturated silicate melts (Sharma et al., 1988). It is possible, therefore, that the extent of steric hindrance of the CO_3^{2-} triangular geometry controls the relationship between CO_2 solubility and the type of metal cation(s) (Holloway et al., 1976). This proposal implies, for example, that at fixed pressure, temperature and NBO/Si of a melt, the CO_2 solubility depends on cation properties in the order $K^+ > Na^+ > Ca^{2+} > Mg^{2+}$. In other words, the CO_2 solubility in silicate melts depends on the nature of the network-modifying cations, as observed in the example for melts along the join Mg_2SiO_4-Ca_2SiO_4-CO_2 (Fig. 16.4D).

The temperature-dependence and, therefore, the ΔH of equilibrium (16.1a) and (16.1b) also are governed by the melt composition (Morizet et al., 2014; Nowak et al., 2003; Konschak and Keppler, 2014; see Fig. 16.8) with a positive correlation with the NBO/T of the melt, for example. Moreover, the increased slope of the $\ln K_{16.1}$ versus $1/T$ in $NaAlSi_2O_6$ compared with

FIG. 16.8 Temperature dependence of the equilibrium constant, $K_{16.1}$, from phonolite and dacite melts (Konschak and Keppler, 2014), $NaAlSi_2O_6$ and $NaAlSi_3O_8$ glass quenched from high temperature at high pressure (Morizet et al., 2001; Nowak et al., 2003). Dacite melt composition (wt%): SiO_2: 70.7, TiO_2: 0.52, Al_2O_3: 15.5, MgO: 2.33, CaO: 3.08, Na_2O: 4.51, K_2O: 3.05. Phonolite melt composition (wt%): SiO_2: 58.4, Al_2O_3: 23.8, Na_2O: 10.7, K_2O: 5.5.

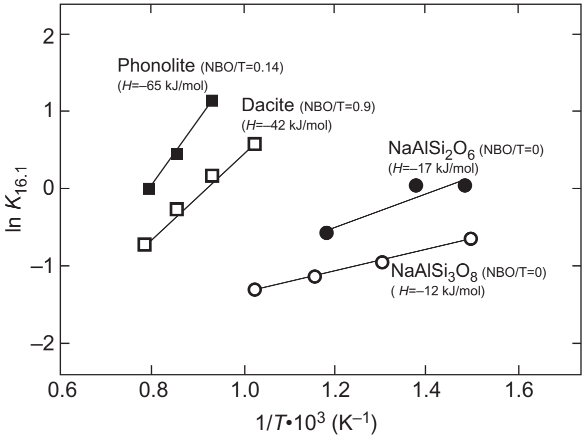

$NaAlSi_2O_8$ melt (Fig. 16.8), might suggest that the Al/(Al+Si) ratio also affects the energetics of the equilibrium. It might also be speculated that the properties of cations involved in the charge-balance of tetrahedrally coordinated Al^{3+} affects the energetics, but experimental data of this kind appear not to be available (see also Chapter 4, Section 4.4.3 and Chapter 9, Section 9.4 for discussion of concepts and energetics of charge-balance of tetrahedrally coordinated Al^{3+}).

In systems containing both CO_2 and H_2O, simple reactions such as;

$$CO_2 + H_2O \Leftrightarrow HCO_3{}^- + H^+. \tag{16.4a}$$

and

$$CO_2 + H_2O \Leftrightarrow CO_3{}^{2-} + 2H^+, \tag{16.4b}$$

can be combined together with the Q^n-species equilibrium such as Eq. (16.2) to yield a complete equilibrium between the carbonate species, molecular CO_2, and the Q^n-species in the melts (Mysen, 2015):

$$6Q^{n-1} + 4CO_2 + H_2O \Leftrightarrow 2HCO_3{}^- + 2CO_3{}^{2-} + 6Q^n. \tag{16.5}$$

Hence, in silicate-CO_2-H_2O systems, solution of CO_2 to yield carbonate and bicarbonate species results in melt polymerization albeit at a slower rate than without H_2O (and $HCO_3{}^-$) ($\Delta NBO/Si = 0.25$ per mol CO_2 with H_2O and $\Delta NBO/Si = 0.67$ per mol CO_2 without it). It is slower because H_2O acts to counter the polymerization (as discussed in this chapter). Moreover, the ratio $HCO_3{}^-/CO_3{}^{2-}$ decreases with increasing temperature (Mysen, 2015). In other words, equilibrium (16.5) shifts to the left and the silicate structure becomes increasingly depolymerized. It is also noteworthy that mechanism (16.5) allows for CO_2, CO_3 and HCO_3 groups to coexist in silicate melts, whereas this is not so in pure C-O-H fluid (see Section 16.1–16.3.1) as a result of the structural interaction between the silicate components and the carbonate groups in silicate melts and glasses.

In meta-aluminosilicate melts with nominal $NBO/T = 0$, one can increase CO_2 solubility and the $CO_3{}^{2-}/CO_2$ ratio by increasing Al/Si of the melt (Mysen, 1976; Fine and Stolper, 1985). This involves transforming some of the metal cations used for Al^{3+}-charge-balance to charge-balance carbonate complexes in the melt instead:

$$5\left[\left(M_{1/n}{}^{n+}AlO_2\right)_x \cdot \left(SiO_2\right)_y\right] + CO_2 \Leftrightarrow 3\left[\left(M_{1/n}{}^{n+}AlO_2\right)_{x-4} \cdot \left(SiO_2\right)_y\right]^{4-} + 4xAl^{3+} + 2M_{1/n}CO_3. \tag{16.6}$$

In Eq. (16.6), the $\left[\left(M_{1/n}{}^{n+}AlO_2\right)_{x-4} \cdot \left(SiO_2\right)_y\right]^{4-}$ complex is less polymerized than $\left[\left(M_{1/n}{}^{n+}AlO_2\right)_x \cdot \left(SiO_2\right)_y\right]$, which means than when CO_2 is dissolved in fully polymerized aluminosilicate melts and forms $CO_3{}^{2-}$ complexes, the silicate melt actually becomes depolymerized.

16.3.2 Solubility and Solution Mechanisms of Reduced Carbon

In the C-O-H system of reduced volatiles, the principal fluid species are CO and CH_4 (Fig. 16.2). The solubility of C-bearing species in melts under such reducing conditions depends systematically on silicate and fluid compositions, redox conditions, and pressure (Pawley et al., 1992; Mysen et al., 2009, 2011; Kadik et al., 2004, 2011, 2014; Ardia et al., 2013; Armstrong et al., 2015). In H-free environments, the reduced species in C-O fluids is CO or a polymerized $(CO)_x$ species under redox conditions down to those defined by the $Fe+0.5O_2=FeO$ (IW) buffer reaction (Pawley et al., 1992; Armstrong et al., 2015), whereas methane dominates in H-bearing C-O-H systems (Kadik et al., 2004; Ni and Keppler, 2013).

A number of recent experimental and modeling studies have proposed additional reduced carbon species as possibilities, for example, hydrocarbons heavier than CH_4 in the C-H subsystem at >20 GPa and >1500 K (Lobanov et al., 2013). However, the latter experiments suffered from composition gradients within the samples at high pressure and temperature so this interpretation is subject to uncertainty. Modeling of reduced species in the C-O-H system also has led to proposed complex organic functional groups such as acetate at high temperature and pressure (Sverjensky et al., 2014). In the latter modeling study, it was assumed that a hard-sphere model for H_2O could be used up to mantle pressures even though high-pressure − / − temperature first-principles calculations have indicated a complex structural envionment involving molecular H_2O, OH groups and polymerized H_2O (Karki et al., 2010), which would be inconsistent with a hard-sphere model. Those modeling effort should not, therefore, be considered a realistic representation of solution mechanisms of organic complexes in silicate melts at high temperature and pressure. It has also been proposed that reduced carbon dissolve in iron-bearing silicate melts at high pressure in the form of iron carbonyl, $Fe(CO)_5$ (Wetzel et al., 2013; Kadik et al., 2014). However, in other experimental studies it was concluded that the latter vibrational spectroscopic assignment is consistent with molecular CO and not with carbonyl (Yoshioka et al., 2015).

16.3.2.1 Carbon Monoxide

Carbon monoxide (CO) in silicate melts has been the subject of a handful of experimental studies (Eggler et al., 1979; Pawley et al., 1992; Thibault and Holloway, 1994; Morizet et al., 2010; Yoshioka et al., 2015). Carbon monoxide solubility experiments require consideration of the shift of the equilibria:

$$CO_2 + C \Leftrightarrow 2CO, \tag{16.7}$$

and

$$2CO + O_2 \Leftrightarrow 2CO_2, \tag{16.8}$$

with pressure, temperature, and oxygen fugacity. The highest CO concentrations are reached at the graphite saturation surface. The mol fraction of CO in the fluid, $CO/(CO+CO_2)$, decreases rapidly, however, with increasing pressure at constant temperature and with decreasing temperature at constant pressure (Ni and Keppler, 2013).

Pawley et al. (1992) reported carbon monoxide solubility in basalt to be a linear function of CO_2 fugacity in the 50–150 MPa pressure range and 1200°C (Fig. 16.9). They suggested that CO dissolves in melts in molecular form, which is also consistent with the results from Yoshioka et al. (2015). That suggestion differs from conclusions inferred from the high-pressure experiments on CO solubility in $CaMgSi_2O_6$ and $NaAlSi_3O_8$ melts (Eggler et al., 1979) and from limited infrared spectroscopic information from CO-bearing glasses by Pawley et al. (1992). In both reports, it was suggested that CO_3^{2-} groups were present

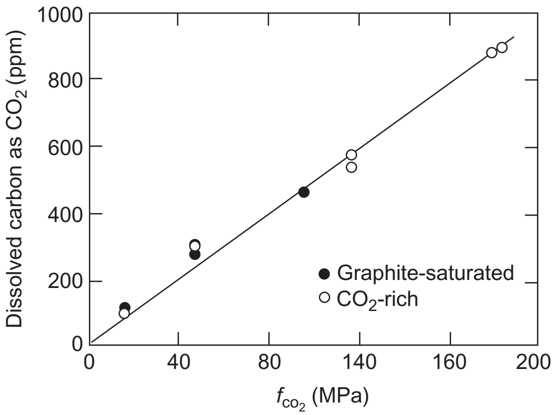

FIG. 16.9 Total carbon solubility (expressed as CO_2) as a function of CO_2 fugacity, f_{CO_2} for a tholeiite melt in equilibrium CO, CO_2, and graphite *(closed symbols)* and in equilibrium with a CO_2-rich fluid *(open symbols)*. Equation represents least-squares fit through all the data points and through the origin (Pawley et al., 1992).

in the quenched glasses after equilibration at temperatures above their liquidus and a few gigapascals of pressure.

Experimental studies of carbon speciation in the glasses formed by quenching melts (Eggler et al., 1979; Thibault and Holloway, 1994) therefore point to formation as $CO_3{}^{2-}$ bearing entities from CO as one of the forms of dissolved carbon. How this takes place is not clear, because transformation of CO to $CO_3{}^{2-}$ requires oxidation of carbon (Pawley et al., 1992). One might propose a reaction such as:

$$2\,CO(\text{fluid}) + O^{2-}(\text{melt}) \Leftrightarrow CO_3{}^{2-}(\text{melt}) + C, \tag{16.9}$$

where O^{2-} (melt) represents the interaction with the silicate melt structure. However, whether or not reactions of this type may occur has not been documented so that we will not consider them further.

16.3.2.2 Carbide

Carbide complexing in silicate melts has been reported, but apparently only in SiO_2 + C-O systems (Renlund et al., 1991; Yurkov and Polyak, 1996). In these studies, various spectroscopic methods were used to determine the nature of the Si—C bonding and how the substitution of C for O in silicate tetrahedra affects properties of oxycarbide melts. There appear to be no data on carbon solubility in oxycarbide melts.

Reduction of carbon to form Si—C bonds can be accomplished via interaction with the silicate network, which in principle can be written as:

$$C + 2Q^n = SiC + Q^{n-2}. \tag{16.10}$$

This equilibrium is, therefore, a very efficient mechanism for depolymerization of the melt. The C/(C+O) ratio of a melt can be accommodated by an increased number of Si—C bonds in the tetrahedral structure observed in ^{29}MAS NMR spectra of such samples (Renlund et al., 1991).

The activation energy of viscous flow of partially substituted oxycarbide SiO_2 melt is somewhat less than that of SiO_2 melt, but the viscosity is greater than that of SiO_2 melt

FIG. 16.10 Viscosity of SiO_2-carbide (oxycarbide—see Table 16.1) and SiO_2 melt. Oxycarbide data from Renlund et al. (1991) and SiO_2 from Urbain et al. (1982).

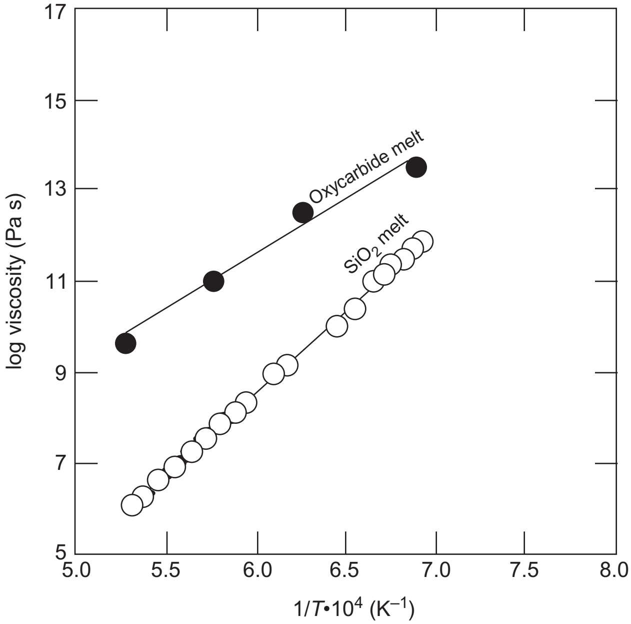

(Fig. 16.10). This effect reflects the stronger Si—C bond, the importance of which increases with increasing C concentration as seen, for example, in the proportions of such units derived from ^{29}Si MAS NMR spectra (Table 16.1). One would expect, therefore, that not only viscosity, but also other transport properties of oxycarbide melts would show analogous effects. Moreover, other physical properties such as thermal expansion, hardness, and elastic modulus also are higher in the oxycarbide glasses compared with vitreous SiO_2 (Renlund et al., 1991). Interestingly, similar features are seen in oxynitride glasses

TABLE 16.1 Mol Fraction of C-Substituted SiO_4 Groups in Silicon Oxycarbide Formed by Pyrolysis at 1400°C of SR350 Resin (Redrawn from ^{29}MAS NMR Data by Renlund et al., 1991)

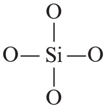 $\mathrm{O{-}\overset{O}{\underset{O}{Si}}{-}O}$	0.43
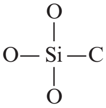 $\mathrm{O{-}\overset{O}{\underset{O}{Si}}{-}C}$	0.28
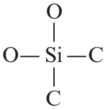 $\mathrm{O{-}\overset{O}{\underset{C}{Si}}{-}C}$	0.29

(see Section 16.5.3). Furthermore, these properties likely will vary with C/O abundance ratio, as this also governs the extent of C,O substitution in the silicate network.

16.3.2.3 *Methane*

Methane (CH_4) is the dominant reduced C-bearing species in the C-O-H fluid system in equilibrium with graphite under conditions more reducing than about three orders of magnitude above that defined by the $2Fe+O_2=2FeO$ (IW) equilibrium (Fig. 16.2). However, when the activity of hydrogen is lowered, reduced carbon species other than hydrocarbons (CH_4) may be stable in melts at high temperature and pressure (Armstrong et al., 2015) although the nature of this C-species is uncertain (see also Yoshioka et al., 2015).

The solubility of carbon in melts and glasses equilibrated with C-O-H fluid at high pressure and temperature decreases systematically with decreasing oxygen fugacity whether in silicate-C-O or silicate-C-O-H melt systems (Fig. 16.11). At given oxygen fugacity, the solubility of reduced carbon species increases with pressure, whether in silicate-C-O or silicate-C-O-H systems, but also decreases as the hydrogen content of the system is lowered (Fig. 16.12) (see also Ardia et al., 2013). Interestingly, the methane solubility increases with H_2O content of the melt (Ardia et al., 2013). This increase might reflect the fact that solution of H_2O results in silicate depolymerization (increasing NBO/T). Hence, there is a strong silicate compositional dependence on CH_4 solubility, one of which is polymerization (Fig. 16.11). This control is analogous to that seen for oxidized carbon (CO_2), the solubility of which also increases with H_2O content (Fig. 16.5). Other melt compositional parameters (silicate structure) also affect the solubility of reduced C-O-H species, perhaps in ways analogous to that seen for oxidized C-species (e.g., Fig. 16.4). Experimental data focusing on the relationship between melt structure and solubility of reduced carbon species are, however, limited.

The solution mechanisms of reduced C-O-H species in silicate melts have been addressed by vibrational spectroscopic methods (Kadik et al., 2004, 2011, 2014; Mysen et al., 2011; Mysen and Yamashita, 2010; Stanley et al., 2014; Armstrong et al., 2015). For redox conditions more reducing than those corresponding to the IW oxygen buffer, CH_4 was reported in most of those studies as a principal species in silicate melts at high pressure.

Carbon-13 MAS NMR and Raman spectroscopic data recorded from both quenched melts (glasses) and hydrous, CH_4-bearing melts at high temperature and pressure are consistent with coexisting molecular CH_4 and CH_3 groups (Mysen and Yamashita, 2010; Kadik et al., 2011; Mysen et al., 2011). A schematic representation of the equilibrium between methyl groups and methane dissolved in hydrous melts is (Mysen et al., 2011):

$$2Q^n + CH_4 \Leftrightarrow Q^{n-1}(CH_3) + Q^{n-1}(OH). \qquad (16.11)$$

In Eq. (16.11), the notations $Q^{n-1}(CH_3)$ and $Q^{n-1}(OH)$ indicate Q-species where at least one of the oxygen atoms in the silicate tetrahedral is replaced by a CH_3 and an OH group, respectively, and that these species are less polymerizing than the reactant Q^{n-}. The formation of $Si—CH_3$ bonds in this fashion is supported by carbon-13 MAS NMR data, which also rule out bonding of the metoxy type, $Si—O—CH_3$ (Mysen et al., 2011). Equilibrium (16.11) shifts to the right with both increasing temperature and increasingly depolymerized silicate melt (Fig. 16.13). These will be affected differently depending on the redox state of carbon.

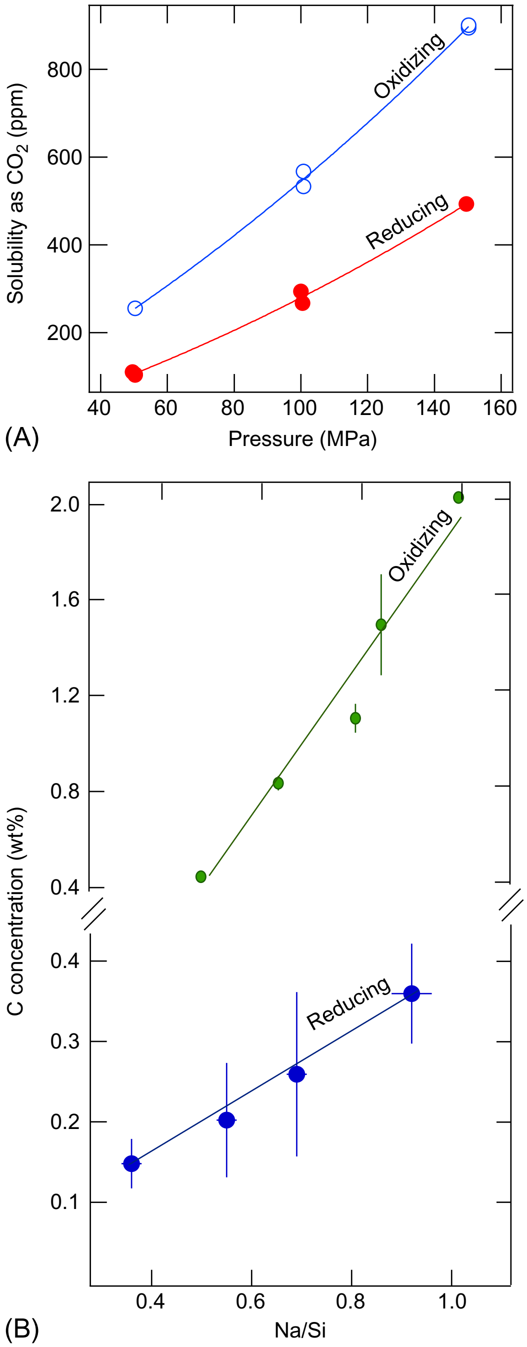

FIG. 16.11 Carbon solubility in melts under reducing and oxidizing conditions at high temperature and pressure. (A) Solubility in basalt melt with C-O fluid, expressed as CO_2 at 1200°C, 50–150 MPa. *Upper curve (open symbols)* shows data for oxidizing conditions (from about the oxygen fugacity defined by the $Ni+0.5O_2=NiO$ (NNO) buffer to about an order of magnitude lower f_{O_2}). *Lower curve (solid symbols)* show solubility in the same composition melt but with f_{O_2} about four orders of magnitude lower than that of the NNO buffer (Pawley et al., 1992). (B) Solubility in Na_2O-SiO_2-C-O-H melt at 1400°C, 1–2.5 GPa under oxidizing conditions defined by the $2Fe_3O_4+0.5O_2=3Fe_2O_3$ (MH) and $Fe^+{\cdot}5O_2=FeO$ (IW) oxygen buffer (Mysen et al., 2011).

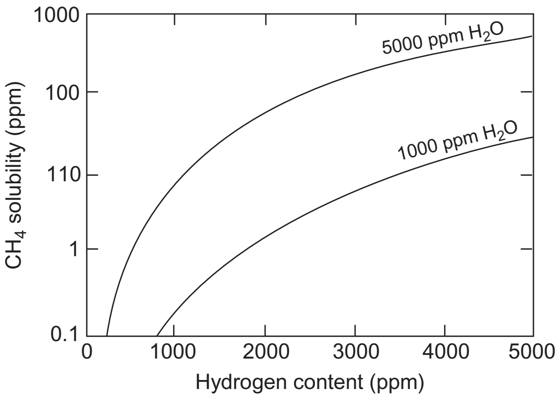

FIG. 16.12 Solubility of CH_4 in basaltic melt as a function of H content for 1000 and 5000pm H_2O as shown (Ardia et al., 2013).

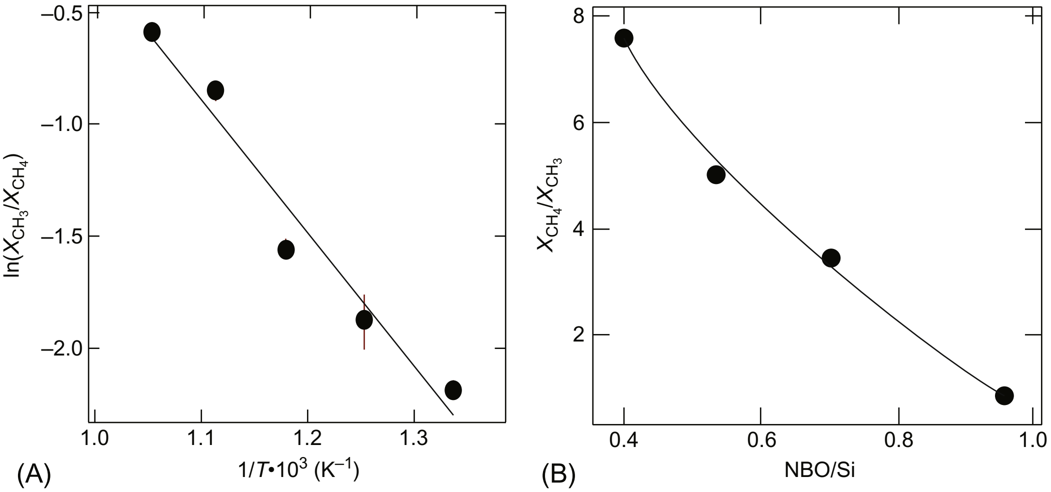

FIG. 16.13 (A) Evolution of CH_3/CH_4 ratio with temperature (Mysen, 2015). (B) Evolution of CH_3/CH_4 ratio with NBO/Si of an Na_2O-SiO_2 melt (Mysen and Yamashita, 2010). The data in both figures were recorded while the samples were at the temperature (and pressure) of interest; see the sources for additional details.

16.3.3 Properties and Solution Mechanisms in (C-O-H) Systems

Solutions of carbon dioxide and methane in silicate melts and glasses have contrasting effects on the properties of these materials, because the degree of melt polymerization is affected in different ways. Dissolved CO_2 results in silicate polymerization (Eq. 16.3), whereas the opposite holds true for methane (Eq. 16.11). Melt properties responding to silicate polymerization include activity-composition relations of silicate components and melting phase relationships, transport, and volume properties.

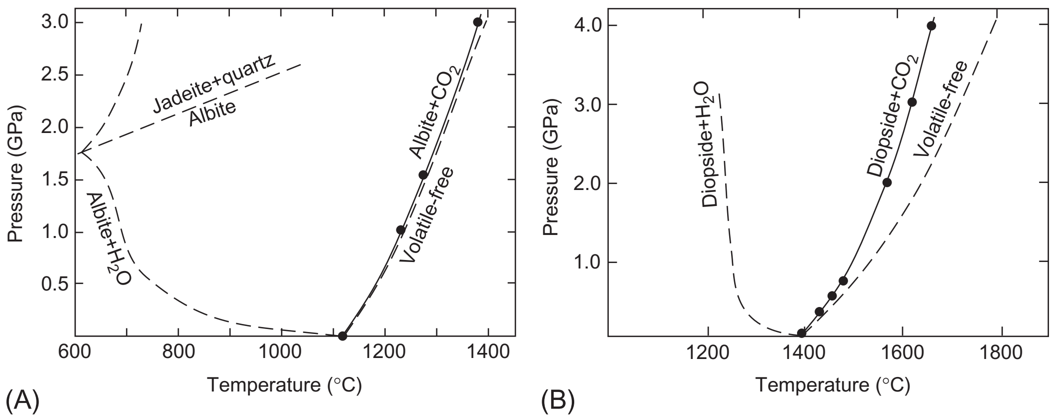

FIG. 16.14 Pressure-temperature trajectories of the liquidus curves of silicates in equilibrium with CO_2 *(solid lines and solid symbols)*, volatile-free and water-saturated *(dashed lines)*. (A) Relationships for albite ($NaAlSi_3O_8$) (Eggler and Kadik, 1979). (B) Relationships for diopside ($CaMgSi_2O_6$). *(B) Redrawn from Eggler and Rosenhauer (1978).*

16.3.3.1 Thermal Properties

The liquidus temperature depression caused by dissolved CO_2 in the partial melt ranges from negligible to several hundred degrees and depends on silicate composition and pressure (Eggler, 1975, 1976; Mysen and Boettcher, 1975; Eggler and Kadik, 1979; Eggler and Rosenhauer, 1978; Boettcher et al., 1987; Boettcher, 1984); see also Fig. 16.14. The extent of this depression is linked to the solubility and solubility mechanism(s) of CO_2 in the melt via the Van't Hoff relationship:

$$\ln a_i = \ln X_i + \ln \gamma_i = \Delta H_i^f / R(1/T - 1/T_o), \tag{16.12}$$

where a_i, X_i, γ_i, and ΔH_i^f are the activity, mol fraction, activity coefficient, and enthalpy of fusion of phase, *i*. Therefore, the greater the solubility of a component, the smaller is the mol fraction, X_i, in the melt and the larger the temperature difference between T_o and T, the liquidus temperature. The CO_2 solubility in $CaMgSi_2O_6$ melt is greater than and is more sensitive to pressure than that of CO_2 in $NaAlSi_3O$ (Fig. 16.14). The greater liquidus temperature depression of $CaMgSi_2O_6$-CO_2 compared with $NaAlSi_3O_8$-CO_2 thus is understandable. Additional complexity is introduced with the activity coefficients of the melt components, but silicate-CO_2 mixing relations are not well known. In general, however, one assumes that molecular CO_2 dissolves with minor deviations from unity of its activity coefficient, γ_i, whereas for CO_3^{2-} and HCO_3^- groups, which are formed through interaction between dissolved CO_2 and melt structure, greater deviations have been observed (Pearce, 1964). It follows, therefore, from the general relations of increasing CO_2(molecular)/CO_3(HCO_3^-) ratio with increasingly polymerized melts (Brooker et al., 2001), that both γ_i and the liquidus temperature depression, $T_o - T$, would also decrease as CO_2-saturated melt becomes increasingly polymerized (i.e., silica-rich). An example of this effect is the liquidus depression of albite and diopside crystals to form $NaAlSi_3O_8$ and $CaMgSi_2O_6$ melts, respectively.

The invariant point olivine + diopside + enstatite + melt in the system Mg_2SiO_4-$CaMgSi_2O_6$-SiO_2 is sensitive to CO_2 content and total pressure (Fig. 16.15). The shift away from the SiO_2

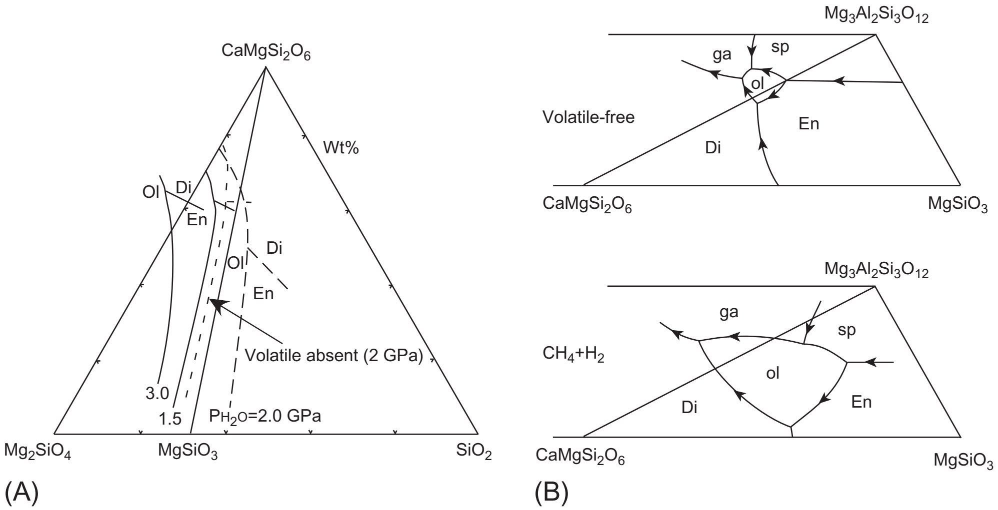

FIG. 16.15 (A) Liquidus phase relations in the system Mg_2SiO_4-$CaMgSi_2O_6$-SiO_2-CO_2 at 1.5 and 3.0 GPa *(solid lines)* compared with the liquidus relations volatile-free and with excess H_2O *(dashed lines)* (Kushiro, 1969). (B) Liquidus phase relations at 2.8 GPa in a portion of the system CaO-MgO-Al_2O_3-SiO_2, either volatile-free or in equilibrium with $CH_4 + H_2$ fluid and graphite. Abbreviations: *Ol*, olivine; *Di*, diopside; *En*, enstatite; *sp*, spinel; *ga*, garnet. *(A) Redrawn from Eggler (1974). (B) Redrawn from Eggler and Baker (1982).*

apex of this invariant point is consistent with an increasing activity coefficient of SiO_2 in the melt (Eggler, 1974), which in turn is in agreement with increasing melt polymerization as illustrated with Eq. (16.3). Interestingly, liquidus phase relations in aluminosilicate-CO-CO_2 systems are essentially identical to those of aluminosilicate-CO_2 (Eggler et al., 1979). From those observations, it may be inferred that mixed CO + CO_2 and pure CO_2 dissolved in silicate melts seem to have similar effects on activity-composition relations in the melt, which is consistent with the fact that CO, at least in part, dissolves to form CO_3 complexes in the melt (see Section 16.3.2.1).

The silicate-CO_2 liquidus relationships contrast with those of silicate-C-O-H systems under reducing conditions. For example, the olivine liquidus volume in the system CaO-MgO-Al_2O_3-SiO_2-CH_4-H_2 expands, compared with the volatile-free CaO-MgO-Al_2O_3-SiO_2 system (Kushiro and Yoder, 1974; Eggler and Baker, 1982) (see also Fig. 16.15B), an effect resembling that of H_2O discussed in this chapter. However, in silicate-CO_2 systems such as CaO-MgO-Al_2O_3-SiO_2-CO_2 the olivine liquidus volume contracts. This olivine liquidus volume expansion with CH_4 reflects the increased abundance of Q^{n-1} depolymerizing species in methane-rich melts compared with more polymerizing Q^n species in volatile free melts (see also Eq. 16.11).

16.3.3.2 *Transport Properties*

In view of the close connections between transport properties (Chapter 4), we will first examine those that can be determined with most confidence before deriving others from their mutual relationships. Diffusion has been most commonly investigated in silicate-C-O-H melt

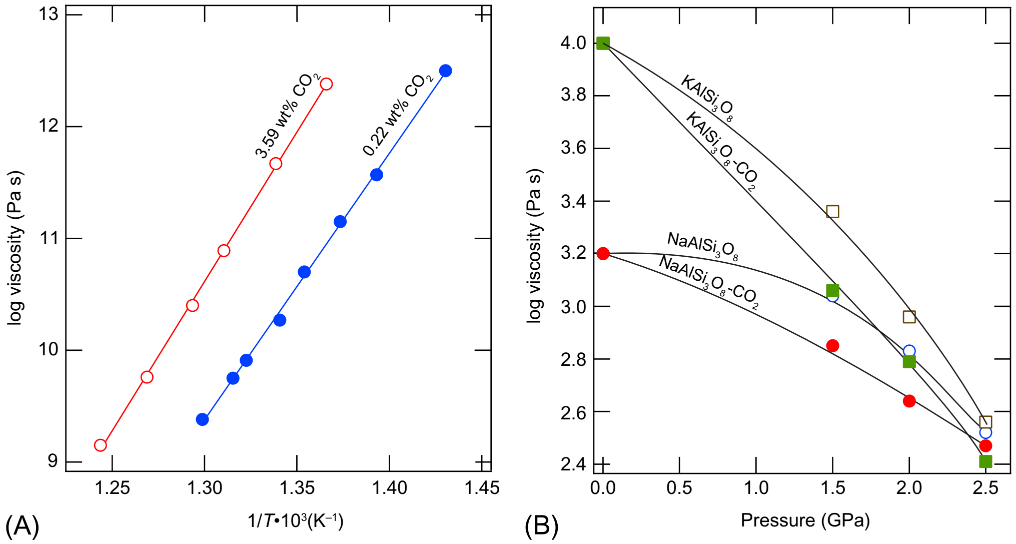

FIG. 16.16 Viscosity of CO_2-bearing silicate melts. (A) Viscosity of $K_2O{\cdot}1.3SiO_2$ melt with 0.22 and 3.79 wt% CO_2 in solution as a function of temperature at ambient pressure (Bourgue and Richet, 2001). (B) Viscosity of aluminosilicate melts as indicated on individual curves with 0.5 wt% CO_2 ~3 mol% CO_2 and without CO_2 as a function of pressure at 1500°C (Brearley and Montana, 1989 and White and Montana, 1990). The ambient pressure points are for volatile-free melts from Urbain et al. (1982).

systems (Nowak et al., 2004; Zhang et al., 2007; Behrens, 2010; Spickenbom et al., 2010). Diffusion of CO_2 and Ar in silica glass at temperatures up to 1097°C is particularly interesting because both the diffusivities activation energies of CO_2 and Ar are essentially the same, whereas the activation energy of H_2O diffusion is only about 50% of those values (Nowak et al., 2004; Behrens, 2010); see Fig. 16.16. These observations have led to the conclusion that diffusion of molecular CO_2 and of Ar may be described with a simple ionic porosity model (Behrens, 2010).

Because these data for silica refer to the glass, however, they cannot be transposed to chemically more complex melt systems at high temperatures. For example, the diffusivity of Ar depends on the NBO/T of the melt, whereas that of total CO_2 does not (Fig. 16.17). This difference led Zhang et al. (2007) to suggest that CO_2 diffusion involves two species, namely, molecular CO_2 and CO_3^{2-} groups. Their diffusivities differ, which is borne out by the structural dependence of the CO_3^{2-} diffusivity in silicate melts (Fig. 16.18). Interestingly, the activation energy of CO_3^{2-} diffusion is only very subtly dependent on melt polymerization (Spickenbom et al., 2010). Moreover, in mixed H_2O-CO_2 systems, the CO_2 diffusivity does increase with increasing water content (Zhang et al., 2007), which is interesting given that the CO_2 diffusivity is not dependent on NBO/T of the melts and water does indeed change NBO/T (Chapter 15). It is possible that this slight effect of dissolved H_2O originates in HCO_3^- complexes that may also participate in the diffusion process.

There exist but only a few data on the effect of dissolved CO_2 on diffusivity of other components in silicate melts and glasses. From first-principles molecular dynamics simulations

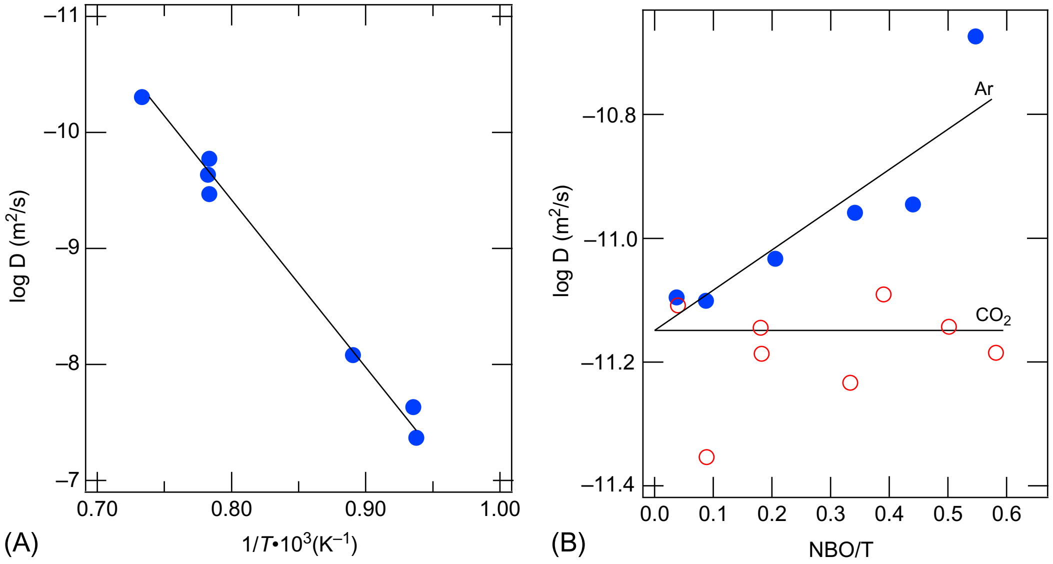

FIG. 16.17 Diffusion of Ar and total CO_2. (A) CO_2 diffusion in silica glass as a function of temperature yielding an activation energy of 105 ± 5 kJ/mol (Behrens, 2010). (B) Diffusion of total CO_2 and of Ar in various silicate melts as a function of melt polymerization, NBO/T, at 1350°C (Nowak et al., 2004).

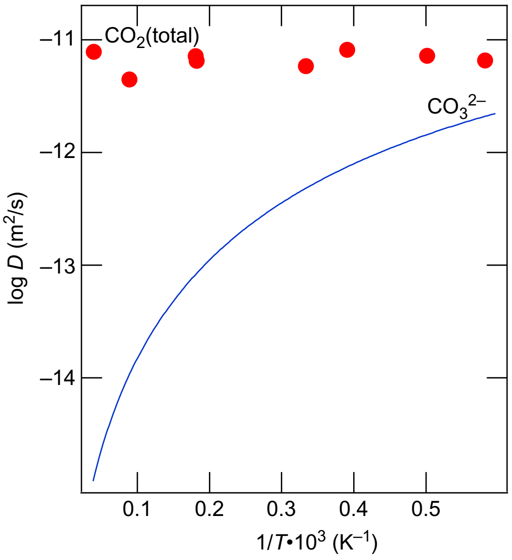

FIG. 16.18 CO_3 diffusivity in melts as a function of melt NBO/T as calculated by Nowak et al. (2004) from proportions of CO_2 and CO_3^{2-} groups in the melt and the diffusion coefficient for total CO_2 (see also Fig. 16.17).

by Vuilleumier et al. (2015), it seems that that dissolved CO_2 results in slightly enhanced diffusivity of network-modifying cations (e.g., Ca and Mg), whereas no effect on Si diffusion in simulated basalt-CO_2 and basalt melt compositions has been reported. To the best of our knowledge, diffusion data (or any other form of transport property data) are lacking for reduced carbon species in melts. However, given the structural similarities of methane and water, it would not be surprising if these two components had analogous influence on transport in silicate melts.

A few viscosity studies also exist for CO_2-saturated melts. Among them, two were conducted on fully polymerized aluminosilicate melts, $NaAlSi_3O_8$ and $KAlSi_3O_8$, at high pressure (Brearley and Montana, 1989; White and Montana, 1990), and one with a depolymerized potassium silicate melt, $K_2O{\cdot}1.3SiO_3$, at ambient pressure (Bourgue and Richet, 2001). In both environments, solution of CO_2 results in decreased melt viscosity (Fig. 16.17A). Notably, the viscosity in highly polymerized melts decreases with increasing pressure in a manner resembling that of the CO_2-free counterparts, which would be consistent with some melt depolymerization of aluminosilicate melts, as implied by Eq. (16.6).

The activation energy of viscous flow for the $K_2O{\cdot}1.3SiO_3$ melt increases only slightly with CO_2 content (about 10% increase with melt containing 0.2 wt% CO_2 to one containing 3.6 wt% (Bourgue and Richet, 2001). This slight increase would be consistent with silicate polymerization as CO_3 groups form in the melt (Eq. 16.3). In the high-pressure experiments with CO_2-bearing $NaAlSi_3O_8$ and $KAlSi_3O_8$ melts, the activation energy could not be derived because temperature was not an experimental variable (Brearley and Montana, 1989; White and Montana, 1990). It is noted, nevertheless, that the viscosity of CO_2-bearing melts shows approximately the same pressure dependence as the viscosity, of CO_2-free melts (Fig. 16.17A).

16.3.3.3 Volume Properties

Volume properties of CO_2-bearing silicate melts and glasses vary with temperature, pressure, and silicate composition. The room-temperature partial molar volume of CO_2 depends on silicate composition (Fig. 16.19). This feature likely reflects differences in CO_2 speciation. The rhyolite melt in Fig. 16.19 contains only molecular CO_2, whereas phonolite melt contains a mixture of molecular CO_2 and $CO_3{}^{2-}$ groups. Basaltic glass comprises only $CO_3{}^{2-}$ groups (Seifert et al., 2013). The bulk moduli of these glasses also are sensitive to composition, which probably reflect differing speciation in the three compositions.

The compression curve of CO_2 in basaltic melts decays exponentially with pressure (Ghosh et al., 2007; Duncan and Agee, 2011; Sakamaki et al., 2011); see Fig. 16.20. This curve resembles that obtained by first-principles molecular dynamics simulation (Guillot and Sator, 2011) although the latter results tend to yield slightly higher partial molar volume values for CO_2 at any pressure than do the results from high-pressure experiments. It is difficult to ascertain whether the compressibility of dissolved CO_2 depends on its solution mechanism, because all existing data appear to be for either basalt or more silica-deficient magmas, under which circumstances dissolved CO_2 likely exists exclusively as CO_3 groups.

The compressibility of CO_2 is less than that of dissolved water (Sakamaki et al., 2009, 2011). A major reason for this difference probably is that for dissolved water, the OH group is a part of the silicate network and follows, therefore, the compressibility curves of the melt and glass (see Chapter 15, Section 15.4.2), whereas the $CO_3{}^{2-}$ group in dissolved basaltic melts and glass forms isolated CO_3 complexes with alkaline earths (Ca and Mg), so that its compressibility is decoupled for that of the silicate network.

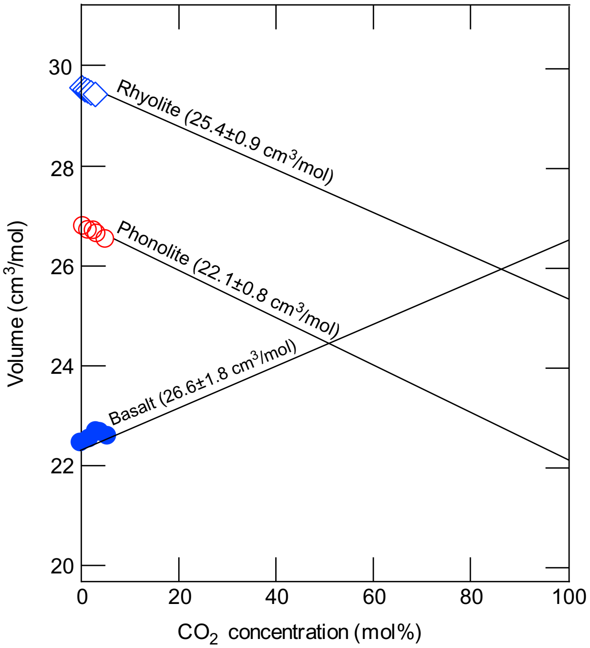

FIG. 16.19 Molar volume of silicate glasses annealed at ambient pressure. Numbers in parentheses denote partial molar volume of CO_2 in the melts (Seifert et al., 2013).

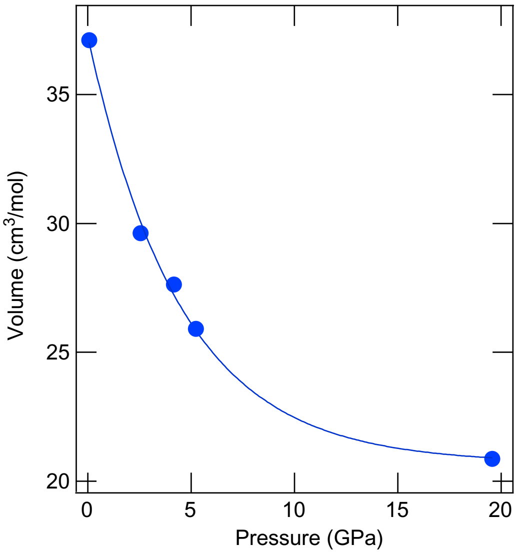

FIG. 16.20 Partial molar volume of CO_2 in basaltic melt as a function of pressure at 2300°C (data and compilation of literature data at <4GPa from Ghosh et al., 2007 and Duncan and Agee, 2011).

16.4 SULFUR IN S-O-H SYSTEMS

This system comprises a variety of volatile species. Here, we will restrict ourselves to simple reduced and oxidized sulfur species (S^{2-}, S^{4+} as in SO_2 or ${SO_3}^{2-}$ groups, and S^{6+} as in SO_3 or ${SO_4}^{2-}$ groups). These may all form complexes with silicate components in glass and melts and are, therefore, reactive components.

The oxidation state of sulfur governs its solubility and solution mechanisms in melts and glasses and, ultimately, its effects on melt properties (e.g., Richardson and Fincham, 1954; Abraham et al., 1960; Nagashima and Katsura, 1973; Sosinsky and Sommerville, 1986; Carroll and Webster, 1994; O'Neill and Mavrogenes, 2002; Paris et al., 2001; Backnaes et al., 2008, 2011; Park and Park, 2012). The principal oxidation and reduction equilibria of sulfur are:

$$\text{Oxidation to } S^{4+}: \quad S + O_2 + O^{2-}(\text{melt}) \Leftrightarrow {SO_3}^{2-}(\text{melt}), \tag{16.13}$$

$$\text{Oxidation to } S^{6+}: \quad SO_2 + 1/2O_2 + O^{2-}(\text{melt}) \Leftrightarrow {SO_4}^{2-}(\text{melt}), \tag{16.14}$$

$$\text{and reduction to } S^{2-}: \quad S_2 + 2O^{2-}(\text{melt}) \Leftrightarrow 2S^{2-}(\text{melt}) + O_2. \tag{16.15}$$

The equilibrium constants for these reactions as a function of oxygen fugacity, f_{O_2}, illustrate how decreasing f_{O_2} leads to increased solubility of reduced sulfur and decreased solubility of oxidized sulfur (Nagashima and Katsura, 1973); see Fig. 16.21. Similarly, at constant oxygen fugacity, the sulfur solubility increases with increasing sulfur fugacity as Eqs. (16.13)–(16.15) shift to the right (O'Neill and Mavrogenes, 2002); see also Fig. 16.22.

FIG. 16.21 Sulfur solubility relations in Na_2O-SiO_2 melts against oxygen fugacity at 1200°C and ambient pressure. *Redrawn from Nagashima and Katsura (1973).*

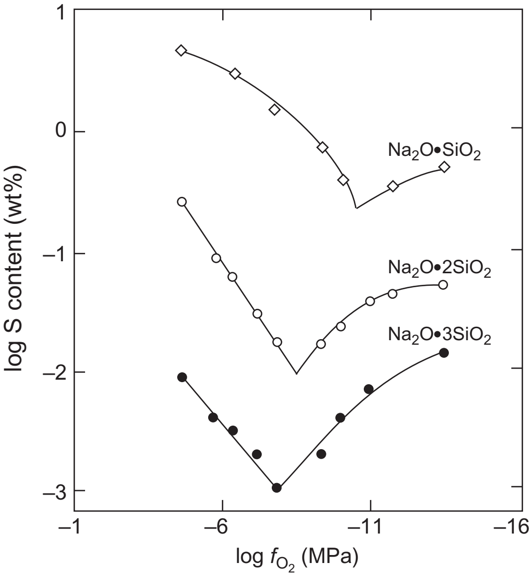

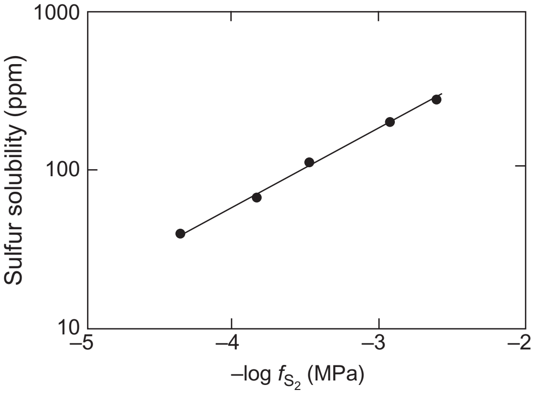

FIG. 16.22 Sulfur solubility in melts at 1400°C and ambient pressure in the system CaO-MgO-Al_2O_3 as a function of f_{S_2} at log $f_{O_2} = -10.28$ (O'Neill and Mavrogenes, 2002).

16.4.1 Solubility and Solution Mechanisms of Oxidized Sulfur

Oxidized sulfur in silicate melts and glasses exists either as SO_2 or SO_3. Their interaction between silicate melts and oxidized sulfur may be described as:

$$SO_x(\text{melt}) + O^{2-}(\text{melt}) \Leftrightarrow {SO_{x+1}}^{2-}(\text{melt}), \tag{16.16}$$

Whether oxidized sulfur in its molecular form, SO_x, does or does not dissolve in silicate melts or whether sulfur exists solely as ${SO_{x+1}}^{2-}$ in melts is not known.

Among the two possible oxidized states of sulfur, S^{6+} tends to dominate, but evidence for S^{4+} also has been reported (Métrich et al., 2002; Bingham et al., 2010; Wilke et al., 2008, 2011). It has been suggested, however, that the observed S^{4+} oxidation state reported in glasses may be the result of interaction between the sample and the intense X-ray beam used for the XANES spectroscopy used to determine the sulfur redox state (Metrich et al., 2009; Wilke et al., 2011). Results obtained with e-beam instruments certainly do show such an effect (Wilke et al., 2011). In light of these uncertainties, we will consider only S^{6+} in this discussion of oxidized sulfur.

Sulfur dioxide solubility in reaction (16.13) has the equilibrium constant:

$$K_{16.13} = a_{SO_4}(\text{melt})/f_{SO_2} \cdot (f_{O_2})^{0.5} a_{O^{2-}}(\text{melt}), \tag{16.17}$$

where a_i denotes the activity of component i and f_{O_2} and f_{S_2} the fugacities of oxygen and sulfur, respectively. By replacing the activity by the mol fraction of dissolved oxidized sulfur X_{SO_4} (Holmquist, 1966; see also Backnaes and Deubener, 2011, for recent review of this situation), one then expresses the solubility of oxidized sulfur as:

$$\log X_{SO_4} = 0.5 \log f_{O_2} + \log f_{SO_2} + \log\left(K_{16.13} + a_{O^{2-}}\right). \tag{16.18}$$

In addition, it can be determined whether or not, or how, a transition from reduced to oxidized sulfur occurs by combining the f_{O_2}-dependent S^{6+}/S^{2-}-relationships via the redox reaction:

$$S^{2-} + 2O_2 \Leftrightarrow {SO_4}^{2-}, \tag{16.19}$$

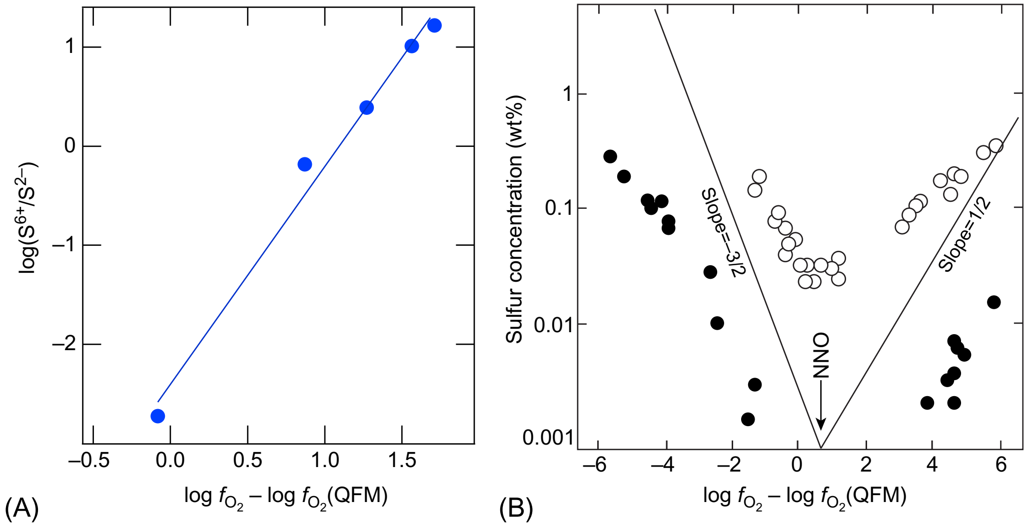

FIG. 16.23 (A) Oxygen fugacity vs oxidation ratio relative to the quartz-fayalite-magnetite oxygen buffer (QFM) for a synthetic basalt composition (Jugo et al., 2010). (B) Sulfur solubility in melts as a function of oxygen fugacity expressed relative to the QFM buffer. *Closed symbols*: 39.4% SiO_2-CaO-Al_2O_3 melts with data from Backnaes and Deubener (2011). *Open symbols*: Na_2O-SiO_2 melts with data from Holmquist (1966). The two sloped lines marked −3/2 and ½, respectively, indicate the slope expected for equilibria of SO_2 reduced to S^{2-} and oxidized to SO_4, respectively.

so that oxygen fugacity is linked to the equilibrium

$$\log f_{O_2} = 0.5 \cdot \left[\log\left(a_{SO_4}/a_{S^{2-}}\right) + \log K_{16.19}\right], \tag{16.20}$$

where $K_{16.19}$ is the equilibrium constant for equilibrium (16.19).

In a linear plot of sulfur redox ratio against f_{O_2}, Jugo et al. (2010) observed that the slope of the curve is about 2, which is consistent with the presence of only S^{2-} and SO_4 (Fig. 16.23). The equilibrium constants for equilibria (16.14) and (16.15) are linear functions of oxygen fugacity, f_{O_2}, from values above the oxygen fugacity buffer, $Ni+0.5O_2=NiO$ (NNO), to two orders of magnitude below it. The implication is that equilibrium (16.15) describes the solubility of SO_4 groups above the NNO buffer, whereas sulfide groups are the sole form of sulfur below about two orders of magnitude below the NNO buffer (Fig. 16.23). At intermediate oxygen fugacity, S^{2-} and $SO_4{}^{2-}$ coexist. The exact oxygen fugacity interval across which this latter situation exists depends on the silicate composition, whether in simple metal oxide-silicate systems (Nagashima and Katsura, 1973; Carroll and Webster, 1994) or more complex systems such as slags or natural magmatic liquids (Klimm et al., 2012; Lesne et al., 2015).

Even in a chemically simple melt or glass system such as Na_2O-SiO_2, increasing Na/Si, which is equivalent to increasing NBO/Si of the melts, results in a gradually increasing slope of the solubility curves (Fig. 16.24). There also appear to be systematic relationships between electronic properties of the metal cation and sulfate solubility (Fig. 16.24). In other words, the solubility of oxidized sulfur in silicate glasses and melts even at fixed silicate polymerization varies with the type of network-modifying cation as seen in the solubility of CO_2 in silicate

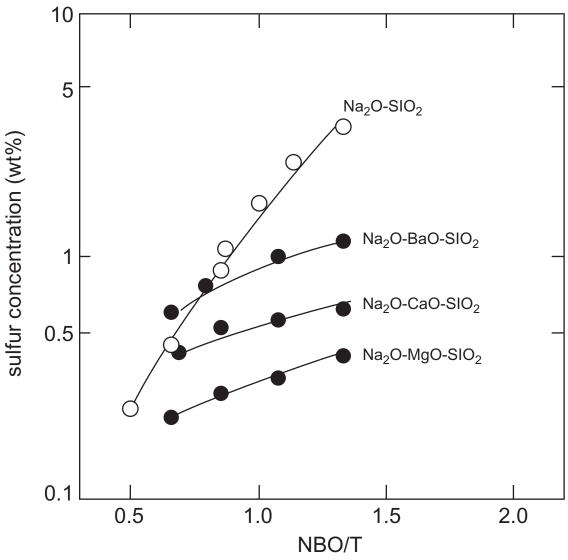

FIG. 16.24 Sulfur solubility in melts as a function of melt NBO/T and other compositional variables, including cation properties. Data are from Ooura and Hanada (1998) *(solid symbols)* and Nagashima and Katsura (1973) *(open symbols)*.

melts (Fig. 16.4). There also may be a general positive correlation between sulfate concentration and water content in a mixed silicate-S-O-H system (Lesne et al., 2015). This correlation may simply reflect the result of dissolved water, which causes silicate depolymerization, because increased silicate depolymerization drives increasing sulfate solubility.

The positive correlation between solubility of oxidized sulfur, SO_4^{2-}, and NBO/T of the silicate network, can be rationalized with a simple solution equilibrium of the type:

$$SO_3(g) + 2Q^n \Leftrightarrow 2Q^{n+1} + SO_4(m) \tag{16.21}$$

In Eq. (16.21), the role of metal cations to form bonding with oxygen in the Q-species and in the SO_4 groups is removed for simplicity. It follows, then, that as the SO_4 concentration in a melt increases and equilibrium (16.21) is shifted to the right, the degree of polymerization of the silicate melt also increases (Q^n is transformed to the more polymerizing Q^{n+1}). This relationship is analogous to that where CO_2 dissolves to form CO_3^{2-} groups and in the process polymerizes the silicate network (Eq. 16.3).

16.4.2 Solubility and Solution Mechanisms of Reduced Sulfur

Sulfur solubility varies with the fugacity of sulfur and oxygen (Richardson and Fincham, 1954; Sosinsky and Sommerville, 1986; Seo and Kim, 1999; O'Neill and Mavrogenes, 2002; Jugo et al., 2005, 2010; Wilke et al., 2011). At oxygen fugacity conditions less oxidizing than about two orders of magnitude below that defined by the NNO oxygen buffer S^{2-} is the stable form of sulfur in silicate glasses and melts (Jugo et al., 2010; Bingham et al., 2010; Backnaes and Deubener, 2011); see also Fig. 16.23.

The transformation of oxidized sulfur, S^{6+} as SO_3, to reduced sulfide is a redox reaction that involves changes in silicate polymerization:

$$Q^n(M) + SO_3 \Leftrightarrow M_2S + Q^{n+1}(M/2) + 2O_2. \tag{16.22}$$

In Eq. (16.22), the Q^n(M) and Q^{n+1}(M/2) notations indicate silicate Q^n-species with a nonbridging oxygen bonded to a network-modifying metal cation. The Q^{n+1}(M/2) implies that the Q^{n+1}-species require only half the number of metal cations for bonding to their smaller number of bridging oxygen, compared with the less polymerizing Q^n(M)-species. The M_2S indicates metal sulfide complex in the melt and glass.

It follows from Eq. (16.22) that, at constant sulfur and oxygen fugacity, the S^{6+}/S^{2-} ratio of a melt tends to increase as the structure is more polymerized in accord with observations (Fig. 16.25) (see also Klimm et al., 2012), although it is clear that other compositional factors also affect this ratio. It also follows that, in mixed S-O-H fluids, the sulfur redox ratio, S^{6+}/S^2, decreases with increasing water content because of the linkage between water content and silicate polymerization (see Chapter 15, Section 15.3).

The solubility of sulfur as S^{2-} in silicate melts and glasses has been linked to the stability of metal sulfide complexes (M_2S or MS type). With this in mind, the concept of sulfur capacity was introduced to express the solubility in terms of weight fraction of metal cations, X_i, oxygen and sulfur fugacity (Fincham and Richardson, 1954):

$$C_S = X_i \cdot (f_{O_2}/f_{S_2}). \tag{16.23}$$

The influence of oxide concentration on the sulfur capacity can be dramatic (Fig. 16.26A), probably reflecting different affinities of S^{2-} for specific cations in the melt such as Fe^{2+} rather than Ca^{2+} (Abraham et al., 1960; Park and Park, 2012). The sulfide capacity also is positively correlated with the ratio of network-modifiers to network-formers but is insensitive to the proportion of different network-formers (Al and Si) (Park and Park, 2012); see also Fig. 16.26B.

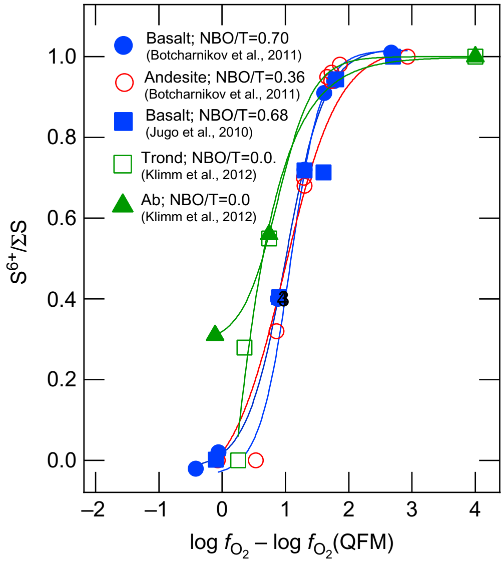

FIG. 16.25 Redox ratio of sulfur in melt with varying NBO/T-values as a function of oxygen fugacity expressed relative to that of the QFM oxygen buffer (Jugo et al., 2010; Botcharnikov et al., 2011; Klimm et al., 2012). Abbreviations: *Trond*, trondhjemite; *Ab*, $NaAlSi_3O_8$.

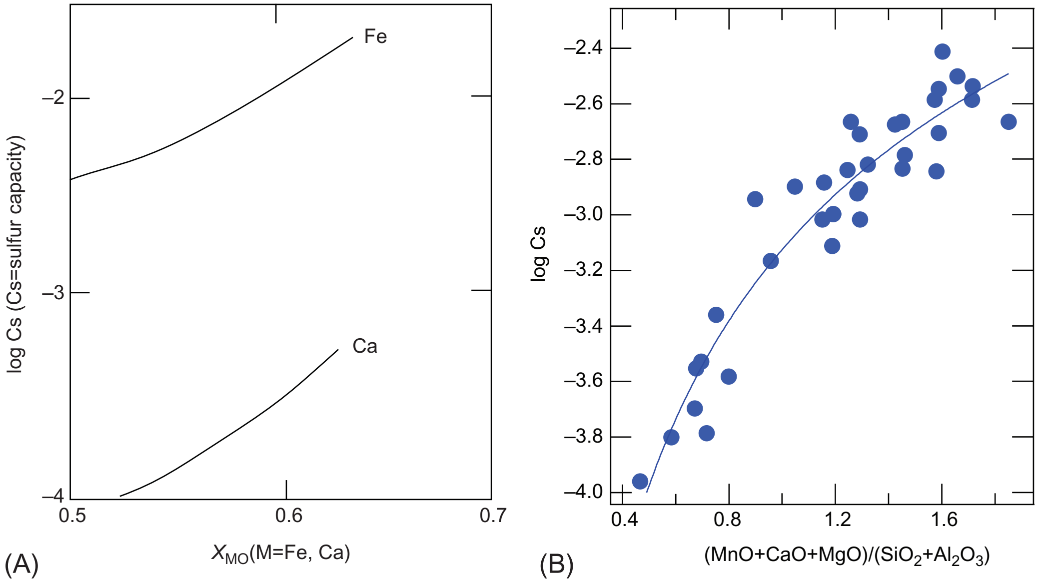

FIG. 16.26 (A) Sulfur capacity, C_s, as a function of the mol fraction of metal oxides, CaO and FeO, in CaO-SiO_2 and FeO-SiO_2 melts (Abraham et al., 1960). (B) Sulfide capacity as a function of proportion of network-modifiers relative to network-formers in the 1400–1600°C range. *Redrawn from Taniguchi et al. (2009) and Park and Park (2012).*

Recent work on oxysulfides, in which some of the oxygens in the silicate tetrahedra are replaced with sulfide, has focused on Li-bearing systems because of the use of such materials in Li-ion battery technology (Hayashi and Tatsumisago, 2018). Sulfur solubility limits in such systems appear not to have been studied. However, from ^{29}Si MAS NMR examination of Li_2S-LiS_2-SiO_2 glasses, sulfur substitution of the oxygen in the silicate tetrahedral does take place in a manner that structurally resembles oxycarbide (see Section 16.3.2) and oxynitride (see Section 16.5.3) substitutions. There appears to be a systematic relationship among species and proportion of sulfur-bearing and sulfur-free structural units (Tatsumisago et al., 2000); see also Fig. 16.27.

16.4.3 Properties and Solution Mechanisms in S-O-H Systems

16.4.3.1 Thermal Properties

Despite the many applications of S-bearing melt and glass systems to industrial and natural processes, the availability of thermal properties of S-bearing silicate systems is surprisingly limited. Some data exist to estimate sulfate activity in Na_2SO_4-bearing Na_2O-SiO_2 glasses and melts (Holmquist, 1966; Buhler, 1999). Here, it was found that the activity coefficient, γ_{Na_2SO4}, shows strong positive deviations from unity and that this deviation increases with increasing Na_2O/SiO_2 abundance ratio (Fig. 16.28). It must be noted, however, that the latter relationships were derived with the assumptions that the activity coefficient of Na_2O does not change as Na_2SO_4 was dissolved in a melt. Buhler (1999) also

FIG. 16.27 Oxysulfide and silicate species in glasses formed by temperature quenching after equilibration at 1000°C (Tatsumisago et al., 2000).

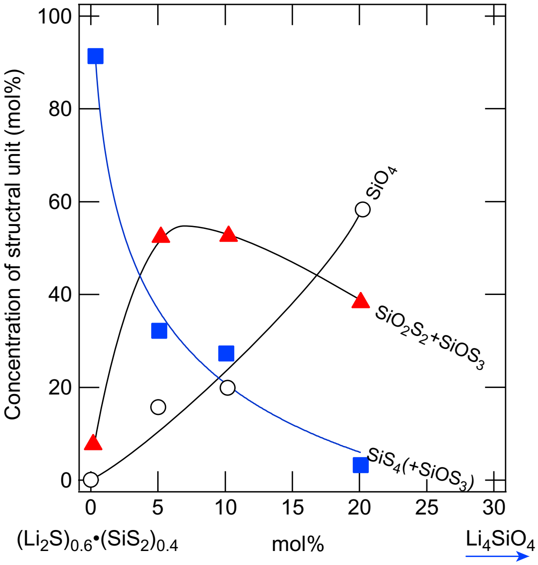

FIG. 16.28 Activity-composition relations in Na_2O-SiO_2-Na_2SO_4 at 1200°C as a function of the mol fraction ratio X_{Na_2O}/X_{Na_2SO4}. *Redrawn from Buhler (1999).*

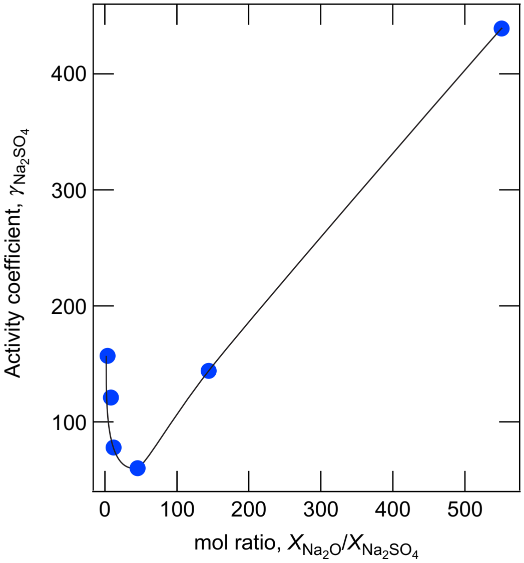

suggested that glasses in the reduced system, Na_2O-SiO_2-Na_2S, exhibited strong deviations from ideal mixing. In that study, it was assumed that there is no interaction between the silicate and S-bearing components in the melts. The latter assumption likely is an oversimplification of the relationships between sulfur solubility, sulfur redox state, and polymerization of silicate structure (Figs. 16.23–16.25). Unfortunately, it appears that no experimental or theoretical data exist with which to evaluate such relationships further.

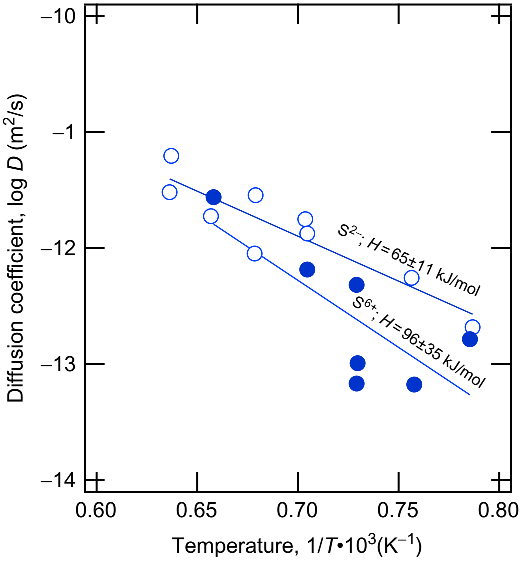

FIG. 16.29 Arrhenius plot for sulfur diffusion Na_2O-CaO-SiO_2 melt composition under reducing conditions (S^{2-} is stable oxidation state) and oxidizing condition (S^{6+} is stable oxidation state). *Redrawn from Behrens and Stelling (2011).*

16.4.3.2 Transport Properties

Transport properties such as sulfur diffusion have been the subject of a significant body of experimental research (Baker and Rutherford, 1996; Freda et al., 2005; de Lemastre et al., 2005; Frischat et al., 2011; Behrens and Stelling, 2011; Backnaes et al., 2011). Taken together, these studies incorporate the effect of silicate composition, redox state of sulfur, and addition of H_2O (see, e.g., Appendix Table 1 in Behrens and Stelling, 2011).

Sulfur diffusivity depends on the oxidation state (Fig. 16.29). Moreover, the activation energies of diffusion under both oxidizing and reducing conditions range between 115 kJ/mol for S^{2-} in hydrous andesite melt (Watson, 1994) to 458 kJ/mol in nominally anhydrous $NaAlSi_3O_8$ melt (Winther et al., 1998) (see also Table 16.2). Such activation energies are in the range of Si—O and Al—O bond energies (see Chapter 2, Section 2.2), which leads to the

TABLE 16.2 Activation Energies of Sulfur Diffusion in Melts and Glasses, kJ/mol (From Data Compilation by Behrens and Stelling, 2011)

Composition	**Activation Energy (kJ/mol)**
Silica glass (sub-Tg)	193
$Na_2Si_3O_7$	177 ± 22
Na_2O-CaO-SiO_2	215 ± 31
$NaAlSi_3O_8$	458 ± 51
Rhyolite (5.8 wt% H_2O)	142 ± 29
Rhyolite	205 ± 24
Dacite	263

suggestion of bond disruption and formation in the silicate network during sulfur diffusion. That would also be consistent with sulfate and sulfide solution mechanisms in silicate melts as represented by Eqs. (16.21), (16.22), which makes it clear that the solution mechanisms of both SO_4 and S^{2-} groups are linked to the silicate network. The transport properties of oxysulfides as a function of S/O ratio appear analogous to those observed of oxycarbides as a function temperature and C/O (Renlund et al., 1991; Ikeda et al., 2001). It cannot be ruled out, therefore, that at least for sulfur diffusion under reducing conditions, rupture and formation of Si—S bonding in oxysulfide complexes could be involved.

16.5 NITROGEN IN N-O-H SYSTEMS

Nitrogen under oxidizing conditions commonly dissolves in glasses and melts in its molecular form,

N_2, and as such is a nonreactive volatile component (see, e.g., Doremus, 1966; Libourel et al., 2003; Miyazaki et al., 2004; Roskosz et al., 2006; Mysen et al., 2008; Kadik et al., 2011, 2013); see also Chapter 17, Section 17.3. However, it has also been reported from ^{15}N MAS NMR studies of alkali silicate glass and melt that oxidized nitrogen may form nitrosyl groups, where nitrogen may be considered a reactive volatile component (Roskosz et al., 2006). The most common form of reactive nitrogen is, however, (N..H) complexes that form in silicate melts under reducing conditions (Mysen and Fogel, 2010; Mysen et al., 2014; Kadik et al., 2013; Li et al., 2015).

16.5.1 Solubility and Solution Mechanisms of Reduced Nitrogen

Nitrogen solubility in silicate melts depends on temperature, pressure, silicate composition, and redox conditions. In this respect, nitrogen behaves in a manner qualitatively similar to other multivalent volatiles in the C-O-H-N-S system (see previous discussion and also Chapters 15 and 17).

Nitrogen solubility as a function of hydrogen fugacity, f_{H_2}, in silicate-N-O-H melts reveal increasing solubility with increasing f_{H_2} (Fig. 16.30) (see also Mysen et al., 2008). Increasing nitrogen solubility in silicate-N-O-H melts with increasing f_{H_2} (and decreasing f_{O_2}) was also reported by Kadik et al. (2011).

There are discrete groups of solubility data defined by different redox conditions (as controlled by oxide + H_2O buffers indicated in Fig. 16.30). Raman spectra of quenched melt (glass) provide structural information in support of the solubility mechanisms (Fig. 16.30B). There is an evolution of the nitrogen-bearing species under increasingly reducing conditions from N_2 molecules under the most oxidizing conditions, to amide groups coexisting with molecular N_2 under intermediate redox conditions to ammine groups coexisting with molecular NH_3 under the most reducing conditions (Fig. 16.30B). Those spectroscopic data are similar to those reported by Kadik et al. (2013) from quenched melts (glasses) in the chemically somewhat more complex system, Na_2O-Al_2O_3-FeO-SiO_2-N-O-H. Li et al. (2015) also reported NH_3 molecules in silicate glasses quenched from melts, but suggested that NH_4 groups may also exist.

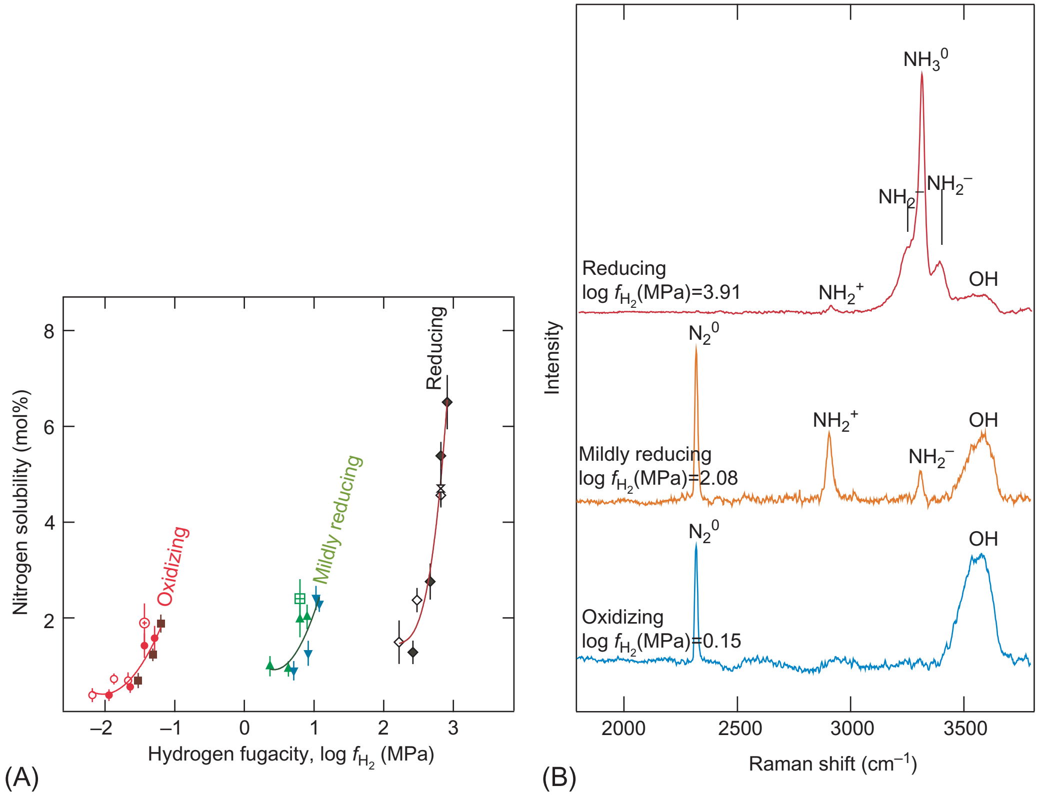

FIG. 16.30 (A) Nitrogen in temperature-quenched Na_2O-SiO_2 melts (from 1400°C and 1–2.5 GPa pressure) as a function of hydrogen fugacity (redox conditions). (B) Raman spectra of temperature-quenched Na_2O-SiO_2 melts (quenched from 1400°C and 2.5 GPa) under various redox conditions as indicated by the hydrogen fugacity on each spectrum (Mysen et al., 2008).

The solubility of reduced nitrogen varies with silicate composition (Fig. 16.31). These variations resemble the solubility of reduced carbon with composition (Fig. 16.11). The solubilities of carbon and nitrogen both increase the less polymerized the silicate.

The solution mechanism of reduced nitrogen in silicate melts can be written in a way analogous to that of reduced carbon (Eq. 16.11):

$$2Q^n + NH_3 \Leftrightarrow Q^{n-1}(NH_2) + Q^{n-1}(OH). \tag{16.24}$$

In other words, there is an equilibrium between molecular NH_3 and NH_2 groups where the NH_2 group substitutes for oxygen in the silicate network. This also means that solution of reduced nitrogen in melt and glasses results in depolymerization of the silicate structure. It also means that when a glass or melt is depolymerized (i.e., Q^{n-1}/Q^n increases), the NH_2/NH_3 ratio should decrease to satisfy the equilibrium constant of reaction (16.24):

FIG. 16.31 Solubility in melts of reduced nitrogen species (NH_2+NH_3 complexes) in glass formed by temperature-quenching from 1400°C at 2.0 GPa pressure as a function of melt NBO/T. Experiments were conducted at the hydrogen fugacity controlled by the IW+HO hydrogen buffer (Mysen and Fogel, 2010). Also shown for comparison are data from Roskosz et al. (2006) for nitrogen solubility in similar melts, but under oxidizing conditions. Note the lack of discernible NBO/T-effect.

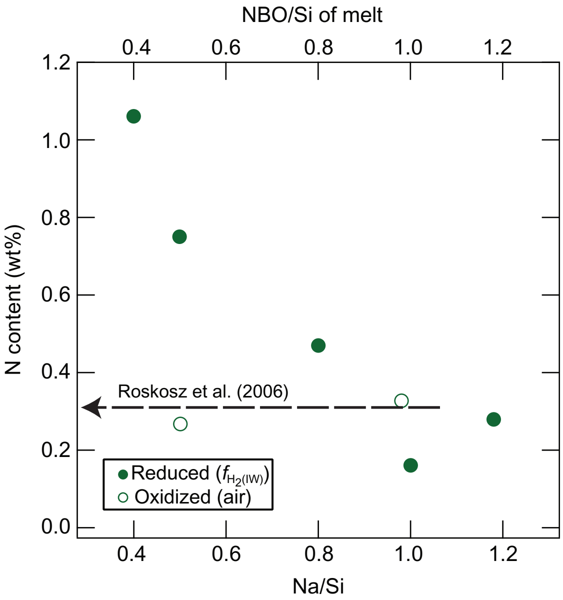

FIG. 16.32 Evolution of abundance ratio, X_{NH_2}/X_{NH_3}, in Na_2O-SiO_2 glass quenched from melt equilibrated at 1400°C and 2 GPa at the redox conditions of the IW-H_2O hydrogen buffer. The proportions are calculated relative their value for a glass composition with NBO/Si = 0.4.

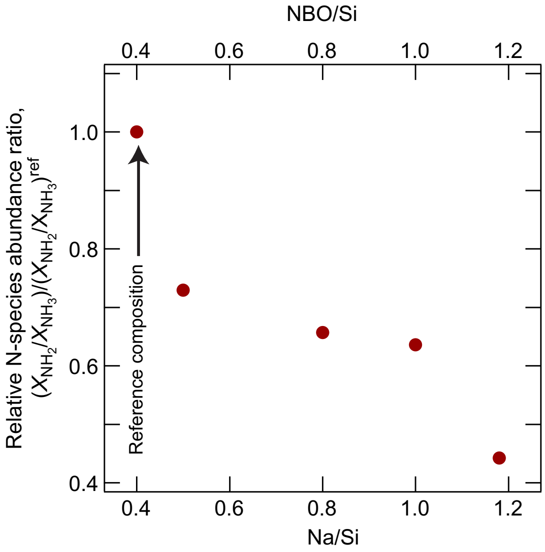

$$K_{16.24} = \left[X_{Q^{n-1}(OH)}/\left(X_{Q^n}\right)^2\right] \cdot \left[X_{Q^{n-1}(NH_2)}/X_{NH_3}\right]. \tag{16.25}$$

This is precisely what happens (Fig. 16.32).

Equilibrium (16.24) likely shifts to the left with increasing temperature because the NH_3/NH_4 ratio increases with temperature (Mysen et al., 2014). This temperature dependence differs, therefore, from that of the CH_3/CH_4 equilibrium, which shifts to the right with temperature (Eq. 16.11 and Fig. 16.13B).

An intermediate redox state of nitrogen, expressed as $NH_2{}^+$ groups (Fig. 16.30), was also reported from the Raman spectra reported by Kadik et al. (2013). Molecular nitrogen, N_2, also is present in such melts and glasses. In this case, the equilibrium between molecular species and $NH_2{}^+$ functional groups in silicate glasses and melts can be expressed as:

$$4Q^n + 2N_2 + 4H_2 + O_2 \Leftrightarrow 4NH_2{}^+ + 4Q^{n-1}. \tag{16.26}$$

This is a redox reaction whereby molecular N_2 is reduced to $NH_2{}^+$ and the $NH_2{}^+$ group effectively serves as a network-modifier and likely bonds to a nonbridging oxygen in the silicate structure.

In summary, the solution mechanisms of nitrogen in silicate-N-O-H melts and glasses can have dramatically different effects on the structure depending on the redox ratio. First, under sufficiently oxidizing conditions where only N_2 molecules are stable, there is no effect of dissolved nitrogen on silicate structure (see Chapter 17). At intermediate redox conditions, molecular NH_3 and H_2 coexist with amide groups, $NH_2{}^+$, which leads to silicate depolymerization (Eq. 16.26). With further reduction of nitrogen, ammine groups replace oxygen in the silicate tetrahedral network so that the glass and melt structure becomes depolymerized (Eq. 16.24).

16.5.2 Oxynitride and Nitrosyl Substitution

Nitrogen may also dissolve in silicate glasses and melts as nitrosyl groups to form Si—O—N bonding (Roskosz et al., 2006). Oxynitrides are formed when oxygen in silicate tetrahedra is replaced by one or more nitrogens (Das, 2000; Hampshire et al., 1994; Hampshire and Pomeroy, 2018). In cases where all nitrogen replaces oxygen in the tetrahedra, we have nitride glasses (Rouxel et al., 1989; Grande et al., 1995; Sakka, 1995; Munoz et al., 2004). Nitrosyl groups can form under highly oxidizing conditions, whereas oxynitride glasses typically are formed under reducing conditions.

16.5.2.1 Nitrosyl Groups

Nitrosyl groups, where nitrogen bonds with oxygen in silicate tetrahedra, have been studied experimentally in silicate glasses formed by temperature quenching from 1400°C at 1–2 GPa, under which conditions the melts were equilibrated with air (Roskosz et al., 2006). These groups were identified with Raman and ^{15}N MAS NMR spectroscopy. The abundance ratio of nitrosyl groups to molecular nitrogen increases as melts become increasingly depolymerized. This abundance ratio also increases with decreasing pressure and with decreasing ionic radius of the network-modifying cation (Roskosz et al., 2006); see also Fig. 16.33.

The solution mechanism that describes formation of nitrosyl groups in H-free silicate glasses and melts can be expressed as:

$$12Q^n(M) + 3O_2 + 2N_2 \Leftrightarrow 2Q^{n-1}(N) + 6Q^{n-1}(M). \tag{16.27}$$

FIG. 16.33 Abundance ratio, nitrosyl groups/total nitrogen for glasses along the Na_2O-SiO_2 join quenched from temperatures at pressures indicated on individual lines in diagram (Roskosz et al., 2006).

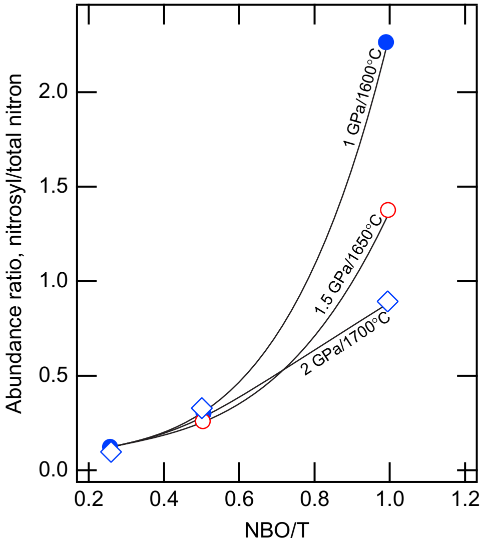

In this reaction, $Q^n(M)$ and $Q^{n-1}(M)$ denote Q-species with M-cations as network-modifiers and forming bonding, therefore, with nonbridging oxygen. The $Q^n(M)$ is more polymerized than $Q^{n-1}(M)$. The $Q^{n-1}(N)$-species is a structural entity where nitrogen as N^{3+} effectively serves as a network-modifying cation in replacement of a metal cation. Such a structure obviously requires that three nonbridging oxygens be linked to the N^{3+}. In other words, formation of nitrosyl groups in a silicate melt and glass results in silicate depolymerization.

Formation of nitrosyl groups affects activity-composition relations of nitrogen in silicate melts. Nitrogen in molecular form, N_2, dissolves according to Henry's Law (Miyazaki et al., 2004; Roskosz et al., 2006). However, upon formation of nitrosyl groups in a melt, the solubility deviates from such a simple relationship because the bulk nitrogen solubility, when extrapolated from high pressure to 1, does not pass through 0, as would be expected if Henry's Law was obeyed (Roskosz et al., 2006); see also Fig. 16.34.

16.5.2.2 Oxynitride Glasses

Oxynitride glasses have nitrogen substituting for oxygen in the silicate network. This substitution enhances melt viscosity, density, glass transition temperatures, compressibility, durability, and crystallization behavior (Sakka, 1995; Deckwerth and Russel, 1997; Pomeroy and Hampshire, 2003; Hampshire, 2003; Richet et al., 2010; Rouxel, 2011; Hampshire and Pomeroy, 2018). For example, the viscosity of aluminosilicate melts with oxynitride functional groups is greater than that of the nitride-free system (Das, 2000); see also Fig. 16.35. These properties have been ascribed to the stronger Si—N bonds compared with Si—O bonds. Similarly, thermodynamic properties such as heat capacity and entropy of oxynitride glasses are smaller than those of oxides (Richet et al., 2010) (see also Fig. 16.36), which also relates to the enhanced strength of the nitride bonds.

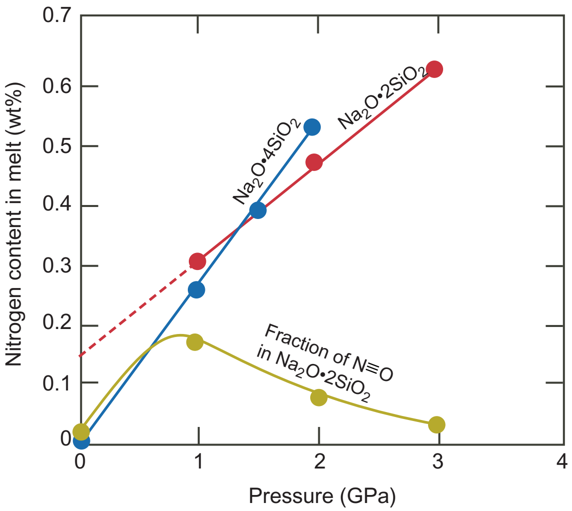

FIG. 16.34 Nitrogen solubility in $Na_2O{\cdot}2SiO_2$ and $Na_2O{\cdot}4SiO_2$ glass quenched from melt equilibrated at 1600°C as a function of pressure. Also shown is the fraction of nitrogen in $Na_2O{\cdot}2SiO_2$ glass that does not dissolve in molecular form (Roskosz et al., 2006).

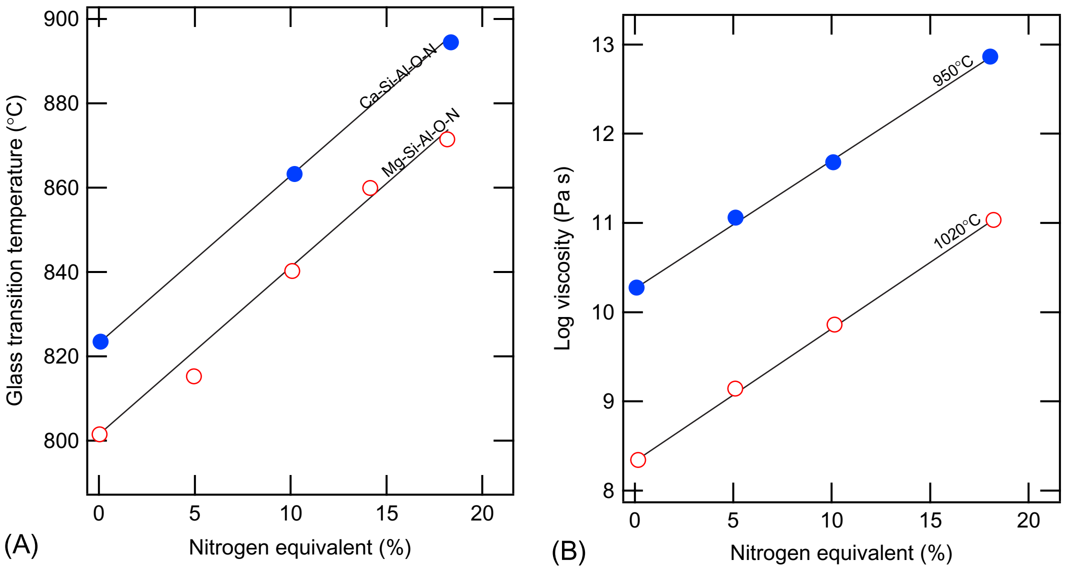

FIG. 16.35 Physical properties of oxynitride, M-Si-Al-O-N, melts. (A) Glass transition temperatures as a function of nitrogen content where M = Ca and Mg as marked. (B) Melt viscosity as a function of nitrogen content for Y-Si-Al-O-N melt at two different temperatures as shown (Das, 2000).

The structural inferences made from such properties of oxynitride glasses are in accord with actual structural measurements. Results of molecular dynamics calculations indicate that the Si—O bond is about 4% longer than the bridging Si—N bond and the Si—N—Si bond angle as much as 15% smaller than the bridging Si—O—Si bonds (Murakami and Sakka, 1988). From multinuclear MAS NMR, it has been shown that in alumino-oxynitride glasses,

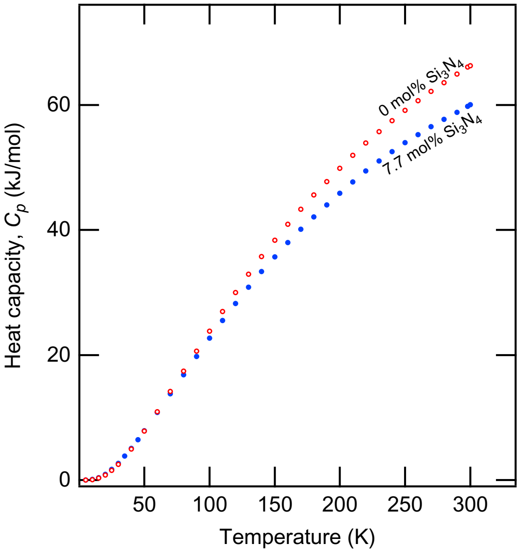

FIG. 16.36 Heat capacity of Si-Al-O-N glasses as a function of Si_3N_4 substitution. Composition, 0 mol% Si_3N_4: $SiO_2 = 65.6$, Al_2O_3: 12.5, Y_2O_3: 21.9. 7.7 mol% Si_3N_4: $SiO_2 = 52.7$, Al_2O_3: 14.4, Y_2O_3: 25.2, Si_3N_4: 7.7 (Richet et al., 2010).

there are systematic relationships between nitrogen content and nitrogen substitution for oxygen in Q-species of the structure (Koroglu et al., 2011) in a manner analogous to oxycarbide and oxysulfide substitution in silicate tetrahedra (Table 16.1, Fig. 16.27).

Nitride solution may be viewed as a redox-driven reaction that involves molecular N_2 and nitride groups:

$$Q^n(M) + N_2 \Leftrightarrow Q_N^{n-2}(M). \tag{16.28}$$

In this equation, Q_N^{n-2} (M) is a more depolymerizing Q-species (by a factor of 2 oxygen bridges/Si) where one of the oxygens is replaced by nitrogen. In other words, formation of oxynitride glasses results in depolymerization of the network.

Despite the depolymerizing effect of nitride substitution, properties that are correlated with melt polymerization, such as for example melt viscosity, actually increase with increasing N/O abundance ratio (Fig. 16.35). Evidently, the enhanced bond strength of Si—N bonding overshadows the effect of melt polymerization on melt transport behavior.

The nitrogen stability in oxynitride melts also can be used to characterize the relationships between increasing nitrogen solubility in melts as the system gets increasingly reduced (Libourel et al., 2003). Such a relationship would be reminiscent of the sulfur solubility in hydrogen-free melts in increasingly reducing environments, as sulfur replaces oxygen in silicate systems (Namur et al., 2016).

16.5.3 Properties and Solution Mechanisms in (N-O-H) Systems

Information on effects of dissolved nitrogen on properties of silicate melts and glasses is quite scarce. One may therefore only be able to predict properties from similarities of nitrogen solution mechanisms with those of other volatiles with analogous solution mechanisms.

These include CH_4 (Section 16.3.2, Eq. 16.11) and H_2O (Chapter 15, Eq. 15.5). For both volatiles, the rate of silicate depolymerization per mol dissolved volatile component in principle is the same, although details of CH_4/CH_3 and NH_3/NH_2 ratio are less well known than H_2O/OH ratio. Quantitative differences between the effects of these different volatiles would, therefore, be expected. The melt properties depending on NBO/Si-dependent are affected by the redox state of nitrogen. For example, liquidus melting temperatures and phase relations are quite sensitive to melt polymerization, as discussed in Chapter 15 on solution mechanisms of water in melts (Section 15.4.4). In analogy with hydrous melts, this would mean that solution of reduced NH_2^- functional groups in melts will lower the activity coefficient of silica, for example. Very likely, NH_2-rich melts will also be less viscous than those without reduced nitrogen species. Associated transport properties such as diffusion and conductivity will follow similar trends. These properties will also be sensitive to variable redox conditions, much like the change in (C-O-H)-saturated melt as the carbon species are reduced from CO_2 to CH_4 (see Section 16.3.3).

References

Abraham, K.P., Davies, M.W., Richardson, F.D., 1960. Sulphide capacities of silicate melts. J. Iron Steel Inst. 196, 309–312.

Ardia, P., Hirschmann, M.M., Withers, A.C., Stanley, B.D., 2013. Solubility of CH_4 in a synthetic basaltic melt, with applications to atmosphere-magma ocean-core partitioning of volatiles and to the evolution of the Martian atmosphere. Geochim. Cosmochim. Acta 114, 52–71.

Armstrong, L.S., Hirschmann, M.M., Stanley, B.D., Falksen, E.G., Jacobsen, S.D., 2015. Speciation and solubility of reduced C-O-H-N volatiles in mafic melt: Implications for volcanism, atmospheric evolution, and deep volatile cycles in the terrestrial planets. Geochim. Cosmochim. Acta 171, 283–302.

Backnaes, L., Deubener, J., 2011. Experimental studies on sulfur solubility in silicate melts at near-atmospheric pressure. Rev. Mineral. Geochem. 73, 143–165.

Backnaes, L., Stelling, J., Behrens, H., Goettlicher, J., Mangold, S., Verheijen, O., Beerkens, R.G.C., Deubener, J., 2008. Dissolution mechanisms of tetravalent sulphur in silicate melts: evidences from sulphur K edge XANES studies on glasses. J. Am. Ceram. Soc. 91, 721–727.

Backnaes, L., Deubener, J., Behrens, H., Stelling, J., Cichy, S.B., Bartels, A., 2011. Diffusion of the ^{35}S isotope in soda–lime–silica and sodium trisilicate glass melts. J. Non-Cryst. Solids 357, 2941–2948.

Baker, L.L., Rutherford, M.J., 1996. Sulfur diffusion in rhyolite melts. Contrib. Mineral. Petrol. 123, 335–344.

Behrens, H., 2010. Ar, CO_2 and H_2O diffusion in silica glasses at 2 kbar pressure. Chem. Geol. 272, 40–48.

Behrens, H., Gaillard, F., 2006. Geochemical aspects of melts: volatiles and redox behavior. Elements 2, 275–280.

Behrens, H., Stelling, J., 2011. Diffusion and redox reactions of sulfur in silicate melts. Rev. Mineral. Geochem. 73, 79–111.

Behrens, H., Misiti, V., Freda, C., Vetere, F., Botcharnikov, R.E., Scarlato, P., 2009. Solubility of H_2O and CO_2 in ultrapotassic melts at 1200 and 1250 degrees C and pressure from 50 to 500 MPa. Am. Mineral. 94, 105–120.

Bingham, P.A., Connelly, A.J., Hand, R.J., Hyatt, N.C., Northrup, P.A., Mori, R.A., Glatzel, P., Kavcic, M., Zitnik, M., Bucar, K., Edge, R., 2010. A multi-spectroscopic investigation of Sulphur speciation in silicate glasses and slags. Glass Technol. Eur. J. Glass Sci. Technol. A 51, 63–80.

Boettcher, A.L., 1984. The system SiO_2-H_2O-CO_2: melting solubility mechanisms of carbon and liquid structure to high pressures. Am. Mineral. 69, 823–834.

Boettcher, A.L., Luth, R.W., White, B.S., 1987. Carbon in silicate liquids: the systems $NaAlSi_3O_8$-CO_2, $CaAl_2Si_2O_8$-CO_2, and $KAlSi_3O_8$-CO_2. Contrib. Mineral. Petrol. 97, 297–304.

Botcharnikov, R.E., Behrens, H., Holtz, F., 2006. Solubility and speciation of C-O-H fluids in andesitic melt at T = 1100–1300 degrees C and P = 200 and 500MPa. Chem. Geol. 229, 125–143.

Botcharnikov, R.E., Linnen, R.L., Wilke, M., Holtz, F., Jugo, P.J., Berndt, J., 2011. High gold concentrations in sulphide-bearing magma under oxidizing conditions. Nat. Geosci. 4, 112–115.

Bourgue, E., Richet, P., 2001. The effects of dissolved CO_2 on the density and viscosity of silicate melts: a preliminary study. Earth Planet. Sci. Lett. 193, 57–68.

Brearley, M., Montana, A., 1989. The effect of CO_2 on the viscosity of silicate liquids at high pressure. Geochim. Cosmochim. Acta 53, 2609–2616.

Brooker, R.A., Kohn, S.C., Holloway, J.R., McMillan, P.F., 2001. Structural controls on the solubility of CO_2 in silicate melts. Part I: bulk solubility data. Chem. Geol. 174, 225–239.

Buhler, P., 1999. Thermodynamics of reactions between oxide glass melts and gases: II. Solubility of gases containing sulfur (SO_3, SO_2, and S^{-2}). *Glass Phys.* Chem. 25, 434–440.

Carroll, M.R., Webster, J.D., 1994. Solubilities of sulfur, noble gases, nitrogen, chlorine, and fluorine in magmas. Rev. Mineral. 30, 231–279.

Das, T., 2000. Oxynitride glasses – an overview. Bull. Mater. Sci. 23, 499–507.

de Lemastre, R.E., Jomard, F., Majimel, J., Bernas, H., 2005. Diffusion properties of chalcogens (S, Se, Te) into pure silica. J. Non-Cryst. Solids 351, 3031–3039.

Deckwerth, M., Russel, C., 1997. Crystallization of oxynitride glasses in the system Mg-Ca-Al-Si-O-N prepared with the aid of a polymeric precursor. J. Non-Cryst. Solids 217, 55–65.

Doremus, R.H., 1966. Physical solubility of gases in fused silica. J. Am. Ceram. Soc. 49, 461–462.

Duncan, M.S., Agee, C.B., 2011. The partial molar volume of carbon dioxide in peridotite partial melt at high pressure. Earth Planet. Sci. Lett. 312, 429–436.

Duncan, M.S., Dasgupta, R., 2014. CO_2 solubility and speciation in rhyolitic sediment partial melts at 1.5–3.0 GPa – implications for carbon flux in subduction zones. Geochim. Cosmochim. Acta 124, 328–347.

Eggler, D.H., 1974. Effect of CO_2 on the melting of peridotite. In: Carnegie Instn. Washington Year Book.vol. 73. pp. 215–224.

Eggler, D.H., 1975. CO_2 as a volatile component in the mantle: the system Mg_2SiO_4-SiO_2-H_2O-CO_2. Phys. Chem. Earth 9, 869–881.

Eggler, D.H., 1976. Does CO_2 cause partial melting in the low-velocity layer of the mantle? Geology (2), 69–72.

Eggler, D.H., Baker, D.R., 1982. Reduced volatiles in the system C-H-O: Implications to mantle melting, fluid formation and diamond genesis. In: High-Pressure Research in Geophysics. D. Reidel/Kluwer Academic Publishers, Boston/Dordrecht, pp. 237–250.

Eggler, D.H., Kadik, A.A., 1979. The system $NaAlSi_3O_8$-H_2O-CO_2: I. Compositional and thermodynamic relations of liquids and vapors coexisting with albite. Am. Mineral. 64, 1036–1049.

Eggler, D.H., Rosenhauer, M., 1978. Carbon dioxide in silicate melts. II. Solubilities of CO_2 and H_2O in $CaMgSi_2O_6$ (diopside) liquids and vapors at pressures to 40 kb. Am. J. Sci. 278, 64–94.

Eggler, D.H., Mysen, B.O., Hering, T.C., Holloway, J.R., 1979. The solubility of carbon monoxide in silicate melts at high pressures and its effect on silicate phase relations. Earth Planet. Sci. Lett. 43, 321–330.

Fincham, C.J.B., Richardson, F.D., 1954. The behavior of sulphur in silicate and aluminate melts. Proc. R. Soc. Lond. A223, 40–62.

Fine, G., Stolper, E., 1985. The speciation of carbon dioxide in sodium aluminosilicate glasses. Contrib. Mineral. Petrol. 91, 105–112.

Freda, C., Baker, D.R., Scarlato, P., 2005. Sulfur diffusion in basaltic melts. Geochim. Cosmochim. Acta 69, 5061–5069.

French, B.M., 1966. Some geological implications of equilibrium between graphite and a C-H-O gas phase at high temperatures and pressures. Rev. Geophys. 4, 223–253.

Frischat, G.H., Szurman, M., Pfeiffer, T., 2011. Role of sulfur and its diffusion in silicate glass melts. Int. J. Appl. Glass Sci. 2, 47–51.

Ghosh, S., Ohtani, E., Litasov, K., Suzuki, A., Sakamaki, T., 2007. Stability of carbonated magmas at the base of the Earth's upper mantle. Geophys. Res. Lett. 34.

Grande, T., Jacob, S., Holloway, J.R., McMillan, P.F., Angell, C.A., 1995. High-pressure synthesis of nitride glasses. J. Non-Cryst. Solids 184, 151–154.

Guillot, B., Sator, N., 2011. Carbon dioxide in silicate melts: a molecular dynamics simulation study. Geochim. Cosmochim. Acta 75, 1829–1857.

Hampshire, S., 2003. Oxynitride glasses, their properties and crystallisation – a review. J. Non-Cryst. Solids 316, 64–73.

Hampshire, S., Pomeroy, M.J., 2018. Oxynitride glasses. In: Richet, P. (Ed.), Encyclopedia of Glass Science, Tehnology, History and Culture. Wiley and Sons, Hoboken.

Hampshire, S., Flynn, R., Morrissey, V., Pomeroy, M., Rouxel, T., Besson, J.L., Goursat, P., 1994. Hoffmann, M.J., Becher, P.F., Petzow, G. (Eds.), Effects of temperature on viscosities and elastic modulus of oxynitride glasses. Silicon Nitride '93pp. 351–355.

Hayashi, A., Tatsumisago, M., 2018. Sulfide-glass electrolytes for all-solid-state batteries. In: Richet, P. (Ed.), Encyclopedia of Glass Science, Tehnology, History and Culture. Wiley & Sons, Hoboken.

Holloway, J.R., Blank, J.G., 1994. Application of experimental results to C-O-H species in natural melts. In: Carroll, M.R., Holloway, J.R. (Eds.), Volatiles in Magmas. Mineralogical Society of America, Washington, DC, pp. 187–230.

Holloway, J.R., Mysen, B.O., Eggler, D.H., 1976. The solubility of CO_2 in liquids on the join CaO-MgO-SiO_2-CO_2. In: Carnegie Instn. Washington Year Book.vol. 75. pp. 626–630.

Holmquist, S., 1966. Oxygen ion activity and the solubility of sulfur trioxide in sodium silicate melts. J. Am. Ceram. Soc. 49, 467–473.

Iacono-Marziano, G., Morizet, Y., Le Trong, E., Gaillard, F., 2012. New experimental data and semi-empirical parameterization of H_2O-CO_2 solubility in mafic melts. Geochim. Cosmochim. Acta 97, 1–23.

Ikeda, Y., Kitade, T., Kojhjiya, S., Hayashi, A., Matsuda, A., Tatsumisago, M., Minami, T., 2001. Ion conducting composites from Li_2S-SiS_2-Li_4SiO_4 oxysulfide glass and poly(oxyethylene)s. Polymer 42, 7225–7228.

Jugo, P.J., Luth, R.W., Richards, J.P., 2005. An experimental study of the sulfur content in basaltic melts saturated with immiscible sulfide or sulfate liquids at 1300 degrees C and 1.0 GPa. J. Petrol. 46, 783–798.

Jugo, P.J., Wilke, M., Botcharnikov, R.E., 2010. Sulfur K-edge XANES analysis of natural and synthetic basaltic glasses: implications for S speciation and S content as function of oxygen fugacity. Geochim. Cosmochim. Acta 74, 5926–5938.

Kadik, A., Pineau, F., Litvin, Y., Jendrzejewski, N., Martinez, I., Javoy, M., 2004. Formation of carbon and hydrogen species in magmas at low oxygen fugacity. J. Petrol. 45, 1297–1310.

Kadik, A.A., Kurovskaya, N.A., Ignat'ev, Y.A., Kononkova, N.N., Koltashev, V.V., Plotnichenko, V.G., 2011. Influence of oxygen fugacity on the solubility of nitrogen, carbon, and hydrogen in FeO-Na_2O-SiO_2-Al_2O_3 melts in equilibrium with metallic iron at 1.5 GPa and 1400 degrees C. Geochem. Int. 49, 429–438.

Kadik, A.A., Litvin, Y.A., Koltashev, V.V., Kryukova, E.B., Plotnichenko, V.G., Tsekhonya, T.I., Kononkova, N.N., 2013. Solution behavior of reduced N-H-O volatiles in FeO-Na_2O-SiO_2-Al_2O_3 melt equilibrated with molten Fe alloy at high pressure and temperature. Phys. Earth Planet. Inter. 214, 14–24.

Kadik, A.A., Koltashev, V.V., Kryukova, E.B., Plotnichenko, V.G., Tsekhonya, T.I., Kononkova, N.N., 2014. Solution of C-O-H volatiles in FeO-Na_2O-Al_2O_3-SiO_2 melts in equilibrium with iron alloy and graphite at 4 GPa and 1550 degrees C. Geochem. Int. 52, 707–725.

Karki, B.B., Bhattarai, D., Mookherjee, M., Stixrude, L., 2010. Visualization-based analysis of structural and dynamical properties of simulated hydrous silicate melt. Phys. Chem. Miner. 37, 103–117.

King, P.L., Holloway, J.R., 2002. CO_2 solubility and speciation in intermediate (andesitic) melts: the role of H_2O and composition. Geochim. Cosmochim. Acta 66, 1627–1640.

Klimm, K., Kohn, S.C., Botcharnikov, R.E., 2012. The dissolution mechanism of sulphur in hydrous silicate melts. II: Solubility and speciation of sulphur in hydrous silicate melts as a function of fO(2). Chem. Geol. 322, 250–267.

Konschak, A., Keppler, H., 2014. The speciation of carbon dioxide in silicate melts. Contrib. Mineral. Petrol. 167.

Koroglu, A., Thompson, D.P., Apperley, D.C., Harris, R.K., 2011. N-15 and O-17 MAS NMR studies of yttrium oxynitride glasses. Phys. Chem. Glasses Eur. J. Glass Sci. Technol. B 52, 175–180.

Kushiro, I., 1969. The system forsterite-diopside-silica with and without water at high pressures. Am. J. Sci. 267-A, 269–294.

Kushiro, I., Yoder, H., 1974. Formation of eclogite from garnet lherzolite: liquidus relations in a portion of the system $MgSiO_3$-$CaSiO_3$-Al_2O_3 at high pressure. In: Carnegie Instn. Washington Year Book.vol. 73. pp. 266–269.

Lesne, P., Scaillet, B., Pichavant, M., 2015. The solubility of sulfur in hydrous basaltic melts. Chem. Geol. 418, 104–116.

Li, Y., Huang, R.F., Wiedenbeck, M., Keppler, H., 2015. Nitrogen distribution between aqueous fluids and silicate melts. Earth Planet. Sci. Lett. 411, 218–228.

Libourel, G., Marty, B., Humbert, F., 2003. Nitrogen solubility in basaltic melt. Part I. Effect of oxygen fugacity. Geochim. Cosmochim. Acta 67, 4123–4136.

Lobanov, S.S., Chen, P.-N., Chen, X.-J., Zha, C.-S., Litasov, K., Mao, H.-k., Goncharov, A.F., 2013. Carbon precipitation from heavy hydrocarbon fluid in deep planetary interiors. Nat. Commun. 4. https://dx.doi.org/10.1038/ncomms3446.

Metrich, N., Bonin-Mosbach, M., Susini, J., Meneaz, B., Galoisy, L., 2002. Presence of sulfite (SIV) in arc magmas: implications for volcanic sulfur emissions. Geophys. Res. Lett. 29, 331–334.

Metrich, N., Berry, A.J., O'Neill, H.S.C., Susini, J., 2009. The oxidation state of sulfur in synthetic and natural glasses determined by X-ray absorption spectroscopy. Geochim. Cosmochim. Acta 73, 2382–2399.

Miyazaki, A., Hiyagon, H., Sugiura, N., Hirose, K., Takahashi, E., 2004. Solubilities of nitrogen and noble gases in silicate melts under various oxygen fugacities: implications for the origin and degassing history of nitrogen and noble gases in the earth. Geochim. Cosmochim. Acta 68, 387–401.

Morizet, Y., Kohn, S.C., Brooker, R.A., 2001. Annealing experiments on CO_2-bearing jadeite glass: an insight into the true temperature dependence of CO_2 speciation in silicate melts. Mineral. Mag. 65, 701–707.

Morizet, Y., Paris, M., Gaillard, F., Scaillet, B., 2009. Raman quantitifcation factor calibration for CO-CO_2 gas mixture in synthetic fluid inclusions: application to oxygen fugacity calculation in magmatic systems. Chem. Geol. 264, 58–70.

Morizet, Y., Paris, M., Gaillard, F., Scaillet, B., 2010. C-O-H fluid solubility in haplobasalt under reducing conditions: an experimental study. Chem. Geol. 279, 1–16.

Morizet, Y., Brooker, R.A., Iacono-Marziano, G., Kjarsgaard, B.A., 2013. Quantification of dissolved CO_2 in silicate glasses using micro-Raman spectroscopy. Am. Mineral. 98, 1788–1802.

Morizet, Y., Paris, M., Gaillard, F., Scaillet, B., 2014. Carbon dioxide in silica-undersaturated melt part II: effect of CO_2 on quenched glass structure. Geochim. Cosmochim. Acta 144, 202–216.

Morizet, Y., Vuilleumier, R., Paris, M., 2015. A NMR and molecular dynamics study of CO_2-bearing basaltic melts and glasses. Chem. Geol. 418, 89–103.

Munoz, F., Benne, D., Pascual, L., Rocherulle, J., Marchand, R., Russel, C., Duran, A., 2004. Silicon oxynitride glasses produced by ammonolysis from colloidal silica. J. Non-Cryst. Solids 345, 647–652.

Murakami, M., Sakka, S., 1988. Ab initio molecular orbital calculation of the interatomic potential and force constants in silicon oxynitride glass. J. Non-Cryst. Solids 101, 271–279.

Mysen, B.O., 1976. The role of volatiles in silicate melts: solubility of carbon dioxide and water in feldspar, pyroxene, feldspathoid melts to 30 kb and 1625 degrees C. Am. J. Sci. 276, 969–996.

Mysen, B., 2015. Hydrogen isotope fractionation and redox-controlled solution mechanisms in silicate-COH melt plus fluid systems. J. Geophys. Res.-Solid Earth 120, 7440–7459.

Mysen, B.O., Boettcher, A.L., 1975. Melting of a hydrous mantle. I. Phase relations of natural peridotite at high pressures and temperatures with controlled activities of water, carbon dioxide and hydrogen. J. Petrol. 16, 520–548.

Mysen, B.O., Fogel, M.L., 2010. Nitrogen and hydrogen isotope compositions and solubility in silicate melts in equilibrium with reduced (N+H)-bearing fluids at high pressure and temperature: effects of melt structure. Am. Mineral. 95, 987–999.

Mysen, B.O., Popp, R.K., 1980. Solubility of sulfur in $CaMgSi_2O_6$ and $NaAlSi_3O_8$ melts at high pressure and temperature with controlled f_{O2} and f_{S2}. Am. J. Sci. 280, 78–92.

Mysen, B.O., Yamashita, S., 2010. Speciation of reduced C-O-H volatiles in coexisting fluids and silicate melts determined in-situ to similar to 1.4 GPa and 800 degrees C. Geochim. Cosmochim. Acta 74, 4577–4588.

Mysen, B.O., Yamashita, S., Chertkova, N., 2008. Solubility and solution mechanisms of NOH volatiles in silicate melts at high pressure and temperature – amine groups and hydrogen fugacity. Am. Mineral. 93, 1760–1770.

Mysen, B.O., Fogel, M.L., Morrill, P.L., Cody, G.D., 2009. Solution behavior of reduced C-O-H volatiles in silicate melts at high pressure and temperature. Geochim. Cosmochim. Acta 73, 1696–1710.

Mysen, B.O., Kumamoto, K., Cody, G.D., Fogel, M.L., 2011. Solubility and solution mechanisms of C-O-H volatiles in silicate melt with variable redox conditions and melt composition at upper mantle temperatures and pressures. Geochim. Cosmochim. Acta 75, 6183–6199.

Mysen, B.O., Tomita, T., Ohtani, E., Suzuki, A., 2014. Speciation of and D/H partitioning between fluids and melts in silicate-D-O-H-C-N systems determined in-situ at upper mantle temperatures, pressures, and redox conditions. Am. Mineral. 99, 578–588.

Nagashima, S., Katsura, T., 1973. The solubility of sulfur in Na_2O-SiO_2 melts under various oxygen partial pressures at 1100°C, 1250°C, and 1300°C. Bull. Chem. Soc. Jpn. 46, 3099–3103.

Namur, O., Charlier, B., Holtz, F., Cartier, C., McCammon, C., 2016. Sulfur solubility in reduced mafic silicate melts: implications for the speciation and distribution of sulfur on mercury. Earth Planet. Sci. Lett. 448, 102–114.

Ni, H.W., Keppler, H., 2013. Carbon in silicate melts. Rev. Mineral. Geochem. Carbon Earth 75, 251–287.

Nowak, M., Porbatzki, D., Spickenbom, K., Diedrich, O., 2003. Carbon dioxide speciation in silicate melts: a restart. Earth Planet. Sci. Lett. 207, 131–139.

Nowak, M., Schreen, D., Spickenbom, K., 2004. Argon and CO_2 on the race track in silicate melts: a tool for the development of a CO_2 speciation and diffusion model. Geochim. Cosmochim. Acta 68, 5127–5138.

O'Neill, H.S.C., Mavrogenes, J.A., 2002. The sulfide capacity and sulfur content at sulfide saturation of silicate melts at 1400°C and 1 bar. J. Petrol. 43, 1049–1087.

Ooura, M., Hanada, T., 1998. Compositional dependence of solubility of sulphate in silicate glasses. Glass Technol. 39, 68–73.

Pan, V., Holloway, J.R., Hervig, R.L., 1991. Pressure and temperature dependence of carbon dioxide solubility in tholeiitic melts. Geochim. Cosmochim. Acta 55, 1587–1595.

Paris, E., Giuli, G., Carroll, M.R., Davoli, I., 2001. The valence and speciation of sulfur in glasses by x-ray absorption spectroscopy. Can. Mineral. 39, 331–339.

Park, J.H., Park, G.-H., 2012. Sulfide capacity of CaO-SiO_2-MnO-Al_2O_3-MgO slags at 1 873 K. ISIJ Int. 52, 764–769.

Pawley, A.R., Holloway, J.R., McMillan, P.F., 1992. The effect of oxygen fugacity on the solubility of carbon-oxygen fluids in basaltic melt. Earth Planet. Sci. Lett. 110, 213–225.

Pearce, M.L., 1964. Solubility of carbon dioxide and variation of oxygen ion activity in sodasilicate melts. J. Am. Ceram. Soc 47, 342–347.

Pomeroy, M.J., Hampshire, S., 2003. Composition - structure - property relationships for Si-Al-O-N glasses containing mixed modifiers. Ann. Chim.-Sci. Mater. 28, 63–70.

Renlund, G.M., Prochazka, S., Doremus, R.H., 1991. Silicon oxycarbide glasses. 2. Structure and properties. J. Mater. Res. 6, 2723–2734.

Richardson, F.D., Fincham, C.J.B., 1954. Sulphur in silicate and aluminate slags. J. Iron Steel Inst. 178, 4–15.

Richet, N.F., Kawaji, H., Rouxel, T., 2010. The boson peak of silicate glasses: the role of Si-O, Al-O, and Si-N bonds. J. Chem. Phys. 133.

Roskosz, M., Mysen, B.O., Cody, G.D., 2006. Dual speciation of nitrogen in silicate melts at high pressure and temperature: an experimental study. Geochim. Cosmochim. Acta 70, 2902–2918.

Rouxel, T., 2011. Thermodynamics of viscous flow and elasticity of glass forming liquids in the glass transition range. J. Chem. Phys. 135.

Rouxel, T., Besson, J.L., Gault, C., Goursat, P., Leigh, M., Hampshire, S., 1989. Viscosity and Young's modulus of an oxynitride glass. J. Mater. Sci. Lett. 8, 1158–1160.

Sakamaki, T., Ohtani, E., Urakawa, S., Suzuki, A., Katayama, Y., 2009. Measurement of hydrous peridotite magma density at high pressure using the X-ray absorption method. Earth Planet. Sci. Lett. 287, 293–297.

Sakamaki, T., Ohtani, E., Urakawa, S., Terasaki, H., Katayama, Y., 2011. Density of carbonated peridotite magma at high pressure using an X-ray absorption method. Am. Mineral. 96, 553–557.

Sakka, S., 1995. Structure, properties and application of oxynitride glasses. J. Non-Cryst. Solids 181, 215–224.

Seifert, R., Malfait, W.J., Lerch, P., Sanchez-Valle, C., 2013. Partial molar volume and compressibility of dissolved CO_2 in glasses with magmatic compositions. Chem. Geol. 358, 119–130.

Seo, J.-D., Kim, S.-H., 1999. The sulphide capacity of CaO-SiO_2-Al_2O_3-MgO (-FeO) smelting reduction slags. Steel Res. 70, 203–208.

Sharafat, A., Grins, J., Esmaeilzadeh, S., 2009. Properties of high nitrogen content mixed alkali earth oxynitride glasses $(AE_xCa_{1-x})_{1.2(1)}SiO_{1.9(1)}N_{0.86(6)}$, AE = Mg, Sr, Ba. J. Non-Cryst. Solids 355, 1259–1263.

Sharma, S.K., Yoder Jr., H.S., Matson, D.W., 1988. Raman study of some melilites in crystalline and glassy states. Geochim. Cosmochim. Acta 52, 1961–1967.

Shishkina, T.A., Botcharnikov, R.E., Holtz, F., Almeev, R.R., Portnyagin, M.V., 2010. Solubility of H_2O- and CO_2-bearing fluids in tholeiitic basalts at pressures up to 500 MPa. Chem. Geol. 277, 115–125.

Sosinsky, D.J., Sommerville, I.D., 1986. The composition and temperature dependence of the sulfide capacity of metallurgical slags. Metall. Trans. B 17B, 331–337.

Spickenbom, K., Sierralta, M., Nowak, M., 2010. Carbon dioxide and argon diffusion in silicate melts: insights into the CO_2 speciation in magmas. Geochim. Cosmochim. Acta 74, 6541–6564.

Stanley, B.D., Hirschmann, M.M., Withers, A.C., 2011. CO_2 solubility in Martian basalts and Martian atmospheric evolution. Geochim. Cosmochim. Acta 75, 5987–6003.

Stanley, B.D., Hirschmann, M.M., Withers, A.C., 2014. Solubility of C-O-H volatiles in graphite-saturated martian basalts. Geochim. Cosmochim. Acta 129, 54–76.

Sverjensky, D.A., Stagno, V., Huang, F., 2014. Important role for organic carbon in subduction-zone fluids in the deep carbon cycle. Nat. Geosci. 7, 909–913.

Tamic, N., Behrens, H., Holtz, F., 2001. The solubility of H_2O and CO_2 in rhyolitic melts in equilibrium with a mixed CO_2-H_2O fluid phase. Chem. Geol. 174, 333–347.

Taniguchi, Y., Sano, N., Seetharaman, S., 2009. Sulphide capacities of CaO–Al_2O_3–SiO_2–MgO–MnO slags in the temperature range 1 673–1 773 K. ISIJ Int. 49, 159–163.

Tatsumisago, M., Yamashita, H., Hayashi, A., Morimoto, D., Minami, T., 2000. Preparation and structure of amorphous solid electrolytes based on lithium sulfide. J. Non-Cryst. Solids 274, 30–38.

Thibault, Y., Holloway, J.R., 1994. Solubility of CO_2 in a Ca-rich leucitite: effects of pressure, temperature, and oxygen fugacity. Contrib. Mineral. Petrol. 116, 216–224.

Tokuda, Y., Uchino, T., Yoko, T., 2003. Ab initio study of NMR spectra of Li_2S–SiS_2 glass system. J. Non-Cryst. Solids 330, 61–65.

Urbain, G., Bottinga, Y., Richet, P., 1982. Viscosity of liquid silica, silicates and alumino-silicates. Geochim. Cosmochim. Acta 46, 1061–1072.

Vetere, F., Holtz, F., Behrens, H., Botcharnikov, R.E., Fanara, S., 2014. The effect of alkalis and polymerization on the solubility of H_2O and CO_2 in alkali-rich silicate melts. Contrib. Mineral. Petrol. 167.

Vuilleumier, R., Seitsonen, A.P., Sator, N., Guillot, B., 2015. Carbon dioxide in silicate melts at upper mantle conditions: insights from atomistic simulations. Chem. Geol. 418, 77–88.

Watson, E.B., 1994. Diffusion in volatile-bearing magmas. In: Carroll, M.R., Holloway, J.R. (Eds.), Volatiles in Magmas. Mineralogical Society of America, Washington, DC, pp. 371–411.

Wetzel, D., Rutherford, M.J., Jacobsen, S.D., Hauri, E.H., Saal, A.E., 2013. Degassing of reduced carbon from planetary basalts. Proc. Natl. Acad. Sci. 110, 8010–8013.

White, W.B., 1974. The carbonate minerals. In: Farmer, V.C. (Ed.), Infrared spectra of minerals. Mineralogical Society of London, London (chapter 12).

White, B.S., Montana, A., 1990. The effect of H_2O and CO_2 on the viscosity of sanidine liquid at high pressures. J. Geophys. Res. 95, 15683–15693.

Wilke, M., Jugo, P.J., Klimm, K., Susini, J., Botcharnikov, R., Kohn, S.C., Janousch, M., 2008. The origin of S4+ detected in silicate glasses by XANES. Am. Mineral. 93, 235–240.

Wilke, M., Klimm, K., Kohn, S.C., 2011. Spectroscopic studies on sulfur speciation in synthetic and natural glasses. Rev. Mineral. Geochem. 73, 41–78.

Winther, K.T., Watson, E.B., Korenowski, G.M., 1998. Magmatic sulfur compounds and sulfur diffusion in albite melt at 1 GPa and 1300-1500 degrees C. Am. Mineral. 83, 1141–1151.

Yoshioka, T., McCammon, C., Shcheka, S., Keppler, H., 2015. The speciation of carbon monoxide in silicate melts and glasses. Am. Mineral. 100, 1641–1644.

Yurkov, A.L., Polyak, B.I., 1996. Contact phenomena and interactions in the system SiC-SiO_2-R_xO_y in condensed matter. 2. Interactions between silicon carbide and silicate glasses at elevated temperatures. J. Mater. Sci. 31, 2729–2733.

Zhang, C., Duan, Z.H., 2009. A model for C-O-H fluids in the mantle. Geochim. Cosmochim. Acta 73, 2089–2102.

Zhang, Y., Xu, Z., Zhu, M., Wang, H., 2007. Silicate melt properties and volcanic eruptions. Rev. Geophys. 45, RG4004. https://dx.doi.org/10.1029/2006RG000216.

CHAPTER

17

Noble Gases, Molecular Species, Hydrogen, and Halogens

OUTLINE

17.1 INTRODUCTORY COMMENTS

When dissolved in silicate melts, molecular species such as CO_2, CH_4, N_2, NH_3, H_2, O_2, H_2O, and halogens are in equilibrium with anionic complexes such as CO_3^{2}, HCO_3^-, CH_3^-, NH_2^-, OH^-, F^-, Cl^-, Br^-, and I^- through reaction with the silicate components. Except for halogen anions, the solubility of these species and their influence on structure and properties have been discussed in the two previous chapters. As exemplified by CO_2 and H_2O, however, these species partly dissolve also in a molecular form. Along with noble gases, these molecular species are then helpful probes of silicate structure such as the way in which cavities form upon physical interactions to accommodate them under a variety of imposed temperatures and pressures. The solubilities of such components in melts are often simple functions of atomic or molecular radii (Doremus, 1966; Lux, 1987; Roselieb et al., 1992; Shibata et al., 1998; Niwa et al., 2013; see also Fig. 17.1).

Silicate Glasses and Melts
https://doi.org/10.1016/B978-0-444-63708-6.00017-X

FIG. 17.1 Henry's Law constant for molecular species (He, Ne, H_2, and O_2) in fused silica at 800–1000°C (Doremus, 1966).

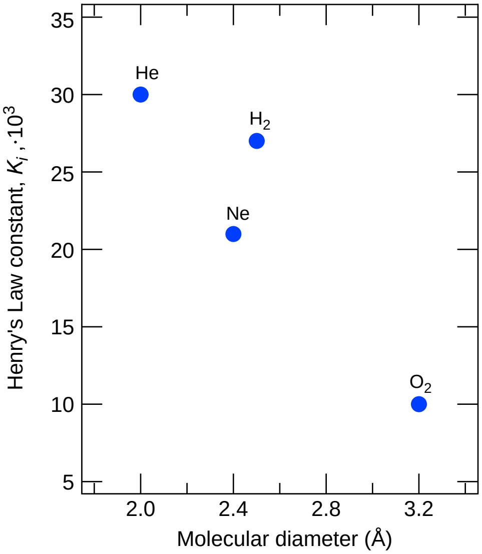

In addition, these molecular gas species, and especially noble gases, have a strong geological interest because their solubilities and partitioning between silicate melts and crystals are useful to decipher degassing events throughout the earth's history, beginning with the formation of the atmosphere and hydrosphere (Lux, 1987; Broadhurst et al., 1992; Jambon, 1994; Ozima, 1998; Miyazaki et al., 2004; Guillot and Sarda, 2006; Heber et al., 2007).

17.2 NOBLE GASES

17.2.1 General Remarks

Noble gases are special solutes in silicates because of their small size and chemical inertness. As a result, they are the only species that can diffuse within a *glass* (i.e., below T_g) and fit within adequate preexisting cavities at an atomic scale they find along the way. The well-known example of noble gases in glasses has in fact led to a common oversimplification. It consists of stating that the solubility of noble gases and other volatiles in a molecular form in *melts* is determined by the availability of cavities. Seen in such a passive way, however, this picture is basically incorrect and misleading because it neglects any physical interactions of a solute with its solvent.

17.2.2 Solubility and Solution Mechanisms

The solubility of noble gases in aluminosilicate and silicate melts varies systematically with silicate composition. Particularly important factors are the Al/(Al+Si) of the silicate, how Al^{3+} is charge-balanced when in tetrahedral coordination, whether the silicate is peralkaline or peraluminous, and, finally, the types and proportions of alkalis and alkaline earths

17.2.2.1 *Glasses and Melts Along Silica-Meta-Aluminate Joins (SiO_2-$M^{x+}_{1/x}AlO_2$)*

The dissolution of noble gases in silica glass and melt has been used as a tool with which to probe voids and void size distribution in SiO_2 glass (Shackleford, 1999; Malavasi et al., 2006; Zhang et al., 2010). There is, for example, a simple relationship between noble gas content in SiO_2 glass and melt and the noble gas atomic radius at any given temperature and pressure. The noble gas content also increases with increasing temperature and pressure (at least at pressures below several gigapascals) and decreases with increasing atomic radius (Shackleford et al., 1972; Carroll and Stolper, 1991; Guillot and Guissani, 1996; see Fig. 17.2). From the temperature dependence of solubility, the enthalpy of solution of noble gases in vitreous silica increases with increasing atomic radius from about 30 kJ/mol for Ne solubility to as much as ~150 kJ/mol for solution of Xe (Shelby, 1976; Shibata et al., 1998). The enthalpy of solution is, however, also dependent on silicate composition, and typically decreases with increasing silicate polymerization (Shibata et al., 1998).

For pressure up to several hundred megapascals, noble gas solubility in melts is a linear or near linear function of pressure (Shackleford et al., 1972; Shelby, 1976; Walter et al., 2000; see also Figs. 17.2 and 17.3), and therefore obeys Henry's Law:

$$K_i = X_i/f_i, \tag{17.1}$$

where f_i is fugacity of gas i, X_i is mol fraction, and K_i is Henry's Law constant. However, as pressure is increased beyond ambient, the solubility deviates from linearity and eventually reaches a maximum value before further pressure increase results in decreasing solubility (Fig. 17.4; see also Schmidt and Keppler, 2002; Chamorro-Perez et al., 1996; Bouhifd et al., 2008; Zhang et al., 2010; Niwa et al., 2013).

Substitution of Si^{4+} with charge-balanced Al^{3+} in melts along meta-aluminosilicate joins results in decreasing noble gas solubility (Walter et al., 2000; Bouhifd et al., 2008; see also Fig. 17.3). The high pressure at which this solubility reaches its maximum before decreasing

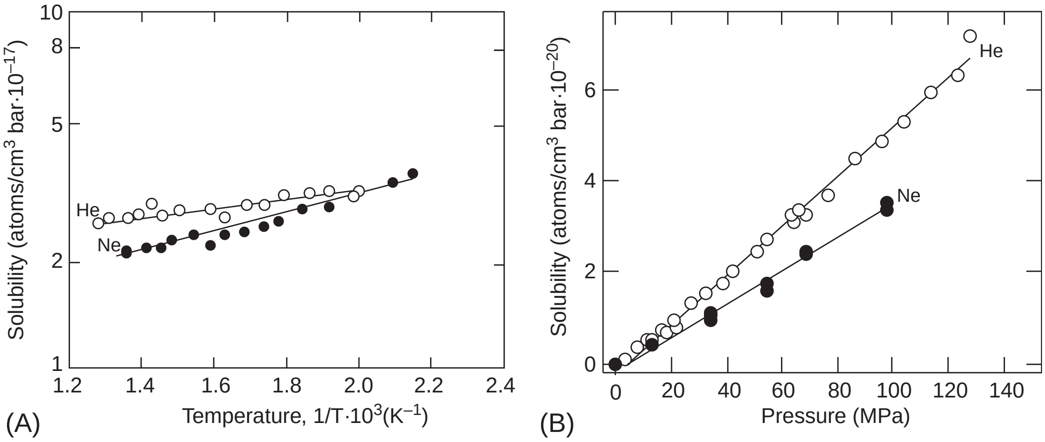

FIG. 17.2 Solubility of He, Ne in fused silica (A) As a function of temperature. This temperature-dependent solubility translates of an enthalpy of solution of −41 and −76 kJ/mol, for He and Ne solution in vitreous SiO_2, respectively. (B) Solubility as a function of pressure (Shelby, 1976).

FIG. 17.3 Solubility of Ar in SiO_2-$NaAlSi_2O_6$ glasses formed by temperature-quenching super-cooled liquids as a function of Al/(Al+Si) and pressure. SiO_2 liquid was equilibrated at 1200°C, $NaAlSi_3O_8$ at 750–1000°C, and $NaAlSi_2O_6$ at 800°C (Walter et al., 2000).

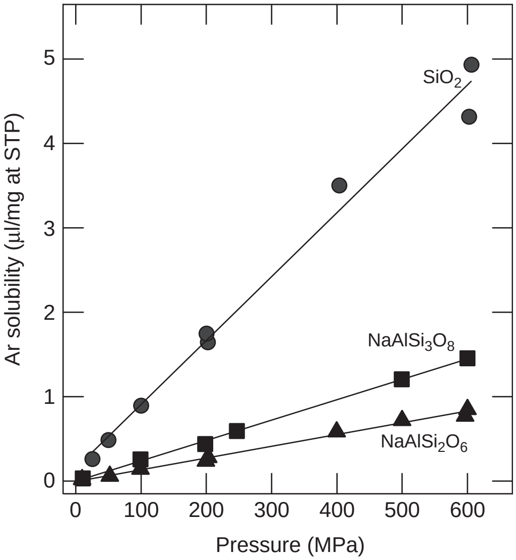

FIG. 17.4 Calculated Ar solubility range (gray field) in SiO_2 melt with pressure from Zhang et al. (2010). Also shown are experimental data from Bouhifd et al. (2008) and Chamorro-Perez et al. (1996).

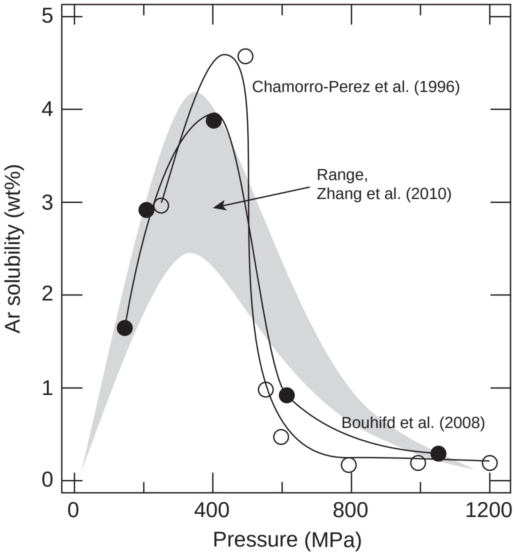

with further pressure increases with increasing Al/(Al+Si) (Bouhifd et al., 2008). This turnover pressure also varies with the type of electrical charge balance of tetrahedrally coordinated Al^{3+} (Bouhifd et al., 2008).

The solution mechanism of noble gases in a fully polymerized structure such as that of fused SiO_2 (see also Chapter 5, Sections 5.4 and 5.5) has been described in terms of nonoverlapping interstitial sites or voids in the structure larger than those of the noble gas

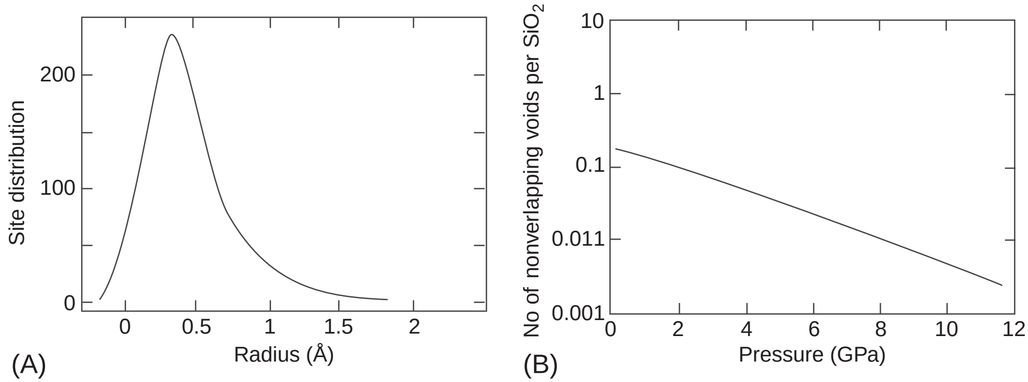

FIG. 17.5 Noble gas solubility in silica and interstitial site distribution. (A) Site distribution as a function of atomic radius (Malavasi et al., 2006). (B) Available nonoverlapping sites per SiO_2 for Ar as a function of pressure (modified after Zhang et al., 2010).

under consideration (Fig. 17.5) (Nakayama and Shackelford, 1990; Carroll and Stolper, 1991; Wulf et al., 1999; Zhang et al., 2010). The decreasing noble gas solubility in silica melt with increasing atomic radius of the noble gas (Fig. 17.2) is then understood in terms of the distribution of interstitial sites (Fig. 17.5A). This model also is consistent with structural data inferred from Wulf et al. (1999) from X-ray absoprtion data.

With increasing pressure, the concentration of nonoverlapping sites larger than the size of a given noble gas decreases (Zhang et al., 2010; see also Fig. 17.5B). This evolution has the effect of decreasing the noble gas solubility. However, at the same time the increasing noble gas fugacity with pressure tends to cause increased noble gas solubility (Shelby, 1976; Roselieb et al., 1992; Walter et al., 2000). The net result is a solubility maximum at some pressure (Fig. 17.4). The different pressures at which experimentally determined solubility turnovers take place is a reflection of the compressibility of the intertetrahedral angles in three-dimensional network structures. This compressibility varies with Al/(Al+Si) and with changes in type of cations for charge-balancing cations (see also Chapter 9, Section 9.4). Of course, solution of a noble gas causes the compressibility of Si—O—Si angles to decrease (Shen et al., 2011), but such effects have not been quantified except for He in silica glass.

A melt structure adjusts itself more or less easily to accommodate dissolved atoms or molecules. The Gibbs free energy of transfer from the gaseous to the dissolved state accounts for various interactions between the solvent and solute (electrostatic, dispersive, and repulsive), a cavitation term (related to the size of the atoms), as well as differences in the energies of the internal degrees of freedom between the two states. In spite of its complex nature, the Gibbs free energy has been evaluated for noble gases in silicate melts with the aid of first-principles calculations (Ottonello and Richet, 2014). With this approach, the critical parameters are the dielectric properties of the solvent and the mean diameter of its particles and not the details of its structure. The same formalism could thus be applied to a nonpolar solvent such as benzene (C_6H_6) and a polar one, such as H_2O, and silicate melts, which have an intermediate character between them. Argon was first used as a probe to derive solvent diameters consistent with a simple functional form based on the molecular volumes of benzene, water, and five different melt compositions ranging from andesite to ugandite. Solubility calculations were then extended to He, Ne, and Kr, whose dispersive and repulsive coefficients were theoretically available. In this way the ab initio-derived Henry's constants at high temperatures satisfactorily reproduce the experimental observations for a wide range of silicate compositions. The major advantage of the method is not only that any temperature and pressure may be considered, but also that the microscopic structure does not need to be known at all, because only the average solvent diameter and its dielectric properties are needed. This advantage has its drawbacks, however, in that macroscopic solubility-structure relationships cannot be derived.

The molar volume of noble gases in melt can be derived from their solubility (Walter et al., 2000),

$$\mathrm{Ln}(f_i/X_i) = \ln K_i + V_i(P - P_o)/RT, \tag{17.2}$$

where P is pressure and P_o reference pressure, R is the gas constant, and T is temperature (K). From this expression and the experimental data, Walter et al. (2000) found that the molar volume, V_i, of noble gases in melts along the SiO_2—$NaAlO_2$ join increases with the atomic diameter, and for a given gas, with increasing Al/(Al+Si) (Table 17.1). This observation would imply that the interstitial site distribution gets broader as a glass along an SiO_2—$NaAlO_2$ join becomes increasingly aluminous.

Most likely, the distribution of interstitial sites (Fig. 17.5) would also explain why the diffusivity of noble gases at given temperature decreases and the activation energy increases with increasing atomic radius (Roselieb et al., 1996; see also Fig. 17.6). The linear square-root relationship in Fig. 17.6 could be explained by the relationship (McElfresh and Howitt, 1986):

$$E_i = 4\pi G r_{Di}(r_i - r_{Di})^2, \tag{17.3}$$

where G is the bulk modulus, and $(r_i - r_{Di})$ is the enlargement of the cavity required for accomodation of moving particle, i.

The increased enthalpy of solution of noble gases in silica glass with increasing radius (Shibata et al., 1998) probably also is a reflection of the energy needed to enlarge a cavity to accommodate the noble gas in the structural cavities. As this enlargement, $(r_i - r_{Di})$, necessarily increases with atomic radius, so does the enthalpy of solution and the activation energy of diffusion in any given glass and melt.

TABLE 17.1 Molar Volume (cm^3/mol) of Noble Gases Dissolved in *Supercooled* Liquids Along the Join SiO_2-$NaAlO_2$ (Walter et al., 2000)

Al/(Al+Si)				
Gas		0.00	0.25	0.333
Ne	–	9.4 ± 3.9	–	–
Ar	25.9 ± 1.3	21.1 ± 1.6	21.1 ± 0.7	7.19 ± 0.1
Kr	24.3 ± 1.8	27.8 ± 0.8	24.7 ± 0.9	12.9 ± 0.2
Xe	–	28.5	–	–

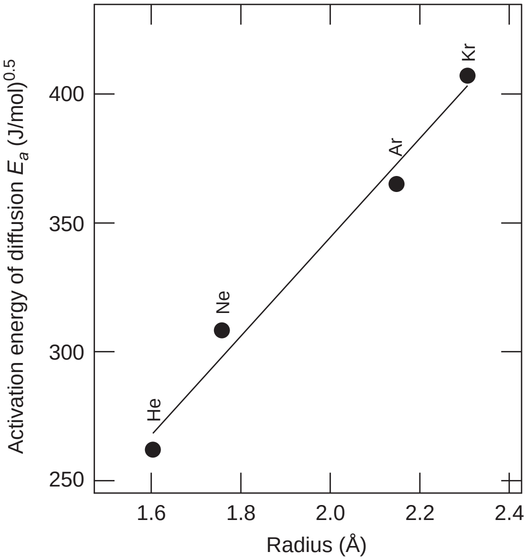

FIG. 17.6 Activation energy of noble gas diffusion as a function of atomic radius. Note how the data follow the relationship outlined in Eq. (17.3) (Roselieb et al., 1992).

17.2.2.2 Peralkaline and Depolymerized Glasses and Melts

Peralkaline compositions, where there is an excess of alkalis or alkaline earths over that required for charge-balance of tetrahedrally coordinated Al^{3+}, will now be addressed. Peralkaline glass and melt compositions are depolymerized.

In these materials, three structural variables will be described to assess whether or how they might also govern noble gas solubility. These are (i) the Al/(Al+Si)-ratio, which can affect interstitial site or three-dimensional cavity dimensions and distributions, and therefore contribute to noble gas solubility and its pressure dependence (see Figs. 17.3 and 17.4); (ii) the abundance ratio of network-modifying/network-forming cations governs the silicate polymerization and Q-species distribution (see Chapter 7; Section 7.3), and therefore the availability of cavities, which play a role in controlling how neutral atoms and molecules might be dissolved; (iii) the proportion of different types of network-modifying cations, because these govern Q-species distribution (Chapter 7, Section 7.3), which in turn affect solubility of atoms and nonreactive molecules.

There is a rather broad range in solubility for each of the noble gases (often more than an order of magnitude; see Fig. 17.7), a range that most likely is a reflection of the influence of the previously mentioned structural variables. This is clear, for example, from the distinctively different slopes of the relationship between solubility and atomic radius when separating out rhyolite melt, which is a nearly fully polymerized ($NBO/T \sim 0$) and essentially an alkali aluminosilicate melt, and a basalt melt, which is predominantly alkaline earth aluminosilicate melt and is also considerably more depolymerized than rhyolite (typical NBO/T values between ~0.7 and 1.0). The NBO/T value of the silicate does indeed have a strong influence on noble gas solubility (Shibata et al., 1996, 1998; Paonita, 2005; Iacono-Marziano et al., 2010; see also Fig. 17.8). It also is clear that the effect of melt polymerization becomes more

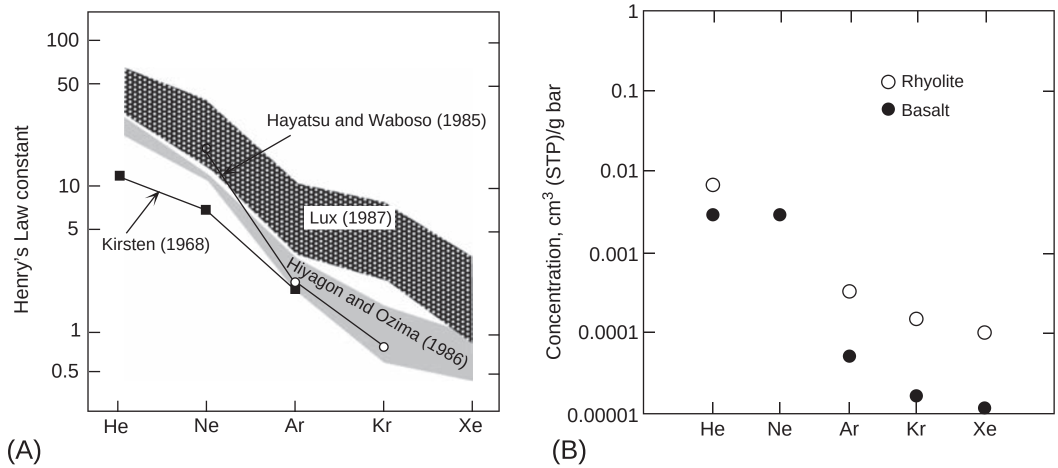

FIG. 17.7 (A) Henry's Law constant, *K*, from noble gas solubility measurements in natural and synthetic silicate melts (Eq. 17.1) (Kirsten, 1968; Hayatsu and Waboso, 1985; Hiyagon and Ozima, 1986; Lux, 1987). (B) Noble gas solubility in basalt and rhyolite melts from Paonita (2005). Melts were equilibrated at temperatures between 1300°C and 1600°C at 0.1–200 MPa pressure and temperature-quenched to glass prior to chemical analysis.

FIG. 17.8 Solubility of Ne, and Ar, and Kr and Xe vs NBO/Si of melt equilibrated at 1400–1500°C and ~100 MPa before temperature-quenching to glass. Samples are in the systems Na_2O-SiO_2, Na_2O-CaO-SiO_2, MgO-SiO_2, and CaO-MgO-SiO_2 (Shibata et al., 1998).

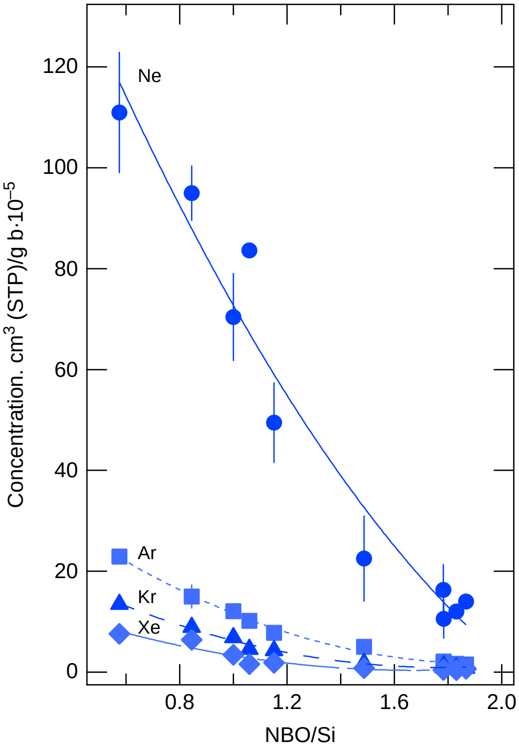

important as the atomic radius of the noble metal decreases. There may also be a slight effect of Al/(Al+Si) (Paonita, 2005), in particular for the melts with small NBO/*T* values (highly polymerized).

Solution of water in melt results in depolymerization, whereas solution of CO_2 causes the silicate structure to be more polymerized (Chapter 16, Section 16.30 and Section 17.3). One would expect, therefore, that noble gas solubility decreases with increasing water content and increases with increasing CO_2 concentration in a melt. This is what has been observed (Fig. 17.9). The Henry's Law constant depends on melt polymerization because the noble gas concentration does (Eq. 17.1). The relationship between Henry's Law constant and dissolved volatiles is therefore consistent with dissolved CO_2 resulting in melt polymerization, whereas dissolved H_2O results in melt depolymerization.

The noble gas solubility in depolymerized melts can be correlated with the proportion of bridging and nonbridging oxygen (Shibata et al., 1998; Paonita, 2005). For a simple relationship to proportion of bridging and nonbridging oxygen (BO and NBO, respectively), Paonita (2005) proposed the relationship for the structural control on the Henry's Law constant, K_i:

$$\ln K_i = X_i^{\mathrm{BO}} \ln K_i^{\mathrm{BO}} + X_i^{\mathrm{NBO}} \ln K_i^{\mathrm{NBO}}, \tag{17.4}$$

where X_i^{BO}, etc., are mol fractions of bridging and nonbridging oxygen and K_i^{BO}, etc., are Henry's Law constants of noble gas i, for bridging and nonbridging oxygen. A more detailed relationship, using Q-species, also has been proposed (Shibata et al., 1998):

$$K_i = \sum_{j-0}^{j} X_{Q^j} K_{Q^j} \tag{17.5}$$

where X_{Q^j} and K_{Q^j} are mol fraction and Henry's Law constant for individual Q-species. The fully polymerized species, Q^4, dominates the K_i-value variations (Shibata et al., 1998).

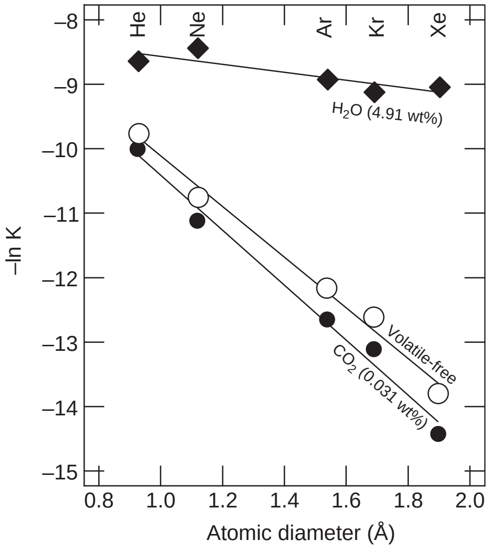

FIG. 17.9 Henry's Law constant (see Eq. (17.1) of noble gases in basalt melt (1150°C/200 MPa) as a function of their atomic radius (calculated results from Nuccio and Paonita, 2000).

FIG. 17.10 Enthalpy of solution, $\triangle H_s$, in Na_2O-SiO_2 melts as a function of noble gas size and melt polymerization (Shibata et al., 1998).

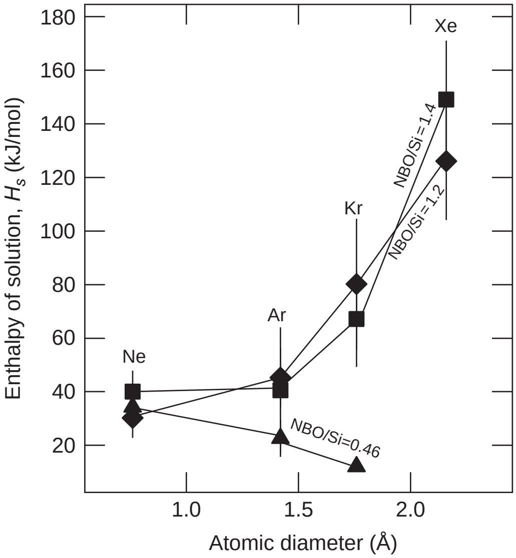

The X_{Q^j} values in silicate melts and glasses in Eq. (17.5) are governed by chemical composition, temperature, and pressure (see Chapter 7, Section 7.3, and Chapter 9, Sections 9.3 and 9.4). It follows, therefore, that the Henry's Law constant would also be a function of composition, temperature, and pressure in addition to the atomic radius of the noble gas.

The temperature dependence of noble gas solubility is slight and can be either positive or negative (Shackleford et al., 1972; Lux, 1987; Shibata et al., 1998). The enthalpy of solution, ΔH_s, derived from the temperature-dependent solubility is positive and ranges from near 5 to about 20 kJ/mol (Lux, 1987). For Ar and larger noble gases in binary metal oxide silicate melts, the ΔH_s decreases with increasing atomic radius (Shibata et al., 1998; see also Fig. 17.10). Furthermore, ΔH_s becomes increasingly sensitive to melt polymerization with increasing atomic radius (equivalent to metal/silicon ratio).

The noble gas solubility in depolymerized, but Q^4-containing, melts is also dependent on pressure (White et al., 1989; Malavasi et al., 2006; Zhang et al., 2010; Guillot and Sator, 2012; see also Fig. 17.11). This effect is in part because the interstitial vacancy dimensions and distribution in Q^4-species change with pressure (Zhang et al., 2010), and in part because increasing pressure results in increased noble gas fugacity. Of course, in depolymerized melts, the Q-distribution is also pressure dependent (Dickinson et al., 1990; Gaudio et al., 2008), which also contributes to how noble gas solubility in depolymerized melts is affected by pressure.

17.3 MOLECULAR SPECIES

Molecular species in silicate glass and melt solution do not interact chemically with the silicate structure. Among the molecular species under consideration here, H_2, CH_4, H_2O, CO_2, and NH_3 molecules typically are in equilibrium with functional groups that do interact chemically with the silicate structure (see also Chapters 15 and 16).

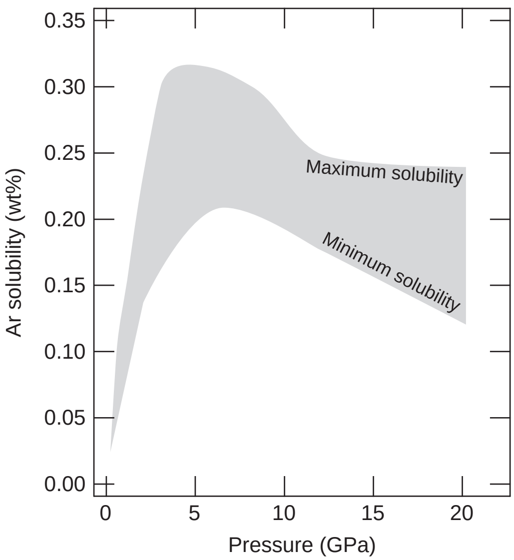

FIG. 17.11 Calculated range of Ar solubility in basalt melt as a function of pressure (Guillot and Sator, 2012).

17.3.1 Solubility and Solution Mechanisms

The molecule species in melts and glasses tend to occupy interstices or cavities in the structure. In other words, the principles governing their solubility are pretty much the same as those used to describe solution of noble gases (Nakayama and Shackelford, 1990; Carroll and Stolper, 1991; Wulf et al., 1999; Zhang et al., 2010)

Although there appear to be only limited experimental data describing the structural roles of the H_2O molecules, the availability of appropriately sized cavities for containment of the H_2O molecule plays an integral role in the solution mechanism of hydrous species (Le Losq et al., 2015). The behavior of molecular CO_2 often is compared with that of argon so that the structural control of Ar solubility might also apply to the solution of molecular CO_2 (Nowak et al., 2004; Behrens, 2010). However, such comparisons carry significant uncertainty because the solution and properties of bulk CO_2 involve both molecular CO_2 and chemically active CO_3^{2-} and HCO_{3-} Groups in the melt and glass structure (see Chapter 16, Section 16.3.3). One might speculate that similar solution mechanisms could describe solution of molecular CH_4 and NH_3 in equilibrium with CH_3 and NH_2 functional groups, respectively (see Chapter 16, Sections 16.3 and 16.5). However, experimental or theoretical data relevant to this question appear not to be available

17.3.1.1 Nitrogen (N_2)

Molecular nitrogen in silicate glasses and melts in the absence of hydrogen is inferred stable at oxygen fugacities ranging from that of air to those defined by the FeO + $0.5O_2$ = FeO (IW) oxygen buffer (Fig. 17.12; see also Libourel et al., 2003; Miyazaki et al., 2004; Li et al., 2015). This behavior is also consistent with N_2 solubility in silicate melts lining up with the solubilities of noble gases in basalt melt as a function of noble gas atomic radius (Miyazaki et al., 1995). In hydrogen-free silicate—N—O systems, the nitrogen solubility

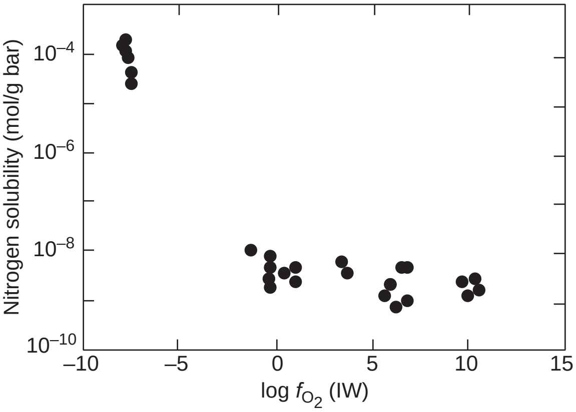

FIG. 17.12 Solubility of nitrogen in basalt melt (glass quenched from melt in the 1300–1500°C range) at ambient pressure as a function of oxygen fugacity, expressed as the difference from that of the iron-wustite oxygen buffer (IW). (Fogel, 1994; Miyazaki et al., 1995, 2004).

increases with decreasing oxygen fugacity at values lower than those of the IW buffer (Fogel, 1994; Miyazaki et al., 2004; Libourel et al., 2003). Under those conditions, nitrogen may substitute for oxygen in silicate tetrahedra to form oxynitride and nitride glasses and melts (Chapter 16, Section 16.5.3). In the presence of hydrogen, vibrational spectra of silicate glasses with volatile components in the N—O—H system indicate that nitrogen is dissolved in molecular form (N_2) at the oxygen fugacity defined by the NNO buffer ($Ni+0.5O_2=NiO$), whereas a lower f_{O2} leads to the formation of N—H species in melts (Mysen et al., 2008; Li et al., 2015; see also Fig. 16.30B). This transformation also leads to an increased solubility of nitrogen (Fig. 16.30A)

17.3.1.2 Hydrogen (H_2)

Hydrogen can dissolve in silicate melts and glasses either in physical form, where presumably solution is in the form of H_2 molecules, through chemical reaction with silicate components, or a combination of both (Doremus, 1966; Shackleford et al., 1972; Luth et al., 1987; Schmidt et al., 1998; Mysen and Fogel, 2010; Hirschmann et al., 2012; Kadik et al., 2015). In the former form, hydrogen simply dissolves as H_2 molecules, so that its solubility is linked to its molecular radius in a manner similar to N_2, O_2 molecules, and noble gases (Doremus, 1966; Shackleford et al., 1972; see also Fig. 17.1).

The H_2 solubility appears essentially independent of the degree of polymerization (Fig. 17.13). In this respect it differs from that of noble gases and N_2, the solubility of which decreases as a melt becomes increasingly depolymerized (Fig. 17.8). A slight positive temperature-dependent H_2 solubility yields an enthalpy of solution near −13 kJ/mol, which is about 30% of the value for dissolution of He (Shackleford et al., 1972; Shelby, 1976). This smaller enthalpy likely reflects a greater availability of cavities in the silica melt and glass structure wherein the smaller H_2 molecules can dissolve, compared with the large noble gases

Above the glass transition of SiO_2 (near 1200°C), the hydrogen solubility is proportional to the square root of pressure, suggesting therefore a chemical interaction between hydrogen and the silicate structure (Shackleford et al., 1972). Such an interaction has been documented via infrared and Raman spectra of quenched glasses (Luth et al., 1987; Schmidt et al., 1998; Mysen and Fogel, 2010). As can be seen in Fig. 17.14, Raman spectra provide evidence for

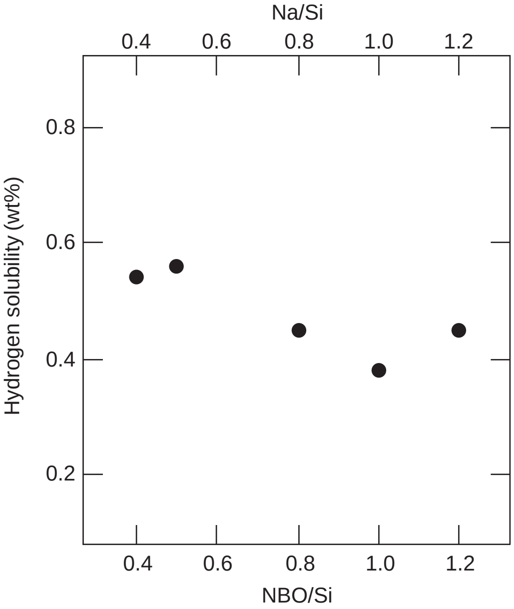

FIG. 17.13 Hydrogen solubility with NBO/Si of quenched melts (quenched from 1400°C at 1.5 GPa pressure at oxygen fugacity defined by the IW buffer) (Mysen and Fogel, 2010).

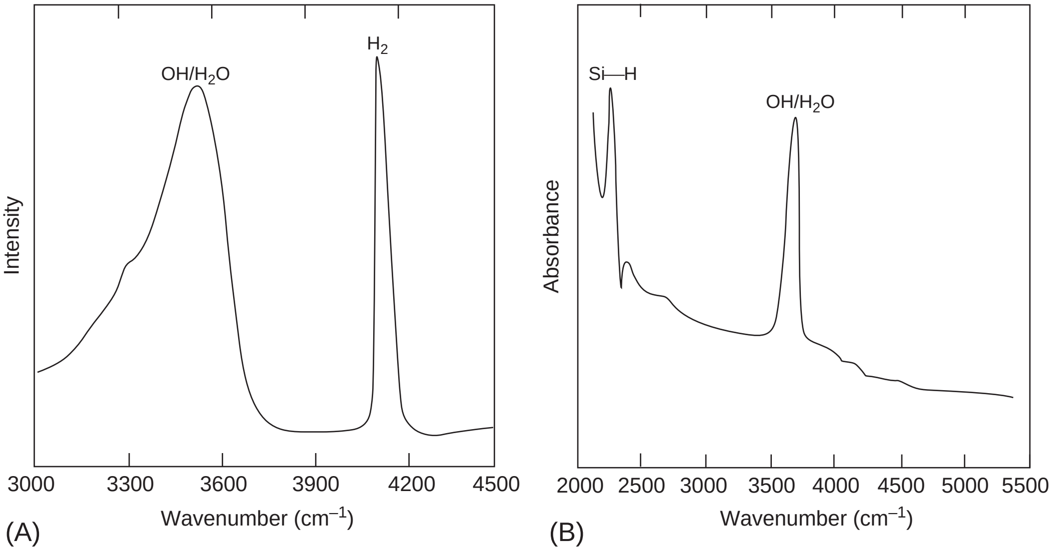

FIG. 17.14 Vibrational spectra of hydrogenated silicate glasses. (A) Raman spectrum of $NaAlSi_3O_8$ glass quenched from melt equilibrated at 1400°C and 2.5 GPa with hydrogen fugacity controlled with the Fe-FeO-H_2O-H_2 buffer (Luth et al., 1987). (B) Infrared absorption spectrum of SiO_2 glass hydrogenated at 800°C and 200 MPa.

formation of OH groups in addition to physically dissolved molecular H_2. Schmidt et al. (1998) also demonstrated formation of Si—H bonding with solubilities in SiO_2—H_2 between 800 and 900 ppm for samples quenched at 200 MPa pressure (Fig. 17.14B)

The structural and chemical information contained in Fig. 17.14 led Schmidt et al. (1998) to follow up on a proposed solution mechanism by Bell et al. (1962) where a solution equilibrium for H_2 in polymerized silicate melts involves bond breakage of the type

$$\mathrm{Si-O-Si+H_2=Si-OH+Si-H}. \tag{17.6}$$

In Eq. (17.6), Si—O—Si denotes a bridging oxygen bond, Si—OH a nonbridging bond terminated with a proton, and Si—H an Si-hydride

The information contained in Eq. (17.6) can be expanded to illustrate that an equilibrium between molecular H_2, Si-hydride and Si—OH is a silicate depolymerization reaction

$$3Q^n + 4H_2 = 2Q^{n-2}(H) + SiH_4. \tag{17.7}$$

Here, two oxygen/silicate tetrahedra are transformed from bridging to nonbridging to form Si—OH bonds. This is expressed as a $Q^{n-2}(H)$ species in Eq. (17.7). This solution nechanism is a very efficient silicate depolymerization reaction

The solution mechanism outlined in Eq. (17.7) would explain the extent of freezing-point depression of silicates caused by H_2-rich H_2O+H_2 fluids (Fig. 17.5; see also Luth and Boettcher, 1986). This temperature depression cannot result from H_2 being simply considered an ideal diluent of H_2O (illustrated as component "X" in Fig. 17.15) because the liquidus

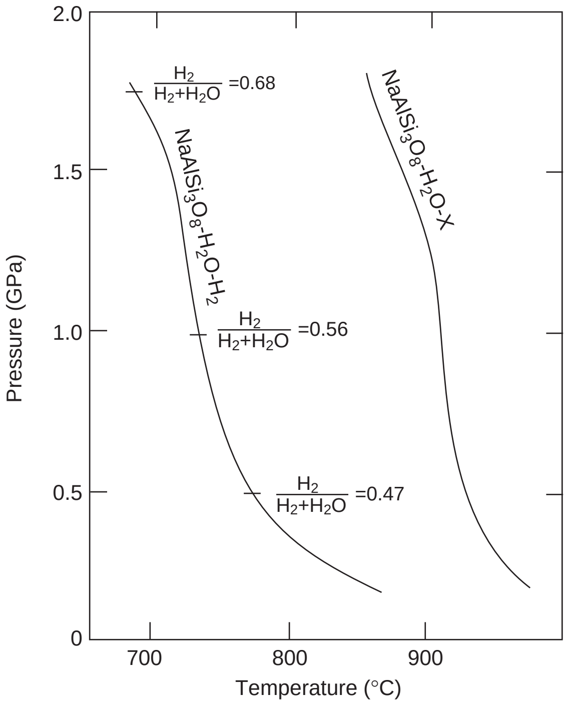

FIG. 17.15 Pressure-temperature trajectory of the $NaAlSi_3O_8$-H_2O-H_2 liquidus equilibrated at the hydrogen fugacity of the Fe-FeO-H_2O-H_2 buffer The evolution of the molar proportion, $H_2/(H_2+H_2O)$, is also shown. The curve marked $NaAlSi_3O_8$-H_2O-X is the calculated liquidus curve with an ideal aqueous fluid mixture that contain a hypothetical component, X, (and Boettcher, 1984).

temperature-depression would then be smaller than actually observed. The effects of hydrogen on freezing-point depression of silicates are either the result of greater deviations from unity of the activity coefficient of H_2O in H_2O+H_2 mixtures than in H_2O+X ("X" denotes a component in ideal mixing with H_2O), or hydrogen interacts chemically with the silicate melt structure. Luth and Boettcher (1986), relying on results of gas mixing calculations by Kerrick and Jacobs (1981) and Boettcher (1984), suggested that the activity coefficients are nearly unity in H_2O+H_2 gas mixtures under these pressures and temperatures. That conclusion accords with more recent examination of H_2O-H_2 fluids at high temperature and pressure, which indicates activity coefficients in the 1.0–1.1 range (Bezmen et al., 2011). Thus, the liquidus temperature depressions of silicates in equilibrium with H_2O+H_2 volatiles indicate chemical reaction between hydrogen and the silicate melt structure (Bell et al., 1962; Luth and Boettcher, 1986; Schmidt et al., 1998).

17.4 HALOGENS

Most property and structure information of halogen-bearing glasses and melts is limited to fluorine and chlorine, data for Br- and I-bearing silicate melts and glasses being much less common. Fluorine information tends to focus on materials properties often relevant to ceramic and glass problems, whereas information on chlorine (and Br and I) tends to be important in Earth and planetary science and often focus on solubility in melts and glasses.

17.4.1 Fluorine

Thermal and transport properties of F-bearing silicate melts are among the most commonly studied. Quantitative fluorine solubility data is comparatively rare.

17.4.1.1 Solubility

Fluorine solubility in silicate melts has been extracted from fluorine effects of liquidus phase relations. For example, the fluorine content of alkaline earth silicate melts in equilibrium with fluorine-rich immiscible melts in the 1450–1565°C range decreases with increasing ionization potential of the alkaline earth cation (Ershova, 1957; Ershova and Olshanskii, 1957; see also Fig. 17.16). These and other liquidus phase equilibrium data indicate that the fluorine solubility also increases with decreasing SiO_2 and with increasing Al_2O_3 contents (see Manning, 1981, for data from Al-bearing systems).

The influence of Al_2O_3 on fluorine solubility is a complex function of silicate composition. Dolejs and Baker (2005) studied various alkali aluminosilicate compositions with 10% H_2O and various amounts of CaF_2 added to the systems with melts equilibrated at 100 MPa and 800–950°C. They found that fluorine solubility in this environment is dependent on whether the melt is peraluminous and peralkaline (Fig. 17.17). The fluorine solubility in peraluminous melts increases with Al_2O_3, whereas it increases with peralkalininity for peralkaline melts. Meta-aluminous silicate melts seem to exhibit minimum fluorine solubility.

A positive correlation of fluorine content with Al/(Al+Si) also has been reported from 1.5 GPa/1400°C experiments in water-free Na_2O-Al_2O_4-SiO_2 and K_2O-Al_2O_4-SiO_2 systems

FIG. 17.16 Extent of two-liquid field in systems Me-AlO_3-SiO_2, where Me is an alkaline earth cation. *Redrawn from Ershova (1957).*

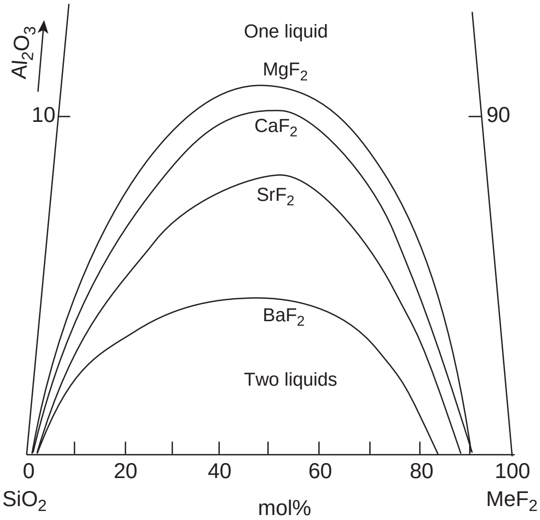

FIG. 17.17 Fluorine solubility in Na_2O-K_2O-CaO-Al_2O_3-SiO_2 glasses formed by temperature-quenching from 1400°C to 1600°C (Dolejs and Baker, 2005).

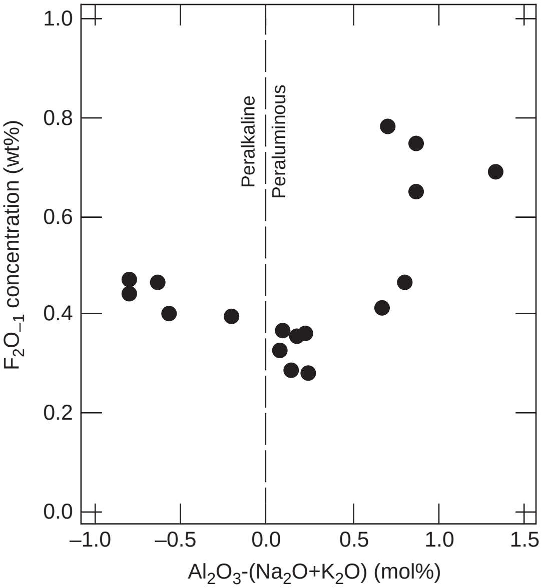

(Dalou et al., 2015; see Fig. 17.18). There is a simple linear relationship between solubility and Al/(Al+Si). The relationships in K- and Na-aluminosilicate systems are nearly indistinguishable from one another (Fig. 17.18). The correlation of solubility with Al/(Al+Si) remains when H_2O is added to the system (Fig. 17.18B). However, the fluorine solubility in alkali aluminosilicate melts also is positively correlated with total H_2O content of the melts and the effect of H_2O increases the more aluminous the melt (Fig. 17.18B).

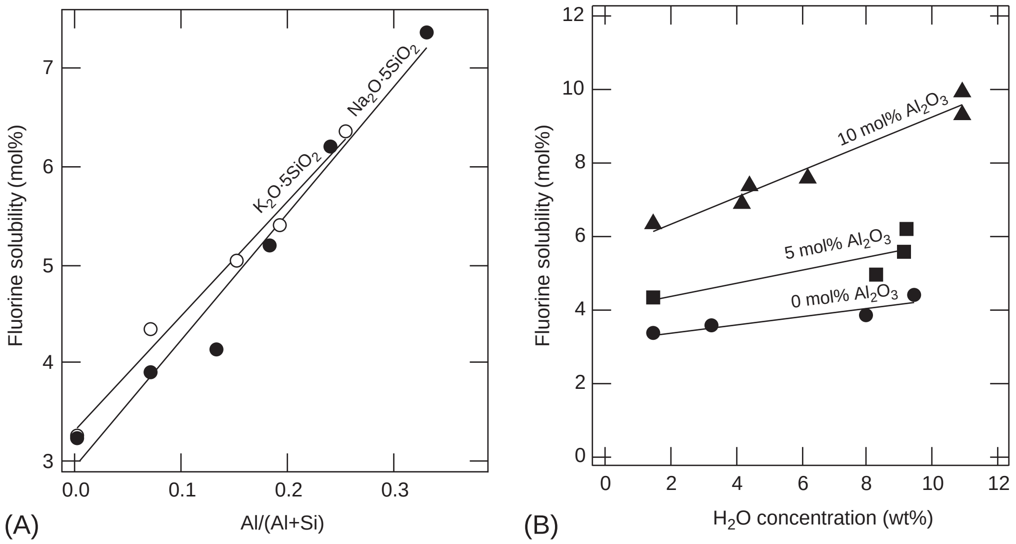

FIG. 17.18 (A) Fluorine solubility in Na_2O-K_2O-Al_2O_3-SiO_2 glasses as a function of Al/(Al+Si) formed by quenching from 1400°C and 1.5 GPa (Dalou et al., 2015). (B) Fluorine solubility in Na_2O-Al_2O_3-SiO_2 glasses as a function of H_2O content for different Al_2O_3 concentration as indicated. Glasses were quenched from 1400°C and 1.5 GPa (Dalou and Mysen, 2015).

17.4.1.2 Solution Mechanisms

Structural studies of F-bearing silicate glasses and melts have been carried out mostly with vibrational and NMR spectroscopic tools. Structural models have also been developed via numerical simulations.

In chemically simple systems such as SiO_2-F, Raman spectra of glasses have been interpreted in terms of depolymerization of the SiO_2 structure via replacement of one or more bridging oxygen with F (Rabinovich, 1983; Yamamoto et al., 1983). In principle, this mechanism is similar to the replacement of bridging oxygen with OH groups in SiO_2-H_2O melts (see Chapter 16, Section 16.3.1).

Vibrational and NMR spectroscopic data of F-bearing metal oxide-silica and melts have led to suggestions that fluorine is dissolved by forming metal fluoride complexes (Takusagawa, 1980; Luth, 1988; Stebbins and Zeng, 2000; Kiczenski and Stebbins, 2002, 2006; Mysen et al., 2004). Interestingly, Luth (1988) proposed that in the system CaO-SiO_2-F_2, formation of Ca—F species may, in fact, result in polymerization of the silicate network of glasses and melts because Ca^{2+} is scavenged from its network-modifying position in F-free melts to form Ca—F bonds in F-bearing melts. This interpretation, in principle, accords with the solution model from the ^{19}F MAS NMR spectra of F-bearing metal oxide-silicate glass, which offer evidence for metal fluoride species where both the alkalis and alkaline earths may serve as metal cations (Mysen et al., 2004; Kiczenski and Stebbins, 2006; see also Fig. 17.19).

In general, for metal-fluoride complexes Na—F bonding dominates over K—F in F-bearing mixed K—Na silicate glasses and Ca—F over Na—F in mixed Ca,Na systems (Stebbins and

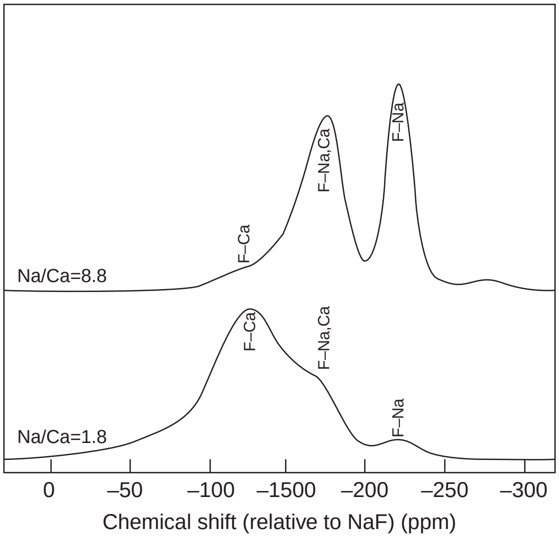

FIG. 17.19 ^{19}F MAS NMR spectra of glasses in the system Na_2O-CaO-SiO_2 with different Na/Ca abundance ratio as indicated and total F content = 1 atom %. Samples were quenched to fictive temperatures near 500°C (Kiczenski and Stebbins, 2006).

Zeng, 2000). In other words, in Al-free metal oxide glasses, fluorine exhibits preference for metals with the largest ionization potential. In this regard, the structural role of metal fluoride species resembles that of metal chloride species in silicate melts, as is discussed further immediately following (Section 17.6.2).

The solution mechanisms of fluorine in silicate melts may be divided into three different types. Fluorine may replace oxygen in silicate tetrahedra and form fluoride complexes with Al^{3+} whether in tetrahedral or other coordination environments, and form simple fluoride complexes with various metal cations (alkalis, alkaline earths, and perhaps more highly charged cations). Combinations of all or some of these solution mechanisms may be present in chemically complex silicate melts.

In fluorinated SiO_2 melt, the simplest substitution involves exchanging a bridging oxygen with F^- (Rabinovich, 1983; Youngman and Sen, 2004; Fan et al., 2015). This mechanism is in many ways equivalent to breaking Si—O—Si bridges with water in solution whereupon two OH groups are formed by dissolving one H_2O molecule, which interacts with bridging oxygen (see Chapter 16, Eq. 16.5). In both situations (F or OH-exchange), the silicate structure is depolymerized. For fluorine, we may write a simple reaction:

$$2Q^n + F^- = 2Q_F{}^{n-1}. \tag{17.8}$$

In this equation, Q_F^{n-1} denotes a Q-species where one of the oxygens in the Q^{n-1} structure has been replaced with F. In principle, more than one oxygen could be replaced with fluorine in this way. This possibility has been found viable through MD calculations (Hayakawa and Hench, 2000). Some vibrational spectroscopic data can also be interpreted to be consistent with multiple F for O exchanges (Rabinovich, 1983; Yamamoto et al., 1983; Duncan et al., 1986). The O—F exchange appears statistically random (Duncan et al., 1986).

Fluoride complexes that involve alkali metals, alkaline earths, and even rare earth fluorides have been reported in F-bearing metal oxide-silicate glasses and melts (Kiczenski and

Stebbins, 2006; Mysen et al., 2004). From ^{19}F MAS NMR data of such materials, there is clear evidence for simple metal fluoride complexes (Fig. 17.19) that involve specific cations (e.g., Na—F and Ca—F) as well as mixed fluoride complexes (Fig. 17.19).

A fraction of Si—F bonding also has been detected (Kiczenski and Stebbins, 2006; Ko and Park, 2013). From examination of glasses with different fictive temperature, the temperature dependence of a simple exchange reaction with terms of bond types can be determined (Kiczenski and Stebbins, 2006):

$$\mathrm{Si-O-Si+M-F=Si-F+Si-O-M}. \tag{17.9}$$

From the temperature dependence (Fig. 17.20), the $\triangle H$ value varies with the nature of the M-cation. For alkali and alkaline earth melts, the $\triangle H$ is in the 70–78 kJ/mol range (Kiczenski and Stebbins, 2006).

Fluorine-19 MAS NMR data, combined with ^{29}Si MAS NMR and high-temperature Raman spectroscopic data, have been used to illustrate the interaction between F and the silicate networks (Toplis and Reynard, 2000; Mysen et al., 2004). With monovalent metal cations, M^+, in peralkaline silicate melts, one can write several solution reactions to illustrate how these F-bearing entities can be formed:

$$2\mathrm{Q}^n(\mathrm{M})+\mathrm{MF}\Leftrightarrow 2\mathrm{Q}^{n+1}+\mathrm{M_3OF}. \tag{17.10}$$

Formation of mixed F- and O-bearing species, M_3OF, causes silicate polymerization. However, given that equilibria such as (17.9) and (17.10) both operate in F-bearing metal oxide-silicate melts, the stability of the various fluoride complexes governs the extent to which the degree of polymerization silicate structure will occur. Moreover, as such equilibra also are temperature dependent (Fig. 17.20), variations in temperature will result in changes in polymerization of silicate melts.

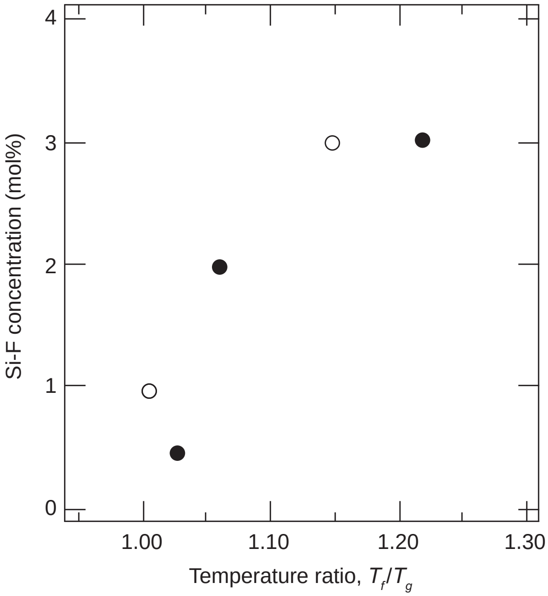

FIG. 17.20 Proportion of Si—F bonding (Si—F) relative to total abundance of fluoride bonding, Si—F/(Si—F+M—F), where M=Na in $Na_2O{\cdot}3SiO_2$ (closed symbols) and $BaO{\cdot}2SiO_2$ (open symbols. T_f denotes fictive temperature and T_g glass transition temperature (Kiczenski and Stebbins, 2006).

Nuclear magnetic resonance and, to a lesser extent, Raman and infrared spectroscopy of F-bearing aluminosilicate glasses have shed considerable additional light on the details of how F interacts with the aluminosilicate network of meta-aluminosilicate melts. The importance of Al—F bonding has, for example, been clearly demonstrated (Schaller et al., 1992; Zeng and Stebbins, 2000; Liu and Nekvasil, 2001; Mysen et al., 2004; Baasner et al., 2014). However, the Al-F-bearing species cannot simply be AlF_3 but must involve both oxygen and metal cations other than Si^{4+} and Al^{3+} (Zeng and Stebbins, 2000; Liu and Tossell, 2003; Mysen et al., 2004). Under certain circumstances, some of the aluminum may undergo transformation from four- to five- and sixfold coordination, at least for highly aluminous melts such as $CaAl_2Si_2O_8$ (Stebbins et al., 2000).

There are several solution mechanisms of fluorine in Al-rich aluminosilicate glasses and melts. For the topaz-like species, one can write (Mysen et al., 2004):

$$6MA1Si_4O_{10} + 3F_2 \Leftrightarrow 2Al_2\left(Al_3\right)F_2 + 4Q^3(M) + Q^2(M) + 19Q^4. \qquad (17.11)$$

In this type of reaction, some of the tetrahedrally coordinated Al^{3+} in the aluminosilicate melt structure is released to form species that may resemble $Al_2(AlO_3)F_2$. The result of this mechanism is depolymerization of the silicate melt structure.

Formation of cryolite-like species in Al-rich aluminosilicate melts was originally inferred from liquidus phase relations in hydrous quartzo-feldspathic systems (Manning et al., 1980; Manning, 1981). That inference is consistent with spectroscopic data (Mysen et al., 2004), and we can write:

$$3MA1Si_4O_{10} + 3F_2 \Leftrightarrow M_3AlF_6 + 2Al^{3+} + 6Q^3 + 6Q^4. \qquad (17.12)$$

Equivalent expressions could be written for mixed (O,F)-containing species such as $M(M_3AlF_5O)$. This is also a depolymerization reaction.

For peralkaline F-bearing aluminosilicate melts, with low Al_2O_3 abundance, on the order of several mol%, there is little or no spectroscopic evidence for Al—F type bonding (Mysen et al., 2004; Dalou et al., 2015). Instead, metal fluoride and Si-fluoride complexes coexist. In other words, a mechanism such as that illustrated with Eq. (17.8) would describe the situation. However, as the Al/(Al+Si) of peralkaline aluminosilicate increases, structures that involve Al—F bonding begin to appear. The detailed nature of the species containing Al—F bonding have been identified via combinations of numerical simulation, ^{19}F MAS NMR and ^{29}Si MAS NMR (Liu and Nekvasil, 2001; Liu and Tossell, 2003; Schaller et al., 1992; Zeng and Stebbins, 2000; Mysen et al., 2004). A variety of Al-bearing complexes are consistent with the experimental and theoretical data, the abundance of which changes systematically with the bulk Al/(Al+Si) (Fig. 17.21).

This abundance of the different F-bearing complexes as a function of Al/(Al+Si) (Fig. 17.22) has different effects on overall aluminosilicate polymerization (Fig. 17.22). In peralkaline aluminosilicate glasses and melts, initial Al^{3+} substitution for Si^{4+} and interaction between F and Al results in melt polymerization, but as the Al/(Al+Si) increases, the net effect of fluorine solution on aluminosilicate polymerization is negligible (Fig. 17.22). This evolution reflects the changing abundance of individual Q-species as a function of Al/(Al+Si) ratio. In F-free melts, this effect is driven predominantly by nearly all Al^{3+} substituting for Si^{4+} in Q^4 species, which, therefore, shifts the Q-species equilibrium to the right;

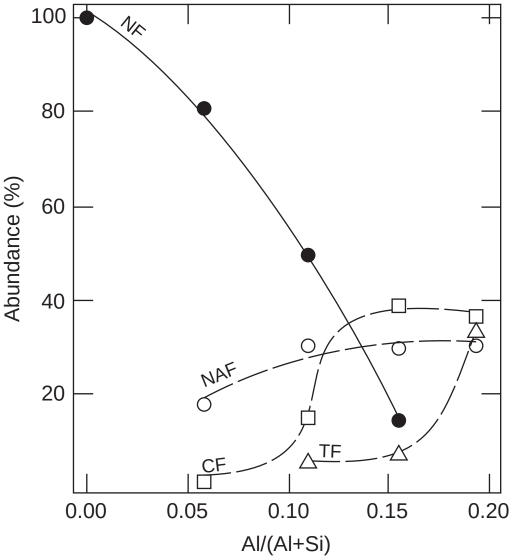

FIG. 17.21 Different types of F-bonding in Na_2O-Al_2O_3-SiO_2 glasses with 3 mol% F and ~80 mol% SiO_2 from ^{19}F MAS NMR spectra of Mysen et al. (2004). Abbreviations: NF: Na—F bonding, NAF: Al—F bonding in cryolite or chiolite-like structures, CF: cryolite-like structure with bridges of oxygen in aluminosilicate network, TF: topaz—like structure. Glasses were formed by 100°C/s temperature quenching of melts quenched from 1400°C at ambient pressure.

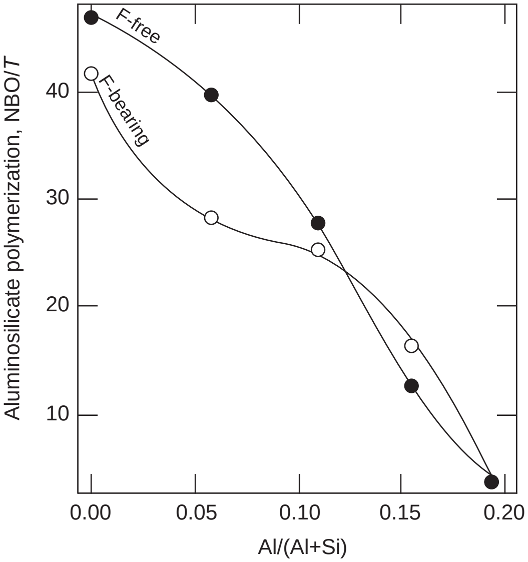

FIG. 17.22 Evolution of NBO/*T* of Na_2O-Al_2O_3-SiO_2 glasses with 3 mol% F as a function of Al/(Al+Si). Glasses were formed by 100°C/s temperature quenching of melts quenched from 1400°C at ambient pressure (Mysen et al., 2004).

$$2Q^3 = Q^2 + Q^4. \tag{17.13}$$

In F-bearing aluminosilicate melts, equilibrium (17.13) is retained, but the proportions of the species in glasses and melts change, as does the temperature-dependence of the equilibrium constant for equilibrium (17.13) (Fig. 17.23):

$$K_{17.13} = X_{Q2} \bullet X_{Q4}/(X_{Q3})^2. \tag{17.14}$$

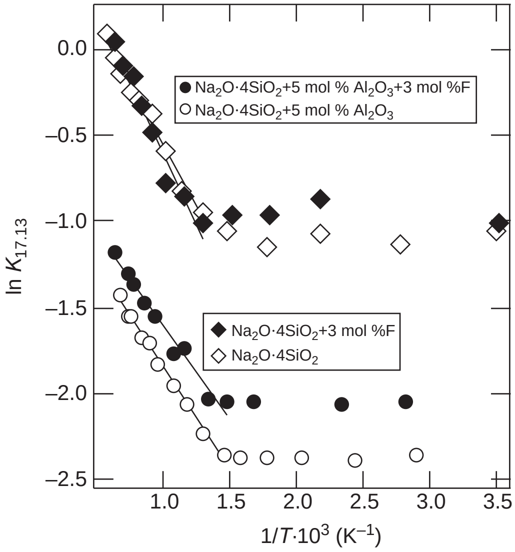

FIG. 17.23 Equilibrium constant, $K_{17.13}$, as a function of $1/T$. The straight slopes extend from the glass transition temperature into the super-cooled liquid and liquid region. The slopes convert to a $\triangle H$ for reaction (17.13) between 9 and 10kJ/mol for Al-free melts and between 11.9 and 14kJ/mol for Al-bearing melts (Mysen et al., 2004).

As the bulk Al/(Al+Si) increases, the $K_{17.13}$-difference between Fe-bearing and F-free glasses and melts reaches a maximum and then decreases with further increase of Al/(Al+Si) (Fig. 17.23).

The enthalpy of equilibrium (17.13) is 9–10kJ/mol for Al-free and 11.9–14kJ/mol for Al-bearing melts. There may be a small effect of dissolved F on the $\triangle H$ values of Al-bearing melts, whereas for Al-free melts the small changes in silicate polymerization via formation of Na—F complexes does not affect the equilibria significantly. The $\triangle S$ difference between F-free and F-bearing melts, defined by the intercept of the $\ln K_{17.13}$ with the temperature axis in Fig. 17.23, diminishes as the melts become increasingly aluminous.

Addition of H_2O to F-bearing aluminosilicate melts has comparatively small effects (Dalou and Mysen, 2015). To illustrate them, we will use a combination of Q-species and aluminate complexes where we may add $MAlO_2$ as a reactant in a reaction that involves a partially fluorinated Q^n species, Q^n(F) metal fluoride, MF, and a more depolymerized silicate species, Q^{n-1}(Al), where the (Al) means that Al^{3+} serves as a network-modifier:

$$Q^n(F) + MAlO_2 = Q^{n-2}(Al) + MF. \tag{17.15}$$

By adding H_2O to this equilibrium, we can write (modified from Dalou and Mysen, 2015):

$$2Q^n(F) + Q^{n+1} + H_2O + 2MAlO_2 = 2Q^{n-2}(Al) + 2MF + Q^{n-1}(H), \tag{17.16}$$

where Q^{n-1}(H) denotes a Q-species with protons, H^+, which bonds to nonbridging oxygen in the Q^{n-1} species. Both reactions (17.15) and (17.16) result in depolymerization of the silicate network. The effect of dissolved F+H_2O on the NBO/T-values of the melts is, nevertheless, essentially the same (Dalou and Mysen, 2015).

17.4.2 Chlorine

A major reason for the interest in Cl in melts is that this fluid component plays a critical role in the enrichment of economically important metals and in volcanic degassing processes (Webster, 1997; Aiuppa et al., 2009; Webster et al., 2009).

17.4.2.1 Solubility

Most experimental studies of the equilibrium between aqueous, Cl-bearing fluids and silicate melts have been carried out under unusual conditions where Cl solubility decreases with increasing pressure (e.g., Webster and Holloway, 1988; Shinohara et al., 1989; Metrich and Rutherford, 1992; Signorelli and Carroll, 2000, 2002). This feature reflects a large partial molar volume difference of chloride complexes between the fluid and the melt (Metrich and Rutherford, 1992; Webster and De Vivo, 2002). However, in water-undersaturated melt systems, the relationship with pressure is positive (Webster and De Vivo, 2002; Dalou and Mysen, 2015).

In anhydrous aluminosilicate-chlorine systems, the chlorine solubility is positively correlated with pressure. However, it is negatively correlated with Al/(Al+Si) of the melt (Dalou et al., 2015; see also Fig. 17.24), in contrast to fluorine solubility, which is a positive function of this parameter (Fig. 17.18). The chlorine solubility is also similar to that observed for fluorine in hydrous silicate melts, because it appears to be at a minimum value for melt compositions near meta-aluminosilicates (Fig. 17.25).

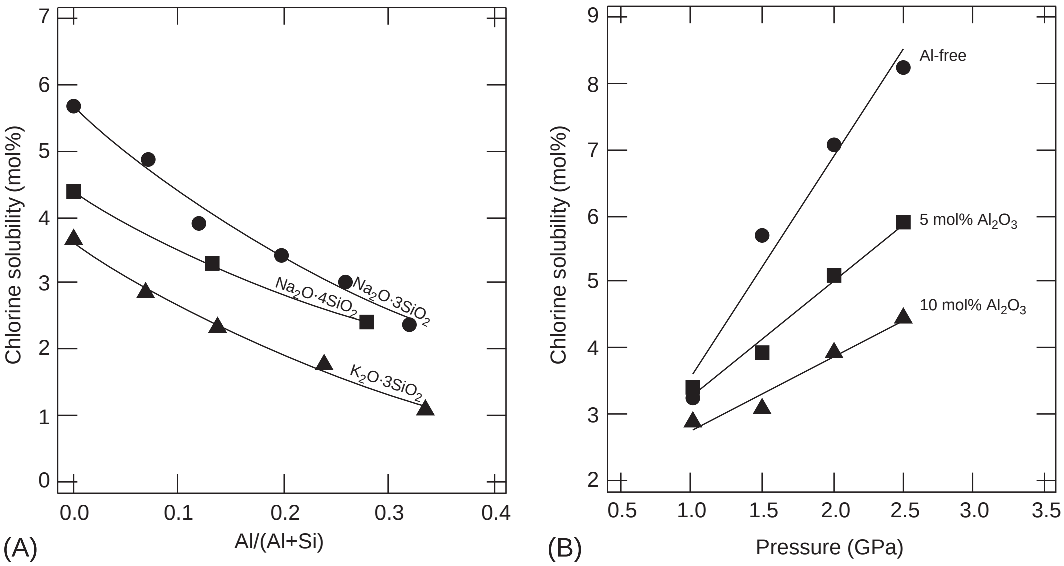

FIG. 17.24 Chlorine solubility in anhydrous aluminosilicate glasses quenched from melt equilibrated at 1400°C. (A) As a function of Al/Al+Si for the Al-free silicate compositions given on the individual Figs. (B) As a function of pressure for the composition $Na_2\cdot4SiO_2$ with Al_2O_3 added (0, 5, and 10 mol% as indicated on individual lines) (Dalou et al., 2015).

FIG. 17.25 Cl solubility in hydrous rhyolite melt as a function of the proportion of alumina relative to alkalis. The dashed line defines the composition of meta-aluminous melts, with peralkaline and peraluminous melts (excess alkalis and excess alumina, respectively) on either side of this divide (Webster and De Vivo, 2002).

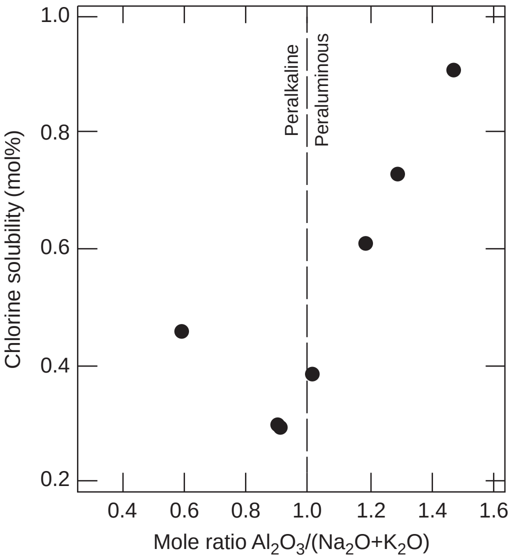

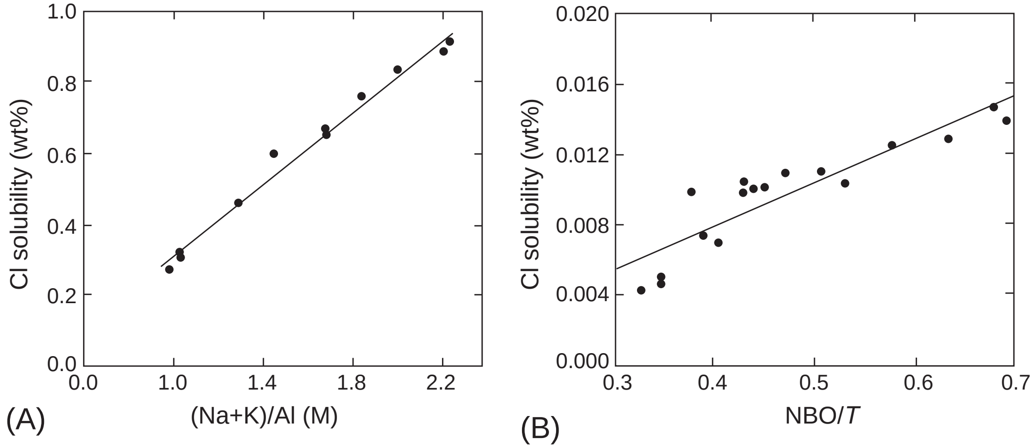

FIG. 17.26 Chlorine solubility (A) as a function of (Na + K)/Al of natural and synthetic phonolite melts (Signorelli and Carroll, 2002) and (B) as a function of NBO/*T* for natural and synthetic rhyolite and trachyte melts (Metrich and Rutherford, 1992; Signorelli and Carroll, 2002).

In water-saturated melts, the chlorine solubility is positively correlated with the (Na + K)/Al ratio of the melt as well as its NBO/*T*-value (Signorelli and Carroll, 2002; Fig. 17.26). It should be noted, though, that increasing the (Na + K)/Al ratio likely results in increasing NBO/*T* of the melt. Thus, it is not clear whether the correlations of chloride solubility with both (Na + K)/Al and NBO/*T* are, in fact, interrelated. Finally, the chlorine solubility varies systematically with water content of a melt (Stelling et al., 2008). It is insensitive to H_2O content for an initial several percent water content in melt before decreasing rapidly as the

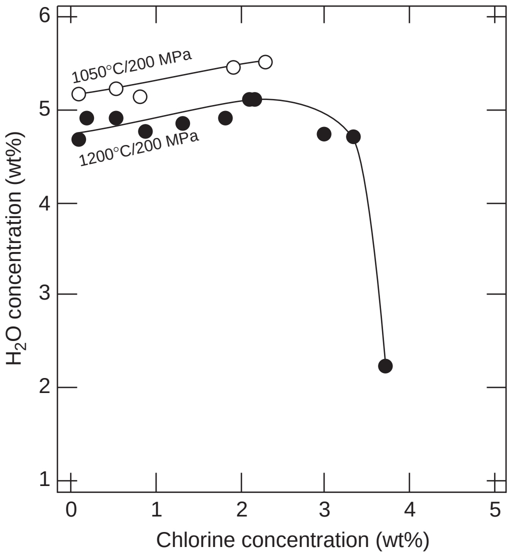

FIG. 17.27 Relationship between H_2O content and chlorine saturation of basalt melt equilibrated at temperatures and pressure indicated and then quenched isobarically to a glass (Stelling et al., 2008).

water concentration increases further (Fig. 17.27). This trend resembles that of CO_2 solubility in hydrous melts (see Section 17.3.1), and reflects an analogous two-solution mechanism. One is increased NBO/T of melt with increasing dissolved water, which enhances Cl solubility. On the other hand, increasing H_2O content in the fluid decreases chloride activity and will therefore tend to decrease the Cl solubility in the melt.

17.4.2.2 Solution Mechanisms

Chlorine-35 MAS NMR and chlorine XANES data of silicate and aluminosilicate glasses suggest that chloride speciation in silicate melts is dominated by alkali chloride or alkaline earth chloride complexes or both (Stebbins and Du, 2002; Sandland et al., 2004; Evans et al., 2008; Baasner et al., 2014; Dalou et al., 2015). In the system Na_2O-CaO-Al_2O_3-SiO_2 with Na>>Ca, results from multinuclear MAS NMR, including ^{35}Cl MAS NMR, indicate that for peralkaline glasses (melts quenched after equilibration as melt at high temperature), Na-chloride complexes dominate (Baasner et al., 2014). Baasner et al. (2014) suggested, however, that for peraluminous glasses, Ca-chloride complexes might be more abundant. Those authors detected no evidence for mixed (Na,Ca)-Cl complexes. In fact, Evans et al. (2008), from their chlorine XANES spectra, concluded that Cl shows distinctive preference for alkaline earths relative to alkali metals in silicate melts. This conclusion is in contrast with that of Sandland et al. (2004), who reported that their ^{35}Cl MAS NMR spectra were best interpreted as mixtures of Na- and Ca-chloride complexes. There was no compelling evidence for Al—Cl bonding in the glasses, whether in the system CaO-MgO-$Al_2O_3SiO_2$ or Na_2O-CaO-Al_2O_3-SiO_2 (Sandland et al., 2004; Evans et al., 2008; Baasner et al., 2014; Dalou et al., 2015).

The structures of Cl-bearing silicate and aluminosilicate glasses and melts differ from those of their Cl-free equivalents (Baasner et al., 2014; Dalou et al., 2015). Baasner et al. (2014) noted changes in ^{29}Si MAS NMR chemical shifts that would be consistent with silicate polymerization, although those authors did not attempt to quantify these effects. Dalou et al.

(2015) observed a small but distinct decrease in the NBO/T of the melts from Raman spectra of Al-free and Al-bearing peraluminous glasses quenched from high temperature at 1.5 GPa pressure.

One may, therefore, write a simply polymerization reaction to describe the solution mechanism of chlorine in silicate melts:

$$2Q^n(M) + MCl = 2Q^{n+1} + M_3OCl. \tag{17.17}$$

This expression is analogous to the fluorine solution mechanism in Eq. (17.10) for Al-free silicate melts. In this regard, fluorine and chlorine solution mechanisms resemble one another. However, in Al-bearing systems, fluorine forms bonding with Al^{3+}, which results in silicate depolymerization (Eqs. 17.11 and 17.12). No such equivalent reaction exists for chlorine in aluminosilicate melts and glasses.

17.4.2.3 *Other Halogens*

The solubility and solution mechanisms in silicate glasses and melts of the larger halogens, Br and I, have received considerably less attention. That scarcity notwithstanding, some data exist (Bureau et al., 2000, 2010; Bureau and Metrich, 2003; Cochain et al., 2015). For example, the same silicate compositional variables seem to govern the solubility of both Cl and Br in hydrous silicate melts, which is positively correlated with Na + K/Al, for example, with a minimum near the meta-aluminosilicate composition (Bureau and Metrich, 2003; see Figs 17.25 and 17.28), Cl (Fig. 17.25). The Br solubility is also a positive function of melt NBO/*T* (Bureau and Metrich, 2003) just like Cl and F solubility (Figs. 17.24 and 17.17). It is also clear that the solubility of Br is lower than that of Cl. In fact, for hydrous melts in equilibrium with halogen-bearing aqueous solutions at high temperature and pressure, the solubility is a simple function of the ionic radius of the halogen when expressed as halogen partition coefficient between aqueous fluid and water-saturated $NaAlSi_3O_8$ melt (Bureau et al., 2000; see also Fig. 17.29)

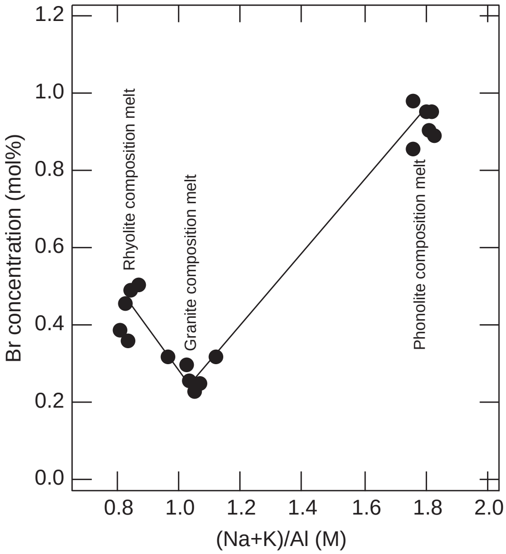

FIG. 17.28 Br Concentration in glasses quenched from melts equilibrated at 900–1000°C and 100–200 MPa pressure (Bureau and Metrich, 2003).

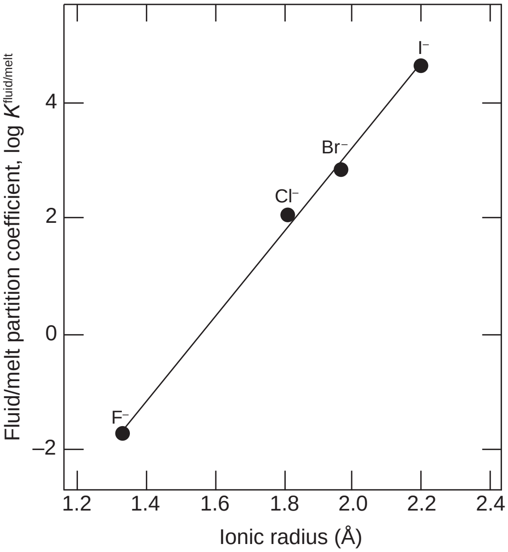

FIG. 17.29 Partition coefficients of halogens between coexisting aqueous fluid and fluid-saturated hydrous $NaAlSi_3O_8$ melt based glass and fluid analyses after quenching experiments from 900°C/200MPa to ambient temperature and pressure conditions (Bureau et al., 2000).

$$\ln K_{\text{fluid/melt}} = -11.7 + 7.3^{*}\text{ionic radius}\left(\text{Å}\right). \tag{17.18}$$

17.4.3 Properties and Solution Mechanisms

Properties of fluorine-bearing glasses and melts have been of major interest among halogen-bearing glasses. There is less information on Cl-bearing melts and glasses. In the latter case, the focus has been on Cl partitioning between aqueous fluids and hydrous silicate melts, because of the importance of such information in many geological processes (Filiberto and Treiman, 2009; Aiuppa et al., 2009; Alletti et al., 2009; Böhm and Schmidt, 2013; Joachim et al., 2015). Fluorine, on the other hand, is not only important in geological processes. However, chlorine also has many commercially important applications (Kyoto et al., 1993; Hosono et al., 1999; Ueda et al., 2000; Kansal et al., 2012). It seems that property data for silicate glasses and melts with Br or I have not been reported extensively. It appears reasonable to assume, however, that the components may have effects similar to Cl, but only to a lesser extent because of their lesser solubility in melts and glasses.

17.4.3.1 Liquidus Phase Relations

Liquidus phase relations in F-bearing silicate and aluminosilicate systems point to complicated relationships between solubility and silicate composition and suggest that effects on liquidus phase relations are considerably greater by dissolving F than Cl (Van Groos and Wyllie, 1967, 1969; Foley et al., 1986; Filiberto and Treiman, 2009; Filiberto et al., 2012; Giehl et al., 2014). Addition of HF to $NaAlSi_3O_8$-H_2O at a few hundred megapascals total pressure depresses the solidus temperature significantly more than addition of equal concentrations of HCl (Fig. 17.30). In fact, in a comparison of effects on liquidus temperature depressions of a natural basalt by H, F, and Cl, fluorine has the greatest effect, followed by hydrogen (water),

FIG. 17.30 Influence of HCl and HF on melting temperature of $NaAlSi_3O_8$ (albite) as a function of temperature. *Redrawn from Wyllie and Tuttle (1964).*

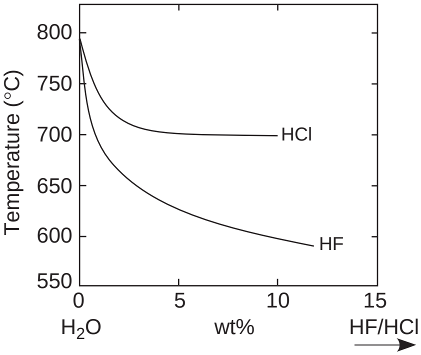

FIG. 17.31 Liquidus phase relations in the system $NaAlSi_3O_8$-$KAlSi_3O_8$-SiO_2-H_2O with fluorine added as indicated on figure (Manning, 1981).

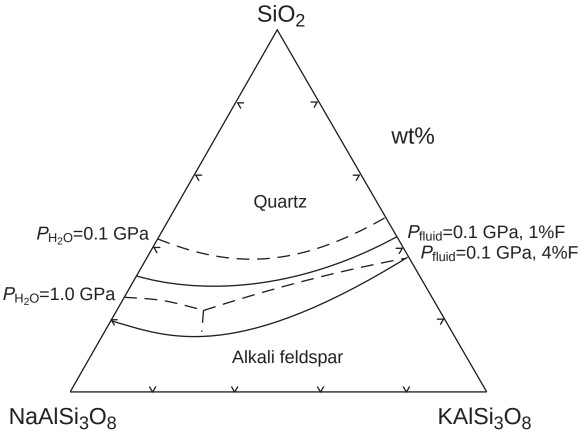

and finally chlorine (Filiberto et al., 2008, 2012; Filiberto and Treiman, 2009). Liquidus phase relations of F- and Cl-bearing systems also differ. Wyllie and Tuttle (1964) noted, for example, that the liquidus volume of quartz in the $NaAlSi_3O_8$-H_2O-HF system is considerably larger than in the equivalent $NaAlSi_3O_8$-H_2O-HCl. In the hydrous "haplogranite" system ($NaAlSi_3O_8$-$KAlSi_3O_8$-SiO_2-H_2O), addition of fluorine leads to an expansion of the quartz relative to the feldspar liquidus volume (Fig. 17.31). These differences between F- and Cl-bearing silicate systems are in direct response to the lower Cl solubility in melts compared with the solubility of fluorine. Moreover, this reflects the greater structural change caused by dissolved fluorine compared with chlorine.

17.4.3.2 Transport Properties

Transport properties such as diffusion and viscosity of silicate melts are profoundly affected by dissolved fluorine, which may, at times, have greater effect on such properties than dissolved water (Dingwell and Mysen 1985; Dingwell and Hess, 1998; Alletti et al., 2007; Baasner et al., 2013). Furthermore, in mixed H_2O-F systems, the combined effect on the viscosity of peralkaline melts of these two volatiles is greater than that which would be expected simply by mixing linearly the effect of H_2O and F (Dingwell and Mysen, 1985). Moreover, the effect on melt viscosity, on a molar basis, of F as compared with OH groups or simply alkali oxides also differ (Fig. 17.32). These effects and their relative importance depend on their concentration. They likely reflect the fact that the solution mechanisms of these components depend not only on their nature, but also on their concentrations.

Solution of chlorine in silicate melts can have a variety of effects on viscosity. For example, for peralkaline compositions, viscosity increases with increasing Cl concentration, whereas the opposite effect is observed for peraluminous melts (Alletti et al., 2007; Zimova and Webb, 2007; Baasner et al., 2013; see also Fig. 17.33). These changes probably reflect changing forms of chloride complexing, perhaps driven by the changing structural role of Al^{3+} in peraluminous melts where charge-compensation of Al^{3+}, accomplished with alkali and alkaline earth cations, differs significantly from that of peralkaline aluminosilicates glasses and melts.

Experimental data on halogen diffusion in silicate melts are somewhat more limited than on viscosity. Some information on F, Cl, and Br diffusion with and without H_2O for a natural phonolite composition, however, has been reported (Balcone-Boissard et al., 2009; Baker and Balcone-Boissard, 2009; Böhm and Schmidt, 2013). In anhydrous melts, chlorine diffuses more slowly than fluorine—by about an order of magnitude in peralkaline compositions. However, this difference diminishes with increasing K/Na ratio and H_2O content of peralkaline aluminosilicate melts (Balcone-Boissard et al., 2009; Böhm and Schmidt, 2013; see also Fig. 17.34). Moreover, the activation energy of diffusion of F and Cl differ significantly, which is consistent with the different solution mechanisms of the two halogens (Sections 17.6.1.2 and 17.6.2.2), whereas those of H_2O and F resemble one another.

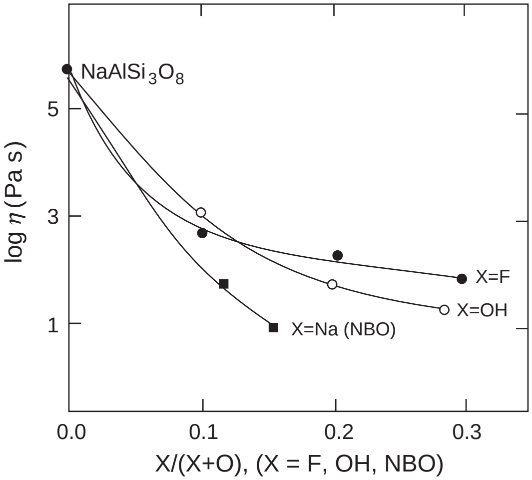

FIG. 17.32 Viscosity at 1200°C and ambient pressure of $NaAlSi_3O_8$ melt as a function of fluorine, H_2O, or Na_2O added (Dingwell and Webb, 1992).

FIG. 17.33 Viscosity change of melts at their glass transition temperature in the system Na_2O-CaO-Al_2O_3-SiO_2 with Cl or F added. The viscosities of peraluminous and peralkaline melts were measured at 815°C and 608°C, respectively (Baasner et al., 2013).

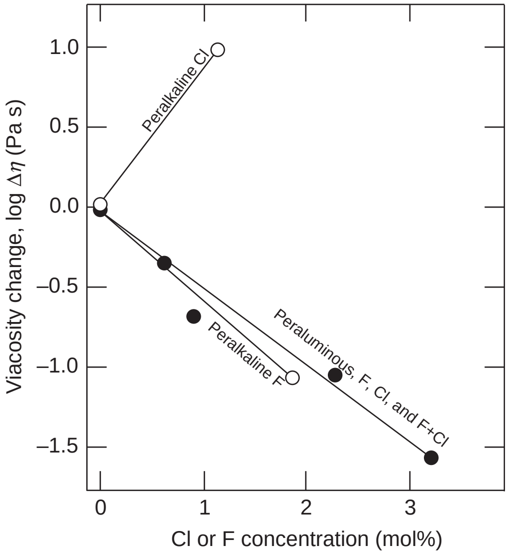

FIG. 17.34 Water, fluorine and chlorine diffusion in potassic trachyte (Balcone-Boissard et al., 2009). The activation energy of diffusion, is shown on each curve.

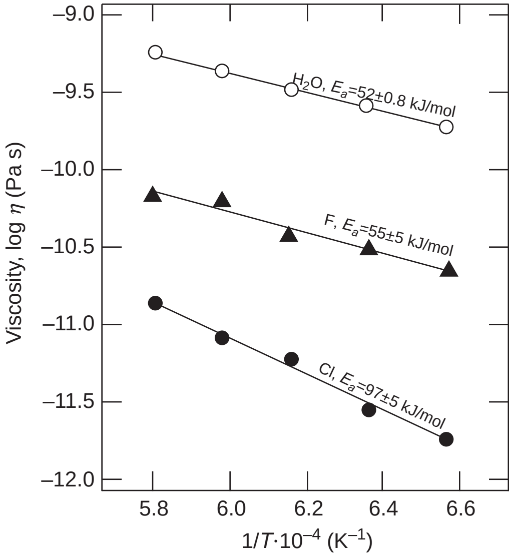

References

Aiuppa, A., Baker, D.R., Webster, J.D., 2009. Halogens in volcanic systems. Chem. Geol. 263, 1–18.

Alletti, M., Baker, D.R., Freda, C., 2007. Halogen diffusion in a basaltic melt. Geochim. Cosmochim. Acta 71, 3570–3580.

Alletti, M., Baker, D.R., Scaillet, B., Aiuppa, A., Moretti, R., Ottolini, L., 2009. Chlorine partitioning between a basaltic melt and H_2O-CO_2 fluids at Mount Etna. Chem. Geol. 263, 37–50.

Baasner, A., Schmidt, B.C., Webb, S.L., 2013. The effect of chlorine, fluorine and water on the viscosity of aluminosilicate melts. Chem. Geol. 357, 134–149.

Baasner, A., Schmidt, B.C., Dupree, R., Webb, S.L., 2014. Fluorine speciation as a function of composition in peralkaline and peraluminous Na_2O CaO-Al_2O_3-SiO_2 glasses: a multinuclear NMR study. Geochim. Cosmochim. Acta 132, 151–169.

Baker, D.R., Balcone-Boissard, H., 2009. Halogen diffusion in magmatic systems: our current state of knowledge. Chem. Geol. 263, 82–88.

Balcone-Boissard, H., Baker, D.R., Villemant, B., Boudon, G., 2009. F and Cl diffusion in phonolitic melts: influence of the Na/K ratio. Chem. Geol. 263, 89–98.

Behrens, H., 2010. Ar, CO_2 and H_2O diffusion in silica glasses at 2 kbar pressure. Chem. Geol. 272, 40–48.

Bell, T., Hetherington, G., Jack, K.H., 1962. Water in vitreous silica. Part 2: some aspects of hydrogen-water-silica equilibria. Phys. Chem. Glasses 3, 141–146.

Bezmen, N.I., Zavel'sky, V.O., Salova, T.P., 2011. Solubility of water-hydrogen fluid in haplogranite, albite, and sodium disilicate melts. Petrology 19, 183–197.

Boettcher, A.L., 1984. The system SiO_2-H_2O-CO_2: melting solubility mechanisms of carbon and liquid structure to high pressures. Am. Mineral. 69, 823–834.

Böhm, A., Schmidt, B.C., 2013. Fluorine and chlorine diffusion in phonolitic melt. Chem. Geol. 346, 162–171.

Bouhifd, M.A., Jephcoat, A.P., Kelley, S.P., 2008. Argon solubility drop in silicate melts at high pressures: a review of recent experiments. Chem. Geol. 256, 252–258.

Broadhurst, C.L., Drake, M.J., Hagee, B.E., Bernatowicz, T.J., 1992. Solubility and partitioning of Ne, Ar, Kr, and Xe in minerals and synthetic basalt melts. Geochim. Cosmochim. Acta 56, 709–723.

Bureau, H., Metrich, N., 2003. An experimental study of bromine behaviour in water-saturated silicic melts. Geochim. Cosmochim. Acta 67, 1689–1697.

Bureau, H., Keppler, H., Metrich, N., 2000. Volcanic degassing of bromine and iodine: experimental fluid/melt partitioning data and applications to stratospheric chemistry. Earth Planet. Sci. Lett. 183, 51–60.

Bureau, H., Foy, E., Raepsaet, C., Somogyi, A., Munsch, P., Simon, G., Kubsky, S., 2010. Bromine cycle in subduction zones through in situ Br monitoring in diamond anvil cells. Geochim. Cosmochim. Acta 74, 3839–3850.

Carroll, M.R., Stolper, E.M., 1991. Argon solubility and diffusion in silica glass: implication for the solution behavior of molecular gases. Geochim. Cosmochim. Acta 55, 211–226.

Chamorro-Perez, E., Gillet, P., Jambon, A., 1996. Argon solubility in silicate melts at very high pressures. experimental set-up and preliminary results for silica and anorthite melts. Earth Planet. Sci. Lett. 145, 97–107.

Cochain, B., Sanloup, C., de Grouchy, C., Crepisson, C., Bureau, H., Leroy, C., Kantor, I., Irifune, T., 2015. Bromine speciation in hydrous silicate melts at high pressure. Chem. Geol. 404, 18–26.

Dalou, C., Mysen, B.O., 2015. The effect of H_2O on F and Cl solubility and solution mechanisms of in aluminosilicate melts at high pressure and high temperature. Am. Mineral. 100, 633–643.

Dalou, C., Le Losq, C., Mysen, B.O., Cody, G.D., 2015. Solubility and solution mechanisms of chlorine and fluorine in aluminosilicate melts at high pressure and high temperature. Am. Mineral. 100, 2272–2283.

Dickinson, J.E., Scarfe, C.M., McMillan, P.M., 1990. Physical properties and structure of $K_2Si_4O_9$ melt quenched from pressures up to 2.4 GPa. J. Geophys. Res. 95, 15675–15681.

Dingwell, D.B., Hess, K.-U., 1998. Melt viscosities in the system Na-Fe-Si-Si-O-Cl-F; contrasting effects of F and Cl in alkaline melts. Am. Mineral. 83, 1016–1021.

Dingwell, D.B., Mysen, B.O., 1985. Effects of water and fluorine on the viscosity of albite melt at high pressure: a preliminary investigation. Earth Planet. Sci. Lett. 74, 266–274.

Dingwell, D.B., Webb, S.L., 1992. The fluxing effect of fluorine at magmatic temperatures (600-800oC): a scanning calorimetric study. Am. Mineral. 77, 30–33.

Dolejs, D., Baker, D.R., 2005. Thermodynamic modeling of melts in the system Na_2O-$NaAlO_2$-SiO_2-F_2O_{-1}. Geochim. Cosmochim. Acta 69, 5537–5556.

Doremus, R.H., 1966. Physical solubility of gases in fused silica. J. Am. Ceram. Soc. 49, 461–462.

Duncan, T.M., Douglass, D.C., Csensits, R., Walker, K.L., 1986. Study of fluorine in silicate glass with 1 9F nuclear magnetic resonance spectroscopy. J. Appl. Phys. 60.

Ershova, Z.P., 1957. Equilibrium of immiscible liquids in the systems of the MeF_2-Al_2O_3-SiO_2 type. Geochem. Int. 4, 350–358.

Ershova, Z.P., Olshanskii, Y.I., 1957. Equilibrium of immiscible liquids of the MeF_2-MeO-SiO_2 type. Geochem. Int. 3, 257–267.

Evans, K.A., Mavrogenes, J.A., O'Neill, H., Keller, N.S., Lang, L.Y., 2008. A preliminary investigation of chlorine XANES in silicate glasses. G3. 9Q10003.

Fan, G.Z., He, S.P., Wu, T., Wang, Q., 2015. Effect of fluorine on the structure of high Al_2O_3-bearing system by molecular dynamics simulation. Metall. Mater. Trans. B Process Metall. Mater. Process. Sci. 46, 2005–2013.

Filiberto, J., Treiman, A.H., 2009. The effect of chlorine on the liquidus of basalt: first results and implications for basalt genesis on Mars and Earth. Chem. Geol. 263, 60–68.

Filiberto, J., Treimann, A.H., Le, L., 2008. Crystallization experiments on a Gusev Adirondack basalt composition. Meteor. and Planet. Sci. 43, 1137–1146.

Filiberto, J., Wood, J., Dasgupta, R., Shimizu, N., Le, L., Treiman, A.H., 2012. Effect of fluorine on near-liquidus phase equilibria of an Fe–Mg rich basalt. Chem. Geol. 312-313, 118–126.

Fogel, R.A., 1994. Nitrogen solubility in aubrite and E chondrite melts. Lunar Planet. Sci. Conf. 25, 383–384.

Foley, S.F., Taylor, W.R., Green, D.H., 1986. The effect of fluorine on phase relationships in the system $KAlSiO_4$-Mg_2SiO_4-SiO_2 at 28 kbar and the solution mechanism of fluorine in silicate melts. Contrib. Mineral. Petrol. 93, 46–55.

Gaudio, S.J., Sen, S., Lesher, C., 2008. Pressure-induced structural changes and densification of vitreous $MgSiO_3$. Geochim. Cosmochim. Acta 72, 1222–1230.

Giehl, C., Marks, M.A.W., Nowak, M., 2014. An experimental study on the influence of fluorine and chlorine on phase relations in peralkaline phonolitic melts. Contrib. Mineral. Petrol.. 167.

Guillot, B., Guissani, Y., 1996. The solubility of rare gases in fused silica: a numerical evaluation. J. Chem. Phys. 105, 255–270.

Guillot, B., Sarda, P., 2006. The effect of compression on noble gas solubility in silicate melts and consequences for degassing at mid-ocean ridges. Geochim. Cosmochim. Acta 70, 1215–1230.

Guillot, B., Sator, N., 2012. Noble gases in high-pressure silicate liquids: a computer simulation study. Geochim. Cosmochim. Acta 80, 51–69.

Hayakawa, S., Hench, L.L., 2000. AM1 study on infrared spectra of silica clusters modified by fluorine. J. Non-Cryst. Solids 262, 264–270.

Hayatsu, A., Waboso, C.E., 1985. The solubility of rare gases in silicate melts and implications for K-Ar dating. Chem. Geol. 52, 97–102.

Heber, V.S., Brooker, R.A., Kelley, S.P., Wood, B.J., 2007. Crystal-melt partitioning of noble gases (helium, neon, argon, krypton, and xenon) for olivine and clinopyroxene. Geochim. Cosmochim. Acta 71, 1041–1061.

Hirschmann, M.M., Withers, A.C., Ardia, P., Foley, N.T., 2012. Solubility of molecular hydrogen in silicate melts and consequences for volatile evolution of terrestrial planets. Earth Planet. Sci. Lett. 345, 38–48.

Hiyagon, H., Ozima, M., 1986. Partition of noble gases between olivine and basalt melt. Geochim. Cosmochim. Acta 50, 2045–2057.

Hosono, H., Mizuguchi, M., Skuja, L., Ogawa, T., 1999. Fluorine-doped SiO_2 glasses for F_2 excimer laser optics: fluorine content and color-center formation. Opt. Lett. 24, 1549–1551.

Iacono-Marziano, G., Paonita, A., Rizzo, A., Scaillet, B., Gaillard, F., 2010. Noble gas solubilities in silicate melts: new experimental results and a comprehensive model of the effects of liquid composition, temperature and pressure. Chem. Geol. 279, 145–157.

Jambon, A., 1994. Earth degassing and large-scale geochemical cycling of volatile elements. Rev. Mineral Volatiles Magmas 30, 479–517.

Joachim, B., Pawley, A., Lyon, I.C., Marquardt, K., Henkel, T., Clay, P.L., Ruzie, L., Burgess, R., Ballentine, C.J., 2015. Experimental partitioning of F and Cl between olivine, orthopyroxene and silicate melt at Earth's mantle conditions. Chem. Geol. 416, 65–78.

Kadik, A.A., Koltashev, V.V., Kryukova, E.B., Plotnichenko, V.G., Tsekhonya, T.I., Kononkova, N.N., 2015. Solubility of nitrogen, carbon, and hydrogen in FeO-Na_2O-Al_2O_3-SiO_2 melt and liquid Iron alloy: influence of oxygen fugacity. Geochem. Int. 53, 849–868.

Kansal, I., Goel, A., Tulyaganov, D.U., Rajagopal, R.R., Ferreira, J.M.F., 2012. Structural and thermal characterization of CaO-MgO-SiO_2-P_2O_5-CaF_2 glasses. J. Eur. Ceram. Soc. 32, 2739–2746.

Kerrick, D.M., Jacobs, G.K., 1981. A modified Redlich-Kwong equation for H_2O, CO_2 and H_2O-CO_2 mixtures at elevated pressures and temperatures. Am. J. Sci. 281, 735–767.

Kiczenski, T.J., Stebbins, J.F., 2002. Fluorine sites in calcium and barium oxyfluorides: F-19 NMR on crysalline model compounds and glasses. J. Non-Cryst. Solids 306, 160–168.

Kiczenski, T.J., Stebbins, J.F., 2006. The effect of fictive temperature on the structural environment of fluorine in silicate and aluminosilicate glasses. J. Am. Ceram. Soc. 89, 57–64.

Kirsten, T., 1968. Incorporation of rare gases in solidifying enstatite melts. J. Geophys. Res. 73, 2807–2810.

Ko, K.Y., Park, J.H., 2013. Effect of CaF2 addition on the viscosity and structure of CaO-SiO_2-MnO slags. ISIJ Int. 53, 958–965.

Kyoto, M., Ohoga, Y., Ishikawa, S., Ishiguro, Y., 1993. Characterization of fluorine-dpoed silica glasses. J. Mater. Sci. 28, 2738–2744.

Le Losq, C., Cody, C.D., Mysen, B.O., 2015. Alkali influence on the water speciation and the environment of protons in silicate glasses revealed by ^{1}H MAS NMR spectroscopy. Am. Mineral. 100, 466–482.

Li, Y., Huang, R.F., Wiedenbeck, M., Keppler, H., 2015. Nitrogen distribution between aqueous fluids and silicate melts. Earth Planet. Sci. Lett. 411, 218–228.

Libourel, G., Marty, B., Humbert, F., 2003. Nitrogen solubility in basaltic melt. Part I. Effect of oxygen fugacity. Geochim. Cosmochim. Acta 67, 4123–4136.

Liu, Y., Nekvasil, H., 2001. Ab initio study of possible fluorine-bearing four- and five-fold coordinated Al species in aluminosilicate glasses. Am. Mineral. 86, 491–497.

Liu, Y., Tossell, J.A., 2003. Possible Al-F bonding environment in F-bearing Na-aluminosilicate glasses: from calculation of ^{19}F NMR shifts. J. Phys. Chem. B 107, 11280–11289.

Luth, R.W., 1988. Raman spectroscopic study of the solubility mechanisms of F in glasses in the system CaO-CaF_2-SiO_2. Am. Mineral. 73, 297–305.

Luth, R.W., Boettcher, A.L., 1986. Hydrogen and the melting of silicates. Am. Mineral. 71, 264–276.

Luth, R.W., Mysen, B.O., Virgo, D., 1987. Raman spectroscopic study of the behavior of H2 in the systemNa_2O-Al_2O_3-SiO_2-H_2. Am. Mineral. 72, 481–486.

Lux, G., 1987. The behavior of noble gases in silicate liquids: solution, diffusion, bubbles and surface effects, with application to natural samples. Geochim. Cosmochim. Acta 51, 1549–1560.

Malavasi, G., Menziani, M.C., Pedone, A., Segre, U., 2006. Void size distribution in MD-modelled silica glass structures. J. Non-Cryst. Solids 352, 285–296.

Manning, D.A.C., 1981. The effect of fluorine on liquidus phase relationships in the system Qz-Ab-Or with excess water at 1 kb. Contrib. Mineral. Petrol. 76, 206–215.

Manning, D.A.C., Hamilton, C.M.B., Herderson, C.M.B., Dempsey, M.J., 1980. The probable occurrence of interstitial Al in hydrous F-bearing and F-free aluminosilicate melts. Contrib. Mineral. Petrol. 75, 257–262.

McElfresh, D.K., Howitt, D.G., 1986. Activation energy for diffusion in glass. J. Am. Ceram. Soc. 69, C237–C238.

Metrich, N., Rutherford, M.J., 1992. Experimental study of chlorine behavior in hydrous silicic melts. Geochim. Cosmochim. Acta 56, 607–616.

Miyazaki, A., Hiyagon, H., Sugiura, N., 1995. Solubility of nitrogen and argon in basalt melt under oxidizing conditions. In: Farley, K.A. (Ed.), Volatiles in the Earth and Solar System: American Inst. Physics.pp. 276–283.

Miyazaki, A., Hiyagon, H., Sugiura, N., Hirose, K., Takahashi, E., 2004. Solubilities of nitrogen and noble gases in silicate melts under various oxygen fugacities: implications for the origin and degassing history of nitrogen and noble gases in the earth. Geochim. Cosmochim. Acta 68, 387–401.

Mysen, B.O., Fogel, M.L., 2010. Nitrogen and hydrogen isotope compositions and solubility in silicate melts in equilibrium with reduced (N+H)-bearing fluids at high pressure and temperature: effects of melt structure. Am. Mineral. 95, 987–999.

Mysen, B.O., Cody, G.D., Smith, A., 2004. Solubility mechanisms of fluorine in peralkaline and meta-aluminous silicate glasses and melts to magmatic temperatures. Geochim. Cosmochim. Acta 68, 2745–2769.

Mysen, B.O., Yamashita, S., Chertkova, N., 2008. Solubility and solution mechanisms of NOH volatiles in silicate melts at high pressure and temperature—amine groups and hydrogen fugacity. Am. Mineral. 93, 1760–1770.

Nakayama, G.S., Shackelford, J.F., 1990. Solubility and diffusivity of argon in vitreous silica. J. Non-Cryst. Solids 126, 249–254.

Niwa, K., Miyakawa, C., Yagi, T., Matsuda, J., 2013. Argon solubility in SiO_2 melt under high pressures: a new experimental result using laser-heated diamond anvil cell. Earth Planet. Sci. Lett. 363, 1–8.

Nowak, M., Schreen, D., Spickenbom, K., 2004. Argon and CO_2 on the race track in silicate melts: A tool for the development of a CO_2 speciation and diffusion model. Geochim. Cosmochim. Acta 68, 5127–5138.

Nuccio, P.M., Paonita, A., 2000. Investigation of the noble gas solubility in H_2O-CO_2 bearing silicate liquids at moderate pressure II: the extended ionic porosity (EIP) model. Earth Planet. Sci. Lett. 183, 499–512.

Ottonello, G., Richet, P., 2014. The solvation radius of silicate melts based on the solubility of noble gases and scaled particle theory. J. Chem. Phys. 140044506 https://dx.doi.org/10.1063/1.4862737.

Ozima, M., 1998. Noble gases under pressure in the mantle. Nature 393, 303–304.

Paonita, A., 2005. Noble gas solubility in silicate melts: a review of experimentation and theory, and implications regarding magma degassing processes. Ann. Geophys. Italy 48, 647–669.

Rabinovich, E.M., 1983. On the structural role of fluorine in silicate glasses. Phys. Chem. Glasses 24, 54–56.

Roselieb, K., Rammensee, W., Buttner, H., Rosenhauer, M., 1992. Solubility and diffusion of noble gases in vitreous albite. Chem. Geol. 96, 241–266.

Roselieb, K., Buttner, H., Eicke, U., Kohler, U., Rosenhauer, M., 1996. Pressure dependence of Ar and Kr diffusion in a jadeite melt. Chem. Geol. 128, 207–216.

Sandland, T.O., Du, L.S., Stebbins, F., Webster, J.D., 2004. Structure of Cl-containing silicate and aluminosilicate glasses: a Cl-35 MAS-NMR study. Geochim. Cosmochim. Acta 68, 5059–5069.

Schaller, T., Dingwell, D.B., Keppler, H., Knoller, W., Merwin, L., Sebald, A., 1992. Fluorine in silicate glasses: a multinuclear magnetic resonance study. Geochim. Cosmochim. Acta 56, 701–707.

Schmidt, B.C., Keppler, H., 2002. Experimental evidence for high noble gas solubilities in silicate melts under mantle pressures. Earth Planet. Sci. Lett. 195, 277–290.

Schmidt, B.C., Holtz, F.M., Beny, J.M., 1998. Incorporation of H-2 in vitreous silica, qualitative and quantitative determination from Raman and infrared spectroscopy. J. Non-Cryst. Solids 240, 91–103.

Shackleford, J.F., 1999. Gas solubility in glasses; principles and structural implications. J. Non-Cryst. Solids 253, 231–241.

Shackleford, J.F., Studt, P.L., Fulrath, R.M., 1972. Solubility of gases in glass. II. He, Ne, and H_2 in fused silica. J. Appl. Phys. 43, 1619–1626.

Shelby, J.E., 1976. Pressure dependence of helium and neon solubility in vitreous silica. J. Appl. Phys. 47, 135–139.

Shen, G., Mei, Q., Prakapenka, V.B., Lazor, P., Sinogeikin, S., Meng, Y., Park, C., 2011. Effect of helium on structure and compression behavior of SiO_2 glass. Proc. Natl. Acad. Sci. U. S. A. 108. https://dx.doi.org/10.1073/pnas.1102361108.

Shibata, T., Takahashi, E., Matsuda, J., 1996. Noble gas solubility in binary CaO-SiO_2 system. Geophys. Res. Lett. 23, 3139–3142.

Shibata, T., Takahashi, E., Matsuda, J., 1998. Solubility of neon, argon, krypton, and xenon in binary and ternary silicate systems: a new view on noble gas solubility. Geochim. Cosmochim. Acta 62, 1241–1253.

Shinohara, H., Iiyama, J.T., Matsuo, S., 1989. Partition of chlorine compounds between silicate melt and hydrothermal solutions: I. Partition of NaCl-KCl. Geochim. Cosmochim. Acta 53, 2617–2630.

Signorelli, S., Carroll, M.R., 2000. Solubility and fluid-melt partitioning of Cl in hydrous phonolitic melts. Geochim. Cosmochim. Acta 64, 2851–2862.

Signorelli, S., Carroll, M.R., 2002. Experimental study of Cl solubility in hydrous alkaline melt: constraints on the theoretical maximum amount of Cl in trachytic and phonolitic melts. Contrib. Mineral. Petrol. 143, 209–218.

Stebbins, J.F., Du, L.-S., 2002. Chloride sites in silicate and aluminosilicate glasses: a preliminarystudy by ^{35}Cl solid-state NMR. Am. Mineral. 87, 359–363.

Stebbins, J.F., Zeng, Q., 2000. Cation ordering at fluoride sites in silicate glasses: a high-resolution 19F NMR study. J. Non-Cryst. Solids 262, 1–5.

Stebbins, J.F., Kroeker, S., Lee, S.K., Kiczenski, T.J., 2000. Quantification of five- and six-coordinated aluminum ions in aluminosilicate and fluoride-containing glasses by high-field. High-resolution ^{27}Al NMR. J. Non-Cryst. Solids 275, 1–6.

Stelling, J., Botcharnikov, R.E., Beermann, O., Nowak, M., 2008. Solubility of H_2O- and chlorine-bearing fluids in basaltic melt of Mount Etna at $T = 1050$-1250 degrees C and $P = 200$ MPa. Chem. Geol. 256, 102–110.

Takusagawa, N., 1980. Infared absorption spectra and structure of fluorine-containing alkali silicate glasses. J. Non-Cryst. Solids 42, 35–40.

Toplis, M.J., Reynard, B., 2000. Temperature and time-dependent changes of structure in phosphorus containing aluminosilicate liquids and glasses: in situ Raman spectroscopy at high temperature. J. Non-Cryst. Solis 263&264, 123–131.

Ueda, S., Koyo, H., Ikeda, T., Kariya, Y., Maeda, M., 2000. Infrared emission spectra of CaF_2-CaO-SiO_2 melt. ISIJ Int. 40, 739–743.

Van Groos, K., Wyllie, P.J., 1967. Melting relationships in the system NaAlSi3O8-NaF-H2O to 4 kb pressure. J. Geol. 76, 50–70.

Van Groos, A.F.K., Wyllie, P.J., 1969. Melting relationships in the system $NaAlSi_3O_8$-NaCl-H_2O at one kilobars pressure, with petrological applications. J. Geol. 77, 581–605.

Walter, H., Roselieb, K., Buttner, H., Rosenhauer, M., 2000. Pressure dependence of the solubility of Ar and Kr in melts of the system SiO_2-$NaAlSi_2O_6$. Am. Mineral. 85, 1117–1127.

Webster, J.D., 1997. Chloride solubility in felsic melts and the role of chloride in magmatic degassing. J. Petrol. 38, 1793–1807.

Webster, J.D., De Vivo, B., 2002. Experimental and modeled solubilities of chlorine in alulminosilicate melts, consequences for mamgma evolution, and implicatios for exsolution of hydrous chloride melt at Mt. Somma-Vesuvius. Am. Mineral. 87, 1046–1061.

Webster, J.D., Holloway, J.R., 1988. Experimental constraints on the partitioning of Cl between topaz rhyolite melt and H_2O and H_2O+CO_2 fluids: new implications for granitic differentiation and ore deposition. Geochim. Cosmochim. Acta 52, 2091–2105.

Webster, J.D., Sintoni, M.F., De Vivo, B., 2009. The partitioning behavior of Cl, S, and H_2O in aqueous vapor- +/- saline-liquid saturated phonolitic and trachytic melts at 200 MPa. Chem. Geol. 263, 19–36.

White, B.S., Brearley, M., Montana, A.L., 1989. Solubility of argon in silicate liquids at high pressures. Am. Mineral. 74, 513–529.

Wulf, R., Calas, G., Ramos, A., Buttner, H., Roselieb, K., Rosenhauer, M., 1999. Structural environment of krypton dissolved in vitreous silica. Am. Mineral. 84, 1461–1463.

Wyllie, P.J., Tuttle, O.F., 1964. Experimental investigation of silicate systems containing two volatile components. III. The effects of SO_3, P_2O_5, HCl, and Li_2O in addition to H_2O on the melting temperatures of albite and granite. Am. J. Sci. 262, 930–939.

Yamamoto, K., Nakanishi, T., Kasahara, H., Abe, K., 1983. Raman scattering of SiF_4 molecules in amorphous fluorinated silicon. J. Non-Cryst. Solids 59-60, 213–216.

Youngman, R.E., Sen, S., 2004. The nature of fluorine in amorphous silica. J. Non-Cryst. Solids 337, 182–186.

Zeng, Q., Stebbins, J.F., 2000. Fluoride sites in aluminosilicate glasses: high-resolution ^{19}F NMR results. Am. Mineral. 85, 863–867.

Zhang, C., Duan, Z., Li, M., 2010. Interstitial voids in silica melts and implication for argon solubility under high pressures. Geochim. Cosmochim. Acta 74, 4140–4149.

Zimova, M., Webb, S.L., 2007. The combined effects of chlorine and fluorine on the viscosity of aluminosilicate melts. Geochim. Cosmochim. Acta 71, 1553–1562.

CHAPTER

18

Chemically Complex Melts and Natural Magma

OUTLINE

18.1 INTRODUCTORY COMMENTS

Natural melts are formed by partial melting of rocks in the interior of the earth and in terrestrial planets. Their composition is governed by the composition of the source rock, pressure, and temperature of melting, and by partial crystallization of minerals before final emplacement in the planet's interior or on its surface. The properties of such melts are therefore central to our understanding of planetary formation and evolution (see, e.g., Fei et al., 1999, for an edited view of relevant contributions). The melts ultimately cooled to form magmatic or igneous rock, either in the form of glass or partially or fully crystallized. They comprise about 10 major element oxides when ferrous and ferric iron are counted separately. The range of individual oxide components for given major rock types is indicated by the standard error on average of a large number of analyses, shown in Table 18.1.

Chemically complex melts, including such materials as formed by natural processes, have commercial applications: for example, glass formed by remelting of the rocks and cooling of

https://doi.org/10.1016/B978-0-444-63708-6.00018-1

TABLE 18.1 Average Compositions of Major Magmatic Liquids

No. of Analyses	Tholeiite 532	Phonolite 560	Andesite 1997	Rhyolite 764
SiO_2	50.29 ± 2.37	56.56 ± 3.72	57.51 ± 4.08	72.18 ± 3.52
TiO_2	2.06 ± 0.82	0.87 ± 0.63	0.93 ± 1.55	0.39 ± 0.29
AlO_2O_3	14.79 ± 1.82	18.31 ± 5.40	16.93 ± 1.45	13.23 ± 1.50
FeO(T)	10.94 ± 1.59	4.02 ± 1.73	7.08 ± 1.85	2.90 ± 1.79
MnO	0.18 ± 0.03	0.24 ± 1.05	0.14 ± 0.05	0.10 ± 0.19
MgO	7.15 ± 2.5	2.47 ± 1.86	3.90 ± 1.82	0.48 ± 0.51
CaO	10.09 ± 1.38	1.18 ± 2.28	7.17 ± 1.85	1.53 ± 1.24
Na_2O	2.41 ± 0.55	8.21 ± 1.57	3.42 ± 0.77	4.03 ± 1.09
K_2O	0.53 ± 0.38	5.23 ± 1.01	1.51 ± 0.86	3.79 ± 1.42
P_2O_5	0.26 ± 0.12	0.21 ± 0.20	0.23 ± 0.13	0.09 ± 0.09

Redrawn from http://earthchem.org.

the melts. The specific applications of such materials include thermal insulation, soundproofing, and filtration (Siligardi et al., 2017; Palencia et al., 2016; Moretti et al., 2016; Yue and Solvang, 2018), and especially steelmaking, with an annual production of SiO_2-poor slags of 300 million tons, which is four times bigger than that of glass (Mills, 2018).

The objective of this chapter is to describe structure and properties of such melts and glasses. We will do this by applying the data often obtained from chemically simple systems, such as those of binary metal silicate and ternary metal aluminosilicate melts, to the much more complicated natural glasses and melts, and to combine this information with data obtained by direct characterization of natural melts and glasses.

18.2 STRUCTURE

Direct determination of the structure of natural melts poses major challenges because most spectroscopic methods cannot resolve individual signals from materials where multiple components may be in similar structural positions. For example, typical network-formers in silicate and aluminosilicate melts and glasses are Si^{4+} and Al^{3+}, whereas the alkali and alkaline earths are dominated by Na, K, Ca, and Mg, which may serve either to charge-balance Al^{3+} in tetrahedral coordination or as network-modifers (Chapter 4, Section 4.4.3). These compositional factors have direct effects on the resolution of spectra from the various methods used for structure analysis. So with the possible exception of average intertetrahedral angles and major coordination transformations obtained by X-ray diffraction (Sanloup et al., 2013; Wang and Shen, 2014), it is generally not possible to extract detailed structural information. In this chapter, we will therefore employ experimental and simulation data obtained for chemically simpler systems to derive (calculate) important structural features of major types of molten igneous rocks.

18.2.1 Degree of Polymerization, Network Formers, and Network Modifiers

The degree of polymerization of natural melts at or near ambient pressure at temperatures above their liquidus is quantified with the ratio NBO/T (where Fe^{3+}, Ti^{4+}, and P^{5+} are included in the tetrahedrally coordinated cations T). The value of this ratio can be calculated from chemical composition with the procedure summarized in Chapter 4 (Section 4.3.3). The distribution of NBO/T is nearly Gaussian within each major group of magmatic rocks (Fig. 18.1). Each has a distinct maximum in its distribution function, although there is some overlap in NBO/T values whose maxima decrease systematically as the melts become more SiO_2-rich. The average NBO/T is 0.83 ± 0.21, 0.41 ± 0.16, 0.20 ± 0.18, and 0.09 ± 0.08, for tholeiite, andesite, phonolite, and rhyolite melts, respectively. Interestingly, though, there is little or no correlation between these NBO/T values and the abundance ratio, Al/(Al+Si) (Fig. 18.2). In fact, it seems that, if anything, the Al/(Al+Si) of the most siliceous melts, rhyolite, tends to be slightly lower than for the other groups of magmatic liquids.

Tetrahedrally coordinated Al^{3+} in natural magmatic liquids and glasses requires charge-balance just as in simple systems (Chapter 4, Section 4.4.3). An understanding of how it is accomplished in natural melts is important, because the structural environment near alkalis and alkaline earths differs depending on whether they serve this role or act as network-modifiers (e.g., Ispas et al., 2002; Cormier et al., 2003; Xue and Stebbins, 1993; Lee and Stebbins, 2003). When multiple such cations coexist, they may be distributed between network-modifying and charge-balancing roles, as governed by the relative stabilities of the various Al-bearing complexes (see Chapter 9, Section 9.3.2). Moreover, Al^{3+} shows distinctive distribution factors among coexisting Q^n-species, and this distribution likely varies with the nature of the charge-balancing cation (Mysen et al., 1981, 2003; Merzbacher et al., 1990; Neuville et al., 2008).

We can calculate the fractions of charge-balancing cations from structural and thermodynamic data of aluminosilicate melts (Chapters 8 and 9). Structural data are consistent with all or nearly all Al^{3+} residing in Q^4-species in silicate melts and glasses (see Chapter 9,

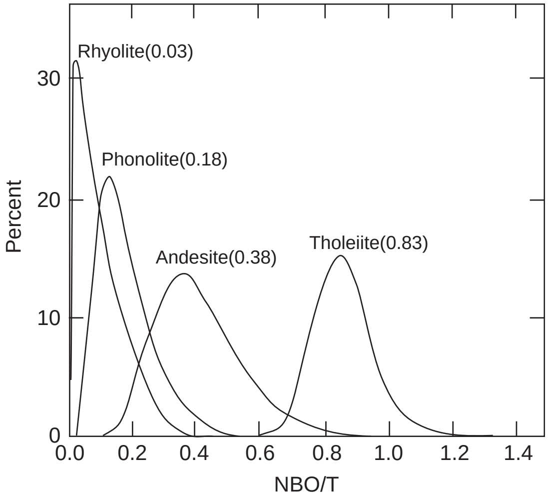

FIG. 18.1 Distribution of nonbridging oxygens per tetrahedrally coordinated cations, NBO/T, of melts of major rock groups as indicated. Numbers in parentheses are the NBO/T values corresponding to the maximum of the individual distribution curves. *Redrawn from http://Earthchem.org.*

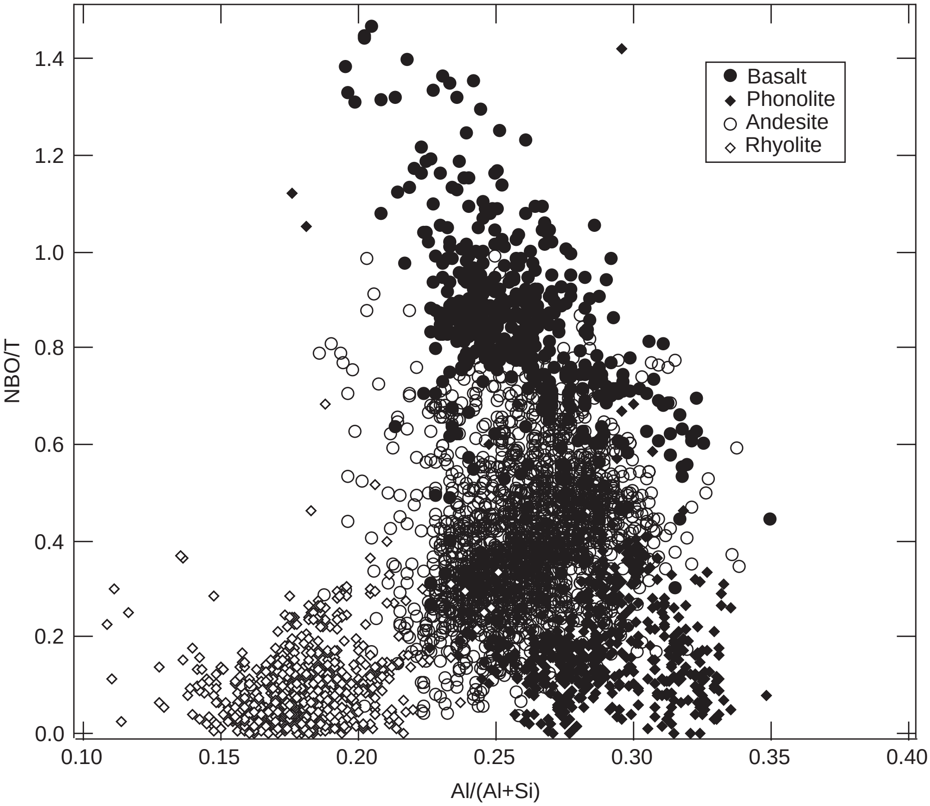

FIG. 18.2 Correlation between NBO/T and bulk Al/(AlSi) of major groups of magmatic liquids. *Redrawn from http://Earthchem.org.*

Section 9.4.2), at least in the NBO/T-range relevant to natural magmatic liquids. The enthalpies of solution of glasses near meta-aluminosilicate joins (Navrotsky et al., 1985) can be used to establish the relative stabilities of alkali and alkaline earth charge-balanced Al^{3+}. Those thermodynamic data indicate near equal stability of $(KAl)^{4+}$ and $(NaAl)^{4+}$ charge-balance followed by $(Ca_{0.5}Al)^{4+}$ and, finally, $(Mg_{0.5}Al)^{4+}$. This hierarchy is in accord with that suggested by Hess and Wood (1982) from their study of Al partitioning between immiscible silicate melts.

From the several thousand analyses of natural melts considered in the computation of these features, K^+, Na^+, and Ca^{2+} for all practical purposes are the cations that charge-balance tetrahedrally coordinated cations in melts of natural composition (Fig. 18.3). Ferrous iron and Mg^{2+} rarely if ever serve in such a role. For andesitic and less felsic (lower SiO_2 contents) melts, the main charge-balancing cation is Ca^{2+}. The proportion of Ca^{2+} relative to $(Na+K)^+$, however, decreases when the materials become more felsic so that alkali charge-balanced Al^{3+} dominates over Ca^+ in rhyolite and phonolite melts (Fig. 18.3). Among the four groups, phonolite melts have the highest proportion of alkali charge-balanced Al^{3+} and tholeiites melts the lowest. In andesitic and tholeiitic melts, all available Na+K is consumed

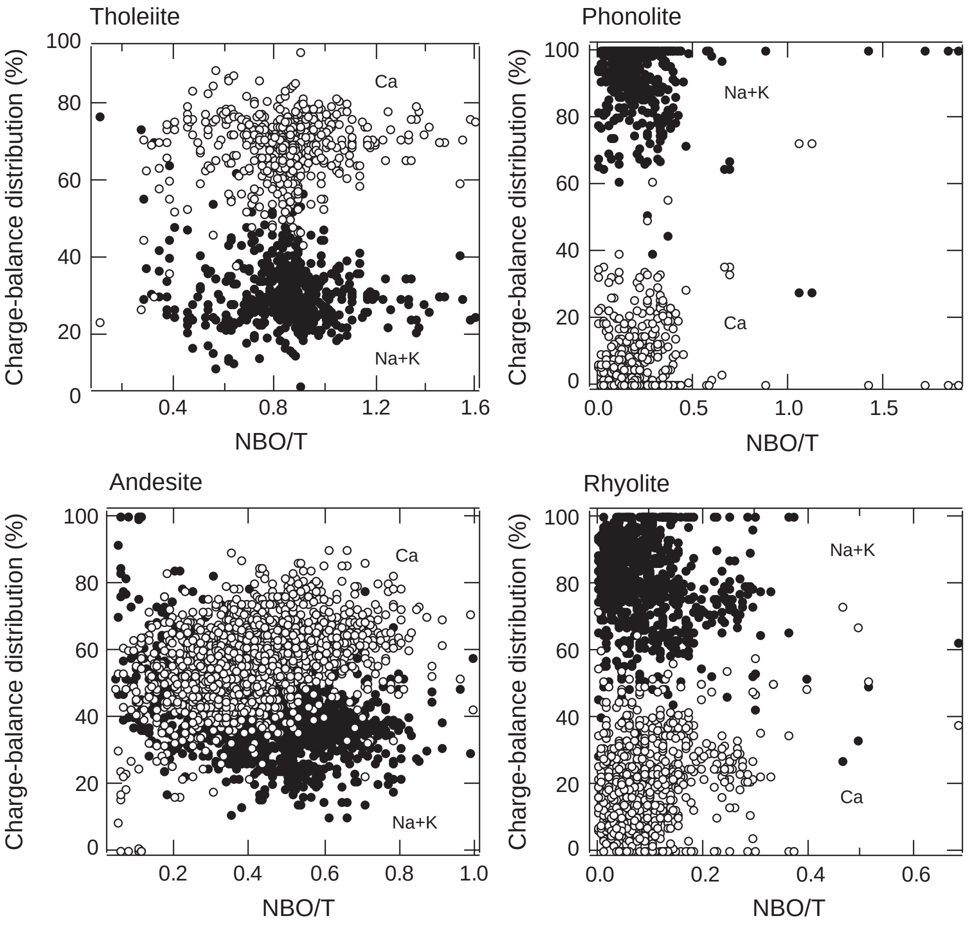

FIG. 18.3 Percentage of Na + K and Ca that charge-balance Al^{3+} in tetrahedral coordination in magmatic liquids as indicated on individual panels. *Redrawn from http://Earthchem.org.*

for this purpose, whereas there exist some compositions among rhyolites and phonolites where there is excess Na + K over that required to charge-balance Al^{3+} (see also Fig. 18.3). This means that relationships between Al/Si ratio and properties of natural magmatic liquids also change because of the greater ordering of Al^{3+} and Si^{4+} in more basaltic melt compositions (Chapter 9, Sections 9.3.2 and 9.4.2).

A consequence of the results in Fig. 18.3 is that in the most felsic liquids (phonolite and rhyolite), about 80% or less of total alkalis serve to charge-balance tetrahedrally coordinated Al^{3+}, and between 20% and 80% of total Ca^{2+} serve as network-modifiers (Figs. 18.4 and 18.5). In less felsic melts such as andesite and tholeiite, alkali metals are never network-modifiers because Na + K serves exclusively to charge-balance Al^{3+} in tetrahedral coordination. A fraction of Ca^{2+} is also a network-modifier in such melts, whereas Mg^{2+} and Fe^{2+} are always network modifiers (Fig. 18.5).

FIG. 18.4 Summary distribution of different forms of charge-compensated Al complexes in major rock types (data from Mysen, 1987).

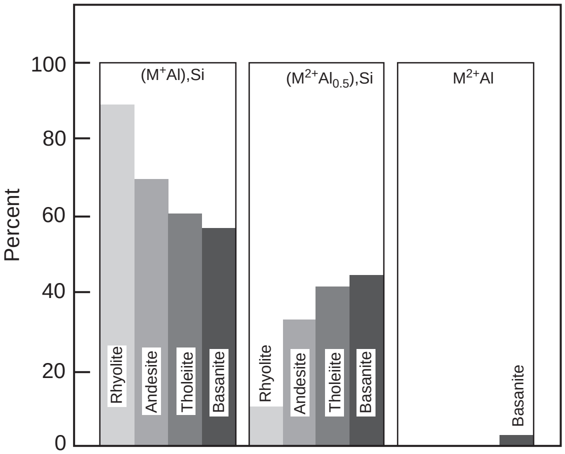

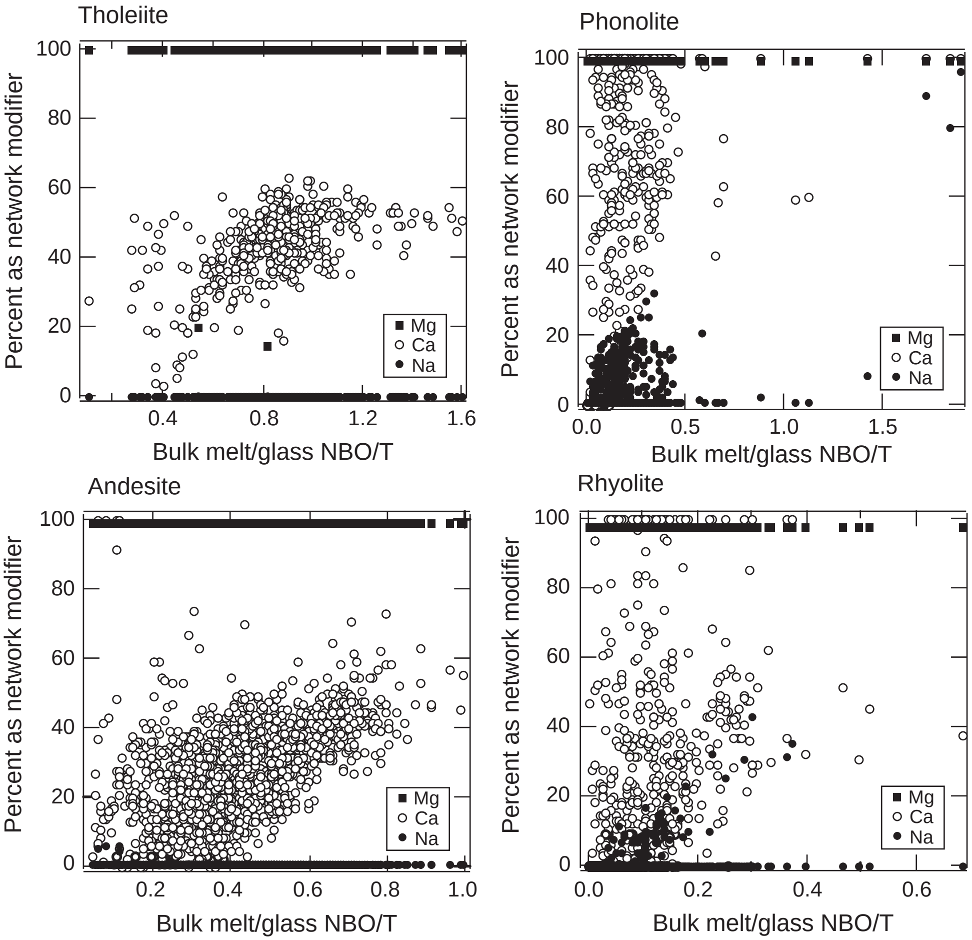

FIG. 18.5 Percentage of Na + K and Ca serving as network-modifiers in magmatic liquids as indicated on individual panels. Note that the percent of Mg is offset by 1% from 100% for clarity. *Redrawn from http://Earthchem.org.*

18.2.2 Q^n-Species in Complex Systems

The distribution of alkali metals and alkaline earths between charge-balancing and network-modifying structural positions (Figs. 18.3 and 18.4) leads to the conclusion that Q^n-speciation in natural melts for the most part is best modeled after alkaline earth aluminosilicate melts. Alkali aluminosilicate structure components contribute only to some rhyolitic and phonolitic melts. Alkali metals only very rarely serve as network-modifiers in natural magmatic liquids at ambient and near ambient pressure.

Without exception, the structural data available for alkali and alkaline earth aluminosilicate melts are consistent with an equilibrium of Q^n-species of the type discussed in Chapter 9 (Section 9.4); see Eq. (9.8). For alkali aluminosilicate melts in the NBO/T-value range less than unity, >98% of the structure can be described with $n=3$. About 95% of the rock analyses used in this discussion of molten rock have NBO/T <1, which suggests that Q^4, Q^3, and Q^2 are the principal species in most natural magmatic liquids. To some extent, however, this conclusion depends on the alkali/alkaline earth ratio, because alkaline earths tend to stabilize more depolymerizing Q^n-species (Chapter 7, Section 7.3).

As alkaline earths rather than alkalis are the principal network-modifying cations in natural magmatic liquids, we need to consider how these cations may affect the equilibria among the Q^n-species. Structural data for $CaO\text{-}SiO_2$ and $MgO\text{-}SiO_2$ melts do not reach compositions even as polymerized as NBO/Si $=1$ because liquid immiscibility is reached at or before melts with NBO/Si $=1$ in these binary compositions (Osborn and Muan, 1960); see also Fig. 6.1. For melts with NBO/Si >1, Raman data lead to the suggestion that the abundance of Q^3-species is suppressed compared with alkali silicate melts (Frantz and Mysen, 1995). Addition of Al^{3+} to any metal oxide melt system drives reaction (9.8) further to the right, because this Al^{3+} exhibits a strong preference for Q^4-species (Mysen et al., 1981; Merzbacher et al., 1990; Mysen, 1999; Lee and Stebbins, 2000; Cormier et al., 2003; Neuville et al., 2004). This preference can also lead to formation of even less polymerizing species, such as Q^1 (Mysen, 1999).

The evolution of Q^n-species as a function of the overall extent of polymerization, NBO/T, in magmatic liquids is shown in Fig. 18.6. The results were calculated from all available structural data from binary and ternary silicate and aluminosilicate glasses, with no consideration of either mixed alkali effects or of how equilibrium (9.8) may be affected by temperature. It is evident from the overall topology of the speciation data (Fig. 18.6) that, when considering magmatic liquids, the general evolutionary trend of the Q^n-species resembles those seen in the simplest of melt compositions (Chapter 7, Section 7.3; Fig. 7.17).

It is clear therefore, from existing data that the three dominant species are Q^4, Q^3, and Q^2 with minor fractions of Q^1-species. Most likely Q^4- and Q^3-species dominate in rhyolite and phonolite melts, whereas Q^2 species are more significant in andesite and less felsic magmatic liquids. In all melts, Al^{3+} resides primarily in Q^4 structural units.

18.3 PROPERTIES

A large experimental database of melt and glass properties and mineral/melt equilibria has been developed. Some of these data have been used to create empirical models describing and predicting properties. However, use of empirical models without theoretical basis to

FIG. 18.6 Estimated Q^n-species abundance evolution as a function of bulk melt NBO/T of melts at ambient pressure from common igneous rocks. *Redrawn from http://Earthchem.org.*

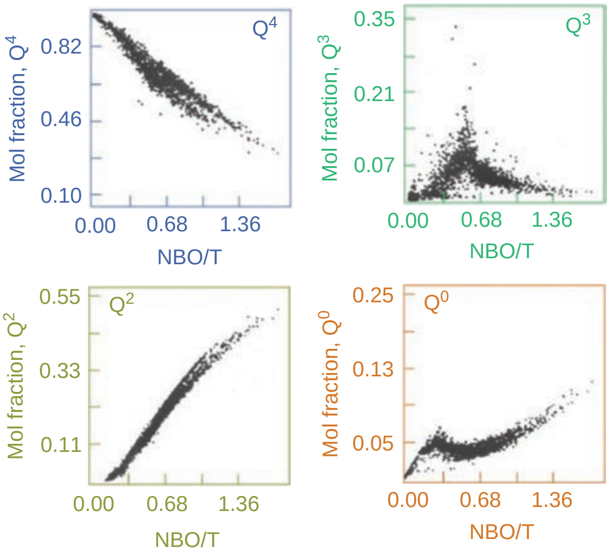

model properties of melts outside the range of compositions used to formulate the model must be exercised with great caution.

From the information discussed in the previous chapters, qualitative and sometimes semiquantitative comments can be made on how the structure and properties of natural melts can be correlated. Some principles will be presented here. Purely empirical models based on regression of properties as a function of oxide composition will not be discussed unless the results of such regression can be evaluated in melt structural terms.

Application of property data from chemically simple systems to magmatic liquids raise such questions as mixing of multiple network-modifying cations, which in principle require consideration of the so-called "mixed alkali effect" (Day, 1976) (see also Chapters 6 and 7), the nature of charge compensation of tetrahedral Al^{3+}, and the extent to which these cations are distributed between charge-balancing and network-modifying roles. These effects can result in variations in physical properties that cannot be explained in terms of simple endmember mixing models and that occur whenever either alkalis or alkaline earths compete for specific sites in silicate melts (Yap and Elliott, 1995; Habasaki et al., 1995; Park and Cormack, 1999). Existing simulations and experimental data, however, are insufficiently detailed to be applied quantitatively to natural silicate melts. Substitution of Al^{3+} for Si^{4+} and variations in the type of cations utilized for charge-compensation offer a series of property and structure variations that may be relevant to our understanding of magmatic liquids (Chapters 8 and 9). Similar observations can be made for solution of various volatiles (Chapters 14–17).

18.3.1 Chemical Properties

In some cases, such as melting and crystallization of complex silicate systems at or near ambient pressure, reasonably successful semiempirical models for natural systems have been proposed (Ghiorso and Sack, 1995). We emphasize that the latter model, commonly termed MELTS, is not based on structural information. Thus, it is not possible to discuss liquidus phase relations calculated by MELTS in such structural terms. Calculation of liquidus phase relations in terms of known structural components rarely has been carried out and to our knowledge never for natural magmatic compositions.

Thermodynamic modeling of activity-composition relations in hydrous systems have been employed to compute melting temperatures and solubility of H_2O in chemically complex systems (Burnham, 1975; Burnham and Nekvasil, 1986). Perhaps surprisingly, however, such models have not improved greatly since they were first proposed. So, even though data from chemically simple systems provide qualitative and semiquantitative guidance as to what to expect in chemically more complex systems (Mysen, 2014), quantitative information often requires direct experimental studies.

18.3.1.1 Melting and Crystallization

In a compositional environment such as natural rocks, initial melting occurs at temperatures often hundreds of degrees lower than those where the last vestiges of crystalline materials disappear. Characteristically, five or six different crystalline phases coexist with melt at the solidus. These then disappear, typically one by one, at specific temperatures as temperature increases, until no crystalline phases are left at the liquidus.

Both solidus and liquidus temperatures are sensitive to chemical composition, SiO_2 content, Si/Al and Fe/Mg ratios being the dominant composition variables. At ambient pressure, both solidus and liquidus temperatures decrease as a sample becomes increasingly SiO_2-rich, so that the solidus temperature of a basalt is in the 1100–1200°C range, whereas that of rhyolite or granite composition is in the 850–950°C range (Thompson, 1972; Fujii and Kushiro, 1977; Gibbon and Wyllie, 1969; Piwinskii and Wyllie, 1970).

The temperature interval between initial and complete melting for basalt compositions is on the order of 200°C at ambient pressure (Yoder and Tilley, 1962). It is <150°C for felsic systems such as granite (Piwinskii and Wyllie, 1970). In basaltic systems, an additional variable with serious effects on melting temperatures is the Mg/Fe ratio, governed by ferromagnesian minerals such as $(Mg,Fe)SiO_3$ (pyroxene) and $(Mg,Fe)_2SiO_4$ (olivine) in the temperature interval between the solidus and liquidus (Yoder and Tilley, 1962). In felsic systems such as rhyolite, granite, and related compositions, the Si/Al and alkali/alkaline earth ratios are the principal compositional factors determining melting temperatures because quartz (SiO_2)/plagioclase ($NaAlSi_3O_8$-$CaAl_2Si_2O_8$) are the dominant minerals in equilibrium with melts between the solidus and liquidus (Piwinskii and Wyllie, 1970; Piwinskii, 1973).

Melting and crystallization of magmatic rocks change with pressure. The pressure–temperature trajectories have positive slopes. The temperature difference between the solidus and liquidus also varies (Fig. 18.7) in response to changes in the mineral assemblages in equilibrium with the melt as a function of increasing pressure. For example, crystalline aluminosilicate materials such as feldspars ($KAlSi_3O_8$, $NaAlSi_3O_8$, and $CaAl_2Si_2O_8$), where Al^{3+} substitutes for Si^{4+} in fourfold coordination, transform to crystal structures with Al^{3+} in sixfold coordination in the multigigapascal pressure range (Johannes et al., 1971; Boettcher et al., 1984). As a result, both the volume and enthalpy of melting, ΔV and ΔH, vary. Therefore, from the Clapeyron equation:

FIG. 18.7 Solidus and liquidus pressure-temperature trajectories of basalt (Cohen et al., 1967) and andesite (Eggler, 1972) as indicated on individual lines.

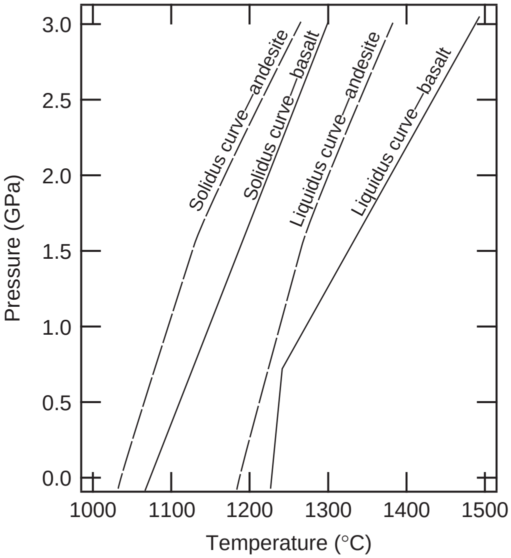

$$dP/dT = \Delta H/T\Delta V, \tag{18.1}$$

the slopes of the solidii and liquidii will also change. Additional variations in the solidus and liquidus temperature-pressure slopes may take place when the pressure gets sufficiently high to result in coordination transformations of Al^{3+} and Si^{4+} in the melt (see also Chapters 5 and 9). However, those pressures are higher than the pressures of the analogous transformations found for crystalline materials, and typically are not encountered until between 5 and 10 GPa. Such structural changes would not, therefore, affect the solidus and liquidus curves in Fig. 18.7.

Addition of a chemical component to a system results in changes in melting phase relations. In simple systems that melt congruently, the temperature depression of liquidus temperatures is a simple function of the activity of the added component and the enthalpy of fusion of the crystalline phase in question:

$$\ln a_X = \left[\Delta H^{\text{fusion}}/R\right] \cdot [(1/T) - (1/T_o)], \tag{18.2}$$

where x is the added component and a_x its activity, ΔH^{fusion} is the enthalpy of fusion of the congruently melting phase, T_o is the melting temperature (K) of the pure phase, and T is the melting temperature when the new component is added.

When this component is a volatile species such as H_2O or CO_2, its activity in the melt is governed by both its solubility (Chapters 14–17, and see also Section 18.3.1.4 following) and its interaction with the silicate components in the melts. Such an interaction, in turn, affects the activity of volatiles in the system. An example of this phenomenon in complex melts such as basalt is provided by volatiles that exist both in a molecular form and in units bonded to the silicate structure. The most notable examples are H_2O and CO_2, which can form OH and CO_3^{2-} groups via interactions with the silicate structure (see Chapters 14–17).

In magmatic liquids, H_2O is by far the most important volatile component. When present during melting of silicate materials, water can depress the solidus temperatures by >500°C,

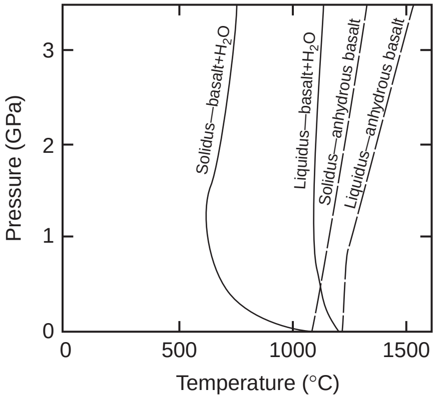

FIG. 18.8 Solidus and liquidus pressure-temperature trajectories of basalt composition in the presence of H_2O and under anhydrous conditions (data from Lambert and Wyllie, 1972).

whereas the effect on the liquidus temperature is considerably smaller—perhaps 100–150°C for basalt (Fig. 18.8). The magnitude of these effects is sensitive to the bulk chemistry of the sample, because the bulk chemistry governs both solubility and solution mechanisms of dissolved water (see Chapter 15, Section 15.4.4, and Chapter 16, Sections 16.3–16.5). In general, the solidus temperature depressions of felsic systems such as granite or rhyolite are considerably greater than in basalt because the ratio OH/H_2O is also greater (Lambert and Wyllie, 1972; Allen et al., 1975). The nature of the reactions resulting from stabilization of OH groups also depends on the bulk composition of the melt. In hydrous systems, isolated metal-OH groups likely are more common basalt than in andesite or rhyolite melts, because the stabilization of such complexes is related to the overall SiO_2 content and to the proportion of alkali metals relative to alkaline earths (Xue and Kanzaki, 2004, 2008; Cody et al., 2005).

18.3.1.2 Crystal/Liquid Equilibria

Element partitioning between minerals and melts is another area subject to considerable effort because this knowledge is central to the characterization of the evolution of igneous rocks. Partition coefficients (element concentration in mineral/element concentration in melts) can vary widely, however, as a function of melt composition (e.g., Watson, 1977; Jurewicz and Watson, 1988; Libourel, 1999; Jaeger and Drake, 2000; Walter, 2001; Toplis and Corgne, 2002; Mysen, 2007a,b, 2008). An example with rare earth partitioning between garnet and magmatic liquids illustrates the effects of melt composition (Fig. 18.9). The activities of high field-strength cations in silicate melts are in fact often simple functions of SiO_2 content (e.g., Watson and Harrison, 1983; Ellison and Hess, 1986). In the experiments reported by Ellison and Hess (1986), melts of differing SiO_2 contents were equilibrated with respective crystalline oxides so that by definition, the activity of the oxides was equal to unity. The decreasing solubility with increasing SiO_2 concentration in the melt (Fig. 18.10) indicates increasing activity coefficient of the three oxides as their SiO_2 concentration increased. This solution behavior, and therefore activity-composition relations, may also be affected by the stabilization of oxyanion complexes involving these high field-strength cations (Mysen, 2012, 2015). The extent to which oxyanion complexes will form is governed by the major element composition of the melts.

FIG. 18.9 Rare earth element (REE) partition coefficients between garnet and melt (wt ratio, garnet/melt) from phenocryst/matrix pairs of natural rocks as indicated (data from Irving and Frey, 1978).

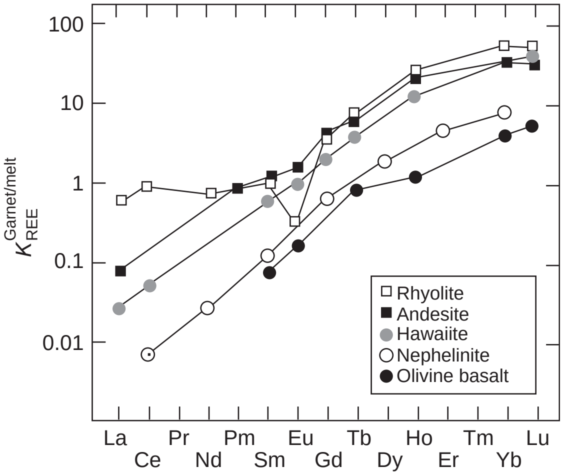

FIG. 18.10 Solubility of oxides of high field strength cations, Ti^{4+}, Zr^{4+}, and Hf^{4+}, in silicate melts in equilibrium with the respective crystalline oxides, TiO_2, ZrO_2, and HfO_2 at 1400°C and ambient pressure (data from Ellison and Hess, 1986).

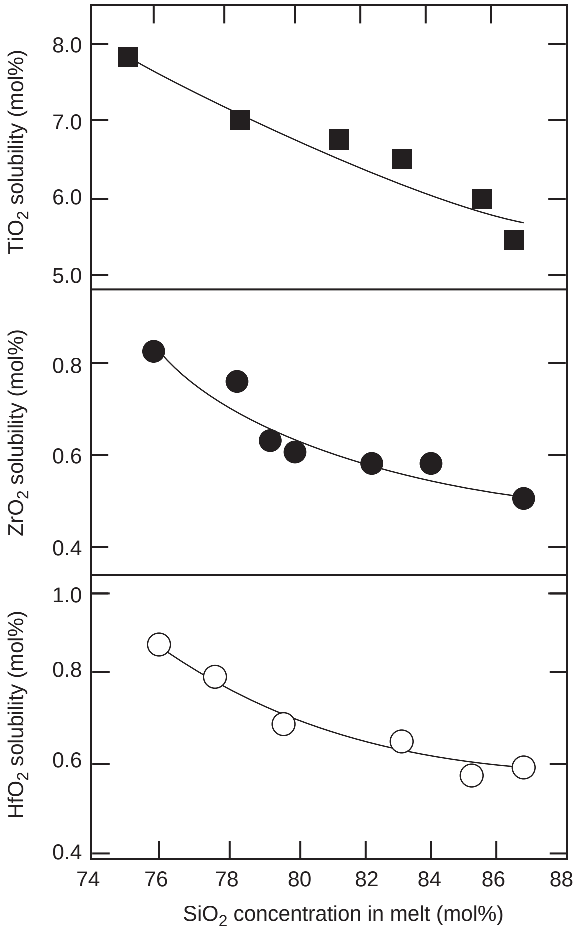

It follows that the activity-composition relations depend on melt composition and therefore on structure. To a first approximation, it has been proposed that melt polymerization, NBO/T, can also be used to quantify effects of composition of partition coefficients (Mysen and Virgo, 1980; Thibault and Walter, 1995; Jana and Walker, 1997; Jaeger and Drake, 2000). The necessary NBO/T values may be calculated provided that the proportion of tetrahedrally coordinated cations (T-cations) is known. However, there is no unifying relationship between partition coefficients and the NBO/T of the melt. These relationships are sometimes linear functions of NBO/T (Mysen and Virgo, 1980; Jaeger and Drake, 2000), but more often they are not (Watson, 1977; Jurewicz and Watson, 1988; Colson et al., 1988; Libourel, 1999; Kushiro and Mysen, 2002; Mysen, 2007a,b); see also Fig. 18.11. Moreover, the functional form differs, even for relatively similar cations (in terms of charge and ionic radius), such as Fe^{2+} and Mg. Given that the (Fe^{2+},Mg) solid solution in olivine is nearly ideal (Olsen and Bunch, 1970), these variations likely reflect different and nonideal solution behavior of Fe^{2+} and Mg in the melts.

It is likely that there exist relations between partition coefficients and NBO/T of the melt because most cations in silicate melts are network-modifiers. The exceptions are Si^{4+} (Chapter 5), Al^{3+} (Chapter 9), Fe^{3+} (sometimes, see Chapter 11), Ti^{4+} (sometimes, see Chapter 12) and P^{5+} (most of the time, see Chapter 13). Network-modifying cations exhibit a preference for nonbridging oxygen in individual Q^n-species in silicate melts and, sometimes, even for specific nonbridging oxygen locations in the melt structure (Chapter 7, Section 7.3.2).

One would expect that the activity/solution relations of such elements, and therefore their mineral/melt partitioning, would reflect the abundances of Q^n-species whether in simple or

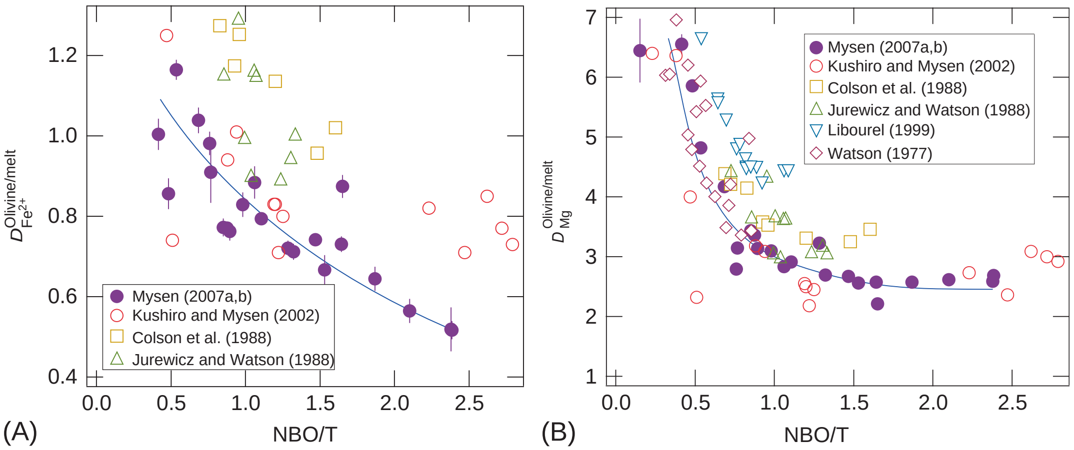

FIG. 18.11 Partition coefficient of Fe^{2+} (A) and Mg (B) between olivine and melt, where the partition coefficients are the wt ratios of the cation between olivine and melt (*solid circles*, data from Mysen, 2007a, at 1350–1380°C. *Open symbols* from various authors, Watson, 1977; Jurewicz and Watson, 1988; Colson et al., 1988; Kushiro and Mysen, 2002; Libourel, 1999, are from various different chemical systems at different and variable temperatures). Those data indicate qualitatively similar trends with NBO/T, but exhibit much more scatter because both silicate composition and temperatures vary over the NBO/T range investigated.

natural systems. Moreover, the Q^n-speciation in melts also varies with Al/Si ratio (Chapter 9, Section 9.4.2). Such structural features can be seen in exchange equilibriia between coexisting melts and crystalline materials at constant temperature and pressure, for which the principal exchange equilibrium of two components, i and j, is written:

$$i(\text{melt}) + j(\text{melt}) \Leftrightarrow i(\text{mineral}) + j(\text{melt}). \tag{18.3}$$

The exchange equilibrium constant then is:

$$K_{D(i-j)}^{\text{Crystal/melt}} = \frac{a_i(\text{crystal}) \cdot a_j(\text{melt})}{a_i(\text{melt}) \cdot a_j(\text{crystal})}, \tag{18.4}$$

where a_i(mineral/melt) is the activity of i in the mineral/melt. Now, the exchange equilibrium constant is proportional to the activity coefficient ratio of components, i and j, in the melt:

$$K_{D(i-j)}^{\text{Crystal/melt}} = \text{constant} \cdot \frac{\gamma_i(\text{melt})}{\gamma_j(\text{melt})}, \tag{18.5}$$

provided that solution of the elements in the crystalline material is Henrian or Raoultian, in which case the activity coefficient ratios in the crystal are unity.

There are several examples of how variations in Q^n-species abundance resulting from variations in alkali/alkaline earth or Al/Si abundance ratios governs exchange equilibria, such as in Eqs. (18.3), (18.5). First, the Fe^{2+}-Mg olivine/melt exchange equilibrium coefficients and NBO/T of the melts in the eight-component system K_2O-Na_2O-CaO-MgO-MnO-FeO-Al_2O_3-SiO_2 evolve as a parabolic function of NBO/T (Kushiro and Mysen, 2002) (Fig. 18.12). The activity coefficient ratio of Fe^{2+} and Mg in the melt should exhibit a similar form in Fig. 18.12, but would be offset relative to the exchange coefficient by the value of the constant in Eq. (18.5). Notably, at least in simple silicate systems, the Q^3-abundance evolution with NBO/T of the melt resembles that of the exchange equilibrium coefficients. One might suggest therefore that this Q^3 evolution may, at least qualitatively, govern the shape of the

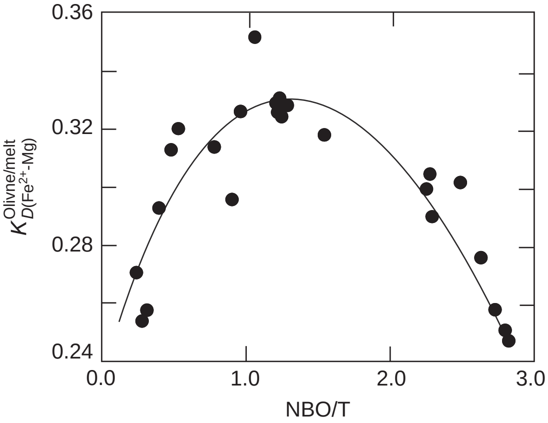

FIG. 18.12 Exchange equilibrium coefficients (see Eq. 18.4) for Fe^{2+} and Mg between coexisting olivine and silicate melt at 1350–1380°C, ambient pressure and $\log f_{O_2} = -6.5$ (MPa) (data from Kushiro and Mysen, 2002).

curves in Fig. 18.12. In addition to metal/(Al+Si) ratio (Fig. 18.12), other variables that can also change the NBO/T of the melt include $Fe^{3+}/\Sigma Fe$ (Section 11.4.2). This means that variations in the iron redox ratio might also cause variations in crystal-liquid partition coefficients, and therefore in activity-composition relations of solutes in silicate and aluminosilicate melts. Such features have indeed been found when dissolving divalent transition metals (e.g., Mysen, 2007a).

Structural data from simple binary and ternary silicate systems indicate that when multiple network-modifying cations exist, they sometimes exhibit a preference for specific types of nonbridging oxygens. Here, the cation with the largest ionization potential (Z/r^2) shows this preference in the most depolymerized silicate structures (see Chapter 7, Section 7.3.2). An example would be coexisting Na^+ and Ca^{2+} (Lee and Stebbins, 2003). Such effects can also be observed in crystal/liquid partitioning, which, of course, is a direct reflection of how cation preferences affect activity-composition relationships in melts, as long as the activity coefficient ratio of the pair of elements, *i* and *j*, does not vary with chemical composition. This effect is particularly evident when the overall melt structure comprises mostly Q^4, Q^3, and Q^2 units. This means that with increasing alkaline earths/alkali ratio, the Q^n-speciation equilibrium:

$$2Q^3 \Leftrightarrow Q^4 + Q^2 \tag{18.6}$$

shifts to the right with increasing $Na^+/(Na^+ + Ca^{2+})$. In this system, the Ca^{2+} likely bonds to a nonbridging oxygen in Q^2 and less polymerized species, whereas, owing to steric hindrance, Na^+ tends to bond to a nonbridging oxygen in Q^3 species. The exchange of Ca^{2+} for Mg^{2+} (Fig. 18.13A) will then be affected because the smaller cation, Mg^{2+}, likely will show preference for the most depolymerized Q^n-species over Ca^{2+}. Given that the abundance of the relevant nonbridging oxygens also is affected by the Na/(Na+Ca) ratio, the exchange

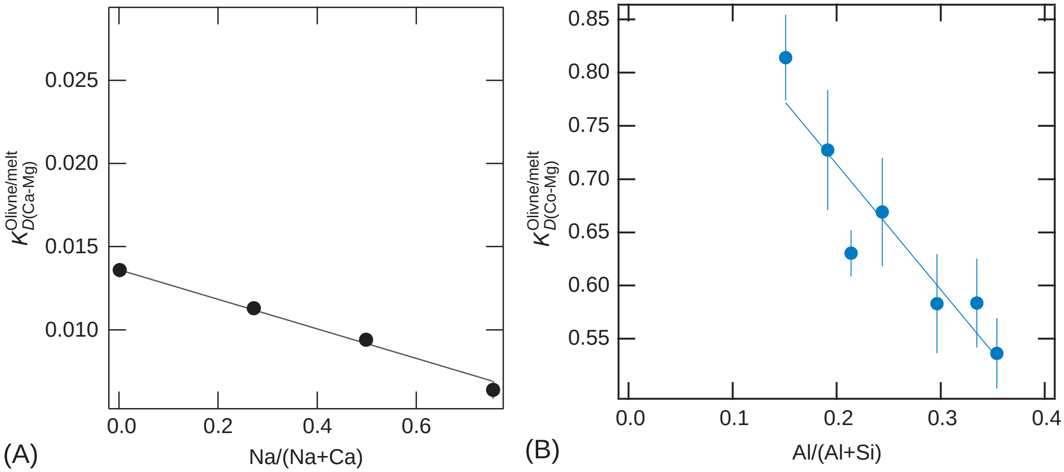

FIG. 18.13 (A) Ca, Mg exchange equilibria between olivine and melt at ambient pressure as a function of Na/(Na+Ca) and constant NBO/T (data from Mysen, 2007a). (B) Co, Mg exchange equilibria between olivine melt at constant NBO/T and temperature at ambient pressure and as a function of Al/(Al+Si) of melt (data from Mysen, 2007b).

equilibrium coefficient for Ca^{2+} and Mg^{2+} becomes dependent on this ratio even though the overall melt polymerization is constant, as is temperature (in the case of Fig. 18.13A, 1350°C at ambient pressure).

There are at least two additional compositional (and, therefore, structural) variables that affect the activity coefficients of network-modifying cations. These are the Al/(Al+Si) and $Fe^{3+}/\Sigma Fe$ ratios (Mysen, 2007a,b). The former will have an effect because an equilibrium such as (18.6) shifts to the right when it increases (Mysen et al., 2003); see also Chapter 9, Section 9.4.2. In other words, increasing Al/(Al+Si) affects equilibrium (18.6) in a manner analogous to decreasing the alkali/alkaline earth ratio, thus affecting olivine/melt exchange equilibria (Fig. 18.13).

All the compositional variables discussed in this section are encountered in magmatic liquids and all do, therefore, affect activity-composition relations of any solute added to such a melt system. Only some cations have been examined experimentally (Kushiro and Walter, 1998; Kushiro and Mysen, 2002; Toplis, 2004; Mysen and Shang, 2005; Mysen, 2007a,b), but very likely the behavior of all will be affected.

18.3.1.3 Redox Relations of Iron

The redox ratio of iron is important because it is not only a probe of the redox conditions under which it was fixed, but also a factor affecting the structure through the distinct roles of Fe^{3+} and Fe^{2+} (Carmichael and Ghiorso, 1990; Kress and Carmichael, 1991; Cottrell and Kelley, 2011). Although the matter has already been discussed in detail in Sections 11.2–11.4, it may be convenient to present again the main points of interest in this chapter.

The structural role of Fe^{3+} and Fe^{2+} in complex melts in many ways resembles those observed in simple systems (see Chapter 11). Results obtained with Fe K-edge X-ray absorption spectroscopy (XANES) of natural glasses are consistent with the average coordination number of both Fe^{3+} and Fe^{2+} between 4 and 6 (Wilke et al., 2005; Metrich et al., 2006; Giuli

FIG. 18.14 Pre-edge intensity vs centroid position from XANES spectroscopy for peralkaline rhyolite glass. *Arrow* indicates direction of relationship with increasing peralkalinity, (Al+K)/Al, of the glasses (data from Giuli et al., 2012).

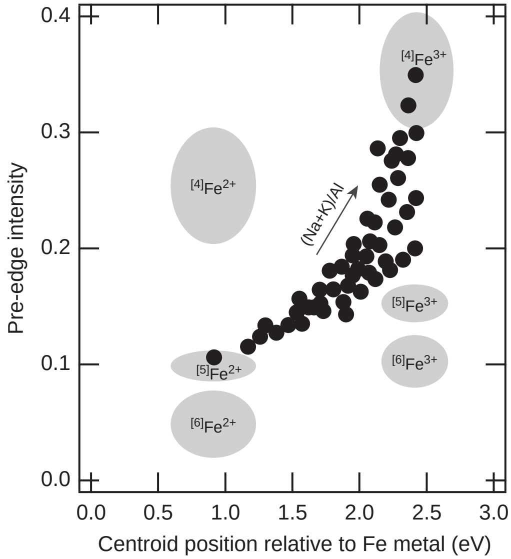

et al., 2012); see also Fig. 18.14. The average Fe^{2+} coordination number is very near 5, whereas that of Fe^{3+} is somewhat lower, but still above 4, which indicates that in a mixed coordination environment, at least some of the Fe^{3+} in these materials actually occupies coordination numbers >4.

The speciation evolution of ferrous and ferric iron seen for peralkaline silica-rich glasses has been reported for both rhyolite and more mafic basalt compositions (Fig. 18.14) (Metrich et al., 2006). Notably, however, from relationships analogous to those of Fig. 18.14, the average coordination numbers of Fe^{2+} and Fe^{3+} in basaltic glasses are about 20%–25% higher than in rhyolitic, more silica-rich glasses (Metrich et al., 2006).

There exist also a number of determinations of the redox state and structure of Fe^{2+} and Fe^{3+} in magmatic liquids as a function of temperature, pressure, and oxygen fugacity (Wilke, 2005; Metrich et al., 2006; Giuli et al., 2012; Zhang et al., 2015). The influence on redox state of water dissolved in natural magma has also attracted attention (Moore et al., 1995; Baker and Rutherford, 1996; Gaillard et al., 2001; Botcharnikov et al., 2005; Schuessler et al., 2008) as well as other, often minor, components such as TiO_2, B_2O_3, P_2O_5, F, and H_2O (Toplis et al., 1994; Botcharnikov et al., 2005; Maia and Rüssel, 2006; Borisov et al., 2013; Cochain et al., 2012).

Variations of the proportions of all those oxides can induce changes in redox ratio at constant temperature, pressure, and oxygen fugacity, just as in simple melts (see Chapter 10, Section 10.4). Therefore, ever since the first experiments of Kennedy (1948) and Fudali (1965), the importance of knowing the iron redox ratio of natural melts and glasses has motivated efforts to predict it as a function of temperature and composition. The first model seems to be that of Lauer (1977) and Lauer and Morris (1977) not only for Fe, but also for Ce and Cr, whose redox states were measured by electron paramagnetic resonance. The composition dependence of the activity coefficient of oxygen ions in simple silicate liquids was related empirically to the ionization potential of network-modifying cations. However, no attempt has been made to extend such a formalism to more complex compositions.

A purely empirical approach was initiated by Sack et al. (1980) and expanded upon by Kilinc et al. (1983) and Kress and Carmichael, 1991. In these treatments, it was assumed that the effects of oxygen fugacity and temperature on the redox ratio do not depend on composition and that, at constant T and f_{O_2}, the redox ratio is an additive function of oxide concentration. The expression they fitted to available and new redox data for melts of geochemical interest ranging from mafic to felsic was thus:

$$\ln\left(x_{Fe_2O_3}/x_{FeO}\right) = a\ \ln f_{O_2} + b/T + c + \sum d_i x_i, \tag{18.7}$$

where x designates an oxide mol fraction; a, b and c are constants; and the d_i are specific parameters for SiO_2, Al_2O_3, "FeO," MgO, CaO, Na_2O, and K_2O. In most cases, multiple regression, using oxide compositions to express c, has been employed (Sack et al., 1980; Kress and Carmichael, 1991; Jayasuriya et al., 2004). Attempts by using regular solution modeling also have been reported (Jayasuriya et al., 2004; Borisov, 2010). Another alternative involves multiple regression of the distribution of nonbridging oxygen in melts associated with the various network-modifying cations (alkalis and alkaline earths) (Mysen, 1987).

There are, however, objections to the assumptions made in these models. These assumptions are, for example, inconsistent with the nonlinear dependence of redox ratio on total iron content (see Chapter 10, Figs. 10.13 and 10.14). Besides, network formers and modifiers should influence the redox state in differing ways as has been documented in simple binary metal oxide-silicate systems (e.g., Virgo et al., 1981). When the "FeO" content is not small, variations of the redox state are, in addition, synonymous with changes in melt polymerization, oxygen activity, and energetics of the redox reaction. All such factors make it difficult to neglect the influence of composition on the variation of redox state with temperature and oxygen fugacity, which is indicated by other data for higher temperatures or lower oxygen fugacities. Models have been proposed that utilize Margules parameters to account for the deviations from ideality (Jayasuriya et al., 2004; Borisov, 2010). However, it is not clear whether they may be applied for chemical compositions outside the range within which the calibration was performed.

To distinguish the effects of network-forming and -modifying cations, Mysen (1987) modified Eq. (18.7) as follows:

$$\ln\left(x_{\mathrm{Fe}^{3+}}/x_{\mathrm{Fe}^{2+}}\right) = a\ \ln f_{\mathrm{O}_2} + b/T + c + d\Big(\mathrm{Al}/(\mathrm{Al}+\mathrm{Si}) + e\left(\mathrm{Fe}^{3+}/\mathrm{Fe}^{3+}+\mathrm{Si}\right) + \sum f_i x_i, \tag{18.8}$$

where x_i designates the NBO/T value pertaining to the network-modifying cation i. Although a better fit to the input database of Kilinc et al. (1983) was obtained in this way, this model has not been extensively used in the literature. As already stated, probable reasons are the need for structural information and the iterative nature of the calculation due to the fact that the model is a function of both FeO and Fe_2O_3 contents.

As described in Chapters 10 and 11, deviations from the nominal 0.25 value of the coefficient, a, in Eqs. (18.7), (18.8) are a measure of nonideal mixing of Fe^{2+} and Fe^{3+}. Such deviations are also observed for natural melts. One may, of course, try to cope with thermodynamic nonideality via the choice of components such that the stoichiometry coefficient remains close to 0.25. Kress and Carmichael (1988) used in this fashion FeO and $FeO_{1.464}$, the latter being thought to reflect a fundamental aspect of the structure of natural melts. The equation:

$$\ln\left(x_{\mathrm{FeO}_{1.464}}/x_{\mathrm{FeO}}\right) = 0.232\ \ln f_{\mathrm{O}_2} - \left(\Delta H + \sum W_i x_i\right)/RT + \Delta S/R, \tag{18.9}$$

was then fitted to a data set complemented by new measurements made at very low oxygen fugacities.

Effects of pressure on redox ratio, Fe^{3+}/Fe^{2+}, were incorporated by Kress and Carmichael (1991) as part of a study of the compressibility of Fe-bearing melts. This is necessary because the partial molar volumes of FeO and $FeO_{1.5}$ differ, which implies a pressure of effect on redox relations of iron in silicate melts (Chapter 10, Section 10.4.2). Kress and Carmichael (1991) reanalyzed some of their previous results and, abandoning Eq. (10.16), reverted to Eq. (10.14) to which they added pressure-dependent terms:

$$\begin{aligned} \ln\left(x_{\mathrm{Fe_2O_3}}/x_{\mathrm{FeO}}\right) &= a\ \ln f_{\mathrm{O}_2} + b/T + c + \sum d_i x_i \\ &+ e[1 - T_0/T - \ \ln T/T_0] + fP/T + g(T - T_0)P/T + hP^2/T, \end{aligned} \tag{18.10}$$

where e, f, g, and h are fit parameters and T_0 (1673 K) a reference temperature. These various models have been tested by Nikolaev et al. (1996). In spite of their differences, they were found to give similar results, with typical deviations of 0.03–0.05 from the measured redox ratios. Less reliable predictions were observed for felsic melts of the andesite-rhyolite series. Eq. (18.10) remains the most commonly used for calculating the iron redox ratio of magmatic liquids.

As tested by Partzsch et al. (2004) with new measurements, the latest models of Kress and Carmichael (1991) and Nikolaev et al. (1996) generally reproduce the observed Fe^{3+}/Fe^{2+} ratios to within 0.05. Deviations of up to 0.1 are nonetheless observed, particularly for felsic compositions or strongly oxidizing conditions. The fact that composition effects are averaged out in complex systems ensures the interest of the predictions, but at the same time prevents them from being made outside the composition range on which they were calibrated. The paradox is that further progress will require better understanding of basic mechanisms to be achieved from the study of simple systems to which current models cannot be applied.

The Mössbauer study of an aluminosilicate melt by Jayasuriya et al. (2004) illustrates this point. A definite interaction was detected between Fe^{2+} and Fe^{3+} whose neglect is the reason why available models do not work well at low iron content. In a development of ln $(x_{FeO^{1.5}}/x_{FeO})$ of expression (18.7), Jayasuriya et al. (2004) thus included a regular solution interaction term derived from their results. In this very simple way, they showed how models could account for the dependence of the redox ratio on total iron content. This method was also employed by Borisov (2010).

Several experimental studies have focused on the effects of dissolved H_2O on the redox ratio of iron in magmatic liquids. Notably, no effect was reported for basalt and other depolymerized melts (Moore et al., 1995; Wilke et al., 2005; Botcharnikov et al., 2005). For more silicic composition, however, increasing H_2O concentration tends to result in increasing $Fe^{3+}/\Sigma Fe$ (Baker and Rutherford, 1996; Schuessler et al., 2008; Lesne et al., 2011); see also Fig. 18.15. In this respect, the effect on the redox ratio of iron resembles that of an increased alkali content in similar melts (Giuli et al., 2012). Increasing $Fe^{3+}/\Sigma Fe$ with increasing water concentration (and water activity) is consistent with the conclusions discussed in Chapters 11 and 15 that an increasing proportion of H_2O dissolved results in depolymerization, which is known to correlate positively with $Fe^{3+}/\Sigma Fe$.

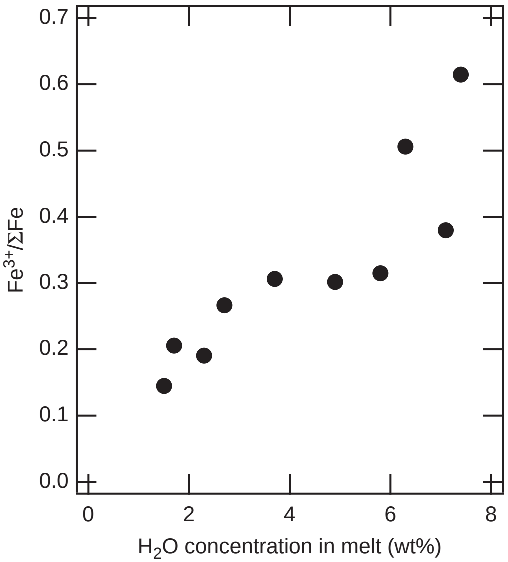

FIG. 18.15 Redox ratio of iron, $Fe^{3+}/\Sigma Fe$, as a function of H_2O concentration in rhyolite melt, equilibrated at 200 MPa and 143 ± 50°C at an oxygen fugacity equal to that of the NNO ($Ni + 0.5O_2 = NiO$) oxygen buffer (data from Baker and Rutherford, 1996).

18.3.1.4 Volatiles in Magmatic Liquids

In natural melts, the most important volatiles are H_2O, CO_2, and sulfur species. Even in the case of water, however, our understanding of its effects in natural melts often is incomplete and not quantitative. This most likely results from the fact that the complexity of its solution mechanisms has yet to be fully appreciated because of restricted compositional ranges of the melts investigated. From the existing experimental studies of water solubility in binary and ternary silicate and aluminosilicate melts, the major compositional variables (see Chapter 15, Sections 15.2 and 15.3).

WATER

Water solubility in simple and complex melts increases systematically with increasing pressure until the second critical endpoint is reached (Paillat et al., 1992). Silicate-rich fluids can no longer be distinguished from hydrous melts beyond this point, which varies from near 1 GPa and near 1000°C for a rhyolite felsic melt (Bureau and Keppler, 1999) to near 5 GPa and near 1400°C for a basalt composition (Kessel et al., 2005). Below these pressures water solubility in complex melts (as in simple melts) increases systematically with increasing pressure (Zhang, 1999; Lesne et al., 2011); see Fig. 18.16A. It has first a negative temperature dependence at low pressure before gradually shifting to a positive one at higher pressure (Holtz et al., 1995; Shishkina et al., 2014). The water solubility also depends on all the compositional variables reported in simple systems (see Chapters 14 and 15). This relationship is illustrated for a range of SiO_2 contents of complex natural melts, where it is clear that water solubiluty at given temperature and pressure does indeed increase with SiO_2 content

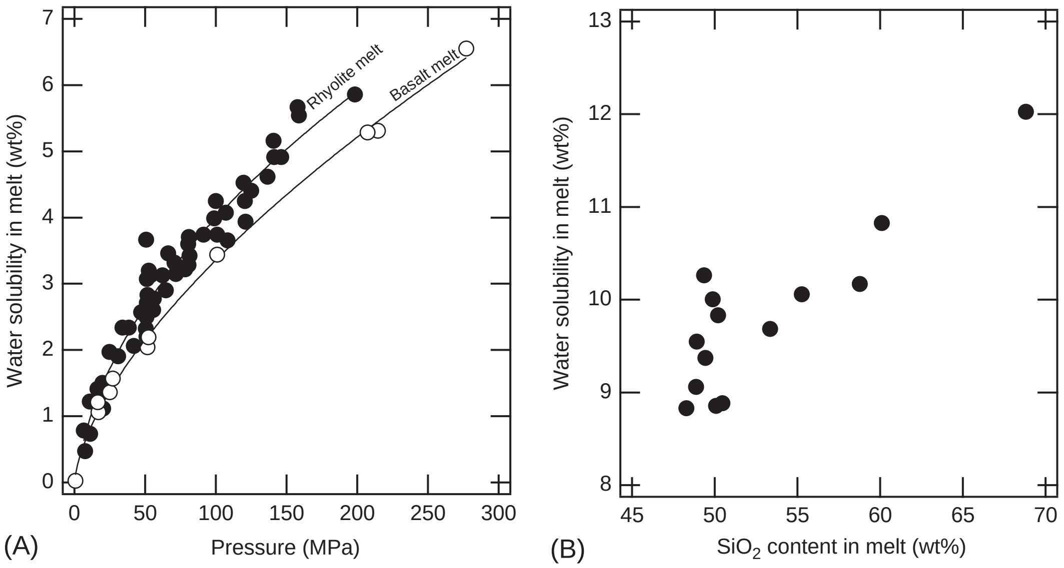

FIG. 18.16 Solubility of water in natural silicate melt compositions. (A) In rhyolite and basalt composition melts as a function of pressure at 850°C from data compilation by Zhang (1999). (B) Water solubility in natural melts as a function of their SiO_2 content at 500 MPa in the 1200–1250°C range (data compilation by Shishkina et al., 2014).

(Shishkina et al., 2014) (see also Fig. 18.16B). Furthermore, the nature of the network-modifying cations can have significant effects. In fact, even an increase of the Na/(Na+K) ratio results in increased water solubility in granitic melt compositions (Dingwell et al., 1997) (see Fig. 18.17A). This is further illustrated in Fig. 18.17B, where Dingwell et al. (1997) increased the alkali contents at the expense of SiO_2 for alkalis changing from Cs to

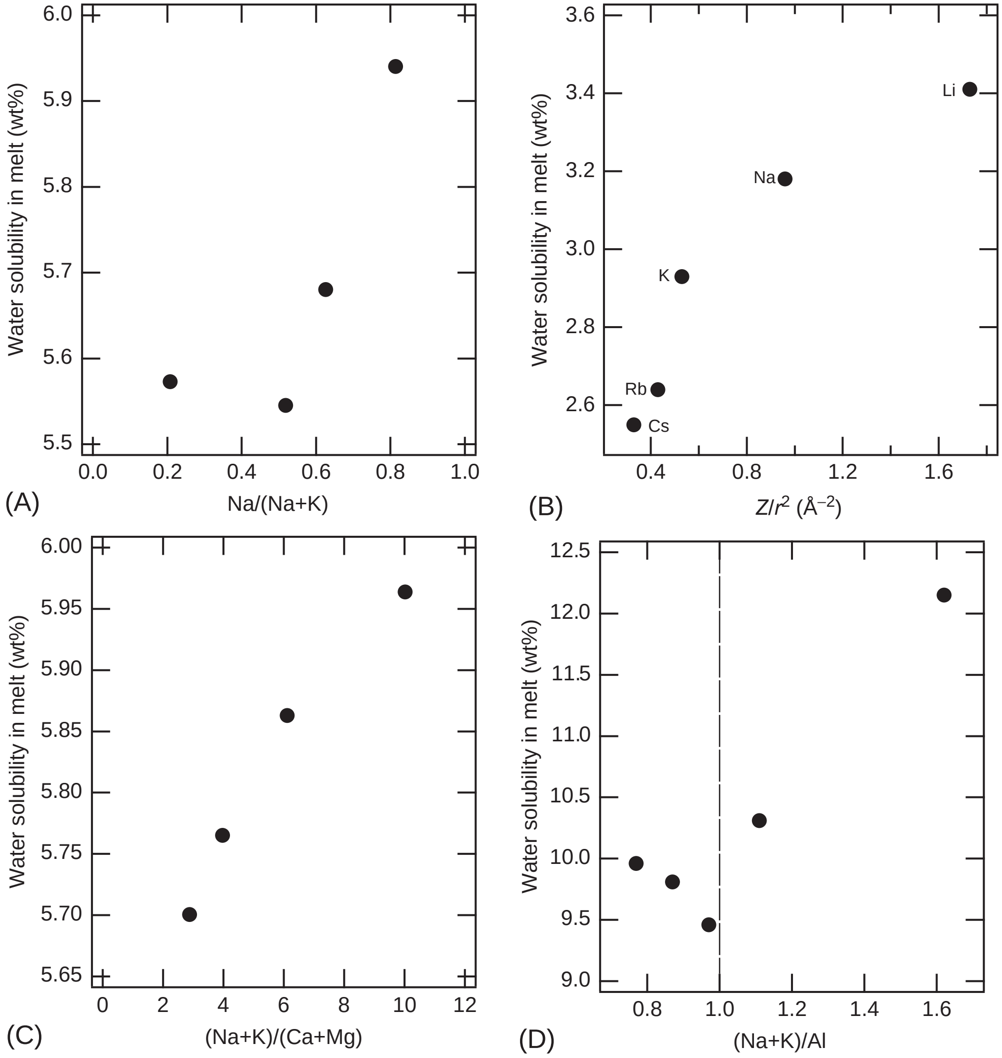

FIG. 18.17 Solubility of water in felsic melts as a function of compositional variables. (A) Solubility in phonolite composition melt as a function of Na/(Na+K) (data from Schmidt and Behrens, 2008). (B) Solubility of water in haplogranite composition as a function of alkali metal addition (data from Dingwell et al., 1997). (C) Solubility in phonolite composition melt as a function of alkali/alkaline earth abundance ratio (data from Schmidt and Behrens, 2008). (D) Solubility of water in haplogranite composition as a function of (Na+K)/Al. *Dashed lines* mark the meta-aluminosilicate composition (data from Dingwell et al., 1997).

Li in a haplogranite melt composition. There is a very clear positive correlation between water solubility and the ionization potential of the added alkali metal. However, when alkali metals are exchanged with alkaline earths (e.g., Ca + Mg for Na + K as seen in Fig. 18.17C), the water solubility, at least in a phonolite composition (essentially that of an alkali-rich and aluminous granite) actually decreases (Schmidt and Behrens, 2008) (see Fig. 18.17C). Finally, as noted by Dingwell et al. (1997), in felsic melt the water solubility increases with increasing peralkalinity and increasing peraluminosity from a minimum value near the meta-aluminosilicate melt (Fig. 18.17D). This trend is similar to that observed in simple ternary aluminosilicate melts (Mysen and Acton, 1999).

The speciation of dissolved water is a systematic function of melt and glass composition, temperature, pressure, and total water concentration (see Chapter 15, Section 15.2 and Eq. 15.1). In natural, complex magmatic glasses, equivalent relationships have been reported (Dixon et al., 1995; Ohlhorst et al., 2001; Mandeville et al., 2002; Lesne et al., 2011); see Fig. 18.13. The proportion of molecular H_2O in complex glasses increases with total water content, more rapidly than that of OH groups (Fig. 18.18). Again, this is the trend already seen in various binary and ternary systems (see Chapter 16, Fig. 16.3). Interestingly, for given total water concentration, the proportion of OH groups in rhyolite glass is considerably greater than that in the less polymerized basalt compositions (Fig. 18.18). This is also the same relationship as seen in compositionally simple systems (Le Losq et al., 2015). The proportion of OH groups in hydrous glass also increases as the glass becomes increasingly polymerized (Deubner et al., 2003); see also Chapter 15, Fig. 15.3B. These differences probably are minimum values, at least for hydrous basalt glass, because the OH/H_2O (molecular) ratio increases with temperature, is that quenched in at the glass transition temperature, and the glass transition temperature of hydrous basalt likely is greater than the glass transition temperature of hydrous rhyolite.

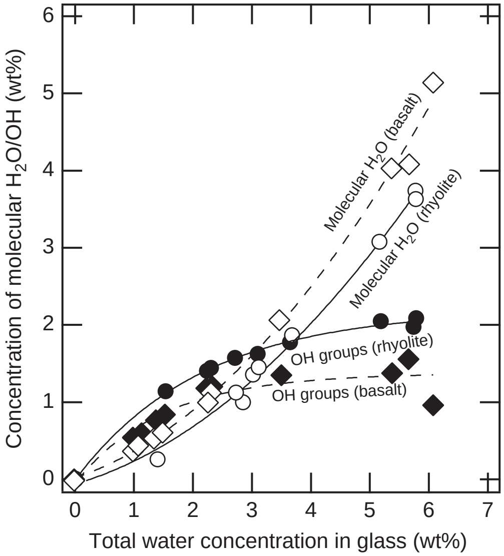

FIG. 18.18 Speciation of water dissolved in quenched melt (glass). (A) For rhyolite composition (data from Ohlhorst et al., 2001). (B) For basalt composition (data from Lesne et al., 2011).

A number of models have been proposed to compute water solubility in magmatic liquids (Spera, 1974; Burnham, 1975; Dixon and Stolper, 1995; Moore et al., 1998; Duan, 2014; Lesne et al., 2011) although most of these are limited to the ranges of conditions of their input data. With the exceptions of the models developed by Stolper and coworkers and by Burnham (1975) (which incorporated thermodynamic data for simple aluminosilicates), all these models are largely empirical and based on limited solubility data (see Zhang, 1999, for a review). Their broader applicability cannot be tested rigorously, so we will restrict ourselves to the approach developed by Silver and Stolper (1985, 1989) and Dixon and Stolper (1995).

The advantage of this model is its potential for rigorously characterizing water solubility, thanks to its structural foundation. It takes advantage of the fact that water dissolves partly as molecular H_2O and partly as OH groups,

$$H_2O(\text{melt}) \Leftrightarrow O(\text{melt}) + 2OH\,(\text{melt}), \tag{18.11}$$

where O(melt) denotes oxygen without distinguishing between bridging and nonbridging oxygens. By fitting spectroscopic data of the proportion of molecular H_2O and OH groups in silicate glasses, and combining those results with an evaluation of the equilibrium between water as molecular H_2O in melts and H_2O in coexisting fluid, Dixon and Stolper (1995) reproduced the water solubility in a range of chemically simple as well as more complicated natural basalt melts (Fig. 18.19).

This model requires experimentally determined concentrations of OH groups and molecular H_2O at high temperature and pressure, which were derived from glasses in the earliest applications (e.g., Silver et al., 1990). The OH/H_2O ratio depends, however, on temperature above the glass transition, but how these variations may affect the water solubility in magmatic liquids is not known (Chapter 15) (see also Dingwell and Webb, 1990; Nowak and Behrens, 1995, 2001; Shen and Keppler, 1995; Sowerby and Keppler, 1999). Moreover, the model assumes that the partial molar volume of H_2O in silicate glasses and melts is the same, which is not borne out by measurements and analyses, even though a range of values has

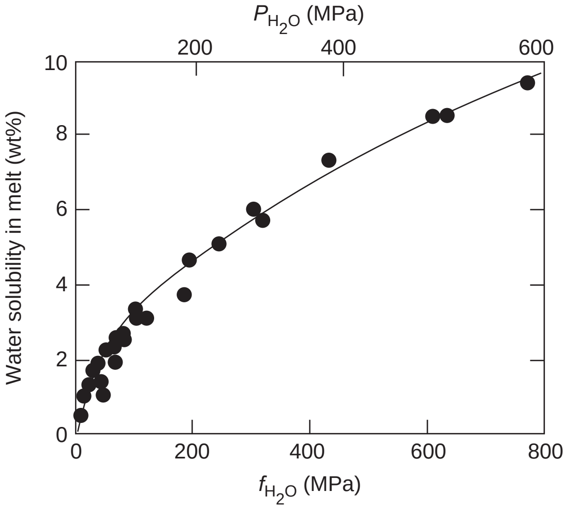

FIG. 18.19 Water solubility in silicate melts calculated by Dixon et al. (1995) *(line)* compared with experimental determination of solubility *(data points)*.

recently been reported (Silver et al., 1990; Ochs and Lange, 1997, 1999; Richet and Polian, 1998; Richet et al., 2000; Mysen, 2002; Le Losq et al., 2015; Bouhifd et al., 2015).

Even though the Stolper solution model has the potential to characterize the solubility of water in natural magmatic liquids, much additional experimental data are needed before it can be used with confidence for all melt compositions. It thus carries more promise than more recent empirical models (Moore et al., 1998; Liu et al., 2005; Lesne et al., 2011) or thermodynamically based models where numerous fitting parameters are needed, absent comprehensive thermodynamic data (Burnham, 1975; Duan, 2014; Ghiorso and Gualda, 2015). In this case, as for other difficult situations, first-principles calculations could represent the most powerful approach. Following the calculation of the SiO_2-H_2O phase diagram and of the associated water solubility (Ottonello et al., 2015), all available solubilities have been reproduced with a surprisingly good precision (Ottonello et al., 2018).

MIXED H_2O-CO_2

The fluid species in the COH system are CO_2 and H_2O under conditions more oxidized than those of the quartz-magnetite-fayalite oxygen buffer. In such systems, the water and carbon dioxide solubility in melts varies as a function of the CO_2/H_2O ratio. The solubility of CO_2 is only a fraction (<10%) of that of H_2O under equivalent conditions except for very silica-deficient and Ca-rich magmatic liquids, such as basanite (Jendrzejewski et al., 1997; Botcharnikov et al., 2005; Shishkina et al., 2014). Moreover, the CO_2 solubility at any temperature and pressure is quite sensitive to bulk composition (Brey and Ryabchikov, 1994) and decreases rapidly as a complex melt becomes increasingly polymerized (decreasing NBO/T) (Brooker et al., 2001; Guillot and Sator, 2011); see also Fig. 18.20. This solubility is a positive function of NBO/T in a similar manner as in chemically simpler systems (Chapter 16, Section 16.3.1). Of course, other variables such as the proportion and type of network-modifier likely are also important, but experimental data relevant to such questions do not appear to be available.

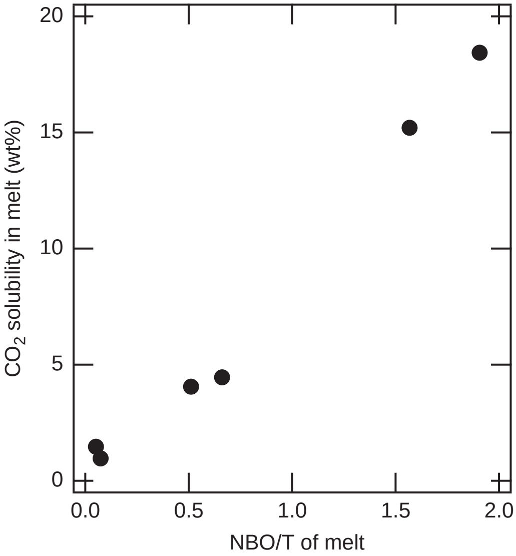

FIG. 18.20 Carbon dioxide solubility in natural magmatic liquids as a function of their NBO/T with Si^{4+}, Al^{3+}, and Fe^{3+} considered as tetrahedrally coordinated cations at 2GPa total pressure (data from Brooker et al., 2001).

The carbon speciation in complex glasses and melts can also be described with the simple equilibrium described for chemically simpler systems in Chapter 16, Eqs. (16.1a), (16.1b):

$$CO_2 + O^{2-} = CO_3{}^{2-}, \tag{18.12}$$

where O^{2-} is an expression of oxygen activity, CO_2 denotes molecular CO_2 and $CO_3{}^{2-}$ species linked to the silicate structure (Pearce, 1964; Brey and Ryabchikov, 1994; Pan et al., 1991). From the scarce temperature- and pressure-dependent variations of equilibrium (18.12), the speciation ratio, $CO_2(\text{molecular})/CO_3{}^{2-}$, appears to increase with both temperature and pressure (Nowak et al., 2003; Guillot and Sator, 2011).

The solubilities of both CO_2 and H_2O are systematic functions of the CO_2/H_2O ratio in melts equilibrated with mixed $CO_2 + H_2O$ fluid (Fig. 18.21; see also Tamic et al., 2001). Both volatile components do affect the silicate structure and in addition mixing of the two volatiles affects their respective activities (Fogel and Rutherford, 1990; Tamic et al., 2001; Behrens et al., 2004; Botcharnikov et al., 2006; Shishkina et al., 2010; Iacovino et al., 2013; Duncan and Dasgupta, 2014). Solution of H_2O results in depolymerization (Chapter 15, Section 15.3), which tends to enhance CO_2 solubility (Chapter 16, Section 16.3). On the other hand, decreasing the CO_2/H_2O ratio results in decreasing CO_2 activity, which leads to a lowered CO_2 solubility. These two contrasting mechanisms together result in a wide CO/HO range where the CO_2 solubility in hydrous melts is relatively insensitive to CO_2/H_2O. This feature is, however, dependent on total pressure (Botcharnikov et al., 2006).

These features in silicate-COH melt systems will, of course, vary with redox conditions because the carbon species in COH systems changes as the hydrogen fugacity is increased (Kadik et al., 2004, 2006; Mysen et al., 2011; Stanley et al., 2014). Reduced carbon is less soluble than CO_2 in silicate melts and likely will exhibit different relationships to mixing in the COH system. However, details of such information for natural complex magmatic systems are not available.

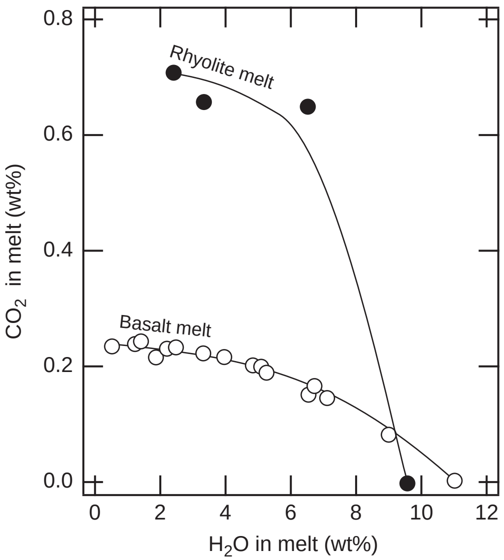

FIG. 18.21 Solubility of CO_2 and H_2O in silicate-CO_2-H_2O mixtures with rhyolite (data from Tamic et al., 2001) and basalt melt (Botcharnikov et al., 2005) at 500 MPa.

SULFUR

Sulfur solubility in magmatic liquids has been studied fairly extensively, in particular for mafic liquids, because such information has some bearing on economically viable sulfur deposits, as well as on the stability of sulfur species in hazardous waste environments (Katsura and Nagashima, 1974; Buchanan and Nolan, 1979; Wallace and Carmichael, 1992, 1994; Mavrogenes and O'Neill, 1999; Metrich and Mandeville, 2010; Backnaes and Deubener, 2011; Yang, 2012; Gorbachev and Bezmen, 2012). The solubility follows the same principles as determined for simpler systems (see Chapter 16, Section 16.4) although the extent of this effect from changing pressure, temperature, composition, f_{S_2} and f_{O_2} differs in simple and complex compositions.

The sulfur solubility is sensitive to sulfur speciation and silicate composition, whether under hydrous or anhydrous compositions. As in the case of chemically simple systems, the more mafic (less polymerized) a melt, the greater is the sulfur solubility (Fig. 18.22). Just as for simple systems (Chapter 16, Eq. 16.13), one can write an expression that relates SO_4^{2-} formation in the melt to the activity of oxygen, $a_{O^{2-}}$, or the proportion of nonbridging to bridging oxygen, as first proposed by Papadopoulos (1973). So the higher the oxygen activity (less silicate polymerization), the greater is the sulfur concentration at saturation. Analogous expressions may be written for sulfide (Chapter 16, Eq. 16.19), so that we may write an expression for coupled sulfur and oxygen fugacity relations (Fincham and Richardson, 1954), which applies equally well to natural melt compositions:

$$0.5S_2\,(\text{gas}) + O^{2-}\,(\text{melt}) = 0.5O_2\,(\text{gas}) + S^{2-}\,(\text{melt}). \tag{18.13}$$

This reaction also accounts for the link between sulfur solubility and fugacity of both sulfur and oxygen (see also Buchanan and Nolan, 1979; Backnaes and Deubener, 2011).

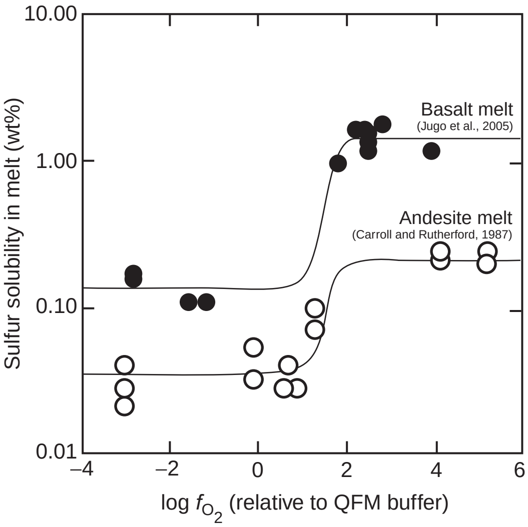

FIG. 18.22 Solubility of sulfur as a function of oxygen fugacity (relative to that of the quartz-magnetite-fayallite, QFM, buffer) for basaltic and andesitic melts (data from Jugo et al., 2005 and Carroll and Rutherford, 1985).

In many ways, one may simplify the solution equilibria for oxidized sulfur in magmatic liquid to that between a simple sulfur oxide, SO_2 or SO_3, and a sulfate, $SO_4{}^{2-}$ species (see also Eq. 16.16).

$$SO_x\,(\text{melt}) + O^{2-}\,(\text{melt}) \Leftrightarrow SO_{x+1}{}^{2-}\,(\text{melt}). \tag{18.14}$$

Given that in general oxidized sulfur exists as 6+ (Wilke et al., 2011), x is equal to 3 in Eq. (18.13).

The activity of oxygen, O^{2-} (melt), can be controlled by composition where the more depolymerized a melt, the greater the activity of O^{2-}. This can be accomplished, for example, by increased proportion of network-modifying cations such as alkalis and alkaline earths (Liu et al., 2007) (see also Fig. 18.23) or by increasing the amount of dissolved H_2O (Moune et al., 2009).

18.3.2 Physical Properties

Transport and volume properties are physical properties of complex magmatic liquid systems and their glasses (see, e.g., Bottinga et al., 1982; Richet et al., 2000; Giordano and Dingwell, 2003; Goto et al., 2005; Ni et al., 2011; Hack and Thompson, 2011; Di Genova et al., 2013; Bouhifd et al., 2015). A number of models of both volume and transport relationships have been proposed (Bottinga et al., 1982; Lange and Carmichael, 1987; Kress and Carmichael, 1991; Knoche et al., 1995; Hess and Dingwell, 1996; Hui and Zhang, 2007).

18.3.2.1 Volume Properties

Molar volume (density) information is critical for our understanding of magmatic processes in the earth, as density driven buoyancy differences govern energy and mass transport in the

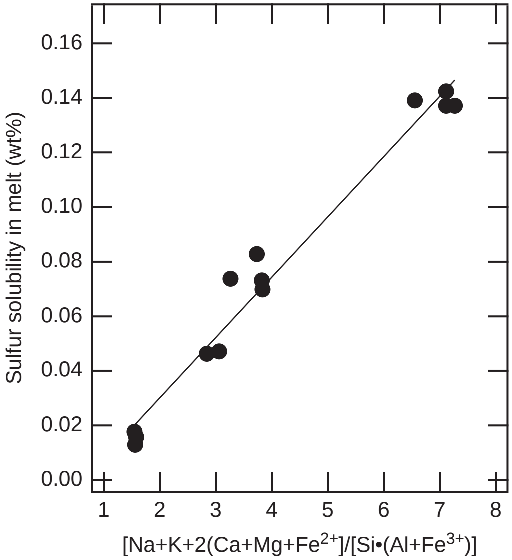

FIG. 18.23 Sulfur solubility in basalt, andesite, and rhyolite melt expressed as a function of composition expressed as indicated at 1250°C and 1 GPa and an oxygen of $10^{-8.98}$ bar (data from Liu et al., 2007).

earth's interior. Following the seminal work by Bottinga and Weill (1970), measurements for the most part have been carried out so as to extract partial molar volumes, thermal expansion, and compressibility of oxide components in the melts (see previous discussion) with a smaller subset of data focused on detailed studies of behavior of specific oxides or small groups of oxides (e.g., Dingwell and Brearley, 1988; Kress and Carmichael, 1991; Lange and Carmichael, 1987).

For melts containing all the major components in natural magmatic liquids, Bottinga and Weill (1970) concluded that the molar volume, V, of a melt (with the exception of Ti-bearing melts) can be described with an additive expression:

$$V = \sum_{i=1}^{i} X_i \cdot \overline{V}_i, \tag{18.15}$$

where X_i is mol fraction and $\overline{V}_i$ is partial molar volume of oxide, i. In this treatment, the partial molar volumes of the individual components are considered independent of melt composition. Thermal expansion and compressibility were considered constant and are therefore independent of composition, temperature, and pressure.

The experimental input data to an equation such as Eq. (18.15) are in general agreement (Bottinga et al., 1983; Lange and Carmichael, 1987; Knoche et al., 1995). However, there may be some variation in the partial molar volume of Al_2O_3 (as well as thermal expansion and compressibility) because of the different structural forms (including different charge-balance, triclusters, etc.—see Chapter 8, Section 8.4.2) (see also Lange and Carmichael, 1987; Bottinga et al., 1982, 1983). There are also issues with temperature-dependent volumes such as for TiO_2, which can undergo coordination changes as a function of temperature (and TiO_2 concentration) (see Chapter 12, Section 12.5.2). For example, whereas the Lange and Carmichael (1987) data were obtained with chemically complex melts resembling natural compositions, Bottinga et al. (1982, 1983) used data from simple binary and ternary melt systems to develop a database and algorithms that could be used to calculate molar volume and thermal expansion of natural silicate melts. The latter treatment has the advantage in that effects of individual oxides, and in particular those that require charge-compensation when in tetrahedral coordination (Al^{3+}, Fe^{3+}, and P^{5+}), could be more clearly identified.

At constant temperature, the molar volume in this treatment is:

$$V = \sum_{i=1}^{i} X_i \cdot \overline{V}_i + X_K \left(V^c + X_K \frac{\sum_j X_j \cdot K_j}{\sum_j X_j} \right), \tag{18.16}$$

where V^c is a constant, j represents components Al_2O_3 as well as possible charge-compensating cations Na_2O, K_2O, MgO, CaO, and FeO, X_K is the mol fraction of an oxide requiring charge-compensation, and K_j are constants associated with components j. This treatment does, therefore, take into account effects of bulk composition and, in particular, the role of Al_2O_3. There is also an exponential term needed to account for thermal expansion, but this will not be discussed here.

The molar volume of natural magmatic liquids shows distinct distribution within tholeiite, andesite, phonolite, and rhyolite melts where the volume maxima increases the more felsic is the melt (Fig. 18.24A). The average molar volumes for each group of melt follow the same

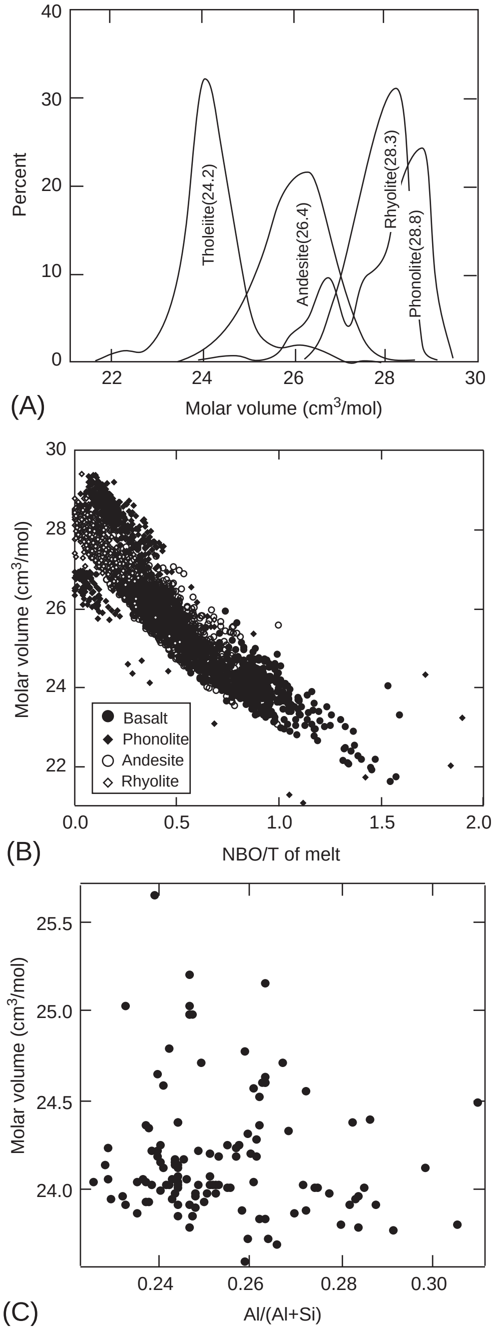

FIG. 18.24 Calculated molar volume and molar volume distribution of magmatic liquids at ambient pressure. Molar volume calculated as described in the text (analyses from http://Earthchem.org). (A). Distribution of molar volumes of melts of major rock groups as indicated. Numbers in parentheses are the volumes corresponding to the maximum of the individual distribution curves. (B) Molar volume of natural melts indicated as a function of their NBO/T. (C) Molar volume of natural melts as a function of Al/(Al+Si) with NBO/T = 0.80 ± 0.05.

trend (24.2 ± 0.8, 25.9 ± 0.8, 27.9 ± 1.1, and $27.9 \pm 0.5\,cm^3/mol$ for tholeiite, andesite, phonolite, and rhyolite melts, respectively). Expressed in terms of molar volume as a function of NBO/T of the melts, it decreases systematically with decreasing degree of melt polymerization (Fig. 18.24B), a trend resembling those observed in binary metal oxide melt systems (Chapter 6, Section 6.4.1). This evolution is due to the fact that partial molar volume of nonbridging oxygens is lower than that of bridging oxygens (Bottinga and Richet, 1995).

The volume relationship of natural magmatic liquids does show a spread of about $1\,cm^3/mol$ for any NBO/T value (Fig. 18.25). So even though the main control on volume likely is the proportion of nonbridging oxygens, other factors such as alumina content and the type of charge-compensation of tetrahedrally coordinated Al^{3+} also contribute. However, a simple relationship between volume and Al/(Al+Si) ratio alone does not show much of a correlation even at constant bulk melt NBO/T, because the nature of the charge balancing has important influence on the partial molar volume of Al_2O_3 in melts, a feature seen clearly in volume relationships of ternary aluminosilicate melts (Fig. 18.24C; see also Chapter 8, Fig. 8.27). An additional refinement relates to the observation that most, and perhaps all, of Al^{3+} resides in Q^4-species in natural melts (see also Chapter 9, Section 9.4.2, for detailed discussion of Al^{3+} distribution among structural units in aluminosilicate melts). Finally, the proportion of nonbridging oxygen in each of the Q^n-species of the melt differs. As the partial molar volume of each of the Q^n-species must be different, any variation in Q^n-species abundance driven by different network-modifying cations (i.e., mixed alkali effects) or Al^{3+} charge-balance will cause the molar volume to change.

Pressure affects molar volume because of compression of intertetrahedral angles, even without coordination transformation of tetrahedrally coordinated cations. Intertetrahedral angle compression necessarily is the most pronounced in the three-dimensionally interconnected Q^4 network structures. Furthermore, intertetrahedral angles are more compressible with charge-balance by alkali metals as contrasted with alkaline earths, as seen

FIG. 18.25 Calculated density evolution with pressure of basalt and peridotite melt. *Redrawn from Ghiorso and Kress (2004).*

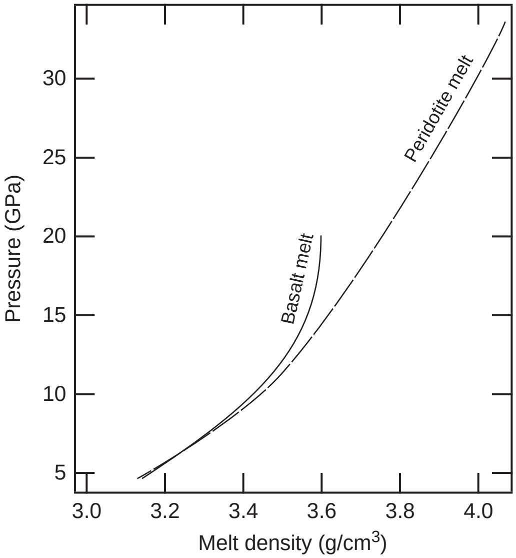

in the different compressibilities of aluminosilicate melts along the $NaAlO_2$-SiO_2 and $CaAl_2O_4$ joins (Chapter 9, Section 9.4.2). These differences imply that felsic magmatic liquids such as andesitic and rhyolitic compositions are more compressible than more depolymerized and mafic basalt or peridotite magmas.

Thermal expansion is affected in an analogous manner. Felsic (SiO_2 rich and lower NBO/T values) magmatic liquid shows greater thermal expansion than basalt and peridotite compositions. Furthermore, basalt melt is more compressible than peridotite melt (Fig. 18.25) because of its considerably higher polymerization, with NBO/T values in the 0.8–1.0 range, as compared with >2.

Solution of water in silicate melts and glasses has profound influence on the density of the material (Ochs and Lange, 1999; Richet et al., 2000). Provided that the partial molar volume of H_2O in solution in magmatic liquids can be determined accurately, the molar volume, and therefore density, can be calculated accurately with equations such as Eqs. (18.15), (18.16).

Perhaps somewhat surprisingly, the partial molar volume of H_2O dissolved in such melts, and most certainly in glasses, commonly has been concluded to be independent of melt composition and water concentration with a value near $12\,\text{cm}^3/\text{mol}$ (Richet and Polian, 1998; Ochs and Lange, 1997; Bouhifd et al., 2001). However, composition-independent partial molar volume appears somewhat unlikely, because the water solubility is indeed composition dependent and solubility and partial molar volume are related.

Transport Properties

Rheological data are needed to assess how the structure of natural silicate melts governs their viscosity. One could accomplish this goal by measuring the viscosity of all possible types of magmatic liquids, or models may be developed with which melt and glass viscosity could be calculated. An early and successful approach to this problem was the model by Bottinga and Weill (1972). More recently, often empirical models follow many of the original principles, but rather than using assumed structural components for which a viscosity contribution was derived (Bottinga and Weill, 1972), simple combinations of oxide components commonly have been used (Baker, 1996; Hess and Dingwell, 1996; Giordano and Dingwell, 2003; Hui and Zhang, 2007). In a more advanced form with temperature and fragility as additional parameters, Giordano et al. (2008) presented a comprehensive empirical model, which can also incorporate effects of water on melt viscosity.

In the early viscosity model of Bottinga and Weill (1972), it was assumed that the viscosity of a silicate melt can be expressed as an additive function of the mol fractions of their oxide components, X_i, within narrow ranges of their concentration (10 mol%):

$$\eta = \sum_{i=1}^{i} X_i \cdot D_i, \tag{18.17}$$

except in the case of Al^{3+} where aluminate components were used and an equivalent fraction of charge-balancing cations was subtracted from the appropriate oxide. The D_i is a regression coefficient obtained by fitting viscosity melt data from a variety of chemically simple systems.

A fundamental question about the Bottinga and Weill (1972) model, and for that matter analogous models, is whether melt viscosity is additive. In other words, are the D_i coefficients independent of melt composition? In light of more recent work on melt viscosity (see, e.g., Toplis, 1998), constant D_i values are not likely to be accurate. This is in part, at least, because the structural roles of metal cations, and for that matter components such as Al^{3+} and Fe^{3+}, likely can serve in multiple structural roles where their exact behavior varies with bulk composition, temperature, and pressure.

A fairly comprehensive viscosity model (in terms of the size of the experimental database for model calibration) is that of Giordano and Dingwell (2003, 2004) with subsequent refinements in 2008 (Giordano et al., 2008). The input data are experimental measurements for natural compositions, which carry the potential of canceling composition effects, as is, of course, also true for other similar models. Moroever, this model does not have a structural basis either, so it should be used with care. We will nevertheless use calculated viscosities of natural melts with this model, to develop a sense of how the viscosity of magmatic liquids varies.

In the Giordano and Dingwell (2003, 2004) model, viscosity is related to a number of fitting parameters, c_2, c_2, and c_3, together with a composition variable, SM:

$$\log \eta = c_1 + [c_2 c_3/(c_3 + SM)], \tag{18.18}$$

where c_1, c_2, and c_3 are the parameters derived by least-squares fitting. The SM is the molar oxide sum, $Na_2O + K_2O + CaO + MgO + MnO + FeO_{total}/2$. The fact that SM does not contain contributions from either of the major components forming the aluminosilicate tetrahedral framework of the melt structure, SiO_2 and Al_2O_3, is cause for concern, because the concentration of these two oxides are important factors in melt viscosity (Chapters 6 and 8). Most likely, their influence is hidden in the complex nature of the c_{1-3} parameters.

Viscosity in the 1200–1600°C range was calculated with the Giordano and Dingwell (2003, 2004) model to derive a high-temperature activation enthalpy of viscous flow, ΔH_η, with the assumption of an Arrhenian viscosity. This assumption is generally correct for anhydrous magmatic liquids at ambient pressure above the liquidus (Bottinga and Weill, 1972; Giordano et al., 2008). However, when both low- and high-temperature viscosity is taken into account, there are significant deviations from linearity (increasing melt fragility), which tend to become more important the more depolymerized and mafic the magmatic liquid (Richet, 1984; Giordano et al., 2008); see Fig. 18.26. The latter evolution is understandable because in more mafic melts there is increased alkaline earth/alkali abundance ratio and also a broader range of Q^n-species.

FIG. 18.26 Viscosity of rhyolite and basanite melts at ambient pressure as a function of temperature (data from Giordano et al., 2008).

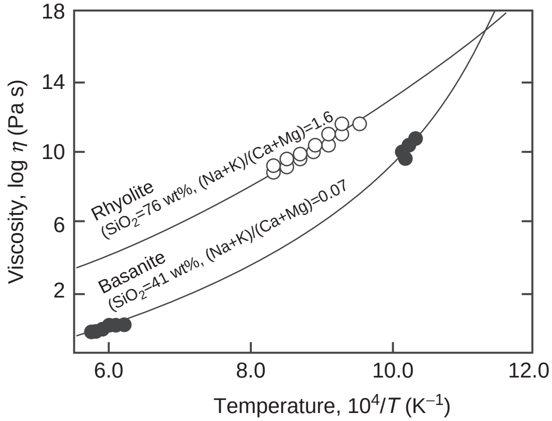

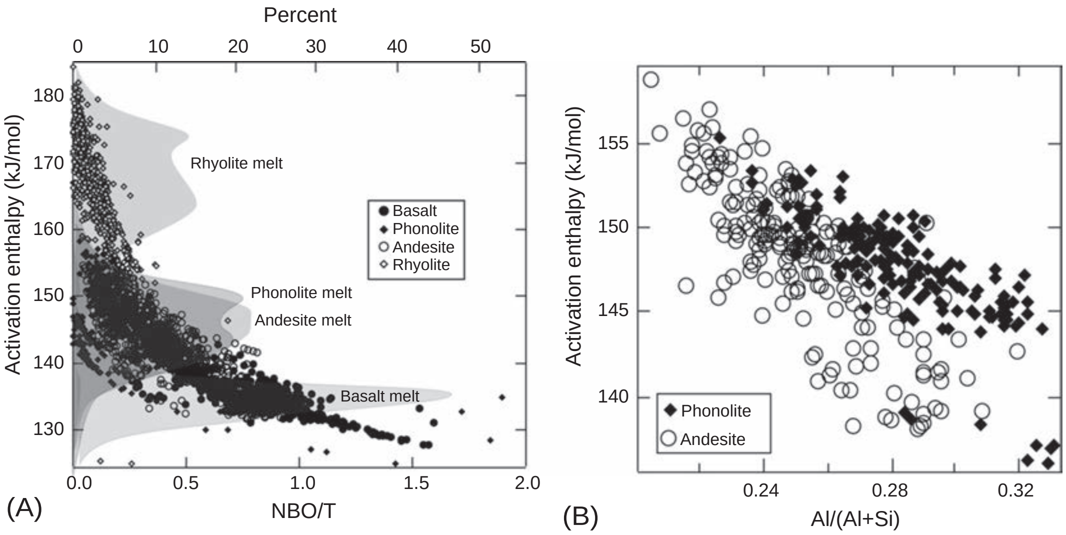

FIG. 18.27 (A) High-temperature (1200–1600°C) activation enthalpy of viscous flow of natural melts indicated as a function of their NBO/T superimposed on which is the distribution of high-temperature (1200 – 1600°C) activation enthalpy of viscous flow of the major melts of major rock groups as indicated. (B) High-temperature (1200 – 1600°C) activation enthalpy of viscous flow of phonolite and andesite melt as a function of their Al/(Al+Si) at NBO/T = 0.20 ± 0.05. Activation enthalpies were calculated with the model of Giordano and Dingwell (2003, 2004) (analyses from http://Earthchem.org).

The activation enthalpies of high-temperature viscous flow for tholeiite, andesite, phonolite, and rhyolite melts from the high-temperature viscosity calculation are shown in Fig. 18.27. The maxima in the enthalpy distribution of individual groups cover about 50 kJ/mol with, broadly speaking, an increase in both the maximum values and in the average activation enthalpies as the melts become more felsic (average $\Delta H_\eta = 135 \pm 3$, 142 ± 5, 146 ± 5, and 167 ± 7 kJ/mol, for tholeiite, andesite, phonolite, and rhyolite melts, respectively).

The calculated activation enthalpy of viscous flow of these natural melts decreases as an exponential function of NBO/T, with the most rapid decrease in the NBO/T range between about 0 and about 0.3 and a much slower decrease as the NBO/T increases further (Fig. 18.27). This trend is similar to that of high-temperature activation enthalpy of viscous flow of melts along binary metal oxide-silica joins where ΔH_η is nearly independent of metal/silicon ratios above 0.3–0.5, depending somewhat on the nature of the metal cation (Bockris et al., 1955, 1956).

There is considerable scatter in the ΔH_η trend, in particular for intermediate melt compositions such as those of andesite and phonolite (Fig. 18.27). This scatter in part results from the significant proportions of Al^{3+} found in natural melts. Alumina causes distinct reductions in ΔH_η (Riebling, 1964, 1966; Toplis et al., 1997). In particular, the activation enthalpy of viscous flow of phonolite melt has a maximum value of about 20 kJ/mol, which is lower than that of rhyolite melt, even though the NBO/T distribution in the two groups is nearly the same (Fig. 18.1). This conclusion is consistent with observations from simple aluminosilicate systems where there is a negative correlation between Al/(Al+Si) and the high-temperature activation enthalpy (Riebling, 1966; Toplis et al., 1997; Webb et al., 2007). Interestingly, the activation enthalpy is more sensitive to Al/(Al+Si) for andesite than for phonolite melts, probably because a larger fraction of tetrahedrally coordinated Al^{3+} is charge-balanced by alkalis in phonolite than in andesite melt (Fig. 18.3). We also note that at nearly constant Al/(Al+Si) the scatter in the ΔH_η versus NBO/T is considerably reduced. The remaining scatter in Fig. 18.27B is probably related to the fact that, even in binary metal oxide systems, the high-temperature activation enthalpy of viscous flow also depends somewhat on the type of network-modifying cations (Bockris et al., 1955, 1956). In natural melts, there are several different network-modifying cations (for the most part Ca, Mg, and Fe^{2+}).

VISCOSITY, PRESSURE, AND TEMPERATURE

The extent to which temperature-dependent viscosity of volatile-free magmatic liquids deviates from Arrhenian variations at ambient pressure seems governed by composition variables similar to those observed for simpler systems (Chapters 6 and 8, Sections 6.4.2 and 8.4.2, respectively). This means that in the context of the configurational entropy model of viscosity (Richet, 1984), for example, as structural contributions to the entropy of mixing increases, the greater is the deviation from Arrhenian viscosity. One can accomplish such changes by exchanging alkaline earths for alkalis, changing from alkali to alkaline earth charge-balance of tetrahedral Al^{3+}, and decreasing the SiO_2 concentration of melts. Such structural and compositional evolutions are those that occur when considering viscosity changes from a felsic rhyolite to a mafic melt (Fig. 18.26).

The effect of pressure on silicate melt viscosity is quite dependent on silicate composition and, in particular, on the degree of melt polymerization, NBO/T (Scarfe et al., 1987). In general, whether for simple system or complex melts, the viscosity increases with pressure for depolymerized melts such as, for example, basalt (Persikov et al., 2015). On the other hand, for more felsic melts such as dacite, andesite, and rhyolite composition, the viscosity increases upon application of a few gigapascals of pressure (Liebske et al., 2003; Ardia et al., 2008; Hui et al., 2009).

VISCOSITY AND WATER

Solution of water in silicate melts results in rapid decrease of melt viscosity (see, e.g., Chapter 14, Section 14.4.2). Such effects increase with decreasing temperature and with increasing degree of melt polymerization. Deviations from Arrhenian viscosity (increasing melt fragility) are positively correlated with H_2O content because of an increase of the entropy of mixing in hydrous as compared with anhydrous melt (Mysen, 1995). Increased water concentration also results in decreasing glass transition temperature and an increase in the configurational heat-capacity change across the glass transition temperature (Bouhifd et al., 2006; Di Genova et al., 2014).

References

Allen, J.C., Boettcher, A.L., Marland, G., 1975. Amphiboles in andesites and basalt. I. Stability as a function of P-T-f_{O2}. Am. Mineral. 60, 1069–1085.

Ardia, P., Giordano, D., Schmidt, M.W., 2008. A model for the viscosity of rhyolite as a function of H_2O-content and pressure: a calibration based on centrifuge piston cylinder experiments. Geochim. Cosmochim. Acta 72, 6103–6123.

Backnaes, L., Deubener, J., 2011. Experimental studies on sulfur solubility in silicate melts at near-atmospheric pressure. Rev. Mineral. Geochem. 73, 143–165.

Baker, D.R., 1996. Granitic melt viscosities: empirical and configurational entropy models for their calculation. Am. Mineral. 81, 126–134.

Baker, L.L., Rutherford, M.J., 1996. The effect of dissolved water on the oxidation state of silicic melts. Geochim. Cosmochim. Acta 60, 2179–2187.

Behrens, H., Ohlhorst, S., Holtz, F., Champenois, M., 2004. CO_2 solubility in dacitic melts equilibrated with H_2O-CO_2 fluids: Implications for modeling the solubility of CO2 in silicic melts. Geochim. Cosmochim. Acta 68, 4687–4703.

Bockris, J.O.'.M., Mackenzie, J.O., Kitchner, J.A., 1955. Viscous flow in silica and binary liquid silicates. Trans. Faraday Soc. 51, 1734–1748.

Bockris, J.O.M., Tomlinson, J.W., White, J.L., 1956. The structure of the liquid silicates. Partial molar volumes and expansivities. Trans. Faraday Soc. 52, 299–310.

Boettcher, A.L., Guo, Q., Bohlen, S., Hanson, B., 1984. Melting of feldspar-bearing systems to high pressures and the structures of aluminosilicate liquids. Geology 12, 202–204.

Borisov, A.A., 2010. Ferric-ferrous ratio in liquid iron oxides: analysis and applications to natural basaltic melts. Petrology 18, 471–481.

Borisov, A., Behrens, H., Holtz, F., 2013. The effect of titanium and phosphorus on ferric/ferrous ratio in silicate melts: an experimental study. Contrib. Mineral. Petrol. 166, 1577–1591.

Botcharnikov, R.E., Koepke, J., Holtz, F., McCammon, C., Wilke, M., 2005. The effect of water activity on the oxidation and structural state of Fe in a ferro-basaltic melt. Geochim. Cosmochim. Acta 69, 5071–5085.

Botcharnikov, R.E., Behrens, H., Holtz, F., 2006. Solubility and speciation of C-O-H fluids in andesitic melt at $T = 1100$-1300 degrees C and $P = 200$ and 500 MPa. Chem. Geol. 229, 125–143.

Bottinga, Y., Richet, P., 1995. Silicate melts: the "anomalous" pressure dependence of the viscosity. Geochim. Cosmochim. Acta 59, 2725–2732.

Bottinga, Y., Weill, D.F., 1970. Densities of liquid silicate systems calculated from partial molar volumes of oxide components. Am. J. Sci. 269, 169–182.

Bottinga, Y., Weill, D.F., 1972. The viscosity of magmatic silicate liquids: a model for calculation. Am. J. Sci. 272, 438–475.

Bottinga, Y., Weill, D., Richet, P., 1982. Density calculations for silicate liquids. I. Revised method for aluminosilicate compositions. Geochim. Cosmochim. Acta 46, 909–919.

Bottinga, Y., Richet, P., Weill, D.F., 1983. Calculation of the density and thermal expansion coefficient of silicate liquids. Bull. Mineral. 106, 129–138.

Bouhifd, M.A., Whittington, A., Richet, P., 2001. Partial molar volume of water in phonolitic glasses and liquids. Contrib. Mineral. Petrol. 142, 235–243.

Bouhifd, M.A., Whittington, A., Roux, J., Richet, P., 2006. Effect of water on the heat capacity of polymerized aluminosilicate glasses and melts. Geochim. Cosmochim. Acta 70, 711–722.

Bouhifd, M.A., Whittington, A.G., Richet, P., 2015. Densities and volumes of hydrous silicate melts: new measurements and predictions. Chem. Geol. 418, 40–50.

Brey, G.P., Ryabchikov, I.D., 1994. Carbon dioxide in strongly silica undersaturated melts and origin of kimberlite magmas. Neues Jb. Miner. Monat. 449–463.

Brooker, R.A., Kohn, S.C., Holloway, J.R., McMillan, P.F., 2001. Structural controls on the solubility of CO_2 in silicate melts. Part I: bulk solubility data. Chem. Geol. 174, 225–239.

Buchanan, D.L., Nolan, J., 1979. Solubility of sulfur and sulfide immiscibility in synthetic tholeiite melts and their relevance to Bushveld complex rocks. Can. Mineral. 17, 483–494.

Bureau, H., Keppler, H., 1999. Complete miscibility between silicate melts and hydrous fluids in the upper mantle; experimental evidence and geochemical implications. Earth Planet. Sci. Lett. 165, 187–196.

Burnham, C.W., 1975. Water and magmas; a mixing model. Geochim. Cosmochim. Acta 39, 1077–1084.

Burnham, C.W., Nekvasil, H., 1986. Equilibrium properties of granite pegmatite magmas. Am. Mineral. 71, 239–263.

Carmichael, I.S.E., Ghiorso, M.S., 1990. Controls on oxidation-reduction relations in magmas. In: Nicholls, J., Russell, J.K. (Eds.), Modern Methods of Igneous Petrology: Understanding Magmatic Processes. The Mineralogical Society of America, Washington, DC, pp. 191–212.

Carroll, M.R., Rutherford, M.J., 1985. Sulfide and sulfate saturation in hydrous silicate melts. J. Geophys. Res. 90, C601–C612.

Cochain, B., Neuville, D.R., Henderson, G.S., McCammon, C.A., Pinet, O., Richet, P., 2012. Effects of the iron content and redox state on the structure of sodium borosilicate: a Raman, Mossbauer and boron K-Edge XANES spectroscopy study. J. Am. Ceram. Soc. 95, 962–971.

Cody, G.D., Mysen, B.O., Lee, S.K., 2005. Structure vs. composition: a solid state ^{1}H and ^{29}Si NMR study of quenched glasses along the Na_2O-SiO_2-H_2O join. Geochim. Cosmochim. Acta 69, 2373–2384.

Cohen, H., Keisuke, I., Kennedy, G.C., 1967. Melting and phase relations in an anhydrous basalt to 40 kilobars. Am. J. Sci. 265, 475–518.

Colson, R.O., McKay, B.A., Taylor, L.A., 1988. Temperature and composition dependencies of trace element partitioning: olivine/melt and low-Ca pyroxene/melt. Geochim. Cosmochim. Acta 52, 539–553.

Cormier, L., Ghaleb, D., Neuville, D.R., Delaye, J.M., Calas, G., 2003. Chemical dependence of network topology of calcium aluminosilicate glasses: a computer simulation study. J. Non-Cryst. Solids 332, 255–270.

Cottrell, E., Kelley, K.A., 2011. The oxidation state of Fe in MORB glasses and the oxygen fugacity of the upper mantle. Earth Planet. Sci. Lett. 305, 1–13.

Day, D.E., 1976. Mixed alkali glasses – their properties and uses. J. Non-Cryst. Solids 21, 343–372.

Deubner, J., Müller, R., Behrens, H., Heide, G., 2003. Water and the glass transition temperature of silicate melts. J. Non-Cryst. Solids 330, 268–273.

Di Genova, D., Romano, C., Hess, K.U., Vona, A., Poe, B.T., Giordano, D., Dingwell, D.B., Behrens, H., 2013. The rheology of peralkaline rhyolites from Pantelleria Island. J. Vocanol. Geoth. Res. 249, 201–216.

Di Genova, D., Romano, C., Giordano, D., Alletti, M., 2014. Heat capacity, configurational heat capacity and fragility of hydrous magmas. Geochim. Cosmochim. Acta 142, 314–333.

Dingwell, D.A., Brearley, M., 1988. Melt densities in the CaO-FeO-Fe_2O_3-SiO_2 system and the compositional dependence of the partial molar volume of ferric iron in silicate melts. Geochim. Cosmochim. Acta 52, 2815–2825.

Dingwell, D.B., Webb, S.L., 1990. Relaxation in silicate melts. Eur. J. Mineral. 2, 427–449.

Dingwell, D.B., Holtz, F., Behrens, H., 1997. The solubility of H_2O in peralkaline and peraluminous granitic melts. Am. Mineral. 82, 434–437.

Dixon, J.E., Stolper, E.M., 1995. An experimental study of water and carbon dioxide solubilities in mid-ocean ridge basaltic liquids; part II, applications to degassing. J. Petrol. 36, 1633–1646.

Dixon, J.E., Stolper, E.M., Holloway, J.R., 1995. An experimental study of water and carbon dioxide solubilities in mid-ocean ridge basaltic liquids. Part 1. Calibration and solubility models. J. Petrol. 36, 1607–1631.

Duan, X., 2014. A general model for predicting the solubility behavior of H_2O-CO_2 fluids in silicate melts over a wide range of pressure, temperature and compositions. Geochim. Cosmochim. Acta 125, 582–609.

Duncan, M.S., Dasgupta, R., 2014. CO_2 solubility and speciation in rhyolitic sediment partial melts at 1.5–3.0 GPa – implications for carbon flux in subduction zones. Geochim. Cosmochim. Acta 124, 328–347.

Eggler, D.H., 1972. Water saturated and undersaturated melting relations of a Paricutin andesite and an estimate of water content in natural magma. Contrib. Mineral. Petrol. 34, 261–271.

Ellison, A.J., Hess, P.C., 1986. Solution behavior of +4 cations in high silica melts: petrologic and geochemical implications. Contrib. Mineral. Petrol. 94, 343–351.

Fei, Y., Bertka, C.M., Mysen, B.O., 1999. Mantle Petrology: Field Observations and High Pressure Experimentation: A Tribute to Francis R. (Joe) Boyd. Geochemical Society, Houston, TX.

Fincham, C.J.B., Richardson, F.D., 1954. The behavior of sulphur in silicate and aluminate melts. Proc. R. Soc. London A223, 40–62.

Fogel, R.A., Rutherford, M.J., 1990. The solubility of carbon dioxide in rhyolitic melts: a quantitative FTIR study. Am. Mineral. 75, 1311–1326.

Frantz, J.D., Mysen, B.O., 1995. Raman spectra and structure of BaO-SiO_2, SrO-SiO_2, and CaO-SiO_2 melts to 1600°C. Chem. Geol. 121, 155–176.

Fudali, F., 1965. Oxygen fugacity of basaltic and andesitic magmas. Geochim. Cosmochim. Acta 29, 1063–1075.

Fujii, T., Kushiro, I., 1977. Melting relations and viscosity of an abyssal tholeiite. In: Carnegie Instn. Washington Year Book.vol. 76. pp. 461–465.

Gaillard, F., Scaillet, B., Pichavant, M., Beny, J.M., 2001. The effect of water and f_{O2} on the ferric-ferrous ratio of silicic melts. Chem. Geol. 174, 255–273.

Ghiorso, M.S., Gualda, G.A.R., 2015. An H_2O–CO_2 mixed fluid saturation model compatible with rhyolite-MELTS. Contrib. Mineral. Petrol. 169, 53. https://dx.doi.org/10.1007/s00410-015-1141-8.

Ghiorso, M.S., Kress, V.C., 2004. An equation of state for silicate melt. II. Calibration of volumetric properties at 10^5 Pa. Am. J. Sci. 304, 679–751.

Ghiorso, M.S., Sack, R.O., 1995. Chemical mass transfer in magmatic processes: IV. A revised and internally consistent thermodynamic model for the interpolation and extrapolation of liquid-solid equilibria in magmatic systems at elevated temperatures and pressures. Contrib. Mineral. Petrol. 119, 197–212.

Gibbon, D.L., Wyllie, P.J., 1969. Experimental studies of igneous rock series: the Farrington Complex, North Carolina and Star Mountain rhyolite, Texas. J. Geol. 77, 221–240.

Giordano, D., Dingwell, D.B., 2003. Non-Arrhenian multicomponent melt viscosity: a model. Earth Planet. Sci. Lett. 208, 337–349.

Giordano, D., Dingwell, D.B., 2004. Erratum to "Non Arrhenian multicomponent melt viscosity: a model" [Earth Planet. Sci. Lett. 208 (2003) 337–349]. Earth Planet. Sci. Lett. 221, 449.

Giordano, D., Potuzak, M., Romano, C., Dingwell, D.B., Nowak, M., 2008. Viscosity and glass transition temperature of hydrous melts in the system $CaAl_2Si_2O_8$–$CaMgSi_2O_6$. Chem. Geol. 256, 203–215.

Giuli, G., Alonso-Mori, R., Cicconi, M.R., Paris, E., Glatzel, P., Eeckhout, S.G., Scaillet, B., 2012. Effect of alkalis on the Fe oxidation state and local environment in peralkaline rhyolitic glasses. Am. Mineral. 97, 468–475.

Gorbachev, P.N., Bezmen, N.I., 2012. Sulfur solubility in fluid-bearing basic silicate melts in dependence on redox conditions. Dokl. Earth Sci. 443, 517–520.

Goto, A., Taniguchi, H., Kitakaze, A., 2005. Viscosity measurements of hydrous rhyolitic melts using the fiber elongation method. Bull. Volcanol. 67, 590–596.

Guillot, B., Sator, N., 2011. Carbon dioxide in silicate melts: a molecular dynamics simulation study. Geochim. Cosmochim. Acta 75, 1829–1857.

Habasaki, J., Okada, I., Hiwatari, Y., 1995. MD study of the mixed alkali effects in lithium-potassium metasilicate glass. J. Non-Cryst. Solids 183, 12–21.

Hack, A.C., Thompson, A.B., 2011. Density and viscosity of hydrous magmas and related fluids and their role in subduction zone processes. J. Petrol. 52, 1333–1362.

Hess, K.-U., Dingwell, D.B., 1996. Viscosities of hydrous leucogranitic melts: a non-Arrhenian model. Am. Mineral. 81, 1297–1300.

Hess, P.C., Wood, M.I., 1982. Aluminum coordination in meta aluminous and peralkaline silicate melts. Contrib. Mineral. Petrol. 81, 103–112.

Holtz, F., Behrens, H., Dingwell, D.B., Johannes, W., 1995. H_2O solubility in haplogranitic melts: composition, pressure, and temperature dependence. Am. Mineral. 80, 94–108.

Hui, H.J., Zhang, Y.X., 2007. Toward a general viscosity equation for natural anhydrous and hydrous silicate melts. Geochim. Cosmochim. Acta 71, 403–416.

Hui, H.J., Zhang, X., Xu, Z., Del Gaudio, P., Behrens, H., 2009. Pressure dependence of the viscosity of rhyolitic melts. Geochim. Cosmochim. Acta 73, 3680–3693.

Iacovino, K., Moore, G., Roggensack, K., Oppenheimer, C., Kyle, P., 2013. H_2O-CO_2 solubility in mafic alkaline magma: applications to volatile sources and degassing behavior at Erebus volcano, Antarctica. Contrib. Mineral. Petrol. 166, 845–860.

Irving, A.J., Frey, F.A., 1978. Distribution of trace elements between garnet megacrysts and host volcanic liquids of kimberlitic to rhyolitic composition. Geochim. Cosmochim. Acta 42, 771–787.

Ispas, S., Benoit, M., Jund, P., Jullien, R., 2002. Structural properties of glassy and liquid sodium tetrasilicate: comparison between ab initio and classical molecular dynamics simulations. J. Non-Cryst. Solids 307, 946–955.

Jaeger, W.L., Drake, M.J., 2000. Metal-silicate partitioning of Co, Ga, and W; dependence on silicate melt composition. Geochim. Cosmochim. Acta 64, 3887–3895.

Jana, D., Walker, D., 1997. The influence of sulfur on the partitioning of siderophile elements. Geochim. Cosmochim. Acta 61, 5255–5277.

Jayasuriya, K., O'Neill, H.S.C., Berry, A.J., Campbell, S.J., 2004. A Mossbauer study of the oxidation state of Fe in silicate melts. Am. Mineral. 89, 1597–1609.

Jendrzejewski, N., Trull, T.W., Pineau, F., Javoy, M., 1997. Carbon solubility in Mid-Ocean Ridge basaltic melt at low pressures (250-1950 bar). Chem. Geol. 138, 81–92.

Johannes, W., Bell, P.M., Mao, H.K., Boettcher, A.L., Chipman, D.W., Hays, J.F., Newton, R.C., Seifert, F.A., 1971. An interlaboratory comparison of piston-cylinder pressure calibration using the albite breakdown reactions. Contrib. Mineral. Petrol. 32, 24–38.

Jugo, P.J., Luth, R.W., Richards, J.P., 2005. An experimental study of the sulfur content in basaltic melts saturated with immiscible sulfide or sulfate liquids at 1300 degrees C and 1.0 GPa. J. Petrol. 46, 783–798.

Jurewicz, A.J.G., Watson, E.B., 1988. Cations in olivine. Part I: calcium partitioning and calcium-magnesium distribution between olivines and coexisting melts, with petrological applications. Contrib. Mineral. Petrol. 99, 176–185.

Kadik, A.A., Pineau, F., Litvin, Y., Jendrzejewski, N., Martinez, I., Javoy, M., 2004. Formation of carbon and hydrogen species in magmas at low oxygen fugacity. J. Petrol. 45, 1297–1310.

Kadik, A.A., Litvin, Y.A., Koltashev, V.V., Kryukova, E.B., Plotnichenko, V.G., 2006. Solubility of hydrogen and carbon in reduced magmas of the early Earth's mantle. Geochem. Int. 44, 33–47.

Katsura, T., Nagashima, S., 1974. Solubility of sulfur in some magmas at 1 atmosphere. Geochim. Cosmochim. Acta 38, 517–531.

Kennedy, G.C., 1948. Equilibrium between volatiles and iron oxides in rocks. Am. J. Sci. 246, 529–549.

Kessel, R., Ulmer, P., Pettke, T., Schmidt, M.W., Thompson, A.B., 2005. The water-basalt system at 4 to 6 GPa: Phase relations and second critical endpoint in a K-free eclogite at 700 to 1400 degrees C. Earth Planet. Sci. Lett. 237, 873–892.

Kilinc, A., Carmichael, I.S.E., Rivers, M.L., Sack, R.O., 1983. The ferric-ferrous ratio of natural silicate liquids equilibrated in air. Contrib. Mineral. Petrol. 83, 136–141.

Knoche, R., Dingwell, D.B., Webb, S.L., 1995. Melt densities for leucogranites and granitic pegmatites: partial molar volumes for SiO_2, $A1_2O_3$, Na_2O, K_2O, Li_2O, Rb_2O, Cs_2O, MgO, CaO, SrO, BaO, B_2O_3, P_2O_5, $F_2O_{\_1}$, TiO_2, Nb_2O_5, Ta_2O_5, and WO_3. Geochim. Cosmochim. Acta 59, 4645–4652.

Kress, V.C., Carmichael, I.S.E., 1988. Stoichiometry of the iron oxidation reaction in silicate melts. Am. Mineral. 73, 1267–1274.

Kress, V.C., Carmichael, I.S.E., 1991. The compressibility of silicate liquids containing Fe_2O_3 and the effect of composition, temperature, oxygen fugacity and pressure on their redox states. Contrib. Mineral. Petrol. 108, 82–92.

Kushiro, I., Mysen, B.O., 2002. A possible effect of melt structure on the Mg-Fe^{2+} partitioning between olivine and melt. Geochim. Cosmochim. Acta 66, 2267–2273.

Kushiro, I., Walter, M., 1998. Mg-Fe partitioning between olivine and mafic-ultramafic melts. Geophys. Res. Lett. 25, 2337–2340.

Lambert, I.B., Wyllie, P.J., 1972. Melting of gabbro (quartz eclogite) with excess water to 35 kilobars, with geological applications. J. Geol. 80, 695–708.

Lange, R.A., Carmichael, I.S.E., 1987. Densities of Na_2O-K_2O-CaO-MgO-Fe_2O_3-Al_2O_3-TiO_2-SiO_2 liquids: new measurements and derived partial molar properties. Geochim. Cosmochim. Acta 51, 2931–2946.

Lauer, H.V., 1977. Effect of glass composition on major element redox equilibria: Fe^{2+}- Fe^{3+}. Phys. Chem. Glasses 18, 49–52.

Lauer, H.V., Morris, R.V., 1977. Redox equilibria of multivalent ions in silicate glasses. J. Am. Ceram. Soc. 60, 443–451.

Le Losq, C., Cody, C.D., Mysen, B.O., 2015. Alkali influence on the water speciation and the environment of protons in silicate glasses revealed by ^{1}H MAS NMR spectroscopy. Am. Mineral. 100, 466–482.

Lee, S.K., Stebbins, J.F., 2000. The structure of aluminosilicate glasses: high-resolution ^{17}O and ^{27}Al MAS and 3Q MAS NMR study. J. Phys. Chem. B 104, 40091–44100.

Lee, S.K., Stebbins, J.F., 2003. Nature of cation mixing and ordering in Na-Ca silicate glasses and melts. J. Phys. Chem. B 107, 3141–3148.

Lesne, P., Scaillet, B., Pichavant, M., Iacono-Marziano, G., Beny, J.-M., 2011. The H_2O solubility of alkali basaltic melts: an experimental study. Contrib. Mineral. Petrol. 162, 133–151.

Libourel, G., 1999. Systematics of calcium partitioning between olivine and silicate melt: implications for melt structure and calcium content of magmatic olivines. Contrib. Mineral. Petrol. 136, 63–80.

Liebske, C., Behrens, H., Holtz, F., Lange, R.A., 2003. The influence of pressure and composition on the viscosity of andesitic melts. Geochim. Cosmochim. Acta 67, 473–485.

Liu, Y., Zhang, Y.X., Behrens, H., 2005. Solubility of H_2O in rhyolitic melts at low pressures and a new empirical model for mixed H_2O-CO_2 solubility in rhyolitic melts. J. Volcanol. Geotherm. Res. 143, 219–235.

Liu, Y., Samaha, N.-T., Baker, D.R., 2007. Sulfur concentration at sulfide saturation (SCSS) in magmatic silicate melts. Geochim. Cosmochim. Acta 71, 1783–1799.

Maia, L., Rüssel, C., 2006. The effect of fluoride on the Fe^{2+}/Fe^{3+} redox equilibrium in glass melts in the system Na_2O/NaF/CaO/Al_2O_3/SiO_2. J. Non-Cryst. Solids 352, 4082–4087.

Mandeville, C.W., Webster, J.D., Rutherford, M.J., Taylor, B.E., Timbal, A., Faure, K., 2002. Determination of molar absorptivities for infrared absorption bands of H_2O in andesitic glasses. Am. Mineral. 87, 813–821.

Mavrogenes, J.A., O'Neill, H.S.C., 1999. The relative effects of pressure, temperature, and oxygen fugacity on the solubility of sulfide in mafic magma. Geochim. Cosmochim. Acta 63, 1173–1180.

Merzbacher, C.I., Sherriff, B.L., Hartman, J.S., White, W.B., 1990. A high-resolution ^{29}Si and ^{27}Al NMR study of alkaline earth aluminosilicate glasses. J. Non-Cryst. Solids 124, 194–206.

Metrich, N., Mandeville, C.W., 2010. Sulfur in magmas. Elements 6, 81–86.

Metrich, N., Susini, J., Foy, F., Farges, F., Massare, D., Sylla, L., Lequin, S., Bonnin-Mosbah, M., 2006. Redox state of iron in peralkaline rhyolitic glass/melt: X-ray absorption micro-spectroscopy experiments at high temperature. Chem. Geol. 231, 350–363.

Mills, K.C., 2018. Metallurgical slags. In: Richet, P. (Ed.), Encyclopedia of Glass Science, Technology, History and Culture. J. Wiley & Sons, Hoboken, NJ.

Moore, G., Righter, K., Carmichael, I.S.E., 1995. The effect of dissolved water on the oxidation state of iron in natural silicate liquids. Contrib. Mineral. Petrol. 120, 170–179.

Moore, G., Vennemann, T., Carmichael, I.S.E., 1998. An empirical model for the solubility of H_2O in magmas to 3 kilobars. Am. Mineral. 83, 36–42.

Moretti, E., Belloni, E., Agosti, F., 2016. Innovative mineral fiber insulation panels for buildings: thermal and acoustic characterization. Appl. Energy 169, 421–432.

Moune, S., Holtz, F., Botcharnikov, R.E., 2009. Sulphur solubility in andesitic to basaltic melts: Implications for Hekla volcano. Contrib. Mineral. Petrol. 157, 691–707.

Mysen, B.O., 1987. Magmatic silicate melts: relations between bulk composition, structure and properties. In: Magmatic Processes: Physiochemical Principles. The Geochemical Society, University Park, PA, pp. 375–399. (special publication).

Mysen, B.O., 1995. Experimental, in-situ, high-temperature studies of of properties and structure of silicate melts relevant to magmatic temperatures. Eur. J. Mineral. 7, 745–766.

Mysen, B.O., 1999. Structure and properties of magmatic liquids: from haplobasalt to haploandesite. Geochim. Cosmochim. Acta 63, 95–112.

Mysen, B., 2002. Water in peralkaline aluminosilicate melts to 2 GPa and 1400 degrees C. Geochim. Cosmochim. Acta 66, 2915–2928.

Mysen, B.O., 2007a. Partitioning of calcium, magnesium, and transition metals between olivine and melt governed by the structure of the silicate melt at ambient pressure. Am. Mineral. 92, 844–862.

Mysen, B.O., 2007b. Olivine/melt transition metal partitioning, melt composition, and melt structure – influence of Si^{4+}, Al^{3+} substitution in the tetrahedral network. Geochim. Cosmochim. Acta 71, 5500–5513.

Mysen, B.O., 2008. Olivine/melt transition metal partitioning, melt composition, and melt structure – melt polymerization and Q^n-speciation in alkaline earth silicate systems. Geochim. Cosmochim. Acta 72, 4796–4813.

Mysen, B.O., 2012. High-pressure/-temperature titanium solution mechanisms in silicate-saturated aqueous fluids and hydrous silicate melts. Am. Mineral. 97, 1241–1251.

Mysen, B.O., 2014. Water-melt interaction in hydrous magmatic systems at high temperature and pressure. Prog. Earth Planet. Sci. 1, 4. https://dx.doi.org/10.1186/2197-4284-1-4.

Mysen, B.O., 2015. An in-situ experimental study of Zr^{4+} transport capacity of water-rich fluids in the temperature and pressure range of the deep crust and upper mantle. Prog. Earth Planet. Sci. 2, 22. https://dx.doi.org/10.1186/s40645-015-0052-7.

Mysen, B.O., Acton, M., 1999. Water in H_2O-saturated magma-fluid systems: solubility behavior in K_2O-Al_2O_3-SiO_2-H_2O to 2.0 GPa and 1300 degrees C. Geochim. Cosmochim. Acta 63, 3799–3815.

Mysen, B.O., Shang, J., 2005. Evidence from olivine/melt element partitioning that nonbridging oxygen in silicate melts are not equivalent. Geochem. Cosmochim. Acta 69, 2861–2876.

Mysen, B.O., Virgo, D., 1980. Trace element partitioning and melt structure: an experimental study at 1 atm pressure. Geochim. Cosmochim. Acta 44, 1917–1930.

Mysen, B.O., Virgo, D., Kushiro, I., 1981. The structural role of aluminum in silicate melts; a Raman spectroscopic study at 1 atmosphere. Am. Mineral. 66, 678–701.

Mysen, B.O., Lucier, A., Cody, G.D., 2003. The structural behavior of Al^{3+} in peralkaline melts and glasses in the system Na_2O-Al_2O_3-SiO_2. Am. Mineral. 88, 1668–1678.

Mysen, B.O., Kumamoto, K., Cody, G.D., Fogel, M.L., 2011. Solubility and solution mechanisms of C-O-H volatiles in silicate melt with variable redox conditions and melt composition at upper mantle temperatures and pressures. Geochim. Cosmochim. Acta 75, 6183–6199.

Navrotsky, A., Geisinger, K.L., McMillan, P., Gibbs, G.V., 1985. The tetrahedral framework in glasses and melts—influences from molecular orbital calculations and implications for structure, thermodynamics, and physical properties. Phys. Chem. Miner. 11, 284–298.

Neuville, D.R., Cormier, L., Massiot, D., 2004. Al environment in tectosilicate and peraluminous glasses: an Al-27 MQ-MAS NMR, Raman, and XANES investigation. Geochim. Cosmochim. Acta 68, 5071–5079.

Neuville, D.R., Cormier, L., Montouillout, V., Florian, P., Millot, F., Rifflet, J.C., Massiot, D., 2008. Structure of Mg- and Mg/Ca aluminosilicate glasses: Al-27 NMR and Raman spectroscopy investigations. Am. Mineral. 93, 1721–1731.

Ni, H., Keppler, H., Behrens, H., 2011. Electrical conductivity of hydrous basaltic melts: implications for partial melting in the upper mantle. Contrib. Mineral. Petrol. 162, 637–650.

Nikolaev, G.S., Borisov, A.A., Ariskin, A.A., 1996. Calculation of the ferric-ferrous ratio in magmatic melts: testing and additional calibration of empirical equations for various magmatic series. Geochem. Int. 34, 641–649.

Nowak, M., Behrens, H., 1995. The speciation of water in haplogranitic glasses and melts determined by in-situ near-infrared spectroscopy. Geochim. Cosmochim. Acta 59, 3445–3450.

Nowak, M., Behrens, H., 2001. Water in rhyolitic magmas: getting a grip on a slippery problem. Earth Planet. Sci. Lett. 184, 515–522.

Nowak, M., Porbatzki, D., Spickenbom, K., Diecrich, O., 2003. Carbon dioxide speciation in silicate melts: a restart. Earth Planet. Sci. Lett. 207, 131–139.

Ochs, F.A., Lange, R.A., 1997. The partial molar volume, thermal expansivity, and compressibility of H_2O in $NaAlSi_3O_8$ liquid: new measurements and an internally consistent model. Contrib. Mineral. Petrol. 129, 155–165.

Ochs, F.A., Lange, R.A., 1999. The density of hydrous magmatic liquids. Science 283, 1314–1317.

Ohlhorst, S., Behrens, H., Holtz, F., 2001. Compositional dependence of molar absorptivities of near-infrared OH- and H_2O bands in rhyolitic to basaltic glasses. Chem. Geol. 174, 5–20.

Olsen, E., Bunch, T.E., 1970. Empirical derivation of activity coefficients for the magnesium-rich portion of the olivine solid solution. Am. Mineral. 55, 1829–1842.

Osborn, E.F., Muan, A., 1960. Plate 2. The System CaO-MgO-SiO_2: Phase Equilibrium Diagrams of Oxide Systems. Amer. Ceram. Soc., Columbus, OH

Ottonello, G., Richet, P., Vetuschi Zuccholini, M., 2015. The wet solidus of silica: predictions from the Scaled Particle Theory and Polarized Continuum Model. J. Chem. Phys. 142, 054503. https://dx.doi.org/10.1063/1.4906745.

Ottonello, G., Richet, P., Papale, P., 2018. Bulk solubility and speciation of H_2O in silicate melts. Chem. Geol. 479 (2018), 176–187.

Paillat, O., Elphick, E.C., Brown, W.L., 1992. The solubility behavior of H_2O in $NaAlSi_3O_8$ melts: a re-examination of Ab-H_2O phase relationships and critical behavior at high pressure. Contrib. Mineral. Petrol. 112, 490–500.

Palencia, P., Bordonaba, J.G., Martinez, F., Terry, L.A., 2016. Investigating the effect of different soilless substrates on strawberry productivity and fruit composition. Sci. Hortic. 203, 12–19.

Pan, V., Holloway, J.R., Hervig, R.L., 1991. Pressure and temperature dependence of carbon dioxide solubility in tholeiitic melts. Geochim. Cosmochim. Acta 55, 1587–1595.

Papadopoulos, K., 1973. The solubility of SO_3 in soda-lime silica melts. Phys. Chem. Glasses 14, 60–65.

Park, B., Cormack, A.N., 1999. Molecular dynamics simulations of structural changes in mixed alkali (Li-K) silicate glasses. J. Non-Cryst. Solids 255, 112–121.

Partzsch, G.M., Lattard, D., McCammon, C., 2004. Mössbauer spectroscopic determination of Fe^{3+}/Fe^{2+} in synthetic basaltic glass: a test of empirical f_{O2} equations under superliquidus and subliquidus conditions. Contrib. Mineral. Petrol. 147, 565–580.

Pearce, M.L., 1964. Solubility of carbon dioxide and variation of oxygen ion activity in soda-silicate melts. J. Am. Ceram. Soc. 47, 342–347.

Persikov, E.E., Bukhtiyarov, P.G., Sokol, A.G., 2015. Change in the viscosity of kimberlite and basaltic magmas during their origin and evolution (prediction). Russ. Geol. Geophys. 56, 885–892.

Piwinskii, A.J., 1973. Experimental studies of igneous rock series, central sierra Nevada batholith, California: Part II. N. Jb. Mineral. Mh. 5, 193–215.

Piwinskii, A.J., Wyllie, P.J., 1970. Experimental studies of igneous rock series: felsic body suite from the Needle Point Pluton, Wallowa Batholith, Oregon. J. Geol. 78, 52–77.

Richet, P., 1984. Viscosity and configurational entropy of silicate melts. Geochim. Cosmochim. Acta 48, 471–483.

Richet, P., Polian, A., 1998. Water as a dense icelike component in silicate glasses. Science 281, 396–398.

Richet, P., Whittington, A., Holtz, F., Behrens, H., Ohlhorst, S., Wilke, M., 2000. Water and the density of silicate glasses. Contrib. Mineral. Petrol. 138, 337–347.

Riebling, E.F., 1964. Structure of magnesium aluminosilicate liquids at 1700°C. Can. J. Chem. 42, 2811–2821.

Riebling, E.F., 1966. Structure of sodium aluminosilicate melts containing at least 50 mole % SiO_2 at 1500°C. J. Chem. Phys. 44, 2857–2865.

Sack, R.O., Carmichael, I.S.E., Rivers, M., Ghiorso, M.S., 1980. Ferric-ferrous equilibria in natural silicate liquids at 1 bar. Contrib. Mineral. Petrol. 75, 369–377.

Sanloup, C., Drewitt, J.W.E., Konopkova, Z., Dallady-Simpson, P., Morton, D.M., Rai, N., van Westrenen, W., Morgenroth, W., 2013. Structural change in molten basalt at deep mantle conditions. Nature 503, 104–107.

Scarfe, C.M., Mysen, B.O., Virgo, D., 1987. Pressure dependence of the viscosity of silicate melts. In: Mysen, B.O. (Ed.), Magmatic Processes: Physicochemical Principles. Geochemical Society, University Park, pp. 59–68.

Schmidt, B.C., Behrens, H., 2008. Water solubility in phonolite melts: influence of melt composition and temperature. Chem. Geol. 256, 259–268.

Schuessler, J.A., Botcharnikov, R.E., Behrens, H., Misiti, V., Freda, C., 2008. Oxidation state of iron in hydrous phonotephritic melts. Am. Mineral. 93, 1493–1504.

Shen, A., Keppler, H., 1995. Temperature-dependence of water speciation in silicate melts: in-situ FTIR spectroscopy to 10 kbars and 1000°C. Eos 76, 647.

Shishkina, T.A., Botcharnikov, R.E., Holtz, F., Almeev, R.R., Portnyagin, M.V., 2010. Solubility of H_2O- and CO_2-bearing fluids in tholeiitic basalts at pressures up to 500 MPa. Chem. Geol. 277, 115–125.

Shishkina, T.A., Botcharnikov, R.E., Holtz, F., Almeev, R.R., Jazwa, A.M., Jakubiak, A.A., 2014. Compositional and pressure effects on the solubility of H_2O and CO_2 in mafic melts. Chem. Geol. 388, 112–129.

Siligardi, S., Miselli, P., Francia, E., Gualtieri, M.L., 2017. Temperature-induced microstructural changes of fiber-reinforced silica aerogel (FRAB) and rock wool thermal insulation materials: a comparative study. Energy Build. 138, 80–87.

Silver, L., Stolper, E., 1985. A thermodynamic model for hydrous silicate melts. J. Geol. 93, 161–178.

Silver, L., Stolper, E., 1989. Water in albitic glasses. J. Petrol. 30, 667–710.

Silver, L., Ihinger, P.D., Stolper, E., 1990. The influence of bulk composition on the speciation of water in silicate glasses. Contrib. Mineral. Petrol. 104, 142–162.

Sowerby, J.R., Keppler, H., 1999. Water speciation in rhyolitic melt determined by in-situ infrared spectroscopy. Am. Mineral. 84, 1843–1849.

Spera, F.J., 1974. A thermodynamic basis for predicting water solubilties in silicate melts and implications for the low velocity zone. Contrib. Mineral. Petrol. 45, 175–186.

Stanley, B.D., Hirschmann, M.M., Withers, A.C., 2014. Solubility of C-O-H volatiles in graphite-saturated Martian basalts. Geochim. Cosmochim. Acta 129, 54–76.

Tamic, N., Behrens, H., Holtz, F., 2001. The solubility of H_2O and CO_2 in rhyolitic melts in equilibrium with a mixed CO_2-H_2O fluid phase. Chem. Geol. 174, 333–347.

Thibault, Y., Walter, M.J., 1995. The influence of pressure and temperature on the metal-silicate partition coefficients of nickel and cobalt in a model C1 chondrite and implications for metal segregation in a deep magma ocean. Geochim. Cosmochim. Acta 59, 991–1002.

Thompson, R.N., 1972. Melting behavior of Snake River lavas at pressures up to 35 kb. In: Carnegie Instn. Washington, Year Book.vol. 71. pp. 406–411.

Toplis, M.J., 1998. Energy barriers associated with viscous flow and the prediction of glass transition temperatures of molten silicates. Am. Mineral. 83, 480–490.

Toplis, M.J., 2004. The thermodynamics of iron and magnesium partitioning between olivine and liquid: criteria for assessing and predicting equilibrium in natural and experimental systems. Contrib. Mineral. Petrol. 149, 22–39.

Toplis, M.J., Corgne, A., 2002. An experimental study of element partitioning between magnetite, clinopyroxene and iron-bearing silicate liquids with particular emphasis on vanadium. Contrib. Mineral. Petrol. 144, 22–37.

Toplis, N.J., Libourel, G., Carroll, M.R., 1994. The role of phosphorus in crystallization processes of basalt: an experimental study. Geochim. Cosmochim. Acta 58, 797–810.

Toplis, M.J., Dingwell, D.B., Hess, K.U., Lenci, T., 1997. Viscosity, fragility, and configurational entropy of melts along the join SiO_2-$NaAlSiO_4$. Am. Mineral. 82, 979–990.

Virgo, D., Mysen, B.O., Seifert, F.A., 1981. Relationship between the oxidation state of iron and structure of silicate melts. In: Carnegie Instn. Washington, Year Book.vol. 80. pp. 308–311.

Wallace, P., Carmichael, I.S.E., 1992. Sulfur in basaltic magma. Geochim. Cosmochim. Acta 56, 1863–1874.

Wallace, P.J., Carmichael, I.S.E., 1994. Speciation in submarine basaltic glasses as determined by measurement of SKa x-ray wavelength shifts. Am. Mineral. 79, 161–167.

Walter, M.J., 2001. Core formation in a reduced magma ocean: New constraints from W, P, Ni, and Co. In: Walter, M.J. (Ed.), Transport of Materials in the Dynamic Earth. Okayama University, Misasa, pp. 152–153.

Wang, Y., Shen, G., 2014. High-pressure experimental studies on geo-liquids using synchrotron radiation at the advanced photon source. J. Earth Sci. 25, 939–958.

Watson, E.B., 1977. Partitioning of manganese between forsterite and silicate liquid. Geochim. Cosmochim. Acta 41, 1363–1374.

Watson, E.B., Harrison, T.M., 1983. Zircon saturation revisited; temperature and composition effects in a variety of crustal magma types. Earth Planet. Sci. Lett. 64, 295–304.

Webb, S.L., Banaszak, M., Kohler, U., Rausch, S., Raschke, G., 2007. The viscosity of Na_2O-CaO-Al_2O_3-SiO_2 melts. Eur. J. Mineral. 19, 681–692.

Wilke, M., 2005. Fe in magma - an overview. Ann. Geophys. 48, 609–617.

Wilke, M., Partzsch, G.M., Bernhardt, R., Lattard, D., 2005. Determination of the iron oxidation state in basaltic glasses using XANES at the K-edge. Chem. Geol. 220, 143–161.

Wilke, M., Klimm, K., Kohn, S.C., 2011. Spectroscopic studies on sulfur speciation in synthetic and natural glasses. Rev. Mineral. Geochem. 73, 41–78.

Xue, X.Y., Kanzaki, M., 2004. Dissolution mechanisms of water in depolymerized silicate melts: constraints from H-1 and Si-29 NMR spectroscopy and ab initio calculations. Geochim. Cosmochim. Acta 68, 5027–5057.

Xue, X.Y., Kanzaki, M., 2008. Structure of hydrous aluminosilicate glasses along the diopside-anorthite join: a comprehensive one- and two-dimensional H-1 and Al-27 NMR study. Geochim. Cosmochim. Acta 72, 2331–2348.

Xue, X.Y., Stebbins, J.F., 1993. Na-23 chemical shifts and local Na coordination environments in silicate crystals, melts, and glasses. Phys. Chem. Miner. 20, 297–307.

Yang, X.-M., 2012. Sulphur solubility in felsic magmas: implications for genesis of intrusion-related gold mineralization. Geosci. Can. 39, 17–32.

Yap, A.T.-W., Elliott, S.R., 1995. A study of mixed alkali effect in disilicate glasses using ^{7}Li nuclear magnetic resonance. J. Non-Cryst. Solids 192&193, 207–211.

Yoder Jr., H.S., Tilley, C.E., 1962. Origin of basalt magmas; an experimental study of natural and synthetic rock systems. J. Petrol. 3, 342–532.

Yue, Y., Solvang, M., 2018. Stone and glass wool. In: Richet, P. (Ed.), Encyclopedia of Glass Science, Technology, History and Culture. J. Wiley & Sons, Hoboken, NJ.

Zhang, Y.X., 1999. H_2O in rhyolitic glasses and melts: measurements, speciation, solubility, and diffusion. Rev. Geophys. 37, 493–516.

Zhang, H.L., Solheid, P.A., Lange, R.A., von der Handt, A., Hirschmann, M.M., 2015. Accurate determination of $Fe^{3+}/\Sigma Fe$ of andesitic glass by Mossbauer spectroscopy. Am. Mineral. 100, 1967–1977.